10th HEAT POWERED CYCLES 2023
Conference Proceedings

10th Heat-Powered Cycles Conference

3-6 September 2023, Edinburgh, Scotland, UK

The University of Edinburgh, Appleton Tower

These *Conference Proceedings* have been prepared with the final submissions that were accepted by the Organizing Committee of the Tenth Heat Powered Cycles Conference. This material aims to serve as a publication of research papers presented at the conference, assisting future research in new developments.

Art Work and information related to the Conference, Organizing Committee, Executive Committee, and Advisory Board were taken from the conference's website.

Edited by:
Prof. Dr. Roger R. Riehl - GamaTech Thermal Solutions - Brazil

Reviewed by:
Prof. Dr. Giulio Santori, The University of Edinburgh (UK)

Prof. (FH) Dr.-Ing. Markus Preißinger - Energy Research Center, University of Applied Sciences Vorarlberg, Austria

Welcome to the 10th Heat Powered Cycles Conference

This is the 10th Heat Powered Cycles Conference. The first was held at Nottingham in 1997. This time the event is being co-organized by the *University of Edinburgh*, (Edinburgh, Scotland)*, The University of Applied Sciences, Vorarlberg*, (Austria), and *Universidade Paulista - UNIP*, (Brazil). The conference is hosted by the University of Edinburgh by *Prof. Giulio Santori*. In addition to formal presentations of technical papers, including invited Keynote papers, the event includes poster sessions and a Special Session on *Joint Talk on Materials and Processes for Carbon Dioxide and Water*. The *Kenneth Denbigh Medal Lecture* will also be presented during the conference. The conference is concerned with scientific and technological innovations relating to the efficient and economic use of heat, derived from all its sources, for the production of cooling, heating, and mechanical power either independently or co-generatively.

University of Edinburgh

Subject areas of particular interest include; hybrid cycles, ORCs, Stirling cycle machines, thermo-acoustic engines and coolers, sorption cycle refrigerators, heat pumps, jet-pump (ejector) machines, temperature amplifiers (heat transformers), chemical heat pumps, new working fluids, mass and heat transfer phenomena, desalination of brackish water and seawater, compact heat exchanger research (including foams and other micro-channel research), thermo-economics, process optimization, and modeling, process, and cycle thermodynamics.

History

	2022: Bilbao The ninth Heat Powered Cycles conference was hosted by the University of the Basque Country, Bilbao, Spain.
	2018: Bayreuth The eighth Heat Powered Cycles conference was hosted by the Bayreuth University, Germany.
	2016: Nottingham The seventh Heat Powered Cycles conference was co-organised by the Universities of Nottingham and Bristol. The conference was held at the University of Nottingham and was hosted by the HVASCR & Heat Transfer Group.
	2012: Alkmaar The sixth Heat Powered Cycles conference was hosted by Energy research Center of the Netherlands (ECN) in the Golden Tulip Hotel in Alkmaar.
	2009: Berlin The fifth Heat Powered Cycles conference was hosted by the Technical University of Berlin.
	2006: Newcastle The fourth Heat Powered Cycles conference was hosted by University upon Tyne Newcastle.

Two Special Issues after HPC 2023

The Organizing Committee of the Heat Powered Cycles Conference will select some of the presented manuscripts, after the conference is finished, to be invited for publication in a special issue of *Applied Thermal Engineering* (Elsevier), and *Carbon Neutrality* (Springer). The selection of the manuscripts will be based on their quality and presentation. The selected manuscripts will undergo a normal review process for those journals.

Organizing Committee
Local Conference Chair
Prof. Dr. Giulio Santori, The University of Edinburgh (UK)

Local Organising Committee
Daniel Friedrich, The University of Edinburgh (UK)
Enzo Mangano, The University of Edinburgh (UK)
Daniel Orejon, The University of Edinburgh (UK)
Bob Critoph, University of Warwick (UK)
Steven Metcalf, University of Warwick (UK)
Ángeles Rivero Pacho, University of Warwick (UK)
Stan Shire, University of Warwick (UK)
Zacharie Tamainot-Telto, University of Warwick (UK)

Executive Committee
Prof. Dr. Roger R. Riehl, GamaTech Thermal Solutions - Brazil
Prof. (FH) Dr.-Ing. Markus Preißinger, Energy Research Center, University of Applied
Sciences Vorarlberg, Austria
Prof. Dr. Ian W. Eames, University of Nottingham, UK
Prof. Dr. Mike Tierney, University of Bristol, UK

Program and Review Chair
Prof. Dr. Roger R. Riehl
GamaTech Thermal Solutions
Faculty of Thermal/Fluid Sciences - Universidade Paulista - Brazil

Scientific Advisory Panel
Roger Riehl, GamaTech Thermal Solutions (Brazil)
Markus Preißinger, Vorarlberg University of Applied Sciences (Austria)
Tommaso Toppi, Polytechnic of Milan (Italy)
Angelo Freni, CNR - ICCOM (Italy)
Gerrit Fueldner, Fraunhofer ISE (Germany)
Majid Bahrami, Simon Fraser University (Canada)
Kyle Glusenkamp, Oak Ridge National Laboratory (USA)
Mario Motta, Polytechnic of Milan (Italy)
Marco Noro, University of Padova (Italy)
Elizabeth Thiele, TU Berlin (Germany)
Valeria Palomba, CNR - Istituto di Tecnologie Avanzate per l'Energia (Italy)
Annelies Vandersickel, DLR (Germany)
Giorgio Besagni, Polytechnic of Milan (Italy)
Jesús María Blanco Ilzarbe, Universidad del País Vasco (Spain)

Jesús Esarte San Martín, NAITEC (Spain)
Robert Hanlon, MIT (USA)
Rayah Al-Dadah, University of Birmingham (UK)
Zacharie Tamainot-Telto, University of Warwick (UK)
Bob Critoph, University of Warwick (UK)
Giulio Santori, The University of Edinburgh (UK)
David A. Reay, David Reay & Associates (UK)
Larisa Gordeeva, Boreskov Institute of Catalysis (Russia)
Michel van der Pal, ECN (Alkmar, Netherlands)
Yukitaka Kato, Tokyo Institute of Technology (Japan)
Yuri Aristov, Boreskov Institute of Catalysis (Russia)
Florian Heberle, Universität Bayreuth (Germany)

Secretariat
Diane Reid, The University of Edinburgh (UK)
Samantha Bain, The University of Edinburgh (UK)

Operations Team
Isabella Cavalcante Quaranta, The University of Edinburgh (UK)
Eloise Bevan, The University of Edinburgh (UK)
Shihab AL-Hasni, The University of Edinburgh (UK)
Marwan Mohammed, The University of Edinburgh (UK)
Anam Abbas, The University of Edinburgh (UK)
Khaloud Al Balushi, The University of Edinburgh (UK)
Janice To, The University of Edinburgh (UK)

The 10th Heat Powered Cycles (HPC) Conference has been sponsored by the following partners.

Table of Contents

desorption of atmospheric water vapor.
Matteo Calò, Vincenzo Gentile

Heat Powered Cycles Conference 2023
Edinburgh
Heat in the new energy system

Oscillating heat pipe operated with a heterogeneous mixture of water and particles

R. Riehl[1] and M.H. Buschmann[2*]

[1]GamaTech Thermal Solutions Ltda, São José dos Campos, SP Brazil

[2]Institut für Luft- und Kältetechnik gGmbH Dresden, 01309 Dresden, Germany

[*]Corresponding author: Matthias.Buschmann@ilkdresden.de

Abstract

The study presents experimental investigations on a glass oscillating heat pipe. Subsidising the reference fluid deionised water by a mixture of deionised water and particles shows an increase of the thermal performance by about 10 %. However, this effect quickly disappears due to the chemical reactions occurring during operation.

Keywords: oscillating heat pipe, heterogeneous working fluid

Introduction/Background

Heat exchangers and other heat engineering equipment are of outstanding importance for the energy transition. With the currently feared drastic shortage or increase in the price of fossil primary energy sources, there is also a growing need to use previously unavailable reservoirs of regenerative thermal energy. The need of users to have such systems at their disposal or to increase their effectiveness is noticeable in all sectors of the economy. Oscillating heat pipes (OHP) operating at low temperatures could be such a system. To increase the thermal performance of OHP's and to avoid an instantaneous heat flux at the condenser, new working fluids need to be investigated.

Discussion and Results

Figure 1 shows the ILK OHP test rig. The OHP consists of a glass body with four loops ($d_i = 3$ mm). A resistant heater heats the lower part (evaporator) of the glass body. The condenser (upper part of device) is cooled by a water stream (volume flux, $V_e = 6$, 20 & 40 l/h; inlet temperature $t_{ein} = 15$ °C) provided by a thermostat. After evacuation the glass body is filled with 9 ml working fluid ($FR = 66$ %). The employed working fluids are either deionised water (DI water) or a mixture of DI water and galinstan (EGa). Galinstan is the eutectic alloy of gallium, indium and tin (77.2 / 14.4 / 8.4 at. %) [1]. Its appearance is metallic bright and its melting point is at about 10.7°C.

The nominal content of galinstan in the working fluid amounts to 0.5 vol. %. For the working fluid, liquid galinstan is added to DI water and sonicating for 4 hours.

The efficiency – ratio of thermal energy retrieved at condenser to heat input at evaporator – at a condenser volume flux of 6 l/h shows Fig. 2. At day one, the efficiency of the OHP operated with the water/galinstan mixture (left plot, orange symbols) is about 10 % higher than for pure water (Fig. 3, left plot). Repeating the experiment 24 hours later shows the fading of this effect (Fig. 2, right plot).
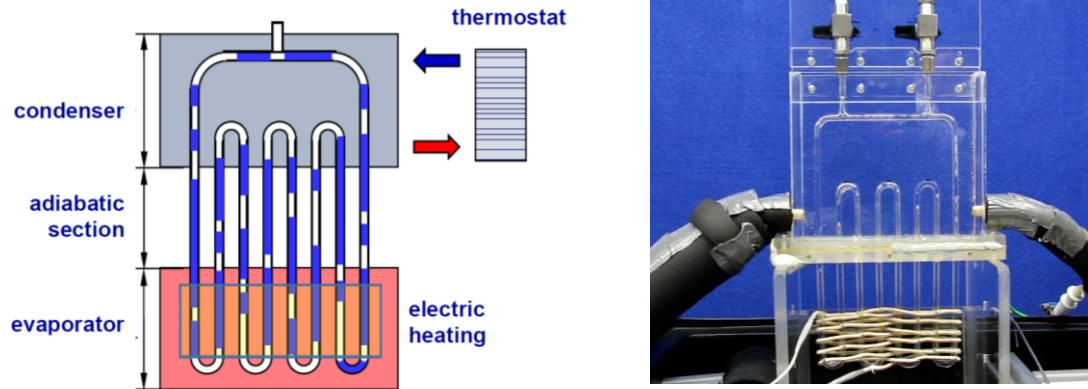
Figure 1. Working principle of OHP (left) and ILK test rig without insulation.
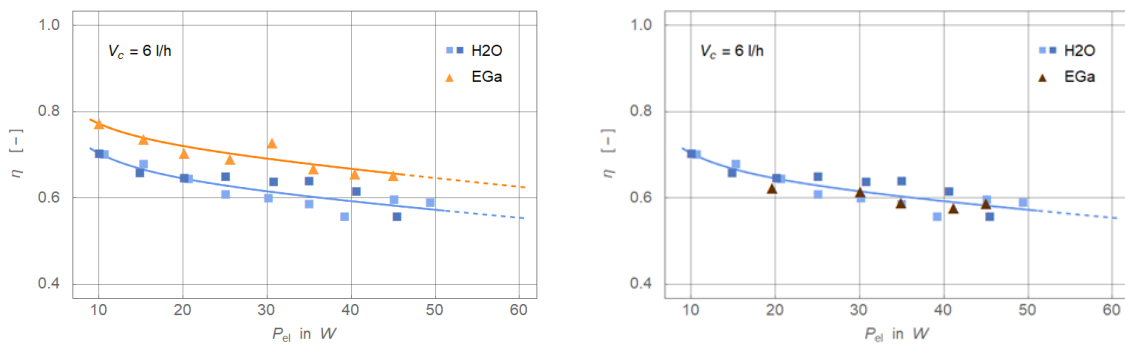
Figure 2. Efficiency of OHP first day (left) and second day. Condenser volume flux 6 l/h.
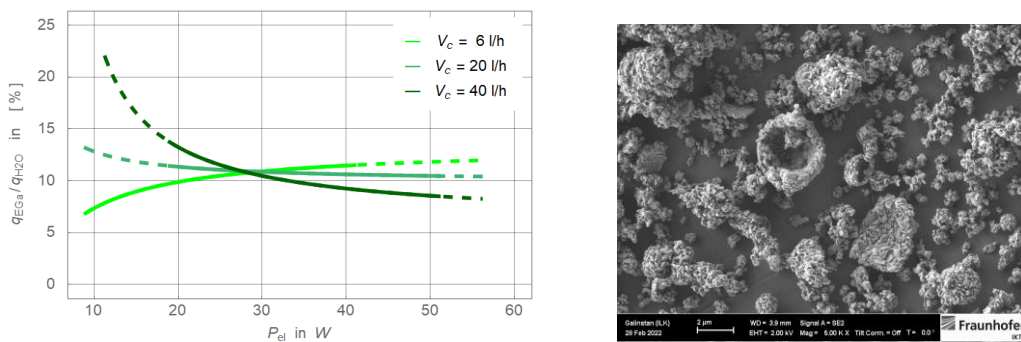
Figure 3. Left plot shows increase of heat received at condenser at day one for three condenser volume fluxes. Right a SEM-image (magnification 5.000) shows the agglomerates formed in the working fluid.

SEM images (Fig. 3, right) reveal the size and structure of the particles formed in the working fluid. The originally liquid alloy has obviously turned into solid agglomerates with sizes up to 2 μm. In some cases, the shape is reminiscent of hollow granules. Based on a quantitative phase analysis, it is determined that the compounds making up these particles are $GaO(OH)$, $In(OH)_3$, $InSn_4$ and pure indium. The summary of these results leads to the conclusion that hydrolysis takes place in the OHP. Larger solid agglomerates and non-condensable gases – probably hydrogen and oxygen – form. While the former may support the OHP's thermal performance, the latter definitively increase its thermal resistance. Figure 4 represents the instantaneous temperature difference at the condenser. Large break down events occur for DI water with low heat input at the evaporator (20 W, Fig. 4, left diagram). Employing the mixture of DI water and particles eliminates these disturbances of the heat flow. At high evaporator heat loads, the heat flux is very similar for both working fluid.

Summary/Conclusions

The conclusion from the experiments is that a heterogeneous mixture of water and any gallium alloy is a complex problem when it comes to working fluids for phase change probes. The reason for this is the extraordinarily high reactivity of gallium towards oxygen. However, the experiments also suggest that the addition of particles (not only nanoparticles) is a way to improve the thermal performance of OHP's significantly.

Probably the best hypothesis to describe the processes taking place inside the OHP is the following.

1. In the first minutes / hours of operation, gallium compounds coat the evaporator surface. This coating make the glass rougher. An open-porous, wick-like surface structure may even form. In both cases, the heat transfer at the evaporator is enhanced either by increasing the number of nucleation sites (roughness) or by wicking. In the latter case, basefluid is transported under the developing bubbles and accelerate their growth.
2. During operation, chemical reactions of the alloying partners (Ga, In & Sn) with the basefluid (water) take place. These reactions are likely to generate hydrogen and oxygen both non-condensable gases (NCG) that accumulate in the condenser. The high operation temperature accelerates this process. That of course increases the thermal resistance of the entire OHP.

In the experiments on the first day, the amount of NCG is small and the coating improves the heat transfer at the evaporator and thus the thermal performance of the OHP. We assume that large particles/agglomerates further improve heat transfer by enhancing capillary instabilities. Furthermore, small particles can influence the thermal performance of the OHP by accumulating at the interface at the liquid/gas phase interface, thus changing the surface tension of the working fluid. In the experiments on the second day, the NCG thwart all these positive effects by impeding the heat transfer at the condenser.

Acknowledgments

References:

[1] Handschuh-Wang, S., Stadler, F. J., Zhou, X., "Critical review on the physical properties of gallium-based liquid metals and selected pathways for their alteration", Journal Physal Chemistry, 2021.

Isochoric Vapour Engine – Introduction, Discussion and Evaluation of a New Approach for Low Grade Waste Heat Recovery

P.Streit[1*], **A. P. Weiß**[1], **D.Stümpfl**[1], **A. Lesser**[2], **F.Stadler**[3]

[1]University of Applied Sciences Amberg-Weiden, Center of Excellence for Cogeneration Technologies, Kaiser-Wilhelm-Ring 23, 92224 Amberg

[2]University of Applied Sciences Regensburg, Turbomachinery Laboratory, Galgenbergstraße 30, 93053 Regensburg

[3]UAS Messtechnik GmbH, Prof.-Hermann-Staudinger-Straße 4, 94234 Viechtach

[*]Corresponding author: ph.streit@oth-aw.de

Abstract

In the light of the energy crisis and the extreme fluctuations of prices for e.g., gas and electricity, domestic microgeneration and low temperature waste heat recovery is more required than ever. For WHR of internal combustion engines, gas turbines and more energy demanding processes like steel, glass and cement industry (>500 kW$_{el}$) an Organic Rankine Cycle is the method of choice and has already established itself over the years. This ORC systems contain a pump, an evaporator, an expander, a recuperator, and a condenser to make ideal use of the low temperature waste heat. For low power WHR (<5 kW$_{el}$) this complexity of the ORC plant aggravates its miniaturization and is only partially suitable. Therefore, the authors aim for a disruptive approach with a so-called isochoric vapour engine (IVE), which has no need for the already named system containments. The IVE performs a complete thermodynamic cycle, is completely self-contained and requires a much smaller assembly space than a comparable ORC system. In the following, the architecture and the thermodynamics of the IVE are introduced, pros and cons are elaborated, first theoretical results are presented and discussed, and next steps are described.

Keywords: Heat-Engine, Isochoric, Vapour, WHR, decentralized

Nomenclature		Subscripts	
h	Specific Enthalpy, (J/kg)	*comp.*	Compression
m	Mass, (kg)	*exp.*	Expansion
p	Pressure, (bar)	*in*	Input
Q	Heat, (J)	*l*	Large
T	Temperature, (°C)	*max*	Maximum
u	Specific Internal Energy, (J/kg)	*min*	Minimum
v	Specific volume (m³/kg)	*out*	Output
W	Work, (J)	*s*	Small
x	Vapour Quality, (-)	*v*	Volume
η	Efficiency, (-)		

Acronyms

EU	European Union
IVE	Isochoric Vapour Engine
ORC	Organic Rankine Cycle
WHR	Waste Heat Recovery
0D	0-Dimensional
1D	1-Dimensional

Introduction

About 800 TWh of waste heat are still discharged by industrial processes into the environment every year in the EU alone [1]. An ORC system would be capable of using this waste heat and convert it partially into electric energy. However, for most of this decentralized waste heat, smaller ORC systems would be needed [2]. The Organic Rankine Cycle is already a mature, economic technology in the power output range of 100 kW_{el} to several MW [1] but not in the region of a few kW. This is, because the downsizing of the technology comes with several challenges, that need to be solved. One of them is the plant specific cost (€/kW), and therefore the return of investment, which is still unattractive for most of the commercial uses. This point is clarified by the ORC market capacity in the power range between 1-100 kW. The capacity of ORC units in this range is only at about 4.95 MW – worldwide [3]. Despite the large potential of the market, an ORC in this power range is uncompetitive due to the high specific costs - even a micro-ORC plant needs a pump, a boiler, an expander and a condenser. Another reason for the low market capacity is, that for these small-scale ORC-Units, a simpler scheme of the plant is preferred due to its usage in civil, industrial, or domestic environment

Despite the facts, that ORC-Units in the power range below 100 kW_{el} are mostly unattractive for commercial use, there are companies, that sell these units in the beforementioned power range, but most of them are still developing prototypes. In the range around 100 kW_{el}, the market analysis shows, that there are some companies available, that sell ORC´s commercially, e.g., Exergy Italy, Rainbow France, GE clean energy USA etc. [4–6]. In the region of a lower power output (<20 kW_{el}) there are only very few companies, that provide ORC plants. ORCAN– Munich provides units from 20 kW_{el} which use a Scroll-Expander. They are able to use waste heat from 80 °C and claim cycle efficiencies of about 5 % [2]. The French Company Enogia sells a ORC unit with a power output down to 10 kW_{el} using a radial turbine coupled with a high speed generator and a total mass of about 450 kg [7]. Below 5 kW_{el}, there is no commercially available unit offered by any company – to the authors knowledge. In research, there are units tested with a power output below 5 kW_{el}, like [8] that investigated a 2,5 kW_{el} ORC for the domestic use with a scale of 0,74 m x 0,74 m x 1,6 m in size without the evaporator. Research is mostly focused on the appropriate choice of the expander unit in the ORC e.g. screw, scroll or reciprocating [9–13].

Another approach could be small Stirling engines, which are an alternative to micro-ORC systems [14] They generally consist of a working cylinder and a displacement cylinder with associated pistons and a crankshaft. Stirling Engines without a crankshaft are the free-piston

versions [15] such as those offered by Viessmann, Vaillant or Senertec with approx. 1 kW$_{el}$ installed in gas boilers for building heating in the 2010s. This is possible due to their compactness and quiet running. In the Stirling hot gas engine, heat is supplied on principle after initial compression of the working gas (some 10s of bars). After that, the expansion of the hot gas takes place under work output. The useful work is only the small difference between the large compression work and the somewhat larger expansion work. To ensure that a usable difference is available as useful work even with friction and heat losses occurring in reality, these small Stirling machines require relatively high upper process temperatures (450 °C-750 °C; [15]) and are thus ruled out for low temperature (waste heat) utilization. To the authors knowledge, only one Stirling engine for low-temperature heat utilization is currently under development at MACH1881 [16]. With all of this information and considerations, the question raises whether there are other, completely detached, disruptive approaches that could take advantage of this unused low-grade waste heat?

This is where the IVE - Isochoric Vapour Engine comes in place. The IVE is the concept (patent pending) of a new type of heat engine with isochoric evaporation and condensation. It does not require a feed pump and recuperates part of the waste heat internally. The compression or pumping work is omitted, and the expansion work is almost fully useful work. This, and the use of low-boiling, organic working fluids, makes heat sources with temperatures below 100 °C exploitable. The IVE concept combines the advantages of the ORC plant in terms of low-temperature application and the simplicity of design of the Stirling engine in terms of its compactness.

IVE Working Principle

First, the new working principle of the IVE is explained in detail to clearly illustrate the differences to other cycles. From this statement, it already becomes clear: The Isochoric Vapour Engine aims to undergo a complete thermodynamic cycle and is not just a newly designed expansion machine. Due to the big differences to other engines, the working principle of the IVE is explained step by step. First its architecture and second, the corresponding thermodynamics. Fluid dynamics will not be addressed, as it would exceed the scope.

Architecture and basic thermodynamics of the new heat engine

To clearly illustrate the mechanical working principle of the IVE, a very simple schematic representation is used below (Fig.1.). In this representation, the process of heating, cooling, and the expansion of the working medium in the cell wheel is described. The description is supplemented by the TS-diagram displayed in Figure 2.

The IVE is based on an outer rotating cell wheel and an inner "expander wheel" - which can be either a turbine (Fig. 1 left) or e.g., a rotary vane expander (Fig. 1 right). The non-rotating housing (grey), which contains the flow channel (red arrows) is mounted around the expander unit. It ensures, that the overflow of the fluid from heated cells B to cooled cells C is only possible at a certain section of the engine. The cell wheel and the inner expander wheel are

coupled and are rotating in the counterclockwise direction as shown by the black arrows. The cell wheel can be either in direct connection with the expander-wheel or via a gear, to implement different rotational speeds of the cell and expander wheel, if reasonable. A shaft is connected to the expander wheel, where excess i.e., net work is extracted.
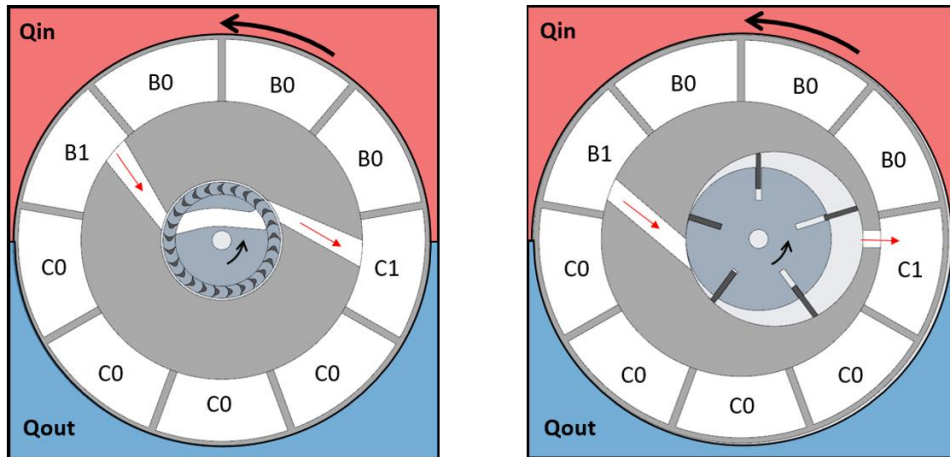
Fig. 1 Schematic mechanical representation of the IVE, left considering a turbine and right volumetric expander
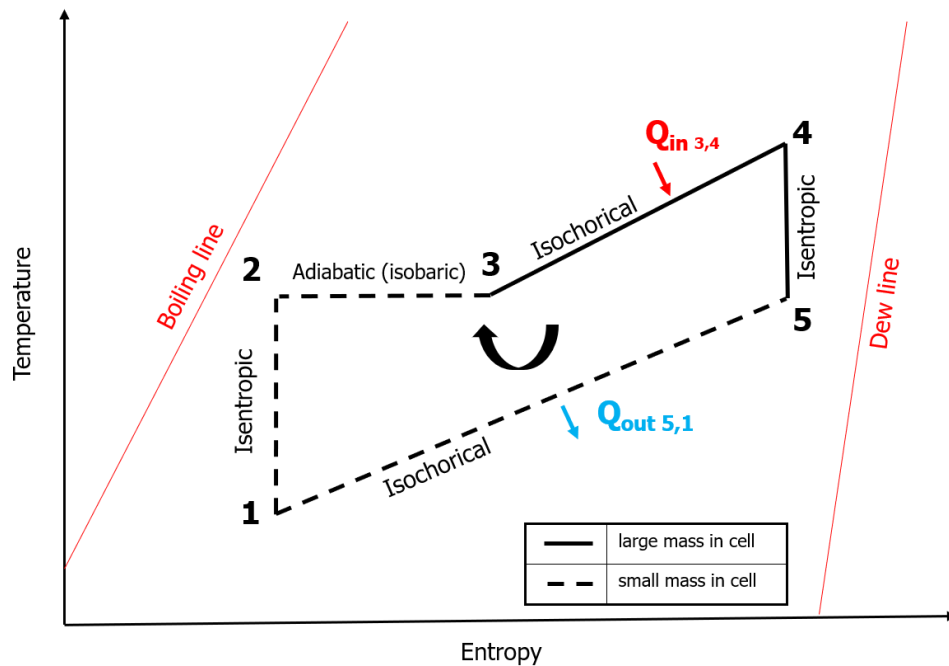
Fig. 2 Schematic Ts-diagram of the IVE cycle in the wet vapour region of an organic working fluid

For about half of the circumference, the cell wheel is in contact with the heat source, e.g., hot water (red area). For the other half to the cooling sink, e.g., cold water (blue area). To be able to clearly define the cells in the next steps, they will be named from now on. Cells that are heated isochorical are now called B0 (Fig. 1), the corresponding change of state 3-4 is shown in Figure 2. Cells that are cooled are called C0 (Fig. 1), the corresponding change of state 5-1 is shown in Figure 2. Isochoric heating and cooling take place because the cell volume and the

cell mass content remain constant while heat addition or rejection. However, while heating, the mass in a cell B0 is larger than while cooling in a cell C0. This fact is indicated by solid and dashed lines in Fig. 2. At the end of the heating or the cooling hemicycle, respectively, cell now named B1 and cell now named C1 are connected via the flow channel. The working fluid expands from the warmer cell B1 with high temperature T_4, high pressure p_4 and high vapour quality X_4, into the cooled down cell C1 and expands thereby to $v_5 = v_1$ at lower temperature T_5 and lower pressure p_5 . As displayed in Fig. 2, the expansion from this certain mass fraction (m_l-m_s) from B1 to C1 is considered as isentropic. Flow work is done which is partly used for turning the cell wheel partly available as net shaft work of the expander. The overflowing of the difference between the large mass in B1 and the small mass in C1 (change of state 1-2-3) is considered in two steps. First, it is assumed that the overflowing hot, high pressure vapour (state 4, Fig. 2) from B1 is compressing isentropically the cold low pressure vapour (state 1) in C1 till pressure equilibrium $p_2 = p_5$ is achieved (1-2, Fig. 2). Because the entire cycle takes place in the wet vapor region of the organic working fluid, pressure equilibrium also means temperature balance. The second step (2-3, Fig. 2) is considered as adiabatic mixing of two vapour fractions with identical pressures, identical temperatures but different vapour qualities. Now the cycle starts again.

It must be pointed out, that in contrast to an Organic Rankine Cycle plant, all IVE components like evaporator and condenser cells, the expander will always work in transient condition, even the IVE works stationary (fixed rotational speed). Furthermore, the IVE cycle could principally also be considered as supercritical cycle, completely working in the superheated (gaseous) region of a working fluid. However, because heat transfer with an evaporating or condensing working fluid is by far stronger than without phase change, the current investigations concentrate on a wet vapour engine.

The simple illustration in Figure 1 shows, that the IVE is made from much fewer components than a comparable ORC plant. There is no need for a feed pump because the heat is added isochoric and therefore, also the pressure increases in the heated cells, while heating. The expander is not a separate unit, it sits directly in the middle of the housing. The cells serve as an evaporator and condenser, depending on which position - either source or sink semicircle – they are. The cells are always in contact with the evaporator- or condenser-side until they are connected with each other via the flow channel. Thus, there is no extra need for an evaporator or condenser unit, pressure and heat losses through piping to and from these units are therefore non-existent. Through the continuous mass exchange between the cells, a storage tank is needles. This mass exchange also serves the advantage, that a portion of the heat is recuperated internally. The residual heat out of cell B1 is automatically transported into cell C1 before C1 gets into B0 and is heated up again.

Thermodynamic-Modeling

Based on these basic considerations, the five changes of state (Fig. 2) of the IVE cycle are expressed in 0D equations. To support the derivation of the governing equations, the cell wheel has been simplified in Figure 3 as neighboring boxes, without expander. The partition between

**Heat Powered Cycles
Conference 2023**
Edinburgh

Heat in the new energy system

*3rd to 6th of September 2023
The University of Edinburgh, Scotland*

the boxes is intended to be movable and acts as a piston. The cells are numbered in the upper right corner, to see in which state they are. Furthermore, the name of the cell is in the upper left corner and the mass distribution, so either the large mass m_l or the small mass m_s are shown in the lower left corner. Also, all the known thermodynamic quantities are presented in the core of the cells. In this box representation, two changes of state are also always represented in parallel since they happen simultaneously.
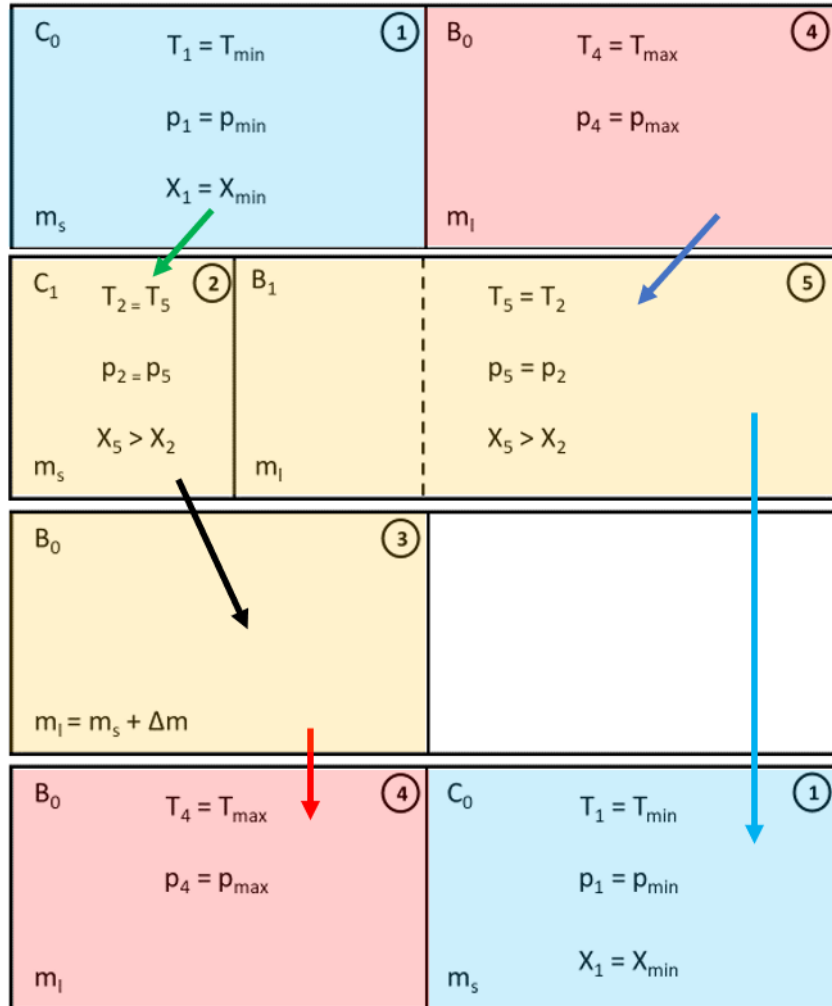
Fig. 3 Schematic changes of state of the IVE, 0D-Model

The change of state from 1 to state 2 is an isentropic compression of the fluid in the small-mass m_s cell C_1, with the lowest temperature and pressure and vapour quality in the cycle, by the overflowing fluid (4-5) from the large-mass cell B1, with the highest fluid temperature, and pressure (green arrow Fig. 3.; closed system). Cold vapour (B1) and overflowing hot vapour (C1) are still separated by the partition.

$$1 \rightarrow 2: \qquad W_{v12} = -\int_1^2 p\,dV = W_{comp.} = m_s * (u_2 - u_1)(> 0) \qquad (1)$$

Simultaneously, from 4 to 5, the hot vapour with the large mass m_l in B1, expands isentropically into cell C1 by pushing the moveable partition. The work output 4-5 serves to a small extent to compress the cold vapour in C1 (1-2), and to a large extent it is useful work (dark blue arrow Fig.3.; closed system):

$$4 \rightarrow 5: \qquad W_{v45} = - \int_4^5 p dV = W_{ex} = m_l * (u_5 - u_4)(< 0) \qquad (2)$$

The small mass m_s is thus compressed just enough, that the pressure of the compressed mass m_s equals the pressure of the expanded mass m_l (p2 = p5). Since the change of state occurs in the wet vapor region, the pressure equalization also means a temperature equalization (T2 = T5). The resulting net work is:

$$W_{Net} = W_{v45} + W_{v12} = W_{ex} + W_{comp.} \qquad (3)$$

From state 2 to 3 (black arrow Fig.3.), the overflown mass from cell B1 with its high vapour content get mixed adiabatically with low quality vapour in cell C1. For this, the partition is now considered to be permeable.

$$2 \rightarrow 3: \qquad m_s * h_2 + \Delta m * h_5 = m_l * h_3 \qquad (4)$$

From state 3 to 4 (red arrow Fig. 3.), the large mass (m$_l$) of working fluid (solid line Fig.2.) in the cells B0 is isochorical heated from the hot water source (Q$_{in3,4}$). Because the heat is supplied isochorical, the temperature, pressure and the vapour content of the fluid increase (closed system):

$$3 \rightarrow 4: \qquad Q_{in3,4} = m_l * (u_4 - u_3) \qquad (5)$$

From state 5 to state 1 (light blue arrow Fig.3.), the remaining low mass fraction m_s in cell C0 is cooled by the cold-water source (Q$_{out5,1}$). The heat is discharged isochorical and therefore, the temperature, pressure and vapour content of the fluid decrease – the cycle gets repeated.

$$5 \rightarrow 1: \qquad Q_{out5,1} = m_s * (u_1 - u_5)(< 0) \qquad (6)$$

It is obvious, that the changes of state from 1 to 2 and 2 to 3 would actually be combined into continuous changes. The lower mass fraction in cell C1 is compressed by the overflowing mass and both mass fractions are simultaneously adiabatically mixed. For first assumptions and 0D calculations of the cycle, the authors used this partitioning for the sake of simplicity.

Heat Powered Cycles
Conference 2023
Edinburgh

Heat in the new energy system

Model Calculations and assumptions

Using the equations above, initial calculations of the IVE can now be performed for specific boundary conditions.
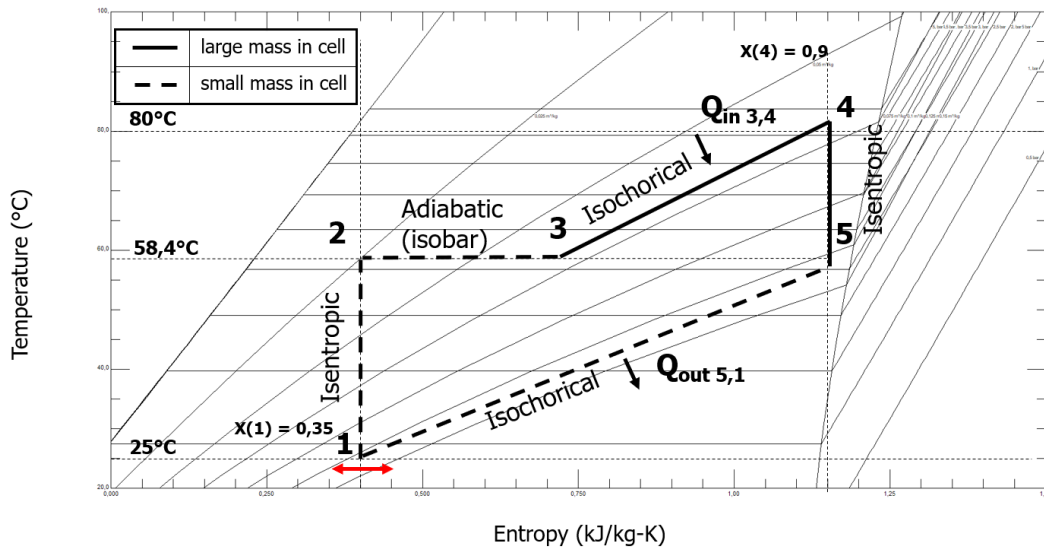
Fig.5 Quantitative Ts-Diagram for Isopentane with first assumptions

Figure 5 shows the quantitative TS-Diagram of the IVE cycle for defined boundary conditions. A constant heat-source temperature of 80 °C $=T_4$ and a constant cold-sink temperature of 25 °C $= T_1$ were selected. This temperature range was chosen because the IVE should be able to cope with domestic temperatures, e.g., hot water from a rooftop solar system or other low temperature heat sources. For a given temperature in the wet Isopentane vapour region, there is a given pressure, as for state 4 it is $p_4 = 4.57$ bar and for state 1 it is $p_1 = 0.92$ bar. As a first step, a fixed point is then defined for state 4, in which the vapour quality must be specified. An x_4 of 0.9 was chosen– which of course will be adjusted empirically after the first measurements have been carried out. Next, a vapour quality needs to be defined for point 1, e.g., $x_1 = 0.35$. By these definitions, points 4 and 1 are now fixed. Since the change of state 5-1 is isochoric, the isentropic expansion is drawn from 4 to 5 to the same specific volume as state 1. As described above, the hot vapour out of B1 will overflow in cell C1 until pressure equilibrium $p_2=p_5$ is achieved. By this determination, point 2 is also determined. Now, state 3 can be calculated via adiabatic mixing of the two mass fractions m_s and m_l. Since $Q_{in3,4}$ and $Q_{out5,1}$ are implemented isochorical, points 3 - 4 and 5 - 1 can now be connected. Due to the two specifications of the vapour qualities and temperatures of points 4 and 1, the 0D system is overdetermined. For this reason, an iteration must now ensure that:

$$Q_{in3,4} + Q_{out5,1} = W_{exp.} + W_{comp.} \quad [kJ] \tag{7}$$

Heat Powered Cycles
Conference 2023
Edinburgh
Heat in the new energy system

3rd to 6th of September 2023
The University of Edinburgh, Scotland

The vapour quality x_1 must now be varied (red arrows Fig.5) until the expression above becomes true and x_1 for state 1 is found.

One can already assume, that for this small temperature range and low upper process temperature, the cycle efficiency and therefore the efficiency of the IVE is not going to be very high. The maximum reachable cycle efficiency or Carnot-efficiency is:

$$\eta_{Carnot} = 1 - \frac{298K}{353K} = \mathbf{15.58}\ \% \tag{8}$$

For the calculation of the cycle efficiency of the IVE, a cell volume must be specified (here, for the sake of simplicity, $V_{cell} = 1dm^3$). With this volume, the thermodynamic quantities obtained by the equations above and the REFPROP Database, the heat input, output and the expansion and compression work can be calculated. The calculation of the cycle efficiency follows as:

$$\eta_{cycle} = \frac{Q_{in3,4} + Q_{out5,1}}{Q_{in3,4}} = \frac{2044J + (-1886J)}{2044J} * 100 = \mathbf{7.73}\ \% \tag{9}$$

and the exergy efficiency:

$$\eta_{exergy} = \frac{\eta_{cycle}}{\eta_{carnot}} = \frac{7.73\%}{15.58\%} = \mathbf{49.61}\ \% \tag{10}$$

These 0D calculations were carried out with many simplifications to be able to assess whether the IVE can deliver useful work in this low temperature range, which can be confirmed herewith. The Carnot efficiency and the actual cycle efficiency make clear that this is not a high-efficient engine. This is due to the fact, that there is now pressure increase before heat addition like in a Rankine cycle. However, it is possible with the IVE to produce useful work even at these small temperature differences.

Discussion and Results

The IVE can be a viable engine to use for small-scale, low temperature waste heat utilization. Of course, as already mentioned and confirmed by the calculations, not too large efficiencies can be achieved due to the lack of pressure i.e., temperature increase before heat supply. Furthermore, because the net work output is the small difference of a large amount of added ($Q_{in3,4}= 2044J$) and rejected heat ($Q_{out5,1}= -1886J$), it can easily become zero, if the cycle is not implemented properly. Nevertheless, the compact, simple design which enables low specific costs (€/kW), could make up for this low energy yield. Of course, some more precise calculations of the IVE must be performed to prove the assumptions. In a proposed follow-up project, a complete IVE prototype and a digital twin (1D-modelled) will be built. The digital twin shall be validated by experimental results of the prototype and the IVE is opposed to become a production-ready product.

Still, there are some questions, that need to be solved in the scope of the planed project:

- What is the most favourable IVE architecture for heat transfer and energy conversion? How should the cells be designed (volume to surface ratio, area, shape) which expander design (turbo or displacement) can be integrated best, with direct or indirect coupling between cell wheel and expander?

- The transient heat transfer between cells and heating/cooling medium (e.g., water) and the organic working fluid in the two-phase region must be physically captured and modelled in the 0D and future 1D design tools.

- Depending on the selected IVE architecture and proportions (cell shape, number of cells, diameter (ratios), volume to area ratio), the question of the most favourable angular velocity of the IVE cell wheel arises to absorb and convert maximum energy per revolution.

- The question of the most favourable expander type, a turbine (radial, axial, impulse, overpressure, etc.) or a volumetric expander (vane, Wankel, scroll, etc.) must be resolved in interaction with the overall architecture.

- To be able to design, compare and evaluate the design variants of the cellular wheel and expander, simple 0D/1D design tools are required and must be created. Despite its structurally simple design, the thermodynamics and fluid mechanics in the IVE concept are too complex, due to the transience and the continuous phase change, for the IVE engine to be designed completely in 3D space using CFD - as is already being done, for example, for the ORC turbines.

- The IVE concept represents a complete, very compact heat engine whose components all operate transiently even in stationary operation. Due to the compact design, all components are also very closely coupled with each other. To analyse and predict the coupled, transient overall behaviour and ultimately optimize the IVE, a digital twin is essential. Thus, in addition to an experimental demonstrator, a one-dimensional transient twin will also be built. In addition to the design and optimization of the IVE, the aim is to improve the scientific analysis of the transient behaviour of such a thermal engine.

Summary/Conclusions

The paper introduced a new, disruptive concept of a so-called isochoric vapour engine – IVE – for low grade waste heat recovery. The engine concept was introduced, and the working principle was presented both mechanically and thermodynamically. First calculations were performed in the 0D as well as in the 1D-Model. The results were compared and deviations from each other were discussed. It turns out, that the IVE could still be successful on the market due to its simple structure and thus potentially low specific costs regardless its efficiency limitations.

Acknowledgments

References

1. *China and Europe's partnership for a more sustainable world*: *Challenges and opportunities;* Spigarelli, F.; Curran, L.; Arteconi, A., Eds.; Emerald: Bingley, England, 2016, ISBN 9781786353313.

2. ORCAN: Orcan Website. Available online: http://www.orcan-energy.com (accessed on 04.10.22).

3. ORC World Map: ORC World Map Website. Available online: http://orc-world-map.org (accessed on 4 October 2022).

4. Exergy: Exergy Website. Available online: http://exergy-orc.com (accessed on 04.10.22).

5. Enertime: Enertime-Rainbow Website. Available online: http://www.enertime.com (accessed on 04.10.22).

6. General Electric: General Electric Website. Available online: https://powergen.gepower.com (accessed on 04.10.22).

7. Enogia: Enogia Website. Available online: http://www.enogia.com (accessed on 04.10.22).

8. Żywica, G.; Kaczmarczyk, T.Z.; Ihnatowicz, E.; Turzyński, T. Experimental investigation of the domestic CHP ORC system in transient operating conditions. *Energy Procedia* **2017**, *129*, 637–643, doi:10.1016/j.egypro.2017.09.123.

9. Weiß, A.P. Volumetric expander versus turbine - which is the better choice for small ORC plants? In *ASME-ORC2015*, Proceedings of the 3rd International Seminar on ORC Power Systems, Brussels, Belgium, 12–14 Oct. 2015; University of Liège and Ghent University, Ed., 2015, ISBN 978-2-9600059-2-9.

10. Qiu, G.; Liu, H.; Riffat, S. Expanders for micro-CHP systems with organic Rankine cycle. *Applied Thermal Engineering* **2011**, *31*, 3301–3307, doi:10.1016/j.applthermaleng.2011.06.008.

11. Saghlatoun, S.; Zhuge, W.; Zhang, Y. Review of Expander Selection for Small-Scale Organic Rankine Cycle. In *Volume 1B, Symposia: Fluid Machinery; Fluid-Structure Interaction and Flow-Induced Noise in Industrial Applications; Flow Applications in Aerospace; Flow Manipulation and Active Control: Theory, Experiments and Implementation; Multiscale Methods for Multiphase Flow; Noninvasive Measurements in Single and Multiphase Flows.* ASME 2014 4th Joint US-European Fluids Engineering Division Summer Meeting collocated with the ASME 2014 12th International Conference on Nanochannels, Microchannels, and Minichannels, Chicago, Illinois, USA, 03–07 Aug. 2014; American Society of Mechanical Engineers, 2014, ISBN 978-0-7918-4622-3.

12. Zywica, G.; Kaczmarczyk, T.Z.; Ihnatowicz, E. A review of expanders for power generation in small-scale organic Rankine cycle systems: Performance and operational aspects. *Proceedings of the Institution of Mechanical Engineers, Part A: Journal of Power and Energy* **2016**, *230*, 669–684, doi:10.1177/0957650916661465.

13. Jakub Mascuch, Vaclav Novotny, Vaclav Vodicka, Zbynek Zeleny and Jan Spale. SET-UP AND PILOT OPERATION OF AN IN-HOUSE DEVELOPED BIOMASS ORC μCHP IN THE CZECH REPUBLIC. *ORC2019*.

14. *Piston Engine-Based Power Plants;* Elsevier, 2018, ISBN 9780128129043.

15. Zare, S.; Tavakolpour-Saleh, A. Free piston Stirling engines: A review. *Int J Energy Res* **2020**, *44*, 5039–5070, doi:10.1002/er.4533.

16. Mach 1881: Mach 1881 Website. Available online: https://www.mach1881.de/ (accessed on 04.10.22).

Heat Powered Cycles
Conference 2023
Edinburgh

Heat in the new energy system

Integration of high-temperature heat pumps into geothermal energy systems

J. Jeßberger[*], F. Heberle, and D. Brüggemann

Chair of Engineering Thermodynamics and Transport Processes (LTTT), Center of Energy Technology (ZET),

University of Bayreuth, Prof.-Rüdiger-Bormann-Strasse 1, DE-95447 Bayreuth, Germany

*Corresponding author: jaromir.jessberger@uni-bayreuth.de

Abstract

For a long time, the energy transition has been regarded as a pure electricity transition. However, due to the high share of the heating market in Europe´s final energy consumption, it is mandatory to intensify the decarbonisation in this sector as well. High-temperature heat pumps (HTHP) could make a major contribution in different areas of application, like the supply of existing heating networks or the utilisation of industrial waste heat. However, there are still open research questions regarding the technical aspects like fluidselection or part load behaviour as well as economical aspects.

With this motivation, the part load behaviour of a HTHP is investigated on the basis of a quasi-steady state simulation model, which is validated from experimental data of a test rig with a thermal output of 30 kW. The simulation results are used for thermo-economic analyses of the integration of HTHPs in geothermal energy systems. In this context two potential applications are considered. On the one hand, the increase of the supply temperature of a medium-deep energy system for a district heating network is analysed. On the other hand, the peak load coverage by means of HTHP in case of a deep geothermal heat plant is investigated. The first measurements show a coefficient of performance (*COP*) of 3.99 at the design point (DP) with a thermal output of 30 kW and a temperature lift of 37.4 K. The simulation model is based on off-design correlations for the heat exchanger according to Toffolo et al. [1] and an extrapolated compressor characteristic curve. The *COP* shows a relative deviation compared to the experiments below 5.8 % for the considered part load conditions and reproduces the measurements qualitatively well. The thermo-economic analyses show that the integration of HTHPs into the two systems mentioned is economical, taking into account the current subsidies in Germany. Thus, in the peak load application the levelized costs of heat (*LCOH*) of gas can be reduced in the basis scenario by 7.1 % and by 20.1 % in the medium-deep application. Extensive sensitivity analyses were carried out to make the influence of the various parameters on the economic viability clear.

In further work, the submodels on component level will be further developed based on extended measurement campaigns.

Keywords: high-temperature heat pump, geothermal, part load, techno-economic analyses, simulation

Introduction

Stopping global warming is one of the biggest tasks of our time. However, renewable energy sources still play a minor role in the heating sector with about 21 % in 2018, although this sector accounts for over 50 % of final energy consumption in Europe [2]. In order to provide thermal energy in a sustainable and resource-efficient way, the integration of high-temperature heat pumps (HTHPs) into renewable energy systems is a promising approach. Potential applications are geothermal systems or the upgrading of waste heat from industrial processes. The use of HTHPs offers the possibility to ensure sustainable peak load coverage, to increase the thermal output of different systems or to raise supply temperatures.

The term HTHP is not clearly defined in literature. For example, Arpagaus et al. [3] label heat pumps with supply temperatures higher than 363 K as high-temperature systems. The International Energy Agency [4] defines classic industrial heat pumps with a heat source temperature of up to 313 K and a heat sink temperature of up to 353 K as HTHP. In case of heat sink temperatures higher than 373 K the term very-high-temperature heat pumps is proposed. In this work, the classification according to the International Energy Agency is applied, without the distinction between very-high-temperature and HTHPs.

There are many publications regarding the techno-economic analysis of HTHPs combined with industrial systems or district heating networks (DHN). Mateu-Royo et al. [5] investigated the integration of HTHPs into DHNs. In their work, the DHN can be used as a heat sink and a heat source. Kosmadakis et al. [6] investigated the integration into industrial processes and thereby the upgrade of waste heat up to 423 K. They also examined different plant configurations with following sensitivity analyses. Sartor et al. [7] also investigated the integration into DHN, but focussed on the steam production and the behaviour of the coefficient of performance (*COP*) of the HTHP. Dumont et al. [8] examined the integration of HTHPs in the food and beverages industry. Their results indicated, that HTHPs could meet 12 TWh of process heat demand in the German food and beverages industry. Some studies have been carried out in the experimental field as well. Hassan et al. [9] examined an HTHP with the hydrochlorofluoro olefin (HCFO) refrigerant R1233zd(E) and developed a simulation model. The HTHP was designed to operate at heat sink temperatures above 403 K, with the possibility to vary the compressor speed from 500 to 1500 rpm. The aim of this work was, to reach a *COP* of greater 4 in every operation point and to find the boundary conditions to reach this goal. Jiang et al. [10] used the same refrigerant and supply temperatures up to 373 K. They reached a *COP* of 3.67 at a temperature lift of 50 K, which is the highest efficiency among published lab-scale and prototype-scale units and developed a simulation model as well. Arpagaus and Bertsch [11] made an experimental comparison between R1224yd(Z) and R1233zd(E) in an HTHP. The laboratory HTHP had a thermal output of 10 kW and the performance was examined at three different temperature lifts.

The heat pump market is growing and Arpagaus [12] identified 26 already commercially available HTHPs with maximum flow temperatures above 363 K. Overall, market-ready technologies already achieve heating capacities between 20 kW and 20 MW. Jiang et al. [13] published a review of the state of the art of HTHPs, focussed on the different fluids, plant configurations and fields of application.

As described, there are many publications in the filed of simulation, thermo-economic analyses as well as experimental investigations. The published experimental investigations mostly focussed on a high temperature lift or high efficiency. So, the literature research points out a large research gap in the integration into geothermal systems and the investigation of the part load behaviour. However, the integration of HTHPs into renewable systems requires flexibility and good part load characteristics. Exemplarily, the heat pumps have to provide short-term peak loads or meet fluctuating heat demands. Thus, the aim of this work can be derived from the experimental investigation of the part load behaviour of a HTHP on a laboratory scale. The

test rig is a HTHP with a thermal output of 30 kW and a supply temperature of up to 378 K. The working medium is the HCFO refrigerant R1233zd(E), with low global warming potential (GWP) and ozone depletion potential (ODP). The conducted measurement series are analysed both at system and component level. Parallel to the construction of the test rig, a quasi-stationary simulation model is built in ASPEN Plus® in on- and off-design, which is validated by experimental data. The developed simulation model is used for thermo-economic analyses of geothermal systems under consideration of the off-design behaviour of the HTHP. In the following chapters, the methodology, followed by a discussion of the results from the experimental investigations and the thermo-economic analyses is presented.

Methodology

Experimental setup

The test rig represents a HTHP with a thermal output of 30 kW at the design point (DP) and a maximum flow temperature of 378 K. The system is based on a customized heat pump from the manufacturer FM Automation. Additionally, the test rig was modified by the following technical measures:

- Invasive temperature and pressure devices at the inlet and outlet of each component
- Software-controlled expansion valve
- Software-controlled mass flow of the water circuits
- Stepless power control by means of a frequency converter
- Oil management system
- Cylinder head cooling of the compressor
- Use of a higher viscosity oil
- Optimisation of insulation
- Four sampling points for fluid data analysis

A priniciple scheme of the HTHP in the laboratory can be seen in Figure 1.
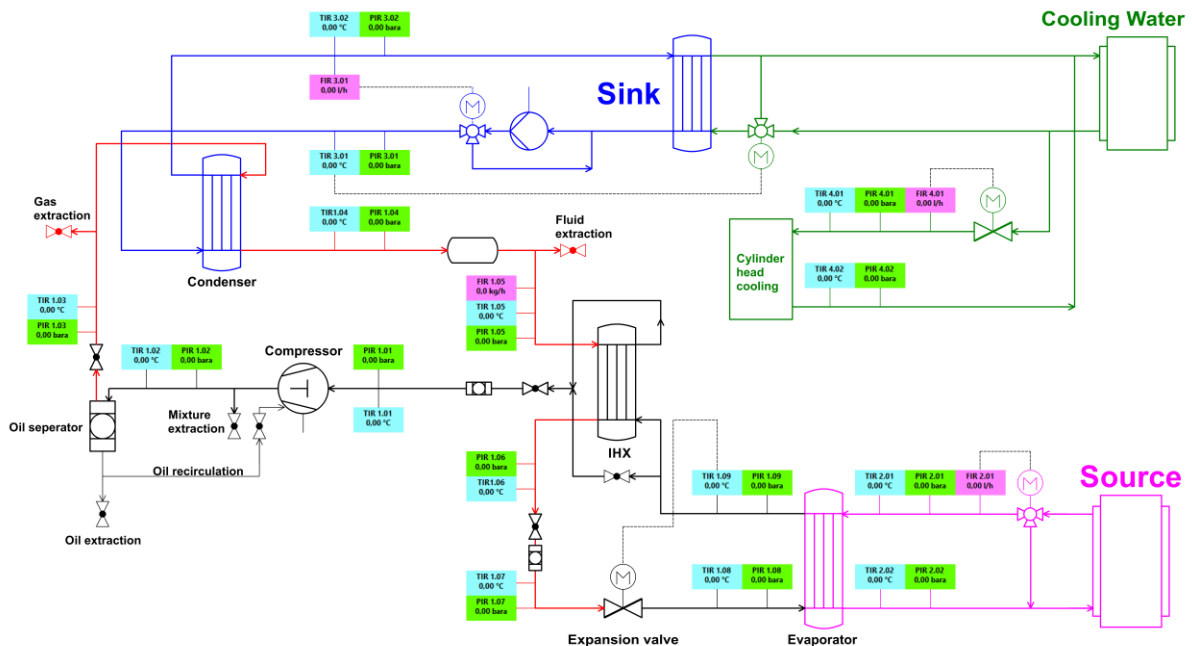
Figure 1: RI-Scheme high-temperature heat pump

The HB-THERM heater, type Thermo-5, is used as heat source. To control the mass flow rate, a three way valve is implemented. As heat sink the cooling water of the building is used, so that the inlet temperature, outlet temperature and the mass flow rate of the heat sink are variable.

The HCFO refrigerant R1233zd(E) is used as the working fluid. The refrigerant has a global warming potential (GWP) of 1 CO_2e and an ozone depletion potential (ODP) of 0.00034 [14]. Due to the overhanging wet steam area in the *p-h* diagram, shown in Figure 2, superheating of the gas phase (at the outlet of the evaporator; state point 1.09) is necessary to avoid compressor damage due to droplet erosion.
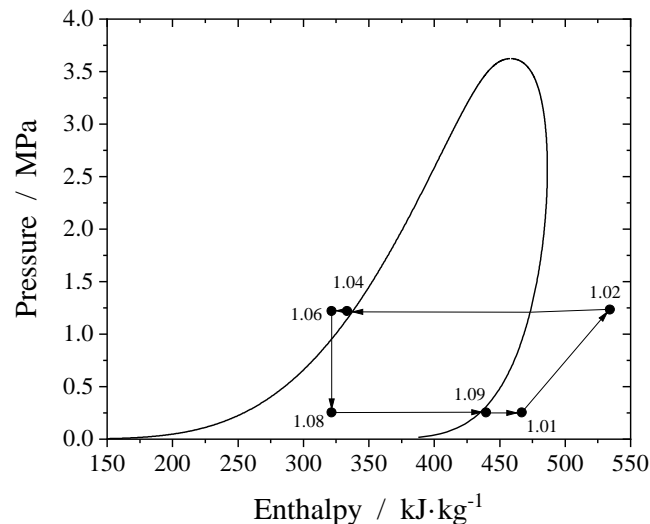
Figure 2: *p,H*-diagram R1233zd(E)

Therefore, an internal heat exchanger (IHX) is used as a recuperator and transfers heat from stream 1.05 to stream 1.09 (see Figure 1). From the outlet of the recuperator, the superheated refrigerant is led to the compressor, where the maximum process pressure of 1.23 MPa is obtained. From the compressor outlet, the refrigerant is led to the condenser. There, a phase change takes place at a temperature (T_c) of 380 K. Finally, the fluid is subcooled by 3 K at state point 1.04. The fluid enters the recuperator and at state point 1.05, the liquid phase is expanded to the lower pressure level by the expansion valve. At the outlet of the expansion valve, the refrigerant has a vapour content (*x*) of 0.37, temperature of 318 K and a pressure of 0.25 MPa. The expansion valve is software controlled and ensures a superheat of 5 K at the outlet of the evaporator (state point 1.02).The compressor, is a Bitzer reciprocating compressor (type 4JE-22Y) with four cylinders on two banks. The compressor oil used is a polyester oil (POE) from Bitzer, designated BSE-85 K. Two different systems are installed for capacity control, one is the VARISTEP system from Bitzer. With this system, one cylinder bank can be switched off and the compressor can operate at 50 % of the maximum capacity. To use a compressor capacity between 50 % and 100 %, the cylinder bank can be switched intermittently. Thus, the compressor operates at 100 % for 5 s and then at 50 % for 5 s, resulting in a compressor capacity of 75 %. On the other hand, a frequency converter is installed, which can control the compressor with a frequency between 25 Hz and 70 Hz. In addition, the cylinder head cooling enables operation at heat sink temperatures ($T_{sink, out}$) higher than 378 K.

PT100 sensors from Omega are used as temperature sensors. These have a measuring range of 243 K to 623 K and accuracy class 1/3 DIN B. This allows the maximum deviation to be determined according to equation (1):

$$dT = \pm\frac{1}{3} \cdot (0{,}30°C + 0{,}005 \cdot T) \tag{1}$$

The uncertainty of the connected measuring card, which amounts to $\pm\,0.15$ K at room temperature, must also be taken into account. The pressure sensors used, type PAA23SY, are also from Omega. Different sensors are used in the low-pressure and high-pressure ranges to improve accuracy. The measuring range for low pressure is up to 0.5 MPa and for high pressure up to 2 MPa. The measurement uncertainties are $\pm\,0.7\,\%$ or $\pm\,0.5\,\%$ depending on the temperature, plus the inaccuracy of the measuring card of $\pm\,0.76\,\%$.

Simulation model

A simulation model of a HTHP is developed in the Aspen Plus® software environment. In a first step the test rig at design conditions is simulated. In the following, the control strategies and the implemented part-load behaviour of the individual components will be briefly described.

The on-design model is extended by several off-design models in order to describe the part load behaviour of the system. The design conditions can be described as follows. The evaporator provides superheating at the outlet of 5 K, the condenser subcooling of 3 K. The expansion valve thus has a fixed outlet pressure of about 0.25 MPa. The condensate flow is cooled by 8 K in the internal heat exchanger. Subsequently, the output pressure of 1.234 MPa, an isentropic efficiency η_{isen} of 0.8 and a mechanical efficiency η_{mech} of 0.93 are specified as boundary conditions for the compressor.

In the off-design model, the part load behaviour of the individual components has to be implemented. For the heat exchangers, the correlation according to Toffolo et al [6] (see equation (2)) is used.

$$UA = UA_{DP} \cdot \left(\frac{\dot{m}}{\dot{m}_{DP}}\right)^n \tag{2}$$

Where U is the overall heat transfer coefficient, $\dot{m}$ is the mass flow of the working medium, A is the heat exchanger surface and n is the exponent that reflects the behaviour of the heat exchanger depending on type and design. For the evaporator and condenser, n is set to 0.15 according to Toffolo et al [6]. For the IHX, n is assumed by 0.67 according to Toffolo et al [6]. The n values differ due to the different heat transfer media. Thus, the course of the heat transfer capacity UA in part load operation can be described as shown in Figure 3.
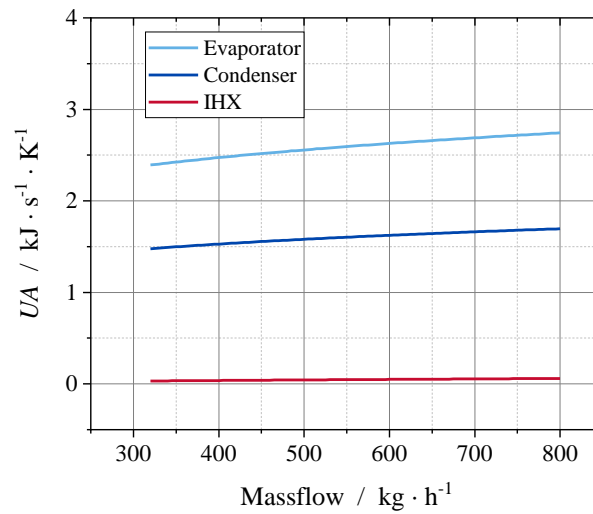
Figure 3: Heat transfer capacity as function of massflow

For the part-load behaviour of the compressor, extrapolated characteristic curves of the manufacturer based on reference refrigerants are used, since no measured data are available for the refrigerant, yet. In Figure 4, the isentropic efficiency of the compressor is plotted against the mass flow, as well as the *COP* resulting from the simulation model. It can be seen that the isentropic efficiency shows a maximum at 730 kg/h. The *COP*, on the other hand, decreases considerably with increasing mass flow. According to Jiang et al. [10], this behaviour is mainly due to the increasing enthalpy difference between compressor inlet and outlet and the increasing mass flow rate. Analogously, the temperature lift ΔT_lift, presented in equation (3), increases with increasing massflow.

$$\Delta T_\text{lift} = T_\text{sink,out} - T_\text{source,in} \tag{3}$$

The influence of the part load behaviour of the heat exchangers on the *COP* behaviour needs to be carried out in the following studies.
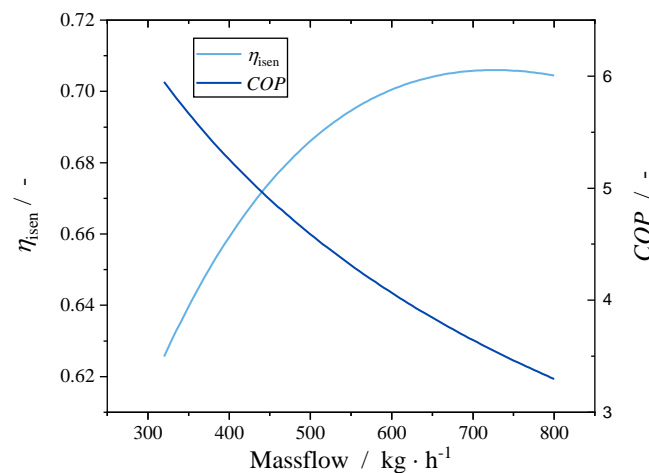
Figure 4: *COP* of the system and isentropic efficiency of the compressor as function of massflow

Heat Powered Cycles
Conference 2023
Edinburgh

Heat in the new energy system

3rd to 6th of September 2023
The University of Edinburgh, Scotland

The expansion valve is controlled in the off-design model as on the test plant itself and ensures a superheat of 5 K at the outlet of the evaporator. The correlations and characteristic curves presented for the part-load behaviour of the individual components are examined and evaluated in the next chapter regarding their validity.

Annuity method regarding VDI 2067

The applications are evaluated with regard to their levelized cost of heat (*LCOH*) using the annuity method according to VDI 2067 [15]. The annuity method is a dynamic investment calculation and is used for the evaluation of energy technology projects. It uses the annuity factor *a* (equation (4)) to predict the annual costs, depending on the interest rate *q*, in the observation period *T*.

$$a = \frac{q^T(q-1)}{q^T - 1} \tag{4}$$

Further calculation methods and boundary conditions for the economic analyses were carried out analogously to Jeßberger et al [16]. Furthermore, the energy costs from the first quarter of 2021 (Q1/21) as well as the German funding programme "Modelvorhaben Wärmenetze 4.0" are taken into account [17]. In a second economic scenario also prices from the first quarter of 2022 (Q1/22) and the new funding programme "Bundesförderung für effiziente Wärmenetze (BEW)" [18] are applied. On this basis, the HTHP is compared with the fossil alternatives. In addition to the operating costs for oil and gas boilers, there are also the CO_2 levies which are set at 60 €/t CO_2 in this study. The corresponding energy cost scenarios considered are shown in Table 1:

Table 1: Energy costs for the evaluated periods

Energy source	costs Q1/21 [€/MWh]	costs Q1/22 [€/MWh]
Oil	64	100
Gas	40	100
Electricity	190	300

The investment costs of the oil and gas boiler are set at 100 €/kW$_{th}$ in the basic scenario and those of the HTHP at 500 €/kW$_{th}$. In the following, the specific boundary conditions for each application are presented and then the results are discussed. Additionally, a ratio between the gas and the electricity price is introduced in equation (5), which indicates the point from which the integration of HTHPs is just as economical as gas.

$$r_{price} = \frac{c_{elect}}{c_{gas}} \tag{5}$$

c_{elect} represents the electricity costs and c_{gas} represents the gas costs of the considered time.

Results and Discussion

The test rig is analysed at 10 different part load points. The boundary conditions of the heat source and heat sink are kept constant. The inlet temperatures are 333 K in each case, the heat source is cooled down to 322 K. Depending on the operating point, the heat sink was heated

up to a maximum temperature of 377 K. The system was measured in 5 Hz steps from 25 Hz to 70 Hz, i.e. the range approved by the compressor manufacturer. Figure 5 shows the *COP* and temperature lift depending on compressor frequency.With increasing frequency and thus an increase in the mass flow rate of the working medium, the *COP* decreases and the temperature lift increases.
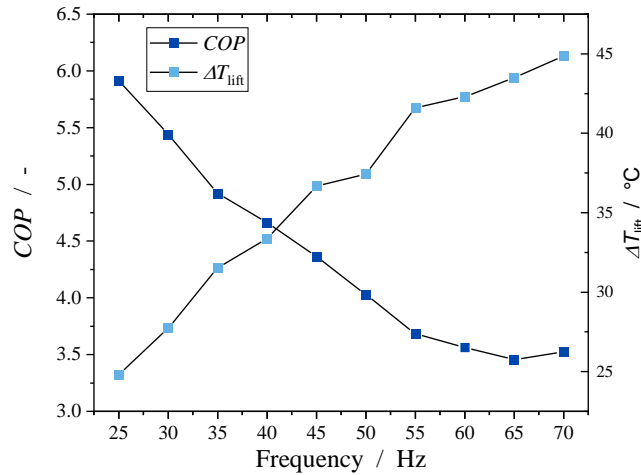
Figure 5: Measurement results *COP* and temperature lift as function of compressor frequency

In consequence, at 25 Hz, a maximum *COP* of 5.92 is obtained with a heating power of 18.8 kW and a temperature lift of 24.8 K. On the other hand, the maximum temperature lift of 44.9 K is measured at a frequency of 70 Hz. The thermal power at this operating point is 35.2 kW and the *COP* 3.52. Figure 6 shows the thermal power of the heat source and heat sink, as well as the electrical power consumed by the system ($P_{el,\ compressor}$). The lines represent the values determined with the simulation model.
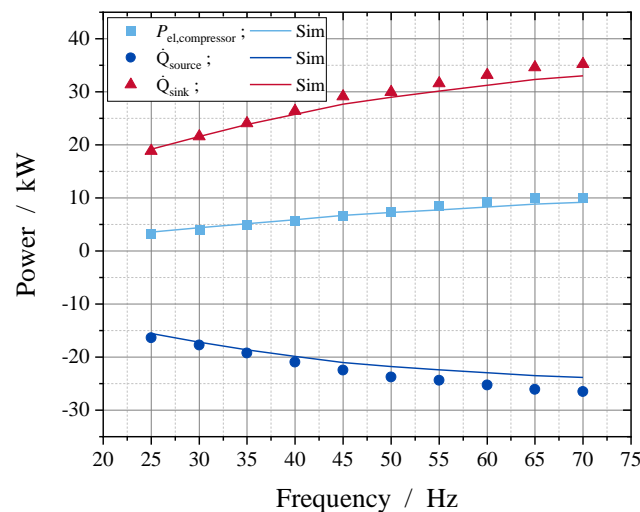
Figure 6: Thermal and electrical power from measurements and simulation as function of compressor frequency

The medium relative deviation of the heat source power leads to 7.4 %, with a maximum deviation of 11 % at 70 Hz and a minimal deviation of 2.9 % at 30 Hz. The medium relative

deviation of the power of the heat sink is significantly smaller and leads to 3.8 %, with a maximum deviation of 7 % at 65 Hz and a minimal deviation of 0.1 % at 30 Hz. The consumed electrical power shows a medium relative deviation of 7.7 %, with a maximum deviation of 13.5 % at 65 Hz and a minimal deviation of 0.25 % at 45 Hz. The trend shows that the calculated consumed electrical power deviates below the DP at 50 Hz positive and over the DP negative. The measured capacities are the capacities absorbed or emitted by the heat source ($\dot{Q}_{source}$) and heat sink ($\dot{Q}_{sink}$). This means that the water circuits are considered here and the heat losses to the environment are taken into account. These are not taken into account in the simulation model yet. So, in the measurements, a higher power can be achieved on the side of the heat sink and a higher power is introduced into the system on the side of the heat source. This, and the not adjusted heat exchanger and compressor models can explain the deviations.
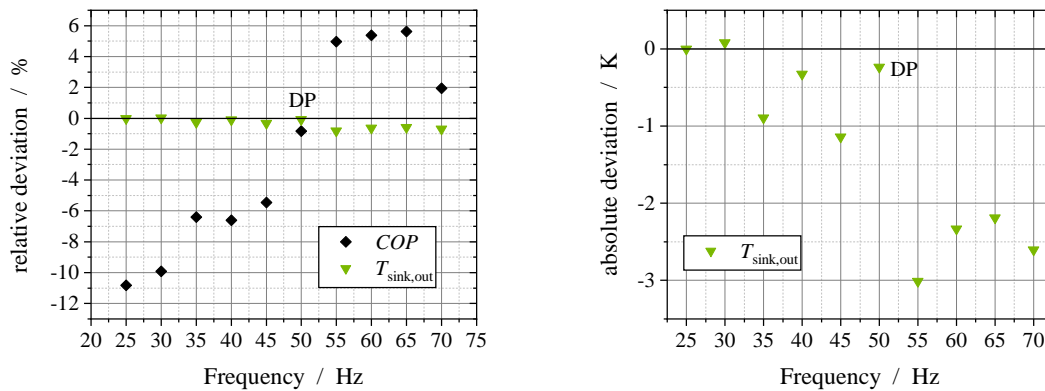
Figure 7: Relative deviation of the *COP* and $T_{sink,out}$ and absolute deviation of $T_{sink,out}$ as function of compressor frequency

This is also illustrated by the relative deviation of the calculated *COP* and the calculated heat sink output temperature $T_{sink,out}$ from the measured values shown in Figure 7. The medium relative deviation of the *COP* leads to 5.8 % and is thus in the same order of magnitude as the results from studies by Jiang et al. [10] and Kosmadakis et al. [6]. Therefore, the results can be used in the thermo-economic analyses. On the right the absolute deviation of $T_{sink,out}$ is presented and shows more accurate calculations with a medium absolute deviation of 1.3 K. The maximum relative deviation of $T_{sink,out}$ is 0.8 % at 55 Hz. The calculations show good deviations to the measurements, but with adaptions of the heat exchanger and compressor models, the performance of the model will be improved in the following studies.

Thermo-economic analyses

In the following chapter, the results of the thermo-economic analyses for the integration of HTHPs into geothermal systems are presented. First, the substitution of existing peak load systems such as oil or gas boilers in geothermal heating plants is examined in application 1 (AP1). In addition, the increase of the supply temperature in medium-deep geothermal energy systems (AP2) is investigated.

AP1: Peak load coverage by means of HTHP in a geothermal heating plant

The heating plant underlying AP1 is located in the South German Molasse Basin, south of Munich, and has an installed thermal capacity of 15 MW [19]. The heating plant has two production wells and one reinjection well. Oil boilers with a capacity of 8 MW are used for peak load coverage, which are to be replaced by an HTHP in this application. The HTHP would be installed after the DHN heat exchanger and would cool down the thermal water before it will be reinjected into the ground. Since the part load behaviour of the HTHP is particularly relevant in the area of peak load coverage, this was used for the calculation of the off-design simulation (Figure 4) and the annual load profile of the peak load system of 2015 was used as input parameters (see Figure 8).
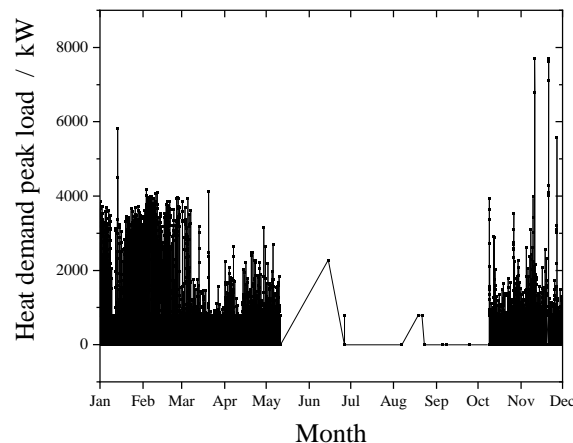
Figure 8:Annual load curve of the peak load system of a geothermal heating plant in the Southern German Molasse Basin

The corresponding *COP* of the HTHP is calculated for each operating point (every 15 min) and coupled to the economic model. In the heating plant, the oil boilers are not only used to cover peak loads, but also for redundancy and to compensate for maintenance-related failures of the heating plant. Due to the comparatively high investment costs of an HTHP, these two areas of application are not considered in the study. As can be seen in Figure 8, between mid-May and mid-October, the heating plant can completely cover the heat demand of the district heating network (DHN), apart from a few exceptions. From mid-October, the heat demand then increases to remain roughly constant at around 4 MW from January to mid-March. After that, the demand flattens out again. The curve shows that with an installed thermal capacity of 8 MW, the heat pump must predominantly supply less than 50 % of the possible capacity. Furthermore, a fixed output of 800 kW of the HTHP is implemented in the model when the demand is between 0 % and 10 % part load. Figure 9 shows the results of the economic analysis. On the left side, the annuities for the four scenarios considered (gas, oil, HTHP and HTHP considering the subsidy options) are plotted with their components. The resulting *LCOH*

are shown on the right. The capital-related costs play a very important role in AP1, as the full load hours in 2015 were only 308 h/a due to the pure peak load coverage.
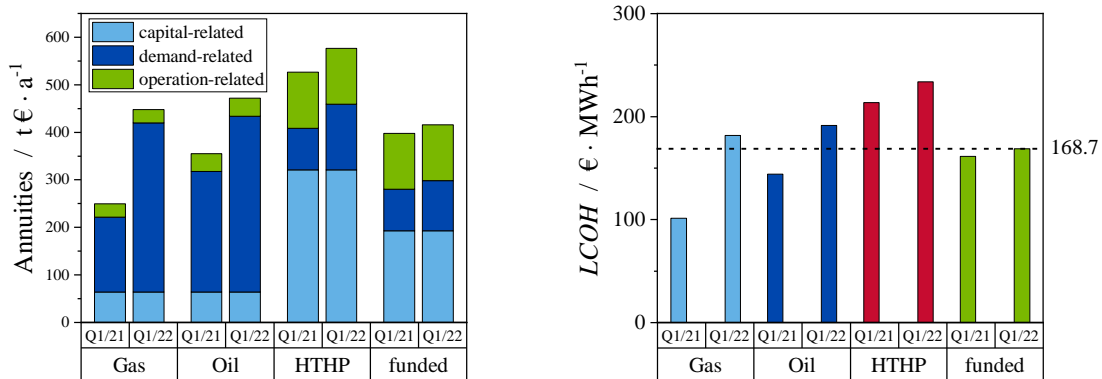
Figure 9: Annuities and *LCOH* AP1

In addition to the different energy sources, the graph also shows the impact of price changes between Q1/21 and Q1/22. Thus, the demand-related costs increase by 45.75 % for oil, 121.61 % for gas and 57.23 % for HTHP (electricity costs). In the case of the subsidised HTHP, this cost share increases only by 20.55 % as the BEW includes an operating cost subsidy for heat pumps of 70 €/MWh. Thus, the results show that the *LCOH* of the subsidised HTHP were still about double that of a gas boiler in 2021, but in Q1/22 they were 7.12 % lower at about 169 €/MWh. The results show the great influence of parameters such as energy prices, *COP* and others. The energy price ratio r_{price} increseases from Q1/21 to Q1/22 from 3 to 3.33

Therefore, the results for AP2 are presented below and sensitivity analyses are carried out to show the influence of the individual parameters on the *LCOH*.

AP2: Supply temperature increase at medium-deep geothermal

In the second application, a more general approach is applied. Here, the part load behaviour is not taken into account. For a medium-deep geothermal energy system, a *COP* of the HTHP of 4 is assumed, with a temperature range ΔT_{lift} of 25 K and 4000 full load hours [2]. The geothermal fluid temperature is assumed to be 333 K and the reinjection temperature 313 K. This leads to a thermal power of the geothermal brine of 7.678 MW$_{th}$ at a mass flow rate of 100 kg/s and a specific heat capacity c_p of 3.839 kJ/kgK according to Bauer [20]. Figure 10 shows this concept for integrating an HTHP to raise the flow temperature for medium-deep geothermal energy. The drilling depth is 2000 m. On the side of the heat sink, the return temperature of the DHN should be 333 K and the supply temperature 358 K. Based

Figure 10: Use of an HTHP to increase the flow temperature for medium-depth geothermal energy

on the given data, the energy balance of the HTHP and neglecting the heat losses in the heat pump circuit, the output for the heat sink and thus for the DHN can be calculated by 10.1 MW$_{th}$. In this case, oil and gas boilers are again examined as alternative technologies. In order to analyse the system economically, the boundary conditions for the geological conditions listed in Table 2 have been assumed [16].

Table 2: Economic boundary conditions for the geothermal heat plant [8]

Drilling costs	3000 €/m
Central heating system	2.83 M €
Land costs	2.06 M €
Additional costs	3.6 M €
Electrical submersible pump	0.8 M €

The electrical submersible pump (ESP) represents the borehole pump in the geothermal water circuit. Its installation depth depends on the water level in the borehole and the maximum drawdown. The installation depth in the heating plant from AP1 is 600 m. Since test drillings and pumping tests are necessary for the exact determination of the installation depth, an installation depth of 700 m is assumed in order to be able to compensate for any geological boundary conditions that negatively influence the result. This leads to an electrical output of about 490 kW_{el}. Due to the highly mineralized geothermal water and high temperatures, the ESP has a lifetime of about 3 to 7 years and must then be replaced. In the case of medium-deep geothermal energy, a lifetime of 7 years was assumed, due to the lower load caused by the comparatively low temperatures.
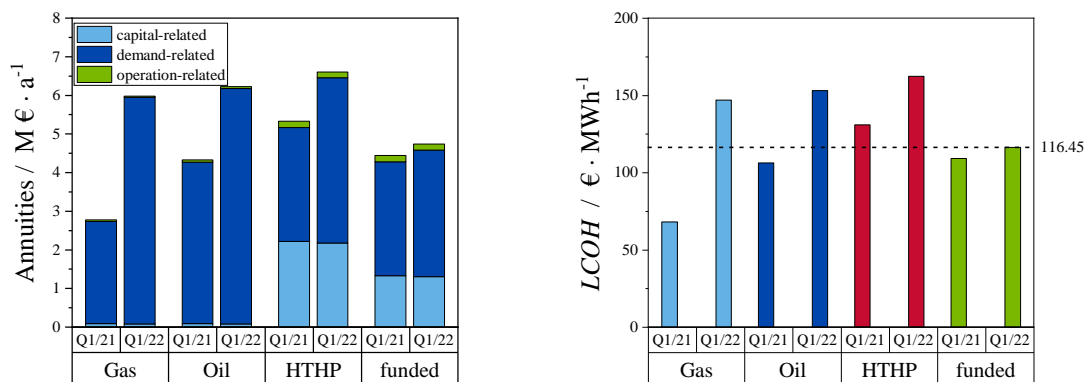
Figure 11: Annuities and *LCOH* AP2

In Figure 11, as in the previous chapter, the annuities as well as the resulting *LCOH* are plotted. In the scenario for Q1/21, the *LCOH* of gas are 68 €/MWh and the *LCOH* for the HTHP with considered subsidies lead to 109 €/MWh. Thus, the HTHP is 60 % less economical. In the scenario for Q1/22 the ratio changes. Due to the huge increase of the demand related costs for gas of 122 %, the *LCOH* of gas lead to 147 €/MWh. With the operating subsidies in the considered funding program, the demand related costs of the HTHP increase by 11 %, what results in *LCOH* of 116.5 €/MWh. The investment costs of the HTHP stay constant between both scenarios, for gas and oil the investment costs do not play a major role due to the large share of demand-related costs. It follows that the subsidised HTHP is more economical than gas or oil boilers. The energy price ratio r_{price} increseases from Q1/21 to Q1/22 from 2.4 to 3.6.

Sensitivity analyses AP2

For the sensitivity analyses, 8 parameters are selected that have a major influence on the *LCOH*. Two parameters have always been varied at the same time so that a result space is created which represents different combinations of the two parameters and their interaction. Figure 12 thus shows the influence of the lifetime ($ESP_{lifetime}$) and the observation period (T) on the left-hand side. On the right, the influence of the full load hours (t_{fh}) and the electricity price (c_{elect}).
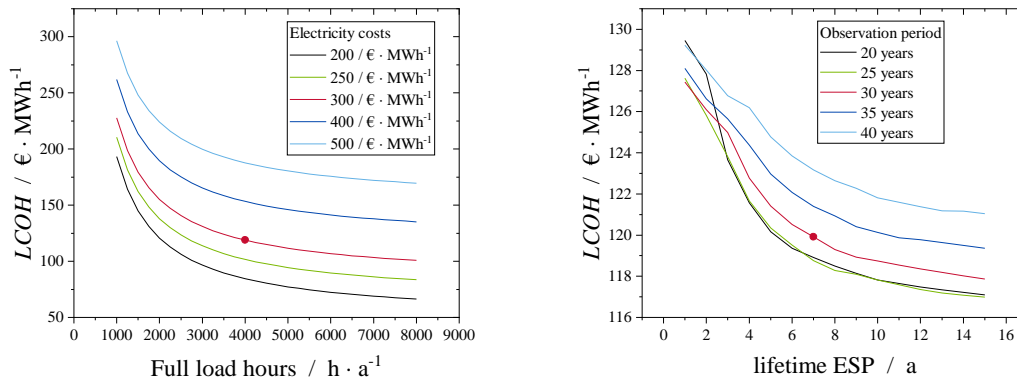
Figure 12: Sensitivity analyses AP2 – variation of $ESP_{lifetime}$, t_{fh}, T and t_{fh}

By varying the observation period, an optimum arises, at 25 years, which is caused by necessary replacements for ESP and heat exchangers. The influence of the lifetime clearly shows that through further development of the technology, the *LCOH* can be reduced by up to 2 €/MWh, with otherwise constant conditions, compared to the base case. In the case of deep geothermal energy, where the lifetime is shorter, the savings would be correspondingly greater. With an increase of the full load hours up to 8000 h/a, the *LCOH* could be reduced by 15 %. Reducing the electricity costs from 300 €/MWh to 200 €/MWh, would result in a decrease of the *LCOH* of 29 %, down to 84.5 €/MWh$_{thermal}$.
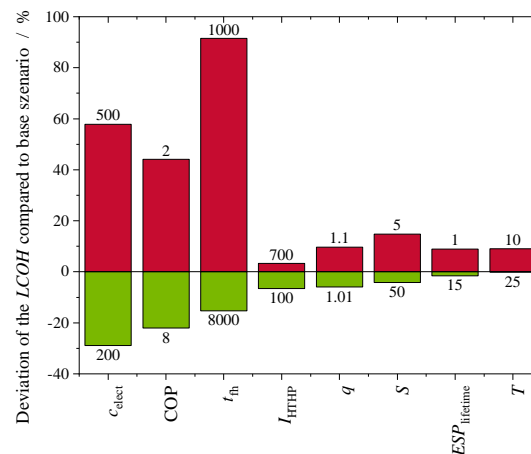
Figure 13: Results of the sensitivity analyses for AP2

To summarize, Figure 13 shows the influence of the individual parameters on the *LCOH*. It can be seen that the *LCOH* reacts most sensitively to the electricity price, with a reduction of 29 %, followed by the *COP*, with a reduction of 22 % and the full load hours, with a reduction of 15 %. From the sensitivity analyses presented, steps can now be derived to increase economic efficiency and reduce environmental impact. Intelligent heat network planning with

thermal storage, for example, can increase the full load hours so that the *LCOH* can be reduced. The development of energy prices can only be passively influenced by operating cost subsidies, as in the BEW. By increasing the efficiency of the heat pumps, through new system concepts such as cascade connection, absorption-compression heat pumps or new refrigerants, the environmental impact can be reduced and profits increased.

Summary and outlook

In this work, an experimental setup of an HTHP was used to validate a quasi-steady state simulation model. The developed off-design model was applied for thermo-economic analyses of the HTHP in geothermal energy systems under consideration of part load behaviour. A comparison of experimental data and simulation results shows a sufficient accuracy. The medium relative deviation of the *COP* is below 5.8 %. The part load measurements of the test rig show a maximum *COP* of 5.92 at a temperature lift of 24.8 K and a maximum temperature lift of 44.9 K at a *COP* of 3.52.

The thermo-economic analyses show that the integration of HTHPs into the two systems mentioned is economical, taking into account the current subsidies in Germany. Thus, in the peak load application, the levelized costs of heat (*LCOH*) of gas can be reduced in the basis scenario by 7.1 % and by 20.1 % in the medium-deep application. Extensive sensitivity analyses were carried out, for the medium-deep application to make the influence of the various parameters on the economic viability clear. The *LCOH* reacts the most sensitively to the electricity price, with a saving potential of 29 %, followed by the increase of the *COP*, with a saving potential of 22 %. The increase of the full load hours would result in a reduction of the *LCOH* of 15 %.

In further work, the submodels on component level will be optimised in an iterative process. Exemplarily, the exponent *n* in the model of Toffolo et al. [1] will be adapted to plate heat exchangers in the heat pump application. This will lead to a optimization of the economic analysis in an iterative process.

Acknowledgement

References

1. A. Toffolo, A. Lazzaretto, G. Manente, and M. Paci: *An Organic Rankine Cycle off-design model for the search of the optimal control strategy*, in The 25th international conference on efficiency, cost, optimization, simulation amd environmental impact of energy systems, vol. 295, 1–14 .

2. World Energy Council, *Der europäische Wärmemarkt: Überblick und Herausforderungen* (2020). https://www.weltenergierat.de/publikationen/energie-fuer-deutschland/der-europaeische-waermemarkt-ueberblick-und-herausforderungen/ [German].

3. C. Arpagaus, F. Bless, M. Uhlmann, J. Schiffmann, and S. Bertsch: *High Temperature Heat Pumps: Market Overview, State of the Art, Research Status, Refrigerants, and Application Potentials,* International Refrigeration and Air Conditioning Conference, 2018.

4. International Energy Agency, *Application of Industrial Heat Pumps: EA Industrial Energy-related Systems and Technologies Annex 13; IEA Heat Pump Programme Annex 35; Final Report Part 1* (2014). https://iea-industry.org/app/uploads/annex-xiii-part-a.pdf.

5. C. Mateu-Royo, S. Sawalha, A. Mota-Babiloni, and J. Navarro-Esbrí: *High temperature heat pump integration into district heating network,* Energy Conversion and Management 210, 2020.

6. G. Kosmadakis, C. Arpagaus, P. Neofytou, and S. Bertsch: *Techno-economic analysis of high-temperature heat pumps with low-global warming potential refrigerants for upgrading waste heat up to 150 °C,* Energy Conversion and Management 226, 2020.

7. K. Sartor, V. Lemort, and P. Dewallef: *Improved district heating network operation by the integration of high-temperature heat pumps,* International Journal of Sustainable Energy 37, 9, 2018.

8. M. Dumont, R. Wang, D. Wenzke, K. Blok, and R. Heijungs: *The techno-economic integrability of high-temperature heat pumps for decarbonizing process heat in the food and beverages industry,* Resources, Conservation and Recycling 188, 2023.

9. A. H. Hassan, J. M. Corberán, M. Ramirez, F. Trebilcock-Kelly, and J. Payá: *A high-temperature heat pump for compressed heat energy storage applications: Design, modeling, and performance,* Energy Reports 8, 2022.

10. J. Jiang, B. Hu, R. Z. Wang, T. Ge, H. Liu, Z. Zhang, and Y. Zhou: *Experiments of advanced centrifugal heat pump with supply temperature up to 100 °C using low-GWP refrigerant R1233zd(E),* Energy 263, 2023.

11. C. Arpagaus and S. Bertsch: *Experimenteller Vergleich von R1224yd(Z) und R1233zd(E) in einer Hochtemperatur-Wärmepumpe,* KI Kälte, 03, 2020 [German].

12. C. Arpagaus, *Hochtemperatur-Wärmepumpen: Marktübersicht, Stand der Technik und Anwendungspotenziale* (VDE VERLAG GMBH, Berlin, Offenbach, 2019) [German].

13. J. Jiang, B. Hu, R. Z. Wang, N. Deng, F. Cao, and C.-C. Wang: *A review and perspective on industry high-temperature heat pumps,* Renewable and Sustainable Energy Reviews 161, 2022.

14. IPCC, *Climate Change 2014: Synthesis Report. Contribution of Working Groups I, II and III to the Fifth Assessment Report of the Intergovernmental Panel on Climate Change* (Geneva, Switzerland, 2014).

15. Verein Deutscher Ingenieure, *Wirtschaftlichkeit gebäudetechnischer Anlagen* (Beuth Verlag GmbH, Berlin, 2012), 2067 [German].

16. J. Jeßberger, F. Heberle, and D. Brüggemann: *Integration of high temperature heat pumps into geothermal systems*, in European Geothermal Congress 2022 .

17. Bundesamt für Wirtschaft und Ausfuhrkontrolle: *Modellvorhaben Wärmenetze 4.0 Modul II* (2019) [German].

18. Bundesamt für Wirtschaft und Ausfuhrkontrolle: *BEW-Merkblatt Antragstellung* (2022) [German].

19. enercharge 2022, *Informationsportal Tiefe Geothermie*. https://www.tiefegeothermie.de/projekte/pullach. Accessed 11 October 2022 [German].

20. Wolgang Bauer, *Reservoirberechnungen Hassfurt* (2021) [German].

Economic Overview for Four Applications of Hydrochar

E. Bevan [1*], M. Luberti [1] and G. Santori [1]

[1]The University Of Edinburgh

[2] Institute for Materials and Processes, School of Engineering, Kings Buildings, The University of Edinburgh, Edinburgh, EH9 3FB, UK

*Bevan.eloise@gmail.com

Abstract

Different applications of hydrochar produced from the hydrothermal carbonisation (HTC) of sewage and food waste generated by a small town in the UK (Chirnside; 2,250 residents) are assessed [1]. These are: as a solid biofuel for use in domestic biomass boilers (DBB), for use in biomass combined heat and power (BCHP) plant, as a precursor to activated carbon, and as a soil conditioner. For each application, the process had a positive net energy when using a portion of the hydrochar to power the HTC plant. The highest potential revenue of £10,371 - 41,162 can be obtained when activating all the hydrochar produced (99.08 t yr^{-1}), with revenues dependant on the characteristics of the final product.

Keywords: Hydrothermal Carbonisation; Hydrocahr; Domestic Biomass Boiler; Combined Heat and Power; Activated Carbon; Soil Conditioner

Introduction/Background

HTC is a thermochemical conversion process capable of converting waste biomass in a water medium at elevated temperatures and pressures (typically 180-250 °C and 10-40 bar [1]) into a solid product known as hydrochar. As an energy-dense and carbon-rich material, hydrochar is exhibiting a wealth of potential for use in a multitude of modern-day applications. This study aims to evaluate four alternative applications of hydrochar produced from a previously modelled plant [1]. As such, the co-derivation of a hydrochar from the sewage and food waste (99.08t yr^{-1}) produced from a small town in the UK (Chirnside: 2,250 residents) is to be compared for the following applications: Scenario (1) as a solid biofuel for use in BCHP (as previously determined in [1]), Scenario (2) as a solid biofuel for use in domestic biomass boilers (DBB), Scenario (3) as a soil conditioner; 3a) all aged, 3b) part used to fuel HTC, remaining aged [2] and 3c) part used to fuel HTC, remaining thermally treated [3], Scenario (4) as a precursor to activated carbon; 4a) all activated and 4b) part used to fuel HTC, remaining activated.

Results and Conclusions

Based on an economic potential revenues-only perspective, the most economically viable option was determined to be as a precursor for activated carbon. The results show that producing activated carbon from hydrochar could lead to the highest potential revenues, even when part of the hydrochar is used in an integrated industrial biomass boiler as a means to supply the plant with its thermal energy demands. However, the revenues are highly dependent on the quality of the product, which is in turn dependant on feedstock, activation method, time and temperature. In turn, activated hydrochar is recommended to increase the application of HTC.

Table 1 – Outputs and potential revenues of four alternative applications of Hydrochar

Application	Output	Est. Rev. (£ yr^{-1})
1) BCHP	77.91 $MW_{th}yr^{-1}$	1,987 [4]
	121.20 $MW_{e}yr^{-1}$	2,885 [4]
2) DBB	239.98 $MW_{th}yr^{-1}$	9,352 [5]
3A) Soil Conditioner	99.08 t yr^{-1}	3,961 [6]
3B) Soil Conditioner	55.01 t yr^{-1}	4,346 [6]
3C) Soil Conditioner	60.36 t yr^{-1}	7,134 [6]
4A) Activated Carbon	32.01 t yr^{-1}	10,371-41,162 [7-8]
4B) Activated Carbon	12.29 t yr^{-1}	3,982-15,804 [7-8]

References

[1] Bevan, E., Fu, J., Luberti, M. & Zheng, Y. Challenges and opportunities of HTC in the UK; case study in Chirnside. *RSC Adv.* **11**, 34870–34897 (2021).
[2] Puccini, M., Stefanelli, E., Hiltz, M. & Seggiani, M. Activated Carbon from Hydrochar Produced by Hydrothermal Carbonization of Wastes. **5**, 6 (2017).
[3] Hitzl, M., Mendez, A., Owsianiak, M. & Renz, M. Making hydrochar suitable for agricultural soil: A thermal treatment to remove organic phytotoxic compounds. *J. Environ. Chem. Eng.* **6**, 7029–7034 (2018).
[4] Medick, J., Teichmann, I. & Kemfert, C. Hydrothermal Carbonization (HTC) of Green Waste: An Environmental and Economic Assessment of HTC Coal in the Metropolitan Region of Berlin, Germany. *SSRN Electron. J.* (2017) doi:10.2139/ssrn.3050324.
[5] Lucian, M. & Fiori, L. Hydrothermal Carbonization of Waste Biomass: Process Design, Modeling, Energy Efficiency and Cost Analysis. *Energies* **10**, 211 (2017).
[6] Zhengzhou Zhongchuang Water Purification Material Co., Ltd., 'Plant Organic Fertilizer Biochar For Organic Agriculture', Alibaba.com. (Accessed Mar. 31, 2021).
[7] Zhengzhou Bo Yue Purification Materials Co., Ltd., Activated Carbon Granular Activated Carbon Product, Alibaba.com. (Accessed Mar. 29, 2021).
[8] Shanghai Xinjinhu Activated Carbon Co. Ltd., Wood Based Activated Carbon By Steam Method, Act Granular, Coalivated Carbon For Food, Activated Carbon For Water Product on Alibaba.com. (Accessed Mar. 29, 2021

Automotive hybrid compressor ejector heat recovery cooling system

Ľ. Kollár[1*], S. Polasa[1] and A. Hrdý[1]

[1]Hanon Systems Autopal Services s.r.o., Závodní 1007, 687 25 Hluk, Czech Republic

[*]Corresponding author: lkollar@hanonsystems.com

Abstract

Decreasing energy consumption of compressor cooling systems becomes highly important problem to solve in all electric vehicles. Efficiency of typical refrigeration cycle decreases when gascooler is exposed to reject the heat at high ambient temperature which results to high electric energy consumption, this is one of the most significant factors limiting driving distance range. Efficient energy consumption of electric vehicles also supports efforts to reduce CO2 emissions in atmosphere in connection with global warming. High temperature ambient conditions make higher demands to rejects the heat to the ambient, which increases the demand to compressor operating performance. The rejected heat becomes more potential to drive a heat powered cycle to generate additional cooling capacity [1]. In this study a hybrid compressor ejector heat recovery (HCEHR) refrigeration cycle is analyzed which uses R744 as a working fluid with focus to recover heat which is normally rejected by gascooler in typical refrigeration system. The cooling system shown in Fig.1 consists of primary compressor driven loop with integrated secondary ejector cooling loop. It is driven by high temperature heat after the compressor outlet where is transferred from gascooler to generator in the ejector loop, both systems are integrated in one complex loop uses same working fluid. Ejector loop creates additional cooling capacity by heat recovery and this uses to subcool [2] compressor loop gascooler below ambient temperature which allows refrigerant expand to higher liquid content ratio and increases the system cooling capacity. From the point of the ejector loop it allows to pump subcooled refrigerant which minimize demand of pump work and support its efficiency. Primary objective of this concept study is to clarify a possibility for performance improvement of vehicle cooling system with better energy efficiency. A basic principle in this study is using of high enthalpy fluid as a power source to run internal heat recovery system.

Keywords: R744, hybrid, heat recovery, ejector, subcooling, automotive, cooling, supercritical

Introduction/Background

In mobile air conditioning (MAC) and heat pump applications, CO2 systems discharge in the supercritical region and are said to be operate in a transcritical cycle because evaporation is in the subcritical region and heat rejection is in the supercritical region. At high ambient conditions, discharge pressures and temperatures are high, efficiency is reduced and problems with heat transfer at temperatures close to the critical point can be experienced [3].

The process that deviates most from the conventional vapor compression cycle is the supercritical heat rejection process, indicating the temperature glide in the gas cooler. The significantly higher discharge temperature and larger temperature change for CO2 than those for conventional refrigerants at the high pressure region are the most visible differences. In this configuration, high temperature refrigerant leaving the gas cooler is cooled more by additionally utilizing an internal heat exchanger for obtaining sufficient subcooling effect prior to being throttled to the evaporation pressure by an expansion device [4].

An integrated ejector refrigeration loop is proposed to extract heat after the compressor to generate additional cooling capacity uses to subcool the system. Subcooling reduces the

Heat Powered Cycles
Conference 2023
Edinburgh
Heat in the new energy system

3rd to 6th of September 2023
The University of Edinburgh, Scotland

gascooler outlet temperature below the ambient temperature and increases the refrigeration effect.
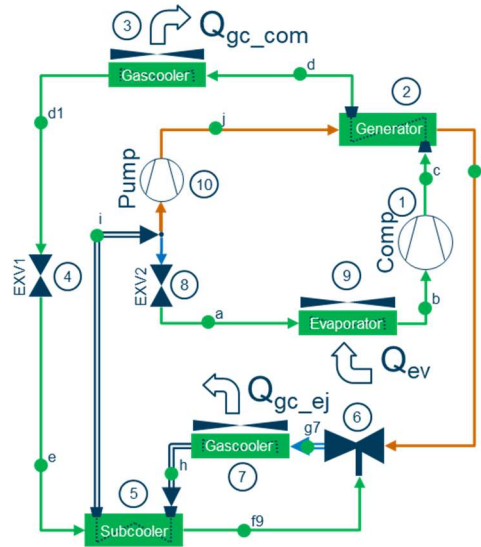
Fig. 1: Schematic of HCEHR cycle

The COP of the system is determined [2, 5] from the first law analysis of the system. It is the ratio of the cooling capacity Q_e to the compressor work input (W_{com}) and the pump work input (W_{pump}). Pump operation is shifted in supercritical gas phase area, but with low energy consumption to pressurize the refrigerant. Even though it is working with fluid in supercritical region it is called as pump (10) in this study.

System description

Schematic of the system is derived from basic compressor cooling cycle and heat driven ejector cycle. Integration both of them into one system is shown on Fig.2.
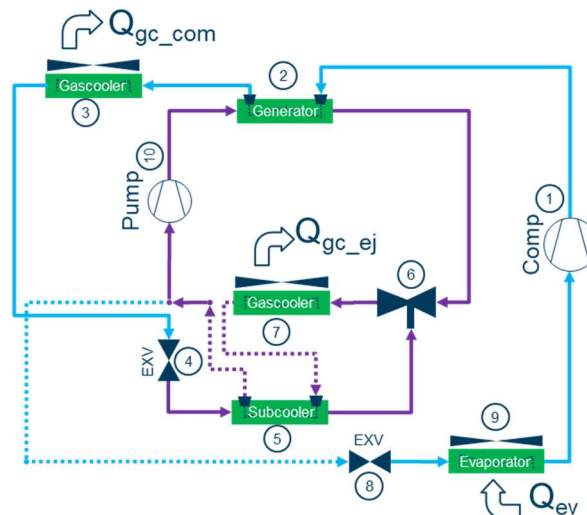
Fig. 2: Schematic of integration compressor and ejector cycle into single system

A compressor cycle colored by blue line consists of basic components as a compressor 1, gascooler 3, expansion valve 8 and evaporator 9. Where the generator 2 of the heat driven cycle shown by purple lines is located in between compressor and gascooler and similarly subcooler 5 between gascooler 7 and expansion valve 4. Generator together with subcooler are heat exchange components between compressor and ejector cooling loop. The heat driven ejector cycle consists with additional components as pump 10, ejector 6, gascooler 7 and expansion valve 4.

While the generator and subcooler ensure heat exchange between both loops, the switching of expansion valves shown by blue dashed line merge them into one system. This integration allows direct mass flow and pressure interaction between compressor and ejector cycle.
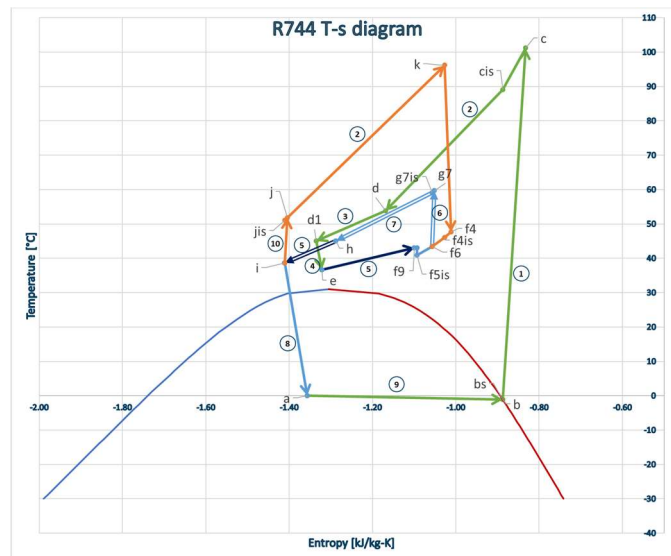
Fig. 3: T-s diagram of HCEHR cycle
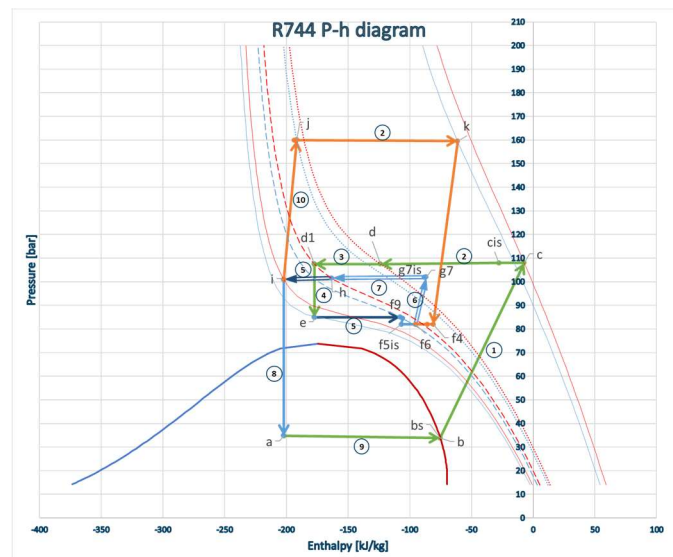
Fig. 4: P-h diagram of HCEHR cycle

Working principle of complete system with related temperatures is shown on T-s diagram Fig.3. It is defined for evaporation temperature 0°C and gascooler outlet temperature 45°C on refrigerant side. Compressor part of system shown by green lines is merged with ejector part through its suction port to expansion valve shown by blue lines. Finally, the motion nozzle of ejector loop part run by pump shown by orange lines closes the cycle.

P-h diagram on Fig.4 shows pressure profiles related to enthalpies of each part described above and differentiated by same line colors. Refrigerant enters evaporator at state point (a) and vaporizes by absorbing heat while cooling down the passenger cabin air. It leaves evaporator at state point (b) as dry saturated vapor and it is sucked by compressor. Compressed vapor is rejected at the pressure 108 bar and temperature 101°C in point (c) to generator. Heat is transferred in the generator from compressor part to ejector loop of system and the temperature of refrigerant decreases to point (d) at the outlet of generator. Next the refrigerant temperature is decreasing to ambient to state point (d_1) in gascooler which releases excess heat from system to ambient air. From this point is the refrigerant expanded through first expansion valve to the pressure of point (e) and concurrently temperature drops to corresponding value and enters the subcooler. Refrigerant at this state point allows to obtain additional cooling capacity when is sucked by ejector through subcooler to ejector suction port. This cooling capacity has good potential for use in the internal heat exchange of the system by absorbing heat after ejector loop gascooler. Despite the previous expansion process, the refrigerant state is still in supercritical region and subcooler thus works only with the gaseous state of the working fluid. Its temperature increases to state point (f_9) and enters the suction port of ejector as a secondary stream. Now the process run in ejector where occurs small expansion of fluid in suction nozzle to point (f_{5is}) and consequently enters mixing chamber where is mixed with primary stream in state point (f_6) and undergo a pressure recovery process in diffuser to point (g_7). After exiting of ejector, the fluid enters primary gascooler where all the heat is rejected to the ambient air and fluid temperature drops close to ambient at 45°C in point (h). Subsequently it flows again to subcooler in counterflow direction where it is cooled down and exits to point (i). Subcooling of working fluid allows its next expansion with higher liquid content ratio in point (a) which improves cooling capacity and at same time it supports efficiency of ejector loop when compressing of colder refrigerant to point (j) is less energy demanding. As is obvious the refrigerant mass flow splits in point (i) in between compressor cooling loop and ejector loop with ratio 1.27. Refrigerant enters generator at point (j) and absorbs heat from compressor loop before entering ejector motive nozzle in state point (k). It recovers portion of heat normally rejected by gascooler by expanding in ejector motive nozzle to run an internal heat driven cooling loop and support internal heat exchange to improve overall cooling performance of system.

Thermodynamic analysis

Cycle energy balance analysis

Thermodynamic analysis of the cycle comes from five balance equations. The objective of the first step is to determine mass flow rate m_{gen} of ejector motive loop. For this we will assume a known mass flow rate of compressor loop $m_{com.}$ Next assumptions are related to ambient temperature with supposed outlet refrigerant temperature from gascoolers. All the balance is correlated with ejector mass, momentum and energy conservation. For the overall cycle prediction is supposed isentropic expansion of motive stream in primary nozzle with efficiency 0.8 and isentropic compression of mixture flow in diffuser with same efficiency.

Heat Powered Cycles
Conference 2023
Edinburgh

Heat in the new energy system

3rd to 6th of September 2023
The University of Edinburgh, Scotland

Mixing enthalpy of fluid is based on energy difference of motive and secondary stream just before entering mixing chamber in ejector.

$$\Delta H_m = \Delta H_s \tag{1}$$

After substitution of individual enthalpies is as follows,

$$(h_{f4} - h_{f6})m_{gen} = (h_{f6} - h_{f5is})m_{com} \tag{2}$$

This is in relation with isentropic expansion $\Delta h_{ej\_ex\_is}$ with initial efficiency 0.8.

$$\Delta h_{ej\_ex} = \Delta h_{ej\_ex\_is} * \eta_{ej\_ex\_is} \tag{3}$$

In which enthalpy f$_4$ of exit motive streams is determined from,

$$(h_k - h_{f4}) = (h_k - h_{f4is})\eta_{ej\_ex\_is} \tag{4}$$

Energy balance of motive nozzle expansion and compression of ejector diffuser is defined as,

$$\Delta H_{ej\_ex} = \Delta H_{ej\_comp} \tag{5}$$

This is expressed by enthalpy change with related mass flow in nozzle and diffuser as follows,

$$(h_k - h_{f4})m_{gen} = (h_{g7} - h_{f6})(m_{gen} + m_{com}) \tag{6}$$

Where compressed flow exiting of ejector diffuser is defined based on isentropic compression with initial efficiency 0.8.

$$\Delta h_{ej\_comp} = \frac{\Delta h_{ej\_comp\_is}}{\eta_{ej\_comp\_is}} \tag{7}$$

After substitution, the enthalpy g$_7$ at the ejector diffuser outlet is determined from,

$$(h_{g7} - h_{f6}) = \frac{(h_{g7is} - h_{f6})}{\eta_{ej\_comp\_is}} \tag{8}$$

Analysis of overall energy balance of complete cooling cycle is done with assumptions that all of the cooling capacity of ejector loop is used to internal heat exchange,

$$Q_{ej\_ev} = Q_{subc} \tag{9}$$

$$(h_{f9} - h_e)m_{com} = (h_h - h_i)(m_{gen} + m_{com}) \tag{10}$$

and generator absorbs the necessary heat to run the motive flow from compressor loop discharge by internal heat exchange.

$$Q_{gc\_gen} = Q_{gen} \tag{11}$$

$$(h_c - h_d)m_{com} = (h_k - h_j)m_{gen} \tag{12}$$

So, input energy to the cycle consists of evaporator cooling capacity of compressor loop, compressor work and pump to run the ejector loop. This is balanced with heat rejection by gascoolers after compressor and ejector.

$$Q_{ev} + W_{com} + W_{pump} = Q_{gc\_com} + Q_{gc\_ej} \tag{13}$$

Detailed breakdown of the equation to see all the enthalpies entering the energy balance is following:

$$(h_b - h_a)m_{com} + (h_c - h_b)m_{com} + (h_j - h_i)m_{gen} \tag{14}$$
$$= (h_d - h_{d1})m_{com} + (h_{g7} - h_h)(m_{gen} + m_{com})$$

COP of the system

The coefficient of performance COP of the system is defined as ratio of overall cooling capacity to all energy inputs. The energy input of compressor loop consists from evaporator heat input and power consumption of compressor. Ejector loop primary drive energy is heat absorbed by generator and secondary power consumed by compressor/pump. Considering the heat is extracting by generator after compressor, it is not included into input of system because it's part of internal energy. Final COP is then defined as a ratio of evaporator cooling capacity to power input of compressor and pump.

$$COP = \frac{Q_{ev}}{W_{com} + W_{pump}} \tag{15}$$

Implementation of Internal heat exchanger

Internal heat exchanger (IHX) is common component in system using R744 as a working fluid. It has significant effect on COP improvement with low impact on complexity of the system. It is also easily applying in the HCEHR cycle as it is shown on Fig. 5. The IHX (3') is located after generator in the HCEHR cycle in compressor loop where replaces secondary gascooler.
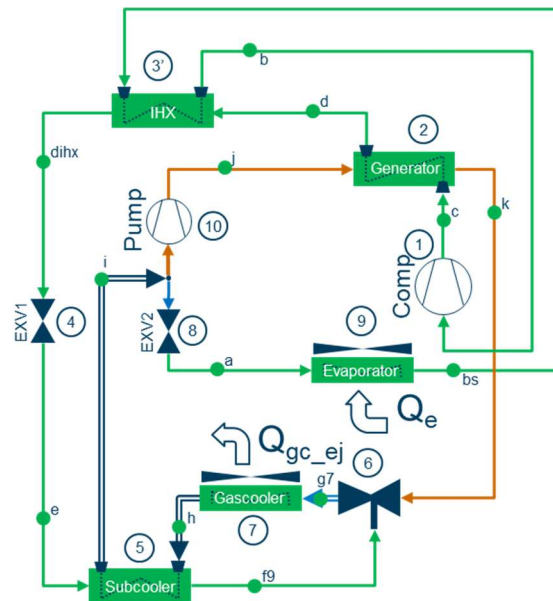
Fig. 5: Schematic of HCEHR cycle with integration of IHX

Its performance is expressed by the following enthalpic balance equation based on equilibrium of absorbed heat before compressor suction and heat extracted at the secondary gascooler location after generator where mass flow both sides is equal.

$$\Delta h_{ihx\_com} = \Delta h_{ihx\_gc} \tag{16}$$

Detailed enthalpic breakdown is following,

$$(h_b - h_{bs}) = (h_d - h_{dihx}) \tag{17}$$

Comparison of both system without and with IHX in T-s diagram is shown on Fig. 6.
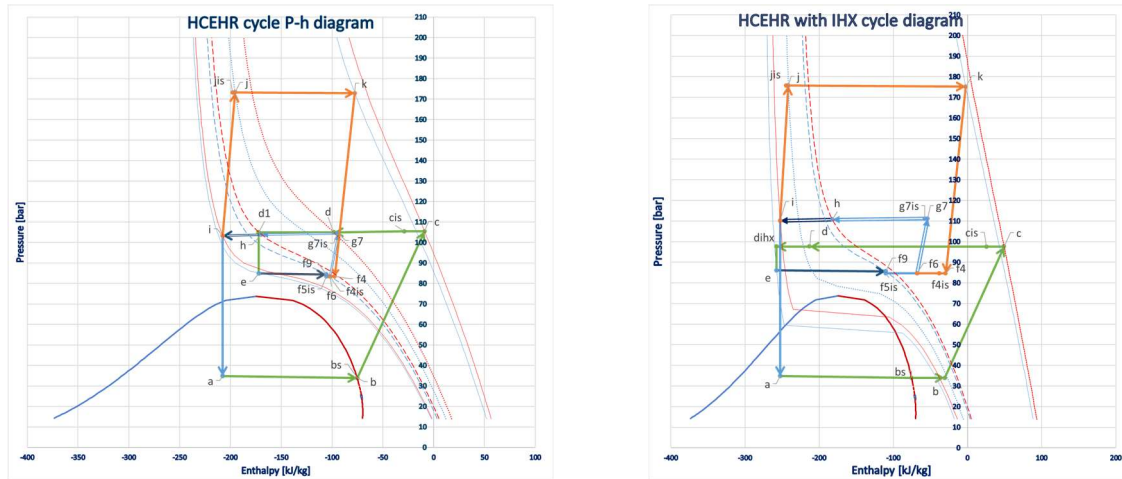
Fig. 6: P-h diagrams of HCEHR cycle without (left) and with (right) integration of IHX

Despite the fact that integration of ejector loop is focused to maximize internal heat exchange and recovery, the IHX still can be applicated. This option was investigated how it can improve cooling capacity of subcooler and COP of system.

Ejector performance analysis

The design of ejector can be categorized into 2 different designs based on the position of nozzle, the nozzle exit which is situated in the constant mixing area section is known as "constant area mixing ejector" and on the other hand if the nozzle exit is with in the suction chamber is known as "constant pressure mixing ejector" [7]. In constant pressure mixing ejector model the assumption is made as follows the primary and secondary streams mix at constant pressure [8]. For this research 1D ejector model which was introduced by [6].
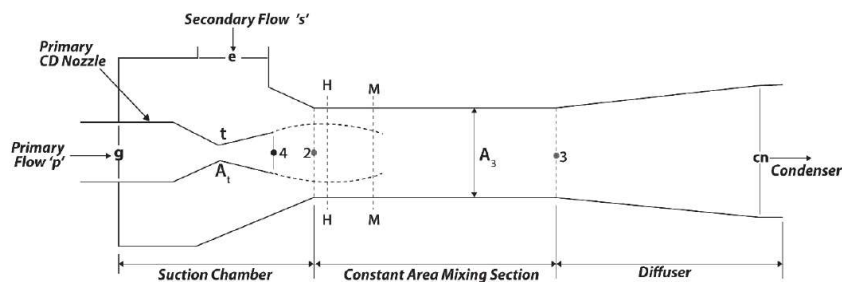
Ejector schematic diagram [9]

Heat Powered Cycles
Conference 2023
Edinburgh

Heat in the new energy system

3rd to 6th of September 2023
The University of Edinburgh, Scotland

For the analyzation following assumptions are to be made:

1. The working fluid is an ideal gas with constant C_p and γ.
2. The flow inside the ejector has to be steady state flow.
3. The kinetic energy has to be negligible at primary & suction inlets and the diffuser exit.
4. The isentropic relations are used. But for non-ideal process, the effects of frictional and mixing losses are considered by using some coefficients introduced in the isentropic relations. These coefficients are related to the isentropic efficiency and needs to be determined experimentally [7].
5. After exiting from the nozzle, the primary stream flows without mixing with the suction stream until cross section H-H which is a hypothetical throat.
6. Both streams will be mixed at the cross-section H-H (hypothetical throat) with constant pressure ($P_m = P_{pH} = P_{sH}$).
7. At the cross-section H-H (hypothetical throat) the entrained flow is chocked ($M_{sH}=1$).
8. The wall of ejector is adiabatic.

Primary flow through the nozzle:

According to isentropic relations with respect to nozzle flow for given inlet stagnation qualities (pressure P_g & temperature T_g), the chocked mass flow rate through the nozzle is given as:

$$\dot{m}_p = \frac{P_g A_t}{\sqrt{T_g}} \sqrt{\frac{\gamma}{R}\left(\frac{2}{\gamma+1}\right)^{\frac{(\gamma+1)}{(\gamma-1)}}} \sqrt{\eta_p} \tag{18}$$

η_s = isentropic efficiency of primary flow

By application of Area Mach number relation from the isentropic relations to obtain Mach number at the exit of the nozzle M_{p4} and the exit pressure P_{p4}.

$$\frac{A_{p4}}{A_t} = \frac{1}{M_{p4}^2}\left[\frac{2}{\gamma+1}\left(1 + \frac{\gamma-1}{2}M_{p4}^2\right)\right]^{\frac{\gamma+1}{\gamma-1}} \tag{19}$$

$$\frac{P_g}{P_{p4}} = \left[1 + \frac{\gamma-1}{2}M_{p4}^2\right]^{\frac{\gamma}{\gamma-1}} \tag{20}$$

Primary flow from section 4-4 to section H-H:

The Mach number M_{pH} is calculated by following isentropic relation at section H-H:

$$\frac{P_{sH}}{P_{p4}} = \frac{\left[1 + \frac{\gamma-1}{2}M_{p4}^2\right]^{\frac{\gamma}{\gamma-1}}}{\left[1 + \frac{\gamma-1}{2}M_{pH}^2\right]^{\frac{\gamma}{\gamma-1}}} \tag{21}$$

Heat Powered Cycles
Conference 2023
Edinburgh

Heat in the new energy system

3rd to 6th of September 2023
The University of Edinburgh, Scotland

For the calculation of area of the primary stream at the section H-H (A_{pH}), the following isentropic relation is used with an arbitrary coefficient φ_p (isentropic coefficient) [9] is included into the equation for the loss of the primary flow from section 4-4 to H-H.

$$\frac{A_{pH}}{A_{p4}} = \frac{\left(\frac{\varphi_p}{M_{pH}}\right)\left[\frac{2}{\gamma + 1}\left(1 + \frac{\gamma - 1}{2}M_{pH}^2\right)\right]^{\frac{\gamma+1}{2(\gamma-1)}}}{\left(\frac{1}{M_{p4}}\right)\left[\frac{2}{\gamma + 1}\left(1 + \frac{\gamma - 1}{2}M_{p4}^2\right)\right]^{\frac{\gamma+1}{2(\gamma-1)}}} \tag{22}$$

Secondary flow from inlet to section H-H:

For given inlet stagnant pressure P_e, the secondary flow reaches to the chocking condition $(M_{sH}) = 1$

$$P_{sH} = \frac{P_e}{\left(1 + \frac{\gamma - 1}{2}M_{sH}^2\right)^{\frac{\gamma}{\gamma-1}}} \tag{23}$$

Secondary mass flow rate at chocking conditions is

$$\dot{m}_s = \frac{P_e A_{sH}}{\sqrt{T_e}}\sqrt{\frac{\gamma}{R}\left(\frac{2}{\gamma + 1}\right)^{\frac{(\gamma+1)}{(\gamma-1)}}}\sqrt{\eta_s} \tag{24}$$

$\eta_s = $ isentropic efficiency of secondary flow

Cross section area at section H-H:

The sum of primary flow cross section area and the secondary flow cross section area is the cross sectional at section H-H which is area of constant area mixing chamber (A_3).

$$A_3 = A_{pH} + A_{sH} \tag{25}$$

Temperatures at section H-H:

The equations for primary and secondary streams at section H-H, with respect to temperatures are as follows

$$\frac{T_g}{T_{pH}} = 1 + \frac{\gamma - 1}{2}M_{pH}^2 \tag{26}$$

$$\frac{T_e}{T_{sH}} = 1 + \frac{\gamma - 1}{2}M_{sH}^2 \tag{27}$$

Mixed stream at section m-m:

According to momentum balance relation

$$\varphi_m\left[\dot{m}_p V_{pH} + \dot{m}_s V_{sH}\right] = \left(\dot{m}_p + \dot{m}_s\right)V_m \tag{28}$$

$\varphi_m = $ mixed flow friction loss coefficient [10].

V_{pH} & V_{sH} are the gas velocities of the primary and secondary flows at section H-H, they are obtained followingly

Heat Powered Cycles
Conference 2023
Edinburgh

Heat in the new energy system

3rd to 6th of September 2023
The University of Edinburgh, Scotland

$$V_{pH} = M_{pH} a_{pH} \qquad (29) \qquad\qquad a_{pH} = \sqrt{\gamma R T_{pH}} \qquad (30)$$

$$V_{sH} = M_{sH} a_{sH} \qquad (31) \qquad\qquad a_{sH} = \sqrt{\gamma R T_{sH}} \qquad (32)$$

From energy balance equation

$$\dot{m}_p \left(C_p T_{pH} + \frac{V_{pH}^2}{2} \right) + \dot{m}_s \left(C_p T_{sH} + \frac{V_{sH}^2}{2} \right) = (\dot{m}_p + \dot{m}_s)\left(C_p T_m + \frac{V_m^2}{2} \right) \qquad (33)$$

The Mach number of mixed flow is calculated as follows

$$M_m = \frac{V_m}{a_m} \qquad (34) \qquad\qquad a_m = \sqrt{\gamma R T_m} \qquad (35)$$

The pressure P$_3$ & Mach number M$_3$ inside the constant area mixing section is solved as follows

$$\frac{P_3}{P_m} = 1 + \frac{2\gamma}{\gamma + 1}(M_m^2 - 1) \qquad (36)$$

According to assumption 6 $P_m = P_{pH} = P_{sH}$

$$M_3 = \sqrt{\frac{1 + \left(\frac{\gamma - 1}{2}\right) M_m^2}{\gamma M_m^2 - \left(\frac{\gamma - 1}{2}\right)}} \qquad (37)$$

Mixed flow through the diffuser:
The equation for the pressure at exit of diffuser is

$$P_{Cn} = P_3 \left(1 + \left(\frac{\gamma + 1}{2}\right) M_3^2 \right)^{\frac{\gamma}{\gamma - 1}} \qquad (38)$$

Discussion and Results

System performance results

A 1-D simulation [6] of final cycle was performed for high temperature ambient conditions. The default outlet temperature for primary and secondary gascooler was determined to 45°C and for the evaporator inlet temperature 0°C. The results show positive effect of subcooling the system below ambient temperature on COP. They were compared with typical compressor cooling system with internal heat exchanger (IHX) of 70% efficiency. Final results of HCEHR cycle COP shows optimum value 1.76 compared to 1.67 of typical system. This represents 5.19% of improvement. The same condition setting was used for simulation of HCEHR cycle with integrated IHX. It shows COP 1.92 which is 14.72% of improvement compared to typical system. A similar trend of results is observable for compressor discharge pressure, where the optimal pressure is lower for HCEHR cycle and it drops down more with integration of IHX.

All off the cycles were subsequently analyzed for gascooler discharge temperatures 50°C, 40°C and 35°C which is shown on Fig.7. The basic HCEHR cycle displayed by blue line slightly improves COP along the line of typical cycle with gascooler exit temperature decreasing. Consequently, the simulation of cycle HCEHR with integrated IHX displayed by purple line shows significantly increasing trend of COP improvement with gascooler exit temperature decreasing comparing to typical cycle. It reaches maximum COP improvement at the lowest simulated outlet gascooler temperature 35°C and 0°C evaporation temperature where it is 3.46 compared to 2.43 of typical system which represents 42.43% of improvement. IHX in cycle improves cooling capacity of subcooler which reduces gascooler outlet temperature. This simultaneously increases heat capacity of generator by lowering inlet temperature which consequently results also in lower IHX inlet temperature which leads to higher evaporator performance and COP.
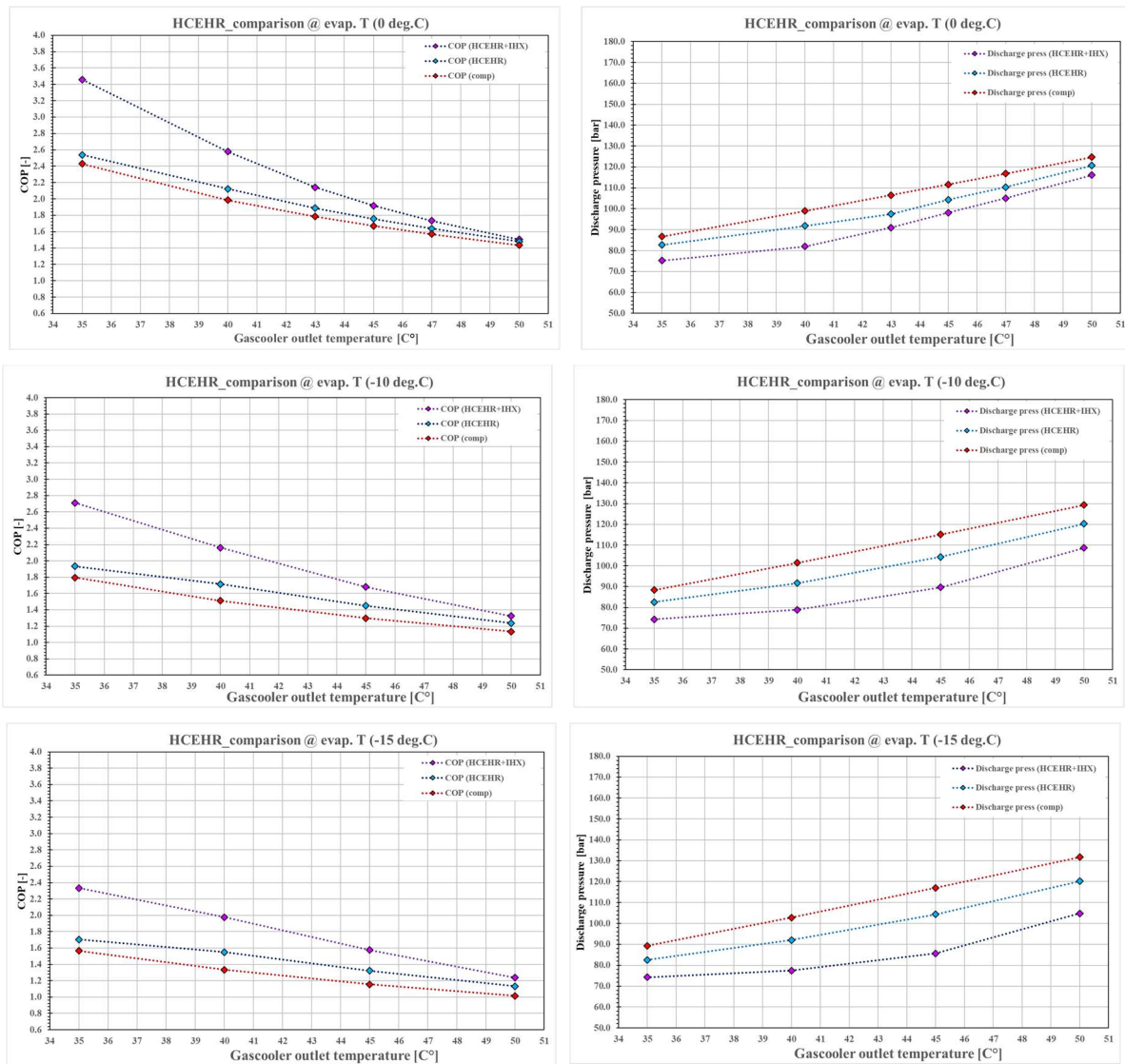
Fig. 7: Comparison of HCEHR cycle COP (left) and compressor discharge pressure (right) at 0°C, -10°C and -15°C evaporation temperature and 35°C, 40°C, 45°C and 50°C gascooler outlet temperature.

Ejector performance results

Analysis of the ejector performance was required from the point of view of verifying the attainability of the required parameters of cycle. This is done based on constant pressure mixing ejector model mentioned in [7] and also described in "Ejector performance analysis" in this article with related assumptions.

The model provides promising results, which can be considered that it is possible to optimize the design of the ejector for the required parameters of the cycle. Results for 1-D ejector model are obtained by varying secondary flow pressure P_e for two different sets of primary flow parameters P_g, T_g which is shown in Fig. 8.

P_g	T_g	P_e	T_e	φ_m	m_s	m_p	P_{Cn}	m_{Cn}
[bar]	[oC]	[bar]	[oC]	-	[kg/sec]	[kg/sec]	[bar]	[kg/sec]
192.28	105	60	38	0.592	0.066	0.06	77.17	0.126
192.28	105	67	38	0.592	0.074	0.06	112.91	0.134
129.3	95	60	38	0.592	0.072	0.044	87.48	0.116
129.3	95	62	38	0.592	0.074	0.044	96.8	0.118

Fig. 8: Table of results based on constant pressure mixing ejector model

Summary/Conclusions

This study presents theoretical investigation of hybrid compressor ejector heat recovery cooling system for automotive application. It shows the possibility of the ejector loop integration into primary compressor cooling system. It allows to work all in one cycle and with the same refrigerant. Based on the results obtained from the 1-D simulation is possible to evaluate different effect of ejector loop on COP at different ambient condition which are represented by gascooler outlet temperature and evaporation temperature. Its improvement declines with increasing ambient temperature and decreasing evaporation temperature. Similar trend can be observed for the compressor discharge pressure decreasing by the ejector loop at different temperatures. Less energy demand of the cooling system has significant effect on range of electric vehicles and it is also positive for overall electric energy consumption. In contrast of that the complexity of new proposed system can make it difficult to run at optimal performance under different conditions. The simulations were done at the theoretical base and needs to be correlated by measurements with respect to real components performance.

Nomenclature

A Area, m^2

a Sonic velocity, m/s

C_p Specific heat of gas at constant pressure, $kJ\ kg^{-1}\ K^{-1}$

C_v Specific heat of gas at constant volume, $kJ\ kg^{-1}\ K^{-1}$

D Diameter, m

M Mach number

$\dot{m}$ Mass flowrate, $kg\ s^{-1}$

P_e Refrigerant pressure at the suction port of the ejector, pa

P_g Refrigerant pressure at the nozzle inlet of the ejector, pa

R Gas constant, $kJkg^{-1}K^{-1}$

T Temperature, K

T_e Refrigerant temperature at the suction port of the ejector, K

T_g Refrigerant temperature at the nozzle inlet of the ejector, K

V Refrigerant velocity, $m\ s^{-1}$

h	Enthalpy, kJ kg^{-1}
ΔH	Energy difference, kJ
γ	Ratio of specific heats, (C_p/C_v)
η	Isentropic efficiency
φ	Coefficient for flow losses

Subscripts

com	Compressor
comp	Ejector compression
C_n	Ejector exit
ej	Ejector
exp	Ejector expansion
ev	evaporator
subc	Subcooler
is	Isentropic
g	Primary nozzle inlet
gen	Generator
m	Ejector motive flow
M	Mixed flow
t	Primary nozzle throat
p4	Primary flow at nozzle exit
pH	Primary flow at hypothetical throat
sH	Entrained flow at hypothetical throat
s	Ejector secondary flow

References:

[1] Giorgio Besagni n, Riccardo Mereu, Fabio Inzoli, *Ejector refrigeration: A comprehensive review,* Elsevier's Renewable and Sustainable Energy Reviews 53, 2016.

[2] Xiangjie Chen, Mark Worall, Siddig Omer, Yuehong Su, Saffa Riffat, *Theoretical studies of a hybrid ejector CO_2 compression cooling system for vehicles and preliminary experimental investigations of an ejector cycle,* Elsevier's Applied Energy 102, 2013.

[3] Stefan Elbel, *Historical and present developments of ejector refrigeration systems with emphasis on transcritical carbon dioxide air-conditioning applications,* Elsevier's International journal of refrigeration 34, 2011.

[4] Sung Chul Kim, Jong Phil Won, Min Soo Kim, *Effects of operating parameters on the performance of a CO2 air conditioning system for vehicles,* Elsevier's Applied Thermal Engineering 29, 2009.

[5] M. Worall, S. Omer and S.B. Riffat, *A hybrid jet-pump CO2 compression system for transport refrigeration,* International Journal of Low-Carbon Technologies 2011.

[6] B.J. Huang, J.M. Chang, C.P. Wang, V.A. Petrenko, *A 1-D analysis of ejector performance,* Elsevier's International Journal of Refrigeration 22, 1999.

[7] D.-W. Sun and I. W. Eames, "Recent developments in the design theories and applications of ejectors," *Journal of the institute of energy ,* Vols. -, p. 16, 1995.

[8] R. Yapıcı and H. Ersoy, "Performance characteristics of the ejector refrigeration system based on the constant area ejector flow model," *Energy Conversion and Management,* pp. 1-20, 2005.

[9] H. A. Muhammad, H. M. Abdullah, Z. Rehman, B. Lee, Y.-J. Baik, J. Cho, M. Imran, M. Masud, M. Saleem and M. S. Butt, "Numerical Modeling of Ejector and Development of Improved Methods for the Design of Ejector-Assisted Refrigeration System," *energies,* pp. 1-19, 2020.

[10] V. J. d. o. marium, in *Efficiency analysis of an incompressible flow ejector using CFD simulations and mathematical modeling ,* Sao Paulo , University of Sao Paulo , 2020, pp. 47 - 48.

Evaluating the Performance of Adsorption Chillers with Water, Methanol, and Ethanol: IR-LTJ Experiments and Model-Based Scale-Up

M. Henninger[1], **D. Tuchlinski**[1], **M. Ismail**[1] , **J. Seiler**[2], and **A. Bardow**[2*]

[1]Institute of Technical Thermodynamics (LTT), RWTH Aachen University, 52062 Aachen, Germany
[2]Energy and Process Systems Engineering (EPSE), ETH Zürich, 8092 Zurich, Switzerland
*Corresponding author: abardow@ethz.ch

Abstract
An efficient workflow is presented to evaluate the performance of adsorption chillers for a wide variety of working fluids. The workflow employs dynamic models parametrized by isobars and Infrared Large-Temperature-Jump (IR-LTJ) experiments. For the studied refrigerants water, methanol, and ethanol, we find that, for an evaporation temperature of 5 °C, methanol is preferred over ethanol with a maximum volumetric cooling power of 265 W/L and a maximum coefficient of performance of 0.44 J/J. When increasing the evaporator temperature to 10 °C, the maximum values for methanol increase to 415 W/L and 0.58 J/J, which is on par with the investigated water adsorption chillers at 10 °C with SG123 and Siogel.

Keywords: Dynamic model, Pareto front, adsorption kinetics, adsorption equilibrium.

Introduction and Background
The performance of adsorption chillers depends on the employed working pair consisting of an adsorbent and a refrigerant. Research on the choice of a working pair, however, often only varies either the refrigerant [1] or the adsorbent [2]. Furthermore, the kinetics (e.g. heat and mass transfer) of the working pair are often neglected. However, only considering thermodynamic equilibrium properties is insufficient to assess the process performance [3,4]. Here, we propose an efficient workflow to evaluate the performance of adsorption chillers with the promising working pairs Siogel/water [3], SG123/water [5], CarboTech A35/methanol [2], and CarboTech A35/ethanol: Siogel is a well-studied benchmark silica gel [3,6] provided by Oker Chemie, SG123 was the silica gel commercially used in adsorption chillers by the InvenSor GmbH [5], and CarboTech A35 had the highest volumetric uptake, bulk density, and surface area in a comparative study between activated carbons [2].

Two temperature triples are studied. The adsorption chillers are compared using dynamic models in Modelica [7], based on equilibrium and kinetic properties from small-scale experiments: Heat and mass transfer coefficients of mono-layer adsorbent samples were determined using the IR-LTJ experiment [8] and inserted into a dynamic two-bed adsorption chiller model. The adsorbers of the dynamic model are commonly used lamella heat exchangers with parametrization from Kummer et al. [9] while evaporator and condenser are modelled as ideal. The performance is then evaluated using two competing performance indicators: The volumetric cooling power (VCP) which can be written as

$$\text{VCP} = \frac{\int_0^{\tau_{\text{cycle}}} \dot{Q}_{\text{Evaporation}} \, \mathrm{d}t}{V_{\text{Adsorber}} \cdot \tau_{\text{cycle}}} \qquad (1)$$

where the cooling power $\dot{Q}_{\text{Evaporator}}$ is averaged over the full cycle time τ_{cycle} and related to the adsorber volume V_{Adsorber}. The cycle time τ_{cycle} is defined as the timespan to complete

both a full adsorption and desorption phase in the two adsorbers. Furthermore, the coefficient of performance (COP) is defined according to

$$\text{COP} = \frac{\int_0^{\tau_{\text{cycle}}} \dot{Q}_{\text{Evaporation}} \, dt}{\int_0^{\tau_{\text{cycle}}} \dot{Q}_{\text{Desorption}} \, dt} \tag{2}$$

where the cooling power is integrated over time and put in relation to the required integrated power for regeneration $\dot{Q}_{\text{Desorption}}$. A trade-off exists between VCP and COP regarding the cycle time: While small cycle times maximize the VCP (because of the cycle time in the denominator) and minimize the COP (because of a small integration interval), large cycle times lead to the opposite result. Therefore, we varied the cycle time in our dynamic models for all investigated working pairs, resulting in Pareto fronts, which enable a comprehensive comparison of the working pairs' performance in an adsorption chiller.

Discussion and Results

The two investigated temperature triples are 10/30/80 °C and -5/25/80 °C for evaporator, condenser/adsorber, and desorber respectively. For 10/30/80 °C (Figure 1), Siogel/water has the maximum volumetric power density VCP with 557 W/L while SG123/water has the maximum COP with a value of 0.62 J/J. Furthermore, the methanol adsorption chiller with CarboTech A35 can compete with both water adsorption chillers and even outperforms the commonly used working pair SG123/water with regard to VCP: CarboTech A35/methanol has a maximal VCP of 415 W/L compared to 349W/L for SG123/water while having the same maximal COP as Siogel/water. Water and methanol dominate ethanol regarding both COP and VCP.
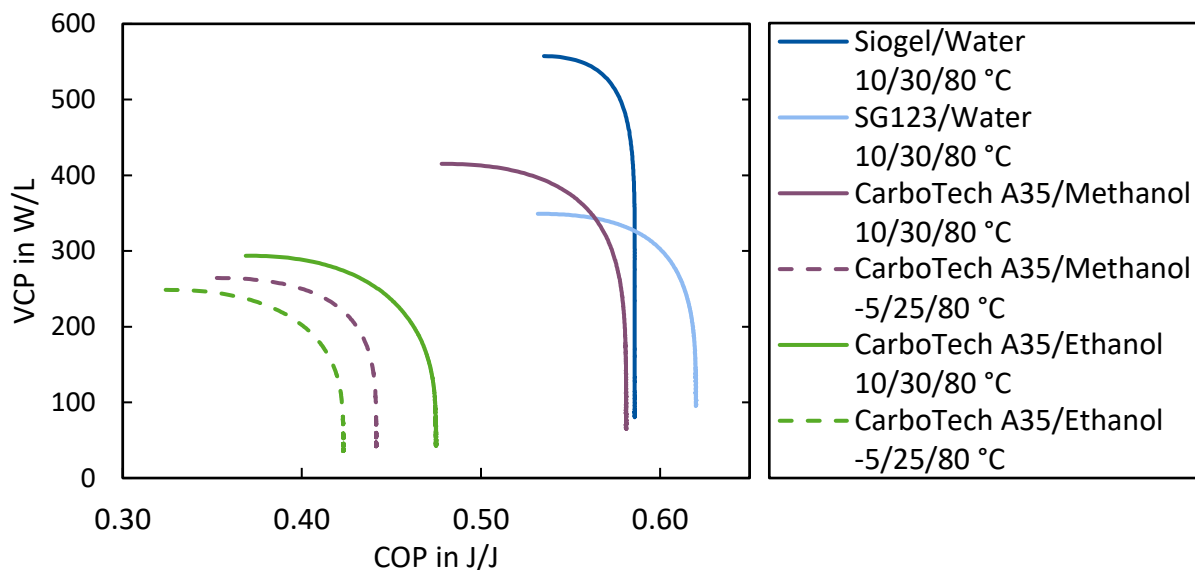
Figure 1: Pareto fronts of power density VCP (Equation (1)) over coefficient of performance COP (Equation (2)) for the refrigerants water (blue), methanol (purple), and ethanol (green) with varying adsorbents Siogel, SG123, and CarboTech A35. Pareto fronts for the temperature triple 10/30/80 °C (solid lines) and for 5/25 /80 °C (dashed lines).

For the temperature triple -5/25/80 °C, the performance of methanol and ethanol decreases for both performance indicators compared to 10/30/80 °C, as expected, due to the lower driving forces. Nevertheless, COPs above 0.4 J/J are still possible for a lower condenser temperature of 25 °C (Figure 1). The maximum VCP decreases by 36 % from 415 W/L to 264 W/L for

methanol and by 15 % from 294 W/L to 249 W/m³ for ethanol. The performance decreases less for ethanol than for methanol compared to the temperature triple 10/30/80 °C since the equilibrium properties of CarboTech A35/ethanol allow for a more flexible operation: While COPs and VCPs are higher with methanol, a lower chilling temperature affects the methanol working pair more than with ethanol as a refrigerant. Further analysis showed that the temperature dependence of the heat and mass transfer coefficients played a minor role compared to the decrease in driving force from the shift in the equilibrium.

Summary and Conclusions

A workflow was presented and employed to assess the performance of adsorption chillers with water, ethanol, and methanol as refrigerants with respect to the volumetric cooling power (VCP) and the coefficient of performance (COP) by evaluating Pareto fronts of each working pair with dynamic models in Modelica. We found that, at a chilling temperature of 10 °C, the working pair CarboTech A35/methanol outperformed CarboTech A35/ethanol. CarboTech A35/methanol could also compete with the investigated water working pairs with regard to COP, but still lacked in VCP when compared to the best water working pair, which was Siogel/water. When decreasing the chilling temperature to -5 °C, the condenser temperature needed to be decreased by 5 K, to still achieve COPs above 0.4 J/J. Methanol was still the preferred refrigerant over ethanol for a chilling temperature of -5 °C, although by a much smaller margin than for 10 °C.

Our study is the first to compare the three most common refrigerants for adsorption chillers with varying working pairs and temperature boundaries based on LTJ experiments including a model-based scale-up. Furthermore, we showed that methanol adsorption chillers can in fact compete with water adsorption chillers when chilling above 0 °C while also providing the possibility to chill below 0 °C.

Acknowledgments

References

[1] D.B. Boman, D.C. Hoysall, D.G. Pahinkar, M.J. Ponkala, S. Garimella, Screening of working pairs for adsorption heat pumps based on thermodynamic and transport characteristics, Appl. Therm. Eng. 123 (2017) 422–434.

[2] S.K. Henninger, M. Schicktanz, P.P.C. Hügenell, H. Sievers, H.-M. Henning, Evaluation of methanol adsorption on activated carbons for thermally driven chillers part I: Thermophysical characterisation, International Journal of Refrigeration 35 (2012) 543–553.

[3] S. Graf, F. Redder, U. Bau, M. de Lange, F. Kapteijn, A. Bardow, Toward Optimal Metal-Organic Frameworks for Adsorption Chillers: Insights from the Scale-Up of MIL-101(Cr) and NH2-MIL-125, Energy Technol. 341 (2019) 1900617.

[4] X. Liu, X. Wang, F. Kapteijn, Water and Metal–Organic Frameworks: From Interaction toward Utilization, Chem. Rev. 120 (2020) 8303–8377.

[5] Green Cooling Initiatives, InvenSor GmbH, https://www.green-cooling-initiative.org/network/member/invensor-gmbh.

[6] A. Sapienza, A. Velte, I. Girnik, A. Frazzica, G. Füldner, L. Schnabel, Y. Aristov, "Water - Silica Siogel" working pair for adsorption chillers: Adsorption equilibrium and dynamics, Renewable Energy 110 (2017) 40–46.

[7] Modelica Association, Modelica - A Unified Object-Oriented Language for Systems Modelling, Language Specification Version 4.0

https://doc.modelica.org/Modelica%204.0.0/Resources/helpDymola/Modelica_UsersGuide_ReleaseNotes.html#Modelica.UsersGuide.ReleaseNotes.Version_4_0_0 (2020).

[8] S. Graf, F. Lanzerath, A. Bardow, The IR-Large-Temperature-Jump method: Determining heat and mass transfer coefficients for adsorptive heat transformers, Appl. Therm. Eng. 126 (2017) 630–642.

[9] H. Kummer, F. Jeremias, A. Warlo, G. Füldner, D. Fröhlich, C. Janiak, R. Gläser, S.K. Henninger, A Functional Full-Scale Heat Exchanger Coated with Aluminum Fumarate Metal–Organic Framework for Adsorption Heat Transformation, Ind. Eng. Chem. Res. 56 (2017) 8393–8398.

Thermal-driven water production using sorbent-coated adsorber

Yaohui Feng[1], and Tianshu Ge[1*]

[1]Insititute of Refrigeration and Cryogenics, Shanghai Jiao Tong University, Shanghai, 200240, China

[*]Corresponding author: baby_wo@sjtu.edu.cn (T.G.)

Abstract

Sorption-based atmospheric water harvesting (SAWH) provides a fruitful solution to the global water crisis. Even though great progress has been made, improving water productivity and lowering energy consumption remain a challenge. Herein, we report an engineering design of SAWH using sorbent-coated adsorber with cooling-assisted sorption, thermal-driven desorption, and ambient-based dewing processes. Benefiting from the lower adsorption temperature, the enhancement of water productivity was more obvious compared with providing a higher desorption temperature and lower condensation temperature. The results suggested that introducing a cooling source in the adsorption stage will contribute to the 1.84-8.30 times improvement of water productivity compared with that without a cooling source at 25°C/60%RH. By utilizing the waste cooling energy in the condensation process, the sorbent can be regenerated by low-grade thermal energy with the range of 45-62°C, providing great potential for thermal-driven water production.

Keywords: Atmospheric water harvesting, Sorption, Cooling source, sorbent-coated adsorber.

Introduction

Water scarcity threatens global sustainable development[1]. It was predicted that more than 2/3 global population will face water shortage problems by 2050[2]. Thus, seeking a clean, sustainable, accessible water production technology is imperative and has been extensively explored by scientific and engineering communities[3]. Although desalination has been regarded as an effective water solution, the requirement of auxiliary equipment and high operational cost limited its development, especially for remote and arid regions[4]. It also was ignored that the atmosphere is a huge water container. More than 13 trillion kilolitres of water existed in the atmosphere, around six times of water content in total rivers[5]. Dewing, fogging and sorption are the three main methods for harvesting water from the air. Among them, sorption-based atmospheric water harvesting (SAWH) deems to be the only way in the arid area[6].

Over the past five years, SAWH obtained enormous attention from all over the world arising from the development of materials science[7–9]. Different from traditional desiccants (such as silica gel and zeolite), the tailored porous structure and the high-water sorption capacity of metal-organic frameworks (MOFs) are promising for water harvesting in the arid area[10]. Besides, the hydrogel and composite sorbent also received overwhelming interest[9,11]. However, it can be found that even if the properties of sorbents are exceptional with high working capacity and low regeneration temperature, the improvement of practical water productivity is limited. The basic reason behind this problem is the lack of a well-designed AWH device. Recently, although the device design obtained attention, such as dual-stage AWH[12], advanced heat transfer design and thermal management[5,13], the total daily yield

still cannot meet the practical demands[14]. The design of AWH needs reconsideration from the basic thermodynamic principle.

A typical AWH process includes the sorption, desorption and condensation processes. Atmospheric moisture is captured by the porous sorbent driven by the humidity difference between the ambient air and pores of sorbents. When the sorbent is saturated with moisture, the heating-powered desorption is trigged by low-grade thermal energy like solar energy, and then the moisture is released, condensed and collected. Almost all designs only consider the importance of desorption temperature and condensation process, but the potentials in the sorption process are not sufficiently tapped[15]. For most sorbents, the sorption capacity tightly depends on the ambient humidity. Followed by the temperature-humidity relationship, introducing cooling in the adsorption stage will contribute to the improvement of relative humidity (RH), thus the sorption capacity can be dramatically promoted[16,17].

In this paper, we report a design of AWH with cooling-assisted adsorption, thermal-driven desorption, and air-cooled dewing processes. The basic principles of the water harvesting device and cooling effect are revealed. Compared with increasing the heating temperature and reducing condensation temperature, introducing cooling into the sorption stage will bring benefits to water harvesting. As a result, the water sorption capacity can be enhanced dramatically and the water production rate is up to 95.1 g/h, which shows 96.1% promotion compared with that in the control case.

Discussion and Results

The basic configuration of SAWH is illuminated in Figure 1. The water harvester consists of three main parts, adsorber units, water bath units, and condenser. The adsorber units are fabricated using two identical adsorbers by coating sorbents on the heat exchanger. Two water baths were used to simulate the heating and cooling source. The cooling and heating temperature of the water can be controlled by the water baths and then flowed into the inner side of copper cubes of adsorbers. Two four-way valves (or one eight-way valve) are employed to switch the sorption and desorption stages. For air side, ambient air flows into the adsorber with a cooling temperature and the moisture was captured by the sorbents. On the desorption side, the air flows to the desorber and was humidified and heated. The high humidity and temperature air pass through the air-cooled condenser and then back to the desorber, forming a closed loop. The cooling and dry air after sorption was exchanged with desorption air to further reduce the condensation temperature. Two air valves were assembled to switch the airflow to release the water continuously.
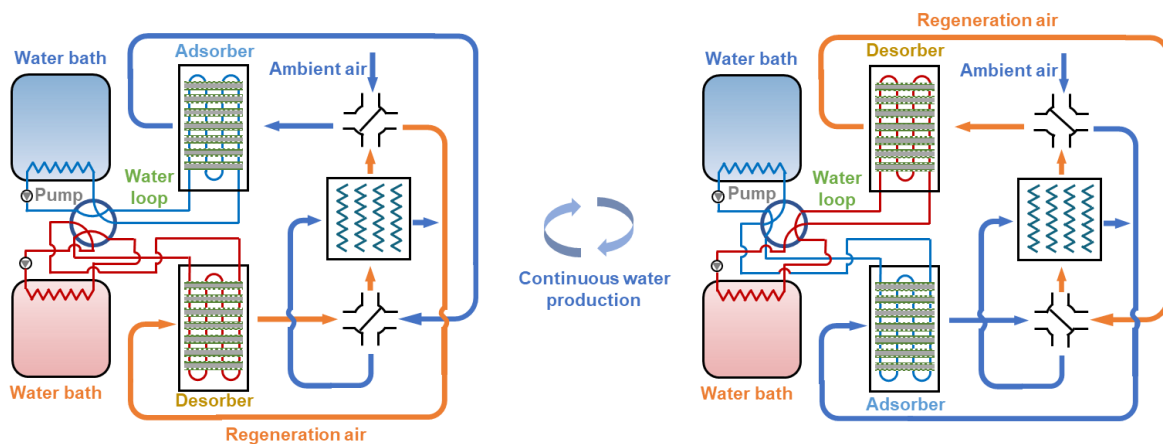
Figure 1. Experimental setup of water harvesting using sorbent-coated adsorber.

Heat Powered Cycles
Conference 2023
Edinburgh

Heat in the new energy system

3rd to 6th of September 2023
The University of Edinburgh, Scotland

Silica gel was used as the sorbent and then coated on the surface of heat exchangers by spraying methods, and its water sorption isotherms and images can be found in Figure 2a. The isotherm shape of silica gel was similarly S shape, and its water sorption capacities are around 0.06 g/g, 0.15 g/g, and 0.21 g/g at 50%RH, 70%RH, and 90%RH with the temperature of 20°C, respectively. Although the water uptake is limited at low humidity, it can be improved by the cooling effect due to the increased local humidity. The relative pressure at different temperatures can be transferred to the absolute water vapor pressure, as shown in Figure 2b. From the water sorption curves, the working capacity of the sorbent can be determined. For instance, the water uptake is ΔW_d when sorption, desorption and condensation temperature are respective 25°C, 45°C and 25°C. Traditionally, increasing the heating temperature for desorption and reducing the cooling temperature for condensation are common approaches for improving water productivity. However, the improvements using the above methods are limited. As indicated in Figure 2b, when increasing the desorption temperature at 54°C and decreasing the condensation temperature at 20°C, the working capacities are enhanced to $\Delta W_{d,h}$ and $\Delta W_{d,c}$, respectively. Interestingly, lowering the sorption temperature at 20°C contributes to the significant improvement of working capacity to $\Delta W_{d,a}$. That is the design principle of this work. In addition, the waste cooling energy from the sorption stage can be further harnessed to cool the desorption airflow, providing another chance for reducing condensation temperature, as fabricated in Figure 1a.

Such an enhancement brought by the cooling effect is not unique to silica gel. The main reason behind this is that the water uptake of most sorbents tightly depends on the relative humidity. With the RH increasing, the sorption capacity increases owing to the huge humidity difference between ambient air and the pore of sorbents. Reduced humidity with heating sorbent to low local humidity is obviously lower than elevated humidity with cooling sorbent to high local humidity. Thus, introducing cooling into the sorption stage could provide a benefit for water production, not limited to silica gel.
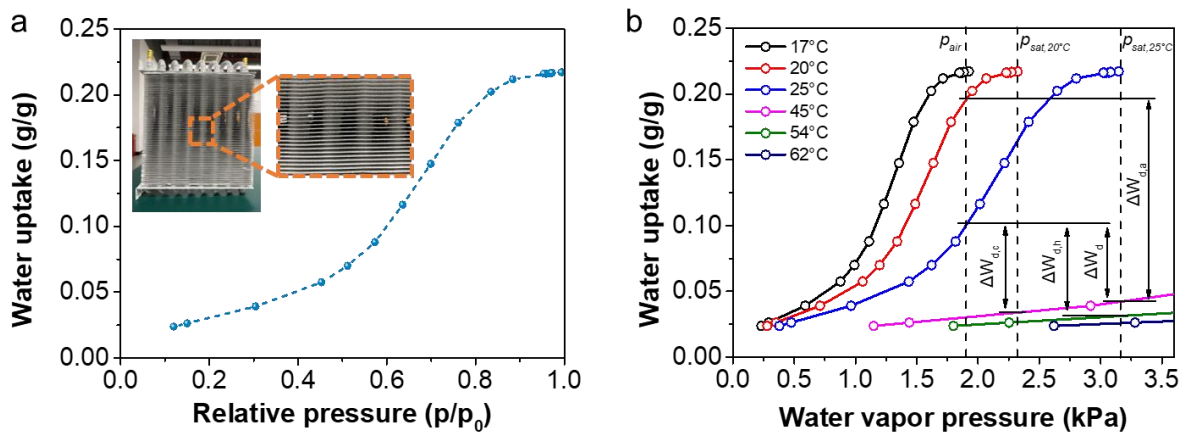
Figure 2. Water vapor sorption isotherms of silica gel. (a) Water uptake varied with relative humidity at 20°C. (b) Water uptake varied with water vapor pressure with different temperatures.

With this proposed SAWH device, the performance was then tested and evaluated. As mentioned in the working principle, the cooling temperature for sorption is critical for the performance of the device. Typical dynamic results with different cooling temperatures under 25°C/60%RH are shown in Figure 3. The control case was conducted by keeping the cooling temperature at 25°C. Figure 3a depicts the outlet air temperature of the adsorber and RH of the condenser. Switching operation leads to fluctuations of temperature and RH once the airflow

and water flow were changed. For a low adsorption temperature of 17°C, the outlet air temperature is always lower than ambient air, which is a benefit for the condensation process. When the adsorption is at 20°C, the initial state of outlet air is higher than the ambient and then reduced below ambient air. While for the control case (adsorption temperature at 25°C), the outlet air temperature is always higher than ambient air due to the switching operations at the initial state and heat transfer resistance during the later period. The changes in RH indicate that the condensation occurs in the condensation (humidity is near 100%RH). But a lower sorption temperature leads to a longer condensation period arising from a higher water sorption capacity at the sorption stage. About 80% of the sorption period is expensed to desorption and condensation when the sorption temperature is 15°C. And that was decreased to 69.5% and 42.4% when sorption temperature was maintained at 20 and 17°C, respectively. Figure 3b reveals the humidity ratio of the inlet and outlet air of the condenser and adsorber with different sorption temperatures. The changes between the inlet and outlet air of the adsorber indicate that the sorption capacity will dramatically be enhanced by lowering the adsorption temperature. That also can be explained by the isotherms with different sorption temperatures. The changes between the inlet and outlet air of the condenser represent how much moisture is released. As seen, low sorption temperature proceeds the sorption capacity and thus more humidity can be released, leading to a large humidity difference between inlet and outlet air.
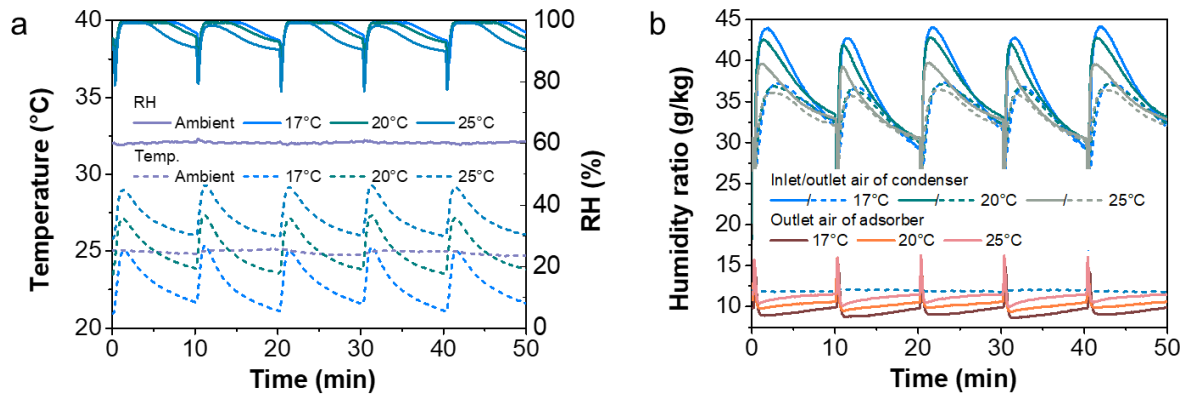
Figure 3. Dynamic results of temperature and humidity with different adsorption temperatures under 25°C/60%RH. (a) Outlet air temperature of the adsorber and outlet air RH of the condenser. (b) Humidity ratio changes between the outlet and inlet air of the adsorber and condenser.

Afterward, the performances with different desorption temperatures are investigated by keeping the sorption temperature at 20°C, as shown in Figure 4. Since the heating and cooling water are encountered with each other during the switchover, the outlet air temperature of the adsorber will be affected by the heating temperature. As seen in Figure 4a, the outlet air temperature of the adsorber is increased with the increase of desorption temperature. When the desorption temperature is 45°C, the time when the outlet air temperature of the adsorber is lower than the ambient temperature is about 74.5% sorption time. But this period will be reduced to 50.1% and 30% sorption time when the desorption temperature is increased to 54 and 62°C, respectively. However, the condensation time (RH approaching 100%) is prolonged with a low desorption temperature since the moisture releasing rate is relatively low and higher temperature features faster releasing rate, as revealed by the RH changes in Figure 4a. The humidity ratio changes of inlet and outlet air of the adsorber and condenser can be found in Figure 4b. As displayed, the sorption side is similar due to the same sorption temperature. Although the desorption temperature is different, the much longer time is dominated by the sorption temperature.

Heat Powered Cycles
Conference 2023
Edinburgh

Heat in the new energy system

3rd to 6th of September 2023
The University of Edinburgh, Scotland

Therefore, increasing the heating temperature will present little influence on sorption performance. However, for the desorption side, the inlet and outlet air of the condenser is quite different. High heating temperature leads to a high inlet and outlet air humidity of the condenser, but more water is released, as indicated in Figure 4b.
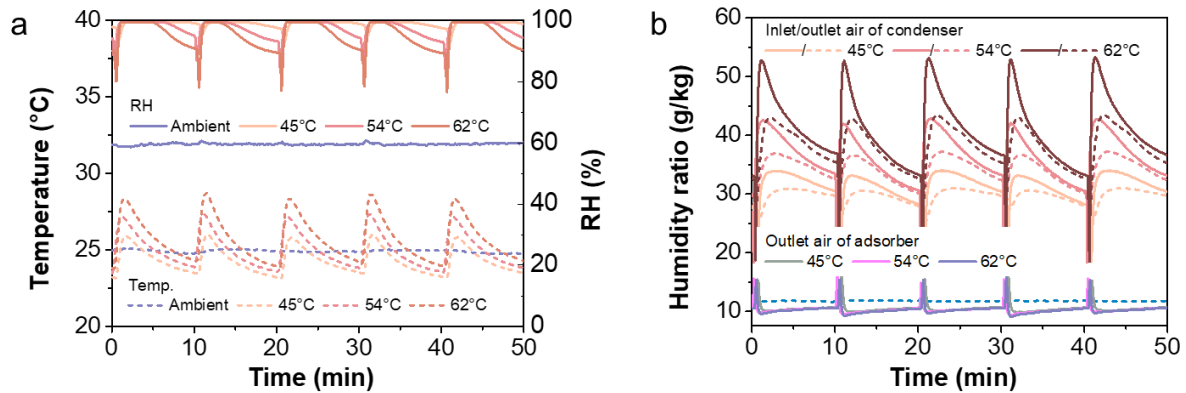
Figure 4. Dynamic results of temperature and humidity with different desorption temperatures under 25°C/60%RH. (a) Outlet air temperature of the adsorber and outlet air RH of the condenser. (b) Humidity ratio changes between the outlet and inlet air of the adsorber and condenser.

With the dynamic sorption and desorption characteristics with different cooling and heating temperatures, the practical collected water is evaluated, as shown in Figure 5. Obeyed to the above-mentioned results, the water production rate also shows a similar trend. With the decrease of cooling temperature for sorption, the water production rate is increased. The water production rate can be up to 80.76 and 45.74 g/h with the cooling temperature of 17°C and 20°C when the heating temperature is 45°C, which is 8.30- and 4.65-times improvement compared with the control case (25/45°C). And these improvements will be 5.01 and 2.93 times when the heating temperature is increased to 54°C. At the high temperature of 62°C, although the promotions of water production caused by the cooling effect are reduced slightly, there are still 2.60- and 1.84-times improvements compared with the control case (25/62°C).
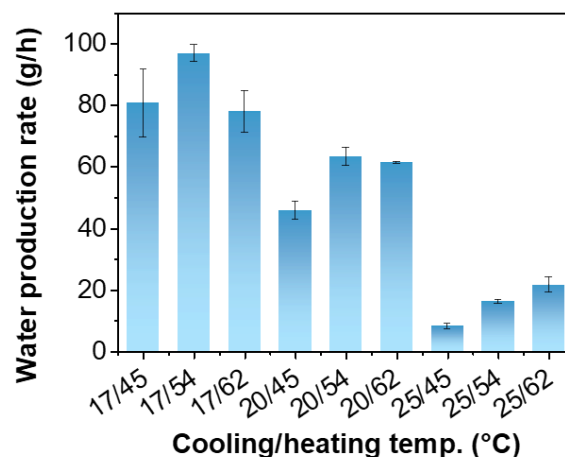
Figure 5. Water production rate with different cooling/heating temperatures under 25°C/60%RH.

It should be noted that the water productivity presents a trend of increase first and then decrease with the increase of heating temperature when the cooling temperature of 17°C and 20°C. The

reason for these trends is that with the increase in heating temperature, the desorbed water is improved, leading to the boosted water production. While the heating temperature further rises, the huge temperature differences between sorption and desorption are not benefited to water harvesting. This trend is not obvious with a relatively high cooling temperature, as indicated by the water production with a cooling temperature of 20°C. For the control case with the cooling temperature of 25°C, the trends of water production obey the traditional rule- high heating temperature promotes high-water production. In addition, the outlet air temperature of the adsorber (to cool the condenser, as shown in Figure 1) is then increased, weakening the condensation efficiency. In this case, performing a heat recovery will give help to improve water production. Nevertheless, all results of water production reveal that introducing a cooling source into the sorption stage will provide an extra advantage for improving water yield.

Conclusions

In summary, we report a design of water harvesting with cooling-assisted sorption. The cooling effect could bring enhanced sorption capacity and rapid kinetics for water harvesting. The impacts of changing sorption, desorption and condensation temperatures were analyzed, indicating that introducing a cooling source into the sorption stage is most effective. Besides, utilizing the waste cooling energy from the sorption stage in the condensation process will give extra merit for condensation, but it was ineffective for high sorption temperatures. By testing the performance of the water harvester, the maximum water production rate of 95.1 g/h is acquired.

An appropriate heating and cooling source should be considered in a real-world application since both heating and cooling are required in this work. This work proved that low-temperature thermal energy with the temperature of 45-62°C is suitable for driving the desorption process. To this end, a heat pump is a suitable selection to provide heating and cooling simultaneously. In this case, the evaporator could provide the cooling demands for sorption and the condenser heat can be used to desorption. Besides, separate heating and cooling sources also can be used to drive this water harvester, like solar energy, waste heat, radiative cooling, ad/absorption cooling, etc.

Acknowledgments

References:

[1] Mekonnen, M.M., Hoekstra, A.Y., "Four billion people facing severe water scarcity", Science Advances, 2016;2: e1500323.

[2] Yang, K., Pan, T., Lei, Q., Dong, X., Cheng, Q., Han, Y., "A Roadmap to Sorption-Based Atmospheric Water Harvesting: From Molecular Sorption Mechanism to Sorbent Design and System Optimization", Environmental Science & Technology 2021;55:6542–60.

[3] Tu, Y., Wang, R., Zhang, Y., Wang, J., "Progress and Expectation of Atmospheric Water Harvesting", Joule 2018;2:1452–75.

[4] Elimelech, M., Phillip, W.A., "The Future of Seawater Desalination: Energy, Technology, and the Environment", Science, 2011;333:712–7.

[5] Xu, J., Li, T., Yan, T., Wu, S., Wu, M., Chao, J., Huo, X., Wang, P., Wang, R., "Ultrahigh solar-driven atmospheric water production enabled by scalable rapid-cycling

water harvester with vertically aligned nanocomposite sorbent", Energy Environmental Science 2021;14:5979–94.

[6] Ejeian, M., Wang, R., "Adsorption-based atmospheric water harvesting", Joule 2021;5:1678–703.

[7] LaPotin, A., Kim, H., Rao, S.R., Wang, E.N., "Adsorption-Based Atmospheric Water Harvesting: Impact of Material and Component Properties on System-Level Performance", Account of Chemical Research, 2019;52:1588–97.

[8] Lu, H., Shi, W., Guo, Y., Guan, W., Lei, C., Yu, G., "Materials Engineering for Atmospheric Water Harvesting: Progress and Perspectives", Advanced Materials 2022;34:2110079.

[9] Shi, W., Guan, W., Lei, C., Yu, G., "Sorbents for Atmospheric Water Harvesting: From Design Principles to Applications", Angewandte Chemie International Edition, 2022;61.

[10] Hanikel, N., Prévot, M.S., Yaghi, O.M., "MOF water harvesters", Nature Nanotechnology, 2020;15:348–55.

[11] Guo, Y., Bae, J., Fang, Z., Li, P., Zhao, F., Yu, G., "Hydrogels and Hydrogel-Derived Materials for Energy and Water Sustainability", Chemical Reviews, 2020;120:7642–707.

[12] LaPotin, A., Zhong, Y., Zhang, L., Zhao, L., Leroy, A., Kim, H., Rao, S.R., Wang, E.N., "Dual-Stage Atmospheric Water Harvesting Device for Scalable Solar-Driven Water Production", Joule, 2021;5:166–82.

[13] Shan, H., Li, C., Chen, Z., Ying, W., Poredoš, P., Ye, Z., Pan, Q., Wang, J., Wang, R., "Exceptional water production yield enabled by batch-processed portable water harvester in semi-arid climate", Nature Communications, 2022;13:5406.

[14] Poredoš, P., Shan, H., Wang, C., Deng, F., Wang, R., "Sustainable water generation: grand challenges in continuous atmospheric water harvesting", Energy Environmental Science, 2022;15:3223–35.

[15] Hua, L., Xu, J., Wang, R., "Exergy-efficient boundary and design guidelines for atmospheric water harvesters with nano-porous sorbents", Nano Energy, 2021;85:105977.

[16] Feng, Y., Wang, R., Ge, T., "Pathways to Energy-efficient Water Production from the Atmosphere", Advanced Science, 2022:2204508.

[17] Feng, Y., Ge, T., Chen, B., Zhan, G., Wang, R., "A regulation strategy of sorbent stepwise position for boosting atmospheric water harvesting in arid area", Cell Reports Physical Science, 2021:100561.

Steam Rankine Cycle Pilot Plant – Long-term operating experience and lessons learnt for future plants regarding reliability and economic efficiency

F. Raab[1*], H. Klein[2], F. Opferkuch[1]

[1]Technische Hochschule Nürnberg Georg Simon Ohm, Distributed Energy Conversion and Storage, Fürther Str. 246b, 90429 Nürnberg, Germany

[2]Technische Universität München, Institute of Plant and Process Technology, Boltzmannstraße 15, 85748 Garching, Germany

[*]Corresponding author: florian.raab@th-nuernberg.de

Abstract

Waste Heat Recovery is becoming increasingly relevant in times of dwindling and more expensive fossil resources. Nevertheless, many energy-intensive processes do not sufficiently utilise high-quality waste heat sources. Reasons often lie on the one hand in the low profitability and on the other in the limited reliability of such systems. This research work describes long-term measurement data and operating experience with a Steam Rankine Cycle pilot plant for the conversion of high-temperature waste heat into electricity using water as the working medium, techno-economic optimisation approaches in various fields of application as well as an optimized plant design.

Keywords: Steam Rankine Cycle, SRC, Pilot Plant, Waste Heat Recovery, WHR, long-term operation experience, techno-economic optimization.

Introduction/Background

Energy-intensive industrial sectors, especially in the forming industry, have profited significantly in recent years from low-cost electricity and gas. A Waste Heat Recovery (WHR) often remained out of reach due to required payback periods of only a few years. Efforts to save CO_2 and the growing pressure on the global energy market are forcing these sectors to look more closely at the utilisation of unused energy flows.

When a suitable in-process use is not possible, an end-of-pipe solution to convert the remaining heat into electrical energy using a Rankine cycle is often the most appropriate approach. For different temperature levels and waste heat flows, a variety of working fluids have been established in Rankine Cycles in recent years. In addition to refrigerants in the low-temperature range up to approx. 180 °C waste heat temperature, hydrocarbons from approx. 180-250 °C and siloxanes above approx. 250 °C [1], water offers comparable efficiencies at waste heat temperatures above approx. 400 °C [2,3], depending on the plant size.

Since the Steam Rankine Cycle (SRC) plant technology for distributed WHR with water as the working fluid has not yet exhausted its full potential compared to centralised large-scale power plant technology, where water is the state of the art, a pilot plant for WHR with water was set up by the TH Nürnberg. This plant converts the waste heat of a sewage gas CHP (Combined Heat and Power) engine into electricity and was described in detail in previous work of the authors [4]. A picture of the plant can be seen in Figure 1, the simplified flow chart with the main measuring points in Figure 2.

Since its commissioning in 2020, this pilot plant has been operated in long-term conditions by the TH Nürnberg, running for 8,212 h and supplying 224 MWh of electrical energy (21.01.2023). In the last half year of operation, the test plant achieved an availability of 73.4 %.

In this paper, detailed measurement data during operation as well as lessons-learned and optimisations for future plants in terms of reliability and economic efficiency are presented and discussed.

Figure 1: MicroRankine pilot plant at the sewage treatment plant in Nürnberg
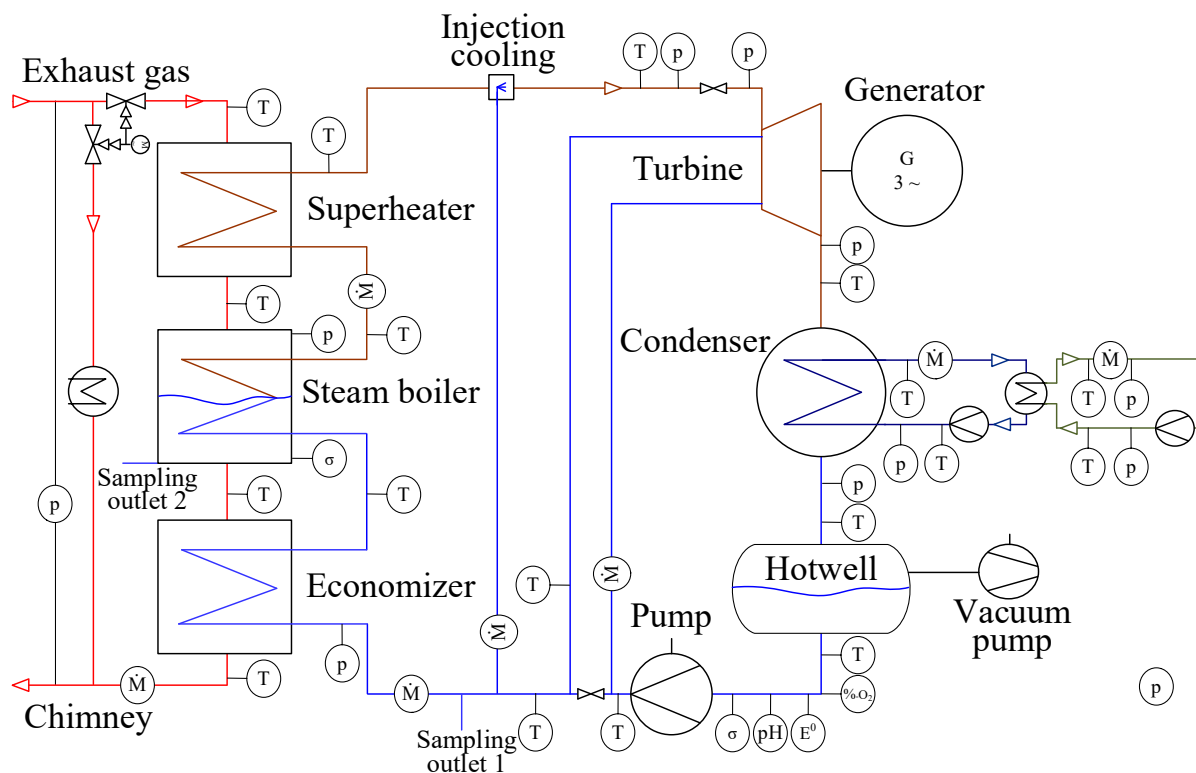
Figure 2: Flow chart of the MicroRankine pilot plant with the main measuring points

Discussion and Results

In the following, first the optimum operating parameters on the high and low pressure side are discussed. Then the measured data of the water-chemical parameters and the effects on corrosion are described. Finally, the new, techno-economically optimised design is presented.

Operating parameters heat source
Following the steady-state model of the Rankine Cycle and the waste heat situation according to [3], the operating parameters of the high-pressure side were varied to identify the most efficient design point. Figure 3 (left) shows the net efficiency of the entire plant, related to the maximum heat flow that can be transferred from the exhaust gas, as a function of the turbine inlet temperature. Figure 3 (right) shows the same efficiency with varied turbine inlet pressure. In all cases, condensation takes place at a temperature of 50 °C, the pinch point of the steam

generator and the summarized transfer capability (kA [W/m²/K]) were kept constant at the level of the MicroRankine plant, which leads to a more insufficient utilisation of the exhaust gas as the steam temperature and pressure increase. The black line represents the classic SRC with pump, steam generator, turbine and condenser. The dashed line represents the additional use of an Internal Heat Exchanger (IHX), which uses the remaining energy in the exhaust steam after the turbine and preheats the water before the economizer.
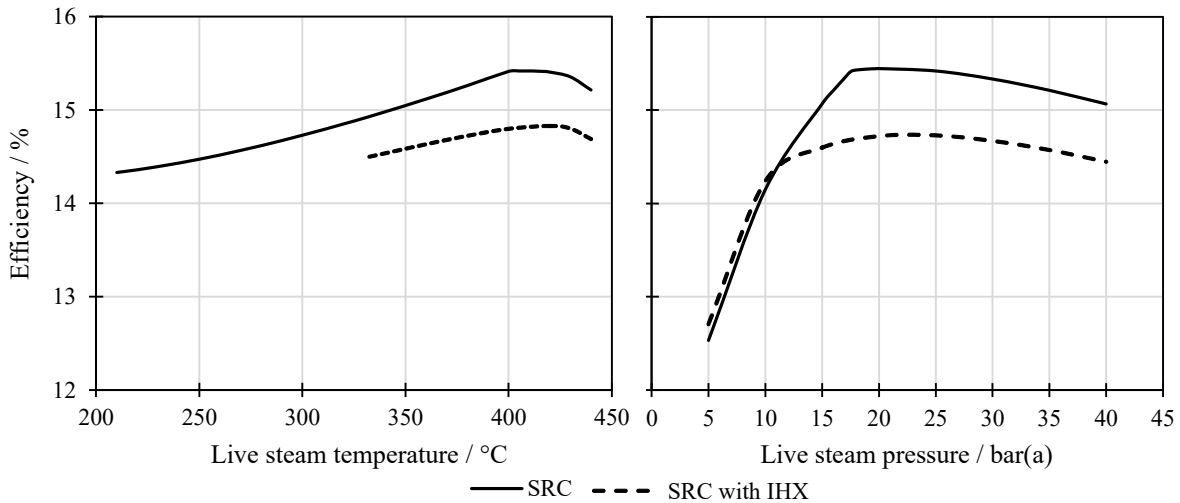
Figure 3: Efficiency of the SRC plant with and without internal heat exchanger as a function of turbine inlet temperature (left) and pressure (right)

The variation of the live steam temperature at constant pressure (17.5 bar) shows that a live steam temperature of 410 °C brings the maximum efficiency. From approx. 400 °C, the efficiency no longer increases, as the mass flow rate must be reduced significantly to reach the temperature with the fixed transfer capability. An IHX does not bring any efficiency benefits. When the live steam pressure is varied, the technical maximum is at 19.9 bar, but there is a break at 17.5 bar, after which the efficiency only rises slightly and then declines. The reason for this is the defined pinch point of 30 °C, causing the waste heat source to be insufficiently utilised as the pressure rises. The IHX does not provide advantage in this case again.

Subsequently, valves and tubes were investigated regarding operating parameters. According to the valve manufacturer, 1.4408 stainless steel is mainly used in this area. According to DIN EN 1092-1 [5], this allows a maximum pressure of 27 bar at 400 °C at PN40. Since these upper limits must never be exceeded during operation, a certain buffer is required by the accredited inspection body. The safety chain of the system regulates the pressure in a first step according to the measurement parameters. In the event of failure of this regulation, a safety pressure switch next switches off the heating by means of hardware equipment; in the event of its failure, a mechanical safety valve finally opens and blows off the steam. The temperature sensor regulates the pump and thus the maximum steam temperature. In the event of failure, a safety temperature limiter switches off the heating by hardware. From these safety functions, only 380 °C/25 bar would be possible with the material of the valves. Since the pressure-litre product according to Directive 2014/68/EU [6] has a decisive influence on acceptance, testing and maintenance, the pressure must be kept as low as possible. For this reason, the break at 17.5 bar selected from Figure 3 (right) was chosen as the design parameter, since the maximum efficiency at 19.9 bar would be only 0.03 % higher.

The alternative high-strength stainless steel for the valves 1.4581 in the comparison would be approved up to 30 bar/530 °C. This would make the optimum design parameters possible, but only a gain in efficiency of 0.22 % would be achieved. According to the manufacturer, however, the valves would be 10-15 % more expensive. With an operating time of 8,000 h/year and

Heat Powered Cycles
Conference 2023
Edinburgh

Heat in the new energy system

3rd to 6th of September 2023
The University of Edinburgh, Scotland

0.15 €/kWh remuneration, there would only be an additional profit of 102 € per year, which is why the use of a high-strength material is not economical.

Therefore, 17.5 bar and 380 °C were selected as the steady-state design steam parameters after the superheater.

Operating parameters heat sink

In the MicroRankine plant, the heat sink is realised by a cooling water system of the sewage treatment plant. In a distributed SRC concept, it cannot be assumed that a cooling system is available, which is why an air cooler with electric fan is necessary. The heat sink through air cooling is accordingly dependent on the ambient temperature, which varies with the season.

The most efficient operation between the area and the power of the air cooler, the intermediate circuit pump and the turbine represents a techno-economic conflict of targets. With higher power of the air cooler or the intermediate circuit pumps, the exhaust turbine pressure decreases and the turbine power increases accordingly, but at the same time the electrical self-consumption increases.

For this purpose, the mass flow rate of the intermediate circuit pump was varied in the Micro-Rankine plant in a first step. In Figure 4, the condensation pressure is plotted against the mass flow rate, which decreases from 0.177 to 0.107 bar at the operating point. As a result, the turbine output increases from 25.7 to 27.6 kW_{el}. At the same time, the pump's own consumption increases from 0.13 to 3.2 kW_{el}, which leads to an optimum of the total output at 3.1 kg/s (black line). An increase beyond this point does not further improve the heat transfer between condensate and cooling water, the condensation heat transfer coefficient is then the determining parameter.
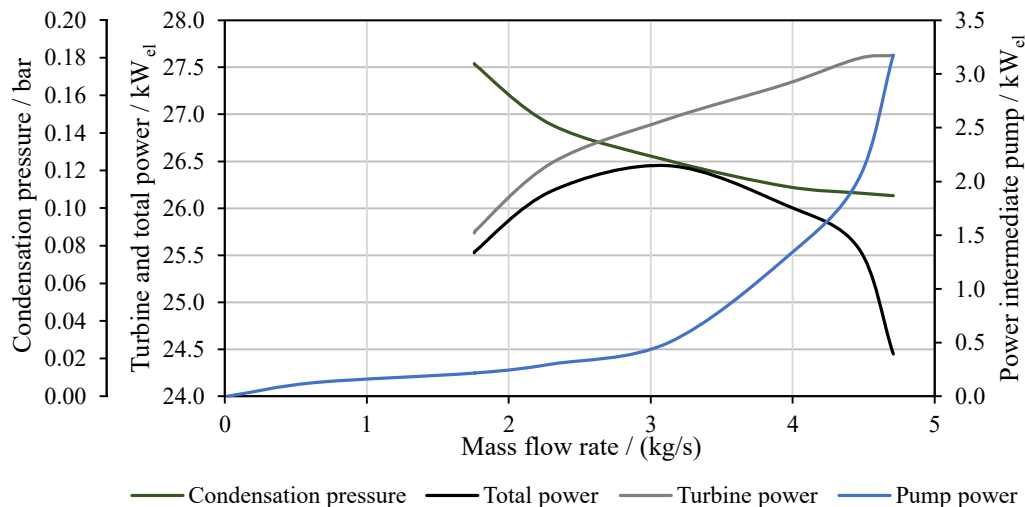
Figure 4: Measured condensation pressure, turbine output, pump power and total output with varied intermediate circuit mass flow rate

For the design of a table air cooler, 200 dry coolers which can basically solve the cooling task were compared with each other in the Güntner Procduct Configurator [7]. The number and power of the fans, the pressure loss of the water and the associated increased intermediate circuit pump power with increased heat transfer surface, the temperature level in the intermediate circuit and the therefore varying turbine power as well as the investment costs were varied. These costs were compared over an operation period of 10 years and an assumed remuneration of 0.15 €/kWh in a simulation of the average ambient temperature in Nürnberg and an economic optimum was determined. The table cooler GFHCFD050,1/23-49-0189157M with six fans turned out to be the techno-economic optimum. An optimal operating point results for each ambient temperature. Figure 5 (left) shows the net output of the SRC system at an ambient

Heat Powered Cycles
Conference 2023
Edinburgh

Heat in the new energy system

3rd to 6th of September 2023
The University of Edinburgh, Scotland

temperature of exemplary 20 °C with varying table cooler power. An optimum results at 38.2 %, the condensation pressure here is 0.12 bar. Figure 5 (right) shows the optimum net power of the system plotted against the ambient temperature, which varies between 32.9 and 25.5 kW$_{el}$ at ambient temperatures of 0 to 35 °C with condensation pressures of 0.05 to 0.25 bar. Because condensation pressures of less than 50 mbar are unrealistic due to the leakages and the limited power of the vacuum pump, lower theoretical values are not displayed.
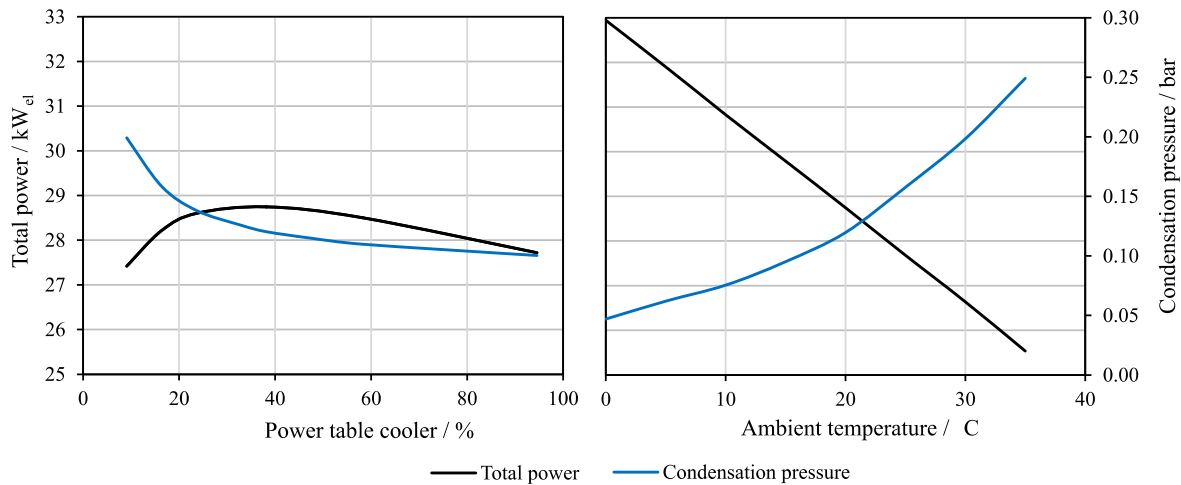
Figure 5: (left): Net power and condensation pressure over table cooler power (for 20 °C ambient temperature)
(right): Optimum net power and condensation pressure over ambient temperature in Nürnberg

Water chemical properties

In the original system with steam boiler, different alloyed and non-alloyed materials are used (Economiser and steam boiler made of P250GH, the rest of the system made of alloyed steal [4]). Although a compact optimised system could be completely made of stainless steel, the problem of the unalloyed materials will remain with larger scaled systems, which is why the development of corrosion in the system and various countermeasures are discussed below. Corrosion in water-steam systems is mainly caused by two processes, surface corrosion by oxygen and acid corrosion, which leads to pitting. To avoid this, the water-chemical regulations for steam generators are summarised in DIN EN 12953-10 [8]. A distinction is made between the water in the steam boiler and the refill water, which in the closed SRC systems correspond to the values in the steam and condensate.

The following table summarises the specifications for the pH-value, oxygen content and electrical conductivity for the use of deionised water without additives at pressure below 20 bar.

Table 1: Specifications for the water-chemical parameters according to DIN EN 12953-10

		Steam boiler	Condensate
pH-value	-	10.0 - 11.0	>9.2
Oxygen content	mg/l	<0.05	<0.05
Electrical conductivity	µS/cm	<1,500.0	<30.0

Since the shell boiler is in category IV according to Directive 2014/68/EU [6], these values must be checked every 72 h in accordance with TRD 604 [9] and DIN EN 12953-10 [8]. Further parameters must be monitored if additives are added. Because the system is filled with deionised water from two mixed-bed filters connected in series, no noticeable impurities such as silicic acid and chloride ions enter the system that could lead to deposits or corrosion. This is monitored via the conductivity after the filters when refilling.

Since these regulations were drawn up on the basis of open steam boiler systems in which the water is rarely reused, the application to a hermetic SRC is not necessarily given. For this

reason, the limit values and specifications are discussed below in the case of the closed SRC and the results of the experimental investigation using the MicroRankine system are presented.

In a first series of experiments, the system was filled exclusively with deionised water from two mixed-bed filters connected in series, the conductivity of the water was <1 µS/cm. The following Figure 6 shows the measured values for the pH-value, the electrical conductivity and the oxygen content in the steam boiler and the condensate collector over one month. Mainly due to the sampling of the water of the boiler and the condensate every 72 h, but also due to minimal leaks at the mechanical safety valve and the vacuum pump, the system loses water during operation. On average, 4.2 litres of the 1,400 litres of water in the system are lost per day, which are regularly refilled by the mixed bed filters. As shown in Figure 2, a water sample can be taken at two points in the system, after the condenser and the pump to examine the condensate and from the steam generator via a sampling cooler to examine the kettle water.
In order to avoid distortion of the measured values due to a reaction of dissolved iron(II) with atmospheric oxygen after taking the sample and the associated acidic dissociation of the iron(III) forming in the present of extremely low-mineral and almost unbuffered water [10], the filling water samples were measured in a flow-through vessel.

In addition, the iron and copper content in the evaporator were regularly measured as indicators of corrosion. Further damage in the system can be triggered by silicic acid and chloride ions. Although these should not enter the system through the mixed bed filters, they were examined at regular intervals. The iron content in continuous operation did not tend to increase and was normally <100 mg/l. The copper content was below the limit of 10 mg/l that could be detected in the commissioned laboratory. The silicic acid content did not increase and was on average approx. 1.5 mg/l. The chloride content in the boiler was 0.7 mg/l in a sample measurement and 0.3 mg/l in the condensate.
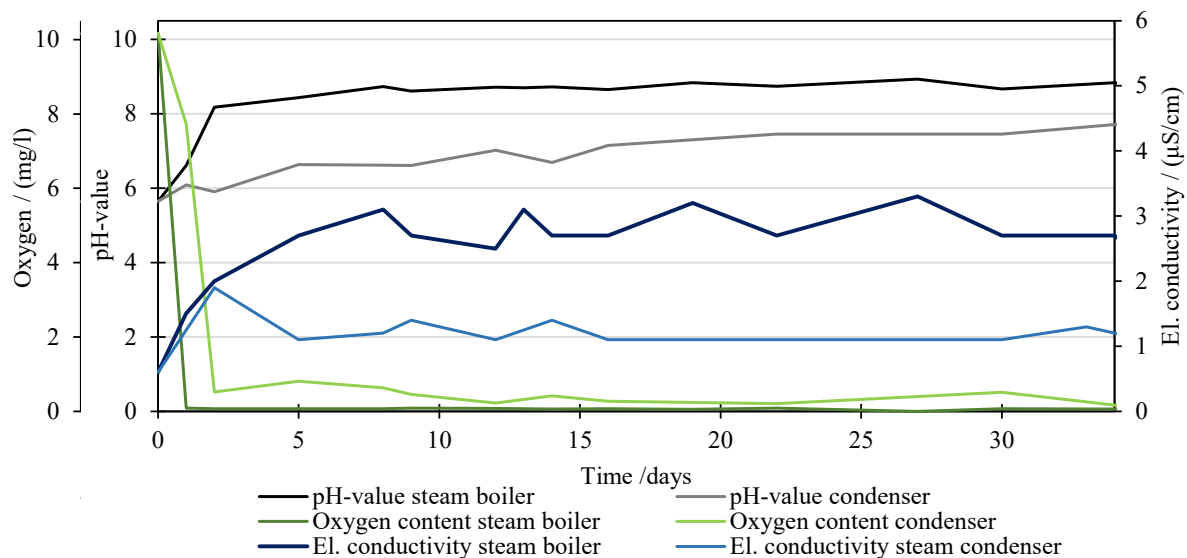
Figure 6: Water-chemical properties during operation with deionised water

The conductivity in the system rises slightly because of remaining impurities in the evaporator due to pool boiling, which leads to a slightly higher conductivity in the kettle (2.9 µS/cm) than in the condenser (1.2 µS/cm).
The oxygen content of the filling water is mostly expelled by the evaporation within the first hours of operation and extracted via the vacuum pump. In steady-state operation, the measured oxygen content in the steam boiler was between 0.03 and 0.1 mg/l, in the condensate between 0.17 and 0.64 mg/l. Since the low-pressure side lies below ambient pressure and the apparatus

and valves of the pilot plant are mostly flanged for maximum flexibility, oxygen is constantly drawn into the system until the vacuum pump is reactivated. But even with mostly welded systems, there will still be a small input of oxygen in the vacuum region. Figure 7 shows the increasing oxygen content in the condensate measured on different days, plotted over time after vacuum draw.
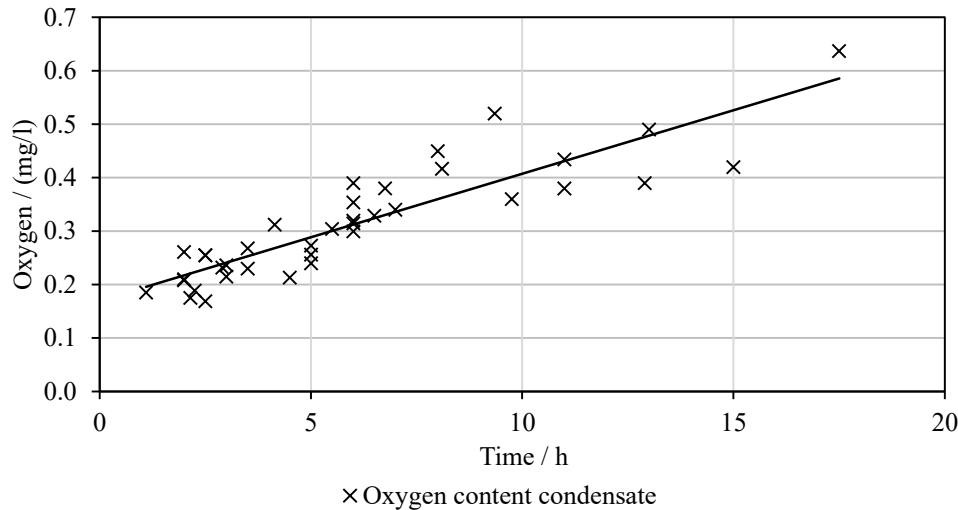
Figure 7: Oxygen content in the condensate over time after vacuum draw

Since oxygen measurement is prone to errors, measurements were also taken with a high-precision measuring apparatus [11] under complete exclusion of ambient air. The oxygen content in the steam boiler was approx. 0.047 mg/l, in the condensate approx. 0.100 mg/l, which principally confirms the regular measurements in this paper.

The pH-value in the condensate increases only slightly to 7.2 because the water hardly reacts with the stainless steel in this area. In the kettle water, CO_2 and caustic soda are formed from the carbonates and hydrogen carbonates at the high temperatures (soda decomposition) [12]. The sodium hydroxide solution, which is not vapour-volatile, alkalises the boiler water, which is why the pH-value in the boiler of approx. 8.7 is higher than in the condensate. Due to the oxidation of the iron(II) that goes into solution in the kettle, the pH-value in the condenser drops significantly [10].

The measured values of the electrical conductivity of the circuit water fully comply with the manufacturer's specifications and the standards, what significantly reduces corrosion according to VDI 2035, even with a higher oxygen content [13]. The oxygen content in the steam boiler appears to be close to the specifications during evaporation. In the condensate, however, the limit value is exceeded by up to 10 times. Since the condensate first flows through the unalloyed preheater, this value is critical. The oxygen content in the system becomes even more critical during standstill. When the system cools down, the high-pressure side also falls into a vacuum, drawing air into the system there as well. The pH-value in the condensate, i.e. in the feed water, is approx. 2 too low, in the steam boiler approx. 1.3 too low. The low pH-value prevents the formation of a magnetite layer that protects against corrosion.

As a result of this experiment, it can be stated that a system made of alloyed and unalloyed steel cannot be operated with the specified water-chemical parameters. Although e.g. Bursik [14] also describes a slightly oxygenated, neutral to slightly alkaline operation as sufficient protection against corrosion, the specifications must be fulfilled for warranty and insur-

ance. Steam boilers of this type are sometimes operated for several decades, resulting in profitable plants, which is the aim of this project. Therefore, countermeasures are discussed and tested in the following for protection against oxygen and acid corrosion.

According to [12], four substances are commonly used for alkalisation, caustic soda, ammonia, sodium phosphate and hydrazine. The effects of different concentrations of these on the pH-value in a steam boiler are shown in Figure 8. Since hydrazine is a highly toxic and carcinogenic medium, it is excluded for this application. Caustic soda and sodium phosphate as non-steam volatile agents remain exclusively in the steam boiler and do not increase the pH-value in the condensate system and thus also not in the preheater. Ammonia is a steam-volatile alkalising agent. The effects of adding ammonia to the system of the MicroRankine plant after refilling and stable water-chemical measurement data can be seen in Figure 9 from day 80. Since the condenser is copper-brazed, it had to be taken into account that the ammonia content must not exceed 0.5 mg/l according to the manufacturer. For this reason, 2.9 ml of a 25% ammonia solution was dosed into the filling water via the condensate tank.
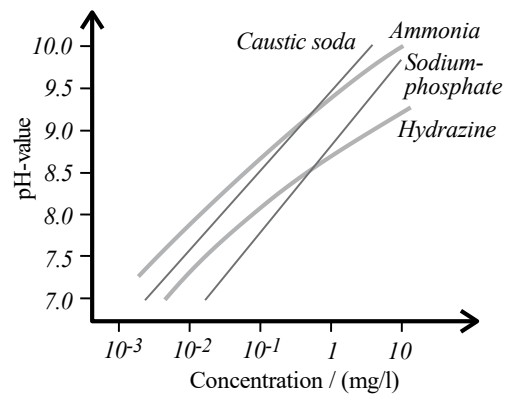
Figure 8: Resulting pH-value with various substances for alkalisation [12]
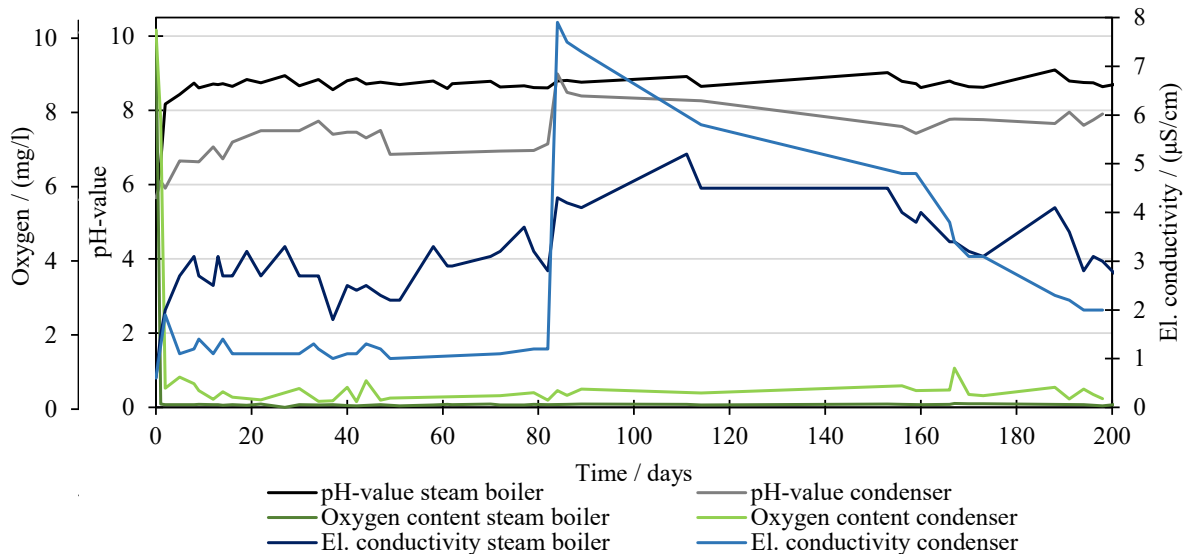
Figure 9: Water-chemical properties during operation with deionised water and ammonia for alkalisation

As can be seen, the electrical conductivity increases noticeable in the condensate, but only slightly in the steam boiler. The pH-value increases analogously in the condensate to over 10, in the steam boiler no influence on the pH-value is recognisable. The oxygen content remains unchanged, as expected.

In the course of approx. 120 days of operation of the plant with the added ammonia, the increased values fall back to the initial level. The reason for this is that ammonia only partially goes into the aqueous solution in the condenser and does not condense at the prevailing temperatures. The vacuum pump, which draws the air out of the system several times a day, also expels some ammonia. Only regular dosing of ammonia would therefore cause an alkalisation of the condensate system, including the preheater, according to the previous experiment. In SRC plants that do not expand into the vacuum e.g. for heat extraction, the effect of alkalisation

by ammonia would be more sustainable because the vacuum pump only operates after stand-still. However, since there is no alkalisation effect in the water of the steam boiler, it is not suitable for exclusive use in the SRC.

Since incorrect dosing of caustic soda for alkalisation in the boiler water can lead to stress corrosion cracking, alkalisation with non-vapour volatile trisodium phosphate was carried out in the following test. The measurement data of the water chemical parameters after refilling with deionised water and steady-state operation as well as alkalisation on day 22 with approx. 2 litres of trisodium phosphate are shown in Figure 10.
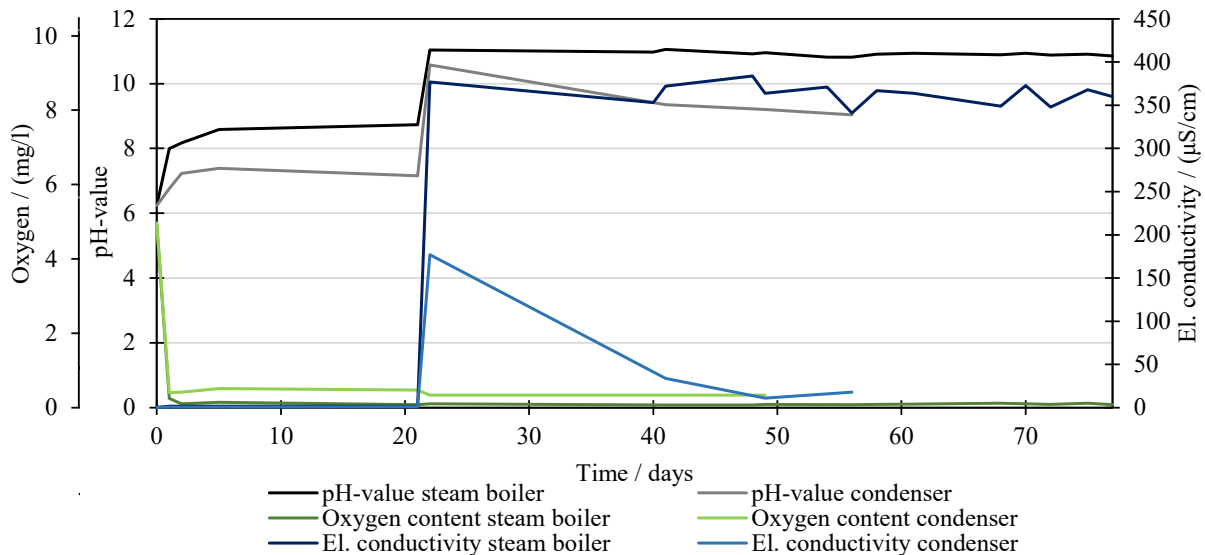
Figure 10: Water-chemical properties during operation with deionised water and trisodium phosphate for alkalisation

As intended, the pH-value in the boiler rises to approx. 10.9 and remains stable over approx. 50 days of operation. Analogously, the conductivity in the boiler increases, as trisodium phosphate is a salt that increases the conductivity in the solution. As it is not vapour volatile, it should have no effect on the condensate system. When adding the alkalising agent just before the pump in the negative pressure area, it seems that some of the trisodium phosphate has flowed back into the condensate collector due to the vacuum. Therefore, the conductivity and the pH-value in the collector increase after dosing. This should be avoided in continuous operation because the condensate could also be used for injection before the turbine and can thus cause damage. After approx. 30 days of operation, the el. conductivity of the condensate system returned to the initial state.

For alkalisation in the steam boiler, trisodium phosphate is therefore a suitable agent that does not require weekly re-dosing. However, since the pH-value in the condensate system is not affected and thus the preheater remains unprotected, the exclusive use of trisodium phosphate in the SRC is not sufficient. A combined addition of ammonia to alkalise the condensate system and trisodium phosphate to alkalise the steam boiler seems to be a solution, but involves some maintenance. The design of the preheater made of stainless steel and the exclusive dosing of trisodium phosphate would be an alternative, which, however, would cause higher investment costs.

Since the oxygen content in the system remains unchanged during all alkalisation processes and the preheater in particular is stressed by high oxygen concentrations from the condensate system, oxygen corrosion must be counteracted. In addition, many transient modes of operation of the SRC require shutdowns where oxygen enters the entire system through the resulting vacuum. According to DIN EN 12953-10 [8], in the case of intermittent operation or operation

without degasser, as is often the case with the SRC, the use of oxygen binding agents or film formers are prescribed. Oxygen binding agents in the SRC would have the disadvantage that sludge produced would have to be regularly removed from the system, which conflicts with the goal of a hermetic process. For this reason, the use of a film former, octadecylamine-$C_{18}H_{39}N$ (ODA), provided by the company *REICON Wärmetechnik & Wasserchemie Leipzig GmbH*, is investigated below. ODA builds up a protective layer on metallic oxide surfaces in the system at the molecular level through ionic bonding [15]. This protective layer is also present during standstill over a longer period of time and is intended to protect against both acid corrosion and oxygen corrosion. Furthermore, the reduced surface tension of the water and the smaller droplets should increase the efficiency during evaporation and condensation, deposits of anions should be removed by the adsorption of the ODA molecules and the efficiency of the turbine could be increased [16]. After an initial conservation with approx. 33 litres of a 0.5% ODA emulsion over a few days, the filling water was changed again, as a significant increase in iron in the system was noticeable as a result of the adsorption of the ODA and the detachment of already oxidised iron. After refilling, the ODA content in the system was tried to be kept at 0.3-0.5 mg/l in the condenser. This surplus is necessary so that there is always enough free ODA in the water to renew a possible abrasion of the protective layer. It is essential to avoid overdosing with ODA, as high excess and low cooling temperatures in the condenser or during standstill at the same time can cause ODA to agglomerate in the collector, which in turn restricts the functionality of the pump. The measured data of the water chemistry during steady-state operation after refilling with surplus ODA are shown in Figure 11 up to day 98. In the course of the complete 164 test days, 730 l of water were refilled, 77 l of the 0.5 % ODA emulsion were necessary for conservation.
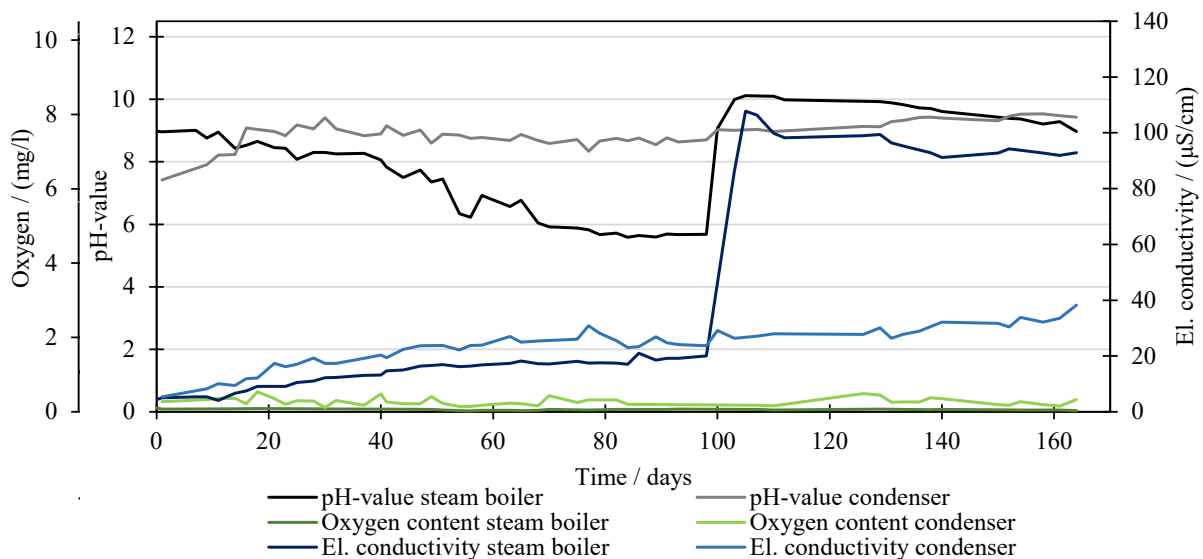
Figure 11: Water-chemical properties during operation with deionised water and octadecylamine for conservation

While the pH-value in the condensate rises until it is higher than in the boiler and stabilises at approx. 8.7, the pH-value in the boiler drops significantly to approx. 5.6 at day 97. In parallel, the conductivities in both parts rise slowly to approx. 19 µS/cm in the boiler and 25 µS/cm in the condensate.

Octadecylamine as a natural and non-toxic preserving agent is thermally decomposable from a temperature of 80 °C, from approx. 450 °C the molecule decomposes completely. It remains relatively stable up to approx. 300 °C. No acetic or formic acids are formed. The decomposition produces carbon dioxide, methane, hydrogen and ammonia. [17]

The ammonia generated is responsible for the increase in pH-value in the condensate. Since the decomposition process is continuous, the pH-value does not decrease as in the case of alkalisation by ammonia alone. The water in the steam boiler is analogously not affected by ammonia as a steam-volatile medium. The resulting CO_2 dissolves in the condensate and forms carbonic acid, which counteracts the effect of the ammonia. In the boiler, the solubility of CO_2 decreases with increasing temperature, which is why no carbonic acid can be present in the boiler water during evaporation. The remaining gases are expelled via the vacuum pump. The pH-value in the boiler does not increase as it does when operating with pure water, because through the ODA layer the depletion reaction on the unalloyed steel cannot take place.

Since in the previous results only the direct conductivity was measured, which as a sum parameter covers all ions and compounds, this value is only of limited informative value for the hazards associated with increased conductivity. In addition to the harmful ions such as chlorides, silicates, sodium, etc., which lead to deposits and increased corrosion, the effect of volatile components such as CO_2 and ammonia, which are formed during decomposition and do not enhance corrosion, are also recorded. Therefore, the conductivity was additionally measured after strongly acidic cation exchanger (acid conductivity). In the live steam directly after the steam boiler as well as in the condensate, this conductivity was approx. 10.1 µS/cm, while in the sample water of the steam boiler it was approx. 20.9 µS/cm. According to DIN EN 12953-10 [8], if the conductivity of the condensate downstream of the strongly acidic cation exchanger is <0.2 µS/cm, phosphate injection would not be necessary to increase the pH-value, and at <5 µS/cm, operation with a steam-volatile alkalizing agent such as ammonia would be permitted.

Although corrosion is significantly reduced by conservation with ODA even under slightly acidic conditions according to [18], the specifications of the standards must be fulfilled. Since the required acid conductivity is not present in the application of the MicroRankine system and the pH-value in the boiler is significantly below the additionally required pH-value ≥ 8.0, alkalization must be applied in addition to the conservation. Since the pH-value in the condensate meets the requirements, 1.25 litre of trisodium phosphate was dosed directly into the boiler water starting on day 98, as can also be seen in Figure 11. As a result, the pH-value in the steam boiler rises to over 10, the conductivity to over 100 µS/cm. These values remain largely stable within the 66 days of the remaining test series but are slowly decreasing. The dosing with trisodium phosphate would have to be repeated afterwards to raise the pH-value again. The condensate seems not to be affected by this alkalization but the pH-value is higher than the required 9.2 in this case.

The correct adjustment of the water chemistry is a challenge for the distributed conversion of waste heat into electricity with a hermetic Rankine cycle. In addition to the danger of corrosion and the associated financial risks, international and national regulations must be complied with. These have been developed and constantly improved over decades, but seem to be not always appropriate for use in a hermetic cycle. Literature sources and also the studies presented suggest that a slightly oxygenic and slightly alkaline operation does not cause any critical corrosion. The iron value in the steam boiler was in the range of <100 mg/l in all the investigations presented, with no upward trend. Nevertheless, the limit values should be observed, as steam generators always pose a danger. For the MicroRankine plant constellation, the combination of conservation with ODA and alkalisation of the steam boiler with trisodium phosphate seems to be suitable. A combination of ammonia for alkalisation of the condensate and trisodium phosphate for alkalisation of the steam boiler water also seems to be a suitable solution for plants without major shutdowns.

In smaller systems that are exclusively made of stainless steel, oxygen corrosion does not occur. According to DIN EN 12502-4 [19] and DIN 50930-4 [20], acid corrosion would only occur at pH-values below 4, which is not the case in systems with pure water [20].

Optimised apparatuses and overall system design

With the help of these optimisations and the parameters to be achieved, the individual devices in the MicroRankine plant were considered and techno-economically optimised for various applications in the range of 40-200 kW$_{el}$.

The evaporator as a shell boiler offers the possibility of exploiting new applications due to its storage capacity. For steady-state conversion of waste heat to electricity, however, forced flow steam generators offer advantages in terms of investment, operating costs and compactness. In the course of the research project *KompACT*, various steam generator designs in the target output range were compared and selected according to the total cost of ownership [21]. For the smallest plant size, which converts approx. 250 kW of thermal energy into approx. 40 kW of electrical energy, a double-walled tube evaporator was developed, in which the water evaporates in the annular gap. In order to keep within the installation height of a container, the preheater and evaporator were planned in one unit, the superheater in a separate one. Due to the small volume of the steam-carrying part, the apparatus can be operated in accordance with category III [6]. In this case, the apparatus is not subject to authorization and can be maintained by a competent person instead of the accredited inspection body.

A micro steam turbine was also newly developed by the partners in the project [22]. The magnetic-bearing machine runs at a design speed of 36,000 rpm, with the rotor attached directly to the turbine wheel and no rotating shaft protruding from the steam chamber, resulting in a hermetic design. The turbine can be operated between 1 bar and 0.2 bar exhaust pressure, for optional provision of heat at a higher temperature level or for maximum cooling capacity analogous to Figure 5. A newly designed regenerative unit concept with certified converters in the power range delivers the electricity into the grid.

As in the MicroRankine plant, an asymmetrical plate heat exchanger is planned as the condenser in the new plant design, which directs the condensate into the condensate tank. In combination with the original steam kettle boiler, the pump that delivers the water back to operating pressure in the economizer was designed as a single-piston membrane-type pump. This pump tended to cavitate at maximum power. The remedy was to limit the power and increase the time between activating the vacuum pump, which increased the subcooling. However, even with an additional pulsation damper, it still produced a highly oscillating mass flow, which would not be suitable for a forced flow steam generator concept. Therefore, a new pump system was designed in a techno-economic selection between different pump types. Due to the tendency of a single pump to cavitate when raising the pressure of the low mass flow rate from below ambient conditions to operating pressure, with subcooling of only 5 K, a two-stage pump concept was chosen. A centrifugal pump delivers a higher mass flow rate back into the condensation tank and slightly increases the pressure. The second pump, a three-piston membrane-type pump, feeds the water into the preheater with low pulsation.

The condenser is supplied with an intermediate medium that transfers the heat to the table cooler in summer. If thermal power is required for heating purposes in winter, heat can be extracted via a further heat exchanger in the intermediate circuit.

Compared with the MicroRankine pilot plant, 9 armatures and 18 measuring points can be avoided in the new concept. Figure 12 shows a simplified flow chart of the *KompACT* plant setup. Figure 13 shows a 3D model of the optimized design for a waste heat output of approx. 250 kW$_{th}$.
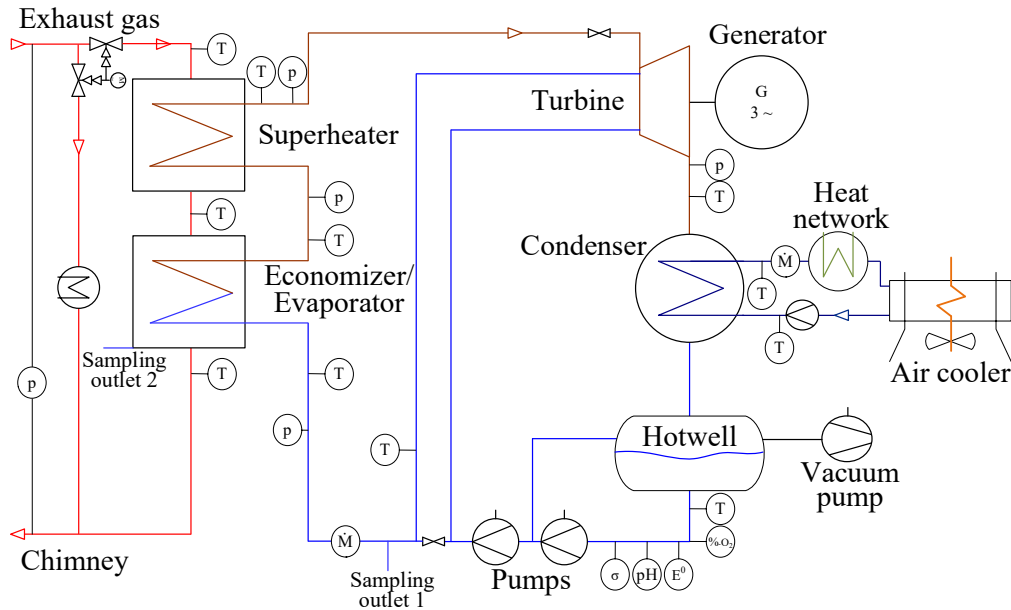
Figure 12: Simplified flow chart of the optimized plant concept with the main measuring points
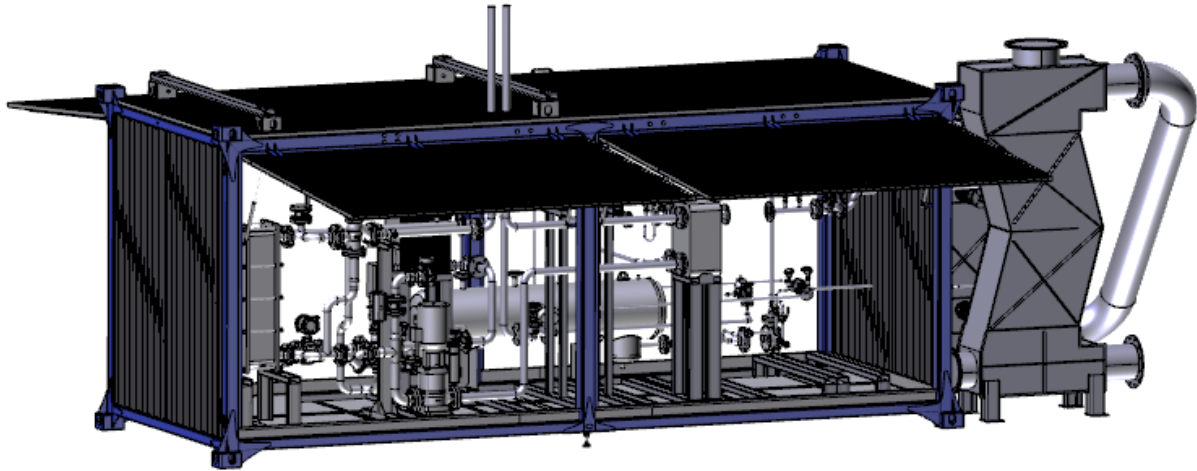
Figure 13: 3D model of the optimized WHR plant design [23]

Summary/Conclusions

High temperature waste heat recovery with water as working fluid faces the challenge of economic feasibility and reliability. While the profit is increasing due to high energy prices, raw material and production costs are rising at the same time. An economic operation is given primarily in continuous operation over many years, with little maintenance and defects. The optimizations and long-term measurement results of the MicroRankine test plant, which have been summarized in the present study, contribute to overcoming these hurdles and to making comprehensive use of previously unused waste heat. In addition to techno-economic optimizations of the operating parameters both on the side of the heat source and the heat sink for the use case of the MicroRankine pilot plant, analyses and countermeasures of corrosion were carried out. In long-term measurements, the water-chemical parameters were adjusted in order to meet the national and international requirements and thus reduce corrosion to a minimum. Verified solution proposals were given for different applications. Finally, an optimized overall plant concept was presented, in which the individual apparatuses were optimized from a techno-economic point of view, resulting in a compact, reliable and profitable plant design.

Acknowledgments

References:

[1] Vélez, F., Segovia, J., Martín, M., Antolín, G., Chejne, F., Quijano, A., *A technical, economical and market review of organic Rankine cycles for the conversion of low-grade heat for power generation*, Renewable and Sustainable Energy Reviews, 2012.

[2] Zhang, X., Wu, L., Wang, X., Ju, G., *Comparative study of waste heat steam SRC, ORC and S-ORC power generation systems in medium-low temperature*, Applied Thermal Engineering, 2016.

[3] Raab, F., Klein, H., Opferkuch, F., *Steam Rankine Cycle instead of Organic Rankine Cycle for Distributed Waste Heat Recovery – Pros and Cons*, 6th International Seminar on ORC Power Systems, 2021.

[4] Raab, F., Klein, H., Opferkuch, F., *A Steam Rankine Cycle Pilot Plant for Distributed High Temperature Waste Heat Recovery*, 9th Heat Powered Cycles Conference, 2022.

[5] DIN EN 1092-1, *Flanges and their joints - Circular flanges for pipes, valves, fittings and accessories, PN designated - Part 1: Steel flanges*, Beuth Verlag GmbH, 2018.

[6] DIRECTIVE 2014/68/EU of the European Parliament and of the Council of 15 Mai 2014 *on the harmonisation of the laws of the Member States relating to the making available on the market of pressure equipment*, Beuth Verlag GmbH, 2014.

[7] Güntner Product Configurator (myGPC), Güntner GmbH & Co. KG, https://www.myguentner.com/#/mygpc.

[8] DIN EN 12953-10, *Shell boilers - Part 10: Requirements for feedwater and boiler water quality*, Beuth Verlag GmbH, 2003.

[9] TRD 604, *Operation of steam boiler plants with steam generators of group IV without permanent supervision*, 1986.

[10] Opel, O., *Bericht Korrosionsmessung an MicroRankine-Versuchsanlage*, Dr. Opel UG, 2021.

[11] Zargari, M., Opel, O., Wiegand, M., *Vermeidung von Korrosion in hydraulischen Systemen*, DKV-Tagung Bremen, 2017.

[12] Zimmermann, H., Rümler, K., Fiebelmann, R., *Grundlagen Wasserchemie, Kessel- und Speisewasser Korrosion und Beläge Wasseraufbereitung*, SPIRAX SARCO GmbH, 2017.

[13] VDI 2035, *Prevention of damage in water heating installations - Scale formation and waterside corrosion*, Beuth Verlag GmbH, 2021.

[14] Bursik, A., *Vergleichende Untersuchungen zum Kondizionierung von Kesselspeisewasser*, VGB Kraftwerkstechnik, Jg. 62 (1), S. 36-41, 1982.

[15] Wagner, R., Czempik, E., Arent, E., *Konservierung der GuD Kraftwerke Knapsack 1 und 2 mit dem filmbildenden Amin Octadecylamin (ODA), Betriebserfahrung nach einem Jahr*, VGB PowerTech 11, 2016.

[16] Dooley, B., Petrova, T., Svoboda, B., *The Possible Effect of FFP on Steam Turbine Performance*, IAPWS International Conference Film Forming Products, Lucerne, Switzerland, 2017.

[17] Bäßler, R., *Beitrag zur Charakterisierung der Inhibierenden Wirkung von Octadecylamin auf die Korrosion des Stahles, 1.5541 bis 250 °C*, Doctoral Thesis, TU Dresden, 1997.

[18] IAPWS TGD11-19*, Technical Guidance Document: Application of Film Forming Substances in Industrial Steam Generators*, 2019.

[19] DIN EN 12502-4, *Protection of metallic materials against corrosion - Guidance on the assessment of corrosion likelihood in water distribution and storage systems - Part 4: Influencing factors for stainless steels*, Beuth Verlag GmbH, 2004.

[20] DIN 50930-4, *Korrosion der Metalle; Korrosion metallischer Werkstoffe im Innern von Rohr-leitungen, Behältern und Apparaten bei Korrosionsbelastung durch Wässer; Beurteilung der Korrosionswahrscheinlichkeit nichtrostender Stähle*, Beuth Verlag GmbH, 1993.

[21] Ambros, P., Raab, D., Keite, M., Raab, F., Opferkuch, F., *Compact and High Efficient Rankine-Evaporator following Economical Targets*, 6th International Seminar on ORC Power Systems, 2021.

[22] Streit, P., Weiß, A., *Parameterized, numerical design of a two-wheel Curtis steam turbine for small scale WHR,* 20th Conference on Power System Engineering, MATEC Web Conf., Volume 345, 2021.

[23] Hagengruber, T., UAS Messtechnik GmbH.

Demand-Side Management for Direct Air Carbon Capture and Storage: An Enabler for Low-Cost Negative Emissions?

P. Postweiler[1], **M. Engelpracht**[1], **D. Rezo**[1], **B. Nilges**[1] and **N. von der Assen**[1*]

[1]Institute of Technical Thermodynamics, RWTH Aachen University, Aachen, Germany

[*]Corresponding author: niklas.vonderassen@ltt.rwth-aachen.de

Abstract

Adsorption-based Direct Air Carbon Capture and Storage (DACCS) can help to limit the average global temperature rise below 2 °C by removing CO_2 from the atmosphere. To enable net-negative CO_2 emissions, DACCS must be powered by low-carbon energy sources to help mitigate climate change. However, most low-carbon energy sources are highly volatile, thus challenging energy system integration. One way to integrate volatile energy sources cost-effectively into an energy system is by demand-side management. In demand-side management, flexible energy consumers adjust their load to synchronise the demand with the volatile energy production and getting financial benefits in return. In this work, we present a framework that allows investigating whether it can be economically advantageous to enhance the load flexibility of the DACCS system and, thus, use DACCS for demand-side management. For this purpose, we extend the typical steam-assisted temperature vacuum swing adsorption cycle with (1) two additional phases and (2) variable air and steam mass flows during the adsorption and desorption phases, respectively, to gain more flexibility. Then, we introduce a detailed dynamic DACCS system model to evaluate the advantages of flexible operation. Finally, we combine a rolling horizon algorithm with a particle swarm optimisation algorithm for the process design optimisation in a flexible operation mode. While optimisation results are pending, this paper focuses on the framework and methodology.

Keywords: negative emission technologies, flexible operation, life-cycle carbon footprint, net removal costs.

Abbreviations:	
AF	Annuity Factor
CapEx	Capital Expenditure
CE	Carbon Dioxide Emissions
CRE	Carbon Removal Efficiency
DAC	Direct Air Capture
DACCS	Direct Air Carbon Capture and Storage
DSM	Demand-Side Management
GCRC	Gross Carbon Removal Cost
HTHP	High-Temperature Heat Pump
IPCC	Intergovernmental Panel on Climate Change
KPIs	Key Performance Indicators
NCRC	Net Carbon Removal Cost
NETs	Negative Emission Technologies
OpEx	Operational Expenditure
PP	Plant Productivity
S-TVSA	Steam-Assisted Temperature Vacuum Swing Adsorption Cycle
TVSA	Temperature Vacuum Swing Adsorption Cycle

Introduction

Limiting anthropogenic climate change below 1.5-2 °C is one of humanity's major challenges. First and foremost, a massive and rapid reduction in CO_2 emissions is crucial and urgently necessary [1]. Nevertheless, to a certain extent, Negative Emission Technologies (NETs) are mandatory according to almost all integrated assessment model pathways of the IPCC that reach the 1.5-2 °C goal [1]. NETs are imperative as they can compensate for hard-to-abate or unavoidable emissions and the overshooting of the earth's carbon budget.

Possible NETs range from enhancing natural carbon sinks to technical capturing CO_2 from the atmosphere combined with permanent storage. Among the wide range of possible NETs being discussed in science, adsorption-based Direct Air Carbon Capture and Storage (DACCS) is considered particularly promising due to its (1) high removal potential [2], (2) low operating temperatures (i.e., 80-130 °C) [3], and (3) minimal land use [4]. Despite the advantages, adsorption-based DACCS is still an expensive and energy-intensive process and thus requires further research.

The energy intensity of DACCS leads to the need for low-carbon energy sources. Otherwise, large amounts of CO_2 are emitted by the energy supply leading to high net removal costs or even more CO_2 emitted by the energy supply than removed [5]. Thus, low-carbon energy sources are crucial for DACCS. However, low-carbon energy sources like wind or solar energy are highly volatile, making system integration difficult. A way to cost-efficiently integrate volatile energy sources into an energy system is to manage the load, called Demand-Side Management (DSM) [6,7]. With DSM, processes that do not necessarily have to operate continuously are switched on or off, throttled, or ramped up as required. In return, the operators of flexible processes for DSM benefit from financial incentives like temporarily low energy costs. Thus, DSM for DACCS could help to reduce the overall removal costs of CO_2.

Even though studies have already examined the first theoretical benefits of flexible DACCS operation [7–9], a detailed assessment of DSM application for DACCS systems is still lacking to the best of the authors' knowledge:

(1) No suggestions have been made on how the standard cycles for adsorption-based DACCS (i.e., Temperature Vacuum Swing Adsorption cycle (TVSA) and Steam-assisted Temperature Vacuum Swing Adsorption cycle (S-TVSA)) have to be adjusted to enhance flexible DACCS operation.
(2) No analysis has been performed on the flexible operation of a DACCS system based on dynamic models capturing the transient and discontinuous behaviour.
(3) No DACCS system model combined with a suitable procedure has been proposed that allows a holistic evaluation of the net carbon removal cost for a flexible operation of a DACCS system for DSM.

Therefore, in this work, we suggest how the standard cycle of adsorption-based DAC(CS) can be adapted to enhance the flexibility of the energy demand without using energy storage. Furthermore, we introduce a dynamic DACCS model, which examines the economic benefits of a flexible operating DACCS system. Thus, this work presents a framework that allows for a holistic analysis of the potential of a flexible DACCS operation for DSM.

Method

This chapter is divided into four subchapters, representing the framework's steps for a holistic evaluation of a flexible DACCS operation for DSM. These steps are (1) cycle adaptations for flexible operation, (2) dynamic DACCS system model, (3) system performance evaluation, and (4) process design optimisation.

Cycle adaptations for flexible operation

The standard adsorption cycles for amine functionalised sorbents for DAC(CS) applications are the TVSA or the S-TVSA. Both cycles have 4 or 5 phases [10,11]: (1) Adsorption, (2) blowdown, (3) heating, (4) desorption (TVSA without and S-TVSA with a steam mass flow), and (5) cooling (optional phase to reduce sorbent degradation [10]). A detailed description of all phases can be found in the literature [5,10,11].
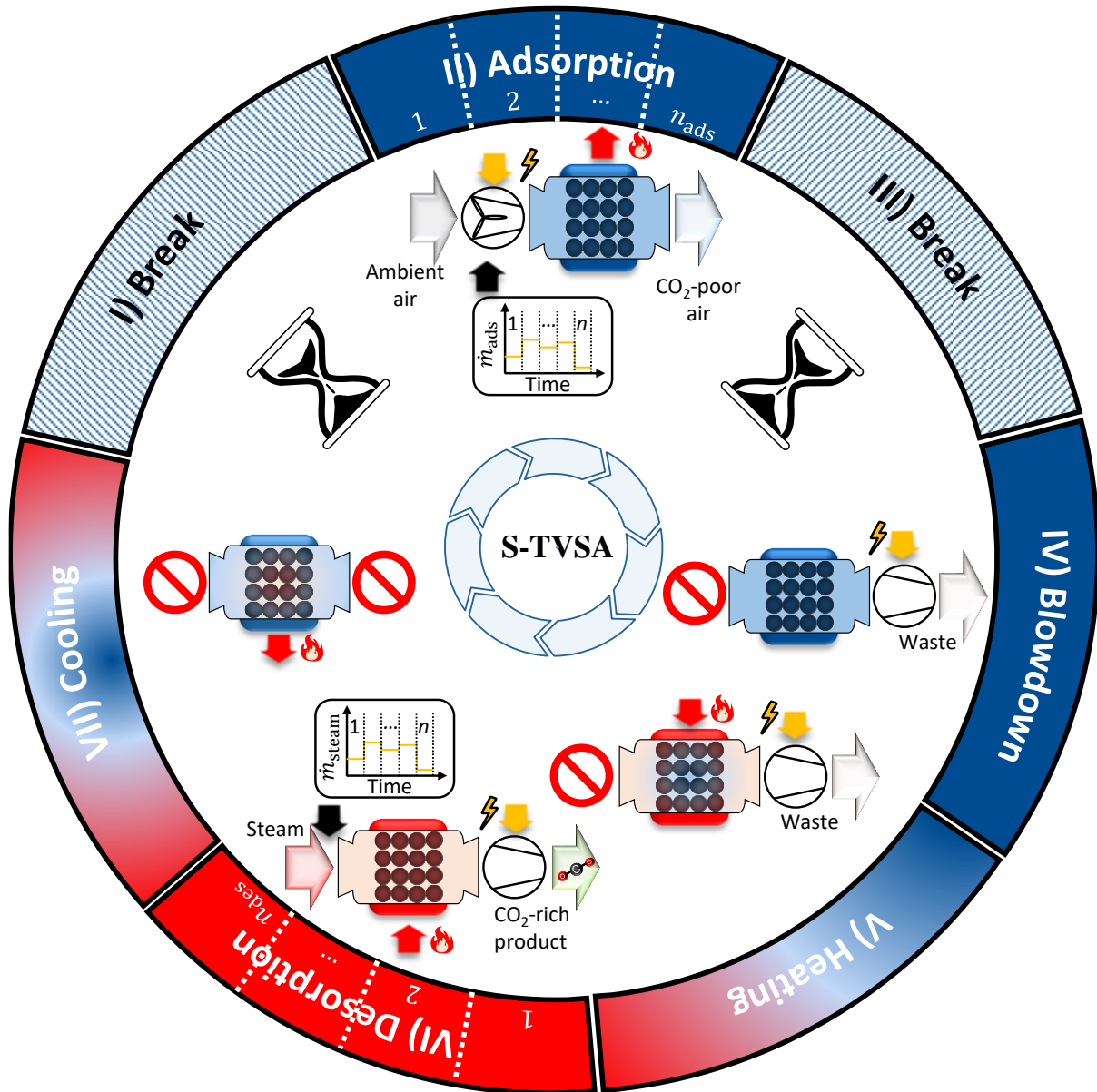
Figure 1: Illustration of the flexibility-enhanced steam-assisted temperature vacuum swing adsorption cycle with the main phases II) adsorption, IV) blowdown, V) heating, VI) desorption, VII) cooling, and the two breaks before I) and after adsorption III). The adsorption and desorption phases are divided into n sub-phases. For each sub-phase, different mass flow rates are possible (i.e., air mass flow during adsorption and steam mass flow during desorption). The colour code of the outer ring represents the temperature trajectory in the DAC adsorption column: From ambient temperature (blue) to desorption temperature (red).

To increase the flexibility of both cycles, we recommend two measures: (1) The extension by two additional phases and (2) the division of the adsorption and desorption phases into several

sub-phases (see **Figure 1**). The two additional phases are a break before and after the adsorption phase, where nothing happens. These breaks can be used to pause the entire cycle operation in case of high electricity prices or a high carbon footprint of the electricity. With high electricity prices and carbon footprints, it may be reasonable to suspend operations for a specific time from economic and ecological perspectives. In addition to the two new phases, the adsorption and desorption phases are subdivided into n sub-phases (n_{ads} and n_{des}), where the air or steam mass flow can be independently changed. Since the mass flow rates are directly correlated to the capture process's specific energy demand and the plant productivity of the DACCS system, the mentioned sub-phases enhance the flexibility of the operation.

During the adsorption phase, a high air mass flow results in high velocities within the column and, in turn, a large pressure drop. High pressure drops increase the fan's energy demand, which drives the air through the column. However, in return, an increased air mass flow accelerates the adsorption phase and, thus, increases plant productivity.

For the steam mass flow during the desorption phase, similar correlations apply. A higher steam mass flow increases the specific energy demand since additional heat is needed to heat, evaporate, and superheat the water. Despite this additional heat demand, the superheated steam also heats the sorbent very quickly and displaces new desorbed CO_2. Thus, desorption is faster, and consequently, plant productivity increases. Hence, adapting both mass flow rates (air and steam) results in a trade-off between specific energy demand and plant productivity. This trade-off results in varying economically optimal mass flow rates depending on the fluctuating electricity prices. Note that the more sub-phases are used, the better the mass flow can be adapted to the electricity price. In the ideal case, the number of sub-phases corresponds to the interval length of constant electricity prices (e.g., 15 min.). With fewer sub-phases, it is impossible to respond to every change in electricity prices but it is still possible to respond to main trends.

For all other phases, nothing is changed from the phases described in the literature, as added values of making the process more flexible do not justify additional efforts. For example, pauses in or between phases IV) blowdown and VII) cooling would be possible to increase flexibility. However, the adsorption column is in a vacuum from the blowdown phase, and it can be assumed that an adsorption column is not perfectly sealed. Hence, air would infiltrate the column. Furthermore, pauses are even more harmful between the V) heating and VII) cooling phase because the adsorption column is heated, which causes heat losses. Minimising these heat losses would require an enormous design effort, not proportional to the slightly increased flexibility. Hence, we argue that further cycle changes than the proposed ones to increase flexibility are not beneficial. Overall, the proposed changes greatly increase the cycle flexibility, making the presented 7-phase S-TVSA practical for DSM.

Dynamic DACCS system model

In order to conduct a sound and holistic evaluation of a DSM operation of a DACCS system, many system-specific indicators are needed. In this work, we use a detailed dynamic DACCS system model to calculate these system-specific indicators. **Figure 2** illustrates the flexible DACCS system model, its components, and system boundaries. The entire DACCS system model is written in the modelling language Modelica and based on components of our model library SorpLib [12], freely available on Gitlab [13].
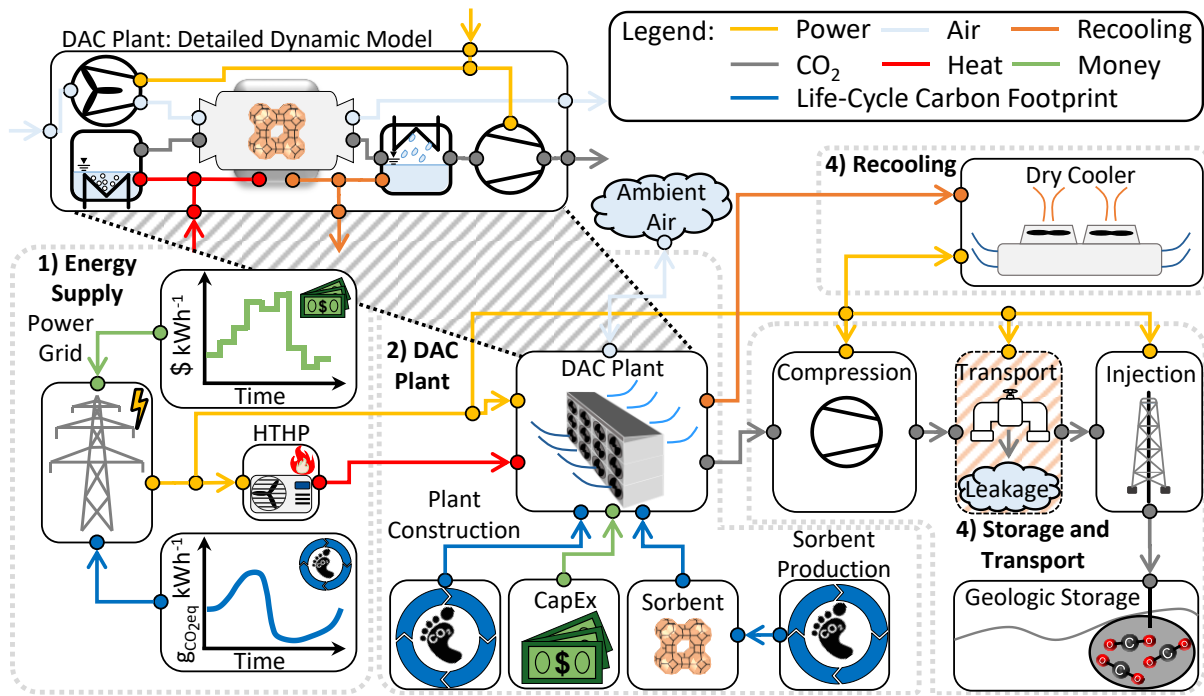
Figure 2: Illustration of the DACCS system model, including the main components 1) energy supply, 2) DAC plant, 3) storage and transport, and 4) recooling. Electricity flows are yellow and heat flows are red. Life-cycle carbon footprints are blue, CO₂ mass flows are grey, and money is green.

The DACCS system model **(Figure 2)** consists of four main components:

(1) **Energy supply [14,15]:** The energy supply model consists of inputs for the trajectories of the electricity price and the carbon footprint of the grid electricity. Furthermore, a high-temperature heat pump (HTHP) converts electricity into heat and provides all required process heat. Thus, the energy supply model detects all energy needs of the DACCS system and allocates the costs and carbon footprint for the required energy flows on a time-resolved basis.

(2) **DAC plant [5,14]:** The main model component of the DACCS system model is the DAC plant model. The DAC plant model consists of a adsorption column model [5] that is linearly scaled up to 4 kt yr^{-1} for a reference process design. The DAC adsorption column is parameterised according to the model published by Stampi-Bombelli et al. [11]. Further, the DAC plant includes the carbon footprint of the plant construction, sorbent production, and sorbent consumption, according to Deutz et al. [14]. Finally, the DAC plant requires Capital Expenditure (CapEx) for construction. The CapEx of a DAC plant is still uncertain and will decrease as the installed capture capacity increases [16]. Therefore, we do not use a fixed value for the CapEx and adjust it for each case study.

(3) **Storage and transport [15,17,18]:** The model component storage and transport includes the power demands for the CO₂ compression from ambient to pipeline pressure, the recompression to compensate for pressure losses during transport, and the injection into the geological storage reservoir. Further, the storage and transport component considers CO₂ leakage during pipeline transport.

(4) **Recooling [19]:** The last model component of the DACCS system is recooling. For recooling, we used a simple model of a dry cooler, which has a specific power demand for a fan per discharged heat.

Detailed explanations of the DACCS system model, including equations, can be partly found in our previous work [5] and references given in each part of the main components.

The DACCS system under investigation is designed to function as a standalone system, utilising an HTHP as its heat source. However, there is potential for DACCS systems to integrate fluctuating or constant waste heat from nearby industries, offering promising options. However, using constant waste heat generally reduces the benefits of DSM. On the other hand, it is challenging to predict the impact of DSM on fluctuating waste heat, as it could either increase or decrease the potential benefits. Thus, future research should investigate the positive effects of DSM on waste heat-powered DACCS systems.

System performance evaluation

The DACCS system model allows for determining the performance of the DACCS system in a DSM operation. However, sound Key Performance Indicators (KPIs) are crucial for evaluating and optimising DACCS systems [5]. From a "techno-ecological" point of view, Carbon Removal Efficiency (CRE) is a sound KPI. The CRE is defined as [14,15]

$$CRE = 1 - \frac{CE_{cap.} + CE_{stor.}}{m_{co_2,rem}} \qquad \text{Eq. 1}$$

and is calculated using the total amount of equivalent Carbon Dioxide Emissions (CE) during the capturing $(CE_{cap.})$ and storage process $(CE_{stor.})$ and the total amount of removed CO_2 from the atmosphere $(m_{co_2,rem})$. Thus, the CRE indicates the net removed percentage of the total amount of captured CO_2. It is important to note that all values between 1 and 0 mean a net removal of CO_2 from the atmosphere. On the contrary, the process has emitted more CO_2 than captured for negative CREs.

In addition to a "techno-ecological" assessment with the CRE, an economic assessment is equally important. Therefore, Gross Carbon Removal Cost (GCRC) is suitable for determining the levelised cost of the removal process and reads as [20]

$$GCRC = \frac{CapEx_{DACCS} \, AF + OpEx_{DACCS}}{PP}. \qquad \text{Eq. 2}$$

Thus, the Capital Expenditure $(CapEx_{DACCS})$ of the DACCS system, the Annuity Factor AF , the Operational Expenditure $(OpEx_{DACCS})$, and the Plant Productivity (PP) (gross captured mass of CO_2 per year for a specific DAC plant) calculate the GCRC.

Combining the KPIs CRE and GCRC forms an enhanced KPI, the Net Carbon Removal Cost (NCRC), which merges the two dimensions techno-ecological and economical [16,21]:

$$NCRC = \frac{1}{CRE \, (\boldsymbol{p_c})} \, GCRC \, (\boldsymbol{p_c}). \qquad \text{Eq. 3}$$

The NCRC is a particularly meaningful KPI, as it gives a price to the actual benefit, i.e., the net removed CO_2 mass from the atmosphere. Hence, we use the NCRC as KPI to evaluate the performance of the flexible DACCS system for DSM. Furthermore, as indicated in Eq. 3, both the CRE and the GCRC are directly related to the process design variables $\boldsymbol{p_c}$, allowing to optimise the process design to minimise the NCRC.

Process design optimisation

The process design variables $\boldsymbol{p_c}$ include at least $7 + n_{\text{ads}} + n_{\text{des}}$ variables ranging from the mass flow rates in each sub-phase of the adsorption and desorption phase to the phase times. Each cycle can have an individual process design in a flexible operation mode to provide the highest possible flexibility for the DSM. However, as the process design is being optimised, the number of process design variables is also the number of degrees of freedom for the optimisation problem. Ideally, the number of sub-phases (n_{ads} and n_{des}) leads to a sub-phase length of 15 minutes so that the process design is adjustable to any change in electricity prices. A sub-phase length of 15 min and a cycle time of 6 hours would result in 31 degrees of freedom for optimisation of just one cycle. The number of degrees of freedom reduces by longer sub-phase lengths. However, longer sub-phases also lead to slightly worse optimisation results. Hence, it still has to be tested with how many degrees of freedom the optimisation problem can be reliably solved without worsening optimisation results. Further, the number of degrees of freedom scales with the number of cycles considered. Consequently, the computational effort disproportionately increases with the number of cycles.

To deal with the increasing computational effort for more cycles and the problem of ideal foresight, we use a rolling horizon algorithm for process design optimisation. In a rolling horizon optimisation, the examined time period is divided into certain short time intervals [22,23]. The length of the time intervals varies based on the application. To keep the computational effort low, the time interval length is equal to the length of one cycle. For each step k of the rolling horizon algorithm, a process design optimisation is carried out for the time intervals k and $k + 1$. Hence the optimisation horizon is two cycles. The result for the time interval $k + 1$ is discarded, as it is only used to consider the effects of the time interval k on the time interval $k + 1$ in the process design optimisation and thus realizing an overlapping of each individual optimisation step. The time intervals are run consecutively, and each process design optimisation gets (1) all data from previous cycles (i.e., DACCS system model is initialised with end values of the previous cycle) and (2) the input data (i.e., time-resolved electricity prices and carbon footprints) from the time intervals k and the $k + 1$. For each time interval k of the rolling horizon algorithm, the process design optimisation problem reads as follows:

$$
\min_{x(\cdot), z(\cdot), \boldsymbol{p_{c,k}}, \boldsymbol{p_{c,k+1}}} \quad
\begin{aligned}
&\text{NCRC}_k\big(x(\tau_{\text{cycle},k}), z(\tau_{\text{cycle},k}), \boldsymbol{p_{c_k}}\big) + &&\text{objective}\\
&\text{NCRC}_{k+1}\big(x(\tau_{\text{cycle},k+1}), z(\tau_{\text{cycle},k+1}), \boldsymbol{p_{c_{k+1}}}\big) &&\text{function}
\end{aligned}
$$

$$
\text{s.t.} \quad
\begin{aligned}
\dot{x} &= f(x(\tau), z(\tau), \boldsymbol{p_c}) &&\text{dynamic}\\
0 &= g(x(\tau), z(\tau), \boldsymbol{p_c}) &&\text{model}\\
x(t = \tau_{\text{start},k}) &= x(t = \tau_{\text{end},k-1}) &&\text{initialisation.}
\end{aligned}
$$

Eq. 4

Thus, the NCRC are minimised for each time interval k and the next time interval $+1$. The optimisation is subject to the differential-algebraic system of equations of the dynamic model and the initial values from the previous time interval of the rolling horizon algorithm. The optimisation problem is solved with a heuristic particle swarm algorithm included in the Python package Pymoo [24]. Thus, with the presented method, we can look at the performance of a DACCS system for DSM over a long period of time, which is the basis for a fair and holistic evaluation and to answer if it is economically feasible and worthwhile.

Summary

In this work, we propose a new 7-phase steam-assisted temperature vacuum swing adsorption cycle where the flexibility of the process design is enhanced by extending established cycles for direct air capture. This enhanced flexibility in process design can be used to operate a direct air carbon capture and storage system in a demand-side management mode and to react to changes in the electricity market (such as price or carbon footprint) during operation. Furthermore, a complete system model is developed to study the impact of flexible operation and, thus, of demand-side management on the net carbon removal costs. Finally, an optimisation framework is presented, combining a rolling horizon algorithm and a heuristic optimiser, which allows for determining optimal process designs of the direct air carbon capture and storage system while applying demand-side management for a broad period of time. Overall, our framework allows future work to answer whether demand-side management of direct air carbon capture and storage can reduce the cost of negative emissions.

Acknowledgments

References

[1] IPCC, *Global warming of 1.5°C. An IPCC Special Report on the impacts of global warming of 1.5°C above pre-industrial levels and related global greenhouse gas emission pathways, in the context of strengthening the global response to the threat of climate change, sustainable development, and efforts to eradicate poverty,* 2018.

[2] National Academies of Sciences, Engineering, and Medicine. *Negative Emissions Technologies and Reliable Sequestration: A Research Agenda*, 2019.

[3] Fasihi, M., Efimova, O., Breyer, C., "Techno-economic assessment of CO_2 direct air capture plants", Journal of Cleaner Production, 2019.

[4] Fuhrman, J., McJeon, H., Patel, P., Doney, S. C., Shobe, W. M., Clarens, A. F., "Food–energy–water implications of negative emissions technologies in a +1.5 °C future", Nature Climate Change, 2020.

[5] Postweiler, P., Engelpracht, M., Gibelhaus, A., von der Assen, N., "Environmental Process Optimisation of Adsorption-based Direct Air Capture of CO2", 9th HPC Conference Proceedings, 2022.

[6] Paulus, M., Borggrefe, F., "The potential of demand-side management in energy-intensive industries for electricity markets in Germany", Applied Energy, 2011.

[7] Warren, P., "A review of demand-side management policy in the UK", Renewable and Sustainable Energy Reviews, 2014.

[8] Wohland, J., Witthaut, D., Schleussner, C.-F., "Negative Emission Potential of Direct Air Capture Powered by Renewable Excess Electricity in Europe", Earth's Future, 2018.

[9] Singh, U., Colosi, L. M., "Capture or curtail: The potential and performance of direct air capture powered through excess renewable electricity", Energy Conversion and Management: X, 2022.

[10] Young, J., García-Díez, E., Garcia, S., van der Spek, M., "The impact of binary water–CO 2 isotherm models on the optimal performance of sorbent-based direct air capture processes", Energy & Environmental Science, 2021.

[11] Stampi-Bombelli, V., van der Spek, M., Mazzotti, M., "Analysis of direct capture of CO2 from ambient air via steam-assisted temperature-vacuum swing adsorption, 2020.

[12] Bau, U., Lanzerath, F., Gräber, M., Graf, S., Schreiber, H., Thielen, N.,Bardow, A., "Adsorption energy systems library - Modeling adsorption based chillers, heat pumps, thermal storages and desiccant systems", 10th International Modelica Conference, 2014.

[13] Institute of Technical Thermodynamics, RWTH Aachen University, "SorpLib: Dynamic simulation of adsorption energy systems, https://git.rwth-aachen.de/ltt/SorpLib.

[14] Deutz, S., Bardow, A., "Life-cycle assessment of an industrial direct air capture process based on temperature–vacuum swing adsorption", Nature Energy, 2021.

[15] Terlouw, T., Treyer, K., Bauer, C., Mazzotti, M., "Life Cycle Assessment of Direct Air Carbon Capture and Storage with Low-Carbon Energy Sources", Environmental science & technology, 2021.

[16] Young, J., McQueen, N., Charalambous, C., Foteinis, S., Hawrot, O., Ojeda, M., Pilorgé, H., Andresen, J., Psarras, P., Renforth, P., Garcia, S., van der Spek, M., The cost of direct air capture and storage: the impact of technological learning, regional diversity, and policy, 2022.

[17] Volkart, K., Bauer, C., Boulet, C., "Life cycle assessment of carbon capture and storage in power generation and industry in Europe", International Journal of Greenhouse Gas Control, 2013.

[18] IPCC, *2006 IPCC guidelines for national greenhouse gas inventories*: *Carbon Dioxide Transport, Injection and Geological Storage;* 2006

[19] Deutsches Institut für Normung e. V., *Energy efficiency of buildings -Calculation of the net, final and primary energy demand for heating, cooling, ventilation, domestic hot water and lighting,* DIN V 18599-7:2011-12

[20] Breyer, C., Fasihi, M., Aghahosseini, A., "Carbon dioxide direct air capture for effective climate change mitigation based on renewable electricity: a new type of energy system sector coupling", Mitigation and Adaptation Strategies for Global Change, 2020.

[21] McQueen, N., Gomes, K. V., McCormick, C., Blumanthal, K., Pisciotta, M., Wilcox, J., "A review of direct air capture (DAC): scaling up commercial technologies and innovating for the future", Progress in Energy, 2021.

[22] Baumgärtner, N., Deutz, S., Reinert, C., Nolzen, N., Kuepper, L. E., Hennen, M., Hollermann, D. E., Bardow, A., "Life-Cycle Assessment of Sector-Coupled National Energy Systems: Environmental Impacts of Electricity, Heat, and Transportation in Germany Till 2050", Frontiers in Energy Research, 2021.

[23] Grossmann, I. E., "Advances in mathematical programming models for enterprise-wide optimization", Computers & Chemical Engineering, 2012.

[24] Blank, J., Deb, K., "Pymoo: Multi-Objective Optimization in Python", IEEE Access, 2020.

Methanol – Activated Carbon Sorption Thermal Energy Storage

N. Tzabar, Y. Garfinkel, N. Lempel

Thermal Energy Science and Technology (TEST) Laboratory, Department of Mechanical Engineering, Ariel University, Ariel, 40700, Israel

Extended Abstract

Due to the rise in demand for renewable energies, several problems have emerged, such as how to best store the energy at times when production is higher than demand, how to discharge the stored energy when the grid demand rises, as well as how long the energy can stay stored with minimal losses. To mitigate these problems, we focus on sorption technology as a storage medium due to its relatively high energy storage density and because it has the potential for long-term (seasonal) storage.

In the current research, a time-dependent numerical thermal analysis of Sorption Thermal Energy Storage (STES) systems is developed, which can undergo heating and cooling cycles to charge and discharge the stored energy system. The numerical model describes bank-tube heat exchangers, and it is fully parametric to allow the investigation of various dimensions, materials, smooth or finned tubes, and different operating conditions. Figure 1 shows a schematic view of the finite-differences mesh, which models an axisymmetric single tube and the adsorbent around it, where the lowest row is the heat transfer fluid (HTF), the second row is the tube wall, and all the upper rows are the adsorbent. In cases of finned-tubes, the fins are modeled in the adsorbent rows. The model calculates the charging and discharging times, which are necessary to obtain a sufficient unified temperature distribution in the sorbent bed. In addition, the model calculates the required energy to be stored in the system. Figure 2 shows an example for presenting the numerical model results, where the temperatures at points A – D (their locations are indicated in Figure 1) are presented as a function of time. This presentation provides information about the sorbent bed temperature distribution as a function of time, in a single view. The results in Figure 2 refer to a 1 m copper tube in length, ¼ inch in diameter, and the largest radius of the system (points A and C) is 20 mm. The initial sorbent bed temperature is 298.15 K and a HTF (water) inlet temperature of 358.15 K.

In order to validate the numerical model, a demonstrator experimental system is constructed in our lab, see figure 3, and it is currently operating and generate data. Left side in Figure 3 shows a photo of the system, and the right side shows the schematics of the system. This well instrumented apparatus completes our research facility for the development of advanced STES systems.
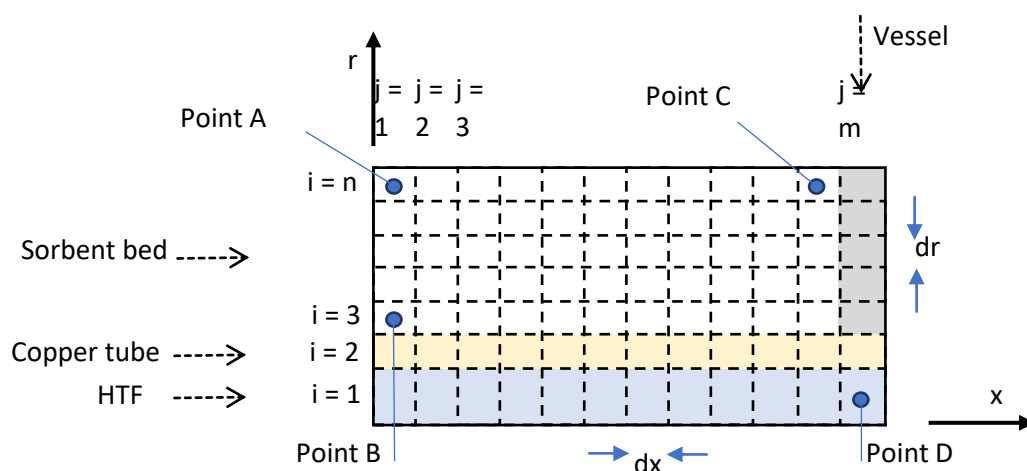
Figure 1 - A schematic view of modeling a single tube of the heat exchanger.

1
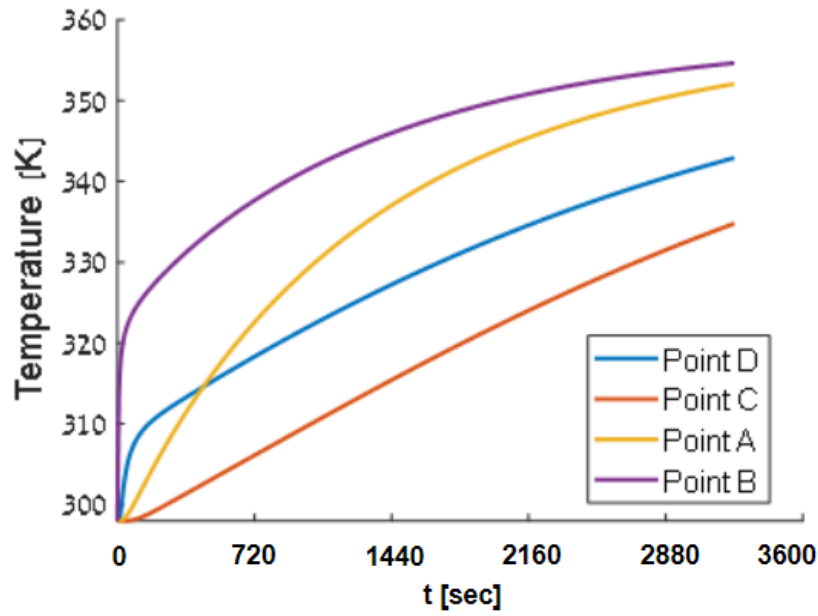
Figure 2 – An example of the numerical model results, presented by temperatures A – D as a function of time.
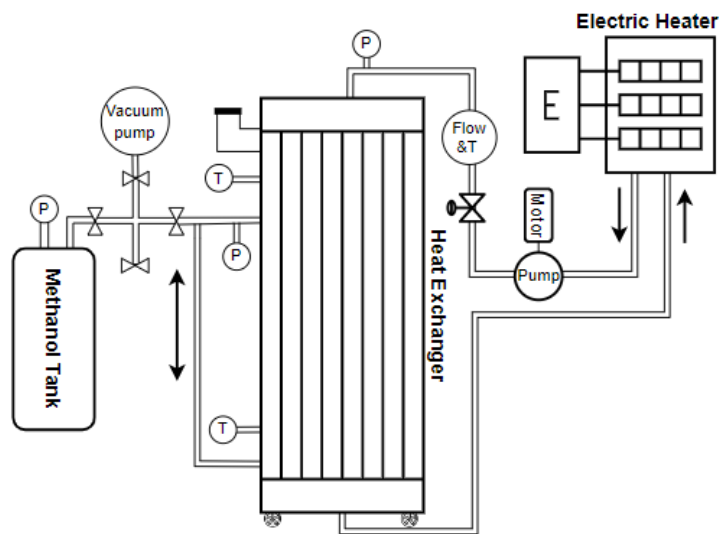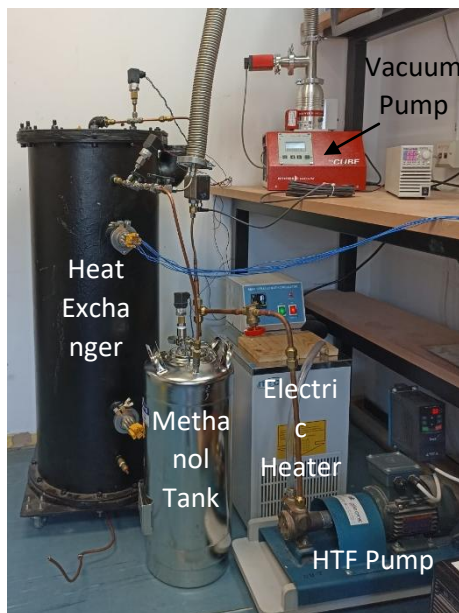
Figure 3 – Experimental demonstrator of a STES.

2

Mapping the Global Carbon Capture Efficiency of DAC

Daniel Rezo[1], **Patrik Postweiler**[1], **Mirko Engelpracht**[1] , and **Niklas von der Aßen**[1*]

[1] Institute of Technical Thermodynamics, RWTH Aachen University,
Schinkelstr. 8, 52062 Aachen, Germany

[*]Corresponding author: niklas.vonderassen@ltt.rwth-aachen.de

Abstract

Adsorption-based direct air capture is a promising technology to limit anthropogenic climate change by directly removing CO_2 from the atmosphere. Recent studies show that DAC performance strongly depends on ambient temperature and humidity, which vary widely across global regions. Moreover, the regional carbon footprint of the energy supply significantly impacts the environmental performance of DAC. Therefore, a comprehensive assessment is needed combining regional DAC performance and the carbon footprint of the energy supply. For this purpose, we present an approach for the global assessment of the carbon capture efficiency of DAC. We identify 11 countries where DAC can achieve a carbon capture efficiency of at least 85 % using today's grid electricity. Furthermore, DAC powered by wind electricity can reach a carbon capture efficiency above 95 % for most global regions. Finally, we show that the optimal placement of DAC powered by wind electricity can reduce the needed global DAC capacity by up to 4.3 % (1.36 Gt/a) in 2100.

Keywords: direct air capture, negative emission technologies, global assessment, life-cycle CO_2 emissions

1 Introduction

Climate change is mainly caused by the increased concentration of greenhouse gases (GHGs) in the atmosphere [1,2]. To combat climate change, GHG emissions must be reduced, e.g., by utilizing renewable energy sources, such as wind and solar. However, unavoidable emissions will still result from human activities like agriculture and aviation [3]. Compensating for these emissions will require active removal of CO_2 from the atmosphere, i.e., negative emissions [3]. Direct Air Capture (DAC) with subsequent storage of CO_2 is a promising approach to achieve negative emissions by capturing CO_2 directly from the atmosphere and storing it in geological formations.

Most DAC systems discussed in the literature capture CO_2 either by adsorption on a solid sorbent or absorption in a liquid solvent [4]. Adsorption-based processes typically use amine-functionalized solid sorbents to capture CO_2 from the atmosphere, while solvent-based processes typically use alkaline solutions [4,5]. Many adsorption-based processes require lower regeneration temperatures (80-130 °C) than solvent-based processes (up to 900 °C) [4,5]. Consequently, adsorption-based DAC can be exergetically advantageous, allowing for the use of heat pumps for heat provision.

Previous numerical studies of adsorption-based DAC examine the impact of ambient conditions on thermodynamic performance metrics, such as specific energy demand (SED) and productivity [6–8]. In general, these studies find that ambient temperature and humidity significantly affect the performance of DAC. By optimization of a dynamic DAC model, Wiegener et al. calculate the optimal SED and productivity for given ambient conditions [8]. For this purpose, the authors derive a linearized representation of the optimized DAC model,

reducing computational effort and allowing for a simplified assessment of DAC at varying ambient conditions. Sendi et al. conduct a geospatial analysis of DAC, integrating global hourly weather data into a dynamic DAC model [7]. The authors provide global maps of the SED and productivity of DAC. Their analysis shows that hot and dry regions decrease the SED, while relatively cold and dry regions increase the productivity of DAC [7].

Recent Life Cycle Assessments (LCA) investigate the environmental performance of adsorption-based DAC [9–11]. In this context, many studies use the carbon capture efficiency (CCE) as a performance metric [9,12,13]. The CCE represents the captured amount of CO_2 after subtracting the CO_2 emissions from the DAC process relative to the captured amount of CO_2. The emissions from the DAC process encompass the construction, operation, and end-of-life of the DAC plant. CCE values of more than 95 % can be achieved using wind electricity [9]. On the other hand, DAC systems driven by fossil energy may exhibit negative CCE values resulting in additional instead of negative emissions. Hence, the carbon footprint of the energy supply significantly impacts the CCE and, thus, the environmental performance of DAC.

Terlouw et al. further investigate the interplay of energy supply and environmental performance using a static DAC model and regionalized data on the carbon footprint of the energy supply [11]. The authors identify countries where a DAC system with subsequent CO_2 storage can achieve negative emissions using solar energy and today's grid electricity, respectively. However, the static DAC model does not account for the effect of regional climates on DAC performance.

In sum, recent assessments of DAC show that climate conditions greatly impact the SED. Furthermore, LCA studies indicate that the CCE of DAC strongly depends on the energy supply's carbon footprint, which varies widely across global regions. However, a comprehensive analysis of the CCE is lacking, which considers both climate-dependent DAC performance and regional carbon footprints of the energy supply. Hence, we examine the CCE of DAC on a global level combining the climate-dependent performance of DAC and the regional carbon footprints of the energy supply in this work. For this purpose, we present an approach for the global assessment of the CCE of DAC.

Global Assessment of the Carbon Capture Efficiency of DAC

To assess the CCE of DAC on a global level, we use the 3 step approach illustrated in **Figure 1**.
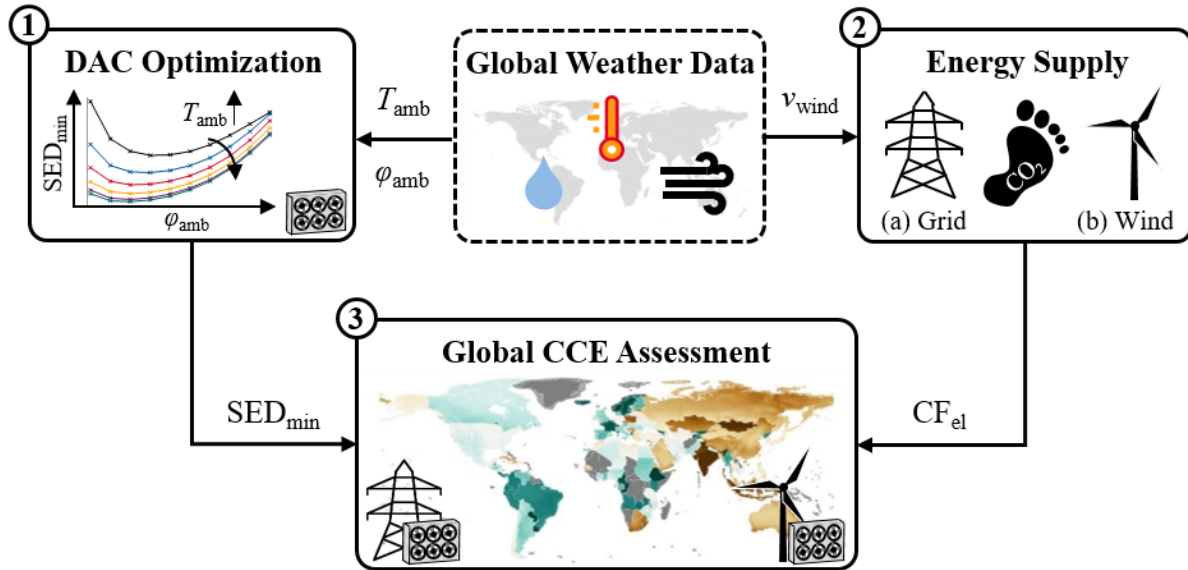
Figure 1: Geospatial assessment of the carbon capture efficiency (CCE) of DAC. For the assessment, data on global ambient temperature (T_{amb}), humidity (φ_{amb}), and wind speed (v_{wind}) is used to determine the regionalized minimum specific energy demand (SED_{min}) of DAC and the regionalized carbon footprint of the energy supply (CF_{el}).

In the first step, a performance map is derived by optimization of a dynamic DAC model. The performance map is a linearized representation of the model that allows for quick calculation of the minimum achievable SED values at different ambient temperature and humidity levels [8].

In the second step, two scenarios for the carbon footprint of the electricity supply (CF_{el}) are defined: (a) A DAC system powered by grid electricity as today's scenario and (b) a DAC system solely powered by wind electricity as best case scenario. For scenario (a), country-specific data on regional carbon footprints of grid electricity is obtained from the LCA database ecoinvent [14]. For scenario (b), we calculate regionalized carbon footprints of wind electricity.

To this end, we use high-resolution global weather data on wind speed (v_{wind}) and ambient temperature (T_{amb}) to calculate regional wind energy yields. Subsequently, we determine regional carbon footprints of wind electricity by combining regional wind energy yields and LCA data of a wind power plant. To calculate the regional SED of DAC, we combine global data on ambient temperature (T_{amb}) and relative humidity (φ_{amb}) with the performance map determined in the first step. Global weather data is obtained from NASA's MERRA-2 dataset [15]. MERRA-2 provides hourly resolved weather data on a high-resolution global grid with a tile size of 0.5 ° lat x 0.625 ° lon. Data access is based on a framework developed by Held et al. [16]. MERRA-2 provides weather data from 1980 to the present. For this study, weather data from 2019 is used to demonstrate our approach.

In the third step, we generate a global map of the CCE of DAC by combining regional data on the SED of DAC and carbon footprints of the electricity supply.

Modelling and Optimization of DAC

We investigate a four-phase temperature-vacuum swing (TVS) DAC process based on a dynamic model implemented by Postweiler et al. [13] in the programming language Modelica, using the Modelica library SorpLib developed at our institute [17,18]. As sorbent we use amine-functionalized cellulose called APDES-NFC. For explanatory purposes, the 4 phases of the process are reduced to an adsorption phase and a general desorption phase. For a detailed description of the four-phase TVS process, please refer to [13,19].

In the adsorption phase, a fan blows air at ambient conditions, i.e., ambient temperature (T_{amb}) and relative humidity (φ_{amb}), through the adsorption column. The sorbent adsorbs H_2O and CO_2 from the airflow, and CO_2-poor air leaves the column. To overcome the pressure drop of the adsorption column, the fan uses electrical power ($\dot{W}_{fan}$). In the subsequent general desorption phase, the column is evacuated by a vacuum pump until it reaches the desorption pressure (p_{des}). In the process, the vacuum pump consumes electrical power ($\dot{W}_{vac}$). The heat flow ($\dot{Q}_{des}$) is supplied to heat up thermal masses and drive endothermic desorption of CO_2 and H_2O, regenerating the sorbent. After the sorbent is regenerated, the cyclic process continues with the next adsorption phase.

In our study, the heat flow during the general desorption phase is supplied by a heat pump using electrical power ($\dot{W}_{hp}$). Thus, the entire DAC system is powered electrically, in total consuming the electrical power ($\dot{W}_{el,total}$). The heat pump's coefficient of performance (COP) is described as a function of the temperature lift (ΔT) between the ambient air and the required heating temperature during desorption. This function is based on empirical data by Schlosser et al. [20]:

$$COP = 15.68\,\Delta T^{-0.355} \tag{1}$$

Figure 2 shows the investigated DAC system.
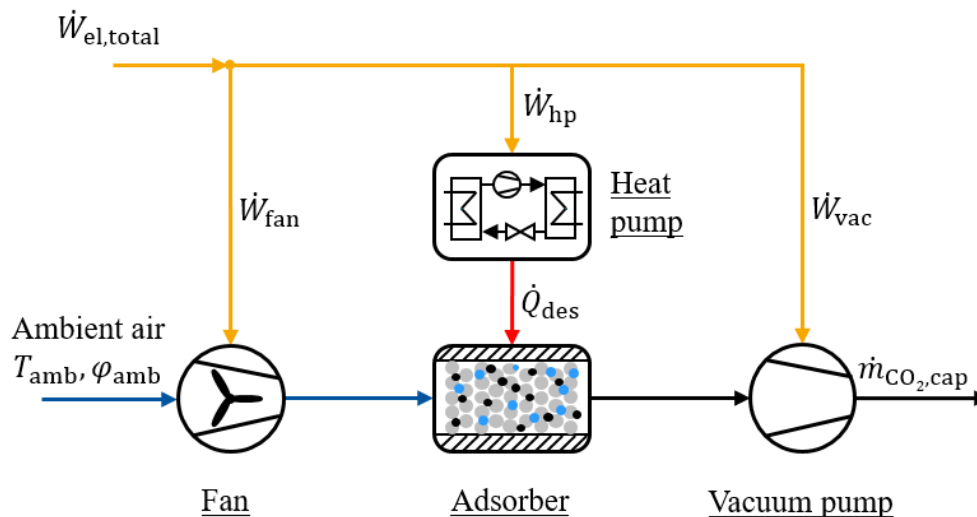
Figure 2: Model of the investigated DAC system capturing the CO_2 mass flow $\dot{m}_{CO_2,cap}$ from ambient air with temperature T_{amb} and relative humidity φ_{amb}. Yellow lines indicate electrical power flows: total system ($\dot{W}_{el,total}$), fan ($\dot{W}_{fan}$), heat pump ($\dot{W}_{hp}$), and vacuum pump ($\dot{W}_{vac}$). The red line marks the supplied heat flow to the adsorber ($\dot{Q}_{des}$).

The SED of the DAC system is defined as the electricity consumption of the entire system over the cycle length τ_{cycle} relative to the captured mass of CO_2 within a cycle:

$$\text{SED} = \frac{\int_{\tau_0}^{\tau_{cycle}} \dot{W}_{el,total}\, d\tau}{\int_{\tau_0}^{\tau_{cycle}} \dot{m}_{CO_2,cap}\, d\tau} = \frac{\int_{\tau_0}^{\tau_{cycle}} (\dot{W}_{fan} + \dot{W}_{hp} + \dot{W}_{vac})\, d\tau}{\int_{\tau_0}^{\tau_{cycle}} \dot{m}_{CO_2,cap}\, d\tau} \qquad (2)$$

An optimization problem is formulated to ensure optimal design of the DAC process at various ambient conditions (equation 3). In this case, optimal design means optimizing phase times τ_i and desorption pressure p_{des} in order to minimize the SED. Therefore, the SED is the objective function, while the phase times and the desorption pressure are decision variables grouped in vector p_c. Previous numerical assessments of the same model show that the optimal desorption temperature is in the range of 93 °C to 100 °C due to the equilibrium data of the sorbent [13]. Therefore, the desorption temperature is fixed at 100 °C to reduce computational effort.

$$\min_{\substack{x(\cdot), z(\cdot), \\ p_c}} \qquad \text{SED}\big(x(\tau_{cycle}), z(\tau_{cycle}), T_{amb}, \varphi_{amb}, p_c\big) \qquad \text{(objective function)} \qquad (3)$$

$$\text{s.t.} \qquad \dot{x} = f\big(x(\tau), z(\tau)\big) \qquad\qquad\qquad\qquad \text{(dynamic model)}$$

$$0 = g(x(\tau), z(\tau))$$

$$x(\tau = 0) = x(\tau = \tau_{cycle}) \qquad\qquad\qquad \text{(cyclic steady-state)}$$

The differential states of the dynamic model are summarized in x and the algebraic states in z. The dynamic DAC model is exported as a functional mock-up unit to solve the optimization problem. Subsequently, the dynamic model is optimized using Python, with the genetic optimization algorithm NASGA II included in the DEAP toolbox [21].

In total, the optimization problem is solved 60 times for pairs of 6 ambient temperature and 10 relative humidity values with $T_{amb} \in [-10\,°C, 40\,°C]$ and $\varphi_{amb} \in [10\,\%, 100\,\%]$. Ambient temperature and relative humidity stay constant throughout the entire DAC cycle for each optimization. **Figure 3** shows the resulting performance map that provides the minimal SED as a function of ambient temperature and relative humidity. The performance map's general trend agrees with the findings by Sendi et al. [7].
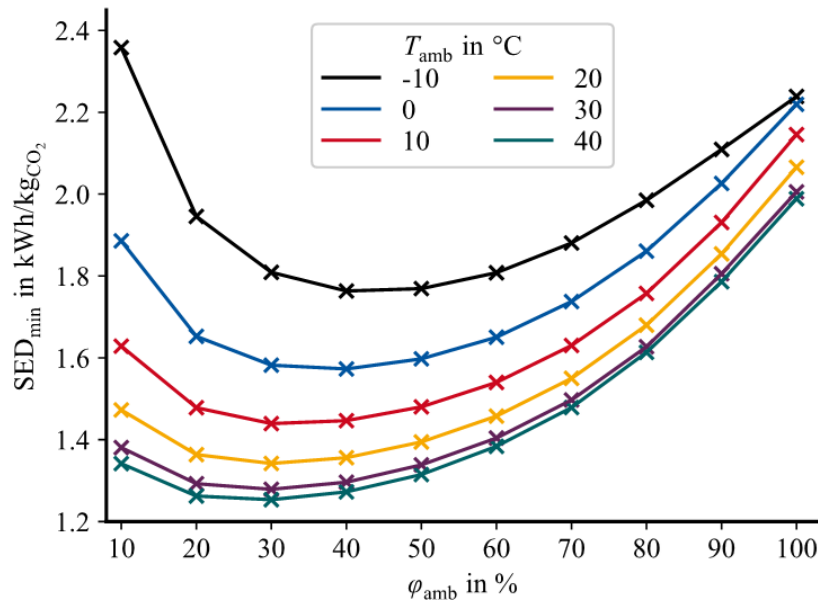
Figure 3: Performance map of the minimal SED of a heat pump driven DAC system for different ambient temperatures (T_{amb}) and humidity levels (φ_{amb}). Crosses indicate optimized data points. Lines are added to enhance readability.

Starting from 10 % relative humidity, the SED decreases with increasing relative humidity and forms a temperature-dependent minimum at a relative humidity of 20 to 40 %. With further increasing relative humidity, the SED increases again. The reasons for this trend are two opposing effects of the relative humidity on the SED [7,8]: (1) CO_2 uptake is enhanced by the co-adsorption of water, which increases CO_2 capacity per cycle and, thus, reduces SED. (2) Co-adsorbed water must be desorbed, increasing energy demand for regeneration. At higher ambient humidity levels, the increased energy demand for regeneration is dominant, increasing the SED.

Regarding the impact of ambient temperature on the SED, lower ambient temperatures decrease the COP of the heat pump due to the increased temperature lift. Thus, the SED increases with decreasing ambient temperature and decreases with increasing ambient temperature.

For the global assessment of the SED, hourly data is used for ambient temperature and relative humidity from the MERRA-2 dataset to determine the SED for every hour of the investigated year 2019. Subsequently, the SED is averaged over all hours of the year. Linear interpolation is used to calculate the SED for pairs of ambient temperature and relative humidity within the limits of the optimized data points. For pairs outside the limits, the SED is calculated based on the closest optimized data point. For example, for ambient temperatures below -10 °C the SED is set to the SED value at -10 °C.

The Carbon Capture Efficiency of DAC

The CCE of the DAC system is defined as

$$\text{CCE} = \frac{m_{\text{CO2,captured}} - \text{CC}}{m_{\text{CO2,captured}}}, \qquad (4)$$

where $m_{\text{CO}_2,\text{captured}}$ denotes the total mass of CO_2 captured over the lifetime of a DAC system, and CC is the cumulated GHG emissions due to DAC. For the CC, only the carbon footprint of energy provision is considered. This assumption is made since recent LCA studies show that the largest share of the climate change impact of DAC results from energy provision [9–11]. All data on carbon footprints is taken from the LCA database ecoinvent version 3.8 using the cut-off system model and the LCA method ReCiPe V1.13 [14]. Ecoinvent provides data on the carbon footprint of grid electricity for 142 countries [14]. If multiple sub-grids are given for one country, the carbon footprint is averaged over all sub-grids, and a uniform carbon footprint is assumed. To assess the carbon footprint of wind electricity, we make five key assumptions:

1. The onshore wind power plant Enercon E-82/2300 is used for all locations, having a peak power output of 2.3 MW and a hub height of 108 m. For this type of turbine, ecoinvent provides reliable LCA data.

2. The LCA data accounts for GHG emissions from plant material production ($m_{\text{CO2,Con}}$) and from decommissioning of the wind power plant ($m_{\text{CO2,Dec}}$).

3. The Python library windpowerlib is used to determine the energy output of the wind power plant [22]. The extrapolation of two reference wind speeds at 10 m and 50 m provided by MERRA determines the wind speed at hub height. For the extrapolation, we use the Hellmann power law [22]. For density correction, the ambient air is assumed to be an ideal gas, and the temperature is linearly extrapolated to hub height from two reference values at 2 m and 10 m.

4. According to ecoinvent, the Enercon E-82 has a lifetime of 20 years [14]. Assuming that the yearly energy output of the reference year 2019 ($W_{\text{el,ref}}$) remains constant, the carbon footprint of wind electricity (CF_{wind}) is determined by

$$\text{CF}_{\text{wind}} = \frac{m_{\text{CO2,Con}} + m_{\text{CO2,Dec}}}{20\, W_{\text{el,ref}}}. \qquad (5)$$

5. Regions are excluded from the analysis when the investigated wind turbine achieves a capacity factor of less than 15 %. By comparison, the International Renewable Energy Agency reports that global capacity factors of wind power plants averaged 34 % in 2018 [23]. Therefore, using the investigated wind power plant in excluded regions would lead to high carbon footprints and, most likely, uneconomical performance. Hence, these regions are excluded from the analysis. Typically, using these regions for wind power generation would require taller wind power plants to increase average wind speed and, thus, the capacity factor [8]. However, the analysis of different wind power plants is out of scope for the present study due to limitations in LCA data availability.

Results and Discussion

Figure 4a shows the global map for the SED calculated using the performance map from **Figure 3**. **Figure 4b** illustrates the carbon footprint of grid electricity provided by ecoinvent, while **Figure 4c** illustrates the carbon footprint of wind electricity calculated based on the approach described in the previous section.
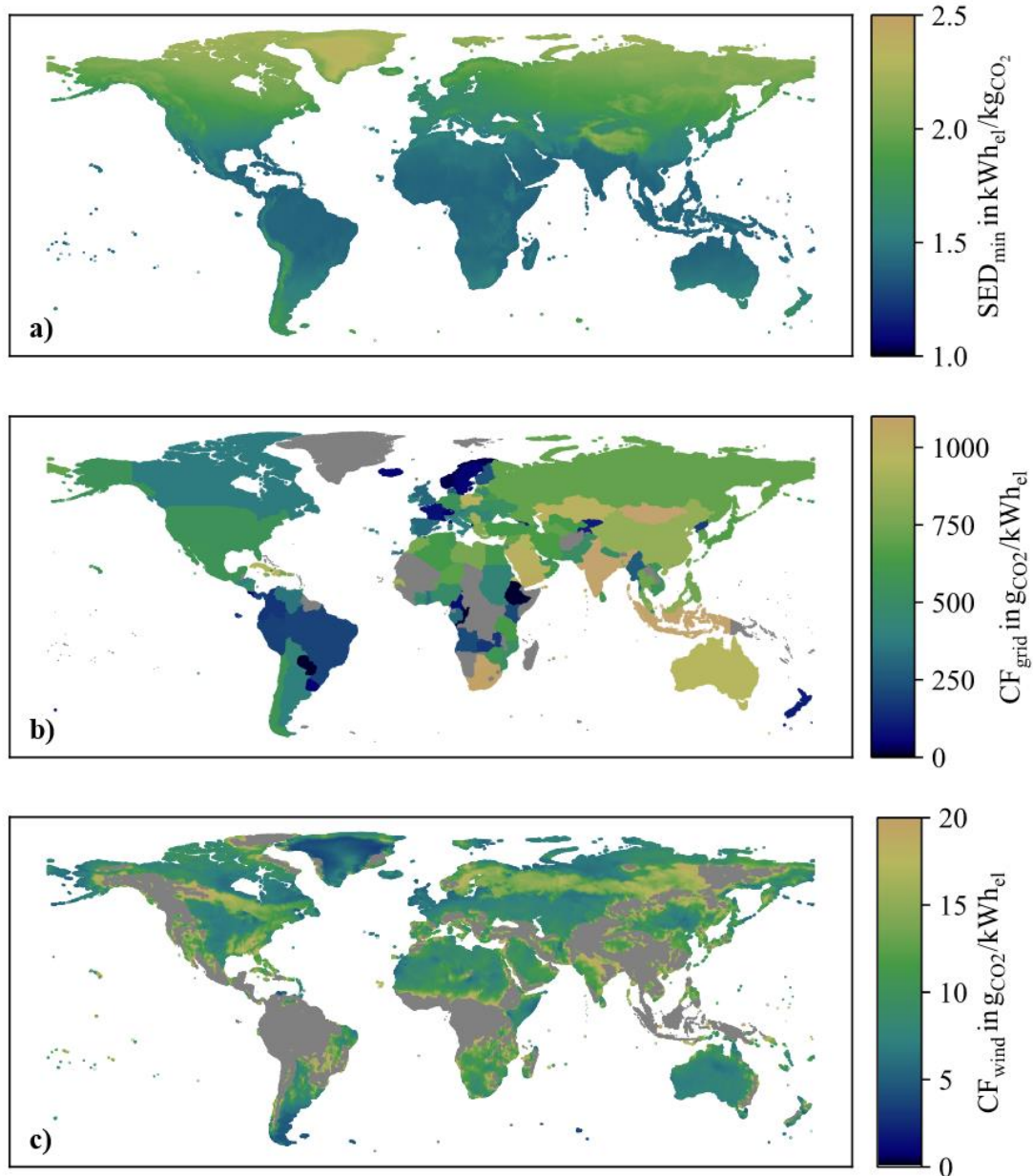
Figure 4: Global maps of the SED of DAC, the carbon footprints of grid electricity (CF_{grid}), and the carbon footprints of wind electricity (CF_{wind}). Greyed-out areas are excluded from the assessment.

Globally, SED values for DAC vary between 1.3 and 2.4 kWh/kg_{CO2}. The lowest SED values are primarily located in dry and warm climates, such as the subtropics in Africa, the Arab Peninsula, and Australia. In humid regions, such as the tropics, the SED is higher due to increased water adsorption. These results agree with the findings by Sendi et al.

Heat Powered Cycles
Conference 2023
Edinburgh
Heat in the new energy system

3rd to 6th of September 2023
The University of Edinburgh, Scotland

The carbon footprint of grid electricity varies widely, ranging from below 30 g_{CO2}/kWh for countries with great shares of renewable energy to 1200 g_{CO2}/kWh for countries heavily relying on fossil-based power plants. Greyed-out countries indicate that there is no ecoinvent data on the carbon footprint of grid electricity.

The carbon footprint of wind electricity ranges between 4 and 20 g_{CO2}/kWh. Greyed-out regions are excluded from the analysis since the investigated wind power plant has a capacity factor of less than 15 % (see Section 2.2). The lowest carbon footprints are found near the coast, with high wind energy yields. In contrast, most greyed-out regions coincide with forests since wind energy yields are low in these regions. Thus, the general trend of wind carbon footprints is in line with data on mean wind power density from the global wind atlas [24]. Moreover, the wind electricity carbon footprints of 4 to 20 g_{CO2}/kWh agree with wind energy datasets from the LCA databases ecoinvent and Gabi that report country-specific carbon footprints of wind electricity mostly in the range of 10 - 35 g_{CO2}/kWh [14,25].

Figure 5 shows the CCE of DAC powered by grid electricity (CCE_{grid}). The CCE_{grid} varies widely ranging from -160 % to 98 %. Deutz et al. find that the first generation DAC plant by Climeworks in Hinwil achieves a CCE of at least 85 % [9]. For demonstration purposes, we use this value as lower bound for our assessment. There are 11 countries in which DAC has on average a CCE_{grid} above 85 %. Therefore, DAC combined with CO_2 storage can achieve negative emissions in these countries using today's grid electricity. However, in most countries, the CCE_{grid} of DAC powered by grid electricity is low due to large fossil shares in energy generation.
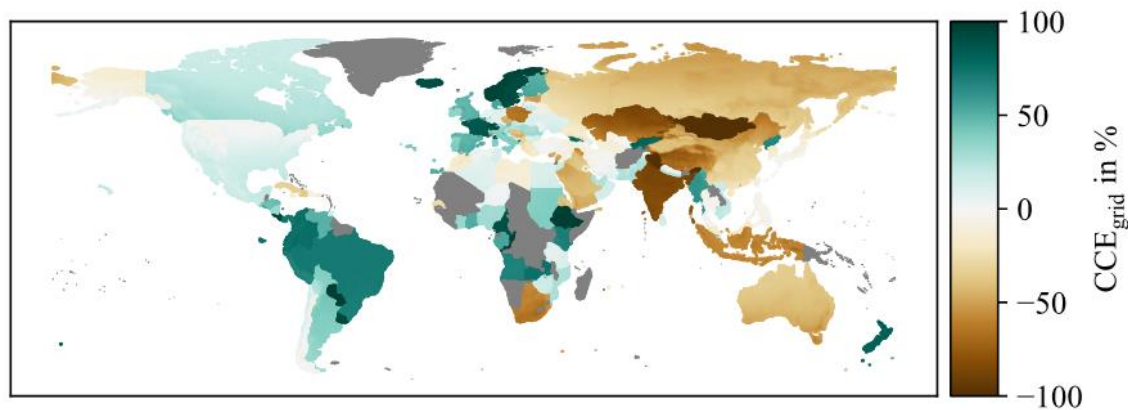
Figure 5: Carbon Capture Efficiency of DAC using grid electricity (CCE_{grid}). For greyed greyed-out countries, there is no data available on the carbon footprint of grid electricity.

A comparison of the CCE_{grid} in **Figure 5** to the SED (**Figure 4a**) and the CF_{grid} (**Figure 4b**) suggests that the CCE_{grid} is mainly affected by the carbon footprint of the electricity supply, whereas the SED has little influence. For example, DAC in Scandinavia has a high CCE_{grid} despite the high SED. Consequently, the low carbon footprint of Scandinavia's grid electricity outweighs the high SED. Conversely, DAC in some North African countries has a low CCE_{grid}, despite the low SED.

Nevertheless, combining the carbon footprint of grid electricity and the regional SED of DAC can help to avoid suboptimal placement within a country. For example, in the USA, DAC could achieve negative emissions in warm climates found in California with a CCE_{grid} > 20 %. In contrast, the CCE_{grid} is approximately 0 in colder climates on the east coast: I.e., DAC combined with CO_2 storage would result in no negative emissions on the east coast. The same

**Heat Powered Cycles
Conference 2023**
Edinburgh

Heat in the new energy system

3rd to 6th of September 2023
The University of Edinburgh, Scotland

can be found in Canada, with CCE values ranging from 10 % in northern regions to 50 % at the U.S.-Canadian border. Since the carbon footprint of grid electricity is assumed constant within a country (see. **Figure 4b**), the CCE gradient can be entirely attributed to the varying ambient conditions across the USA and Canada.

Figure 6 shows the CCE of DAC powered by wind electricity (CCE_{wind}).
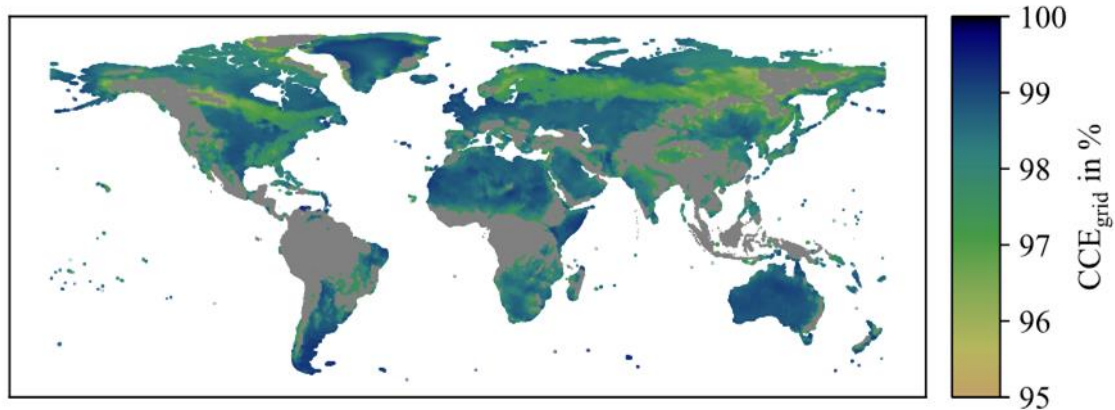
Figure 6: Carbon Capture Efficiency of DAC using wind electricity (CCE_{wind}). Greyed-out countries are excluded from the assessment.

DAC powered by wind electricity achieves a CCE_{wind} above 95 % in all assessed locations. The CCE_{wind} has a minimum of 95.3 % and a maximum of 99.6 %. Hence, for wind-powered DAC, the CCE_{wind} can be increased by 4.3 percentage points between the worst and the best location. Considering that current research suggests a need for negative emissions up to 30 Gt/a until 2100 [26,2,27], optimal placement of DAC plants with a net removal capacity of 30 Gt/a can reduce the needed gross CO_2 capture capacity by up to 1.36 Gt/a. Thus, a thorough assessment of DAC considering regionalized DAC performance and regionalized renewable energy availability is important to optimize environmental performance.

Furthermore, the assessment of the CCE_{wind} shows that advantageous locations for DAC are again found in the subtropics, in North Africa, Australia, and the Arabian Peninsula. This result coincides with the results of the SED assessment (**Figure 4a**). However, DAC also achieves high CCE_{wind} values of more than 98.5 % in North America and large parts of Central Europe. In contrast, an assessment based purely on the SED would classify these regions as suboptimal. However, the high wind yield in these regions reduces the carbon footprint of wind power and thus lowers the CCE_{wind}. This effect compensates for the non-optimal SED of DAC in these regions. Therefore, an assessment based purely on the SED would have excluded numerous regions in which DAC has a high CCE. Hence, both the regional performance of DAC and the yield of renewable energies must be considered for optimal DAC site selection.

Conclusion

In the present study, we conduct a comprehensive analysis of the carbon capture efficiency (CCE) of DAC, considering both climate-dependent DAC performance and regional carbon footprints of the electricity supply. We investigate two case studies for DAC powered by grid and wind electricity. Grid-powered DAC can achieve an average CCE_{grid} of more than 85 % in 11 countries enabling negative emissions using today's grid electricity when combined with CO_2 storage. However, in most countries, the carbon footprint of grid electricity is high due to large shares of fossil energy making DAC less viable. DAC powered by wind electricity has a CCE_{wind} of more than 95 % for all assessed locations, with a minimum value of 95.3 % and a maximum of 99.6 %. Therefore, optimal placement of wind-powered DAC can lower the CCE_{wind} by up to 4.3 percentage points when comparing the best and worst locations. This can reduce the needed global capture capacity of DAC by up to 1.36 Gt/a when a target of 30 Gt/a of net CO_2 removal is met. Assessing wind-powered DAC solely based on SED classifies many locations as sub-optimal, in which DAC could achieve high CCE values. Therefore, the CCE should be preferred over the specific energy demand (SED) for DAC site assessment.

Acknowledgments

References

[1] Montzka, S. A., Dlugokencky, E. J., Butler, J. H., "*Non-CO2 greenhouse gases and climate change*", Nature, 2011.

[2] IPCC, *Global warming of 1.5°C - An IPCC Special Report on the impacts of global warming of 1.5°C above pre-industrial levels and related global greenhouse gas emission pathways, in the context of strengthening the global response to the threat of climate change, sustainable development, and efforts to eradicate poverty*, 2018.

[3] Fawzy, S., Osman, A. I., Doran, J., Rooney, D. W., "*Strategies for mitigation of climate change: a review*", Environmental Chemistry Letters, 2020.

[4] McQueen, N., Gomes, K. V., McCormick, C., Blumanthal, K., Pisciotta, M., Wilcox, J., "*A review of direct air capture (DAC): scaling up commercial technologies and innovating for the future*", Progress in Energy, 2021.

[5] Fasihi, M., Efimova, O., Breyer, C., "*Techno-economic assessment of CO2 direct air capture plants*", Journal of Cleaner Production, 2019.

[6] Schellevis, H. M., van Schagen, T. N., Brilman, D., "*Process optimization of a fixed bed reactor system for direct air capture*", International Journal of Greenhouse Gas Control, 2021.

[7] Sendi, M., Bui, M., Mac Dowell, N., Fennell, P., "*Geospatial analysis of regional climate impacts to accelerate cost-efficient direct air capture deployment*", One Earth, 2022.

[8] Wiegner, J. F., Grimm, A., Weimann, L., Gazzani, M., "*Optimal Design and Operation of Solid Sorbent Direct Air Capture Processes at Varying Ambient Conditions*", Industrial & Engineering Chemistry Research, 2022.

[9] Deutz, S., Bardow, A., "*Life-cycle assessment of an industrial direct air capture process based on temperature–vacuum swing adsorption*", Nature Energy, 2021.

[10] Madhu, K., Pauliuk, S., Dhathri, S., Creutzig, F., "*Understanding environmental trade-offs and resource demand of direct air capture technologies through comparative life-cycle assessment*", Nature Energy, 2021.

[11] Terlouw, T., Treyer, K., Bauer, C., Mazzotti, M., "*Life Cycle Assessment of Direct Air Carbon Capture and Storage with Low-Carbon Energy Sources*", Environmental science & technology, 2021.

[12] Jonge, M. M. de, Daemen, J., Loriaux, J. M., Steinmann, Z. J., Huijbregts, M. A., "*Life cycle carbon efficiency of Direct Air Capture systems with strong hydroxide sorbents*", International Journal of Greenhouse Gas Control, 2019.

[13] Postweiler, P., Engelpracht, M., Gibelhaus, A., Aßen, N. von der, "*Environmental Process Optimisation of Adsorption-based Direct Air Capture of CO2*, 2022.

[14] Wernet, G., Bauer, C., Steubing, B., Reinhard, J., Moreno-Ruiz, E., Weidema, B., "*The ecoinvent database version 3 (part I): overview and methodology*", The International Journal of Life Cycle Assessment, 2016.

[15] NASA Global Modeling and Assimilation Office, "*MERRA-2 tavg1_2d_slv_Nx: 2d,1-Hourly,Time-Averaged,Single-Level,Assimilation,Single-Level Diagnostics V5.12.4*, 2022.

[16] Held, M., *Technological CO2 Mitigation Strategies for the European Transport Sector*. ETH Zurich, 2021.

[17] Bau, U., Lanzerath, F., Gräber, M., Graf, S., Schreiber, H., Thielen, N., Bardow, A., "*Adsorption energy systems library - Modeling adsorption based chillers, heat pumps, thermal storages and desiccant systems*", 10th International ModelicaConference, 2014.

[18] Chair of Technical Thermodynamics, "*SorpLib - Adsorption Systems Library*, https://git.rwth-aachen.de/ltt/SorpLib.

[19] Stampi-Bombelli, V., van der Spek, M., Mazzotti, M., "*Analysis of direct capture of CO2 from ambient air via steam-assisted temperature–vacuum swing adsorption*", Adsorption, 2020.

[20] Schlosser, F., Jesper, M., Vogelsang, J., Walmsley, T. G., Arpagaus, C., Hesselbach, J., "*Large-scale heat pumps: Applications, performance, economic feasibility and industrial integration*", Renewable and Sustainable Energy Reviews, 2020.

[21] Fortin, F.A., De Rainville, F.-M., Gardner, M.-A., Parizeau, M., Gagné, C., "*Deap: Evolutionary algorithms made easy*", Journal of Machine Learning Research, 2012.

[22] Haas, S., Krien, U., Schachler, B., Shivam, K., Bosch, S., "*wind-python/windpowerlib*, 10.5281/zenodo.4591809, 2021.

[23] International Renewable Energy Agency, *Future of wind: Deployment, investment, technology, grid integration and socio-economic aspects (A Global Energy Transformation paper)*, 2019.

[24] Technical University of Denmark, "*Global wind atlas 3.0*, https://globalwindatlas.info/, 2022.

[25] thinkstep AG, *GaBi 9.2.0.58: Software-System and Database for Life Cycle Engineering, DB 8.7 - SP 39*, 2019.

[26] Realmonte, G., Drouet, L., Gambhir, A., Glynn, J., Hawkes, A., Köberle, A. C., Tavoni, M., "*An inter-model assessment of the role of direct air capture in deep mitigation pathways*", Nature communications, 2019.

[27] Rogelj, J., Popp, A., Calvin, K. V., Luderer, G., Emmerling, J., Gernaat, D., Fujimori, S., Strefler, J., Hasegawa, T., Marangoni, G., Krey, V., Kriegler, E., Riahi, K., van Vuuren, D. P., Doelman, J., Drouet, L., Edmonds, J., Fricko, O., Harmsen, M., Havlík, P., Humpenöder, F., Stehfest, E., Tavoni, M., "*Scenarios towards limiting global mean temperature increase below 1.5 °C*", Nature Climate Change, 2018.

Carbon-Dioxide Sorption Compressors for Refrigeration and Air-Conditioning Systems

S. Iraqi, N. Tzabar

Thermal Energy Science and Technology (TEST) Laboratory, Department of Mechanical Engineering, Ariel University, Ariel, 40700, Israel

Extended Abstract

Air-conditioning and refrigeration systems are an integrated part of our lives for everyday use, in residential, medical, commercial, industrial and transportation uses. Nowadays, most air conditioning and refrigeration systems use electrically driven compressors to drive the vapor cycle. Air-conditioning systems consume a major part of the global generated electric power (25 – 40 %), which constantly increases due to the growing demand for electricity. This growth requires more power plants and larger distribution infrastructure. Our aim in developing thermally driven air-conditioning and refrigeration systems is to reduce the global electricity consumption, by using available heat sources, such as waste heat, solar radiation, biofuels combustion, and more.

Thermally driven sorption compressors technology was initiated for cryogenic Joule-Thomson cooling for space applications, in the 1970s. In previous work we investigated sorption compressors for Joule-Thomson cryocooling [1-2], both for pure and mixed refrigerants. Recently, we started a research which aims to use the sorption compressor technology for air-conditioning and refrigeration systems, which operate in the well-known vapor cycle. The target is to replace existing mechanical compressors, while maintaining all the other components of the system: refrigerant, evaporator, condenser, and expansion valve. This means that the technology may be implemented with any refrigerant for any cooling temperature. The current research initially focuses on carbon-dioxide as the refrigerants, which is environmental friendly and has attractive cooling performances. The main reason that carbon-dioxide is not widely in use is its relatively high operating pressures. While this characteristic is a disadvantage for mechanical compressor, sorption compressors similarly operate at high and low pressures.

In previous research on sorption compressors for cryogenic cooling systems, a numerical model was developed for multi-stage adsorption compressors [2-4], and an experimental system was built to verify the numerical model [5]. We currently use the numerical model and the existing experimental apparatus to investigate the operation of sorption compressors with carbon-dioxide, in order to develop a sorption compressor demonstrator, which shall be tailored for carbon-dioxide.

Figure 1 shows a comparison between numerical model results and experimental results, of a single sorption cell compressor which operates with carbon-dioxide. In this operation the filling pressure is 2.83 MPa, the high and low temperatures of the cycle are 300 °C and 100 °C, respectively, the flow rate is 1.5 mg/s, and the obtained high and low pressures are 3.60 MPa and 1.03 MPa, respectively. The results in Figure 1, among additional similar results, provided a basic proof for the ability to compress carbon-dioxide with sorption compressors. As a consequence, the numerical model is used to develop the next experimental apparatus, as a stage in the development of a full compressor demonstrator, which shall drive a real air-conditioner. Figure 2 shows numerical results of a single sorption cell compressor, which demonstrate the ability to obtain the desired operating pressures of carbon-dioxide in refrigeration systems. The results in Figure 2 refer to high and low pressures of 8.3 MPa and 3.5 MPa, respectively, and a flow rate of 0.12 g/s, per a single sorption cell, where the high and low temperatures of the cycle are 33 °C and 104 °C, respectively. The research is in progress and additional results are constantly generated, also for air-conditioning systems. The plan is to fabricate the first demonstrator and tests it during this year, and later to design and test a full demonstrator of a sorption compressor for carbon-dioxide.

1

Heat Powered Cycles
Conference 2023
Edinburgh

Heat in the new energy system

3rd to 6th of September 2023
The University of Edinburgh, Scotland
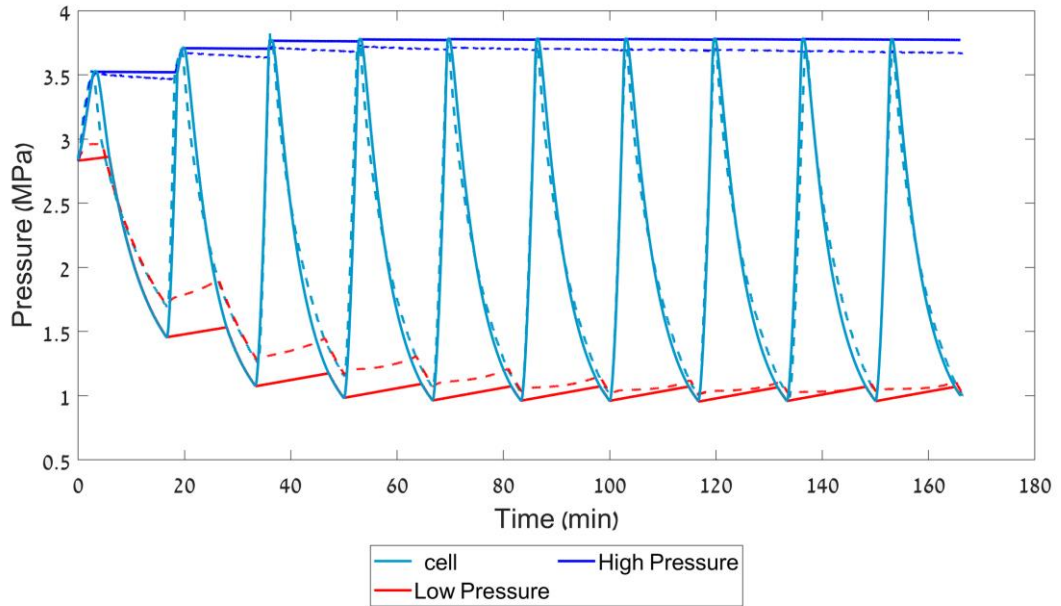
Figure 1 - Experimental results (dashed lines) versus numerical results (continuous lines), of an existing single-cell sorption compressor, operating with carbon-dioxide.
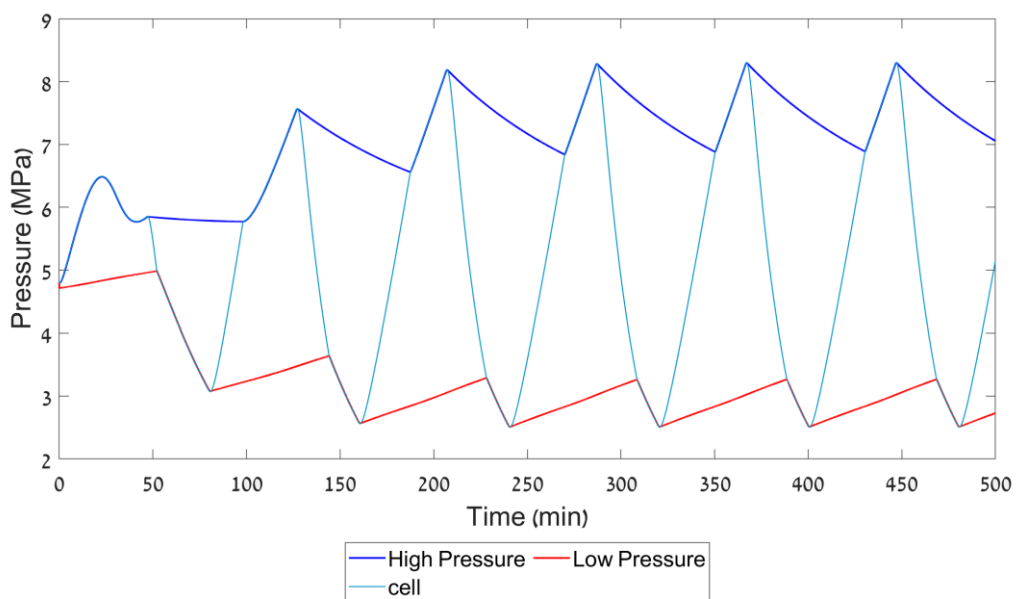
Figure 2 - Numerical results of a single-cell sorption compressor, operating with carbon-dioxide at the desired operating pressures for refrigeration systems.

References

[1] N. Tzabar and G. Grossman, *Cryogenics* 52 (2012), 491-499
[2] A. Hamersztein and N. Tzabar. International Journal of Refrigeration, 124 (2021) 105–113
[3] A. Davidesko and N. Tzabar. *Cryogenics* 108 (2020), 103074
[4] A. Davidesko and N. Tzabar. *Adsorption* 27 (2021), 117-128
[5] N. Tzabar and A. Hamersztein. *Renewable Energy*, 181 (2022), 666-674

2

A Mathematical Model to Predict the Properties of Desiccant Coated Heat Exchanger with Different Adsorbent by Self-refining Meshing Method

Qian Li[1] and T.S.Ge[1*]

[1]Institute of Refrigeration and Cryogenics, Shanghai Jiao Tong University, 800 Dongchuan Road, Minhang District, Shanghai 200240, China

[*]Corresponding author: baby_wo@sjtu.edu.cn (T.G.)

Abstract

The Desiccant coated heat exchanger (DCHE), utilizing an inner cooling source to remove sorption heat, are promising alternatives for traditional evaporators and condensers in vapor compression (VC) heat pumps. A mathematical model is necessary to facilitate the design, analysis and performance prediction of the component and the relevant systems. In this study, a three-dimensional model of DCHE with self-refining meshing method is proposed, accounting for the two-phase phenomena, the mass transfer resistance in adsorbent, the fluid transport in multiple directions and the coupled heat and mass transfer. Study reveals that, owing to the advanced iteration method, computation speed, accuracy and astringency are promoted. Latent load (inlet humidity) reduces the sensible heat handling capacity of the DCHE, while the total heat transfer capacity is improved because the latent heat and sensible heat are addressed by different approach. Meanwhile, the performances of DCHEs coated with three different adsorbents is simulated. Results manifest MOF shows better stability and speed of dehumidification than silica gel and hygroscopic salt, which may be a promising material of the future DCHE.

Keywords: Simulation, DCHE, Adsorption, Heat and mass transfer, Self-refining meshing.

Introduction

Desiccant coated heat exchanger (DCHE), which refers to the fin-tube exchanger with adsorbent applied on the fins is widely used in many fields, such as dehumidification and atmospheric water harvesting (AWH)[1]. Owing to the large areas of the fins, the adsorbent can be scattered uniformly and forms a thin coating (usually about 200um), which dramatically intensifies the processes of heat and mass transfer, and thus enable the DCHE to be driven by low grade heat sources. In addition, the refrigerant flowing in the tubes can cool down the adsorbent and carry off the adsorption heat, which benefits the adsorption process in the aspects of both adsorption rate and adsorbing capacity. What's more, the performance of adsorbent can also be regulated by varying the temperatures of refrigerant to adapt different humidity conditions[2]. Equipped with these dominant advantages, DCHE shows the potential to substitute traditional air handing systems (such as liquid desiccant dehumidification devices and rotary wheels)[3-8] and AWH systems (such as condensation-based AWH using traditional vapour compression cooling system, and sorption-based AWH using traditional sorption beds). When combined with heat pumps, named after solid desiccant heat pump (SDHP), DCHE realizes dehumidification above the dew point and enjoys a high COP (6.3)[9] and the SDHP has been demonstrated to be an effective way to humidify the air in winter.

The heat and mass transfer occurring on the DCHE is complicated and coupled with each other, which involves plenty of factors like the properties of adsorbent, refrigerant, structural parameters and operating conditions. Consequently, the experimental results of a given

DCHE are hard to be generalized. Numerical studies of DCHE are then expected to reveal the mechanism of the coupled heat and mass transfer, predict the performances of DCHE in different conditions, screening the proper adsorbents and guide the optimization of structural design. Previous numerical studies concerning about the adsorption process mainly focused on desiccant wheels[10-11]. The models of desiccant wheels can be divided into gas-side resistance (GSR) model, pseudo-gas-side (PGS) model, gas and solid side (GSS) model and parabolic concentration profile (PCP) model, among which the GSS model is known as high precision. In this paper, GSS model is introduced to depict the mass transfer in the adsorbent. Meanwhile, contrast with the former GSS model, the diffusion of the gas phase in adsorbents is also comprised, in consideration that the adsorbents applied to DCHE usually feature as mesoporous. Studies concentrating on DCHE simulations mainly depend on experimental data or make several, simplifying assumptions at the expense of model accuracy. Yuan, Jagirdar and Lee[12-13] extend the empirical correlations of fin efficiency in traditional heat exchangers to the heat transfer analysis of DCHE. The one-dimensional GSR model is widely used in literature to identify mass transfer performance. Meanwhile a two-dimensional GSS one is believed to be more accurate. Li[14] proposes a more simplified method by assuming constant mass and heat resistance. Recent study also reports a detailed three-dimensional mathematical model to predict the performance of the DCHE driven by the two-phase refrigerant, which is much more accurate than the models mentioned above and consistent with the experimental results[15]. However, this model only applies to a certain DCHE coated with silica gel and a few working conditions, and only surface diffusion is considered in the adsorbent. Besides, attribute to the complexity of the governing equations, this model is time-consuming and can cause severe divergence in some extreme cases. In fact, speed and astringency are ambivalent for a given algorithm. A better astringency requires refined time and space interval, which inevitably slows down the calculation speed. In the field of numerical simulation like CFD, the mesh is usually refined at the place easy to be divergent like discrete boundaries. Nevertheless, so many efforts should be paid to find out a proper mesh that a fast performance prediction of DCHE seems like impossible in this way, because even though for a given DCHE the mesh structure can varies tremendously in different working conditions.

In this paper, a self-refining meshing method is proposed to give a possible solution to this dilemma, which realizes a fast calculation and convergence, and guarantees a high accuracy. Different from traditional meshing method, this method can automatically identify the place which needs refining, according to the local astringency. Meanwhile, a GSS model involving the gaseous diffusion is employed to further promote the accuracy of results. At last the performances of DCHE with different adsorbents (silica gel, MOFs and hygroscopic salt) driven by two-phase refrigerant (R134a) are predicted by this model and the simulation results are compared with experiments.

Discussion and Results

2.1 Structure of DCHE and mesh

Fig.1(a) demonstrates the configuration of a sample desiccant coated heat exchanger and the fluids (air and refrigerant) flowing through it. The DCHE is equivalent to a cuboid, whose structural parameters are 320mm (length:x axis), 88mm (width:y axis) and 320mm (height:z axis). A Cartesian coordinate is established to derive the governing equations of air, heat exchanger adsorbent and refrigerant as shown in Fig.1(a). Because the governing equations of refrigerant are complicated and nonlinear, it's better to segment the DCHE along the flow passage of refrigerant to simplify the calculation. The corresponding mesh is shown in Fig.1 (b) (c) and (d), where 12, 4, 6 layers are divided along z, y, x axis respectively and the total number of elements is 288. Fig.1(e) shows the structural parameters of one element, which contains 21

fins and one tube. We suppose all heat and mass transfer processes occur in the 288 elements, and the corresponding governing equations can be deduced.

(a) Structure of DCHE

(b) Mesh along z axis

(c) Mesh along y axis

(d) Mesh along x axis

(d) Structure of one element
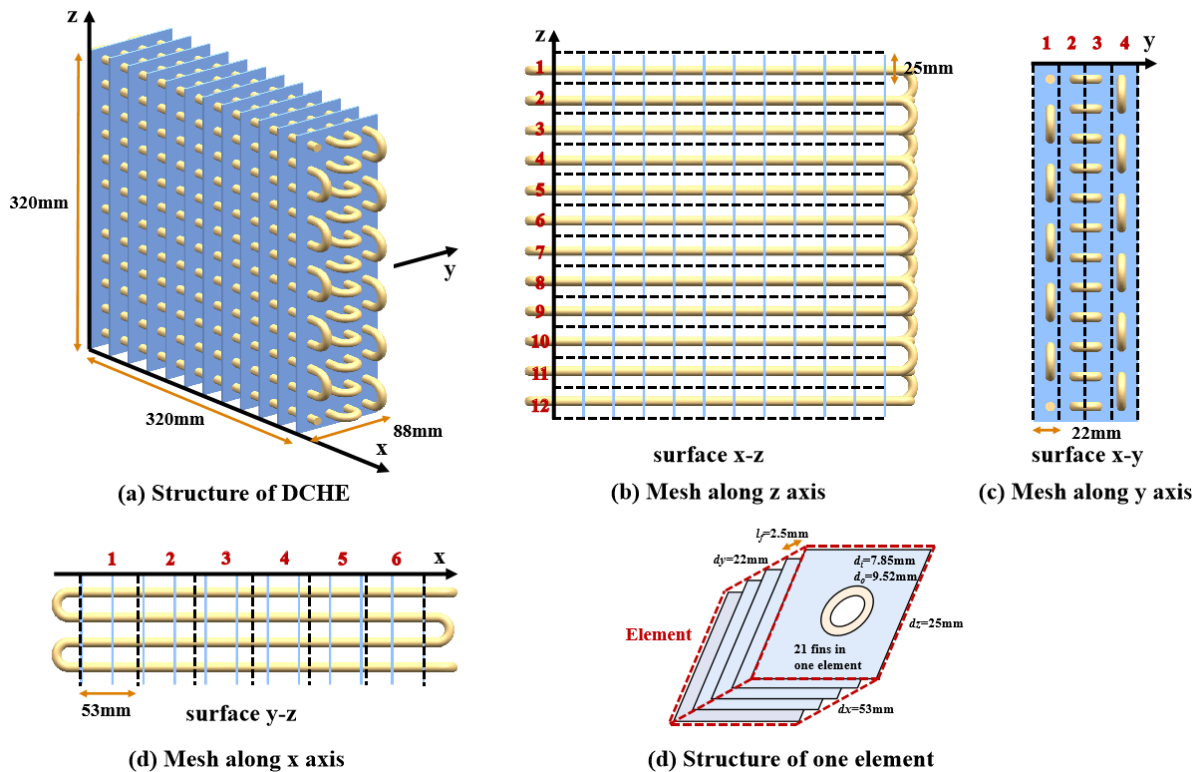
Figure.1 Detailed configuration of the example DCHE and its corresponding mesh.(a) Structure of DCHE (b) Mesh along z axis (c) Mesh along y axis (d) Mesh along x axis (e) Structural parameters of one element

2.2 Working principles of DCHE and adsorbent

Fig.2(a) demonstrates the working principle of DCHE. When the air passes the fins of DCHE, the dry air was cooled down and the moisture (blue dots) contained in the air is captured by the adsorbent on the fins (yellow layers). The refrigerant flowing along the tube provide cooling source for DCHE to facilitate the adsorption process and provide heat source to drive the adsorbent to release the moisture in the desorption process. The coupled heat and mass transfer occurring on the fins can be explain by the picture in the middle. When the vapour adsorbed by the adsorbent, the adsorption heat is emitted to the heat exchanger and is carried off by the refrigerant through heat conduction between the tube and refrigerant. This latent heat, equaling to adsorption rate multiplying the specific adsorption heat, can change the temperature of the fins, affect the heat conduction rate and influence the sensible heat of the air. On the other hand, adsorption rate is also sensible to the temperature of the fins. It's reported that at least for physical adsorption, adsorption rate can be greatly boosted by cooling. Therefore, only the heat and mass transfer equations are solved simultaneously the behaviour of DCHE can be explained clearly. The principle of adsorption is depicted by the last picture in Fig.2(a). For these mesoporous or macroporous adsorbents, both gaseous and liquid diffusion can occur. The free vapour molecules (blue dots), deemed as gas phase, move into the pores driven by concentration difference and split into 2 situations. Some of the free vapour are adsorbed by the adsorbents (blue and yellow arrows) and turn into adsorbed state (red dots), which are usually treated as liquid phase. The movement of these adsorbed vapour can be explained by the theory of surface diffusion. Other free vapour continuously permeates towards the deeps of the pore (green arrows), which can be described by Knusen

diffusion and molecular diffusion[16]. Fig.2(b) presents the isotherms of selected adsorbents, which represent the 3 main categories applied to DCHE: silica gel, hygroscopic salt (silica gel @LiCl) and MOFs (MIL-101 Cr). The dash lines are the fitting curves of isotherms by the experimental data, which are used to calculate the adsorption rate.
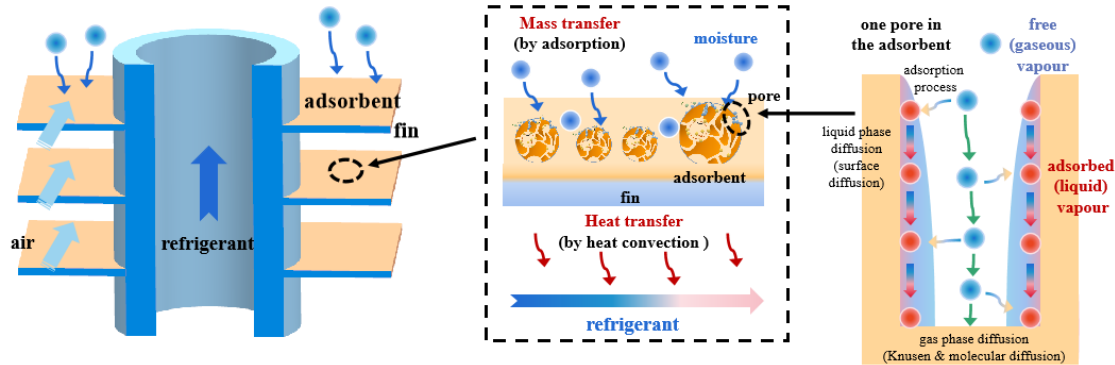
(a) Schematic of the principle of DCHE and the diffusion in adsorbent
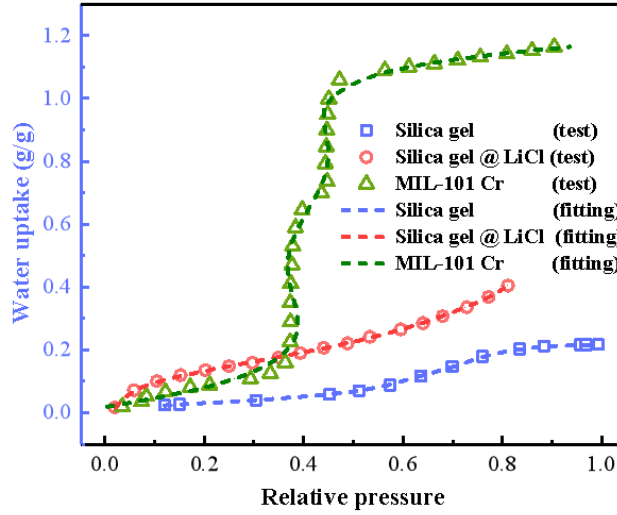
(b) Isotherms of the selected adsorbents
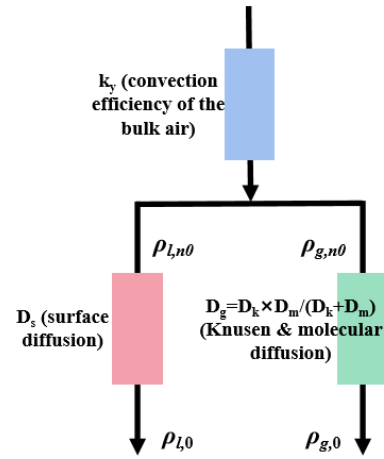
(c) Mass transfer resistance in adsorbent

Fig.2 Working principle of DCHE and the properties of selected adsorbent. (a) Schematic of the principle of DCHE and the diffusion in adsorbent (b) Isotherms of the selected adsorbents and the corresponding fitting curves (c) Mass transfer resistance in adsorbent.

2.3 Governing equations

The governing equations of the air side include the mass transfer and heat transfer equations as Eq.(1) and Eq.(2) respectively. Eq.(1), originated from mass conservation, is derived via dimension reduction, only considering lateral (perpendicular to x-z surface in Fig.1) velocity and supposing the mass transfer along the normal direction of the fins. $\rho_a u_a Y_a c_a$ and T_a represent the density, velocity, humidity ratio, specific heat and temperature of the air. m_w means the adsorption rate, which is positive for adsorption and negative for desorption and v_a is the volume of the air in one element.

$$\frac{\partial(\rho_a Y_a)}{\partial t} + \frac{\partial(\rho_a u_a Y_a)}{\partial y} = -\frac{m_w}{v_a} \tag{1}$$

$$\frac{\partial(c_a \rho_a T_a)}{\partial t} + \frac{\partial(c_a \rho_a u_a T_a)}{\partial y} = \frac{h_a(T_{hx} - T_a)}{v_a} \cdot \eta_f \tag{2}$$

The heat transfer equation derived from energy conservation is shown in Eq.(2), with the assumptions of negligible pressure variation, gravity and friction. In order to get simplified, one dimensional formulations, only temperature and velocity gradient in the x-z plane are counted. h_a, the convective heat coefficient can be calculated via Eq.(3), and the corresponding convective mass coefficient can be deduced by Eq.(4)[13], which indicates that the Sherwood number and the Nusselt number are interconnected by Chilton-Colburn analogy[17]. The fin efficiency η_f can be calculated by Eq.(5).

$$h_a = j\frac{c_a\rho_a u_a}{\Pr_a^{2/3}}, j = 0.086\mathrm{Re}^{c_1} N_{tx}^{c_2}(\frac{P_f}{d_c})^{c_3}(\frac{P_f}{D_h})^{c_4}(\frac{P_f}{\delta_z})^{-0.93}$$

$$c_1 = -0.361 - \frac{0.042N_{tx}}{\ln(\mathrm{Re})} + 0.158\ln\left[N_{tx}(\frac{P_f}{d_c})^{0.41}\right]$$

$$c_2 = -1.224 - \frac{0.076(\delta_x/D_h)^{1.42}}{\ln(\mathrm{Re})} \tag{3}$$

$$c_3 = -0.083 - \frac{0.058N_{tx}}{\ln(\mathrm{Re})}, c_4 = -5.735 + 1.21\ln(\frac{\mathrm{Re}}{N_{tx}})$$

$$\mathrm{Re} = \frac{\rho_a u_a d_c}{\mu_a}, \Pr_a = \frac{\mu_a C_a}{\lambda_a}$$

$$k_y = \frac{A_a}{v_a}\rho_a D_a Sh_a, D_a = 2.302\times10^{-5}$$

$$\frac{Sh_a}{\mathrm{Re}\cdot Sc^{1/3}} = \frac{Nu_a}{\mathrm{Re}\cdot\Pr^{1/3}}, Sc_a = \frac{\mu_a}{\rho_a D_a}, Nu_a = \frac{h_a v_a}{A_a \lambda_a} \tag{4}$$

$$\eta_f \Leftrightarrow \frac{\overline{T}_f - T_a}{T_f - T_a}$$

$$= \frac{r_0\sqrt{2h_a k_f t_f}(T_f - T_a - \frac{q_{sorption}}{h_a})\frac{K_1(mr_0)I_1(mr_2) - I_1(mr_0)K_1(mr_2)}{K_0(mr_0)I_1(mr_2) - I_0(mr_0)K_1(mr_2)} + q_{sorption}(r_2^2 - r_0^2)}{h_a(r_2^2 - r_0^2)(T_f - T_a)} \tag{5}$$

$$m = \sqrt{\frac{2h_a}{k_f t_f}}, q_{sorption} = q_{st}k_y(Y_a - Y_{dn})$$

The DCHE is considered as a homogeneous mixture of copper, aluminum and desiccant. Thermal energy variation of the component is attributed to 3 contributors, the adsorption heat emitted or assimilated by adsorbent, the air convection and the refrigerant convection. These 3 factors constitute the heat transfer equation of heat exchanger as shown in Eq.(6), derived from energy conservation. Because the tube and fins are so thin that the area of heat conduction is as small as $10^{-6}\mathrm{m}^2$, which means the heat conduction along tube and fins can be neglected, compared with the former 3 contributors.

$$v_{hx}c_{hx}\rho_{hx}\frac{\partial T_{hx}}{\partial t} = \pi d_i dx h_r(T_r - T_{hx}) + h_a S_a(T_a - T_{hx})\eta_f + r_w m_w \tag{6}$$

Where v_{hx} c_{hx} ρ_{hx} T_{hx} is the volume, specific heat, density and temperature of heat exchanger. T_r h_r is the temperature and convective heat coefficient of refrigerant, S_a is the total area of fins in one element and r_w is the specific adsorption heat.

Heat Powered Cycles
Conference 2023
Edinburgh

Heat in the new energy system

3rd to 6th of September 2023
The University of Edinburgh, Scotland

Sub-graph in the right of Fig.2(a) clarifies the mass transfer in the desiccant. To be specific, desiccant normally has interconnected pores exposed to air and substrate atoms and strongly affiliated to free vapour molecules. Hence, the water molecules inside air can easily penetrate into the pores of unsaturated adsorbent, then partially trapped into the potential field of adsorption of the adsorbent, becoming adsorbed water. Also note that the water molecules, both the free ones and the adsorbed ones, are in most cases distributed unevenly inside the desiccant, which yield liquid diffusion (surface diffusion) and gaseous diffusion (molecular diffusion and Knudsen diffusion) respectively. In desorption process, the direction of the concentration gradient and thus diffusion are inverted by heating, adsorbed water is then desorbed from the adsorbent atoms. It's obvious that at the top surface of adsorbent (edge of the pores), mass transfer can only take place by gaseous diffusion, which is related to the convection efficiency (k_y) of the bulk air, and at the bottom of adsorbent the concentration gradient of both liquid and gas phase must be zero. These two equations confirm the boundary conditions of the diffusion process. Fig.2(c) illustrates the mass transfer process and the resistance in the pores. Based on the law of mass conservation and the assumption of even coating thickness, negligible lateral (along the surface of fins) diffusion, negligible vapor-phase mass and constant physical properties (porosity and density of the desiccant), governing equation of mass transfer inside desiccant (Eq.(7)), along with the initial and boundary conditions (Eq.(8)), can be derived as followed.

$$\frac{\partial \rho_l}{\partial t} + \frac{\partial \rho_g}{\partial t} = D_s \frac{\partial^2 \rho_l}{\partial n^2} + D_g \frac{\partial^2 \rho_g}{\partial n^2}$$

$$m_w = \int_0^{n_0} \frac{\partial \rho_l}{\partial t} dn \tag{7}$$

$$\rho_l = k_0 \rho_g, k_0 = k_{iso} \frac{\rho_d(1-\varepsilon_d)}{\varepsilon_d \rho_s(T_{hx})}$$

$$\varepsilon_d(k_0 D_s + D_g)\frac{\partial \rho_g}{\partial n}\Big|_{n=n_0} = k_y(\rho_v - \rho_{g,n_0})$$

$$\frac{\partial^2 \rho_g}{\partial n^2} + \frac{\partial^2 \rho_l}{\partial n^2}\Big|_{n=0} = 0 \tag{8}$$

Where ρ is the density of vapour, subscribe l g v mean liquid (absorbed) water, gaseous (free) water in the adsorbent and the vapour contained in the bulk air. n is the normal direction of the fins. ε_d ρ_d k_{iso} are the porosity density of adsorbent and slope of the isotherm. Eq.(7) is a coupled differential equation, involving the diffusion of both liquid and gas phase, which can be solved by a widely used assumption that the gas and liquid phase are in equilibrium, determined by the isotherms[16]. In this way, as shown in Eq.(7), the ratio of liquid and gas density (k_0) can be calculated by the slope of isotherm (k_{iso}). D_s and D_g are diffusion efficiency of liquid phase and gas phase respectively, which can be calculated by Eq.(9). The former is surface diffusion and the latter is a series connection of molecular diffusion and Knusen diffusion.

$$D_s = \frac{\varepsilon_d}{\tau} D_0 \exp(-0.974 \times 10^{-6} \times \frac{r_w}{T_{hx}}), D_0 = 0.8 \times 10^{-6}$$

$$D_g = \frac{D_k D_m}{D_k + D_m}, D_k = \frac{d_p}{3}\sqrt{\frac{8RT_{hx}}{\pi M}}, D_m = D_0 \frac{P_0}{P}(\frac{T}{T_0})^{1.81} \tag{9}$$

Where D_s D_k D_m means surface, Knusen, molecular diffusion coefficient. τ is the tortuous factor (usually 1~4), d_p is the diameter of the pores, R is the gas universal constant (8.31 J/K) and M is the relative molecular mass of vapour (18 g/mol).

The heat transfer between refrigerant and heat exchanger is complex, which involves the flow of compressible, two phase fluid. According to former studies[18-22], the following continuity, momentum and energy conservation Eq.(10) can be used to demonstrate the flow pattern of the single-phase refrigerant. In super-heating and sub-cooling zones, the refrigerant (R134a) is treated as a homogeneous mixture at thermal equilibrium. One-dimensional flow is assumed and the effects imposed by the viscosity, gravity, heat conduction and spatial variation of pressure are ignored.

$$\frac{\partial \rho_r}{\partial t} + \frac{\partial(\rho_r v_r)}{\partial x} = 0$$

$$\frac{\partial(\rho_r v_r)}{\partial t} + \frac{\partial(\rho_r v_r^2)}{\partial x} = -\frac{\partial p_r}{\partial x} - f_r \qquad (10)$$

$$\frac{\partial U_r}{\partial t} + \frac{\partial(\rho_r v_r i_r)}{\partial x} = \frac{\partial p_r}{\partial t} + \frac{h_r(T_{hx} - T_r)}{0.25 \times d_i}$$

Where ρ_r v_r p_r U_r i_r is the density, velocity, pressure, internal energy and enthalpy of refrigerant, h_r is the convection coefficient between refrigerant and heat exchanger, f_r is the fanning friction coefficient which can be estimated by Eq.(11).

$$\rho_r = \alpha_r \rho_{rg} + (1 - \alpha_r)\rho_{rl}$$

$$U_r = \alpha_r U_{rg} + (1 - \alpha_r)U_{rl}$$

$$i_r = x_r i_{rg} + (1 - x_r)i_{rl}$$

$$\alpha_r = \frac{x_r}{\rho_{rg}}\left\{[1 + 0.12(1 - x_r)](\frac{x_r}{\rho_{rg}} + \frac{1 - x_r}{\rho_{rl}}) + \frac{1.18(1 - x_r)\left[g\sigma_r(\rho_{rl} - \rho_{rg})\right]^{0.25}}{(\rho_r v_r)^2 \rho_{rl}^{0.5}}\right\}^{-1}$$

$$h_r = 1.061\exp(\frac{0.042}{(1 - x_r)^{0.8}/x_r^{0.8}}\frac{\rho_{rl}}{\rho_{rg}}) \times 0.023\text{Re}_{rl}^{0.8}\text{Pr}_{rl}^{0.4}\frac{\lambda_{rl}}{d_i} + 0.238\left[(\frac{1 - x_r}{x_r})^{0.8}\frac{\rho_{rl}}{\rho_{rg}}\right]^{0.238}$$

$$\times (\frac{d_i}{\sqrt{\sigma_r/g(\rho_{rl} - \rho_{rg})}})^{1.11} \times 55(\frac{p_r}{p_{rc}})^{0.12}\left[-\lg(\frac{p_r}{p_{rc}})\right]^{-0.55} M_r^{-0.5}h_r(T_{hx} - T_r)$$

$$f_r = \left\{1 + \left[x_r + 4(x_r^{1.8} - x_r^{10})\right] \times \left[\frac{\frac{\rho_{rl}}{\rho_{rg}}}{(\frac{\rho_{rl}}{\rho_{rg}})^{0.25}} - 1\right]\right\} \times \frac{0.158}{\text{Re}_r^{0.25}d_i\rho_{rl}}(v_r\rho_r)^2$$

$$\text{Re}_{rl} = \frac{(1 - x_r)\rho_r v_r d_i}{\mu_{rl}}, \text{Re}_r = \frac{\rho_r v_r d_i}{\mu_{rl}}$$

(11)

When it comes to two-phase flow, relative 'slip' can be observed between the vapor and liquid velocities. Thus, new definitions, such as the void fraction (α_r), vapour weight fraction (x_r), average density, average internal energy and average flowing enthalpy should be introduced as shown in Eq.(11)[23,24]. It's observed that the velocity always combines with the density, so the mass flow rate m_r can substitute v_r to simplify the expressions. The

Heat Powered Cycles
Conference 2023
Edinburgh

Heat in the new energy system

3rd to 6th of September 2023
The University of Edinburgh, Scotland

interaction among the 3 equations above should also be clarified. The continuity equation (top) can calculate the refrigerant flow mass and density field in the tube and then help the momentum equation (middle) to derive the pressure distribution. The refrigerant temperature of two phase can be directly obtained by the saturation curve of R134a under the known pressure. The energy equation (bottom) can then deduce the vapour weight fraction and void fraction under the known T_r, and the new density field can be calculated by Eq.(11). In the single-phase section, x_r and α_r is constant and the density is related to T_r, which can also be obtained by the energy equation. The refrigerant properties, including ρ_{rg} ρ_{rl} U_r i_{rg} i_{rl} μ_{rg} μ_r λ_{rl} σ_r can be obtained by calling the corresponding programs of REFPROP 9.1.

2.4 Calculation algorithm

All differential equations above (Eq.(1)-(11)) are discretized at first in implicit format, indicating all variables appears in the equations are written as current forms like Eq.(12), which are unknown. The implicit format enjoys much better than explicit format (variables are written as past forms, which are foregone). The numerical solution can be deduced based on the discrete computational domain in Section 2.1, provided that necessary geometric, material physical and operating parameters are available. The general calculation algorithm is that in every time steps (t=i+1) the physical variables like mass, pressure, temperature in every elements are updated based on these variables in the past time (t=i). The initial and boundary conditions are set according to the environmental and other known conditions. Although Eqs.(1)-(11) are coupled and nonlinear, considering the great mass and heat capacity of heat exchanger, once the temperature of heat exchanger (T_{hx}) in this time step (t=i+1) is substituted with the past time (t=i), which means T_{hx} is rewritten in explicit format, the equations of adsorption rate (Eq.(7)) heat transfer of air (Eq.(2)) and heat exchanger (Eq.(6)) are decoupled and linear. These three equations can be solved directly by Gaussian elimination in MATLAB and complicated iterations are averted. The remained equations, mainly including the equations of refrigerant are heavily coupled and must be solved by iteration of fixed point theorems. However, iteration process is a explicit format, whose astringency severely depends on the fineness of time/space steps and the intensity of the change of variables like pressure, temperature, density. Traditional iteration method usually chooses a constant time and space step, in every iteration cycle all variables in all elements are updated until the results are convergent. This method at least contains 2 defects, that when the time or space step is too large the iteration can be vibrant and divergent. On the other hand, not all of the elements are divergent, which indicates a time waste as shown in Fig.3(a). A better way is to identify the divergent place and make the iteration aiming to these elements. Meanwhile the space steps are refined to avoid vibration, which is the self-refining iteration method mentioned at the beginning. Taking the continuity equation in Eq.(10) for example, the discretized equation can be written as Eq.(12).

$$\frac{\rho(i+1, j+1) - \rho(i, j+1)}{dt} + \frac{m_r(i+1, j+1) - m_r(i+1, j)}{dx} = 0$$

$$\Rightarrow m_r(i+1, j+1) = m_r(i+1, j) - \frac{\rho(i+1, j+1) - \rho(i, j+1)}{dt} \cdot dx \tag{12}$$

The letter i means time steps and j means the number of elements. It can be seen that when the variation of density is too sharp $m_r(i+1, j+1)$ can be negative, which is obviously impossible. The solution is to reduce the space step dx and impair the sharpness of variation, and is also suitable for the other 2 equations in Eq.(10). The space step in the self-refining iteration obtains two types: dx-normal (53mm) using in the pre-computation and dx-iterate (5.3mm) using in the iteration cycles. Pre-computation is first carried out to determine whether mesh refining need to be implemented. Only when the pre-computation is divergent,

is *dx*-itertate employed. After iteration of the divergent elements, *dx*-normal is used again for next element, as illustrated by Fig.3(b).

(a) Traditional iteration method

(b) Self-refining iteration method
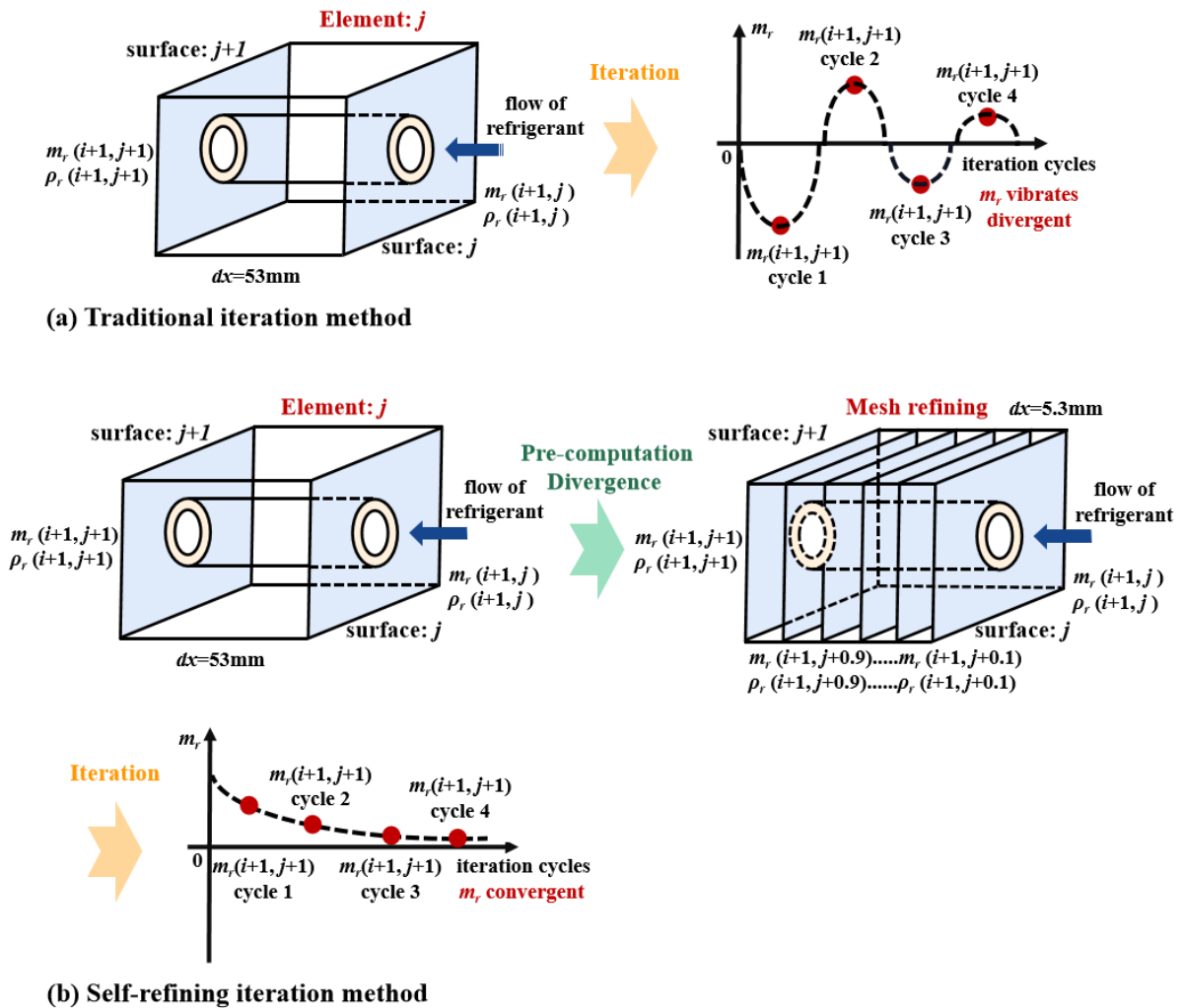
Fig.3 Schematics of iteration methods (a) Traditional iteration method (b) Self-refining iteration method.

2.5 Simulation results and validation

At first a DCHE coated with silica gel is simulated by the model, and the results are validated by the experimental data. Fig.4(a) shows the working principle of the desiccant heat pump in the experiment and the real structure. Refrigerant first flow into the DCHE in evaporation side (DE) to cool down the air and drive the adsorbent to capture the moisture. Then the compressor compress the gaseous refrigerant to the condensation pressure and the refrigerant begin to condense in the DCHE of condensation side (DC). The latent heat of condensation is used to driven the adsorbent release the water in the pores and realize continuous running. The evaporation and condensation temperatures of refrigerant, air temperature humidity ratio and speed at the inlet is 15 ^{o}C, 55 ^{o}C, 23.2 ^{o}C, 9.2 g/g and 0.86 m/s respectively, measured by the sensors. The vapour weight fraction at the inlet of DE ($x_r$in) is 0.316, calculated by the properties of refrigerant shown as Eq.(13). The flow mass of the refrigerant is 5g/s, estimated by the total heat transfer and the latent heat of refrigerant as shown in Eq.(14). The boundary and initial conditions are set as these parameters. Fig.4(b) compares the air temperature and humidity ratio of the experiment and simulation. It's obvious that the simulation results show satisfied consistency with the experimental data. The air temperature can reach 50 ^{o}C because the DCEH is at high temperature (about 53 ^{o}C) at the

beginning and the adsorption rate is very fast, generating a large amount of heat. Then the air temperature start to declines and keeps stable after 7 min. The final temperature stabilise at 17 ^{o}C. The humidity ratio also reach a high level at the beginning because the high temperature of DCHE drive adsorbent desorb the water. Then the humidity ratio drop sharply and then gradually increases because the adsorbent becomes close to saturation as the adsorption proceeds. The humidity ratio stabilise at 9 g/kg after 10 min.

(a)

(b)

(c)

(d)
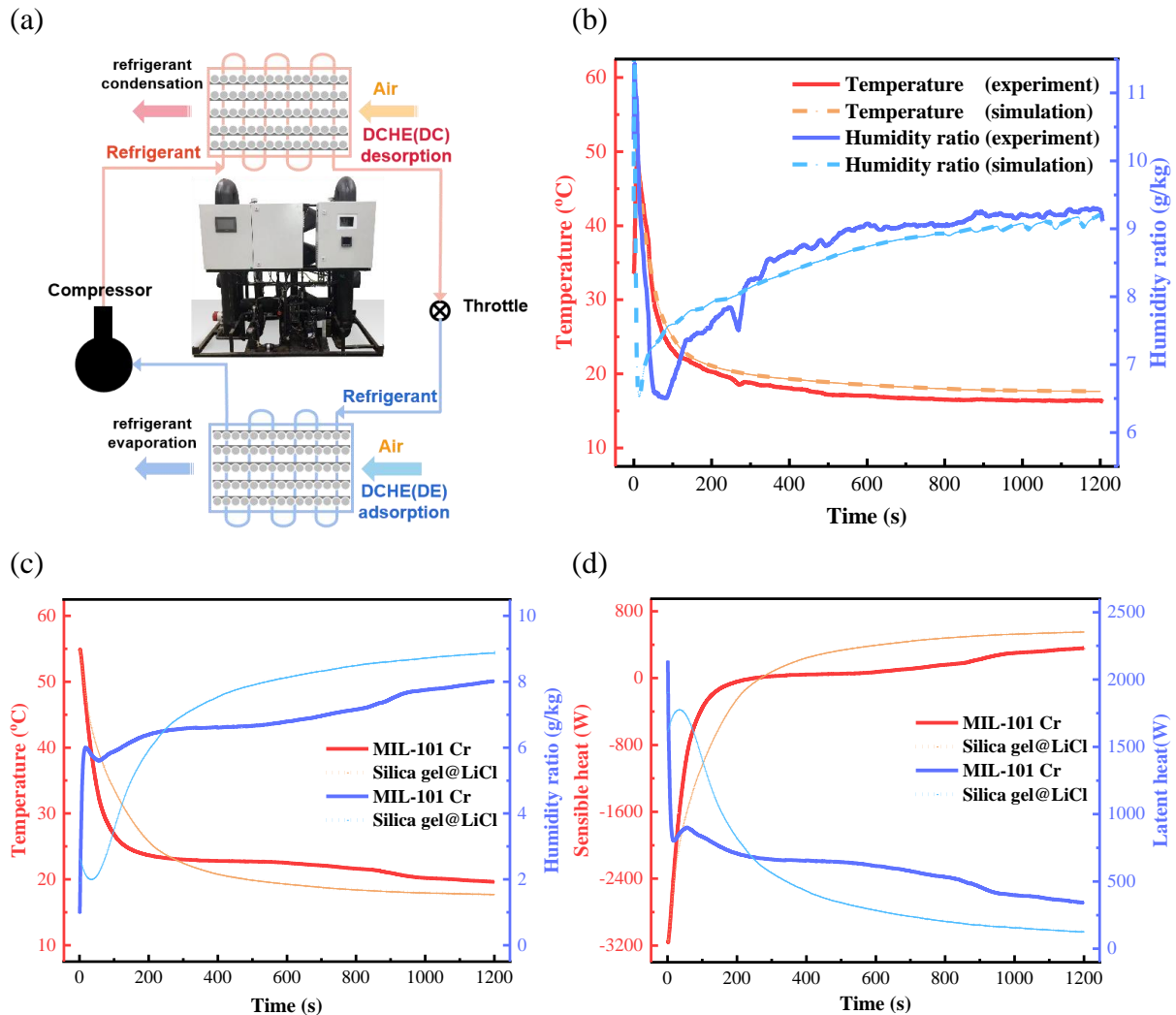
Fig.4(c) shows the air temperature and humidity ratio of DCHE coated with different adsorbent. The horizontal line of humidity ratio from 200s to 800s manifests the dehumidification rate keeps almost constant, indicating MOF possesses a better stability of dehumidification, because of the stepwise type isotherm. Besides MOF distinctly obtains large dehumidification capacity, which may be a promising material of the future DCHE. Fig.4(d) shows the heat transfer of DCHE, including sensible heat and latent heat. It's apparent that the total heat transfer between refrigerant and heat exchanger gradually decrease as time passes by. The reason is that the latent heat and sensible heat are addressed by mass transfer of the adsorbent and heat transfer of the heat exchanger respectively, which is different from traditional heat exchanger that both latent and sensible heat are handled by heat conduction. Therefore, by introducing DCHE, the energy loss during heat transfer can be reduced and the condensation temperature can be reduced, which benefits to improve the COP of heat pump.

Conclusions

In this paper, a mathematical model is built on the DCHE adopting R134a as refrigerant, followed by the validation and discussion over the model. Afterwards, we conclude that:

1. The three-dimensional model on DCHE overcomes the challenges aroused by the two-phase phenomena, the multidimensional of flow transport, the periodical switch over, the solid-side resistance and the coupled heat and mass transfer. It is independent on experimental data and validated to be accurate and robust.

2. With self-refining meshing method, our calculation algorithm yields a quick and convergent solution of the mathematical model, with a satisfied accuracy compared with the experimental data.

3. DCHE, coupling both heat and mass transfer, possesses higher heat exchange capacity (sensible and latent heat) and can reduce the energy loss during heat transfer and hence the condensation temperature, which may benefit to improve the COP of heat pump.

Acknowledgments

References:

[1] Vivekh, P., et al., 2018. Recent developments in solid desiccant coated heat exchangers – A review. *Appl Energy* 229, 778-803.

[2] Yaohui Feng, Tianshu Ge, et al., A regulation strategy of sorbent stepwise position for boosting atmospheric water harvesting in arid area, *Cell Report Physical Science* (2021)

[3] Simonetti, M., et al., 2016. Experimental testing of the buoyant functioning of a coil coated with SAPO34 zeolite, designed for solar DEC(Desiccant evaporative cooling)systems of buildings with natural ventilation. *Appl. Therm. Eng.* 103, 781-789.

[4] Tu, Y.D., et al., Comfortable, high-efficiency heat pump with desiccant-coated, water-sorbing heat exchangers, *Scientific Reports*. 7 (2), 2017, 40437.

[5] Tu, Y.D., Wang, R.Z., Ge, T.S., 2018. New concept of desiccant-enhanced heat pump. *Energy Conv. Manag.* 156, 568-574.

[6] Zhao, Y., et al., 2016. A high performance desiccant dehumidification unit using solid desiccant coated heat exchanger with heat recovery. *Energy Build*. 116, 583-592.

[7] Park, B., Lee, S., Kato, S., 2016. Technical feasibility study of a compact desiccant-based outdoor air system using cogenerated hot water. *Appl. Therm. Eng.* 106, 968-980

[8] Aynur, T.N., Hwang, Y., Radermacher, R., 2010. Integration of variable refrigerant flow and heat pump desiccant systems for the cooling season. *Appl. Therm. Eng.* 30 (8), 917-927.

[9] L.J. Hua, Y. Jiang, T.S. Ge,.Experimental investigation on a novel heat pump system based on desiccant coated heat exchangers. *Energy.* 142 (2018) 96-107

[10] Ge, T.S., et al., 2008. A review of the mathematical models for predicting rotary desiccant wheel. *Renew. Sustain. Energy Rev*. 12 (6), 1485-1528.

[11]Ge, T.S., Ziegler, F., Wang, R.Z., 2010. A mathematical model for predicting the performance of a compound desiccant wheel (A model of compound desiccant wheel). *Appl. Therm. Eng*. 30 (8), 1005-1015.

[12] Yuan, W.X., et al., 2008. Study of a new modified cross-cooled compact solid desiccant dehumidifier. *Appl. Therm. Eng*. 28 (17), 2257-2266.

[13] Jagirdar, M., Lee, P.S., 2018. Mathematical modeling and performance evaluation of a desiccant coated fin-tube heat exchanger. *Applied Energy*. 212, 401-415.

[14] Li, Z., Michiyuki, S., Takeshi, F., 2015. Experimental study on heat and mass transfer

characteristics for a desiccant-coated fin-tube heat exchanger. *Int. J. Heat Mass. Transf.* 89,641-651.

[15] L.J. Hua, T.S. Ge, R.Z. Wang,. A mathematical model to predict the performance of desiccant coated evaporators and condensers. *Int. J. Heat Mass. Transf.* 109 (2020) 188-0

[16] Medveď,I.,Cerný,R., Surface diffusion in porous media: a critical review. *Microporous Mesoporous Mater*. 2011. 142 (2), 405-422.

[17] Higashi, T., et al., 2017. Theoretical and experimental studies on isothermal adsorption and desorption characteristics of a desiccant-coated heat exchanger. *Int. J. Refri* 84, 228-237.

[18] Collier, J.G., Thome, J.R., 1973. Convective boiling and condensation. *Chem. Eng*. 28 (9), 1775.

[19] Macarthur, J.W., Grald, E.W., 1989. Unsteady compressible two-phase flow model for predicting cyclic heat pump performance and a comparison with experimental data. *Int. J. Refri* 12 (1), 29-41.

[20] Zhang W.J., Zhang C.L. and Ding G.L., On three forms of momentum equation in transient modeling of residential refrigeration systems, *Int. J. Refri*. 32 (5), 2009, 938-944.

[21] Jia, X., et al., 1996. A distributed model for prediction of the transient response of an evaporator. *Fuel and Energy Abstracts* 37 (5), 48.

[22] Koury, R.N.N, Machado, L., Lsomail, K.A.R., 2001. Numerical simulation of a variable speed refrigeration system. *Int. J. Refrig*. 24 (2), 192-200.

[23] Ding,G.L.,et al.,2007. Extension of the applicable range of the implicit curve-fitting method for refrigerant thermodynamic properties to critical pressure. *Int. J. Refrig*. 30 (3), 418-432.

[24] Ding, G.L.,et al., 2009. Extension of the implicit curve-fitting method for fast calculation of thermodynamic properties of subcooled refrigerants. *HVAC&R Research*. 15 (5), 875-888.

Dynamic Modelling of Adsorption Chillers Using Refrigerant Mixtures: Impacts of Equilibrium and Dynamics on Performance

M. Lache[1], M. Engelpracht[1], S. Leidolf[1], S. Seiler[2], and A. Bardow[2*]

[1]Institute of Technical Thermodynamics, RWTH Aachen University, Aachen, Germany
[2]Energy & Process Systems Engineering, ETH Zurich, Switzerland

[*]Corresponding author: abardow@ethz.ch

Abstract

Adsorption chillers provide cooling using renewable or waste heat and environmentally friendly pure refrigerants. Pure refrigerants limit operating conditions such as the cooling temperature or the operating pressure. In contrast, refrigerant mixtures allow adjustment of operating conditions by changing their composition. Still, refrigerant mixtures have rarely been studied for adsorption chillers. Studies based on thermodynamic equilibrium models showed a great potential for mixtures but neglected the process dynamics. However, dynamics are known to influence the performance of adsorption chillers strongly. Hence, we develop a dynamic adsorption chiller model exemplarily using water-ethanol as the refrigerant mixture and silica gel 123 as the adsorbent. With the dynamic model, we investigate the effect of ethanol concentration on the performance of the adsorption chiller: the performance decreases by up to 55 % when using an ethanol mole fraction of 5 mol-% compared to pure water for the investigated operating temperature of 10 °C. Dynamics impact performance even more than equilibrium, which shows the importance of dynamic modeling when evaluating the performance of adsorption chillers.

Keywords: adsorption chiller, water/ethanol on silica gel, dynamic modeling, co-adsorption.

Introduction/Background

Adsorption chillers sustainably provide cooling by using renewable or waste heat, thus reducing fossil fuel consumption[1]. Moreover, adsorption chillers offer the opportunity of using environmentally friendly refrigerants such as water, methanol, or ethanol [2]. Typically, refrigerants are applied as pure refrigerants [1]. However, pure refrigerants have only one degree of freedom during phase change, limiting the adsorption chiller's operating conditions (e.g., cooling temperature or operating pressure). Adding a second refrigerant introduces the composition of the refrigerant mixture as a new degree of freedom. Thus, refrigerant mixtures enable, for example, lower cooling temperature by reducing the freezing point of water by adding an antifreeze [3,4]. Furthermore, the system pressure can be increased to atmospheric pressure to improve cost and safety using an ethanol-ammonia mixture [5]. Hence, refrigerant mixtures seem promising to increase the practical applicability of adsorption chillers.

Reinforcingly, a recent review suggests the investigation of binary refrigerant mixtures like ethanol-water, methanol-water, ammonia-water, or ethanol-ammonia [1]. However, experimental investigations of adsorption chillers are time-consuming and resource-intensive already when using pure refrigerants [6,7]. Hence, experimental investigations of adsorption chillers using refrigerant mixtures would be even more resource-intensive due to the second degree of freedom. In contrast, dynamic models avoid resource-intensive experiments [2] and can reliably predict experimental results of adsorption chillers, as shown for pure refrigerants [8]. For refrigerant mixtures, thermodynamic equilibrium models already exist in the literature [5,4], but dynamic models are lacking to the best of the author's knowledge. However,

adsorption dynamics strongly affect the adsorption chiller performance [7,9], thus often limiting the practical application.

In this work, we therefore develop a dynamic model of a two-bed adsorption chiller (AC model) using water-ethanol & silica gel 123 as the working pair. With this AC model, we demonstrate the strength of a dynamic model for evaluating the performance of adsorption chillers.

The AC model (see **Figure 1**) uses the open-source Modelica library *SorpLib* [10], developed at our institute and freely available at GitHub [11]. The AC model is based on the AC model for pure water described and validated by Bau et al. [8]. To consider a water-ethanol mixture instead of pure water, we implemented three modifications:

(1) The multicomponent adsorption equilibrium is described by the ideal adsorbed solution theory (IAST). The IAST model is then represented by an extended isotherm model to reduce computational effort [12]. The equilibrium data of pure water and ethanol were taken from the literature [13]. The adsorption enthalpy of the mixture is calculated by the theoretical approach presented by Sircar [14].

(2) We extended the phase separator model of the evaporator and condenser by a flash calculation and added the Wilson equation [15] to consider non-idealities in the vapor-liquid equilibrium.

(3) The mass transfer of the mixture is described by superposing the linear driving force (LDF) approach for both components water and ethanol.
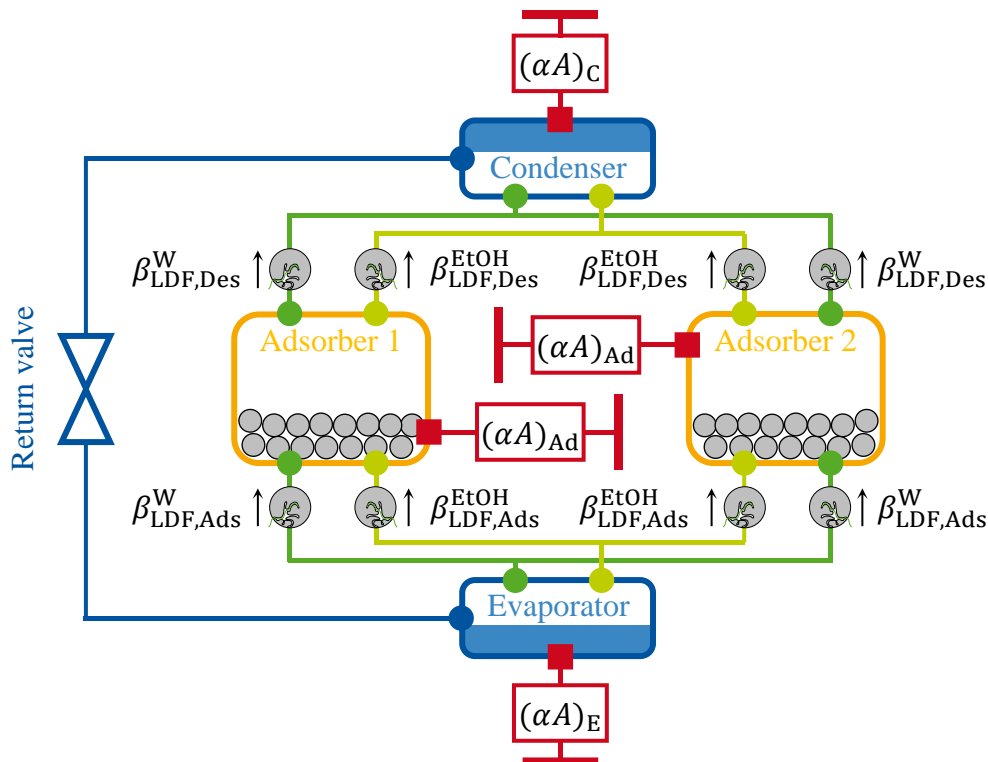
Figure 1. Scheme of the dynamic two-bed adsorption chiller model with water-ethanol as the refrigerant mixture. Heat and mass transfer coefficients are shown: Heat transfer coefficients αA_i of all main components i (Adsorber (Ad), Evaporator (E), Condenser (C)), as well as mass transfer coefficients $\beta_{\mathrm{LDF},j}^{n}$ of water (W) and ethanol (EtOH) for adsorption (Ads) and desorption (Des).

Heat Powered Cycles
Conference 2023
Edinburgh
Heat in the new energy system

3rd to 6th of September 2023
The University of Edinburgh, Scotland

Effective heat and mass transfer coefficients ($(\alpha A)_i$ and $\beta_{LDF,j}^W$, respectively) of pure water were taken from Bau et al. [8]. The effect of ethanol is considered by correction coefficients derived from (a) literature for mass transfer [16] and condensation [17] and (b) own experiments for evaporation [18].

To evaluate the adsorption chiller, we used the performance indicators coefficient of performance (COP) and specific cooling power (SCP):

$$\text{COP} = \frac{Q_E}{Q_H + Q_{Des}} \qquad (1)$$

$$\text{SCP} = \frac{Q_E}{\Delta\tau_{cycle}m_{sor}} \qquad (2)$$

The COP relates the provided cooling energy during evaporation Q_E to the heating input at the adsorber during isosteric heating Q_H and desorption Q_{Des}. The SCP is the ratio of the provided cooling energy during evaporation Q_E to the product of cycle time $\Delta\tau_{cycle}$ and mass of adsorbent m_{sor}. As COP and SCP have a trade-off, adsorption and desorption phase times were set equal and varied to determine the Pareto frontier regarding COP and SCP. The inlet temperatures of the heat transfer fluids during evaporation T_E, condensation T_C, adsorption T_{Ads}, cooling T_{Cool}, desorption T_{Des}, and heating T_H were exemplarily selected as $T_E = 10\,°C \,|\, T_C = T_{Ads} = T_{Cool} = 20\,°C \,|\, T_{Des} = T_H = 85\,°C$.

Discussion and Results

Figure 2 shows the trade-off between SCP and COP of the AC model for pure water and three water-ethanol mixtures. The highest SCP and COP are obtained with pure water. All water-ethanol mixtures lower the performance.

To understand the source for the reduced performance, we varied the heat and mass transfer coefficients for the water-ethanol mixtures: In Case (1), the coefficients are equal to pure water, assuming ethanol only affects the adsorption and vapor-liquid equilibrium (Equilibrium Only), and in Case (2) the coefficients calculated by the derived correction factors, thus assuming that ethanol influences equilibrium and dynamics (Equilibrium + Dynamics).

For the "Equilibrium Only" case, the maximal COP remains the same, and the maximal SCP decreases slightly by 11 % compared to pure water for the lowest total ethanol mole fraction $z_{EtOH} = 0.05$ mol mol^{-1}. At higher total ethanol mole fraction of at $z_{EtOH} = 0.15$ mol mol^{-1}, maximal SCP and COP drop by up to 30 and 40 %, respectively. SCP and COP drop due to a lower enthalpy of vaporization and loading difference.

For the "Equilibrium + Dynamics" case, SCP and COP decline twice as much as in the "Equilibrium Only" case with increasing total ethanol mole fraction. Here, SCP and COP are further limited by a reduced mass transfer during adsorption.

The results show that dynamics affect the performances of the AC model at least as strong as the equilibrium when using water-ethanol as the refrigerant mixture. Thus, dynamics should be considered when evaluating adsorption chillers with refrigerant mixtures. Furthermore, the dynamic model allows identifying the critical kinetic influences to which the performance reacts most sensitively. Thus, the developed model enables the target-oriented identification of the most significant potential for improvement.
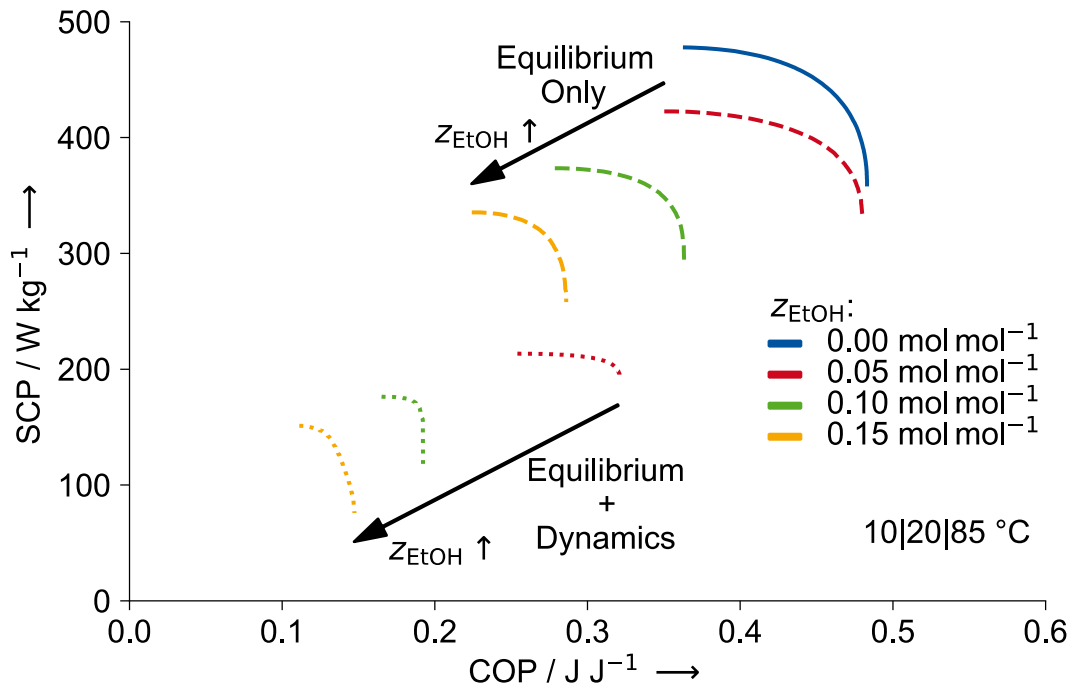
Figure 2. Specific cooling power (SCP) and coefficient of performance (COP) calculated with the AC model for pure water and three water-ethanol mixtures for two cases, where Heat and mass transfer coefficients of the water-ethanol mixtures are (1) equal to pure water (Equilibrium Only) and (2) calculated by the derived correction factors (Equilibrium + Dynamics). The total ethanol mole fraction in the adsorption chiller is z_{EtOH}. The inlet temperatures of the AC model correspond to the temperature triple 10|20|85 °C.

Summary/Conclusions

In this study, we modeled an adsorption chiller using water-ethanol and silica gel 123 as the working pair. With the adsorption chiller model, we investigated the effect of ethanol on the COP and SCP. Both COP and SCP decrease with increasing ethanol mole fraction. The dynamics of the adsorption chiller are shown to affect the COP and SCP at least as strongly as the equilibrium. Therefore, dynamic modeling is important for evaluating adsorption chillers using refrigerant mixtures.

Acknowledgments

References:

[1] Aristov, Y. I., "Adsorption heat conversion and storage in closed systems: What have we learned over the past decade of this century?", Energy, 2022.

[2] Sah, R. P., Choudhury, B., Das, R. K., Sur, A., "An overview of modelling techniques employed for performance simulation of low–grade heat operated adsorption cooling systems", Renewable and Sustainable Energy Reviews, 2017.

[3] Seiler, J., Hackmann, J., Lanzerath, F., Bardow, A., "Refrigeration below zero °C: Adsorption chillers using water with ethylene glycol as antifreeze", International Journal of Refrigeration, 2017.

[4]   Girnik, I. S., Aristov, Y.I., "Water as an adsorptive for adsorption cycles operating at a temperature below 0 °C", Energy, 2020.

[5]   Luberti, M., Di Santis, C., Santori, G., "Ammonia/Ethanol Mixture for Adsorption Refrigeration", Energies, 2020.

[6]   Yong, L., Sumathy, K., "Review of mathematical investigation on the closed adsorption heat pump and cooling systems", Renewable and Sustainable Energy Reviews, 2002.

[7]   Graf, S., Eibel, S., Lanzerath, F., Bardow, A., "Validated Performance Prediction of Adsorption Chillers: Bridging the Gap from Gram-Scale Experiments to Full-Scale Chillers", Energy Technology, 2020.

[8]   Bau, U., Baumgärtner, N., Seiler, J., Lanzerath, F., Kirches, C., Bardow, A., "Optimal operation of adsorption chillers: First implementation and experimental evaluation of a nonlinear model-predictive-control strategy", Applied Thermal Engineering, 2019.

[9]   Liu, X., Wang, X., Kapteijn, F., "Water and Metal-Organic Frameworks: From Interaction toward Utilization", Chemical reviews, 2020.

[10] Bau, U., Lanzerath, F., Gräber, M., Graf, S., Schreiber, H., Thielen, N., Bardow, A., "Adsorption energy systems library – Modeling adsorption based chillers, heat pumps, thermal storages and desiccant systems", The 10th International Modelica Conference, 2014.

[11] RWTH Aachen University, *SorpLib: Dynamic simulation of adsorption energy systems*, https://git.rwth-aachen.de/ltt/SorpLib, 2018.

[12] Postweiler, P., Zenk, K., Engelpracht, M., Bardow, A., von der Aßen, N., "Extended-isotherm surrogates for Dynamic Simulation and Optimization of IAST-based Multicomponent Adsorption Equilibria", 14. International Conference on Fundamentals of Adsorption, 2022.

[13] Lambert, B., Foster, A. G., "Studies of gas-solid equilibria. Part III.—Pressure-concentration equilibria between silica gel and (a) water, (b) ethyl alcohol, directly determined under isothermal conditions", Proceedings of the Royal Society of London. Series A, Containing Papers of a Mathematical and Physical Character, 1931.

[14] Sircar, S., "Excess properties and thermodynamics of multicomponent gas adsorption", Journal of the Chemical Society, Faraday Transactions 1: Physical Chemistry in Condensed Phases, 1985.

[15] Wilson, G. M., "Vapor-Liquid Equilibrium. XI. A New Expression for the Excess Free Energy of Mixing", Journal of the American Chemical Society, 1964.

[16] Guevara-Carrion, G., Vrabec, J., Hasse, H., "Prediction of self-diffusion coefficient and shear viscosity of water and its binary mixtures with methanol and ethanol by molecular simulation", The Journal of chemical physics, 2011.

[17] Li, Y., Yan, J., Qiao, L., Hu, S., "Experimental study on the condensation of ethanol–water mixtures on vertical tube", Heat and Mass Transfer, 2008.

[18] Entrup, M., Nissen, T., Unkhoff, J., Seiler, J., Bardow, A. "Charakterisierung der Dünnfilmverdampfung von Wasser-Ethanol-Gemischen als Kältemittel für Kälteanwendungen unter 0 °C", Thermodynamik-Kolloquium, 2021.

Development of a latent heat thermal energy storage system for waste heat recovery on ships

P. Niknam[1], **L. Ciappi**[1], **R. Fisher**[1], **and A. Sciacovelli**[1*]

[1]School of Chemical Engineering, Birmingham Centre for Energy Storage,
University of Birmingham, UK,
[*]Corresponding author: p.niknam@bham.ac.uk, l.ciappi@bham.ac.uk, r.fisher@bham.ac.uk
a.sciacovelli@bham.ac.uk

Abstract

This paper focus on Thermal energy storage (TES) for an emerging application field: decarbonization of ships and of the wider maritime sector. Heat wasted on-board of ships, for example from engines exhausts and cooling jackets, is a main source of inefficiency and hard to abate. Further, the intermittency in waste heat, primarily due to variation of ship sailing speed, makes traditional waste heat recovery (WHR) solutions less viable. The present paper therefore presents a TES technological solution aimed at mitigate such on-board waste heat intermittency, enabling enhanced recovery of energy otherwise wasted. The present research evaluates a latent heat TES designed to capture onboard waste heat. The proposed TES system consists of a bundle of pillow plate heat exchangers, while the phase change material (PCM) surrounds the plates and serves as the storage medium. The heat storage capacity, heat flow, operating temperature, and charging time are tailored for linking the onboard waste heat sources and energy sinks in either passenger or cargo vessels. The proposed configuration is developed to be adequately light and compact for loading onboard. The TES thermal evaluation during the charging and discharging cycle is assessed by a detailed 3D computational fluid dynamics (CFD) model. The influence of the PCM latent heat and melting temperature (80-130°C), the HTF flow and the source/sink temperature (50-160°C) on TES performance is investigated. The results show that the charging time is highly sensitive to the source temperature rather than the HTF mass flow. The other cross-cutting aspects considered are the scaling up from the laboratory to the onboard scale, discussing how the charging and discharging times can be adjusted between 50 and 180 minutes to align other WHR technologies.

Keywords: Thermal energy storage, latent heat, maritime application, waste heat recovery, numerical modelling.

1. Introduction and background

For decades the maritime sector and its regulator, the International Maritime Organisation (IMO), set plans for improving energy efficiency and taking actions to reduce the emissions from international shipping. Now, pressure is mounting on the shipping industry to chart a course to zero emissions by 2050 [1]. On the other hand, without greater action, emissions from shipping are expected to grow anywhere between 50% to 250% by 2050. [2]. Therefore, the shipping industry, alongside all other sector must quickly embrace new solutions that will lay the groundwork for low and eventually net zero carbon operations. Studies suggest that there

are several opportunities to curb ships' emission emissions, including switching to alternative fuels and recovery of the waste heat available onboard.

Regarding on-board waste heat, the main sources are the high-temperature heat carried away with exhaust gases and low-temperature heat, which is mainly found in the jacket water, scavenge air/charge air cooling water. All of these waste heat sources can be integrated into onboard WHR technologies and increase vessel energy efficiency and reduce fuel consumption. A proven WHR technology for improving efficiency is converting the high-temperature heat from exhaust gases into service steam by boilers and economisers, and this steam can be used for hotel loads or introduced into a steam turbine for generating electricity. Another promising exhaust heat recovery technology is Organic Rankine Cycle (ORC) which is widely used to convert low-grade thermal energy to electricity; however, the application of ORC and similar technologies is currently under investigation, and efforts are being made to adapt those to the onboard energy system [3], and recently some commercial ORCs has been introduced to the market by Alfa Laval AB and Climeon AB with an output range scalable from modules of 150 kW each [4].

Several other technologies could be integrated for onboard WHR, including TES, which may enable other technologies to operate at maximum efficiency. This is because the waste heat available onboard is intermittent and cannot be dispatched on-demand; therefore, TES is a solution that might addresses such issue and allows a greater amount of waste heat to be recovered and reintroduced into the onboard energy system. Onboard TES has a historical record back to the 19th century when some short-distance submarines used steam-TES to power a piston engine and drive the propeller. However, TES solutions, particularly latent heat storage technologies, continue to emerge and mature with costs being driven down, and today, a wide range of phase change materials (PCM) with different thermal characteristics are available in the market [5]. The values of melting temperature (50-220°C) and sensible heat (120-300 kJ/kg) comprise a wide range of use in onboard TESs supporting other WHR technologies [6, 7]. The TES potential for maritime applications stems from the applicability of the technology itself in a wide temperature range and the availability of waste heat within 50-350°C, which is presented in Fig 1. The TES system can be tailored by selecting and utilising a proper energy storage material and mechanical design to maximise its efficiency within the waste heat recovery system. Therefore, although literature suggests that onboard TES shows promise and merits further development and demonstration, there is still significant uncertainty around the viability of TES onboard integration at scale. In order to help address this gap, a detailed analysis of TES performance is conducted in the present study.

The present study proposes, investigate and discuss the merits of a novel latent heat TES system with pillow-plate configuration for onboard application. Scale, energy storage capacity and thermal performance of TES system are addressed; Second the ability of the TES to provide a favourable response time in discharging to be coupled with other WHR technologies is studied. Overall, the performance of the proposed TES are thoroughly predicted by means of CFD analysis and considering a range of operating conditions aligned with the onboard WHR.
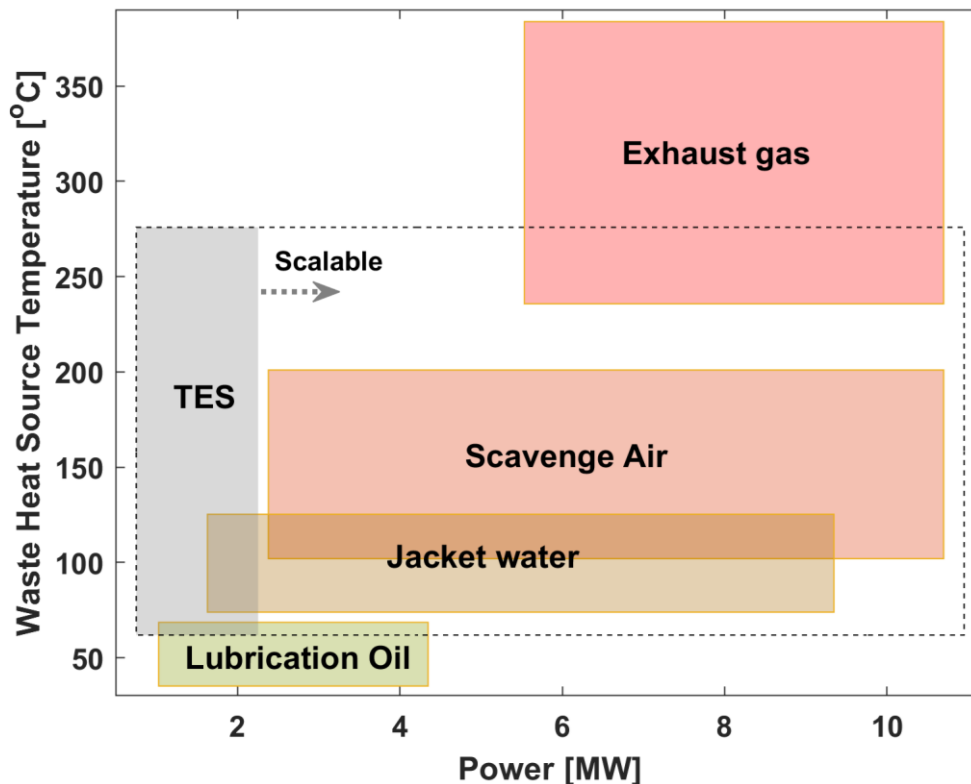
Fig 1-Characteristics of the available waste heat sources and the TES capacity

2. Methodology

2.1. Subject of the study

The structure of the heat exchangers considered in the present research is based on pillow plates, as illustrated in Figure 2. Two different devices were analysed: one at the real scale and one at the laboratory scale. In both cases, a set of pillow plates, stacked parallel to each other in the horizontal direction, is bundled in a box. A plenum pipe connects all the plates with the inlet or outlet pipe at each extremity. This can be achieved with direct joints between the plates and the plenum pipes, as for the real-scale device, or indirectly through dedicated pipes for each plate, as for the laboratory-scale device.

The heat transfer fluid enters the system from the inlet pipe, passes through the pillow plates and exits from the outlet pipe. The plates are surrounded by the phase change material, which acts as the medium for heat storage. In particular, every pillow plate comprises two metal sheets with equivalent wall thickness welded together. The channels for the fluid passage are created between the sheets through an inflation process, expanding them until the attainment of the required height. A path with a U-shape is created inside the plates with three opposite septa to lead the flow which increases heat exchange and reduces bulk.
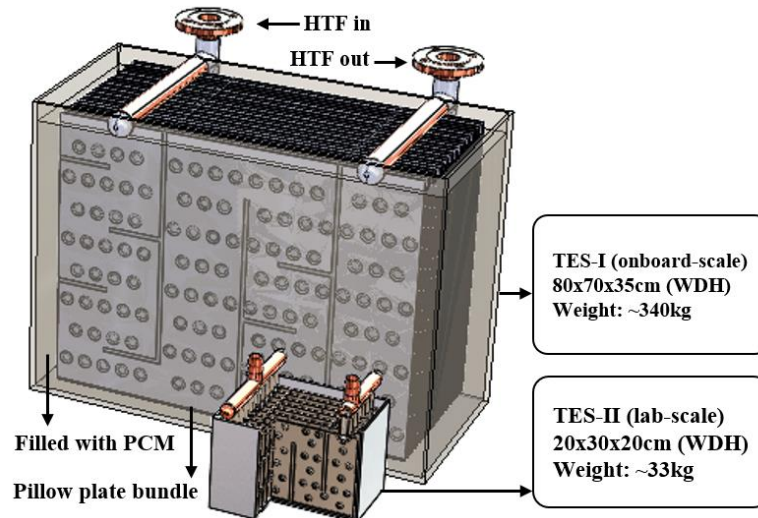
Fig 2 – Schematic representation of pillow plates heat exchangers embedded in PCM at two scales
The principal geometric specifications and operating conditions of the device analysed are listed in Table 1.

Table 1. Main parameters of the geometry and functioning of the heat exchanger with pillow plates

Parameter	Value
Inlet and outlet pipe diameter (D_e)	26.77 mm
Plate pipe diameter (D_p)	21.34 mm
Plate dimensions (I_p x F_p x W_p)	200 x 300 x 6 mm
Welding external diameter (D_{we})	15.80 mm
Welding internal diameter (D_{wi})	6.00 mm
Plate number (n_p)	10
Welding number (n_w)	34
Septum number (n_s)	3

During operation, the heat transfer fluid enters the inlet piping and is distributed to each pillow plate. In the charging phase, the hot HTF passing through the plates acts as the energy source, releasing heat to the phase change material, which absorbs the latent heat, acting as an energy sink. In the reverse discharging phase, the cold HTF is heated up by the thermal energy stored in the PCM. This allows to reserve thermal energy to resolve the mismatch between its availability and demand.

2.2. Design of experiment

The approach of Latin Hypercube sampling (LHS) is utilised to produce 100 sets of four random samples. The LHS sampling substantially reduces the number of samples required for a given accuracy and improves the coverage of parameter space with a fixed number of samples in a multidimensional space. Table 2 summarises the ranges of parameters for LHS and the distribution of samples are shown in Fig 3.

Table 2. Range of parameters applied to LHS of PCMs

Property	Unit	Range
Mass flow rate	kg/s	0.06… 0.6
Charging temperature (heat source)	°C	80…120
Phase change temperature	°C	80 …95
Latent heat	kJ/kg	100…250

Prior to applying each set to the CFD, the latent heat and phase change temperature of all sets are corrected to the nearest value belonging to the commercially available PCMs, which are S83, S89, A82, A95, X90, X80 and the properties are listed in table 3.
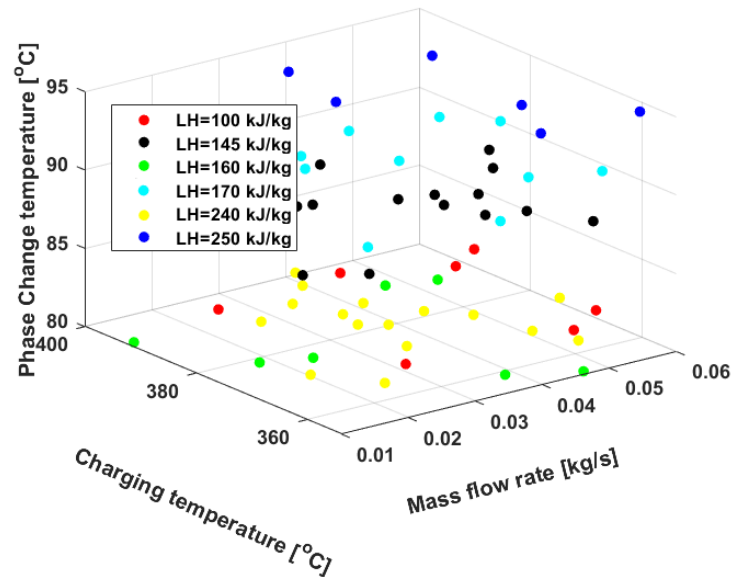
Fig 3- Characteristics of the available waste heat sources and the TES capacity

2.3. CFD model

Three-dimensional CFD models were realised to analyse the thermo-fluid dynamics of the flow crossing the thermal energy storage device. The computational domain was generated with SolidWorks and ANSYS SpaceClaim, its spatial discretisation was obtained with ANSYS Meshing, and ANSYS Fluent was applied for the numerical simulations. Version 21.1 was utilised for the software.

All the pillow plates of the TES device have the same geometry, which is symmetrical regarding the longitudinal plane, as visible in Figure 4(a). The flow conditions of the heat transfer fluid passing through them can be approximated as equal due to the plenum pipes upstream and downstream of the plates. Moreover, the effects of the box walls on the global heat exchange with the PCM and the two plates at the extremes of the set are limited, considering the significant plate number present. This implies that the symmetry of the geometry and thermo-fluid dynamics enables performing simulations on the computational domain comprising half of a pillow plate and the PCM surrounding it, shown in Figure 4(b). As a consequence, the computational time and power of the analyses are markedly decreased as needed for conducting an adequate sensitivity analysis and performing a wide variety of simulations on various cases.
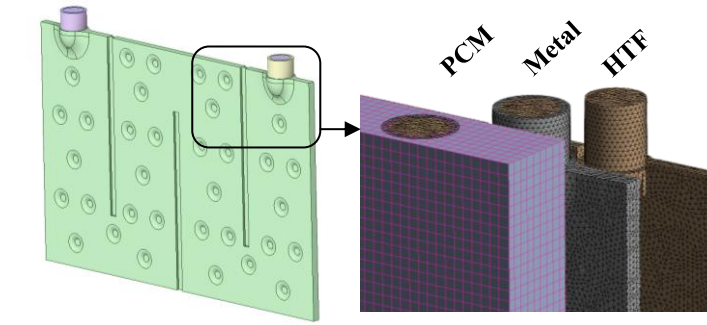
Fig. 4 – Rendering of (**a**) one of the pillow plates and (**b**) the computational mesh of the CFD analyses for the TES device at the laboratory scale

The computational domain is divided into three stationary zones, corresponding to the heat transfer fluid, the pillow plate metal and the phase change material. Interface surfaces were created between the HTF and metal zones and the metal and PCM zones for solving heat transfer.

The spatial discretisation of the computational domain was achieved with either mapped or unmapped approaches. In particular, an unmapped mesh with polyhedral elements was created for the HTF and metal zones; in contrast, a mapped mesh with hexahedral elements and an H-type topology was generated for the PCM zone. A grid refinement is applied for the latter zone in the proximity of the inlet and outlet surfaces and corresponding to the circular weldings of the pillow plate. The sufficiently refined grid allows for solving all relevant flow features for the objectives of the analyses.

The mesh consists of about 0.97 million elements, of which 0.50 million compose the HTF zone, 0.41 million constitute the metal zone, and 0.06 form the PCM zone. The quality of the grid ensures that solutions are reached while respecting the convergence criteria of the mass conservation within 10^{-3} and the maximum order of the root mean squares residuals of 10^{-6} for the continuity, momentum, energy and turbulence equations.

A mesh sensitivity analysis was conducted to assess the spatial independence of the computational discretisation. To this end, the outcomes of the primary fluid dynamics quantities were compared by carrying out simulations with various grids with a number of nodes in the interval between 0.3 and 3.0 million. The variations of grid size were obtained by proportional modifications of element number for the three zones regarding the selected mesh.

Unsteady Reynolds averaged Navier-Stokes (URANS) equations were solved for an incompressible liquid. The liquid density, thermal conductivity, and dynamic viscosity were determined based on its static temperature. The governing equations refer to the continuity, momentum, and energy balances and are defined in the following equations (from Eq. (1) to Eq. (3)):

$$\frac{\partial \rho}{\partial t} + \nabla \cdot (\rho \boldsymbol{v}) = 0 \tag{1}$$

where t is the time and $\boldsymbol{v}$ is the liquid velocity vector.

$$\frac{\partial (\rho \boldsymbol{v})}{\partial t} + \nabla \cdot (\rho \boldsymbol{v} \boldsymbol{v}) = -\nabla \cdot p + \nabla \cdot \tau \tag{2}$$

where τ is the stress tensor.

$$\frac{\partial(\rho H)}{\partial t} + \nabla \cdot (\rho \boldsymbol{v} \mathrm{H}) = \frac{\partial p}{\partial t} + \nabla \cdot (k\nabla T + \tau \cdot \boldsymbol{v}) \tag{3}$$

where H is the total specific enthalpy, k is the effective thermal conductivity and T is the temperature.

The total specific enthalpy is calculated through Eq. (4) based on the specific enthalpy h and the specific kinetic energy and velocity magnitude v of the liquid.

$$H = h + \frac{v^2}{2} \tag{4}$$

The phase variations of the PCM are modelled by applying the Solidification and Melting model. This approach couples the energy accumulated or released by the PCM during the charging and discharging processes is coupled with the temperature determined by the energy equation, as defined in Eq. (5).

$$E = \begin{cases} \int_{T_0}^{T_{pcm}} (\rho c_p)_{pcm} dT & T_{pcm} < T_{sol} \\ \int_{T_0}^{T_{pcm}} (\rho c_p)_{pcm} dT + \frac{\rho L}{T_{liq} - T_{sol}}(T_{pcm} - T_{sol}) & T_{sol} < T_{pcm} < T_{liq} \\ \int_{T_0}^{T_{pcm}} (\rho c_p)_{pcm} dT + \rho L & T_{pcm} > T_{sol} \end{cases} \tag{5}$$

where E is the specific energy, L is the latent heat, T_{pcm} is the PCM temperature and T_{sol} and T_{liq} are the PCM solidification and melting temperatures, respectively [8].

The governing equations were discretised with a second-order scheme for the pressure and second-order upwind schemes for the density, momentum and energy. The SIMPLE scheme was utilised to relate the corrections of velocity and pressure. The least-squares and cell-based method were selected for calculating the quantity gradients [9]. Since the Reynolds number of the heat transfer fluid is characteristic of the laminar behaviour, the turbulence closure was obtained with second-order discretisation using the laminar model [10].

The equations were implicitly solved with a pressure-based approach. Fully transient simulations were conducted, and a time step equal to $2 \cdot 10^{-2}$ seconds was imposed for marching the solutions in time.

2.3. Material properties

PCMs and HTF Thermophysical Properties are listed in Table 3. While the HTF in all parts of the analysis is the same, different PCMs are considered for TES performance assessments. The PCMs are tailored by the supplier for different melting temperatures; however, they are mostly mixtures of nitrate salts [11].

Table 3-Thermophysical properties of pillowplate-TES compartment PCM and HTF materials

Parameter			Value
HTF: Therminol 66	C_p [kJ/kgK]	373K	1.84
		473K	2.19
	Density, ρ [kg/m3]	373K	955
		473K	885
PCM	C_p [kJ/kgK]		1.5 … 2.3
	Thermal conductivity [W/mK]		0.36 … 0.51
	Density [kg/m^3]		900 … 1600
	Latent heat (LH) [kJ/kg]	PlusICE® H105	125
		PlusICE® H115	100
		PlusICE® H120	120
		PlusICE® S83	100
		PlusICE® S89	145
		PlusICE® A82	240
		PlusICE® A95	250
		PlusICE® X80	160
		PlusICE® X90	170
	$T_{melting}$ [°C]	PlusICE® H105	105
		PlusICE® H115	115
		PlusICE® H120	120
		PlusICE® S83	83
		PlusICE® S89	89
		PlusICE® A82	82
		PlusICE® A95	95
		PlusICE® X80	80
		PlusICE® X90	90

3. Discussion and Results

This section reports and discusses the dynamic behaviour of the pillow-plate TES under investigation. As part of the overall aims of the paper, the results initially detail how the system undergoes a full charging and discharging cycle. Figure 5 shows the time evolution of PCM temperature and liquid phase fraction. The charging rate is directly proportional to the temperature differential between the HTF fluid as the heat source and the PCM temperature; therefore, the temperature is increased with a progressive reduction in slope, and the temperature is almost stable during the phase change when the heat is absorbed in the form of latent heat. The temperature increases gradually until reaching the source temperature, which indicates that the storage is filled.
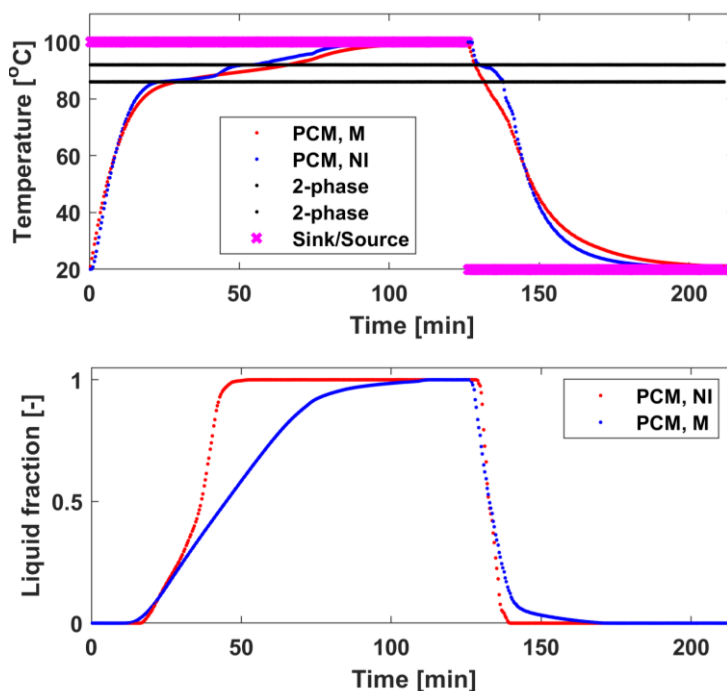
Fig 5-Time evolution of charge-discharging cycle(TES-II)

Based on the literature, the TES discharging process is longer than the charging because of the different heat transfer process, as there is no natural convection or buoyancy effect during the discharging [12]. The discharging rate of the proposed TES is investigated when different sink temperatures are applied. Figure 6 (corresponding to the yellow highlighted area) demonstrates that increasing the sink temperature from 50 to 70°C is led to longer discharging. Because of the different duration of the charging and discharging phases, there is a need for a flexible thermal storage system that can be charged and discharged at different rates. A potential solution would be to charge and discharge the TES with different HTF flow rates. In order to clarify the impact of this parameter, it is investigated in detail in the parametric analysis section.
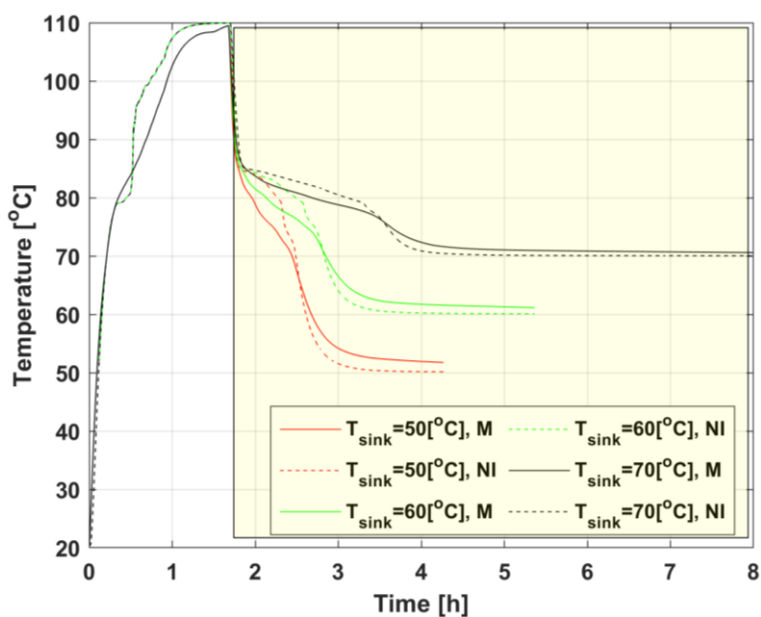
Fig. 6-Discharging time on different sink temperatures (TES-II)

3rd to 6th of September 2023
The University of Edinburgh, Scotland

Heat Powered Cycles
Conference 2023
Edinburgh
Heat in the new energy system

3.1. Parametric analysis

The CFD simulation was conducted for a set of conditions, and the outputs of the simulation are extracted and sorted accordingly. The key questions in TES performance assessment are how much energy can be stored, and the answer can be assessed by quantifying the stored energy in various boundary conditions and settings. The second is charging power which is critical for the overall WHRS to be integrated into other WHR technologies. As shown in Figure 7, There is a clear linear relationship between the charging time variables, while no clear relationship is found for the other three design parameters of mass flow, phase change temperature and latent heat. A good theoretical rationale for the significant impact of charging temperature is directly involved in the temperature difference, which is the driving force of the conduction heat transfer. However, the HTF mass flow does not directly involve heat transfer within the PCM. Moreover, the influence of the phase change temperature and latent heat would be more on the phase change behaviour within the PCM rather than the heat source temperature.
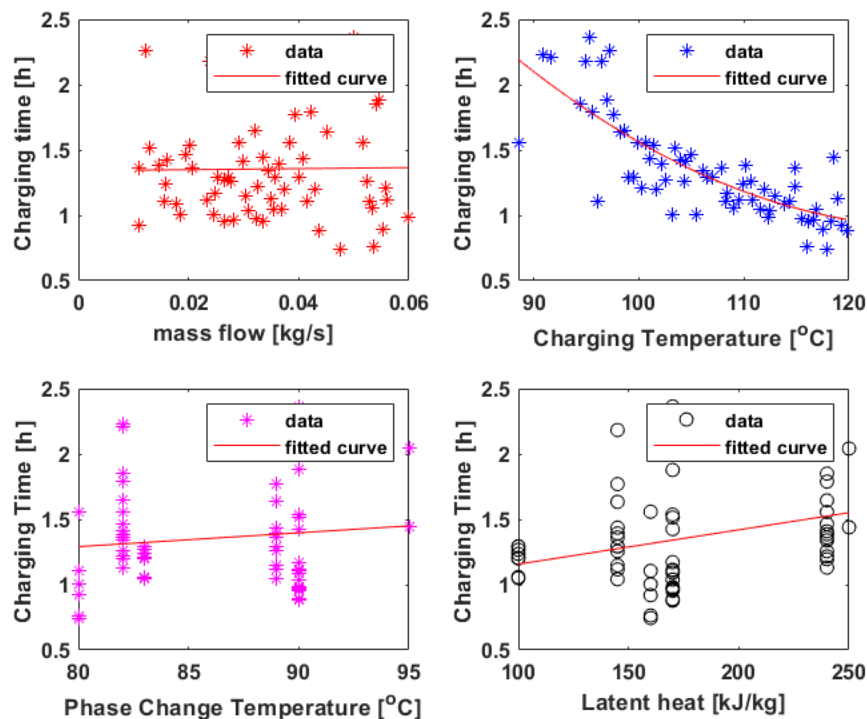
Fig 7-Charging time estimation (TES-II)

Figure 8 complements the results of Figure 7 and reports how the heat load is correlated with the heat source temperature. The average and maximum heat loads for all sets of boundary conditions in the parametric analysis are reported in this figure. Moreover, what stands out in this figure is that the maximum load imposed on the TES at the beginning of charging (maximum temperature difference) is approximately three times the average load.
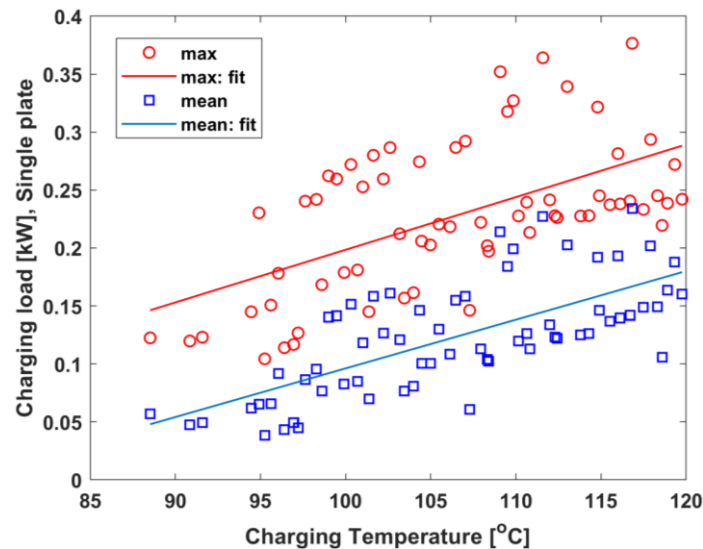
Fig. 8- Charging load in different charging temperatures (TES-II)

The parametric analysis is conducted to assess the influence of key design and operating parameters on optimal thermal performance, and the main focus of this part of the study is on the charging time. The thermal performance of the small-scale storage (TES II) is simulated under various source temperatures (T_s), as shown in Figure 9, and under various mass flow rate shown in Figure 10. These two figures complement the results of Figure 7 and report how the time evolution of the TES charging rate is strongly tied to the source temperature but not to the HTF mass flow rate. The corresponding stored energy in the PCM during the charging is demonstrated for the large scale (TES I) and small scale (TES II) in Figure 10 and Figure 11, respectively. The energy storage capacities shown in these figures are estimated for a single pillow plate, and the plate bundle capacity depends on the number of plates. A ten-plate bundle provide 3kWh on the lab scale and 15 kWh on the onboard scale.
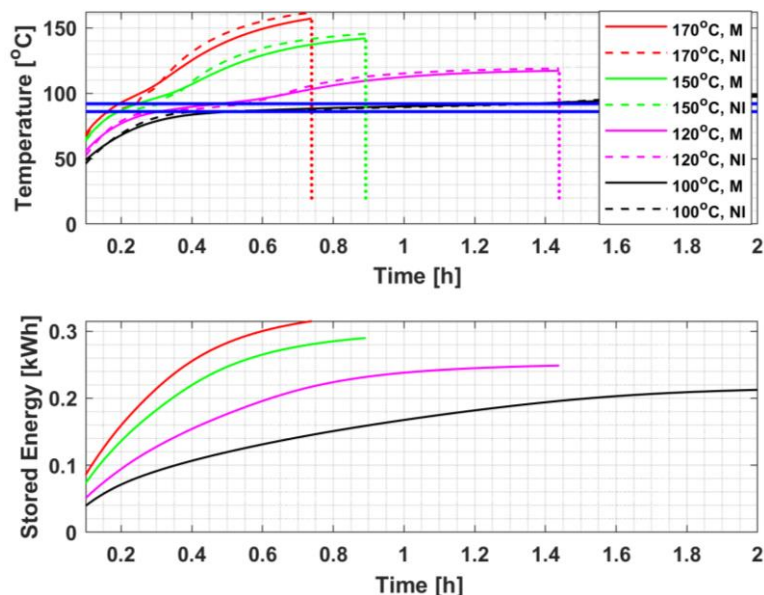
Fig. 9- Temperature and energy of TES in charging under various charing temperatures, TE-II, PCM: a89, $\dot{m}$=0.02 [kg/s] (M:mean, NI:near inlet)
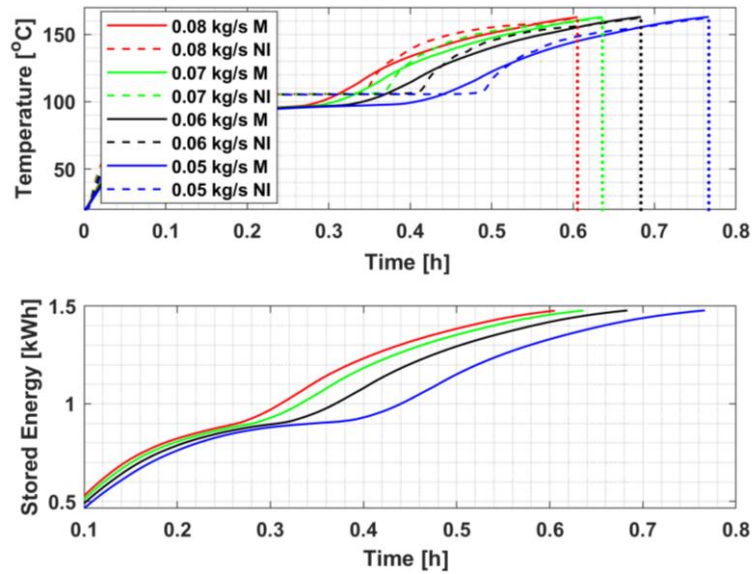
Fig. 10- Temperature and energy of TES in charging under various HTF mass rates, TES-I, T_s=170[°C] (M:mean, NI:near inlet)

The impact of the type of the PCM on the melting process, as well as the influence on the stored energy are investigated, and the results are reported in Figure 11. Although some types of PCM provide a faster response and higher storage capacity, those are not necessarily the best options. For example, a higher mass density implies a larger TES total weight, which is not in favour of onboard applications at scale.
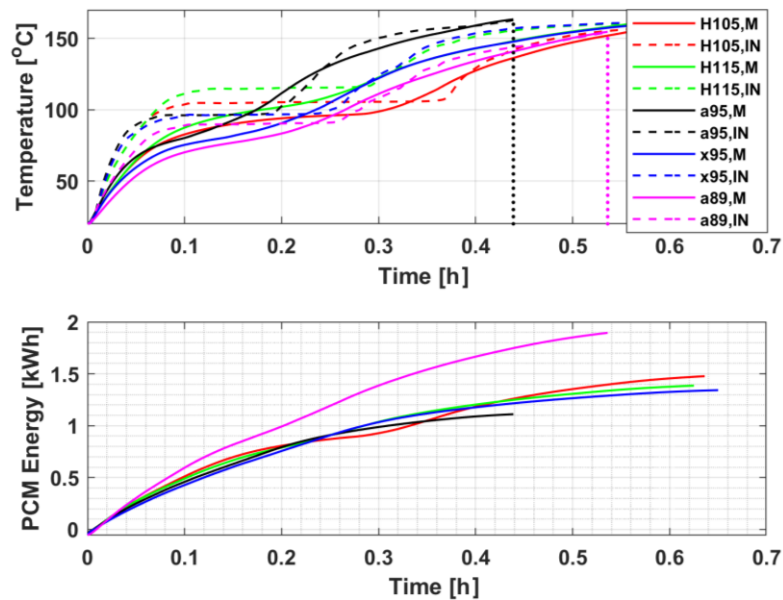
Fig. 11- Temperature and energy of TES with different PCMs in charging, $\dot{m}$=0.02 [kg/s]¸TES-I, T_s=170 [°C] (M:mean, NI:near inlet)

The relative comparison of four types of PCM discussed in the present research, including A-type (organic solutions), S- type (hydrated salts), X-type (solid-solid) and H- type (high temperature), is presented in Figure 12. So, there is a trade-off between density, thermal conductivity and heat capacity for PCM selection, and it can be tailored based on the requirement of thermal power and design limits imposed by the upstream or downstream

conditions. Regardless of the weight limit for onboard equipment, the high-temperature PCMs (H-type) would be preferred; otherwise, A-type support the TES with a higher charging-discharging efficiency.
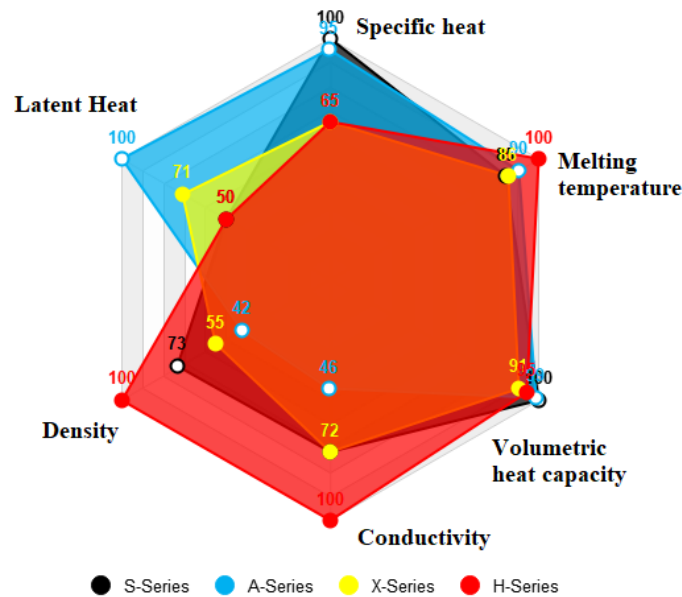
Fig. 12- PCM property comparison (values are relative percentages to the maximum of all types)

4. Conclusion

The present studied addresses the application of TES technology on-board of ships to enable the recovery of waste heat. Specifically, a novel TES configuration combining pillow-plate heat exchangers and PCMs is proposed and investigated. The focus of the study was on the parametric analysis of the TES performance and influence of the main design parameters. It was found that the charging time strongly depends on the source temperature and slightly depends on the PCM type, and the values of the HTF mass flow rate. These outcomes justify the consideration of the TES technology when operating upstream or downstream of other WHR technologies. The simulation results show that the charging time is 45 to 70 minutes (equivalent to an average charging rate of 0.2kW), while the discharging time is longer, as it ranges between 2 and 6 hours (equivalent to an average discharging rate of 0.05 kW) for a single 20x30cm pillow plate. However, the HTF flow adjustment is also shown as a practical solution while specific discharging time is required particularly when TES is expected to support other WHR technologies.

Acknowledgements

References:

[1] Wu, Min, et al. "Carbon Emission Trading Scheme in the shipping sector: Drivers, challenges, and impacts." Marine Policy, 2022. DOI: https://doi.org/10.1016/j.marpol.2022.104989.

[2] Rahim, Mia Mahmudur, Md Tarikul Islam, and Sanjaya Kuruppu. "Regulating global shipping corporations' accountability for reducing greenhouse gas emissions in the seas." Marine Policy, 2016. DOI: 10.1016/j.marpol.2016.04.018.

[3] Mondejar, M. E., et al. "A review of the use of organic Rankine cycle power systems for maritime applications." Renewable and Sustainable Energy Reviews, 2018. DOI: 10.1016/j.rser.2018.03.074.

[4] Konur, Olgun, C. Ozgur Colpan, and Omur Y. Saatcioglu. "A comprehensive review on organic Rankine cycle systems used as waste heat recovery technologies for marine applications." Energy Sources, Part A: Recovery, Utilisation, and Environmental Effects, 2022. DOI: 10.1080/15567036.2022.2072981.

[5] Sciacovelli, Adriano, Vittorio Verda, and Francesco Colella. "Numerical model for storage systems based on phase-change materials." ASME International Mechanical Engineering Congress and Exposition, 2011. DOI: 10.1115/IMECE2011-65393.

[6] https://www.pcmproducts.net/files/PlusICE%20Range%202021-1.pdf

[7] Niknam, P.H. and Sciacovelli, A.,. Hybrid PCM-steam thermal energy storage for industrial processes–Link between thermal phenomena and techno-economic performance through dynamic modelling. Applied Energy, 2023. DOI: 10.1016/j.apenergy.2022.120358.

[8] Bellan, S., Alam, T.E., González-Aguilar, J., Romero, M., Rahman, M.M., Goswami, D.Y. and Stefanakos, E.K. Numerical and experimental studies on heat transfer characteristics of thermal energy storage system packed with molten salt PCM capsules. Applied thermal engineering, 90, pp.970-979, 2015. DOI: 10.1016/j.applthermaleng.2015.07.056.

[9] ANSYS Incorporated, ANSYS Fluent Theory Guide, Southpointe 2600 ANSYS Drive Canonsburg, Pennsylvania 15317, 2021

[10] Launder, B.E., and Spalding, D.B., Lectures in Mathematical Models of Turbulence, Academic Press, London, England, 1972, ISBN 0124380506.

[11] Humbert, G., et al. "Development of a latent heat thermal energy storage unit for the exhaust of a recuperated solar-dish Brayton cycle." Applied Thermal Engineering, 2022. DOI: 10.1016/j.applthermaleng.2022.118994.

[12] Fadl, Mohamed, Daniel Mahon, and Philip C. Eames. "Thermal performance analysis of compact thermal energy storage unit-An experimental study." International Journal of Heat and Mass Transfer, 2021. DOI: 10.1016/j.ijheatmasstransfer.2021.121262.

Nomenclature

A	Area [m^2]	T	Temperature [K]
B	Melt fraction [-]	T_S	Surface temperature [K]
c_p	Specific heat capacity [J/kg.K]	T_s	Source or sink temperature [K]
D_e	Pipe diameter [mm]	T_A	Surface adjacent air temperature [K]
D_p	Plate pipe diameter [mm]		
D_{we}	Welding external diameter [mm]	t	Time [s]
D_{wi}	Welding internal diameter [mm]	$\boldsymbol{v}$	Velocity vector [m/s]
E	Specific energy [J/m^3]	v	Velocity magnitude [m/s]
F_p	Plate heigh [mm]	W_p	Plate width [mm]
g	Gravitational acceleration [m/s^2]	**Greek symbols**	
H	Specific total enthalpy [J/kg]	ρ	Density [kg/m^3]
h	Specific enthalpy [J/kg]	τ	Stress tensor [N/m^2]
I_p	Plate length [mm]	**Other symbols**	
K	Thermal conductivity [W/m.K]	Δt	Time step [s]
k	Effective thermal conductivity [W/mK]	Δx	Finite difference layer thickness [m]
L	Latent heat [J/kg]	HTF	Heat transfer fluid
ṁ	Mass flow rate [kg/s]	LHTES	Latent heat thermal energy storage
n_p	Plate number [-]	PCM	Phase change material
n_s	Septum number [-]	TES	Thermal energy storage
n_w	Welding number [-]	URANS	Unsteady Reynolds averaged Navier-Stokes
p	Pressure [Pa]		
q	Heat flux [W/m^2]	WHR	Waste heat recovery

Salt in porous matrix composites for sorption heat transformers: How to maximize sorption capacity and dynamic performance while avoiding leakage

I. Girnik, C. McCague, and M. Bahrami[*]

Laboratory for Alternative Energy Conversion, School of Mechatronic Systems Engineering, Simon Fraser University, 250-13450 102 Avenue, Surrey, BC, V3T 0A3, Canada

[*]Corresponding author: mbahrami@sfu.ca

Abstract

Salt in porous matrix composites has high sorption capacity and can be tuned to specific applications, e.g. thermally-driven heat transformers, chillers, and thermal storage. However, if prepared incorrectly, salt can leak from the matrix resulting in inconsistent performance, reduced dynamics, and corrosion of metallic components of the system. This study presents a method of calculating optimal salt-to-matrix ratios for sorption cycles considering operating conditions, the matrix pore volume, the sorption equilibrium curve, and the solution density curve. The porous matrix water sorption "flooding thresholds" are plotted for $CaCl_2$, LiCl and LiBr in mesoporous silica gel matrices in comparison to an unsuitable microporous silica gel matrix.

Keywords: Sorption, Hygroscopic salt in porous matrix, Salt Leakage, Hysteresis, Corrosion.

Introduction/Background

Salt in porous matrix composites – such as mesoporous silica gels or vermiculite impregnated by hygroscopic salts ($CaCl_2$, LiBr, LiCl, etc.) – have sorption thermal storage and transformation applications [1]. However, if improperly prepared, such materials are subject to salt solution leakage from the pores and possible sorption-desorption hysteresis both of which can affect the sorption system performance. Salt solution leakage can also lead to corrosion and contamination of system components, i.e., the evaporator, condenser, valves, chambers, and sorber bed. For this reason, it is crucial to determine how the salt-to-porous matrix weight ratio influences the circumstances under which the sorbate solution leak out of matrix pores. In addition, it is important to understand how sorbent composition and system operating conditions influence adsorption-desorption hysteresis.

In this research, salt solution leakage threshold conditions (temperature, T, and relative pressure, P/P_0) and adsorption-desorption hysteresis were studied for different combinations of matrixes (mesoporous silica gels, SiliaFlash B150 and B300, SiliCycle Inc., and microporous silica gel, Fuji RD) and hygroscopic salts ($CaCl_2$, LiCl, and LiBr).

Discussion and Results

Salt solution leakage threshold was calculated as a function of hygroscopic salts ($CaCl_2$, LiCl, and LiBr) composite weight ratios for silica gels with different specific pore volumes, V, and average pore diameters, d. The analysis included the variation in aqueous salt solution density as a function of the mole fraction of salt in solution [2] in the calculation of the leakage threshold point as a function of composite and operating cycle conditions.

It is shown that for $CaCl_2$ in a mesoporous silica gel (B150, $V = 1.05$ cm^3/g, $d = 16.7$ nm) at temperature $T = 30°C$ and relative pressure $P/P_0 = 0.8$, the salt solution will flood the sorbent if $CaCl_2$ is more than 22.5 wt.% of the composite (Fig. 1a; composite which consists only of

silica gel and salt). Therefore, for stability in long term thermal energy storage, for the selected salt and matrix, the salt must be less than 22.5 wt.%. to prevent salt solution leakage and corrosion. For a microporous silica gel matrix (Fuji RD, $V = 0.4$ cm^3/g, $d = 2.2$ nm), the flood point occurs at low CaCl$_2$ content, < 10 wt.% (Fig. 1b), which makes it unsuitable, due to the corresponding low water uptake capacity for stable salt loads.

In the case of LiCl in a mesoporous silica gel (B150), under the same conditions, the salt solution leakage threshold is lower (15 wt.%) than for CaCl$_2$ due to the difference in molecular weight, sorption equilibrium curve, and density of the salt solution, 1.09 g/cm^3 vs 1.21 g/cm^3 for LiCl and CaCl$_2$, respectively.

a   **b**
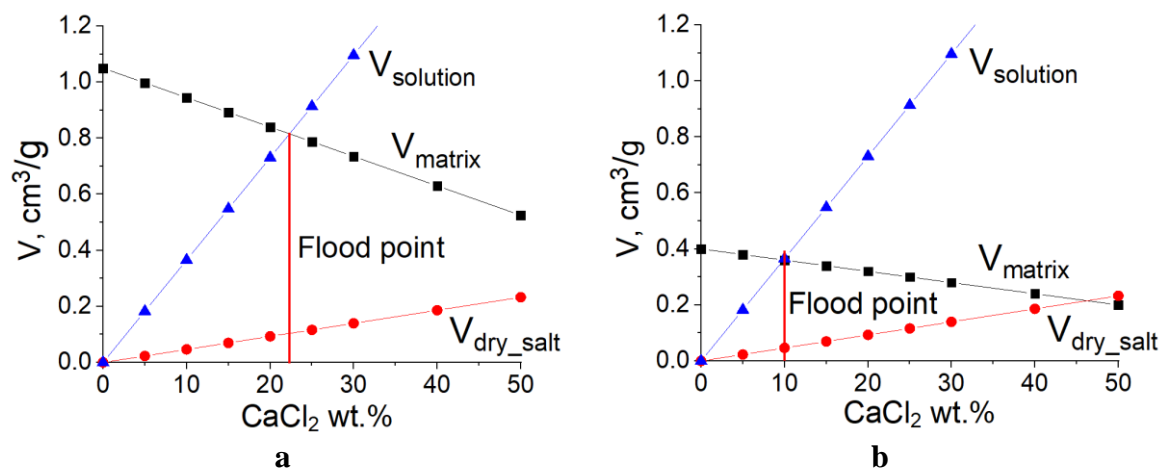
Fig. 1. Specific pore volume (■), specific volume of dry salts (●) and specific volume of salt solution (▲) for "CaCl$_2$ – silica gel" composites for (a) mesoporous silica gel (1.05 cm^3/g) and (b) microporous silica gel (0.4 cm^3/g). The salt solution volume at 30°C and $P/P_0 = 0.8$ is plotted, and the flooding threshold, where the solution volume exceeds the matrix pore volume, is marked.

A thermogravimetric vapor sorption analyser was used to measure the water sorption-desorption isotherms of CaCl$_2$ and LiCl in silica gel composites. The flooding threshold can be observed as an inflection point in the adsorption branch and the initiation of hysteresis in the desorption branch.

Summary

Water sorption-desorption hysteresis and salt solution leakage "flooding points" as a function of salt wt.% were calculated for composites of hygroscopic salts (CaCl$_2$, LiCl or LiBr) in silica gel matrices and were experimentally observed in water sorption isotherms. The presented methods for calculating and measuring water sorption flooding points thresholds can be used to tune salt in porous matrix sorbent composition for specific sorption systems and operating cycles.

Acknowledgments

References:

[1] Aristov, Yu. I., Tokarev, M. M., Cacciola, G., and Restuccia, G., "Selective water sorbents for multiple applications: 1. CaCl$_2$ confined in mesopores of the silica gel: sorption properties", Reaction Kinetics and Catalysis Letters, 1996.

[2] Conde, M.R., "Properties of aqueous solutions of lithium and calcium chlorides: formulations for use in air conditioning equipment design", International Journal of Thermal Sciences, 2004.

Experimental Study on Thermal Contact Resistance in Sorbent Reactors

Salman Hassanabadi, Majid Bahrami*

Laboratory for Alternative Energy Conversion (LAEC), School of Mechatronic Systems Engineering,
Simon Fraser University, 250- 13450 102nd Ave., Surrey, BC, Canada V3T 0A3

ABSTRACT

Thermal contact resistance (TCR) can significantly affect the heat transfer between two solid bodies. In solid sorption systems, thermal contact resistance occurs between the solid adsorbent and the heat exchanger surface. In this study, the thermal contact resistance was measured by a custom-built guarded hotplate for sorbent composite samples with various grain sizes. Consolidated sorbent composites were prepared from silica gel, calcium chloride and binder. Results showed that thermal contact resistance ranges from 1.9 to 2.8 K/W (i.e., 4.5%-6.5% of the total thermal resistance for a 5-mm thick sorbent composite) for the composites made from the smallest to the largest grain size, respectively. There is a need to optimize the composite's grain size and its composition to minimize TCR while enhancing thermal conductivity.

Keywords: sorption system, heat-driven cycles, thermal contact resistance, silica gel, and sorbent composite

1. INTRODUCTION

Thermal contact resistance (TCR) is an interfacial phenomenon and should be addressed independently from thermal conductivity, which is a bulk property [1]. Two main methods exist for measuring TCR: transient and steady state. The steady-state approaches are relatively straightforward and accurate; however, transient approaches are frequently used in order to determine the relationship between the thermophysical properties via optical or acoustics techniques [2]. In this study, we prepared several sorption composites and measured their effective thermal conductivity and the TCR at the interface with the heat exchanger surface (substrate) using a custom-built thermal conductivity measuring test bed, as per ASTM standard C177-13 [3]. To measure the thermal contact resistance between the sorbent and substrate (TCR$_{sorb-NGS}$), the sorbent sample was sandwiched between two natural graphite sheets (NGSs), as a substrate, Figure 1. The thermal resistance of the natural graphite sheet, R$_{NGS}$, and the contact resistance between the flux meter and the graphite sheet, TCR$_{flux-NGS}$, were measured separately using a bare NGS substrate, then, the two-thickness method [1] was used to find the TCR$_{sorb-NGS}$. The two-thickness method is an approach to measure the sample's thermal conductivity and de-convolute the effect of the TCR between the fluxmeters and the sample, see Ref. [1] for more details. The TCR may be precisely excluded from the sample's thermal conductivity using this technique. Equations (1) to (4) show the two-thickness method calculations to find the R$_{sorb}$ and TCR$_{sorb-NGS}$.

$$R_{sample1} = 2TCR_{flux-NGS} + 2R_{NGS} + 2TCR_{sorb-NGS} + R_{sorb1} \tag{1}$$

$$R_{sample2} = 2TCR_{flux-NGS} + 2R_{NGS} + 2TCR_{sorb-NGS} + R_{sorb2} \tag{2}$$

$$R_{sample2} - R_{sample1} = R_{sorb2} - R_{sorb1} = \frac{\Delta T_2}{\dot{Q}_2} - \frac{\Delta T_1}{\dot{Q}_1} \tag{3}$$

$$R_{sorb1} = \frac{t_{sorb1}}{k_{sorb1}\,A} \; ; \; R_{sorb2} = \frac{t_{sorb2}}{k_{sorb2}\,A} \tag{4}$$

where, t is the sorbent sample thickness, A is the sample surface area, $\dot{Q}$ is the heat transfer rate that passes through the fluxmeters, and ΔT is the temperature difference across the sample, respectively.

2. MATERIALS AND METHODS

Four silica gel samples with various particle sizes were prepared for this study, Table 1. Calcium chloride (CaCl$_2$) and polyvinylpyrrolidone (PVP) were used as the impregnating salt and polymeric binder. The thermal contact resistance is a pressure-dependent parameter. However, as we aim to investigate the effect of particle size on the TCR, TCR$_{sorb-NGS}$, was measured at a constant contact pressure of 1 bar, with a maximum of 8 percent uncertainty. Furthermore, a higher contact pressure may damage the samples.

3. RESULTS AND DISCUSSION

The measurements showed that $TCR_{Flux-NGS}$ was less than one percent of the total thermal resistance ($R_{total} = 2TCR_{flux-NGS}+2R_{NGS}+2TCR_{sorb-NGS}+R_{sorb}$). This could be due to the soft and flexible surface of the NGS, which creates an almost perfect contact with the smooth surface of the fluxmeter. Similarly, the bulk resistance of the substrate (natural graphite sheet) was 2% of the total resistance, which was expected because of its relatively higher thermal conductivity (k = 5 W/m.K) and the small thickness of the substrate (0.9 *mm*).

Two main sources of thermal resistance include the sorbent composite itself (the bulk resistance) and the thermal contact resistance between the sorbent composite and the graphite sheet substrate. Figure 2 shows the share of the $TCR_{sorb-NGS}$ for the samples with various silica gel particle sizes compared with their total thermal resistance. The $TCR_{sorb-NGS}$ for the samples ranges from 1.9 to 2.8 K/W which was 4.5% to 6.5% of the total thermal resistance for a 5-mm thick sorbent. However, for most applications, where the sorption composites are thinner, <1 mm, the contribution of the TCR will be notably higher, up to 40%.

The composites with larger grain sizes (SGC-04 and SGC-03) showed higher TCR (SGC-01 and SGC-02), which may be due to the higher intergranular spaces and thus, less solid contact between the grains and substrate, see [4]. Lower intergranular spaces are easier to be filled with binder since the binder itself could fill the gaps better and also adhere to the substrate better. Therefore, the particle size and consequently the binder-to-grain ratio play important roles in the TCR between the composite and substrate. On the other hand, the thermal conductivity of the composites decreased from 0.30 W/m.K to 0.18 W/m.K by increasing the grain size. This 40% reduction also could be due to the decreasing porosity of composites for larger grain sizes. This shows a compromise between the thermal conductivity and TCR.
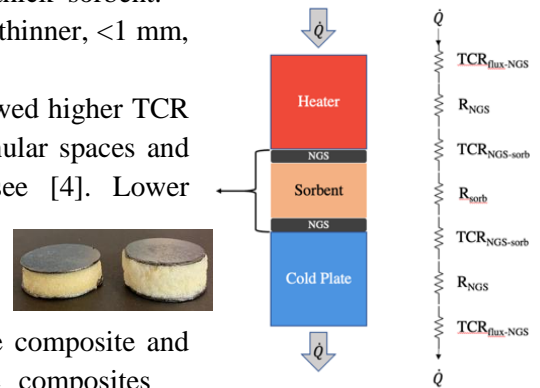
Figure 1. Resistance network to measure the thermal contact resistance between the sorbents and NGS substrate

Samples	Silica gel size range (μm)	Silica gel (wt.%)	Salt (CaCl$_2$) (wt.%)	Binder (PVP40) (wt.%)	Thermal conductivity (W/m.K)	Thermal contact resistance (K/W)
SGC-01	SG-01: 45-60	55	30	15	0.30	2.1
SGC-02	SG-02: 75-250	55	30	15	0.28	1.9
SGC-03	SG-03: 250-500	55	30	15	0.21	2.6
SGC-04	SG-04: 500-1,000	55	30	15	0.19	2.9

Table 1. Silica gels size range and the composition of samples

4. CONCLUSIONS

The thermal contact resistance of four sorbent composites with various grain sizes was measured using a custom-built thermal conductivity measuring test bed. The composites with larger grain sizes showed higher thermal contact resistance, 6.5% of the total resistance vs. 4.5% for smaller grain sizes when the sorbent thickness was 5 mm. The thermal conductivity of the samples varies from 0.19 to 0.3 W/m.K from composite with larger grain size to the smaller grain size.
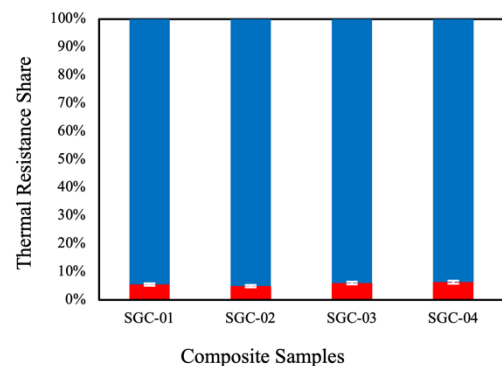
Figure 2. Thermal contact resistance shares (red) in
the total resistance of the composite samples
(sorbent thickness: 5 mm)

REFERENCES

[1] A. Sharafian, K. Fayazmanesh, C. McCague, and M. Bahrami, "Thermal conductivity and contact resistance of mesoporous silica gel adsorbents bound with polyvinylpyrrolidone in contact with a metallic substrate for adsorption cooling system applications," *International Journal of Heat and Mass Transfer*, vol. 79, pp. 64–71, Dec. 2014, doi: 10.1016/j.ijheatmasstransfer.2014.07.086.

[2] Y. Xian, P. Zhang, S. Zhai, P. Yuan, and D. Yang, "Experimental characterization methods for thermal contact resistance: A review," *Applied Thermal Engineering*, vol. 130, pp. 1530–1548, Feb. 2018, doi: 10.1016/j.applthermaleng.2017.10.163.

[3] ASTM Int., "ASTM C177-13, Standard Test Method for Steady-State Heat Flux Measurements and Thermal Transmission Properties by Means of the Guarded-Hot-Plate Apparatus." 2004.

[4] M. Rouhani and M. Bahrami, "Effective thermal conductivity of packed bed adsorbers: Part 2 ─ Theoretical model," *International Journal of Heat and Mass Transfer*, vol. 123, pp. 1212–1220, Aug. 2018, doi: 10.1016/j.ijheatmasstransfer.2018.01.143.

Analytical solutions for the coupled heat and mass transfer in flat and hollow fiber membrane-based adiabatic sorber beds

Mahyar Ashouri and Majid Bahrami[1]

Laboratory for Alternative Energy Conversion (LAEC), School of Mechatronic Systems Engineering, Simon Fraser University, Surrey, BC, Canada, and Pacific Institute for Climate Solutions

Abstract

Adiabatic membrane-based sorber beds offer higher absorption rates than conventional sorber beds for absorption heat pump/chiller application. In this study, we propose two analytical solutions for the coupled heat and mass transfer in flat and hollow fiber membrane-based adiabatic sorber beds. The similarity solution and the Laplace transform method are used to develop the present analytical models. The proposed analytical models are validated with experimental data and numerical results available in the literature with an average relative difference of 12%.

Keywords: absorber beds; sorption reactors; absorption chillers and heat pumps; analytical solution; heat and mass transfer; hollow fiber membrane; and membrane technology.

1. Introduction

Recently, membrane-based sorber beds have received immense attention, as they can improve the coefficient of performance (COP) and reduce the size of absorption chillers/heat pumps. Membrane-based sorber beds can be categorized into two types: i) isothermal membrane-based sorber beds in which the solution film is continuously cooled or heated via a heat transfer fluid [1]; and ii) adiabatic membrane-based sorber beds in which the solution film is not cooled or heated via a heat transfer fluid during absorption process [2]. Isothermal membrane-based sorber beds have shown promising performance. While the adiabatic membrane-based sorber beds have exhibited comparable performance with their isoflux counterparts, they are more compact and less costly. Therefore, we focus on adiabatic membrane-based absorber beds.

In this paper, we developed two new analytical closed-form solutions for heat and mass transfer in flat and hollow fiber membrane-based adiabatic sorber beds used in absorption chillers and heat pumps. To develop these models, two approaches are used: i) the similarity solution; and ii) the Laplace transform method. The models are validated with the numerical studies and experimental data available in the literature.

2. Problem description

Coupled heat and mass transfer in flat and hollow fiber membrane-based adiabatic sorber beds are investigated. LiBr-water is selected as the working fluid, which is the most common solution in absorption chillers/heat pumps; however, the results can be used for other refrigerants. As schematically showed in Fig. 1, in a flat membrane-based adiabatic sorber bed, the LiBr-water solution film is confined by a plate and a microporous/nanofiber membrane. However, in a hollow fiber membrane-based adiabatic sorber bed, the LiBr-water solution flows in hollow fiber membranes. The membrane is impermeable to the LiBr-water solution but allows water vapor to pass, resulting in vapor absorption or desorption at the membrane-solution interface.

---

[1] *Corresponding author's email: mbahrami@sfu.ca*
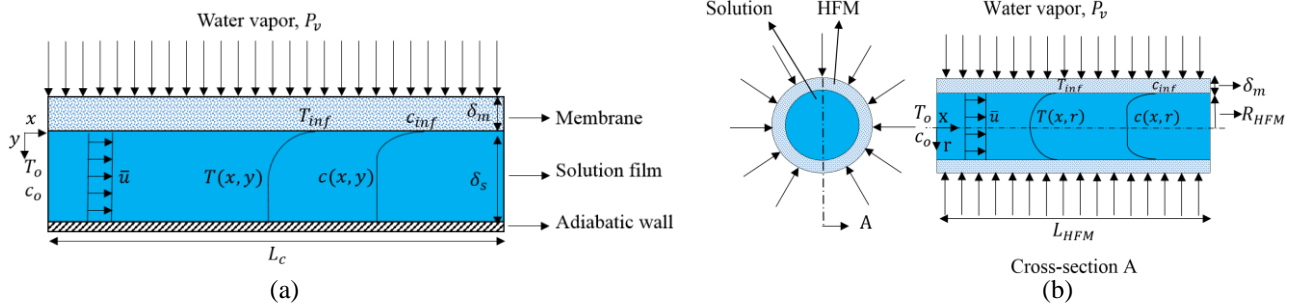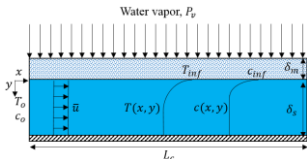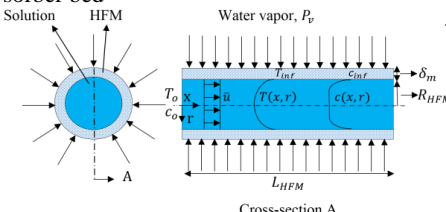
Fig. 1. A schematic diagram of: (a) a flat membrane-based adiabatic sorber bed; and b) a hollow fiber membrane-based (HFM) adiabatic sorber bed.

3. Analytical solutions

To develop the analytical models, the following assumptions are made: The solution film is laminar; the flow is hydrodynamically fully developed; linear estimation is used to find the pressure at the solution-membrane interface; the mean velocity is utilized; the thermo-physical properties of LiBr-water solution are constant; heat transfer from the film to the gaseous phase and membrane is negligible; inlet concentration and temperature distributions are uniform and constant; the absorbent is non-volatile; membrane temperature is constant; and desorption temperature should be less the boiling point of the solution (i.e. nearly 95°C for aqueous LiBr). The developed closed-form solutions are shown in Table 1.

Table 1. The proposed analytical solutions for the heat and mass transfer in flat and hollow fiber membrane-based adiabatic sorber beds.

Geometry	Parameter	
Flat membrane-based adiabatic sorber bed 	$\dot{q}(\xi) = \dfrac{k_s T_o}{\delta_s \sqrt{\pi \xi}} \bar{\theta}_{inf} \quad [\dfrac{w}{m^2}]$	(1)
	$\dot{m}(\xi) = \dfrac{\rho_s D_s c_o}{\delta_s} \sqrt{\dfrac{Le}{\pi \xi}} \, \bar{\gamma}_{inf} \quad [\dfrac{kg}{m^2 s}]$	(2)
Hollow fiber membrane-based adiabatic sorber bed 	$\dot{q}(\xi) = \dfrac{k_s T_o}{R_{HFM}} \dfrac{\partial (ILT(\Theta(s, \eta = 1)))}{\partial \eta}\Big|_{inf} \quad [\dfrac{w}{m^2}]$	(3)
	$\dot{m}(\xi) = \dfrac{\rho_s D_s c_o}{R_{HFM}} \dfrac{\partial (ILT(\Upsilon(s, \eta = 1)))}{\partial \eta}\Big|_{inf} \quad [\dfrac{kg}{m^2 s}]$	(4)

$$\bar{\gamma}_{inf} = [\dfrac{k_m (p_v - p_o)}{k_m b_5 + 2 \dfrac{b_3 \sqrt{Le}}{\sqrt{\pi \xi}} + \dfrac{k_m b_4 \Lambda}{\sqrt{Le}}}] \qquad \bar{\theta}_{inf} = \dfrac{\Lambda}{\sqrt{Le}}[\dfrac{k_m (p_v - p_o)}{k_m b_5 + 2 \dfrac{b_3 \sqrt{Le}}{\sqrt{\pi \xi}} + \dfrac{k_m b_4 \Lambda}{\sqrt{Le}}}] \qquad (5)$$

$$\Theta(s, \eta) = \left[\dfrac{\Lambda}{\sqrt{Le}} \dfrac{I_1(\sqrt{Le.s})}{I_1(\sqrt{s})}\right]\left[\dfrac{\dfrac{k_m(p_v - p_o)}{s}}{b_3 \sqrt{Le.s} I_1(\sqrt{Le.s}) + k_m b_4 \dfrac{\Lambda}{\sqrt{Le}} \dfrac{I_1(\sqrt{Le.s})}{I_1(\sqrt{s})} I_o(\sqrt{s}) + k_m b_5 I_o(\sqrt{Le.s})}\right] I_o(\sqrt{s}\eta) \qquad (6)$$

2

$$\Upsilon(s,\eta) = \left[\frac{\frac{k_m(p_v - p_o)}{s}}{b_3\sqrt{Le.s}\,I_1\left(\sqrt{Le.s}\right) + k_m b_4 \frac{\Lambda}{\sqrt{Le}} \frac{I_1\left(\sqrt{Le.s}\right)}{I_1\left(\sqrt{s}\right)} I_o\left(\sqrt{s}\right) + k_m b_5 I_o\left(\sqrt{Le.s}\right)} \right] I_o\left(\sqrt{Le.s}\,\eta\right) \qquad (7)$$

Inverse Laplace Transform (ILT) using the Stehfest method [3,4]

$$\theta(\xi,\eta) = \frac{ln2}{\xi}\sum_{i=1}^{N} V_i\Theta(\frac{ln2}{\xi}i,\eta) \quad \& \quad \gamma(\xi,\eta) = \frac{ln2}{\xi}\sum_{i=1}^{N} V_i\Upsilon(\frac{ln2}{\xi}i,\eta) \quad \& \quad V_i = (-1)^{\frac{N}{2}+j}\sum_{k=[\frac{j+1}{2}]}^{min\,(j,\frac{N}{2})} \frac{k^{\frac{N}{2}}(2k)!}{(\frac{N}{2}-k)!\,k!\,(k-1)!\,(j-k)!\,(2k-j)!} \qquad (8)$$

Non-dimensional parameters

$$\theta(\xi,\eta) = \frac{T(\xi,\eta) - T_o}{T_o}, \gamma(\xi,\eta) = \frac{c(\xi,\eta) - c_o}{c_o}, \xi = \frac{x}{\delta_s^2}\frac{\alpha_s}{\bar{u}}\,or\,\frac{x}{R_{HFM}^2}\frac{\alpha_s}{\bar{u}}, \eta = \frac{y}{\delta_s}\,or\,\frac{r}{R_{HFM}}, \Lambda = \frac{h_{abs}c_o}{c_s T_o}, Le = \frac{\alpha_s}{D_s}$$

4. Model Validation

Figure 2 shows a comparison between the present models against the numerical results of Venegas et al. [5] and the experimental data of García-Hernando et al. [6] and Hong et al. [7]. The minimum, average, and maximum relative differences between the proposed model and data from Refs. [5–7] are presented in Table 2. The proposed models follow the trend and show a good agreement with the data.

(a)

(b)
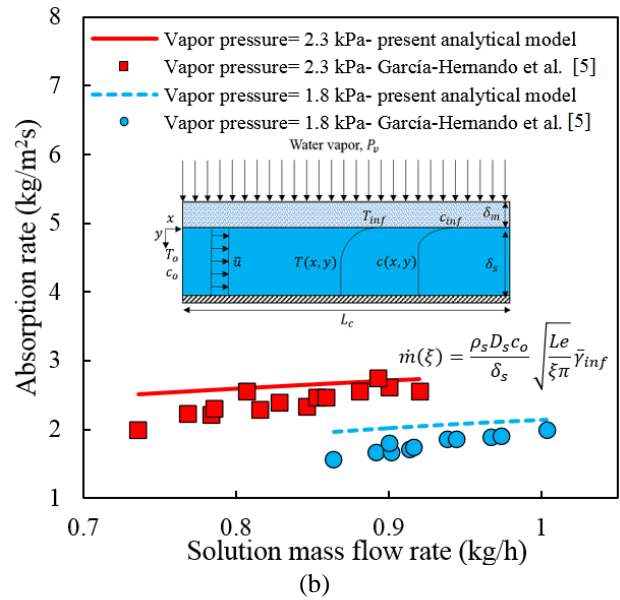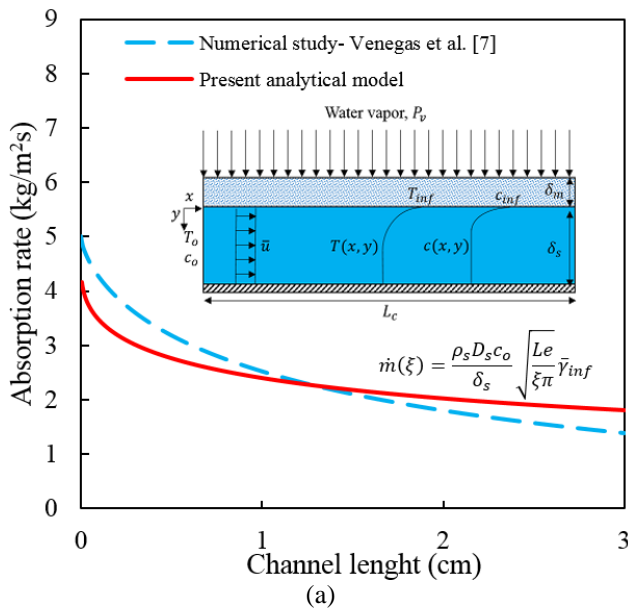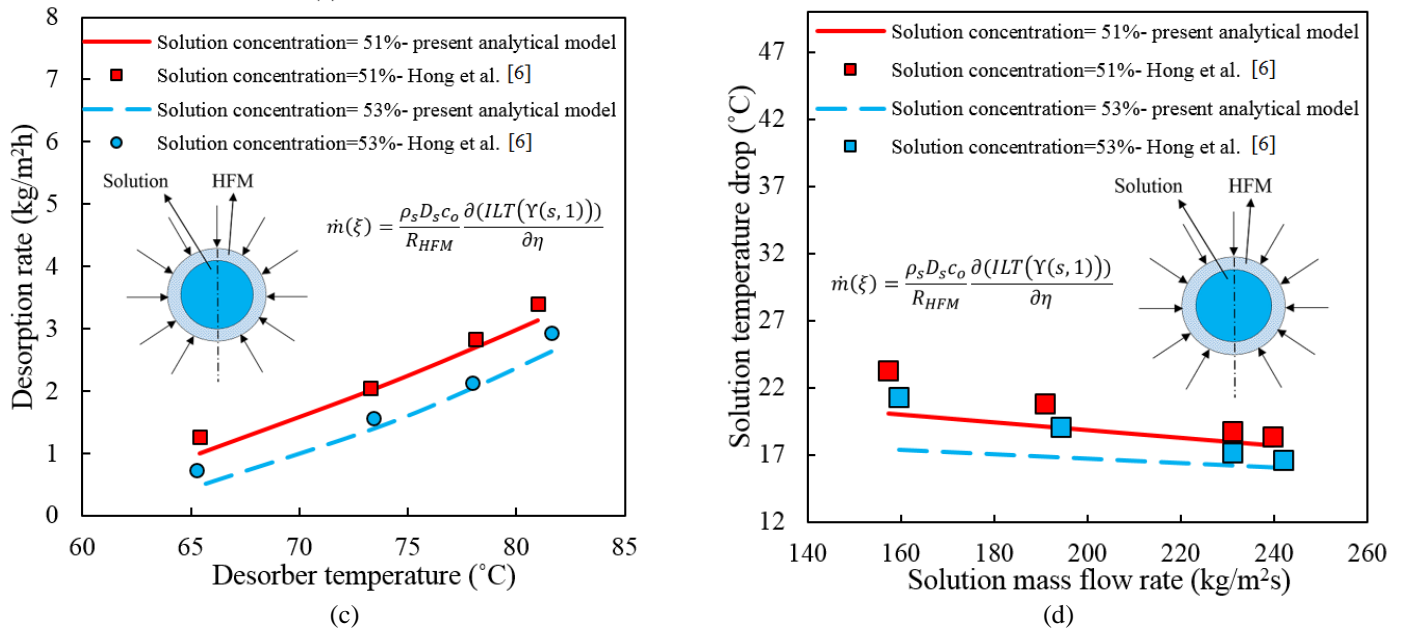
Fig. 2. The comparison between the results from the similarity solution method used for the flat membrane-based adiabatic absorber against: (a) the numerical result of Venegas et al. [5]; and (b) the experimental data of García-Hernando et al. [6]. Also, the comparison between the present Laplace transform model for the hollow fiber membrane-based (HFM) adiabatic desorber against: (c); and (d) the experimental data of Hong et al. [7].

Table 2. The minimum, average, and maximum relative difference between the present models compared to Refs. [5–7].

Study		Min. relative difference (%)	Averaged relative difference (%)	Max. relative difference (%)
Venegas et al. [5]	Fig. 3 (a)	0	12.7	28.7
García-Hernando et al. [6]	Fig. 3 (b)	1.7	15.3	26.5
Hong et al. [7]	Fig. 3 (c)	2.2	12	29.1
	Fig. 3 (d)	5.3	7.9	12.4

Conclusion

This study proposed two analytical solutions for the coupled heat and mass transfer in flat and hollow fiber membrane-based adiabatic sorber beds for absorption heat pump/chiller application. The similarity solution and Laplace transform method were used to develop the analytical models. The presented analytical models were validated with experimental data and numerical results available in the literature with an average relative difference of 12%.

4

References

[1] M. Ashouri, M. Bahrami, Analytical solution for coupled heat and mass transfer in membrane-based absorbers, Int. J. Heat Mass Transf. 192 (2022) 122892.

[2] N. García-Hernando, M. De Vega, M. Venegas, Experimental characterisation of a novel adiabatic membrane-based micro-absorber using H2O-LiBr, Int. J. Heat Mass Transf. 129 (2019) 1136–1143.

[3] H. Stehfest, Algorithm 368: Numerical inversion of Laplace transforms [D5], Commun. ACM. 13 (1970) 47–49.

[4] M. Ashouri, M. Bahrami, Heat and mass transfer in laminar falling film absorption: A compact analytical model, Int. J. Heat Mass Transf. 188 (2022) 122598.

[5] M. Venegas, M. de Vega, N. García-Hernando, U. Ruiz-Rivas, Adiabatic vs non-adiabatic membrane-based rectangular micro-absorbers for H2O-LiBr absorption chillers, Energy. 134 (2017) 757–766. https://doi.org/10.1016/J.ENERGY.2017.06.068.

[6] N. García-Hernando, M. Venegas, M. De Vega, Experimental performance comparison of three flat sheet membranes operating in an adiabatic microchannel absorber, Appl. Therm. Eng. 152 (2019) 835–843.

[7] S.J. Hong, E. Hihara, C. Dang, Analysis of adiabatic heat and mass transfer of microporous hydrophobic hollow fiber membrane-based generator in vapor absorption refrigeration system, J. Memb. Sci. 564 (2018) 415–427.

A machine learning based model for membrane-based absorbers in absorption heat pumps

Mahyar Ashouri, Naghme Kheyrikoochaksarayee, Callum Chhokar, Amir Shabani, and Majid Bahrami[1]

Laboratory for Alternative Energy Conversion (LAEC), School of Mechatronic Systems Engineering, Simon Fraser University, Surrey, BC, Canada, and Pacific Institute for Climate Solutions

Abstract

A new multi-label machine learning-based model is proposed for membrane-based absorbers used in absorption heat pumps and chillers. The model offers the accuracy of a numerical model with the computational efficiency of an analytical model. A comprehensive dataset, comprising of 100,000 data points, is generated using 2D numerical modeling. The dataset consists of 15 input parameters, including operating conditions and geometrical parameters, and four output variables including absorption rate, outlet concentration, solution outlet temperature, and heat transfer fluid outlet temperature. Support Vector Regressor, Random Forest Regressor, and Decision Tree Regressor algorithms are used to develop the present model. The results of the proposed model are validated with the experimental data available in the literature, capturing the trend of the data with a relative difference of 15%. It is shown that the present machine learning-based model can predict the four outputs with an accuracy of over 90%.

Keywords: machine learning; absorption chillers and heat pumps; membrane-based absorber; heat and mass transfer; and membrane technology.

1. Introduction

Several studies have been conducted to analyze a membrane-based absorber's performance using computational fluid dynamics (CFD) and other numerical methods [1–4]. These methods can produce detailed results; however, implementing such models incurs a high computational cost. Analytical models [5,6] offer efficient computation, but they may have limiting assumptions such as isothermal boundary condition at the heat exchanger wall. As such, they cannot consider the temperature lift and heat exchanger wall thickness.

There are only a few studies on membrane-based absorbers that use machine learning, and they are generally for minimizing flow maldistribution in membrane-based absorbers [7], geometry optimization [8], or investigating the available ionic liquid absorbents for absorption heat pumps [9]. In this study, we propose a new multi-label machine learning-based model for membrane-based absorbers used in absorption chillers and heat pumps for the first time. A multi-label machine learning model enables predicting more than one independent variable. A comprehensive dataset, comprising of 100,000 data points, is generated using our 2D numerical model, which was run on Compute Canada's supercomputers, namely, Narval, Cedar, Graham, and Beluga [10].

2. Problem description

Coupled heat and mass transfer in membrane-based absorbers is numerically studied for two configurations: i) the single-sided configuration, where the absorption heat is transferred to the heat transfer fluid only from one side, shown in Fig. 1(a); and ii) the double-sided configuration,

---

1

in which the absorption heat is transferred to the heat transfer fluid from both sides, shown in Fig. 1(b). Lithium bromide-water is used as the solution, which is the most common absorbent in absorption chillers/heat pumps. The liquid solution is constrained by a microporous/nanofibrous membrane and a plate heat exchanger. The membrane is impermeable to the LiBr-water solution, while water vapor can traverse the membrane leading to water vapor absorption at the membrane-solution interface.
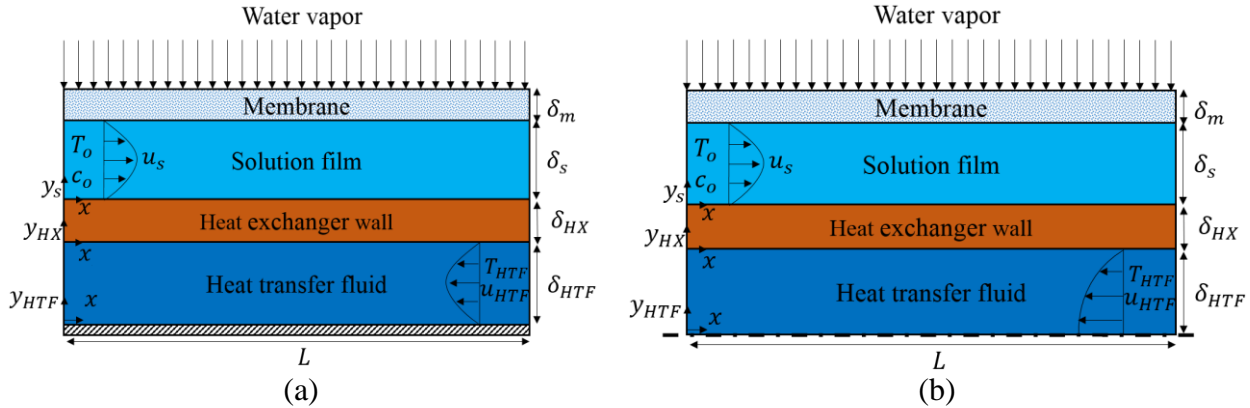
Fig. 1. A schematic diagram of a membrane-based absorber over a heat exchanger. (a) the single-sided configuration; and (b) the double-sided configuration (symmetry boundary condition is applied).

3. Model development

The following governing equations for energy and species conservation can be derived for the advective transport in the flow direction x and diffusivity transport in the y_s direction for the solution domain:

$$u_s \frac{\partial T_s}{\partial x} = \alpha_s \frac{\partial^2 T_s}{\partial y_s^2} \tag{1}$$

$$u_s \frac{\partial c_s}{\partial x} = D_s \frac{\partial^2 c_s}{\partial y_s^2} \tag{2}$$

where, T, α_s, c_s and D_s are the solution's temperature, thermal diffusivity, concentration, and mass diffusivity, respectively. Energy equations for the heat transfer fluid and heat exchanger wall can be written as follows:

$$u_{HTF} \frac{\partial T_{HTF}}{\partial x} = \alpha_{HTF} \frac{\partial^2 T_{HTF}}{\partial y_{HTF}^2} \tag{3}$$

$$\frac{\partial^2 T_{HX}}{\partial y_{HX}^2} + \frac{\partial^2 T_{HX}}{\partial x^2} = 0 \tag{4}$$

where, T_{HTF}, α_{HTF}, and T_{HX} are the heat transfer fluid's temperature, thermal diffusivity, and heat exchangers' temperature, respectively. The Dusty-Gas model [11] is used to model the mass transfer through the membrane:

$$J = k_m(p_v - p_{inf}) \quad [\frac{kg}{m^2.s}] \tag{5}$$

where, k_m, p_v, and p_{inf} are the membrane mass transfer coefficient, vapor pressure, and water vapor partial pressure at the membrane-solution interface, respectively. The governing equations should be solved simultaneously and iteratively. A finite difference method was used to solve the governing equations. The first and second derivatives of the parameters were discretized using a central difference method. Virtual nodes were considered to couple the boundary conditions to

2

the domain to maintain second-order accuracy. All the equations were solved iteratively until a residual of 10^{-8} was reached for each parameter. Thermophysical properties for the solution and the heat transfer fluid were calculated at each iteration, more details can be found in Ref [12]. Computations were performed on Compute Canada's supercomputers, namely, Narval, Cedar, Graham, and Beluga [10].

4. Machine learning process

4.1. Data description

This study generated a dataset, comprising of 100,000 data, using our 2D numerical model for a membrane-based absorber. The dataset includes 15 features, which are the input parameters in a machine learning model, including operating conditions and geometrical parameters listed in Table 1. There are 4 labels, which are the selected output parameters of the model, including absorption rate, outlet concentration, solution outlet temperature, and heat transfer fluid outlet temperature. The range for the selected features has been picked to cover all practical operating conditions and geometrical parameters of an actual absorption setup available in the literature [13–15] to ensure usability of the present machine learning-based model.

Table 1- The features' ranges used for the current machine learning-based model.

Feature name	Feature type	Feature range	Available experimental range in the literature [13–15]
Absorber length L [cm]	Numeric	$1 - 10$	$3 - 5$
Solution thickness δ_s [μm]	Numeric	$50 - 500$	$100 - 200$
Average solution velocity $\bar{u}_s$ [$\frac{mm}{s}$]	Numeric	$0.1 - 20$	$5 - 15$
Solution inlet temperature T_o [^oC]	Numeric	$25 - 55$	$25 - 35$
Water inlet concentration c_o [$\frac{kg\ water}{kg\ solution}$]*	Numeric	$0.38 - 0.55$	$0.4 - 0.45$
Heat transfer fluid inlet temperature T_{HTF} [^oC]	Numeric	$25 - 55$	$25 - 30$
Vapor pressure p_v [kPa]	Numeric	$0.840 - 2.34$	$0.840 - 1.9$
Membrane porosity φ	Numeric	$0.1 - 1$	$0.4 - 0.9$
Membrane pore diameter D_m [μm]	Numeric	$0.2 - 3$	$0.45 - 1$
Membrane thickness δ_m [μm]	Numeric	$10 - 250$	$50 - 150$
Heat exchanger wall thickness δ_{HX} [mm]	Numeric	$0.5 - 5$	N/A
Heat transfer fluid thickness δ_{HTF} [mm]	Numeric	$0.25 - 5$	$0.25 - 5$
Heat exchanger thermal conductivity k_{HX} [$\frac{W}{m.K}$]	Numeric	13-17 Stainless steel / 170-230 Aluminum	Both
Average heat transfer fluid velocity $\bar{u}_{HTF}$ [$\frac{mm}{s}$]	Numeric	$0.1 - 20$ Parallel flow / $-0.1\ to -20$ Counter flow	N/A
Configuration	Binary	0 single-sided configuration / 1 double-sided configuration	Single-sided configuration

* Water concentration $c_o = 1 - X$ where X is the solution concentration.

4.2. Machine learning-based model development

The Support Vector Regressor (SVR) [16], Random Forest Regressor (RFR) [17], and Decision Tree Regressor (DTR) [18] are implemented and combined to improve the model's accuracy. 90% of the dataset is used for training, and 10% is used for testing. Figure 2 shows the predicted label versus the actual label based on the numerical modeling. The following can be observed: i) the absorption rate can be predicted with an accuracy of 90%; ii) the outlet

3

concentration can be predicted with an accuracy of 98%; and iii) the solution outlet temperature and heat transfer fluid outlet temperature can be predicted with an accuracy of ± 99.5%.

(a)

(b)

(c)

(d)
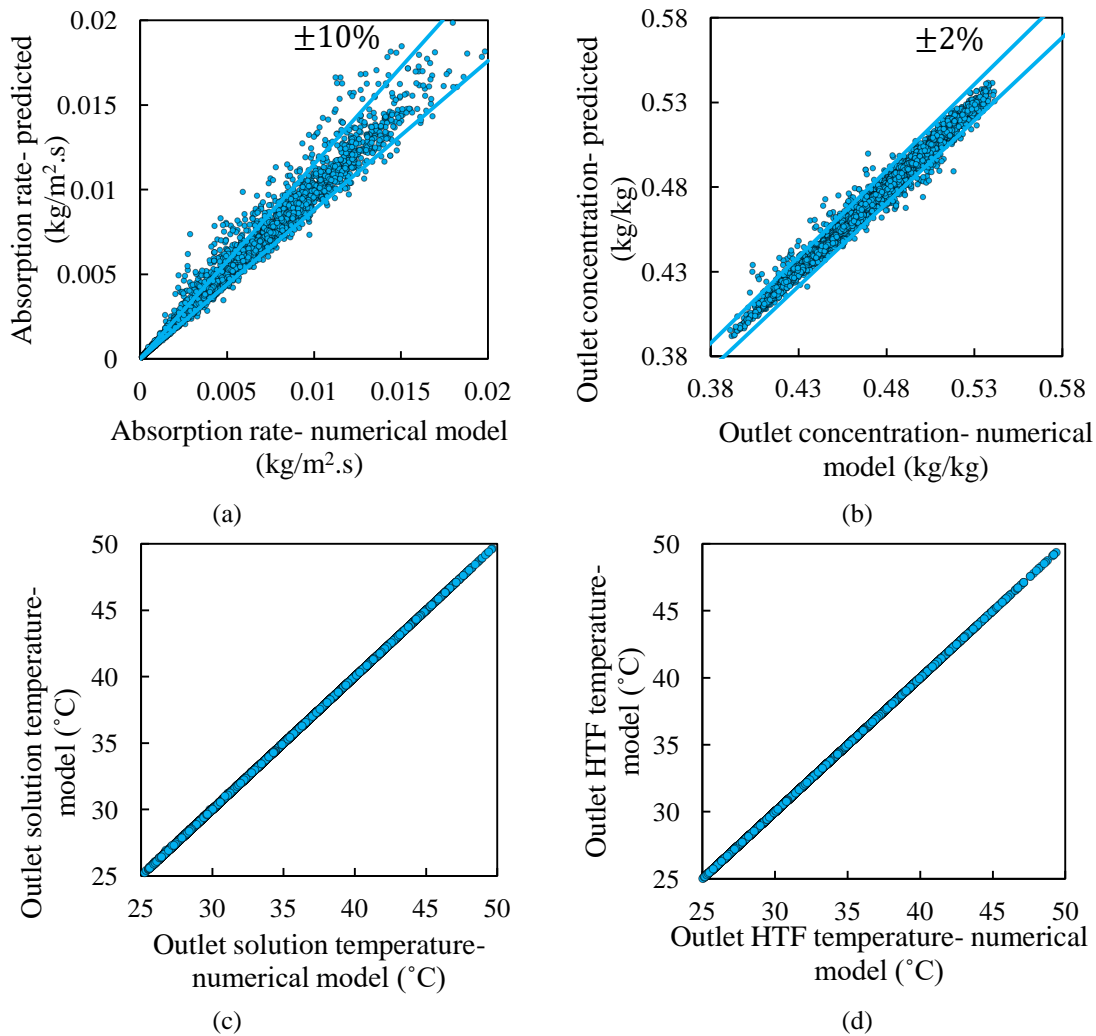
Fig. 2. The predicted label versus the actual label based on numerical modeling for the present labels.

4.3. Validation with experimental data

The machine learning model is validated with experimental data from Isfahani et al. [13,14]. As shown in Fig. 3, the present model can predict the experimental data, capturing data within a relative difference of 15%.

Conclusion

In this study, we proposed a multi-label machine learning-based model for membrane-based absorbers used in absorption heat pumps and chillers for the first time. The generated dataset, comprising of 100,000 data, consists of 15 input parameters, including operating conditions and geometrical parameters, and four output variables, i.e., the
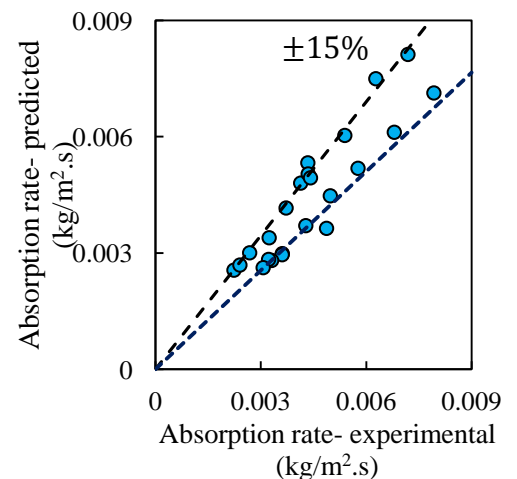
Fig. 3. Validation of the present machine learning based model with experimental data from Refs. [13,14].

4

absorption rate, outlet concentration, solution outlet temperature, and heat transfer fluid outlet temperature. The results of the machine learning-based model were validated with experimental data.

Supplementary data

The present machine learning model and dataset are shared on GitHub, enabling prospective readers to perform real-time absorber control, optimization, and design in an accurate, time-efficient manner.

Acknowledgments

References

[1]   F. Abdollahi, S.A. Hashemifard, A. Khosravi, T. Matsuura, Heat and mass transfer modeling of an energy efficient Hybrid Membrane-Based Air Conditioning System for humid climates, J. Memb. Sci. 625 (2021) 119179.

[2]   M. Venegas, M. De Vega, N. García-Hernando, Parametric study of operating and design variables on the performance of a membrane-based absorber, Appl. Therm. Eng. 98 (2016) 409–419.

[3]   F. Asfand, Y. Stiriba, M. Bourouis, CFD simulation to investigate heat and mass transfer processes in a membrane-based absorber for water-LiBr absorption cooling systems, Energy. 91 (2015) 517–530. https://doi.org/10.1016/J.ENERGY.2015.08.018.

[4]   F. Asfand, Y. Stiriba, M. Bourouis, Performance evaluation of membrane-based absorbers employing H2O/(LiBr+ LiI+ LiNO3+ LiCl) and H2O/(LiNO3+ KNO3+ NaNO3) as working pairs in absorption cooling systems, Energy. 115 (2016) 781–790.

[5]   M. Ashouri, M. Bahrami, Analytical solution for coupled heat and mass transfer in membrane-based absorbers, Int. J. Heat Mass Transf. 192 (2022) 122892.

[6]   M. Ashouri, M. Bahrami, Heat and mass transfer in laminar falling film absorption: A compact analytical model, Int. J. Heat Mass Transf. 188 (2022) 122598. https://doi.org/10.1016/J.IJHEATMASSTRANSFER.2022.122598.

[7]   Z. Sui, W. Wu, AI-assisted maldistribution minimization of membrane-based heat/mass exchangers for compact absorption cooling, Energy. (2022) 125922.

[8]   Z. Sui, Y. Sui, W. Wu, Multi-objective optimization of a microchannel membrane-based absorber with inclined grooves based on CFD and machine learning, Energy. 240 (2022) 122809.

[9]   Y. Sui, C. Zhai, W. Wu, M.K.H. Leung, Multi-scale Computer-aided molecular design of Ionic liquid for absorption heat transformer based on Machine learning, Energy Convers. Manag. 261 (2022) 115617.

5

[10] Home Page | Digital Research Alliance of Canada, (n.d.). https://alliancecan.ca/en (accessed December 20, 2022).

[11] E.A. Mason, M. EA, M. AP, Gas transportin porous media: The dusty-gas model, (1983).

[12] G.A. Florides, S.A. Kalogirou, S.A. Tassou, L.C. Wrobel, Design and construction of a LiBr–water absorption machine, Energy Convers. Manag. 44 (2003) 2483–2508.

[13] R.N. Isfahani, K. Sampath, S. Moghaddam, Nanofibrous membrane-based absorption refrigeration system, Int. J. Refrig. 36 (2013) 2297–2307.

[14] R.N. Isfahani, S. Moghaddam, Absorption characteristics of lithium bromide (LiBr) solution constrained by superhydrophobic nanofibrous structures, Int. J. Heat Mass Transf. 63 (2013) 82–90.

[15] M. De Vega, N. García-Hernando, M. Venegas, Experimental performance of membrane water absorption in LiBr solution with and without cooling, Appl. Therm. Eng. 180 (2020) 115786.

[16] M. Awad, R. Khanna, Support vector regression, in: Effic. Learn. Mach., Springer, 2015: pp. 67–80.

[17] M.R. Segal, Machine learning benchmarks and random forest regression, (2004).

[18] M. Xu, P. Watanachaturaporn, P.K. Varshney, M.K. Arora, Decision tree regression for soft classification of remote sensing data, Remote Sens. Environ. 97 (2005) 322–336.

3rd to 6th of September 2023
The University of Edinburgh, Scotland

Heat Powered Cycles
Conference 2023
Edinburgh

Heat in the new energy system

Development of SrBr$_2$/MOF composites with enhanced water adsorption dynamics for low temperature thermochemical heat storage

Luxi Yang[1], Wenjing Wei[1], Giulio Santori[1] and Xianfeng Fan[1*]

[1] School of Engineering, Institute for Materials and Processes, University of Edinburgh, Robert Stevenson Road, Edinburgh, EH9 3FB Scotland, UK.

[*]Corresponding author: X.Fan@ed.ac.uk

Abstract

Salt hydrates using as thermochemical heat storage materials are attracting increasing interests because of the high storage energy density and low cost. In this research, novel materials SrBr$_2$/MIL-101(Cr) as "composite salt inside porous matrix" (CSPM) has been prepared by the post synthesis methods in solution with excellent pore volume and specific surface area properties. By cycling desorption and adsorption of water vapour, the obtained composites can store and release heat under low temperature. The pore structure within MIL-101(Cr) enables high salt loading inside the pores. The interactions between the salt and matrix enhance the sorption capacities significantly to 0.54 g/g. The composites show good cycling stability under cycling test and achieve good thermal energy storage capacities (1526 J/g). This work presents novel strategy to develop TCES materials with high energy storage capacities as well as excellent water sorption dynamics, providing the inspiration for the design of the sorption heat storage materials.

Keywords: Thermochemical energy storage, Composite salt inside porous matrix (CSPM), Strontium bromide, Metal-organic framework (MOF).

Introduction/Background

Effective energy storage technologies, aiming at the Net Zero emissions target, is required for heat accumulation systems to utilize curtailed renewable energy. These systems will balance the energy demand and supply, and thus guarantee the stable and continuous use of energy, as well as enhance the utilization efficiency of solar energy [1, 2].

Thermal energy storage has an increasingly effect on the development of renewable and sustainable energy [3]. Among various storage methods, thermochemical heat storage (THS) systems based on water sorption, have demonstrated relatively high energy density and environmentally friendly features [4, 5]. Salt hydrate is one of common material for water-sorption based THS. It holds great promises because of their ease reaction and availability. By cycling desorption and adsorption of water vapour, salt hydrates can store and release heat with chemisorption reaction under low temperature. Although some investigations of salt hydrates have been made in THS, there are still some challenges, such as low adsorption capacity and deliquescence, hinder effectiveness of applications [6].

Recently, there is a strategy, namely 'composite salt inside porous matrix' (CSPM), improved the adsorption performance of THS systems by impregnating salt in porous materials [7]. The salt hydrates inside act as active ingredients with energy density, whereas the host matrix could ameliorate the heat and mass transfer of TCMs. The materials commonly used are silica gels, activated alumina, zeolites, expanded vermiculites [8-10]. Currently, ordered porous hybrid materials like Metal Organic Framework (MOFs) have attracted attentions as matrix MOFs are of great potential for thermochemical heat storage systems because of their large diversity in porosity and surface chemistry properties[11, 12]. Large pore volume would

allow higher salt loading rate and the high specific surface would facilitate the processes of heat transfer. MIL-101(Cr) is a very promising candidate with high water uptakes (> 1.0 g/g), accompanied by an extraordinary water stability and the desired S-shape adsorption isotherm [13-15]. However, it shows low vapour adsorption capacity at low relative pressure and slow water adsorption process because of micropore structures.

Herein, we developed a CSPM combining $SrBr_2$ with MIL-101(Cr) to improve the water sorption properties, so to enhance the whole heat storage performance. Salt solution with different ratios (from 10% to 40%) were used to prepare the composites. The ratio would affect the salt content in CSPM, morphology, pore features, water sorption and heat storage performance. The contribution and interaction of each component to the water uptake capacity and sorption dynamics will be investigated, and the optimal ratios of the salt and matrix were chosen. The proposed composites $SrBr_2$ in the MIL-101(Cr) provide a feasible way to realise the thermochemical energy storage with high water sorption capacity and fast dynamics in low temperature, which can also inspire the new researches about CSPM.

Discussion and Results

Nitrogen (N_2) adsorption isotherms of pure MIL-101(Cr) and composites are used to study the specific surface area and pore volume, important properties to evaluate porous materials. The result of MIL-101(Cr) shows a relatively high specific surface area (3222.147 m^2/g) and high pore volume (1.657 cm^3/g), enabling the more sorption sites inside the matrix and more space to combine with salt. From 10% to 40%, the pore volume decreases gradually for SrBr2/MIL-101(Cr): from 1.252 cm^3/g to 0.365 cm^3/g, confirming the higher loading salt inside the pores (Figure 1a).

Additionally, hydration dynamics is also a key parameter to evaluate the water-sorption based heat storage performance. The water uptake amount is recorded as a function of time and the water sorption dynamics is assessed at 30 °C 50% RH (Figure 1b). In order to figure out the promising candidate composite which can achieve high water sorption and fast dynamics, the water sorption processes within 120 minutes are discussed here. Composite with different ratio reaches a relatively stable state within short time. The sample 20% shows higher water uptake amount (0.54 g/g) than other samples. The decrease of water sorption for higher salt contents can be ascribed to the extra salt deposited on the outer surface of MIL-101(Cr) in the high content samples, blocking the pore area and inhibiting the water sorption processes.
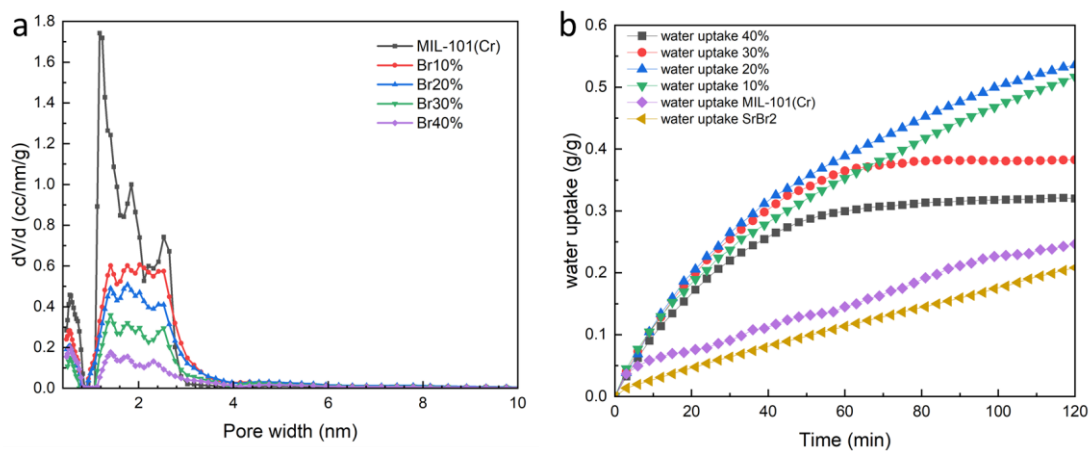
Figure 1 a: Pore distribution of matrix and different composites; b: water sorption dynamics of $SrBr_2$/MIL-101(Cr) at 50% RH.

The water uptake isotherms of the pure MIL-101(Cr) with composites were compared to thoroughly study the water sorption/desorption performance at different water pressures. As shown in Figure 2a, the water sorption isotherm of MIL-101(Cr) exhibits an S-shape curve (type V). As for the water sorption time, it takes relatively long time to reach equilibrium at both adsorption and desorption processes for MIL-101(Cr) at different water pressure, especially at high water pressure region. The isotherm shows that the pure MIL-101(Cr) has a high water uptake capacity at high water pressure above 40% (p/p_0) as well as slow water sorption processes, which can be ascribed to its high surface area and micropore structures. Compared with pure MIL-101(Cr), $SrBr_2$/MIL-101(Cr) shows different water sorption isotherms (Figure 2b), which is a classic type II isotherm. The initial increase of the water uptake and the followed-up increase come from the monolayer and multilayer interactions respectively. This isotherm confirms the performance of the different types of water sorption together. The final water uptake can be the collective effects of three parts: the left micropores inside MIL-101(Cr) without salts which can adsorb water molecules physically, the interface interactions of the surface layer between MIL-101(Cr) and the salt $SrBr_2$, and the monolayer pure salt parts which can react with molecules. The introduction of the salt content $SrBr_2$ enhance the water sorption dynamics, promoting the water uptake performance of the whole composites.
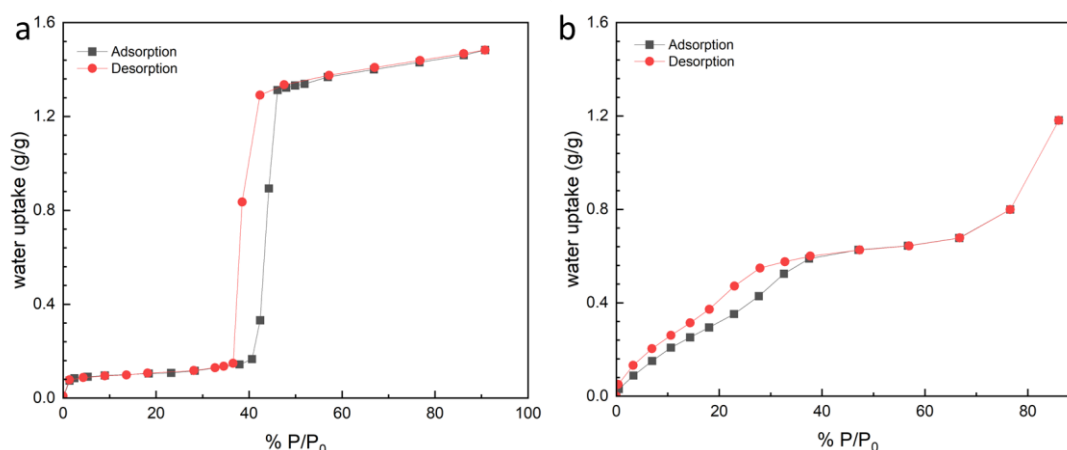
Figure 2 Water vapour sorption/desorption isotherms at 30 °C (a: MIL-101(Cr); b: 20% $SrBr_2$/MIL-101(Cr)).

Summary/Conclusions

In summary, we synthesized a thermochemical energy storage material $SrBr_2$/MIL-101(Cr) with high salt loadings inside the matrix, which attributes to the optimised post synthesis methods in solution and outstanding pore structures of MIL-101(Cr). The composite has a high water uptake capacity (0.54 g/g) compared with pure $SrBr_2$. However, the overloading salts would stack on the surface and block the pores, leading to lower water sorption when the salts contents become too high. The dynamics tests reveal that the water sorption capacities are composed of three parts: the chemical reactions of the salts, the physical sorption of MIL-101(Cr) and the interface interactions between the salts and matrix. The composite also exhibits good energy storage capacities (1526 J/g), enabling good potential for thermochemical heat storage applications.

Acknowledgments

References:

[1] S. Bennici, T. Polimann, M. Ondarts, E. Gonze, C. Vaulot, N. Le Pierrès, "Long-term impact of air pollutants on thermochemical heat storage materials", Renewable and Sustainable Energy Reviews, 2020.

[2] D. Chaatouf, M. Salhi, B. Raillani, S. Amraqui, A. Mezrhab, H. Naji, "Parametric analysis of a sensible heat storage unit in an indirect solar dryer using computational fluid dynamics", Journal of Energy Storage, 2022.

[3] B. Koçak, A.I. Fernandez, H. Paksoy, "Review on sensible thermal energy storage for industrial solar applications and sustainability aspects", Solar Energy, 2020.

[4] E. Bagherisereshki, J. Tran, F. Lei, N. AuYeung, "Investigation into $SrO/SrCO_3$ for high temperature thermochemical energy storage", Solar Energy, 2018.

[5] L. Scapino, H.A. Zondag, J. Van Bael, J. Diriken, C.C. Rindt, "Sorption heat storage for long-term low-temperature applications: a review on the advancements at material and prototype scale", Applied Energy, 2017.

[6] A. Shkatulov, R. Joosten, H. Fischer, H. Huinink, "Core-shell encapsulation of salt hydrates into mesoporous silica shells for thermochemical energy storage", ACS Applied Energy Materials, 2020

[7] B. Ding, C. Xu, Z. Liao, F. Ye, "Study on long-term thermochemical thermal storage performance based on SrBr2-expanded vermiculite composite materials", Journal of Energy Storage, 2021.

[8] R. -J. Clark, M. Farid, "Experimental investigation into the performance of novel SrCl2-based composite material for thermochemical energy storage", Journal of Energy Storage, 2021.

[9] S.Z. Xu, R.Z. Wang, L.W. Wang, J. Zhu, "Performance characterizations and thermodynamic analysis of magnesium sulfate-impregnated zeolite 13X and activated alumina composite sorbents for thermal energy storage", Energy, 2019.

[10] A. Permyakova, S. Wang, E. Courbon, F. Nouar, N. Heymans, P. D'Ans, N. Barrier, P. Billemont, G. D. Weireld, N. Steunou, M. Frère, C. Serre, "Design of salt-metal organic framework composites for seasonal heat storage applications", Journal of Materials Chemistry A, 2017.

[11] B. Tan, Y. Luo, X. Liang, S. Wang, X. Gao, Z. Zhang, Y. Fang, "Composite salt in MIL-101(Cr) with high water uptake and fast adsorption kinetics for adsorption heat pumps", Microporous Mesoporous Materials, 2019.

[12] S. Zhang, Y. Lin, Q. Li, X. Jiang, Z. Huang, X. Wu, H. Zhao, G. Jing, H. Shen, "Remarkable performance of N-doped carbonization modified MIL-101 for low-concentration benzene adsorption", Separation and Purification Technology, 2022.

[13] W. Shi, Y. Zhu, C. Shen, J. Shi, G. Xu, X. Xiao, R. Cao, "Water sorption properties of functionalized MIL-101(Cr)-X (X=-NH_2, –SO_3H, H, –CH_3, –F) based composites as thermochemical heat storage materials", Microporous Mesoporous Materials, 2019.

[14] C. Wang, L. Hua, H. Yan, B. Li, Y. Tu, R. Wang, "A Thermal Management Strategy for Electronic Devices Based on Moisture Sorption-Desorption Processes", Joule 2020.

[15] X. Chen, H. Gao, Z. Tang, G. Wang, "Metal-organic framework-based phase change materials for thermal energy storage", Cell Reports Physical Science, 2020.

A framework for physics based off-design and dynamic modelling and simulation of combined cycle power plants in weight and volume constraint environments

R. M. Montañés[*], M. K. Windfeldt, L. E. Andersson, G. Skaugen

SINTEF Energy Research, Sem Sælands vei 11, 7034 Trondheim, Norway

[*]Corresponding author: ruben.mocholi.montanes@sintef.no

Abstract

In order to decarbonize energy systems, there is an increasing penetration of non-dispatchable renewable energy sources. In the context of island energy systems, such as offshore oil and gas platforms or ships, there is a need for combined cycle power plants with low emissions, that provide flexible power demands at multiple time scales and that are reliable. This can help in providing variation management to the energy system. Unconventional thermal power generation systems are required for implementation in weight and volume constrained environments. This includes compact combined cycles. There is a need for frameworks capable of addressing several aspects of process design and operation. In this work, we present a framework for unconventional thermal power plants design, and for off-design and transient modelling. We illustrate an application of the framework where an existing offshore combined cycle power plant is modelled. An OTSG steady-state process model is validated with three steady-state performance data points from the real system, and a dynamic system model of the combined cycle is developed with real reference plant data, and inputs from the design part of the framework.

Keywords: Combined cycle, dynamic simulations, once-through steam generator, off-design and transients.

Introduction/Background

The increased penetration of non-dispatchable renewable energy sources, together with an increased need for reliability in energy systems, requires thermal power plants to provide variation management services. This often translates into thermal power plants being operated in flexible mode, or being designed to provide flexible heat and/or power outputs to accommodate varying demands [1]. In fossil fuelled thermal power plants, there is also a need for higher energy efficiency and reduced fuel consumption. Traditionally, this has led to highly efficient thermal power plants designs, with focus on cost-minimization in operation. However, providing variation management might also imply challenges for steam-based thermal power plant operation. New design requirements include high product flexibility (large span of operational loads), fast transitions from one operating load to another, and quick and reliable hot start-up capabilities. From that perspective, for design and operation of thermal power plants, there is an increasing need to address both off-design (energy efficiency and emissions) and dynamic conditions (controllability, transients, and discrete events such as start- up and shut-down), while reducing greenhouse gas emissions [2]. In some energy systems, such as a power unit for an offshore oil and gas platform, there are limited weight budgets for equipment and process systems implementation [3]. This is especially important in brownfield applications. The result is a need for power plants that are compact in terms of both volume and footprint, as well as weight. This also applies to FPSOs (Floating, Storage and Offloading) platforms. An FPSO is an alternative to offshore platforms that can lead to advantages. This

![Heat Powered Cycles Conference 2023 logo] Heat Powered Cycles Conference 2023 — Edinburgh — Heat in the new energy system

3rd to 6th of September 2023
The University of Edinburgh, Scotland

includes the possibility to operate petroleum maritime fields located in remote areas. Another possible application is in combined cycles in large cargo ships. Therefore, frameworks to assess in a systematic way, concepts for compact steam bottoming cycle designs can help de-risk and accelerate its implementation.

The aim of this work is to present a framework for optimal process and control structure design of power plants. The framework includes steady-state and dynamic models. It is an advanced framework that allows to understand interactions between a physical system (reference plant) and the implemented controls, for design and operation of innovative compact and low weight steam bottoming cycles. The framework can also allow addressing of design and operation aspects of process flexibility, even before the system is build, or improve operation of existing systems. In this work, the framework is applied with a case application of an existing offshore combined cycle.

Methodology

The framework presented in this work combines three "advanced" areas of model-based systems engineering: process design optimization, dynamic modelling, and control strategies. The main elements of the framework are illustrated in Figure 1.
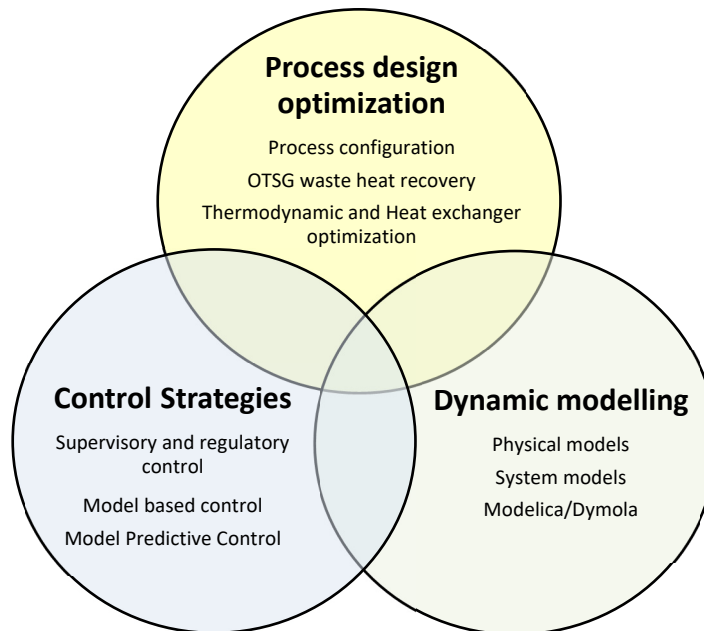
Figure 1: Main elements of the framework for physics-based modelling and simulation of combined cycle power plants in weight and volume constraint environments.

A typical challenge in weight constrained environments is to design bottoming cycles with sufficient compactness. This requires process optimization models that are flexible in terms process configuration (process synthesis) and combined thermodynamic and heat exchanger design optimization [4]. In addition, when using steam as working fluid, the most heavy and unconventional component of the system is the waste heat recovery unit. Process design optimization and steady-state off-design models of the combined cycle and once-through steam generator (OTSG) system are thus key pillars of the framework.

The bottoming cycle design optimization model applies geometry-based correlations for the heat exchanger and constant efficiency models for the turbomachinery and uses provided heat exchanger geometry information and cycle state points to compute the bottoming cycle net

power and the size and weight of heat exchanger. Details have been previously presented in the work by Montañés et al. [5]. The design optimization of the once-through steam generation in this framework utilizes the NLPQL gradient-based optimization algorithm [6].

An additional challenge is related to the OTSG dynamic operation and process dynamics. The once-through steam generator response, and subsequent steam quality response, is very sensitive to gas turbine load changes due to the thermal inertia. This makes it important to understand the dynamics and control of an OTSG in operation. The impact of the OTSG operational dynamics on the overall performance of the combined cycle system is therefore included using physics-based combined cycle system models, developed in the Modelica language based on commercially available libraries. Studying the system using dynamic models in this way is useful for optimization of control, such as PID tuning or model-predictive control design, as well as for understanding interactions between the implemented controls and the physical system. This also allows implementing supervisory and regulatory control layers of both existing or new systems [7].

In this work, the framework is applied to an existing offshore platform reference system, with the focus on the interface between the process design optimization models, and in particular, the OTSG steady-state model and the dynamic models. In this paper, the OTSG steady-state models and their validation and the dynamic model of the system is presented, with illustrative results under load changes.

Steady-state modelling of the once-through steam generator

The most complex and unconventional component in this type of systems is the OTSG. This is a heat exchanger unit capable of producing superheated steam from cold feedwater in a single heat source cooling process. Although it internally can consist of different sections emulating the traditional economizer, evaporator, and superheater units, it must be treated as a single unit with only the inlet and outlet streams normally available for measurements and control. Thus, while the OTSG model presented here consisted of three heat exchangers with distinct geometries, they were solved together as if they were one.

The model is built using an optimization framework designed for flexible simulation of different heat exchanger geometries [8], and the particular method used for the OTSG has been described in detail by Montañés et al. [5]. It consists of three interlinked cross-flow finned tube bundles, each with individual fin and tube geometries and circuit configuration. The model was discretized in two dimensions, namely the directions of flow for both gas and water. Effects of maldistribution of exhaust gas was thus not considered. The OTSG duty was solved for by integrating the transferred heat between the flue gas and the water/steam side and the pressure drop for both streams using local thermophysical properties along the circuits. A 4$^{'th}$ order Runge-Kutta scheme was used in this integration, while the system was solved using the NLPQL gradient-based algorithm [6]. For this particular model, the water/steam side was integrated backwards from a known temperature and pressure for the generated steam and solved for the feed water flow rate in an outer iteration loop.

The thermodynamic properties of the exhaust gas was modelled using the Peng-Robinson equation of state [9], while ESCOA-based correlations as implemented by Ganapathy [10] were used for gas side heat transfer and pressure drop. On the water/steam side, in-house reference tables were used for thermodynamic properties, while heat transfer was modelled using the Gnielinski correlation [11] in the single-phase regions and the Bennett-Chen correlation [12] in the two-phase region.

Dynamic modelling of the steam cycle

Dynamic process modelling and simulation of thermal power generation is a modelling paradigm that has received increased attention in recent years and has proliferated in the literature [13]. Dynamic modelling allows to describe the transient behaviour and response of a continuous process [14]. The applications of these models are multiple, such as conducting optimization of control, including control structure design and virtual tuning of controllers [15,16], exploring model-based control concepts [7], and as reference models for testing model predictive control strategies [17]. The models also allow to conduct "what-if" studies, such as sudden start-stop of a process [18]. The dynamic models in this work are based on physical principles and semi-empirical correlations [13]. They are written using the Modelica modelling language in the Dymola software [19], which is an stablished modelling approach for dynamic modelling of thermal power plants [20]. The individual components were for this work modelled using the commercial ThermalPower library by Modelon [21]. They were set up to use case-specific input such as geometry as well as nominal values for flow conditions and process efficiencies as detailed in the following sections.

Gas turbine quasi-static models

Gas turbine closed-loop dynamics are an order of magnitude faster (10 s) than that of steam cycles (10^2 s) [5,22]. Therefore, it is common in dynamic modelling and simulation of thermal power plants to model gas turbines as quasi-static processes. In this work, a look-up table approach to gas turbine modelling is applied, as presented in [23]. The main input is the gas turbine load set-point, while the main outputs are power output, mass flow rate, temperature, and exhaust gas composition. The granularity of the model depends on the input data to the look-up table. The data can be available from validated steady-state off-design or dynamic model from a software simulations or vendor data.

OTSG dynamic model

A dynamic process model of the OTSG was developed using recuperator models from the ThermalPower library [21]. It consisted of three one-dimensional (1D) dynamic heat exchanger models in a counterflow configuration, as detailed by Montañés et al. [5]. Internal and external heat transfer and total heat exchanger (HX) mass was calculated from the input geometry. The geometry supplied included outer dimensions, passes, shell geometry, and fin geometry. In addition, the wall material properties for tubes and fins were introduced as inputs to the dynamic model. In this work, the input geometries to the dynamic model were implemented based on designs obtained from results of the steady-state bottoming cycle design optimization. A soft link based on modelling records from the steady-state model to the dynamic model was implemented for fast model parametrization.

Steam cycle dynamic models

A steam turbine model based on Stodola's Law of the Ellipse [24] was used, which predicts off-design mass flow rate based on nominal values for pressure, backpressure, flow rate and density. Shaft power and outlet enthalpy were calculated using a constant isentropic efficiency. A simple generator component used the shaft power to predict power output of the cycle, which could be used for tuning in a case study.

The condenser was modelled as a tube-in-shell heat exchanger, including an internal volume with a hot well for steam and condensate inventory. A geometry-based heat transfer correlation for film condensation on horizontal tubes based on the works of Fujii et al. [25] was chosen. A

simplified water treatment system was also included, modelled as a mixing volume with a specifiable pressure drop, providing condensate to a deaerator. The component used for the latter was a tank volume kept in two-phase equilibrium and served as the main water inventory for the cycle. As such, excess steam cooled with feedwater was added as a secondary inlet stream.

Two pumps were modelled as part of the cycle, one for condensate from the condenser to the polisher, and one for treated feedwater from the deaerator to the steam generators. Both pumps give off-design flow rate and pressure lift from nominal values for density, pressure head and volume flow, as well as a constant rotational speed. Tuning of the pressure head was done adding a set hydrostatic pressure component before the pump inlet.

Controller blocks

Thermal power plant systems require the implementation of control structures. In dynamic modelling and simulation, it is common to implement the regulatory control (fast time scale with purpose of stabilizing) and supervisory (slow time scale, with purpose of seeking for optimal performance). The safety and ancillary controllers are usually disregarded. In this work, regulatory control layers are implemented by means of controller blocks and available PID controllers in Modelica Standard Library [26] and ThermalPower Library [21].

Case study: combined cycle in offshore oil and gas platform

The framework was applied to an existing combined cycle installed on an offshore platform. In this environment, on-site power production is critical for operation, and constraints on volume and weight are generally very strict compared to onshore sites.

Process and Instrumentation Diagrams (P&IDs) from the manufacturer were available for the steam cycle, which provided nominal values for the fluid between all components, except between the turbine and the condenser. Here, nominal duty values of the two components were used instead. Outer geometry data was available for the condenser and deaerator components, but nominal filling levels and condenser tube layout were not, and were instead tuned to provide the known outlet conditions. Hydrostatic pressure components were also added to satisfy the inlet conditions of the pumps.

A schematic of the steam cycle as implemented in Dymola is shown in Figure 2, with the OTSGs sub-model shown in Figure 3. Only details considered common or industry standard are shown. Horizontal shading indicates a component with volume used for water inventory, while diagonally shaded components are smaller mixing volumes. Dashed lines are used to indicate control structure. Orifice components were used to represent pressure drop over minor water treatment steps not included in the model. The regulatory control and supervisory control main control loop pairing of the steam cycle are described in Table 1. We work with the assumption that live steam pressure sliding control is implemented. The PIC controllers were tuned using the SIMC tuning rules [27].

Figure 2: Schematic of the steam cycle as implemented in the dynamic model.

Table 1: Regulatory control and supervisory control of steam cycle.

Manipulated variable		Controlled variable		Type of controller and function
Condensate valve opening	V_C	Condenser water level	L_C	Feedback PI for condenser inventory control
Make-up water valve opening	V_M	Deareator water level	L_D	Feedback PI for system inventory control
Turbine valve opening	V_T	Turbine inlet pressure	P_T	Unused, test case uses sliding pressure
Deaerator steam valve opening	V_{DS}	Deaerator pressure	P_D	Feedback PI for deaerator pressure control
Deaerator feedwater valve opening	V_{DF}	Deaerator steam inlet temperature	T_D	Feedback PI for deaerator inlet water attemperation
OTSG A flow rate set point	$F_{S,A}$	Live steam temperature	T_{OA}	Feedback PI for OTSG$_A$ steam temperature cascade control
OTSG B flow rate set point	$F_{S,B}$	Live steam temperature	T_{OB}	Feedback PI for OTSG$_B$ steam temperature cascade control
OTSG A valve opening	V_{OA}	Feedwater flow rate	F_A	Feedback PI for live steam temperature control OTSG$_A$
OTSG B valve opening	V_{OB}	Feedwater flow rate	F_B	Feedback PI for live steam temperature control OTSG$_B$
Attemperator A valve opening	V_{AA}	Live steam temperature	T_{AA}	Feedback PI for live steam temperature attemperation
Attemperator B valve opening	V_{AB}	Live steam temperature	T_{AB}	Feedback PI for live steam temperature attemperation

Figure 3: Schematic of the OTSG dynamic sub-model.

For the steady-state OTSG model, all geometry specifications were known for each section. Historical measurement data from three occasions was available for validation. This included temperatures at inlet and outlet for both fluids, pressures at flue gas inlet, feedwater inlet and steam outlet, and flow rate at both fluid inlets. Reference data for validation has been provided by the power plant operator. The data utilized in this work is different steady-state operating points of the OTSG systems. The feedwater flow-rate was reported as both measured and corrected, while the flue gas flow rate was calculated from other measurements, assuming constant heat capacity.

Simulations

The framework application focus in this paper is on OTSG steady-state process model validation and dynamic system model development.
The simulations in this work include:
- Model validation of the steady-state operation data from the OTSG reference system. Reference data is normalized.
- Preliminary results of transient performance of the entire combined cycle operation for a step change of -20% over 5 seconds, both gas turbines changing load and starting from same initial operating point of 70% GT load.

Discussion and Results

The steady-state OTSG model was validated against the historical data on duty and steam production rate. Simulations were done using two different values for the flue gas flow rate: The reported values originally calculated assuming a constant heat capacity, and newly calculated values using a variable heat capacity derived from the Peng-Robinson equation of state. This equated to a 5% reduction in flue gas flow rate.
Compared to the three sets of historical data, the model overpredicted the heat transfer duty by 3.89%, 8.96% and 3.70%. When using the reduced 95% flue gas flow rate, this was reduced to an underprediction of -0.85 %, -2.23 %, and -0.89 %, respectively. A similar trend was observed for the steam production rate as shown in Figure 4. Here, the prediction results for

both cases are compared to the historical values, which were reported as both "measured" and "corrected". The best fit is observed between the measured data and the predictions using reduced flue gas flow rate.
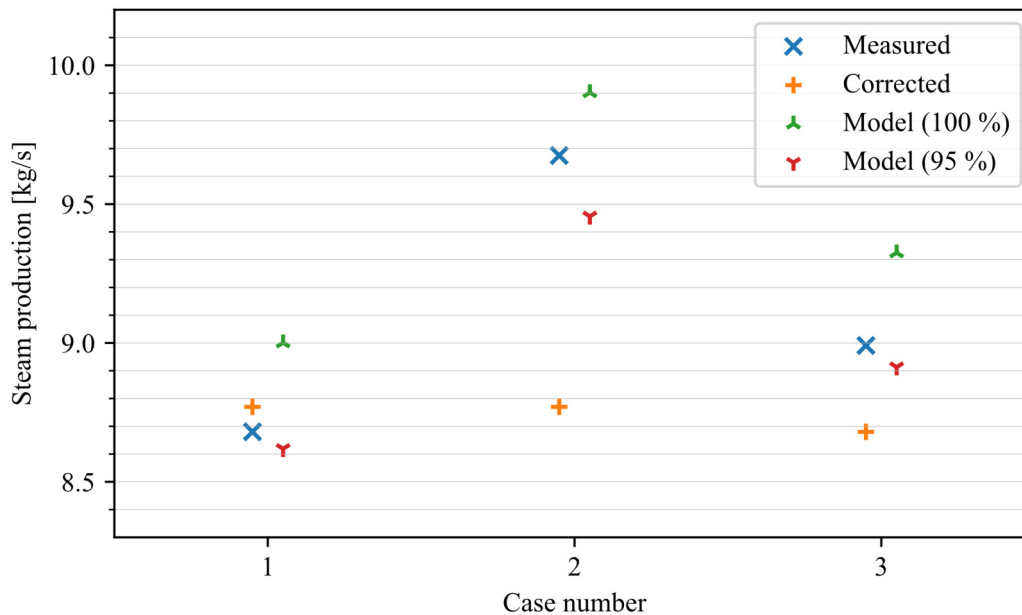
Figure 4: Comparison of predicted and reported steam production rates.

The dynamic model was tested using a gas turbine load ramp of -20 % over 5 seconds. Figure 5 shows the response time and eventual new steady-state values of selected parameters relative to 70 % gas turbine load: Flow rate, pressure and temperature of the produced steam, as well as power production of the gas turbines, steam cycle and the entire combined cycle. The temperature is normalized with Celsius as its unit.

The results in Figure 5 show that the dynamic process model can produce stable initial and final steady-state conditions for the key process output trajectories and variables plotted. The controller tuning is essential for the response of the system. For the level controllers of condenser and deareator a smooth controller tuning was chosen to avoid oscillations. The most challenging control loop is the cascade controlling the live steam temperature of the OTSG (Figure 3). A trade-off between fast disturbance rejection and avoidance of oscillation of the system must be found. With the current tuning the live steam temperature initially reduces 19 °C. Moreover, in the recovery to the set point small oscillation of the live steam temperature is present, but overshooting is avoided. The power production at the steam turbine reduces by about 18% and the new steady-state is reached after about 20 minutes. In the current model power control that regulates the gas turbines is not implemented. In future it will be interesting to explore if a reaction of the gas turbine to the small oscillation of the steam turbine power production has a negative impact on the current system and if retuning of controllers will be necessary.
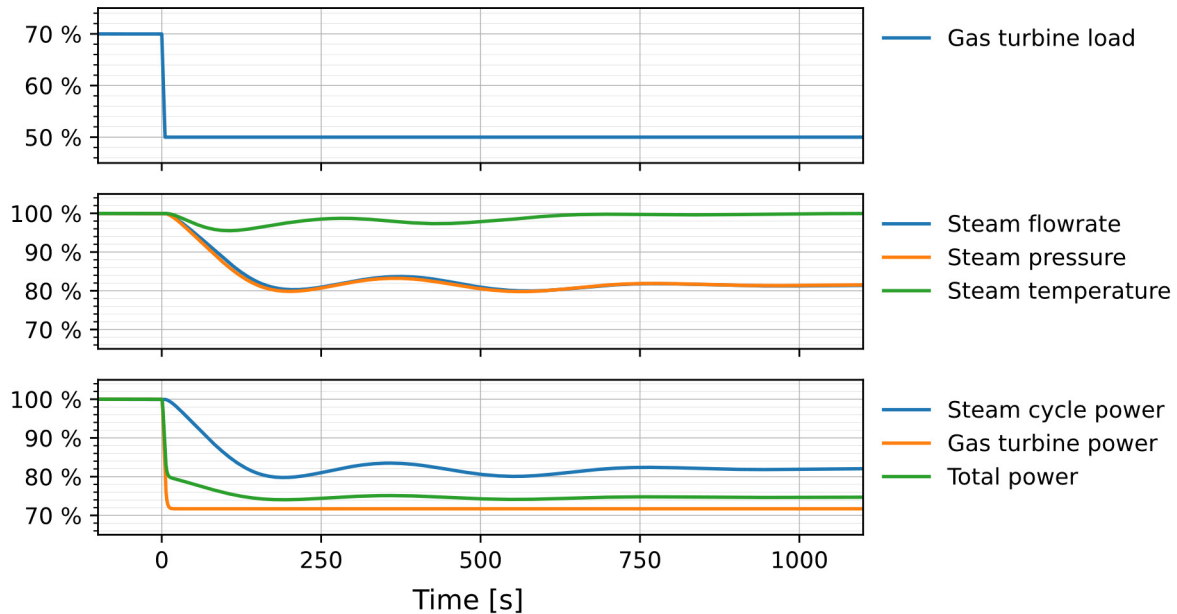
Figure 5: Predicted changes in power output and steam conditions at turbine inlet in response to sudden gas turbine load change, with the system dynamic model.

Conclusion

This work presents a framework for optimal process and control structure design of thermal power plants in weight and volume constraint environments. The framework includes interaction between physical steady-state and dynamic models to study combined cycle power plants. It allows greater understanding of interactions between a physical system (reference plant) and its implemented controls, applied for design and operation of innovative compact and low weight steam bottoming cycles.

In this work, the framework is applied to a case study of an offshore combined cycle, with manufacturer specifications and historical measurement data available. The validation of the steady-state OTSG model shows good agreement with recorded data. The results from the dynamic model show good capabilities to represent process dynamics, illustrated in this work for a sudden load change. However, further work should explore the verification of the dynamic process model with steady-state operational data at different steady-points. Furthermore, further control structures can be implemented including power control, feedforward control for the live steam temperature of the OTSG and attemperator control loops.

Moeover, the framework should be used in addressing operational flexibility, either in the design of a new system, or to improve the operation of existing systems. It will be expanded to incorporate surrogate modelling of key components to allow for more advanced control structure configurations, including model predictive control.

Acknowledgments

References:

[1]   J. Beiron, R. M. Montañés, F. Normann, and F. Johnsson, 'Flexible operation of a combined cycle cogeneration plant – A techno-economic assessment', Applied Energy, 2020, doi: 10.1016/j.apenergy.2020.115630.

[2]   R. M. Montañés, 'Transient performance of combined cycle power plant with absorption based post-combustion CO2 capture: dynamic simulations and pilot plant testing', Doctoral thesis, NTNU, 2018.

[3]   M. J. Mazzetti, B. A. L. Hagen, G. Skaugen, K. Lindqvist, S. Lundberg, and O. A. Kristensen, 'Achieving 50% weight reduction of offshore steam bottoming cycles', Energy, 2021, doi: 10.1016/j.energy.2021.120634.

[4]   H. Deng, G. Skaugen, E. Næss, M. Zhang, and O. A. Øiseth, 'A novel methodology for design optimization of heat recovery steam generators with flow-induced vibration analysis', Energy, 2021, doi: 10.1016/j.energy.2021.120325.

[5]   R. M. Montañés, G. Skaugen, B. Hagen, and D. Rohde, 'Compact Steam Bottoming Cycles: Minimum Weight Design Optimization and Transient Response of Once-Through Steam Generators', Frontiers in Energy Research, 2021.

[6]   K. Schittkowski, 'NLPQL: A fortran subroutine solving constrained nonlinear programming problems', Ann Oper Res, 1986, doi: 10.1007/BF02022087.

[7]   C. Zotică, R. M. Montañés, A. Reyes-Lúa, and S. Skogestad, 'Control of steam bottoming cycles using nonlinear input and output transformations for feedforward disturbance rejection', IFAC-PapersOnLine, 2022, doi: 10.1016/j.ifacol.2022.07.570.

[8]   G. Skaugen, K. Kolsaker, H. T. Walnum, and Ø. Wilhelmsen, 'A flexible and robust modelling framework for multi-stream heat exchangers', Computers & Chemical Engineering, 2013, doi: 10.1016/j.compchemeng.2012.10.006.

[9]   D.-Y. Peng and D. B. Robinson, 'A New Two-Constant Equation of State', Ind. Eng. Chem. Fund., 1976, doi: 10.1021/i160057a011.

[10] V. Ganapathy, 'Evaluate extended surface exchangers carefully', Hydrocarbon Processing; (USA), 1990.

[11] V. Gnielinski, 'On heat transfer in tubes', International Journal of Heat and Mass Transfer, 2013, doi: 10.1016/j.ijheatmasstransfer.2013.04.015.

[12] D. L. Bennett and J. C. Chen, 'Forced convective boiling in vertical tubes for saturated pure components and binary mixtures', AIChE Journal, 1980, doi: 10.1002/aic.690260317.

[13] F. Alobaid, N. Mertens, R. Starkloff, T. Lanz, C. Heinze, and B. Epple, 'Progress in dynamic simulation of thermal power plants', Progress in Energy and Combustion Science, 2017, doi: 10.1016/j.pecs.2016.11.001.

[14] P. J. Dechamps, 'Modelling the Transient Behaviour of Heat Recovery Steam Generators', Proceedings of the Institution of Mechanical Engineers, Part A: Journal of Power and Energy, 1995, doi: 10.1243/PIME_PROC_1995_209_005_01.

[15] L. O. Nord and R. M. Montañés, 'Compact steam bottoming cycles: Model validation with plant data and evaluation of control strategies for fast load changes', Applied Thermal Engineering, 2018, doi: 10.1016/j.applthermaleng.2018.07.012.

[16] G. Martinez Castilla, R. M. Montañés, D. Pallarès, and F. Johnsson, 'Dynamics and control of large-scale fluidized bed plants for renewable heat and power generation', Applied Thermal Engineering, 2023, doi: 10.1016/j.applthermaleng.2022.119591.

[17] H. Zhu, G. Zhao, L. Sun, and K. Y. Lee, 'Local Model Network Based Multi-Model Predictive Control for a Boiler - Turbine System', IFAC-PapersOnLine, 2020, doi: 10.1016/j.ifacol.2020.12.1800.

[18] G. Martinez Castilla, M. Biermann, R. M. Montañés, F. Normann, and F. Johnsson, 'Integrating carbon capture into an industrial combined-heat-and-power plant: performance with hourly and seasonal load changes', International Journal of Greenhouse Gas Control, 2019, doi: 10.1016/j.ijggc.2019.01.015.

[19] Dassault Systemes, 'DYMOLA Systems Engineering'. 2021.

[20] S. Can Gülen and K. Kim, 'Gas Turbine Combined Cycle Dynamic Simulation: A Physics Based Simple Approach', Journal of Engineering for Gas Turbines and Power, 2013, doi: 10.1115/1.4025318.

[21] 'Thermal Power Library', *Modelon*. https://modelon.com/library/thermal-power-library/ (accessed Dec. 09, 2022).

[22] M. K. Windfeldt and R. M. Montañés, 'Investigating the characteristics of a dynamic model of a once-through steam generator for waste heat recovery', presented at the Heat Powered Cycles Conference 2023, Edinburgh, Scotland, 2023.

[23] R. M. Montañés, S. Ó. GarÐarsdóttir, F. Normann, F. Johnsson, and L. O. Nord, 'Demonstrating load-change transient performance of a commercial-scale natural gas combined cycle power plant with post-combustion CO2 capture', International Journal of Greenhouse Gas Control, 2017, doi: 10.1016/j.ijggc.2017.05.011.

[24] D. H. Cooke, 'On Prediction of Off-Design Multistage Turbine Pressures by Stodola's Ellipse', Journal of Engineering for Gas Turbines and Power, 1985, doi: https://doi.org/10.1115/1.3239778.

[25] T. Fujii, H. Uehara, K. Hirata, and K. Oda, 'Heat transfer and flow resistance in condensation of low pressure steam flowing through tube banks', International Journal of Heat and Mass Transfer, 1972, doi: 10.1016/0017-9310(72)90072-5.

[26] Modelica Association, 'Modelica® - A Unified Object-Oriented Language for Systems Modeling', Language Specification, vol. Version 3.4, 2017.

[27] S. Skogestad, 'Simple analytic rules for model reduction and PID controller tuning', Journal of Process Control, vol. 13, no. 4, pp. 291–309, 2003, doi: https://doi.org/10.1016/S0959-1524(02)00062-8.

Systematic Model Selection for Grey Box Modeling of HVAC Systems

V. Seiler[1*], G. Huber[1], P. Kepplinger[1]

[1]Illwerke vkw Endowed Professorship for Energy Efficiency, Research Center Energy,
Josef Ressel Centre for Intelligent Thermal Energy Systems,
Vorarlberg University of Applied Sciences, Hochschulstraße 1, 6850 Dornbirn, Austria

*Corresponding author: valentin.seiler@fhv.at

Abstract

Grey Box models provide an important approach for control analysis in the Heating, Ventilation and Air Conditioning (HVAC) sector. Grey Box models consist of physical models where parameters are estimated from data. Due to the vast amount of component models that can be found in literature, the question arises, which component models perform best on a given system or dataset? This question is investigated systematically using a test case system with real operational data. The test case system consists of a HVAC system containing an energy recovery unit (ER), a heating coil (HC) and a cooling coil (CC). For each component, several suitable model variants from the literature are adapted appropriately and implemented. Four model variants are implemented for the ER and five model variants each for the HC and CC. Further, three global optimization algorithms and four local optimization algorithms to solve the nonlinear least squares system identification are implemented, leading to a total of 700 combinations. The comparison of all variants shows that the global optimization algorithms do not provide significantly better solutions. Their runtimes are significantly higher. Analysis of the models shows a dependency of the model accuracy on the number of total parameters.

Keywords: Grey Box, Modeling, HVAC, Model selection

Introduction
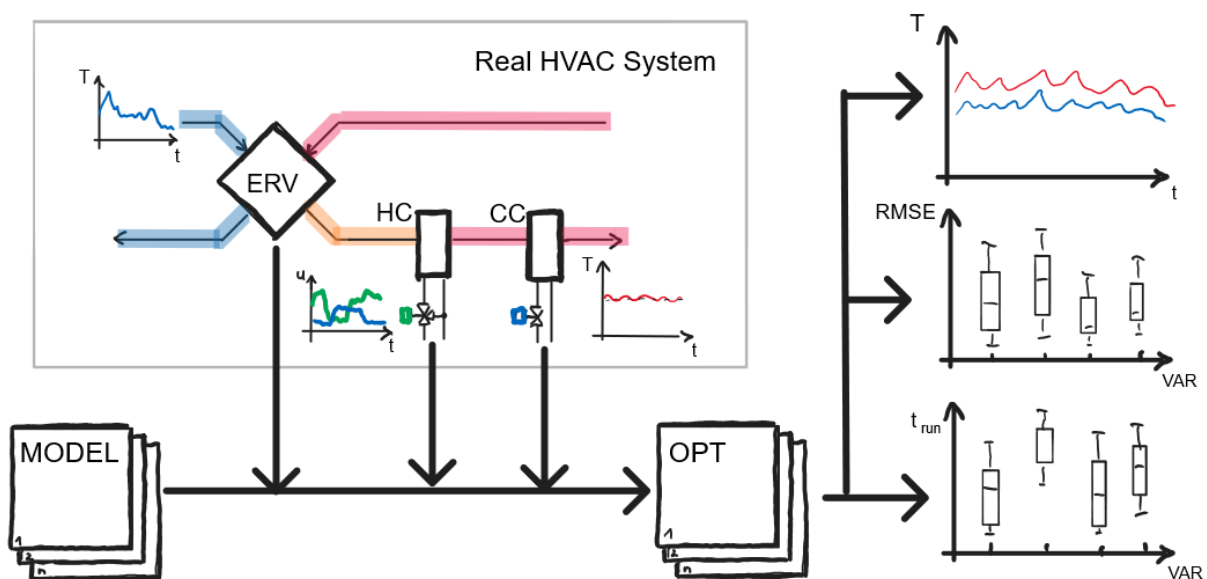
Figure 1. Scheme of the Model Selection

Grey Box modeling of Heating, Ventilation and Air Conditioning (HVAC) systems is used for control analysis and set point optimization [1, 2] and, therefore, provides an important pillar

for efficient system operation. Grey Box models are created by formulating physical (White Box) models and estimating unknown parameters from recorded data of the real system. This parameter estimation is done through nonlinear optimization, e.g., nonlinear least squares [3]. In contrast to Black Box models (also known as data-driven models) and White Box models, being the other common modeling approaches, Grey Box models are reported to have the following benefits [4, 1]:

- usually better generalization capability than Black Box models;
- lower data quality necessary than Black Box models;
- better accuracy possible than White Box models.

In literature, examples for the modeling of HVAC systems with the Grey Box approach can be found and will be outlined in the following.

Afram and Janabi-Sharifi [4] and Afroz et al. [1] review modelling methods in HVAC sector. As part of their analysis, they present common component models. Also, Okochi and Yao [5] present a review of variable-air-volume air-conditioning systems, which also includes component models.

Ghiaus, Chicinas, and Inard [6] performed a Grey Box identification of elements of ventilation systems. Here, the system consists of two electric heating coils (one for preheating and one for heating), a cooling coil, and an evaporator for air humidification. The relative humidity and the temperature of the supply air are controlled. The system is divided into small Single Input Single Output (SISO) elements, which are identified independently. A damped Gauss-Newton algorithm is used to identify the Grey Box parameters.

Koehler et al. [7] create a simple Grey Box model of a ventilation system for use in model predictive control.

Very detailed modeling of an entire HVAC system of a prototype residential building using the Grey Box approach is presented by Afram and Janabi-Sharifi [8]. Among the components considered is the ventilation system with heat recovery and cooling coil. Nonlinear least squares optimization is used to find the parameters of the models.

Systems under consideration generally consist of the same principal components including heating coils (HC), cooling coils (CC), mixing boxes (MB), energy recovery units (ER), humidifiers, ductwork, dampers and valves. Further, components of the energy supply side like heat pumps, buffer tanks and cooling towers as well as the building zones are commonly modeled.

Very little justification is given on how each model type is selected for each component, especially, as there is a great variety of model variants. Particularly for the heat exchanger modeling of ER, HC and CC units, several variations can be found and shall shortly be presented. Common steady state models are based on the so-called Number of Transfer Unit (NTU) approach [9]. Modeling examples can be found in [10, 5, 1] and it is also used in the simulation software TRNSYS® [11] as a simplified model. There, either a constant effectiveness ϵ or a correlation, to determine the effectiveness, is used. Various correlations for different heat exchangers exist, basic correlations can be found in [9], and advanced correlations for air-coils can be found for example in [12]. Dynamic models, mapping time-dependent or capacitive effects, are commonly used for control analysis. Chen and Treado [13] use a model which includes a time constant into the NTU approach, making it dynamic. Other models use simple energy balances over the heat exchanger, either using one thermal mass (for example presented in [14]) or two thermal masses (used by [8]). Those models generally map heat transfer in a simplified manner.

When it comes to a real system, the question one is confronted with is: Which of the given models performs best for the given system and dataset? To do a systematic evaluation, we
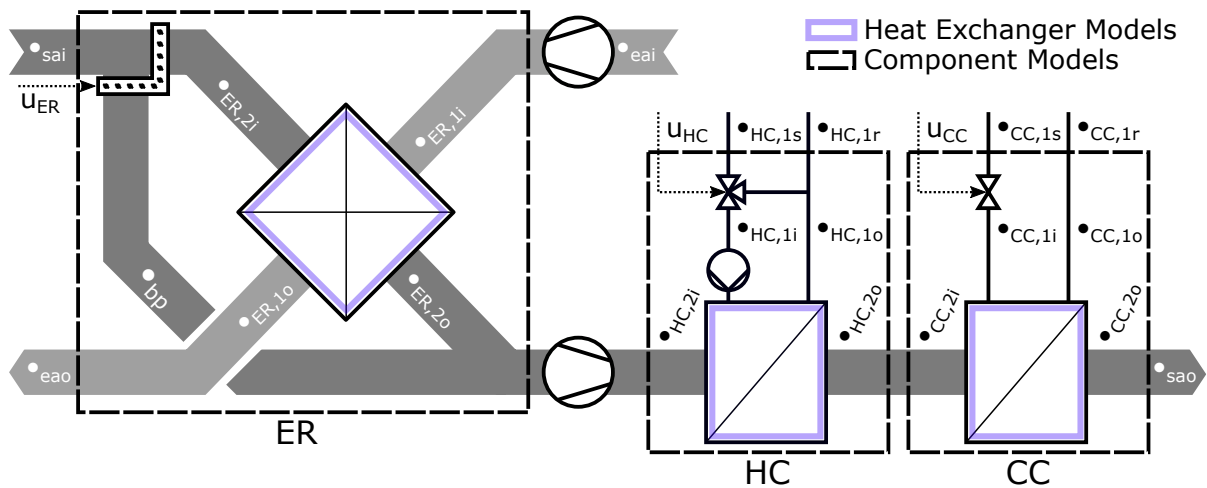
Figure 2. Scheme of the showcase ventilation system. The symbols represent the following: ER - Energy Recovery, HC - Heating Coil, CC - Cooling Coil, sa - supply air, ea - exhaust air, i - in, o - out, s - supply, r - return, bp - bypass and u - control signal

propose a grid search model selection, where suitable models are compared with each other. We present the approach based on a showcase system using real operational data with limited sensor and data availability. The principal methodology can be seen in Figure 1. Suitable model variants are selected representing the above-stated different heat exchanger formulations. Four variants for the ER, five variants of the HC and five variants of the CC are implemented, resulting in a total of 100 model combinations. Furthermore, a comparison of seven different optimization algorithms for system identification (solving the nonlinear least squares problem) is presented on all model variants, leading to a total of 700 combinations evaluated.

Methods

At first, a short description on how the overall grid search is performed on the given system is presented. Then all model variants are presented in detail, starting with general heat exchanger models, followed by the description of the particular component models that are based on the general heat exchanger models. Eventually, the system identification using the nonlinear least squares is described.

The system, subject of this project, is a ventilation system of a salesroom, where several months of recorded operating data is available. It is depicted in Figure 2. Modeling in this particular case is done, to create a test field to improve the temperature controller for the conditioned air. The components that need to be modeled are the ER, the HC, and the CC. The two fans are not modeled as they provide constant airflow, and, are irrelevant for the controller analysis. Therefore, all components are heat exchangers in different configurations. For each component, several models were identified from the literature and are adapted, to be applied to this system.

The project is implemented in Python as it provides good capabilities in data preprocessing, data analysis and optimization. In general, the system identification process developed in this project consists of three steps:

1. A combination of component models is selected.
2. An optimization algorithm is selected.
3. The model parameters are optimized (identified) by solving the nonlinear least squares problem with the chosen optimization algorithm.

Component models will be presented, starting with principal heat exchanger models, which provide the basis of the components modeled

A simplified model using the so-called effectiveness - NTU method [9] is, for example, used for modeling by Schito [10], Okochi and Yao [5], and Afroz et al. [1], and is also used in the simulation software TRNSYS® [11] as a simplified heat exchanger model. The basis of the method is that a fraction, ϵ, of the maximum transferable heat flow is transferred from the hot fluid to the cold fluid. In theory, the maximum transferable heat flow is obtained in a counter-flow heat exchanger of infinite length. Here, the temperature of the fluid with the smaller heat capacity would take on the input temperature of the fluid with the larger heat capacity [9]. The heat capacity flows $\dot{C}$ of each fluid 1 and 2 of the heat exchanger are calculated by $\dot{C}_1 = c_{p1}\dot{m}_1$ and $\dot{C}_2 = c_{p2}\dot{m}_2$, where c_{pn} denotes the specific heat capacity and $\dot{m}_n$ denotes the mass flow of fluid n. With $\dot{C}_{max} = \max(\dot{C}_1, \dot{C}_2)$ and $\dot{C}_{min} = \min(\dot{C}_1, \dot{C}_2)$, the maximum transferable heat can be calculated by

$$\dot{Q}_{max} = \dot{C}_{min}(T_{1i} - T_{2i}). \tag{1}$$

The temperatures at the outputs are then given by

$$T_{1o} = T_{1i} + \frac{\epsilon \dot{Q}_{max}}{\dot{m}_1 c_{p1}} \quad \text{and} \tag{2}$$

$$T_{2o} = T_{2i} - \frac{\epsilon \dot{Q}_{max}}{\dot{m}_2 c_{p2}}, \tag{3}$$

where indices i and o refer to in and out. Due to [9], the effectiveness ϵ can be calculated as an analytical expression for all heat exchanger types as a function $\epsilon = f(NTU, C_r)$. Here, $C_r = \frac{\dot{C}_{min}}{\dot{C}_{max}}$ and the NTU is a dimensionless ratio widely used in heat exchanger analysis. It is defined according to [9] as $NTU = \frac{UA}{\dot{C}_{min}}$, where U is the heat transfer coefficient in W/K and A is the area in m^2 of the heat exchanger. Many ϵ correlations for common heat exchanger types can be found in the literature. For the ER, the following correlation is implemented according to [9], assuming that the heat exchanger is a cross-flow type:

$$\epsilon = 1 - e^{\frac{1}{C_r}(NTU)^{0.22}\left(e^{-C_r(NTU)^{0.78}} - 1\right)}. \tag{4}$$

Detailed ϵ correlations for air coils can be found in [12], for example. However, here we implement an ϵ-correlation for counter flow heat exchangers for the HC and the CC according to [9], as a general assumption, as the exact design of the coil is unknown:

$$\epsilon = \frac{1 - e^{-NTU(1-C_r)}}{1 - C_r e^{-NTU(1-C_r)}} \qquad \text{for} \quad C_r < 1 \tag{5}$$

$$\epsilon = \frac{NTU}{1 + NTU} \qquad \text{for} \quad C_r = 1. \tag{6}$$

However, this NTU method only maps the steady state. Chen and Treado [13] use a heating coil model, that is also based on the $\epsilon - NTU$ method, but models the capacitive dynamics of the coil. In the following, this variant will be referred to as *NTU Dyn*. Here, the equilibrium temperatures are also calculated according to equation (2) and (3). Whereby the dynamic temperatures are additionally calculated by

$$\frac{dT_{1o,dyn}}{dt} = \frac{T_{1o} - T_{1o,dyn}}{\tau} \quad \text{and} \tag{7}$$

$$\frac{dT_{2o,dyn}}{dt} = \frac{T_{2o} - T_{2o,dyn}}{\tau}. \tag{8}$$

According to Chen and Treado, the time constant τ is composed of a capacitive term τ_{c} and a "flush time" τ_{x} as $\tau = \frac{1}{\tau_{\text{c}}^{-1} + \tau_{\text{x}}^{-1}}$. In this paper, however, τ is identified as a single parameter in the system identification.

Another modeling approach is for example used by [14], which will be referred to as *UA1C-*method hereafter. The heat exchanger is modeled using a single energy balance as follows:

$$\frac{\text{d}T_{1\text{o}}}{\text{d}t} = \frac{1}{C} \left[\dot{m}_2 c_{\text{p}2}(T_{2\text{i}} - T_{2\text{o}}) + UA(T_{\text{env}} - T_{1\text{o}}) - \dot{m}_1 c_{\text{p}1}(T_{1\text{i}} - T_{1\text{o}}) \right]. \tag{9}$$

Where T_{env} is the environment temperature. If the heat exchange with the environment $UA(T_{\text{env}} - T_{1\text{o}})$ is neglected, Equation (9) becomes

$$C\frac{\text{d}T_{1\text{o}}}{\text{d}t} = \dot{m}_2 c_{\text{p}2}(T_{2\text{i}} - T_{2\text{o}}) - \dot{m}_1 c_{\text{p}1}(T_{1\text{i}} - T_{1\text{o}}). \tag{10}$$

From Tashtoush, Molhim, and Al-Rousan [14] it is assumed that the return temperature of fluid 2 is constant $T_{2\text{o}} = 10°\text{C}$, since this temperature is not a model output, unlike in the other model variants. In this paper, $T_{2\text{o}}$ is included as a parameter for system identification.

Another approach using two coupled energy balance equations, one for each fluid, can be found in a paper by Afram and Janabi-Sharifi [8]. This method is referred to as *UA2C* hereafter. The ER model is formulated as such, following [8]:

$$\frac{\text{d}T_{1\text{o}}}{\text{d}t} = \frac{1}{C_{\text{am}}} \left[\dot{m}_1 c_{\text{p}1}(T_{1\text{i}} - T_{1\text{o}}) - UA\left(\frac{T_{1\text{i}} + T_{1\text{o}}}{2} - \frac{T_{2\text{i}} + T_{2\text{o}}}{2}\right) \right] + c_1 \tag{11}$$

$$\frac{\text{d}T_{2\text{o}}}{\text{d}t} = \frac{1}{C_{\text{am}}} \left[UA\left(\frac{T_{1\text{i}} + T_{1\text{o}}}{2} - \frac{T_{2\text{i}} + T_{2\text{o}}}{2}\right) - \dot{m}_2 c_{\text{p}2}(T_{2\text{o}} - T_{2\text{i}}) \right] + c_2. \tag{12}$$

C_{am} is the heat capacity of the air and metal in the heat exchanger. Here, C_{am}, UA, c_1 and c_2 are identified in the system identification where parameters c_1 and c_2 represent correction terms intended to compensate for modeling inaccuracies. This variant is implemented in two separate sub-variants, once using the correction terms (named *UA2C c*) and, once, without correction terms to study their influence. Afram and Janabi-Sharifi [8] also present a model for an air handling unit (here equivalent to a cooling coil) model similar to their ER model. Here, heat transfer is characterized by the term $UA(T_{1\text{o}} - T_{2\text{o}})$ unlike with the ER model. Thus, the differential equations are as follows:

$$\frac{\text{d}T_{1\text{o}}}{\text{d}t} = \frac{1}{C_1} \left[\dot{m}_1 c_{\text{p}1}(T_{1\text{i}} - T_{1\text{o}}) - UA(T_{1\text{o}} - T_{2\text{o}}) \right] + c_1 \tag{13}$$

$$\frac{\text{d}T_{2\text{o}}}{\text{d}t} = \frac{1}{C_2} \left[UA(T_{1\text{o}} - T_{2\text{o}}) - \dot{m}_2 c_{\text{p}2}(T_{2\text{o}} - T_{2\text{i}}) \right] + c_2. \tag{14}$$

With $C_2 = 1 * c_{\text{p}2}$, all other parameters are identical to the ER model stated before. Here again, it is implemented in two separate sub-variants with and without correction terms c_1 and c_2.

These mentioned heat exchanger models are then adapted accordingly to fit the test case system. Therefore, power control for each component needs to be modeled. The ER is equipped with a bypass for power control as can be seen in Figure 2. The bypass diverts a part of the air stream around the heat exchanger to control the recovered power. Under the assumption of linear valve behavior, the two air streams after the valve can be modeled as

$$\dot{m}_{\text{ER},2} = \dot{m}_{\text{sai}} u_{\text{ER}} \text{ and} \tag{15}$$

$$\dot{m}_{\text{bp}} = \dot{m}_{\text{sai}} (1 - u). \tag{16}$$

**Heat Powered Cycles
Conference 2023**
Edinburgh

Heat in the new energy system

3rd to 6th of September 2023
The University of Edinburgh, Scotland

Where $\dot{m}_{\mathrm{bp}}$ denotes the air stream through the bypass, $\dot{m}_{\mathrm{ER,2}}$ denotes the air stream through the heat exchanger, $\dot{m}_{\mathrm{sai}}$ denotes the total supply airflow into the ER and u_{ER} denotes the control signal for the three-way valve of the ER. Note, that the notation here is following Figure 2. The mixing temperature at the ER outlet (HC inlet), assuming a constant specific heat capacity of the air, is obtained from the energy balance by

$$T_{\mathrm{HC,2i}} = T_{\mathrm{ER,2o}}u_{\mathrm{ER}} + T_{\mathrm{sai}}(1 - u_{\mathrm{ER}}). \tag{17}$$

For the heat exchanger of the ER, four of the above-mentioned models were used: *NTU, NTU Dyn, UA2C, UA2Cc*. The *UA1C* model was excluded due to expected low performance. The fluid flows 1 and 2 of the heat exchanger models correspond to the exhaust and supply air, respectively.

Similar to the energy recovery, the heating coil is composed of two subcomponents, the water-air heat exchanger and a three-way valve, which controls the power of the coil. The mass flow in the heat exchanger itself is constant and, depending on the valve position, water from the return is proportionally added to the flow through the heat exchanger. The constant mass flow $\dot{m}_{\mathrm{HC,1}}$ can be determined as a parameter of the model during system identification. The temperature at the inlet of the heat exchanger is therefore formed as a mixed temperature from the supply temperature and the return temperature of the heat exchanger. From the energy balance of the three-way valve follows for the mixed temperature $T_{\mathrm{HC,1i}}$ depending on the control input u_{HR} of the valve:

$$T_{\mathrm{HC,1i}} = T_{\mathrm{HC,1s}}u_{\mathrm{HC}} + T_{\mathrm{HC,1o}}(1 - u_{\mathrm{HC}}). \tag{18}$$

For the water-to-air heat exchanger, all five of the above-described variants from the literature were implemented. Fluids 1 and 2 of the heat exchanger models refer to water and air respectively.

The cooling coil power is controlled via a valve to control the power output. Different from the heating coil, this is done with a throttle valve. Therefore, under the assumption of linearity of the valve $u_{\mathrm{CC}} \sim \dot{m}_{\mathrm{CC,1i}}$, the equation for the mass flow can be formulated as follows:

$$\dot{m}_{\mathrm{CC,1i}} = u_{\mathrm{CC}} \cdot \dot{m}_{1,\mathrm{max}}. \tag{19}$$

Here the maximum mass-flow $\dot{m}_{1,\mathrm{max}}$ can be determined as a parameter during system identification. To model the water-to-air heat exchanger, the same variants can be used as in the heating coil. This modeling implies, that there is no condensation taking place during the cooling process.

All used model variants for each component, including their start parameters and bounds for the optimization, are shown in Table 1.

Since the components have no feedback within the system boundaries, they can be solved independently. Thus, the first component of the model forms the input of the second component and the second the input of the third. All components are transformed into general time-discrete input-output models with a time resolution of one minute in the following form:

$$y_i^* = f(y_{i-1}^*, x_i). \tag{20}$$

Where y_i^* is the output vector of model f at time i, y_{i-1}^* is the model output vector at time $i-1$ and x_i is the model input vector at time i. To get all models into the given form, differential equations need to be solved. The solution of the differential equations is obtained analytically. Models containing coupled systems of differential equations are solved, by transformation into

Table 1. Component Models

Component	Model	Parameter	Start value	lb	ub	Unit
ER	NTU	UA	3933.9	1	5000	W/K
	NTU Dyn	UA	3933.9	1	5000	W/K
		τ	60	1	500	s
	UA2C	UA	3933.9	1	5000	W/K
		C_{am}	25000.0	1	500000	J/K
	UA2C c	UA	3933.9	1	5000	W/K
		C_{am}	25000.0	1	500000	J/K
		c_1	0	-10	10	
		c_2	0	-10	10	
HC	NTU	$\dot{m}_{HC,1}$	0.2908	0.1	5	kg/s
		UA	258.76	1	5000	W/K
	NTU Dyn	$\dot{m}_{HC,1}$	0.2908	0.1	5	kg/s
		UA	258.76	1	5000	W/K
		τ	60	1	500	s
	UA1C	$\dot{m}_{HC,1}$	0.2908	0.1	5	kg/s
		C	500000	1	500000	J/K
		T_{1o}	40.0	1	70	°C
	UA2C	$\dot{m}_{HC,1}$	0.2908	0.1	5	kg/s
		UA	258.76	1	5000	W/K
		C_{wm}	250000	1	500000	J/K
	UA2C c	$\dot{m}_{HC,1}$	0.2908	0.1	5	kg/s
		UA	258.76	1	5000	W/K
		$\dot{m}_{HC,1}$	250000	1	500000	J/K
		c_1	0	-10	10	
		c_2	0	-10	10	
CC	NTU	$\dot{m}_{1,max}$	0.4625	0.1	5	kg/s
		UA	1485.2	1	5000	W/K
	NTU Dyn	$\dot{m}_{1,max}$	0.4625	0.1	5	kg/s
		UA	1485.2	1	5000	W/K
		τ	60	1	500	s
	UA1C	$\dot{m}_{1,max}$	0.4625	0.1	5	kg/s
		C	500000	1	500000	J/K
		T_{1o}	18.0	1	20	°C
	UA2C	$\dot{m}_{1,max}$	0.4625	0.1	5	kg/s
		UA	1485.2	1	5000	W/K
		C_{wm}	250000	1	500000	J/K
	UA2C c	$\dot{m}_{1,max}$	0.4625	0.1	5	kg/s
		UA	1485.2	1	5000	W/K
		C_{wm}	250000	1	500000	J/K
		c_1	0	-10	10	
		c_2	0	-10	10	

Heat Powered Cycles
Conference 2023
Edinburgh

Heat in the new energy system

3rd to 6th of September 2023
The University of Edinburgh, Scotland

their eigenbasis. The heating coil, where the return temperature is at the same time its input temperature, requires the models to be solved iteratively for each time step.

The parameters of the models are identified using optimization technics. This optimization aims to minimize the error between the model output and the dataset. In the presented test case, there are two model outputs with corresponding measurements in the dataset. Therefore, the calculated error is the sum of the individual errors of each model output and the minimization can be formulated as

$$\min_p \sum_{i \in \mathcal{I}} \left((y_{1,i}^*(p) - y_{1,i})^2 + (y_{2,i}^*(p) - y_{2,i})^2 \right) \tag{21}$$

$$s.t. \ lb \leq p \leq ub. \tag{22}$$

Where $y_{1,i}^*(p)$ and $y_{2,i}^*(p)$ are the outputs of a model at time i with the parameter-vector p. $y_{1,i}$ and $y_{2,i}$ are the corresponding measurements from the dataset at the same time and lb and ub are the lower and upper bounds for the parameter vector p. Values for the upper and lower bound of each parameter are given in Table 1. For the optimization, the parameters p are scaled logarithmically. The algorithms require an initial guess for the parameters p as a starting point for the optimization (start parameters). These values were taken from the data sheet of the system if available. They are also given in Table 1.

For the optimization algorithms, the choice was made from a selection of global and local optimization algorithms available in the Python SciPy library [15, 16] which provides a selection of common optimization routines. The selection criteria were, that the algorithm has to accept bounds and no derivatives are needed. Furthermore, some algorithms were excluded due to unreasonable long runtimes based on a preliminary study. The selected local optimization algorithms are:

- Nelder-Mead
- L-BFGS-B
- Powell
- TNC

The global optimization algorithms are:

- Differential-Evolution
- Dual-Annealing
- DIRECT

Data for the system identification was extracted from the control unit of the showcase system over several months. Relevant measurement points of the system are displayed in Table 2. T_{sao} and $T_{\text{HC,1r}}$ correspond to outputs of the model and can therefore be used to formulate the error function of the optimization (Equation (21)). However, not all outputs of the model are represented in the dataset, which means they cannot be used in the error calculation. Intermediate measurements of the supply air are, for example, not available which is assumed to limit the accuracy of the model variants. Further, the measurements of the plant are taken in irregular time steps, based on a constant delta. To mimic this behavior in the model, a sensor model is implemented. Also, the data needs to be pre-processed. This preprocessing is done by resampling the irregularly sampled dataset to a one-minute time resolution for usability in the time discrete model. Further, suitable days, when model assumptions hold, and no faulty behavior is detected in the dataset are selected based on formulated conditions, systematically. Further details on the data preprocessing can be found in [17].

Table 2. Measurements of the test case system

Position	Quantity	Unit	Symbol
Supply air	Mass flow	kg/s	$\dot{m}_{\mathrm{sa}}$
Supply air in	Temperature	°C	T_{sai}
Supply air out	Temperature	°C	T_{sao}
Return air	Mass flow	kg/s	$\dot{m}_{\mathrm{ra}}$
Return air in	Temperature	°C	T_{rai}
Heating coil supply	Temperature	°C	$T_{\mathrm{HC,1s}}$
Heating coil return	Temperature	°C	$T_{\mathrm{HC,1r}}$
Cooling coil supply	Temperature	°C	$T_{\mathrm{CC,1s}}$
Controller	Output		$u_{\mathrm{ER}}, u_{\mathrm{HC}}, u_{\mathrm{CC}}$

The available dataset starts on 03/03/2022 and ends on 08/06/2022, thus containing 98 days. After applying the preprocessing rules, only eight days show to be suitable for system identification. Then a training- and a test dataset are selected from the suitable days for parameter identification and model verification respectively. The outdoor temperature provides a good indication of the operating state of the plant. The training and test data sets each contain a range of outdoor temperatures from about 0°C to just over 30°C. However, the distributions are different, so the extrapolation ability of the model can be verified by the test data set.

Results

The model outputs, T_{sao}^{*} and $T_{\mathrm{HC,1r}}^{*}$ of the model with the lowest error can be seen in Figure 3. They are plotted against the corresponding measurements T_{sao} and $T_{\mathrm{HC,1r}}$. Both outputs capture the general swinging dynamics of the system, noting, that the swinging dynamics are already present in the controller output of the dataset. The deviation is mostly (90% of time) below 1.6 K for T_{sao} and below 3.7 K for $T_{\mathrm{HC,1r}}$, however, still significant.
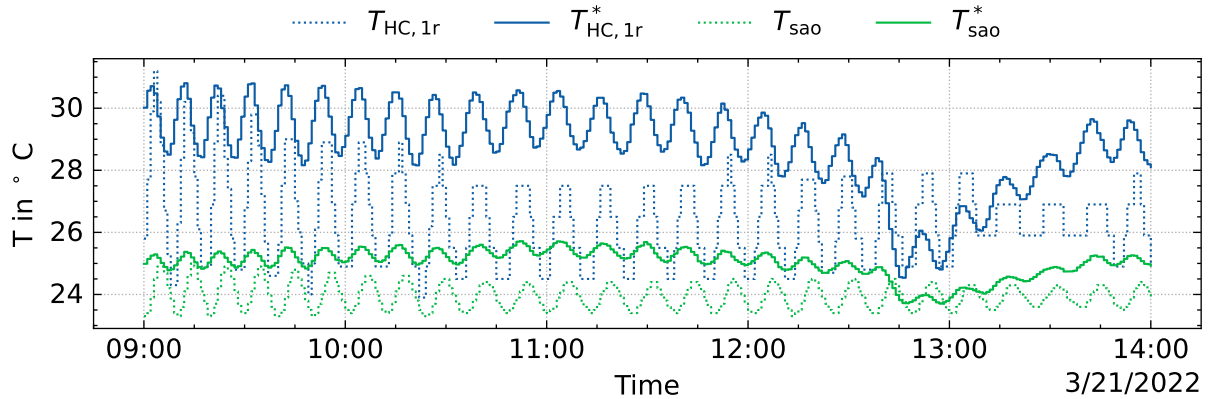
Figure 3. Exemplary model output ($T_{\mathrm{HC,1r}}^{*}$, T_{sao}^{*}) and corresponding measurements ($T_{\mathrm{HC,1r}}$, T_{sao})

Calculated performance metrics of the final model (on training and test data) can be seen in Table 3. Notably, the metrics are comparably worse than other Grey Box modeling approaches, for example Afram and Janabi-Sharifi [8], who reach RMSEs between 0.224 and 1.127, however, for individual component models.

The grid search approach, applied to the test case system, yields a total of 700 combinations of models and optimization algorithms. The test dataset is primarily used, to test the extrapolation

Table 3. Metrics of the final model.

		$T_{\mathrm{HC,1r,train}}$	$T_{\mathrm{HC,1r,test}}$	$T_{\mathrm{sao,train}}$	$T_{\mathrm{sao,test}}$
RMSE	Root Mean Square Error	2.377	2.320	1.050	1.281
R^2	Coefficient of multiple determination	0.992	0.992	0.998	0.997
MSE	Mean Squared Error	5.650	5.381	1.102	1.642
MAE	Mean Absolute Error	1.603	1.430	0.831	0.931

ability of the models or the overfitting tendency of the models. This is done by comparing the achieved errors of the training and test dataset. For analysis purposes, the RMSE (Root Mean Squared Error) of each model is used. Figure 4 shows the division of the RMSE of the training dataset divided by the RMSE of the test dataset. A value smaller than one indicates, that the model performs better on the training dataset than on the test dataset, which indicates a low extrapolation ability or overfitting. Values greater than one indicate, that the model performs better on the test dataset, which can be coincidental. Plot 1 of Figure 4 shows the sum of the errors of both model outputs (T_{sao} and $T_{\mathrm{HC,1r}}$). As the values are close to one, overfitting appears to be insignificant. However, the second and the third plots show, that the RMSE of T_{sao} tends to overfit more significantly, which seems to be compensated by the RMSE of $T_{\mathrm{HC,1r}}$.
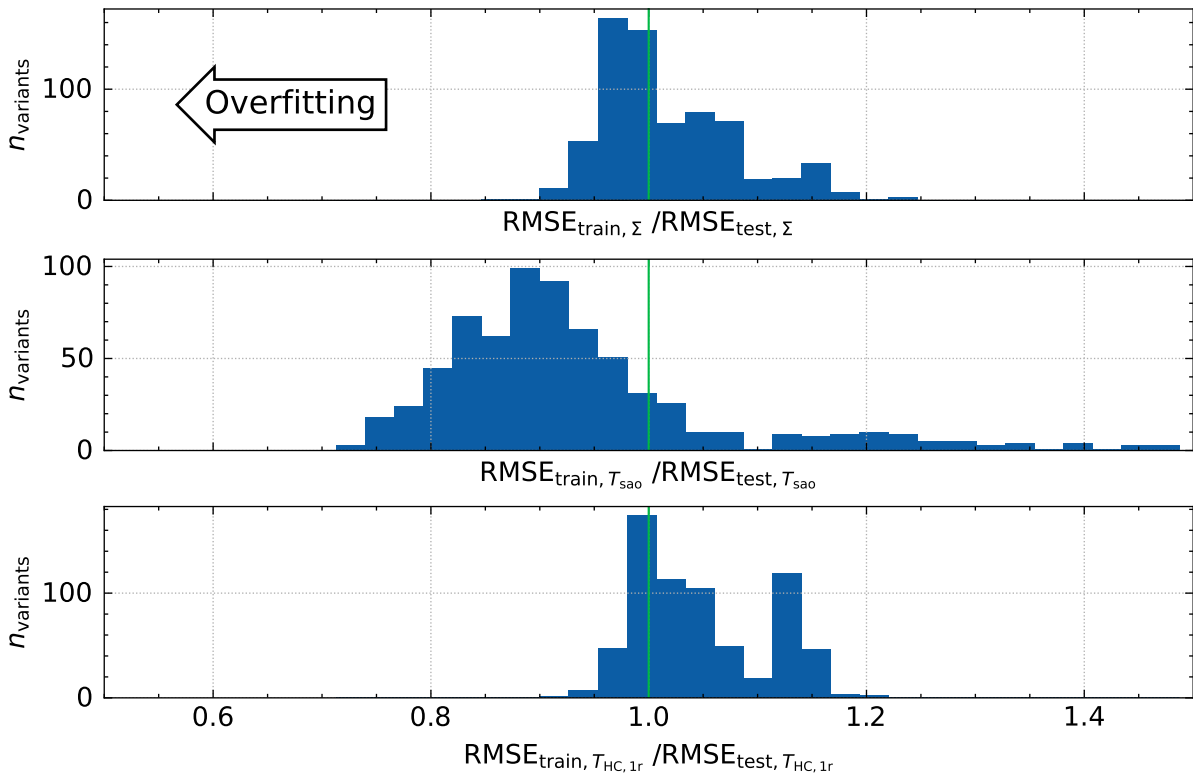
Figure 4. Histogram of the ratios of the $\mathrm{RMSE_{train}}/\mathrm{RMSE_{test}}$ of all 700 model variants, which provide an indicator for overfitting. Plot 1 shows the ratio for the summed errors of both model outputs. Plot 2 shows the ratio for the error of T_{sao}, and plot 3 for $T_{\mathrm{HC,1r}}$.

Figure 5 shows the comparison of the optimization algorithms. Again, the RMSE is used for evaluation. Note, that some algorithms did not converge, however, the results are included, as long as they were returned by the algorithm. As can be seen, the distributions of all optimization algorithms have similar minimum and maximum values except for some outliers of
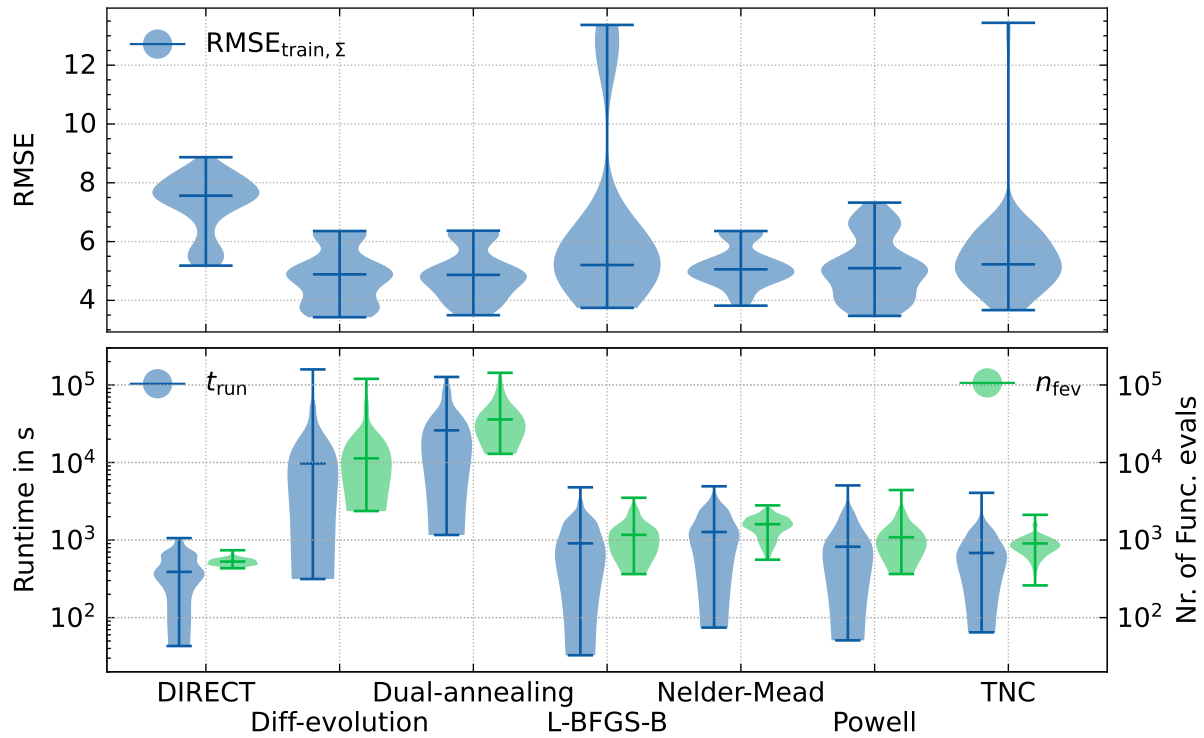
Figure 5. Comparison of performance of optimization algorithms in all 700 variants. Plot 1: Distributions of the sum of RMSE of T_{sao} and $T_{\mathrm{HC,1r}}$ grouped by the optimization algorithm. Plot 2: Distribution of runtimes and the number of function evaluations grouped by the optimization algorithm.

the L-BFGS-B, the TNC algorithms, and the DIRECT method which performs worse in the optimization setting at hand. Further, the second plot shows that the global optimization algorithms Differential-Evolution and Dual-Annealing have significantly higher runtimes and more function evaluations compared to the local optimization algorithms. The global optimizer DIRECT also has lower runtimes and function evaluations. However, the achieved errors are, as mentioned, worse compared to the other algorithm.

Figure 6 shows an analysis grouped by the number of parameters. The first plot shows that with an increasing number of parameters, the mean absolute error decreases up to nine parameters. Then, the error does not decrease significantly with an increase in the number of parameters. The last plot shows that the median of the runtime for each optimization routine and the median of the number of function evaluations tend to increase with the number of parameters.

Discussion

The data selection process shows, that much of the recorded data does not fulfill the requirements for the model fit. This is mainly due to the low resolution and the resampling of the data. The low resolution is also expected to be the main cause of the comparably low model performance compared to results from the literature. A further cause for the low performance in the test case is the lack of intermediate measurements between the components, i.e., only the complete system can be identified as a whole in one process. In Figure 3, the drop in $T_{\mathrm{HC,1r}}$ and T_{sao} at around 12:45 clearly shows that some effects are not represented in the dataset or that some dynamics are not modeled correctly. That shows the difficulties that arise with the usage of real operational data which is only addressed in literature very rarely.

One aspect to consider is, that the component models which are relevant, strongly depend on
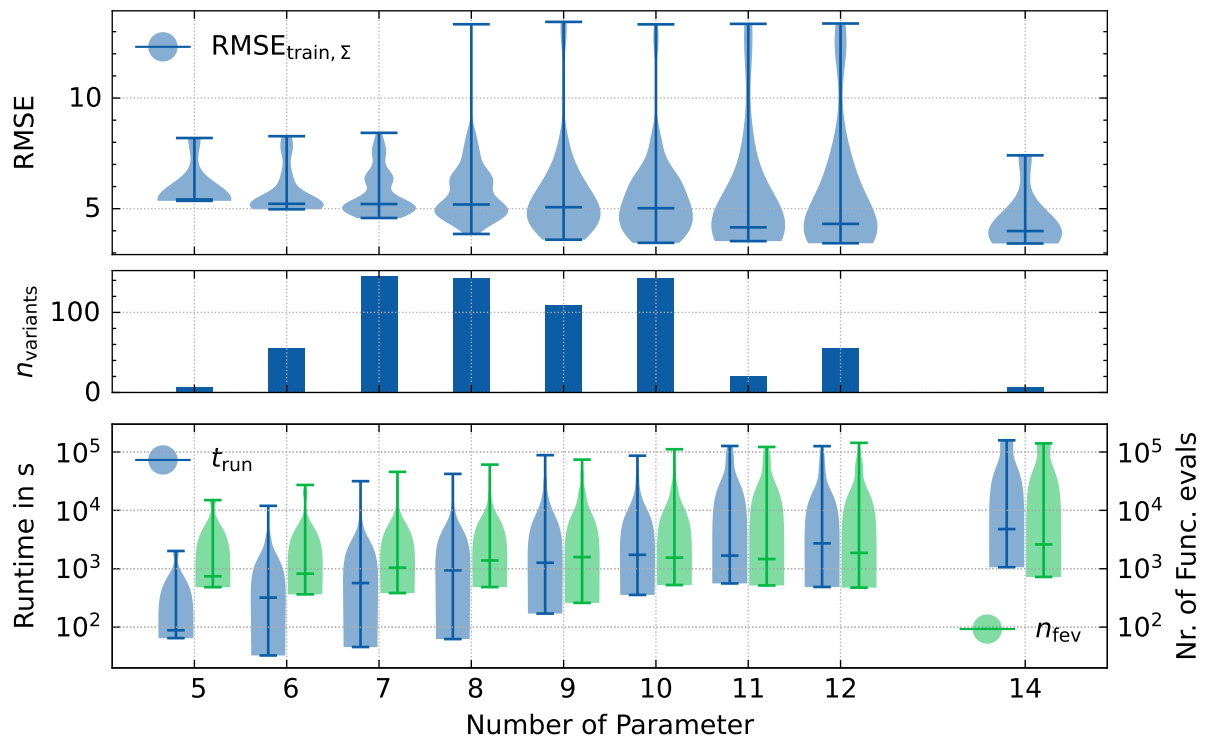
Figure 6. Analysis of sum of RMSE of T_sao and $T_\text{HC,1r}$, runtime and the number of function evaluations in dependency of the number of total model parameters. Note: There are more variants towards the middle of the spectrum as there are more possible component combinations with a given number of parameters, there is no possible combination of components that results in 13 parameters.

the later use case of the model. For example models for control analysis usually need to map capacitive effects, whereas quantitative energy analysis can usually cope with static models. Also, the time necessary for modeling, running system identification and evaluating several model variants for each component presents a significant drawback of the presented approach. This is especially the case, as there are no software solutions available for this kind of analysis. The lack of software solutions in modeling has already been addressed by [18].

However, interesting observations stem from the study results.

First, the runtime of the global optimizers is much longer than that of the local optimizers, the achieved model errors, however, do not show a significant difference in accuracy.

Secondly, the analysis of the number of parameters of the models shows that also simple models can yield results comparable to those of more complex modeling approaches.

Thirdly, the validation of the models with the test dataset shows, that some models tend to overfit on single outputs, whereas the overall error does not. This shows, that overfitting can be a relevant issue and, that the selection of the error function can be of great importance and multi-objective optimization should be considered.

Conclusions

In this project, a methodology for the selection of Grey Box models is presented on a real test case system. Therefore, several component models are identified for each component of the plant that needs to be modeled. Here, the energy recovery is modeled in four different variants and the heating coil and the cooling coil are each modeled in five different variants. For comparison, all possible model combinations are created and the parameters of the model are identified using four different local optimization algorithms and three global optimization algorithms. In total that leads to 700 system identifications.

The comparison of the optimization algorithms shows that the global optimizers have generally much longer runtimes and the achieved model errors are of comparable quality as those achieved by the local optimizers.

The analysis of different model variants shows that there is a dependency of the accuracy of the model and the number of parameters. Here, the achieved errors show a minimum at around nine parameters and the runtimes increase significantly with the number of parameters.

Further work should be done in evaluating the presented approach on different datasets with better quality to be able to make more general statements about suitable model types. A successive reduction in data quality, e.g., reducing the number of sensors and measurement intervals, could further yield results about necessary data quality for each type of model.

Even though the methodology provided probably renders to be too complex and time-consuming for most common modeling tasks, it can give insights into the system behavior and system identification process. Future works with Grey Box models should consider a systematic approach for system identification as this can help to determine the best-suited complexity of the model for a given system or dataset.

Acknowledgement

References

[1] Zakia Afroz et al. "Modeling Techniques Used in Building HVAC Control Systems: A Review". In: *Renewable and Sustainable Energy Reviews* 83 (Mar. 2018), pp. 64–84. DOI: 10.1016/j.rser.2017.10.044.

[2] Mohammad Royapoor, Anu Antony, and Tony Roskilly. "A Review of Building Climate and Plant Controls, and a Survey of Industry Perspectives". In: *Energy and Buildings* 158 (Jan. 2018), pp. 453–465. DOI: 10.1016/j.enbuild.2017.10.022.

[3] Raad Z. Homod. "Review on the HVAC System Modeling Types and the Shortcomings of Their Application". In: *Journal of Energy* 2013 (2013), pp. 1–10. DOI: 10.1155/2013/768632.

[4] Abdul Afram and Farrokh Janabi-Sharifi. "Review of Modeling Methods for HVAC Systems". In: *Applied Thermal Engineering* 67.1-2 (June 2014), pp. 507–519. DOI: 10.1016/j.applthermaleng.2014.03.055.

[5] Godwine Swere Okochi and Ye Yao. "A Review of Recent Developments and Technological Advancements of Variable-Air-Volume (VAV) Air-Conditioning Systems". In: *Renewable and Sustainable Energy Reviews* 59 (June 2016), pp. 784–817. DOI: 10.1016/j.rser.2015.12.328.

[6] Christian Ghiaus, Adriana Chicinas, and Christian Inard. "Grey-Box Identification of Air-Handling Unit Elements". In: *Control Engineering Practice* 15.4 (Apr. 2007), pp. 421–433. DOI: 10.1016/j.conengprac.2006.08.005.

[7] Sarah M. Koehler et al. "Chapter 7 Distributed Model Predictive Control for Forced-Air Systems". In: *Intelligent Building Control Systems*. Ed. by John T. Wen and Sandipan Mishra. Advances in Industrial Control. Cham: Springer International Publishing, 2018. ISBN: 978-3-319-68461-1 978-3-319-68462-8. DOI: 10.1007/978-3-319-68462-8.

[8] Abdul Afram and Farrokh Janabi-Sharifi. "Gray-Box Modeling and Validation of Residential HVAC System for Control System Design". In: *Applied Energy* 137 (Jan. 2015), pp. 134–150. DOI: 10.1016/j.apenergy.2014.10.026.

[9] T. L. Bergman and Frank P. Incropera, eds. *Fundamentals of Heat and Mass Transfer*. 7th ed. Hoboken, NJ: Wiley, 2011. ISBN: 978-0-470-50197-9.

[10] Eva Schito. "Dynamic Simulation of an Air Handling Unit and Validation through Monitoring Data". In: *Energy Procedia* 148 (Aug. 2018), pp. 1206–1213. DOI: 10.1016/j.egypro.2018.08.010.

[11] S A Klein et al. *TRNSYS 16, Mathematical Reference*.

[12] Hélio Aparecido Navarro et al. "Effectiveness - NTU Data and Analysis for Air Conditioning and Refrigeration Air Coils". In: *Journal of the Brazilian Society of Mechanical Sciences and Engineering* 32.3 (Sept. 2010), pp. 218–226. DOI: 10.1590/S1678-58782010000300004.

[13] Yan Chen and Stephen Treado. "Development of a Simulation Platform Based on Dynamic Models for HVAC Control Analysis". In: *Energy and Buildings* 68 (Jan. 2014), pp. 376–386. DOI: 10.1016/j.enbuild.2013.09.016.

[14] Bourhan Tashtoush, M. Molhim, and M. Al-Rousan. "Dynamic Model of an HVAC System for Control Analysis". In: *Energy* 30.10 (July 2005), pp. 1729–1745. DOI: 10.1016/j.energy.2004.10.004.

[15] Pauli Virtanen et al. "SciPy 1.0: Fundamental Algorithms for Scientific Computing in Python". In: *Nature Methods* 17.3 (Mar. 2, 2020), pp. 261–272. DOI: 10.1038/s41592-019-0686-2.

[16] *Optimization and Root Finding (Scipy.Optimize) — SciPy v1.10.0 Manual*. URL: https://docs.scipy.org/doc/scipy/reference/optimize.html (visited on 01/06/2023).

[17] Valentin Seiler. *Grey-Box-Modellierung einer Lüftungsanlage mit realen Betriebsdaten für die Optimierung des Reglers*. 2022. DOI: 10.25924/opus-4580. URL: https://opus.fhv.at/frontdoor/index/index/docId/4580 (visited on 12/01/2022).

[18] Ercan Atam. "Current Software Barriers to Advanced Model-Based Control Design for Energy-Efficient Buildings". In: *Renewable and Sustainable Energy Reviews* 73 (June 2017), pp. 1031–1040. DOI: 10.1016/j.rser.2017.02.015.

Investigating the characteristics of a dynamic model of a once-through steam generator for waste heat recovery

M. K. Windfeldt[1*], R. M. Montañés[1], L. E. Andersson[1]

[1]SINTEF Energy Research, Sem Sælands vei 11, 7034 Trondheim, Norway

*Corresponding author: magnus.windfeldt@sintef.no

Abstract

A dynamic model of a once-through steam generator for bottoming cycles has been investigated. Its response to both continuous and discontinuous load changes was studied to determine its transient characteristics. The characteristic time of the relevant transient output trajectories of the OTSG are found to be in the order of 10^2 seconds, which is suspected to be the longest in the reference combined cycle power plant system. The discretisation of volume elements has been varied to study the accuracy and required simulation time at increasing complexity. A high discretisation of volumes is required for accurate duty calculation, but not for accurate modelling of transient behaviour, indicating possible directions for further model development. The model will be used as basis for further developments of surrogate modelling, including data-driven methods for dynamic modelling.

Keywords: Dynamic Modeling, simulation, transients, heat exchanger, waste heat, accuracy, simulation speed, Modelica.

Introduction

Waste heat recovery (WHR) systems for increased energy efficiency in energy intensive industries must be robust and reliable [1]. Operational flexibility of WHR systems is key in many industrial applications due to fluctuations in the waste heat source. In some industrial sites where a WHR unit is to be installed, there is limited space or system capacity to add more weight, for example in existing offshore oil and gas platforms [2] and other maritime systems such as ships. Achieving low weight, volume, and footprint is thus key for successful implementation of WHR systems. A once-through approach to the design of components for steam generation by heat recovery can eliminate boiler drums and many other pieces of equipment, allowing for lower weight and volume systems [1]. Such a system uses a single heat exchanger for heat recovery, known as a once-though steam generator (OTSG).

Robust control systems must be implemented in order to regulate the superheated steam pressure and temperature over time [3], and to allow the system to cope with fluctuations in the water-to-steam transition point within the OTSG. In principle, OTSGs are highly suitable for flexible or cyclic operation [1], but dynamic modelling and simulation models allow further study of the transient response of the WHR systems and its controls [3]. In some control schemes, such as model predictive control, a dynamic model of the WHR system can be used as part of the optimisation. However, high fidelity dynamic models might not be readily amenable for optimisation applications.

This paper details the work done to characterise a model of a OTSG in the Modelica [4] language with Dymola [5] as environment, which is to be used as a reference for new model development and as a component in a system level dynamic model of an offshore bottoming steam cycle. The dynamic response to both a continuous and discontinuous change in the gas turbine load is investigated, as well as the simulation time and accuracy achieved for different discretisations.

Model description

The OTSG model used in this paper was previously presented in the work by Montañés et al [3], from which the illustrations in Figure 1 also originate. It was built upon a tube-and-shell model from the Thermal Power Library [6] developed by Modelon. It uses geometry parameters from an OTSG already installed off-shore. The models are developed based on principles of continuous system modelling [7]. The modelling paradigm, based on thermo-hydraulic modelling of thermal power plants, is described in the work by Casella and Leva [8]. Modelling principles are further described by Dechamps [9].

OTSG description

In reality, the OTSG would be a cross-flow heat exchanger, where gas flows across bundles of narrow tubes. The water/steam flows inside these tubes, and makes several passes across the gas flow. The heat transfer is normally enhanced on the gas side by use of fins. The OTSG system model was designed for a specific case study on WHR of an off-shore platform in the Norwegian Continental Shelf, focusing on WHR from the exhaust gas of two gas turbines, normally operated at around 85–100% load. Table 1 lists the parameters describing the heat exchanger studied for this work. It contains a brief description and the value used. These values are generated through optimisation using a SINTEF in-house modelling framework [10,11] by tuning known parameters to historical data.

Table 1: Geometry parameters used in OTSG model.

Parameter	Value	Description
Bundle level		
nTubesPerRow	36	Number of tubes at gas inlet
CoreWidth	3.202 m	Length of one pass
TubePitchTransversal	0.076 m	Centre to centre, perpendicular to gas flow
Staggered_tubes	true	False = inline tubes
Layer level		
nPasses	16	Number of times water/steam flows back or forth
nRowsPerPass	2	Parallel water/steam flows
TubePitchLongitudinal	0.066 m	Centre to centre, parallel to gas flow
Tube level		
TubeInnerDiameter	21.18 mm	
TubeOuterDiameter	25.4 mm	
FinHeight	6.60 mm	Distance from tube end to fin end in radial direction
FinThickness	1.05 mm	
FinPitch	3.31 mm	Centre to centre
Serrated_fins	true	False = plain fins
SegmentWidth	4 mm	Width of serrated segments
UnserratedHeight	4.5 mm	Height of unserrated part of fin

Implementation in Modelica/Dymola

The desired OTSG geometry was exported directly to the Dymola environment, where it was stored in a record coupled to the OTSG dynamic model. For simulation this 3-dimensional geometry was translated into a 1-dimensional model preserving the most important flow and heat transfer characteristics, but not representing the actual geometry, and simulated as a counterflow heat exchanger. According to Dechamps [9], this is a valid approach for studying transient behaviour as long as the following characteristics are conserved: Height, gas side free cross-

sectional area, crossing time for water/steam, water mass flow rate, internal heat transfer surface, external heat transfer surface, and mass.
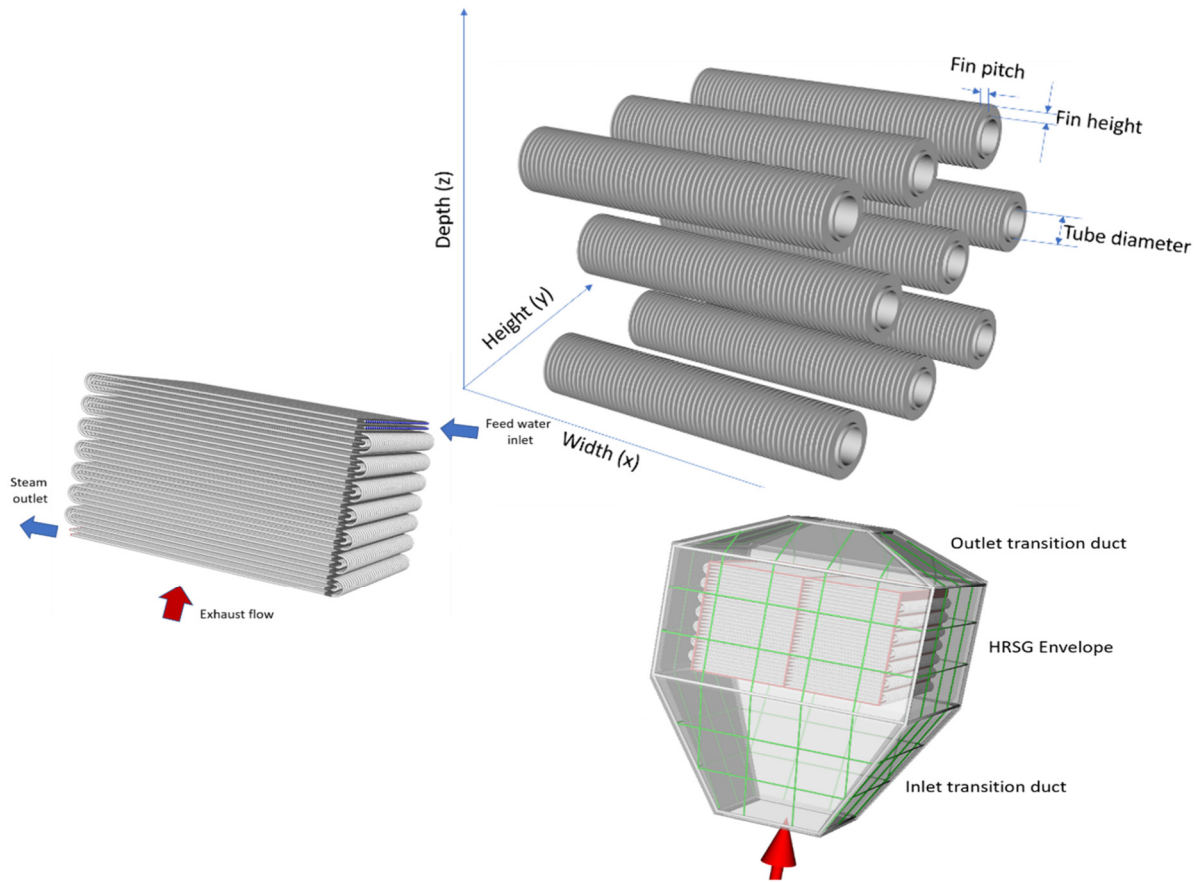
Figure 1: Illustrations of OTSG geometry.
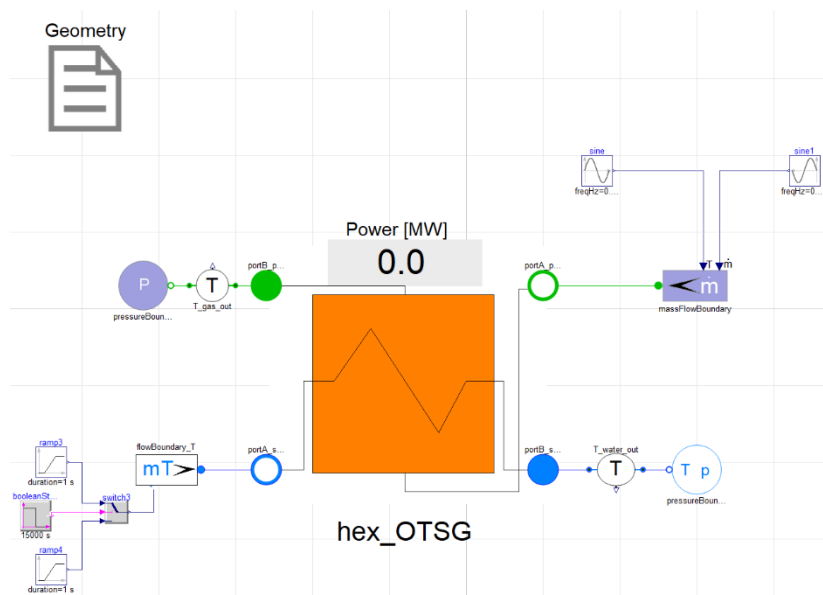
Figure 2: The OTSG model as implemented in the Dymola graphical interface. The inlets are here configured with either step changes or sinusoidal changes.

Figure 2 shows the OTSG model in the graphical interface of Dymola. It has two inlet connections, one for the gas and one for the feed water, and two corresponding outlet connections. When response to change is investigated it mainly entails effects on outlet temperature, as recorded by the sensors shown in the figure, when temperature and/or mass flows are altered at the inlets.

The model uses a discretised volume approach, where mass, momentum and energy balances can be applied to finite volume elements of each fluid as well as the wall between them. The number of discretised volumes in parallel is a parameter of the model. Its default value is equal to the number of water tube rows, which is 32 for the geometry used for this study.

Simulations and model characterisation

Three simulation based studies were conducted in order to characterise the model:

- Response to step change in waste heat load (upstream gas turbine load). Gas inlet temperature and mass flow were reduced from 100 % down to 60 % and up again.
- Response to continuous change in waste heat load (upstream gas turbine load). Periodic oscillations of the gas turbine load were imposed. The time delay characteristic caused by the thermal and fluid damping was analysed and overall time-response of the combined power plant system is shown, following the method proposed by Shin et al. [12] to characterise the amplitude of variation in outlet conditions depending on frequency of inlet variation.
- Model discretisation analysis. Changing the discretisation of the model was investigated. Multiples of the default value of 32 were used, from n = 4 to n = 256. Trade-offs for fast simulations versus low accuracy were analysed.

Results

Response to step change

Model response to a step change in gas turbine load has been investigated, here emulated by a reduction of gas inlet temperature and mass flow from 100 % down to 60 % and up again. The transients studied were the time required for the outlet temperatures to fully transition from one steady state to another. The results of this simulation are shown in Figure 3. There is a distinct time delay in the transition to a new steady state following a step like this, affected by the rate of heat transfer and the volume of both wall and fluid in the system.
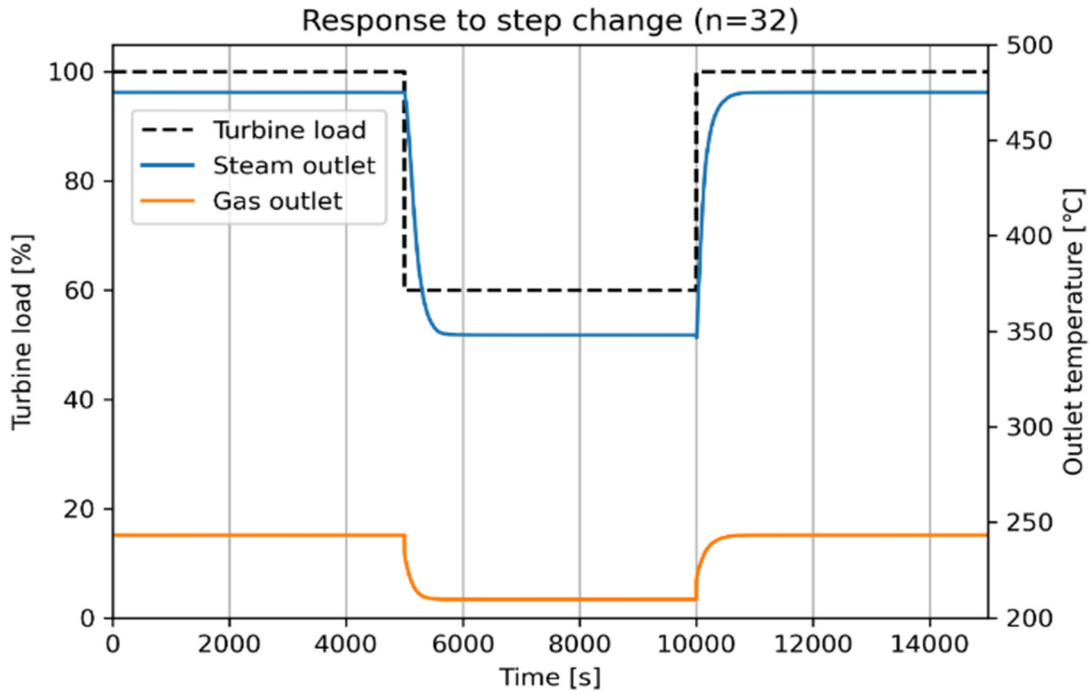
Figure 3: Step change simulation, with turbine load input on the left axis and outlet temperatures on the right axis.

Figure 4 shows the time scale of this transient period in greater detail. It can be seen that the time scales of these transients are in the order of hundreds of seconds, with the gas side being somewhat quicker than the steam side. This is expected to be the slowest response time in all components of a typical steam bottoming cycle, making it a vital parameter for overall system control [13].
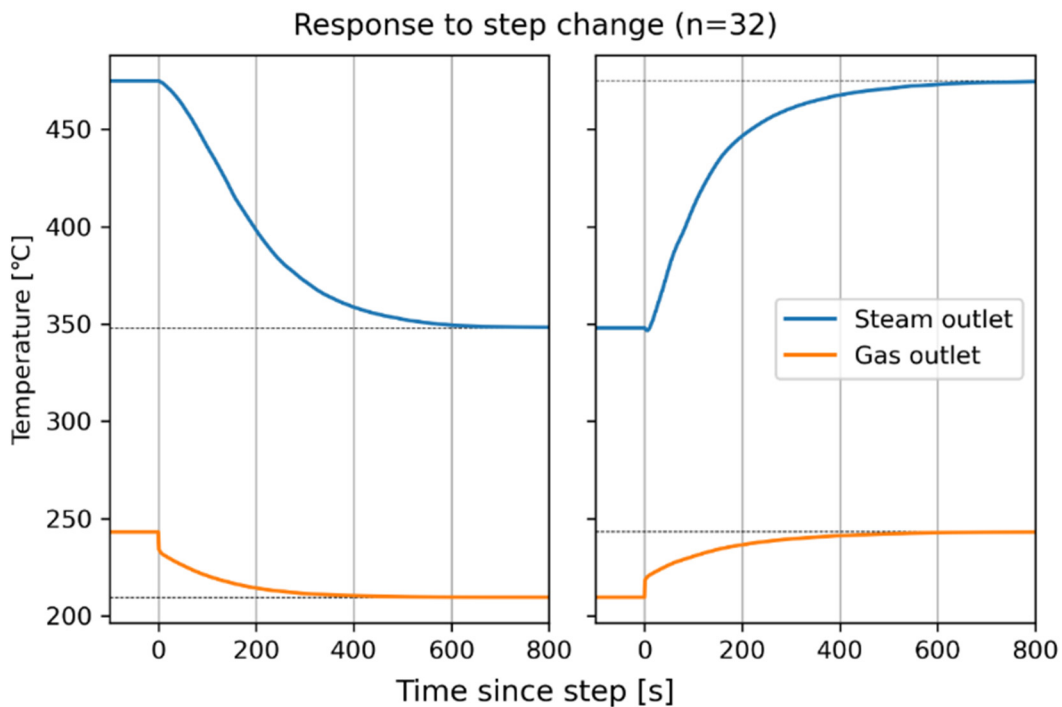
Figure 4: Transients following a step change.

Response to continuous change

The OTSG model has also been studied under continuous change, with the inlet conditions representing gas turbine load were varied between 90 % and 80 % in a sinusoidal manner. Several simulations were performed, with the amplitude being kept constant at 5 %, and the frequency varied between 1 Hz and 10^{-5} Hz. Figure 5 shows the variations in gas turbine load used for the gas inlet and the resulting variations in gas and steam outlet temperature for selected frequencies.
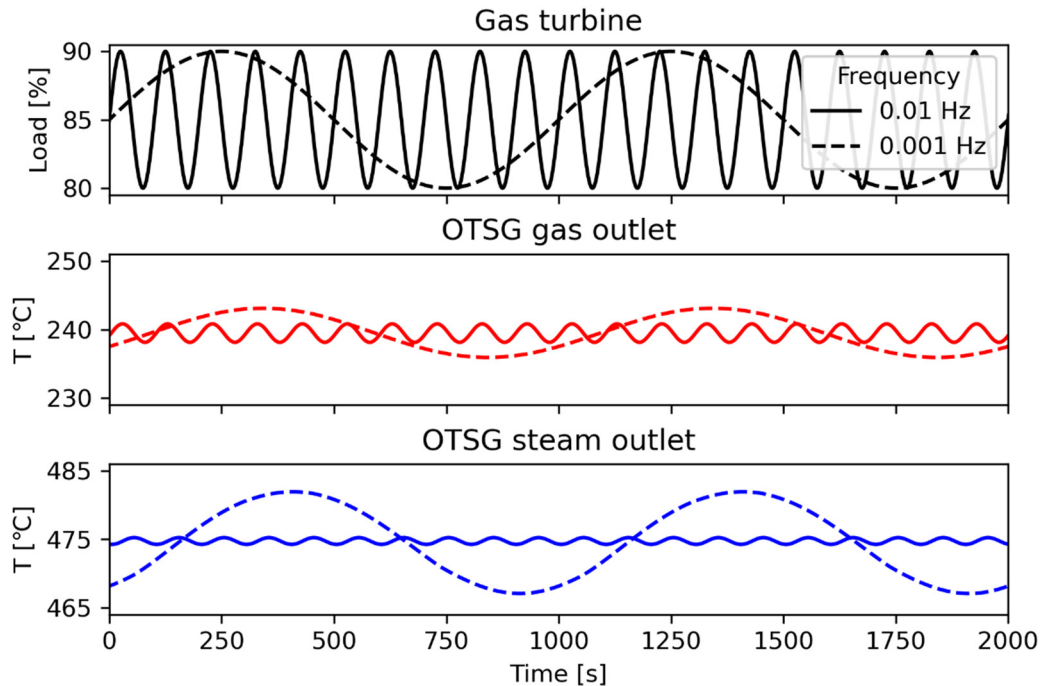
Figure 5: Variations in OTSG gas inlet and resulting variations in gas outlet and steam outlet for frequencies of 10^{-2} and 10^{-3} Hz.

The outlet conditions naturally vary in the same sinusoidal manner as the inlet conditions, with a time delay. This delay prevents the amplitude of the outlet conditions from rising when the frequency is quicker than the time needed for the system to react. These amplitudes are shown as a function of frequency in Figure 6. Here it can be seen that the impact of sinusoidal variations in gas turbine load is negligible when the frequency is significantly quicker than the time delay of the system, and that it reaches a maximum when the frequency is sufficiently slow to where the system is in a quasi-steady state. The frequencies between these states match the characteristic times of the step change transients in order of magnitude.
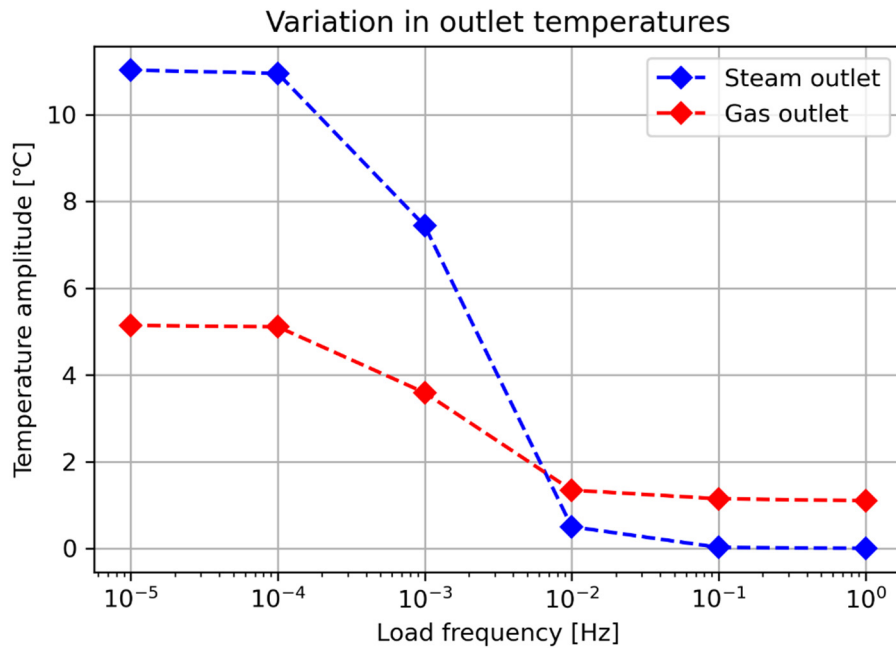
Figure 6: Amplitude of variation in outlet conditions depending on frequency of inlet variation.

Effect of discretisation

Lastly, the effect of changing the discretisation of the model was investigated. Multiples of the default value of 32 were used, from n = 4 to n = 256. The complexity of the model increases with the number of volume elements, as shown in Table 2.

While the number of equations, variables and states all vary linearly with n, their increase has an adverse effect on the simulation speed. Table 2 also includes the time spent simulating the step change from Figure 3 for the various values of n.

Table 2: Selected model statistics at different discretisations.

n	*Original model*		*Translated model*				*Result*
	Variables	Equations	Parameters	States	Nonlinear equations	Equations after manipulation	Simulation time
4	3464	540	9	8	88	14	0.3 s
8	3880	656	13	16	180	26	0.9 s
16	4712	888	21	32	364	50	3.1 s
32	6376	1352	37	64	732	98	15 s
64	9704	2280	69	128	1468	194	73 s
128	16360	4136	133	256	2940	386	438 s
256	29672	7848	261	512	5884	770	4995 s

Heat Powered Cycles Conference 2023
Edinburgh
Heat in the new energy system
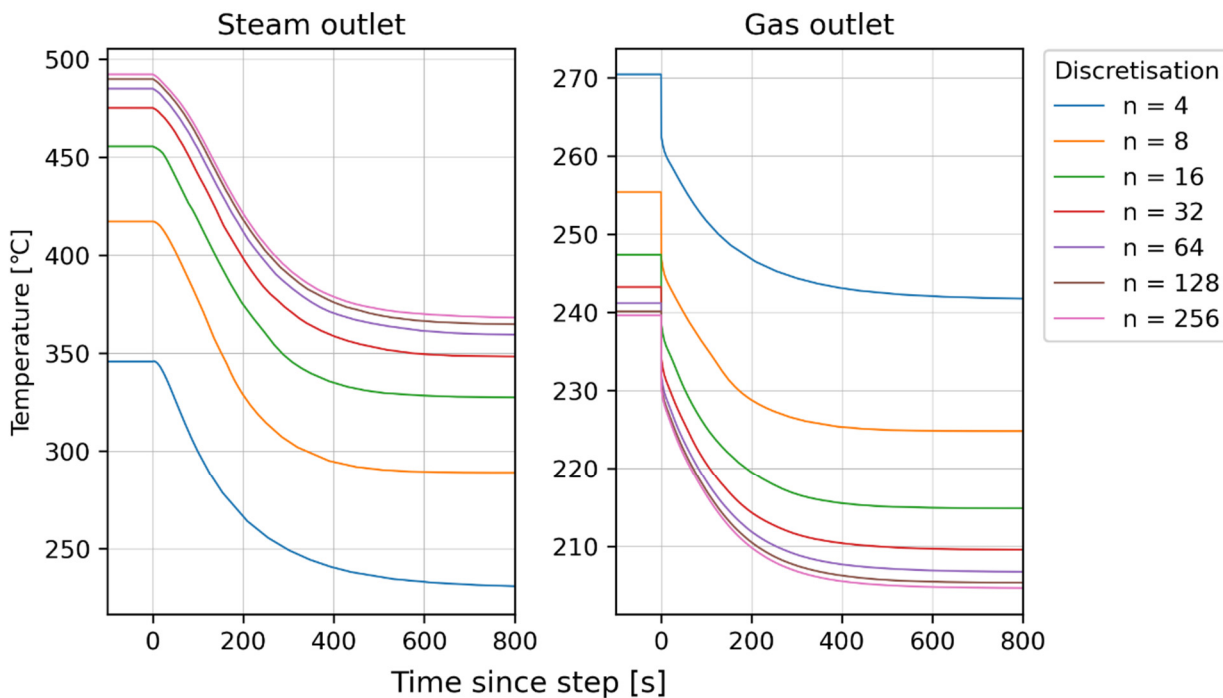
Figure 7: Step change response at various discretisations.

The expected trade-off for fast simulations would typically be low accuracy. Figure 7 shows what the step change simulation results look like for various discretisations. It can be seen that the transient behaviour is similar for all simulations, but that the steady state temperatures of the two fluids vary significantly. They both appear to approach a value as the discretisation increases, and the same is true for the overall duty of the simulated OTSG. Figure 8 compares the steady state temperature of the steam (at 100 % gas turbine load) to the simulation time at various discretisations.
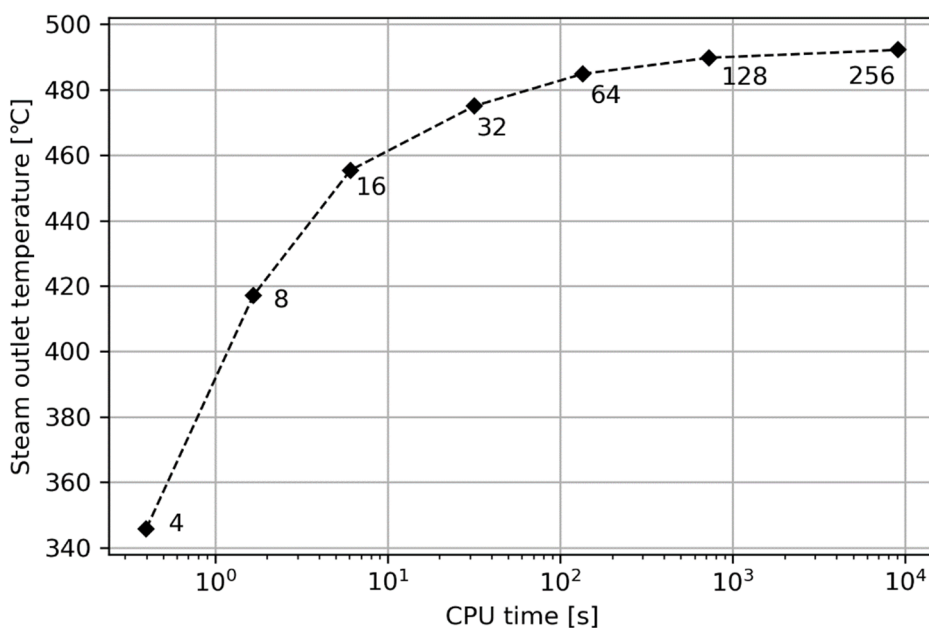
Figure 8: Steady state temperature of steam versus simulation time.

It should be noted that the assumption that the model approaches an increasingly accurate value may be an oversimplification. The default discretisation of 32 is chosen to be equal to the number of rows of water pipes in the original geometry. As the real OTSG is a cross-flow heat exchanger where the gas actually interacts with 32 discrete water tubes in turn, increasing the model discretisation above this may impose false characteristics on the gas side. This does not mean that a model with n = 32 is perfectly accurate either, as it would not account for the water temperature rising along the length of a tube.

Conclusions

From these results it can be seen that the response time of the OTSG model is in the order of several minutes. This supports the assumption that the OTSG is the slowest component in the bottoming cycle, and will be of relevance for control system design.

The transient behaviour appears unaffected by the number of discretised volume elements, but the modelled duty of the OTSG is not. This implies that a low discretisation model could be modified for use in a faster, complete system simulation model of the entire bottoming cycle. A reliable method for determining the true duty would for this approach be required to serve as a reference. Further work should explore surrogate modelling approaches based on data driven methods using this model as a reference to generate synthetic data.

Acknowledgments

References:

[1]   M. F. Brady, 'Design aspects of once through systems for heat recovery steam generators for base load and cyclic operation', Materials at High Temperatures, 2001, doi: 10.1179/mht.2001.024.

[2]   M. J. Mazzetti, B. A. L. Hagen, G. Skaugen, K. Lindqvist, S. Lundberg, and O. A. Kristensen, 'Achieving 50% weight reduction of offshore steam bottoming cycles', Energy, 2021, doi: 10.1016/j.energy.2021.120634.

[3]   R. M. Montañés, G. Skaugen, B. Hagen, and D. Rohde, 'Compact Steam Bottoming Cycles: Minimum Weight Design Optimization and Transient Response of Once-Through Steam Generators', Frontiers in Energy Research, 2021.

[4]   Modelica Association, 'Modelica® - A Unified Object-Oriented Language for Systems Modeling', Language Specification, vol. Version 3.4, 2017.

[5]   Dassault Systemes, 'DYMOLA Systems Engineering'. 2021.

[6]   'Thermal Power Library', *Modelon*. https://modelon.com/library/thermal-power-library/ (accessed Dec. 09, 2022).

[7]   F. E. Cellier, *Continuous System Modeling*. New York, NY: Springer, 1991. doi: 10.1007/978-1-4757-3922-0.

[8]   F. Casella and A. Leva, 'Modelling of thermo-hydraulic power generation processes using Modelica', Mathematical and Computer Modelling of Dynamical Systems, 2006, doi: 10.1080/13873950500071082.

[9]   P. J. Dechamps, 'Modelling the Transient Behaviour of Heat Recovery Steam Generators', Proceedings of the Institution of Mechanical Engineers, Part A: Journal of Power and Energy, 1995, doi: 10.1243/PIME_PROC_1995_209_005_01.

[10] G. Skaugen, K. Kolsaker, H. T. Walnum, and Ø. Wilhelmsen, 'A flexible and robust modelling framework for multi-stream heat exchangers', Computers & Chemical Engineering, 2013, doi: 10.1016/j.compchemeng.2012.10.006.

[11] R. M. Montañés, M. K. Windfeldt, G. Skaugen, and L. E. Andersson, 'A framework for physics based off-design and dynamic modelling and simulation of combined cycle power plants in weight and volume constraint environments', presented at the Heat Powered Cycles Conference 2023, Edinburgh, Scotland, 2023.

[12] J. Y. Shin, Y. J. Jeon, D. J. Maeng, J. S. Kim, and S. T. Ro, 'Analysis of the dynamic characteristics of a combined-cycle power plant', Energy, 2002, doi: 10.1016/S0360-5442(02)00087-7.

[13] L. O. Nord and R. M. Montañés, 'Compact steam bottoming cycles: Model validation with plant data and evaluation of control strategies for fast load changes', Applied Thermal Engineering, 2018, doi: 10.1016/j.applthermaleng.2018.07.012.

Liter-scale sorption based atmospheric water harvester by heat-powered integrated compact module

Zhihui Chen[1], Shuai Du[1] and Ruzhu Wang[1*]

[1]Institute of Refrigeration and Cryogenics, MOE Engineering Research Center of Solar Power and Refrigeration, Shanghai Jiao Tong University, Shanghai 200040, China

[*]Corresponding author: rzwang@sjtu.edu.cn

Abstract

Sorption-based atmospheric water harvesting as an appealing way to address the global water shortage can obtain water from air anytime and anywhere. However, achieving high water yield by using a small-size device in the semi-arid climate is still a challenge. Here, a portable and compact atmospheric water harvester with low-cost composite sorbent SG@Li was proposed to realize high water yield of hundred-gram one cycle and thousand-gram one day (three cycles). The indoor (near no wind) and outdoor (windy) test results presented that the water harvester produced 320 and 370 g clean water with low energy consumption of 606 and 595 mL/kWh in one cycle under the simulated and real semi-arid climate. When the desorption experiment is repeated twice within one day, the accumulated water yield could reach 960~1110 g/day. This remarkable output performance promotes the availability of large-scale atmospheric water production and practical application.

Keywords: Atmospheric water harvesting, Composite sorbent, Water harvester, High water yield.

Introduction

Water scarcity has become a global problem, thus urgently calling for efficient freshwater production techniques to alleviate it.[1] Sorption-based atmospheric water harvesting (SAWH) as a novel way to obtain water from air at anytime and anywhere has great potential to supply clean water for the arid and remote areas.[2]

The output performance of SAWH system mainly depends on the sorbent materials, the device, and the match between the two components.[3] By now, various sorbents have been developed to achieve rapid and sufficient water harvesting such as zeolite, silica gel (SG), hygroscopic salts, hydrogel, metal–organic frameworks (MOFs) and lots of composite sorbents.[4-6] Among these sorbents, SG as a classic hygroscopic material with the features of porous structure, low cost, and easy regeneration, has been commercially mass-produced. However, the weak sorption capacity limits SG's practical applications. By contrast, hygroscopic salts such as LiCl and $CaCl_2$ have strong hygroscopicity which are preferred for AWH in arid regions, but this kind of materials are prone to deliquescence, leakage and corrosion.[7] Therefore, salt-based composite sorbent was proposed to combine the hygroscopic salt with porous matrix, thus resulting in satisfactory water sorption capacity in a wide humidity range.[8] For the material synthesis method, physical immersion method under room temperature is easy to operate and suitable for mass production with cheap cost. Therefore, SG as the porous matrix was immersed into the LiCl solution to synthesize SG@Li composite sorbent.

Although various efficient sorbents were developed, the water yield of SAWH device has not made a great breakthrough in recent years.[9,10] Therefore, structure optimization of the device to enhance the heat and mass transfer for material and device matching is vital for rapid and abundant water production.[11] For the passive SAWH device powered by solar

energy, the water production rate is largely influenced by the intensity of solar desorption, which is unstable and uncontrollable.[12] In comparison, active SAWH device powered by electric heating enables better matching of the sorption and desorption processes by adjusting desorption temperature and duration. When there is a certain demand for daily drinking water, the device supplied by active energy could meet high water yield within a limited time.[13] Besides, if the laboratory results want to be translated into practical product, the cost and benefit also need to be considered.

In this work, a portable and integrated compact atmospheric water harvester with cheap material SG@Li as the sorbent was introduced to achieve high water yield of hundred-gram one cycle and thousand-gram one day (three cycles) under semi-arid climate. The sorbent basket filled with 1.5 kg SG@Li particles exhibited superb water uptake capacity of 159, 267 and 394 g at 30%, 50% and 80% RH within 12 h. Furthermore, in order to narrow the gap between materials science and engineering application, the heat and mass transfer inside the device was carefully designed and optimized to obtain sufficient freshwater within a limited time rapidly. The indoor (near no wind) and outdoor (windy) test results showed that the portable atmospheric water harvester achieved high water production yield of 320 and 370 g with low energy consumption of 0.528 and 0.622 kWh in one sorption-desorption cycle under the simulated and real semi-arid climate. When the desorption experiment is repeated twice within one day which corresponds to a batch operation model (three baskets capture moisture overnight and desorb water in turn during the day), the accumulated water yield could reach 960~1110 g/day with low energy consumption (606~595 mL/kWh). The integrated compact thermal design requested the whole unit only 7.54 liters. This remarkable output performance of the small-size SAWH device brings the SAWH technology one step closer to practical market application.

Results and Discussion

The sorbent SG@Li was synthesized by an impregnation method under room temperature as shown in **Figure 1a**. An LiCl solution with a mass concentration of 35% was pre-prepared. The selection of LiCl solution's mass concentration was based on a series of pre-experiments. Then the silica gel particles were immersed into the LiCl solution for 24 h. During the immersion process, the SG materials were stirred every few hours so that the LiCl solution could penetrate fully into SG's porous structure. Next, the wetted SG particles were transferred into a drying oven at 100 °C for 12 h to completely dry out the remaining water. Finally, the synthesized SG@Li composite was encapsulated carefully. Figure 1b demonstrates the digital photographs of SG@Li composite in its dehydrated and hydrated states. The color of the composite particles changes obviously after capturing moisture. Furthermore, the scanning electron microscope (SEM) image and energy disperse X-ray spectroscopy (EDS) mapping in Figure 1c illustrated that the LiCl particles were uniformly coated on the surface of SG. When the composite was exposed to the air, hydrogen bonds were formed between SG and water molecules, and hydration occurred between LiCl and water molecules.[14]
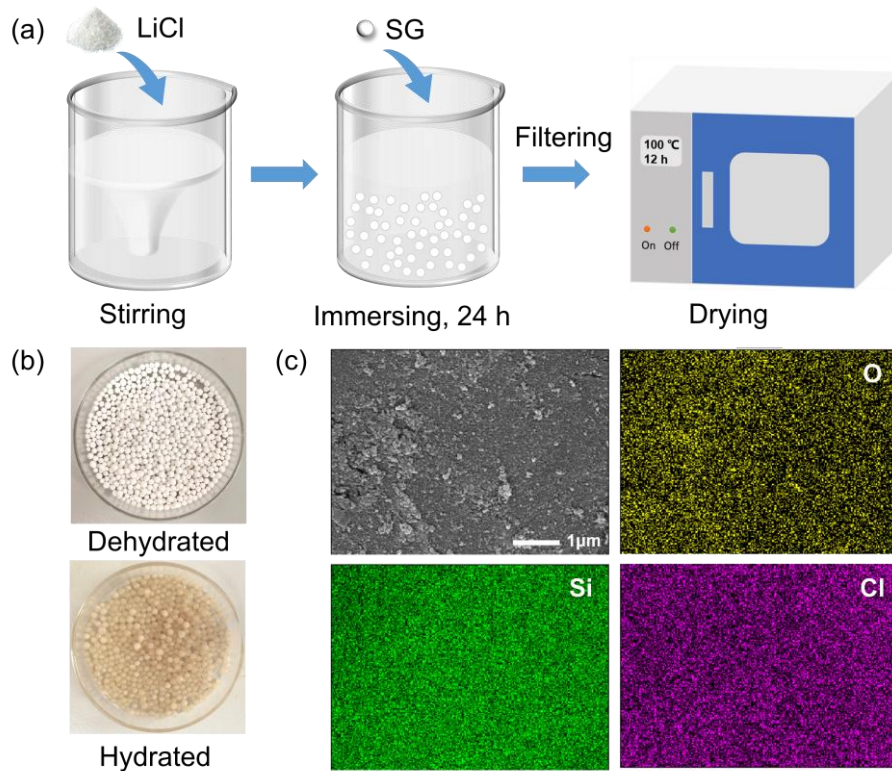
Figure 1. Synthesis and characterization of SG@Li. (a) Synthesis process of the SG@Li composite. (b) Digital photographs of SG@Li in dehydrated and hydrated states. (c) EDS mapping of the synthesized SG@Li composite displaying the element distribution.

For the synthesized sorbent SG@Li, its dynamic water uptake curves under various working conditions (30, 50, 80% RH and 25 °C) were obtained by using 20 g sample. The test results in **Figure 2a** indicated that SG@Li exhibited acceptable hygroscopic performance in the simulated arid, semi-arid and humid conditions with low synthesis cost. Figure 2b presented the water sorption isotherms of both SG and SG@Li obtained by a modified accelerated surface area and porosimeter (ASAP) under 25 °C. By comparing the two curves, it was noticed that the addition of LiCl into SG enhanced its water uptake capacity significantly. Salt-based composite sorbent possessed both the excellent hygroscopicity of hygroscopic salt and intrinsic pore structure of porous matrix, making it more available for AWH.[15] Moreover, the cycling stability of SG@Li was tested through STA test. The sorption and desorption conditions were set as 30 °C, 50% RH and 85 °C, 5% RH respectively. Through eight consecutive sorption-desorption tests in Figure 2c, the material still maintained stable sorption capacity after more than 84 hours testing. All the test results indicated that SG@Li had the potential to be applied for large-scale water production with acceptable water uptake capacity and cheap synthesis cost.

Here a portable water harvester with integrated sorbent basket and fin-enhanced condenser was proposed for daily water production as shown in **Figure 3a**. Before testing the water harvesting performance of the device, the dynamic water uptake curves of the sorbent basket filled with SG@Li particles were also measured under 30, 50, 80% RH and 25 °C. The size of the designed sorbent basket was 230*33*300 mm and the basket was divided into two layers with 15 mm thickness by a metal heating plate in the middle. 1.5 kg sorbent materials were filled inside. The test results in Figure 2d showed that the water uptake capacity of the sorbent basket at 30, 50, 80% RH for 12 h could reach 159, 267 and 394 g, respectively. Although compared with test sample with 20 g, the water uptake capacity of per unit mass material in sorbent basket was low, in practical applications there are usually requirements for the volume, occupied area and weight of

**Heat Powered Cycles
Conference 2023**
Edinburgh

Heat in the new energy system

*3rd to 6th of September 2023
The University of Edinburgh, Scotland*

the device, all of which make tight packing between sorbent particles inevitable.[16] Therefore, optimizing the heat and mass transfer in sorbent layer is vital to narrow the gap between materials science and engineering application.[17] Figure 3b exhibited the basic heat and mass transfer process of this device for water collection. During the desorption process, the heat generated by the electric heating rod desorbed the water inside the sorbent basket. Then the generated water vapor diffused from the desorption chamber to the condensation chamber driven by the concentration and density difference. When the hot vapor made contact with the cold wall, it quickly released heat and condensed into liquid water. The condensed water then fell down the wall by gravity and was collected in the water tank.
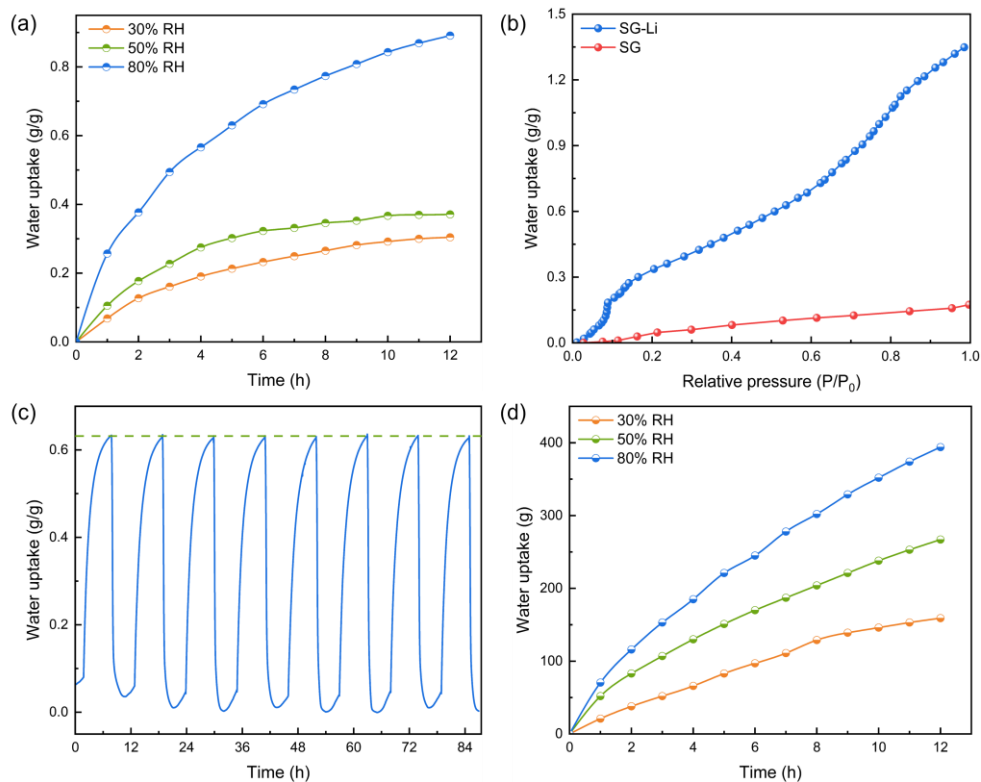
Figure 2. Water sorption performance of SG@Li. (a) Dynamic water uptake curves of SG@Li with 20 g. (b) Water sorption isotherms of both SG and SG@Li. (c) Cycling stability test of SG@Li. (d) Dynamic water uptake curves of SG@Li with 1.5 kg in sorbent basket.

To evaluate the availability of the designed water harvester, an indoor experiment was conducted under laboratory conditions. The device was placed indoors with about 20 °C room temperature and near no wind. The operation model was set as 15-hour sorption process and 3-hour desorption process with a heating temperature of 135 °C to achieve both the high water yield and low power consumption based on pre-experiments. The ambient conditions for sorbent basket to capture moisture were set as 25 °C and 50% RH. Figure 3c illustrated the temperature variations of the top cover (the outer surface of the top cover covered with thermal insulation cotton), inside chamber (the space between the desorption and condensation chamber), finned surface (the surface of the fin radiator sticked to the outside surface of the device), and outside surface (the outside surface of the device without fin radiator) during the whole desorption process. The temperature of the top cover could reach an equilibrium value of 122 °C within 42 min. Both the temperature of outside and finned surfaces also reached equilibrium within 42 min. The temperature difference between desorption and condensation chamber was about 40 °C which ensured an efficient condensation process. Moreover, it was noticed that the equilibrium temperature of the finned surface was about 6 °C lower than that of the outside surface, proving effective heat dissipation to the surroundings.

For this one-cycle water harvesting test in the laboratory, when the desorption time was up to 3 h, the water yield of the device reached 320 g with an energy consumption of 0.528 kWh, which meant an extraordinary water yield index of 606 g/kWh compared with the existing research results. It was worth mentioning that for this single-day experiment, besides 15 h sorption process and 3 h desorption process, there was still 6 h remaining time, which meant that the desorption experiment could be repeated twice. Therefore, a batch type operation model could be used. Three sorbent baskets were placed in the humid environment to capture moisture overnight. During the day, the three sorbent baskets were moved into the atmospheric water harvester to desorb water one by one, so that the accumulated water yield could reach 960 g/day under the laboratory conditions.

Based on the indoor laboratory test, the outdoor field test of the water harvester was conducted in the region of southwest China (Kunming, Yunnan). The operation model also consisted of 15-hour overnight sorption and 3-hour daytime desorption process. Before the sorbent basket was moved into the water harvester to release moisture, it was placed outdoors overnight (average climatic conditions of 12.8 °C and 65% RH) to absorb moisture. The average climate conditions during the daytime were 16.0 °C and 45.3% RH. Compared with the temperature curves in Figure 3c, the temperature of inside chamber in Figure 3d reached about 100 °C after 45 min and remained stable. While the temperature of the outside surface gradually dropped from 88 °C to 49 °C after an initial period of rapid temperature rise. Besides, the temperature of finned surface in this outdoor test was about 15 °C lower than that of the outside surface on average. All of these changes were mainly due to the better heat dissipation conditions caused by outdoor wind. When the condensation heat was dissipated rapidly, the water vapor condensation process could be carried out quickly and continuously. As the remaining uncondensed water vapor gradually decreased, the condensation temperature also decreased.

Figure 3e recorded the water yield (water sorption, desorption and collection capacity) and energy consumption for both the indoor and outdoor experiments. The results illustrated that when the whole AWH system was moved outside, its water yield increased to 370 g with a higher energy consumption of 0.622 kWh under the windy condition. When the desorption experiment is repeated twice as described above, the accumulated water yield could reach 1110 g/day under the real outdoor conditions which was a remarkable promotion. In addition, the quality of collected water was tested by an ion chromatograph. As shown in Figure 3f, the water produced by the atmospheric water harvester met the drinking-water standard of World Health Organization (WHO).[18]
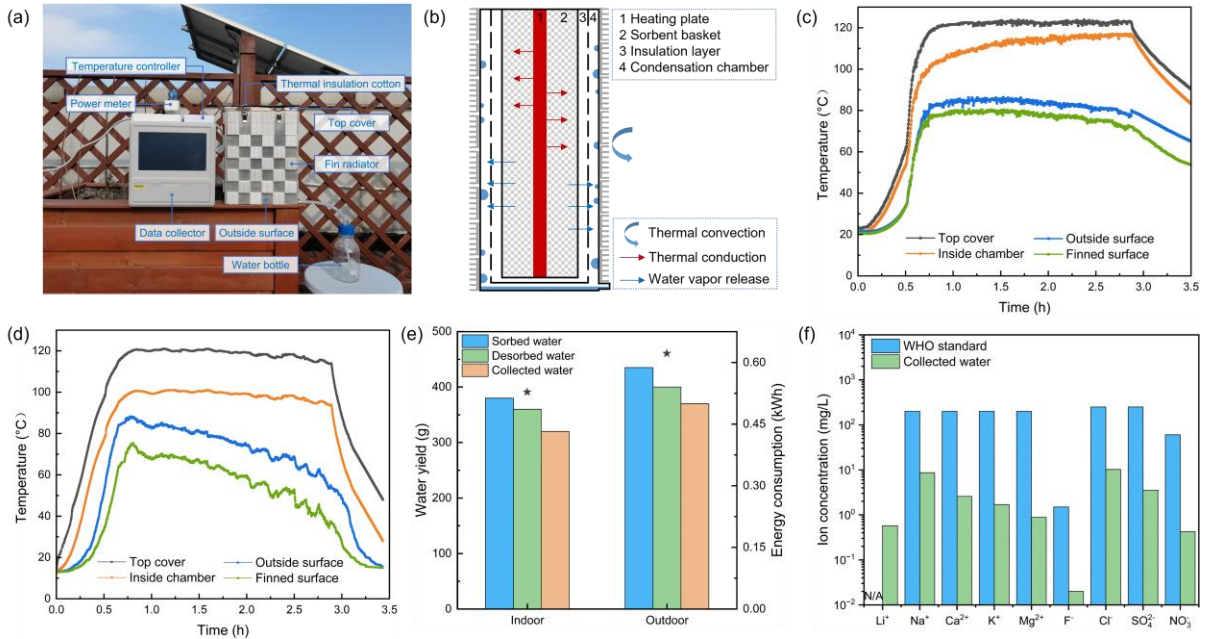
Figure 3. Water harvesting performance of the integrated water harvester. (a) Photo of the whole AWH system. (b) Heat and mass transfer process inside the device during the desorption process. (c) Temperature variations of the top cover, inside chamber, finned surface, and outside surface during the indoor desorption process. (d) Temperature variations of the top cover, inside chamber, finned surface, and outside surface during the outdoor desorption process. (e) Water yield and energy consumption of the water harvester under indoor and outdoor conditions. (f) Test results of the quality of the water produced from the water harvester.

The above indoor and outdoor test results indicated that by implementing multi-cycle desorption strategy as shown in **Figure 4a**, the daily water production yield of small-size AWH device could reach an order of 1,000 grams, which is a remarkable process pushing AWH technology to the future market. This infusive water productivity (960~1110 g/day) with low energy consumption (606~595 mL/kWh) make this portable device a viable approach to relieve the global water crisis. It need to be clarified that the whole integrated unit is only with a volume of 7.54 liters. Furthermore, the SG@Li composite sorbent can be easily mass- synthesized which is suitable for large-scale water production with low material cost. When the AWH device is put into the market, in addition to the water yield, economic factors such as materials cost and energy consumption and quality factors such as cycle stability and service life also need to be taken into account (Figure 4b). Meanwhile, the compact and detachable design concept makes the AWH device more portable and adaptable for practical applications.
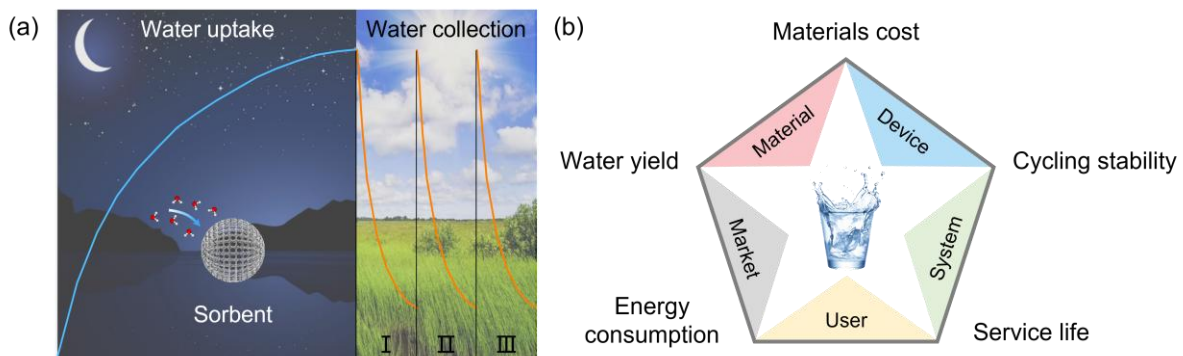
Figure 4. Outlook of the AWH technology. (a) Schematic illustration of multi-cycle desorption strategy for high water yield. (b) A series of factors that need to be considered when AWH devices are put into the market.

Conclusions

In this study, a portable and integrated compact atmospheric water harvester was proposed and fabricated by using a low-cost material SG@Li as the sorbent to capture moisture from air and release water through rapid electric heating method. The SG@Li composite particles were encapsulated in a sorbent basket exposed to the atmosphere overnight obtaining moisture, and transferred to the heat-powered water harvester during the day producing water. By optimizing the heat and mass transfer process inside the device, the compact water harvester showed an extraordinary output performance of high water yield (960~1110 g/day) with low energy consumption (606~595 mL/kWh) in the indoor and outdoor tests under semi-arid climate conditions. Based on the practical application of AWH, this study designed and optimized the water harvester from feasibility, economy, portability, sustainability and other aspects. It is believed that this study could promote AWH towards high water yield, low energy consumption, low cost, small size, scalability and other indicators which are suitable for market application.

Acknowledgments

References:

[1] Lord, J., Thomas, A., Treat, N. et al., "Global potential for harvesting drinking water from air using solar energy", Nature, 2021.

[2] Ejeian, M., Wang, R. Z., "Adsorption-based atmospheric water harvesting", Joule, 2021.

[3] Wang, J. Y., Hua, L. J., Li, C. F., Wang, R. Z., "Atmospheric water harvesting: Critical Metrics and Challenges", Energy & Environmental Science, 2022.

[4] Lu, H. Y., Shi, W., Guo, Y. H. et al., "Materials engineering for atmospheric water harvesting: progress and perspectives", Advanced Materials, 2022.

[5] Xu, W. T., Yaghi, O. M., "Metal-organic frameworks for water harvesting from air, anywhere, anytime", ACS Central Science, 2020.

[6] Deng, F. F., Chen, Z. H., Wang, C. X. et al., "Hygroscopic porous polymer for sorption-based atmospheric water harvesting", Advanced Science, 2022.

[7] Zhang, S., Fu, J. R., Das, S. et al., "Crystalline porous organic salt for ultrarapid adsorption/desorption-based atmospheric water harvesting by dual hydrogen bond system", Angewandte Chemie International Edition, 2022.

[8] Shan, H., Li, C. F., Chen, Z. H. et al., "Exceptional water production yield enabled by batch-processed portable water harvester in semi-arid climate", Nature Communications, 2022.

[9] Hanikel, N., Prévot, M. S., Yaghi, O. M., "MOF water harvesters", Nature Nanotechnology, 2020.

[10] Xu, J. X., Li, T. X., Yan, T. S. et al., "Ultrahigh solar-driven atmospheric water production enabled by scalable rapid-cycling water harvester with vertically aligned nanocomposite sorbent", Energy & Environmental Science, 2021.

[11] LaPotin, A., Kim, H., Rao, S. R., Wang, E. N., "Adsorption-based atmospheric water harvesting: impact of material and component properties on system-level performance", Accounts of Chemical Research, 2019.

[12] Li, Z. T., Xu, X. T., Sheng, X. R. et al., "Solar-powered sustainable water production: state-of-the-art technologies for sunlight-energy-water nexus", ACS Nano, 2021.

[13] Tu, Y. D., Wang, R. Z., Zhang, Y. N., Wang, J. Y., "Progress and expectation of atmospheric water harvesting", Joule, 2018.

[14] Legrand, U., Castillo Sánchez, J. R., Boudreault, R. et al., "Fundamental thermodynamic properties of sorbents for atmospheric water capture", Chemical Engineering Journal, 2022.

[15] Xu, J. X., Li, T. X., Chao, J. W. et al., "Efficient solar-driven water harvesting from arid air with metal-organic frameworks modified by hygroscopic salt", Angewandte Chemie International Edition, 2020.

[16] Chen, Z. H., Shao, Z., Tang Y. C. et al., Study of the scale-up effect on the water sorption performance of MOF materials", ACS Materials Au, 2022.

[17] Tao, Y. l., Wu, Q. N., Huang, C. et al., "Electrically heatable carbon scaffold accommodated monolithic metal–organic frameworks for energy-efficient atmospheric water harvesting", Chemical Engineering Journal, 2023.

[18] World Health Organization, Guidelines for Drinking-Water Quality, 4th edition, 2017.

Experimental evaluation of barium bromide-ammonia equilibrium lines

J. A. Locke[1*], **G. H. Atkinson**[1], **G. S. F. Shire**[1], **R. E. Critoph**[1] and **S. J. Metcalf**[1]

[1]Sustainable Thermal Energy Technologies, University of Warwick, Coventry, UK

[*]Corresponding author: j.a.locke@warwick.ac.uk

Abstract

This work has experimentally evaluated the position of $BaBr_2$ and ammonia equilibrium lines. $BaBr_2$ samples, contained in discs of ENG, were placed in an experimental rig and a new methodology, termed the Fast Temperature Ramp (FTR), was used to reveal adsorption and desorption reactions. Reaction onset points were plotted to generate equilibrium lines and calculate reaction enthalpies and entropies. Significant hysteresis between adsorption and desorption reactions was found, with the degree of hysteresis increasing as the salt becomes more deammoniated. The hysteresis effect was greatest for $BaBr_2$ (2-1)/(1-2) and $BaBr_2$ (1-0)/(0-1) reactions and also increased at higher pressures, exceeding 20°C at 900 kPa for $BaBr_2$ (1-0)/(0-1). Adsorption reactions were found to occur over a very small temperature range, giving rise to a single transition 'zone' less than 20°C wide. TGA experiments confirmed the position of equilibrium lines, although they were not successful in differentiating between two ammoniated states.

Keywords: barium bromide, chemisorption, ammonia, adsorption, desorption.

Introduction/Background

Reversible reactions between metal-halide salts and ammonia have been successfully exploited in recent years for heat pumping, thermal transformation and thermal storage applications. These reversible chemical reactions offer some of the highest reaction enthalpies available. However, there are only a limited number of candidate salts whose reactions occur within the -20°C to 200°C temperature range and 0.1 to 10 bar pressure range, constraining the operating conditions of these technologies. Experimental and theoretical studies over the past three decades have focused overwhelmingly on reactions between single salt-chlorides and ammonia [1], with little attention paid to salt-bromides other than a small number of binary-salt experiments, such as those by Gordeeva et al. [2].

The objectives of this work were to evaluate, experimentally, the position of barium bromide and ammonia equilibrium lines. Unlike many halide-salt and ammonia reactions, literature sources [3] indicate that $BaBr_2$ and NH_3 undergoes four reversible adsorption and desorption reactions in quick succession over a relatively small temperature range:

$$BaBr_2 + NH_3 \leftrightarrow BaBr_2 \cdot NH_3 \qquad (1)$$
$$BaBr_2 \cdot NH_3 + NH_3 \leftrightarrow BaBr_2 \cdot 2NH_3 \qquad (2)$$
$$BaBr_2 \cdot 2NH_3 + 2NH_3 \leftrightarrow BaBr_2 \cdot 4NH_3 \qquad (3)$$
$$BaBr_2 \cdot 4NH_3 + 4NH_3 \leftrightarrow BaBr_2 \cdot 8NH_3 \qquad (4)$$
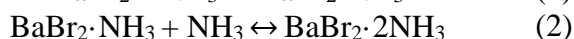
The methodology used in this work is similar to previous work carried out by Wu [4] and further developed by Atkinson [5] and Hinmers [6], where $BaBr_2$ samples, contained in discs of ENG to improve mass transfer and thermal conductivity, were placed in a LTJ experimental rig.

In this work, ENG, $\rho = 150$ kg·m^3 (Sigratherm$^®$ L10/1500, SGL Carbon), was used as a host matrix, onto which barium bromide was deposited using a wet impregnation technique. 10 mm diameter discs were waterjet cut from 10 mm thick ENG board and a 1 mm hole drilled through the centre to allow for the placement of a thermocouple. The samples were then dried and weighed, before being placed into a barium bromide solution for 24 hours at a pressure of 0.1 bar. The solution contained 43.5 g of barium bromide dihydrate (Alfa Aesar, $\geq$ 99.3%) and 100 g water, so that the resulting composite samples contained a greater mass of salt than graphite. Following their removal from solution, the samples were dried at 180°C in an oven until their mass remained constant to remove all water and to ensure that only anhydrous barium bromide was present. Figure 1 shows the appearance of the composite salt-ENG sample prior to ammoniation. Characteristics of the samples used in this work are shown in Table 1.

Figure 1. Waterjet cut ENG discs after impregnation with salt and drying.

Table 1. Sample characteristics

Experiment	Number of discs	ENG mass (g)	Salt mass (g)	Mass ratio (salt:ENG)	Moles of salt
FTR	5	0.633	0.867	1.37:1	2.92x10^{-3}
TGA	2	0.249	0.390	1.57:1	1.31x10^{-3}

The FTR method used an apparatus similar to that used for previous LTJ experiments [6]. Five ENG-salt discs were placed in the inner tube side of a tube-in-tube heat exchanger with the heat transfer fluid, Huber M20.235.20 silicone oil, flowing around the outside. The fluid was connected to an air-cooled circulating bath that provided the fast temperature ramp. The inner tube-side reactor was connected to 7 litre buffer vessels containing ammonia gas, which was all contained inside a temperature-controlled box. A diagram of the FTR experimental setup is shown in Figure 2.
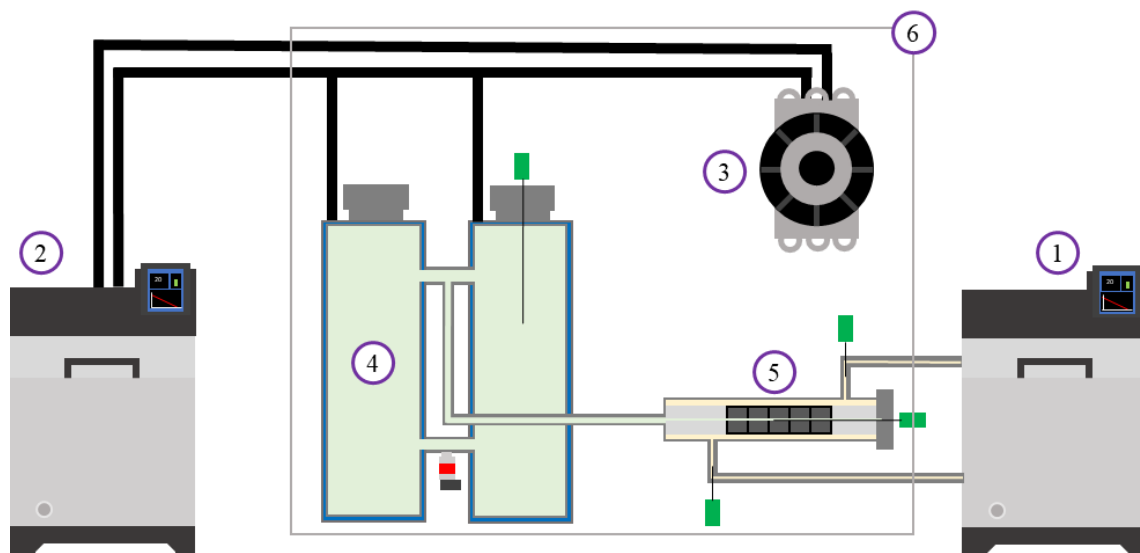
Figure 2. Simplified schematic of the Fast Temperature Ramp (FTR) apparatus, showing (1) reactor bath, (2) bath feeding buffer vessels and fan, (3) fan, (4) buffer vessels, (5) tube-in-tube reactor containing samples and (6) isothermal box. Not to scale.

The samples were then put through a fast temperature ramp, initiating adsorption and desorption reactions, and the resulting pressure change in the attached buffer vessel was then analysed to determine which of the expected ammonia-salt transitions had occurred. The pressure remained near constant throughout the tests.

TGA experiments were also undertaken using a Rubotherm Magnetic Suspension Balance. The instrument separates the sample environment from the balance via a magnetic coupling, allowing for a controlled gaseous environment (in this case ammonia gas) to surround the sample. The pressure was controlled by linking the sample chamber to a receiver containing liquid ammonia. A diagram of the TGA experimental setup is shown in Figure 3.
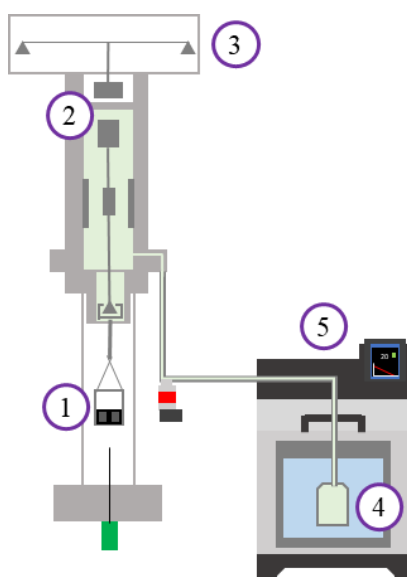
Figure 3. Simplified schematic of the Rubotherm Magnetic Suspension Balance apparatus, showing (1) bucket containing samples, (2) magnetic coupling, (3) balance, (4) receiver containing liquid ammonia and (5) temperature-controlled bath. Not to scale.

Heat Powered Cycles
Conference 2023
Edinburgh
Heat in the new energy system

3rd to 6th of September 2023
The University of Edinburgh, Scotland

Discussion and Results

Figure 4 shows the results of one FTR desorption test. Unlike the LTJ method [5], the FTR test revealed all four reactions. Each reaction onset occurs when the sample temperature deviates away from the reactor wall temperature and is accompanied by a pressure rise. In total, fourteen FTR tests were conducted at a variety of pressures between 1 and 7 bar.
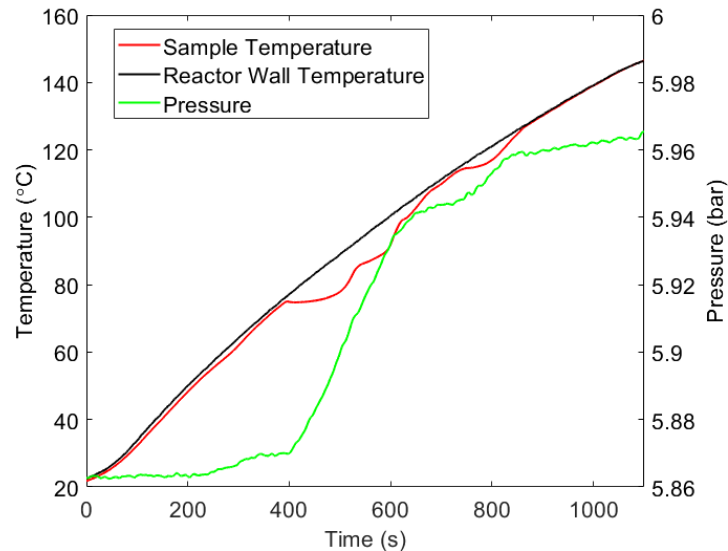
Figure 4. FTR desorption test results showing the four deammoniaton steps of $BaBr_2$.

These results were then further analysed by producing two plots and using a method first introduced by Atkinson [5], where the test results are plotted as (1) temperature against time and (2) pressure against temperature on ln(p) vs -1000/T axes. Figure 5 shows the test results from Figure 4 plotted in this way. The onset of each reaction can be seen by a distinct temperature plateau on Figure 5 (a) and a sharp pressure increase on Figure 5 (b). An equilibrum point was then manually selected at the point that each of the four reactions begin, and the corresponding temperature and pressure values were recorded.

(a)   (b)
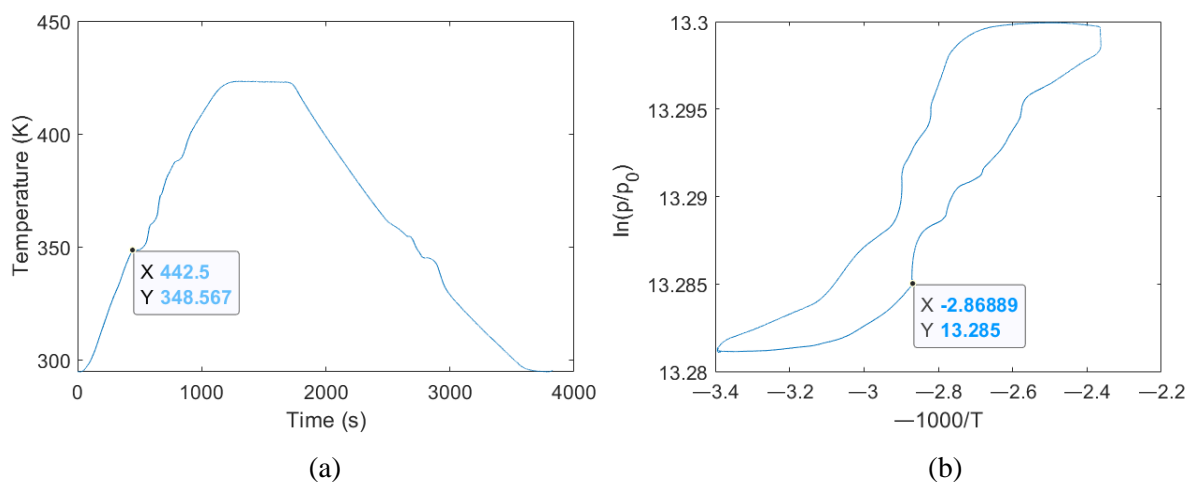
Figure 5. FTR desorption test results showing the four deammoniaton steps of $BaBr_2$.

The Clapyron diagram generated from the FTR tests is shown in Figure 6. A linear regression fit was used to generate the solid adsorption and desorption lines. Also shown in Figure 6 are equilibrium lines derived from literature values obtained from Blitz [7]. The results show that significant hysteresis exists between adsorption and desorption for all four reactions, and that all four adsorption reactions occur over a much smaller range than the desorption reactions. The results also show that the barium bromide and ammonia reaction enthalpy and entropy values are significantly different from the published values previously obtained [7].
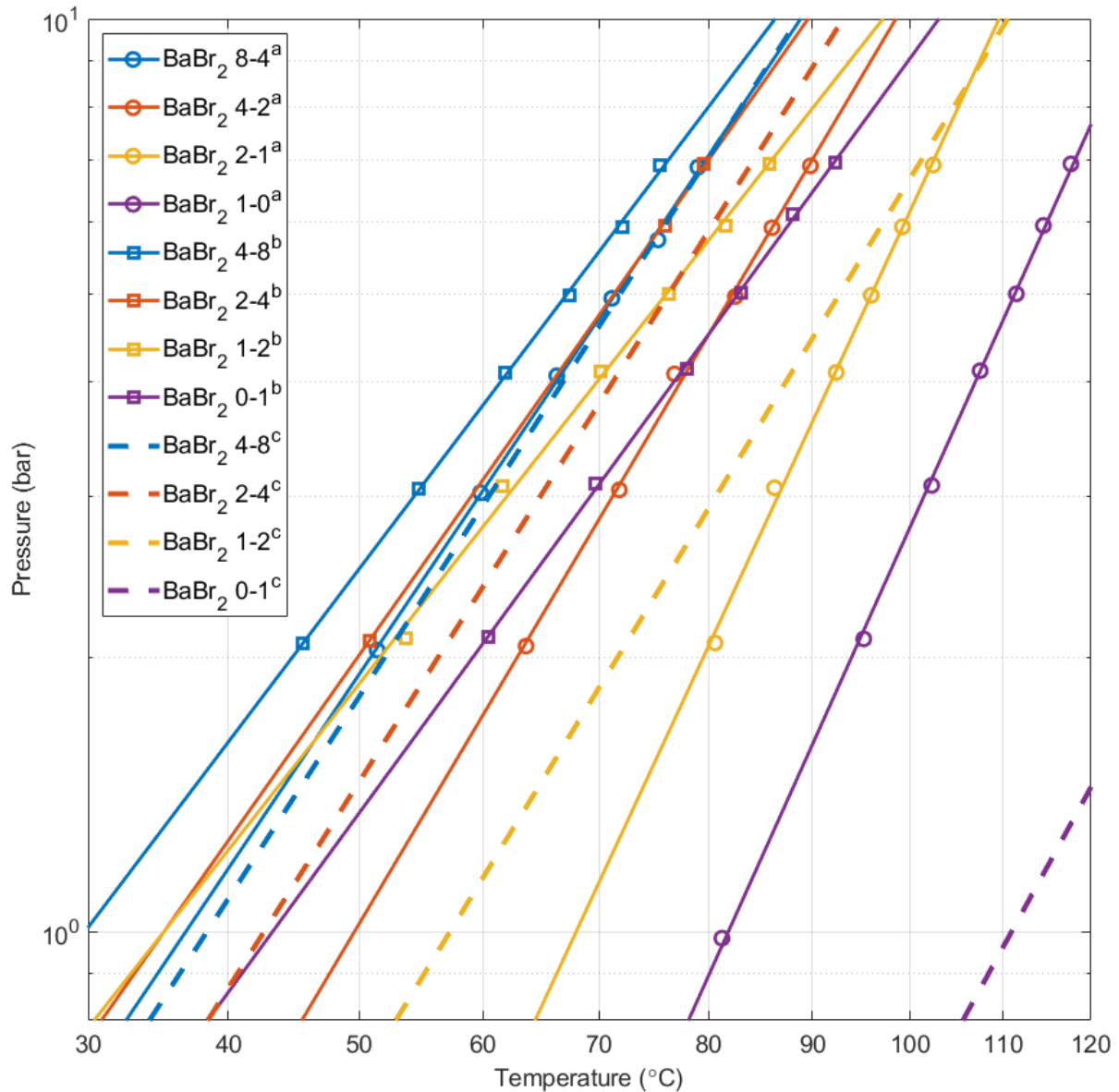
Figure 6. Clapeyron diagram showing FTR derived desorption ([a]) and adsorption ([b]) equilibrium lines for $BaBr_2 \cdot nNH_3$ (n = 0, 1, 2, 4, 8) reactions ($r^2 > 0.99$), alongside literature values ([c]) published by Blitz [7].

3rd to 6th of September 2023
The University of Edinburgh, Scotland

Heat Powered Cycles
Conference 2023
Edinburgh

Heat in the new energy system

Table 2. Calculated reaction enthalpies and entropies versus literature values[a]

Reaction	Calculated reaction enthalpy ΔH (J mol^{-1})	Calculated reaction entropy ΔS (J mol^{-1}K^{-1})*	Literature reaction enthalpy[a] ΔH (J mol^{-1})	Literature reaction entropy[a] ΔS (J mol^{-1}K^{-1})*
BaBr$_2$ (0-1)	38160	226	50700	227.7
BaBr$_2$ (1-2)	35363	238	45600	233.7
BaBr$_2$ (2-4)	39476	268	43900	234.7
BaBr$_2$ (4-8)	36840	267	43000	233.7
BaBr$_2$ (1-0)	62001	215	50700	227.7
BaBr$_2$ (2-1)	60118	221	45600	233.7
BaBr$_2$ (4-2)	46961	208	43900	234.7
BaBr$_2$ (8-4)	41354	214	43000	233.7

*Reference pressure, P_0 = 1 Pa   [a]Taken from Blitz 1922 [7]

The isobaric adsorption and desorption characteristics of barium bromide were studied at a range of pressures using the TGA setup. Figure 7 shows the experimental results at 700 kPa using 1 K steps and a heating rate of 1.5 K·h^{-1}. In all cases, three distinct reactions were visible. The reactions BaBr$_2$ (8-4)/(4-8) and BaBr$_2$ (4-2)/(2-4) occurred as expected, however the reactions BaBr$_2$ (2-1)/(1-2) and BaBr$_2$ (1-0)/(0-1) occurred as a single step. This differed from the FTR results, where four distinct transitions were visible. The TGA results were also analysed in the same way as Figure 5, however the reaction onset points were less clear due to the discreet temperature steps of 1 K and the slow temperature ramp rate used. The molar fraction (X) of ammonia adsorbed and desorbed was >99% in all cases.
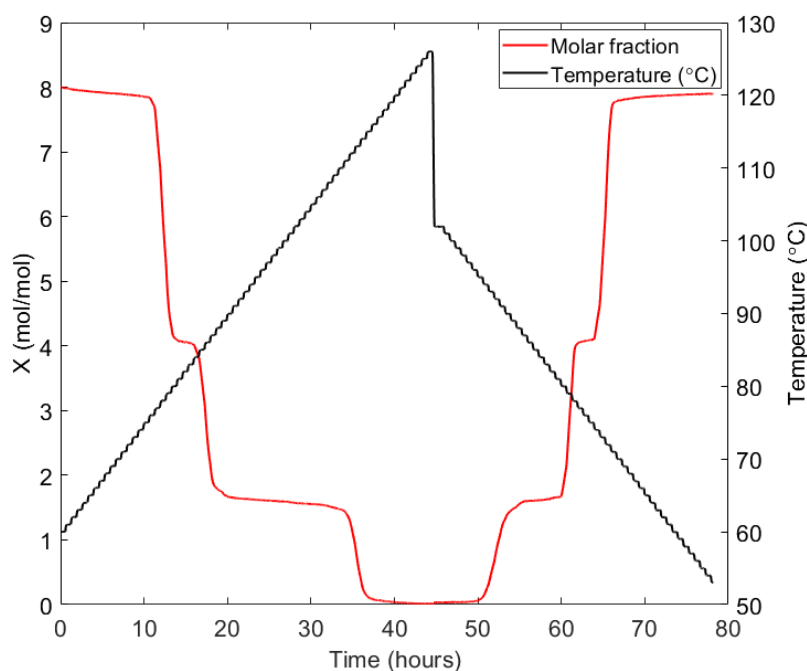
Figure 7. Isobaric adsorption and desorption curve of barium bromide at 700 kPa.

All three visible reactions showed significant hysteresis at all investigated pressures, as shown in Figure 8. For example, the onset of reaction BaBr$_2$ (2-4) and decomposition BaBr$_2$ (4-2) occurred at 77°C and 81°C degrees, respectively, at 600 kPa, a difference of 4°C. At 900 kPa, the reactions occurred at 85°C and 91°C, a difference of 6°C. The onset of the BaBr$_2$ (0-2) reaction and (2-0) decomposition displayed the greatest hysteresis, but also the greatest

uncertainty in onset temperature. The temperatures at X = 1, equivalent to BaBr2·NH₃, were 98°C and 119°C for adsorption and desorption, respectively, at 900 kPa, a difference of 21°C.
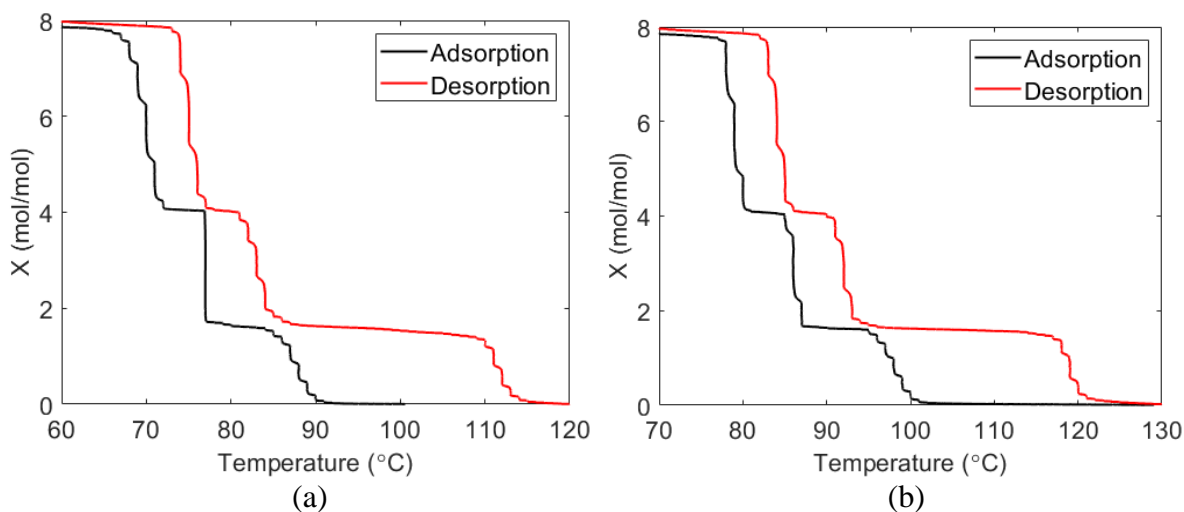
Figure 8. Isobaric adsorption and desorption curves of barium bromide at (a) 600 kPa and (b) 900 kPa.

Conclusions

This work has developed a new method for evaluating the multi-transition reactions of ammoniated salts, termed the Fast Temperature Ramp (FTR). This method, alongside TGA, was used to determine the location of barium bromide-ammonia equilibrium lines, showing that TGA alone is not sufficient to reveal all transitions. Significant hysteresis between adsorption and desorption was found, in particular for the $BaBr_2$ (2-1)/(1-2) and $BaBr_2$ (1-0)/(0-1) reactions. This hysteresis effect increased at higher pressures, exceeding 20°C at 900 kPa. Most significantly, this work showed that the published values of entropy and enthalpy are different to the experimentally found values. Adsorption reactions were found to occur over a smaller temperature range than desorption, giving rise to a single adsorption transition 'zone' less than 20°C wide. This suggests that $BaBr_2$ is a viable candidate salt for use in heat pumping, thermal transformation and thermal storage applications.

References

[1] Neveu, P. and Castaing, J. "Solid-gas chemical heat pumps: Field of application and performance of the internal heat of reaction recovery process," Heat Recovery Systems and CHP, 1993.
[2] Gordeeva, L. et al. "Composites 'binary salts in porous matrix' for adsorption heat transformation," Applied Thermal Engineering, 2013.
[3] Donkers, P. et al. "Deammoniation and ammoniation processes with ammonia complexes," AIMS Energy, 2016.
[4] Wu, S. et al. "Experimental identification and thermodynamic analysis of ammonia sorption equilibrium characteristics on halide salts," Energy, 2018.
[5] Atkinson, G. et al. "Ammonium chloride (NH₄Cl)—Ammonia (NH₃): Sorption characteristics for heat pump applications," Energies, 2021.
[6] Hinmers, S. et al. "Modelling and analysis of ammonia sorption reactions in halide salts," International Journal of Refrigeration, 2022.
[7] Blitz, W. "Beiträge zur systematischen Verwandtschaftslehre XXIV. Über das Vermögen kristallisierter Salze, Ammoniak zu binden," Z Anorg Chem, 1923.

Entransy based heat transfer irreversibility analysis for cascaded absorption-compression heat pumps

Jinfang You[1], **Xi Zhang**[1], **Ruzhu Wang**[1] **and Zhenyuan Xu**[1*]

[1] Engineering Research Center of Solar Power and Refrigeration (MOE), Institute of Refrigeration and Cryogenics, Shanghai Jiao Tong University, Shanghai 200240, China
[*]Corresponding author: xuzhy@sjtu.edu.cn

Abstract

The cascaded absorption-compression high-temperature heat pumps achieve high temperature lift and high system performance through thermal coupling between sub-cycles. Irreversible losses in thermal coupling part and other components have a serious effect on the heat pump performance. In this study, the entransy dissipation was used for the heat transfer irreversibility analysis on heat transfer components in heat pumps; heat and mass transfer process models and entransy dissipation calculation methods for complex transfer components such as absorber and generator were proposed; exergy loss and entransy dissipation of the same heat transfer component but in different heat transfer temperature differences were obtained and compared; the effect of thermal coupling temperature on the exergy based and entransy based heat pump system parameters was investigated. The results indicated that the trend of the heat pump component entransy dissipation with the heat transfer temperature difference is in good agreement with that of exergy loss, which proved that the entransy dissipation calculation method is correct and available for the heat transfer irreversibility analysis for high-temperature heat pump components. In addition, the unique *T-Q* diagram obtained by the entransy dissipation analysis visually illustrates the heat and mass transfer processes in each heat transfer component, which is difficult to obtain in traditional exergy loss analysis. Therefore, entransy dissipation has its own characteristics and advantages over exergy loss.

Keywords: Heat pump, Absorber and generator, Heat transfer irreversibility, Entransy.

Introduction

High-temperature heat pumps, as clean and efficient technologies to replace boilers for effective industrial and building heating, have been extensively studied[1–3]. Through the thermal coupling between condensers of low-temperature stages and evaporators of high-temperature stages, cascaded multi-stage compression heat pumps can achieve high temperature lift [4]. However, for large scale and high temperature heat demands, conventional cascaded multi-stage compression heat pumps are often difficult to satisfy it due to limitations of compressor design and work media[5]. Cascaded absorption-compression heat pumps, which usually use the absorption-based sub-cycle instead of the compression-based sub-cycle as the high-temperature stage, are common forms of hybrid absorption-compression high-temperature heat pumps. The compression heat pump has high efficiency and good controllability but is not good at high-temperature output, thus it is used as the low-temperature stage. While the second type absorption heat pump has high output temperature and flexible temperature management ability but needs medium-temperature input, thus it is used as the high-temperature stage. Therefore, two stages, through thermal coupling between condensers of the compression cycle and generator and evaporator of the absorption cycle, are complementary to each other. This makes the cascaded absorption-compression heat pump attractive for high temperature heat output. Moreover, through the internal heat recovery between the condenser of the absorption cycle and the evaporator of the compression cycle, the hybrid absorption-compression heat pump can effectively enhance the

system performance, as shown in Fig. 1[6-7]. In order to further improve the overall performance, it is important to reduce the heat transfer irreversibility of the thermal coupling part and other heat transfer components in the high-temperature heat pump[8-9].
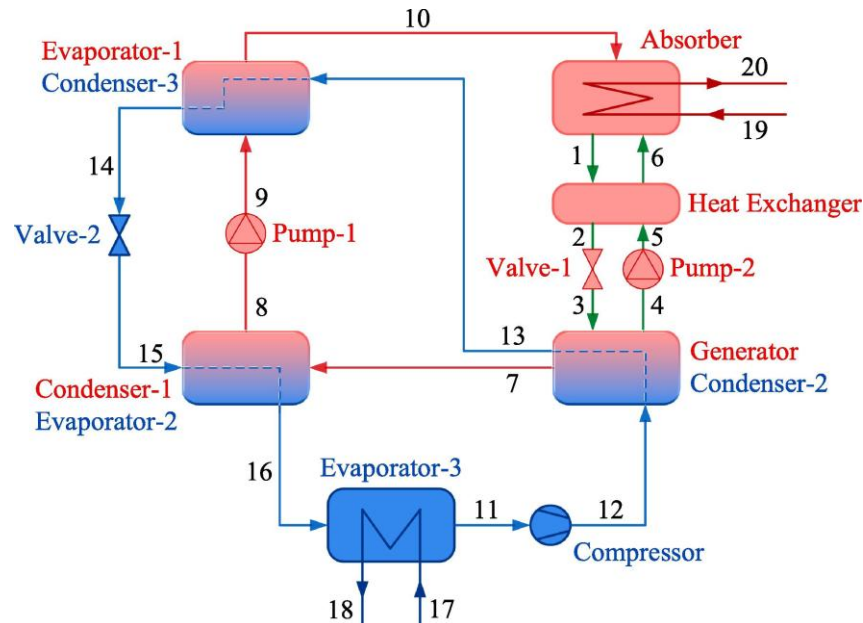
Figure 1. The schematic diagram of the two-stage hybrid absorption-compression heat pump cycle[7].

Entransy was a newly proposed physical quantity which was initially used for the optimization of heat transfer processes through the extremum entransy dissipation principle and had a large number of successful application cases[10]. According to the definition of entransy, it contains the quantity and the quality of energy, and is therefore promising as a second law analysis tool for thermodynamic systems, like exergy. Currently, the entransy analysis for thermodynamic systems is mostly based on heat engine or heat pump cycles considering the work-heat conversion. Concepts such as work entransy were proposed to evaluate the input or output work in cycles so that the entransy analysis for thermodynamic systems can be self-consistent. Chen et al. extended the entransy theory from the heat transfer process optimization to the thermodynamic system optimization by developing the concept of entransy loss for heat engine cycles[11], the concept of entransy increase for heat pump cycles[12], the work entransy theory and the entransy balance equation of thermodynamic processes. The derived maximum entransy loss principle was used in the optimization of closed [13] and open [14] cycles with heat-work conversion. Especially for endo-reversible Carnot heat engine and heat pump cycles under specific given optimization conditions, the entransy theory can be used successfully [15-17].

However, the entransy analysis method for thermodynamic systems is still controversial due to the unclear physical meaning of work entransy and the debate about whether entransy is a state or process quantity[18-19]. Moreover, the work entransy based entransy analysis is difficult to be used for non-work driven thermodynamic cycles, such as absorption cycles. Therefore, in this study, entransy was mainly used to analyze the heat transfer irreversibility in hybrid absorption-compression heat pumps, not involving the non-heat transfer processes. Entransy dissipation based heat transfer irreversibility analysis is quite mature and widely used, and entransy dissipation analysis is most suitable for the description of heat transfer processes irreversibility, other than other thermodynamic processes[20]. While the entransy

Heat Powered Cycles
Conference 2023
Edinburgh

Heat in the new energy system

3rd to 6th of September 2023
The University of Edinburgh, Scotland

dissipation and *T-Q* diagram based heat transfer irreversibility is desired for the analysis and the optimization of heat pumps. Hu et al. proposed a heat pump system, and plotted *T-Q* diagrams of its condensers and evaporators to demonstrate that the proposed heat pump cycle had an improved performance due to the reduction of the entransy dissipation under the same working condition[8]. Yang et al. proposed a high-temperature combined heat pump system and used its *T-Q* diagram to illustrate a better temperature match in the heating supply process[9].

The entransy dissipation calculation for a simple two-fluid heat exchanger is based on the energy conservation equation and the thermodynamic property equation of work media. Then the temperature relationship with the heat transfer process for the hot and cold fluid, i.e., the *T-Q* diagram is derived. Finally, the entransy dissipation of the heat transfer process can be obtained from the area surrounded by the hot and cold fluid temperature curve of the *T-Q* diagram[10,21]. However, absorption and generation processes in absorption cycles, which include the mass transfer between the solution and the refrigerant and the heat transfer between the solution, the refrigerant, and the surrounding, have complex irreversibility and are difficult to calculate their entransy dissipations. To solve this problem, Zhang et al. proposed the concept of concentration entransy, and derived calculation equations for the mass and heat transfer entransy dissipation of absorbers and generators based on the one-dimensional absorption and generation micro-element model[22]. This method was successfully used to analysis the entransy dissipation of absorbers and generators in first type absorption heat pumps[22-23]. However, negative entransy dissipations were obtained in some operating conditions when applied this method to second type absorption heat pumps, as shown in Table 1. This is obviously not in accordance with the second law of thermodynamics. The main problem comes from the non-conservation of energy due to flawed heat and mass transfer process model assumptions. From the perspective of the energy quantity, when considering the solution absorption process, this method calculates the latent heat of steam liquefaction, rather than the heat released by mixing the solution with the steam, and results in the heat input less than the heat output when considering the overall process. The direct evidence is that there is a big difference between entransy dissipations of absorber according to Kelvin temperature and Celsius temperature. This contradicts the conclusion that entransy dissipation is proportional to the heat transfer temperature difference but not related to the absolute value of the heat transfer temperature. Moreover, in the mathematical model of first type absorption heat pumps, the solution at the absorber inlet (i.e., the solution throttle outlet) is saturated and has higher temperature than outlet, while in the mathematical model of second type absorption heat pumps, the solution at the absorber inlet is usually unsaturated and has lower temperature than outlet. Therefore, it is necessary to consider inlet and outlet states of work media in absorbers and generators, while assume heat and mass transfer processes, so as to conduct a correct entransy dissipation analysis.

Table 1. A case where the entransy dissipation is negative according to Ref. [22], the absorber operating conditions are taken from the high-pressure absorber (HPA) of the three-stage heat pump cycle (HACHP-2) in Ref. [7].

items	values
vapor in (point 16)	$t_{16} = 86\ °C$, $p_{16} = 60.07\ kPa$, $m_5 = 0.0224\ kg/s$
solution in (point 4)	$t_4 = 130\ °C$, $p_5 = 60.07\ kPa$, $m_5 = 0.6169\ kg/s$, $x_5 = 0.6057$

Heat Powered Cycles
Conference 2023
Edinburgh

Heat in the new energy system

3rd to 6th of September 2023
The University of Edinburgh, Scotland

solution out (point 5)	$t_5 = 135\ °C,\ p_5 = 60.07\ kPa,\ m_5 = 0.6393kg/s,\ x_5 = 0.5845$	
cooling water in (point 25)	$t_{25} = 100\ °C,\ p_{25} = 200\ kPa,\ m_{25} = 0.0217\ kg/s$	
cooling water out (point 26)	$t_{26} = 130\ °C,\ p_{26} = 200\ kPa,\ m_{26} = 0.0217kg/s$	
vapor entransy change	-4417.04 kW·°C	-18446.29 kW·K
solution concentration entransy change	-2647.66 kW·°C	-2647.66 kW·K
solution heat entransy change	1241.28 kW·°C	3800.21 kW·K
cooling water entransy	6003.13 kW·°C	19682.87 kW·K
total entransy dissipation	-179.72 kW·°C	-2389.13 kW·K

Here, inspired by the heat transfer irreversibility analysis of the absorption process in once-through discharging absorption thermal storage systems[24], the entransy dissipation calculation and *T-Q* diagram plotting method for absorbers and generators in second type absorption heat pumps was proposed. In addition, to evaluate the effect of the heat transfer component improvement on the hybrid absorption-compression high-temperature heat pump system performance, the effect of the heat transfer temperature difference on the entransy dissipation of each component was investigated and compared with the exergy analysis.

Entransy dissipation and *T-Q* diagrams of heat transfer components in the heat pump

In this section, the irreversibility of each heat transfer component in the cascaded absorption-compression high-temperature heat pump (Fig. 1) that has the optimal coupling temperature under the air temperature of 20.0 °C and the output temperature of 130.0 °C will be analyzed. As mentioned before, in order to calculate the entransy dissipation of heat transfer components, the key is to know temperature change relationships of the hot and cold fluid as a function of the heat transfer process. This can be obtained from the conservation of energy within each micro-element stepping heat transfer process, as will be shown below. The micro-element stepping heat transfer process is denoted by the relative heat exchange amount, *r*, varying from 0 to 1. This is a differential variable that can be used both as a micrometric multiplier in the energy conservation equation and as a differential variable in the integral entransy equation. Taking condenser-3 (subscript "con3") & evaporator-1 (subscript "eva1") as an example, its entransy dissipation can be calculated as follows.

$$r_{con3}Q_{con3} = m_{13}(h_{13}-h_{con3}) \tag{1}$$

$$T_{con3} = T_{R134a}(p_{13},h_{con3}) \tag{2}$$

$$G_{con3} = -\int_0^1 T_{con3}Q_{con3}\,dr_{con3} \tag{3}$$

Heat Powered Cycles
Conference 2023
Edinburgh

Heat in the new energy system

3rd to 6th of September 2023
The University of Edinburgh, Scotland

$$r_{\text{eva1}} Q_{\text{eva1}} = m_9 (h_{\text{eva1}} - h_9) \tag{4}$$

$$T_{\text{eva1}} = T_{\text{Water}}(p_9, h_{\text{eva1}}) \tag{5}$$

$$G_{\text{eva1}} = \int_0^1 T_{\text{eva1}} Q_{\text{eva1}} \mathrm{d}r_{\text{eva1}} \tag{6}$$

$$G_{\text{dis,con3,eva1}} = -(G_{\text{con3}} + G_{\text{eva1}}) \tag{7}$$

where, Eq. 1 ~ Eq. 3 calculate the entransy transfer rate of the hot fluid R134a in condenser-3, G_{con3}; Eq. 2 calculates the temperature at the corresponding pressure and specific enthalpy based on the thermophysical property of R134a; Eq. 4 ~ Eq. 6 calculate the entransy transfer rate of the cold fluid water in evaporator-1, G_{eva1}; Eq. 7 calculates the entransy dissipation rate of condenser-3 & evaporator-1, $G_{\text{dis,con3,eva1}}$; r_{con3} and Q_{con3} represent the relative heat exchange amount and the total heat exchange amount of condenser-3, respectively; h_{con3} represents the specific enthalpy of R134a after completing the corresponding relative heat exchange process r_{con3}. The negative sign in G_{con3} represents the entransy transfer rate accompanying with heat is output.

Other two-fluid heat exchangers, including condenser-1 (subscript "con1") & evaporator-2 (subscript "eva2") and evaporator-3 (subscript "eva3" for the cold R134a and subscript "air" for the hot air), can calculate their entransy dissipation in the similar way.

Unlike simple two-fluid heat exchangers, in the absorber and generator, the mass and heat transfer process is complex. In the solution, there is not only the heat transfer, but also the absorption and generation of work media (steam). As shown in Fig. 2(a), considering the solution thermodynamic states at the inlet (point 6) and outlet (point 1) of the absorber and the solution flowing process in the heat pump system, the following simplified two-stage absorption and exothermic process of the solution inside the absorber was assumed.

(a)   (b)
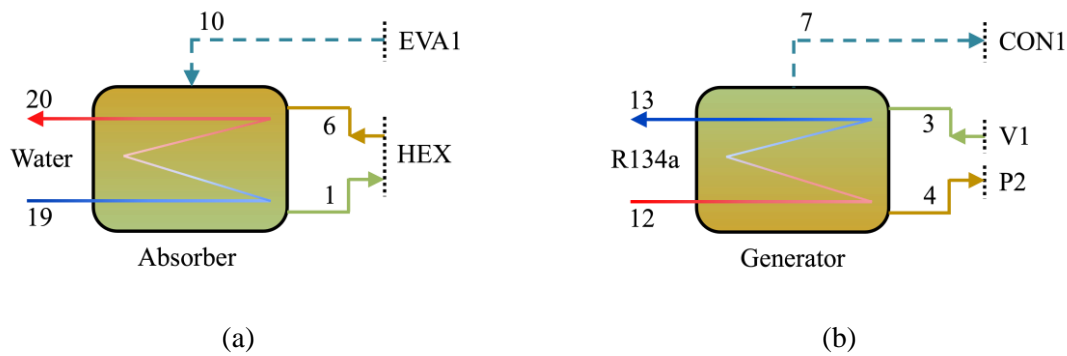
Figure 2. The schematic diagrams of the inlet and outlet state points and heat and mass transfer processes in the absorber (a) and generator (b). The color gradient of the refrigerant from blue to red or from red to blue indicates being heated or cooled, respectively; the color gradient of the solution from brown to green or from green to brown indicates being weak or strong, respectively.

In the first stage, at the beginning, the strong solution (point 6) from the solution heat exchanger (HEX) is in the state of pressure p_6 and concentration x_6, but the temperature has not yet reached the corresponding saturation state ($T_6 < T_{\text{LiBr}}(p_6, x_6)$). Therefore, after the

strong solution enters the absorber, it rapidly absorbs a portion ($m_{abs,vapor,1}$) of the high-pressure steam (point 10) from evaporator-1 (EVA1), while the concentration decreases and the temperature increases simultaneously until the solution reaches the saturated solution state (subscript "abs, weak, 1") under the absorption pressure. During the first stage, all the heat absorbed by the strong solution from the steam is used to increase the solution temperature and allow the solution to be saturated quickly. Therefore, this stage can be considered as an adiabatic process, i.e., no heat transfer to water is considered. Balance equations (Eq. 8 ~ Eq. 10) and property equations (Eq. 11 ~ Eq. 12) for the first stage are shown below.

$$m_6 + m_{abs,vapor,1} = m_{abs,weak,1} \tag{8}$$

$$m_6 x_6 = m_{abs,weak,1} x_{abs,weak,1} \tag{9}$$

$$m_6 h_6 + m_{abs,vapor,1} h_{10} = m_{abs,weak,1} h_{abs,weak,1} \tag{10}$$

$$T_{abs,weak,1} = T_{LiBr}\left(p_6, x_{abs,weak,1}\right) \tag{11}$$

$$h_{abs,weak,1} = h_{LiBr}\left(T_{abs,weak,1}, x_{abs,weak,1}\right) \tag{12}$$

where, Eq. 11 refers to the calculation of temperature at the corresponding pressure and solution mass concentration based on the thermophysical property of the LiBr-H$_2$O solution; Eq. 12 refers to the calculation of specific enthalpy at the corresponding temperature and solution mass concentration, based on the thermophysical property of the LiBr-H$_2$O solution. This set of equations (Eq. 8 ~ Eq. 12) can be solved by iterating with the variable $x_{abs,weak,1}$ until the LiBr solution saturated (Eq. 11).

In the second stage, the saturated solution before exotherm (subscript "abs, weak, 1") starts to release heat to water through the heat exchanger in the absorber, while the solution cools down and continues to absorb the remaining ($m_{abs,vapor,2}$) high pressure steam (point 10) from evaporator-1 (EVA1) to maintain the saturated state at all times (subscript "abs, weak, 2") until the solution completes all the exotherm process and becomes the weak solution (point 1). Balance equations (Eq. 13 ~ Eq. 15) and property equations (Eq. 16 ~ Eq. 17) for the second stage, including entransy transfer of the solution in the absorber, G_{abs} (Eq. 18), are shown below.

$$m_{abs,weak,1} + m_{abs,vapor,2} = m_{abs,weak,2} \tag{13}$$

$$m_6 x_6 = m_{abs,weak,2} x_{abs,weak,2} \tag{14}$$

$$r_{abs} Q_{abs} = m_{abs,weak,1} h_{abs,weak,1} + m_{abs,vapor,2} h_{10} - m_{abs,weak,2} h_{abs,weak,2} \tag{15}$$

$$T_{abs,weak,2} = T_{LiBr}\left(p_6, x_{abs,weak,2}\right) \tag{16}$$

$$h_{abs,weak,2} = h_{LiBr}\left(T_{abs,weak,2}, x_{abs,weak,2}\right) \tag{17}$$

$$G_{abs} = -\int_0^1 T_{abs,weak,2} Q_{abs} \, dr_{abs} \tag{18}$$

Heat Powered Cycles
Conference 2023
Edinburgh
Heat in the new energy system

3rd to 6th of September 2023
The University of Edinburgh, Scotland

For the entransy transfer rate of water, G_{water}, and the entransy dissipation rate of the heat transfer process in the absorber, $G_{dis,abs}$, a similar method as simple two-fluid heat exchangers can be used, as shown below.

$$r_{water}Q_{abs} = m_{19}(h_{water}-h_{19}) \tag{19}$$

$$T_{water} = T_{water}(p_{19},h_{water}) \tag{20}$$

$$G_{water} = \int_0^1 T_{water}Q_{abs}\,dr_{water} \tag{21}$$

$$G_{dis,abs} = -(G_{abs}+G_{water}) \tag{22}$$

Similarly, as shown in Fig. 2(b), the solution thermodynamic states at the inlet (point 3) and outlet (point 4) and the solution flowing process were considered. The weak solution (point 3) from valve-1 (V1) has been partially flash (refrigerant vapor quality q_3) to saturation. Thus, unlike the two-stage absorption and exothermic process in the absorber, the weak solution in the generator is always saturated. It directly absorbs heat and generates steam simultaneously, accompanied by a continuous increment in the temperature and concentration until the solution completes all the heat absorption and steam generation process and becomes the strong solution (point 4). Therefore, the entransy dissipation of condenser-2 (subscript "con2") & generator (subscript "gen") can be calculated as follows.

$$r_{con2}Q_{con2} = m_{12}(h_{12}-h_{con2}) \tag{23}$$

$$T_{con2} = T_{R134a}(p_{12},h_{con2}) \tag{24}$$

$$G_{con2} = -\int_0^1 T_{con2}Q_{con2}\,dr_{con2} \tag{25}$$

$$m_{gen,strong} = m_3 - m_{gen,vapor} \tag{26}$$

$$m_3(1-q_3)x_3 = m_{gen,strong}x_{gen,strong} \tag{27}$$

$$r_{gen}Q_{gen} = m_{gen,strong}h_{gen,strong}+m_{gen,vapor}h_{gen,vapor}-m_3h_3 \tag{28}$$

$$T_{gen,strong} = T_{LiBr}(p_4,x_{gen,strong}) \tag{29}$$

$$h_{gen,strong} = h_{LiBr}(T_{gen,strong},x_{gen,strong}) \tag{30}$$

$$h_{gen,vapor} = h_{Water}(T_{gen,strong},p_7) \tag{31}$$

$$G_{gen} = \int_0^1 T_{gen,strong}Q_{gen}\,dr_{gen} \tag{32}$$

$$G_{dis,con2,gen} = -(G_{con2}+G_{gen}) \tag{33}$$

where, Eq. 23 ~ Eq. 25 calculate the entransy transfer rate of the hot R134a in condenser-2, G_{con2}; Eq. 26 ~ Eq. 32 calculate the entransy transfer rate of the cold LiBr-H$_2$O solution in

generator, G_{gen}; Eq. 33 calculates the entransy dissipation rate of condenser-2 & generator, $G_{dis,con2,gen}$.

The case of the solution heat exchanger (subscript "hex") is special. Because the hot and cold fluid involved in the solution heat exchanger is not saturated, the temperature of solution cannot be obtained from the property equation. Hence, the heat capacity was used here.

$$r_{hex,hot}Q_{hex} = m_1 c_{p,hex,hot}\left(t_1 - T_{hex,hot}\right) \tag{34}$$

$$c_{p,hex,hot} = c_{p,LiBr}\left((T_{hex,hot}+t_1)/2, x_1\right) \tag{35}$$

$$G_{hex,hot} = -\int_0^1 T_{hex,hot}Q_{hex}\,dr_{hex,hot} \tag{36}$$

$$r_{hex,cold}Q_{hex} = m_5 c_{p,hex,cold}\left(T_{hex,cold}-t_5\right) \tag{37}$$

$$c_{p,hex,cold} = c_{p,LiBr}\left((T_{hex,cold}+t_5)/2,,x_5\right) \tag{38}$$

$$G_{hex,cold} = \int_0^1 T_{hex,cold}Q_{hex}\,dr_{hex,cold} \tag{39}$$

$$G_{dis,hex} = -\left(G_{hex,hot}+G_{hex,cold}\right) \tag{40}$$

where, Eq. 34 ~ Eq. 36 calculate the entransy transfer rate of the hot fluid in heat exchanger, $G_{hex,hot}$; Eq. 37 ~ Eq. 39 calculate the entransy transfer rate of the cold fluid in heat exchanger, $G_{hex,cold}$; Eq. 35 and Eq. 38 refer to the calculation of the specific heat capacity at the corresponding arithmetic average temperature and solution mass concentration based on the thermophysical property of the LiBr solution; Eq. 40 calculates the entransy dissipation rate of the solution heat exchanger, $G_{dis,hex}$; $T_{hex,hot}$ and $T_{hex,cold}$ represent the solution temperature after completing the corresponding relative heat exchange process $r_{hex,hot}$ and $r_{hex,cold}$, respectively.

Besides, *T-Q* diagrams of all heat transfer processes in the heat pump can be obtained, as shown in Fig. 3. Considering the counter-current arrangement, for the cold fluid, when drawing the *T-Q* diagram, its horizontal coordinate should be 1-*r*. Intuitively, the entransy transfer value of the hot fluid and the cold fluid can be expressed in terms of the area enclosed by the horizontal axis and their temperature change curves on the *T-Q* diagram, while the area between the two curves is the entransy dissipation.

(a) Absorber (ABS)

(b) Condenser-2 & Generator (CON2-GEN)

(c) Condenser-3 & Evaporator-1
(CON3-EVA1)

(d) Condenser-1 & Evaporator-2
(CON1-EVA2)

(e) Heat Exchanger (HEX)

(f) Evaporator-3 (EVA3)
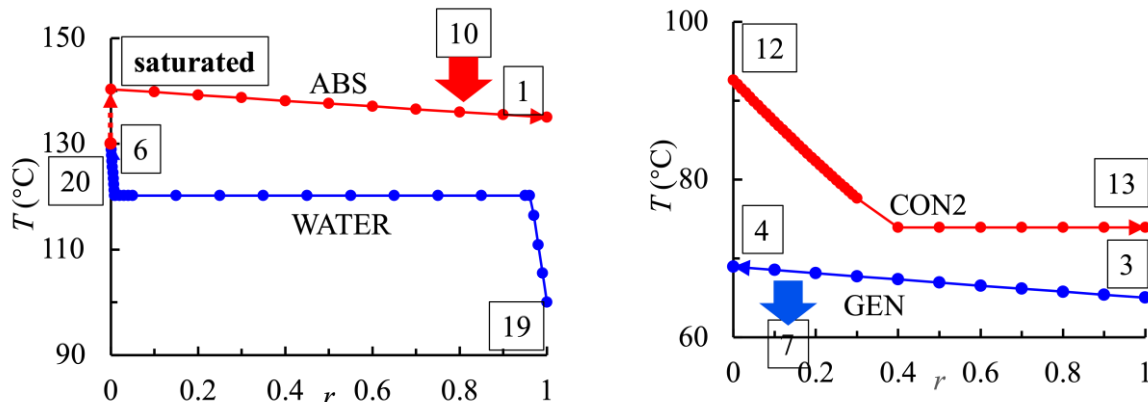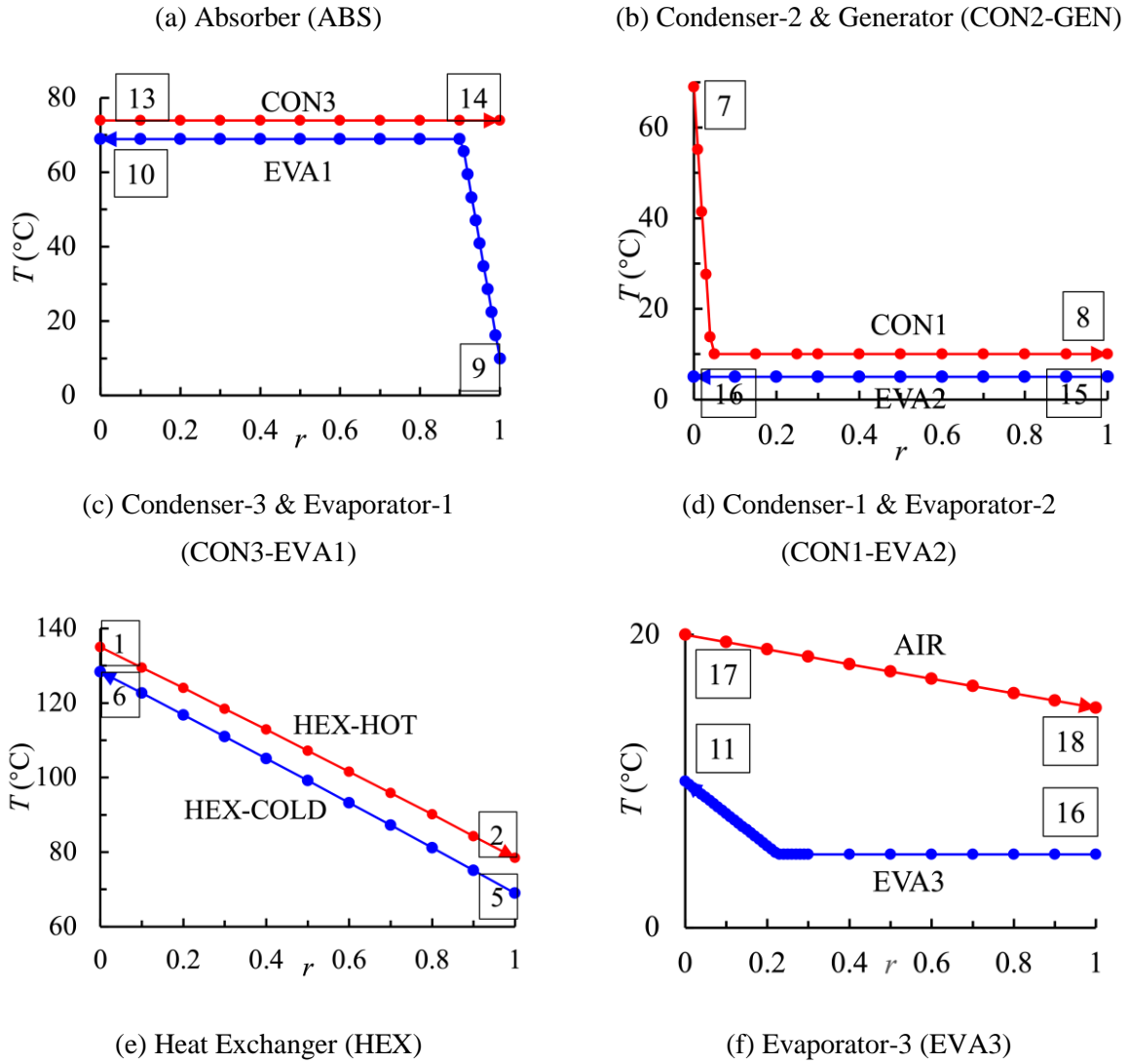
Figure 3. *T-Q* diagrams of each heat transfer component in the heat pump, illustrating inlet and outlet state points and temperature change processes of work media in each component.

As can be seen from *T-Q* diagrams, besides the temperature change curve in the latent heat transfer stage is a horizontal straight line, the temperature change curve in the sensible heat transfer stage can also be approximated as a straight line. Therefore, for simplicity, the whole heat transfer process was segmented according to sensible and latent heat transfer. And the arithmetic average temperature in each segment was used. Taking the absorber as an example, the entransy transfer calculation is shown below.

$$G_{abs} = -\frac{T_{abs,weak,1}+T_1}{2}Q_{abs} \tag{41}$$

$$\begin{aligned}G_{water} = &\frac{T_{19}+T_{water}(p_{19})}{2}m_{19}\left[h_{water}(p_{19},x=0)-h_{19}\right]\\&+T_{water}(p_{19})m_{19}\left[h_{water}(p_{19},x=1)-h_{water}(p_{19},x=0)\right]\\&+\frac{T_{water}(p_{19})+T_{20}}{2}m_{19}\left[h_{20}-h_{water}(p_{19},x=1)\right]\end{aligned} \tag{42}$$

The entransy dissipation results of all heat transfer components in the two-stage hybrid absorption-compression heat pump under the state in Table 2 of Ref. [7] are shown in Table 2. It indicates that the relative error (RE) between the integral calculation and the approximate calculation is not significant.

Table 2. Comparisons between entransy dissipation results using integral and simplified calculation.

G_{dis}	ABS	CON1-EVA2	CON2-GEN	CON3-EVA1	EVA3	HEX	total
Integral (kW·°C)	885.9	332.8	522	414	171.5	451	2777
Simplified (kW·°C)	887.6	332	529.1	413.6	171.5	428.3	2762
RE	0.19%	0.24%	1.36%	0.10%	0.00%	5.03%	0.54%

Entransy dissipation based heat transfer irreversibility analysis and improvement guide

In order to verify the reasonableness of the entransy based heat transfer irreversibility analysis method, exergy loss and entransy dissipation results of each heat transfer component, when the absorber heat transfer temperature difference Δt_{abs} varied from 10 °C to 0 °C, are shown in Fig. 4. The consistency between the trend of exergy loss and entransy dissipation with heat transfer temperature difference suggests that both of them can be used to quantify the heat transfer components irreversibility in heat pumps.

Taking the absorber (Fig. 2(a)) as an example, the exergy loss of heat pump components is calculated as follows.

$$I_{abs} = T_0(m_1 s_1 + m_{20} s_{20} - m_6 s_6 - m_{10} s_{10} - m_{19} s_{19}) \tag{43}$$

where T_0 refers to the ambient temperature and s refers to the special entropy. It can be seen that the exergy loss calculation of heat transfer components in the heat pump only considers inlet and outlet states but ignores internal heat and mass transfer processes. Moreover, inquiring the special entropy of work media and pre-setting the ambient temperature are required, which means that the value of the exergy loss may be affected by factors other than the heat transfer irreversibility.

Heat Powered Cycles
Conference 2023
Edinburgh
Heat in the new energy system

3rd to 6th of September 2023
The University of Edinburgh, Scotland
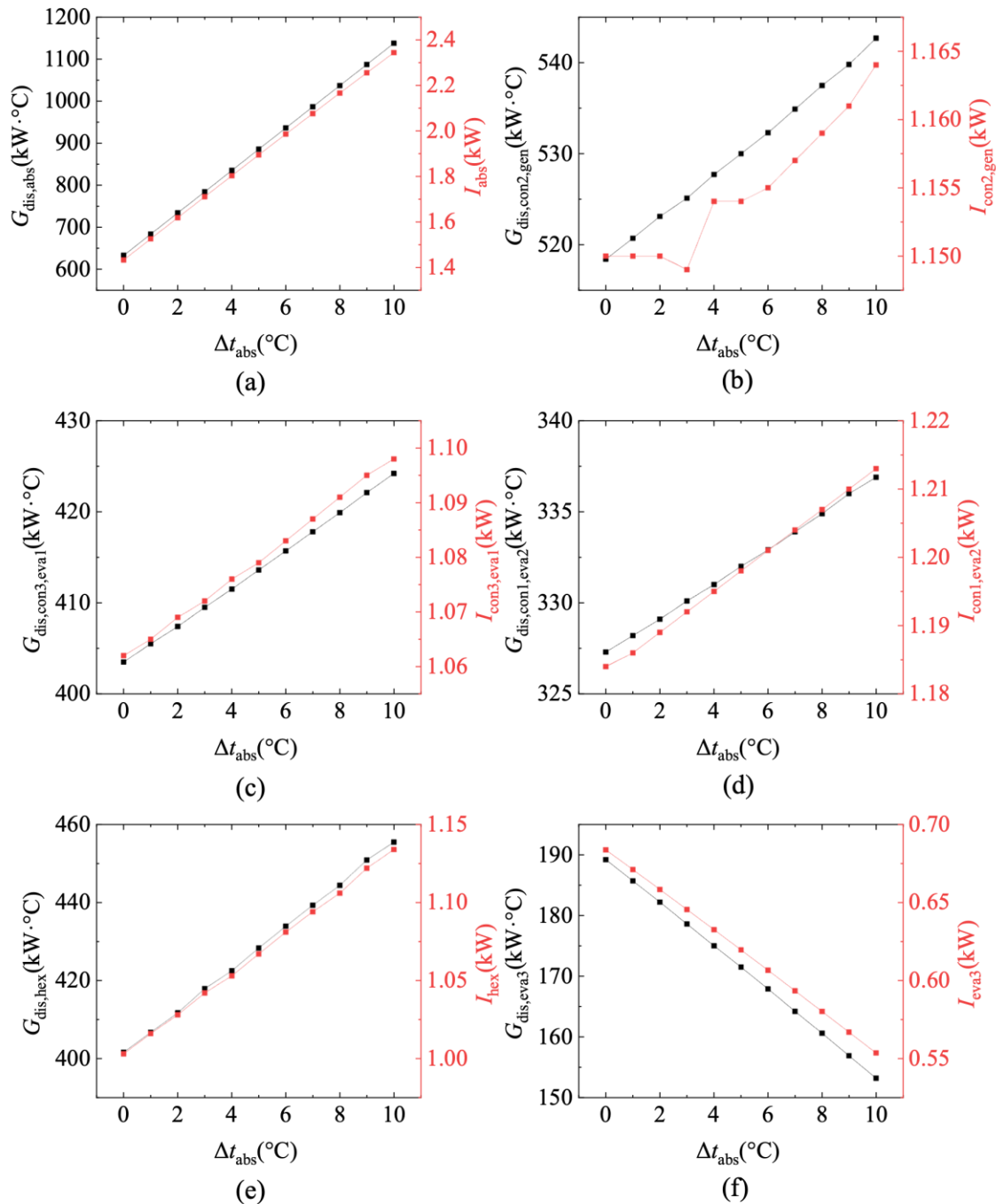
Figure 4. Comparisons of the effect of the absorber heat transfer temperature difference Δt_{abs} on exergy loss I and entransy dissipation G_{dis} of each heat transfer component: (a) ABS; (b) CON2-GEN; (c) CON3-EVA1; (d) CON1-EVA2; (e) HEX; (f) EVA3.

In order to show the irreversibility improvement of each heat transfer component and its effect on system coefficient of performance (COP), reducing the minimum heat transfer temperature difference in the calculation model was considered. The minimum heat transfer temperature difference of the liquid-liquid heat exchanger (ABS, CON2-GEN, CON3-EVA1, CON1-EVA2, and HEX) was decreased from original 5 °C to 2 °C, and the minimum heat transfer temperature difference of the liquid-gas heat exchanger (EVA3) was decreased from the original 10°C to 7 °C. Besides, in order to show the irreversibility improvement of the

non-heat transfer component, compressor (COM), in the heat pump, its isentropic efficiency was increased from the original 0.8 to 0.9. The effects of the irreversibility improvement on the entransy dissipation of each component and COP of the heat pump are shown in the Fig. 5. It can be seen that:

(1) The irreversibility improvement of each heat transfer component reduce its own entransy dissipation most, while the irreversibility improvement of the compressor reduce the entransy dissipation of the condenser-2 & generator most.

(2) As shown in Table 2, the absorber has the highest entransy dissipation under the original operating condition. Correspondingly, the reduction of the total entransy dissipation caused by the heat transfer irreversibility improvement of the absorber is the most. But interestingly, the COP improvement is not the largest (from 1.404 to 1.438) under the absorber improvement. While the heat transfer irreversibility improvement of the condenser-1 & evaporator-2 (moderate entransy dissipation under the original operating condition) results the best COP improvement (from 1.404 to 1.459).

(3) Moreover, it is more interesting that the irreversibility improvement of some components causes an increment rather than a reduction in the entransy dissipation of other heat transfer components. For example, the entransy dissipation of evaporator-3 always increased when components other than itself had irreversibility improvements.
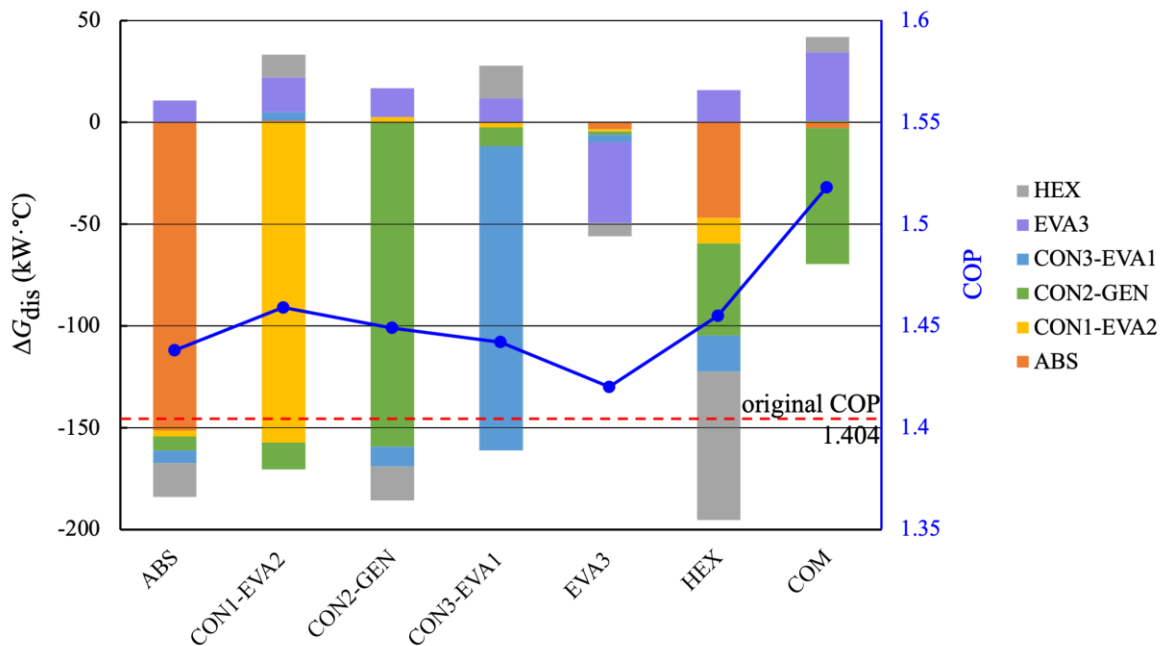
Figure 5. The effect of the irreversibility improvement of each component (horizontal coordinates, for example, "ABS" means that only the absorber gets its own irreversibility improvement and other component dose not) on the entransy dissipation of all heat transfer components and the COP of the heat pump system.

Entransy metrics perspective of the coupling temperature optimization for the heat pump

For cascaded absorption-compression heat pumps, the coupling temperature t_m usually needs to be optimized for the maximum COP requirement under a given external operating

Heat Powered Cycles
Conference 2023
Edinburgh
Heat in the new energy system

3rd to 6th of September 2023
The University of Edinburgh, Scotland

condition. In order to investigate the availability of exergy and entransy analysis relevant parameters for the COP optimization, the COP (Eq. 44), total exergy loss I_{total}, exergy efficiency ϕ (Eq. 45), total entransy dissipation $G_{\text{dis,total}}$ and entransy increment G_{inc} (Eq. 46) of the system under the same external operating condition but different coupling temperatures were calculated.

$$\text{COP} = \frac{Q_{\text{out}}}{W_{\text{in}}} \tag{44}$$

$$\phi = \frac{Ex_{\text{out}}}{W_{\text{in}}} \tag{45}$$

$$
\begin{aligned}
G_{\text{inc}} &= G_{\text{Q,H,out}} - G_{\text{Q,C,in}} = Q_{\text{out}}T_{\text{out}} - Q_{\text{in}}T_{\text{in}} \\
&= Q_{\text{out}}T_{\text{out}} - \left(Q_{\text{out}} - W_{\text{in}}\right)T_{\text{in}} = Q_{\text{out}}\left(T_{\text{out}} - T_{\text{in}}\right) + W_{\text{in}}T_{\text{in}}
\end{aligned}
\tag{46}
$$

where, Q_{out}, W_{in}, Ex_{out}, $G_{\text{Q,H,out}}$, $G_{\text{Q,C,in}}$, T_{out}, Q_{in}, and T_{in} represent the high-temperature heat output, power input, exergy of the high-temperature heat output, entransy of the high-temperature heat output, entransy of the low-temperature heat input, heat output temperature, low-temperature heat input, and heat input temperature, respectively.

The results are shown in Fig. 6. As seen in the figure, the coupling temperatures corresponding to the optimal I_{total}, ϕ, and G_{inc}, as well as COP, are consistent. This is because that I_{total} and ϕ reflect the total irreversible losses and exergy utilization efficiency, respectively. While G_{inc} is inversely proportional to COP under fixed Q_{out}, as can be seen from Eq. 45. These parameters are evaluated from the global perspective of the whole system. However, $G_{\text{dis,total}}$ only indicates the heat transfer irreversibility but excludes the non-heat transfer irreversibility, so there is a bias in the coupling temperature optimization.
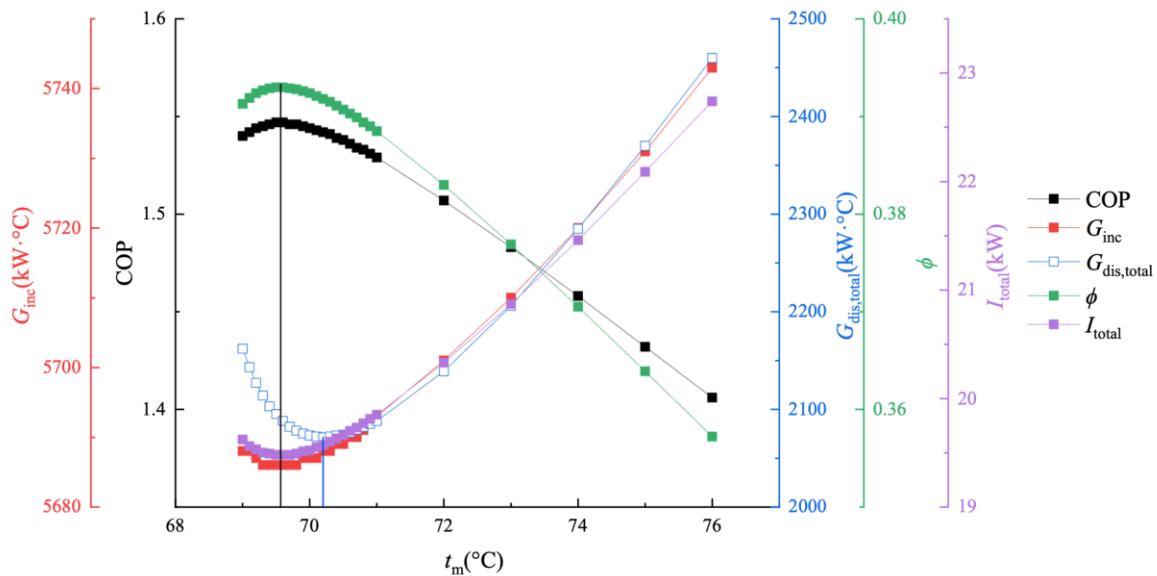
Figure 6. Exergy and entransy metrics perspective of the coupling temperature optimization for the cascaded absorption-compression high-temperature heat pump.

Summary

Entransy, as a newly proposed physical quantity, is expected to be used in the analysis of thermodynamic systems in addition to the successful application in heat transfer systems. However, the thermodynamic entransy theory, such as work entransy, is still controversial and cannot yet be used for the analysis of absorption heat pumps. Hence, the entransy analysis here for cascaded absorption-compression heat pumps only includes the entransy dissipation based heat transfer irreversibility analysis and the entransy increment based heat pump performance characterization. In summary, following conclusions could be obtained.

(1) The entransy dissipation calculation method for the absorber and generator in heat pumps was constructed. By comparing the entransy dissipation and exergy loss under variable heat transfer temperature differences, it can prove the correctness of entransy dissipation as an evaluation indicator for the irreversibility of heat transfer components in heat pumps. By comparing the exergy based and entransy based heat transfer irreversibility analysis processes, it can conclude that the entransy dissipation analysis achieves a graphical visual illustration of the heat transfer process, which is difficult to be achieved by the exergy loss analysis.

(2) The effect of heat transfer temperature difference on the entransy dissipation and exergy loss of components, as well as the total entransy dissipation and COP of the system, was investigated. Under the same temperature difference improvement, the heat transfer improvement of the component with the largest entransy dissipation in the original working condition does not obtain the best COP improvement results, which needs further research on changes of heat pump parameters.

(3) The optimized coupling temperatures at the extremum of the entransy increment, exergy destruction and exergy efficiency, are same as the optimized coupling temperature at the maximum COP. Therefore, the entransy increment can be used for the coupling temperature optimization of cascaded absorption-compression heat pumps, but the total entransy dissipation cannot.

Acknowledgments

References:
[1] Rosenow, J., Gibb, D., Nowak, T., Lowes, R., "Heating up the global heat pump market", Nature Energy, 2022.
[2] Jiang, J.T., Hu, B., Wang, R.Z., Deng, N., Cao, F., Wang, C.C., "A review and perspective on industry high-temperature heat pumps", Renewable and Sustainable Energy Reviews, 2022.
[3] Arpagaus, C., Bless, F., Uhlmann, M., Schiffmann, J., Bertsch, S.S., "High temperature heat pumps: Market overview, state of the art, research status, refrigerants, and application potentials", Energy, 2018.
[4] Qu, M.L., Fan, Y.N., Chen, J.B., Li, T.R., Li, Z., Li, H., "Experimental study of a control strategy for a cascade air source heat pump water heater", Applied Thermal Engineering, 2017.
[5] Farshi, L. G., Khalili, S., Mosaffa, A. H., "Thermodynamic analysis of a cascaded compression – Absorption heat pump and comparison with three classes of conventional heat pumps for the waste heat recovery," Applied Thermal Engineering, 2018.
[6] Gao, J. T., Xu, Z. Y., Wang, R. Z., "An air-source hybrid absorption-compression heat pump with large temperature lift", Applied Energy, 2021.

[7] Zhang, X., Wang, R. Z., Xu, Z. Y., "Air-source hybrid absorption-compression heat pumps with three-stage thermal coupling configuration for temperature lift over 150 °C", Energy Conversion and Management, 2022.

[8] Hu, B., Xu, S.Z., Wang, R.Z., Liu, H., Han, L.Y., Zhang, Z.P., Li, H.B., "Investigation on advanced heat pump systems with improved energy efficiency", Energy Conversion and Management, 2019.

[9] Yang, W.W., Cao, X.Q., He, Y.L., Yan, F.Y., "Theoretical study of a high-temperature heat pump system composed of a CO2 transcritical heat pump cycle and a R152a subcritical heat pump cycle", Applied Thermal Engineering, 2017.

[10] Guo, Z.Y., Zhu, H.Y., Liang, X.G., "Entransy—A physical quantity describing heat transfer ability", International Journal of Heat and Mass Transfer, 2007.

[11] Cheng, X.T., Liang, X. G., "Entransy, Entransy Dissipation and Entransy Loss for Analyses of Heat Transfer and Heat-Work Conversion Processes", Journal of Thermal Science and Technology, 2013.

[12] Cheng, X.T., Liang, X. G., "Entransy and entropy analyses of heat pump systems," Chinese Science Bulletin, 2013.

[13] Cheng, X.T., Liang, X. G., "Entransy loss in thermodynamic processes and its application", Energy, 2012.

[14] Cheng, X.T., Wang, W.H., Liang, X.G., "Entransy analysis of open thermodynamic systems", Chinese Science Bulletin, 2012.

[15] Wang, W.H., Cheng, X.T., Liang, X.G., "Analyses of the endoreversible Carnot cycle with entropy theory and entransy theory", Chinese Physics B, 2013.

[16] Açıkkalp, E., "Entransy analysis of irreversible heat pump using Newton and Dulong–Petit heat transfer laws and relations with its performance", Energy Conversion and Management, 2014.

[17] Wu, Y.Q, "Output power analyses of an endoreversible Carnot heat engine with irreversible heat transfer processes based on generalized heat transfer law", Chinese Physics B, 2015.

[18] Xu, S.Z., Guo, Z.Y., "Entransy transfer analysis methodology for energy conversion systems operating with thermodynamic cycles", Energy, 2021.

[19] Xu, S.Z., Zhao, T., Chen, Q., Liang, X.G., Guo, Z.Y., "State functions/quantities in thermodynamics and heat transfer", Fundamental Research, 2022.

[20] Wang, W.H., Cheng, X.T., Liang, X.G., "Entransy dissipation and irreversibility of some thermodynamic processes", Chinese Science Bulletin, 2012.

[21] Xu, S. Z., Wang, R. Z., Wang, L. W., "Temperature–heat diagram analysis method for heat recovery physical adsorption refrigeration cycle – Taking multi-stage cycle as an example", International Journal of Refrigeration, 2017.

[22] Zhang, X.Y., Wu, J.D., Li, Z., "Irreversibility characterization and analysis of coupled heat and mass transfer processes in an absorption system," International Journal of Heat and Mass Transfer, 2019.

[23] Yang, L., Huang, S.H., Lu, Z.N., Gong, Y.L., Li, H.S., "Application and discussion on entransy analysis of ammonia/salt absorption heat pump systems", International Journal of Low-Carbon Technologies, 2021.

[24] Xu, Z.Y., Wang, R.Z., "High-Performance Absorption Thermal Storage with Once-Through Discharging," ACS Sustainable Chemistry & Engineering, 2022.

3rd to 6th of September 2023
The University of Edinburgh, Scotland

Heat Powered Cycles
Conference 2023
Edinburgh

Heat in the new energy system

A Dual-Purpose Innovative Cooling Cycle for Future Sustainability

Muhammad Ahmad Jamil, Muhammad Wakil Shahzad

[1]Mechanical & Construction Engineering Department, Northumbria University, Newcastle Upon Tyne NE1 8ST, United Kingdom

[*]Corresponding author: muhammad2.ahmad@northumbria.ac.uk

Abstract

A surge in cooling demand is observed in the last few decades because of rising temperatures, growing population, high urbanization, and improved living standards. Therefore global air conditioner possession is increasing continuously with the maximum rise in developing countries. Therefore, air conditioning-related energy demand and emissions are also increasing exponentially. Conventional vapor compression systems are energy intensive and result in harmful emissions. Therefore, there is a need to develop unconventional water-based cooling systems with lower energy consumption and benign emissions. In this regard, a dual-purpose innovative indirect evaporative cooling system is proposed and tested. The system aimed to address the major limitations in existing systems like water consumption, complex wall, low heat transfer rate, and intensive maintenance requirements. The experimental investigation revealed that the proposed system achieved a temperature drop of as high as 19 ^{o}C, a cooling capacity of 118 W, and a coefficient of performance of 29 (only for cooling) at a higher outdoor air temperature of 46 ^{o}C. Moreover, the system produced the supply air temperature at 21±0.5 ^{o}C for different outdoor air temperatures varying between 30 to 46 ^{o}C. Furthermore, the proposed IEC system can be used as a cooling tower to cool the intake water while simultaneously providing cool air. The experiments show that water in a humidifier achieves wet bulb temperature irrespective of water intake temperature. For experimentation, the water intake varied from 15 to 45 ^{o}C. Therefore, developing this advanced system is potentially a remarkable step toward the commercial-scale realization of indirect evaporative cooling technology.

Keywords: dual purpose, indirect evaporative cooling, innovative cooling system, energy efficiency, sustainable development

Introduction/Background

The global cooling demand is increasing continuously because of some of the key drivers. These include rising global surface temperature (1.5°C–1.8°C/century) [1], Population Growth which is expected to surpass 9.9 billion by 2050 [2], high urbanization rate (57%) [3], and high living standards. Meanwhile, the surge in cooling demand also increases the energy demand and emissions as well. For instance, the air conditioner stock is expected to cross 5.6 billion by 2050 [4]. The corresponding, AC energy demand is predicted to surpass 7700 terawatt-hours (TWh) and the emissions are expected to cross 170 Gt. Conventional vapor compression chillers have high energy consumption and work on the typical simple cooling coil-based working cycle. This working cycle operates by maintaining rigid temperatures and pressure conditions across the evaporator and condenser [5,6]. This fixed temperature limitation poses pressure limitations across the compressor which increases

energy consumption. Also, the fixed temperature differential across the evaporator and condenser prohibits any significant improvement in the energy efficiency of the system and hence the system COP is restricted < 4 for the last three decades [7]. Meanwhile, these systems also operated on high global warming potential chemical-based refrigerants which makes them environmentally unfriendly. Therefore, the current focus in the cooling market is unconventional cooling systems. Particularly, the systems based on water are encouraged because of safe operation. In this regard, indirect evaporative cooling (IEC) has emerged as one of the viable unconventional cooling solutions operated by water. Moreover, the systems do not involve any compressor and hence have significantly lower energy demand than conventional systems [8]. However, the traditional IEC systems are only tested at a laboratory scale and have not yet been commercialized. This is because the typical design suffer various design limitations which hinder the system expansion on the large scale.

A novel dual-purpose indirect evaporative cooler is proposed and experimentally tested. The cooler can provide humidity-controlled cool air as well as can be employed to cool the hot water. This is because the proposed system has a novel operational configuration that includes a dedicated humidifier for the working airside. The humidifier simultaneously cools the working as well as showered water by harnessing the evaporative potential of air and water. The subsequent section provides details about the proposed system.

Proposed system description.

The proposed system schematic is shown in Figure 1 which shows that the system consists of a heat exchanger and a humidifier. Two fans are used to maintain the flow rates of outdoor air and working air. A pump and misting nozzle are used to shower fine mist in the humidifier. The small particle size of the mist increases the evaporation rate in the humidifier thus improving the cooling performance of the system. The heat exchanger part of the system cools the hot outdoor air by releasing its heat to the working air stream. While the humidifier is used to generate cold and humid working air by direct mixing and evaporation of water in the humidifier. This proposed arrangement addresses the design limitations of the traditional IEC systems. For example, the inclusion of a humidifier eliminates the requirements of special wall manufacturing with low thermal conductivity hydrophilic material like felt, cotton and wick, etc. Rather, the wall can be manufactured using any high thermal conductivity metal sheet which is aluminum in this case with thermal conductivity > 235 W/m. Because of simple construction the system achieves high heat transfer, no water accumulation problems, fewer fouling issues, and low capital investment. Moreover, the system does not need excessive maintenance and has high operational availability. Moreover, in the proposed arrangement, the working air enters the wet channel at the lowest temperature of wet bulb $T = T_{wb}$ with relative humidity RH = 100% which boosts the heat transfer process. The psychrometric chart of the system is shown in Figure 2. The sensible cooling of the outdoor air takes place in the dry channel (1-2). The working air is cooled and dehumidified in the humidifier (1-3), and then the working air extracts heat from the outdoor air in the wet channel (3-4). It is also important to emphasize that the heat exchanger in the proposed system always receives working air at wet bulb temperature and hence the cooler is minimally affected by the outdoor air temperature conditions. Moreover, the heat transfer process in the heat exchanger and working air humidification in the humidifier can be independently controlled and optimized. The air-water interaction through proper water showering, recirculation, and replenishment can significantly reduce water footprints thus improving overall system efficiency.
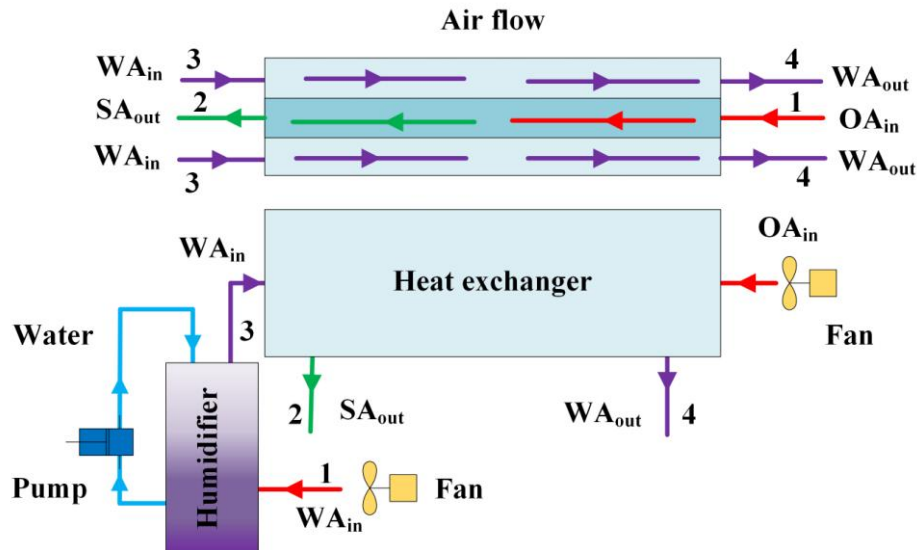
Fig. 1. Schematic of the proposed IEC.
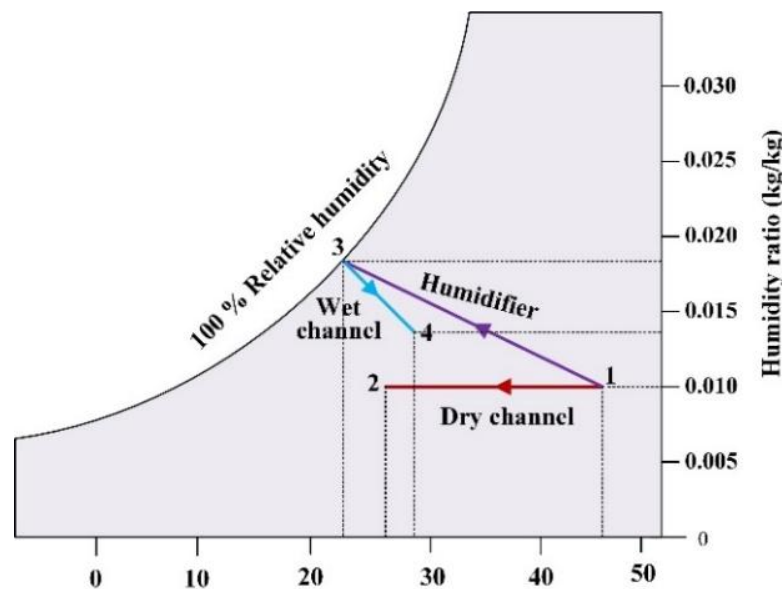
Fig. 2. Process description on the psychrometric chart.

Experimental facility

A lab-scale testing facility for the proposed IEC system was designed and fabricated as shown in Figure 3. It consists of a heat exchanger containing one dry channel in the middle and two wet channels on the sides. The system was fully instrumented with temperature sensors and flow meters to monitor and record the temperature and flow rates of air streams. The process involved the flow of outdoor air in the dry channel and the working air in the humidifier. The humidified and cooled working air enters the heat exchanger and extracts heat from the outdoor air thus cooling it to the supply air temperature. The supply air is then directed to the conditioned space and the high-humidity hot working air is discarded to the ambient. The system performance was tested under assorted operating conditions of the outdoor air temperature and the system performance was measured in terms of temperature drop, cooling capacity, and coefficient of performance as given below.
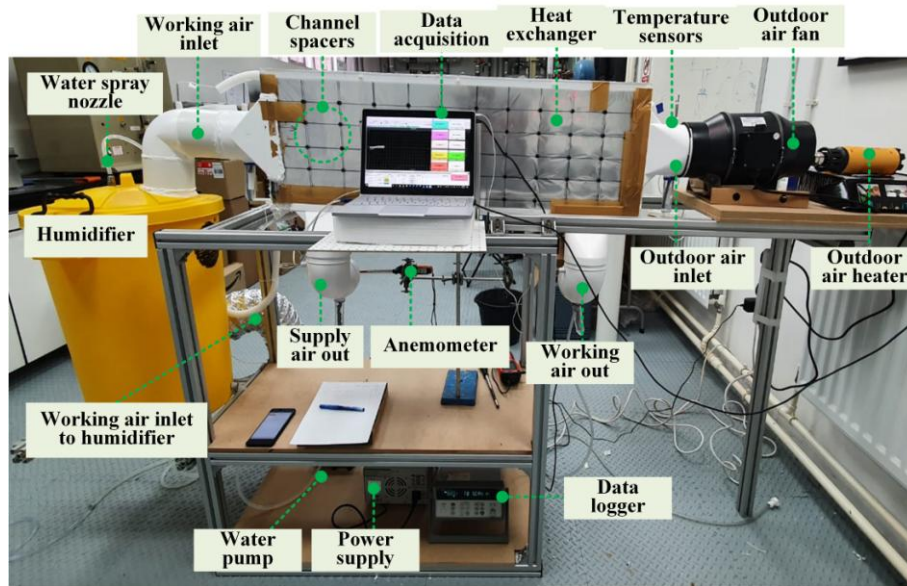
Fig. 3. Experimental test facility.

The temperature drop represents the degree of cooling achieved in the outdoor air stream and is given as the difference between the outdoor air temperature and the supply air temperature.

$$\Delta T = T_{OA,i} - T_{SA,o} \tag{1}$$

The cooling capacity is the amount of heat extracted from the outdoor air in watts and is given in terms of flow rate, specific heat, and temperature drop.

$$Q = \dot{m}_{OA} \, c_{p,OA} \left(T_{OA,i} - T_{SA,o} \right) \tag{2}$$

The coefficient of performance (COP) is calculated based on the cooling produced and the total power supplied.

$$COP = \frac{Q}{P_{input}} \tag{3}$$

Discussion and Results

The typical temperature trend for the outdoor air and supply of the system at an outdoor air temperature of 41 ± 0.5^{o}C and absolute humidity of 10 g/kg is shown in Figure 4. It is observed that the system achieved a supply air temperature of 25 ± 0.5 ^{o}C during the continuous run for 6 hours. It indicates that the system achieved a ΔT of 15 ± 0.5 ^{o}C during operation. It is also observed that the system attained stable operation and did not suffer any heat accumulation or longitudinal heat transfer across the plate.

Meanwhile, the humidifier was also performed to humidify and cool the working air as shown in Figure 5. It was seen that the working air intake in the humidifier was at 41 ± 0.5 ^{o}C and 42% relative humidity which achieved 100% relative humidity and wet-bulb temperature of 21 ± 0.5 ^{o}C. The cool, humid air carrying mist particles extracted heat from the outdoor air in the dry channel. The working air leaves the wet channel at 28 ± 0.5 ^{o}C with a temperature rise of 6 ± 0.5 ^{o}C. Meanwhile, it is also important to mention that in the working air channel, evaporation takes place which extracts the major portion of the heat from the dry channel in the form of latent heat.

Heat Powered Cycles
Conference 2023
Edinburgh
Heat in the new energy system

3rd to 6th of September 2023
The University of Edinburgh, Scotland
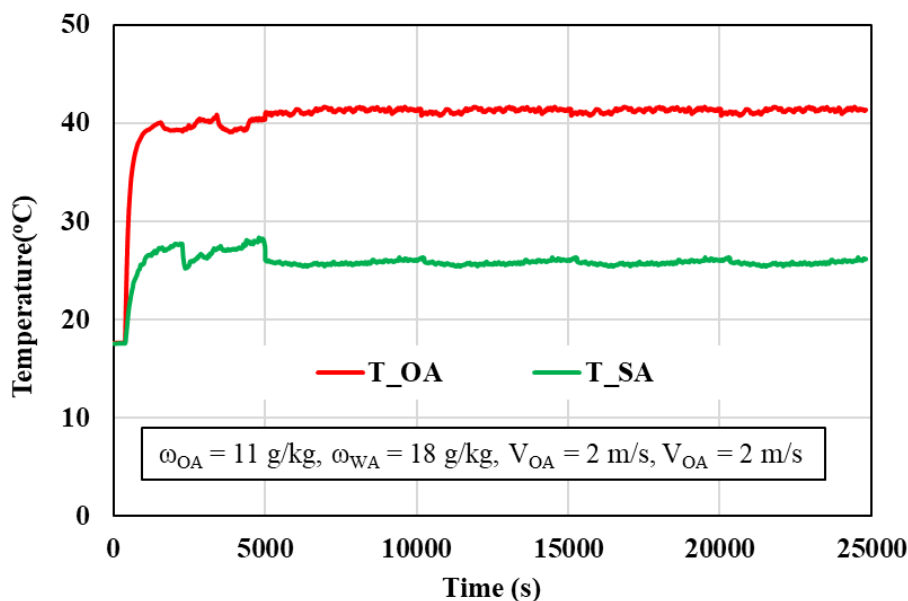
Figure 4. Outdoor and supply air temperature trends.
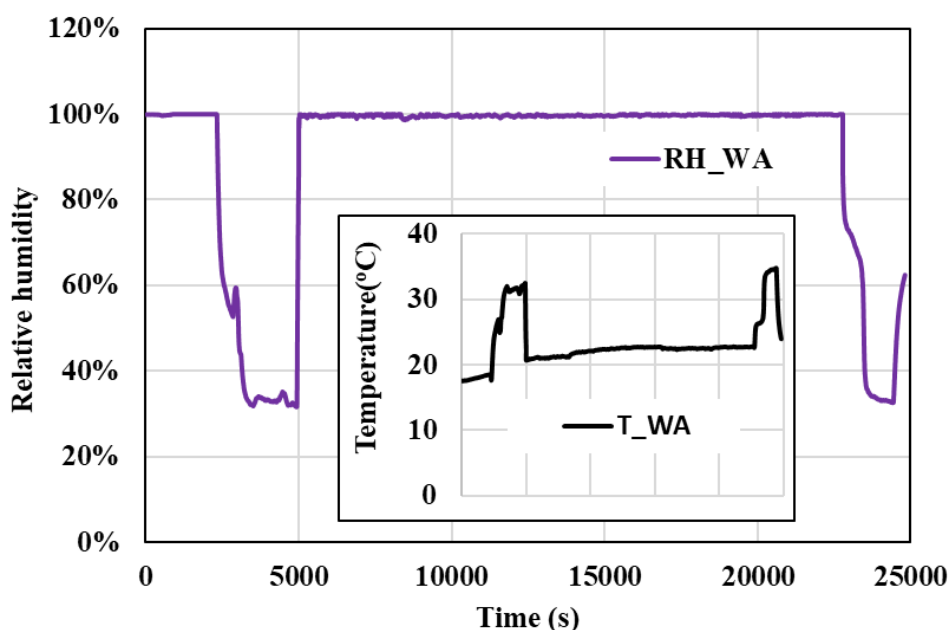
Figure 5. Working air temperature and humidity trend at humidifier outlet/channel inlet.

The system analysis on varying outdoor air temperature conditions was conducted. For this purpose, the outdoor air temperature increased from 30-46 $^{\circ}$C as shown in Table 1. It was observed that the supply air temperature varied between 23.2 to 26.8 $^{\circ}$C while T_{OA} increased from 30 to 46 $^{\circ}$C. The largest temperature drop was achieved against the maximum outdoor air temperature of 19.13 $^{\circ}$C and 48 $^{\circ}$C, respectively. Therefore, the maximum cooling capacity of 118 W was obtained against 46 $^{\circ}$C of the outdoor air temperature. Similarly, the coefficient of performance was observed to be a maximum of 29.5 (only for cooling) at an outdoor air temperature of 46 $^{\circ}$C. The decrease in cooling capacity and COP at lower outdoor air temperatures is because of a drop in the temperature differential across the air streams.

Table 1. Performance parameters at different outdoor air temperature conditions.

$T_{OA,i}$ (^oC)	$T_{SA,o}$ (^oC)	ΔT (^oC)	Q (W)	COP
30	23.24	6.76	45	11.25
34	23.96	10.04	61	15.25
38	24.56	13.44	76	19
42	25.69	16.31	102	25.5
46	26.87	19.13	118	29.5

Furthermore, the proposed IEC system can be used as a cooling tower to cool the intake water while simultaneously providing cool air. The experiments show that water in a humidifier achieves wet bulb temperature irrespective of water intake temperature. For experimentation, the water intake varied from 15 to 45 ^oC. As depicted in Figure 6, the sump water in the humidifier achieved wet bulb temperature within first hour of operation irrespective of intake temperature. It indicated that the proposed system is suitable for assorted operating scenarios.
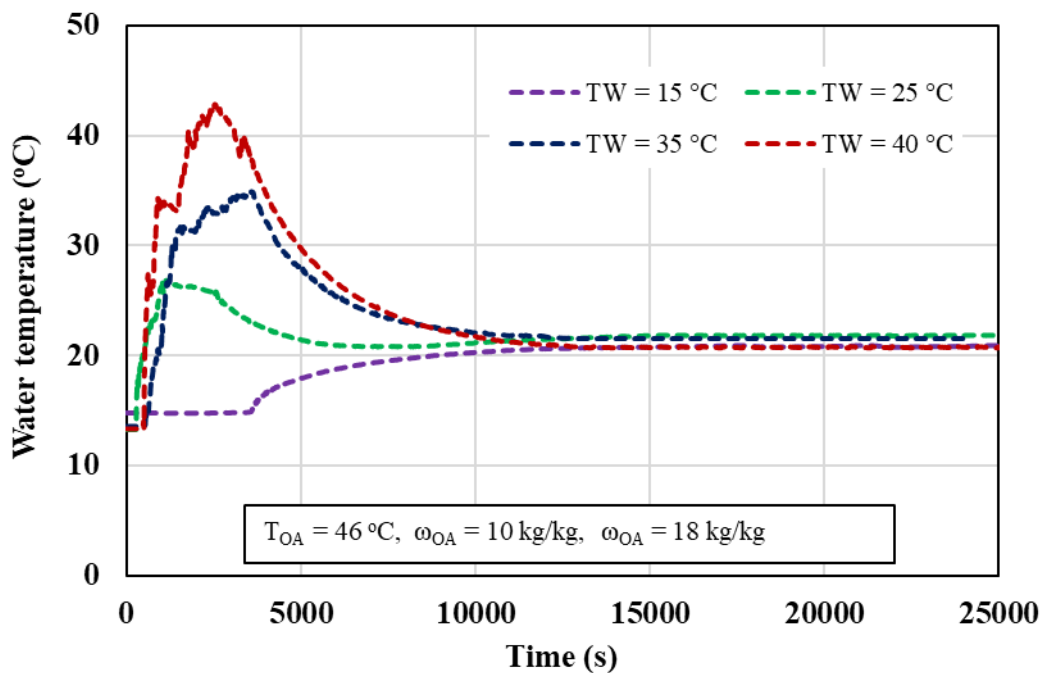
Figure 6. Water temperature trends during IEC operation.

Summary/Conclusions

A dual-purpose innovative indirect evaporative cooling system is proposed to address the major constraints in conventional systems. These include water consumption, complex wall, low heat transfer rate, and intensive maintenance requirements. The experimental investigation revealed that the proposed system achieved a temperature drop of as high as 19 ^{o}C, a cooling capacity of 118 W, and a coefficient of performance of 29 (only for cooling) at a higher outdoor air temperature of 46 ^{o}C. Moreover, the system produced the supply air temperature at 21±0.5 ^{o}C for different outdoor air temperatures varying between 30 to 46 ^{o}C. Furthermore, the proposed IEC system can be used as a cooling tower to cool the intake water while simultaneously providing cool air. The experiments show that water in a humidifier achieves wet bulb temperature irrespective of water intake temperature. For experimentation, the water intake varied from 15 to 45 ^{o}C. As The sump water in the humidifier achieved wet bulb temperature within half an hour of operation irrespective of intake temperature. It indicated that the proposed system is suitable for assorted operating scenarios. The system performance under all conditions is competitive with the existing IEC systems with additional benefits of high heat transfer, resilient design, easy operation, and low maintenance requirements. Therefore, developing this advanced system is potentially a remarkable step toward the commercial-scale realization of IEC technology.

Acknowledgments

References

[1]   Blunden J, Hartfield G, Arndt DS. State of the climate in 2017. Bull Am Meteorol Soc 2018;99:1–330. https://doi.org/10.1175/2018BAMSSTATEOFTHECLIMATE.1.

[2]   PRB. (Population Reference Bureau): World Population Data Sheet 2018. https://www.prb.org/resources/2018-world-population-data-sheet-with-focus-on-changing-age-structures/ (accessed July 10, 2021).

[3]   UN. United Nations: World Urbanization Prospects - Population Division - 2018. https://population.un.org/wup/ (accessed July 10, 2021).

[4]   Campbell BI, Kalanki A, Sachar S, Hartley B. Solving the Global Cooling Challenge: How to Counter the Climate Threat from Room Air Conditioners. 2018.

[5]   Howarth N, Odnoletkova N, Alshehri T, Almadani A, Lanza A, Patzek T. Staying Cool in A Warming Climate: Temperature, Electricity and Air Conditioning in Saudi Arabia. Climate 2020;8:4. https://doi.org/10.3390/cli8010004.

[6]   Air conditioning use emerges as one of the key drivers of global electricity-demand growth - News - IEA 2018. https://www.iea.org/news/air-conditioning-use-emerges-as-one-of-the-key-drivers-of-global-electricity-demand-growth (accessed January 23, 2021).

[7]   Min Y, Chen Y, Shi W, Yang H. Applicability of indirect evaporative cooler for energy recovery in hot and humid areas: Comparison with heat recovery wheel. Appl Energy 2021;287:116607. https://doi.org/10.1016/j.apenergy.2021.116607.

[8]   Shahzad MW, Burhan M, Ybyraiymkul D, Oh SJ, Choon K. An improved indirect evaporative cooler experimental investigation. Appl Energy 2019;256:113934.

Innovative Process Integrating Waste Heat Source Heat Pumps and Direct Air Capture Processes

Bingyao Ge[1], Man Zhang[1], Xuancan Zhu[1*]

[1]Research Center of Solar Power & Refrigeration, School of Mechanical Engineering, Shanghai Jiao Tong University, 800 Dongchuan Road, Shanghai, 200240, China

Corresponding author: zhuxc19@sjtu.edu.cn (X.C. Zhu)

Abstract

Direct air capture (DAC) technology has become crucial in mitigating the effects of global warming by directly capturing CO_2 from the atmosphere. The high thermal energy consumption associated with DAC is a major challenge due to the ultra-dilute CO_2 concentration in the air. In this study, two different thermal integration strategies are proposed combining waste-heat source heat pump (WH-HP) with solid adsorbent DAC technology. In Aspen Plus models, the simple DAC with WH-HP system reduced the energy consumption by 67.5% to 536.8 kWh/tonCO_2 comparing the traditional DAC system. The novel deeply integrating DAC with WH-HP would provide a cost-effective, energy-efficient solution to enhance DAC performance.

Keywords: Heat Integration, Thermal Modelling, CO_2 capture, Waste heat source heat pump

Introduction

The cumulative amount of CO_2 emitted into the atmosphere is directly proportional to the global average temperature rise[1]. To achieve the temperature rise target below 2 °C in Paris Agreement of the 2015 Climate Conference (COP 21), it is necessary to maintain atmospheric concentration levels of CO_2 between 430–480ppm in 2100[2]. Negative emissions technologies (NETs) are required for stabilizing climate through removal of CO_2 from the atmosphere[3].

Direct air capture (DAC) is an important NET that can capture CO_2 from the air directly. According to the Net Zero Emissions by 2050 Scenario of the International Energy Agency, DAC capture capacity would be up to almost 90 MtCO_2/year in 2030 and increase significantly to 980 MtCO_2/year (13% of all CO_2 emissions) in 2050[4]. DAC was first proposed to mitigate climate change in 1999[5] and has been at high technology readiness level (TRL 6) via lots of plants in 2022[4].

Considering the ultradilute CO_2 in the air (400 ppm), removing CO_2 from the atmosphere requires a higher energy input and cost than other traditional capturing technologies. Wohland et al.[6] showed that to ensure negative CO_2 emissions, at least 80% of the electricity needs to be from renewable energy when operating DAC plants entirely on electricity. However, the average thermal and electric power requirement of DAC is 80% and 20% respectively[7]. Using high-quality electric energy completely for regeneration (enrich captured CO_2) heat demand is not an optimal solution.

There are two main technology approaches for DAC: high-temperature (~800 °C) aqueous solution (HT DAC) and low-temperature (80–100 °C) solid sorbent (LT DAC) systems[8]. LT DAC systems do not require high-temperature demand. Therefore, it has considerable potential for cost reduction by acquiring thermal energy from low-temperature waste heat.

Heat pumps can absorb low-grade heat from waste heat or even ambient heat to improve energy efficiency[9]. Combining the waste heat source heat pump (WH-HP) to meet the thermal energy of the DAC system can greatly reduce the system energy consumption, further lessen the

dependence of the DAC system on renewable energy power and increase the flexibility of the DAC system layout. G. Leonzio and N. Shah[10] applied air source heat pump (ASHP) to supply hot water for DAC by taking heat from air. By simulating different working fluids (CO_2, CO_2-ethane, CO_2-R41) in Aspen Plus software, the integrated process can save energy consumption of 55%, 60%, and 53% respectively.

At present, there is no detailed study on DAC coupled waste heat source heat pump systems. In this study, two system schemes for DAC with WH-HP system are proposed: simple DAC with WH-HP system and deeply integrating DAC with WH-HP system (named HP-DAC). Simulations were conducted in the Aspen Plus based on the same CO_2 capture capacity and thermal requirements. Compared with the simple DAC with WH-HP system, HP-DAC can save construction costs and occupied area due to the minor components. Furthermore, it displayed lower energy consumption via inner thermal integration which improved efficiency of energy utilization.

Discussion and Results

Modeling and parameter setting of DAC

The main components of a DAC unit are an adsorption tower and a desorption tower for continuous CO_2 production. The cyclic capture of the DAC unit is realized by the regeneration at high temperature and re-adsorption at low temperature of the adsorbent in the same tower. As shown in **Figure 1**, the simplified DAC process consists of cooling/adsorption stage and heating/desorption stage. In the cooling/adsorption stage, air flows into the adsorption tower while achieving adsorbent cooling and CO_2 adsorption. At the same time, to speed up the cooling stage and maintain the temperature stability of the adsorption, another cold fluid that does not directly contact with the adsorbent is also sent into the adsorption tower. In the heating/desorption stage, the adsorbents are heated to desorption temperature, and captured CO_2 is released due to the hot fluid flows.
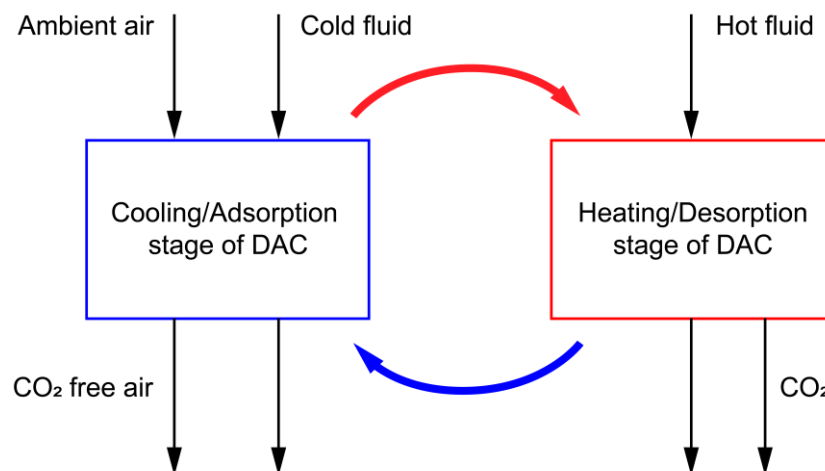
Figure 1. Diagram scheme of the DAC unit

The adsorbent in the adsorption/desorption tower is the aminosilane-functionalized nanofibrillated cellulose sorbent material (abbreviated as APDES-NFC-FD), and its characteristic parameters are displayed in **Table 1**. The DAC unit has a CO_2 capture capacity of 152 kg_{CO2}/day[11].

Heat Powered Cycles
Conference 2023
Edinburgh

Heat in the new energy system

3rd to 6th of September 2023
The University of Edinburgh, Scotland

Table 1 Main data of the APDES-NFC-FD sorbents[12]

Parameter	Value
working capacity (mol/kg)	0.771
specific heat capacity of sorbent (J/kg/K)	2070[13]
adsorption temperature (°C)	25
desorption temperature (°C)	100
heat of CO_2 adsorption (J/mol)	60000
captured CO_2 per unit (kg/day)	152

The energy consumption of the DAC part includes external heat, external electricity, and internal heat. 1: External heat is the industrial waste heat input to the system. 2: External electricity includes power consumption of compressors and hot water pumps. Fan power consumption is not considered due to consistent air flow in both systems. 3: Internal heat is the thermal energy for regeneration which considers the sensible heat and adsorption heat and can be calculated according to the following equation[14].

$$Q_{in} = \frac{1}{q_w} C_{p,s}(T_{de} - T_{ad}) + \Delta H_{CO_2} \qquad (1)$$

In the above equation, Q_{in} is the regeneration heat (J/mol), q_w is the working capacity of adsorbent (mol/kg), $C_{p,s}$ is the specific heat capacity of adsorbent (J/kg/K), T_{de} and T_{ad} are the desorption and adsorption temperature, respectively (K), and ΔH_{CO_2} is the heat of CO_2 adsorption (J/mol). Calculated results show that the regeneration heat of the APDES-NFC-FD sorbents is 1650 kWh/tonCO_2. Therefore, 104.5 kW thermal energy needs to be provided to ten DAC units, producing 1520 kg/day CO_2. The sensible heat and adsorption heat require 64.4 kW and 40.1 kW, respectively.

Simple DAC with WH-HP system

The flowsheet of the simple DAC with WH-HP system is shown in **Figure 2**. To simplify the simulation, WH-HP is a single-stage compression heat pump with a single waste-heat source. The WH-HP provides hot water to meet the regeneration thermal needs of DAC by a water pump. The regenerated CO_2 from adsorbents in the desorption tower will be collected for further sequestration or utilization. At the same time, the CO_2 from air will be captured in an adsorption tower. After adsorption saturation, exchange the hot water and air flow destination to the adsorption tower and desorption tower shown in **Figure 2** respectively so that the DAC system can operate continuously.
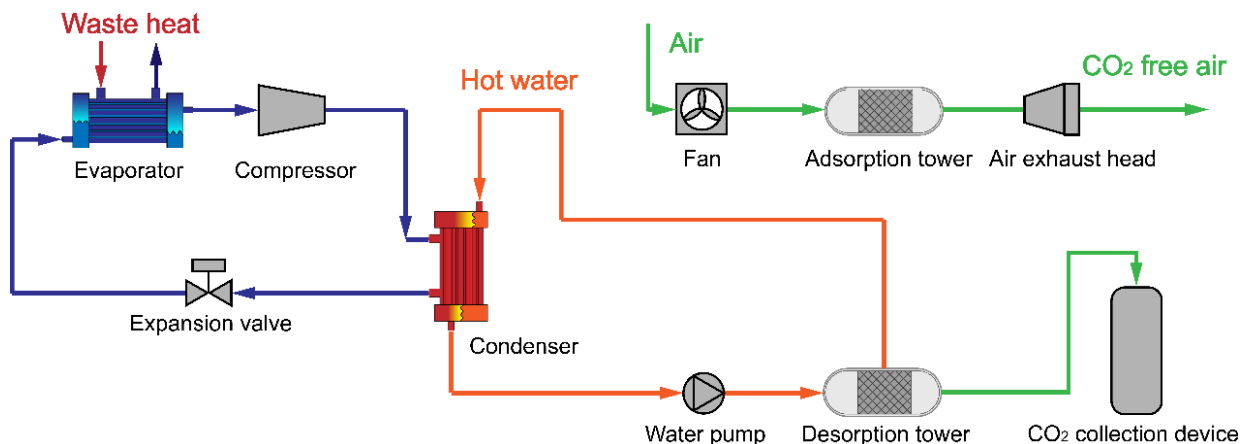
Figure 2. The flowsheet of simple DAC with WH-HP system

The waste hot water at 60 °C is considered an external low-temperature heat source for the WH-HP system in the Aspen Plus model. And the working fluid of the WH-HP cycle is

Heat Powered Cycles
Conference 2023
Edinburgh
Heat in the new energy system

3rd to 6th of September 2023
The University of Edinburgh, Scotland

conventional R245fa. **Table 2** presents the main data of the WH-HP system. The heat pump constantly generates hot water at 100 °C in order to meet the regeneration of DAC units. For the simple DAC with WH-HP system of capturing 1520 kg_{CO_2}/day, 34 kW of electrical energy was required. Compared with the traditional DAC with the same thermal demand of regeneration (1650 $kWh/tonCO_2$), it reduced energy consumption by 67.5% to 536.8 $kWh/tonCO_2$. The coefficient of performance (COP) of WH-HP was 3.07.

Table 2 Main data of the WH-HP system

Parameter	Value
waste heat temperature (°C)	60
evaporation temperature (°C)	50
condensation temperature (°C)	110

Deeply integrating DAC with WH-HP

For the DAC system, the adsorption tower is an exothermic component including the latent heat when adsorbing CO_2 and sensible heat from switching the high temperature (100 °C) to a suitable adsorption temperature (25 °C). The desorption tower needs to absorb thermal energy oppositely. Considering the energy consumption of DAC units and WH-HP, the deeply integrating DAC units with the WH-HP system is proposed in **Figure 3**. On the condensation side, the desorption tower as a condenser is directly heated by the refrigerant. Therefore, the electrical power consumption of hot water pumps can be saved compared with the conventional DAC systems. On the evaporation side, the refrigerant splits into two streams: one enters the waste heat exchanger, and the other flows through the adsorption tower to cool the sorbents. Noting the refrigerant entering the adsorption tower needs to be throttled down to 25 °C again due to the operating conditions of the sorbents. Therefore, the HP-DAC system need not require additional cooling water to the adsorption tower for rapid cooling and staying the temperature at 25 °C.
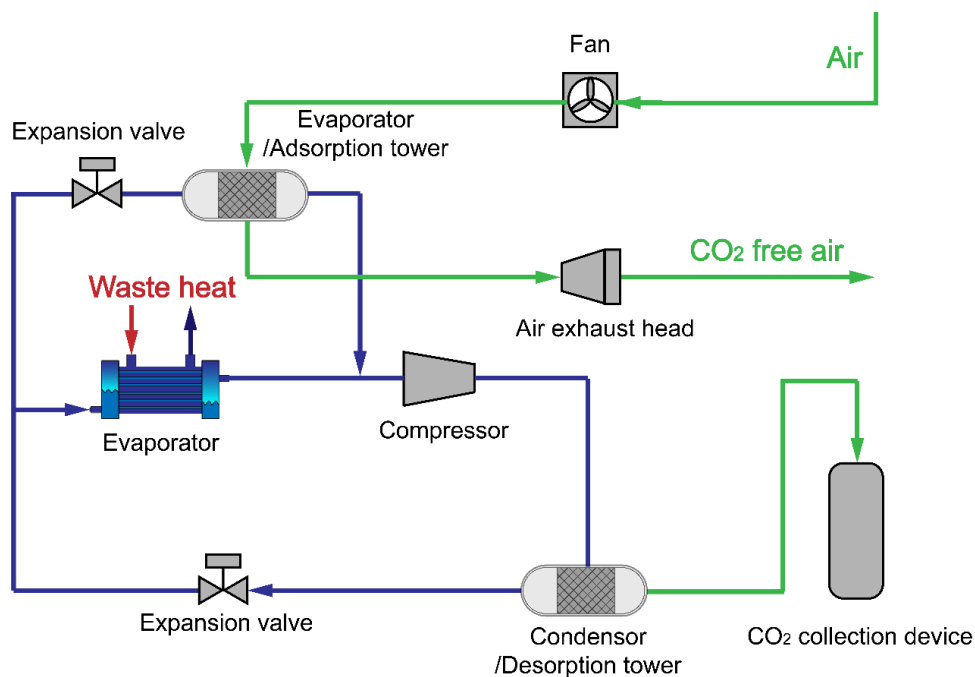
Figure 3. The flowsheet of deeply integrating DAC with heat pump (HP-DAC)

In the simulated model of the HP-DAC system, the temperature and working fluid were set to be the same as the simple DAC with WH-HP system. **Table 3** provides the main data of the HP-DAC system. Especially, the setting condensation temperature is lower than that in the

simple DAC with WH-HP system due to fewer heat transfer times (the working fluid exchanges thermal energy with adsorbents directly). The HP-DAC have enormous advantages in energy saving in our above analysis. Different refrigerants with negligible global warming potential (GWP) such as 1233zd, 600a, and CO_2 would also be applied and investigated in the HP-DAC system except for R245fa. Detailed cost-saving values of this novel system will be provided after further calculation.

Table 3 Main data of heat pump in HP-DAC system

Parameter	Value
waste heat temperature (°C)	60
primary evaporation temperature (°C)	50
secondary evaporation temperature (°C)	25
condensation temperature (°C)	105

Conclusions

To decrease the high energy consumption of DAC, especially since the thermal energy demand accounts for ~80%, the WH-HP was applied to supply the thermal energy (100 °C) from the low-temperature waste water (60 °C) for the DAC system. This paper presents two various thermal integrated systems and corresponding models in Aspen Plus.

For the simple one, WH-HP directly provides hot water (100 °C) to meet the regeneration thermal needs of DAC. The COP of single-stage compression WH-HP can reach 3.07 in this situation. And the participation of WH-HP saved the regenerative thermal energy consumption of 67.5% compared to a conventional DAC system. It means energy demand decreased to 536.8 kWh/tonCO$_2$ from 1650 kWh/tonCO$_2$.

For the deep thermal integration system, exothermic adsorption tower and endothermic desorption tower of DAC units replaced the evaporation and condensation of the heat pump, respectively. An extra-evaporation set parallel with the adsorption tower (inner heat source) is the outside heat source from waste heat water. The novel DAC system deeply integrating WH-HP was first proposed (denoted as HP-DAC). Therefore, the refrigerant can exchange thermal energy with adsorbents directly so that the additional water pumps and chiller for the cooling stage can be saved. The system with low energy consumption and low cost would be investigated by applying different refrigerants with low GWP in further research.

Acknowledgments

References:

[1] al, J. R. e. Zero emission targets as long-term global goals for climate protection. Environ. Res. Lett. 2015.

[2] Fuss, S.; Canadell, J. G.; Peters, G. P.; Tavoni, M.; Andrew, R. M.; Ciais, P.; Jackson, R. B.; Jones, C. D.; Kraxner, F.; Nakicenovic, N.; et al. Betting on negative emissions. Nature Climate Change 2014.

[3] Smith, P.; Davis, S. J.; Creutzig, F.; Fuss, S.; Minx, J.; Gabrielle, B.; Kato, E.; Jackson, R. B.; Cowie, A.; Kriegler, E.; et al. Biophysical and economic limits to negative CO2 emissions. Nature Climate Change 2016.

[4] Direct Air Capture A key technology for net zero; International Energy Agency (IEA), 2022.

[5] Lackner, K., Ziock, Hans-Joachim, and Grimes, Patrick. . Carbon Dioxide Extraction from Air: Is It An Option? 1999.

[6] Wohland, J.; Witthaut, D.; Schleussner, C.-F. Negative Emission Potential of Direct Air Capture Powered by Renewable Excess Electricity in Europe. Earth's Future 2018.

[7] National Academies of Sciences, E.; Medicine. Negative Emissions Technologies and Reliable Sequestration: A Research Agenda; The National Academies Press, 2019.

[8] Fasihi, M.; Efimova, O.; Breyer, C. Techno-economic assessment of CO2 direct air capture plants. Journal of Cleaner Production 2019.

[9] Yan, H.; Zhang, C.; Shao, Z.; Kraft, M.; Wang, R. The Underestimated Role of the Heat Pump in Achieving China's Goal of Carbon Neutrality by 2060. Engineering 2022.

[10] Leonzio, G.; Shah, N. Innovative Process Integrating Air Source Heat Pumps and Direct Air Capture Processes. Industrial & Engineering Chemistry Research 2022.

[11] Gebald, C.; Wurzbacher, J. A.; Tingaut, P.; Zimmermann, T.; Steinfeld, A. Amine-Based Nanofibrillated Cellulose As Adsorbent for CO2 Capture from Air. ENVIRONMENTAL SCIENCE & TECHNOLOGY 2011.

[12] Leonzio, G.; Fennell, P. S.; Shah, N. A Comparative Study of Different Sorbents in the Context of Direct Air Capture (DAC): Evaluation of Key Performance Indicators and Comparisons. APPLIED SCIENCES-BASEL 2022.

[13] Wurzbacher, J. A. Development of a temperature-vacuum swing process for CO2 capture from ambient air. ETH Zurich, 2015.

[14] Gray, M. L.; Hoffman, J. S.; Hreha, D. C.; Fauth, D. J.; Hedges, S. W.; Champagne, K. J.; Pennline, H. W. Parametric Study of Solid Amine Sorbents for the Capture of Carbon Dioxide. Energy & Fuels 2009.

Experimental testing of an adsorption thermal energy storage system

S. Vasta[1*], A.J. Di Cicco[2], T. Toppi[2], M. Motta[2,3], A. Freni[3]

[1]CNR - Institute of Advanced Energy Technology "Nicola Giordano" (ITAE), Messina, Italy

[2]Department of Energy, Politecnico di Milano, via Lambruschini 4, 20156, Milano, Italy

[3]CNR - Institute of Chemistry of Organo Metallic Compounds (ICCOM), Pisa, Italy

[*]Corresponding author: salvatore.vasta@itae.cnr.it

Abstract

The objective of this work is to test and characterize a lab-scale silica gel/water test bench realized at POLIMI labs and operating as Thermal Energy Storage (TES) system for domestic applications. Several charging and discharging cycles were performed setting 20-35, 30-50, and 80-90 °C as heat transfer fluid temperatures for the evaporation, condensation/adsorption and desorption processes. The system performance is evaluated in terms of energy efficiency, charge and discharge rate, and operating cost.

Keywords: Adsorption, Silica Gel/Water, Thermal Energy Storage

Introduction

Despite the fact that 2020 emissions were lower than in 2019 as a result of the COVID-19 crisis and subsequent countermeasures, GHG concentrations in the atmosphere continue to rise, with the immediate reduction in emissions predicted to have a minor long-term influence on climate change. In 2019, global GHG emissions increased for the third year in a row, reaching a new high of 52.4 GtCO2e without land-use change (LUC) emissions and 59.1 GtCO2e when LUC emissions are included. Total GHG emissions are dominated by fossil carbon dioxide (CO2) emissions (from fossil fuels and carbonates). Fossil CO2 emissions in 2019 set a new high of 38.0 GtCO2 [1]. In contrast, global GHG emissions in 2030 need to be approximately 25% and 55% lower than in 2017 to put the world on a least-cost pathway to limiting global warming to 2 °C and 1.5 °C, respectively [2].

Global CO2 emissions are above the targets set by the agreements on Mitigation of Climate Change and the national governments. The major reason is that although energy efficiency considerably improved and renewables have been installed at a large scale, this was overcompensated by economic growth resulting in an increase in emissions. Furthermore, heating/cooling and domestic hot water production represent an important share of the primary energy demand in the residential sector. In such a context, Thermal Energy Storage (TES) systems have the potential to revolutionize the way households meet their energy demands, but the development of efficient and cost-effective units is crucial. In this work, we present the experimental testing of a lab-scale silica gel/water test bench realized at POLIMI labs and operating as a Thermal Energy Storage (TES) system for domestic applications.

Adsorption technology is a promising method for thermal energy storage in residential applications [3, 4]. The technology involves the use of adsorbent materials to store thermal energy in the form of heat. These materials have the ability to adsorb heat by attracting and retaining heat energy at high temperatures. The most commonly used adsorbents are silica-gel and zeolites. Zeolites are porous minerals that have a high surface area, making them ideal for heat storage. They can store heat at high temperatures and release it when needed, making them a promising material for residential thermal energy storage.

Adsorption technology is highly attractive for residential applications due to its high energy storage density, low cost, and ease of integration with existing heating systems. It has the potential to significantly reduce energy costs and improve energy efficiency in residential homes.

Discussion and Results

The studied system is based on a sorption storage technology, which relies on the reversible reaction, associated with a high amount of thermal energy, occurring between a sorbent and a sorbate. Such a process is limited by the slow reaction kinetics, because of the large amount of heat associated as well as the heat and mass transfer diffusion resistance within the material. However, this feature is extremely useful in a residential-type application, since it allows the reaction to be controlled and the discharge power to be regulated precisely. In the proposed concept, the solar (or alternatively, the district) heat is employed to drive a desorption process, which means that solar heat is stored in the form of adsorption potential energy. Moreover, the heat is stored without any loss until the refrigerant fluid (adsorbate) is kept separated from the adsorbent enabling in fact the long-term storage of solar energy. Generally, there are two system configurations for adsorption TES: closed and open cycle. The studied heat storage system belongs to the closed-cycle sorption storage category.
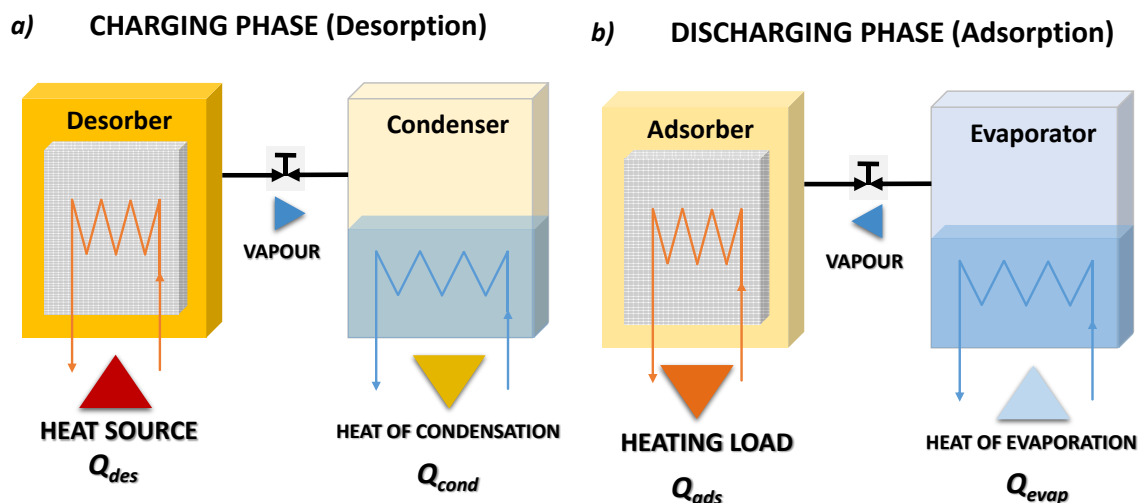
Figure 1: A closed adsorption heat storage cycle: (a) charging phase; (b) discharging phase

Figure 1 reports the working phases of closed adsorption. During the charging phase, the adsorber, in which the adsorbent material is saturated with adsorbate, is regenerated by exploiting heat coming from the solar field. The desorbed vapour is then condensed in the condenser, and the heat of condensation, Qcond, is either dissipated in the ambient or delivered to a proper load if the temperature level is adequate. Once the charging process is completed, and the adsorbent material is dry, the connection between the condenser and adsorber is closed. In this condition, the system can keep the stored energy for an indefinite time since the thermal energy is stored as adsorption potential between adsorbate and adsorbent material. To recover the stored thermal energy the connection between the liquid adsorbate reservoir, which in this phase acts as an evaporator, and the adsorber is again opened. During this discharging phase, the adsorbate is evaporated adsorbing heat from the ambient, Qevap, or providing a cooling effect to the domestic user. Then, the vapour fluxes to the adsorber and, since the adsorption process is exothermic, the heat stored is released to the load. It is self-evident that in this heat storage system, the adsorbate is continuously condensed/evaporated in a closed device without any mass exchange with the ambient, thus ensuring proper operation in dry climates.

Next Fig 2a, b reports the schematic layout and a photo of the experimental set-up that has been built at POLIMI labs to test adsorption units and their components. The core of the system consists of a single adsorbent bed, a falling-film evaporator equipped with a recirculation pump to improve the heat transfer efficiency and a condenser. The adsorbent bed was made of granular RD silica gel embedded in a finned heat exchanger. The three components are connected by two electric-actuated valves to allow the passage of water vapour enabling the ad/desorption phase. The external sinks/sources consist of three hydraulic circuits with a nominal capacity of 2 kW for the evaporator and condenser and 5 kW for the adsorber, with flow rates between 200 and 1000 L/h. The test bench is provided with several Pt100 temperature sensors, pressure transducers and flow meters to measure the relevant quantities required to monitor the system's evolution and performance. A real-time control and data acquisition software was realised employing the LabView™ language. More details on the test bench realized at POLIMI are reported elsewhere [5].
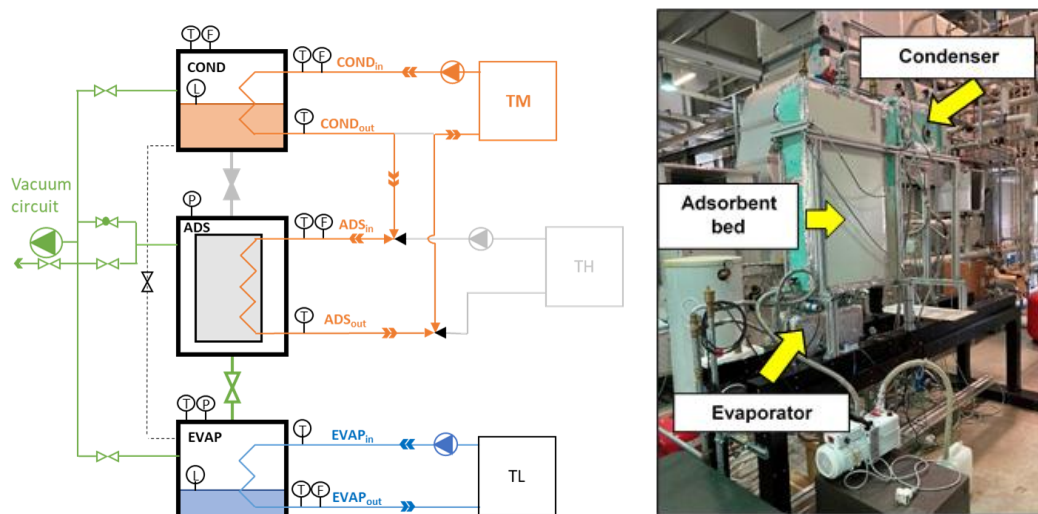
Figure 2a, b – Adsorption test rig schematic and photo

Testing activity is currently in progress according to the typical operating conditions of an adsorption TES system driven by a low-grade heating source (80-90°C) at different temperatures of evaporation and adsorption/condensation. The system performance is evaluated in terms of energy efficiency, charge and discharge rate, and operating cost. Preliminary testing results confirm the high potential for adsorption thermal energy storage systems in the residential sector and highlight the importance of continued research and development in this field.

References:

[1] United Nations Environment Programme, Emissions Gap Report, 2020th ed., United Nations Environment Programme (UNEP) and UNEP DTU Partnership (UDP)., Nairobi, 2020. https://www.unep.org/emissions-gap-report-2020.

[2] J. Delbeke, A. Runge-Metzger, Y. Slingenberg, J. Werksman, The paris agreement, Towar. a Clim. Eur. Curbing Trend. (2019) 24–45. doi:10.4324/9789276082569-2.

[3] Wei, Y., Han, X., Zhang, Y., & Zhang, X. (2017). Adsorption heat storage materials and systems for building heating and cooling. Energy and Buildings, 150, 78-93.

[4] L. Scapino, H. A. Zondag, J. Van Bael, J. Diriken, C.C.M. Rindt, Sorption heat storage for long-term low-temperature applications: A review on the advancements at material and prototype scale, Applied Energy, 190, 920-948 (2017).

[5] T. Toppi, T. Villa, S. Vasta, W. Mittelbach, A. Freni, Testing of a falling-film evaporator serving a silica gel/water adsorption chiller, Energies, 15 (5), 1709 (2022).

Assessment of coated monoliths for Direct Air Capture

I.C.C Quaranta[1], M. Luberti[2], S. Brandani[1] and G. Santori[1*]

[1] The University of Edinburgh, School of Engineering, Institute for Materials and Processes, Robert Stevenson Road, Edinburgh, EH9 3FB, United Kingdom
[2] The University of Manchester, Oxford Road, M13 9PL, Manchester, United Kingdom

[*]Corresponding author: g.santori@ed.ac.uk (G. Santori)

Abstract

Zinc-based Metal-Organic Framework (MOF) CALF-20 is a promising material for carbon capture due to its high CO_2 capacity and reduced water uptake. This study assesses the use of a monolith coated with CALF-20 to capture ultra-dilute CO_2 from air in order to contain the energy required to process large air flows through a contactor with reduced pressure drops. The monolith is designed taking into account the superficial velocity through the channels and the multicomponent adsorption of N_2, CO_2, and H_2O. Different desorption temperatures are analysed, showing the possibility to regenerate the monolithic adsorption bed with low temperature heat below 80 °C.

Keywords: Direct Air Capture, Carbon Dioxide, CALF-20, Monolith, Adsorption.

Introduction

It has been almost a decade since the 2015 Conference of Parties in Paris, where several countries set an ambitious goal to contain climate change by limiting global warming in below 2 °C. Despite the current efforts global temperature continues to rise each year, reaching its peak since the 19th century [1, 2]. Containing new emissions alone cannot revert the ongoing situation. The removal of CO_2 that is present in the atmosphere has become a mandatory measurement to reduce this gas concentration levels.

Direct Air Capture (DAC) is a promising negative emission technology (NET) that targets CO_2 removal from air by using reversible adsorption processes. In contrast to post-combustion carbon capture, DAC needs to capture ultra-dilute CO_2 (approximately 400 ppm in ambient air), compress and purify it to at least 95% by volume to be used in a downstream processes or stored underground [3]. The development of sorbent materials that have a high CO_2 working capacity and a small water uptake is one of the key requirements to enable a wider deployment of DAC. Several sorption-based DAC processes are heat-powered and low-temperature heat is preferable for regenerating the sorbent since it makes the process more economically attractive [4, 5], for the possibility to recover energy sources that would be otherwise wasted.

This work aims to evaluate the use of monoliths of CALF-20 for DAC. This Metal-Organic Framework (MOF) shows high CO_2 capacity, while maintaining some degree of hydrophobicity [6]. The use of coated monoliths as adsorption beds allow reduced pressures drops, less energy input and a closer contact between the gas and the adsorbent [7, 8].

Methodology

A plug flow isothermal mass balance was elaborated considering the following assumptions: (i) gas phase described by ideal gas law; (ii) equilibrium theory; (iii) negligible radial profiles; (iv) the bed was initially filled with pure nitrogen at 101.325 kPa and 298.15 K; (v) adsorption multicomponent equilibrium is described by the Ideal Adsorbed Solution Theory (IAST) [9]. Pressure drop model is reported in [10]. The overall and component mass balances are described in Equations 1 and 2.

Heat Powered Cycles
Conference 2023
Edinburgh
Heat in the new energy system

3rd to 6th of September 2023
The University of Edinburgh, Scotland

$$\frac{\partial (u.C_T)}{\partial z} + \varepsilon_b.\frac{\partial C_T}{\partial t} + (1 - \varepsilon_b).\rho_B.\sum_i \frac{\partial q_i}{\partial t} = 0 \tag{1}$$

$$\frac{\partial (u.C_i)}{\partial z} + \varepsilon_b.\frac{\partial C_i}{\partial t} + (1 - \varepsilon_b).\rho_B.\frac{\partial q_i}{\partial t} = 0 \tag{2}$$

Where u (m/s) is the gas superficial velocity, C_T (mol/m³) is the total concentration in the gas phase, C_i (mol/m³) is the concentration of component i in the gas phase, ε_b is the external void fraction, ρ_B (kg/m³) is the particle density, and q_i (mol/kg¹) is the adsorbed amount of component i.

Air composition in feed is assumed to contain only N_2, CO_2 and H_2O, and all other atmospheric gases are lumped in N_2 concentration. Adsorption isotherms are described by Equations 3 to 5 [6].

$$q_{N2} = q_{s1,N2} \frac{b_{1,N2}\, C_{N2}}{(1 + b_{1,N2}\, C_{N2})} \tag{3}$$

$$q_{CO2} = q_{s1,CO2} \frac{b_{1,CO2}\, C_{CO2}}{(1 + b_{1,CO2}\, C_{CO2})} + q_{s2,CO2} \frac{b_{2,CO2}\, C_{CO2}}{(1 + b_{2,CO2}\, C_{CO2})} \tag{4}$$

$$q_{H2O} = q_{s1,H2O} \frac{b_{11,H2O}\, C_{H2O} + 2b_{12,H2O}(C_{H2O})^2 + 3b_{13,H2O}(C_{H2O})^3}{(1 + b_{11,H2O}\, C_{H2O} + b_{12,H2O}(C_{H2O})^2 + b_{13,H2O}(C_{H2O})^3)} + q_{s2,H2O} \frac{b_{2,H2O}\, C_{H2O}}{(1 + b_{2,H2O}\, C_{H2O})} \tag{5}$$

Where $q_{s,i}$ (mol/kg) is the saturation capacity (of site n) and b_i (m³/mol) is the adsorption equilibrium constant (of site n). The values of those parameters are reported in Table 1. The parameter b (m³/mol) is dependent of temperature following Equation 6.

$$b_i = b_0.\exp\left(-\frac{\Delta U_i}{RT}\right) \tag{6}$$

Table 1: Pure components isotherm parameters [6]

Parameter	Value	Unit	Parameter	Value	Unit
N_2 isotherm			H_2O isotherm		
$q_{s1,N2}$	5.6583	mol/kg	$q_{s1,H2O}$	1.6290	mol/kg
$b_{01,N2}$	$8.143\ 10^{-7}$	m³/mol	$b_{011,H2O}$	$-2.685\ x\ 10^{-17}$	m³/mol
ΔU_{N2}	$-17.96\ x10^3$	J/mol	$b_{012,H2O}$	$1.158\ x10^{-16}$	(m³/mol)²
CO_2 isotherm			$b_{013,H2O}$	$5.374\ x10^{-17}$	(m³/mol)³
$q_{s1,CO2}$	2.3870	mol/kg	$\Delta U_{1,H2O}$	$-97.99\ x10^3$	J/mol
$b_{01,CO2}$	$5.519\ x10^{-7}$	m³/mol	$q_{s2,H2O}$	5.7810	mol/kg
$\Delta U_{1,CO2}$	$-35.06\ x\ 10^3$	J/mol	$b_{02,H2O}$	$8.773\ x10^{-12}$	m³/mol
$q_{s2,CO2}$	3.2711	mol/kg	$\Delta U_{2,H2O}$	$-64.72\ x10^3$	J/mol
$b_{02,CO2}$	$5.187\ x10^{-8}$	m³/mol			
$\Delta U_{2,CO2}$	$-28.95\ x\ 10^3$	J/mol			

The process cycle was characterized by two steps: adsorption and desorption. A twin-bed system was assumed in phased cycle design, synchronizing the adsorption of one bed the desorption of the other. Initially, ambient air is fed to the contactor bed until it is saturated with CO_2. After that, part of the clean air produced in the twin-bed is heated and fed counter-currently to purge the system. Boundary conditions used in the model are described in Table 2. The mathematical model was implemented in gPROMS software [11] to solve the system of partial differential and algebraic equations. The system was discretized in 50 axial nodes and with a tolerance of 10^{-5}.

Table 2: Boundary conditions for adsorption and desorption steps

Adsorption		Desorption	
$C_{i,(z=0)} = C_{i,ads}$	$\left.\dfrac{\partial C_i}{\partial z}\right\|_{z=L} = 0$	$\left.\dfrac{\partial C_i}{\partial z}\right\|_{z=0} = 0$	$C_{i,(z=L)} = C_{i,des}$
$\left.\dfrac{\partial P}{\partial z}\right\|_{z=0} = 0$	$P_{(z=L)} = P_{atm}$	$P_{(z=0)} = P_{atm}$	$\left.\dfrac{\partial P}{\partial z}\right\|_{z=L} = 0$
$u_{(z=0)} = \dfrac{\dot{V}_{ads}}{A}$	$\left.\dfrac{\partial u}{\partial z}\right\|_{z=L} = 0$	$\left.\dfrac{\partial u}{\partial z}\right\|_{z=0} = 0$	$u_{(z=L)} = \dfrac{\dot{V}_{des}}{A}$

where $\dot{V}$ ($m^3 s^{-1}$) is the gas volumetric flowrate, and A (m^2) is the cross-sectional area, P is the pressure and P_{atm} is the atmospheric pressure (101.325 kPa). Axial position is represented by z and varies from 0 to L, where L (m) is the length of the adsorption column. The subscript i refers to the component (N_2, CO_2, and H_2O). The subscription 0, ads and des refer to the feed, adsorption, and desorption step, respectively.

A cordierite monolith (200 CPSI, 0.20 mm wall thickness, 60% wall porosity) was assumed as a support for the coating layer. Due to the high porosity of the wall of the monolith, we considered the monolith pores filled of adsorbent. The mathematical model described in this section was applied to each individual monolith channel. Multiple coating layer thicknesses were analysed to evaluate adsorption time and adsorption capacity. The monolith size was defined using the CO_2 adsorption capacity at the feed conditions in a multicomponent adsorption.

An air stream of 1 m³/h at ambient conditions (101 kPa, 298 K) containing nitrogen, carbon dioxide and water was used to feed the coated monolith. Air had a fixed CO_2 composition of 400 ppm and 1% relative humidity (RH). Different regeneration temperatures were investigated at a given air flowrate to allow adsorption and desorption steps to be similar in duration. The analysis was performed considering only equilibrium, given reliable kinetic data of the multicomponent mixture on CALF-20 are not available yet.

Results and Discussion

Bed sizing and dynamic of the adsorption step

Understanding the adsorbent working capacity is essential to size the adsorption bed. Although IAST over-predicts the water content in CALF-20 at low water concentrations, the competitive adsorption of CO_2 can be well described for relative humidity below 40% [6]. Therefore, at 298 K and 101.32 kPa, each gram of empty CALF-20 can capture 0.028 mmol of CO_2. This means that, if adsorption lasts for 1 minute, at least 10 g of adsorbent are required to capture 400 ppm of CO_2 from an air stream of 1 m^3/h.

The monolith diameter was calculated by the superficial velocity in each channel. For packed beds, typical gas superficial velocities are 0.1–0.5 m s^{-1}, but in monoliths this value can go up to 2–3 m/s [12]. A value of 1 m/s was chosen to reduce pressure drop and control residence time for a better contact between the gas and the adsorbent. To ensure that the superficial velocity in each channel does not exceed this value, the monolith was designed with a diameter of 2.5 cm.

Lastly, the monolith length was calculated as a function of the coating thickness. Typical thicknesses in range of 20–100 µm [13] were analysed and a monolith with 20 cm length and a coating layer with 50 µm was assumed. A breakthrough curve was calculated to evaluate the duration of the actual adsorption step, as shown in Figure 1.
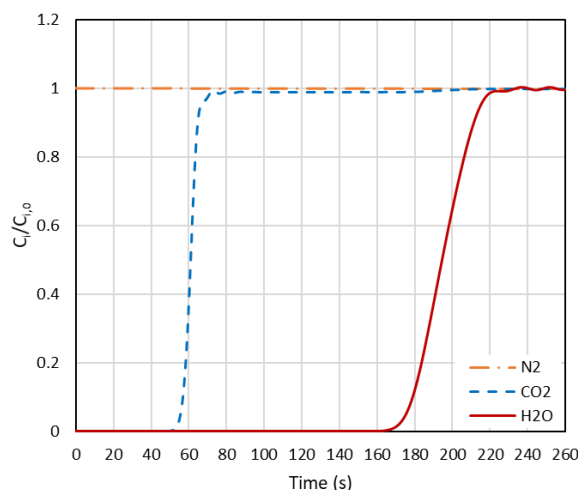
Fig. 1. *Dynamic column breakthrough for CALF-20 at 298 K and 101 kPa in a monolith channel. C_i (mol/m³) is the gas concentration of component i at z = L. $C_{i,0}$ (mol/m³) is the component concentration of the feed gas. For N_2, CO_2 and H_2O values of $C_{i,0}$ are 40.845 mol/m³, 0.016 mol/m³, and 0.013 mol/m³, respectively.*

Among the three components, nitrogen is the least strongly adsorbed, followed by CO_2, and lastly, we can observe that water breakthroughs at around 160 s. As the desired component in DAC is CO_2, the adsorption can be terminated after it reaches saturation throughout the monolith (after 70 s). The concentration change between 70 and 180 s does not justify extending the adsorption step for 110 more seconds.

Despite being the least strongly adsorbed component, nitrogen has the highest concentration in the gas phase. Therefore, N_2 has a larger loading on the adsorbed phase. Figure 2 shows the concentration profile of the adsorbed phase distributed along the length of the column at the end of the adsorption. For the conditions simulated, pressure drop across the monolith was below 30 Pa.
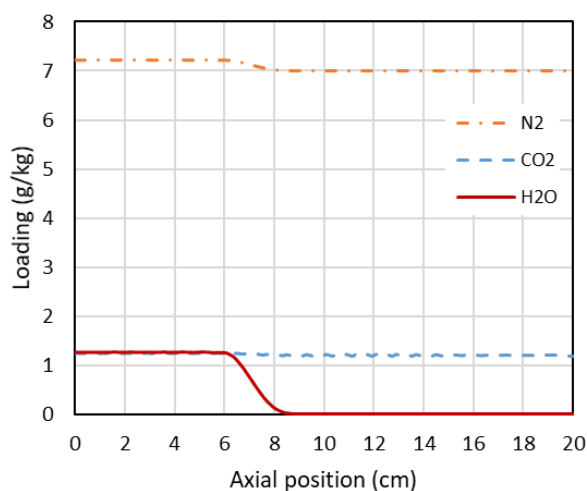
Fig. 2. *Adsorbed amount profile in the monolith channel at the end of the adsorption (70 s).*

Desorption Temperature

Recovery of the adsorption material needs a driving force to move the system to a new equilibrium. This can be done by a change in pressure, such as in Pressure Swing Adsorption, or by increasing the temperature. A combination of those can also occur, but this work limits the analysis to Temperature Swing Adsorption (TSA) only.

To simplify the initial analyses, we considered that the heating and cooling steps are instantaneous between the air and the coated layer (thermal equilibrium). Three desorption temperatures were then evaluated: 50 °C, 60 °C and 70°C, all of them below the state-of-the-art desorption temperature (around to 80 °C) for similar processes [5]. The water concentration was kept at 1% RH.

A fraction of clean air produced by the twin column (during the adsorption step) was fed at the product end ($z = L$) of the contactor bed. The purge flowrate was adjusted for each temperature to obtain a duration of 70 s. For the temperatures of 50 °C, 60 °C and 70 °C, desorption flowrates were assessed as 0.28 m³/h, 0.21 m³/h and 0.14 m³/h, respectively.
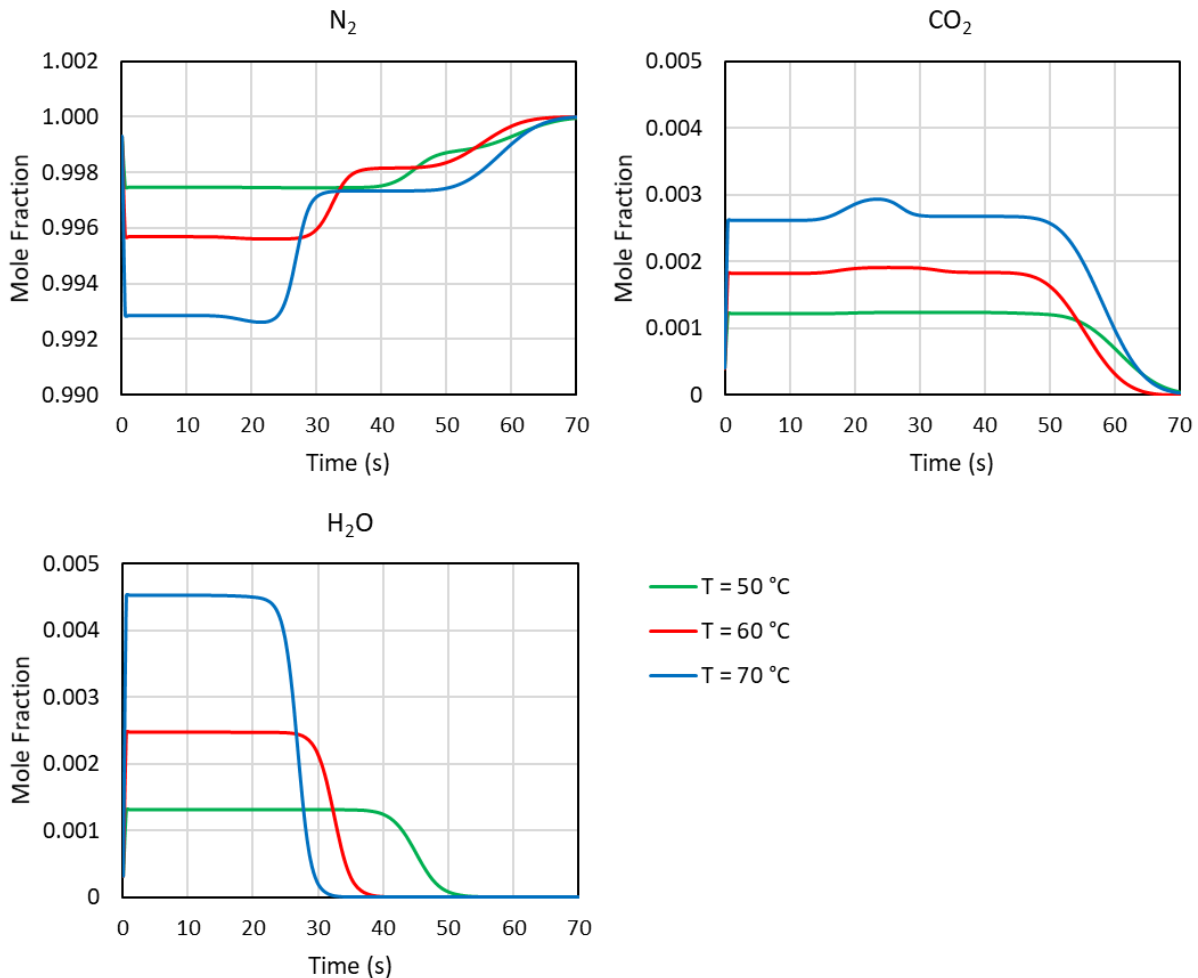
Fig. 3. *Gas phase mole fraction for N_2, CO_2 and H_2O at $z = 0$. Results for different desorption temperatures of 50 °C (── green), 60 °C (── red), and 70 °C (── blue).*

For the lowest temperature, water is desorbed almost at constant concentration during all the purge extent. By increasing desorption temperature, as it can be seen in Figure 3, water is more easily desorbed, migrating from the adsorbed phase to the gas phase. When the column is desorbed at 50 °C, water and CO_2 concentrations are similar (0.046 mol/m³ for CO_2 and 0.049 mol/m³ for H_2O) along the purge. This profile changes with the increase of desorption temperature. Both H_2O and CO_2 show a raise in concentration in the gas phase. However, water is more sensitive to this increase, desorbing faster than CO_2. For the highest desorption temperature, at 70 °C, all water is desorbed in half of the time for CO_2 desorption.

For all three temperatures the material was fully regenerated, confirming that low grade heat can regenerate CALF-20. From an energetic viewpoint, the reduction of purge flow at 70 °C

compensated the increase in temperature, being the least energy demanding among the three temperatures evaluated in this work.

Conclusions

Due to the low CO_2 concentration, the efficient removal and concentration of CO_2 from atmospheric air is a challenge. To achieve the ambitious goal of engineering energy efficient DAC processes, an appropriate adsorption material is pivotal. CALF-20, a recent hydrophobic MOF, shows promising results when used in a temperature swing adsorption process. Further studies in purification of the extracted carbon dioxide are required to achieve a low energy process. Furthermore, arranging CALF-20 in monoliths allows to reduce pressure drops across a contactor bed without compromising the energy efficiency of the whole DAC process.

Acknowledgments

References:

[1] NOAA National Centers for Environmental Information;, "Monthly Global Climate Report for Annual 2021," 2022. Available: https://www.ncei.noaa.gov/access/monitoring/monthly-report/global/202113

[2] NASA, "World of Change: Global Temperatures," 2022. https://earthobservatory.nasa.gov/world-of-change/global-temperatures (accessed Jan. 26, 2023).

[3] C. Charalambous, G. Santori, E. Vilarrasa-Garcia, M. Bastos-Neto, C. L. Cavalcante, and S. Brandani, "Pure and Binary Adsorption of Carbon Dioxide and Nitrogen on AQSOA FAM Z02," *J. Chem. Eng. Data*, vol. 63, no. 3, pp. 661–670, Mar. 2018, doi: 10.1021/acs.jced.7b00864.

[4] K. Madhu, S. Pauliuk, S. Dhathri, and F. Creutzig, "Understanding environmental trade-offs and resource demand of direct air capture technologies through comparative life-cycle assessment," *Nat. Energy*, vol. 6, no. 11, pp. 1035–1044, Nov. 2021, doi: 10.1038/s41560-021-00922-6.

[5] C. Beuttler, L. Charles, and J. Wurzbacher, "The Role of Direct Air Capture in Mitigation of Anthropogenic Greenhouse Gas Emissions," *Front. Clim.*, vol. 1, pp. 1–7, 2019, doi: 10.3389/fclim.2019.00010.

[6] J. Bin Lin *et al.*, "A scalable metal-organic framework as a durable physisorbent for carbon dioxide capture," *Science*, vol. 374, no. 6574, pp. 1464–1469, 2021, doi: 10.1126/science.abi7281.

[7] T. A. Nijhuis, M. T. Kreutzer, A. C. J. Romijn, F. Kapteijn, and J. A. Moulijn, "Monolithic catalysts as efficient three-phase reactors," *Chem. Eng. Sci.*, vol. 56, pp. 823–829, 2001.

[8] T. A. Nijhuis, A. E. W. Beers, T. Vergunst, I. Hoek, F. Kapteijn, and J. A. Moulijn, "Preparation of monolithic catalysts," *Catal. Rev. - Sci. Eng.*, vol. 43, no. 4, pp. 345–380, 2001, doi: 10.1081/CR-120001807.

[9] A. L. Myers and J. M. Prausnitz, "Thermodynamics of Mixed-Gas Adsorption," *AiChE J.*, vol. 11, no. 1, pp. 121–127, 1965.

[10] R. Mennitto, I. Sharma, and S. Brandani, "Extruded monoliths for gas separation

processes: Height equivalent to a theoretical plate and pressure drop correlations,"
AIChE J., vol. 68, no. 6, pp. 1–11, 2022, doi: 10.1002/aic.17650.

[11] Process Systems Enterprise, "gPROMS." 1997. [Online]. Available: www.psenterprise.com/products/gproms

[12] S. Roy, A. K. Heibel, W. Liu, and T. Boger, "Design of monolithic catalysts for multiphase reactions," *Chem. Eng. Sci.*, vol. 59, no. 5, pp. 957–966, 2004, doi: 10.1016/j.ces.2003.12.001.

[13] B. Mitra and D. Kunzru, "Washcoating of different zeolites on cordierite monoliths," *J. Am. Ceram. Soc.*, vol. 91, no. 1, pp. 64–70, 2008, doi: 10.1111/j.1551-2916.2007.02032.x.

Thermosyphon geysering shows characteristic pressure pattern

M.H. Buschmann[1], T. Grab[2], R. Riehl[3*]

[1]Institut für Luft- und Kältetechnik gGmbH Dresden, 01309 Dresden, Germany

[2]Lehrstuhl für Technische Thermodynamik, TU Bergakademie Freiberg

[3]GamaTech Thermal Solutions Ltda, São José dos Campos, SP Brazil

[*]Corresponding author: Matthias.Buschmann@ilkdresden.de

Abstract

Geysering is an instantaneous state of operation that may occur during start-up or under low-pressure conditions thermosyphon. The study presents experimental results of two independent thermosyphons operated with a KOH-water solution and diamond nanofluid. The pressure pattern occurring during the geyser cycle is analysed in detail. The results show a characteristic pattern similar in both devices. The investigation does not indicate significant difference between the two working fluids water and diamond nanofluid.

Keywords: thermosyphon, geysering, instantaneous pressure

Introduction/Background

Geyser boiling is a commonly observed instantaneous pressure pattern in thermosyphons (TS) [1]. It occurs at low pressure, small filling ratio, or during transient operation (start / end). Geysering is characterised by a cycle consisting of several phases. The first phase is the superheating of the working fluid in the evaporator. It follows the emergence of a big bubble. If the pressure difference between the inner of this bubble and its surrounding is large enough, the bubble expands in vertical direction and propels working fluid toward the condenser. After that, the working fluid returns to the sump and a new geyser cycle may start. The scope of this study is first to characterise the geysering cycle in more detail and second to examine how geysering changes when a diamond nanofluid is employed as working fluid.

Discussion and Results

Two independent test rigs (Fig. 1) one located at TU Bergakademie Freiberg and the other at ILK Dresden are used to detect instantaneous pressure pattern related to geysering. The first device consists of four vertical stainless steel thermosyphons each with an inner diameter of 100 mm and 1,440 mm long. The second device (copper) has an inner diameter of 20 mm and a length of 1,800 mm. The amount of working fluid is in the first case 1,500 ml and in the second 85 ml. For further technical details, it is referred to [1, 2]. In both systems, either a reference fluid or a diamond nanofluid (NF) with a concentration of 2 vol. % is employed. The latter is a suspension of nanodiamonds with a size of 59 nm. The NF is only mildly stabilised employing KOH (potassium hydroxide) to achieve a pH-value of 10.4 (corrosion minimum of cooper). The volume ratio KOH/diamond is about 1/50. The reference fluid is a water-KOH solution to exclude special effects for the boiling process following from the stabilisation. Pressure transmitters (TRAFAG 8842) with a measurement range of 0 … 400 Pa and an accuracy of 0.5 Pa measure the internal pressure in both devices with a frequency of 1 kHz.

With both test rigs a large number of different parameter sets with respect to heat input at the evaporator, cooling water flux at condenser etc. is realised. Under all these conditions internal
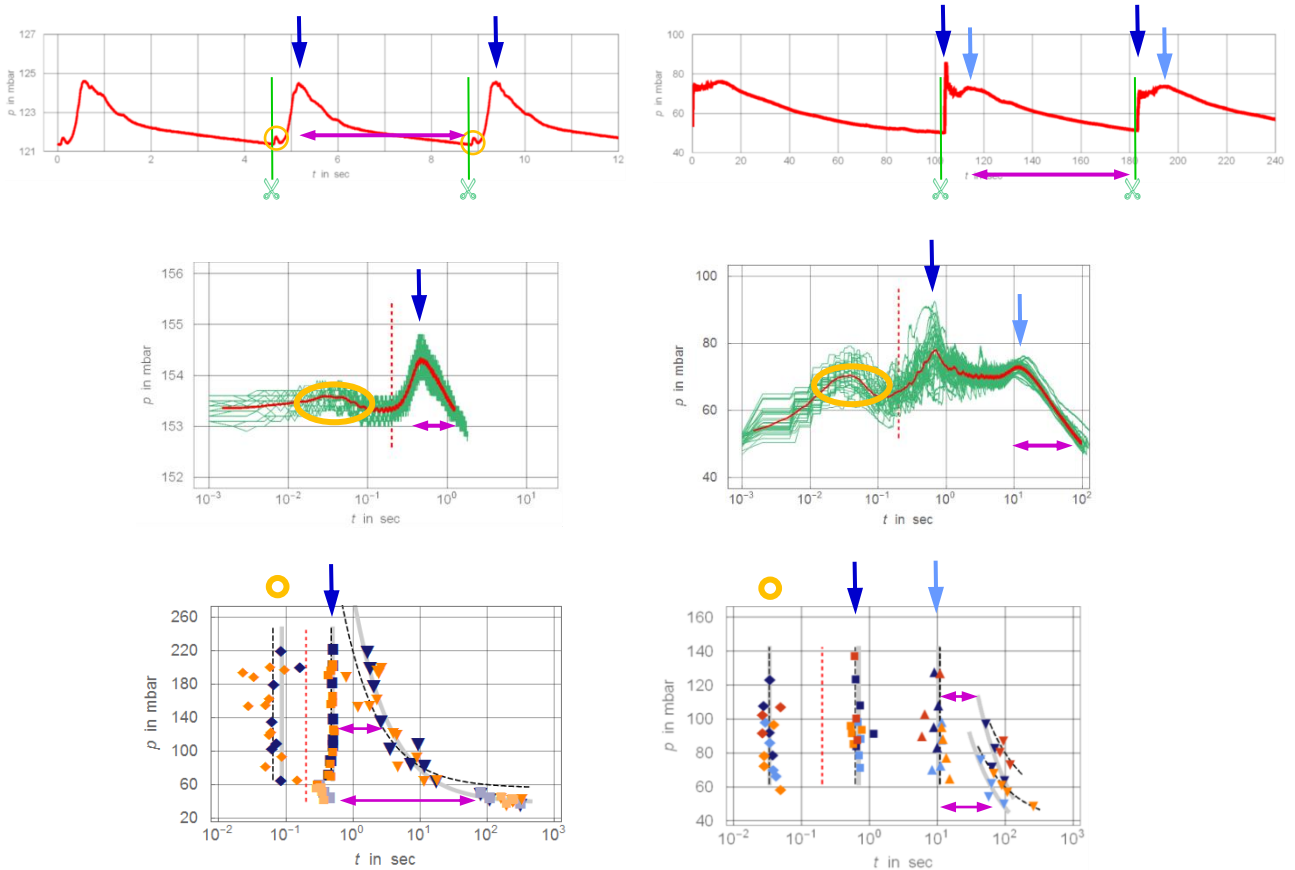
Figure 1. Thermosyphon test rigs at TU Bergakademie Freiberg (left) and at ILK Dresden. Second line: Characteristic pressure signals of geysering. The dark blue arrows indicate first and light blue arrows second pressure peak. Orange circles mark the pre-peak and pink arrows the relaxation period. Green scissor show start of geyser cycle where pressure distribution is split apart. Third line: Twenty individual geyser cycles superimposed (green) and averaged (red). Fourth line: Peak pressures over time. Blue symbols indicate water and orange diamond nanofluid with 2 vol. %. Light blue symbols show results for evaporator inlet temperature of 15 °C and dark blue symbols for 25 °C (ILK device only).

pressure is measured over time. Examples give the second line of Fig. 1. For both devices, the pressure pattern of a geyser cycle shows characteristic sequences of peaks and relaxation

periods. The third line of Fig. 1 depicts 20 superimposed individual geyser cycles (green) for the each devise. The red curves indicate the mean of these cycles. The dark blue arrows specify the ejection of working fluid by the major bubble. A pre-curser of this is marked with an orange ellipse. The ILK device shows a second pressure peak (light blue arrows) before the relaxation time starts (vertical purple double-arrows).

The plots in the fourth raw of Fig. 1 represent on the horizontal axis the time intervals between start of geyser cycle, pre-curser peak (orange circle), first (dark blue arrow) and second pressure peak (light blue) and end of cycle. The vertical axis show the averaged values of the pressure reached at these distinguished events (peaks etc.) for different heat loads at the evaporator. The mean pressure (vertical axis of diagrams) represents these different heat loads. Data predicted by averaging groups of 20 geyser cycles similar as shown in the second row of Fig. 1 with the red curves.

For both test rigs, the time intervals between onset of the geyser cycle and the pre-curser peak, onset and the main peak (dark blue arrow) and onset and the second peak are nearly independent of the imposed heat load at the evaporator. However, these time intervals are different for the two thermosyphons. The Freiberg-device (left column) shows no significant differences for the two working fluids. The same is true for the ILK-device except for the relaxation period from the second pressure peak to the end of the geyser cycle. However, here a temperature effect is already visible which the adding of the diamond particles enhances.

After opening the ILK-device, the inside of the evaporator is inspected employing an endoscopic camera. Differently to [1] where surfactant stabilised nanofluids are employed in a similar TS no wall coating is found. While the surfactants fix the gold, nanohorn and silica particles employed in [1] to the evaporator this is not the case for the diamond particles. The reason is that while KOH dissociates in the suspension surfactants like sodium dodecyl sulphate and polyvinyl-pyrrolidone support the formation of stable coating layers. However, operation agglomerates the diamond nanoparticles that are found at the lowest point of the TS after opening. Similar results deliver the TSs at TU Bergakademie Freiberg.

Summary/Conclusions

Experiments with two closed loop thermosyphons employing a reference fluid and a diamond nanofluid are carried out. The two devices show very similar pressure distributions over time. The stabilisation of the nanofluid with KOH does not allow the formation of an open porous layer on the inner evaporator surface. Therefore, the pressure pattern of the two working fluids are also nearly identical.

Acknowledgments

References:

[1] A. Kujawska, A., Zajaczkowski, B., Wilde, L.M., Buschmann, M.H., Geyser boiling in a thermosyphon with nanofluids and surfactant solution. *J. Therm. Sci.* **139**:195-216, 2019.
[2] T. Grab, U. Gross, U. Franzke, M.H. Buschmann, Operation performance of thermosyphons employing titania and gold nanofluids, *J. Therm. Sci.* **86**:352-364, 2014.

Sustainable Sorption Heat Pumps for Residential Applications

A. Zivariravan[1,2], **G. Santori**[2,] **and A. Arteconi**[1,3*]

[1]Department of Mechanical Engineering, KU Leuven, B-3000, Leuven

[2]School of Engineering, The University of Edinburgh

[3]Dipartimento di Ingegneria Industriale e Scienze Matematiche, Università Politecnica delle Marche, via Brecce Bianche 1, 60131 Ancona,

[*]Corresponding author: alessia.arteconi@kuleuven.be

Abstract

This work is focused on adsorption heat pumps (AHP) in renewable heating applications. The research activities presented in this paper are two folds: (i) a holistic modelling approach will be developed to optimize both the design and control of AHPs; (ii) novel and performing sorption materials will be proposed and tested. Thanks to the approach from nano (material level scale) to meter (system level scale) scale, it will be defined a holistic methodology for AHP design and it will be supported the development of commercial AHPs with novel and affordable adsorbent materials.

Keywords: adsorption heat pumps; renewable heating; ionogels; system modelling.

Introduction/Background

As stated by the European Technology and Innovation Platform on Renewable Heating and Cooling, "the decarbonisation of the heating and cooling sectors is an essential milestone to achieve the ambitious climate and energy targets of the European Union" [1]. Among the others, Heat Pumps represent a promising technology to achieve this goal. Within this category sorption heat pumps are very interesting for their eco-friendly properties. They can be, indeed, powered by thermal energy sources like solar energy or waste heat rather than electricity. AHP presents still a lot of space for performance improvements. The choice of the adsorbent/adsorbate working pair has a huge relevance on the system performance and operation and a lot of work has been done in studying the most suitable ones [2]. The heat and mass transfer depend on the adsorbent-adsorbate pair kinetics and the bed design (i.e. adsorbent thickness, use of thermal enhancing material between adsorbent and bed structure, fins configuration, etc.). Therefore it is paramount to optimally design the system to improve performance; however, a consistent increase of the COP can be achieved only with breakthrough innovative materials and thermodynamic enhancements.

Studies of a complete AHP system considering all its aspects and components cannot be found in literature: research has been done on different topics, but treated separately. In the end, there are no tools that are able to address synchronously all interrelated technology aspects and this limits the possibility of achieving optimal solutions competitive with traditional technologies [3]. In addition, new adsorbent-adsorbate working pairs with low heat and mass transfer resistances, which can be regenerated at lower temperatures are needed.

Discussion and Results

In order to overcome the existing limitations of AHPs and to improve their design, this work proposes a novel design approach. It is based on the two pillars described below.

Physical model of the entire AHP system: A physical model that can be used as a dimensioning and optimization tool for an AHP system for heating applications wants to be developed. It is

important that the model can represent the dependency among the different parameters in a detailed way (i.e. adsorbent material physical and thermodynamic properties, adsorber configuration and operating modes) but at the same time it cannot be too much complex in order to allow the implementation of optimization algorithms. A 3 layers approach will be implemented: (i) component scale; (ii) system scale; (iii) control level. The first two layers are linked to the design of the machine, while the third one is related to its operation, so that the influence of the mutual interaction between design and control is taken into account.

Advanced sorption materials: Typical sorption materials must meet the specific thermodynamic, kinetic, and thermophysical requirements, which primarily influence the COP and the Specific Heating/Cooling Power. Unrivalled improvement in these performance indicators can arise from a transition in fundamental material science from sorption in nanoporous materials to sorption onto ionic interfaces supported on high surface area solids (e.g. Ionogels). Ionogels are an emerging class of solid-state ionic materials that retain some of the properties of the constituent ionic liquid. Ionogels have shown unrivalled performance for heat-powered sorption desalination [4] but their applicability to heat pumps is still unknown and these aspects want to be further explored.

Summary/Conclusions

This work focuses on adsorption heat pumps and proposes a novel approach for their design aimed at improving the system's performance. The method proposed is based on developing a system-level model including simultaneously the optimization of the adsorption equilibrium and kinetics, adsorbent bed specifications, operating conditions, and the relationship between all system components. Furthermore, new adsorbent materials that offer a good trade-off between technical and economic performance thanks to their physical and thermodynamic properties will be analysed. In particular, considering heating applications, they should be able to be regenerated at lower temperature levels, thus solar thermal energy can be used as a prime mover also in colder climates.

Acknowledgments

References:

[1] RHC Platform 2020. 2050 vision for 100% renewable heating and cooling in Europe. https://www.rhc-platform.org/publications

[2] A. Freni, G. Maggio, A. Sapienza, A. Frazzica, G. Restuccia, S. Vasta, Comparative analysis of promising adsorbent/adsorbate pairs for adsorptive heat pumping, air conditioning and refrigeration, Applied Thermal Engineering 104 (2016) 85–95

[3] J.M.S. Dias, V.A.F. Costa, Adsorption heat pumps for heating applications: A review of current state, literature gaps and development challenges, Renewable and Sustainable Energy Reviews 98 (2018) 317–327

[4] A. Askalany, C. Olkis, E. Bramanti, D. Lapshin, L. Calabrese, E. Proverbio, A. Freni, G. Santori, Silica-Supported Ionic Liquids for Heat-Powered Sorption Desalination, ACS Appl. Mater. Interfaces 2019, 11, 40, 36497–36505

Experimental Investigation and Visualisation of Water Condensation Inside an Asymmetric Plate Heat Exchanger acting as a Condenser in a single-bed Adsorption Chiller

S.Nowak[1], M. Mikhaeil[1,2], A. Salama[3], M. Gaderer[4] and B. Dawoud[1*]

[1] East Bavarian Technical University of Applied Sciences (OTH Regensburg), Faculty of mechanical Engineering, Laboratory of Sorption Processes, Galgenberg street 30, 93053 Regensburg, Germany

[2] Menofia University, Faculty of Engineering, Mechanical Power Engineering Department, Shebin-El-Kom, Egypt,

[3] Department of Process System Engineering, University of Regina, Regina, SK, S4S 0A2, Canada

[4] TUM Campus Straubing for Biotechnology and Sustainability, Chair Regenerative Energy Systems, Technical University of Munich, Schulgasse 16, 94315 Straubing, Germany

*Corresponding author: belal.dawoud@oth-regensburg.de

Abstract

This study presents an experimental investigation and visualization of the condensation mechanism in a closed-structure, asymmetric plate heat exchanger (PHEx) employed as a stagnant water condenser for the application in a single-bed, intermittent adsorption chiller. To this aim, an experimental unit is constructed, which comprises two identical PHEs, one acting as a condenser/evaporator and the other one as a desorber/adsorber. Two endoscope cameras are mounted inside the investigated condenser heat exchanger to visualize the condensation mechanism taking place upon performing desorption-condensation processes. It turned out that, the condensation mechanism is dropwise condensation. A dedicated heat transfer analysis is conducted to evaluate the condensation heat transfer coefficient (h_{cond}) inside the investigated condenser. The obtained condensation heat transfer coefficient varies between zero and 2500 [W·m^{-2}·K^{-1}] over the investigation time of the desorption-condensation processes, which were performed under typical operating conditions of an adsorption chiller..

Keywords: Condenser; Plate heat exchanger; Desorption-condensation; Dropwise condensation

Introduction

Size and cost reduction are the two major challenges in the development of adsorption systems. To reduce the size and cost, the research in the field of adsorption systems is mainly concerned with developing efficient working pairs [1-6], improving the adsorption and desorption kinetics [7-11], increasing the performance of the adsorber heat exchanger [12-16], and increasing the performance by applying efficient management for the adsorption system [17-19].

Indeed, there are many research communications dealing with the evaporator/condenser heat exchanger (HEx) applied generally in the cooling and heating appliances. However, there is a noticeable lack in the research dealing with the application of plate-type heat exchanger to act as evaporator/condenser in adsorption appliances. Applying plate heat exchanger (PHEx) instead of fin-and-tube or falling film ones can reduce the sizing of the adsorption system, as they are more compact. The application of asymmetric plate heat exchangers (APHEx), which are characterized by heat transfer between two separated domains of unequal volume, to act as evaporator/condenser in the adsorption systems could come with the advantage of realizing

high heat transfer coefficients and low-pressure drops leading to a significant enhancement in the heat and mass transfer rates [20]. Various studies dealing with the application of plate heat exchanger for condensation of water under atmospheric conditions [21] and condensation of hydrofluorocarbon (HFC) refrigerants, such as R134a, R22, R290 R245fa and ammonia [22-31], were found in the literature. However, nothing has been found that addresses the condensation of water in plate heat exchanger under sub-atmospheric conditions.

It can be concluded, that so far, no experimental studies on the application of asymmetric plate heat exchangers acting as a condenser under the operating conditions of adsorption heat transformation appliances exist in the literature. To the authors' knowledge, most of the research deals with finned circular and flat tube heat exchangers with Hydrofluorocarbon (HFC) refrigerants [29,32], and water under atmospheric conditions [33]. Indeed, few research articles addressed the application of vertical plate heat exchanger as water condenser [21], however, studies investigating the water condensation in a horizontal plate heat exchangers don't exist. This gap shall be filled by the present work, which aims at investigating the application of an asymmetric plate heat exchanger as a condenser of an adsorption heat transformation appliance. Hereby, two endoscopes are utilized to visualize the condensation mechanism inside a commercially available asymmetric plate heat exchanger mounted horizontally and tested as a stagnant condenser against a desorber heat exchanger under typical operating conditions of an adsorption chiller.

Experimental setup and test procedure

Test Unit

For investigating the performance of an asymmetric closed-structure PHE acting as an evaporator/condenser for the application in adsorption heat transformation processes, a pair of identical "GL50" PHEs [34] produced by Alfa Laval©, Sweden, is employed. The two "GL50" PHEs assembling the test setup are of the same size, namely each PHE consists of 20 plates. The test setup with the two identical PHEs is depicted in

Figure 1, with a schematic illustrated in Fig. 1a, and a 3D-drawing of the assembled components of the test setup constructed at the Laboratory of Sorption Processes (LSP) of OTH Regensburg depicted in Fig. 1b. The heat exchanger (top-left) adapted to work as adsorber/desorber as described in [35, 36] is filled with 790 [g] of the loose microporous Siogel (Oker Chemie, Germany) with grain size range of 0.71 to 1.00 [mm]. The evaporator/condenser heat exchanger has been filled with 225 [g] of degassed water, with the filling procedure being described elsewhere [36].
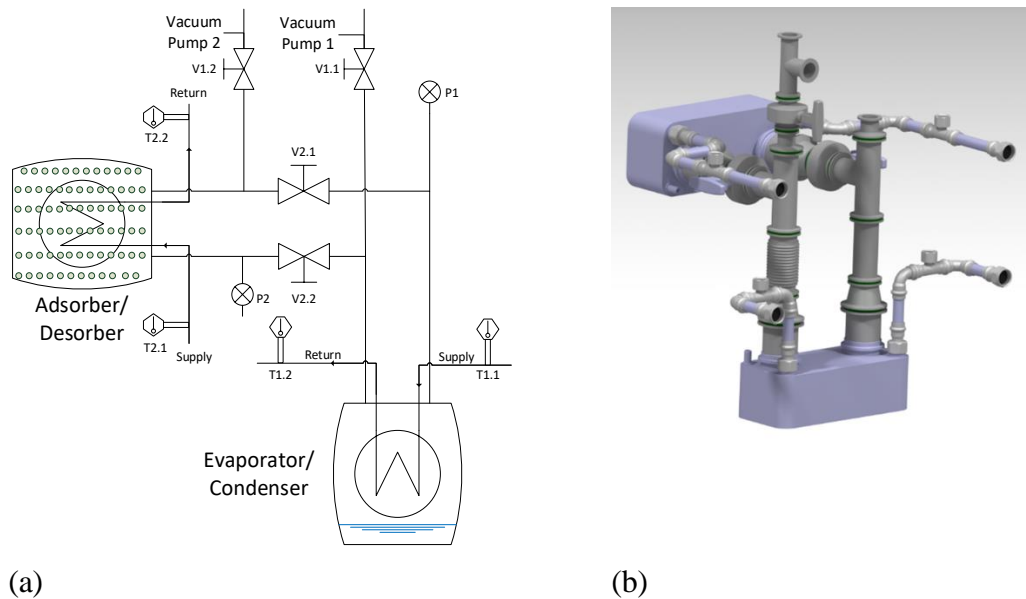
Figure 1: Layout of the test setup. (a) Schematic layout including the most important sensors, (b) 3D-drawing of the assembled components

Fixation of the endoscopes

For the visualization of the condensation process inside the investigated condenser heat exchanger, two different endoscope cameras (BS-3.9/1m QVGA and BS-350XIPSD, from VOLTCRAFT©) are applied. The characteristics of the cameras as well as the exact fixation is described in [48]. The installation positions of the endoscopes inside the condneser heat exchanger are schematically illustrated Fig. 2, where it can be seen that one endoscope, namely endoscope (1), is positioned inside the fifth refrigerant channel to visualize the condensation mechanism. Endoscope (2) is positioned in one of the two refrigerant vapour manifolds of the condenser heat exchanger to observe the bottom of the manifold as well as the inlet of the refrigerant channels interfaced with the vapour manifold.
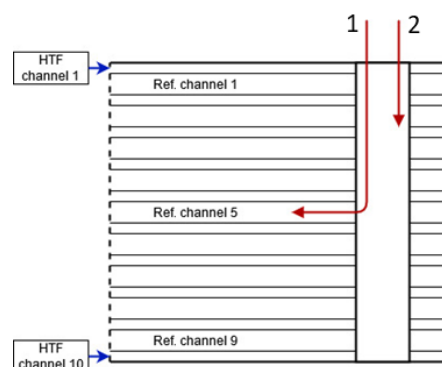
Figure 2: Schematic drawing for illustrating the position of endoscopes (1) and (2) inside the condenser heat exchanger

Test conditions and experimental procedure

Throughout the course of this work, the desorption-condensation processes have been conducted following the Large Temperature Jump (LTJ) technique under different operating conditions of a real adsorption chiller. Fig. 3 presents the ideal adsorption chiller process (in black) versus those

**Heat Powered Cycles
Conference 2023**
Edinburgh
Heat in the new energy system

*3rd to 6th of September 2023
The University of Edinburgh, Scotland*

taking place in a real adsorption chiller (in red). As the evaporator-condenser heat exchanger is not of infinite size, the pressure can't be kept constant. At the beginning of each process, the adsorption or desorption sucks or drives out more water vapour than that producible by the evaporator or condensable by the condenser. As the system is an adsorption unit represented thermodynamically as a closed system, the pressure shall decrease/increase at the beginning of the adsorption/desorption process, respectively, the case of the red lines 4-1 for adsorption and 2-3 for desorption in Fig. 3. Approaching the final equilibrium state, the rate of adsorption/desorption decreases, so that the size of the evaporator/condenser becomes big enough to retain the initial pressure level according to the inlet temperature into the heat exchanger.
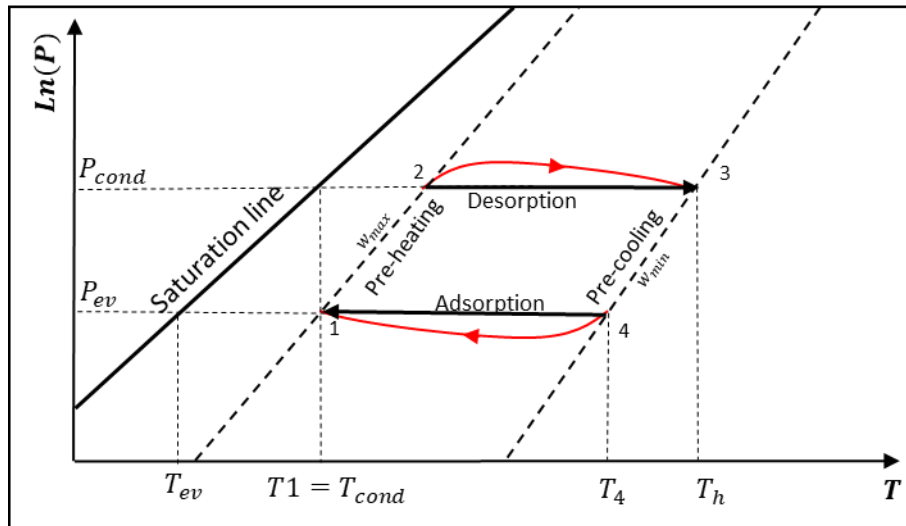
Figure 3: Schematic representation of both ideal and real adsorption and desorption processes of an adsorption chiller in a Clapeyron diagram

The LTJ desorption-condensation processes have been conducted at condenser temperatures (T_{cond}) of 30 and 35[°C], driving heat source (desorption-end) temperature (T_h) of 90[°C] and evaporator temperatures (T_{evap}) of 10 and 15[°C]. The desorption-start temperature (des-start), i.e., the temperature of state 2 (T_2) has been determined using the equilibrium model developed in [37] for water adsorption in Siogel at all defined sets of operating conditions and listed in Table 1.

Table 1: Boundary conditions of the conducted desorption-condensation processes

#	Process	T_{cond} [°C]	$T_{des-start}$, T_2 [°C]	$T_{des-end}$, T_3 [°C]
1	10/30/90	30.0	50.5	
2	10/35/90	35.0	58.8	90.0
3	15/30/90	30.0	44.5	
4	15/35/90	35.0	55.1	

The test procedure of a LTJ desorption-condensation process consists of the following two phases, during which the gate valves (V2.1 and V2.2) connecting the desorber to the condenser are kept open:

1. The preparation phase, which aims at realizing the desorption start condition. This is done by setting the desorber heat exchanger to the desorption start temperature (T_2) and, at the same time, setting the temperature of the condenser heat exchanger to the required

condensation temperature (T_{cond}). This preparation phase takes 2 hours to ensure reaching the equilibrium state 4.

2. The second phase is the LTJ-quasi-isobaric desorption phase, in which the temperature of the HTF feeding the desorber experiences a step-change to the desorption-end temperature (T_3). The LabVIEW code written to control the whole set-up allows setting the desired end-temperature and realizing it at the inlet of the desorber heat exchanger in about 2 minutes after finishing phase one. The desorption phase is measured over 2 hours to ensure reaching the equilibrium condition at the end of the process.

The investigation results of the adsorption-evaporation processes (4-1 in Fig. 3) along with the identified evaporation mechanism, with the help of the mounted endoscopes, are the subject of a separate communication, which is under publication [35].

Evaluation of the condenser performance

A MATLAB® code has been developed to estimate the condenser power out of the recorded experimental data, the overall and the individual heat transfer coefficients of the investigated condenser heat exchanger for all conducted desorption-condensation processes (see Table 1). The achieved condenser power has been calculated according to Eq. (1),

$$\dot{Q}_{cond} = \dot{V}_{HTF} \cdot \rho_{HTF} \cdot c_{p,HTF} \cdot \left(T_{HTF,in} - T_{HTF,out}\right) \tag{1}$$

Where $\dot{Q}_{cond}$ [W] is the condenser power, $\dot{V}_{HTF}$ [m³·s⁻¹] is the measured volume flow rate of the heat transfer fluid (HTF), ρ_{HTF} [kg·m⁻³] is the density of the HTF, $c_{p,HTF}$ [J·kg⁻¹·K⁻¹] is its specific heat capacity and $T_{HTF,in}$[K] and $T_{HTF,out}$[K] are the measured inlet and outlet temperature of the HTF. The thermodynamic properties of the HTF (water) have been determined at the mean temperature between the inlet and outlet of the HTF passing through the condenser heat exchanger using the thermophysical property database *CoolProp*, which is coupled to MATLAB®.

Having calculated the condenser power, the overall heat transfer coefficient U [W·m⁻²·K⁻¹] in the condenser can be estimated by the following equation.

$$U = \frac{\dot{Q}_{cond}}{A_{total} \; LMTD} \tag{2}$$

Where A_{total} [m²] is the heat transfer area of the condenser and $LMTD$ [K] is the logarithmic mean temperature difference, which is defined by Eq. (3).

$$LMTD = \frac{T_{HTF,in} - T_{HTF,out}}{\ln\dfrac{T_{HTF,in} - T_{ref}}{T_{HTF,out} - T_{ref}}}. \tag{3}$$

T_{ref} is the saturation temperature of the refrigerant (water) inside the condenser heat exchanger. T_{ref} is measured implicitly during the conducted desorption-condensation processes by means of measuring the temporal vapour pressure in the condenser (P_{cond}). Tetens equation is used to estimate the temporal T_{ref} out of the measured pressure inside the condenser [38] as presented in Eq. (4).

$$T_{ref}(t) = T_{sat}\big(P_{cond}(t)\big) = -237.3\left(\frac{ln(P_{cond}(t)/6.1078)}{ln(P_{cond}(t)/6.1078) - 17.27}\right) \tag{4}$$

In Eq. (4), P_{cond} is in [mbar] and the obtained T_{ref} is in [°C].

Heat Powered Cycles
Conference 2023
Edinburgh
Heat in the new energy system

3rd to 6th of September 2023
The University of Edinburgh, Scotland

The total thermal resistance of the condenser heat exchanger can be represented as a series connection of three resistances as shown in Fig. 4. Accordingly, the overall thermal resistance R_{total}[K·W^{-1}] can be expressed as:

$$R_{total} = R_{cond} + R_{plate} + R_{HTF} \tag{5}$$

Where R_{ref} [K·W^{-1}] is the thermal resistance of the condensed water from the channel's wall, R_{HTF} [K·W^{-1}] is the convective heat transfer resistance between the HTF and the channel's wall and R_{plate}[K·W^{-1}] is the conductive thermal resistance through the channel's wall.

$$R_{HTF}$$
$$R_{plate}$$
$$R_{cond}$$
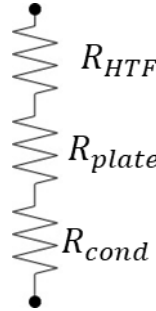
Figure 4: Thermal resistances of the condenser HEx

Based on the basic heat transfer relationship (Eq. (6)), between the overall heat transfer coefficient and the total thermal resistance, the unknown condensation heat transfer coefficient on the refrigerant (water) side h_{cond} [W·m^{-2}·K^{-1}] can be determined by Eq. (7).

$$U \cdot A_{total} = \frac{1}{R_{total}} \tag{6}$$

$$h_{cond} = \left(\frac{1}{U} - \frac{1}{h_{HTF}} - \frac{1}{h_{plate}} \right)^{-1} \tag{7}$$

where the heat transfer coefficient h_{plate} [W·m^{-2}·K^{-1}] represents the conduction through the wall (see Eq. (8)) and h_{HTF} [W·m^{-2}·K^{-1}] is the convective heat transfer coefficient between the wall and the HTF (cf. Eqs. (9) and (10)).

$$h_{plate} = \frac{k_{plate}}{L_{plate}} \tag{8}$$

Where k_{plate} is the thermal conductivity of the plate, amounts 15 [W·m^{-1}·K^{-1}] and L_{plate} [m] is the plate thickness, amounts to 0.35 [mm].

The heat transfer coefficient h_{HTF} between the wall and the HTF is determined using the correlation proposed by Gnielinski [39].

$$Nu = 0.664 \cdot Re_{HTF}^{1/2} \cdot Pr^{1/3} \tag{9}$$

$$h_{HTF} = 1.5 \cdot Nu \cdot \frac{k_{HTF}}{d_{h,HTF}} \tag{10}$$

Where Nu is the Nusselt number, Re is the Reynolds number of the HTF and Pr its Prandtl number. k_{HTF}[W.m^{-1}K^{-1}] is the thermal conductivity of the HTF and $d_{h,HTF}$[m] the hydraulic diameter of the HTF channel. $d_{h,HTF}$ is estimated using the 3D drawings of the "GL50" plates and equals 7.5E-3 [m]. The factor 1.5 is to account for the effect of the dimples on the h_{HTF} [40-42].

Results

Condenser power and the condensation heat transfer coeffcient

The measured temporal condenser powers of all conducted desorption-condensation processes are depicted in Fig. 5. The condenser power obtained from the desorption-condensation process conducted at 15/30/90[°C] is nearly twice as high as that conducted at 10/35/90 [°C], whereas the condenser power obtained at 15/35/90 [°C] is almost equal that obtained at 10/30/90 [°C]. This implies that the time rate of change of the refrigerant discharge from the desorber at operating conditions 15/30/90 [°C] is almost twice as high as that at 10/35/90 [°C]. The time integral of the condenser power is directly proportional to the differential water uptake Δw [kg.kg^{-1}] of the desorber. Strictly speaking, Δw equals 0.182 [kg.kg^{-1}] at 15/30/90 [°C], and 0.093 [kg.kg^{-1}] at 10/35/90 [°C] [37]. At the operating conditions 15/35/90[°C] and 10/30/90[°C], almost the same differential water uptakes (Δw) have been obtained; namely, 0.131 [kg.kg^{-1}] and 0.138 [kg.kg^{-1}], respectively. The measured condenser power curves at both boundary conditions (green and blue curves in Fig. 5) are almost identical, which implies similar temporal course of variation of their respective $\frac{dw}{dt}$.
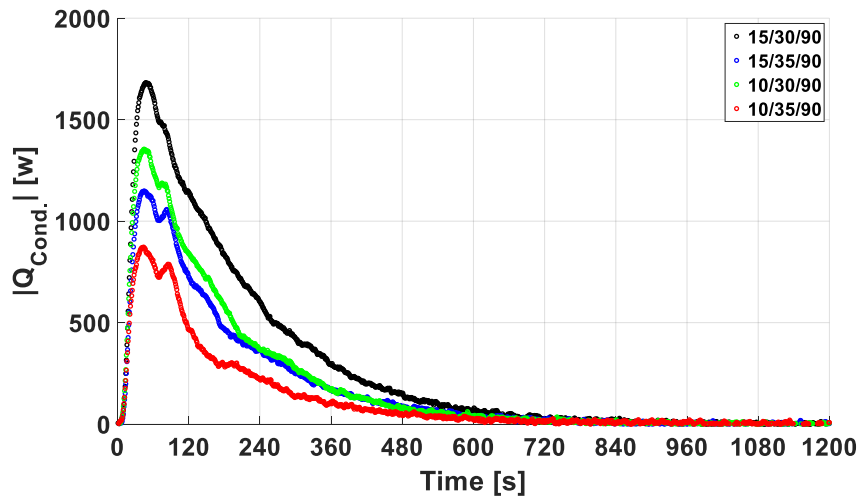
Figure 5: Calculated condenser power for all applied operating conditions.

To estimate the total heat transfer coefficient (U) and then the condensation heat transfer coefficient (h_{cond}) for all conducted experiments, the $LMTD$ has been calculated according to Eq. (3). Fig. 6 shows the time variation of the refrigerant temperature in the condenser heat exchanger (T_{ref}) and the inlet and outlet temperatures of the heat transfer fluid (HTF) flowing through the condenser heat exchanger ($T_{HTF,inlet}$ and $T_{HTF,outlet}$) for one of the conducted experiments, namely the one conducted under the operating conditions 15/30/90 [°C]. The time variation of $LMTD$ at 15/30/90 °C is also shown in Fig. 6. Fig 6b clearly depicts the variation in the values of $T_{ref}, T_{HTF,inlet}$, $T_{HTF,outlet}$ and $LMTD$, in the first 20 [s] after the start of condensation at 15/30/90 [°C].

For all other operating conditions, the time variation of $LMTD$ has been computed. Fig. 7 compares between the temporal $LMTD$ values obtained for the different operating conditions. As shown in Fig. 7, for each operating condition, the $LMTD$ reaches its highest absolute value in the first few seconds after the start of the condensation. The highest values exist between 1.4 (at 10/35/90) to 2.5 [°C] (at 15/30/90). Then, the $LMTD$ value decreases continually till the end of the condensation process. Although, for all applied operating conditions, the condenser power reaches almost zero after less than 780 [s] from the start of the desorption-condensation (Fig. 5),

the *LMTD* does not reach zero even after 1200 [s], as depicted in Fig. 7. This implies that the zero power of the investigated condenser is due to the approximately zero *U*-values obtained after 780 [s] from the start of the condensation for all applied operating conditions.

(a)   (b)
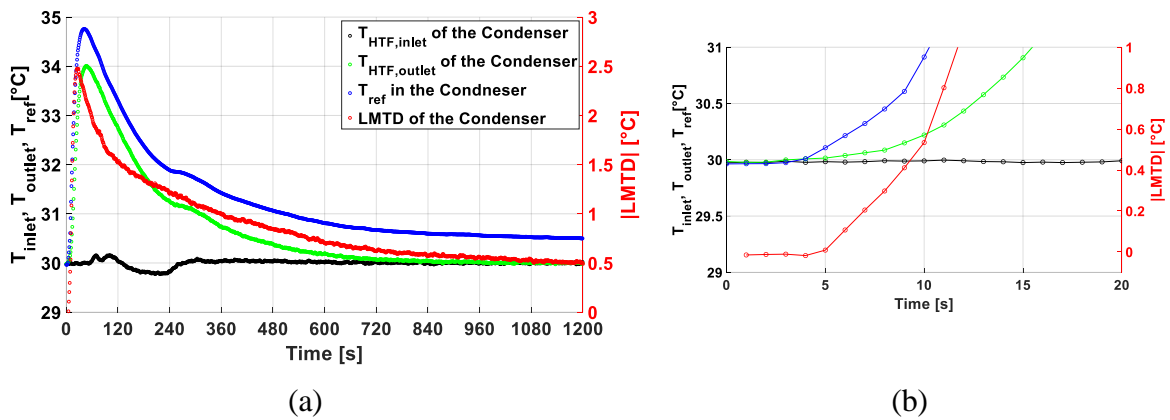
Figure 6: Experimentally obtained temporal variation of $T_{HTF,inlet}$, $T_{HTF,outlet}$, T_{ref} and *LMTD* of the investigated condenser at set of operating conditions 15/30/90 [°C], (a) during 1200 [s], (b) during the first 20 [s] from the beginning of the desorption-condensation process
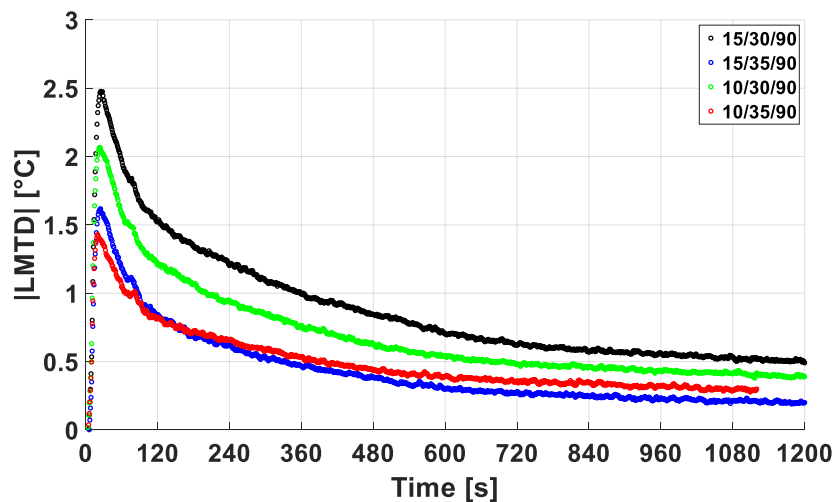
Figure 7: Experimentally obtained temporal variation of the *LMTD* of the investigated condenser at all applied operating conditions.
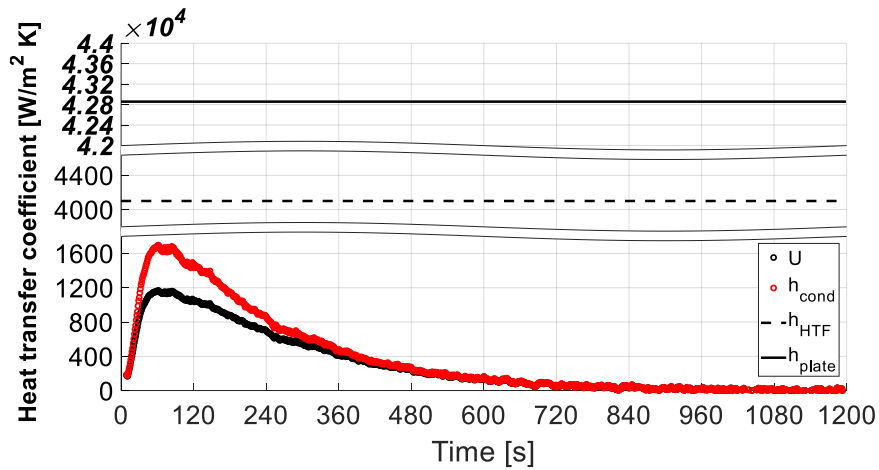
Figure 8: Contributions to the overall heat transfer coefficient.
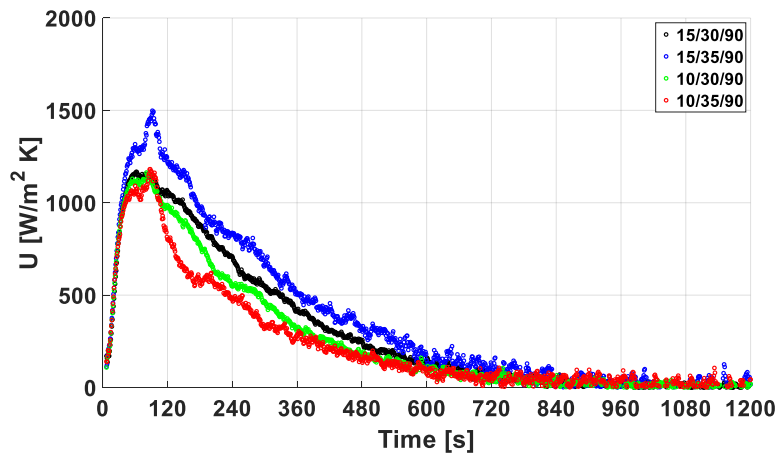
(a)
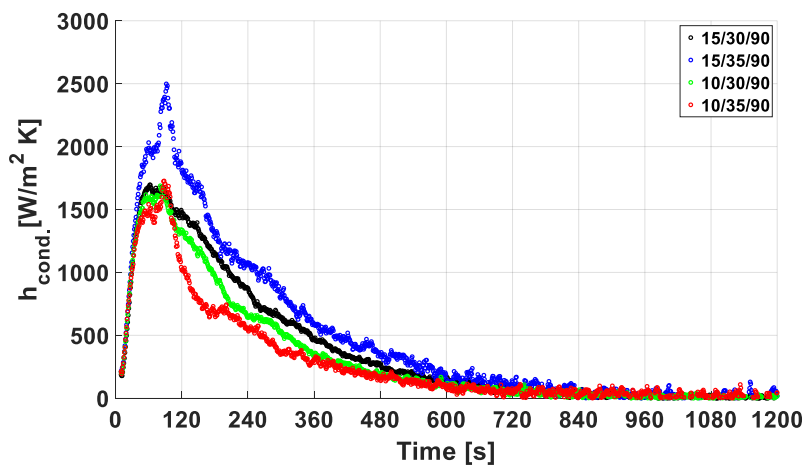
(b)

Figure 9: Experimentally obtained U and h_{cond} of the investigated condenser, (a) U,

(b) h_{cond}

By applying Eq. (1) to (10), the contribution of each individual heat transfer coefficient to the overall heat transfer coefficient can be estimated at each set of operating conditions. Since the experimental data of $\dot{Q}_{cond}$ and the $LMTD$ obtained at the beginning of the desorption-condensation processes are close to zero, the calculated U-values at the first a few seconds from the beginning of each process are characterized by fluctuations with a higher level of uncertainty. The same is valid after long time from the beginning of each process, where the equilibrium condition is approached and, consequently, the temperature difference becomes so low that the uncertainty in measuring that temperature difference and, accordingly, the U-value does remarkably increase. Therefore, we fixed the analysis of the experimental results to the period between 7 [s] and 1200 [s].

Fig. 8 depicts the contribution of each individual heat transfer coefficient to the overall heat transfer coefficient of the process conducted at 15/30/90 [°C]. It is a basic heat transfer knowledge that the overall heat transfer coefficient (U) shall be less than the least heat transfer coefficient in the serial connection according to Fig. 4, for which the total heat transfer resistance is expressed by Eq. (5).

It is clearly visible that the condensation heat transfer coefficient on the refrigerant side h_{cond} is the one with the major influence on U, followed by the heat transfer coefficient on the HTF side (h_{HTF}) and the heat transfer coefficient due to conduction through the plate's wall h_{plate}.

Figs. 9a and 9b show the estimated total condenser heat transfer coefficient (U) and condensation heat transfer coefficient (h_{cond}), respectively, for all conducted desorption-condensation processes. As can be seen in Fig. 9, the values of U and h_{cond} are close to zero at the beginning of each conducted process. During the first few seconds ($t < 90$ [s]), U and h_{cond} increase until they reach peak values, then they decrease until reaching almost zero at $t < 780$ [s]. As shown in the figure, the highest U and h_{cond} values are obtained at 15/35/90 [°C], amounting to 1500 2500 [W·m^{-2}·K^{-1}] and 2500 [W·m^{-2}·K^{-1}], respectively.

Visualized investigation on the condensation mechanism

The visualization of the water condensation on the surface of one of the refrigerant channels and one of the two refrigerant vapour manifolds inside the investigated condenser plate heat exchanger is utilized to determine the condensation mechanism prevailing during the conducted desorption-condensation processes. A number of screenshots taken from the video film recorded by endoscope (1) during the desorption-condensation process under the operating condition of 15/30/90[°C] are presented in Fig. 10, showing the vision of endoscope (1) between two successive HTF channels. Six inclined surfaces of different dimples and the flat horizontal surfaces connecting them can be distinguished [43]. The dimples appearing in the vision of endoscope (1) are categorized into (i) two opposite, deep and concave dimples, (ii) two opposite, shallow and concave dimples, and (iii) two opposite and convex dimples brazed together at their interfacial surface.

It is observable that the refrigerant channel was initially dry (Fig. 10a). At the beginning of the condensation process, small droplets formed in the upper and lower deep concave dimples as well as on the two convex dimples brazed together (Fig. 10b). With ongoing time, the droplets coalesced to bigger ones (Fig. 10c), until they formed a liquid film at the end of the condensation process. Based on the visual investigation, it can be concluded that dropwise condensation is the condensation mechanism taking place in the investigated asymmetric plate heat exchanger acting as a horizontally placed, stagnant condenser for the adsorption chilling unit presented in Fig. 1.

Fig. 11 depicts three screenshots taken from a video film of endoscope (2), which has been recorded simultaneously with the video film of endoscope (1). The visualization of endoscope (2) presented in Fig.11a illustrates that at the beginning of the condensation process, there was a thin liquid film at the edge of the manifold bottom (Fig. 11a). With ongoing time, droplets condensed at the bottom of the manifold as depicted in Fig. 11b. With further condensation, more refrigerant condensed at the bottom of the manifold (Fig. 11c) until finally a large area of the manifold bottom is covered with a liquid film, see Fig. 11c. Similar results were received in the repetition tests and the tests with the other boundary conditions. However, the intensity of the forming of the droplets during the condensation was not always the same.

.

(a)

(b)

(c)
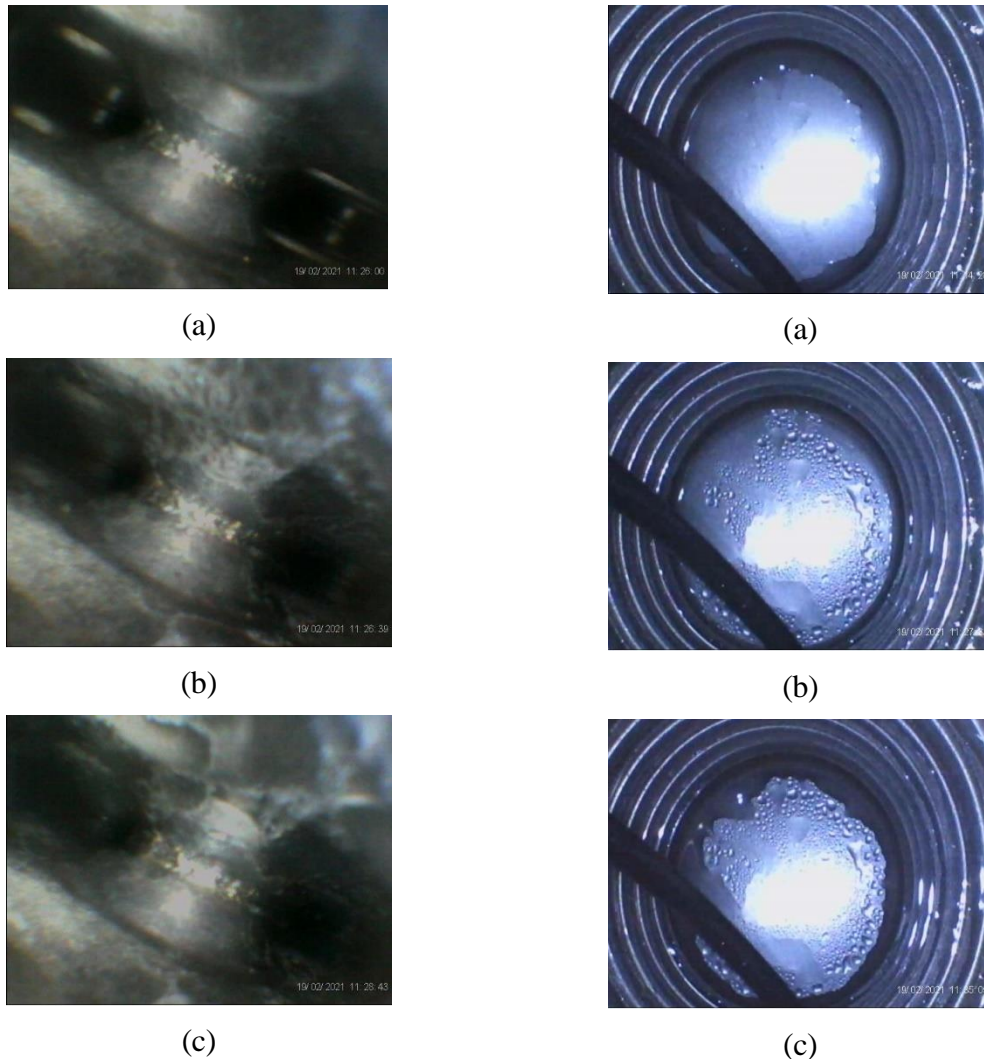
Figure 10: Screenshots from endoscope (1) between the plates. (a) at the start of the condensation, (b) formation of small droplets, (c) at the end of the condensation.

(a)

(b)

(c)

Figure 11: Screenshots from endoscope (2) in the manifold (a) at the start of the condensation, (b) formation of small droplets, (c) formation of liquid film at the circular edge of the bottom.

Conclusion

This communication presents the first experimental study on the application of an asymmetric plate heat exchanger, with a closed structure and a horizontal orientation, to act as a stagnant water

condenser under typical operating conditions of an adsorption chiller. The main outcomes of this study can be summarized as follows:

- Dropwise condensation was identified as the condensation mechanism inside the investigated plate heat exchanger.

- The thermal resistance related to the condensation heat transfer coefficient (R_{cond}) dominates the total heat transfer resistance and, consequently, the overall heat transfer coefficient of the investigated condenser.

- The condensation heat transfer coefficient (h_{cond}) of the investigated condenser varies between zero and 2500 [W·m^{-2}K^{-1}] over the investigated desorption-condensation time and boundary conditions.

The introduced plate heat exchanger as a condenser of an adsorption system is associated with several advantages in terms of system compactness and, accordingly, the specific power density of the adsorption chiller. Besides, the construction cost of the adsorption appliance can be considerably reduced if closed structure PHEs are adopted for use, as there is no need to place the evaporator/condenser inside a vacuum tight chamber, which is quite bulky and costly. The extremely durable operation because of the no corrosion potential is a special added value of the introduced technology (Nickel brazing of Stainless-Steel sheets). More investigations are needed, however, to develop appropriate heat transfer correlations and to develop the design rules of such special plate heat exchangers for application in different adsorption heat transformation appliances.

Acknowledgements

References

[1] A. Allouhi, T. Kousksou, A. Jamil, T. El Rhafiki, Y. Mourad, and Y. Zeraouli, "Optimal working pairs for solar adsorption cooling applications," Energy, vol. 79, no. C, 2015, doi: 10.1016/j.energy.2014.11.010.
[2] D. B. Boman, D. C. Hoysall, D. G. Pahinkar, M. J. Ponkala, and S. Garimella, "Screening of working pairs for adsorption heat pumps based on thermodynamic and transport characteristics," Appl. Therm. Eng., vol. 123, 2017, doi: 10.1016/j.applthermaleng.2017.04.153.
[3] Q. Cui, G. Tao, H. Chen, X. Guo, and H. Yao, "Environmentally benign working pairs for adsorption refrigeration," in Energy, 2005, vol. 30, no. 2-4 SPEC. ISS., doi: 10.1016/j.energy.2004.05.005.
[4] A. Frazzica and A. Freni, "Adsorbent working pairs for solar thermal energy storage in buildings," Renew. Energy, vol. 110, 2017, doi: 10.1016/j.renene.2016.09.047.
[5] A. N. Shmroukh, A. H. H. Ali, and S. Ookawara, "Adsorption working pairs for adsorption cooling chillers: A review based on adsorption capacity and environmental impact," Renewable and Sustainable Energy Reviews, vol. 50. 2015, doi: 10.1016/j.rser.2015.05.035.
[6] L. W. Wang, R. Z. Wang, and R. G. Oliveira, "A review on adsorption working pairs for refrigeration," Renewable and Sustainable Energy Reviews, vol. 13, no. 3. 2009, doi: 10.1016/j.rser.2007.12.002.

[7] I. S. Glaznev and Y. I. Aristov, "Kinetics of water adsorption on loose grains of SWS-1L under isobaric stages of adsorption heat pumps: The effect of residual air," Int. J. Heat Mass Transf., vol. 51, no. 25–26, 2008, doi: 10.1016/j.ijheatmasstransfer.2008.04.061.

[8] B. Dawoud, "On the effect of grain size on the kinetics of water vapor adsorption and desorption into/from loose pellets of FAM-Z02 under a typical operating condition of adsorption heat pumps," J. Chem. Eng. Japan, vol. 40, no. 13, 2007, doi: 10.1252/jcej.07WE163.

[9] B. Dawoud and Y. Aristov, "Experimental study on the kinetics of water vapor sorption on selective water sorbents, silica gel and alumina under typical operating conditions of sorption heat pumps," Int. J. Heat Mass Transf., vol. 46, no. 2, 2003, doi: 10.1016/S0017-9310(02)00288-0.

[10] R. H. Mohammed, O. Mesalhy, M. L. Elsayed, S. Hou, M. Su, and L. C. Chow, "Physical properties and adsorption kinetics of silica-gel/water for adsorption chillers," Appl. Therm. Eng., vol. 137, 2018, doi: 10.1016/j.applthermaleng.2018.03.088.

[11] L. Schnabel, M. Tatlier, F. Schmidt, and A. Erdem-Şenatalar, "Adsorption kinetics of zeolite coatings directly crystallized on metal supports for heat pump applications (adsorption kinetics of zeolite coatings)," Appl. Therm. Eng., vol. 30, no. 11–12, 2010, doi: 10.1016/j.applthermaleng.2010.02.030.

[12] M. Mikhaeil, M. Gaderer, and B. Dawoud, "On the development of an innovative adsorber plate heat exchanger for adsorption heat transformation processes; an experimental and numerical study," Energy, vol. 207, 2020, doi: 10.1016/j.energy.2020.118272.

[13] K. C. A. Alam, B. B. Saha, Y. T. Kang, A. Akisawa, and T. Kashiwagi, "Heat exchanger design effect on the system performance of silica gel adsorption refrigeration systems," Int. J. Heat Mass Transf., vol. 43, no. 24, 2000, doi: 10.1016/S0017-9310(00)00072-7.

[14] S. W. Hong, O. K. Kwon, and J. D. Chung, "Application of an embossed plate heat exchanger to adsorption chiller," Int. J. Refrig., vol. 65, 2016, doi: 10.1016/j.ijrefrig.2016.02.012.

[15] M. Mahdavikhah and H. Niazmand, "Effects of plate finned heat exchanger parameters on the adsorption chiller performance," in Applied Thermal Engineering, 2013, vol. 50, no. 1, doi: 10.1016/j.applthermaleng.2012.08.033.

[16] T. Miyazaki and A. Akisawa, "The influence of heat exchanger parameters on the optimum cycle time of adsorption chillers," Appl. Therm. Eng., vol. 29, no. 13, 2009, doi: 10.1016/j.applthermaleng.2009.01.005.

[17] A. El Fadar, "Novel process for performance enhancement of a solar continuous adsorption cooling system," Energy, vol. 114, 2016, doi: 10.1016/j.energy.2016.07.149.

[18] A. Sapienza, S. Santamaria, A. Frazzica, and A. Freni, "Influence of the management strategy and operating conditions on the performance of an adsorption chiller," Energy, vol. 36, no. 9, 2011, doi: 10.1016/j.energy.2011.07.020.

[19] S. K. Yeboah and J. Darkwa, "A critical review of thermal enhancement of packed beds for water vapour adsorption," Renewable and Sustainable Energy Reviews, vol. 58. 2016, doi: 10.1016/j.rser.2015.12.134.

[20] S. Zhang, X. Niu, Y. Li, G. Chen, and X. Xu, "Numerical simulation and experimental research on heat transfer and flow resistance characteristics of asymmetric plate heat exchangers," Front. Energy, vol. 14, no. 2, pp. 267–282, 2020, doi: 10.1007/s11708-020-0662-7.

[21] R. Würfel and N. Ostrowski, "Experimental investigations of heat transfer and pressure drop during the condensation process within plate heat exchangers of the

herringbone-type," Int. J. Therm. Sci., vol. 43, no. 1, pp. 59–68, 2004, doi: 10.1016/S1290-0729(03)00099-1.

[22]   R. Eldeeb, V. Aute, and R. Radermacher, "A survey of correlations for heat transfer and pressure drop for evaporation and condensation in plate heat exchangers," Int. J. Refrig., vol. 65, pp. 12–26, 2016, doi: 10.1016/j.ijrefrig.2015.11.013.

[23]   J. R. García-Cascales, F. Vera-García, J. M. Corberán-Salvador, and J. Gonzálvez-Maciá, "Assessment of boiling and condensation heat transfer correlations in the modelling of plate heat exchangers," Int. J. Refrig., vol. 30, no. 6, pp. 1029–1041, 2007, doi: 10.1016/j.ijrefrig.2007.01.004.

[24]   Y. Y. Yan, H. C. Lio, and T. F. Lin, "Condensation heat transfer and pressure drop of refrigerant R-134a in a plate heat exchanger," Int. J. Heat Mass Transf., vol. 42, no. 6, pp. 993–1006, 1999, doi: 10.1016/S0017-9310(98)00217-8.

[25]   G. A. Longo, "Refrigerant R134a condensation heat transfer and pressure drop inside a small brazed plate heat exchanger," Int. J. Refrig., vol. 31, no. 5, pp. 780–789, 2008, doi: 10.1016/j.ijrefrig.2007.11.017.

[26]   Z. Y. Shi, J. P. Chen, V. Grabenstein, and S. Kabelac, "Experimental investigation on condensation heat transfer and pressure drop of R134a in a plate heat exchanger," Heat Mass Transf. und Stoffuebertragung, vol. 46, no. 10, pp. 1177–1185, 2010, doi: 10.1007/s00231-010-0699-y.

[27]   K. Sarraf, S. Launay, G. El Achkar, and L. Tadrist, "Local vs global heat transfer and flow analysis of hydrocarbon complete condensation in plate heat exchanger based on infrared thermography," Int. J. Heat Mass Transf., vol. 90, pp. 878–893, 2015, doi: 10.1016/j.ijheatmasstransfer.2015.07.036.

[28]   A. Jokar, M. H. Hosni, and S. J. Eckels, "Dimensional analysis on the evaporation and condensation of refrigerant R-134a in minichannel plate heat exchangers," Appl. Therm. Eng., vol. 26, no. 17–18, pp. 2287–2300, 2006, doi: 10.1016/j.applthermaleng.2006.03.015.

[29]   H. S. Wang and J. W. Rose, "Film condensation in horizontal microchannels: Effect of channel shape," Int. J. Therm. Sci., vol. 45, no. 12, pp. 1205–1212, 2006, doi: 10.1016/j.ijthermalsci.2006.03.004.

[30]   D. Jung, K. H. Song, Y. Cho, and S. J. Kim, "Flow condensation heat transfer coefficients of pure refrigerants," Int. J. Refrig., vol. 26, no. 1, pp. 4–11, 2003, doi: 10.1016/S0140-7007(02)00082-8.

[31]   A. Cavallini, S. Bortolin, D. Del Col, M. Matkovic, and L. Rossetto, "Condensation heat transfer and pressure losses of high- and low-pressure refrigerants flowing in a single circular minichannel," Heat Transf. Eng., vol. 32, no. 2, pp. 90–98, 2011, doi: 10.1080/01457631003769104.

[32]   J. Zhang, W. Li, and S. A. Sherif, "A numerical study of condensation heat transfer and pressure drop in horizontal round and flattened minichannels," Int. J. Therm. Sci., vol. 106, pp. 80–93, 2016, doi: 10.1016/j.ijthermalsci.2016.02.019.

[33]   A. Grzebielec and A. Rusowicz, "Thermal Resistance of Steam Condensation in Horizontal Tube Bundles," J. Power Technol., vol. 91, no. 1, pp. 41–48, 2011.

[34]
    "https://www.alfalaval.com/contentassets/11dca8962e464b58932c125e47fa8eeb/gl50---gln50_product-leaflet.pdf." .

[35]   M. Mikhaeil, S. Nowak, V.Palomba, A. Frazzica, M. Gaderer and B. Dawoud, "Experimental and analytical investigation of applying an asymmetric plate heat exchanger as an evaporator in a thermally driven adsoprtion appliance", Under final editorial approval for publication in Appl. Therm. Eng. (2023).

[36]   D. Malzkorn, M. Mikhaeil, and B. Dawoud, "Assembly and Investigation of a Compact Adsorption Heat Storage Module," in Regensburg Applied Research Conference, 2020, pp. 111–120.

[37]   A. Sapienza, A. Velte, I. Girnik, A. Frazzica, G. Füldner, L. Schnabel, Y. Aristov, "'Water - Silica Siogel' working pair for adsorption chillers: Adsorption equilibrium and dynamics," Renew. Energy, vol. 110, pp. 40–46, 2017, doi: 10.1016/j.renene.2016.09.065.

[38]   John Monteith, Mike Unsworth, Principles of Environmental Physics, 3rd ed., Academic 954 Press, 2007.

[39]   V. Gnielinski, G4 Heat Transfer in Flow Past a Plane Wall, in: VDI Heat Atlas, Springer 914 Berlin Heidelberg, Berlin, Heidelberg, 2010: pp. 713–716. doi:10.1007/978-915 3-540-77877-6_37.

[40]   J. Turnow, N. Kornev, V. Zhdanov, and E. Hassel, "Flow structures and heat transfer on dimples in a staggered arrangement," Int. J. Heat Fluid Flow, vol. 35, pp. 168–175, 2012, doi: 10.1016/j.ijheatfluidflow.2012.01.002.

[41]   N. K. Burgess and P. M. Ligrani, "Effects of dimple depth on channel nusselt numbers and friction factors," J. Heat Transfer, vol. 127, no. 8, pp. 839–847, 2005, doi: 10.1115/1.1994880.

[42]   Y. Rao, B. Li, and Y. Feng, "Heat transfer of turbulent flow over surfaces with spherical dimples and teardrop dimples," Exp. Therm. Fluid Sci., vol. 61, no. C, pp. 201–209, 2015, doi: 10.1016/j.expthermflusci.2014.10.030.

[43]   Marcello Masgrau, Plate for a heat exchanger and a heat exchanger, Wo-2015/057115 882 A1, 2015.

New CO_2-water co-adsorption measurements and modelling of amine-functionalized polymeric resins for direct air capture

Katia Piscina[1]*, John Young[1], Susana Garcia[1], Mijndert van der Spek[1]

[1] Research Centre for Carbon Solutions, Heriot-Watt University, Edinburgh, UK

*Corresponding author: kp2037@hw.ac.uk

Abstract

This study advances our recently published CO_2-water co-adsorption model [1] using new experimental isotherm data from two amine-functionalized polymeric adsorbents (sorbents A and B). It presents new isotherm data for water, CO_2, and water-CO_2 co-adsorption, as well as heat capacities and other adsorbent properties key to process modelling.

Today's atmospheric concentrations of greenhouse gases such as carbon dioxide, nitrous oxide, and methane pose a threat to Earth's climate system, demanding action from all sides to combat the effects [2]. With current Paris agreement pledges, limiting warming to 2°C will require the implementation of carbon dioxide removal (CDR) strategies in addition to deep decarbonization [2]. It is therefore necessary for technologies that pull carbon dioxide directly from the air – CDR technologies – to be developed and deployed. Direct Air Capture (DAC) using amine-functionalized adsorbents is one such technology that employs solid adsorbents to chemically bind to the carbon dioxide in the air. Current theory suggests that in this process, CO_2 chemically reacts with the amine-functionalized adsorbents to form carbamates, bicarbonates, or (stabilized) carbamic acid depending on local surface chemistry, temperature, and critically, humidity [1, 3]. Stoichiometrically, the amine efficiency of producing carbamate is 0.5, whereas for bicarbonate it is 1, leading previous authors to suggest that we can obtain double the carbon dioxide adsorbed per available amine group in the presence of water [1]. However, in our previous work on a different amine-functionalized adsorbent, Lewatit® VP OC 1065, we have shown that the maximum increase of CO_2 uptake is larger than 2 at low CO_2 partial pressures, while it is much smaller, or even *decreasing* at partial pressures of 0.1 bar and above, also subject to temperature and humidity [1]. Stoichiometric enhancement alone cannot explain these results. Instead, we postulated a CO_2-water co-adsorption model that accounts for blocking of amine sites by water molecules, stoichiometric enhancement, and changes in the CO_2 heat of adsorption in the presence of water.

Here, we add new isotherm data to the existing body of literature and adjust our published co-adsorption model to the new insights generated. The isotherms for water, CO_2 and water-CO_2 co-adsorption were measured for two proprietary polymeric resins that may be suitable for DAC. All isotherms were measured in a DVS Vacuum system, supplied by Surface Measurement Systems. In addition, we measured heat capacity data, nitrogen isotherms at 77K, and sorbent stability.

An example of our results presented in Figure 1 shows water isotherms for the two new sorbents tested. Hysteresis can be seen between the adsorption and desorption steps for both sorbents, which is typical for water's monolayer-multilayer adsorption [1, 4]. The shape of both isotherms is very similar, while sorbent A shows more water adsorption over the whole relative humidity range. Both are expected given the two sorbents differ in the amount of amine included in the polymer matrix.

With our results we add new data to update our co-adsorption model, allowing future research to improve process modelling and optimize DAC for location and sorbent based on the effects of humidity and ambient temperature.

Water Isotherms (25°C)
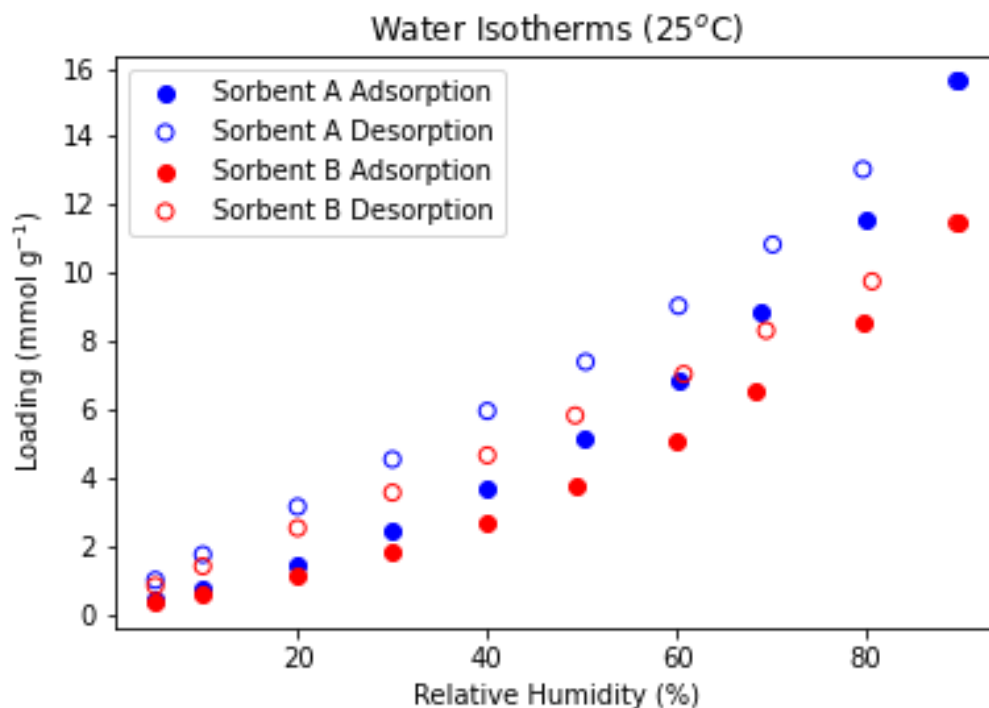
Keywords: CO_2 removal (CDR), adsorption processes, co-adsorption modelling

References:

[1]   Young J, García-Díez E, Garcia S, et al. The impact of binary water–CO_2 isotherm models on the optimal performance of sorbent-based direct air capture processes. *Energy Environ Sci* 2021; 14: 5377–5394.

[2]   Pathak M, Slade R, Shukla PR, et al. *Technical Summary*. Cambridge, UK and New York, NY, USA, 2022.

[3]   Varghese AM, Karanikolos GN. CO2 capture adsorbents functionalized by amine – bearing polymers: A review. *International Journal of Greenhouse Gas Control* 2020; 96: 103005.

[4]   Scheufele FB, Módenes AN, Borba CE, et al. Monolayer–multilayer adsorption phenomenological model: Kinetics, equilibrium and thermodynamics. *Chemical Engineering Journal* 2016; 284: 1328–1341.

Life Cycle Assessment (LCA) of CO2-Adsorbing Metal Organic Framework "CALF-20".

Edgar Contreras* [1,2] ; Isaac Herraiz [1,2] ; Enrique Moliner [1].

1: LOMARTOV S.L. Applied Innovation Engineering. C/Alfarería 3. 46100 Burjassot (Valencia), Spain.
2: Universitat Politècnica de València. Camino de Vera s/n. 46022 Valencia, Spain.

* Corresponding author. Edgar Contreras: econtreras@lomartov.com

ABSTRACT

Calgary Framework-20 (CALF-20) is a zinc-based metal organic framework (MOF) with high water stability and excellent CO_2 adsorption properties. Several studies have proven CALF-20 to reach optimal performance in CO_2 capture from air with several N_2/CO_2 compositions. Currently, the European Project "SOLDAC" tests and implements different morphologies of CALF-20 for the Direct Air Capture unit of its breakthrough CO_2-to-ethylene solar conversion technology. In an effort to maintain the implementation of CALF-20 for CO_2 capture as environmentally responsible as possible, a Life Cycle Assessment (LCA) is performed. The aim of the LCA is to determine the overall environmental impacts associated with the synthesis of CALF-20, tracking them from the extraction of raw materials, through the synthesis of precursors, to the final synthesis of the MOF. Implementing this environmental screening approach allows for comprehensive and environmentally aware decision-making when developing CALF-20-enabled technologies.

KEYWORDS: Metal-organic framework CALF-20; Life cycle assessment; Direct air capture.

1. **INTRODUCTION**

Calgary Framework 20 (CALF-20) is a metal-organic framework (MOF) comprised of a crystallographic arrangement of two-dimensional zinc(II) triazolate grids pillared by oxalate anions perpendicular to the layers, creating a three-dimensional porous structure with no open coordination sites.

CALF-20 has shown the ability to take up 4.07 mmol/g at conditions of 1.2 bar and 20ºC with a CO_2/N_2 selectivity of 230, by ideal adsorbed solution theory, for a 10:90 CO_2/N_2 mixture. Additionally, it showed low water-affinity and sustained CO_2 capacity up to and above a relative humidity of 40%, making it favorable for direct air capture applications (Lin et al., 2021).

Studies on the binding sites of CALF-20 for guest molecules show that CO_2 has its most probable binding in the middle of the framework's pores, with interatomic distances between consistent with physisorption. Furthermore, analysis of the binding energy proved attractive dispersion interactions to contribute in 85% to the CO_2-CALF20 interaction, with electrostatics providing the balance.

However, implementing the use of CALF-20 for said application requires a prior screening of the environmental impacts associated to its synthesis, as doing so allows for a better understanding of the actual alleviation on CO_2 emissions that it enables.

As a response, a life cycle assessment (LCA) on the traditional synthesis of CALF-20 – as reported by Lin et al., 2021 – is presented in this study, aiming to assess its implementation in the European Project "SolDAC: Solar Direct Air Capture and Conversion" (G.A. 101069359).

The principal aim of the SolDAC project is to produce sustainable ethylene and ethanol from the electrochemical conversion of atmospheric CO_2 by means a novel technology that supposes the integration of three unit operations – a direct air capture (DAC) unit for the capture, purification,

and compression of the atmospheric CO_2; a photoelectrochemical (PEC) stack for the conversion into ethylene and ethanol; and a full-spectrum solar (FSS) collector to provide the energy and heat duties of the prior two units.

CALF-20 is currently being studied as a potential candidate for the material composition of the nanoporous adsorption beds of SolDAC's direct air capture unit. Consequently, the development of this study is motivated by the need to ensure the environmental responsibility of the project.

2. <u>GOAL AND SCOPE</u>

The intended application of the LCA – and general <u>objective</u> of the study – is to report the environmental impacts of the synthesis of CALF-20 across the complete range of impact categories provided by the employed assessment method, providing a baseline for future environmental screenings on CALF-20-enabled technologies, including the SolDAC project. The target audience for this study is the general scientific community working in the topic.

The system that is being assessed in this study is the manufacturing process of CALF-20 powder for its application as CO_2 adsorbent. The functional unit (FU) of the system is one kilogram of synthesized CALF-20, meaning that all environmental impacts will be determined per unit mass of the assessed material.

Additionally, the boundaries of the system follow a cradle-to-gate approach, meaning that the environmental impacts are determined from the extraction of raw materials (cradle) to the final manufacture of the MOF (gate). This system boundary is fit for the application of the assessment, providing an environmental baseline for CALF-20, because the next phases of its life cycle (i.e., use phase, end-of-life, disposal) are defined by the specific technology where it is to be implemented.

Following the European Commission's recommendation on "methods to measure and communicate the life cycle environmental performance of products and organizations" (The European Commission, 2021), the impact assessment method employed in this assessment is Environmental Footprint (EF) 3.0, along with its characterization, weighting, and normalization standards.

Both the modelling of inventories and the impact assessment are performed with the SimaPro 9.2 software. The building of inventories into SimaPro is made using the materials available in the Ecoinvent 3.6 database.

3. <u>LIFE CYCLE INVENTORY (LCI) ANALYSIS</u>

The life cycle inventory (LCI) for the synthesis of one kilogram of CALF-20 was built according to the procedure reported by Lin et al., 2021 and peer-reviewed by partners from the University of St. Andrews. The resulting inventory is presented ahead, in **Table 1.**

Table 1. LCI for the synthesis of one kilogram of CALF-20 powder

Type of input	Input	Quantity	Units
Synthesis precursor	Zinc oxalate dihydrate	950.00	g
Synthesis precursor	1,2,4-triazole	1,404.70	g
Solvent	Methanol	19,782.50	g
Solvent	Water	16,616.67	g
Energy	Heating	20.44	kWh
Type of output	**Output**	**Quantity**	**Units**
Product	CALF-20 powder	1,000.00	g
Waste	Wastewater	37,753.33	g

The data regarding required mass of synthesis precursors and solvents, as well as of obtained product were directly disclosed by the team at University of St. Andrews, while the energy input and wastewater output had to be calculated from the procedure reported by them.

3.1 Calculation of energy input

The energy input was obtained by modelling the consumption of the reported heating needs for the procedure: two sets of heating in a conventional laboratory oven, one at 100 ºC for 84h and another at 60ºC overnight. The energy consumption of each set was calculated by considering the use of a commercially available laboratory oven with the technical specifications presented in **Table 2**.

Table 2. Modelled oven specifications.

Concept	Quantity	Unit
Max. Temp.	204	ºC
Max. Power	1.2	kW
Max. Load	91	kg

(ITW EAE, 2020)

A linear trend is assumed to determine the power (P) of the oven as a function of its temperature (T) setting, where a power of 0 kW is needed for a 20ºC setting and 1.2 kW are needed for a 204ºC setting. The resulting function – illustrated in **Figure 1** – is obtained as follows, using the definition of a slope:

$$P = mT + b$$

$$m = \frac{P_2 - P_1}{T_2 - T_1} = \frac{1.2 - 0}{204 - 20} = \frac{3}{460}$$

$$P = \frac{3}{460}T - \frac{3}{23}$$
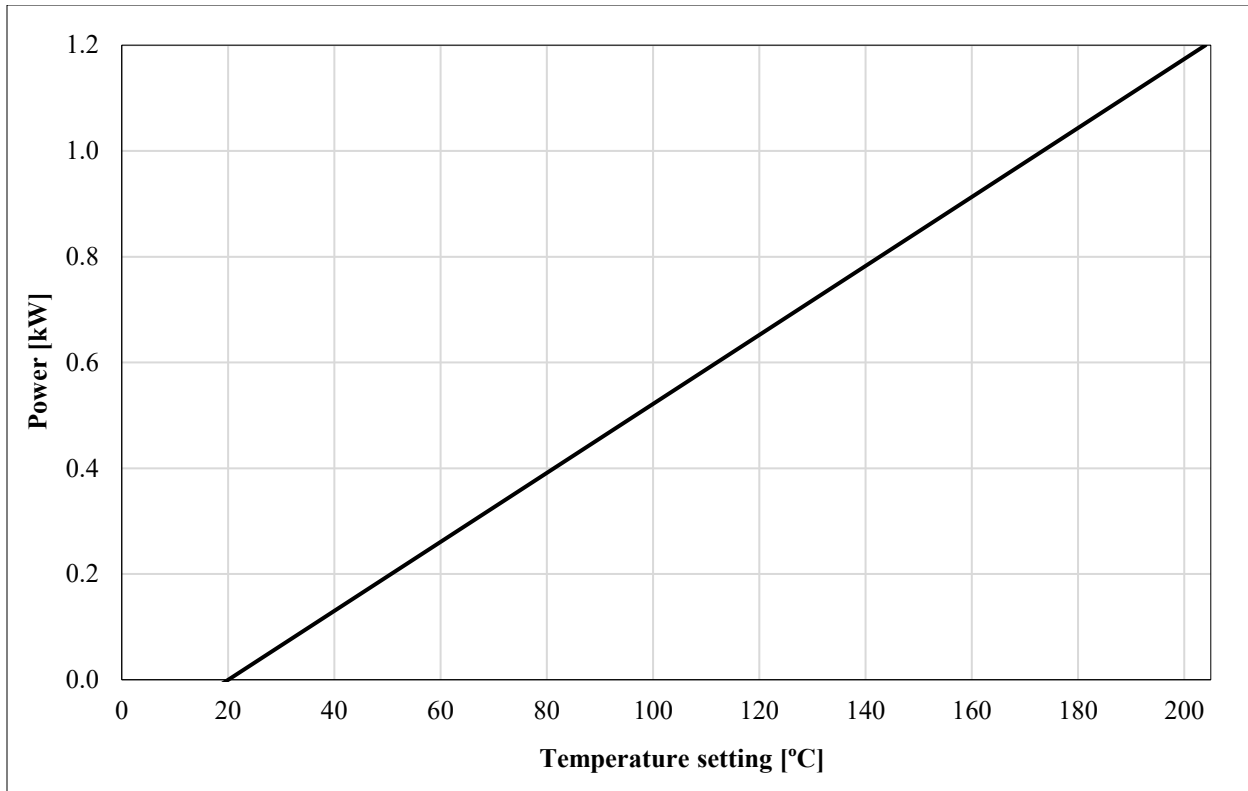
Figure 1. Function for power determination from oven's temperature setting.

Applying the obtained function, the power for both heating sets were calculated and then multiplied by their corresponding heating times to obtain the energy of each set. However, because these sets are considered to be made at the oven's full load, the resulting energy values were divided by its load capacity to obtain a "mass-specific" energy consumption value per set. Finally, said value is multiplied by the actual load of the oven, according to the mass inputs of the inventory. All values are presented in **Table 3.**

The sum of the actual energy consumption for both heating sets results in a total energy input of 20.44 kWh, as reported in **Table 1.**

Table 3. Energy consumption data per heating set

Concept	Set 1	Set 2
Temp. setting [ºC]	100	60
Estimated power [kW]	0.522	0.261
Heating time [h **(s)**]	84 **(302,400)**	16 **(57,600)**
Estimated energy [kJ]	157,773.913	15,026.087
Full load capacity [g]	91,000	91,000
Mass-specific consumption [kJ/g]	1.734	0.165
Actual load [g]	38,753.33	38,753.33
Actual energy consumption [kJ]	67,189.726	6,399.022

3.2 Calculation of wastewater

The mass of generated wastewater was calculated by a mass balance, subtracting the mass of produced CALF-20 powder from the total mass of material inputs, resulting in 37,753 g; as reported in **Table 1.**

3.3 Modelling of precursors

Both synthesis precursors – 1,2,4-triazole and zinc oxalate dihydrate – are not readily available in the Ecoinvent database for direct input when modelling the LCI for the synthesis of CALF-20 in SimaPro. Consequently, both precursors must be previously modelled from their respective synthesis procedures, enabling their later input into the final LCI of the CALF-20 synthesis.

1,2,4-triazole was modelled from the synthesis procedure reported in patent US4267347A, issued to Petree et al., 1981. This patent claims a method for its direct preparation from hydrazine and formamide, precursors that are readily available in the Ecoinvent database.

A process flow diagram (PFD) of the synthesis procedure – presented in **Figure 2** – was built from the claims of the patent, adjusted to the production of 1 kg of 1,2,4-triazole. The material inputs and outputs of the process were calculated according to the stoichiometry and the yields of reaction and purification reported in the patent.

Figure 2. PFD for the synthesis of 1,2,4-triazole according to pat. USA4267347A.
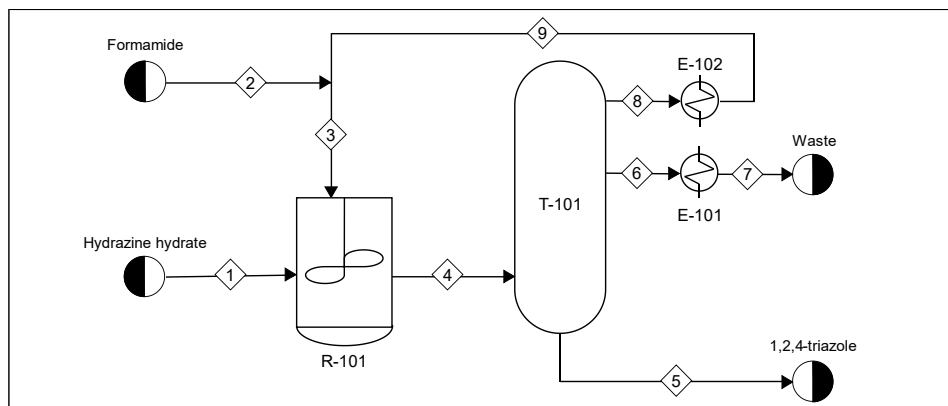
Stream #	1	2	3	4	5	6	7	8	9
Temperature [ºC]	25	25	25	170	130	107.5	107.5	117.5	117.5
Vapor fraction	0	0	0	0	0	1	0	1	0
Mass flowrate [kg]	0.77	2.14	2.79	3.55	1.06	1.89	1.89	0.66	0.66
Flowrates [mol]									
1,2,4-triazole				14.95	14.49275	0.31	0.31	0.149512	0.149512
Water	15.48783			29.90		29.90	29.90	0	0
Ammonia				29.90		29.90	29.90	0	0
Formic Acid				14.95		14.95	14.95	0	0
Hydrazine	15.48783			0.54		0.54	0.54	0	0
Formamide		47.49	61.95	17.10		2.63	2.63	14.46284	14.46284
Flowrates [kg]									
1,2,4-triazole	0	0	0	1.031635	1	0.021318	0.021318	0.010316	0.010316
Water	0.278781	0	0	0.538244	0	0.538244	0.538244	0	0
Ammonia	0	0	0	0.508342	0	0.508342	0.508342	0	0
Formic Acid	0	0	0	0.687756	0	0.687756	0.687756	0	0
Hydrazine	0.495611	0	0	0.017171	0	0.017171	0.017171	0	0
Formamide	0	2.136982	2.787809	0.769394	0	0.118566	0.118566	0.650828	0.650828

Unit	R-101	T-101	E-101	E-102
Energy duty [kWh]	0.96	0.87	3.22	2.95

Mass balances:

2,9,3 node
INPUTS 2.798 kg
OUTPUTS 2.788 kg
Reactor
INPUTS 3.562 kg
OUTPUTS 3.553 kg
Distillator
INPUTS 3.553 kg
OUTPUTS 3.616 kg
Overall balance
INPUTS 2.911 kg
OUTPUTS 2.955 kg

Substance	M.W.
1,2,4-triazole	69
Water	18
Ammonia	17
Formic Acid	46
Hydrazine	32
Formamide	45

Meanwhile, the energy inputs were determined considering the requirements of the process related to: (1) the energy duty of the reactor, and (2) the energy required for the separation and isolation of 1,2,4-triazole from the reactor's output solution.

These were calculated with the temperatures reported by the patent for each stage of the synthesis, as well as with the specific properties of the different materials involved.

Firstly, the energy duty of the reactor was determined by calculating the heat of reaction associated with the synthesis of triazole, following **equation 1**.

$$\Delta H_{rxn} = \sum n_j \cdot \left[\Delta \widehat{H}^o_{f\,j} + C_{p\,j} \cdot (T_{out} - 298K) \right] - \sum n_i \cdot \left[\Delta \widehat{H}^o_{f\,i} + C_{p\,i} \cdot (T_{in} - 298K) \right] \quad \textbf{(Eq. 1)}$$

Symbol	Meaning	Units
$i\,;j$	Input species; output species	-
ΔH_{rxn}	Heat of reaction	kJ
n	Moles	Mol
$\Delta \widehat{H}^o_f$	Standard heat of formation	$kJ \cdot mol^{-1}$
C_p	Specific heat capacity	$kJ \cdot mol^{-1} \cdot K^{-1}$
$T_{out}\,;T_{in}$	Outflow reaction temperature; feedstock temperature	K

On the other hand, the energy for purification was calculated in two parts: the heating requirement for the distillation of the reactor's output solution, following **equation 2**; and the refrigeration requirement for the condensation of the obtained distillate, according to **equation 3.**

$$\Delta H_{dist.} = n \cdot \left[\bar{C}_p \cdot (T_{ovh.} - T_{in}) + \Delta \bar{H}_{vap} \right] \quad \textbf{(Eq. 2)}$$

$$\Delta H_{cond.} = n \cdot \Delta \bar{H}_{vap} \quad \textbf{(Eq. 3)}$$

Symbol	Meaning	Units
$\Delta H_{dist.}$	Heat requirement for distillation	kJ
$\Delta H_{cond.}$	Refrigeration to condensate distillates	kJ
n	Moles of output reaction solution	Mol
$\bar{C}_p$	Average specific heat of reaction solution	$kJ \cdot mol^{-1} \cdot K^{-1}$
$T_{ovh.}\,;T_{in}$	Overhead distillation temp.; initial solution temp.	K
$\Delta \bar{H}_{vap}$	Average latent heat of reaction solution	$kJ \cdot mol^{-1}$

All calculated energy demands were adjusted to account for the scaling-up to an industrial process by applying the correction factors used by (Cuéllar-Franca et al., 2016), who performed a similar model of the same synthesis procedure based on patent US4267347A as well. The correction

factors have values of 4.2 for heating (assuming the use of natural gas) and 3.2 for cooling (assuming the use of electricity for refrigeration equipment).

The resulting inventory, presented in **Table 4**, enabled modeling 1,2,4-triazole as a new material in SimaPro. The outputs correspond to the mass of produced 1,2,4-triazole and the "average wastewater treatment" item available in Ecoinvent. The wastewater volume was obtained by calculating an average density of stream 7 in the PFD and multiplying it times the total mass of the stream.

Table 4. Inventory for the production of 1 kg of 1,2,4-triazole.

Type of input	Input	Quantity	Units
Synthesis precursor	Hydrazine	495.61	g
Synthesis precursor	Formamide	2,136.98	g
Solvent	Water	278.78	g
Energy	Reaction heat	0.96	kWh
Energy	Purification energy	7.05	kWh
Type of output	**Output**	**Quantity**	**Units**
Product	1,2,4-triazole	1,000.00	g
Waste	Wastewater	2,114.59	mL

On the other hand, the inventory for the synthesis of the second precursor of CALF-20, **zinc oxalate dihydrate**, was built based on the experimental procedure reported by Qi et al., 2014.

The procedure described in the study states that equimolar parts of zinc oxide and oxalic acid dihydrate are mixed, milled, and then aged for 7 days, obtaining a molar equivalent of zinc oxalate. All the procedure is carried out in solid phase, with no solvents, and a 100% reaction yield is assumed for the sake of this study.

To calculate the energy demand of the milling process, the technical specifications of an industrial batch ball mill were consulted. The selected mill, from HengXing Engineering, reported a nominal power of 2.2 kW with a nominal load capacity of 200 kg (HengXing Engineering, n.d.).

In order to scale the power demand per unit mass, a specific power was calculated by dividing the nominal power over the nominal load capacity, giving a value of 0.011 kW/kg. This value was then used to calculate the adjusted electricity demand for an assumed milling time of 3 hours and a load of one kilogram.

The resulting inventory is presented in **Table 5**. Both reaction precursors are available in the Ecoinvent database, making it possible to model zinc oxalate in SimaPro using this inventory.

Table 5. Inventory for the production of 1 kg of zinc oxalate.

Type of input	Input	Quantity	Units
Synthesis precursor	Zinc oxide	429.54	g
Synthesis precursor	Oxalic acid dihydrate	665.42	g
Energy	Mill electric consumption	0.03	kWh
Type of output	**Output**	**Quantity**	**Units**
Product	Zinc oxalate dihydrate	1,000.00	g

However, when looking into the model prepared by Ecoinvent of the zinc oxide precursor, it came up that no elemental flow of zinc was considered for its composition; meaning that virtually, there is no actual zinc in the Ecoinvent model of zinc oxide. This is relevant and non-neglectable for the scope of the study as zinc accounts for the metallic part of the CALF-20 metal-organic framework, which is fundamental to its characterization; this is especially true for any future work that takes on the reported impacts from this study to compare CALF-20 with other MOFs for similar applications.

To account for this situation, the "elemental zinc" item from the Ecoinvent database was implemented as a substitute (proxy) for zinc oxalate in the LCI for the synthesis of CALF-20. To determine the mass of elemental Zn to be considered in the inventory, the mass fraction of elemental zinc within zinc oxalate dihydrate was determined by dividing the mass of one mole of Zn over the mass of on mole of Zinc oxalate dihydrate (as there is one atom of Zn per molecule of Zn oxalate). The obtained fraction – 0.3453 – was then multiplied by the total mass of zinc oxalate in the inventory for the standard synthesis of one kilogram of CALF-20, which has a value of 950.00 g, as reported in **Table 1.** The resulting inventory after implementing these changes is presented in **Table 6.**

Table 6. Corrected LCI for the synthesis of one kilogram of CALF-20 powder

Type of input	Input	Quantity	Units
Synthesis precursor	Zinc oxalate dihydrate	328.04	g
Synthesis precursor	1,2,4-triazole	1,404.70	g
Solvent	Methanol	19,782.50	g
Solvent	Water	16,616.67	g
Energy	Heating	20.44	kWh
Type of output	**Output**	**Quantity**	**Units**
Product	CALF-20 powder	1,000.00	g
Waste	Wastewater	37,753.33	g

4. LIFE CYCLE IMPACT ASSESSMENT

Based on its LCI, the impacts for the synthesis of CALF-20 across all categories offered by the EF3.0 methodology were assessed. **Table 7** presents the calculated impacts disaggregated by the contribution of each input/output of the inventory to the total impact. These values are shaded with a color scale per category, where red represents the highest value, and green the lowest. Impact categories have been abbreviated as indicated int the table footer.

Table 7. Impact reporting for the synthesis of CALF-20.

Impact category	Unit	Share of impact per input/output						Total impact
		1,2,4-triazole	Zinc oxalate	Methanol	Deionised water	Electricity	Wastewater	
CC	kg $CO_{2,eq}$	22.87	0.86	13.36	4.2E-03	7.68	0.01	44.78
OD	kg $CFC11_{eq}$	5.5E-06	6.1E-08	4.4E-06	1.1E-09	4.7E-07	4.8E-10	1.0E-05
IR	kBq $U-235_{eq}$	1.04	0.09	0.16	1.9E-04	1.52	7.0E-04	2.82
Ph	kg $NMVOC_{eq}$	0.04	0.01	0.04	1.1E-05	0.02	4.3E-05	0.10
PM	disease inc.	6.2E-07	4.0E-08	1.8E-07	3.0E-10	9.7E-08	8.1E-10	9.5E-07
HT-NC	CTUh	3.9E-07	1.5E-07	7.6E-08	1.6E-10	6.3E-08	3.8E-09	6.9E-07
HT-C	CTUh	4.0E-09	5.0E-09	2.2E-09	1.7E-12	1.5E-09	6.2E-11	1.3E-08
Ac	mol H^+_{eq}	0.08	0.01	0.05	4.0E-05	0.04	1.7E-04	0.18
EuF	kg P_{eq}	6.4E-04	9.1E-05	3.0E-04	1.5E-07	8.5E-04	3.9E-05	1.9E-03
EuM	kg N_{eq}	0.03	1.9E-03	0.01	3.2E-06	0.01	8.4E-04	0.04
EuT	mol N_{eq}	0.16	0.02	0.10	3.4E-05	0.06	5.0E-04	0.33
ET	CTUe	3342.24	195.20	213.65	17.65	82.41	16.44	3867.60
LU	Pt	29.73	5.14	2.85	0.00	24.42	0.01	62.15
WU	m^3 depriv.	27.26	0.91	3.04	0.50	2.44	-1.61	32.53
RU-F	MJ	303.49	12.73	616.90	0.05	168.12	0.08	1101.38
RU-MM	kg Sb_{eq}	1.6E-05	5.0E-04	3.6E-05	2.0E-09	2.8E-06	3.1E-09	5.5E-04

CC = Climate change

OD = Ozone depletion

IR = Ionizing radiation

PhOF = Photochemical ozone formation

PM = Particulate matter

HT-NC = Human toxicity, non-cancer

HT-C = Human toxicity, cancer

Ac = Acidification

EuF = Eutrophication, freshwater

EuM = Eutrophication, marine

EuT = Eutrophication, terrestrial

ET = Ecotoxicity

LU = Land use

WU = Water use

RU-F = Resource use, fossils

RU-MM = Resource use, minerals and meta

5. INTERPRETATION OF RESULTS

To further improve the visibility of the share of impact that each input/output of the CALF-20 synthesis procedure has on its overall impacts, **Figure 3** presents the resulting data in a stacked bar chart, using the same abbreviations key as **Table 7.**

From the chart is clear to see that 1,2,4-triazole supposes the largest share of impact in most categories, even accounting for more than half of the total impact in seven out of sixteen categories. A clear exception on this trend is the category corresponding to the use of mineral and metallic resources; this is expected, as the component that supposes the largest share in this category is the zinc oxalate precursor, as it comprises the metallic part of the CALF-20 MOF.
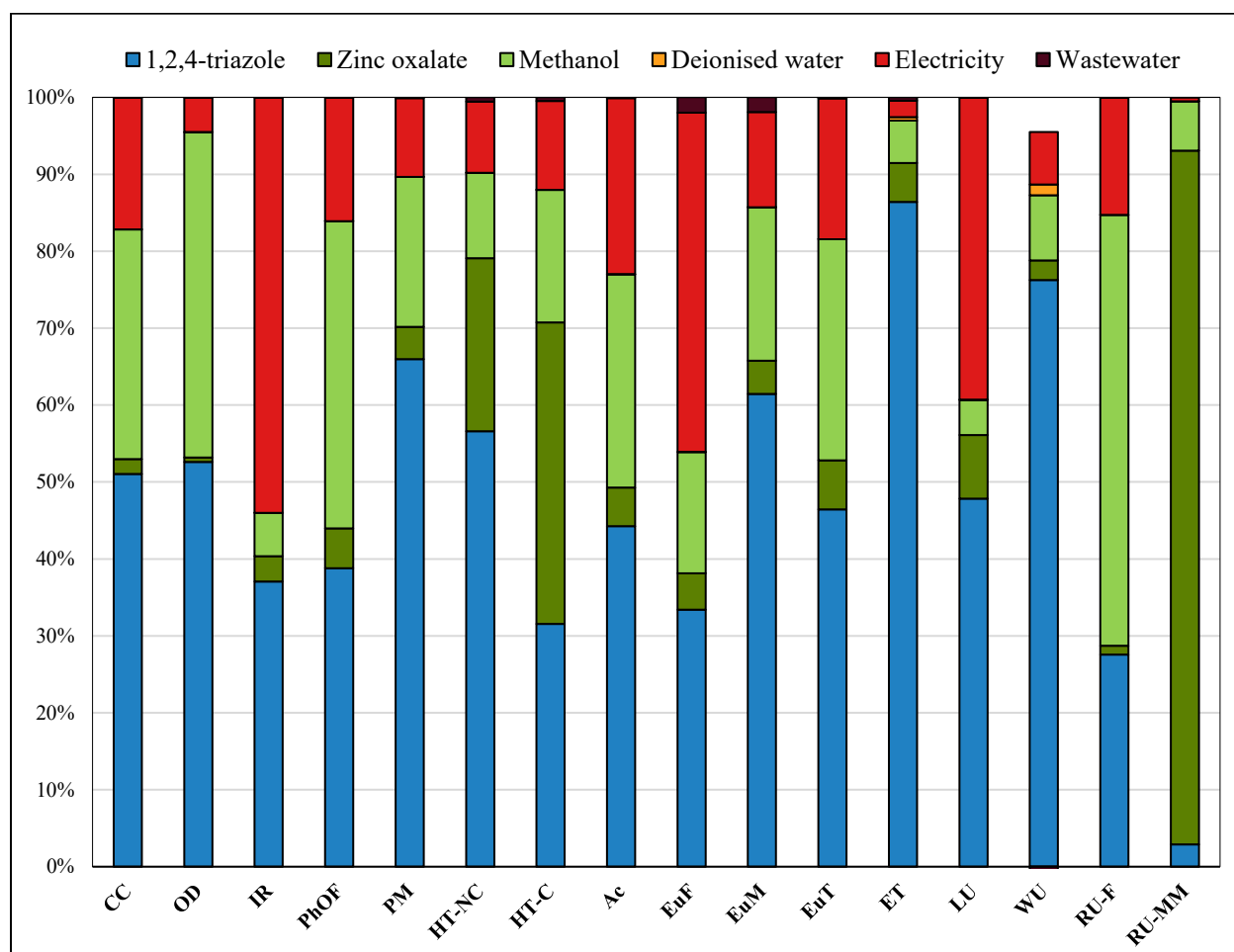
Figure 3. Contribution per input/output component to impacts of the CALF-20 synthesis.

Another element to be noted from the chart is that the wastewater output supposes a "negative" impact in the water use category. This is because the "wastewater treatment" item in the Ecoinvent database accounts for avoided impacts in the deprivation of water from natural sources, as it considers the potential reutilization of a fraction of the treated wastewater.

To further visualize the contribution of 1,2,4-triazole as an environmental hotspot to the synthesis of CALF-20, **Figure 4** illustrates the impact network for the process. The network is presented as a Sankey diagram, where the arrows indicate the connection between substances and their precursors, while the widths of the arrows are proportional to the share that the precursor has on the overall impacts of the material that it synthesizes.
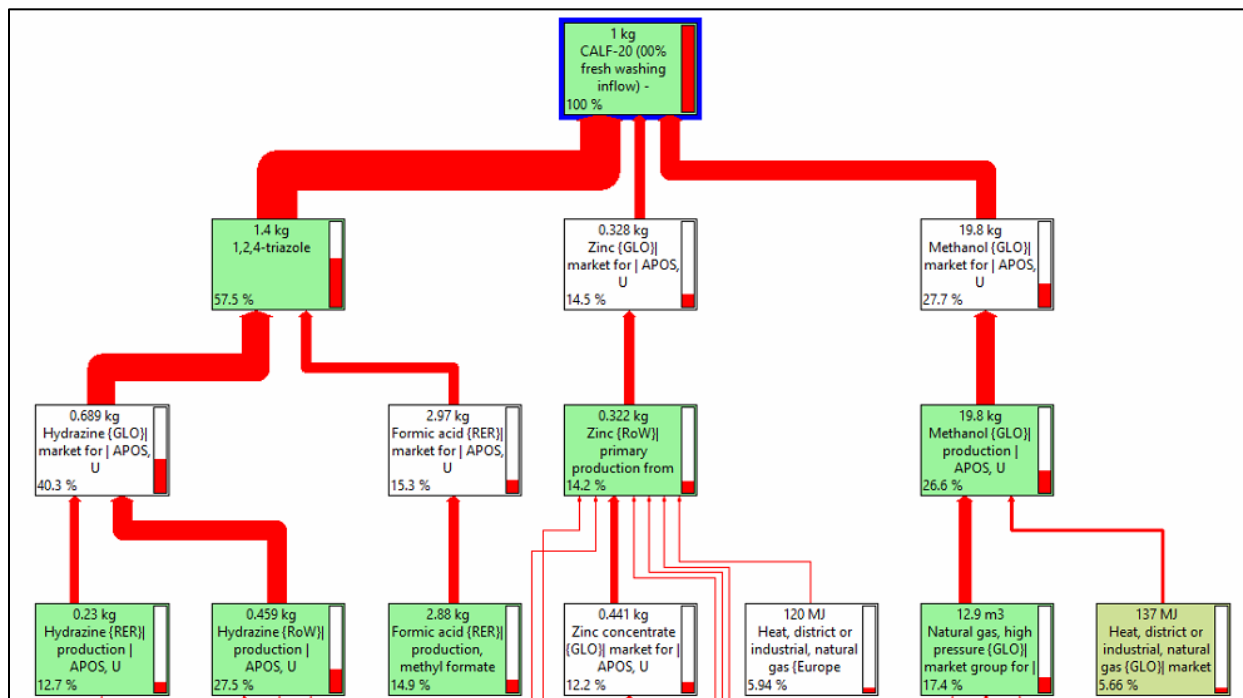
Figure 4. Impact network for the synthesis of one kilogram of CALF-20.

The network is generated by SimaPro, where an overall single-score environmental impact is calculated for every element within it. This single-score impact is calculated by the software using the characterization, weighting, and normalization factors of the Environmental Footprint method, making a weighted aggregate of the normalized impacts of every element across all impact categories.

When analyzing the network, it becomes evident that 1,2,4-triazole is the primary contributor to the overall impact of the synthesis procedure – accounting for 57.5% of the overall single-score impact. This suggests that optimizing the consumption of 1,2,4-triazole when synthesizing CALF-20 becomes mandatory to optimize the magnitude of the environmental impacts of the process.

6. CONCLUSIONS

The insights presented in the interpretation of results suppose relevant information that satisfies the general objective of the study, which is to report the environmental impacts of the synthesis of CALF-20, simultaneously providing a baseline for future environmental screenings of CALF-20-enabled technologies, including the SolDAC project.

It is especially important to highlight that when assessing the calculated impacts, 1,2,4-triazole came up as an environmental hotspot, accounting for more than half of the overall impacts of the CALF-20 synthesis procedure. Within the framework of the SolDAC project – and of any other future technology that seeks to implement CALF-20 for CO_2 capture purposes – this information supposes an alert to optimize the use of 1,2,4-triazole when synthetizing the MOF. It then becomes relevant to study intensification techniques on the use of organic synthesis precursors to achieve this optimization at its highest potential.

Future work

It is imperative to thoroughly evaluate the functionality of CALF-20 with respect to its ability for CO2 uptake. This is key to enable the future development of a future LCA that considers CO2 uptake as its functional unit, rather than the mass of CALF-20.

ACKNOWLEDGEMENTS

REFERENCES

Cuéllar-Franca, R., García-Gutiérrez, P., Taylor, S., Hardacre, C., & Azapagic, A. (2016). A novel methodology for assessing the environmental sustainability of ionic liquids used for CO_2 capture. *Faraday Discussions*, *192*, 283–301. https://doi.org/10.1039/C6FD00054A

HengXing Engineering. (n.d.). *Batch Ball Mill*. Despatch Industries. http://www.hengxingmill.com/products/grinding-mills/99.html

ITW EAE. (2020). *LBB Forced Convection Oven*. HengXing Mill. https://www.despatch.com/pdfs/LBB%20spec%20sheet.pdf

Lin, J.-B., Nguyen, T. T. T., Vaidhyanathan, R., Burner, J., Taylor, J. M., Durekova, H., Akhtar, F., Mah, R. K., Ghaffari-Nik, O., Marx, S., Fylstra, N., Iremonger, S. S., Dawson, K. W., Sarkar, P., Hovington, P., Rajendran, A., Woo, T. K., & Shimizu, G. K. H. (2021). A scalable metal-organic framework as a durable physisorbent for carbon dioxide capture. *Science*, *374*(6574), 1464–1469. https://doi.org/10.1126/science.abi7281

Petree, H. E., Pociask, J. R., & Gupton, J. T. (1981). *Method for direct preparation for 1,2,4-triazole from hydrazine and formamide* (Patent No. USA4267347A).

Qi, F., Stein, R. S., & Friščić, T. (2014). Mimicking mineral neogenesis for the clean synthesis of metal–organic materials from mineral feedstocks: coordination polymers, MOFs and metal oxide separation. *Green Chem.*, *16*(1), 121–132. https://doi.org/10.1039/C3GC41370E

The European Commission. (2021). Commission Recommendation (EU) 2021/2279 of 15 December 2021 on the use of the Environmental Footprint methods to measure and communicate the life cycle environmental performance of products and organizations. *Official Journal of the European Union. Recommendations.*

Dynamics of water vapour sorption on composite LiCl/(silica gel):

comparative study of loose adsorbent grains vs. coatings

S.V. Strelova, Yu.I. Aristov, L.G. Gordeeva[*]

Boreskov Institute of Catalysis, Ak. Lavrentiev av. 5, Novosibirsk, 630055, Russia

[*]Corresponding author: gordeeva@catalysis.ru

Abstract

Adsorption Heat Conversion (AHC) is considered an energy and environment saving alternative to conventional compression chillers and heat pumps. The growth of the Specific Power (SP) of AHC systems is prerequisite for wider spreading of this technology. The SP of AHC systems is mainly affected by ad/desorption dynamics in an Adsorber - Heat Exchanger (Ad-HEx) unit, which is governed by coupled heat and mass transfer in the adsorbent bed and between the bed and HEx. Two basic Ad-HEx configurations are loose adsorbent grains loaded between the HEx fins, and compact adsorbent coating on the fins. The main goal of this work was a comprehensive comparative study of the water vapour adsorption dynamics on loose grains and coatings of a composite sorbent LiCl/silica, intently developed for AHC. Thin coatings of the adsorbent on an aluminum foil were prepared with different binders of both organic and inorganic nature, and the water vapour adsorption dynamics on these coatings was and compared with that for loose adsorbent grains. The effect of the binder nature was studied. The effective heat transfer coefficients were evaluated under typical conditions of adsorption cooling cycles. The main findings are: (a) the effective heat transfer coefficient is increased when heat conductive compound CPTD, bentonite, and aluminium oxynitrate were used as binders; (b) organic binders, polyvinyl alcohol and polyvinylpyrrolidone, do not affect heat transfer; (c) intensification of heat transfer results in acceleration of the initial stage of the ad/desorption process; (d) on the contrary, at longer time, sorption deceleration is observed, probably due to hindered mass transfer. Recommendations for designing the optimal adsorbent bed configuration are formulated.

Keywords: Adsorption heat conversion, composite LiCl/silica, water adsorption dynamics, adsorbent coating vs. loose grains.

Introduction/Background

In recent years, the growing energy demand and environment pollution caused by the extensive use of fossil fuels have inspired considerable research interest to adsorptive heat conversion (AHC) [1]. This technology offers effective utilization of low-grade solar or waste thermal energy, which is available in abundance, to produce cooling and heating. Due to utilization of environmentally benign working fluids (water, methanol, ammonia, etc.) and low consumption of electric power, the AHC is characterised by a weak environment impact and represents a promising alternative to compression chillers and heat pumps. However, despite a noteworthy potential of AHC to fulfil the growing demands for cooling and heating, there are some research gaps hindering the practical implementation of these systems. Accordingly, till now the share of AHC systems in the market is small as compared to absorption chillers and particularly to common compression ones [2]. Therefore, there is a big room for improving the AHC systems performance.

Low specific power (SP) and, as a result, large size of AHC systems, are the main drawbacks which severely limit the commercialization and wider dissemination of AHC systems. The SP is mainly affected by adsorption dynamics of a working fluid, and its acceleration is a

key-stone for increasing the competitiveness of AHC systems [3]. The sorption dynamics in AHC systems depends on coupled heat and mass transfer in an Adsorber – Heat Exchanger (Ad-HEx) unit, and optimization of its configuration is a subject of numerous researches. A common and very usable Ad-HEx configuration is finned HEx loaded with loose adsorbent grains. Such a HEx configuration is generally considered to provide fast mass transfer due to large porosity of the bed (voids between grains), but the heat transfer is slow due to a high contact resistance between the grains and the HEx surface. Indeed, the "grain size insensitive" mode was detected for water and methanol vapour adsorption on thin granulated beds of silica [4], FAM-Z02 [5], activated carbon [6], composite LiCl/MWCNT [7], metal-organic frameworks NH_2-MIL-125 [8], MOF-801 [9], etc. For this mode, the adsorption dynamics is invariant with respect to the ratio S/m_{ad} = <heat transfer surface area>/<adsorbent mass> regardless the grain size; and the initial adsorption rate is proportional to this ratio. This indicates sufficiently fast intra- and intergrain mass transport and control of adsorption rate by heat transfer.

To reduce the contact resistance and enhance the heat transfer, thin adsorbent layers (coating) consolidated with the HEx surface with or without a binder were suggested [10]. Coating offer a high heat transfer between the adsorbent and HEx due to large contact surface. However, mass transfer can be slower because of a high density and low porosity of the consolidated layer, which can become a new factor limiting the sorption dynamics [11].

To date, several methods for the coating synthesis have been suggested, including dip-coating, drop-coating, spray-coating, electrospinning, binderless in-situ coating [**Erro! Indicador não definido.**, 12], etc. These techniques were applied to prepare thin consolidated layers based on zeolites [13], aluminophosphates [14], composite sorbents [15], MOFs [16, 17], etc. Furthermore, several lab-scale AHC units employing coated HExs were built and tested [18, 19, 20]. Freni et al. studied a chiller with HEx coated by commercial SAPO-34 with a uniform thickness of 0.1 mm, prepared with a silane binder. The chiller delivered a high SP of 675 W/kg_adsorbent, which exceeds SP = 498 W/kg obtained for the fixed bed of the SAPO-34 granules of 0.6-0.7 mm size loaded to the same HEx [21]. However, the volumetric specific power VSP = 93 W/dm^3_HEx and the Coefficient Of Performance COP = 0.24 were lower than those for the granulated adsorbent bed (VSP = 212 W/dm^3 and COP = 0.4). McCague et al. [22] compared a chiller based on a commercial fined-tube HEx with FAM-Z02 coating supplied by Mitsubishi Plastic Ltd. of 0.33 mm thickness with the same HEx loaded with FAM-Z02 pellets of 1.2-2.4 mm size. The SP equal to 300-456 W/kg and VSP of 60-90 kW/m^3 were obtained for the coated HEx. For fixed bed, the SCP was significantly lower (50-60 kW/kg), whereas, the VSP was higher (100-150 W/m^3). Thus, for thin adsorbent coatings of 0.1-0.3 mm, high SP-values related to the unit mass of the adsorbent can be achieved. However, a small amount of adsorbent loaded in such coated HExs increases the ratio m_{HEx}/m_{ad} of HEx to the adsorbent masses, and lowers both VSP and COP. At increasing coating thickness, the reduction of vapour transport occurs, which can become the process limiting the adsorption rate [23, 24].

Thus, a smart compromise between the heat and mass transfer is needed for the optimization of Ad-HEx configuration. A deeper understanding of the relative contribution of the heat and mass transfer resistances, and their affects on the adsorption kinetics is prerequisite to achieve such a compromise and enhance the SP of AHT units. Furthermore, the heat and mass transfers are inevitably coupled in the adsorption process, since faster adsorption releases larger amount of heat. Therefore, their differentiation and clarification of which transport mechanism is limiting, are welcome. Meanwhile, to the best of our knowledge, there is a scarcity of reports on detailed and accurate comparative study of the adsorption kinetics on the consolidated and granulated beds [7, 25, 26]. Particularly, the S/m_{ad} - ratio is key factor

Heat Powered Cycles
Conference 2023
Edinburgh
Heat in the new energy system

3rd to 6th of September 2023
The University of Edinburgh, Scotland

affecting the adsorption dynamics. Accordingly, to reveal the effect of adsorbent consolidation with the HEx surface on the AHC dynamics the correct comparison has to be performed at the same S/m_{ad} values.

In this paper, we report the results on the dynamics of water vapour adsorption on a sorbent specifically developed for AHC, namely the composite "LiCl inside silica gel pores" [27, 28]. Coatings were prepared with various binders of both inorganic and organic nature and characterized by microscopy and low-temperature nitrogen adsorption. The dynamics was studied under conditions of a typical adsorption cooling cycle. To distinguish the effect of the binder and the adsorbent consolidation from other factors affecting the dynamics, we fixed the S/m_{ad}-ratio for all adsorbent bed configurations. The effects of the binder nature and content as well as the coating thickness were studied. The effective heat transfer coefficient was measured in the air and calculated from an initial part of the kinetic curves. Based on the obtained results, factors controlling the kinetics were determined and recommendations on the adsorbent bed configuration were formulated.

Discussion and Results

The adsorbent coatings characterization

Lithium Chloride and silica gel Davisil Gr. 646 (specific surface area $S_{sp} = 267$ m^2/g, pore volume $V_p = 1.1$ cm^3/g, average pore size $d_{av} = 15.9$ nm) were used for the composite synthesis. The composite was prepared by a dry impregnation method [27]. Two adsorbent configurations were studied: the loose grains of 0.4-0.5 size, placed as monolayer on the surface of aluminium foil and the grains "glued" to the aluminum foil with a binder. Common binders of both inorganic (bentonite, pseudoboehmite AlOOH, aluminum oxynitrate AlONO$_3$, ceramic-polymer heat-conducting compound CPTD 1/3T) and organic natures (polyvinyl alcohol (PVA), polyvinylpyrrolidone (PVP)), often used for the coating synthesis, were selected. To avoid blocking of the salt particles inside pores by the binder, we first prepared the silica gel coatings, then impregnated them with the salt solution and finally dried them.

The microscopic images of the coatings presented in Fig. 1 showed that the morphology of LiCl/silica grains remains unchanged after gluing to the foil. Small bentonite particles deposited on the surface of LiCl/silica grains are observed for the coating with bentonite (Fig. 1 b). Some filamentous particles are also detected on the surface of LiCl/silica/CPTD, which can be CPTD or LiCl, partially removed from the silica pores on the external surface of the grains during the coating preparation. PVA, PVP, and aluminum oxynitrate form films on the foil surface and are not observed on the grain surface.

According to data of nitrogen porosimetry, the aluminum oxynitrate, pseudoboehmite, and PVP only slightly alter the porous structure of the adsorbents (Table 1). The pore blocking degree calculated as

$$\delta = [V_{p.ads} - V_{p.coating}] \, 100\% \, /V_{p.ads} \qquad (1)$$

(here $V_{p.ads}$ and $V_{p.coat}$ are the specific pore volumes of the adsorbent and the coating, related to the adsorbent mass) does not exceed 12%. CPTD reduces both pore volume and surface area of the composite due to partial pore blockage ($\delta = 20\%$), which is in accordance with the microscopy images. The texture characteristics of silica gel grains glued on the foil by PVP and PVA are similar to those of the pristine silica. However, pore volume and surface area are reduced strongly after impregnation the salt, giving the pore blockage $\delta = 29\%$. The increase in pore volume and surface area is observed for the coatings prepared with bentonite ($\delta = -38\%$) due to internal porosity of the binder. Indeed, an additional pick is observed on

Heat Powered Cycles
Conference 2023
Edinburgh
Heat in the new energy system

3rd to 6th of September 2023
The University of Edinburgh, Scotland

the pore size distribution at d = 3-4 nm along with the pick at d = 10-20 nm corresponding to mesopores of the silica gel. Thus, CPTD leads to significant blockage of the coating's pores. PVA, PVP and aluminum oxynitrate slightly affect the porous structure of the coatings. Coating with bentonite is characterized by formal negative pore blockage due to internal porosity of the binder.

(a) LiCl/SiO$_2$ (b) LiCl/SiO$_2$/bentonite   (c) LiCl/SiO$_2$/PVP   (d) LiCl/SiO$_2$/PVA   (e) LiCl/SiO$_2$/CPTD
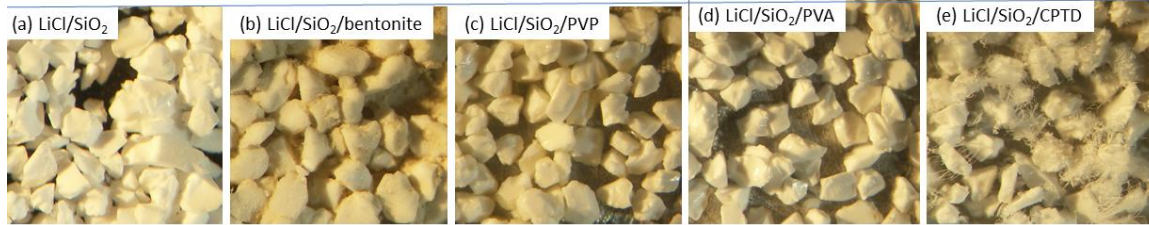
Fig. 1. Microscopic images of coatings LiCl/silica/binder.

Table 1. Composition and texture characteristics of the coatings: salt and binder contents C_{LiCl} and C_b, average pore size d_{av}, specific pore volume V_p and surface area S_{sp}, pore blockage degree δ.

Sample	C_{LiCl}, wt.%	C_b, wt.%	d_{av}, nm	V_p^*, см^3/г	S_{sp}^*, м^2/г	δ, %
SiO$_2$	-	-	15.9	1.1	267	0
LiCl/SiO$_2$	32	-	12.7	0.66	155	0
LiCl/SiO$_2$/AlONO$_3$	34	31	12.4	0.62	163	6
LiCl/SiO$_2$/CPTD	32	51	12.6	0.53	112	20
LiCl/SiO$_2$/bentonite	27	33	12.6	0.91	284	-38
LiCl/SiO$_2$/pseudoboehmite	34	46	15.9	0.58	160	12
SiO$_2$/PVA	-	14	19.2	1.1	267	0
LiCl/SiO$_2$/PVA	34	9	12.5	0.47	126	29
SiO$_2$/PVP	-	30	19.1	1.1	266	0
LiCl/SiO$_2$/PVP	33	18	12.3	0.47	141	29

* for the coatings with the binders the data are related to the unit mass of the composite.

Water vapour adsorption kinetics

Water vapour sorption kinetics was studied under conditions of a typical cooling cycle (water vapour pressure P = 12.4 and 42.8 for adsorption and desorption stages, respectively, which correspond to the temperature of the evaporator T_{ev} = 10°C and condenser T_{con} = 30°C; the temperature of adsorption T_{ad} = 30, 35, 40°C and desorption T_{des} = 80, 90, 100°C. The S/m$_{ad}$ - ratio was equal to 5.9 m^2/kg for all Ad-Hex configurations, which corresponds to monolayer of 0.4-0.5 mm grains. The kinetics was studied by a volumetric temperature jump method under quasi-isobaric conditions [29].

The loose grains of LiCl/silica exchange Δw = 0.47±0.01 g/g under conditions of the cooling cycle at T_{ad} = 35°C and T_{des} = 100°C. The binders CPTD, bentonite, pseudoboehmite, PVA does not affect the adsorption capacity, the water uptake related to the composite mass Δw = 0.46 ± 0.01 g/g. It is worth noting that despite pore blockage by CPTD and pseudoboehmite, the uptake on the coatings does not decreases, because LiCl as introduced into the coatings is

available for water vapour. Aluminum oxynitrate reduces the uptake to $\Delta w = 0.42 \pm 0.01$ g/g, probably due to a chemical interaction with the salt.

An initial parts of the kinetic curves (Fig. 2) obey the first order-kinetic equation

$$w(t) = w_{t\to\infty}(1 - \exp(-t/\tau)), \qquad (2)$$

where $w_{t\to\infty}$ is the final uptake variation, t is time, and τ is the characteristic time. For the loose grains bed, the characteristic time τ equal 63 and 34 s for adsorption at $T_{ad} = 35°C$ and desorption at $T_{des} = 100°C$, respectively (Table 2).
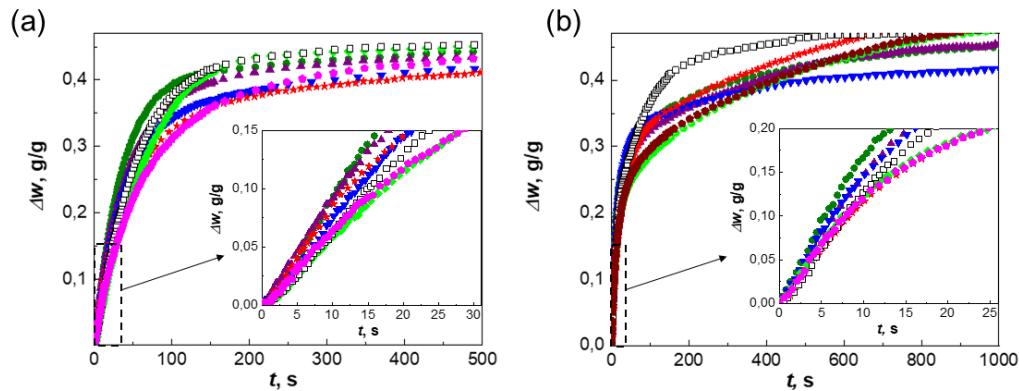
Fig. 2. Kinetic curves of water adsorption at $T_{ad} = 35$ °C (a) and desorption at $T_{des} = 100$ °C, for loose grains (□) and coatings of the composite LiCl/silica, prepared by gluing with CPTD (●), pseudoboehmite (★), bentonite (▲), AlONO$_3$ (▼), PVP (⬠), and PVA (◆).

The gluing of the grains with inorganic binders CPTD, pseudoboehmite, bentonite, AlONO$_3$ results in some acceleration of ad/desorption at initial times (Fig. 2 inserts). The strongest effect was observed for CPTD, the characteristic times τ reduces to 44 and 22 s for adsorption and desorption, respectively. The accelerating effect for bentonite, and AlONO$_3$ is smaller, the characteristic time $\tau_{ad} = 48 - 53$ s and $\tau_{des} = 23\text{-}24$ s. The acceleration is probably caused by the reduction of the contact thermal resistance between the grains and the aluminium surface due to the binder presence. The organic binders PVA and PVP do not accelerate ad/desorption, probably due to their low thermal conductivity or poor adhesion to the adsorbent grains.

Table 2. Characteristic times τ and $t_{0.8}$, the maximum specific power W_{max} and the specific power $W_{0.8}$, released/consumed in the cycle restricted by the conversion $q = 0.8$ in the beds of the LiCl/silica loose grains and coatings.

T, °C	τ, c	W$_{max.}$, Вт/г	t$_{0.8}$, c	W$_{0.8}$, Вт/г	Δw, г/г
Adsorption					
Loose grains LiCl/silica					
40	67	20.7	102	10.7	0.42
35	63	24.9	97	12.6	0.47
30	60	29.8	96	14.6	0.53
LiCl/silica /CPTD					
40	45	29.4	79	13.1	0.39
35	44	34.3	80	16.8	0.46
30	40	45.4	79	18.0	0.54
LiCl/silica/AlONO$_3$					
40	47	23.4	90	9.5	0.33
35	50	28.3	96	11.7	0.42
30	52	34.1	100	13.8	0.53
LiCl/silica/pseudoboehmite					

40	49	25.4	120	7.7	0.35
35	53	30.1	140	8.5	0.45
30	53	34.1	135	10.2	0.53
LiCl/silica/bentonite					
40	49	25.4	90	11.1	0.38
35	48	31.3	95	12.5	0.45
30	50	35.0	110	12.7	0.53
LiCl/silica/PVA					
40	72	18.2	113	9.3	0.39
35	68	22.2	106	11.4	0.46
30	63	27.8	94	14.9	0.53
LiCl/silica/PVP					
40	77	16.6	195	5.3	0.39
35	68	22.1	170	7.0	0.46
30	62	28.3	150	9.3	0.53
Desorption					
Loose grains LiCl/silica					
80	25	27.8	59	9.5	0.23
90	25	36.7	72	10.4	0.31
100	34	43.6	123	9.5	0.49
LiCl/silica /CPTD					
80	17	40.7	120	4.7	0.22
90	19	55.0	290	2.7	0.33
100	22	63.4	185	6.0	0.46
LiCl/silica/AlONO$_3$					
80	21	37.2	49	12.1	0.26
90	22	48.5	71	11.9	0.35
100	23	55.5	89	10.4	0.41
LiCl/silica/pseudoboehmite					
80	31	25.3	140	4.5	0.26
90	33	33.6	250	3.5	0.37
100	39	39.2	320	3.8	0.51
LiCl/silica/bentonite					
80	21	30.8	50	10.9	0.21
90	21	46.7	80	9.8	0.32
100	24	55.2	170	6.3	0.44
LiCl/silica/PVA					
80	18	32.3	30	15.2	0.19
90	22	38.6	70	9.6	0.28
100	35	43.5	440	2.8	0.51
LiCl/silica/PVP					
80	26	26.7	115	4.9	0.23
90	29	34.7	200	4.1	0.33
100	35	40.3	380	3.0	0.47

At high dimensionless conversion $q = w(t)/w_{t \to \infty} > 0.5\text{-}0.8$ the ad/desorption for the coatings becomes slower than for the loose grains. To describe the kinetics at high conversion, the time $t_{0.8}$ corresponding to conversion $q = 0.8$ was determined, which equals 97 s for adsorption at $T_{ad} = 35°C$ and 123 s for desorption at $T_{des} = 100°C$ (Table 2) for the loose grains. The adsorption deceleration is strongest for pseudoboehmite and PVP as binders, resulting in the increase in time $t_{0.8ads}$ to 140 and 170 s, respectively. For desorption runs the deceleration is even more pronounced, for the coatings with PVP, PVA, and pseudoboehmite the time $t_{0.8des} = 320\text{-}440$ s at $T_{des} = 100°C$.

Heat transfer coefficients

The analysis of the initial part of the kinetic curves measured on the loose grains (Fig. 3) at different temperatures T_{ad} = 30, 35, and 40°C and T_{des} = 80, 90, and 100°C showed that the initial adsorption rate R_0 and, consequently, the specific maximum power W_{max}, released/consumed at t = 0 are proportional to the driving temperature difference $\Delta T = T_{ad} - T_{in}$:

$$R_0 = \frac{d\Delta w(t)}{dt}\Big|_{t=0} = \Delta w_{t\to\infty}/\tau = A(T_s - T_{in}), \text{ and} \tag{3}$$

$$W_{max} = R_0\Delta H_s = A\Delta H_s (T_s - T_{in}), \tag{4}$$

where ΔH_s is the adsorption heat, T_s and T_{in} are the ad/desorption temperatures and the initial adsorbent temperature. This indicates that at t = 0, the heat transfer between the foil and the adsorbent bed controls the adsorption rate. A similar linear dependence is detected for the coatings LiCl/silica/binder.
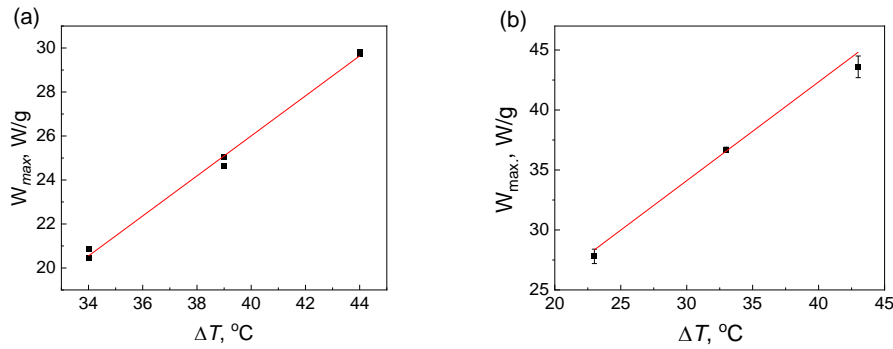
Fig. 3. Maximum specific power W_{max} released during adsorption (a) and consumed during desorption (b) for the bed of loose LiCl/silica grains vs the driving temperature difference ΔT.

The heat balance in the bed at t = 0 can be expressed as

$$\alpha_c \left(\frac{S}{m_{ad}}\right) \cdot (T_s - T_{in}) = R_0\Delta H_s + C_p(T_s - T_{in}) \tag{5}$$

where α_c is the effective heat transfer coefficient, and C_p is the specific heat capacity of the adsorbent and adsorbed water. Then, the effective heat transfer coefficient α_c between the metal support and the adsorbent bed under conditions of the adsorption cycles can be estimated from eqs. (2) and (3) assuming that the second summand on the right can be neglected. The effective heat transfer coefficient in the bed of LiCl/silica loose grains (Table 3) equals 155 and 140 ± 15 W/(m²K) for adsorption and desorption runs, respectively. LiCl/silica/binder coatings with CPTD, bentonite, and aluminum oxynitride show the higher coefficients α_c = 170-260 and 160-210 ± 15 W/(m²K) for adsorption and desorption, respectively. The effect of PVA, PVP and pseudoboehmite the effective heat transfer coefficients is minor.

Table 3. Effective heat transfer coefficients for LiCl/silica loose grains and LiCl/silica/binder coatings of under conditions of the adsorption cycle.

Sample	α_c, W/(m²· K)	
	Adsorption	Desorption

Loose grains LiCl/silica	155	140
LiCl/silica/CPTD	260	180
LiCl/silica/bentonite	170	210
LiCl/silica/AlONO$_3$	180	160
LiCl/silica/pseudoboehmite	160	120
LiCl/silica/PVP	190	110
LiCl/silica/PVA	160	100

These data are in accordance with the data on the thermal resistance R and coefficient α_{air} of the silica gel loose grains and coatings measured by a thermal probe method in atmospheric air (Table 4). The heat transfer resistance of the silica/binder coatings prepared with CPTD, bentonite, pseudoboehmite, and aluminum oxynitrate, varies in the range R = 0.015-0.022 m^{2}K/W, which is lesser that for the loose grains, R = 0.027 m^{2}K/W. Again, the effect of PVP and PVS as binders is minor (R = 0.027-0.032 m^{2}K/W). Thus, using inorganic binders (CPTD, bentonite, pseudoboehmite, and aluminum oxynitrate) affords to reduce the thermal resistance of the adsorbent coatings.

Table 4. Thermal resistance R and the heat transfer coefficients of the thin bed of loose silica grains and coatings.

Sample	R, m^2·K/W	α_{air}, W/(m^{2}K)
Loose silica grains	0.027	74
silica/CPTD	0.015	138
silica/bentonite	0.015	133
silica/pseudoboehmite	0.020	100
silica/AlONO$_3$	0.022	91
silica/PVA	0.032	63
silica/PVP	0.027	74

Specific power estimation

The data on the water vapour sorption kinetics were used to evaluate the specific power, which can be realized in a typical adsorption cooling cycle for the studied adsorbent beds. The maximum specific power released/consumed at the beginning of ad/desorption stages is calculated according to the expression

$$W_{max} = R_0 \Delta H_s = \Delta w_{t \to \infty} \Delta H_s / \tau . \tag{6}$$

The average power $W_{0.8}$ released and consumed during adsorption and desorption is calculated for the cycle restricted by the conversion q = 0.8 as

$$W_{0.8} = \Delta w_{t \to \infty} \Delta H_s / t_{0.8}, \tag{7}$$

where $t_{0.8}$ is the time corresponding to q = 0.8.
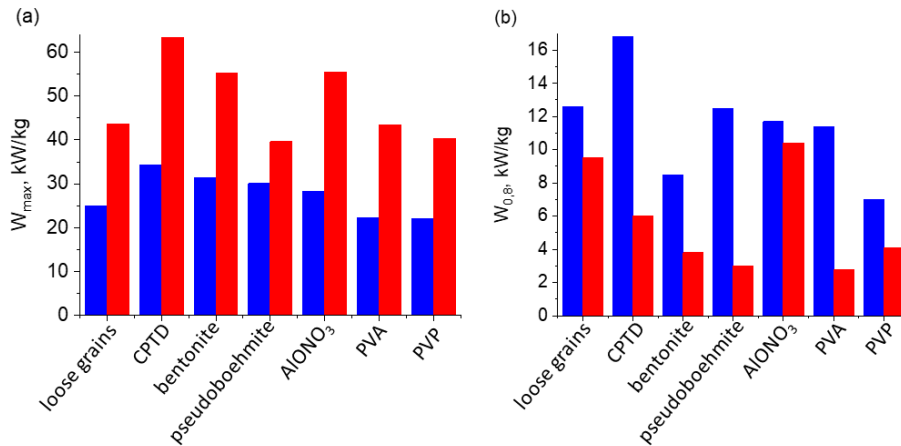
Fig. 4. Maximum W_{max} (a) and average $W_{0.8}$ (b) specific powers, released during adsorption at $T_{ad} = 35°C$ (■) and consumed during desorption $T_{des} = 100°C$ (■) on thin beds of LiCl/silica loose grains and coatings.

Very high maximum specific power W_{max} equal to 21 - 30 kW/kg is released during adsorption for bed of LiCl/silica loose grains (Table 2, Fig. 4a). Even larger is the power consumed during desorption $W_{max} = 28-44$ kW/kg. It can be further increased by using LiCl/silica/binder coatings. Thus, coatings prepared with CPTD and bentonite show higher initial powers $W_{max} = 25-45$ and $30-63$ kW/kg during adsorption and desorption stage, respectively. For the coatings with pseudoboehmite and aluminium oxynitrate, the power enhancement is smaller (Fig. 4a) according to their lower accelerating effect (see above).

The average power $W_{0.8}$ released and consumed on the loose grains during adsorption and desorption is also high and varies in the range 11-15 and 10-11 kW/kg (Table 2, Fig. 3b), respectively. Contrary to the initial power W_{max}, the consolidation of LiCl/silica grains with the surface of the aluminum support by the binders does not increase the average power $W_{0.8}$ (Fig. 4b). This is because the acceleration of the sorption at short times is completely compensated by the deceleration of adsorption and, particularly, desorption at longer times (Fig. 3). As the result, no increase in the average power $W_{0.8}$ is observed.

In sum, the consolidation of LiCl/silica with CPTD, bentonite, and aluminium oxynitrate allows essential increase in the effective heat transfer coefficients (Fig. 5a,b), which accelerate the water vapour ad/desorption at short times. Accordingly, the maximum specific power, released/consumed at the beginning of ad/desorption is significantly increased. At longer times, corresponding to q > 0.5 – 0.7, the deceleration of adsorption and, particularly, desorption for coatings was observed compared to the bed composed of loose grains. The slowing down of ad/desorption for LiCl/silica/binder coatings can be caused by the following reasons:

- For the coatings LiCl/silica benders the mass transfer inside the coating can be partially hindered by the binder. At long times, it becomes the main factor limiting the sorption rate, which slows down the ad/desorption for the coatings (Fig. 5b).
- When preparing the LiCl/binder/silica coating, first, the silica grains are glued to the foil with the binder, and then, impregnated with the aqueous LiCl solution. The solution is imbibed inside the silica pores and can be, at least partially, located between the grains and the binder. Accordingly, during the coating drying, the salt can precipitate not only inside silica pores, but also form large crystals between the grains. The water ad/desorption for these large salt crystals can be severely hampered by the mass transfer inside the salt particles or chemical reaction between the salt and water (Fig. 5c).

As the result of the sorption deceleration at long times, no enhancement of the average specific power $W_{0.8}$ was observed for coatings LiCl/silica/binder.
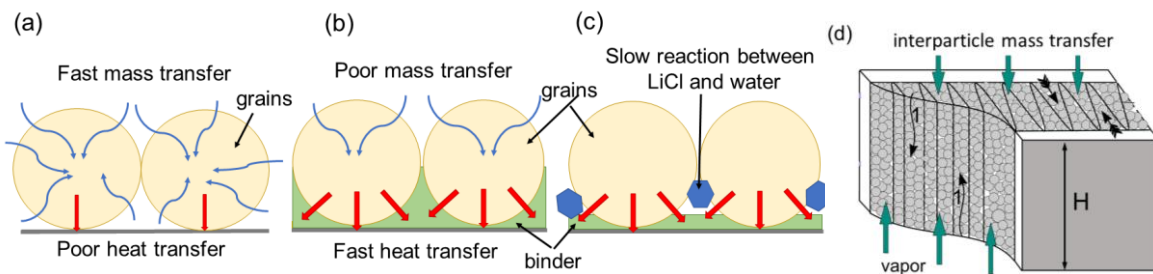
Fig. 5. Scheme of mass and heat transfers for thin beds of loose grains (a) and coating (b) and finned flat-tube HEx (c).

Taken into account the obtained results, the simple and usable Ad-HEx configuration composed of loose LiCl/silica grains can be recommended for AHC systems. The probable drawback of the granulated beds based on common commercial HExs, such as finned [22, 30] and finned flat-tube [31] Hex, could be an additional resistance to interparticle mass transfer in the direction parallel to fins (Fig 5d). For HExs with large height H, this resistance can control the adsorption dynamics. Indeed, it was shown for the loose grains of activated carbon [32], composite LiBr/silica [33], and water adsorption on AQSOA FAM-Z02 [34] loaded into finned flat-tube HExs that at the heights H > 20-40 mm the ad/desorption was essentially controlled by the inter-grain mass transfer. To avoid this, the height should be restricted by a certain value, which depends on the adsorbent and adsorptive nature, operating vapour pressure, grain size, etc.

Summary/conclusions

In this paper, the results of comprehensive study of the dynamics of water vapor adsorption on thin beds of composite sorbent LiCl/silica are presented. Two adsorbent bed configurations are thoroughly compared, namely thin beds of loose grains placed on the aluminium foil and coatings of this sorbent with various binders. To reveal the effect of the binder, both configurations were prepared with the same ratio <heat transfer surface area>/ <adsorbent mass>. The bed of LiCl/silica loose grains demonstrates the high values of the specific power W_{max} = 21-30 and 28-44 kW/kg kW/kg, released and consumed at the beginning of ad/desorption stages, respectively. The average specific power for the cycle restricted by conversion q = 0.8 reaches $W_{0.8}$ = 11-15 and 10-11 kW/kg for adsorption and desorption. The consolidation of LiCl/silica grains to the aluminium foil with CPTD, bentonite, and aluminium oxynitrate affords to increase the effective heat transfer coefficient α_c from 155 to 170-260 kW/(m^{2}K) and from 140 to 180-210 W/(m^{2}K), respectively. The enhanced heat transfer results in the acceleration of ad/desorption at initial times, and in the growth of the maximum specific power W_{max}, realized at the beginning of ad/desorption, to 25-45 and 30-63 kW/kg for adsorption and desorption, respectively. At longer time, the deceleration of water adsorption and desorption on coatings is observed, probably due to increased resistance to intraparticle mass transfer. For LiCl/silica/binder coatings, this deceleration completely compensates the growth of the ad/desorption rate at initial times, so that no increase in the average specific power $W_{0.8}$ is observed. Given the obtained results, the adsorbent bed configuration composed of loose grains can be recommended.

Acknowledgments

References:

[1] Wang, R., Wang, L., Wu, J., *Adsorption Refrigeration Technology: Theory and Application*, John Wiley & Sons, Singapore, 2014.

[2] Chauhan, P.R., Kaushik, S.C., Tyagi, S.K., "Current status and technological advancements in adsorption refrigeration systems: A review", Renew. Sustain. Energy Rev., 2022, 154, 111808

[3] Aristov, Yu., "Adsorptive transformation and storage of renewable heat: review of current trends in adsorption dynamics", Renewable Energy, 2017, 110, 105-114.

[4] Aristov, Yu. I., Glaznev, I. S., Girnik, I. S., "Optimization of adsorption dynamics in adsorptive chillers: Loose grains configuration", Energy, 2012, 46, 484-492.

[5] Girnik, I. S., Aristov, Yu. I., "Dynamic optimization of adsorptive chillers: The "AQSOA™-FAM-Z02 - water" working pair", Energy, 2016, 106, 13-22.

[6] Gordeeva, L. G., Aristov, Yu. I., "Dynamic study of methanol adsorption on activated carbon ACM-35.4 for enhancing the specific cooling power of adsorptive chillers", Appl. Energy 2014, 117, 127–133.

[7] Grekova, A., Gordeeva, L., Lu, Z., Wang, R., Aristov, Yu., "Composite LiCl/MWCNT as advanced water sorbent for thermal energy storage: sorption dynamics", Sol. Energy Mater. Sol. Cells, 2018, 176, 273–279.

[8] Solovyeva, M. V., Aristov, Yu. I., Gordeeva, L. G., "NH2-MIL-125 as promising adsorbent for adsorptive cooling: Water adsorption dynamics", Appl. Therm. Eng., 2017, 116, 541–548.

[9] Solovyeva, M. V., Gordeeva, L. G., Krieger, T. A., Aristov, Yu. I., "MOF-801 as a promising material for adsorption cooling: Equilibrium and dynamics of water adsorption", Energy Convers. Manag., 2018, 174, 356–363.

[10] Guilleminot, J.J., Choisier, A., Chalfen, J.B., Nicolast S., Reymoney, J.L., "Heat transfer intensification in fixed bed adsorbers", Heat Recovery Systems & CHP, 1993, 13, 297-300.

[11] Gordeeva, L.G., Aristov, Y.I., "Adsorbent Coatings for Adsorption Heat Transformation: From Synthesis to Application", Energies, 2022, 15, 7551.

[12] Caprì, A., Frazzica, A., Calabrese, L., "Recent Developments in Coating Technologies for Adsorption Heat Pumps: A Review", Coatings, 2020, 10, 855.

[13] Wang, L., Zhu D., Tan, Y., "Heat Transfer Enhancement of the Adsorber of an Adsorption Heat Pump", Adsorption, 1999, 5, 279–286.

[14] Calabrese, L., Mittelbach, W., Bonaccorsi, L., Freni, A., "An Industrial Approach for the Optimization of a New Performing Coated Adsorber for Adsorption Heat Pumps", Energies, 2022, 15, 5118.

[15] He, F., Nagano K., Seol, S.-H., Togawa, J., "Thermal performance improvement of AHP using corrugated heat exchanger by dip-coating method with mass recovery", Energy, 2022, 239, 122418.

[16] Kummer, H., Baumgartner, M., Hügenell, P., Fröhlich, D., Henninger, S.K., Gläser, R., "Thermally driven refrigeration by methanol adsorption on coatings of HKUST-1 and MIL-101(Cr)", Appl. Therm. Eng., 2017, 117, 689–697.

[17] Cui, S., Qin, M., Marandi, A., Steggles, V., Wang, S., Feng, X., Nouar, F., Serre, C., "Metal-Organic Frameworks as advanced moisture sorbents for energy-efficient high temperature cooling", Sci. Reports, 2018, 8, 15284.

[18] Bauer, J., Herrmann, R., Mittelbach, W., Schwieger, W., "Zeolite/aluminum composite adsorbents for application in adsorption refrigeration", Int. J. Energy Res., 2009, 33, 1233–1249.

[19] He, F., Nagano, K., Togawa, J., "Experimental study and development of a low-cost 1 kW adsorption chiller using composite adsorbent based on natural mesoporous material," Energy, 2020, 209, 118365.

[20] Kummer, H., Jeremias, F., Fröhlich, D., Warlo, A., Füldner, G., Janiak, C., Gläser, R., Henninger, S., "A Functional Full-Scale Heat Exchanger Coated with Aluminum Fumarate Metal-Organic Framework for Adsorption Heat Transformation", Ind. Eng. Chem. Res., 2017, 56, 8393-8398.

[21] Freni, A., Bonaccorsi, L., Calabrese, L., Caprì, A., Frazzica, A., Sapienza, A., "SAPO-34 coated adsorbent heat exchanger for adsorption chillers", Appl. Therm. Eng., 2015, 82, 1-7.

[22] McCague, C., Huttema, W., Fradin, A., Bahrami, M., "Lab-scale sorption chiller comparison of FAM-Z02 coating and pellets", Appl. Therm. Eng., 2020, 173, 115219.

[23] Wang, L., Zhu D.,Tan, Y., "Heat Transfer Enhancement of the Adsorber of an Adsorption Heat Pump", Adsorption, 1999, 5, 279–286.

[24] Zhao, L.H., Wang, R.Z., Ge, T.S., "Desiccant coated heat exchanger and its applications", Int. J. Refrig., 2021, 130, 217–232.

[25] Girnik, I.S., Grekova, A.D., Gordeeva, L.G., Aristov, Yu.I., "Dynamic optimization of adsorptive chillers: compact layer vs. bed of loose grains", Appl. Therm. Eng., 2017, 125, 823-829.

[26] Solovyeva, M.V., Gordeeva, L.G., Aristov, Yu.I., "MIL-101(Cr) - methanol" as working pair for adsorption heat transformation cycles: adsorbent shaping, adsorption equilibrium and dynamics", Energy Conv. Manag., 2019, 182, 299-306.

[27] Gong, L. X., Wang, R. Z., Xia, Z. Z., Chen, C. J., Adsorption Equilibrium of Water on Composite Adsorbent Employing Lithium Chloride in Silica Gel, J. Chem. Eng. Data, 2010, 55, 2920–2923.

[28] Shkatulov, A., Gordeeva, L. G., Girnik, I. S., Huinink, H., Aristov, Yu. I., "Novel adsorption method for moisture and heat recuperation in ventilation: Composites "LiCl/matrix" tailored for cold climate", Energy, 2020, 201, 117595

[29] Aristov, Yu.I., Dawoud, B., Glaznev, I.S., Elyas, A., "A new methodology of studying the dynamics of water sorption/desorption under real operating conditions of adsorption heat pumps: experiment"' Int. J. Heat Mass Transf. 2008, 51, 4966-4972.

[30] Gkaniatsou, E., Chen, C., Cui, F.S., Zhu, X., Sapin, P., Nouar, F., Boissiere, C., Markides, C.N., Hensen, J., Serre, C., "Producing cold from heat with aluminum carboxylate-based metal-organic frameworks", Cell Reports Phys. Sci., 2022, 3, 100730.

[31] Freni, A., Bonaccorsi, L., Calabrese, L., Caprì, A., Frazzica, A., Sapienza, A., "SAPO-34 coated adsorbent heat exchanger for adsorption chillers", Appl. Therm. Eng., 2015, 82, 1-7.

[32] Brancato, V., Gordeeva, L., Sapienza, A., Freni, A., Frazzica, A., "Dynamics study of ethanol adsorption on microporous activated carbon for adsorptive cooling applications", Appl. Therm. Eng., 2016, 105, 28–38.

[33] Gordeeva, L., Frazzica, A., Sapienza, A., Aristov, Yu., Freni, A., "Adsorption cooling utilizing the "LiBr/silica – ethanol" working pair: Dynamic optimization of the adsorber/heat exchanger unit", Energy, 2014, 75, 390–399,

[34] Santamaria, S., Sapienza, A., Frazzica, A., Freni, A., Girnik, I. S., Aristov, Yu. I., "Water adsorption dynamics on representative pieces of real adsorbers for adsorptive chillers", Applied Energy, 2014, 134, 11–19.

Ammonia-salt resorption heat pump development and analysis

G. H. Atkinson[1, *], S. J. Metcalf[1], R. E. Critoph[1] and G. S. F. Shire[1]

[1] Sustainable Thermal Energy Technologies, University of Warwick, Coventry, UK

[*] Corresponding author: George.H.Atkinson@warwick.ac.uk

Abstract

Testing and subsequent modelling of ammonia-salt reactions in Large Temperature Jump (LTJ) and slow-ramp equilibrium tests has proved successful [1], and has led to the design [2] and manufacture [3] of a kW-scale resorption heat pump test bench (with scope for future development as a thermal transformer). Ammonia is selected as the refrigerant in a resorption cycle with manganese chloride ($MnCl_2$) as the high temperature salt (HTS) and sodium bromide (NaBr) as the low temperature salt (LTS) – both salts are impregnated in a conductive expanded natural graphite (ENG) matrix to improve heat transfer and to eliminate agglomeration. Initial results from the resorption heat pump test bench are encouraging, showing consistent pressure and temperature cycling of the reactors in a repeatable manner. Analysis of the results to-date indicates that the cycle is operating as anticipated, and that improving the heat transfer and minimising thermal mass in the sorbent reactor is key to producing an effective and compact resorption system.

Keywords: ammonia; chemisorption; heat pump; resorption; and thermochemical.

Introduction

Cycles using chemisorption can be applied to refrigeration, heat pumping, and thermal transformation, and may either use a single salt in a reactor, together with a system for evaporating and condensing the refrigerant, or a resorption cycle, in which the refrigerant is adsorbed or desorbed between two salts with the refrigerant maintained in gas form. The reversible reactions of ammonia with halide salts in a resorption setup may present a comparatively inexpensive alternative to existing sorption systems by removing the need for evaporator and condenser components.

The two salts in a resorption cycle are termed a Low Temperature Salt (LTS) and High Temperature Salt (HTS) and are contained in separate reactors (solid-gas adsorbent heat exchangers). The salts are in the presence of ammonia refrigerant, either as an adsorbed phase with the salt, or in gas form. A block diagram and Clapeyron graph example of a resorption cycle are illustrated in Figure 1. Referring to Figure 1 and starting in the high-pressure phase (P_H), the HTS is heated by a high temperature input (T_H), perhaps at between 150-180 °C, and the HTS desorbs ammonia, which at the same pressure is adsorbed by the LTS, yielding a useful heat output at between 40-60 °C (T_M). The HTS is $MnCl_2$, which adsorbs 4 moles of ammonia (6-2 reaction), and the LTS is NaBr, which adsorbs 5.25 moles ammonia (5.25-0 reaction). The choice of salt is not discussed further, but selection methods and discussions can be found in [1, 4, 5]. The reaction proceeds at nominal constant pressure until the reaction completes and the ammonia has moved from the HTS to the LTS (completing both desorption and adsorption respectively). To reach the low-pressure phase, the LTS

reactor is cooled, while the HTS is adiabatic. For a higher COP machine, heat recovery could be used to recover the heat from the LTS reactor. During the low-pressure phase, the LTS is heated from ambient heat between -10 to +10 °C (T_L), desorbing ammonia, which is then adsorbed by the HTS, releasing heat at a middle temperature (T_M), around 40-60 °C. Again, the reaction completes at a nominal constant pressure.
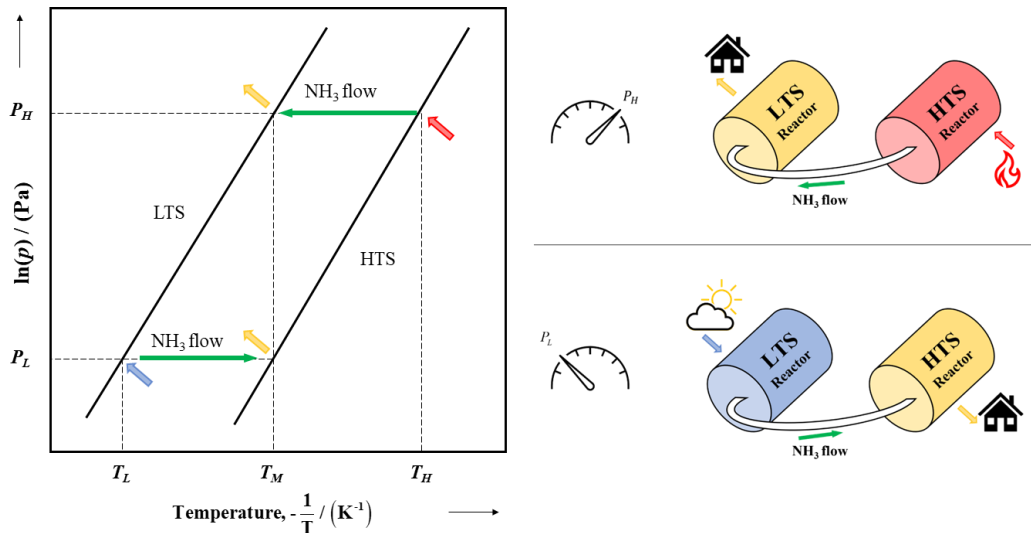
Figure 1. *(Left) Clapeyron diagram LTS and HTS equilibrium lines. (Right) block diagram showing the working operation of a resorption cycle driven by three temperature levels and working between two pressure levels. The coloured arrows match across each section of the figure, with a high temperature and low temperature heat input from a gas burner and ambient respectively, and a middle temperature heat output, which can be used usefully for domestic hot water and space heating.*

Methodology

To assess the performance of a resorption system, a kW-scale resorption heat pump test bench has been designed and manufactured. The system is driven by a high temperature (T_H) source of pressurised water at up to 170 °C (simulating a gas burner), a low temperature (T_L) input is from water between 5 and 15 °C (simulating ambient heat) and the output (T_M) is between 30 and 50 °C (simulating a load). In other words, the system is driven by three temperature levels in operation. It uses a simple cycle consisting of one low-pressure phase followed by a high-pressure phase, without any heat recovery, moving ammonia from the LTS reactor to the HTS reactor and vice versa. A practical machine would have two such sets of reactors and recover heat between the LTS reactors. The heat transfer fluid temperatures are measured using PRTs (PT100s) and the mass flow rate of the water and the ammonia are measured by Coriolis flow meters.

The three temperature levels for resorption operation are provided by the thermal test facility at the University of Warwick – the ThermExS laboratory [6], Figure 2.

Large Temperature Jump (LTJ) experimental work and semi-empirical modelling has informed the design of the composite adsorbent and reactor, providing an understanding of the reaction kinetics and heat transfer [1]. Interestingly, the reactions with ammonia-salts appear to be dominated by heat transfer between the heat transfer fluid and the salt composite, rather than the reaction kinetics, or mass transfer. What follows is an outline of

the completed resorption test bench design, incorporating the composite adsorbent and reactor.
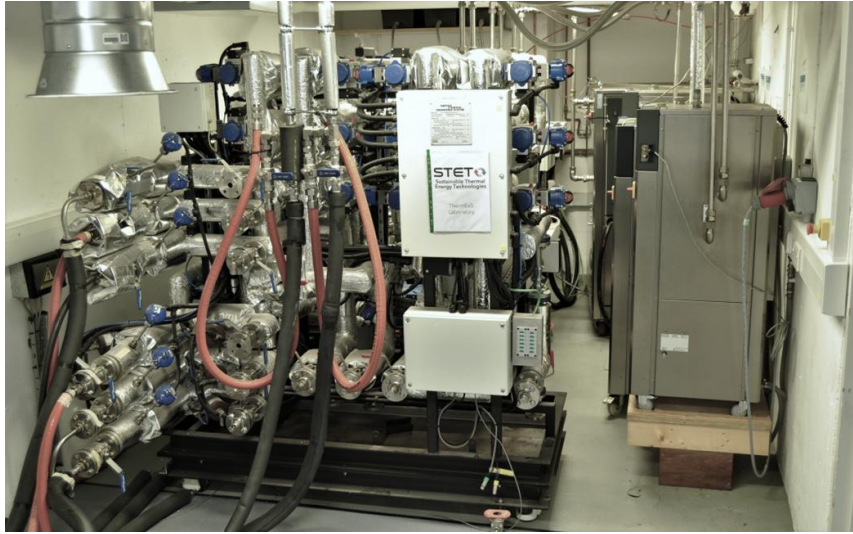
Figure 2. *ThermExS laboratory at the University of Warwick. Huber thermostatic baths (right hand side) provide heating or cooling silicone oil that can be delivered directly to a test bench system, or, sent to the heat exchanger assembly (centre/left hand side) allowing the delivery of pressurised hot water.*

Resorption Test Bench Design

A simple schematic layout of the kW-scale test bench is shown in Figure 3, and the completed system connected in front of the ThermExS facilities is shown in Figure 4. From the schematic, it is clear to see that the advantages of the resorption cycle are in the absence of any condenser, evaporator, or any refrigerant control valves. This is in addition to the wide range of salts available to react with ammonia, from which each reaction can be selected to match the required application.
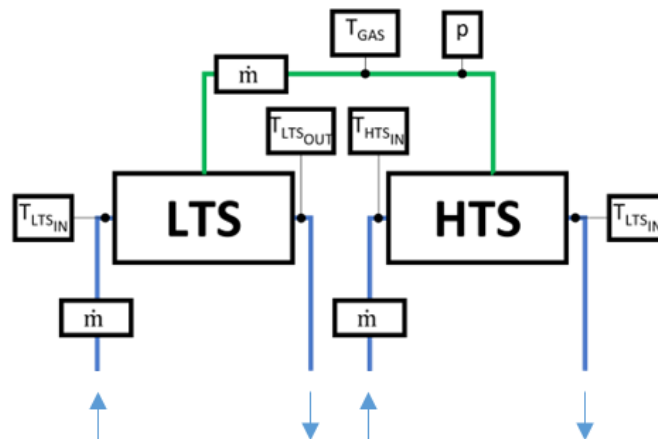
Figure 3. *Schematic of the resorption system, illustrating the simplicity. Blue lines indicate pressurised water inlet and outlet to the LTS and HTS reactors, and the green line connections indicate the ammonia line between the reactors. For measurement: temperatures (T) measured on the water line are measured with calibrated PT100s; mass flow rates (ṁ) are measured with Coriolis flow meters on both the water and ammonia lines; pressure (p) on the ammonia line is measured with a Danfoss ammonia suitable pressure transducer; and the temperature (T) of the ammonia gas is measured with a K-type thermocouple.*

Using techniques employed by van der Pal and Critoph [7], Hinmers et al. [2], and Atkinson et al. [4], the reactors have been manufactured with the ENG-salt composite held on the

shell-side and the heat transfer fluid flowing through the tube-side. The Expanded Natural Graphite (ENG) is used following findings from Karabanova et al. [8] and by researchers at the University of Warwick, that shows by dispersing the salts in a porous and conductive matrix, both agglomeration and heat transfer issues can be overcome.

Figure 4. The completed resorption test bench situated in front of the ThermExS testing facility. The LTS reactor (NaBr) is situated on the top shelf (insulated), with the HTS reactor (MnCl$_2$) on the middle shelf (stainless steel shell visible, uninsulated).

Results and Discussion

A sample of a 160 / 40 / 15 °C (T_H / T_M / T_L) resorption heat pump test output is shown in Figure 5, illustrating the cyclic nature of the pressure between the low- and high- pressure phases of the resorption system. In Figure 5, the system cycles between 0.30 bar and 8.80 bar in a repeatable manner with a total cycle time of 3600 seconds (60 minutes), which is a cycle time designed to fully ammoniate and deammoniate the salt reactors in each half of the cycle.
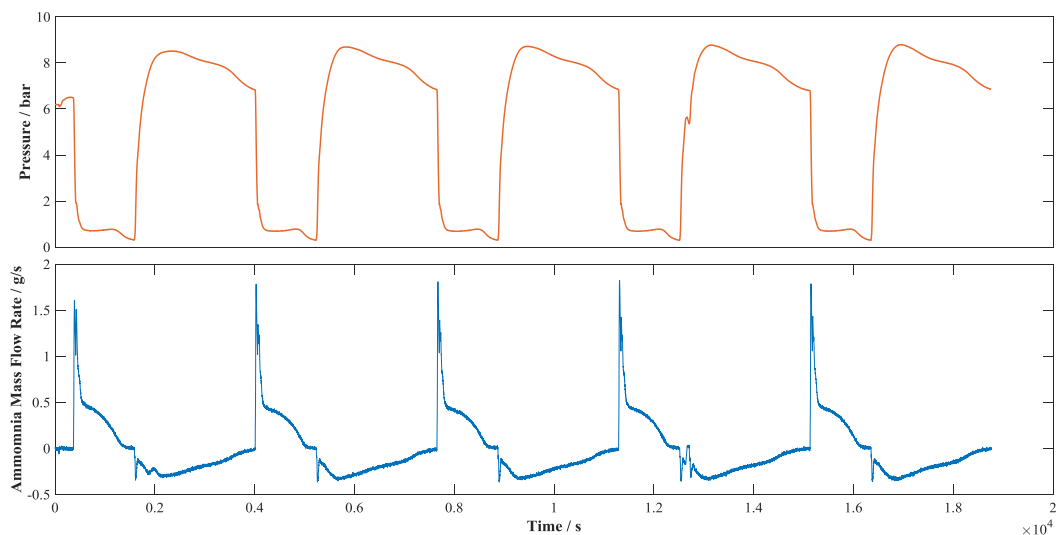
Figure 5. Pressure variation and ammonia mass flow rate between the low- and high- pressure phases during five repeated resorption cycles. The peak mass flow in the low-pressure phase is 1.80 g/s and in the high-pressure phase is -0.35 g/s.

At the time of writing a limited number of test conditions have been conducted and not fully analysed, but the consistency of the cycles is encouraging, albeit with power and COP

outputs that are less than predicted. Initial analysis indicates that the lower COP can be attributed to the high ratio of sensible heat to reaction heat, although the reactor design has achieved a sorbent-to-sensible mass ratio better than previous works in this field. This is particularly prevalent in the LTS reactor during the high-pressure phase, where significant self-heating is required to bring the reactor temperature to the middle (T_M) delivery temperature. Low power outputs are because of the long cycle times which allow the complete adsorption and desorption of the reactors during each half cycle. Heating power output can be improved with shorter cycle times at the expense of a drop in the COP.

Conclusions

A resorption heat pump test bench has been designed and manufactured using knowledge of ammonia-salt reactions gained from LTJ experiments. The solid-gas adsorbent heat exchangers (reactors) use an ENG-salt composite, where the salts are dispersed in the porous ENG structure to improve heat transfer and remove potential for salt agglomeration. LTJ testing on small samples was used to determine the heat transfer and reaction kinetics.

The test bench preliminary results show consistent cycling of the two salt reactors ($MnCl_2$-NaBr, HTS-LTS pair), with results that are consistent and repeatable.

Future work will test the system at a variety of temperature and cycle time conditions to determine overall system performance, as well as reversing the heat flows to operate the resorption setup as a resorption heat transformer. Additional work will also consider using two pairs of reactors and employing heat recovery between the LTS reactors to enhance the performance.

Acknowledgments

References

[1] S. Hinmers, G. H. Atkinson, R. E. Critoph, and M. van der Pal, "Modelling and Analysis of Ammonia Sorption Reactions in Halide Salts," *International Journal of Refrigeration,* 2022, doi: 10.1016/j.ijrefrig.2022.01.032.

[2] S. Hinmers, G. H. Atkinson, R. E. Critoph, and M. van der Pal, "Resorption Thermal Transformer Generator Design," *Energies,* vol. 15, no. 6, 2022, doi: 10.3390/en15062058.

[3] G. H. Atkinson, S. J. Metcalf, R. E. Critoph, G. S. F. Shire, and M. van der Pal, "Design and manufacture of a proof-of-concept resorption heat pump using ammonia-salt chemisorption reactions," *Cleaner Energy Systems,* Under Review.

[4] G. H. Atkinson, S. Hinmers, R. E. Critoph, and M. van der Pal, "Ammonium Chloride (NH4Cl)—Ammonia (NH3): Sorption Characteristics for Heat Pump Applications," *Energies,* vol. 14, no. 18, 2021, doi: 10.3390/en14186002.

[5] Z. Yang, M. Qu, and K. R. Gluesenkamp, "Design screening and analysis of gas-fired ammonia-based chemisorption heat pumps for space heating in cold climate," *Energy,* vol. 207, 2020, doi: 10.1016/j.energy.2020.118213.

[6] Sustainable Thermal Energy Technologies (STET). "ThermExS Laboratory." The University of Warwick. https://warwick.ac.uk/fac/sci/eng/research/grouplist/sustainableenergy/facilities/thermxs/ (accessed 17th November, 2019).

[7] M. van der Pal and R. E. Critoph, "Performance of CaCl2-reactor for application in ammonia-salt based thermal transformers," *Applied Thermal Engineering,* vol. 126, pp. 518-524, 2017, doi: 10.1016/j.applthermaleng.2017.07.086.

[8] A. Karabanova *et al.*, "Small-Angle Neutron Scattering Characterization of SrCl2-ENG Composites for Thermochemical Heat Storage," *ACS Appl Mater Interfaces,* vol. 13, no. 29, pp. 34213-34226, Jul 28 2021, doi: 10.1021/acsami.1c07449.

Adsorption Cryocooler

Z. Tamainot-Telto[*] and R. Smith

School of Engineering, University of Warwick, Coventry, CV4 7AL, UK

[*]Corresponding author: z.tamainot-telto@warwick.ac.uk

Extended Abstract

The current study is aimed at evaluating the potential of Activated Carbon 208C-Nitrogen pair for cryocooling applications. The initial work consists of elaborating Nitrogen refrigerant (R728) uptakes based to a modified form of the Dubinin-Astakhov (D-A) equation **[1]** and a novel technique to estimate the relevant parameters without experimental tests **[2]**. This technique has the advantage of generating multiple isotherms, when the conventional ASAP 2020 Porosimeter measurements provide only one isotherm at 77 K, therefore more accurate expression of Nitrogen uptake within a large spectrum of operating conditions. Based on Activated Carbon 208C–Ammonia pair characteristic, Activated Carbon 208C–Nitrogen pair Dubinin-Astakhov (D-A) equation is established as:

$$x = x_0 \exp[-k\left(\frac{T}{T_{sat}} - 1\right)^n] \quad \#(1)$$

Where:
x is the Nitrogen concentration (kg Nitrogen/kg Carbon); x_o is the Nitrogen concentration under saturation conditions ($x_o = 0.404$ *kg Nitrogen/kg Carbon*); T is the operating temperature (K); T_{sat} is the saturation temperature corresponding to the gas pressure (K); k is defined as the energetic affinity characteristic of adsorbent-refrigerant pair ($k = 2.2148$); n is the characteristic of adsorbent micro-pores size distributions **[3]** *(n=1.187).*

The Nitrogen uptake, shown in **Figure 1**, is elaborated with the saturation temperature (T_{sat}) ranging from 70 K to 120 K and the driving temperature *(T)* for 120 K to 350 K. Beyond *(T/T_{sat} - 1) = 2*, the uptake of Nitrogen becomes marginal. Furthermore, for any saturation temperature between 70 K and 80 K such as 77 K could have experimentally provided limited data (more likely no data below *(T/T_{sat} - 1) = 0.5)* for better characterisation of Activated Carbon 208C–Nitrogen pair.

The cooling performance have been estimated with fixed condensing and evaporating temperatures to 100 K and 70 K respectively, and the driving temperature ranging from 150 K to 350 K. Both Single Bed and 2-Beds (with heat recovery) are considered. With 2-Beds system, the two reactors operate out of phase. Both reactors are briefly linked between phases (Adsorption/Desorption) till the temperature difference between both beds is 5 K. The methodology used to estimate the cooling performance indicators is detailed in the literature **[4]**. The specific cooling is independent of bed configurations as shown in **Figure 2 (a)**. It increases with the driving temperature and ranges between 5 kJ/kg Carbon to 26 kJ/kg Carbon**.** As expected, the 2-Beds system has higher COP (Coefficient of Performance) compared to 1-bed ones (about 30% better on average) as illustrated in **Figure 2 (b)**. Each system has an optimum value of COP estimated to 0.155 at 193 K and 0.208 at 198 K for 1-bed and 2-Beds respectively: this does not necessarily lead to optimum cooling effect (about 18.2 kJ/kg Carbon for 1-Bed and about 18.2 kJ/kg Carbon for 2-Beds).
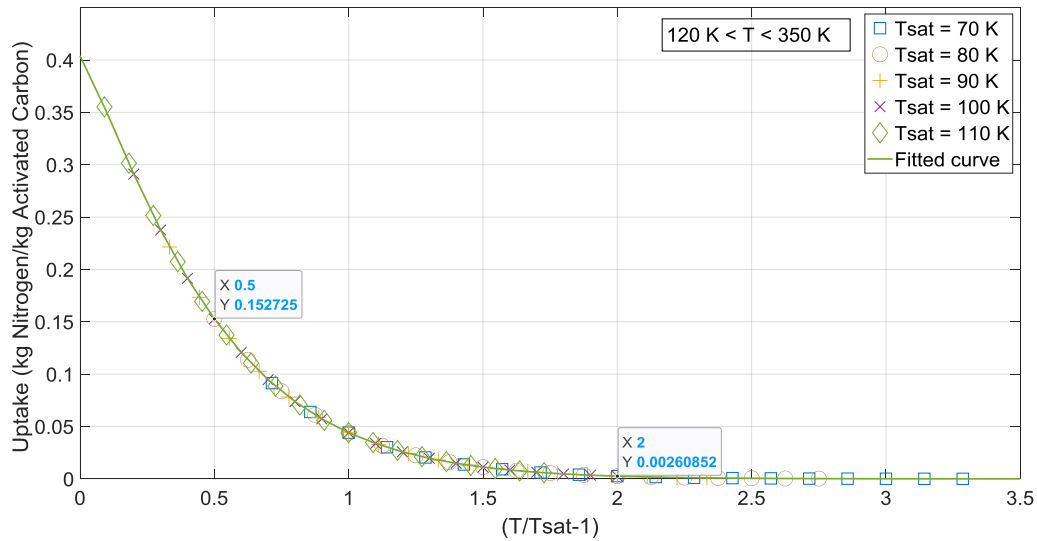
Figure 1: Nitrogen uptake with Activated Carbon 208C
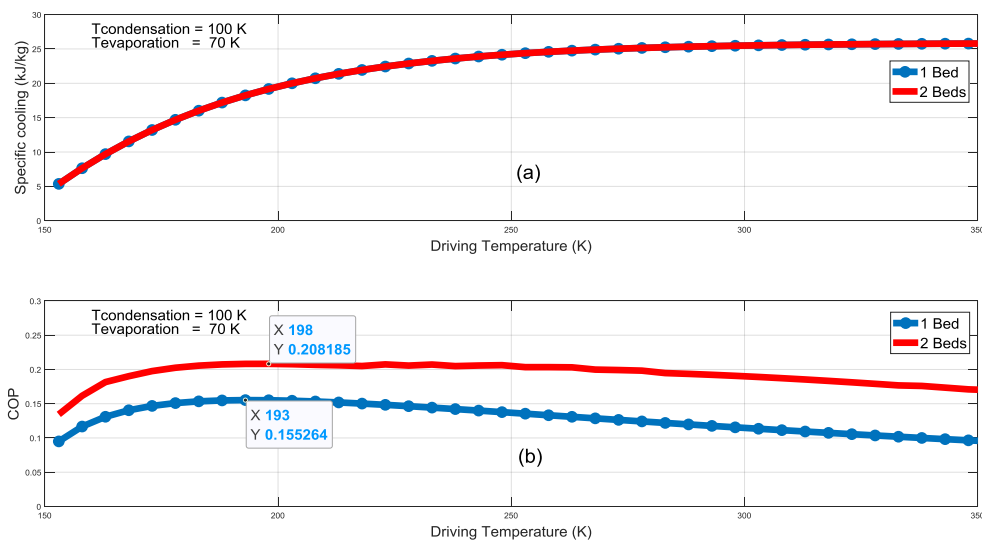
Figure 2: Cooling Performance Indicators – (a) Specific cooling – (b) COP

References:

[1] Z. Tamainot-Telto, Novel method using Dubinin-Astakhov theory in sorption reactor design for refrigeration and heat pump applications, Applied Thermal Engineering, 107, 1123-1129, 2016
[2] R.E. Critoph, Evaluation of alternative refrigerant–adsorbent pairs for refrigeration cycles, Applied Thermal Engineering, 16 (11), 891–900, 1996
[3] R. T. Y. S. G. Chen, Theoretical Basis for the Potential Theory Adsorption Isotherms: the Dubinin-Radushkevich and Dubinin-Astakhov Equations, Langmuir, 10, 4244-4249, 1994
[4] Z. Tamainot-Telto, S.J. Metcalf, R.E. Critoph, Y. Zhong, R.N. Thorpe, Carbon-Ammonia pairs for adsorption refrigeration applications: ice making, air conditioning and heat pumping, International Journal of Refrigeration, 32 (6), pp. 1212-1229, 2009

Preliminary testing and evaluation of two zeolites for integration of a sorption system into industrial tumble dryers

H. Schmit[1*], **A. Velte-Schäfer**[2], **E. Lävemann**[1], **A. Krönauer**[1], **S. Pöllinger**[1], **T. Schubert**[1], **E. Laurenz**[2], **G. Füldner**[2] **and S. Hiebler**[1]

[1]ZAE Bayern, Walther-Meissner-Str. 6, 85748 Garching, Germany

[2]Fraunhofer ISE, Heidenhofstr. 2, 79110 Freiburg, Germany

[*]Corresponding author: henri.schmit@zae-bayern.de

Abstract

Open sorption systems based on the adsorption and desorption of water on zeolites promise energy savings by leveraging either the heat pump effect or the storage effect, or even both. The challenge consists in transferring these potential energy savings to matching applications. An application with high potential are industrial tumble dryers where high humidity and temperature requirements necessitate in-depth material characterisation and testing. It was investigated, if it is possible to acquire equilibrium data with an existing self-built hydrothermal test setup to determine the characteristic curves of zeolites CWK 13XBFK and CWK NaYBFK. The characteristic curve relates the adsorbed water volume to the adsorption potential They were determined for an adsorption potential (ΔF) between $81 \text{ kJ kg}^{-1} \leq \Delta F \leq 2192 \text{ kJ kg}^{-1}$. The obtained characteristic curves are in good agreement with existing ones from other sources. Evaluating CWK 13XBFK and CWK NaYBFK under desorption and adsorption conditions identified for the industrial tumble dryer, similar binding enthalpies of around 180 kJ kg^{-1} and 181 kJ kg^{-1}, respectively, were calculated with the experimentally determined equilibrium data. The equilibrium data also served as input for the method of the characteristic temperature difference. With this method, the driving temperature differences as measures for the potential sorption dynamics in adsorption and desorption under temperature boundary conditions of the application can be assessed. Results show that under the given application conditions, 13XBFK would be the superior choice. Furthermore, preliminary ageing tests were carried out on both zeolites with desorption conditions of 300 °C temperature and 60 °C dew point temperature in a self-built cycling device. After 140 cycles, a decrease of 36.5% in the water uptake of 13XBFK was determined, while the decrease was only 3.3% for NaYBFK. Therefore, these preliminary measurements already allow eliminating 13XBFK as zeolite for application in industrial tumble dryers.

Keywords: Thermal energy storage, Characteristic curve, Characteristic temperature difference, Water sorption

Introduction/Background

Thermal energy storage based on adsorption and desorption of water on adsorbents promises high energy storage densities (ca. 180 kWh m^{-3} on a system level) [1]. Zeolites are well-known adsorbents and those with high water adsorption capacities are potentially interesting for application in thermal energy storage systems [2]. In order to use the high energy storage densities, the selected zeolites have to be a good match for desorption and adsorption conditions of the intended application. Once a matching zeolite is identified, the storage container (packed bed) itself has to be designed and simulated according to the requirements of the application. A good example for the successful integration of a sorption heat storage into a matching application is the dishwasher, developed by Bosch-Siemens-Hausgeräte and

ZAE Bayern. The integration of a sorption heat storage into a dishwasher reduces the thermal energy demand by 30% [3]. Additionally, thermal energy storages become generally economically more viable, the higher the number of cycles [4]. From an economic position, a dishwasher is therefore also a good match for a sorption heat storage.

Industrial tumble dryers with a typical size of 60 to 120 kg are another application where high humidity and high temperatures are a promising match for sorption heat storage with zeolites. Additionally, industrial tumble dryers usually run 12 hours per day with several batches. This makes the integration of a sorption heat storage interesting from an economic position. First estimates yield a reduction of the primary energy demand of around 30%. However, to achieve this reduction, the desorption conditions should be at a temperature of 300 °C and a dew point temperature of 80 °C. Especially the dew point temperature is considerably higher than in the case of the dishwasher. Therefore, in order to find a zeolite that can be used in industrial tumble dryers, extensive material characterisation and testing is needed.

In this work, preliminary tests are carried out on two zeolites to assess them as candidates for the integration in a sorption system in industrial tumble dryers. To evaluate both zeolites on a material level, reliable equilibrium data over a large temperature and dew point temperature range is needed. Therefore, in this work, it is determined if it is possible to acquire the equilibrium data with an existing hydrothermal test setup. With the equilibrium data, it is possible to determine characteristic curves for each zeolite. The characteristic curve relates the adsorbed water volume to the adsorption potential and allows amongst other assessing the binding enthalpy under the boundary conditions given by a specific application. The equilibrium data is furthermore used to apply the method of the characteristic temperature difference to assess the sorption dynamics in adsorption and desorption under application conditions. Additionally, preliminary ageing tests of the zeolites under cycle conditions close to those encountered in the specific application are performed.

Materials and Methods

Materials

Two well-known zeolites with known characteristic curves were selected for preliminary testing and evaluation: 13XBFK and NaYBFK which are both from Chemiewerk Bad Köstritz GmbH (CWK). The two zeolites, although pelletised, are so-called "binderless" or "binder-free", since the binder itself acts as active zeolite.

Determination of the equilibrium data and characteristic curves

At ZAE Bayern, a multiple sample setup was built to test the hydrothermal stability of adsorbents [5]. The setup, shown in Figure 1, has four temperature-controlled sample blocks, each containing four sample containers. Four sample containers of each sample block are connected orthogonally to each other and to one of four temperature-controlled water reservoirs. With this configuration, samples can be exposed to a total of 16 different conditions of temperature and water vapour pressure by setting four different temperatures and four different dew point temperatures. Thereby, the temperature range of each sample block is between 30 °C and 350 °C, while that of each water reservoir is between 5 °C and 70 °C. Due to the large temperature and dew point temperature range, the hydrothermal test setup has potential to acquire the equilibrium data to investigate the zeolites on a material level.
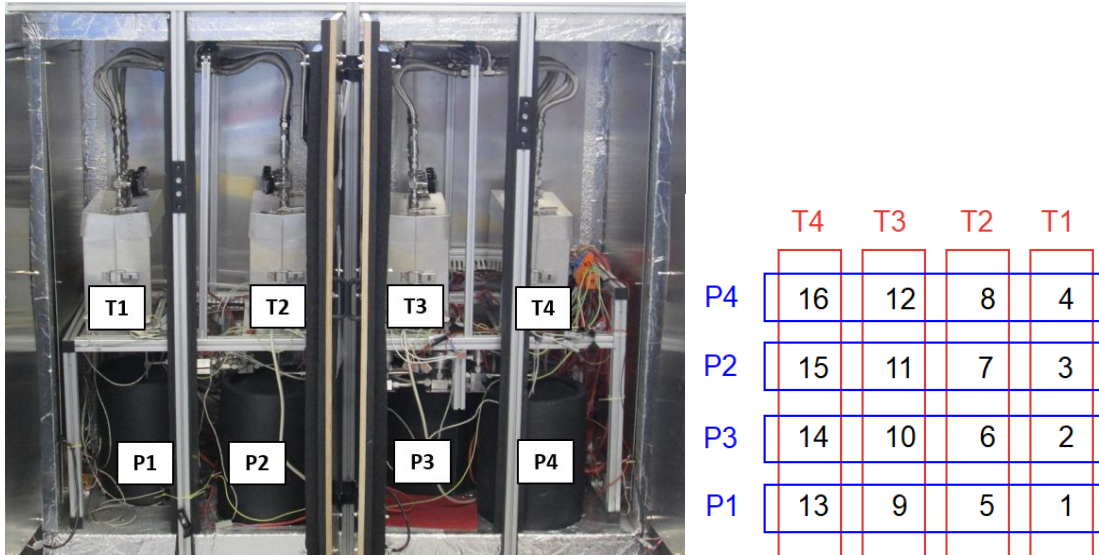
Figure 1. The picture on the left hand side shows the temperature-controlled cabinet of the hydrothermal test setup with four temperature-controlled water reservoirs (P1 to P4) and four sample blocks (T1 to T4). The schematic on the right hand side shows the orthogonal interconnection of the water reservoirs and sample blocks, through which it is possible to subject the samples to 16 different hydrothermal conditions [5].

A measuring procedure starts with introducing around 3 g of a sample into each of the 16 sample containers. The samples are then placed into the sample blocks and gradually dried for around 20 hours at temperatures up to 350 °C under constant evacuation. To determine the dry sample masses, the manual valve on top of each sample container is first closed. Subsequently, the samples are removed from the sample blocks. They are weighted manually after a cooling period at room temperature. The measured equilibrium data necessary for the construction of the characteristic curve is subsequently determined in adsorption. Technically, it is feasible to determine 16 data points in one measurement run. However, in practice, it has proven advantageous to determine eight data points in one measurement run. Thereby, each data point consists of the arithmetic mean value of the results obtained for two samples. Hence, the data points become more reliable and outliers can be identified more easily, while the downside is a longer measurement time. In three measurement runs, 24 data points are determined in adsorption. Before each measurement, the samples are dried under the aforementioned conditions.

For both zeolites, dew point temperatures T_p were varied between 25 °C and 34 °C for the three measurement runs in adsorption. In the same three measurement runs, the temperatures, T, were varied between 43 °C and 315 °C.

Each data point obtained from the measured equilibrium data consists of a temperature T, a dew point temperature T_p and an adsorbed water mass X_{ads}. The necessary quantities for the characteristic curve are then calculated with the equations provided e.g. by Hauer [7]. The adsorption potential ΔF is calculated for each data point based on the measured temperature and dew point temperature. The adsorbed water volume W_{ads} for each data point is calculated based on the experimentally determined adsorbed water mass X_{ads} and a temperature dependent function for the density [7]. Subsequently, the fit from equation (1), proposed by Fischer [2], was used to obtain the characteristic curves based on the 24 data points for each zeolite.

$$W_{ads} = \frac{a + c \cdot \Delta F + e \cdot \Delta F^2 + g \cdot \Delta F^3}{1 + b \cdot \Delta F + d \cdot \Delta F^2 + f \cdot \Delta F^3} \tag{1}$$

Evaluation of the equilibrium data

The equilibrium data collected with the hydrothermal test setup and the determined characteristic curves allow to evaluate both zeolites under application conditions. The heat of adsorption that can be expected under application conditions is composed of the binding enthalpy and enthalpy of evaporation/condensation. In contrast to the enthalpy of evaporation, the binding enthalpy is a material property, and it can be determined with the characteristic curve of a zeolite.

Knowing the adsorption and desorption temperatures and dew point temperatures, the corresponding adsorption potentials can be calculated. On the left hand side of Figure 2, a schematic representation of a characteristic curve is given. Exemplary adsorption potentials during adsorption ΔF_{ads} and desorption ΔF_{des} are indicated on the characteristic curve.
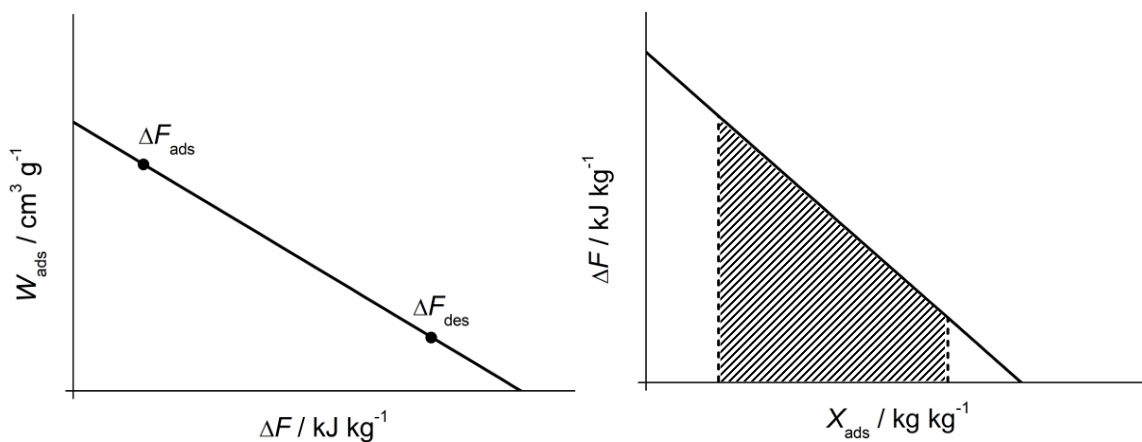
Figure 2. Left hand side: schematic characteristic curve with two exemplary adsorption potentials during adsorption ΔF_{ads} and desorption ΔF_{des} indicated on the curve. Right hand side: schematic representation of the adsorption potential ΔF as a function of the adsorbed water mass X_{ads}. The hatched area under the curve corresponds to the binding enthalpy encountered under application conditions.

With the known characteristic curve, it is possible to determine the binding enthalpy of a zeolite under application conditions. Therefore, the characteristic curve has to be transformed into a representation of the adsorption potential as a function of the adsorbed water mass X_{ads}. If no experimental data is available for X_{ads}, W_{ads} can be converted into X_{ads} using a mean density of the water at temperatures encountered in the potential application. A schematic of ΔF as a function of X_{ads} is shown on the right hand side in Figure 2. The adsorption and desorption conditions of the potential application set the limits for the area under the curve on the right hand side in Figure 2. The integrated area under the curve corresponds to the binding enthalpy.

A further analysis of the equilibrium data can be carried out by using the characteristic temperature difference ΔT_{ch}. The analysis of the characteristic temperature difference allows for a quick evaluation of loading spread and driving temperature differences for a given set of temperatures that are defined out of the targeted application. As an 'easy to use' representation of the equilibrium data it can help to build a bridge between material science and application without converting temperature and pressure into ΔF. The characteristic temperature difference ΔT_{ch} is defined in equation (2) [8]. The characteristic temperature difference is the difference between the measured equilibrium temperature $T_{\text{eqi}}(X,p)$ and the measured dew point temperature T_{p}.

$$\Delta T_{ch} = T_{eqi}(X, p) - T_p \qquad (2)$$

To define the application boundary conditions in terms of characteristic temperature difference the temperature lift ΔT_{lft} and the temperature thrust ΔT_{thr} are defined in equation (3) and (4), respectively.

$$\Delta T_{lft} = T_{ads} - T_{p,ads} \qquad (3)$$

$$\Delta T_{thr} = T_{des} - T_{p,des} \qquad (4)$$

Cycling stability

In order to assess the cycling stability of solid sorbents under application conditions, a cycling device was constructed and built at ZAE Bayern. It basically consists of an air circuit with a humidifier and a suitable air heater to set the intended test conditions. The insulated column containing the 8 sample containers is shown in Figure 3. The dry sample masses typically range from around 50 g to 90 g.

It was mentioned before, that the desorption conditions in the industrial tumble dryer setting are projected to be 300 °C temperature at a dew point temperature of 80 °C. These conditions, especially the dew point temperature, are likely to put a high hydrothermal stress on the zeolites. Additonally, this dew point temperature is at the upper limit of the cycling device. Therefore, a preliminary cycling test was designed with desorption at 300 °C and a reduced dew point temperature of 60 °C. The adsorption conditions were a temperature of 42.5 °C and a dew point temperature of 20 °C (and, thus, also lower then the projected adsorption conditions). A whole cycle consisting of desorption and adsorption takes around two hours. So far, 140 cycles were carried out on both zeolites, CWK 13XBFK and CWK NaYBFK.

The ageing of the samples was regularly checked by running reference cycles. Therefore, a reference desorption with a temperature of 300 °C and a dew point temperature of 12 °C was performed for around 16 hours. The reference adsorption takes place at a temperature of 40 °C and a dew point temperature of 24.8 °C. After each reference adsorption and reference desorption run, the sample containers are removed from the cycling device, covered with lids, and weighted manually after cooling at room temperature.
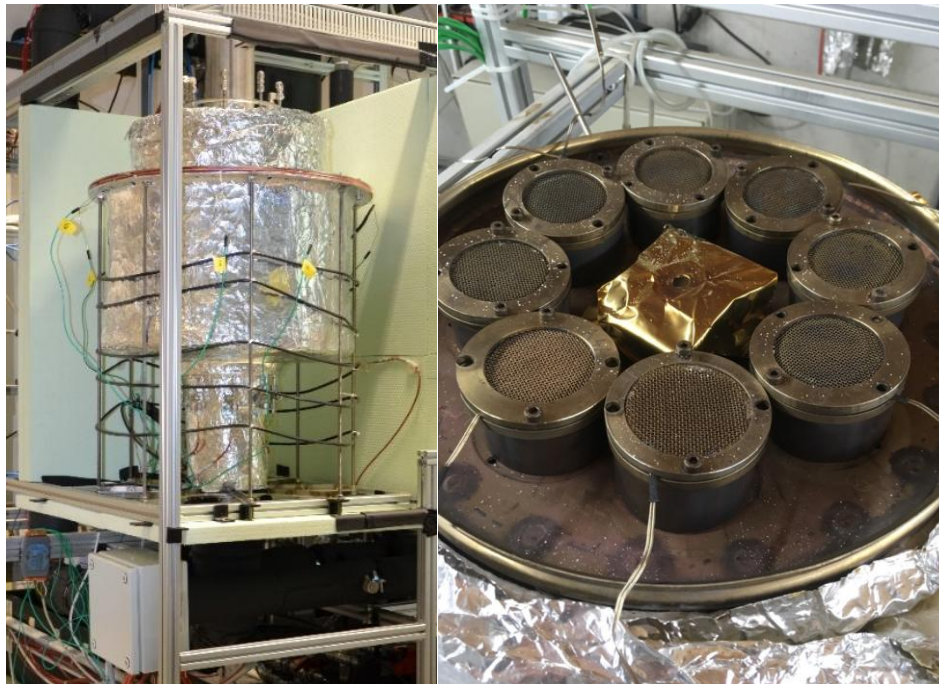
Figure 3. View of the insulated column of the cycling device containing 8 sample containers.

Discussion and Results

Determination of the equilibrium data and characteristic curves

The equilibrium data was successfully acquired for both CWK 13XBFK and CWK NaYBFK over the intended temperature and dew point temperature range. Based on the equilibrium data, the adsorption potential ΔF and adsorbed water volume W_{ads} were calculated for each data point in order to obtain the characteristic curves of the two zeolites.

The mean adsorption volumes $W_{ads,mean}$ of 13XBFK as a function of the adsorption potential ΔF are shown on the left hand side in Figure 4. Since the calculated standard deviations are small (maximum 0.002 cm^3 g^{-1}) compared to the absolute values of $W_{ads,mean}$, they are not visible. The small standard deviations show a good agreement between the two different samples exposed to the same conditions.
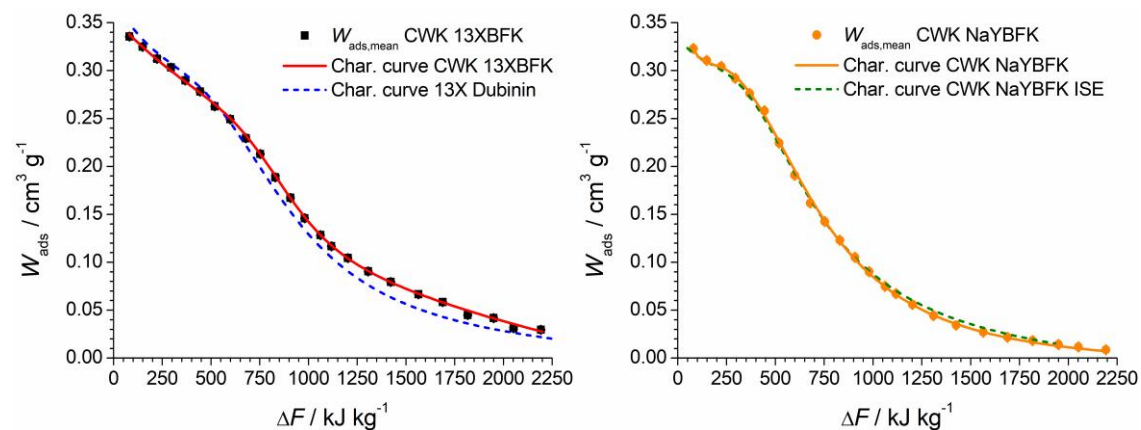
Figure 4. Left hand side: experimentally determined mean adsorption volumes, $W_{ads,mean}$, for CWK 13XBFK (black squares). The characteristic curve fitted to this data is shown as red line. The blue dotted

line is the characteristic curve of 13X based on experimental data from Dubinin ([2][6]). Right hand side: $W_{ads,mean}$ for CWK NaYBFK (orange circles) obtained with the setup presented here. The characteristic curve fitted to this data is shown as orange line. The green dotted line shows the characteristic curve of CWK NaYBFK based on unpublished experimental data from the Fraunhofer ISE.

The characteristic curve of CWK 13XBFK is represented by the fit (red line) through the points representing the adsorption volumes in Figure 4. It is valid for an adsorption potential between 81 kJ kg^{-1} ≤ ΔF ≤ 2192 kJ kg^{-1} and an adsorbed water volume between 0.030 cm^3 g^{-1} ≤ W_{ads} ≤ 0.336 cm^3 g^{-1}. The parameters with 4 significant digits, used to construct the characteristic curve of 13XBFK in Figure 4, are listed in Table 1.

The characteristic curve of 13XBFK determined with the hydrothermal test setup is thereby in good agreement with the characteristic curve of 13X (blue dashed line) based on experimental data from Dubinin ([2][6]). It has to be noted, that the 13X measured by Dubinin was likely not formed into pellets, but instead in form of powder. A comparison with the CWK 13XBFK is thus meaningful, since the 13XBFK, as mentioned before, is a binderless zeolite. Hence, it can be expected, that its adsorption capacity is nearer to a 13X powder than to 13X as pellets containing a non-active binder.

Table 1. Parameters with 4 significant digits for equation (1) to obtain the characteristic curves of CWK 13XBFK and CWK NaYBFK.

Parameter	CWK 13XBFK	CWK NaYBFK
a	0.3550	8.590
b	$-1.467 \cdot 10^{-3}$	1.734
c	$-7.444 \cdot 10^{-4}$	0.4093
d	$2.992 \cdot 10^{-7}$	$-2.393 \cdot 10^{-3}$
e	$5.730 \cdot 10^{-7}$	$-5.323 \cdot 10^{-5}$
f	$5.739 \cdot 10^{-10}$	$4.554 \cdot 10^{-6}$
g	$-1.262 \cdot 10^{-10}$	$-3.395 \cdot 10^{-8}$

On the right hand side of Figure 4, $W_{ads,mean}$ determined for CWK NaYBFK is plotted as a function of the adsorption potential. Again, the standard deviations are small (maximum 0.001 cm^3 g^{-1}) compared to the absolute values of $W_{ads,mean}$. The characteristic curve of NaYBFK is represented by the fit (orange line) through the adsorption volumes in Figure 4. It is valid for an adsorption potential between 81 kJ kg^{-1} ≤ ΔF ≤ 2192 kJ kg^{-1} and an adsorbed water volume between 0.009 cm^3 g^{-1} ≤ W_{ads} ≤ 0.323 cm^3 g^{-1}. The parameters with 4 significant digits, used to construct the characteristic curve of NaYBFK in Figure 4, are listed in Table 1. The green dashed line in Figure 4 represents the characteristic curve of CWK NaYBFK based on unpublished experimental data from the Fraunhofer ISE. The agreement between both characteristic curves is very good.

From the above results, it can be concluded, that the determination of the equilibrium data and the characteristic curves with the existing hydrothermal test setup was successful for the two investigated zeolites CWK 13XBFK and CWK NaYBFK. It can thus be used in the future to

reliably determine the characteristic curves of further zeolites and potentially of other adsorbents.

<u>Evaluation of the equilibrium data</u>

The heat of adsorption that can be expected under application conditions is composed of the binding enthalpy and enthalpy of evaporation/condensation. The binding enthalpy can be determined with the characteristic curve of a zeolite, if the hydrothermal operationg conditions are known. In the case of industrial tumble dryers, the desorption is planned to take place at a temperature of 300 °C and a dew point temperature of 80 °C. These temperatures correspond to an adsorption potential ΔF of 1376 kJ kg^{-1}. The adsorption could take place at a temperature of 60 °C and a dew point temperature of 30 °C, corresponding to a ΔF of 238 kJ kg^{-1}. Both of these adsorption potentials are visualised on the characteristic curve of CWK NaYBFK on the left hand side of Figure 5.
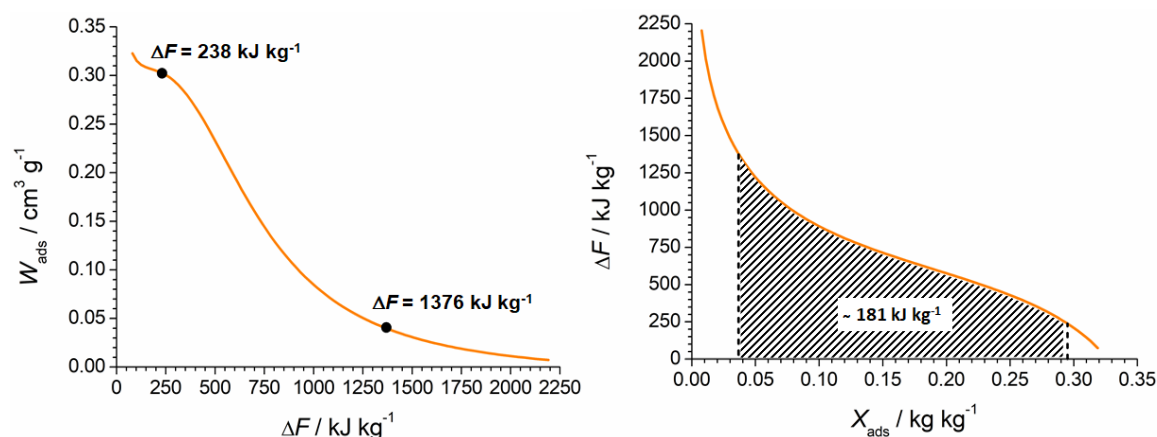
Figure 5. Left hand side: characteristic curve of CWK NaYBFK with the adsorption potential indicated for adsorption ($T = 60$ °C, $T_p = 30$ °C) and desorption conditions ($T = 300$ °C, $T_p = 80$ °C). Right hand side: adsorption potential ΔF in function of the experimentally determined adsorbed water mass X_{ads}, indicated in kg water per kg of adsorbent (NaYBFK).

With the characteristic curve of NaYBFK from Figure 5 and the operation conditions during desorption and adsorption, the binding enthalpy can be calculated. Therefore, the adsorption potential is needed as a function of the adsorbed water mass X_{ads}. Since X_{ads} was determined experimentally in this work, this representation is straightforward. If, however, only a characteristic curve is available the adsorbed water volume has to be converted into an adsorbed water mass, using a mean density of the water at temperatures encountered in the potential application.

The desorption and adsorption under application conditions set the limits for the area under the curve on the right hand side in Figure 5. The integration of this area yields a binding enthalpy of around 181 kJ kg^{-1} for CWK NaYBFK. The same procedure yields 180 kJ kg^{-1} for CWK 13XBFK. The binding enthalpy of both zeolites is therefore similar, and does not allow to favour one zeolite over the other.

A further comparison of both zeolites is performed with the method of the characteristic temperature difference. To assess the characteristic temperature differences of CWK NaYBFK and CWK 13XBFK, the temperature difference given by equation (2) is plotted as a function of the loading for each zeolite in Figure 6.
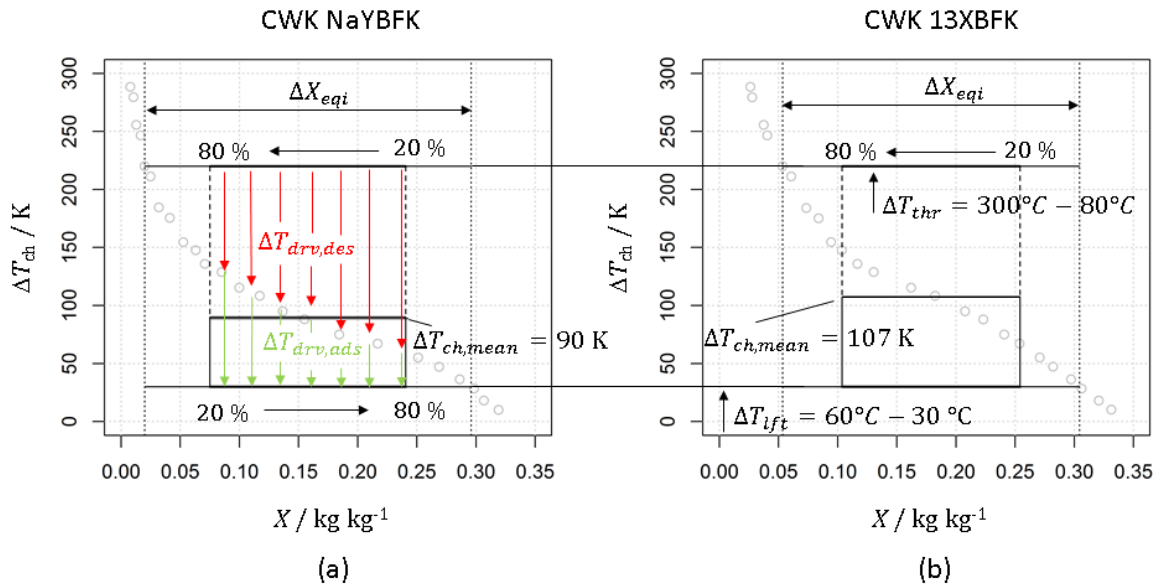
Figure 6. Characteristic temperature difference ΔT_{ch} of CWK NaYBFK (a) and CWK 13XBFK (b). Temperature lift ΔT_{lft} and temperature thrust ΔT_{thr} (horizontal lines) define the lower and the upper boundary of the application window. The equilibrium loading spread ΔX_{eqi} is additionally shown.

The temperature lift and temperature thrust are represented by the two horizontal lines marked with ΔT_{lft} and ΔT_{thr} in Figure 6. At the intersection points of ΔT_{lft} and ΔT_{thr} with ΔT_{ch} two vertical lines are drawn resulting in the equilibrium loading spread ΔX_{eqi}, similar to the bounds of the highlighted area on the right hand side in Figure 5. In a real-world application with finite mass flow rates within the packed bed and finite cycle times a loading spread $\Delta X < \Delta X_{eqi}$ will be achieved. In the following, it is assumed that the loading in the application is in the range between 20 % and 80 % of the equilibrium loading spread as illustrated in Figure 6. With this assumption first estimates regarding the driving temperature differences in the adsorption and desorption half cycle can be gained. The mean characteristic temperature difference $\Delta T_{ch,mean}$ in the investigated range is slightly lower for CWK NaYBFK (90 K) than for CWK 13XBFK (107 K). Together with the heat and mass transfer resistances, the driving temperature differences determine the dynamics of the process [8][9], i.e. the higher the driving temperature differences, the higher the heat flow rate. In the example shown in Figure 6 (a), the mean driving temperature difference in the adsorption half cycle is $\Delta T_{drv,ads} = 90\text{ K} - 30\text{ K} = 60\text{ K}$ and in the desorption half cycle $\Delta T_{drv,des} = 220\text{ K} - 90\text{ K} = 130\text{ K}$. This indicates that desorption will be nearly two times faster than adsorption if the heat and mass transfer resistances are similar in both phases.

These figures also allow to evaluate the two materials CWK NaYBFK and CWK 13XBFK as listed in Table 2.

Table 2. Evaluation of driving temperature differences $\Delta T_{drv,ads}$, $\Delta T_{drv,des}$ and equilibrium loading spread ΔX_{eqi} achievable in an application with $T_{des} = 300\text{ °C}$, $T_{p,des} = 80\text{ °C}$ and $T_{ads} = 60\text{ °C}$, $T_{p,ads} = 30\text{ °C}$ for the two zeolites CWK NaYBFK and CWK 13XBFK.

	CWK NaYBFK	CWK 13XBFK
ΔX_{eqi} / kg kg^{-1}	0.27	0.25
$\Delta T_{drv,ads}$ / K	60	77

$\Delta T_{\text{drv,des}}$ / K	130	113

This evaluation shows that CWK NaYBFK has a slight advantage regarding the achievable equilibrium loading spread. However, since the driving temperature difference of CWK NaYBFK in the adsorption half cycle is lower than it is for CWK 13XBFK, in case of CWK NaYBFK more than 20% more material and thus, a larger heat exchanger are needed to achieve the same thermal power output. Based on this analysis, CWK 13XBFK would be sthe uperior choice for the temperature boundary conditions defined in this study.

Cycling stability

The results obtained for the cycling stability of CWK 13XBFK and NaYBFK are visualised in Figure 7.
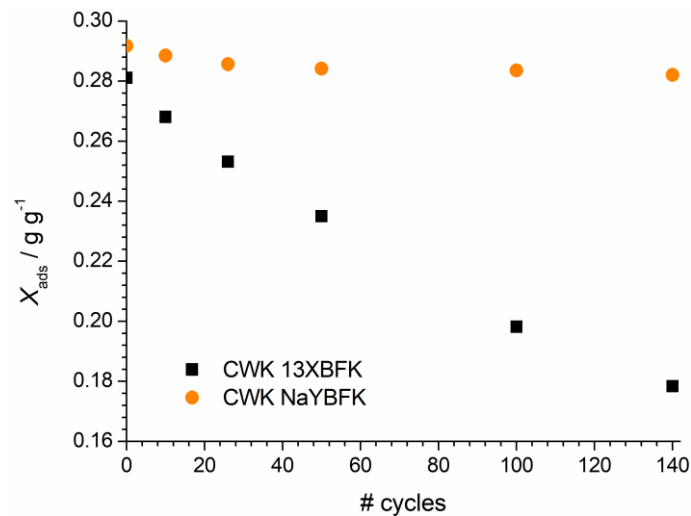
Figure 7. Trend of the absorbed water mass X_{ads} for the reference adsorption of CWK 13XBFK (black squares) and CWK NaYBFK (orange circles) in function of the number of cycles (# cycles).

For 13XBFK, an initially adsorbed water mass of 0.281 g g^{-1} (with regard to the dry mass of the zeolite) was determined. Already after 10 cycles, the adsorbed water mass decreased by 4.6%. With increasing number of cycles, a steady decrease in the adsorbed water mass can be seen in Figure 7. After cycle 140, the decrease was 36,5%. This shows, that already with a lower dew point of 60 °C instead of 80 °C, CWK 13XBFK cannot be used as zeolite in industrial tumble dryers.

The second zeolite, CWK NaYBFK has an initial adsorbed water mass of 0.292 g g^{-1}. After ten cycles, the adsorbed water mass decreased by 1.1 %. The trend of the adsorbed water mass with the number of cycles in Figure 7 shows a decrease up to cycle 140. After 140 cycles, the decrease is 3.3% and thus considerably lower than in the case of CWK 13XBFK. Additionally, the slope of the decrease in the adsorbed water mass decreases with increasing number of cycles. Therefore, it remains to be seen, if after further cycles, the decrease stabilises itself, meaning that the ageing of NaYBFK has reached a steady state and will not go on further. The preliminary cycle tests on CWK NaYBFK show that it should be further tested under the higher dewpoint temperature of 80 °C to assess its potential use in a sorption system in industrial tumble dryers.

Conclusions and Outlook

Open sorption systems based on the adsorption and desorption of water on zeolites promise energy savings by leveraging either the heat pump effect or the storage effect, or even both. The challenge consists in transferring these potential energy savings to matching applications. After the successful integration of a sorption system into commercial dishwashers, the ZAE Bayern is currently investigating the integration of a sorption system into industrial tumble dryers. Besides the high humidity and temperatures attractive for sorption heat storage, the high number of cycles per year make industrial tumble dryers also an economically interesting application.

The two zeolites CWK 13XBFK and CWK NaYBFK were investigated to assess their potential use in a sorption system for industrial tumble dryers. The evaluation on a material level requires equilibrium data over a large temperature and dew point temperature range. Therefore, equilibrium measurements were performed with an existing self-built hydrothermal test setup to check if it can be used to reliably determine the required equilibrium data. Equilibrium data for both zeolites was determined over a temperature range from 43 °C to 315 °C and a dew point temperature range from 25 °C to 34 °C.

With the acquired equilibrium data, characteristic curves were determined for both zeolites. The characteristic curve allows amongst others assessing the binding enthalpy under the boundary conditions given by a specific application. For the two zeolites, characteristic curves were determined for an adsorption potential (ΔF) between 81 kJ kg^{-1} ≤ ΔF ≤ 2192 kJ kg^{-1}. The determined characteristic curve for 13XBFK is valid for an adsorbed water volume (W_{ads}) between 0.030 cm^3 g^{-1} ≤ W_{ads} ≤ 0.336 cm^3 g^{-1}. For NaYBFK the validity is between 0.009 cm^3 g^{-1} ≤ W_{ads} ≤ 0.323 cm^3 g^{-1}. The obtained characteristic curves are in good agreement with existing ones from other sources. These results show, that the hydrothermal test setup can be used to reliably measure the equilibrium data to determine characteristic curves of zeolites.

Evaluating CWK 13XBFK and CWK NaYBFK under desorption and adsorption conditions identified for industrial tumble dryers, binding enthalpies of around 180 kJ kg^{-1} and 181 kJ kg^{-1}, respectively, were calculated with the experimentally determined equilibrium data. These similar values for the binding enthalpies of the two zeolites do not allow to favour one zeolite over the other.

The characteristic temperature difference for the investigated cycle conditions is around 107 K for CWK 13XBFK and around 90 K for CWK NaYBFK. Further analysis shows that CWK NaYBFK has a slight advantage regarding the achievable equilibrium loading spread. However, the driving temperature difference of CWK NaYBFK in the adsorption half cycle is lower than for CWK 13XBFK. This means that for CWK NaYBFK more than 20% more material and thus, a larger packed bed are needed to achieve the same thermal power output. Based on this analysis, CWK 13XBFK would be the superior choice for the temperature boundary conditions defined in this study.

Both, the estimation of the binding enthalpy and the evaluation of the characteristic temperature difference are preliminary tools to evaluate both zeolites under the boundary conditions of the application. Thus, a first assessment is possible using only the experimentally determined equilibrium data. However, the used adsorption and desorption conditions are static, while in the application, dynamic conditions are encountered. The dynamic water sorption process and the dimensioning of the sorption system will therefore be assessed with a packed bed simulation. The packed bed simulation uses amongst others the determined characteristic curves as input. The resulting time-resolved temperature breakthrough curves will be verified experimentally.

The planned desorption conditions are 300 °C and 80 °C. Preliminary ageing tests were carried out on both zeolites with desorption conditions of 300 °C temperature and 60 °C dew point temperature in a self-built cycling device. After 140 cycles, a decrease of 36.5% in the water uptake of 13XBFK was determined, while the decrease was only 3.3% for NaYBFK. Therefore, these preliminary measurements already allow eliminating 13XBFK as zeolite for application in industrial tumble dryers. NaYBFK, however, will be further cycled under harsher conditions to determine if it can be used in a sorption system for industrial tumble dryers. Furthermore, additional candidate zeolites will be tested.

Acknowledgments

References:

[1] Lävemann, E. et al., *Mobile Sorptionsspeicher zur industriellen Abwärmenutzung Grundlagen und Demonstrationsanlage – MobS II*, FKZ 0327383B, TIB Hannover, 2015.

[2] Fischer, F., *Hydrothermale Stabilität von 13X-Zeolithen: Experimentelle Untersuchung und Modellierung*, PhD thesis, TU München, 2018.

[3] Hauer, A., Fischer, F., "Open adsorption system for an energy efficient dishwasher", Chemie Ingenieur Technik, 2011.

[4] Rathgeber, C., Lävemann, E., Hauer, A., „Economic top-down evaluation of the costs of energy storages- A simple economic truth in two equations, Journal of Energy Storage, 2015.

[5] Fischer, F., Lävemann, E., "Multiple sample setup for testing the hydrothermal stability of adsorbents in thermal energy storage applications", Measurement Science and Technology, 2015.

[6] Dubinin, M. M., Adsoprtion in micropores, Journal of Colloid and Interface Science, 1967.

[7] Hauer, A., *Beurteilung fester Adsorbentien in offenen Sorptionssystemen für energetische Anwendungen*, PhD thesis, TU Berlin, 2022.

[8] Laurenz, E., *Frequency response analysis of heat and mass transfer in adsorbent composites and simplified performance estimation for heat transformation applications*, PhD thesis, TU Hamburg, 2021.

[9] Velte, A. et al., Adsorption dynamics and hydrothermal stability of MOFs Aluminium Fumarate, Mil-160(Al), and Cau-10-H, and Zeotype Tiapso for heat transformation applications, http://dx.doi.org/10.2139/ssrn.4230996 (last accessed 14th February 2023).

A benchmark study of supervised learning methods for predicting the live steam production of thermal power plants

G. Prokhorskii[1,2,3*]**, E. Eder**[1,2]**, S. Rudra**[3]**, M. Preißinger**[1,2]

[1]illwerke vkw Endowed Professorship for Energy Efficiency, Research Center Energy,
Vorarlberg University of Applied Sciences, Hochschulstraße 1, 6850 Dornbirn, Austria

[2]Josef Ressel Centre for Intelligent Thermal Energy Systems,
Vorarlberg University of Applied Sciences, Hochschulstraße 1, 6850 Dornbirn, Austria

[3]University of Agder, Jon Lilletuns vei 9, 4879 Grimstad, Norway

*Corresponding author: gleb.prokhorskii@fhv.at

Abstract

Power plant operators increasingly rely on predictive models to diagnose and monitor their systems. Data-driven prediction models are generally simple and can have high precision, making them superior to physics-based or knowledge-based models, especially for complex systems like thermal power plants. However, the accuracy of data-driven predictions depends on (1) the quality of the dataset, (2) a suitable selection of sensor signals, and (3) an appropriate selection of the training period. In some instances, redundancies and irrelevant sensors may even reduce the prediction quality.

We investigate ideal configurations for predicting the live steam production of a solid fuel-burning thermal power plant in the pulp and paper industry for different modes of operation. To this end, we benchmark four machine learning algorithms on two feature sets and two training sets to predict steam production. Our results indicate that with the best possible configuration, a coefficient of determination of $R^2 = 0.95$ and a mean absolute error of $MAE = 1.2$ t/h with an average steam production of 35.1 t/h is reached. On average, using a dynamic dataset for training lowers MAE by 32 % compared to a static dataset for training. A feature set based on expert knowledge lowers MAE by an additional 32 %, compared to a simple feature set representing the fuel inputs. We can conclude that based on the static training set and the basic feature set, machine learning algorithms can identify long-term changes. When using a dynamic dataset the performance parameters of thermal power plants are predicted with high accuracy and allow for detecting short-term problems.

Keywords: Thermal power plant, Live steam prediction, Supervised learning, Monitoring system, Predictive maintenance

Nomenclature

Acronyms

ANN	Artificial neural network
DD	Data-driven
KB	Knowledge-based
KNN	K-nearest neighbors
ML	Machine learning
MLP	Multilayer perceptron
PB	Physics-based
PM	Predictive maintenance
RFR	Random forest regressor

Symbols

α	Regularization parameter $(-)$
$\hat{y}$	Predicted value (t/h)
$\overline{y}$	Arithmetic mean of value (t/h)
n	amount $(-)$
R^2	Coefficient of determination $(-)$
t_{calc}	Calculation Time (s)
y	Value (t/h)
MAE	Mean absolute error (t/h)

Subscripts

l	Layers
max	Maximum
min	Minimum
n	Neighbors
t	Trees

Introduction

The complexity of thermal power plants inevitably leads to downtime, which cannot be completely avoided by maintenance at predefined intervals or based on conditions. Predictive maintenance could be a solution and needs to be investigated more for thermal power plants [1]. The term "predictive maintenance" (PM) consists of the two words "predictive" and "maintenance", which implies that accurate predictions are the foundation of appropriate PM. For thermal power plants, high-accuracy predictions of performance parameters are of particular interest. For such predictions, appropriate models are necessary.

Three general methods to model systems like thermal power plants exists [2]: data-driven (DD), knowledge-based (KB), and physics-based (PB). KB predictions depend on knowledge from operational personnel, and this knowledge is usually not centralized. Shift changes and retirements often lead to the loss of information. Physical or mathematical approaches have limited validity for modeling complex systems, resulting in a high computational effort. On the other hand, DD methods based on machine learning (ML) are ideal for thermal power plant modeling. Predictions based on ML are powerful tools for the operator to detect specific issues and identify the involved equipment in this process. In literature, DD methods are the most used ones either as standalone or in combination with other methods [1].

Performance predictions are generally more meaningful when they are based on actual data. We use the data of a project partner who builds thermal power plants and is interested in a prediction model, which is efficient, accurate, and has a low computational demand. To fulfill such a task, the dataset in use should be consistent, complete, and easy to process. Performance parameters of thermal power plants can then be predicted by means of regression. Regression is commonly understood as the prediction of a continuous target value using attributes or features. It has plenty of real-world applications. However, the performance of the regression methods strongly depends on (1) the feature set, (2) the selected training period, and (3) the algorithm and its working principle.

Khalid et al. [3] developed an optimal sensor selection approach based on ML, however, it just works when normal and abnormal behavior is labeled, and feature selection becomes simple. In the case of unknown labels, expert knowledge, and feature selection must be applied based on the whole dataset. Thota and Syed [4] analyzed different data-driven feature selection methods for predicting boiler efficiency and discovered that dimensionality reduction can improve the model accuracy and that ensemble learning techniques such as random forest classifiers are more robust than other methods. Hundi and Shahsavari [5] compared several supervised and unsupervised learning algorithms such as linear regression, multilayer perceptron (MLP), support vector machine, random forest regressor (RFR), and elliptic envelope for health monitoring of power plants. Their results represent the applicability of ML for health monitoring. Gu et al. [6] investigated a safety assessment of thermal power plants based on 120 Management Systems Safety Assessment of Thermal Power plants records using different ML algorithms. Ismail et al. [7] deployed an early prediction of boiler tube leak trip using an intelligent monitoring system. In this study, two models use artificial neural networks (ANNs) and hybrid techniques to predict tube leakage based on real value prediction. Allen et al. [8] showed the difference between supervised, semi-supervised, and unsupervised ML algorithms in the field of anomaly detection. Additionally, their investigations revealed the necessity of checking training data when the model fails, checking for physical changes to the machinery and non-standard configurations. Mohd Nistah et al. [9] investigated the implementation of an ANN for fault detection to help operators to identify and narrow down the operational boiler parameters that cause the fault quickly. Although, all of these papers show the use of ML techniques for anomaly detection, the results are closely related to real-time value prediction.

However, hardly any literature exists on prediction models for thermal power plants. In a comprehensive work, Tufekci at al. [10] investigated different ML algorithms to predict the power output of two gas turbines and a steam turbine in a combined cycle power plant. The author used ambient conditions and the steam turbine vacuum to show dependencies between the features and the power output. Based on these features, the power output was predicted for the nominal load. In contrast, our project partner has large variations in the steam output, and we aim to predict the live steam for various loads with high accuracy. In the second paper to consider here, the authors created a k-nearest neighbors (KNN) prediction model on power plant data to predict the temperature and differential pressure of a coal mill [11]. Their model shows good accuracy but doesn't allow for extrapolation to unknown states.

We state that the gap in literature is generic recommendations on algorithms, feature handling, and appropriate training periods for predicting performance parameters in thermal power plants. In our research, we intend to address this lack. We benchmark several ML algorithms on actual power plant data to (1) detect and predict short- and long-term changes in the power plant operational behavior, and (2) investigate the sensitivity of our predictions to different settings with respect to (a) the hyperparameters of the algorithms, (b) the feature set, and (c) the training set.

Methods

Steam power plant description

A detailed schematic of the investigated thermal power plant is given in Fig. 1.
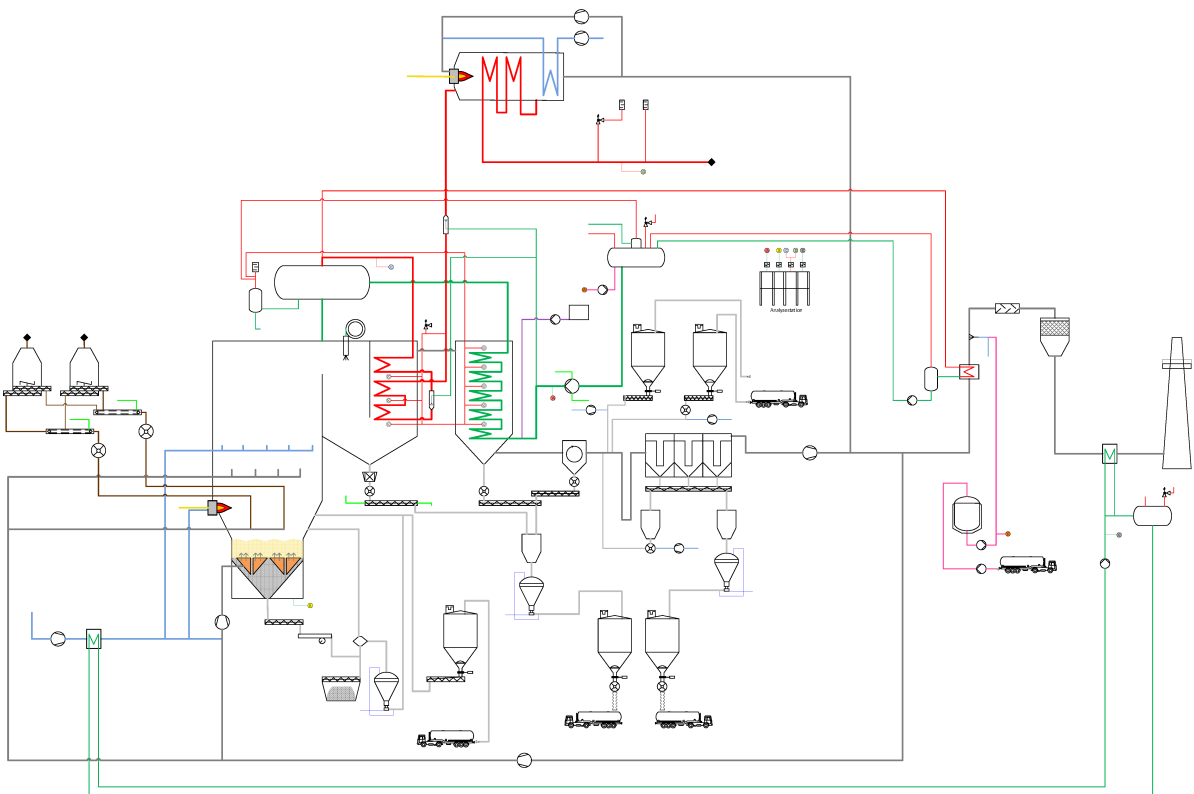
Figure 1. Scheme of the power plant with auxiliary equipment

The steam power plant investigated includes a water treatment system, a deaerator, a boiler with superheaters, and an external superheater on the water side. The fuel side contains solid fuel storages, transporters, feeders, and gas lines with gas burners. Finally, the air side includes heaters, ash removers, air purifiers, and a flue-gas stack. The boiler unit has several

**Heat Powered Cycles
Conference 2023**
Edinburgh

Heat in the new energy system

*3rd to 6th of September 2023
The University of Edinburgh, Scotland*

ash removers and collecting systems to clean the airflow from impurities. It is evident that a steam turbine is not installed as the subsequent pulp and paper production uses the live steam directly. Therefore, the thermal power plant produces live steam with a pressure of $73\,\mathrm{bar}$ and a temperature of $460\,°\mathrm{C}$.

Raw data and preprocessing

Our predictions are conducted using a period of half a year between January 1st and July 5th in 2022. The raw data samples have a resolution of $1\,\mathrm{Hz}$. In the first step, we remove redundant, unnecessary, and incomplete sensor signals, simplifying the dataset to 900 operational features from more than 3500 signals. The features are then resampled to a quarter hour resolution by aggregation or calculation of the arithmetic mean.

Prediction algorithms

Python version 3.8.5 [12] and scikit-learn package [13] version 1.1.1. are used for ML predictions. We benchmark four ML algorithms for predicting the target value of live steam flow.

- **K-nearest neighbors**: When assigning a continuous value to a new sample, the KNN algorithm compares the features of the sample and the training set. It then calculates a target value by averaging the target values of the n_{n} values that are in the closest neighborhood with respect to the features. The model complexity is varied by a parameter representing the number of neighbors n_{n} to consider.
- **Random forest regressor**: RFR is an example of an ensemble learning algorithm. It uses a group of decision trees and averages the prediction of the individual trees to predict a continuous value. The model complexity can be varied using the number of decision trees n_{t}.
- **Multilayer perceptron**: MLP is a representer of ANNs, which utilize a supervised learning technique called backpropagation for training. The ANN consists of at least three layers ($n_{\mathrm{l}} = 3$), and adding additional layers increases the model complexity.
- **Lasso regression**: Lasso is an adaptation of a simple linear regression algorithm. It uses an additional regularization parameter (α) to vary the model complexity. The feature weights are reduced for large values of α, lowering the algorithm's complexity.

Internal parameters, feature and training sets

Most ML algorithms have parameters for varying the complexity. A high complexity indicates that the algorithm tries to extract as much information as possible from the training set, to fit the target most accurately. This can lead to overfitting on the training set and to a specified solution, which doesn't generalize very well. A suitable model complexity, on the other hand, prevents overfitting of the data and leads to a more generic solution. In Tab. 1 the complexity parameters of the individual algorithms are listed with their respective minimum and maximum values. Variations of these hyperparameters have an impact on the accuracy and on the time consumption of the algorithm.

Table 1. Hyperparameters of all algorithms

Algorithm	Complexity parameter	Minimum	Maximum
KNN	n_{n}	1	100
RFR	n_{t}	1	200
MLP	n_{l}	1	500
Lasso	α	0.001	500

We investigate the impact of different training periods and how these periods affect individual predictions by comparing two training sets: a static and a dynamic training set (Fig. 2).

Static training dataset   **Dynamic training dataset**

Figure 2. Different types of training sets (each square represents one day of operation)

- **Static training set:** The first seven days of the investigated period of 185 days are selected as the training period. The live steam flow is then predicted for the entire remaining dataset.

- **Dynamic training set:** To predict a certain day of the 185 days, the previous seven days are used for training the algorithm. Retraining the dataset every day is computationally extensive but allows for an adaption of the algorithm to occurring changes in the power plant operation.

The period of seven days for training the algorithm is not chosen arbitrarily. We conducted preliminary test runs and concluded that a training period between three and ten days gives the best prediction results. As a power plant has weekly patterns regarding the live steam flow we select seven days as the training period. In addition to using two training sets, the impact of the features for training the algorithm is of interest. Two different feature sets are used:

- **Basic feature set:** We use the natural gas and solid fuel flows as features and consider this the basic feature set.

- **Extended feature set:** For the extended feature set, 13 signals are selected based on expert knowledge. All the selected features are related to the target value and influence it to some extent.

Fig. 3 shows the natural gas and solid fuel flows (which comprise the basic feature set) and the target value live steam flow for an exemplary period. The left y-axis represents the fuel flows, while the right y-axis shows the live steam flow.

According to Fig. 3 the boiler works either on gas or solid fuel and sometimes on both to sustain the burning stability. It is also evident that solid fuel usage results in a higher live steam flow. When solid fuel only powers the boiler, the live steam flow is not constant and hasn't reached its maximum.

Fig. 4 represents the correlations between the 13 signals that are chosen based on expert knowledge and the target value. Trivial features like the feed water flow are not considered for the feature selection process. While most of the selected signals are highly correlated, some don't correlate at all. We still included these low-correlated signals in the extended feature set. The reason for this is that while they are not beneficial to the accuracy of the prediction, they are indicators of typical anomalies in thermal power plants. For example, the level in the steam drum is usually constant but will decrease for tube leakages, resulting in a deviation between the prediction and the actual values.

Figure 3. Basic feature set containing natural gas (top) and solid fuel (bottom), and the target value live steam flow with respect to time for nine days

Figure 4. Correlation between selected sensor signals and the target value live steam flow

Flow scheme and quality estimators

Fig. 5 depicts a summary of the conducted methods in a flow chart. The raw dataset consisting of 3518 signals is first pre-processed, then resampled to a quarter hour resolution and finally used for various predictions of the live steam flow. KNN, RFR, MLP and lasso regression are used as ML algorithms. For each of the tested algorithms, the prediction is computed multiple times to find optimized values for the respective hyperparameters. This is done for two different feature sets (the basic feature set consisting of four features and the extended feature set consisting of 13 features) and two different training sets (a static and a dynamic training set).
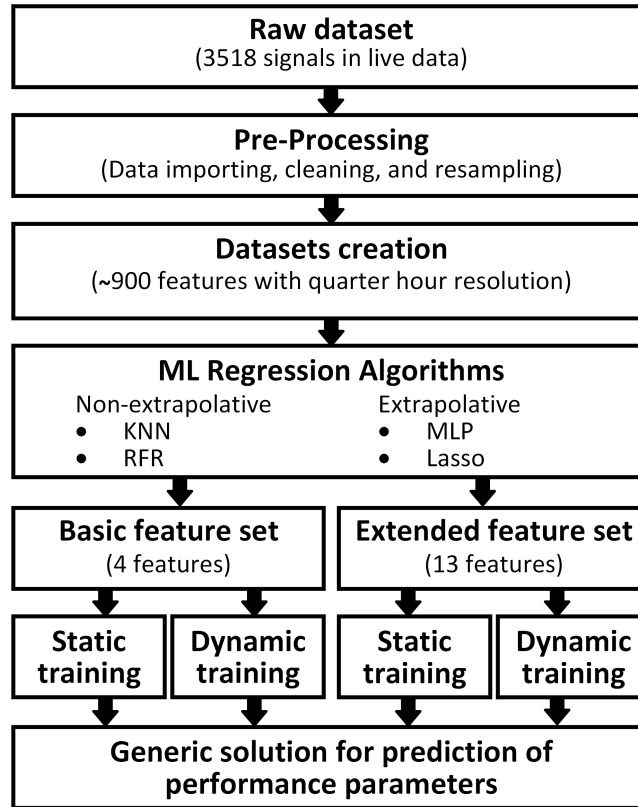
Figure 5. Flow chart of the prediction process

The coefficient of determination R^2 and the mean absolute error (*MAE*) are calculated to estimate the quality of the individual predictions. R^2, as given by Eq. 1, explains how well the variance in the target variable can be explained by the variances of the features.

$$R^2 = 1 - \frac{\sum_i (y_i - \hat{y}_i)^2}{\sum_i (y_i - \bar{y}_i)^2} \tag{1}$$

In addition, we compute *MAE*, a model evaluation metric for regression models. The mean absolute error is computed as the arithmetic mean of the absolute prediction errors of all individual samples in the test set. It is given in Eq. 2:

$$MAE = \frac{\sum_i |\hat{y}_i - y_i|}{n} \tag{2}$$

Although, *MAE* and R^2 typically correlate, mean absolute error is helpful as a quality estimator, as absolute numbers are often more intuitive and aid in interpreting the data.

Discussion and Results

Variation of algorithms

Fig. 5 shows that we use two non-extrapolative (KNN, RFR) and two extrapolative (MLP, Lasso) algorithms. We test the general accuracy and the capability of these algorithms to extrapolate by selecting a designated period of our dataset, where the test period includes values that do not occur in the training period. In Fig. 6 the comparison between the actual and the

predicted values are visualized for the training and the testing period. Fig. 6 shows that the ability to extrapolate has a crucial impact on the algorithm's precision. While KNN and RFR suffer from the lack of information in training data, MLP and lasso can still give a decent prediction quality for values that are outside the range of the target in the training period.
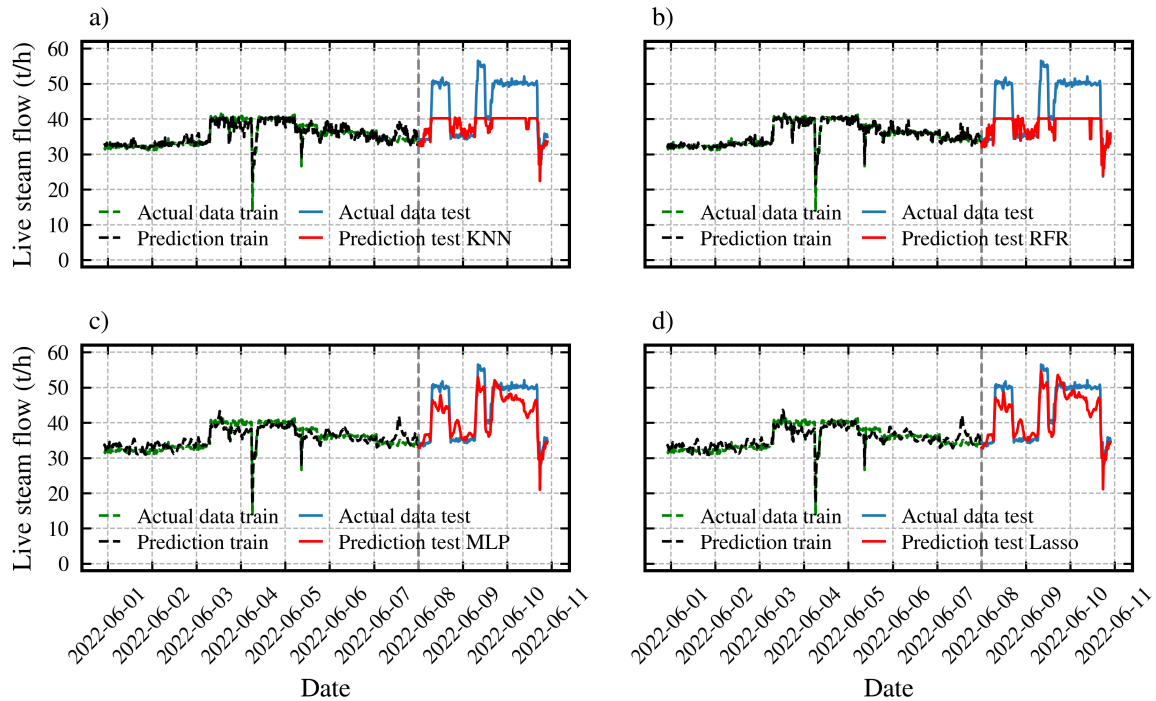
Figure 6. The showcase of algorithms constraints (a) KNN (b) RFR (c) MLP (d) Lasso

Variation of training sets

Fig. 7 visualizes the impact of using a static or a dynamic dataset for training. The average live steam flow is 35.1 t/h in the investigated period. Additionally, a planned shutdown, which is excluded from the prediction, is shown as greyed-out area. We use daily average values to make the figure more presentable. In general, training the algorithms on a dynamic dataset increases the accuracy of the prediction compared to training on the static dataset. Moreover, before the shutdown, the predictions exclusively overestimate the actual live steam flow, whereas, after the shutdown, they underestimate it. This behavior indicates that some critical changes happened during the shutdown period. Due to the higher prediction accuracy, the dynamic training set can be of great use to power plant operators for detecting changes on a much shorter time scale.

Tab. 2 lists the calculation time, the coefficient of performance R^2, the *MAE*, and the relative difference in MAE between the static and the dynamic training set for all investigated algorithms. Calculation time does not include the time needed for the tuning of the hyperparameters. For the static dataset, the fastest algorithm is more than 30 times faster than the slowest algorithm. As for the dynamic dataset, KNN (fastest) is more than 700 times faster than MLP (slowest). Even though we predict half a year of data, it is still possible to use MLP for daily predictions, but not on live data, because training the algorithm is linked to a high computational effort. With the same training dataset, all algorithms perform similarly in terms of *MAE*, while R^2 is approximately 20% lower for KNN and RFR than for MLP and lasso. The usage of a dynamic training set leads to a 33% improvement on average in both *MAE* and R^2, with small variations for the individual algorithms. Although *MAE* never exceeds 3.5 t/h with a 35.1 t/h average, $R^2 \leq 0.73$ and must be improved.
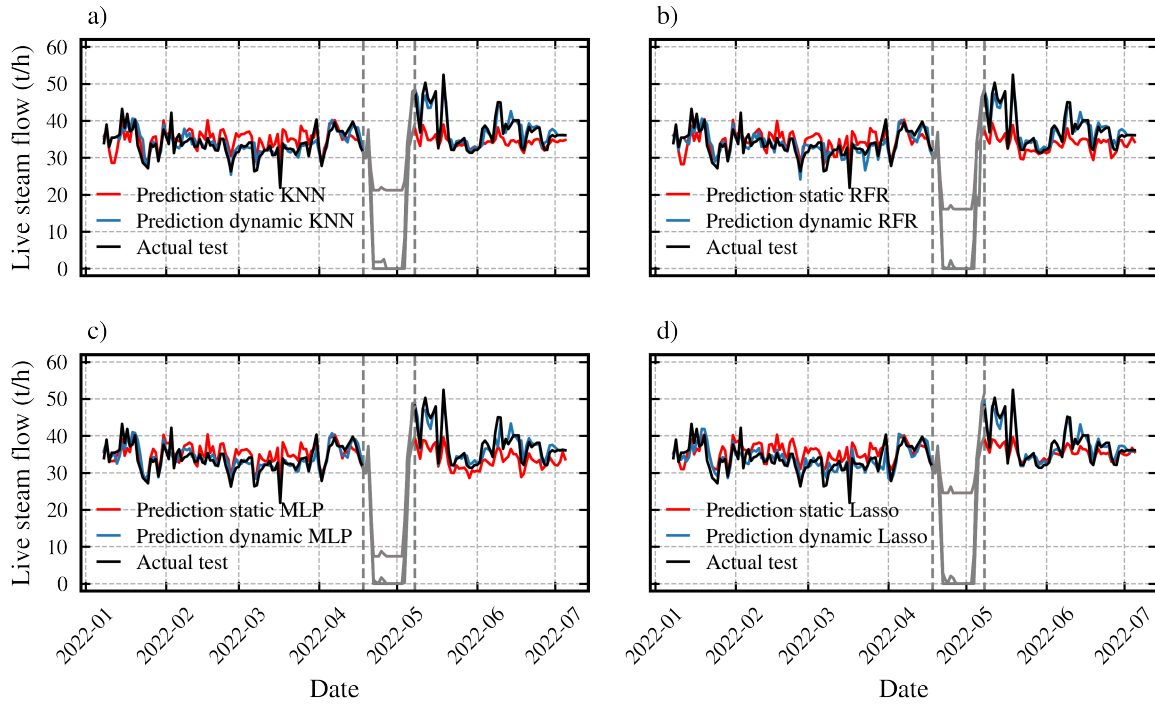
Figure 7. Prediction results in comparison between static and dynamic datasets (a) KNN (b) RFR (c) MLP (d) Lasso (the grey period represents a planned shutdown which was excluded for the prediction)

Table 2. Calculation time, coefficient of performance *MAE* and the relative difference in MAE between the static and the dynamic training set for the basic feature set

Algorithm	Training Set	t_{calc} (s)	R^2 (−)	*MAE* (t/h)	ΔMAE (%)
KNN	Static	1	0.37	3.19	35.6
	Dynamic	1	0.65	2.05	
RFR	Static	1	0.35	3.25	32.6
	Dynamic	8	0.61	2.19	
MLP	Static	22	0.46	3.06	37.6
	Dynamic	718	0.73	1.91	
Lasso	Static	11	0.46	3.06	28.4
	Dynamic	37	0.66	2.19	

Variation of feature sets

Tab. 3 lists the calculation time, the coefficient of performance R^2, and the *MAE* for the extended feature set. For RFR and MLP, the calculation time for the dynamic dataset with an extended feature set is more than 90 times and more than 20 times higher than for the static dataset. KNN and lasso did not notice such a difference. The deviation of *MAE* between the algorithms among training datasets is minor, and only the results of KNN differ from the other three. Directly comparing two training datasets, we see the major *MAE* improvement from 40 % in the case of KNN up to 68 % in the case of RFR, the results of MLP and lasso are in between. In turn, R^2 of algorithms increased up to three times.

If we compare Tab. 2 and Tab. 3, we see that all algorithms become more computationally demanding, but still six out of eight combinations have calculation times less than a minute. For the static dataset, swap from the basic to the extended feature set results in a higher *MAE*.

A possible reason for this is that the additional sensors increase the complexity of the model, resulting in overfitting. Removing some of the less correlated features might improve the prediction in these instances. Meanwhile, the use of the extended feature set in combination with the dynamic training set reduces the *MAE* from 2.05 t/h to 1.92 t/h in the case of KNN, from 2.19 t/h to 1.19 t/h for RFR, from 1.91 t/h to 1.33 t/h for MLP, and from 2.19 t/h to 1.18 t/h for lasso. We also see that KNN isn't profiting from the extended feature set. That is because of its computational ease and the non-complex model. Ultimately, the extended feature set based on expert knowledge increases R^2 in some cases by more than 50 % from 0.61 to 0.93 (RFR).

Table 3. Calculation time, coefficient of performance and *MAE* for the extended feature set

Algorithm	Training Set	t_{calc} (s)	R^2 (−)	*MAE* (t/h)
KNN	Static	3	0.31	3.39
	Dynamic	4	0.89	1.92
RFR	Static	2	0.31	3.73
	Dynamic	186	0.93	1.19
MLP	Static	57	0.41	3.84
	Dynamic	1120	0.94	1.33
Lasso	Static	20	0.52	3.41
	Dynamic	25	0.91	1.18

The results show that detecting long-term changes is possible using an ANN-based MLP algorithm. Fig. 8 visualizes the best configurations for long-term and short-term state detection in the thermal power plant.
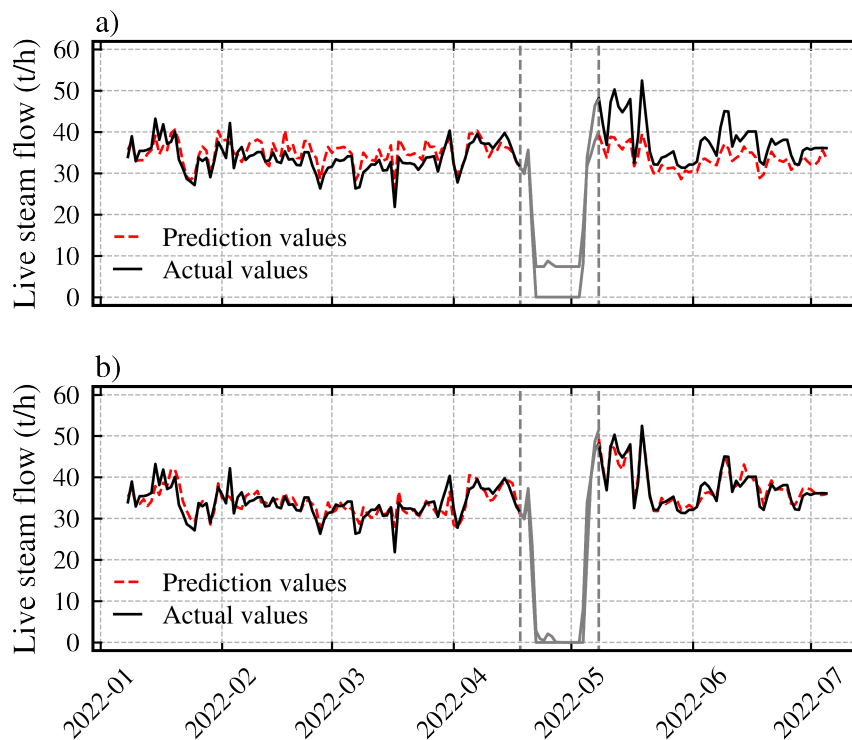
Figure 8. The best results for (a) long-term prediction based on the static dataset, MLP algorithm, and basic feature set (b) short-term prediction based on the dynamic dataset, lasso algorithm, and extended feature set

Heat Powered Cycles
Conference 2023
Edinburgh

Heat in the new energy system

3rd to 6th of September 2023
The University of Edinburgh, Scotland

Fig. 8 (a) visualizes the most appropriate setting for a long-term prediction using the MLP algorithm and four sensors. In our specific case, we can use one week of the data, where we know that the equipment operates in a normal state, and then predict several months. The computational effort is not a crucial criterion, as the algorithm only needs to be computed every couple of months. With the resulting predictions, long-term deterior ation or degradation of the equipment is detected.

Fig. 8 (b) represents the result of the Lasso regressor using a dynamic training set and the extended feature set. Although RFR predicts approximately 3% more accurately than Lasso, it is time-consuming for retraining and suffers from an inability to extrapolate, as shown in Fig. 6. Therefore, all aspects considered we see that lasso is one of the best algorithms in every quality estimation.

Conclusion and Outlook

To predict the live steam flow of a thermal power plant with high accuracy, four different machine-learning algorithms are compared. To detect short-term and long-term developments in the power plant, (1) different training sets, (2) different feature sets, and (3) different hyper-parameter settings are investigated. With this respect, the conducted study has come up with the following findings:

- The dependency of the prediction quality is studied for different settings, and the ideal settings result in a live steam prediction with $R^2 = 0.95$.
- Long-term change in the power plant operation can be tracked by predicting with the basic feature set, which includes only fuel inputs.
- A high accuracy prediction is possible by using a lasso regressor and the extended feature set. It can be used to monitor short-term changes in the power plant operation.

Therefore, ideal configurations to monitor short-term and long-term problems in the power plant operation are recommended in our study. To increase the prediction accuracy even further and to detect typical anomalies in the power plant operation, unsupervised learning methods can be of great use. Therefore, in a following study, we plan to focus on unsupervised learning methods that help power plant operators to react effectively and on time to anomalies and state changes.

Acknowledgment

References

[1] M. Preißinger. Predictive maintenance in thermal power plants: a systematic literature survey. In *9th HPC Conference Proceedings*, pages 496–515, Bilbao, Spain, April 2022. Heat Powered Cycles (HPC).

[2] Juan José Montero Jimenez, Sébastien Schwartz, Rob Vingerhoeds, Bernard Grabot, and Michel Salaün. Towards multi-model approaches to predictive maintenance: A systematic literature survey on diagnostics and prognostics. *Journal of Manufacturing Systems*, 56:539–557, July 2020.

[3] Salman Khalid, Hyunho Hwang, and Heung Soo Kim. Real-World Data-Driven Machine-Learning-Based Optimal Sensor Selection Approach for Equipment Fault Detection in a Thermal Power Plant. *Mathematics*, 9(21):2814, November 2021.

[4] Sailaja Thota and Muzamil Basha Syed. Analysis of feature selection techniques for prediction of boiler efficiency in case of coal based power plant using real time data. *Int J Syst Assur Eng Manag*, July 2022.

[5] Prabhas Hundi and Rouzbeh Shahsavari. Comparative studies among machine learning models for performance estimation and health monitoring of thermal power plants. *Applied Energy*, 265:114775, May 2020.

[6] Dong-Xiao Gu, Chang-Yong Liang, Isabelle Bichindaritz, Chun-Rong Zuo, and Jun Wang. A case-based knowledge system for safety evaluation decision making of thermal power plants. *Knowledge-Based Systems*, 26:185–195, February 2012.

[7] Firas Basim Ismail, Deshvin Singh, and Mohammad Shakir Nasif. ADOPTION OF INTELLIGENT COMPUTATIONAL TECHNIQUES FOR STEAM BOILERS TUBE LEAK TRIP. *MJCS*, 33(2):133–151, April 2020.

[8] Cody W. Allen, Chad Holcomb, and Maurício de Oliveira. Anomaly Detection for Large Fleets of Industrial Equipment: Utilizing Machine Learning With Applications to Power Plant Monitoring. In *Volume 4: Controls, Diagnostics, and Instrumentation; Cycle Innovations; Cycle Innovations: Energy Storage; Education; Electric Power*, page V004T05A016, Virtual, Online, June 2021. American Society of Mechanical Engineers.

[9] Nong Nurnie Mohd Nistah, King Hann Lim, Lenin Gopal, and Firas Basim Ismail Alnaimi. Coal-Fired Boiler Fault Prediction using Artificial Neural Networks. *IJECE*, 8(4):2486, August 2018.

[10] Pınar Tüfekci. Prediction of full load electrical power output of a base load operated combined cycle power plant using machine learning methods. *International Journal of Electrical Power & Energy Systems*, 60:126–140, September 2014.

[11] Vedika Agrawal, Shubham Agrawal, Sayak Nag, Debayan Chakraborty, B. K. Panigrahi, and P. M. V. Subbarao. Application of K-NN regression for predicting coal mill related variables. In *2016 International Conference on Circuit, Power and Computing Technologies (ICCPCT)*, pages 1–9, Nagercoil, India, March 2016. IEEE.

[12] Guido Van Rossum and Fred L. Drake. *Python 3 Reference Manual*. CreateSpace, Scotts Valley, CA, 2009.

[13] F. Pedregosa, G. Varoquaux, A. Gramfort, V. Michel, B. Thirion, O. Grisel, M. Blondel, P. Prettenhofer, R. Weiss, V. Dubourg, J. Vanderplas, A. Passos, D. Cournapeau, M. Brucher, M. Perrot, and E. Duchesnay. Scikit-learn: Machine learning in Python. *Journal of Machine Learning Research*, 12:2825–2830, 2011.

Using Effective Heat and Mass Transfer Resistances and Characteristic Temperature Differences to Predict Performance of Adsorptive Heat Transformation Devices - a Simple and Robust Approach

A. Velte-Schäfer[1*], E. Laurenz[1], T. Weilenmann Weisser[1] and G. Füldner[1]

[1]Fraunhofer ISE, Heidenhofstrasse 2, 79110 Freiburg, Germany

[*]Corresponding author: andreas.velte@ise.fraunhofer.de

Abstract

Adsorptive heat transformation (AHT) devices can be used in thermal energy storage, thermally driven heat pumps and chillers, and heat upgrading applications. Usually, the prediction of efficiency and heat flow rates requires transient numerical modelling. This means a high effort for preliminary evaluations of AHT devices. To accelerate the design process we propose a simple and robust approach by linking methods from basic heat exchanger theory with a characteristic temperature difference and effective heat and mass transfer resistances for adsorption modules. With this approach the performance of AHT devices can be predicted for quick evaluation of their potential. In this study we demonstrate the applicability to adsorption modules for thermally driven heat pumps and chillers, thermal energy storage, and heat upgrading.

Keywords: Adsorptive heat transformation, heat and mass transfer resistances, characteristic temperature difference,

Introduction/Background

Adsorptive heat transformation (AHT) can be applied in thermal energy storage [1], thermally driven heat pumps [2–4] and chillers [5, 6] and also heat upgrading [7]. By using low-grade heat as driving heat source or increasing the efficiency of existing processes this technology can help to reduce CO_2 emissions and to reduce electricity as well as primary energy demand [8–11]. To design the adsorption heat exchanger, the evaporator, and the condenser that are necessary for AHT devices, usually detailed transient models including all relevant heat and mass transfer processes are used [7, 10, 12–18]. With these models the efficiency and heat flow rates can be predicted even if design parameters of the heat exchangers change. Usually, these models require extensive calibration and validation with experimental data. Despite the power of detailed, transient numerical modelling, the main drawback of this method is the huge effort that has to be put into modelling and calibration. Moreover, these models require an equilibrium description of the working pair that describes the dependency between loading, temperature, and pressure. The calibration of the equilibrium model requires fitting of experimentally measured isotherms or isobars to rather complex mathematical functions [19, 20]. Thus, for a quick evaluation of the potential of novel materials or other applications it is desirable to have an approach that reduces this effort. To this end, a simple and robust approach is currently under development that is based on the characteristic temperature difference as proposed by Laurenz [21], the method of heat and mass transfer resistances [22–24], and the well-known methods of basic heat exchanger theory [25]. We aim to demonstrate the great potential of this simple approach in our study.

Adsorptive heat transformation applications can be described as heat exchange between three temperature levels $T_{HT} > T_{MT} > T_{LT}$. The application determines the connection of the

components to the heat sinks and sources as listed in Table 1. With the two temperature differences "temperature lift" ΔT_{lft} and "temperature thrust" ΔT_{thr} as defined in Table 1 the driving temperature differences in the adsorption or desorption half cycle can be calculated as illustrated in Figure 1 (a) [21, 24]. The heat upgrading application was described by Engelpracht et al. [7] recently.

Table 1 – Connections of components with heat sinks and heat sources at low, medium, and high temperature levels for heat pump / chiller / storage application and heat upgrading application. Heat flows > 0 indicate connection with a heat sink, heat flows < 0 indicate the connection with a heat source.

Connections		Heat pump / chiller / storage	Heat upgrading
Adsorption			
ADHX	$\dot{Q}_{s,ads} > 0$	$T_{in,s,ads} = T_{MT}$	$T_{in,s,ads} = T_{HT}$
E	$\dot{Q}_{e,ads} < 0$	$T_{in,e,ads} = T_{LT}$	$T_{in,e,ads} = T_{MT}$
Desorption			
ADHX	$\dot{Q}_{s,des} < 0$	$T_{in,s,des} = T_{HT}$	$T_{in,s,des} = T_{MT}$
C	$\dot{Q}_{e,des} > 0$	$T_{in,e,des} = T_{MT}$	$T_{in,e,des} = T_{LT}$
Temperature differences			
Temperature lift	$\Delta T_{lft,in}$	$T_{in,s,ads} - T_{in,e,ads} = T_{MT} - T_{LT}$	$T_{HT} - T_{MT}$
Temperature thrust	$\Delta T_{thr,in}$	$T_{in,s,des} - T_{in,e,des} = T_{HT} - T_{MT}$	$T_{MT} - T_{LT}$

The characteristic temperature difference is defined in equation (1) as the difference between equilibrium temperature T_{eq} and saturation temperature of the corresponding vapor pressure $T_{sat}(p)$. Thus, ΔT_{ch} can be calculated from any equilibrium data set, resulting from any isothermal or isobaric measurement. As an example, the resulting curve for the TiAPSO-water working pair is shown in Figure 1.

$$\Delta T_{ch} = T_{eqi}(X,p) - T_{sat}(p) \tag{1}$$

With ΔT_{lft} and ΔT_{thr} as horizontal lines the achievable loading spread ΔX_{eqi} for a given working pair with its characteristic temperature difference can be obtained as shown in Figure 1 (b) [21, 24]. The intersection points of ΔT_{lft} and ΔT_{thr} with the characteristic temperature difference curve define the minimum loading X_{min} and maximum loading X_{max}. Since in real-world applications X_{min} and X_{max} are not reached completely, a range between 20% and 80% of the equilibrium loading is defined for the calculation of the mean characteristic temperature difference $\Delta \bar{T}_{ch}$ according to equation (2). For working pairs with a step-like characteristic temperature difference (e. g. TiAPSO, SAPO-34, CAU-10-H) this value will change only little if ΔT_{lft} is below the step and ΔT_{thr} is above the step. In case of a rather linear characteristic temperature difference (e. g. Silicagel-water) $\Delta \bar{T}_{ch}$ strongly depends on ΔT_{lft} and ΔT_{thr}.

$$\Delta \bar{T}_{ch}\left(\Delta T_{lft}, \Delta T_{thr}\right) = \int_{X_{min}(\Delta T_{thr})+0.2\cdot\Delta X_{eqi}}^{X_{min}(\Delta T_{thr})+0.8\cdot\Delta X_{eqi}} \Delta T_{ch}(X) \cdot dX \tag{2}$$

Isotherms

Characteristic temperature difference

(a)

(b)
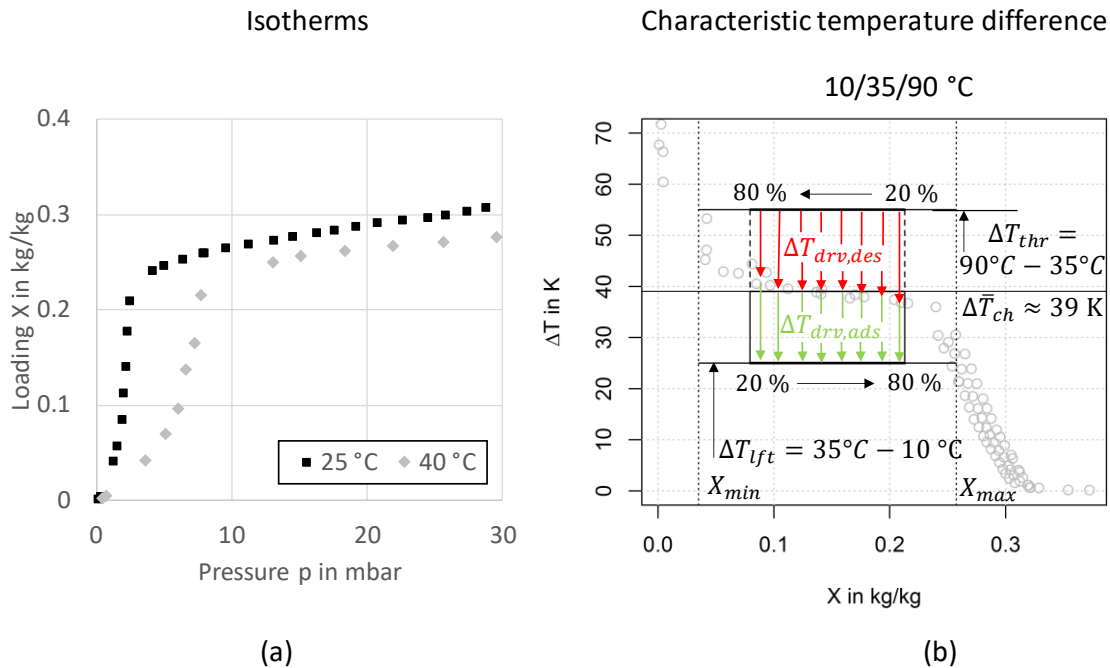
Figure 1 – Measured isotherms of TiAPSO (a), characteristic temperature difference calculated with isotherm data (b), data taken from Velte et al. [24]

In Figure 2 the relationships between the temperature levels in the components and characteristic temperature difference are shown. With a finite mass flow rate of the heat transfer fluid in the components, the outlet temperature of the adsorption heat exchanger is larger than the inlet temperature $T_{out,s,ads} > T_{in,s,ads}$ and the outlet temperature of the evaporator is lower than the inlet temperature $T_{out,e,ads} < T_{in,e,ads}$. It is obvious that lower mass flow rates will reduce the driving temperature differences $\Delta T_{drv,s}$ and $\Delta T_{drv,e}$ for a given characteristic temperature difference, resulting in a lower thermal output. Similar relationships apply to the desorption half cycle.

Evaporator-condenser

Adsorption heat exchanger
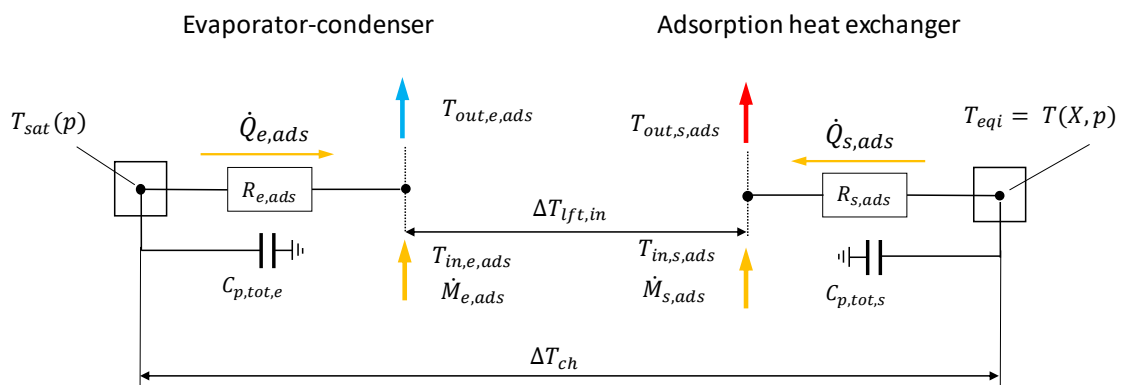
Figure 2 – Relationships between heat and mass transfer resistances, heat flows, inlet- and outlet temperatures, and characteristic temperature difference for the adsorption half cycle. Adapted from Velte et al. [26].

The detailed analysis of the quasi-isobaric phase (i. e. after switching of the hydraulic valves and completing of the quasi-isosteric heat up or cool down of the thermal capacities) of adsorption module measurements as presented by Wittstadt et al. [27], or more recently Velte et al. [26] showed that the heat flow rates can be calculated by using simple $\epsilon - NTU$ relationships [25] in combination with the method of the characteristic temperature difference

presented here. A simple energy balance of the quasi-isobaric part of the process as shown in equation (3) yields the relationship between loading difference ΔX, adsorbent mass M_{sorb}, adsorption enthalpy Δh_{ad}, heat and mass transfer resistance R_s, and driving temperature difference $\Delta T_{drv,s}$. If M_{sorb}, Δh_{ad} and R_s are known, $\Delta T_{drv,s}$ can be calculated with ϵ-NTU relationships. With an assumption about the shape of the time-dependent loading curve (rather linear or exponential shape) a half cycle time t_{hc} can be calculated – or if the half cycle time is fixed, the loading spread ΔX is obtained with equation (3). Similarly, half-cycle time or loading spread can be calculated with equation (4) using the heat and mass transfer from the evaporator-condenser R_e and the corresponding driving temperature difference $\Delta T_{drv,e}$. The heat $Q_{s,ib}$ is the heat of adsorption in the quasi-isobaric phase, $Q_{e,ib}$ is the heat of evaporation or condensation in the quasi-isobaric phase.

$$Q_{s,ib} = \Delta X \cdot M_{sorb} \cdot \Delta h_{ad} = t_{hc} \cdot R_s^{-1} \cdot \Delta T_{drv,s} \tag{3}$$

$$Q_{e,ib} = \Delta X \cdot M_{sorb} \cdot \Delta h_v = t_{hc} \cdot R_e^{-1} \cdot \Delta T_{drv,e} \tag{4}$$

The four heat flow rates $\dot{Q}_{s,ads}$, $\dot{Q}_{s,des}$, $\dot{Q}_{e,ads}$, and $\dot{Q}_{e,des}$ can be calculated with equation (5), (6), (7), and (8), respectively. In these equations the heat of the quasi-isobaric phase Q_{ib} is increased or decreased with the heat needed to heat or cool the thermal capacity of the components. Depending on the application and the type of the module (combined evaporator-condenser or separate components), the thermal capacities have to be considered. In case of heat pump / chiller and heat upgrading application a module with combined evaporator-condenser is considered here. Thermal energy storage needs additional separate components as shown in Figure 3. A further feature of thermal energy storage are the temperature differences $\Delta T_{str,ads}$ and $\Delta T_{str,des}$. These temperature differences depend on the storage duration - $\Delta T_{str,ads}$ will be the temperature difference between desired heat release temperature (i. e. medium temperature level T_{MT}) and ambient temperature for long-term storage, but it could be less if the adsorption heat exchanger does not cool down completely between charging and discharging the storage as detailed by Treier et al. [28] and Schreiber [1].

Table 2 – Calculation of heat flow rates in adsorption, desorption, evaporation, and condensation depending on the application

	Heat pump / chiller	Storage	Heat upgrading	Eq.
$\dot{Q}_{s,ads}$	$\dfrac{Q_{s,ib} + \Delta T_{thr} \cdot C_{p,tot,s}}{t_{hc}}$	$\dfrac{Q_{s,ib} - \Delta T_{str,ads} \cdot C_{p,tot,s}}{t_{hc}}$	$\dfrac{Q_{s,ib} - \Delta T_{lft} \cdot C_{p,tot,s}}{t_{hc}}$	(5)
$\dot{Q}_{s,des}$	$\dfrac{-Q_{s,ib} - \Delta T_{thr} \cdot C_{p,tot,s}}{t_{hc}}$	$\dfrac{-Q_{s,ib} - \Delta T_{str,des} \cdot C_{p,tot,s}}{t_{hc}}$	$\dfrac{-Q_{s,ib} + \Delta T_{lft} \cdot C_{p,tot,s}}{t_{hc}}$	(6)
$\dot{Q}_{e,ads}$	$\dfrac{-Q_{e,ib} + \Delta T_{lft} \cdot C_{p,tot,e}}{t_{hc}}$	$\dfrac{-Q_{e,ib}}{t_{hc}}$	$\dfrac{-Q_{e,ib} - \Delta T_{thr} \cdot C_{p,tot,e}}{t_{hc}}$	(7)
$\dot{Q}_{e,des}$	$\dfrac{Q_{e,ib} - \Delta T_{lft} \cdot C_{p,tot,e}}{t_{hc}}$	$\dfrac{Q_{e,ib}}{t_{hc}}$	$\dfrac{Q_{e,ib} + \Delta T_{thr} \cdot C_{p,tot,e}}{t_{hc}}$	(8)

(a) (b)
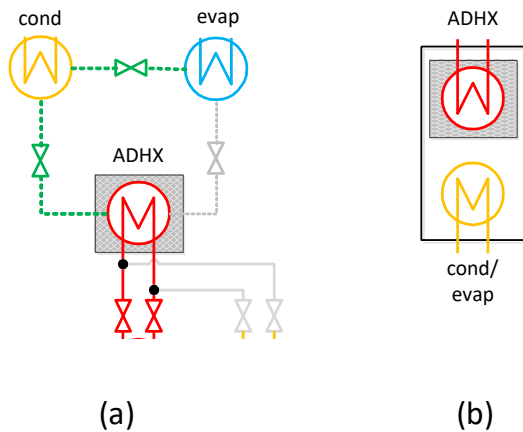
Figure 3 – Adsorption module with separate components for thermal energy storage application (a), adsorption module with combined evaporator-condenser for heat pump / chiller / heat upgrading applications (b)

With given heat and mass transfer resistances and additional component specifications such as effective thermal masses $C_{p,tot}$ and adsorbent mass M_{sorb} the efficiency, the thermal output and other performance indicators can be evaluated as shown in Figure 4 using the set of equations presented here.
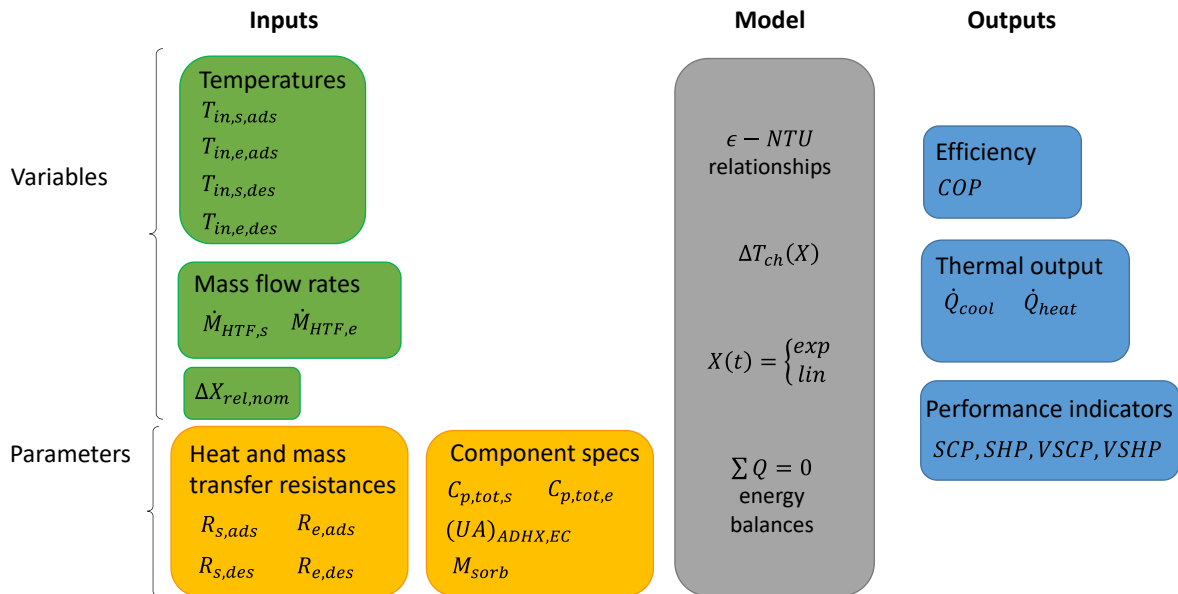
Figure 4 –Structure of the calculation approach with required inputs clustered as variables, parameters and outputs

The calculation of efficiency and thermal output is listed in Table 3 for all cases presented here. Please note that the thermal output in equation (10) is calculated with the overall cycle time t_{cyc} except for the storage. Here the half cycle time $t_{hc,ads}$ of the discharge half cycle is considered since adsorption (discharging) and desorption (charging) are decoupled possibly over a long period of time in this case.

Table 3 – Calculation of efficiency and thermal output for different applications

	Heat pump	Chiller	Storage	Heat upgrading	Eq.
COP	$\dfrac{Q_{s,ads} + Q_{e,ads}}{-Q_{s,des}}$	$\dfrac{Q_{e,ads}}{Q_{s,des}}$	$\dfrac{Q_{s,ads}}{-Q_{s,des}}$	$\dfrac{Q_{s,ads}}{-Q_{s,des} - Q_{e,ads}}$	(9)
Thermal output	$\dfrac{Q_{s,ads} + Q_{e,ads}}{t_{cyc}}$	$\dfrac{Q_{e,ads}}{t_{cyc}}$	$\dfrac{Q_{s,ads}}{t_{hc,ads}}$	$\dfrac{Q_{s,ads}}{t_{cyc}}$	(10)

Discussion and Results

We provide measurement results obtained from three different adsorption modules for heat pump, chiller, and heat upgrading application. The main parameters that characterise the adsorption modules and that are needed for the simulation are listed in Table 4.

Table 4 – Main parameters of different adsorption modules simulated here, all modules have a combined evaporator-condenser.

Parameter	Unit	Fibrous structures 'Size S'	Fibrous structures 'Size L'	Round tube-lamella	
Adsorbent	-	SAPO-34	SAPO-34	Silicagel	
Shape of isotherm	-	step-like	step-like	linear	
Shape of X(t)	-	linear	linear	exponential	
Application	-	heat pump	heat pump	cooling	heat upgrading
Literature	-	Velte et al. [26]	Wittstadt et al. [27]	new measurements	
M_{sorb}	kg	1.5	3.3	20.3	
$R_{s,ads}$	K/kW	2.6	1.5	0.8	0.6
$R_{s,des}$	K/kW	1.2	1.1	0.5	0.5
$R_{e,ads}$	K/kW	2.0	0.5	0.4	0.4
$R_{e,des}$	K/kW	0.5	0.2	0.2	0.2
$C_{p,tot,s}$	kJ/K	13.7	18.2	88.8	
$C_{p,tot,e}$	kJ/K	7.0	17.5	27.0	

The measurement conditions of the 'Size S' and 'Size L' fibrous structure modules are listed in Table 5.

Table 5 – Measurement conditions of 'Size S' and 'Size L' fibrous structure modules

Quantity	Unit	Size S	Size L
Nominal temperatures		15/35/90 °C	
$t_{hc,ads}$, $t_{hc,des}$	s	280, 320	300, 300
$T_{in,s,ads}$	°C	35	33
$T_{in,e,ads}$	°C	15	15
$T_{in,s,des}$	°C	89	88
$T_{in,e,des}$	°C	35	34
$\dot{M}_{s,ads}$, $\dot{M}_{s,des}$	kg/s	0.16, 0.16	0.49, 0.45
$\dot{M}_{e,ads}$, $\dot{M}_{e,des}$	kg/s	0.16, 0.16	0.52, 0.36

The results of the measurements and calculations with the newly developed approach of 'Size S' and 'Size L' fibrous structure modules are shown in Figure 5. The calculation results for 'Size S' modules match the experimental results very good, whereas the 'Size L' simulation overestimates the efficiency. This can be explained mainly with the strong over- and undershoots of the inlet temperature due to imperfections in the test-rig control. An illustration of that behavior can be seen in publications of Wittstadt et al. [27] and Velte [13]. However, the prediction of the heat flow rate matches the experiment in both cases within ±5 %.
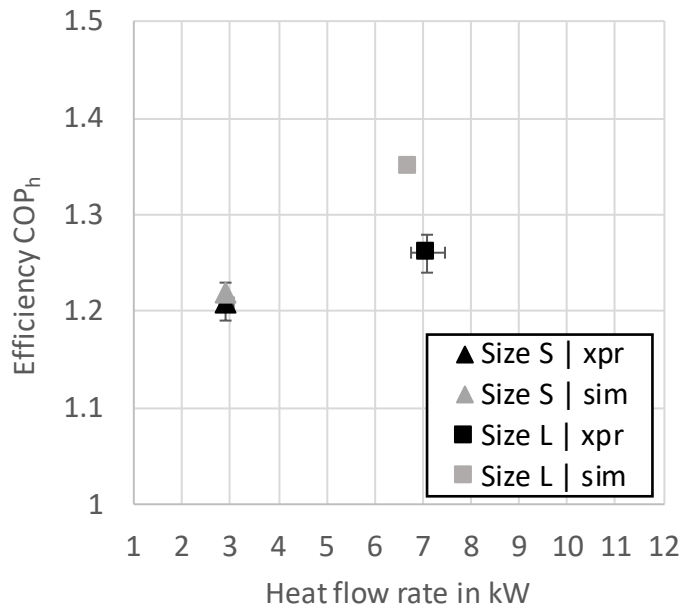
Figure 5 – Measurement and calculation results in terms of efficiency and heat flow rate of 'Size S' and 'Size L' fibrous structure modules, heat pump application, working pair: SAPO-34-water

The measurement conditions of the round fin-and-tube silicagel module are listed in Table 6 for chiller application and heat upgrading application. The mass flow rate was kept constant throughout the experiments at 0.6 kg/s in both the adsorption heat exchanger and the evaporator-condenser.

Table 6 – Measurement conditions of round tube-lamella Silicagel module operating in chiller application and heat upgrading application

Quantity	Unit	Chiller application		Heat upgrading application	
Nominal temperatures		15/28/65 °C		20/55/70 °C	10/50/70 °C
$t_{hc,ads}$, $t_{hc,des}$	s	325	600	600	
$T_{in,s,ads}$	°C	28		70	70
$T_{in,e,ads}$	°C	15		55	50
$T_{in,s,des}$	°C	65		55	50
$T_{in,e,des}$	°C	28		20	10
$\dot{M}_{s,ads}$, $\dot{M}_{s,des}$	kg/s	0.6			
$\dot{M}_{e,ads}$, $\dot{M}_{e,des}$	kg/s				

The results of the measurements and calculations of the chiller application are shown in Figure 6. The calculated efficiency and heat flow rate is lower in the experiment with short half cycle time (325 s) and higher in the experiment with long half cycle time (600 s). However, the deviation is around 15% in both cases, which is quite good, keeping in mind the simplicity of the calculation. It is an interesting point that a longer half cycle time leads to a higher efficiency and equal heat flow rate in the experiment. In the simulation the longer half cycle time even leads to a higher efficiency and a higher heat flow rate. This can be explained with the fact that the half cycle time of both experiments is not sufficient to get close to the equilibrium loading. Thus, a longer half cycle time leads to higher loading spread that is sufficient to keep or even increase the heat flow rate. It was observed for experiments with half cycle time > 1000 s that the heat flow rate decreases as soon as the actual loading spread gets closer to the equilibrium loading spread.
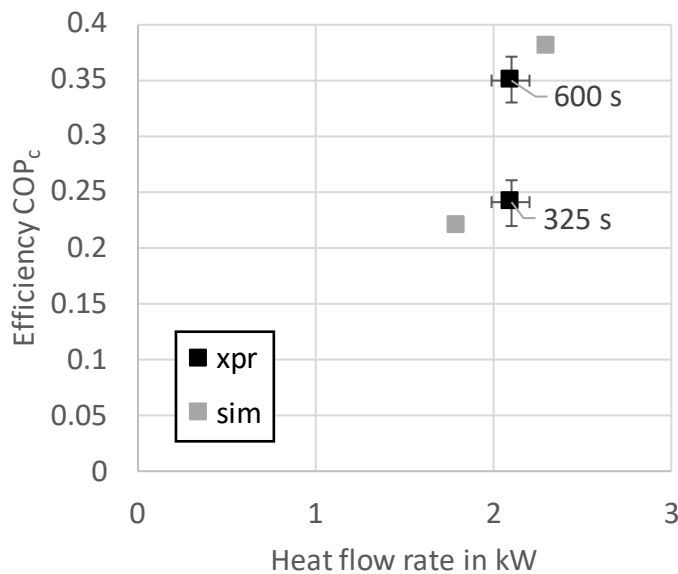
Figure 6 – Measurement and calculation results in terms of efficiency and heat flow rate of round tube-lamella module, chiller application, working pair: Silicagel-water

For the heat upgrading application of the round tube-lamella module the results are shown in Figure 7. The calculation overestimates the efficiency in both experimentally measured points, whereas the simulated heat flow rate is within ±10% of the experimental results. A deeper analysis of the experimentally measured heats reveals that this discrepancy in terms of efficiency can be explained with condensation and evaporation on the metal surface of the housing of the module. At evaporator temperatures of 50…55 °C the water vapour condenses on the metal parts of the housing until the thermal capacity of these parts is heated up to an equilibrium temperature which depends on loading and temperature of the adsorption heat exchanger. Consequently, the heat supplied to the evaporator increases due to heating up the dead thermal capacity of the housing. This dead thermal capacity is until now not part of the calculation approach. As a result, the efficiency in the calculation is overestimated.
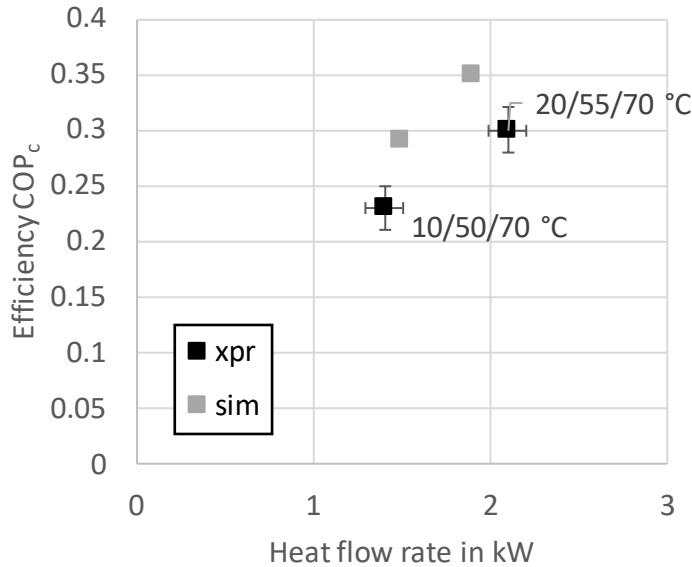
Figure 7 – Measurement and calculation results in terms of efficiency and heat flow rate of round tube-lamella module, heat upgrading application, working pair: Silicagel-water

Summary/Conclusions

In our study we have shown the applicability of a simple and robust approach to predict efficiency and heat flow rate of adsorption modules for AHT applications such as thermally driven heat pumps and chillers and heat upgrading. The simulated heat flow rates match the experimentally measured results within a range of ±15%, which is quite a good basis for the preliminary evaluation of the potential of AHT devices. The measured efficiency of adsorption modules for thermally driven heat pumps and chillers is matched with the simulation results with a reasonable accuracy (±10%, except for an outlier of 'Size L' module). However, the efficiency of the heat upgrading application is overestimated with the calculation approach. The in depth-analysis of the experimental data pointed to evaporation and condensation happening on metal parts of the housing that are not part of the approach yet. In a follow-up publication we aim to overcome this limitation by improving the approach to handle high evaporation temperatures (> 30 °C) necessary for heat upgrading applications.

Acknowledgments

Nomenclature

Symbol	Unit	Description
$C_{p,tot}$	J/K	effective thermal capacity
COP	1	coefficient of performance
Δh_{ad}	J/kg	adsorption enthalpy
Δh_v	J/kg	evaporation / condensation enthalpy
$\dot{M}$	kg/s	mass flow rate
M_{sorb}	kg	adsorbent mass
NTU	1	number of transfer units
p	Pa	pressure
Q	J	heat
$\dot{Q}$	W	heat flow rate
SCP, VSCP	W/kg, W/dm³	(volume) specific cooling power
SHP, VSHP	W/kg, W/dm³	(volume) specific heating power
t	s	time
T	K	temperature
ΔT	K	temperature difference
X	kg/kg	loading
ϵ	1	temperature effectiveness

Index	Description
ads	adsorption half cycle
ch	characteristic
cool	cooling application
cyc	cycle
des	desorption half cycle
drv	driving
e	evaporation, evaporator-condenser
eqi	equilibrium
hc	half cycle
heat	heating application
HT	high temperature
ib	quasi-isobaric
in	inlet
lft	lift
LT	low temperature
max	maximum
min	minimum
MT	medium temperature
nom	nominal
out	outlet
rel	relative
s	sorption, adsorption heat exchanger
sat	saturation
str	storage
thr	thrust

References

[1] H. Schreiber, *Experimentelle Untersuchungen und validierte Modelle eines thermischen Adsorptionsspeichers für Industrie- und Gebäudeheizprozesse*: RWTH Aachen University, 2017.

[2] A. Velte, E. Laurenz, S. Leisner, J. Weber, U. Wittstadt, and G. Füldner, "Experimental Results of a Gas Fired Adsorption Heat Pump and Simulative Prediction of Annual Performance in a Multi-Family House," *Appl. Therm. Eng.*, vol. 212, p. 118581, 2022, doi: 10.1016/j.applthermaleng.2022.118581.

[3] A. M. Rivero-Pacho, R. E. Critoph, and S. J. Metcalf, "Modelling and development of a generator for a domestic gas-fired carbon-ammonia adsorption heat pump," *Renewable Energy*, vol. 110, pp. 180–185, 2017, doi: 10.1016/j.renene.2017.03.089.

[4] S. Metcalf, Á. Rivero-Pacho, and R. Critoph, "Design and Large Temperature Jump Testing of a Modular Finned-Tube Carbon–Ammonia Adsorption Generator for Gas-Fired Heat Pumps," *Energies*, vol. 14, no. 11, p. 3332, 2021, doi: 10.3390/en14113332.

[5] M. Khan, K. Alam, B. B. Saha, A. Akisawa, and T. Kashiwagi, "Performance evaluation of multi-stage, multi-bed adsorption chiller employing re-heat scheme," *Renewable Energy*, vol. 33, no. 1, pp. 88–98, 2008, doi: 10.1016/j.renene.2007.01.012.

[6] B. B. Saha *et al.*, "Performance evaluation of a low-temperature waste heat driven multi-bed adsorption chiller," *International Journal of Multiphase Flow*, vol. 29, no. 8, pp. 1249–1263, 2003, doi: 10.1016/S0301-9322(03)00103-4.

[7] M. Engelpracht, A. Gibelhaus, J. Seiler, S. Graf, N. Nasruddin, and A. Bardow, "Upgrading Waste Heat from 90 to 110 °C: The Potential of Adsorption Heat Transformation," *Energy Technol.*, vol. 9, no. 1, p. 2000643, 2021, doi: 10.1002/ente.202000643.

[8] Y. Aristov, "Review of adsorptive heat conversion/storage in cold climate countries," *Appl. Therm. Eng.*, vol. 180, p. 115848, 2020, doi: 10.1016/j.applthermaleng.2020.115848.

[9] A. Caprì, A. Frazzica, and L. Calabrese, "Recent Developments in Coating Technologies for Adsorption Heat Pumps: A Review," *Coatings*, vol. 10, no. 9, p. 855, 2020, doi: 10.3390/coatings10090855.

[10] A. Pesaran, H. Lee, Y. Hwang, R. Radermacher, and H.-H. Chun, "Review article: Numerical simulation of adsorption heat pumps," *Energy*, vol. 100, pp. 310–320, 2016, doi: 10.1016/j.energy.2016.01.103.

[11] J. M. Pinheiro, S. Salústio, J. Rocha, A. A. Valente, and C. M. Silva, "Adsorption heat pumps for heating applications," *Renewable and Sustainable Energy Reviews*, vol. 119, p. 109528, 2020, doi: 10.1016/j.rser.2019.109528.

[12] G. Füldner, "Stofftransport und Adsorptionskinetik in porösen Adsorbenskompositen für Wärmetransformationsanwendungen," Dissertation, Freiburg, 2015.

[13] A. Velte, "Experimentelle Arbeiten und Entwicklung von numerischen Modellen zur Analyse und Optimierung von erweiterten Adsorptionskreisläufen für die Wärmeversorgung von Gebäuden," Dissertation, Technische Fakultät, Universität Freiburg, Freiburg, 2019.

[14] B. B. Saha, E. C. Boelman, and T. Kashiwagi, "Computer simulation of a silica gel-water adsorption refrigeration cycle--the influence of operating conditions on cooling output and COP," *ASHRAE Transactions*, pp. 348–357, 1995.

[15] H. T. Chua, K. C. Ng, A. Malek, T. Kashiwagi, A. Akisawa, and B. B. Saha, "Modeling the performance of two-bed, sillica gel-water adsorption chillers," *International Journal of Refrigeration*, vol. 22, no. 3, pp. 194–204, 1999, doi: 10.1016/S0140-7007(98)00063-2.

[16] F. Lanzerath, U. Bau, J. Seiler, and A. Bardow, "Optimal design of adsorption chillers based on a validated dynamic object-oriented model," *Science and Technology for the Built Environment*, vol. 21, no. 3, pp. 248–257, 2015, doi: 10.1080/10789669.2014.990337.

[17] U. Bau *et al.,* "Adsorption energy systems library - Modeling adsorption based chillers, heat pumps, thermal storages and desiccant systems," in *Proceedings of the 10th International Modelica Conference, March 10-12, 2014, Lund, Sweden*, 2014, pp. 875–883.

[18] A. M. Rivero-Pacho, R. E. Critoph, and S. J. Metcalf, "Alternative monolithic/composite carbons for adsorption generators and simulation for optimal performance," *Appl. Therm. Eng.*, vol. 126, pp. 350–357, 2017, doi: 10.1016/j.applthermaleng.2017.07.177.

[19] M. Llano-Restrepo and M. A. Mosquera, "Accurate correlation, thermochemistry, and structural interpretation of equilibrium adsorption isotherms of water vapor in zeolite 3A by means of a generalized statistical thermodynamic adsorption model," *Fluid Phase Equilibria*, vol. 283, 1-2, pp. 73–88, 2009, doi: 10.1016/j.fluid.2009.06.003.

[20] A. Desai, V. Schwamberger, T. Herzog, J. Jänchen, and F. P. Schmidt, "Modeling of Adsorption Equilibria through Gaussian Process Regression of Data in Dubinin's Representation: Application to Water/Zeolite Li-LSX," *Industrial & Engineering Chemistry Research*, vol. 58, no. 37, pp. 17549–17554, 2019, doi: 10.1021/acs.iecr.9b03005.

[21] E. Laurenz, "Frequency response analysis of heat and mass transfer in adsorbent composites and simplified performance estimation for heat transformation applications," TUHH Universitätsbibliothek, 2021.

[22] J. Ammann, P. Ruch, B. Michel, and A. R. Studart, "Quantification of heat and mass transport limitations in adsorption heat exchangers: Application to the silica gel/water working pair," *International Journal of Heat and Mass Transfer*, vol. 123, pp. 331–341, 2018, doi: 10.1016/j.ijheatmasstransfer.2018.02.076.

[23] A. Velte, J. Weise, E. Laurenz, J. Baumeister, and G. Füldner, "Zeolite NaY-Copper Composites Produced by Sintering Processes for Adsorption Heat Transformation—Technology, Structure and Performance," *Energies*, vol. 14, no. 7, p. 1958, 2021, doi: 10.3390/en14071958.

[24] A. Velte *et al.,* "Adsorption Dynamics and Hydrothermal Stability of MOFs Aluminium Fumarate, MIL-160 (Al), and CAU-10-H, and Zeotype TiAPSO for Heat Transformation Applications: pre-print," *SSRN Journal*, 2022, doi: 10.2139/ssrn.4230996.

[25] R. K. Shah and D. P. Sekulić, *Fundamentals of heat exchanger design*. Hoboken, NJ: Wiley-Interscience, 2003.

[26] A. Velte, L. Joos, and G. Füldner, "Experimental Performance Analysis of Adsorption Modules with Sintered Aluminium Fiber Heat Exchangers and SAPO-34-Water Working Pair for Gas-Driven Heat Pumps: Influence of Evaporator Size, Temperatures, and Half Cycle Times," *Energies*, vol. 15, no. 8, p. 2823, 2022, doi: 10.3390/en15082823.

[27] U. Wittstadt *et al.,* "A novel adsorption module with fiber heat exchangers: Performance analysis based on driving temperature differences," *Renewable Energy*, vol. 110, pp. 154–161, 2017, doi: 10.1016/j.renene.2016.08.061.

[28] M. S. Treier, G. Munz, A. Velte, S. K. Henninger, and F. P. Schmidt, "Estimations of Energy Density and Storage Efficiency for Cascading Adsorption Heat Storage Concepts," *International Journal of Refrigeration*, no. 105, pp. 59–65, 2018, doi: 10.1016/j.ijrefrig.2018.10.012.

DACCS Roadmap to 2050: Achieving a safe, scalable, and low-cost implementation

S. Aeschlimann[1*], C. Charalambous[1,2], L. Kung[2], M van der Spek[2], S. Garcia[2] and D. Pike[1]

[1]RMI, 22830 Two Rivers Road, 81621 Basalt, Colorado, United States

[2]Research Centre for Carbon Solutions (RCCS), School of Engineering and Physical Sciences, Heriot-Watt University, EH14 4AS Edinburgh, United Kingdom

[*]Corresponding authors: saeschlimann@rmi.org

Extended Abstract

According to the Intergovernmental Panel on Climate Change (IPCC), we will need to remove around 1.3–29 $GtCO_2$ from the atmosphere annually by 2050 to limit global warming to 1.5°C above pre-industrial levels [1]. Direct air carbon capture and storage (DACCS) is a technological solution that has the potential to remove significant amounts of CO_2 from the atmosphere and concentrate it to a stream required for long-term storage. Given the early stage of technical research and development for DACCS, the challenges faced in reducing costs and energy requirements, as well as the uncertainty regarding how both energy and DACCS systems evolution, it is critical that developments and improvements for a range of direct air capture (DAC) technologies are rapidly expedited this decade. This advancement will require a greater understanding of the current state of DACCS and the identification of existing knowledge gaps and obstacles to scaling.

Building on previous literature and with the aim to surface the set of DACCS systems that merit accelerated research, testing, development, and deployment, and to help prioritize activities to support these ends, this work provides: (i) an overview and classification of DACCS systems, (ii) a harmonization of technical and economic performance of DAC technologies, based on publicly available data, (iii) a comprehensive list of technical- and infrastructure-based knowledge gaps and obstacles to scaling DACCS systems, (iv) and a list of priority initiatives for unlocking research, development, demonstration and deployment of DACCS. Our intent is to drive progress against high-impact priority actions, with a focus on accelerating research, development, and deployment of safe, scalable, and lower cost DACCS as a component of the broader carbon dioxide removal portfolio.

To meet these objectives, we firstly classify DAC technologies according to four main CO_2 capture mechanisms: physical and/or chemical binding to either (i) a liquid or (ii) a solid material; (iii) separation based on differences in gas diffusivities; and (iv) separation by freezing point (see Figure 1). We then categorise DAC technologies based on their respective CO_2 release driver (i.e., use of heat, electricity, and/or water/steam/humidity), resulting in 11 DAC technologies. For instance, technologies that bind CO_2 to a liquid can be further categorized as regeneration by high-grade heat, low-grade heat crystallization, low-grate heat stripping, and electricity. Within each of the 11 technologies, multiple configurations can exist, which can differ by material, equipment, process layout, and used energy vector. Configurations reflect the different process implementations, realized either by different DAC companies (or research organizations) pursuing a similar technology, e.g., Climeworks [2] and Global Thermostat [3] both pursuing adsorption with a temperature vacuum swing process, or by a portfolio approach within one company, e.g., Carbon Engineering [4] looking at both natural gas-fired and electric calciners. This analysis resulted in 14 DAC

configurations for which we then looked at their technology performance for selecting the promising ones for achieving a large-scale CO_2 removal.
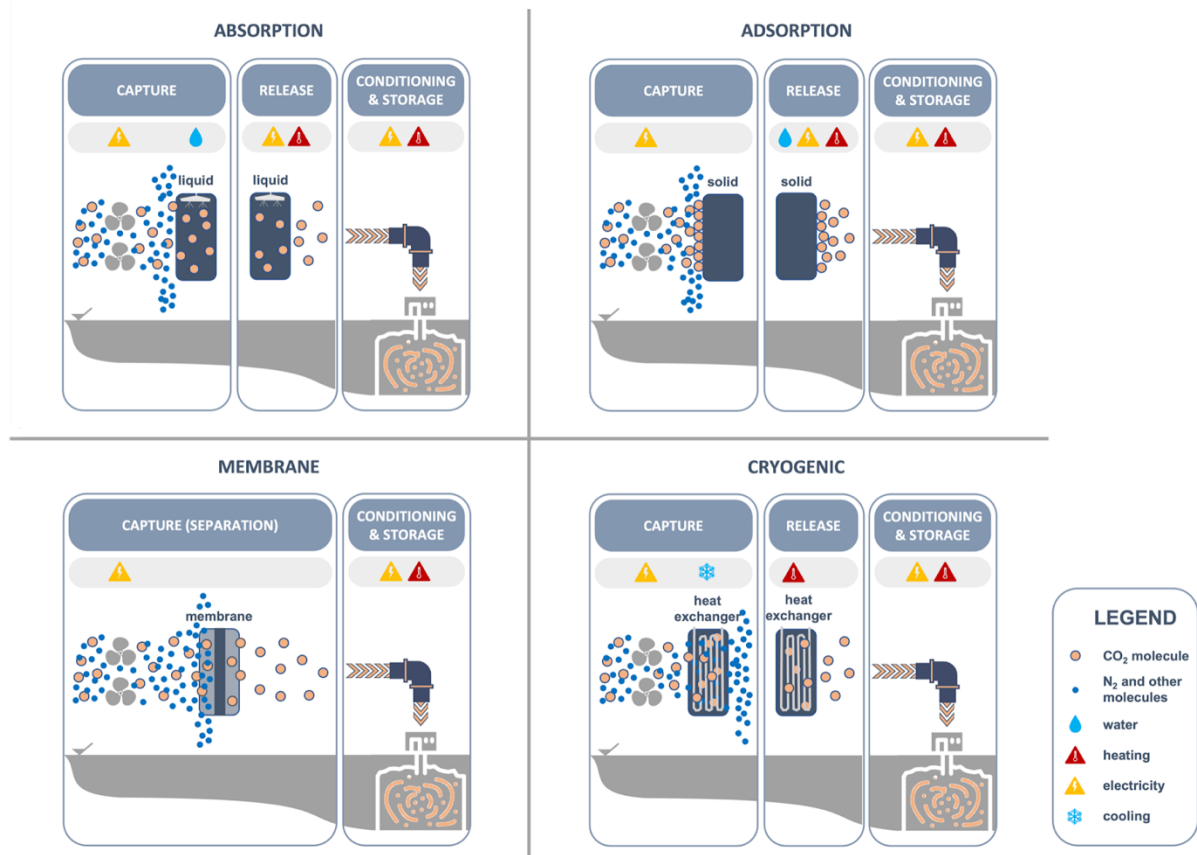
Figure 1. The four primary separation mechanisms of DACCS: *absorption*, *adsorption*, *membrane*, and *cryogenic*. The CO_2 produced from the main separation processes is directed for further conditioning and storage.

We then performed a harmonized techno-economic evaluation of their performance to identify the specific cost drivers and properly quantify them. For this analysis, we firstly screened the available literature on DACCS techno-economics. For the technologies where only process performance evaluation was available, we looked at energy-related costs and extracted lessons from these. For the technologies where capital and operational costs have been published, we compared the cost drivers for each technology on a like-for-like basis by harmonizing the available capital and operational expenditure data.

Given the uncertainty around how energy systems will evolve, how the rate of cost and energy requirements of DACCS will progress, and which DAC technological solutions will have the potential to deliver negative emissions safely and cost-effectively at scale, it is expected that a portfolio of DAC technologies should be advanced up the technology readiness level during the next decade. This is necessary to de-risk technology lock-in and provide first benchmark costs for different DAC technologies which are a prerequisite for realistic cost predictions and cost reduction pathways for DAC technologies. To accelerate unlocking and de-risking DACCS's potential at scale, we identified a comprehensive list of existing knowledge gaps and obstacles and priority initiatives across five categories: (i) materials, (ii) process design, (iii) equipment, (iv) system integration, and (v) infrastructure. Here, we focus on research, development, demonstration, and deployment obstacles and initiatives only, as obstacles related to other supporting elements of a high-functioning carbon dioxide removal (CDR) ecosystem such as demand, human capital, and social acceptance [5]

are expected to apply to CDR solutions more generally and not to DACCS systems specifically.

Considering the predicted installed capacity of DACCS in the next coming decades and our comprehensive list of priority initiatives, we proposed a DACCS Roadmap to 2050. In this roadmap we indicated whether priority initiatives are "very relevant" or "less relevant" in the short (2030), medium (2040) and long term (2050). We also highlighted whether industry, academia or both have currently the skills to address these initiatives or whether no skills are currently existing/accessible and need to be developed.

In conclusion, this study introduced a novel hierarchy for classifying DAC technologies that supports enhanced understanding of the key DAC performance indicators and the quality of the underlying data, on which claims on energy requirements and future cost can be built. A harmonized techno-economic framework was developed based on available energy and cost data to allow for a fair comparison between DAC technologies. For most DAC technologies, plant-level data is unavailable, presenting a major obstacle to cost and energy use reduction efforts. For the technologies where plant-level data exist, future cost ranges of USD100–300/tCO$_2$ seem attainable. Nevertheless, the lower and upper range are extremely ambitious targets. In addition, one-size-fits-all DAC solutions do not appear to exist. Different DAC technologies favour different geographies, pre-existing infrastructure, equipment, and materials, which makes having a portfolio of ready-to-be deployed DAC technologies a necessary precondition for global Gt-scale deployment. For overcoming these barriers, this study proposed a list of critical priority initiatives. As deployment-led innovation alone is unlikely to make DACCS economically feasible, simultaneous investments into research, development, and deployment and the buildout of supporting infrastructure are expected to be crucial. Further research is needed to better quantify the cost of proposed priority initiatives and their attendant research projects.

References

[1] IPCC, "Mitigation of Climate Change Climate Change 2022 Working Group III", contribution to the Sixth Assessment Report of the Intergovernmental Panel on Climate Change, 2022.

[2] Climeworks, "Achieve net zero targets with Climeworks direct air capture", Retrieved February 15, 2023, from https://climeworks.com/.

[3] Global Thermostat, "Core Solution - Direct Air Capture", Retrieved February 15, 2023, from https://globalthermostat.com/.

[4] Carbon Engineering, "Direct Air Capture of CO$_2$", Retrieved February 15, 2023, from https://carbonengineering.com/.

[5] Maesano, C. et al., "Geochemical Negative Emissions Technologies: Part II. Roadmap", Frontiers in Climate, 2022.

Heat Powered Cycles
Conference 2023
Edinburgh

Heat in the new energy system

Experimental study of an isobaric expansion engine – Shaft power and electricity generation

S. Roosjen[1*], M. Glushenkov[2], J. Gül[2], A. Kronberg[2]

[1] Sustainable Process Technology, Faculty of Science and Technology, University of Twente, PO Box 217, 7500 AE Enschede, The Netherlands

[2] Encontech B.V. TNW/SPT, P.O. Box 217, Enschede 7500 AE, The Netherlands

*Corresponding author e-mail: s.roosjen@utwente.nl

Abstract

Modern heat engines for valorisation of ultra low grade heat are too capital intensive especially with a low temperature of heat source ($<$ 100°C). To resolve the technical problems of the current heat conversion technologies a concept of "isobaric expansion" (IE) engine is proposed [1]. This paper presents an IE engine operating as an electric generator, the results of experiments obtained with this engine, as well as a comparison of the experimental results with a thermodynamic model. Experiments were carried out at heat source temperature in the range 30 – 80 ^{o}C and heat sink temperature around 12 ^{o}C; refrigerant R134a was used as the engine working fluid. Depending on the temperature of the heat source the obtained efficiency was 3.5 – 6 %. The relative difference between the experimental and thermodynamic efficiency is less than 4 %, which indicates low mechanical and thermal losses. The results obtained extend upon the previously reported application of the engine as a pump [2]. The IE engine can deliver any pressure of the pumped liquid or gas and convert the hydraulic output to shaft power/electricity, furthermore the IE engines can be integrated to cooling systems of for example: LT-PEM hydrogen fuel cells or internal combustion engines.

Keywords: Heat-driven pump, renewable energy, isobaric expansion, low-grade heat, shaft power, electricity generation.

Introduction

The IE process is an alternative to conventional polytropic gas/vapour expansion accompanied by a pressure decrease typical of all state-of-the-art heat engines.

IE engines are the oldest type of heat engines [3], dating back to the early industrial revolution. The current status of the IE technology and important modifications to make IE machines competitive and cost-effective alternatives to state-of-the-art heat conversion technologies are presented in [1]. The technology is a simple and low-cost alternative to ORC systems as well as other state-of-the-art energy conversion systems. The engine is very versatile; it can be used wherever heat of any grade is available [1].

IE engines present a compelling proposition as vapor-driven pumps and compressors, owing to their simplicity in kinematic structure and reduced energy conversion intricacies. In this way heat can be effectively harnessed for direct pumping and compression, without the need for intervening stages involving the generation of shaft power or electricity, transmissions and re-conversion into conventional mechanical energy—a departure from prevalent practices in modern industry.

Using a differential piston arrangement (a combination of two pistons with different diameters), the IE engine-pump can deliver any pressure of the pumped liquid or gas. This allows the engine-pump to be used for high-pressure applications such as heat-driven water desalination, oil hydraulic power units, cheap compression of hydrogen or other gasses.

The energy from the pumped liquid flows can be converted to shaft power (rotary motion) or electricity using off-the-shelf hydraulic motors. Another option is the so-called pump as turbine (PAT) technology, which uses mass-market centrifugal pumps that operate in reverse mode i.e., as turbines. In this case, the installation is turned into a heat-to-power converter.

The IE engine was studied as a high-pressure pump [2, 3]. Significant advantages of IE engines over similar existing systems were obtained in terms of efficiency and power output. In order to understand and demonstrate the capabilities of the system, the engine was combined with a hydraulic motor producing shaft power that could be used to generate electricity and/or drive centrifugal pumps.

The purpose of this paper is to present an IE engine operating as an electric generator, to show general feasibility for low temperature waste heat recovery and specifically in LT-PEM hydrogen fuel cell systems or cooling systems of internal combustion engines (ICE).

Modified engine and experimental set up

The IE engine-pump presented previously [2] was modified for shaft power generation. Figure 1 shows a scheme of such the new experimental setup. It is similar to the engine operating as a water pump, which was explained in ref. [2].
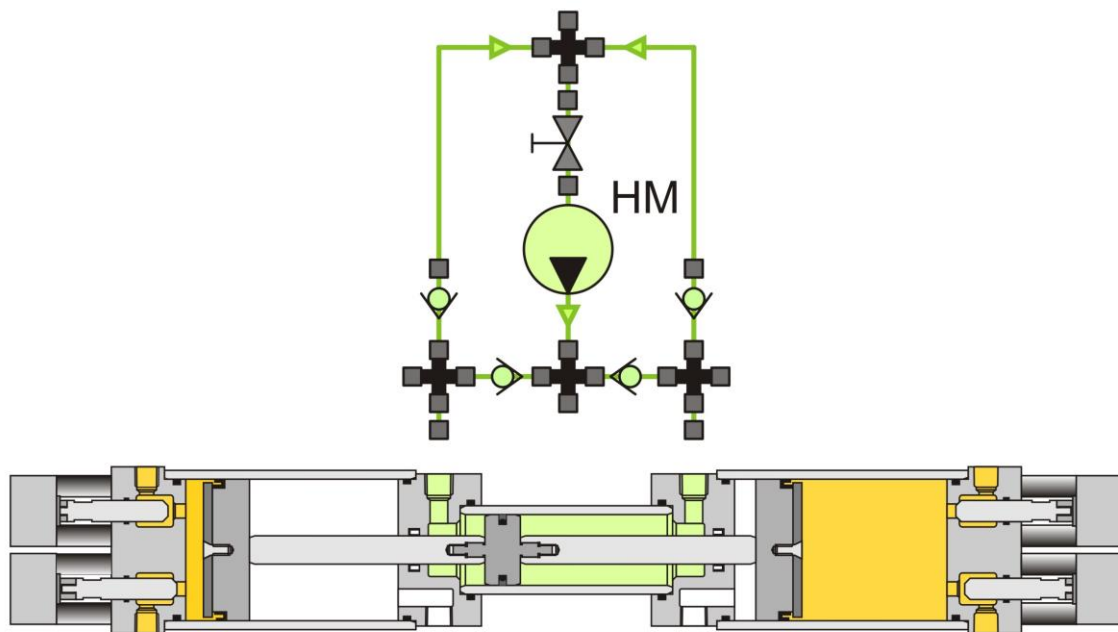
Figure 1. Scheme of the IE engine for production of shaft power.

A difference is that a hydraulic motor HM serves as an engine load and the hydraulic circuit is filled with hydraulic oil instead of water. Also, the inlet and discharge valves were improved.

The engine consists of two power or driving cylinders, pumping cylinder, three pistons, two connecting rods, two driving valve covers, two pumping valve covers, and two pneumatic cylinders. The pneumatic cylinders were used to actuate the inlet and outlet valves in the covers. Each cover of the pumping cylinder is equipped with a non-return (check) suction and discharge valve.

The pistons divide the internal volumes of the cylinders into six chambers: two driving chambers, shown in light brown, two pumping chambers (light green), and two auxiliary

chambers (colourless). The auxiliary chambers can be used for lubricating the pistons and for collecting leaks from the pumping and driving chambers in case of failure of the piston seals. They are connected by a manifold through which the leaks are routed to ventilation.

During operation, the reciprocating movement of the pistons (in two power chambers and in the pumping chamber) under the action of the working fluid (light brown) leads to the pumping of oil (light green) through the hydraulic motor. An important feature of this process is that the pressure of the working fluid in the power cylinders does not change (isobaric expansion) during the entire piston stroke.

The use of oil permits using a wider range of commercially available hydraulic motors. To provide pulseless flow of the hydraulic oil and smooth rotation of the hydraulic motor, a hydraulic accumulator is imbedded into the hydraulic circuit.

As a hydraulic motor MI02 Var-Spe radial pistons hydraulic motor (speed 70-2000 rpm, pressure up to 150 bar; efficiency 96 %) was used. Since this hydraulic motor, as well as other hydraulic motors, is most efficient at a rather high pressure drop of about 80 bar, the original engine-pump was modified to feature smaller pumping chambers as seen in Figure 2.
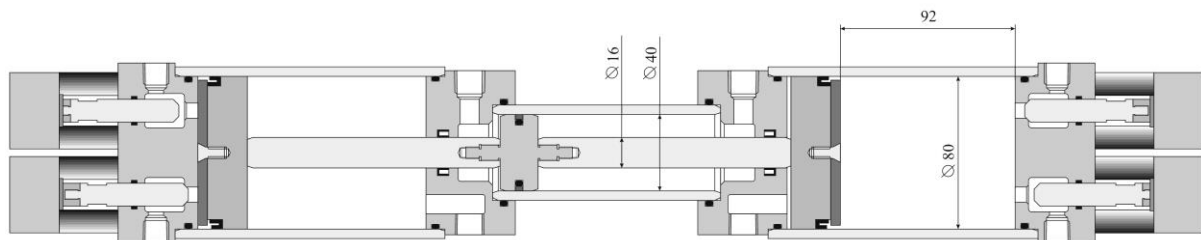
Figure 2. Modified IE engine-pump for increased pumping pressure.

The modified engine, Figure 2, is in fact a differential piston reciprocating inside a differential cylinder, which has a simple design with no mechanical transmission or crank gear etc. The engine dimensions: length without the pneumatic cylinders – 550 mm, length with the pneumatic cylinders – 576 mm, inner diameter of the power cylinders 80 mm, outer diameter – 90 mm, inner diameter of the pumping cylinder – 40 mm, diameter of the connecting rods – 16 mm, length of the piston stroke – 96 mm. Volumes of each driving and pumping chambers of the engine are 0.482 L and 0.101 L respectively.

Reducing the diameter of the pumping cylinder from 80 mm to 40 mm made it possible to increase the pressure of the pumped liquid by about 4 times or up to 80 bar.

Sealing of the power and pumping cylinders and pistons were provided by seals based on materials with high resistance to all refrigerant classes as well as potentially possible ammonia-water mixtures, oxygenates, carbon dioxide, and hydrocarbon-based working fluids. The mating cylinder surfaces were treated by plasma nitriding up to 1100HV on the nitride layer. To extend the lifetime of the dynamic seals Fomblin Compressor Oil YL VAC 16/6 was used.

The experimental set-up (so-called Worthington type IE engine-pump [1]) is shown in Figures 3 and 4. It includes a double acting IE engine-pump **E-P**, working fluid feed pump **FP** actuated by a pneumatic actuator **PA**, hydraulic accumulator **HA**, heater (evaporator) **H**, regenerator **R**, cooler (condenser) **C**, water heater **WH**, pressure indicators **PI**, pressure and temperature transmitters **PT** and **TT**. The operation of such engine-pumps is described elsewhere [1, 2].

To supply low-pressure cold working fluid after the cooler to the heat exchanger at high cycle pressure, a specially designed variable-flow piston feed pump FP was used (Figure 3). It was

driven by a pneumatic actuator PA (double-acting pneumatic cylinder) with a maximum stroke of 100 mm.

The maximum working volume of the feed pump per cycle was 0.232 L. In the operating mode, the working volume of the feed pump was regulated by adjusting the stroke of the pneumatic cylinder depending on the required engine power.

The pneumatic actuator of the feed pump and pneumatic actuators of the engine valves used compressed air at 7 - 9 bar pressure from the laboratory net.
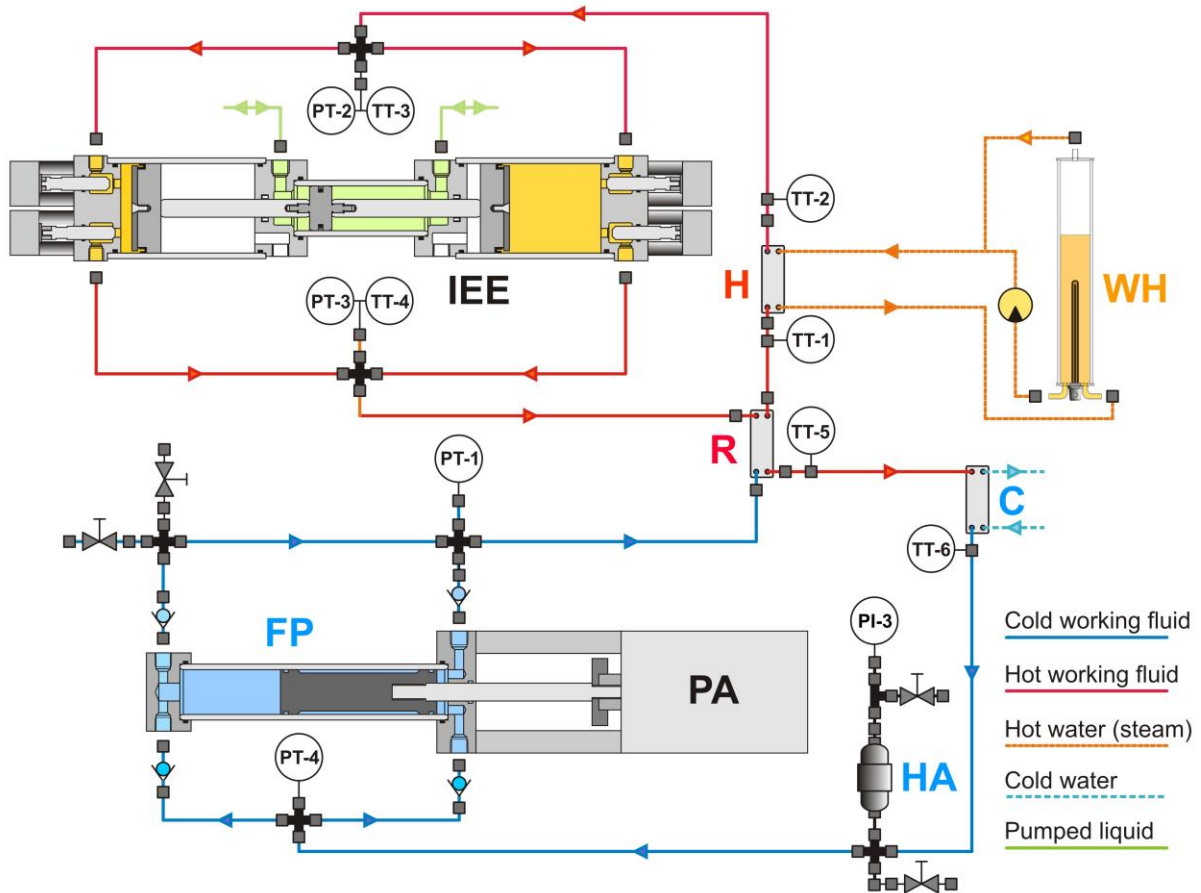
Figure 3. Scheme of the experimental setup

Figure 4. Engine-pump set-up

To generate electricity the hydraulic motor was connected to a 3-phase electric generator (Low Speed 600 W, 12V Gearless Permanent Magnet Generator AC Alternator Wind Turbine DIY). A DC electric load was connected via a full bridge rectifier. Electric power was measured through a digital volt-ammeter.

In experiments without electricity generation, engine power was measured by oil pressure drop and oil flow rate, which is proportional to the rotational speed of the hydraulic motor.

The pressures at the inlet and outlet of the engine and feed pump as well as the pressure of the pumped oil were measured by pressure transmitters PT (Sendo SS302 model, with 0.5% accuracy and 4 ms response time). Independently, the pressures were controlled by Empeo manometers with 1.6% accuracy installed in parallel with the pressure transmitters. The same manometer type was used to indicate the gas pressure in the hydraulic accumulator.

The working fluid temperature was measured using 1 mm shielded K-types thermocouples TT (accuracy ± 1.5 ºC), pre-calibrated in the range of 0 – 100 °C, and installed at the inlet and outlet ports of the heat exchangers and the inlet and outlet of the engine. The inlet and outlet temperature of heating and cooling water was measured with the same thermocouple type. All pressure transmitters have 4 – 20 mA output to avoid any influence of cable lengths. The signal from the transmitters was processed and displayed using a 12 bits PicoLog 1012 data acquisition system with a 10 ms sampling interval. The temperatures were measured using a TC-08 DataLogger with a 100 ms sampling interval.

Refrigerant R134a (T_{crit} = 101.08 °C, p_{crit} = 40.6 bar) was used as working fluid of the engine. This working fluid is not optimal for achieving the highest efficiency. It is also not attractive as it is a greenhouse gas (Global Warming Potential 1430). It was selected from several other

potentially applicable working fluids for safety reasons (low flammability, chemically stable) for the first engine testing only. The total amount of working fluid (R134a) filled into the system was 1.5 – 2.5 kg. There was no noticeable effect of the amount of working fluid on the operation of the engine in this range. Hot water, heated by a 24 kW electric heater, was pumped through the heat exchanger **H**, providing the heat supply. Cold tap water with temperature of 12 °C was supplied to the cooler **C**. The flow rate of the hot water pumped through the heater was 30 L/min and the flow rate of the cold water flowing through the cooler was 20 L/min. From multiple heat exchangers available on the market, three brazed plate heat exchangers (heater **H**, recuperator **R**, and cooler **C,** Figure 3) produced by company SWEP were selected. The main characteristics of the heat exchangers are presented in **Table 1**. All these units are certified to meet 45 bar maximum pressure at 135 $^{\circ}$C temperature. The heat loads and flow rates indicated in the table were used when selecting heat exchangers. In experiments, these parameters varied over a wide range.

Table 1. Specifications of the heat exchanger

Heat exchanger	Heat transfer surface, m^2	Number of plates	Number of channels per pass	Total volume, L
Heater: B25THx30/1P	1.76	30	14 (R134a) 15 (water)	1.55 (R134a) 1.66 (water)
Recuperator: B10THx20/1P	0.558	20	9 (low p) 10 (high p)	0.55 (low p) 0.61 (high p)
Cooler: B25THx40/1P	2.39	40	19 (R134a) 20 (water)	2.11 (R134a) 2.22 (water)

The main variables were: temperature of the hot water (30 to 80°C), frequency of the operation (0.1 – 1.0 Hz), pressure drop of the pumped oil (low and high cycle pressures) controlled by the engine load.

Discussion and Results

For testing and adjustment of the test setup components some preliminary, non-thermal measurements were made at room temperature. Mechanical functionality of the engine-pump was tested using compressed air in the range of 7 - 9 barg pressure as the driving agent for the pistons. These experiments helped to evaluate and reduce friction losses in seals and fluid-mechanical losses in pipes and valves.

The following figures show examples of pressure and temperature changes in different engine-pump parts in the case of low frequency operation of 0.30 – 0.35 Hz. In these examples the pumped oil flow rate was 3.5 – 4.0 L/min at a pressure drop of 6 - 60 bar.
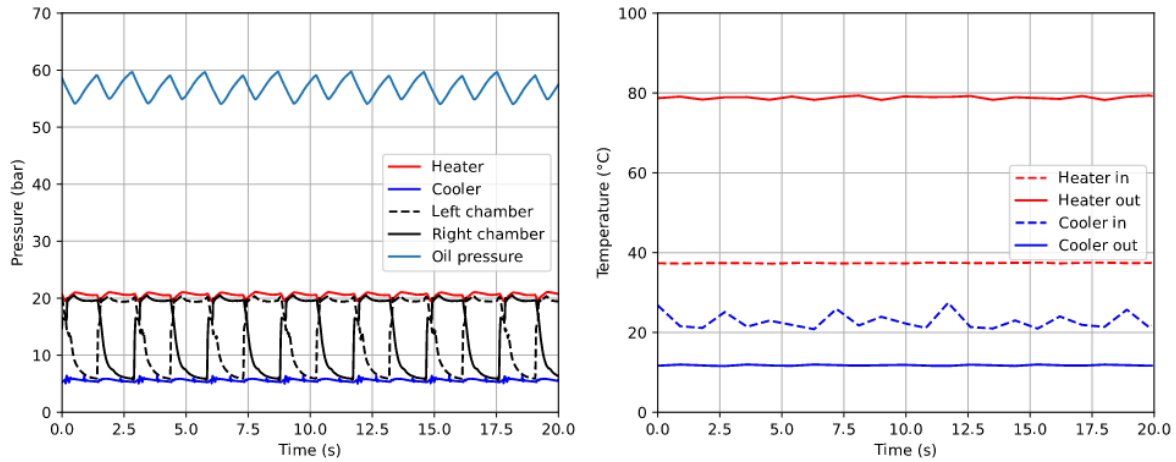
Figure 5. Pressure (left) and temperature (right) changes in the engine-pump parts for heat source temperatures of 80 ºC.
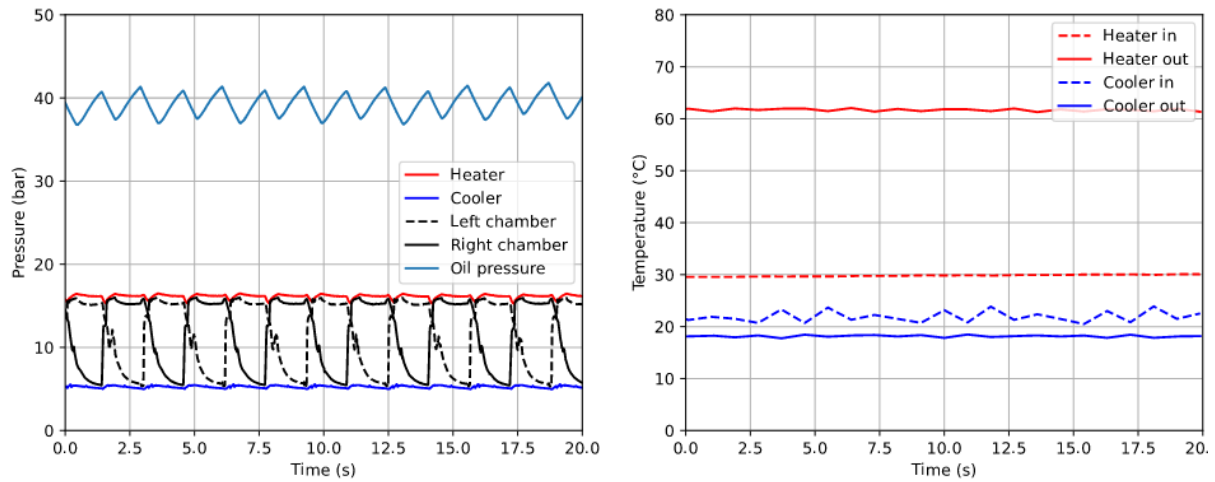
Figure 6. Pressure (left) and temperature (right) changes in the engine-pump parts for heat source temperatures of 60 ºC.
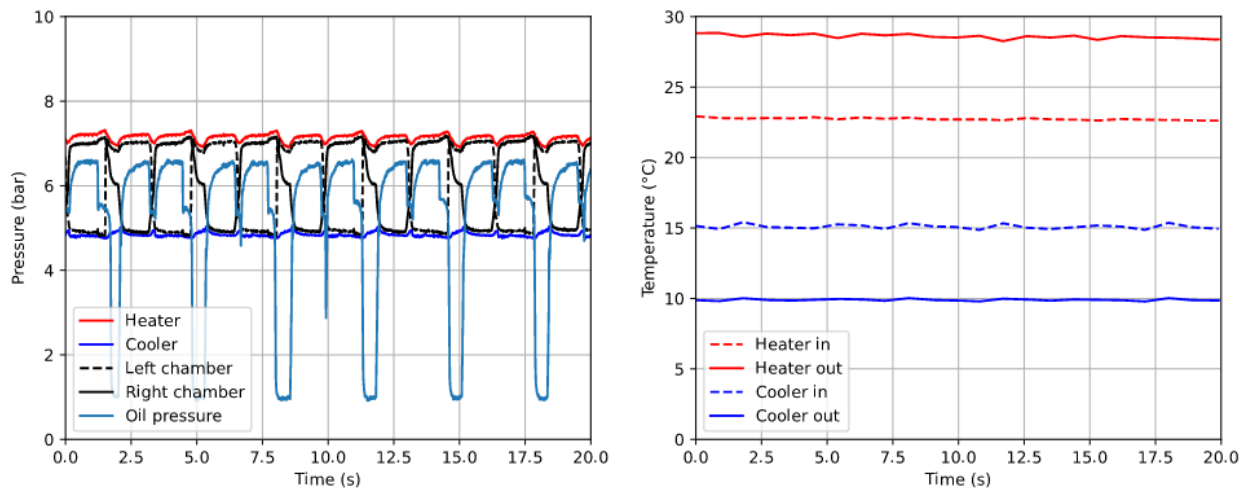
Figure 7. Operation of the setup at extremely low temperature difference.

The hydraulic accumulator, Figure 1, was not adjusted for the lowest temperature operation meaning oil pressure could not be maintained between strokes. However stable operation of the setup is shown to be possible at a temperature difference as low as 18 °C. Increasing engine speed to 1 Hz would constitute a power output of 200 W.

The pressure differences generated by the engine-pump were in the range of 6 – 60 bar, and generated electric power of 35 – 410 W at an operating frequency of 0.3 – 0.35 Hz.

The differential piston principle used in the engine-pump is shown to be able to generate any pressure of the liquid to be pumped. The hydraulic output can be also converted to shaft power/electricity turning the pump into a heat-to-power converter.

Summary/Conclusions

The preliminary outcomes from the experiment are encouraging, reaffirming the anticipated benefits of the IE engine-pumps. This innovative engine showcases remarkable efficiency at low temperature differences, demonstrating its potential applications in electricity generation and powering various rotational equipment. Particularly noteworthy is its ability to effectively harness abundant low-grade heat sources with temperatures below 100°C, a feature that can significantly broaden its usability. A robust and economic integration with hydrogen LT-PEM fuel cells or electrolyser technology is possible. Internal combustion engines also present an opportunity for increasing their thermal efficiency by using IE engines in their waste heat streams.

The engine's efficiency remains high even at extremely low heat source temperatures. In this temperature range conventional heat conversion technologies prove impractical. This characteristic underscores the robustness and adaptability of these uncomplicated yet highly efficient machines, making them a promising avenue for maximizing energy utilization from prevalent low-temperature heat sources.

Acknowledgments

References

[1] Glushenkov, M., Kronberg, A., Knoke, T., Kenig, E. Y. Isobaric Expansion Engines: New Opportunities in Energy Conversion for Heat Engines, Pumps and Compressors, *Energies*, 11(1), 154, 2018.

[2] Glushenkov, M., Kronberg, A. Experimental study of an isobaric expansion engine-pump – Proof of concept. Applied Thermal Engineering, 212 (2022), 118521. https://doi.org/10.1016/j.applthermaleng.2022.118521.

[3] Van der Kooij, B. The Invention of the Steam Engine, Delft: University of Technology. Delft., 2015.

[4] IE engine pump in ECT's laboratory (video): https://www.chester-project.eu/news/ie-engine-pump-in-ects-laboratory-video.

Alternating operation of a façade-integrated adsorption chiller for continuous cooling of lightweight buildings

O. Boeckmann[1*] and M. Schaefer[1]

[1]University of Stuttgart, Pfaffenwaldring 31, 70569 Stuttgart, Germany

[*]Corresponding author: boeckmann@igte.uni-stuttgart.de

Abstract

Due to its high demand for resources and energy, the building sector accounts for almost 40% of the global carbon dioxide emissions. Therefore, in order to achieve the ambitious climate protection goals, it is essential to reduce the required amount of building material in the construction of future buildings as well as to operate these lightweight buildings more energy efficiently or, if possible, energy self-sufficiently. Against this background, a novel, façade-integrated adsorption system for solar cooling of lightweight buildings is being developed and experimentally investigated within the Collaborative Research Centre 1244 "Adaptive skins and structures for the built environment of tomorrow" at the University of Stuttgart. The proposed adsorption system combines the functionality of energy storage and cold production, with minimum occupation of inner building space.
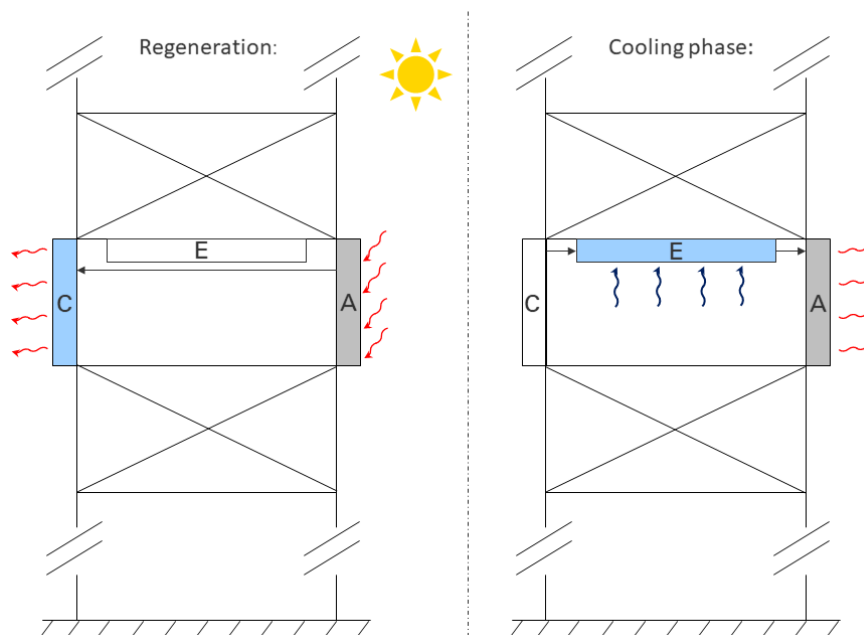
Figure 1: Design scheme and operating principle of the façade-integrated adsorption chiller

The adsorption system consists of the three components adsorber, condenser and evaporator, refer to Figure 1. The adsorber and the condenser are integrated as panel-shaped elements into the building façade. The particular challenge lies in the efficient absorption of solar irradiation by the adsorber during the regeneration phase and the sufficiently high heat release to the ambient during cooling operation. The evaporator is installed as a cooling ceiling in the building. For cooling, the evaporator is connected to the adsorber, whereby the cooling power can be controlled by throttling the vapor mass flow.

For the computational development of the system, detailed component models are created for the three main components, which are coupled by the vapor flow. Simulations of the

components are carried out under realistic boundary condition. The component models describe the internal heat and mass transfer processes as well as the adsorption and condensation/evaporation processes. The simulation of a reference case confirms the general functionality of the proposed cooling system and a broad parameter study provides information about possible optimization to increase the cooling rate and cooling capacity. The compass orientation of the adsorber façade elements, the surface area ratios of the components and the design of the adsorber are identified as promising optimization parameters. Based on these results, a best-case configuration is identified that reveals cooling rates up to 150 W/m².

In order to achieve continuous cooling power throughout the day, an additional adsorber is integrated into a façade with different compass orientation. An alternating operating mode with one adsorber being regenerated while to other supplies cooling power is successfully deployed. Furthermore, it is shown that a realistic cooling demand can be covered for most of the day applying this alternating operation mode as it is shown in Figure 2. Finally, active shading of the adsorbers is studied in order to achieve more flexible cooling power.
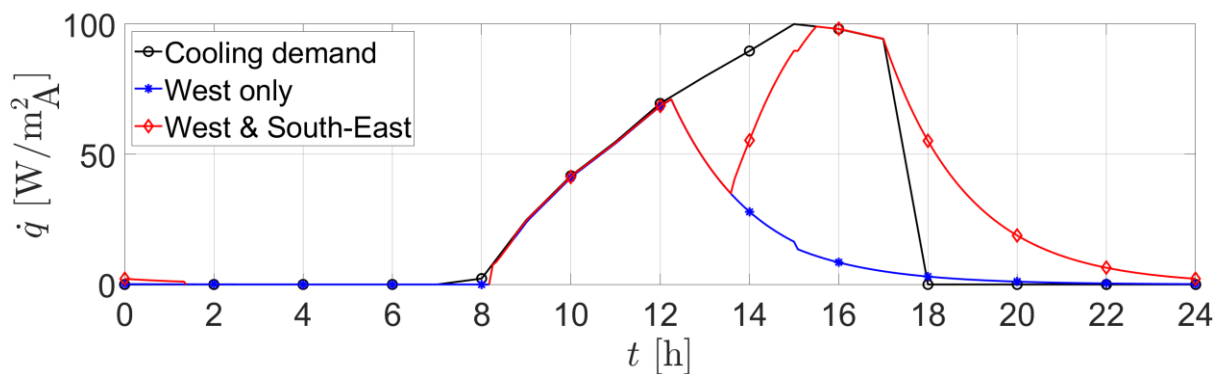
Figure 2: Simulation results of the alternating operation mode for a realistic cooling demand

This work introduces the working principle, describes the alternating operation mode and presents the simulation results of the alternating operating mode for continuous cooling as well as for a realistic cooling demand.

Stability of adsorbent coatings for open-cycle adsorption processes

A. Freni[1]*, E. Mastronardo[2,] S. De Antonellis[3], E. Bramanti[1], L. Calabrese[2,1]

[1] CNR ICCOM - Institute of Chemistry of Organometallic Compounds, Pisa, Italy

[2] Department of Engineering, University of Messina, Messina, Italy

[3] Department of Energy, Politecnico di Milano, Milano, Italy

*Corresponding author: angelo.freni@pi.iccom.cnr.it

Abstract

Aim of this work is to apply a protocol of different characterization techniques to evaluate the stability of novel silica gel/polymer- based coatings developed for open-cycle air dehumidification. Specifically, the following aging conditions have been applied: i) repeated ad/desorption under real operating conditions (open cycles); ii) post-curing at 30, 40 and 60 °C; iii) immersion in water for 30 days; iv) aging in salt-fog chamber for 30 days, v) accelerated aging by wet/dry cycles. Characterisation of fresh and aged samples has been carried out by X-Ray diffraction, Scanning Electron Microscopy (SEM) and Fourier-Transform Infrared spectroscopic analyses. Additionally, mechanical strength has been verified by tensile test.

Keywords: Adsorbent coatings, open-cycle adsorption process, stability verification.

Introduction/Background

Currently, relevant research activities have been focused to develop coated adsorbent heat exchangers for sorption systems. However, for practical utilization of this technology, strict reliability requirements are necessary: i) high hydrothermal stability against repeated cycling over the expected lifetime; ii) high mechanical stability during operation and transport phases; iii) no corrosion issues; no release of inert gases upon repeated ad–desorption cycling, especially for coatings based on polymers. Accordingly, verification of mechanical and hydrothermal stabilities is a key-issue [1-2]. Indeed, the adsorbent coating is normally subjected during its lifetime to repeated ad/desorption processes as well as thermal cycling, which could in principle cause degradation of mechanical and adsorption properties, thus limiting the reliability of the technology. Moreover, the adsorbent material could incidentally be subjected to unexpected conditions such as exposure to liquid (salt) water, mechanical/thermal shock etc. Accordingly, in this work we propose a protocol of different characterization techniques to evaluate the stability of novel silica gel/polymer- based coatings developed for open-cycle air dehumidification and subjected to various aging conditions. Details on the adsorbent coatings preparation procedure and its preliminary testing in a lab-scale prototype are reported in [3]. Specifically, the adsorbent coatings have been subjected to the following aging conditions: i) repeated ad/desorption under real operating conditions (open cycles); ii) post-curing at 30, 40 and 60 °C under dry conditions; immersion in water for 30 days; aging in salt-fog chamber for 30 days, aging with Wet/Dry cycles. Structural characterisation of fresh and aged samples has been carried out by X-Ray diffraction, Scanning Electron Microscopy (SEM) and Fourier-Transform Infrared spectroscopic analyses. Mechanical strength has been verified by tensile test.

Discussion and Results

Repeated ad/desorption tests have been carried out by a thermo-gravimetric adsorption apparatus (Aquadyne DVS analyzer) available at POLIMI lab. The instrument allows the measurement of adsorption isotherms by supplying a dry/wet carrier gas. The aging process consisted of 100 repeated ad/desorption cycles. For each cycle, the sample was kept 30 minutes at T=45°C and RH=80 % and 30 minutes at T=45°C and RH=5%, which allowed to apply on the sample a large water uptake variation ($\Delta w \sim 30$ wt.). Next Fig.1 refers to a sample currently under test and shows the water content and relative humidity profiles during several ad/desorption cycles. It is evident that, for this specific sample water adsorption capacity is unchanged after many cycles, so there is no evidence of performance degradation.
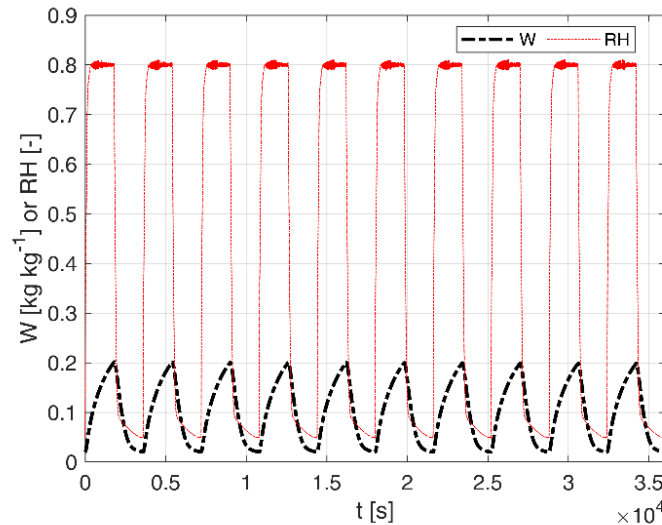
Fig. 1. Water content and relative humidity profiles during repeated ad/desorption aging cycles.

The post-curing aging treatment was carried out at 30 °- 60°C under dry conditions. Fig. 2 shows the mechanical strength of aged samples measured by tensile test. The results obtained indicate that, despite the quite large error bar due to the not homogeneous adsorbent layer composition, the strength increases at increasing curing temperature. This effect is probably due to polymerization of the organic component of the binder.
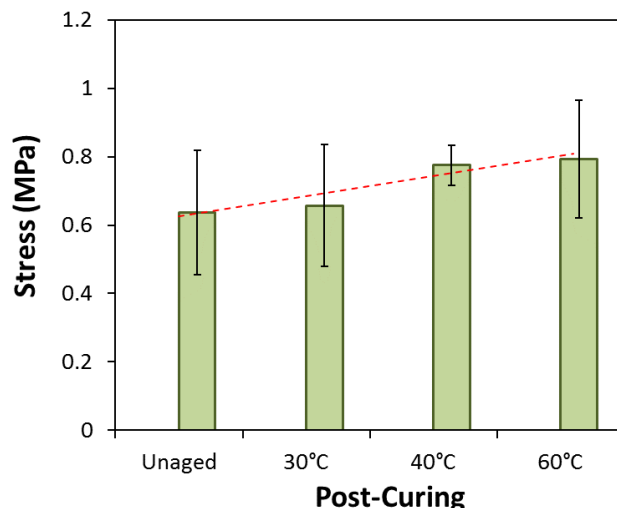
Fig. 2. Tensile strength of samples subjected to post-curing at different temperatures.

Accelerated aging by wet/dry cycles was carried out by a self-made apparatus subjecting each sample to a spraying of liquid water (15 min) and a subsequent drying by a thermoelectric cell (15min at 40°C and 60°C). Tensile strength measurements indicate that the coupled wet-dry cycles at 40°C have a soft degradative effect, compared to post-cured one. On the contrary, the coupled wet-dry cycles at 60°C degrade significantly the material. Immersion tests were carried out by keeping the samples in distilled water for 30 days at ambient temperature and then drying for long time (up to 1000 hours). Tensile strength measurements were carried at different drying times putting in evidence a relevant collapse of mechanical performance. Finally, samples were subjected to a 1-month long continuous spray of salt-fog at controlled temperature (37°C) and very high humidity (RH=98%) by a salt-fog chamber available at UNIME. Mechanical characterization of aged samples indicated a slight degradation effect for low drying time and a mechanical strength similar to post-cured samples for long times..

Summary/Conclusions

In this work we proposed a protocol of different characterization techniques to evaluate the stability of novel silica gel/polymer- based coatings developed for open-cycle air dehumidification. Preliminary characterization results indicate that the combination of the proposed techniques can be effectively employed to verify the occurrence of degradation processes due to aging.

References:

[1] A. Freni, A. Frazzica, B. Dawoud, S. Chmielewski, L. Calabrese and L. Bonaccorsi, Adsorbent coatings for heat pumping applications: verification of hydrothermal and mechanical stabilities, Applied Thermal Engineering, 50, 1658-1663, 2013.
[2] A. Frazzica, V. Brancato, Verification of hydrothermal stability of adsorbent materials for thermal energy storage, International Journal of Energy Research 43 (12), 6161-6170, 2019.
[3] S. De Antonellis, E. Bramanti, L. Calabrese, B. Campanella, A. Freni, A novel desiccant compound for air humidification and dehumidification, Applied Thermal Engineering, 214, 118857, 2022.

An air-charged Stirling-cycle refrigerator with novel isothermalisers

Jafar M. Daoud[1, *] and *Daniel* Friedrich[2]

[1]College of Engineering and Technology, Palestine Technical University-Kadoorie (PTUK), Palestine
[2]Institute for Energy Systems, School of Engineering, University of Edinburgh, EH9 3DW (Scotland)
[*]Corresponding author: j.daoud@ptuk.edu.ps

Abstract

While the Stirling cycle is a simple thermodynamic cycle, energy dense machines are expensive and complex due to the complicated heat exchangers. Heat exchangers are essential to increase the heat transfer but they increase the dead volume, cost and pumping losses. In this contribution, a simple and novel isothermaliser is proposed that improves the cooling power density of the Stirling-cycle refrigerator without adding to the dead volume. Simulations based on the second order polytropic model show that the cooling power and efficiency can be enhanced and the regenerator losses can be significantly reduced. The novel isothermaliser leads to better performance than the conventional Stirling refrigerator at temperatures of 27/7° C achieving higher cooling density per swept volume of 2.5 folds. The increased power density enables the Stirling refrigerator to compete with the vapour compression cycle in both high-lift and near-ambient refrigeration.

Keywords: Stirling cycle, Near-ambient refrigeration, Isothermalisers.

Introduction

The Vapour compression cycle (VCC) is the most widely used refrigeration technology for the near ambient market because it has the highest COP among other cooling technologies [1][2][3]. However, the refrigerants used with the VCC are often non-environmental-friendly since they are considered toxic, flammable, have ozone depletion potency and can participate in global warming. An alternative is the Stirling cycle refrigerator which is simple, has safe and quiet operation, low maintenance requirement, high theoretical efficiency and uses benign gases. It is a good competitor to the VCC in high-lift refrigeration where it achieves better performance and is also cheaper. The performance reaches a peak for an absolute temperature ratio around two in only one stage of refrigeration [4] for which, the performance of the VCC deteriorates [5]. Although, the ideal Stirling cycle has higher COP than the inverse Rankine cycle [66] the Stirling cycle refrigerator has not been successful at low lift refrigeration. The practical Stirling refrigerator lags behind the VCC as its cooling capacity decreases with the COP [6]. The Stirling refrigerator can achieve the efficiency of the VCC at a given cooling load but it is not cost-competitive [7]. Walker et al. doubted that the Stirling cycle refrigerator can compete economically with the VCC refrigerator due to the large number of VCC units produced every year [8]. In contrast, only few Stirling refrigerators are available for limited applications due to their initial and running costs [9]. Berchowitz et al. developed a free piston refrigerator for domestic refrigeration [10] and portable coolers [11][12]. The refrigerator showed a total efficiency of 35% of Carnot efficiency, which is

---

[*]Corresponding author: j.daoud@ptuk.edu.ps

3rd to 6th of September 2023
The University of Edinburgh, Scotland

Heat Powered Cycles
Conference 2023
Edinburgh
Heat in the new energy system

comparable to the VCC. The portable coolers are powered by a PV collector and have a COP of three while the Carnot COP is 9.1. Oguz and Ozkadi [13] tested the free piston Stirling refrigerator for domestic refrigeration and showed that the main challenge is using complicated heat exchangers. Thus, the Stirling cooler can be an alternative to the VCC if the cost and complexity of the heat exchangers is reduced while maintaining the performance.

The Stirling cycle is an external combustion cycle that needs to convey heat from the working gas to the heat source via heat exchangers. Efficient heat exchangers enhance the heat transfer to achieve high refrigeration rates but at the cost of increasing the complexity, dead volume, power losses and machine price [14][15]. The expansion and compression volumes are usually unheated and their operation tends to be adiabatic. Walker [16] reported that the actual COP ratio of the Stirling cycle refrigerator due to the adiabatic cycles has a maximum absolute temperature between 100-150K. Bauwens [4] showed numerically that the adiabatic losses play the major role in decreasing the COP ratio at low-lift refrigeration which is hard to improve without decreasing the refrigeration load. Carlson et al. [17] showed the adiabatic cycle efficiency at low-lift refrigeration tends to less than 50% of the isothermal efficiency and the cooling power decreases for non-ideal adiabatic processes. Walker [16] suggested isothermalising the freezers and coolers as they are designed to maximise the heat transfer. Orlowska [18] suggested adding the isothermaliser in particular to the compression space to improve the COP of a refrigerator. The isothermalisers differ from the external heat exchangers in that they are within the expansion and compression spaces and not in series with them. Accordingly, the expansion and compression processes are neither isothermal nor adiabatic, but polytropic. The polytropic cycle cannot achieve Carnot efficiency for both the Stirling power cycle and heat pump. For example, at the maximum power point, the engine efficiency cannot exceed the Curzon and Ahlborn limit [19] where the working gas temperature is not equal to source temperature. The temperature difference causes irreversibility but helps to increase the heat transfer and hence reduce the gas friction losses. On the other hand, Stirling cycle refrigerators have no maximum cooling power due to the monotonic response of the cooling power to the COP [20][21][22]. Leff and Teeters [23] attributed the monotonic response to possible unbounded temperatures in contrast to the engine that works between two limits. Thus, the Carnot efficiency can be ideally approached when the cooling power is zero and the COP approaches zero for the highest cooling power. However, due to the potential Stirling refrigerator losses, the maximum COP and maximum cooling power might be reached [5][24].

Daoud and Friedrich [25] proposed a novel machine geometry for conveying the heat by the cylinder wall instead of only the end plates. Thus, the Stirling cycle machine benefits from the whole surface of the cylinders and the temperature difference between gas and containing cylinders to transfer heat. In the Franchot arrangement, the conduction and shuttle losses, which are the major thermal loss in the Stirling cycle machine [5][26], are eliminated and the hysteresis losses can be ignored. In a later publication [27], the same authors innovated a new isothermaliser specially tailored for the direct heating and cooling purpose without any intermediate heat exchanger. The isothermalisers resulted in power improvements and reduction in volumetric flow rate. This work is an extension of our previous studies to Stirling refrigeration. It is a theoretical study based on the second-order polytropic model [25] which aims to obtain the performance curves of the isothermalised Franchot refrigerator by varying the phase angle, dead volume, cylinder diameters and the speed. Both, the bare cylinder and isothermalised cylinder are considered and the performance is evaluated for a speed range of 100-500 RPM.

Methodology

The proposed isothermaliser for the Franchot machine is shown in Figure 1. The Franchot machine was invented in 1885. It comprises two opposite alpha Stirling machines each with a distinct gas circuit but both share the same cylinders. The Franchot machine has no shuttle and axial heat conduction losses and the phase angle is controllable. The connecting rod can work as an adiabatic or isothermal fin causing the hydraulic diameter to decrease which increases the heat transfer and decreases the swept volume. The adiabatic fin refers to unheated or uncooled connecting rod whilst the isothermal fin refers to the rod having the same cylinder temperature. The isothermal fins have potential in air conditioning since the expansion cylinder can be directly exposed to the refrigerated space and the compression cylinder can be directly exposed to the ambient. The rod itself can be hollow to reduce its weight and heat capacity.
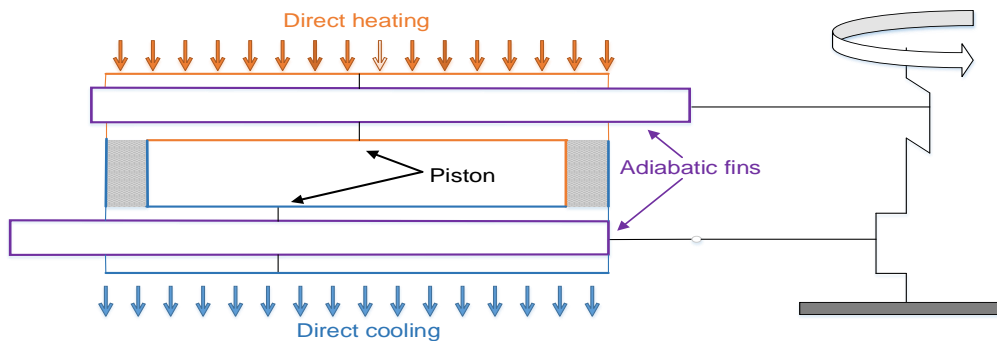
Figure 1: The proposed adiabatic fins inside the Franchot engine cylinders [27].

The heat addition and removal is calculated from Newton's law of cooling

$$\dot{Q}_e = hA\Delta T \qquad\qquad 1$$

The in cylinder heat transfer coefficient h is given by the correlations [28]

$$h_e = 0.042(D-d)^{-0.42}v^{0.58}p^{0.58}T^{-0.19}$$
$$h_c = 0.0236(D-d)^{-0.47}v^{0.53}p^{0.53}T^{-0.11} \qquad\qquad 2$$

where D and d are the diameters of the cylinder and rod, e and c are expansion and compression, respectively. According to the definition, the adiabatic fin, which is externally insulated, has a total heat flow equal to zero

$$\oint \dot{Q}_f = \oint hA_f\big(T_f - T_g\big) = 0 \qquad\qquad 3$$

where h, A_f, T_f and T_g are the coefficient of heat transfer, fin area, fin temperature and gas temperature, respectively. The fluctuation in the connecting rod temperature is ignored because of the higher heat capacity of the stainless-steel rod in comparison to air. Hence, the fin temperature is supposed to be constant during a cycle. So, the average temperature of the adiabatic fin can be calculated as

$$T_f = \frac{\oint hA_f T_g}{\oint hA_f} \qquad\qquad 4$$

The Franchot engine consists of two alpha engines with two separate gas circuits. The pressure variation in each gas circuit is [25]

$$\dot{p} = \frac{-p\left(\frac{\dot{v}_e}{T_{re}} + \frac{\dot{v}_c}{T_{cr}}\right) + \frac{R}{c_p}\left(\frac{\dot{Q}_e}{T_{re}} + \frac{\dot{Q}_c}{T_{cr}}\right)}{\frac{v_e}{\gamma T_{re}} + \frac{V_r}{T_r} + \frac{v_c}{\gamma T_{cr}}} \qquad 5$$

Regenerator end temperatures are calculated from

$$T_{rh} = \frac{-\oint i\dot{m}_e T_e}{\oint(1-i)\dot{m}_e}$$
$$T_{rk} = \frac{-\oint j\dot{m}_c T_c}{\oint(1-j)\dot{m}_c} \qquad 6$$

where the parameters i and j are given by

$$i = \begin{cases} 1, & \dot{m}_e < 0 \\ 0, & \dot{m}_e \geq 0 \end{cases}$$
$$j = \begin{cases} 1, & \dot{m}_c < 0 \\ 0, & \dot{m}_c \geq 0 \end{cases} \qquad 7$$

The average regenerator temperature is

$$T_r = \frac{T_{rh} - T_{rk}}{\ln\frac{T_{rh}}{T_{rk}}} \qquad 8$$

The average engine power for the Franchot engine is calculated as

$$P = 2 * f \oint p(\dot{v}_e + \dot{v}_c) \qquad 9$$

where f is the frequency. The pressure loss in the expansion and compression cylinders is calculated separately from the Zhao correlation for oscillatory turbulent pipe flow [29]:

$$\Delta p = -\frac{2\rho U_{max}^2 L}{X_m}\left(\frac{76.6}{(\frac{2D_h Re_{max}}{X_m})^{1.2}} + 0.40624\right) \qquad 10$$

The power loss in each cylinder is calculated from

$$P_p = \Delta p * \dot{v} \qquad 11$$

where $\dot{v}$ is the volumetric flow rate of the working gas.

The polytropic model is applied to the alpha type engine with annular heat exchanger made by Karabulut [30]. The annular heat exchanger has the cylinder walls heated and the piston dome is of adiabatic fin type as shown in Figure 2.
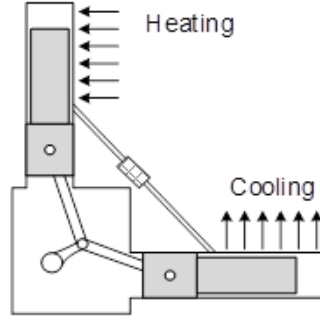
Figure 2: Karabulut alpha engine with annular heat exchangers: schematic diagram [30].

In the Karabulut engine, the heat exchanging area and volume are constant for the annulus and dynamic for the swept space. These conditions are replicated in our model for validation purpose. The technical specification of the engine is shown in Table 1.

Table 1: Technical specifications and operating conditions of the Karabulut engine [30].

Name	*value/unit*
Stroke length	*6 cm*
Bore diameter	*5.24 cm*
Piston dome diameter	*4.74 cm*
Hot annulus length	*13.5 cm*
Cold annulus length	*11 cm*
Connecting pipe length	*30 cm*
Connecting pipe diameter	*0.5cm*
Regenerator matrix	*Woven wire*
Wire diameter	*100 micron*
Regenerator porosity	*0.7*
Regenerator volume	*12 cm³*
Out-of-Phase angle	*90°*
Hot, cold temperatures	*1100°C ,20°C*
Working gas	*Air*
Average gas pressure	*1 bar, 2 bar*

To increase the accuracy of the model the reheat and pressure losses of the regenerator are considered. The effect of imperfect regeneration is considered by modifying the regenerator gas stream temperatures as [31][32]

$$T_{rho} = T_{rk} + \varepsilon(T_{rh} - T_{rk})$$
$$T_{rko} = T_{rh} - \varepsilon(T_{rh} - T_{rk})$$
$$\qquad 12$$

where, T_{rho}, T_{rko} and ε are the hot outlet gas temperature, cold outlet gas temperature and regenerator effectiveness, respectively. The enthalpy loss can be quantified by

$$\dot{Q} = c_p \dot{m} \Delta T (1 - \varepsilon) \qquad 13$$

The effectiveness is calculated according to Tanaka [33] by

$$\varepsilon = \frac{Ntu}{Ntu + 2} \qquad 14$$

where Ntu is the number of transfer units and calculated from

$$Ntu = \frac{4\overline{Nu}L_r}{P_r \overline{R_e} d_h} \qquad 15$$

where $\overline{Nu}, P_r, \overline{R_e}$ and d_h are the average Nusselt number, Prandtl number, average Reynolds number and regenerator hydraulic diameter, respectively. Nusselt number is correlated according to Tanaka as follows

$$\overline{Nu} = 0.33\overline{R_e}^{-0.67} \qquad 16$$

The pressure loss due to the gas friction with the regenerator material is calculated from

$$\Delta p_{loss} = -\frac{0.5 f_h \rho L_r U^2{}_{max}}{d_h} \qquad 17$$

where Δp_{loss} is the pressure loss and f_h is the friction factor calculated according to Tanaka from

$$f_h = 1.6 + \frac{175}{Re_{max}} \qquad 18$$

The pressure loss due to the connecting pipe is calculated as

$$\Delta p_{loss} = -\frac{2 f_{Re} \mu L_r U_{av}}{d_h} \qquad 19$$

where f_{Re} is calculated by [34]

$$f_{Re} = \begin{cases} 16 & Re < 2000 \\ 7.343 * 10^{-4} Re^{1.3142} & 2000 < Re < 4000 \\ 0.0791 Re^{0.75} & Re > 4000 \end{cases} \qquad 20$$

The mathematical model is applied to the Karabulut engine at a range of speeds and two pressures. The comparison between the polytropic model and experimental study is shown in Figure 3. The polytropic model has good agreement with the experimental results especially in predicting the trend of engine performance and location of the maximum brake power. The max relative error was calculated as +22% and +30% for the 1 and 2 bar data sets, respectively. Those errors can be attributed to the roughness of the experimental data, lack of data about gas leakage and mechanical friction.
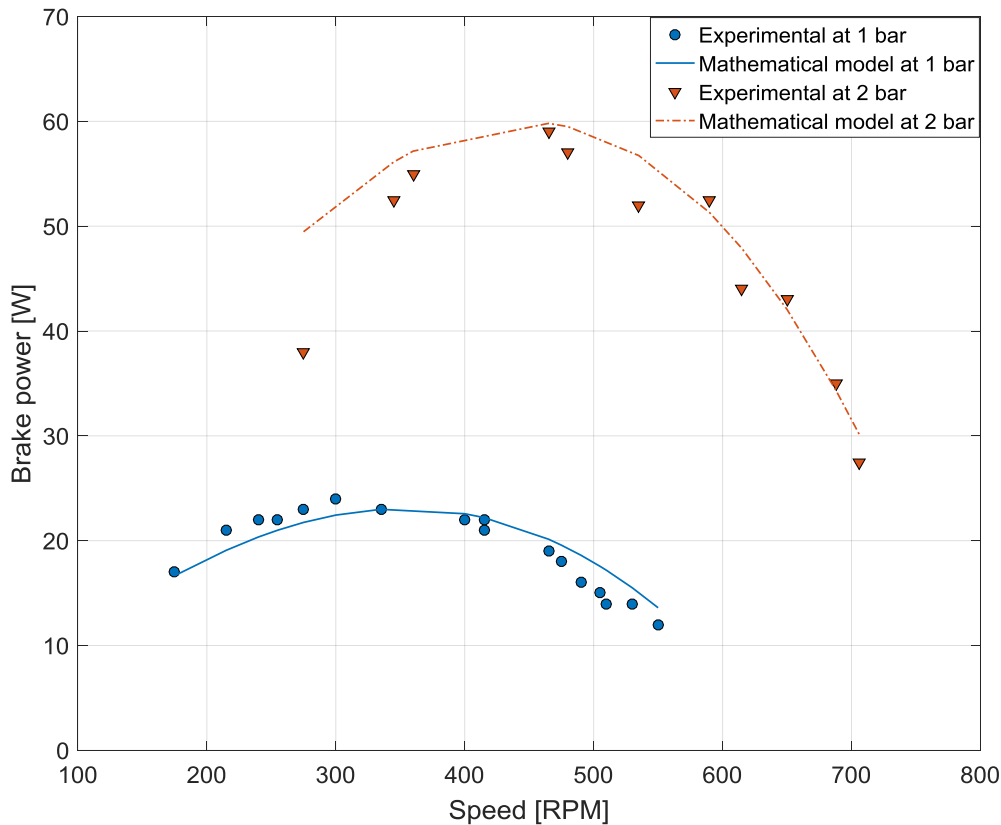
Figure 3: Comparison between the 3 control volume polytropic model with regenerator losses and experimental data of Karabulut alpha type engine [30].

The model is implemented in MATLAB/Simulink and solved using the Runge-Kutta method with a time step of 10^{-4}s. Since the refrigerator has a monotonic response, the parameters are taken from the optimised machine working as a prime mover [27]. The prime mover and the refrigerator have similar phase angle, speed, dead volume, stroke and geometry. All results use the reference machine parameters listed in *Table 2* unless otherwise stated.

Table 2: Parameters of the reference machine

Name	symbol	value/unit
Stroke length	L_e, L_c	50 cm
Bore diameter	D_e, D_c	5 cm
Charge gas density	ρ	1.225 kg/m³
Clearance length	re, rc	0.01 cm
Regenerator volume	V_r	0 cm³
Out of Phase angle	θ	90 degree
Hot, cold temperatures	T_h, T_k	450K/280 K,300 K
Working gas	Air	
Gas constant	R	287 J/kg.K

Discussion and Results

The isothermalised Franchot engine has its optimal performance at the maximum power point at which it reaches Curzon efficiency. On the other hand, the cooling power of the Franchot refrigerator depends on the COP. Hence, the performance of the refrigerator is given with reference to the engine. Figure 4 shows the optimised response of the system at the maximum power point for three different design parameters: phase angle for plain cylinder and diameter

for both adiabatic and isothermal fin. The optimisation was performed manually until the maximum power is reached for the speed range 100-500rpm. Every single speed, phase angle and connecting rod diameter were changed manually with a step size of 50rpm, 1 degree and 1mm, respectively. The step sizes are believed to be responsible for the roughness in the generated figures.
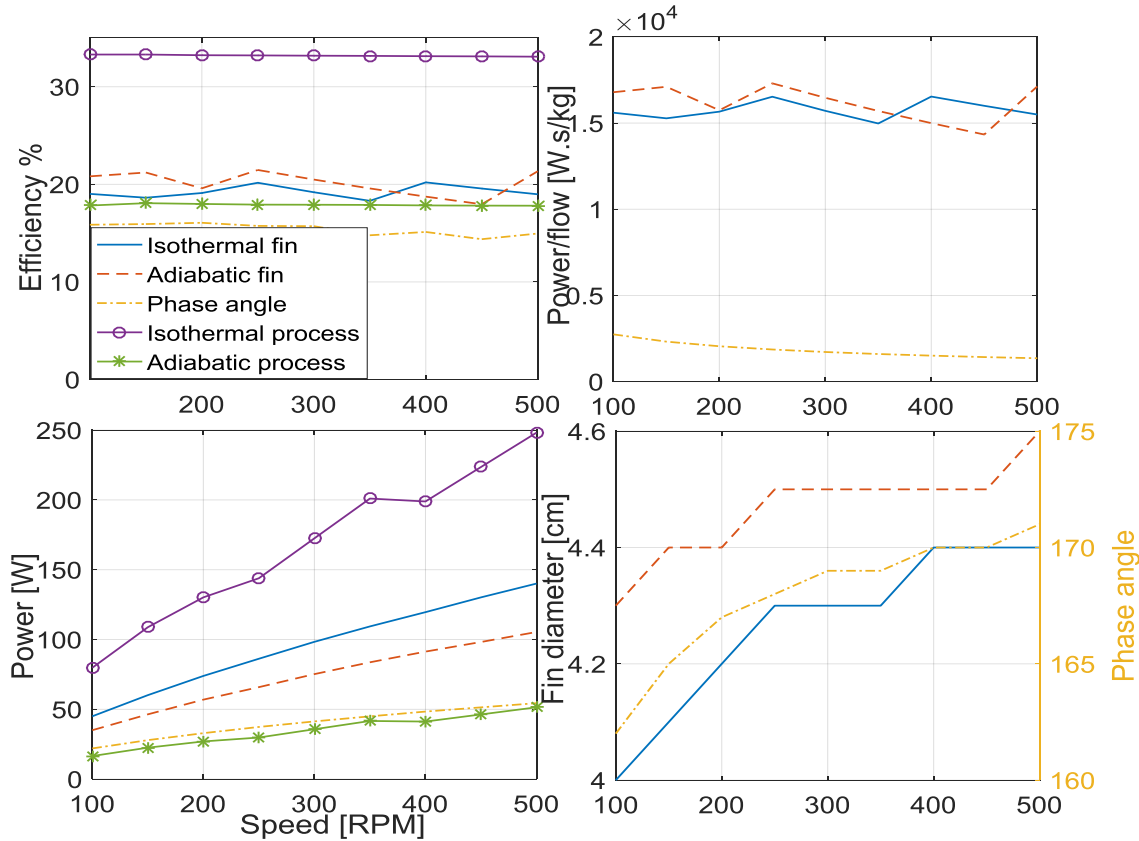
Figure 4: Optimised response based on the maximum power for the Franchot engine using adiabatic and isothermal fins and bare Franchot engine controlled by the phase angle [27].

It is shown that both the isothermal and adiabatic fins are superior to the phase angle control method in terms of power and efficiency. The engine with fins works closer to the Curzon efficiency at the maximum power than the phase angle method. In addition to that, the power obtained is higher for the isothermalised engine than the bare engine optimised by varying the phase angle since the fins increase the heat transfer and heat transfer area. In contrast, the adjustment of the phase angle only optimises the power for a given heat transfer.

It is also shown that optimal cylindrical fin size increases with speed. This is due to the nonlinear increase of the heat transfer in comparison to the swept volume. The fin diameter increases to compensate the increase in the heat required at higher speed by decreasing the hydraulic diameter. It is interesting that the diameter of the isothermal rod is smaller than that of the adiabatic rod, which eases sealing and reduces gas leakage. Most importantly, the bare engine produces much lower power to mass flow rate than the isothermalised engine, which increases regenerator losses. The power to mass flow rate of the isothermalised engine is fixed to a constant value by decreasing the swept volume with increasing speed.

The response of the novel refrigerator is shown in Figure 5 for three different design parameters: phase angle for plain cylinder and diameter for both adiabatic and isothermal fin. The response of the ideal isothermaliser that has ideal expansion and compression processes and the ideal adiabatic engine in which the heaters and coolers are isothermal and the expansion and compression are adiabatic is shown for comparison. Both the ideal isothermal and adiabatic refrigerators have the same swept volume as the isothermal finned design. The isothermal cycle refrigerator presents the maximum possible performance, which gives the Carnot COP.
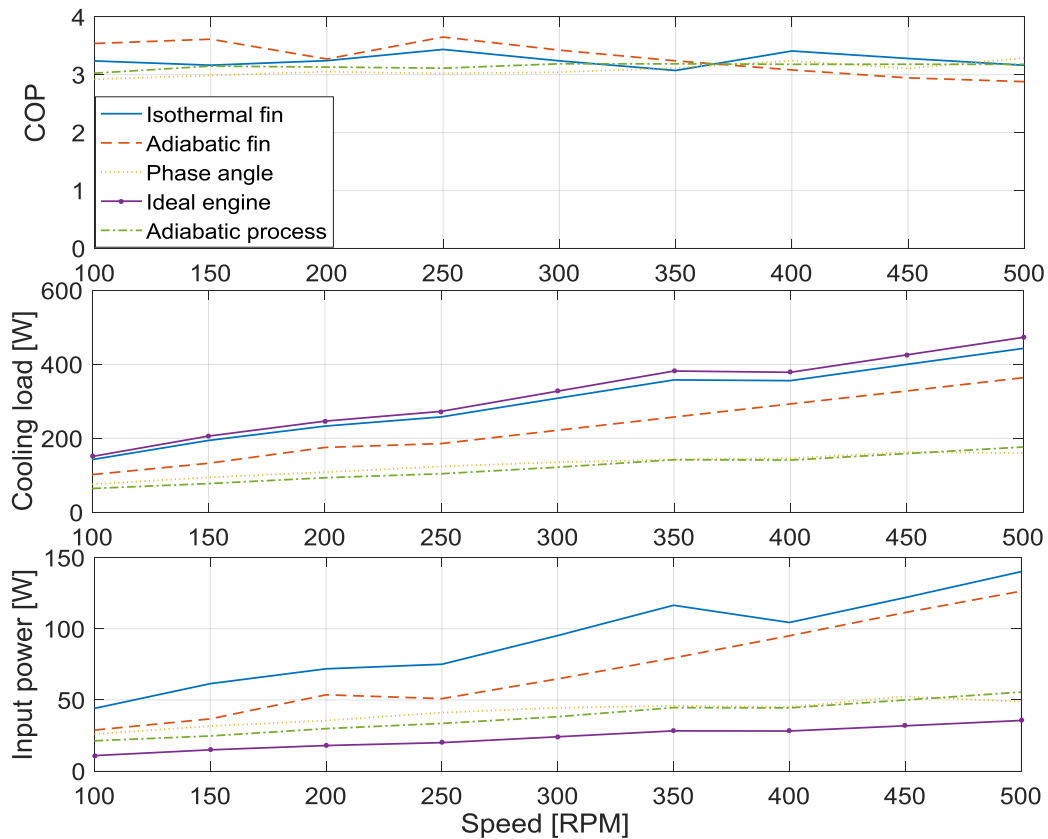
Figure 5: Response of the Franchot cycle refrigerator using adiabatic and isothermal fins and the bare Franchot refrigerator controlled by the phase angle. The response of the ideal refrigerator with isothermal expansion and with adiabatic expansion is shown for comparison.

Finned refrigerators are superior to the phase angle optimised refrigerators as they can achieve higher cooling power at a given efficiency. However, the input power consumed by the refrigerator is higher for the isothermal fin than the bare and adiabatic finned refrigerator. That is expected since the fins increase the heat transfer area and thus the heat transfer.

In comparison to the ideal isothermalisers, which have a COP of 14, the refrigerator with isothermal fins has slightly lower cooling power but has much lower COP. However, the ideal COP is unachievable. In this regard, the ideal adiabatic refrigerator has lower cooling power and efficiency than both the isothermal and adiabatic finned refrigerator at nearly the same COP. On average, the isothermal and adiabatic finned refrigerators have 2.5 and 1.9 times the cooling power of the ideal adiabatic refrigerator at COP of 3.25 and 3.29, respectively. The isothermal and adiabatic finned refrigerator can have an average cooling power of 94% and 72% of the ideal refrigerator. Interestingly, the refrigerators consumed power is comparable to the generated power by the prime mover of the same geometry.

Hence, a duplex engine configuration where the prime mover powers the refrigerator would be suggested for near ambient cooling and medium temperature heat activation.

For near ambient refrigeration, the isothermal finned engine has a COP range comparable to that of the VCC as shown in Figure 6. Thus, the polytropic cycle has greater potential compared to the adiabatic cycle for near ambient cold production. Increasing temperature ratio (ratio of ambient to load temperature) causes the prime mover to speed up hence eventually will reach a steady operation point. On the other hand, decreasing the load temperature increases the required power and hence the engine is anticipated to decelerate. The COP ratio which is the actual COP to Carnot COP reaches zero at load temperature equal to the ambient temperature although the COP is at the maximum. The reason for this is that the gas temperature in the polytropic engine needs to be different from the wall temperature for the heat transfer to take place while the temperature difference in the ideal machine is zero. The improvement in the power density of the polytropic cycle with simple isothermalisers can lead to price reduction and hence can make the Stirling cycle cooler more competitive with the VCC.
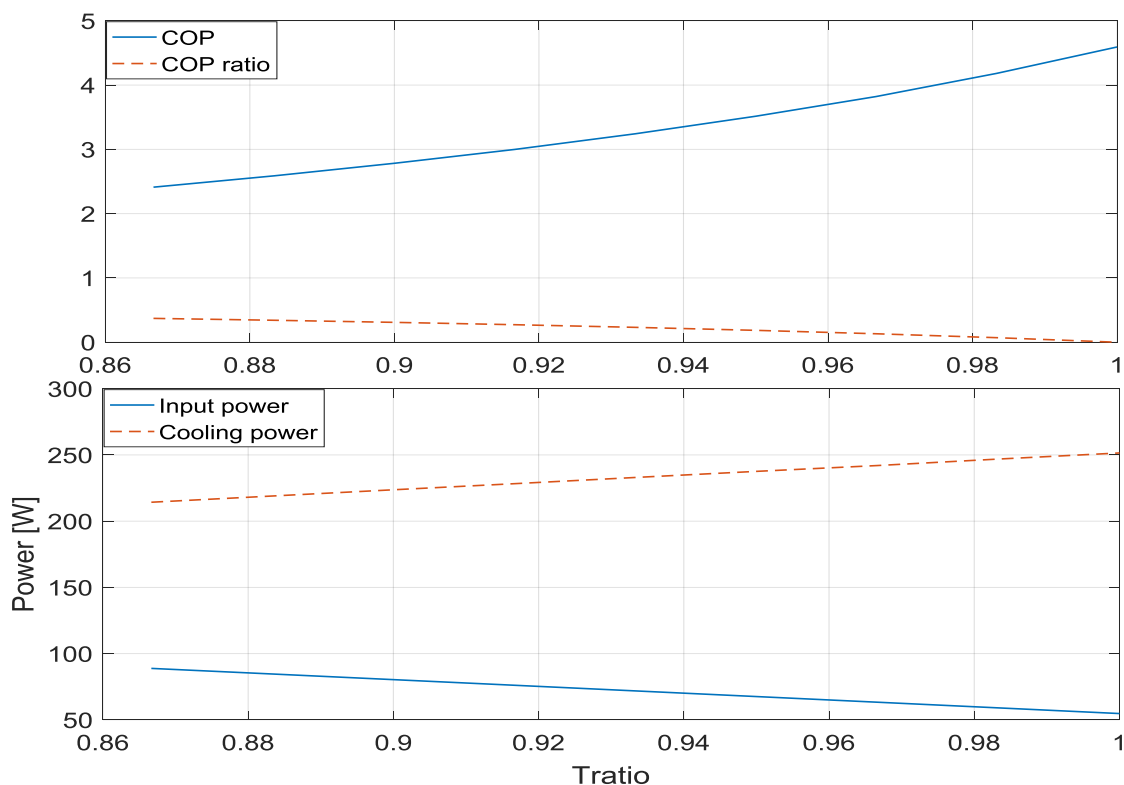
Figure 6: Effect of increasing the temperature ratio of the load to ambient on the COP, COP ratio, input power and cooling power of the isothermal finned cooler at $T_k = 300, n = 200\ rpm$ and $D_e, D_c = 4.2\ cm$.

Conclusion

The machine with isothermalisers resulted in a higher power to mass flow rate in comparison to the bare cylinders for both the engine and refrigerator, which decreases regenerator losses, namely the adiabatic loss that depends on the mass flow rate and the pressure loss that depends on the volumetric flow rate. The simulations show that the Franchot engine can achieve the Curzon efficiency and has the potential to enhance the performance of Stirling engines without using costly and complex heat exchangers. Thus, the performance of the Stirling cycle refrigerators can be improved to be comparable to the conventional VCC in terms of the COP. The isothermalised refrigerator has higher power density than the adiabatic cycle

refrigerator. The isothermal and adiabatic fins achieve an average of 2.5 and 1.9 higher power density than the adiabatic engine, respectively.

Larger than 90° phase angle can be used with some attention to the regenerator losses due to the mass flow rate. However, the finned machine is superior to the adiabatic engine in terms of the power density and hence the regenerator losses.

Acknowledgment

References

[1]   M. Gräber and C. Kirches, "Nonlinear model predictive control of a vapor compression cycle based on first principle models," *Proc. 7th Vienna Int. Conf. Math. Model.*, p. 6, 2012.

[2]   N. Hariharan and B. P. Rasmussen, "Parameter estimation for dynamic HVAC models with limited sensor information," in *Proceedings of the 2010 American Control Conference*, 2010, pp. 5886–5891.

[3]   B. P. Rasmussen and A. G. Alleyne, "Dynamic modeling and advanced control of air conditioning and refrigeration systems," ACRC TR-244, 2006.

[4]   L. Bauwens, "Adiabatic Losses in Stirling Refrigerators," *J. Energy Resour. Technol.*, vol. 118, no. June 1996, pp. 120–127, 1996.

[5]   H. Hachem, R. Gheith, F. Aloui, and S. Ben Nasrallah, "Optimization of an air-filled beta type stirling refrigerator," *Int. J. Refrig.*, vol. 76, pp. 296–312, 2017.

[6]   A. Allouhi, T. Kousksou, A. Jamil, P. Bruel, Y. Mourad, and Y. Zeraouli, "Solar driven cooling systems: An updated review," *Renew. Sustain. Energy Rev.*, vol. 44, pp. 159–181, 2015.

[7]   D. Haywood, "Investigation of Stirling-type Heat-pump and Refrigerator Systems Using Air as the Refrigerant," 2004.

[8]   G. Walker, G. Reader, R. Fauvel, and E. R. Bingham, "Stirling, Near-Ambient Temperature Refrigerators: Innovative Compact Designs," in *27th Intersociety Energy Conversion Engineering Conference*, 1992, p. 5.93-5.96.

[9]   K. Mahkamov, G. Hashem, B. Belgasim, K. Hossin, and I. Mahkamova, "Parametric Analysis of a Dynamic Solar Cooling System Based on a Liquid Piston Converter," *17th Int. Stirling Engine Conf.*, no. December, pp. 59–74, 2016.

[10]   D. M. Berchowitz and R. Unger, "Experimental Performance of a Free-Piston Stirling Cycle Cooler for Non-CFC Domestic Refrigeration Applications," in *18th International congress of refrigeration*, 1991.

[11]   D. M. Berchowitz, "Stirling Coolers for Solar Refrigerators," in *International appliance technical conference,* 1996.

[12]   D. M. Berchowitz, J. Mcentee, and S. Welty, "Design and testing of a 40 W free-piston Stirling cycle cooling unit," in *20th International Congress of Refrigeration*, 1999, no. 1998.

[13]   E. Oguz and F. Ozkadi, "Experimental Investigation Of A Stirling Cycle Cooled Domestic Refrigerator," in *International Refrigeration and Air Conditioning Conference*, 2002.

[14]   D. G. Thombare and S. K. Verma, "Technological development in the Stirling cycle engines," *Renew. Sustain. Energy Rev.*, vol. 12, no. 1, pp. 1–38, Jan. 2008.

[15]   J. D. Van de Ven, "Mobile hydraulic power supply: Liquid piston Stirling engine pump," *Renew. Energy*, vol. 34, no. 11, pp. 2317–2322, 2009.

[16]   G. Walker, *Cryocoolers*, Part 1: Fu. Boston, MA: Springer US, 1983.

[17]   H. Carlson, M. B. Commisso, and B. Lorentzen, "Maximum Obtainable Efficiency For Engines And Refrigerators Based On The Stirling Cycle," in *Proceedings of the 25th Intersociety Energy Conversion Engineering Conference*, 1990, vol. 5, pp. 366–371.

[18]   Anna Helena Orlowska, "An investigation of some heat transfer and gas flow problems relevant to miniature refrigerators," Oxford university, 1985.

[19]   F. L. Curzon and B. Ahlborn, "Efficiency of a Carnot engine at maximum power output," *Am. J. Phys.*, vol. 43, no. 1, pp. 22–24, Jan. 1975.

[20]   C. H. Blanchard, "Coefficient of performance for finite speed heat pump," *J. Appl. Phys.*, vol. 51, no. 5, p. 2471, 1980.

[21]   C. WU, "Maximum Obtainable Specific Cooling Load of a Refrigerator," *Energy Convers.Mgmt*, vol. 36, no. 1, pp. 7–10, 1995.

[22]   J. Chen, "Minimum power inputof irreversible Stirling refrigerators for given cooling rate," *Energy Convers. Manag.*, vol. 39, no. 12, pp. 1255–1263, 1998.

[23]   H. S. Leff and W. D. Teeters, "EER, COP, and the second law efficiency for air conditioners," *Am. J. Phys.*, vol. 46, no. 1, pp. 19–22, Jan. 1978.

[24]   A. Batooei and A. Keshavarz, "A Gamma type Stirling refrigerator optimization: An experimental and analytical investigation," *Int. J. Refrig.*, vol. 91, pp. 89–100, 2018.

[25]   J. M. Daoud and D. Friedrich, "Performance investigation of a novel Franchot engine design," *Int. J. Energy Res.*, Aug. 2017.

[26]   R. Li and L. Grosu, "Parameter effect analysis for a Stirling cryocooler," *Int. J. Refrig.*, vol. 80, pp. 92–105, Aug. 2017.

[27]   J. M. Daoud and D. Friedrich, "Parametric Study of an Air Charged Franchot Engine with Novel Hot and Cold Isothermalizers," *Inventions*, vol. 2, no. 4, p. 35, Dec. 2017.

[28]   F. Toda, S. Iwamoto, M. Matsuo, and Y. Umezane, "Heat Transfer on a Small Stirling Engine," *J. Mar. Eng. Soc. JAPAN*, vol. 25, no. 6, pp. 358–365, 1990.

[29]   T. S. Zhao and P. Cheng, "Experimental studies on the onset of turbulence and frictional losses in an oscillatory turbulent pipe flow," *International Journal of Heat and Fluid Flow*, vol. 17, no. 4. pp. 356–362, 1996.

[30]   H. Karabulut, H. S. YUCESU, and A. Koca, "Manufacturing and testing of a V-type Stirling engine," *Turkish J. Eng. Environ. Sci.*, vol. 24, no. 2, pp. 71–80, 2000.

[31]   C. H. Cheng and Y. J. Yu, "Numerical model for predicting thermodynamic cycle and thermal efficiency of a beta-type Stirling engine with rhombic-drive mechanism," *Renew. Energy*, vol. 35, no. 11, pp. 2590–2601, 2010.

[32]   B. Kongtragool and S. Wongwises, "Thermodynamic analysis of a Stirling engine including dead volumes of hot space, cold space and regenerator," *Renew. Energy*, vol. 31, no. 3, pp. 345–359, Mar. 2006.

[33]   M. Tanaka, I. Yamashita, and F. Chisaka, "Flow and Heat Transfer Characteristics of the Stirling Engine Regenerator in an Oscillating Flow," *JSME Int. J.*, vol. 33, no. 2, pp. 283–289, 1990.

[34]   M. Babaelahi and H. Sayyaadi, "Simple-II: A new numerical thermal model for predicting thermal performance of Stirling engines," *Energy*, vol. 69, pp. 873–890, May 2014.

Experimental analysis of a hybrid thermochemical cycle for simultaneous cold & work productions driven by low grade heat sources

H. GHAZALE[1*], N. MAZET[1], P. NEVEU[1,2], M. PERIER-MUZET[1,2]

[1] CNRS-PROMES. Laboratoire PROcédés, Matériaux et Energie Solaire, Tecnosud, Rambla de la Thermodynamique – 66100 Perpignan

[2] UPVD Université de Perpignan Via Domitia, 52 Avenue Paul Alduy – 66100 Perpignan

[*]Hasan.ghazale@promes.cnrs.fr

Abstract

An original tri-thermal hybrid thermochemical multifunctional cycle is proposed in this study: a sorption cycle based on a reversible endothermic/exothermic solid-gas reaction, whose originality lies in the integration of an expander on the gas line to provide mechanical work. This discontinuous cycle is able to recover medium grade waste heat between 150 and 250 °C during a charging phase, store energy in its intermediate phase, produce cold by the evaporation of the gas working fluid, and produce mechanical power by its expansion during its flow in the production phase. For this purpose, an experimental prototype with $MnCl_2(6/2)$ NH_3 (solid-gas reactants) and a 1 kWe scroll expander, is developed at the laboratory. Primary results of this experimental prototype showed a validation of the hybrid thermochemical cycle concept, where cold and mechanical production are achieved continuously during the production phase. The dynamic behaviours of the components and their couplings are analysed in several thermodynamic conditions (thermodynamic equilibrium deviations (T-P) at the reactor, expander rotational speed and volumetric ratio, mechanical and cold productions…), and such experimental results lead to the validation of a numerical dynamic model to go further in the energetic, exergetic, and global performance optimization studies of the cycle (internal heat recovery of the exothermic reaction, cold temperature at the expander's outlet, control on the coupling between the expander and the electrical generator…).

Keywords: Hybrid thermochemical cycle, Heat waste recovery, Cogeneration, Cold and work production.

Introduction

Energy policies include important issues such as the use of low-temperature heat sources (renewable, industrial waste heat), the management of variabilities in both sources and demands, and a particular attention to the growing demand of electricity and cooling. In order to respond to this, thermochemical processes called 'hybrid' combining energy multigeneration and storage functions are being developed [1, 2]. As with any thermochemical cycle, it's based on a reversible chemical reaction where one of its phases is endothermic and the second is exothermic:

$$S' + \Delta h_r \rightleftarrows S + G.$$
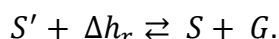
In the forward direction of the reaction, known as the charging or decomposition phase, heat is supplied to the solid-gas compound S' to decompose it into another poor solid-gas compound S. The desorbed gas, G, is condensed and stored at ambient conditions. In the backward direction of the reaction, the discharging or synthesis phase, the condensed reactive fluid evaporates to flow, react with S, and reform again S' releasing the heat of the synthesis reaction. The endo or exothermic effects generated in these processes can be used to produce useful thermal effects: storage, cold and/or heat productions. The hybridization of such a cycle with a vapour power cycle by the integration of an expander between the reactor and the condenser or the evaporator of the thermochemical cycle allows adding to the thermal effects a mechanical

production effect (fig.1). Thus, this hybrid thermochemical cycle is a multifunctional cycle that valorises, beside the thermal energy, the mass flow of the reactive gas between the components.
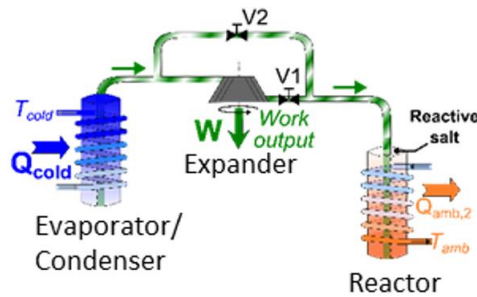
Figure 1- Simultaneous hybrid thermochemical cycle scheme

The thermochemical solid/gas reaction as well as the liquid/vapour phase change process are mono-variant thermodynamic equilibria described by equilibrium lines in the Clausius Clapeyron diagram. In the diagrams, figures 2-4, the high temperature equilibrium (HTE) refers to the solid/gas reaction equilibrium, while the low temperature equilibrium (LTE) refers to the liquid/vapor equilibrium of the reactive fluid.

Hybrid thermochemical cycles can be adapted to a wide range of heat sources temperatures, depending on the chosen reactants and their equilibria with respect to the operating conditions [3]. Several cycle modes that differ in the phase of production of useful effects are defined for this process:

- The separate mode (fig.2), where mechanical production occurs during the charging phase and cold effect is produced during the discharging phase. In this mode, there is no storage of the mechanical work production.
- The simultaneous mode (fig.3), where mechanical and cold productions occur simultaneously during the discharging phase after being stored.
- The combined mode (fig.4) combines the two previous modes and thus mechanical power is produced in both phases of the cycle.
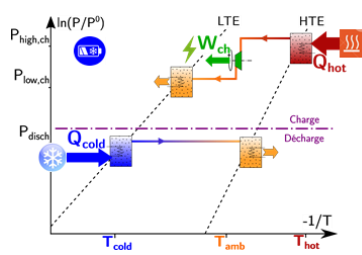
Figure 2- Separate mode of the cycle described in Clausius Clapeyron diagram
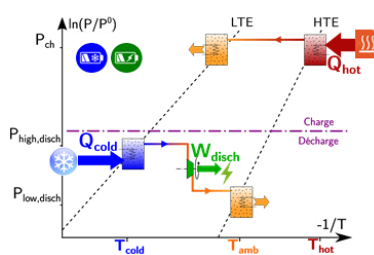
Figure 3- Simultaneous mode of the cycle described in Clausius Clapeyron diagram
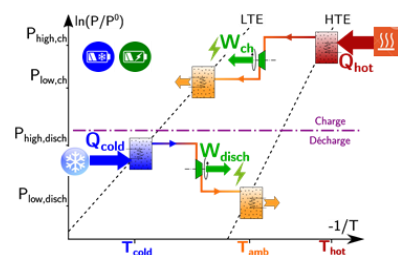
Figure 4- Combined mode of the cycle described in Clausius Clapeyron diagram

The application of the concept of hybridization to the solid/gas sorption cycle has only been in use since the 2010s. Despite being a relatively new area of study, the bibliography on these cycles is limited. An analysis of the available information reveals the following key points:

- Previous studies on this topic have primarily focused on static thermodynamic analyses. They have shown the feasibility of using these cycles to recover heat at low temperatures, below 200°C [1, 4].
- The dynamic behaviour has been investigated in only one study. It highlighted the significant impact of the coupling between the expander and the reactor [5].

- The proposed cycle architectures integrate two thermochemical reactors. Such processes avoid the management of liquid ammonia, but they imply delicate control of the process [6].
- The functionality of these systems in regards to storage has only been addressed in one study, which investigated the use of phase change material in a heat storage system combined with a thermochemical hybrid process [7].
- Only one experimental study has been conducted, but the hybridization concept was not achieved. The failure was attributed to an underestimate of the impact of heat transfer resistances, resulting in an undersized reactor [8].

The main objectives of the research work on these hybrid cycles conducted at CNRS-PROMES since 2016 are to numerically and experimentally analyse the behaviour and performance of single-reactor hybrid thermochemical processes, which seem simpler to control.

This paper provides a summary of the work conducted on the simultaneous mode. The main results of a thermodynamic analysis conducted in a static regime are presented, which was aimed at determining the potential of these cycles. Then, it summarizes the numerical dynamic analysis of the coupling between the expansion device and the thermochemical reactor. Finally, the paper describes the experimental prototype that has been designed to demonstrate the proof of concept, and presents the first results of its experimentation.

Numerical analysis

1- Steady state thermodynamic analysis

The aim of this thermodynamic study, based on equilibrium conditions and energy calculations, is to explore the potential of hybrid thermochemical cycles with different reactive salts and to retrieve the most promising ones.

This study is based on usual assumptions (steady-state process, heat losses and pressure drop inside components are neglected), detailed in a previous work [3]. Several temperature pinches are set for heat exchanges and for the deviation from chemical reaction equilibrium in the reactors. The cold source and ambient sink temperatures are set at $T_{cold} = 0$ °C, $T_{amb} = 20$ °C respectively, and a maximal hot source temperature is set at $T_{hot,max} = 250$ °C, while the required heat source temperature T_{hot} depends on the reactive salt.

A review of 103 reactive ammoniated salts from a database by Touzain and from CNRS-PROMES expertise has been carried out. For given operating conditions (T_{amb} and T_{cold}), the salts selected for the analysis are those that can be decomposed with a hot source temperature $< T_{hot,max}$ and that can be synthesized at a pressure lower than the evaporation pressure of the reactive fluid. For each of these salts, the required heat source temperature, the energy and exergy efficiencies of the cycle, and the mechanical work production ratio are calculated as follows:

- energy efficiency:

$$\eta_I = \frac{|W_{mec}| + Q_{cold}}{Q_{hot}}$$

where W_{mec} is the produced mechanical work, Q_{cold} is the cold production and Q_{hot} is the heat supplied by the hot source.

- exergy efficiency:

$$\eta_{ex} = \frac{|W_{mec}| + Ex_{cold}}{Ex_{hot}}$$

where

$$Ex_{cold} = Q_{cold} \cdot \left(\frac{T_{amb}}{T_{cold}} - 1 \right)$$

and

$$Ex_{hot} = Q_{hot} \cdot \left(1 - \frac{T_{amb}}{T_{hot}} \right)$$

- ratio of mechanical power production:

$$\tau_w = \frac{|W_{mec}|}{|W_{mec}| + Q_{cold}}$$

Figure 5 presents the results for the most common salts. It shows that the required hot source temperature is always higher than 100 °C and that the energetic and exergetic efficiencies of the cycle are weakly dependent on the reactive salts, η_I between 40 and 50 % and η_{ex} between 20 and 30%. However, the ratio of mechanical production (τ_w) is strongly dependent on the salt: this ratio increases with the requested hot source temperature of the cycle. This increase in the ratio of mechanical production is directly related to the equilibrium of the salt: each salt imposes its synthesis reaction pressure at the outlet of the expander leading to variable mechanical productions and thus variable mechanical production ratios.
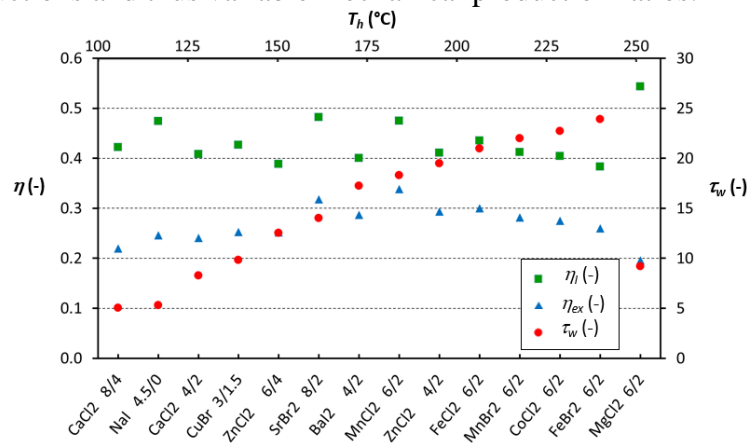
Figure 5- Energetic and exergetic analysis of the cycle as function of several salts and temperatures

Among this set, two salts, CaCl$_2$ and MnCl$_2$, are particularly interesting for the first experimental investigations. Indeed, they are well known (used in commercial thermochemical processes) and stable; they have interesting thermodynamic performances; and their decomposition temperatures are reasonable for experimental developments in a research laboratory.

2- Analysis of the coupling between the expander and the reactor

In order to analyse the dynamic behaviour of hybrid thermochemical processes, numerical models were developed for each component (reactor, condenser, evaporator, and expander). In each component, internal variables (thermodynamic state of the reactive fluid, wall temperature, reaction advancement …) were considered uniform (nodal approach). The model of the reactor, the condenser and the evaporator are based on the 1st law of thermodynamics and mass balances, solid/gas reaction or liquid/vapour phase change kinetics, and the ideal gas assumption. As a first approach, the expander is supposed to operate in steady-state and its global performance is described by two parameters: the isentropic efficiency η_{is} and the volumetric efficiency η_v. Moreover, its exhaust pressure is fixed to simulate user control. The reactant pair of CaCl$_2$.8/4NH$_3$ is chosen and standard heat transfer coefficients have been

employed, with 100 W.m^{-2}.K^{-1} for the heat exchange between the reactive bed and the wall, and 1000 W.m^{-2}.K^{-1} for the heat exchange between the wall and heat transfer fluid. The hybrid cycle, composed of these models, was coded and simulated using the Python programming language (in an object-oriented method).

The coupling between the expander and the reactor involves antagonistic behaviours of these components, and it is a key issue in the operation of thermochemical hybrid cycles [9]. In the discharging phase of the simultaneous mode, the generation of mechanical power by the expander ($\dot{W}_{mec}$) is dependent on the pressure levels of admission (P_{ex}^{in}) and exhaust (P_{ex}^{out}), as well as the mass flow rate of ammonia ($\dot{m}_g$), expressed as:

$$\dot{W}_{mec} = \dot{m}_g. g\left(P_{ex}^{in}, \boldsymbol{P_{ex}^{out}}\right)$$

In the reactor, the advancement of the synthesis reaction (X) is a function of the exhaust pressure of the expander, and expressed as:

$$\frac{dX(t)}{dt} = K_s. \left(1 - X(t)\right). f\left(T_R - T_{eq}(\boldsymbol{P_{ex}^{out}}(t))\right)$$

where, $X(t)$ is the advancement of the chemical reaction defined as the ratio of the number of moles of the synthetized salt (S') to the total mole number of the salt at an instant t, expressed as:

$$X(t) = \frac{n_{s'}(t)}{n_s(t) + n_{s'}(t)}$$

K_s is the kinetics constant coefficient of the synthesis reaction, T_R is the reactive solid temperature and T_{eq} is the equilibrium temperature of the reactant at the pressure of the synthesis reaction i.e. the exhaust pressure of the expander. The numerical analysis of the discharging phase, for a fixed cold source temperature at 0 °C (evaporation pressure $P_{evap} = 4.26$ bar), shows a variation of the mean mechanical power as the outlet pressure at the expander varies (fig. 6). While having low pressure differences at the expander's extremities, the mechanical work production is unfavourable. With varying the outlet pressure at the expander in this dynamic study between 0.5 and 3 bars, the mean mechanical power increases as the outlet pressure at the expander decreases below 3 bars until reaching an optimum of production at 1.5 bar. On the other side, while the pressure decreases more below 1.5 bars, the mean mechanical power decreases due to low mass flow rates of ammonia gas caused by a slow chemical reaction rate while getting closer to the equilibrium of the reaction (the pressure at the outlet of the expander approaches the equilibrium pressure of the synthesis reaction at the imposed temperature). From an energy point of view, as the exhaust pressure decreases, the mechanical energy increases even though the reaction's advancement slows down. This antagonistic behaviour between the expander and the reactor, leads to the definition of the optimum operating conditions for the discharging phase.
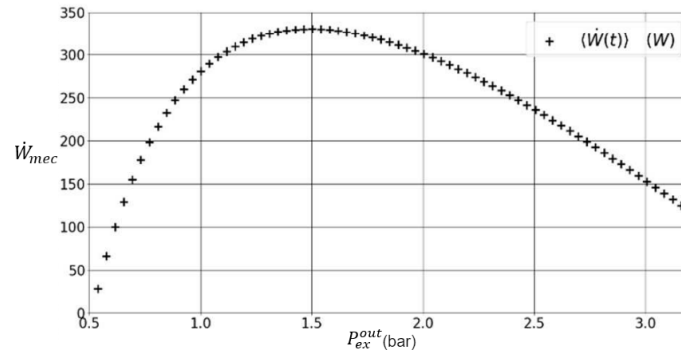
Figure 6- Evolution of the mean mechanical power as function of the exhaust expander's pressure for fixed evaporating conditions

Experimental analysis

1- Prototype description

A prototype of the simultaneous mode has been developed. This prototype schematized in figure 7 includes five main parts: the reactor, the expander coupled to an electric generator, an evaporator, a condenser and a throttling valve.
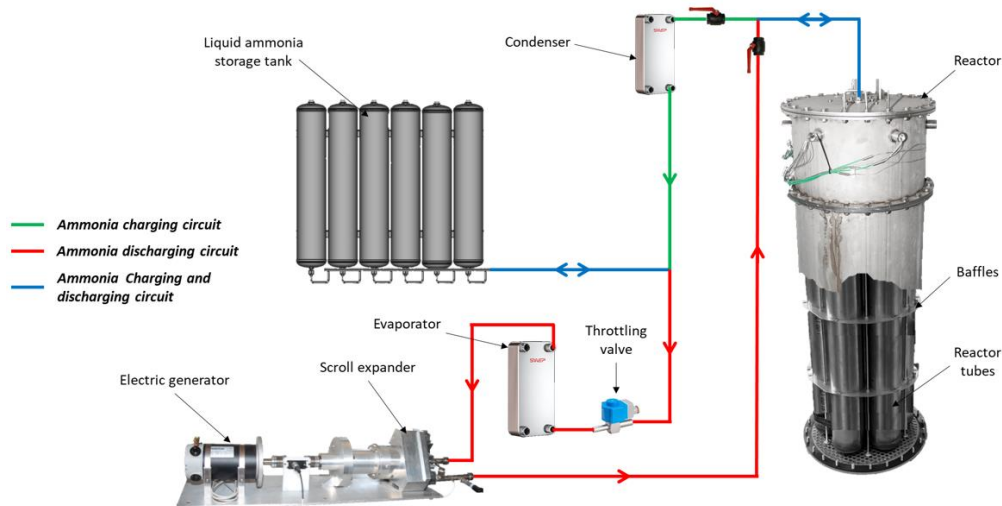
Figure 7- Schematic description of the thermochemical hybrid prototype

7 reactor tubes connected together and placed inside a cylindrical shell with baffle plates consist the whole thermochemical reactor. As noted in the static thermodynamic analysis, $MnCl_2$ salt was selected for this prototype because it shows high thermodynamic performance, and is a well-known salt with good stability. Each reactor tube contains the reactive material composed of 0.69 kg of Expanded Natural Graphite (to enhance conductive transfer), 4.15 kg of $MnCl_2$ charged with 3.35 kg of NH_3. Mineral oil is used as a heat transfer fluid in the reactor shell. A thermo-regulator with a heat power of 14 kW operating between 20 and 180 °C is used to heat the reactor during the decomposition phase and to cool it during the synthesis one. The reversible thermochemical reaction that takes place in the reactor tubes is:

$$MnCl_2. 6NH_3 + \Delta h_r \rightleftarrows MnCl_2. 2NH_3 + 4NH_3$$
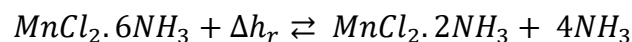
The expander is a scroll type with a nominal mechanical power of 1 kW, volumetric expansion ratio of 3.5, a displacement of 14.5 cm^3/Rev, maximum working pressure of 13.8 bars and a

nominal rotating speed of 3600 rpm bought from Airsquared. The expander is coupled through a magnetic coupling to a DC electrical generator which is electrically coupled to a rheostat ($0 \leq R_{elec} \leq 100$ Ohm) to vary the electrical load of the electrical circuit.

The evaporator is a stainless-steel plates heat exchanger with a total heat transfer area of 0.414 m². The evaporation heat is supplied by glycolic water loop, between 0 °C and 25 °C. An electrical flow heater of 0.6 kW is connected to the outlet of the evaporator to control the superheating of the NH_3 flow.

The condenser is also a stainless-steel plates heat exchanger with a total heat transfer area of 0.276 m². The condensation heat is evacuated by a pressurized water circuit circulating between 10 °C and 30 °C. The throttling valve is an electronic one, coupled to a regulator in order to control the NH_3 flow rate and maintain the superheating condition at the outlet of the evaporator for a fixed value.

After a tuning phase (tightness control at high pressure and vacuum, evacuation of non-condensable gases...), classical thermochemical cycles (bypassing the expander) are carried out to test and validate the thermochemical part of the prototype before integrating the expander. The hybrid cycle is then exploited. A first discharging phase was done in an open circuit electrical condition (at the generator), to validate the concept of the hybrid thermochemical cycle. Once validated, experiments with different electrical charges were done. The purpose of such electrical variations is to study the effect of the variation of the electrical charge on the behaviour of the expander and thus the whole performance of the cycle: cold production, mechanical power, and reaction kinetics.

2- Charging phase: reproducibility and kinetics

The first decomposition was done under the following operating conditions: the inlet temperature of the reactor heat transfer fluid was set at 180 °C and that of the condenser heat transfer fluid at 12 °C imposing a condensation pressure of 7 bars. This experiment was repeated twice under the same conditions for reproducibility tests. Then, the decomposition operating conditions were changed (by decreasing the reactor's inlet temperature) to analyse the evolution of the reaction kinetics at different deviations from the thermodynamic equilibrium conditions. Figure 8 presents the advancement of the reaction for these 6 decomposition phases. It is noteworthy that X equals 1 in the event of complete synthesis of the salt ($MnCl_2.6NH_3$), and X equals 0 in the event of total decomposition of the salt ($MnCl_2.2NH_3$).
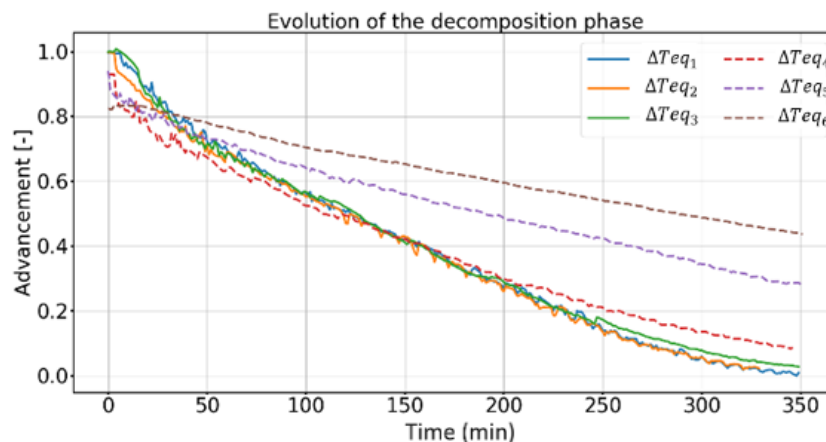
Figure 8- Evolution of the advancement of the decomposition reaction for different deviations from equilibrium

The first three decomposition reactions, carried out in the same conditions, leading to a temperature deviation from the equilibrium of the salt of 43 °C $\left(\Delta T_{eq} = T_{htf,R,in} - T_{eq}(P_R)\right)$, have identical evolution of the advancement demonstrating the reproducibility of the decomposition phase. For the three other decomposition reactions where the inlet temperature of the condenser heat transfer fluid remains at 12 °C and the deviation from the salt's equilibrium decreases to $\Delta T_{eq,4} = 33$ °C, $\Delta T_{eq,5} = 23$ °C and $\Delta T_{eq,6} = 13$ °C: as expected, the reaction's rate becomes slower when the deviation from equilibrium decreases. For instance, at the time when the first three decompositions were finished (X→ 0 i.e., at 350 min), the reaction's advancement was still at X = 0.1, X = 0.3 and X = 0.43 for the 4th, 5th and 6th reactions, respectively.

3- Discharging phase with an open circuit electrical generator

The heat transfer fluid inlet temperature at the evaporator is fixed at 10 °C, the reactor's temperature setpoint is 35 °C and the expander freely rotates with no electrical load. The reaction's advancement and cold production profiles of this experiment are shown in figure 9, and the expander's rotational speed, pressure ratio, and mechanical production are shown in figure 10.

Before the start of the synthesis phase, the solid reactant is kept at low temperature (35 °C) and therefore the pressure in the reactor is low. At the beginning of the synthesis phase (when the reactor is connected to the evaporator through the expander) the reactor sorbs a high flow of ammonia by maintaining a high-pressure difference with the evaporator which results in a peak of cold and mechanical power. Due to the exothermic synthesis reaction, the solid reactant rises in temperature and pressure, reducing the pressure difference across the expander and the sorbed ammonia flow rate is modulated so that the heat of reaction can be dissipated by the coolant. A change in the slope of the advancement and an increase in the cold production are noted after 50 minutes. The cold power production increased from 1.5 kW to 2.5 kW (as average values) and the saturation temperature of ammonia decreased to -5 °C. During the whole discharging phase, the expander is rotating and performing mechanical work (figure 10). In the first 50 mins, the expander rotates freely at 450 rpm producing around 4 W of mechanical work. After, the expander accelerates to around 800 rpm and produces around 10 W of mechanical power. This acceleration in the reaction that favours the production at the second period of the synthesis reaction is referred, as a first hypothesis, to a variable thermal exchange at the level of the reactor where the heat transfer fluid evacuates weakly – but increasingly – the heat of the synthesis reaction.
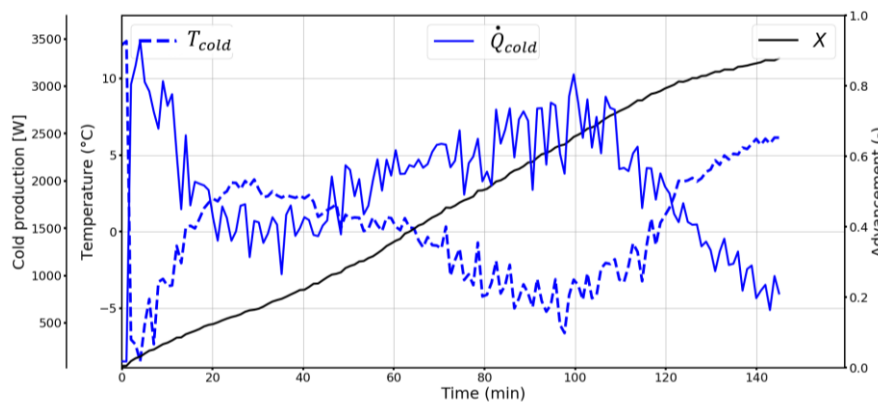
Figure 9- Cold power, cold temperature and advancement of the chemical reaction over time during the discharging phase

Heat Powered Cycles
Conference 2023
Edinburgh

Heat in the new energy system

3rd to 6th of September 2023
The University of Edinburgh, Scotland
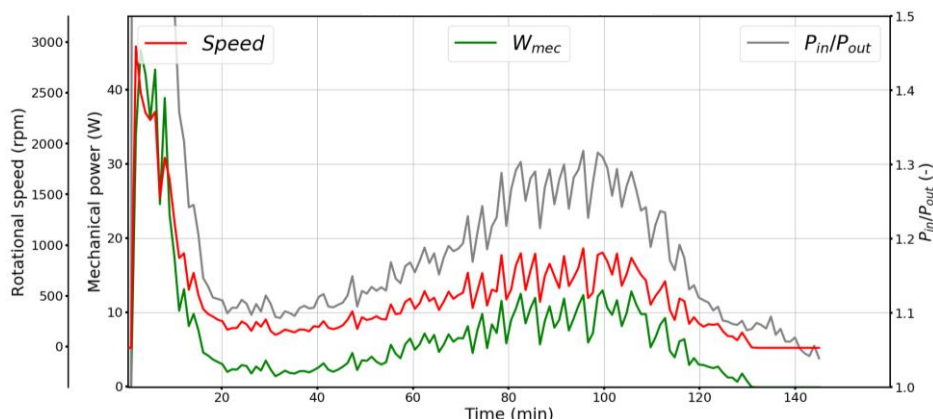
Figure 10- Expander's rotational speed, mechanical power and pressure ratio over time during the whole synthesis phase

4- Discharging phase experiments with fixed evaporating pressure and variable electrical charges

For these experiments, the evaporator's heat transfer fluid inlet temperature is fixed at 10 °C, and the reactor's setpoint is 35 °C. During the first experiment, the expander was blocked mechanically. An electrical resistor of 7 Ω is coupled to the electrical generator in the second experiment, 57 Ω in the third, 100 Ω in the fourth, and an infinity resistor (open circuit) in the fifth experiment. The advancement of the synthesis reaction for each experiment is plotted in figure 11. An inflection point in the curves of advancement is noted where the slope of the advancement profiles increases after 50 minutes. Behind this inflection point, all the advancement curves are bounded by the curves of the blocked and the open circuit conditions, where the faster advancement corresponds to an open circuit condition and the lowest to a blocked expander. This acceleration appears also in the production of cold at the level of the evaporator, where the similar profiles of cold production increase from 1.5 kW to 2.5 kW as shown in figure 12, and no significant effect of the electrical charge is shown by these experiments on the cold production for a maximum difference of 0.5 kW between the boundaries of the cold powers.
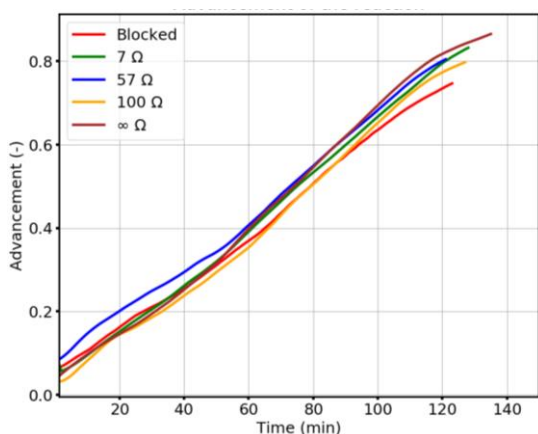
Figure 11- Advancement of the reactions
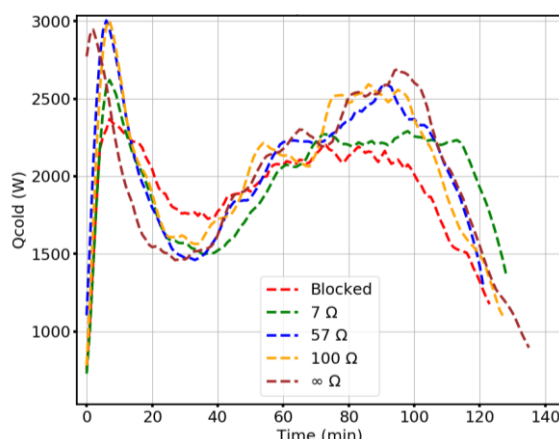
Figure 12- Cold production during the discharging phase

At the level of the expander, during the second period of the discharging phase, the volumetric flowrate of ammonia scores the highest value of $V_5 = 2.75$ m^3/hr for the experiment done in open circuit electrical conditions at the generator (figure 13). While the resistance value

Heat Powered Cycles
Conference 2023
Edinburgh
Heat in the new energy system

3rd to 6th of September 2023
The University of Edinburgh, Scotland

decreases, the volumetric flowrate decreases where a maximum of 2.5, 2.3, 2.25 m^3/hr are achieved for experiments with electrical resistance of 100, 57 and 7 Ω respectively. The blocked expander experiment achieved a maximum of 1.8 m^3/hr during the second period of the discharging phase. This high-volume flow rate of ammonia that circulates in the expander when it is blocked reveals a strong internal leakage flow in the expander which limits significantly the performance of the latter in the operating conditions of these experiments (low speed of rotation compared to the nominal). Beside the volumetric flowrate results, the pressure ratio at the expander's extremities is also evaluated by the change in electrical resistance at the generator's level. The minimum pressure ratio ȶ$_p$ is obtained in experiment 5 where the generator is in an open circuit condition. Decreasing the value of the electrical resistance results in higher pressure ratios as shown in figure 14. For instance, ȶ$_p$ increases from 1.25 to 1.3, 1.35, and 1.6 – as maximum values – while decreasing the resistance value from infinity to 100, 57, and 7 Ω respectively. Similarly, ȶ$_p$ increases to 1.8 when the expander is blocked. This weak pressure difference at the extremities of the expander results from the mass coupling between the expander and the reactor as already discussed in the part 2 of this document.
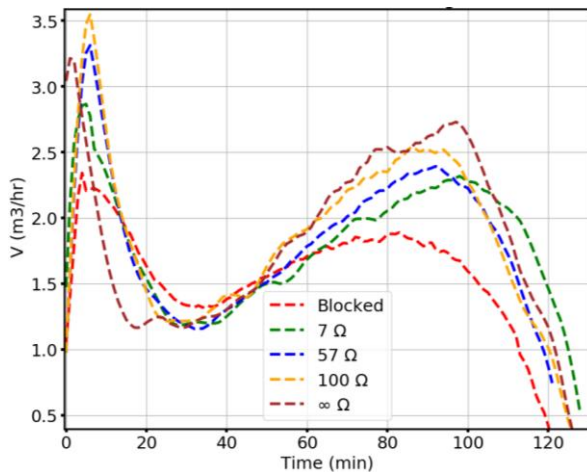
Figure 13 - Ammonia volumetric flowrate at the expander's inlet
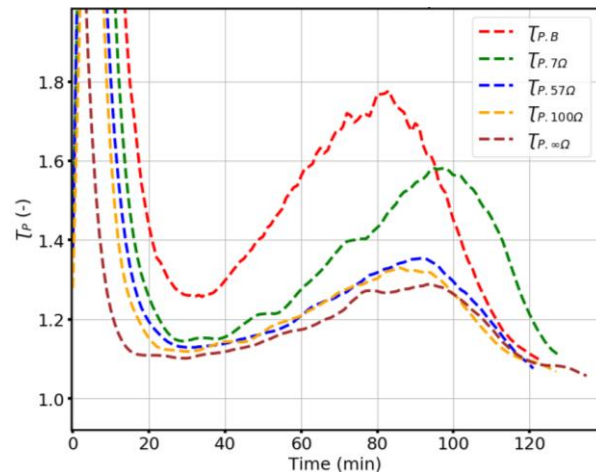
Figure 14- Pressure ratio at the expander's extremities

Furthermore, the dynamic rotational speed and the torque force are also affected by the variation of the electrical resistance. While the expander was freely rotating (open circuit conditions), the rotational speed **ω** reached a maximum of 800 tr/min. Once decreasing the electrical charge to 100, 57 and 7 Ω, the maximum rotational speed decreases to 600, 500 and 300 tr/min respectively, and the blocked expander has no rotation. Contrary, the maximum torque force **T** in the same period of the reaction is at its maximum of 1.2 N.m for a blocked expander and decreases to 0.6, 0.3, 0.2 and 0.1 N.m when increasing the electrical resistance to 7 Ω, 57 Ω, 100 Ω and infinity. These evolutions of the torque forces and rotational speeds at the expander, which vary inversely while changing the electrical resistance, affect the production of mechanical work and thus the expander's efficiency (η_{exp}) – obtained between 0.15 and 0.2 – that are calculated as follows:

$$\dot{W}_{mec} = \frac{2\pi.\boldsymbol{\omega}.\mathbf{T}}{60}$$

$$\eta_{exp} = \frac{\dot{W}_{mec}}{\dot{m}_g \cdot \left(h_{ex}^{in} - h_{ex}^{out,is}\right)}$$

where, $\dot{W}_{mec}$ is the mechanical power of the expander in W, $\boldsymbol{\omega}$ is the rotational speed in tr/min, **T** is the torque force in N.m, η_{exp} is the efficiency of the expander, $\dot{m}_g$ is the mass flowrate of ammonia in kg/s, h_{ex}^{in} and $h_{ex}^{out,is}$ are the inlet enthalpy and outlet isentropic enthalpy at the extremities of the expander respectively in J/kg.
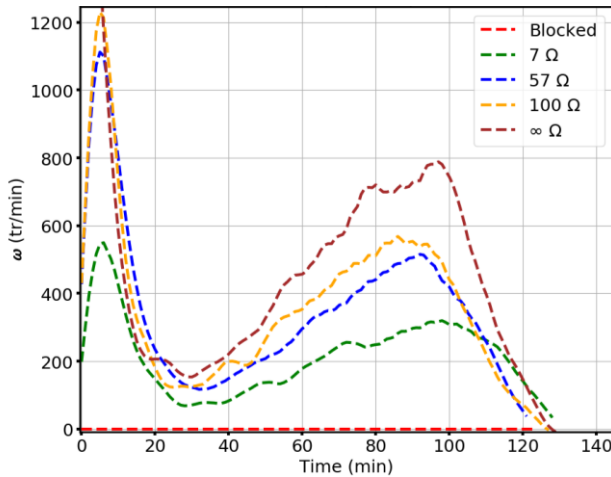
Figure 15- Expander rotational speed
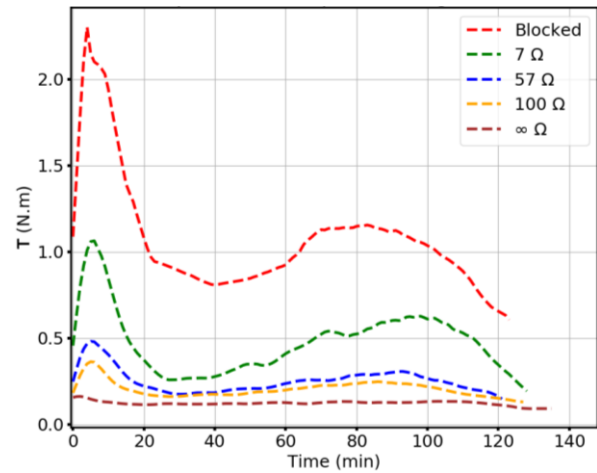
Figure 16- Torque force applied by the generator on the expander
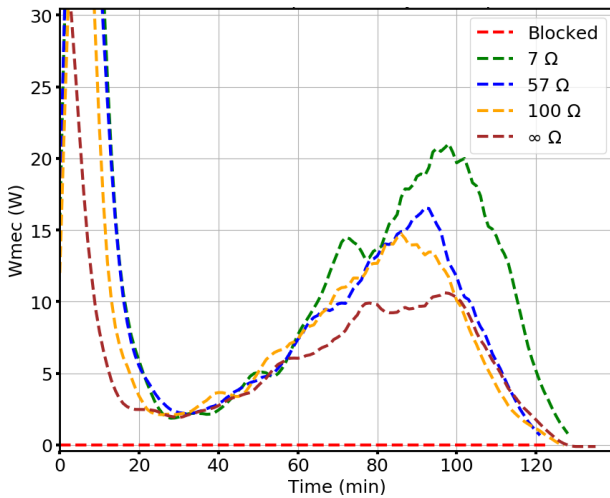
Figure 17- Produced mechanical work during the discharging phases
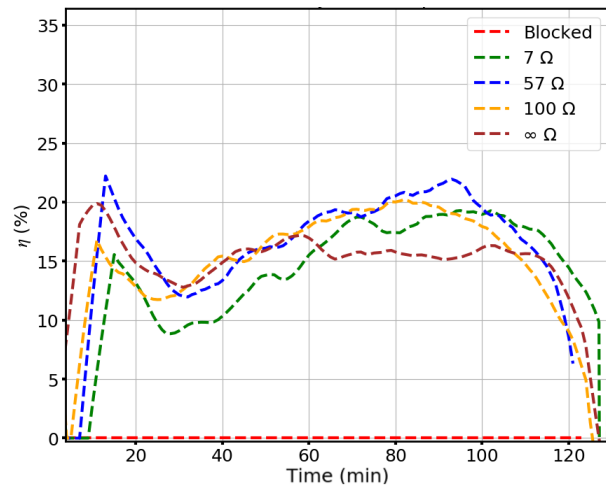
Figure 18- Dynamic efficiencies of the expander

During these experiments, the effects of the electrical resistances are shown on the behaviour of the expander. These effects on the operating conditions of the expander are summarized in table 1. The analysis of these results shows a concave evolution of the maximum mechanical power with the evolution of the electrical resistance. An optimum is obtained for these experiments with a load between 57 Ohm and the blocked expander.

Table 1- Maximum rotational speed, torques and mechanical power of the expander for different electrical resistances

Experiment	Electrical resistance (Ω)	ω_{max} (rev/min)	T_{max} (N.m)	$\dot{W}_{max}$ (W)
1	-	0	1.2	0
2	7	350	0.6	22
3	57	500	0.3	16
4	100	600	0.25	15
5	∞	800	0.1	10

Conclusions

A hybrid thermochemical concept to valorise low or mid-grade heat in cold and mechanical power is analysed numerically and developed experimentally. A prototype involving $MnCl_2NH_3(6/2)$ ammoniated salts and a 1 kWe scroll expander was mounted. First, the reproducibility and kinetics of the cycles were checked for several operating conditions of the reactor. In a second step, the hybrid process with the expander was exploited. A first cycle was done with no electrical charges at the generator's level to validate the concept of the integration of an expander in a thermochemical process. Other experiments were followed where the evaporating conditions were fixed and the electrical resistance at the generator was varied. These experiments showed the effect of the electrical charge on the performance of the expander: by the increase of the electrical charge (electrical potential difference at the generator), the expander rotates faster with lower coupled torque forces applied by the generator. These variations in the behaviour of the expander with the generator affected the mechanical power production and the efficiency of the expander. A presence of an important internal leakage in the expander is observed, reducing the performance of that latter. Furthermore, the synthesis reaction has shown an acceleration, which could be attributed to a possible hypothesis that suggests a weak and gradually improving heat evacuation performance at the reactor level.

More experiments are in progress to better understand the coupling between the elements of the hybrid thermochemical cycle. Several experimental protocols are to be done, such as fixing the electrical resistance at the generator and varying the evaporating pressure to analyse the behaviour of the expander in such conditions. The numerical dynamic model of the cycle is set to be validated with the experimental results to head finally towards sensibility studies, energetic and exergetic studies and analysis of the components irreversibilities, along with a global performance optimization of the cycle.

Acknowledgments

References:

[1] Wang L., Ziegler F., Roskilly A., Wang R., Wang Y., A resorption cycle for the cogeneration of electricity and refrigeration, Applied Energy 2013;106:64-56.
[2] Thiele E., Jahnke A., Ziegler F., Efficiency of the Lamm–Honigmann thermochemical energy storage, Thermal Science and Engineering Progress 2020; 19;100606.
[3] Godefroy A., Perier-Muzet M., Neveu P., Mazet N. Hybrid thermochemical cycles for low-grade heat storage and conversion into cold and/or power. Energy Conversion and Management 2020;225.

[4] H. Bao, Z. Ma, A.P. Roskilly, 2017. Chemisorption power generation driven by low grade heat – Theoretical analysis and comparison with pumpless ORC, Applied Energy (186)282–290

[5] H.Bao, Y.Wang, A.P.Roskilly, 2014. Modelling a chemisorption refrigeration & power cogeneration system, Applied Energy (119)351

[6] L.Jiang, Y.J.Lu, A.P.Roskilly, R.Z.Wang, L.W.Wang, K.Tang, 2018. Exploration of ammonia resorption cycle for power generation by using novel composite sorbent, Applied Energy (215)457–467

[7] L.Jiang, L.W. Wang, X.F.Zhang, C.Z.Liu, R.Z.Wang, 2015. Performance prediction on a resorption cogeneration cycle for power and refrigeration with energy storage Renewable Energy (83)1250- 1259

[8] L.Jiang, L.W.Wang, C.Z.Liu, R.Z.Wang, 2016. Experimental study on a resorption system for power and refrigeration cogeneration, Energy (97) 182-190

[9] Godefroy A. "Analyse thermodynamique et performances dynamiques de cycles hybrides impliquant des procedes a sorption". PhD thesis. Université de Perpignan via Domitia, 2020.

Heat Powered Cycles Conference 2023
Edinburgh
Heat in the new energy system

Model analysis of rotary adsorber in steam-assisted temperature swing adsorption processes for efficient CO$_2$ capture from ambient air

Junye Wu[1,2,3], **Kuihua Wang**[1], **Xuancan Zhu**[1], **Ruzhu Wang**[1], **Chi-hwa Wang**[2,4], **and Tianshu Ge**[1,2*]

[1]Research Center of Solar Power & Refrigeration, Institute of Refrigeration and Cryogenics, Shanghai Jiao Tong University, 800 Dongchuan Road, Shanghai, 200240, China

[2]Energy and Environmental Sustainability Solutions for Megacities (E2S2), Campus for Research Excellence and Technological Enterprise (CREATE), 138602, Singapore

[3]NUS Environmental Research Institute, National University of Singapore, Singapore 138602, Singapore

[4]Department of Chemical and Biomolecular Engineering, National University of Singapore, 4 Engineering Drive 4, Singapore 117585, Singapore

[*]Corresponding author: baby_wo@sjtu.edu.cn)

Abstract

The continuous growth of atmospheric CO$_2$ concentration has motivated widespread research of negative emission technologies (NETs)[1-3]. Direct air capture (DAC) is a promising NET but remains under paced in deployment efforts because of high energy demand and cost[4-6]. Creative implementations are required to lower the barrier to economic applicability of DAC systems[7]. To this end, this work presents an innovative strategy to capture CO$_2$ from air using a rotary adsorber and achieve regeneration with steam purge. The rotary-wheel-shaped amine-modified structured adsorbents are used to reduce the pressure drop and enhance the gas diffusion. A mathematical model that can describe the heat and mass transfer during temperature swing adsorption processes were developed. The CO$_2$ and H$_2$O capacities and kinetics of adsorbents were evaluated in details. By comparing the simulation results to experimental data from prototype tests, a desirable accuracy of ±20% was observed. We elucidated the rotary adsorption operation law by simulating and analyzing the parameter distribution on the wheel outlet surface as well as inside the gas flow microchannels. The effects of both structural parameters (wheel thickness, regeneration section area ratio, adsorbent and substrate linear density) and operation parameters (regeneration temperature, wheel rotation speed, process air flow rate, and steam flow rate) were evaluated. On this basis, comprehensive optimization of multiple parameters was carried out using the orthogonal test method to identify the optimal conditions. Results show that the rotary adsorber presents a high CO$_2$ capture rate of 40–80% and high productivity of 4.2–12.3 kg/m3/h (or 0.15–0.31 g/g/day). By separating the steam in the regeneration gas using the condensation, CO$_2$ with purity of 75–97% can be generated. The adsorption of H$_2$O during steam purge can release heat for CO$_2$ regeneration, which helps to reduce the process energy consumption to 1.8–2.5 kWh/kg. The rotary adsorber offers an efficient CO$_2$ direct air capture process while also boasting a compact design that achieves continuous operation in a single vessel.

Keywords: structured adsorbent, direct air capture, temperature swing adsorption, steam purge regeneration, amine.

References:

[1] Creutzig, F., et al., "The mutual dependence of negative emission technologies and energy systems", Energy & Environmental Science, 2019.

[2] Rogelj, J., et al., "Scenarios towards limiting global mean temperature increase below 1.5 °C", Nature Climate Change, 2018.

[3] Smith, P., et al., "Biophysical and economic limits to negative CO_2 emissions", Nature Climate Change, 2015.

[4] Zhu, X., et al., "Recent advances in direct air capture by adsorption", Chemical Society Reviews, 2022.

[5] Erans, M., et al., "Direct air capture: process technology, techno-economic and socio-political challenges", Energy & Environmental Science, 2022.

[6] Sanz-Perez, E.S., et al., "Direct Capture of CO_2 from Ambient Air. Chemical Reviews", 2016.

[7] Bachman, E., et al., "Rail-based direct air carbon capture". Joule, 2022.

Modeling and optimization of a packed-bed adsorption thermal battery

Ziya Zeng[1,2,3], **Bingchen Zhao**[1,2], **Duc Thuan Bui**[3], **Weidong Chen**[3], **Kian Jon Ernest Chua**[3], **and Ruzhu Wang**[1,2*]

[1]Institute of Refrigeration and Cryogenics, Shanghai Jiao Tong University, Shanghai, 200240, China.

[2]MOE Engineering Research Center of Solar Power and Refrigeration, Shanghai Jiao Tong University, Shanghai, 200240, China.

[3]Department of Mechanical Engineering, National University of Singapore, 9 Engineering Drive 1, Singapore 117576, Singapore.

[*]Corresponding author: rzwang@sjtu.edu.cn

Abstract

Water-based adsorption thermal battery, owing to its advantages of high energy storage density, negligible thermal losses and realizable humidity control, could provide huge possibility in widespread applications of energy saving and low grade heat energy utilization, especially for space heating. A three-dimensional computational model for predicting the overall thermal output performances of a packed-bed adsorption thermal battery was built and validated. By using this model, the influences of structural parameters were firstly investigated for adsorbent bed optimization, and then the effects of the operating parameters on the system performance were evaluated. A strategy of tuning airflow rate for output performance regulation was investigated to realize stable thermal output with satisfactory output temperature and heating power. The simulation results indicated that the effective heating time is 404 min with a discharging threshold temperature of 25 $^{\circ}$C, and the heating power maintains as 19.5 kW m^{-3} for the stable output stage, demonstrating its possibility to achieve stable thermal output in the application of space heating. The output RH change between 35% and 40% along the effective discharging process, which also enables a controllable humidity management in the application of direct space heating considering human thermal comfort.

Keywords: Adsorbent packed bed, Adsorption thermal battery, Numerical simulation, Thermal energy storage

Introduction

Harnessing moisture in the air, which remains as a huge and unexploited source, has becoming popular in significant fields of atmospheric water harvesting to resolve water shortage in arid regions, and dehumidification for living comfort in humid areas [1, 2]. The air humidity assisted adsorption system, based on the reversible reaction between the adsorbent and water as adsorbate, has attracted a lot of interests in recent years [3-5]. Since the adsorption process is accompanied by releasing heat while the desorption process is on the contrary, this intrinsic characteristic of the system has been discovered to provide thermal effect in adsorption thermal battery (ATB) [6]. In the discharging process, the adsorption reaction is exothermic, with the released adsorption heat for thermal demand. While during the charging process, the adsorbent is heated up by an external heat source, triggering a reverse reaction in which the adsorbate is desorbed from the adsorbent and the heat is stored in the adsorbent as a form of chemical energy [7]. Owing to multifarious advantages of high energy storage density, negligible thermal losses and realizable humidity control, ATB could provide huge possibility in widespread applications of energy saving and low grade heat

energy utilization, especially for space heating, which accounts for a large part of the total energy consumption in modern society [8].

From the perspective of thermal energy utilization, one of the most significant issues to be tackled with is thermal energy upgrading. Therefore, most studies concentrate on lifting and stabilizing the output temperature [9-11]. By alternating suitable adsorption materials and system cycles, for example, a 1.3 kWh ATS prototype with a strategy of "dual reactor", adopting activated alumina/LiCl in a main reactor and $SrBr_2 \cdot H_2O$ in a regulatory reactor, is able to heat up the air from 20 ^{o}C to 38.1 ^{o}C for over 5 h [12]. What is overlooked by recent study is that, the heating power of open ATB systems, which is regarded as a more significant performance indicator of space heating, is hard to achieve the optimal value if only the output temperature is emphasized [13]. To date, research on this aspect is desirable but remains a great challenge to investigate. In addition, open ATB systems based on water harvesting/releasing processes assisted with air humidity holds the potential of realizing synchronous management of temperature and humidity for satisfactory thermal comfort.

Herein, a numerical simulation of the packed-bed reactor was performed by using COMSOL Multiphysics. The simulation model is based on an experimental setup of a constructed ATB reactor, the working principle of which will be introduced in the simulation method. The transient flow and heat and mass transfer performances within the reactor were studied. The Adsorption processes of ATB systems working in the open cycle and the loop cycle were numerically investigated here to show different characteristics. And the thermal output performance of the ATB reactor was further demonstrated under various working conditions, in terms of output temperature and relative humidity (RH), heating power, thermal discharging efficiency. The strategy of tuning airflow rate for output performance regulation was investigated to realize stable thermal output with satisfactory output temperature and heating power.
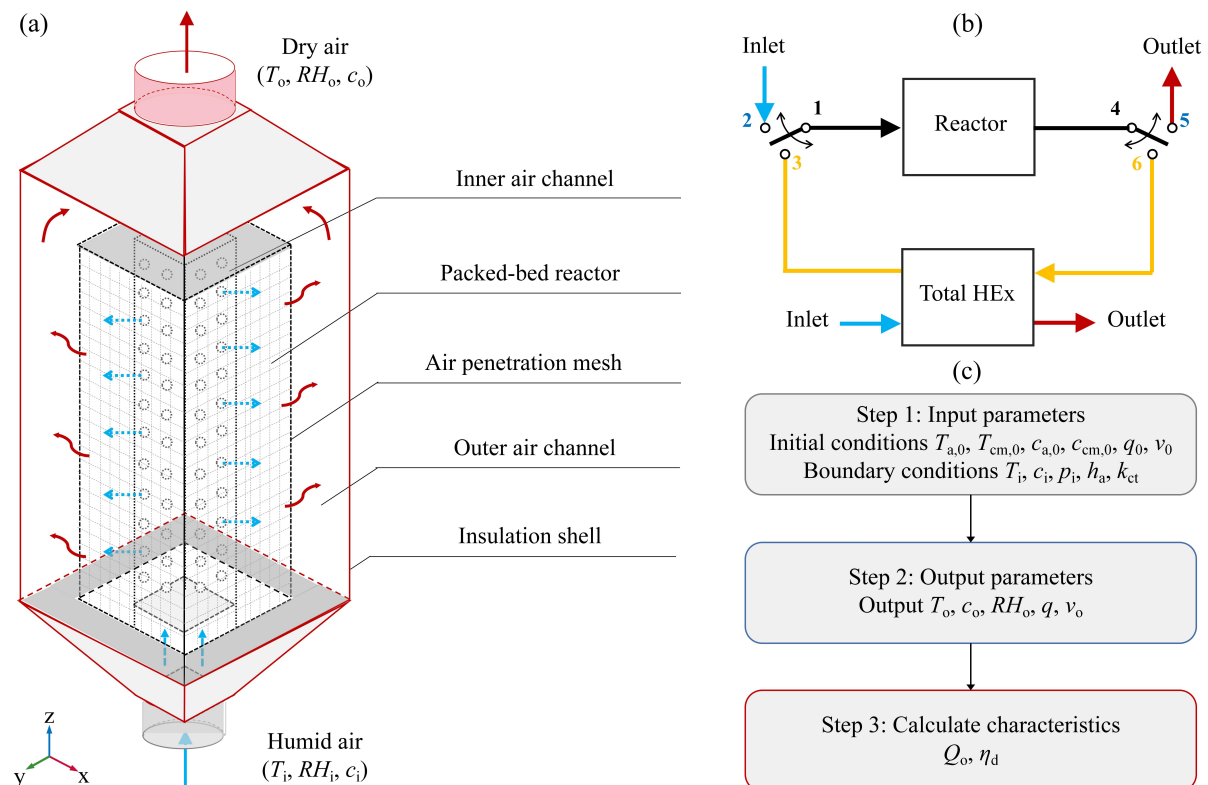
Figure 1. The geometry model of the adsorbent bed unit and simulated 3D illustration. (a) The 3D schematic diagram of the adsorption process in the ATB reactor. (b) The working

principle of open-cycle and loop-cycle adsorption processes applied in the computational model. (c) Schematic diagram of the flow chart.

Simulation methods

Model description

The geometry model of the ATB reactor is presented in Figure 1a. Two operation cycles, including the open cycle and the loop cycle, were applied in the simulation models (shown in Figure 1b). For ATB systems working in open cycle, the input air is introduced into the inlet of the ATB reactor, and the same airflow from the outlet of the reactor is used as the output to evaluate the thermal performance of ATB. For ATB working in loop cycle, two flows, namely the fresh airflow and loop airflow, exchange moisture and heat through the total heat exchanger (HEx) during the adsorption processes. One distinguished characteristic of loop cycle is that, two gradients, the water vapor concentration gradient and temperature gradient, occur in the region of the heat and mass exchanger. The outlet air of the fresh airflow side is denoted as output and used as the supplied air.

To simplify the analysis, a representative ATB reactor model was constructed primarily based on the following simplifications and assumptions: (1) the adsorbent particles are randomly distributed inside the reactor bed, and the porosity is spatially uniform; (2) the laminar flow model is adopted in the model; (3) the boussinessq's hypothesis is applied in solving the air's mass and momentum equation, while the water vapor is regarded as an ideal gas; (4) the boundary condition of ATB bed wall is considered as heat convection with the ambient environment; (5) the inlet air condition is uniform in space, but may vary with time; (6) the HEx is lacked in the model considering the complexity, replaced by a total exchange efficiency of 0.6, thus the outlet air parameter multiplied by which is used as the input parameter of inlet air of the reactor, and the exchanged heat is used as thermal output calculation. The calculation method of the computational model is schematically shown in Figure 1c.

Table 1. Thermophysical properties and operating parameters used in the simulation [14].

Parameter	Value	Units
Specific heat capacity of dry composite adsorbent, $c_{p,cm}$	880	J kg^{-1} K^{-1}
Specific heat capacity of air at 20 ºC and 70%RH, $c_{p,a}$	1013	J kg^{-1} K^{-1}
Density of dry composite adsorbent, ρ_{cm}	1162	kg m^{-3}
Density of air, ρ_a	1.2	kg m^{-3}
Viscosity of air, μ_a	1.8e-5	kg m^{-1} s^{-1}
Thermal conductivity of dry composite adsorbent, k_{cm}	0.2	W m^{-1} K^{-1}
Thermal conductivity of air, k_a	0.0256	W m^{-1} K^{-1}
Porosity of the dry composite adsorbent, ε_s	0.77	1
Porosity of the packed bed, ε_b	0.38	1
Volume of the adsorbent reactor, V_r	0.00972	m^3
vapor molecular diffusivity in the air, D_{vap}	2.491e-5	m^2 s^{-1}
Molecular weight of water, M_w	18	g mol^{-1}

Airflow rate in the open-cycle reactor, Q_a	4, 6, 8, 10	m s^{-1}
Fresh airflow rate in the loop-cycle reactor, Q_F	6	m s^{-1}
Loop airflow rate in the loop-cycle reactor, Q_L	4, 6, 8, 10	m s^{-1}
Inlet air temperature, T_i	15, 20, 25	^{o}C
Inlet air relative humidity, RH_i	30, 50, 70	%
Heat convection coefficient, h_a	5	W m^{-2} K^{-1}
Thermal conductivity of insulation cotton, k_{ct}	0.034	W m^{-1} K^{-1}

Heat and mass transfer during sorption process

In general, the water absorption process of the composite adsorbent can be divided into three stages: i) external diffusion, the gaseous water molecules transport from the free space of air to the external surface of the adsorbent; ii) internal diffusion, the water molecules diffuse in the pores of the composite adsorbent and reach the surface of adsorption sites; and iii) adsorption, water molecules are adsorbed by physical adsorption of SG and chemical adsorption (or absorption) of hygroscopic salt until the adsorption equilibrium is reached, and the water molecules will change from a free state closer to the gas phase to an adsorbed state closer to the liquid phase. The governing equations of mass transfer and mass balance applied to air channel and packed-bed reactor are expressed as follows [15]:

$$\rho_a \frac{\partial \mathbf{u}}{\partial t} + \rho_a (\mathbf{u} \cdot \nabla) \mathbf{u} - \nabla \cdot \left[-p + \mu \left(\nabla \mathbf{u} + (\nabla \mathbf{u})^T \right) - \frac{2}{3} \mu (\nabla \cdot \mathbf{u}) \right] - \rho_a \mathbf{g} = 0 \tag{1}$$

$$\frac{1}{\varepsilon_b} \rho_a \frac{\partial \mathbf{u}}{\partial t} + \frac{1}{\varepsilon_b} \rho_a (\mathbf{u} \cdot \nabla) \mathbf{u} \frac{1}{\varepsilon_b} - \nabla \cdot \left[-p + \mu \frac{1}{\varepsilon_b} \left(\nabla \mathbf{u} + (\nabla \mathbf{u})^T \right) - \frac{2}{3} \mu \frac{1}{\varepsilon_b} (\nabla \cdot \mathbf{u}) \right] - \rho_a \mathbf{g} = 0 \tag{2}$$

$$\frac{\partial c}{\partial t} + \mathbf{u} \cdot \nabla c + \nabla \cdot \left(-D_{vap} \nabla c \right) = 0 \tag{3}$$

$$\frac{\partial c}{\partial t} + \mathbf{u} \cdot \nabla c + \nabla \cdot \left(-D_{eff} \nabla c \right) + \frac{1}{\varepsilon_b} \rho_s \frac{dw}{dt} = 0 \tag{4}$$

The above equations represent the overall mass balance and water vapor mass balance, respectively. ρ_a, c and ρ_s is the density of air, concentration of water vapor and the density of composite adsorbent, respectively. u is the air velocity, D_{vap} is the diffusion coefficient of water vapor, ε_b is the porosity of the ATB packed-bed reactor, w is the water uptake.

Adsorption heat as the reaction enthalpy is generated during the water adsorption process, which is used to heat up the airflow. Equation describes the heat transfer and heat balance in the air channel and packed-bed reactor,

$$\rho_a c_{pa} \frac{\partial T}{\partial t} + \rho_a c_{p,a} \mathbf{u} \cdot \nabla T + \nabla \cdot (-k_a \nabla T) = 0 \tag{5}$$

$$\rho_{eff} c_{p,eff} \frac{\partial T}{\partial t} + \rho_a c_a \mathbf{u} \cdot \nabla T + \nabla \cdot (-k_{eff} \nabla T) - \rho_s \frac{dw}{dt} h_{ads} = 0 \tag{6}$$

where ρ_a, $c_{p,a}$, k_a are the density (kg m^{-3}), heat capacity (J kg^{-1} K^{-1}) and thermal conductivity (W m^{-1} K^{-1}) of the air, ρ_{cm}, $c_{p,cm}$, and k_{cm} are the local density (kg m^{-3}), heat capacity (J kg^{-1} K^{-1}) and thermal conductivity (W m^{-1} K^{-1}) of the composite adsorbent, respectively. Q represents the heat released by the composite layer during adsorption process. h_{ads} means the adsorption enthalpy (J mol^{-1}). The terms from left to right on the left side of the equation are

the total heat capacity, heat convection, thermal conductivity and the released adsorption heat, respectively.

Sorption kinetics reveals the dynamic behaviors of sorption process and indicates the instantaneous adsorption/desorption rates. The linear driving force (LDF) model, established upon the intramolecular transport phenomenon for spherical particles, has been recognized as a well-fitted theoretical method for the assessment of kinetics of the adsorbents in packed-bed reactors [16-18]. In this model, it is assumed that the all adsorption sites always reach equilibrium at local temperatures and pressures. The LDF model was adopted to describe the sorption kinetics in this study. The transient adsorption/desorption rate is given as:

$$\frac{dw}{dt} = k_{LDF}\left(w_{eq}\left(\frac{p_v}{p_{sat}(T)}\right) - w\right) \tag{7}$$

Here, k_{LDF} represents the coefficient of LDF model (s^{-1}), which is acquired by fitting the dynamic water uptake curves of the adsorbent. w_{eq} is the equilibrium water uptake of the sorbent ($g\ g^{-1}$), determined by the adsorption isotherm as a function of adsorption temperature T, and vapor pressure p_v.

Performance index definitions

The sorption and thermodynamics properties of the composite adsorbents are tested using ASAP and STA. The total volume of the ATB reactor V_r is calculated to be 0.0126 m^3. The adsorbents are considered to be fully regenerated before adsorption. The referenced adsorption temperature is set to be 20 ºC. The total mass of the sorbent m_s is 7 kg. The packing density of the sorbent bed ρ_b is 720 kg m^{-3}. The water uptake w [g$_{water}$ g$_{sorbent}^{-1}$] and adsorption enthalpy ΔH [J g$_{water}^{-1}$] of the adsorbents are obtained through experimental measurements using ASAP and STA. The theoretical energy storage density is thus calculated as:

$$ESD_t = w_{max} \cdot \rho_b \cdot \Delta H \ [\text{kWh m}^{-3}] \tag{8}$$

The output heating power, is another significant indicator to understand the behavior of ATB systems, which can be obtained by the equation below:

$$q_v = \frac{\dot{m}_a \cdot (c_{p,o} \cdot T_o - c_{p,i} \cdot T_i)}{V_r} \ [\text{kW m}^{-3}] \tag{9}$$

Discharging efficiency, denoting the effective thermal delivery performance of the ATB device, is calculated as the ratio between the useful heat output and the maximum output:

$$\eta_d = \frac{q_v}{ESD_t} = \frac{\int \dot{m}_a \cdot (c_{p,o} \cdot T_o - c_{p,i} \cdot T_i) dt}{\rho_b \cdot V \cdot w_{max} \cdot \Delta H} \ [\%]. \tag{10}$$
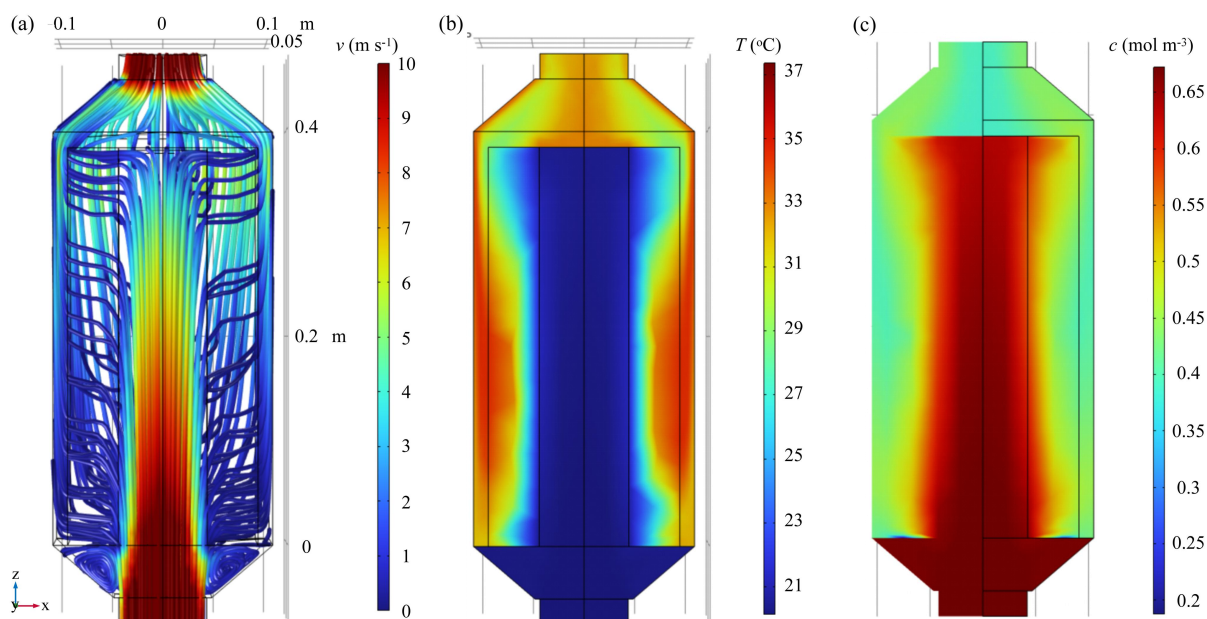
Figure 2. A representative numerical result of the computational model, showing (a) the airflow velocity, (b) temperature distribution and (c) water vapor concentration within the ATB reactor in the 10th min of the adsorption process. The results indicated a good uniformity of heat and mass transfer within the adsorbent bed.

Grid independence and Model validation

Figure 2 shows a representative numerical result of the computational model, which indicates the interior flow field of the ATB reactor. The influences of grid size on the simulation results, selecting the temperature and RH variation at the outlet of the air channel as the examples, were displayed in Figure 3a. The mesh density was refined from 10,000 to 200,000 elements respectively in each case. The results indicated that the transient temperature and RH were hardly invariant to the mesh size when the mesh density was refined from 50,000 to 200,000 elements, which demonstrated the grid independence. Therefore, the number of mesh cell is set to be 50,000 and the time step is selected as 1 min to ensure the reliability of the simulation investigation.

The modeling results are compared with the corresponding experimental results to validate the present model. Validation adsorption condition were performed under the same experimental working condition climates (15–25 ◦C & 30–70% RH), with the structural parameters listed in Table 1. A large number of conditions were compared and it was found that the errors between the experiments and modeling were all acceptable. Thus, one representative conditions (20 ◦C and 70% RH) was compared and shown in Figure 3b. The simulated results of outlet air temperature generally agree well with the experimental data. The discrepancy during the adsorption process could mainly attribute to the less accurate adsorption heat and sorption kinetics adopted in the simulation model, which is hard to determine through experiment.

Heat Powered Cycles
Conference 2023
Edinburgh

Heat in the new energy system

3rd to 6th of September 2023
The University of Edinburgh, Scotland
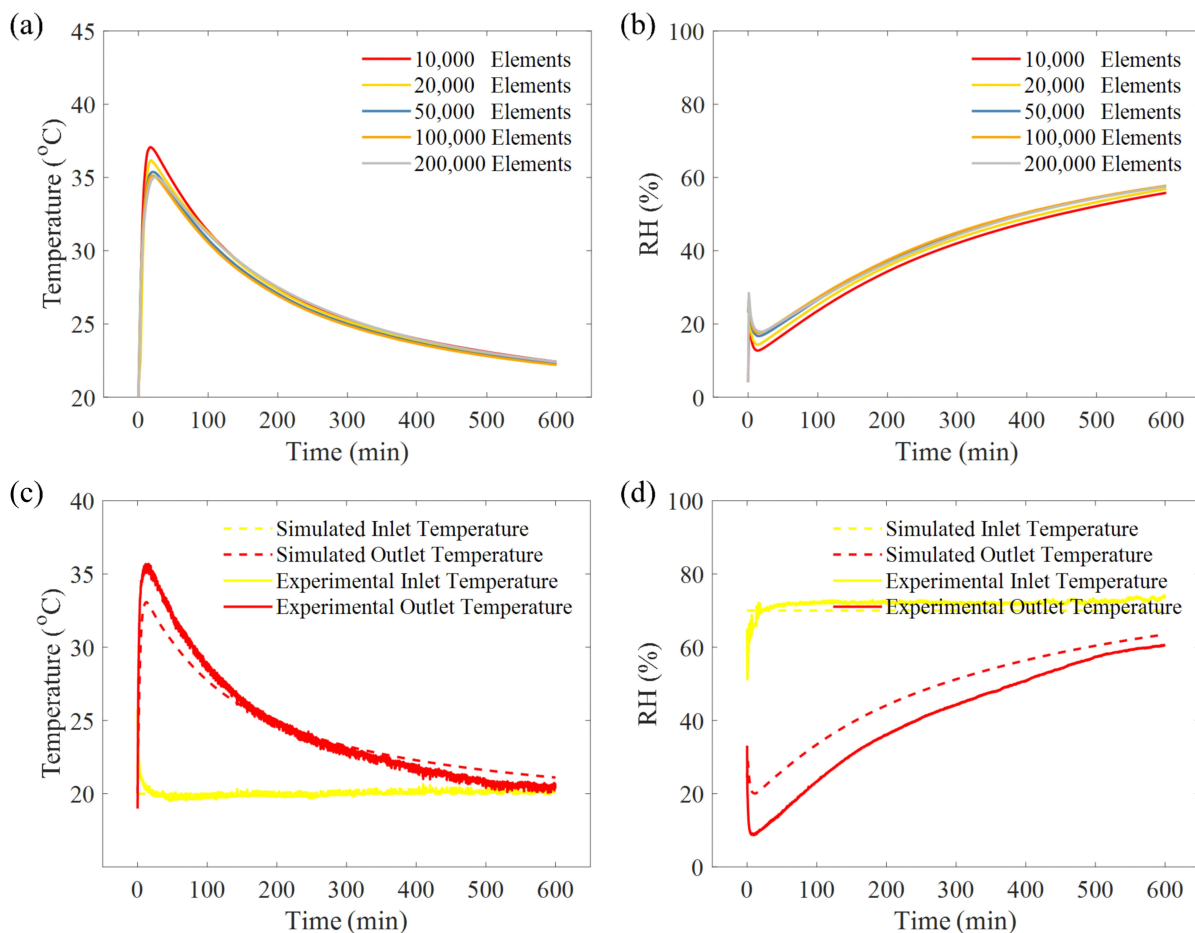
Figure 3. Grid dependence investigation for simulation analysis illustrating the effect of grid size on the simulation output results of the ATB reactor, with (a) the output temperature and (b) output RH results shown. Comparison between the simulated and experimental results under the inlet condition of 20 oC and 70 %RH, with (c) the inlet and outlet temperature, and (d) inlet and outlet RH shown .

Discussion and Results

In the following section, a series of parametric studies were analyzed to show the influence of structural and operating parameters on the thermal output performances. The main thermophysical properties and operating parameters used in the modeling are listed in Table 1.

Effects of reactor geometry

To study the influence of adsorbent bed structure on the system performance, three structural parameters, including the reactor thickness, the reactor height, and the aspect ratio L/H calculated from the ratio of the reactor thickness to the reactor height, were investigated for adsorbent bed structure optimization. In the structural parametric studies, the air temperature and RH at the inlet of the reactor are 20 °C and 70%, respectively. The influences of the reactor geometry on the evolution of output temperature, output RH, instantaneous heating power, and discharging efficiency in the open-cycle model are presented in Figure 4. The simulation results indicated that the thermal output performances of the ATB reactor is greatly dependent on the reactor thickness as well as the reactor height. With a larger height of adsorbent bed, the water uptake capacity is larger, and thus a greater adsorption heat is released, leading to an increased output temperature and heating power. The same reason of larger water capture amount causes a

lower output RH. However, the discharging efficiency (denoted as the blue line in Figure 4) of ATB reactor during the adsorption process is relatively low. When thinner adsorbent bed is applied, the water uptake capacity by the adsorbent decreases, causing less released adsorption heat, which results in a reduced output temperature and heating power. The discharging efficiency is larger in this case due to the faster adsorption process. To achieve the optimal thermal output performance of the ATB reactor considering both the heating power and the discharging efficiency, a bed thickness of 0.048 m and a reactor height of 0.38 m was selected in the following simulation and investigation.
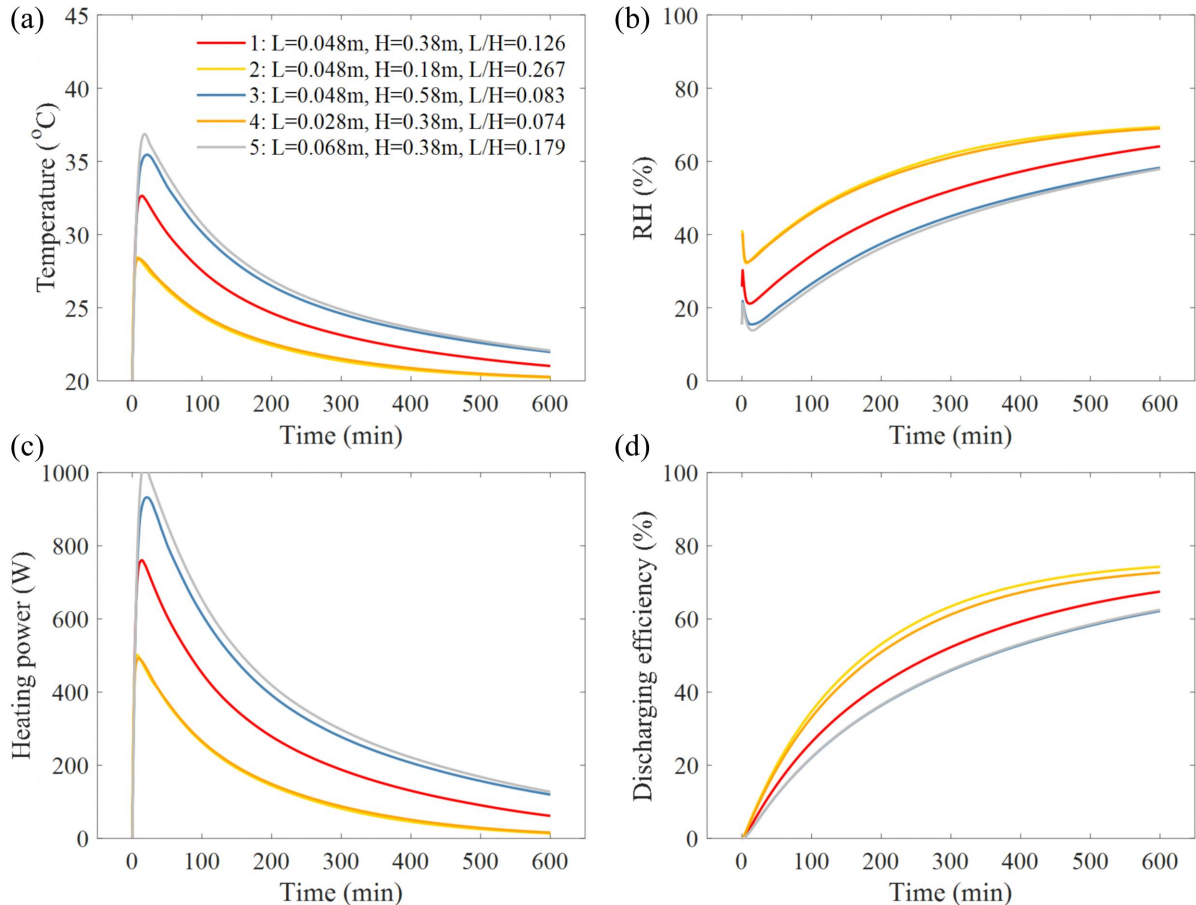
Figure 4. The influence of the geometry parameter L/H (the ratio of the thickness of the adsorbent packed bed and the height of the reactor) upon the output thermal performances: (a) the outlet temperature, (b) outlet RH, (c) heating power, and (d) discharging efficiency of the ATB reactor.

Effects of inlet air temperature and RH

Figure 5a depicts the impact of inlet air temperature on the heat and mass transfer performances of the ATB reactor. By varying the inlet air temperature with the same RH, an increase of temperature lift between the outlet and inlet temperature was obtained, with 14.77 °C, 17.02 °C, and 18.33 °C for the cases of 15 °C, 20 °C, and 25 °C inlet temperature. The reason is that the inlet air with a higher temperature and constant RH contains a larger amount of moisture, a greater water vapor concentration gradient between the air and adsorbent caused by which would lead to a faster adsorption kinetics in the adsorbent bed. Thus, a larger heating power and discharging efficiency is also achieved. The effect of inlet air RH on the output thermal performances of the ATB reactor shares some similarities with the influence of inlet air

temperature, but greater differences are observed in those cases with different RH. As expected, by increasing the inlet air RH, a larger output temperature, output RH, heating power and discharging efficiency is achieved. The temperature lift between the outlet and inlet temperature was obtained, with 8.64 °C, 13.36 °C, and 17.02 °C for the cases of 30%RH, 50%RH and 70%RH, respectively. The difference of temperature lift caused by various RH is larger than that cases with different inlet temperature. The maximum discharging efficiency after 600 min of adsorption processes in these three cases is 43.01%, 62.16%, and 85.95%. This can be explained by two reasons. The inlet air with a higher RH and constant temperature contains a larger amount of moisture, a greater water vapor concentration gradient between the air and adsorbent caused by which would lead to a faster adsorption kinetics in the adsorbent bed. In addition, at higher RH, the equilibrium water uptake of the adsorbent is larger, which determines the maximum capacity of moisture capture of the adsorbent. Both factors will contribute to a larger adsorption heat to release. This simulation results generally agree well with the results obtained in previous studies [19, 20].
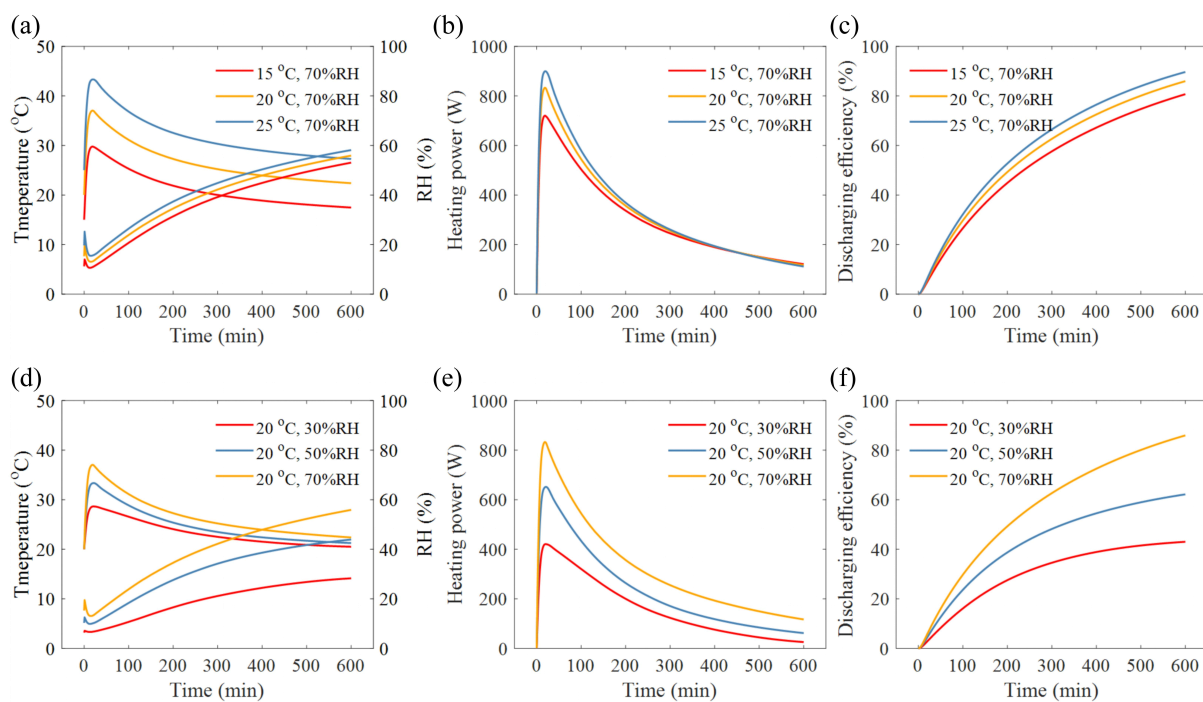
Figure 5. The influence of the inlet temperature upon the output thermal performances: (a) the outlet temperature and outlet RH, (b) heating power, and (c) discharging efficiency of the ATB reactor. The influence of the inlet RH upon the output thermal performances: (d) the outlet temperature and outlet RH, (e) heating power, and (f) discharging efficiency of the ATB reactor.

Effects of airflow rate

The airflow rate, as a crucial parameter determining the heat and mass transfer coefficients and influencing the thermal output performances of the ATB reactor, has been widely investigated in previous studies. Figure 6a evaluates the effects of airflow rate in the open-cycle reactor on the output temperature, output RH, heating power and the discharging efficiency. By increasing the airflow rate, a higher velocity could contribute to a smaller mass transfer resistance and faster adsorption kinetics. The results illustrated that, increasing the airflow rate from 4 m s^{-1} to 10 m s^{-1} leads to an increase in output RH and heating power, and a larger discharging efficiency. A maximum heating power of 879.8 W was obtained when applying an airflow rate of 10 m s^{-1} in the simulation model. However, a drop of temperature lift accompanies the increase of heating

Heat Powered Cycles
Conference 2023
Edinburgh

Heat in the new energy system

3rd to 6th of September 2023
The University of Edinburgh, Scotland

power in the case of high airflow rate. The reason is that the air with high flow rate takes away more adsorption heat, while the adsorption kinetics is not rapid enough to provide sufficient amount of heat. This phenomenon was also observed in many previous research [21, 22]. The disharmony between the change of output temperature and heating power is not expected if to be used in the space heating applications.

In this study, the loop-cycle ATB reactor was proposed to solve this problem. The effects of airflow rate on the overall thermal output performances of the loop-cycle model were investigated. In Figure 6b, it is indicated that as the rise of loop airflow rate from 4 m s^{-1} to 10 m s^{-1}, the output temperature increases, with a maximum temperature lift between outlet and inlet air of 6.30 $^{\circ}$C in the case of 4 m s^{-1} airflow rate improved to 11.19 $^{\circ}$C in the case of 10 m s^{-1} airflow rate. The heating power also increases along the rise of loop airflow rate attributing to the larger temperature lift. The increase of loop airflow rate accelerate the adsorption kinetics in the adsorbent reactor, thus leading to an enhancement of discharging efficiency. These results have illustrated that, by applying the loop-cycle strategy in the ATB system, it is possible to realize satisfactory thermal delivery with a positive feedback between output temperature and heating power. After the 600-min adsorption processes, the maximum discharging efficiency of the loop-cycle reactor with 10 m s^{-1} airflow rate is 50.45%, which is one third less than that of the open-cycle reactor under the same airflow rate (approximately 80%). It should be noted that, the reaction kinetics in the loop-cycle reactor is smaller due to the existing heat and mass exchange efficiency of the HEx, which could hold the potential of supplying long-term discharging heat with stable thermal output.
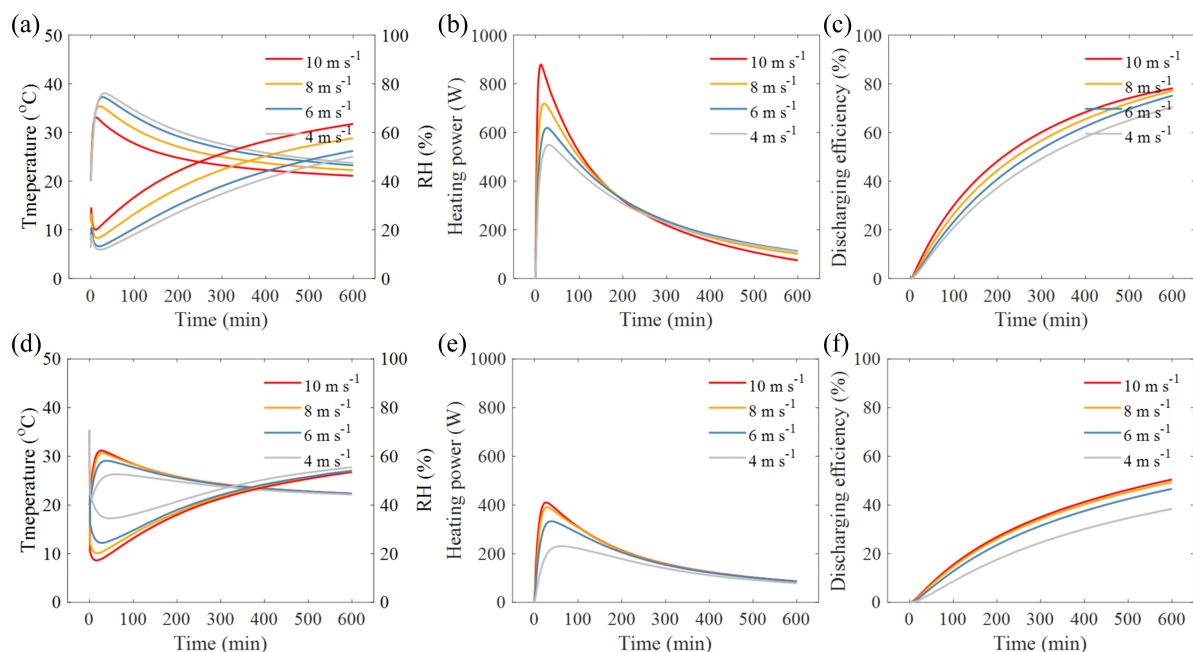
Figure 6. The influence of the fresh air velocity in the open-cycle reactor upon the output thermal performances: (a) the outlet temperature and outlet RH, (b) heating power, and (c) discharging efficiency of the ATB reactor. The influence of the loop air velocity in the loop-cycle reactor upon the output thermal performances: (d) the outlet temperature and outlet RH, (e) heating power, and (f) discharging efficiency of the ATB reactor.

Stable output strategy

To achieve stable thermal output, the overall performances of the loop-cycle ATB reactor were further studied by adopting different tuning strategies (shown in Figure 7). The step-by-step

strategy is to maintain the loop airflow rate as 4 m s^{-1} in the first 180 min of adsorption, and then successively increase the air velocity to 6 m s^{-1}, 8 m s^{-1}, and 10 m s^{-1} in the 180th min, 320th min, and 460th min. Test 1, Test 2, Test 3, Test 4, and Test 5 applied the method of gradual rate increase, with different starting times and various slopes used in each rate range, as denoted in Figure 7. Test 1 adopted the slowest slope of airflow rate, while the increase speed of airflow rate in Test 2, Test 3 and Test 4 was the largest but the starting time of rate increase was different in these cases. Compared with the case of Test 4, Test 5 shared a same starting time in the 180th min, but had a relatively small slope in the range of 4-6 m s^{-1}. The investigated method is for finding possible management strategies to achieve stable thermal output with high discharging temperature and large heating power.
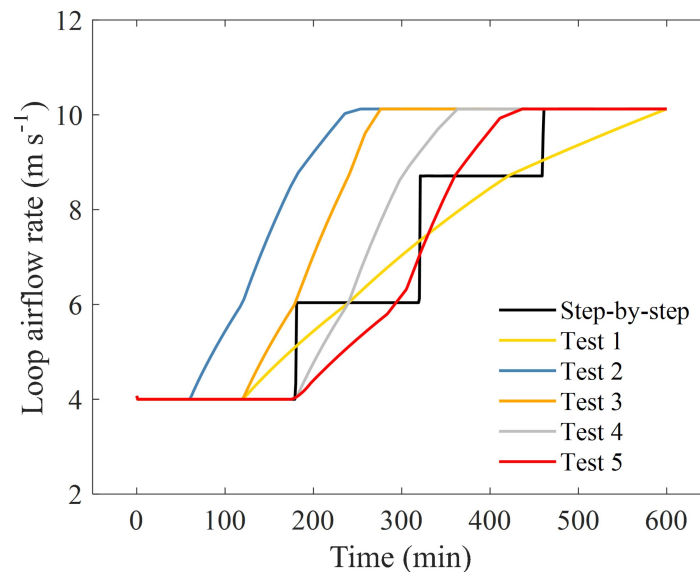
Figure 7. Strategies for stable thermal output by tuning loop airflow rate in the loop-cycle simulation model.

A comparison of output thermal performances of the loop-cycle ATB reactor model under different discharging threshold temperatures was presented in Figure 8. For the step-by step case, as the loop airflow rate increases in each rate step, the adsorption kinetics in the adsorbent bed speeds up, resulting in an increase in water uptake and a larger adsorption heat to release. In addition, due to an increased loop airflow rate, more moisture is exchanged from the fresh air to the loop air, and more heat is exchanged from the loop air to the fresh air through the HEx. With a constant fresh airflow rate, the discharging temperature and heating power obtained at the outlet can be improved. As expected, a sudden increase of output temperature and heating power like the shape of zigzag was observed in each rate step.

For the case of Test 1, the discharging temperature maintains as approximately 26 °C and the heating power is above 220 W for 161 min, which is mainly attributed to a slow rate slope. As the rate slope increases, the adsorption rate is accelerated, leading to the enhancement in output temperature and heating power. With a discharging threshold temperature of 27 °C, the effective heating time (defined as the total discharging duration time when the output temperature is above the discharging threshold temperature) in Test 2 is 172 min. With a discharging threshold temperature of 26 °C, the effective heating time in Test 2 and Test 3 is 250 min and 276 min, respectively.

Heat Powered Cycles
Conference 2023
Edinburgh

Heat in the new energy system

3rd to 6th of September 2023
The University of Edinburgh, Scotland

For the case of Test 4 and Test 5, the results indicated a distinguished platform in the profiles of output temperature, output RH and heating power. A larger discharging temperature and heating power was obtained in Test 4 due to a larger slope of airflow rate in the 4-6 m s^{-1} range compared with that of Test 5. Taking 25 $^{\circ}$C as the discharging threshold temperature, the effective heating time in Test 4 and Test 5 is 380 min and 404 min, respectively. For the stable output stage, the heating power density is 19.5 kW m^{-3} for as long as 252 min. The output RH change between 35% and 40% along the effective discharging process, which also enables a controllable humidity management in the application of direct space heating considering human thermal comfort.
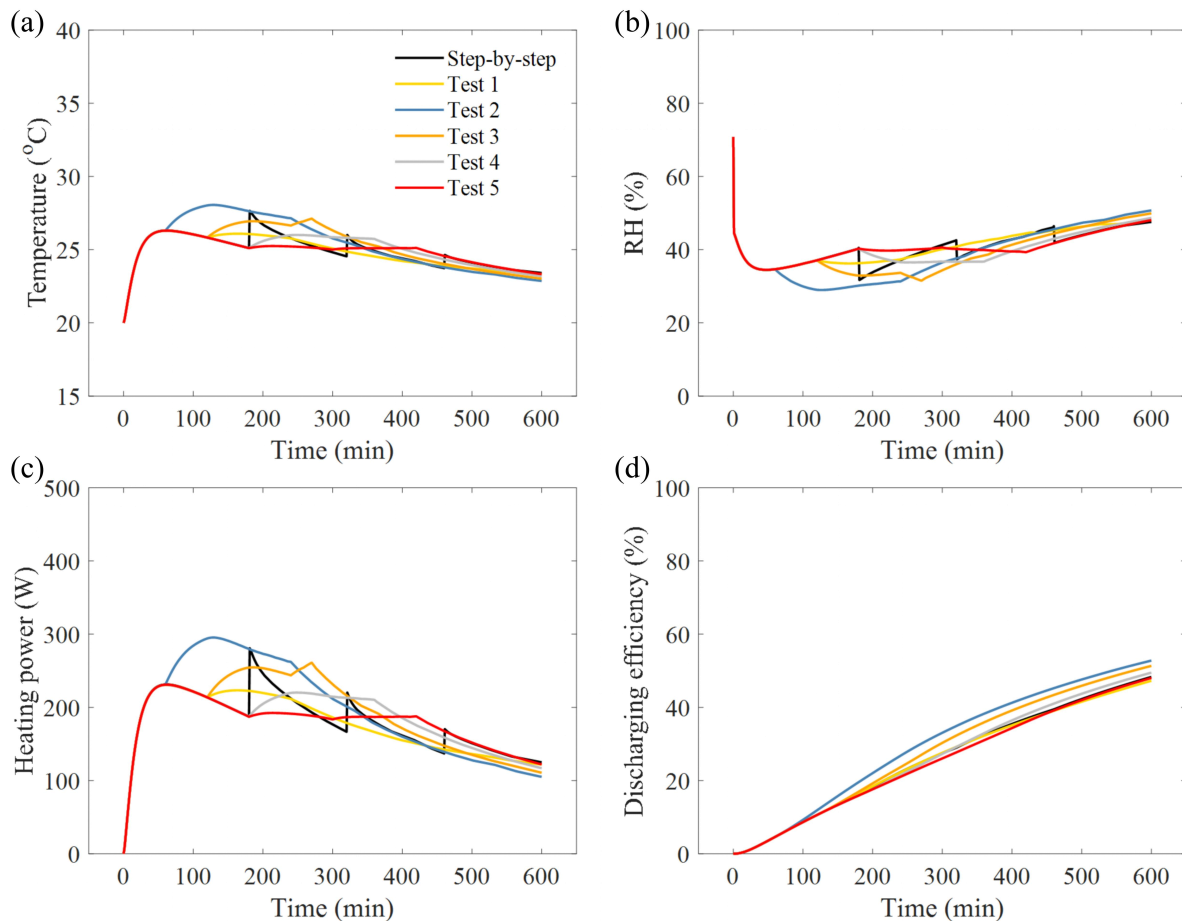
Figure 8. The output thermal performances of the loop-cycle simulation model adopting different loop air velocity to achieve stable output temperature and heating power : (a) outlet temperature, (b) outlet RH, (c) heating power, and (d) discharging efficiency.

Conclusions

A three-dimensional computational model for predicting the overall thermal output performances of a packed-bed adsorption thermal battery was built and validated. By using this model, the influences of structural parameters were firstly investigated for adsorbent bed optimization, and then the effects of the operating parameters on the system performance were evaluated. A possible strategy for stable thermal output by tuning loop airflow rate based on the simulation results is thus proposed in this study.

In summary, the following conclusions can be drawn:

(1) The reactor height and adsorbent bed thickness both impose great influence on the thermal output performances of the ATB reactor. A larger reactor height and bigger bed thickness will induce greater water capture capacity of the adsorbent, contributing to a larger output temperature and heating power but an insufficient discharging efficiency.

(2) The parametric study of the effect of inlet air temperature, RH and airflow rate reveals the various characteristics of the ATB reactor under different operating conditions. Those cases with larger inlet temperature and RH for the adsorption processes benefit to greater thermal output performances. By varying airflow rate, the simulation points out a common phenomenon of the disharmony between the change of output temperature and heating power in the open-cycle reactor.

(3) For ATB working in loop cycle, increasing the loop airflow rate could both enhance the output temperature lift and heating power, which indicates the possibility of realizing satisfactory thermal delivery with a positive feedback between output temperature and heating power. Based on the simulation results, the management strategy proposed in this study by tuning loop airflow rate demonstrated its feasibility to achieve stable thermal output.

Acknowledgments

References:

[1] H. Kim, S. Yang, S.R. Rao, S. Narayanan, E.A. Kapustin, H. Furukawa, A.S. Umans, O.M. Yaghi, E.N. Wang, Water harvesting from air with metal-organic frameworks powered by natural sunlight, Science, 356(6336) (2017) 430-434.

[2] Y. Zhang, L. Wu, X. Wang, J. Yu, B. Ding, Super hygroscopic nanofibrous membrane-based moisture pump for solar-driven indoor dehumidification, Nat Commun, 11(1) (2020) 3302.

[3] C.X. Wang, L.J. Hua, H.Z. Yan, B.J. Li, Y.D. Tu, R.Z. Wang, A Thermal Management Strategy for Electronic Devices Based on Moisture Sorption-Desorption Processes, Joule, 4(2) (2020) 435-447.

[4] M. Ejeian, R.Z. Wang, Adsorption-based atmospheric water harvesting, Joule, 5(7) (2021) 1678-1703.

[5] W. Li, X.Y. Luo, P. Yang, Q.W. Wang, M. Zeng, C.N. Markides, Solar-thermal energy conversion prediction of building envelope using thermochemical sorbent based on established reaction kinetics, Energy Conversion and Management, 252 (2022) 115117.

[6] S. Narayanan, X. Li, S. Yang, H. Kim, A. Umans, I.S. McKay, E.N. Wang, Thermal battery for portable climate control, Applied Energy, 149 (2015) 104-116.

[7] H.L. Zhang, J. Baeyens, G. Caceres, J. Degreve, Y.Q. Lv, Thermal energy storage: Recent developments and practical aspects, Progress in Energy and Combustion Science, 53 (2016) 1-40.

[8] N. Yu, R.Z. Wang, L.W. Wang, Sorption thermal storage for solar energy, Progress in Energy and Combustion Science, 39(5) (2013) 489-514.

[9] L. Scapino, H.A. Zondag, J. Van Bael, J. Diriken, C.C.M. Rindt, Sorption heat storage for long-term low-temperature applications: A review on the advancements at material and prototype scale, Applied Energy, 190 (2017) 920-948.

[10] Y. Zhang, R. Wang, Sorption thermal energy storage: Concept, process, applications and perspectives, Energy Storage Materials, 27 (2020) 352-369.

[11] G.L. An, L.W. Wang, J. Gao, Two-stage cascading desorption cycle for sorption thermal energy storage, Energy, 174 (2019) 1091-1099.

[12] Y.N. Zhang, H.H. Dong, R.Z. Wang, P.H. Feng, Air humidity assisted sorption thermal battery governed by reaction wave model, Energy Storage Materials, 27 (2020) 9-16.

[13] Z. Zeng, B. Zhao, R. Wang, Water based adsorption thermal battery: Sorption mechanisms and applications, Energy Storage Materials, 54 (2023) 794-821.

[14] W.W. Wang, Q.W. Pan, R.Z. Wang, T.S. Ge, Modeling and optimization of a honeycombed adsorbent bed for efficient moisture capture, Applied Thermal Engineering, 200 (2022) 117717.

[15] M. Gaeini, H.A. Zondag, C.C.M. Rindt, Effect of kinetics on the thermal performance of a sorption heat storage reactor, Applied Thermal Engineering, 102 (2016) 520-531.

[16] E. Alpay, D.M. Scott, The linear driving force model for fast-cycle adsorption and desorption in a spherical particle, Chemical Engineering Science, 47(2) (1992) 499-502.

[17] Y.I. Aristov, I.S. Glaznev, A. Freni, G. Restuccia, Kinetics of water sorption on SWS-1L (calcium chloride confined to mesoporous silica gel): Influence of grain size and temperature, Chemical Engineering Science, 61(5) (2006) 1453-1458.

[18] S. Sircar, J.R. Hufton, Why does the Linear Driving Force model for adsorption kinetics work ?, Adsorption, 6(2) (2000) 137-147.

[19] T. Yan, T. Li, J. Xu, J. Chao, R. Wang, Y.I. Aristov, L.G. Gordeeva, P. Dutta, S.S. Murthy, Ultrahigh-Energy-Density Sorption Thermal Battery Enabled by Graphene Aerogel-Based Composite Sorbents for Thermal Energy Harvesting from Air, ACS Energy Letters, 6(5) (2021) 1795-1802.

[20] P. Tatsidjodoung, N. Le Pierres, J. Heintz, D. Lagre, L.G. Luo, F. Durier, Experimental and numerical investigations of a zeolite 13X/water reactor for solar heat storage in buildings, Energy Conversion and Management, 108 (2016) 488-500.

[21] Y.C. Lin, W. Liu, X.J. Zhang, L. Jiang, Performance analysis on open thermochemical sorption heat storage from a real mass transfer perspective, Journal of Energy Storage, 54 (2022).

[22] Y.N. Zhang, R.Z. Wang, T.X. Li, Experimental investigation on an open sorption thermal storage system for space heating, Energy, 141 (2017) 2421-2433.

3rd to 6th of September 2023
The University of Edinburgh, Scotland

Heat Powered Cycles
Conference 2023
Edinburgh

Heat in the new energy system

The effect of polytetrafluoroethylene (PTFE) thin films deposited on aluminium surfaces on Phase Change Material (PCM) solidification.

Ronald Muhumuza[1*], Pawel Dominik Nycz[1], and Philip Eames[1]

[1]Centre for Renewable Energy Systems Technology (CREST), Wolfson School of Mechanical, Electrical and Manufacturing Engineering, Loughborough University, Loughborough, LE11 3TU, UK

*Corresponding author: email address (r.muhumuza@lboro.ac.uk)

Abstract

A thin film Polytetrafluoroethylene (PTFE) coating was applied to as-received (AR), manually polished (MP), and sandblasted (SB) surfaces of 60 mm diameter, 10 mm thick aluminium discs cut from a circular cross section rod to produce samples with different areal surface roughness parameters. This resulted in different water contact angles and different degrees of hydrophobicity. Experiments were performed to determine how the solidification behaviour of two PCMs; erythritol, a polar molecule, and polyethylene glycol 6000 (PEG 6000), a non-polar molecule were influenced by surface characteristics. The coated manually polished sample with measured areal surface roughness parameters, $S_a = 1.02 \pm 1.30 \, \mu m$, $S_{sk} = 0.04$, and $S_{ku} = 2.69$ increased the time to phase change onset of a 2 g sample of erythritol (placed on the surface and then melted) by 93% compared to the aluminium surface without a PTFE thin film. The fabricated surfaces which were superhydrophobic had a strong effect on the shape formed by hot erythritol liquid due to the polar characteristics of the erythritol molecule. Using superhydrophobic thin film coatings on heat exchanger surfaces to modify the solidification behaviour of polar molecules like erythritol, can have potential applications in Latent Heat Thermal Energy Storage (LHTES) systems by modifying charge/discharge performance.

Keywords: superhydrophobicity, superoleophobicity, superomniphobicity, phase change materials, LHTES, thin films

Introduction

When discharging LHTES systems, a layer of solid Phase Change Material (PCM) develops rapidly on the heat transfer surfaces which increases thermal resistance and decreases the rate of heat transfer to the heat exchanger and the heat transfer fluid [1]. To overcome this, active mechanical scrappers [2] and/or electrical resistance heaters [3], and ultrasonic vibrations [4] have been explored to limit the development of PCM solid layers on heat exchanger surfaces during the discharge cycle. Alternative passive approaches have been employed to maintain acceptable rates of heat transfer during charging/discharging of PCM stores, e.g., extended surfaces [5], tilting the thermal store [6], introducing highly conductive particles into the PCMs [7], or utilising different storage container shapes [8] and orientation and location of heat input /extraction locations [9]. Passive approaches employing non-stick thin film coatings can modify the heat transfer boundary layer on surfaces, thus potentially improving the heat discharge cycle. Non-stick coatings have been unsuccessfully trialled [10] in high temperature LHTES (above ~300°C), but to date they have not been evaluated for use in low temperature (up to ~250°C) LHTES. As PCMs advance into various low temperature process heat recovery and storage applications, it is necessary to investigate heat transfer surfaces with potential to deliver improved performance, by employing liquid-repellent thin film coatings.

The potential of liquid-repellent surfaces to passively suppress/delay PCM solid nucleation on the contact heat transfer surface opens possibilities to i) improve the heat discharge cycle and ii) achieve long-term low loss thermal energy storage using suitable PCMs. In the discharge cycle by cooling the liquid PCM to below its normal solidification point at the heat transfer surface it will sink due to buoyancy considerations, if solidification subsequently is initiated at a nucleation point, for example at the base of the store, heat will be released warming the adjacent fluid which will rise and circulate to the heat exchanger, establishing natural convective circulation. The option for low loss, long term storage requires that the liquid PCM can be cooled to ambient without solidification being initiated, and when store discharge is required, solidification is triggered at the base of the store, releasing heat, and establishing a natural convective cycle, allowing heat to be removed at the heat exchanger. Evaluating the solidification of suitable PCMs on liquid-repellent surfaces is important for their practical application in real phase change thermal energy storage systems.

Liquid-repellent surfaces can be achieved by applying low surface-energy thin film materials on rough metallic and non-metallic substrates. The typical roughness on metal substrates can be on microscopic (~50nm-10μm) and nanoscopic (up to ~100 nm) length scales [11], whilst the thicknesses of the thin film coatings can be as low as ~ 0.01 µm [12] depending on the fabrication technique. Roughness is mostly evaluated on a 2-dimensional (2D) line profile [13] but areal 3-dimensioanal (3D) surface roughness parameters, e.g., arithmetic mean height (S_a), root mean square height (S_q), skewness (S_{sk}), kurtosis (S_{ku}), etc. [14] are expected to be used to standardise the future development of liquid-repellent surfaces [15].

Many approaches are available to fabricate liquid-repellent surfaces [16], with durability a major challenge [17] for their large-scale production and application. Simple, low-cost established methods for the cost-effective production of liquid-repellent surfaces for many applications are attractive. Sol-gel methods, dip-coating, spray-coating and spin-coating are considered flexible, low-cost, and widely accessible ways of achieving both good levels of surface roughness and depositing simultaneously liquid-repellent thin films using composite mixtures of micro-nanoparticles and low surface energy materials, (e.g., micro-nanoparticle–polymer mixtures [18]). Liquid-repellent surfaces can also be cost-effectively and conveniently produced at scale by separately introducing surface roughness using abrasive blasting (e.g., sandblasting or bead blasting) [19] and/or chemical etching [20] followed by the deposition of a low surface energy coating. Brinksmeier et al. [21] assessed different methods that can achieve multiscale functional surface texture on materials.

In this work, water-repellent surfaces were achieved using different abrasive methods to introduce surface roughness before applying a Polytetrafluoroethylene (PTFE) aerosol spray coating. Areal surface roughness and wettability parameters were measured and their impact on PCM nucleation was evaluated experimentally. The experiments provided measured temperature data and digital microscopic observations to study transient solidification effects of erythritol and polyethylene glycol 6000 (PEG 6000) - promising PCMs for low temperature LHTES up to ~120°C [22] and ~60°C[23], respectively.

Material and methods

Preparation of samples

Aluminium disc samples were machined from a rod of 60 mm diameter to a consistent thickness of 10 ± 0.5 mm by turning and the surfaces were made flat with the same cutting tool and cutting speed. Abrasive blasting (samples SB-1 and SB-2) and hand polishing (samples MP-1 and MP-3) with different emery paper grades (P480 to P2000) were used to produce surface textures on one side of each aluminium disc. The surface of sample MP-2 was prepared to a near mirror finish by additional polishing using ultra-fine diamond polishing pads (6μm‑1μm) with a manual surface polisher/grinder. Two samples AR-1 and AR-2 were

retained as received after machining to provide control samples. A 2 mm diameter hole was drilled into the circumference of each aluminium disc at a positioned 2 mm below the roughened surface to a depth of 30 mm. This was for inserting a thermocouple to measure the Al disc temperature. The surfaces were cleaned by ultrasonication in deionised (DI) water, washed with acetone and isopropanol (IPA) and dried at ambient temperature. The cleaned samples were kept in a desiccator to minimise corrosion and provided temporary storage during the measurement of their surface morphology before applying thin film coatings.

A thin film coating was deposited on each clean/dry textured surface using a polytetrafluoroethylene (PTFE) aerosol spray. Coated surfaces were heat treated in an oven at a temperature of 150°C for 10 min to evaporate the solvent, subsequently the oven temperature was increased to 290°C for 5 min to sinter the PTFE particles onto the surfaces. The oven was then switched off and the sintered thin film samples allowed to cool to ambient conditions. The samples were returned to the desiccator for protection during the process of measuring water contact angles. **Table 1** summarises the different samples and the conducted surface operations.

Table 1. Sample surfaces on aluminium discs with flat surfaces

Sample	Thickness (mm)	Surface structure preparation	PTFE Spray coated (yes/no)
AR-1	10.01	As received after machining	Yes
AR-2	10.05	As received after machining	No
MP-1	10.09	Roughened with emery paper (grades P600, P800, P1200 and finally P2000)	Yes
MP-2	9.50	Mirror finish (ultra-micro finish/smooth (1μm cloth – polishing machine)	Yes
MP-3	10.17	Roughened with emery paper (grades P480 and finally P600)	Yes
SB-1	10.05	Abrasive blasting using mixed Al2O3 grits (F36 and F120) for ~5 min at 10-15 cm distance and 6 bar air supply pressure	Yes
SB-2	9.90	Abrasive blasting using soda-lime glass beads (Honite 14, grit size 75-150 microns) at ~5 cm distance and 6.5 bar air supply pressure	Yes

Characterisation

A digital microscope (Keyence VHX-6000) mounted with a wide-range zoom lens (VH-Z100R) was used to capture magnified images of the fabricated sample surfaces. The magnification was 200X with a field of view of 1.53 mm x 1.14 mm. Image stitching was used to expand the field of view enabling a surface area of 12.8 mm by 12.8 mm to be recorded for each sample before applying the thin film. The recorded images were used to evaluate changes in areal surface roughness parameters using the 3D profile measurement application (model VHX-H4M) on the microscope computer. Based on an expected profile average surface roughness R_a above the range $0.06 - 1.2$ μm but below the range $1.2 - 6.0$ μm [24], a recommended L-filter nesting index value of 1 mm was selected in accordance with ISO 25178-3:2012 [25] to filter low-frequency/long wavelength spatial structures [26]. A rectangular area of 5 mm x 1 mm (according to the ISO standard) was used to extract measurements from at least six different locations on previously recorded images. Additionally, each 5 mm x 1 mm area was divided into five 1 mm x 1 mm subareas, resulting in a total of at least 30 measurements for each sample. To remove high-frequency noise from the

Heat Powered Cycles
Conference 2023
Edinburgh

Heat in the new energy system

3rd to 6th of September 2023
The University of Edinburgh, Scotland

measurements, an S-filter nesting index value of 10 μm was used, so that the approximate bandwidth ratio between the L-filter and S-filter nesting index values was 100:1.

The measured surface parameters included, S_a, S_q, S_{sk}, and S_{ku} which are standard parameters used in characterising the areal roughness profile of textured surfaces [27]. S_a is the average areal roughness representing the arithmetic mean of the absolute values of all the points of measured area whilst S_q corresponds to the standard deviation of height measurements. S_{sk} and S_{ku} indicate the asymmetric property and sharpness of height distribution of the surface as illustrated by the schematic probability density functions presented in Fig. 1. Liquid-repellent thin film coatings combining surface roughness and thin film coatings demand surface texture characteristics with a low $S_a \pm S_q$. Thin film surfaces whose probability density functions of the surface heights have $S_{sk} < 0$ and $S_{ku} < 3$ can minimise failure of the thin film by liquid-surface-texture penetration or wetting.
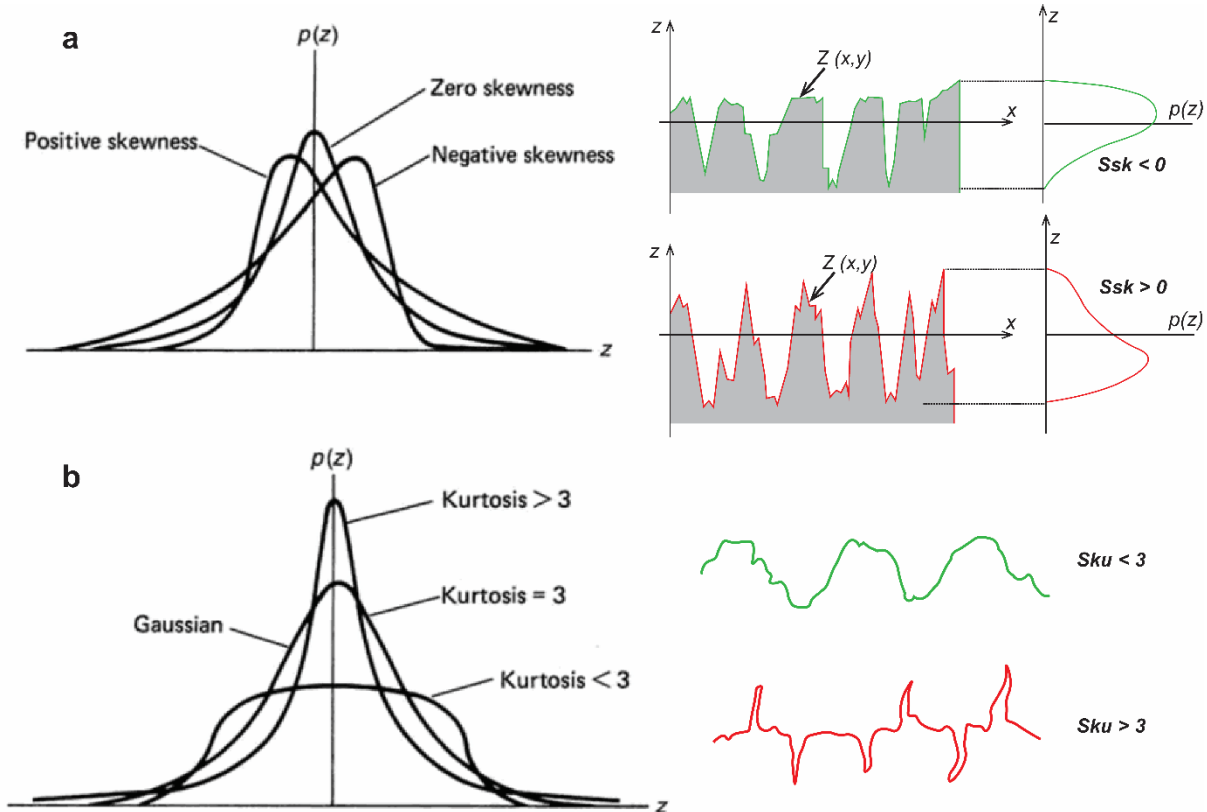
Fig. 1. Probability density distributions for (a) surfaces with different skewness (S_{sk}) values and (b) symmetrical distributions (zero skewness) with different kurtosis (S_{ku}) values [27] and corresponding typical surface roughness profiles. Roughness profile values of $S_{sk} < 0$ and $S_{ku} < 3$ are fundamental for fabricating surfaces resistant to wetting (liquid-repellent surfaces).

A contact angle goniometer (Ossila BV) was used for measuring static contact angles of the fabricated PTFE thin film surfaces using deionised (DI) water droplets of 3 μL in volume dispensed using an adjustable micropipette. At least seven measurements of static contact angle were acquired at different random locations on the surfaces for each sample. Due to manual adjustment of the stage of the contact angle goniometer to locate the baseline, care was taken to minimise the root-mean-square-error (RMSE) in the left and right-contact angle measurements of water droplets on surfaces.

The effect of fabricated thin films on PCMs

Two experiments were performed, i) a digital microscope was used to observe the effect of surfaces on the solidification and melting of polar and non-polar PCMs, i.e., erythritol and PEG 6000 suitable for latent heat storage applications, ii) a more detailed analysis of solidification behaviour of erythritol on the prepared surfaces. In the first set of experiments two surfaces, one from the as-received group (control surface without a PTFE thin film coating) and one from the bead blasted and manually polished groups were selected. These were used to investigate cases of PCM droplet shapes formed by melting single micrometre scale crystals and flakes of erythritol and PEG 6000, respectively under a digital microscope. The second set of experiments were performed in a heated space illustrated in Fig. 2 to evaluate the effect of the different fabricated surfaces on the solidification temperature of erythritol. The hot space was formed of a transparent glass① enclosure which was placed over the aluminium disc substrate⑥ mounted on a thermoelectric heating element⑩, which was in turn placed on a continuously water-cooled heat sink stage⑫.

1. Transparent hot space containment
2. Hot space temperature thermocouple
3. PCM (Erythritol)
4. PCM temperature thermocouple
5. Silicone O-ring
6. Aluminium disc (substrate)
7. Surface of interest on substrate
8. Substrate temperature thermocouple
9. Insulation for substrate K-type thermocouple
10. Thermoelectric heater
11. DC power supply
12. Water-cooled heat sink stage
13. Heat sink stage themocouples
14. Hot air gun on fixed stand
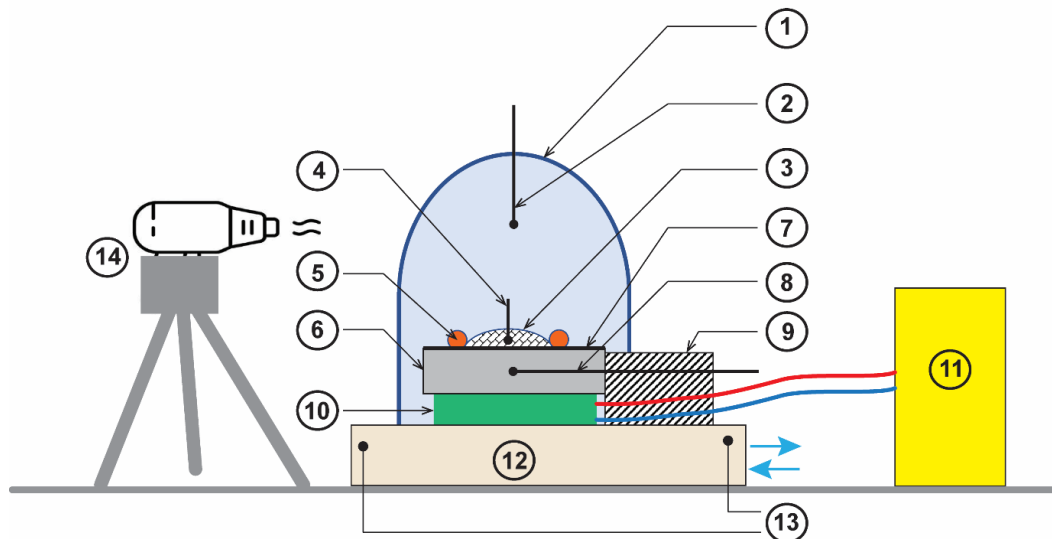
Fig. 2. A schematic diagram of the experimental rig developed for observation of the solidification behaviour of a PCM (erythritol) on the different sample surfaces.

The experimental procedure involved melting erythritol on the sample surface followed by cooling the surface to observe solidification. A cold-water tank at 20°C provided constant temperature cooling water via an inhouse-built cooling loop which circulated cold water through copper tubes in a 15 mm thick-rectangular aluminium heat exchanger. The thermoelectric heater (dimensions 50 mm x 50 mm, $I_{max} = 13A$, $V_{max} = 24.1V$) was connected to a DC power source⑪ (with adjustable current supply) and oriented with the cold side in contact with the cold heat sink stage. Each sample was mounted onto the hot side surface of the thermoelectric heater with care taken to avoid damaging the surface of interest⑦. A silicone O-ring⑤ with inner diameter 25 mm, thickness 3.5 mm, and temperature rating −30°C to 200°C was cleaned using DI water, dried in ambient air, and cleaned with IPA before carefully placing it centrally on the sample surface. An electronic weighing balance was used

to weigh 2.00 g of erythritol crystals which were placed on the sample surface contained by the O-ring. A transparent glass enclosure with two T-type thermocouples internally secured in position using Kapton tape was inverted over the sample so that one of the T-type thermocouples was inserted into the PCM crystals touching the sample surface whilst the second was in the air space above the sample. Temperatures were measured and recorded each second using a datalogger (Datataker 85 Series 4). A digital clock was used for timing the PCM solidification events during the experiments. Table 2 shows the different temperature measurement sensors and their locations in the experimental rig. The thermocouples were calibrated at four different temperatures (25°C, 40°C, 65°C and 85°C) and the calculated absolute error reduced from ±0.61°C to ±0.24°C. Fig. 3 presents the process stages of the conducted experiment and Fig. 4 a photograph of the experimental test rig.

Table 2
Temperature measurement instrumentation

Description of measured quantity	Thermocouple type	Number of thermocouples	Label on schematic in Fig. *2*
Temperature of hot chamber	T-type	1	②
Temperature of PCM	T-type	1	④
Temperature of substrate (at 2mm below the sample surface 30 mm from the circumference)	K-type	1	⑧
Temperature of the water-cooled heat sink stage	T-type	2 (inlet/outlet)	⑬
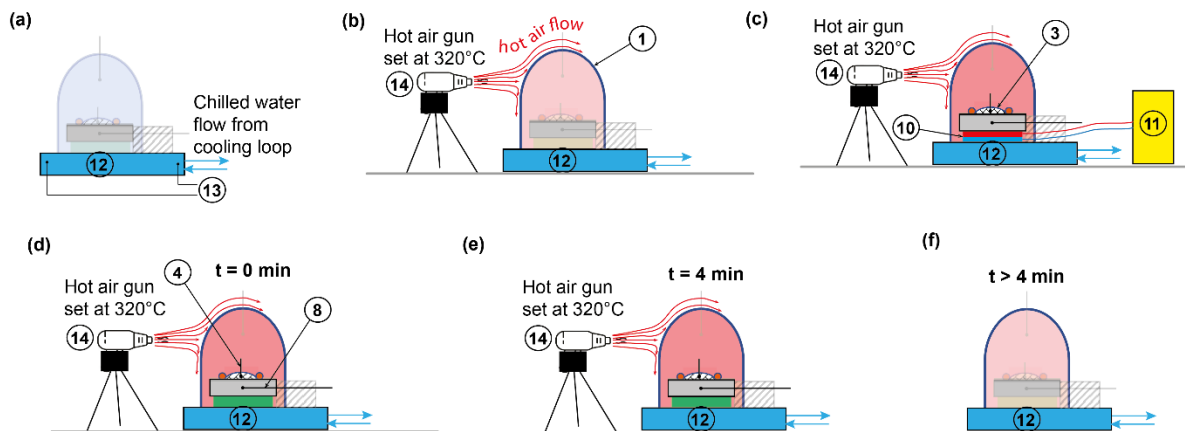
Fig. 3. Experimental procedure with erythritol indicating (a) initial cooling of the cold heat sink stag ⑫ to ~19.8 ± 0.1°C measured continuously using heat sink stage thermocouples⑬, (b) initial heating of the transparent hot air containment① using the hot air gun (Steinel HG2310 LCD 240V~, 2300W)⑭ for the first 4 min at the lowest air flow rate setting (150-250 l/min), (c) powering the thermoelectric heater to melt the erythritol crystals③ on surfaces using a DC power source⑪ with current adjustment between 3.65-3.72 A, (d) DC power source switched off to commence the cooling phase of the experiment when the substrate thermocouple⑧ measured 127 ± 0.6°C and the PCM-surface interface thermocouple④ measured 126 ± 0.3°C, (e) heating of the transparent hot air containment for a further time (t =4 min), after switching off the DC power source and (f) the rest of the cooling period (t > 4 min) without the hot air gun and with the set up left to cool over the cold heat sink stage⑫.
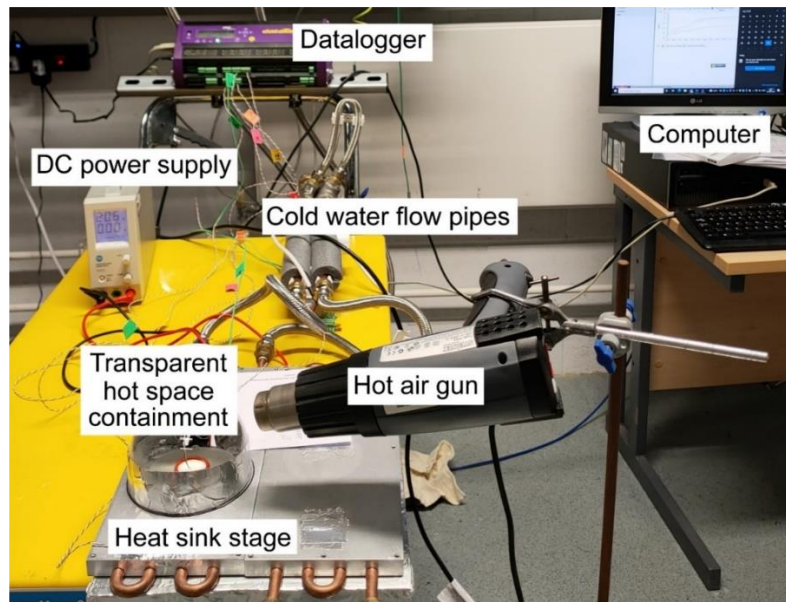
Fig. 4. Photograph of the laboratory set-up used for the investigation of the solidification behaviour of erythritol on the different sample surfaces.

Results and discussion

Surface roughness and wettability

The initial surface appearance with x200 magnification, 3D surface topology images, the typical primary profiles, and the corresponding areal surface roughness parameters of the different samples before applying the PTFE thin films are shown in Fig. 5. The roughness profiles achieved by the various surface texture generating operations on the samples, ranged from 57.9μm to 117.5μm for the as-received samples (AR-1 and AR-2), from 113.4μm to 337.7μm for the manually polished samples (MP-1, MP-2 and MP-3), and from 100.0μm to 127.4μm for the sandblasted samples (SB-1 and SB-2). The shown primary profiles for the surfaces are unfiltered and so represent profiles where form surface factors such as tilt, curvature and sphericity [26] are automatically removed by the microscope software. The variation of the measured areal surface roughness parameters for the different samples is relatively low, indicating similarity of texture generated across the different surfaces.

Table 3 summarises the median values of the measured areal surface roughness parameters before applying PTFE thin films. The arithmetic average surface roughness (S_a) and its root-mean-square value (S_q) for sandblasted surfaces were higher than for as-received and manually polished surfaces. The sandblasted surface (SB-1) had the lowest skewness coefficient ($S_{sk} = -0.6$), indicating that it had deep valleys (refer to Fig. 1). SB-1 also had a higher roughness profile as indicated by S_a and S_q with relatively sharp/high peaks as indicated by a higher kurtosis coefficient ($S_{ku} = 5.82$). Zero skewness indicates a fully symmetrical height distribution, positive skewness indicates a roughness profile dominated by sharper peaks above the mean surface, whilst negative skewness indicates a roughness profile with more rounded peaks above the mean surface [28]. A surface roughness profile with more rounded peaks and valleys will have a kurtosis coefficient, $S_{ku} < 3$, whilst one with sharper peaks and valleys will have $S_{ku} > 3$ [29]. A negative skewness coefficient ($S_{sk} < 0$) and a low kurtosis coefficient ($S_{ku} < 3$) along with S_a on a micro-nano-scale are viable metrics [30] for attaining general Cassie-Baxter behaviour [31] and superhydrophobic properties [32] although the spacing between peaks and valleys can be of additional influence [33]. The x200 times magnified surface appearance of

the different samples after applying the PTFE thin films are shown in Fig. 6. The dark deposits of the sintered aerosol particles are clearly visible on the PTFE treated surfaces in contrast to the shiny surfaces before spray coating. The as-received sample AR-2 was used in the PCM solidification experiment without any surface modification after initial machining.
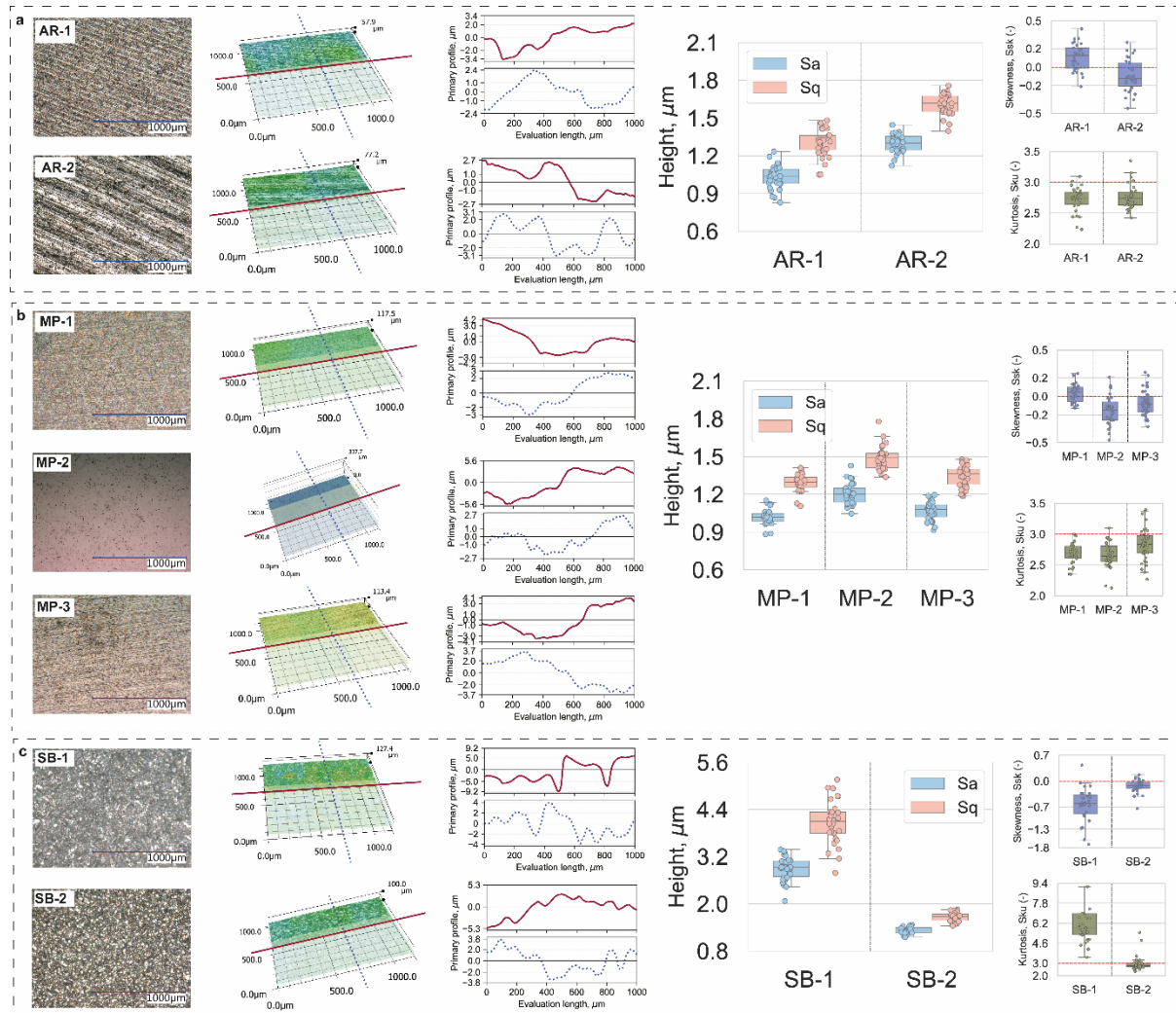
Fig. 5. The x200 magnified microscopic surface appearance, 3D surface topology images and typical primary profiles before coating for the (a) as-received (AR-1 and AR-2) (b) manually polished (MP-1, MP-2, and MP-3), and the (c) sand blasted (SB-1 and SB-2) samples, and their measured areal surface roughness parameters, i.e., arithmetic mean height (S_a, µm), root mean square height (S_q, µm), skewness (S_{sk}) and kurtosis (S_{ku}).

Table 3. Median (50% percentile) values of areal surface roughness parameters before spray coating

Description	Sample	N	S_a, µm	S_q, µm	S_{sk}	S_{ku}
As received	AR-1	30	1.03	1.31	0.12	2.75
	AR-2	30	1.30	1.62	-0.12	2.74
Manually polished	MP-1	30	1.02	1.30	0.04	2.69
	MP-2	30	1.20	1.49	-0.15	2.64
	MP-3	40	1.08	1.37	-0.08	2.84
Sandblasted	SB1	30	2.93	4.10	-0.60	5.82
	SB2	30	1.32	1.67	-0.12	2.81
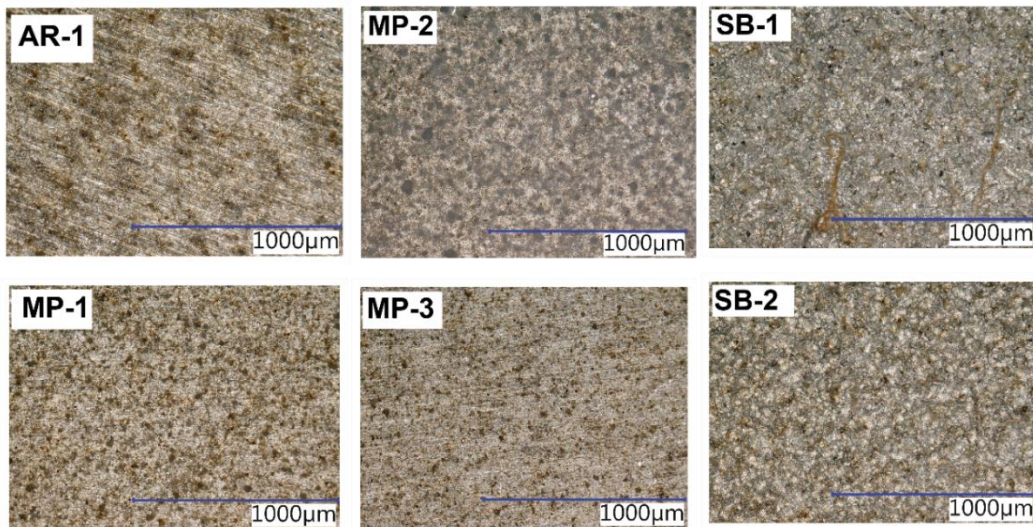
Fig. 6. The x200 magnified surface appearance, after PTFE spray coating for the as-received (AR-1), manually polished (MP-1, MP-2, and MP-3), and the sand blasted (SB-1 and SB-2) samples after applying the PTFE thin film coating.

Fig. 7 shows the measured static water contact angles of the different sample surfaces after applying the PTFE thin film including AR-2 with no thin film. Static contact angle was adopted as a convenient indicator for surface wettability rather than measuring the most stable apparent receding and advancing contact angles [34] on each prepared sample surface which demands more expensive apparatus. The surface roughness parameters for the as-received sample AR-1 resulted in a static water contact angle as high as $161.5 \pm 4.2°$ after applying a PTFE thin film. Any of the employed surface roughness methods enhanced the water contact angle for the PTFE coated surfaces.
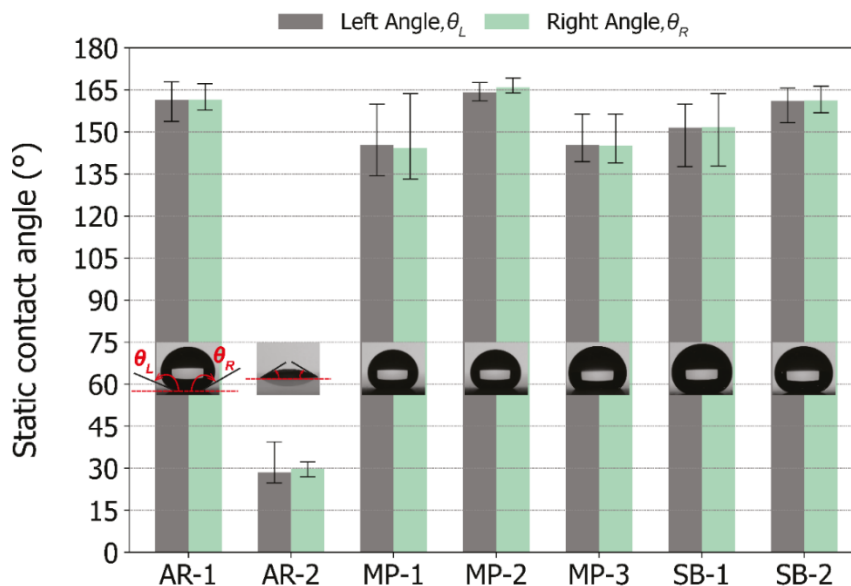
Fig. 7. Static contact angle values for the different samples used in the experiments measured at room temperature (20°C).

Solidification delay of PCMs

The first set of experiments performed were to assess the interaction of a polar molecule PCM (erythritol) and a non-polar molecule PCM (PEG 6000) when melting and solidifying on

the fabricated thin film surfaces with superhydrophobic and hydrophilic properties. Fig. 8 shows the effect of the thin films on the shape of PCM liquid (erythritol) after melting and solidifying on a superhydrophobic surface (MP-2) and a hydrophilic surface (AR-2). Similar crystal sizes of erythritol (as indicated by length, width, and height) were placed on a superhydrophobic (MP-2) sample and a hydrophilic surface (AR-2) sample and melted and then solidified. The erythritol crystal transformed into a spherical bead when melted on the superhydrophobic surface whilst it spread over the hydrophilic surface (Supplementary Video 1). In comparison, the superhydrophobic surface (SB-2) did not produce a similar effect for PEG 6000, as shown in Fig. 9, for similar flake sizes melted and then solidified on the surfaces (Supplementary Video 2). This can be attributed to differences in the chemical bonding [35] of hydrogen atoms and hydrogen functional groups between the two materials that render erythritol polar and PEG 6000, non-polar. A different kind of liquid-repellent surface will be needed to generate a similar effect for non-polar PCMs. Due to the clear difference in behaviour of erythritol on the different surfaces further experiments were performed using this material and experiments with PEG 6000 discontinued.
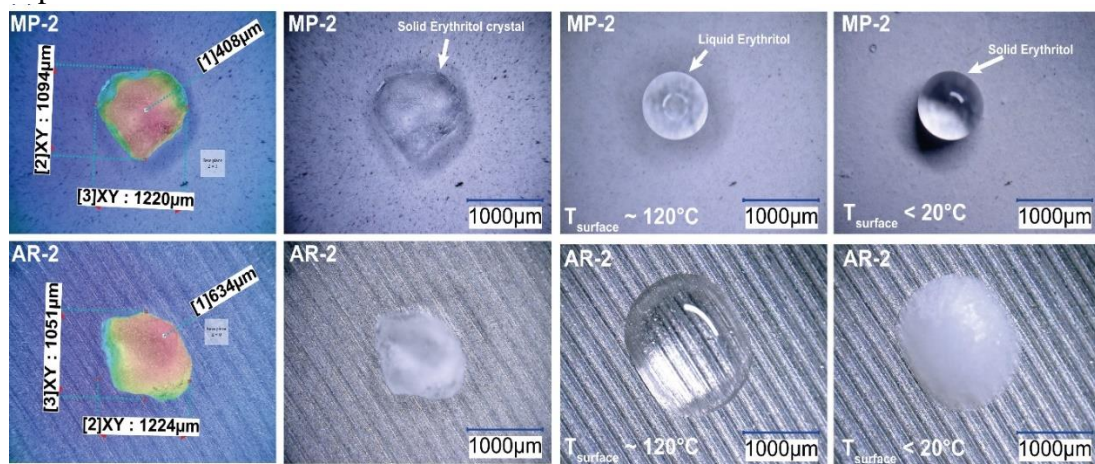
Fig. 8. Material shapes from an erythritol crystal melted and solidified on superhydrophobic (MP-2) and hydrophilic (AR-2) surfaces under a microscope (x100 magnification).
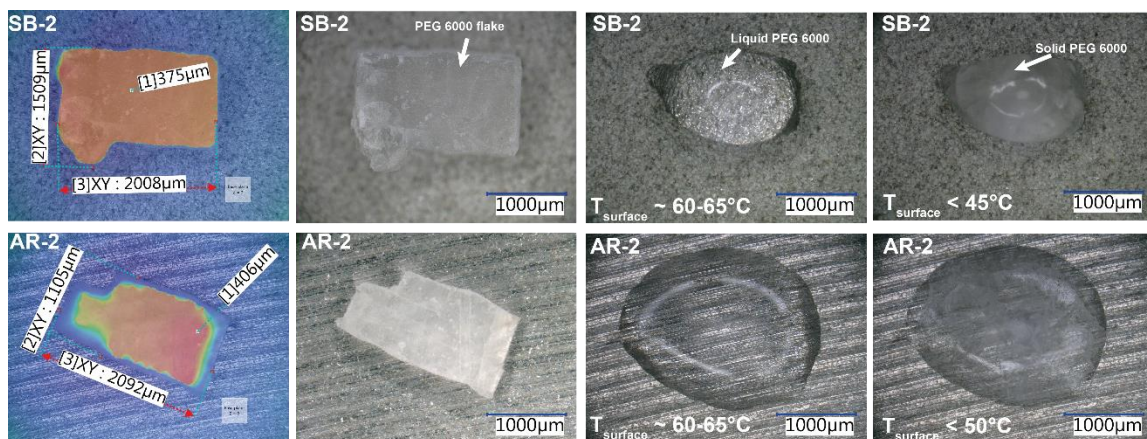
Fig. 9. Material shapes from a PEG 6000 flake melted and solidified on superhydrophobic (SB-2) and hydrophilic (AR-2) surfaces under a microscope (x100 magnification).

The measured temperatures of the hot space, erythritol on surfaces and the cold heat sink stage during an 18 min cooling period are shown for the as-received (Fig. 10a), manually polished (Fig. 10b), and sandblasted (Fig. 10c) samples. Continued operation of the hot air gun for 4 min after $t = 0$ min, established a temperature gradient between the enclosed hot space,

the erythritol and sample surfaces. The temperature measured on the erythritol-sample-surface interface dropped below the hot space temperature within 2 min. At $t = 4$ min when the heat gun was switched off, the temperature of the hot space was within $96.4 \pm 2.1°C$ for all the experiments. The hot space temperature decreased steadily thereafter but remained consistently higher than the erythritol-sample-surface temperature. Erythritol supercooled significantly below the published phase change temperature of $117.4°C$[22] before the onset of nucleation.
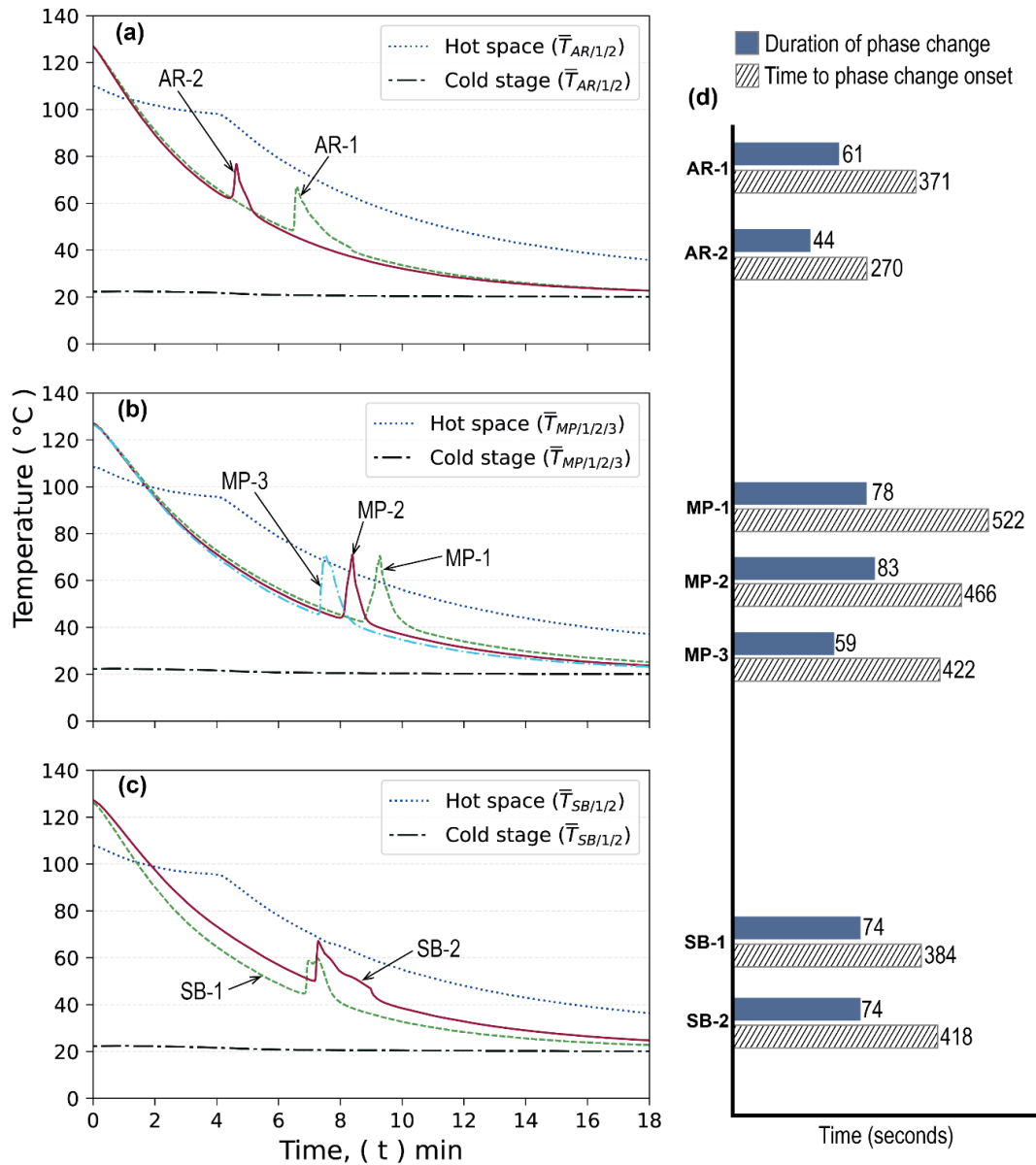
Fig. 10. The measured erythritol, cold stage, and hot space temperatures for the PTFE coated, a) as-received (AR-1, AR-2), b) manually polished (MP-1, MP-2, MP-3), and c) sandblasted (SB-1 and SB-2) surfaces during the solidification/cooling experiments, and (d) their respective duration of phase change and time to phase change onset.

The average cold heat sink stage temperature during the 18 min cooling period varied between $20.8 \pm 0.8°C$, and $20.9 \pm 0.8°C$. At the start of all cooling experiments ($t = 0$ min), the average temperatures of the hot space, erythritol, aluminium disc substrate, and the cold heat sink stage for all samples were $108.7 \pm 1.8°C$, $126.8 \pm 0.4°C$, $127.9 \pm 0.5°C$ and $22.3 \pm 0.1°C$, respectively. At $t = 0$ min, the temperature measured at the erythritol-sample-surface

interface was at least $9.4 \pm 0.4°C$ higher than the published phase change temperature of erythritol in all the experiments.

Fig. 10d presents time in seconds for phase change duration (i.e., the time for full solid formation from the onset of nucleation) and time to the onset of solidification from the start of the cooling experiments). The as-received-uncoated sample (AR-2) had the shortest phase change duration at 44 s. Adding a PTFE thin film coating on a similar as-received sample surface (AR-1) increased the phase change duration to 61 s (an increase of ~39%). Polished surfaces (MP-1 and MP-2) had the longest phase change durations of 78 s and 83 s, respectively due to their finer surface finish. The data suggests that the finer the grade of emery paper or the smaller the bead blasting grits, the longer the phase change duration. Similarly, PTFE thin films applied on manually polished surfaces had a longer delay to the onset of phase change compared to sandblasted and as-received surfaces. Such surface effects if achieved at scale can maintain significant thermal energy below the phase change temperature of PCMs and prolong storage timeframes.
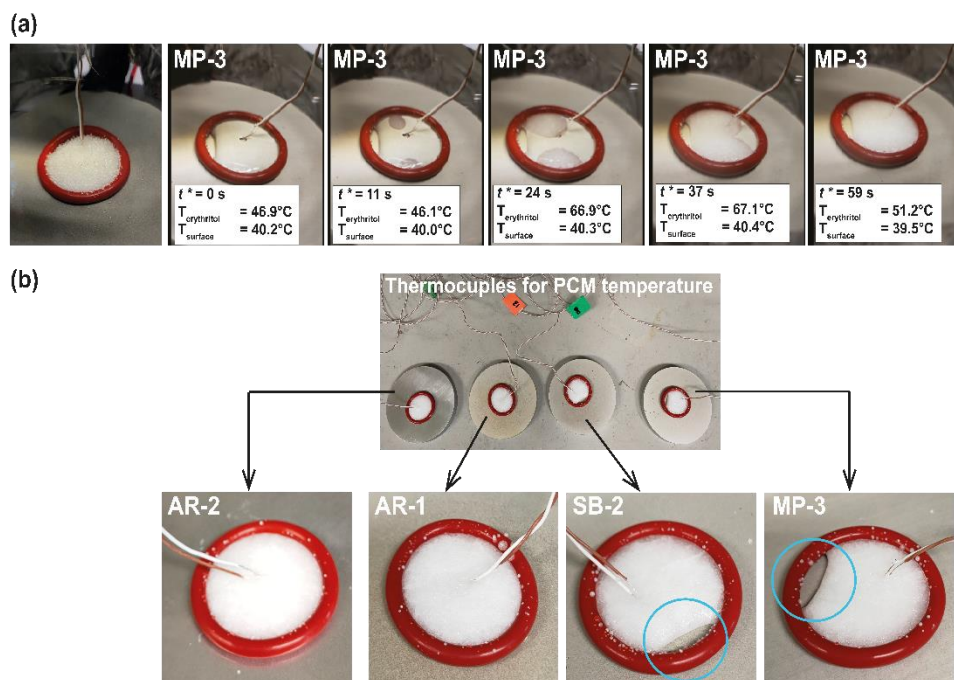
Fig. 11. Progress of solidification of erythritol on (a) PTFE coated MP-3, and (b) the shapes of erythritol solid on the non-coated-as-received (AR-2), spray-coated-as-received (AR-1), sandblasted-spray-coated (SB-2), and manually-polished-spray-coated (MP-3).

Fig. 11 presents images of the observed effect of superhydrophobic thin films on the solidification of erythritol. Fig. 11a shows the progress of erythritol solidification at $t^* = 0$, 11, 24, 37 and 59 s on sample MP-3 over the phase change duration. The time $t^* = 0$ s is the time at the onset of phase change and not time $t = 0$ min when the cooling experiment began. For each experiment, the thermocouple was inserted into the weighed PCM crystals located in the centre of the O-ring. After melting, when erythritol solidification commenced during cooling and began spreading over the contact surface and into the PCM, the measured temperature of the erythritol increased seconds later (e.g., ~ 24 seconds later for sample MP-3). The solid shapes formed after complete solidification for samples AR-1, AR-2, SB-2 and MP-3 are shown in Fig. 11b. Due to the super-liquid-repellence behaviour of the fabricated samples, the melted erythritol did not fill the O-ring completely, leaving a non-wetted surface inside the O-ring as seen for sample MP-3 and sample SB-2.

Multiscale surface features with microscopic (~50nm-10μm) and nanoscopic (up to ~100 nm) roughness are considered a general guideline for achieving super-liquid-repellent

behaviour on metal surfaces with low surface energy thin films [11]. These scale ranges refer to line profile surface roughness measurements (e.g., produced by contact profilometry) as opposed to a 3D non-contact surface profilometry measurements, for which guideline values are yet to be established. The areal arithmetic average surface roughness (S_a) of all the fabricated samples in this study were at least an order of magnitude higher (i.e., ~1000 nm to 2930 nm) than the above suggested guideline but clearly demonstrated superhydrophobicity. Research to determine a suitable benchmark for super-liquid-repellent thin film surfaces on metal substrates based on areal surface roughness measured using 3D non-contact surface profilometry techniques is needed. Abrasive blasting if done with the appropriate size scale of grit particles can be significantly easier and faster for larger system-scale surfaces compared to manual surface polishing.

Conclusion

This research investigated the effect of superhydrophobic PTFE thin film surfaces on the solidification and melting of erythritol and polyethylene glycol 6000 (PEG 6000), potential materials for low temperature LHTES applications. Different texturing operations were conducted on aluminium surfaces, and their wetting properties and areal surface roughness parameters measured before applying PTFE thin films by spray coating. Compared to the as-received control sample, the duration of phase change from onset to full solidification of the same mass (i.e., 2 g) of erythritol crystals when cooled down from a temperature of $\approx 126.8 \pm 0.4°C$ lasted up to ~89% longer for PTFE coated manually polished samples with initial arithmetic average surface roughness of $S_a \approx 1.20 \pm 1.49$ µm. The applied PTFE thin films resulted in longer times to phase change onset (i.e., greater PCM subcooling). Superhydrophobic PTFE thin films have strongly liquid-repellent characteristics for erythritol (a polar molecule) but not for PEG 6000 (a non-polar molecule). Implementing such surfaces for selected PCMs can potentially enhance the heat discharge performance of low temperature LHTES and prolong heat storage timeframes.

Acknowledgement

References

[1] Cabeza, L.F., H. Mehling, S. Hiebler and F. Ziegler, "Heat transfer enhancement in water when used as PCM in thermal energy storage", Applied Thermal Engineering, 2002.

[2] Egea, A., A. García, R. Herrero-Martín and J. Pérez-García, "Experimental performance of a novel scraped surface heat exchanger for latent energy storage for domestic hot water generation", Renewable Energy, 2022.

[3] Lang, C. and C. Wocke, "Phase change material thermal storage with constant heat discharge", *SolarPACES 2017, AIP Conf. Proc.*, AIP Publishing (2018), 1–8.

[4] Oh, Y.K. and H.D. Yang, "Experimental and Numerical Study on the Melting Acceleration of Phase Change Material by Ultrasonic Vibrations", Key Engineering Materials, 2006.

[5] Agyenim, F., P. Eames and M. Smyth, "A comparison of heat transfer enhancement in a medium temperature thermal energy storage heat exchanger using fins", Solar Energy, 2009.

[6] Kamkari, B., H. Shokouhmand and F. Bruno, "Experimental investigation of the effect of

inclination angle on convection-driven melting of phase change material in a rectangular enclosure", International Journal of Heat and Mass Transfer, 2014.

[7] Motahar, S., A.A. Alemrajabi and R. Khodabandeh, "Experimental investigation on heat transfer characteristics during melting of a phase change material with dispersed TiO2 nanoparticles in a rectangular enclosure", International Journal of Heat and Mass Transfer, 2017.

[8] Bashar, M. and K. Siddiqui, "Investigation of heat transfer during melting of a PCM by a U-shaped heat source", International Journal of Energy Research, 2017.

[9] Jevnikar, S. and K. Siddiqui, "Investigation of the influence of heat source orientation on the transient flow behavior during PCM melting using particle image velocimetry", Journal of Energy Storage, 2019.

[10] Laing-Nepustil, D., U. Nepustil, D. Lodemann et al., "Development of an active high temperature PCM storage concept with coated heat exchanger plates", *Proceedings of the ISES Solar World Congress 2019 and IEA SHC International Conference on Solar Heating and Cooling for Buildings and Industry 2019*, (2019), 1229–1235.

[11] Kreder, M.J., J. Alvarenga, P. Kim and J. Aizenberg, "Design of anti-icing surfaces: Smooth, textured or slippery?", Nature Reviews Materials, 2016.

[12] Bottein, T., J. Loizillon and D. Grosso, "Full Investigation of Angle Dependence in Dip-Coating Sol-Gel Films", Journal of Physical Chemistry B, 2017.

[13] Leach, R. and H. Haitjema, "Bandwidth characteristics and comparisons of surface texture measuring instruments", Measurement Science and Technology, 2010.

[14] MacUlotti, G., X. Feng, R. Su, M. Galetto and R. Leach, "Residual flatness and scale calibration for a point autofocus surface topography measuring instrument", Measurement Science and Technology, 2019.

[15] Bordatchev, E. V. and A.M.K. Hafiz, "Advanced measurement and analysis of surface textures produced by micro-machining processes", Measurement Science and Technology, 2014.

[16] Zhang, P. and F.Y. Lv, "A review of the recent advances in superhydrophobic surfaces and the emerging energy-related applications", Energy, 2015.

[17] Zhang, W., D. Wang, Z. Sun, J. Song and X. Deng, "Robust superhydrophobicity: Mechanisms and strategies", Chemical Society Reviews, 2021.

[18] Zhang, Y., S. Zhou, Z. Lv, L. Fan, Y. Huang and X. Liu, "A Facile Method to Prepare Superhydrophobic Coatings for Various Substrates", Applied Sciences (Switzerland), 2022.

[19] Sun, R., J. Zhao, Z. Li, J. Mo, Y. Pan and D. Luo, "Preparation of mechanically durable superhydrophobic aluminum surface by sandblasting and chemical modification", Progress in Organic Coatings, 2019.

[20] Raimondo, M., M. Blosi, A. Caldarelli, G. Guarini and F. Veronesi, "Wetting behavior and remarkable durability of amphiphobic aluminum alloys surfaces in a wide range of environmental conditions", Chemical Engineering Journal, 2014.

[21] Brinksmeier, E., B. Karpuschewski, J. Yan and L. Schönemann, "Manufacturing of multiscale structured surfaces", CIRP Annals, 2020.

[22] Nomura, T., M. Tsubota, T. Oya, N. Okinaka and T. Akiyama, "Heat release performance of direct-contact heat exchanger with erythritol as phase change material", Applied Thermal Engineering, 2013.

[23] Thonon, M., L. Zalewski, S. Gibout, E. Franquet, G. Fraisse and M. Pailha, "Experimental comparison of three characterization methods for two phase change materials suitable for domestic hot water storage", Applied Sciences (Switzerland), 2021.

[24] British Standards Institution, *Geometrical product specifications (GPS) - Surface texture: Profile - Part 3: Specification operators (ISO 21920-3:2022)*, British Standards Institution (BSI), London, 2022.

[25] British Standards Institution, *Geometrical product specifications (GPS) - Surface texture: Areal - Part 3: Specification operators (ISO 25178-3:2012)*, British Standards Institution (BSI), London, 2012.

[26] He, B., S. Ding, C. Wei and Z. Shi, "The Influence of the Choice of a Gaussian Filter on the Determination of Areal Surface Texture Parameters", Instruments and Experimental Techniques, 2021.

[27] Bhushan, B., "Surface roughness analysis and measurement techniques", In B. Bhushan, ed., *Modern Tribology Handbook*. CRC Press, Boca Raton, 2001, 49–119.

[28] Vazirinasab, E., K. Maghsoudi, R. Jafari and G. Momen, "A comparative study of the icephobic and self-cleaning properties of Teflon materials having different surface morphologies", Journal of Materials Processing Technology, 2020.

[29] Talibouya Ba, E.C., M.R. Dumont, P.S. Martins, R.M. Drumond, M.P.M. da Cruz and V.F. Vieira, "Investigation of the effects of skewness Rsk and kurtosis Rku on tribological behavior in a pin-on-disc test of surfaces machined by conventional milling and turning processes", Materials Research, 2021.

[30] Abbott, J.P.R. and H. Zhu, "3D optical surface profiler for quantifying leaf surface roughness", Surface Topography: Metrology and Properties, 2019.

[31] Sahoo, B.N. and B. Kandasubramanian, "Recent progress in fabrication and characterisation of hierarchical biomimetic superhydrophobic structures", RSC Advances, 2014.

[32] Khaskhoussi, A., L. Calabrese, S. Patané and E. Proverbio, "Effect of chemical surface texturing on the superhydrophobic behavior of micro–nano-roughened AA6082 surfaces", Materials, 2021.

[33] Kanungo, M., S. Mettu, K.Y. Law and S. Daniel, "Effect of roughness geometry on wetting and dewetting of rough PDMS surfaces", Langmuir, 2014.

[34] Drelich, J.W., L. Boinovich, E. Chibowski et al., "Contact angles: History of over 200 years of open questions", Surface Innovations, 2020.

[35] G.V. Beketov and O.V. Shynkarenko, "Surface wetting and contact angle: basics and characterisation", Himia, Fizika ta Tehnologia Poverhni, 2022.

High-temperature heat pumps
and zeotropic refrigerant mixtures: A perfect match?

P. Widmaier[1], A. Bardow[1] and D. Roskosch[1*]

[1]Energy and Process Systems Engineering Lab ETH Zürich, Tannenstrasse 3,
Zürich 8092, Switzerland

[*]Corresponding author: droskosch@ethz.ch

Abstract

Refrigerant mixtures can improve the efficiency of high-temperature vapor compression heat pumps by matching their non-isothermal phase change to temperature changes in the heat source and sink. Previous studies suggest that the advantage of mixtures compared to pure refrigerants increases for larger temperature changes of heat sources and sinks. However, the potential efficiency increase has not yet been systematically studied. Thus, the conditions are still unclear under which zeotropic mixtures are particularly beneficial.

In this work, we therefore screen a comprehensive set of pure refrigerants and all their binary mixtures for a broad range of sink and source temperature changes. The refrigerant set includes 33 natural and halogenated refrigerants. To assess the mixture performance, we model the heat pump process. Here, the compressor efficiencies depend upon the refrigerants.

The study confirms the basic theory that mixtures can substantially improve the coefficient of performance (COP) and the benefits increase with the temperature changes of sink and source. However, the temperature change is shown to be more relevant at the heat source: mixtures are already beneficial at small temperature changes of the heat source, while a minimal temperature change of 10 K is needed for the heat sink. The greatest COP increase of a mixture, at 27%, is identified at maximum temperature changes of 40 K in the source and in the sink. The optimal mixture is highly specific to the temperature changes of heat sink and source. However, binary mixtures are identified that show good performance over broad ranges of source and sink temperature changes when their composition is tailored, e.g., pentene/cyclopropane. Such refrigerant mixtures could have the potential for universal use in heat pumps.

Keywords: High-temperature heat pumps, temperature glide, zeotropic mixtures, compressor efficiency

Introduction/Background

Heat pumps are a central element in the decarbonization of both residential and industrial heat supply. While residential heat pumps have already significantly penetrated the market, industrial high-temperature heat pumps have just started to gain interest in the industry.

High-temperature heat pumps still have a lower technological readiness level than residential heat pumps but are currently undergoing intensive development [1]. Development mainly aims to qualify heat pumps for the higher temperatures and heating powers required for industrial applications while also improving their efficiency. Since high-temperature heat pumps generally have smaller COPs, any potential must be exploited to improve efficiency [2]. One promising approach to increase efficiency is through the the use of zeotropic refrigerant mixtures: Zeotropic mixtures differ from pure refrigerants by changing temperature during evaporation and condensation, referred to as temperature glide. The temperature glide can improve the matching of the refrigerant and the secondary fluids within the heat exchangers for non-isothermal heat sources and sinks [3]. An improved matching decreases temperature differences and thus exergy destruction in the heat exchangers and therefore has the potential

to increase the COP. In addition, mixing refrigerants offers an additional degree of freedom to adjust other desirable refrigerant properties, such as low global warming potential (GWP) and flammability [3, 4].

For several decades, the potential and performance of zeotropic mixtures have been investigated for residential heat pumps [5–7]. The studies confirm the theory and demonstrate efficiency benefits of zeotropic mixtures with temperature glide. However, the actual efficiency gains of mixtures compared to pure refrigerants were small and ranged within a few percentage points [6, 8]. The small gain from zeotropic mixtures in the residential sector might be attributed to the typically low temperate changes of residential sources and sinks (order of magnitude 5 – 10 K), reducing the relevance of glide matching. As a result, the temperature glide of zeotropic mixtures is currently not exploited in commercial residential heat pumps.

The situation is different for industrial high-temperature heat pumps: In the industrial sector, heat sinks and sources often change temperatures over several dozen Kelvin. Thus, glide matching becomes much more important to achieving increased heat pump efficiency [4]. To date, initial studies have analyzed the potential for specific conditions of heat source and sink or a limited design space of potential refrigerant mixtures. Yelishala et al. [9] investigated the performance of hydrocarbon and carbon dioxide mixtures in vapor compression cycles. For source and sink temperature changes of 15 K, they found a maximum COP increase of 40% at 30°C – 60°C lift for the best-performing mixture (propylene (20 mass-%)/carbon dioxide (80 mass-%)) compared to its best pure component (propylene). Zühlsdorf et al. [10] studied four combinations of temperature changes of heat source and sink, and a fluid set that includes 14 natural refrigerants. For small temperature changes of the source (5 K), no advantage of mixtures could be found. For high-temperature changes (source 20 K, sink 40 K), they found a COP increase of up to 27% for the best mixture (dimethyl ether (20 mass-%)/ethyl ether (80 mass-%)) compared to the best pure refrigerant (isopentane). In addition, the source's temperature change dominated over the sink's influence. Abedini et al. [11] considered three case studies for the use of refrigerant mixtures in high-temperature heat pumps represented by combinations of heat source and sink temperature profiles (isothermal and non-isothermal). They found only minor or negligible COP improvements of mixtures for an isothermal heat source and sink. Similar findings occurred in an almost isothermal source combined with a large heat sink temperature change. For temperature changes in the source and sink, however, a considerable improvement of the COP,10%, was observed with an ethanol/p-xylene mixture.

To date, however, no study has evaluated the potential COP benefits of mixtures systematically over a broad span of typical temperature changes for industrial heat sources and sinks. Furthermore, other important influencing factors have remained unconsidered, including the behavior of the compressor [12].

In this contribution, we therefore study the potential of zeotropic mixtures for high-temperature applications. For this purpose, we systematically vary the temperature changes of sink and source and perform an extensive screening of pure refrigerants and their mixtures. The screening employs a heat pump process model to optimize the thermodynamic cycle while the fluid dependence of the compressor efficiencies is considered. The results show the potential of mixtures as a function of source and sink temperature changes and identify promising mixture candidates.

Methods and Case Study

The study considers a subcritical heat pump cycle with an internal heat exchanger (IHX) as a component additional to the evaporator, compressor, condenser, and throttle. The IHX is implemented since it usually increases the COP, is comparatively inexpensive to purchase, and

often used in practice [13]. The heat pump model follows a standard approach, which considers the heat exchangers by pinch models and the state change in the compressor by an isentropic compressor efficiency [14]. The isentropic compressor efficiency is determined by a loss-based compressor model that, in particular, accounts for refrigerant dependency [15]. The throttle is isenthalpic and the superheating at the compressor inlet is assumed to be fully realized by the IHX. All other components are considered loss-free and represented by mass-specific energy balances.

During the refrigerant screening, the cycle is optimized for each pure refrigerant and refrigerant mixture under consideration. The evaporation and condensation temperatures as well as the superheating and subcooling are optimized with respect to the COP. The optimization is subject to constraints to maintain minimum approach temperatures in all heat exchangers and pressure limits. The optimization ensures that the heat pump cycle always optimally adapts to the refrigerant (-mixture) considered.

The investigated fluid set includes 33 pure refrigerants from various substance groups (natural and halogenated). The refrigerants are chosen for their low global warming potential (GWP) and ozone depletion potential (ODP) according to current regulatory guidelines. As well as the pure refrigerants, all possible mixture combinations are investigated with a composition increment of 0.1 mol/mol. The mixtures cover a broad range of temperature glides from 0 K to approximately 130 K (at a representative pressure of 20 bar). All refrigerant properties are calculated by REFPROP [16].

For the source's and sink's temperature changes, a range of 0 K to 40 K discretized in 5 K intervals is considered; limiting the study to temperature changes of up to 40 K enables a comprehensive evaluation of the efficiency increase potential for industrial applications at viable computational effort. The temperature changes in source and sink are based on a heat source inlet temperature of 40°C and a heat sink outlet temperature of 100°C, respectively. The best-performing mixture is compared to the best-performing pure refrigerant from the refrigerant set.

Discussion and Results

To map the performance of zeotropic mixtures, the COP of the best mixture is related to the COP of the best pure refrigerant for each combination of sink and source temperature changes (Figure 1). A line at a constant COP ratio is added to emphasize the area of larger mixture benefits (for this study, an isoline at $COP_{ratio} = 1.08$ is chosen).
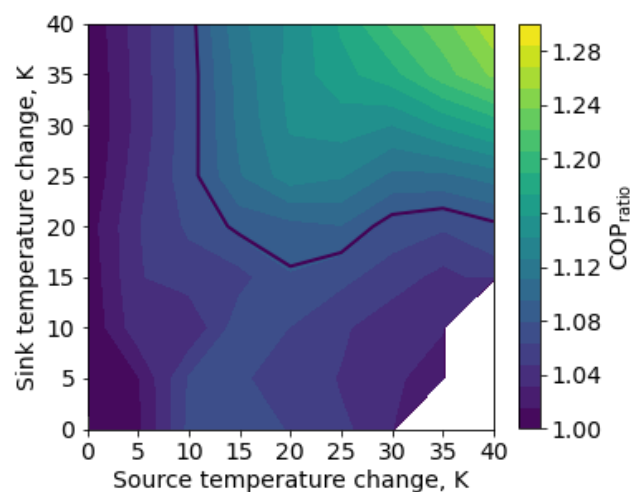
Figure 1: COP ratio of the best mixture COP and best pure refrigerant COP as a function of heat source and sink temperature change. $T_{si,in} = 40°C$; $T_{so,out} = 100°C$. The black line represents a constant COP_{ratio} of 1.08.

Mixtures achieve greater or equal COPs than pure refrigerants throughout the study. The largest COP advantage of 27% is observed for maximum source and sink temperature changes of 40 K, respectively. This result indicates potentially greater benefits for increased temperature changes. In the area of significant COP ratios ($COP_{ratio} > 1.08$), the advantage of mixtures increases toward substantial source and sink temperature changes. However, the shape of the 8% isoline indicates a stronger sensitivity of the COP ratio to temperature changes in the heat source: Exceeding the 8% isoline requires temperature changes of approximately 10 K in the source but 15 – 20 K in the heat sink.

Generally, the COP advantage of mixtures is attributed to the temperature glide (Figure 2). For temperature changes of heat source and sink, the temperature glide increases the thermodynamic mean temperature of evaporation ($\bar{T}_{m,l}$) and decreases it in the condenser ($\bar{T}_{m,h}$). The reduced temperature ratio ($\bar{T}_{m,h}/\bar{T}_{m,l}$) increases the COP.

However, the heat pump process is affected differently by temperature changes in source and sink. Since superheating is performed in the IHX, the pinch point is located at the evaporator inlet (Figure 2, $T_{so,out}$). The evaporation of a pure refrigerant must take place entirely at a temperature below the outlet temperature of the heat source (Figure 2, left). With each Kelvin temperature change increase in the heat source, there is a decrease in the heat source's outlet temperature ($T_{so,out}$) and the mean temperature of evaporation ($\bar{T}_{m,l}$) on a one-to-one basis. Hence, larger temperature changes in the heat source significantly reduce the COP. The temperature glide of mixtures can cushion the COP decrease by increasing the thermodynamic mean temperature. In turn, increasing temperature changes in the heat sink (decreasing $T_{si,in}$) are even slightly beneficial for the COP as the condensation temperature (at dew line) is reduced. The temperature glide of mixtures can further decrease the mean condensation temperature and is therefore beneficial. However, the thermodynamic mean temperature of heat rejection ($\bar{T}_{m,h}$, state 2 to state 3') depends less on the condensation temperature. Subcooling (Figure 2, bubble line to state 3') and the compressor outlet state (state 2) also significantly influence the mean temperature. Thus, a temperature glide during condensation has only a minor effect on the thermodynamic mean temperature. Hence, the potential for COP increase due to the temperature glide of mixtures is greater for larger temperature changes in the heat source. This preference is also shown by the optimal temperature glides (Figure 3). The temperature glides are adjusted to primarily match the temperature changes of the heat source, in particular for unequal temperature changes of the heat source and sink.
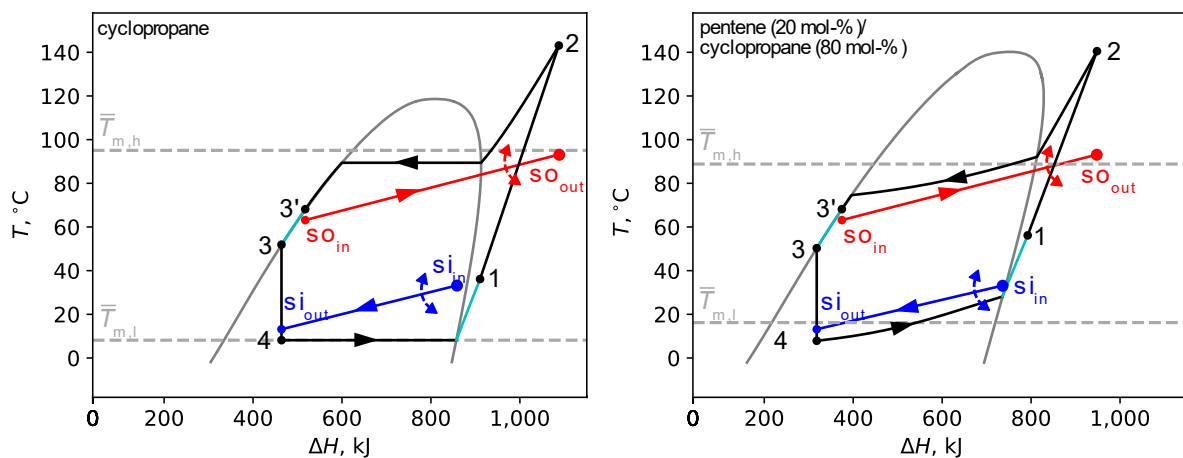
Figure 2: Temperature-enthalpy diagrams of heat pump cycles with a pure fluid (cyclopropane) and a mixture (pentene (20 mol-%)/cyclopropane (80 mol-%)). Source and sink temperature changes of 20 K and 30 K, respectively.

The greater influence of the heat source is also observed outside the area of large COP ratios (Figure 1, $COP_{ratio} < 1.08$). Up to heat source temperature changes of $10 - 15$ K, the COP ratio increases with increasing temperature changes in the heat source. The temperature change of the heat sink has only a minor influence here. The temperature glide is principally optimized to match the temperature change of the heat source (Figure 3). As a result, mixtures are still beneficial for the combination of small temperature changes in the heat source and large temperature changes in the heat sink (Figure 3, upper left quarter).

A different picture is observed for large temperature changes in the heat source ($20 - 40$ K) and small temperature changes in the heat sink ($0 - 15$ K) (Figure 3, lower right quarter). Here, the COP ratios are modest and decrease with increasing heat source temperature changes. In addition, the best-performing mixtures only have minor or no temperature glides.

Large source and small sink temperature changes generally demand extreme requirements on refrigerants. Small heat sink temperature changes require large condensation temperatures (at dew line) and, thus, high critical temperatures, while large heat source temperature changes demand low evaporation temperatures (Figure 2). Refrigerants with high critical temperatures and sufficiently high evaporation pressures at low temperatures are rare. Our screening set includes only few pure refrigerants and mixtures that meet the requirements. For extreme combinations of high source and low sink temperature changes, no pure refrigerants could be found in the screening set that meet the requirements (blank bottom right corner of Figure 1). However, even if suitable refrigerants can be identified, we do not expect considerable advantages of mixtures for such applications. A large temperature change in the heat source would be required to exploit the advantage of mixtures. However, further glide matching in the evaporator would not be beneficial for the COP given the small temperature changes in the heat sink (poor glide matching). The condensation temperature would have to be increased, and the thermodynamic mean temperature would increase.
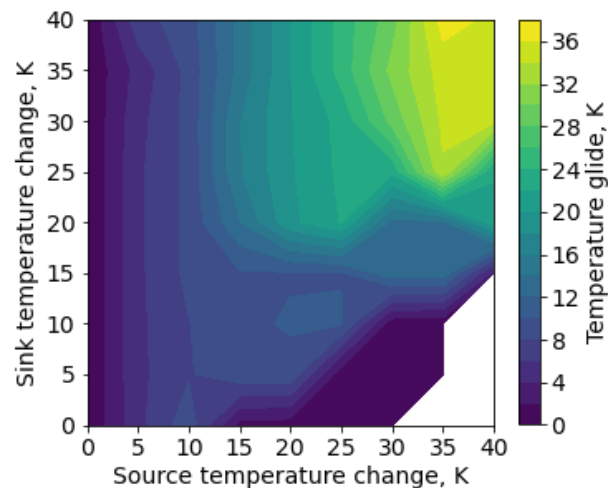
Figure 3: Temperature glide of the respective best mixture for every combination of source and sink temperature change. Calculated from dew to bubble line for the respective mean value of evaporation and condensation pressure.

The best mixture determined during screening is specific for a given combination of source and sink change. The specificity of the best mixture refers to both its components and their respective molar share (composition) in the mixture. The highest COP advantage of mixtures over pure refrigerants is given by diethyl ether (30 mol-%)/propylene (70 mol-%).

An analysis of the mixture COP rankings for every source and sink temperature change shows that there often are several mixtures that rank close to the best-ranked mixture. Under these top-ranked mixtures, often combinations of the same pure refrigerants are repeatedly found,

e.g. cyclopropane, cyclobutene, pentane, R161, diethyl ether. Hence, binary combinations of these components repeatedly yield high ranking positions with COPs close to the best mixture and the composition of these mixtures may vary.

Particularly frequently, pentene/cyclopropane mixtures deliver near-optimal COPs. Figure 4 shows the COP ratio of the best pentene/cyclopropane mixture (optimized composition) and the overall best mixture over all source and sink change combinations considered in this study.
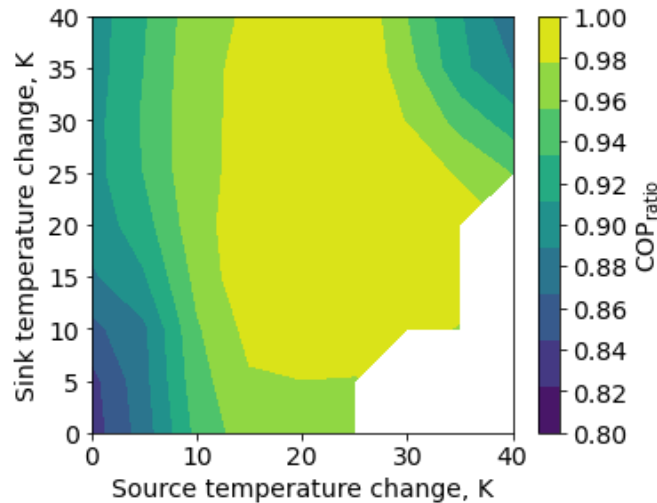
Figure 4: COP ratio of pentene/cyclopropane mixtures and the respectively top-ranked mixture as a function of heat source and sink temperature changes. $T_{si,in} = 40°C$; $T_{so,out} = 100°C$.

Over a wide range of source and sink temperature changes, pentene/cyclopropane shows the overall best COP or achieves COPs that are very close to the overall best for the respective source and sink conditions (yellow area in Figure 4).

At high and low source changes (towards the edges of Figure 4), the COP ratio of pentene/cyclopropane decreases. However, pentene/cyclopropane still delivers better COPs than all considered pure refrigerants for all source and sink specifications. For these temperature changes ($\Delta T_{so} < 15$ K and $\Delta T_{so} > 35$ K), other mixtures can be identified that perform well over a broad range of heat source and sink temperature changes.

Finding mixtures that perform well over a broad range of heat source and sink temperature changes can be hugely beneficial in practice: starting from a basic design, heat pumps can be tailored to a specific application just by adapting the mixture composition. The design effort can be reduced while near-optimal efficiencies can be retained.

Summary/Conclusions

In this study, a model of a high-temperature heat pump was set up to screen a representative set of refrigerants over a broad range of heat source and heat sink temperature changes. The analysis demonstrated how the temperature changes of heat source and sink influence the efficiency increase of mixtures compared to pure refrigerants.

It was identified that the advantage of mixtures generally increases for larger temperature changes of heat source and sink. A maximum COP increase of 27% was observed for the combination of the largest temperature changes of heat source and sink. These findings show the significant potential for efficiency improvements by using refrigerant mixtures with temperature glide for heat pump applications with large temperature changes in sink and source. The COP increase of mixtures compared to pure refrigerants was found to be more sensitive to temperature changes in the heat source

Although the optimal mixture was found to be specific to the temperature changes of heat source and sink, we found that mixtures of pentene/cyclopropane perform very well over a broad range of temperature changes in source and sink. Such mixtures can be of great relevance in practice, as heat pump systems can be tailored to a specific application by only changing the refrigerant mixture composition.

Acknowledgments

References

[1] Gaur, A. S., Fitiwi, D. Z., Curtis, J., "Heat pumps and our low-carbon future: A comprehensive review", Energy Research & Social Science 2021.

[2] Thiel, G. P., Stark, A. K., "To decarbonize industry, we must decarbonize heat". Joule 2021.

[3] Bai, M., Zhao, L., Zhao, R., "Review on Applications of Zeotropic Mixtures", J. Therm. Sci. 2022.

[4] Arpagaus, C., Bless, F., Uhlmann, M., Schiffmann, J., Bertsch, S. S., "High temperature heat pumps: Market overview, state of the art, research status, refrigerants, and application potentials", Energy 2018.

[5] Mohanraj, M., Muraleedharan, C., Jayaraj, S., "A review on recent developments in new refrigerant mixtures for vapour compression-based refrigeration, air-conditioning and heat pump units", Int. J. Energy Res. 2011.

[6] Chang, Y., Kim, M., Ro, S., "Performance and heat transfer characteristics of hydrocarbon refrigerants in a heat pump system", International Journal of Refrigeration 2000.

[7] Park, K.-J., Jung, D., "Performance of heat pumps charged with R170/R290 mixture", Applied Energy 2009.

[8] Park, K.-J., Seo, T., Jung, D., "Performance of alternative refrigerants for residential air-conditioning applications", Applied Energy 2007.

[9] Yelishala, S. C., Kannaiyan, K., Sadr, R., Wang, Z., Levendis, Y. A., Metghalchi, H., "Performance maximization by temperature glide matching in energy exchangers of cooling systems operating with natural hydrocarbon/CO2 refrigerants", International Journal of Refrigeration 2020.

[10] Zühlsdorf, B., Jensen, J. K., Cignitti, S., Madsen, C., Elmegaard, B., "Analysis of temperature glide matching of heat pumps with zeotropic working fluid mixtures for different temperature glides", Energy 2018.

[11] Abedini, H., Vieren, E., Demeester, T., Beyne, W., Lecompte, S., Quoilin, S., Arteconi, A., "A comprehensive analysis of binary mixtures as working fluid in high temperature heat pumps", Energy Conversion and Management 2023.

[12] Roskosch, D., Venzik, V., Schilling, J., Bardow, A., Atakan, B., "Beyond Temperature Glide: The Compressor is Key to Realizing Benefits of Zeotropic Mixtures in Heat Pumps", Energy Tech 2021.

[13] Arpagaus, C., Bless, F., Uhlmann, M., Büchel, E., Frei, S., Schiffmann, J., Bertsch, S. S., "High temperature heat pump using HFO and HCFO refrigerants - System design, simulation, and first experimental results", Purdue e-Pubs, 2018.

[14]   Roskosch, D., Venzik, V., Atakan, B., "Fluid Retrofit for Existing Vapor Compression Refrigeration Systems and Heat Pumps: Evaluation of Different Models", Energies 2019.

[15]   Roskosch, D., Arpagaus, C., Bertsch, S., Bardow, A., "Compressor Design Vs. Refrigerants Properties: What Affects Compressor Efficiency More?", International Compressor Engineering Conference (Ed.) 2022.

[16]   Lemmon, E.W., Bell, I.H., Huber, M.L., McLinden, M.O., "REFPROP: Reference Fluid Thermodynamic and Transport Properties. Standard Reference Data Program", National Institute of Standards and Technology NIST, Gaithersburg 2018.

Second law analysis of polygeneration cycle

B. Chandrakala, **K. Sarath Babu and E. Anil Kumar**[*]

Department of Mechanical Engineering, Indian Institute of Technology Tirupati, India

[*]Corresponding author: anil@iittp.ac.in

Abstract

Polygeneration systems have been considered as a viable technology for efficiently utilizing clean energy sources such as solar and wind. The present study proposes a novel metal hydride-based polygeneration cycle for high temperature solar energy storage, energy upgradation, and cooling. A second law analysis of the proposed polygeneration cycle is performed. The exergy efficiency and exergy COP are calculated for four pairs ($MmNi_{4.4}Al_{0.6}$-Mg_2Ni, $MmNi_{4.4}Al_{0.6}$-Mg_2Fe, $MmNi_{4.4}Al_{0.6}$- Mg_2Co, and $MmNi_{4.4}Al_{0.6}$-Mg_2Cu). Further, the effect of cooling temperature and pressure ratio on efficiency is studied. An exergy efficiency of 56.7 % is obtained at a maximum energy recovery temperature of 399°C for $MmNi_{4.4}Al_{0.6}$-Mg_2Fe. A maximum exergy COP of 0.26 is obtained at a cooling temperature of 5°C.

Keywords: Metal hydride, Polygeneration, Second law, Exergy.

Introduction

The world's energy demands are met majorly by fossil fuels which are limited and non-renewable. The extensive use of fossil fuels contributes to global warming. So, there is an urge to move to renewable energy sources and conserve energy. The use of renewable energy sources such as wind and solar energy reduces the emission of greenhouse gases. The intermittent nature of solar energy demands energy storage and conversion systems. Thermal energy storage systems play a major role in the conversion of energy from renewable energy sources [1]. A polygeneration system produces multiple effects simultaneously such as heating, cooling, hydrogen production, and electricity generation. Polygeneration is one of the techniques to improve system efficiency [2]. Thermal energy storage using metal hydrides draws the attention of several researchers because of their high storage density, long-term storage and environmentally benign [3]. Metal hydride systems such as heat pumps, heat transformers and thermal energy storage systems operate on a pair of reactors; low temperature metal hydride reactor (LTMH) and high temperature metal hydride reactor (HTMH) [4]. The metal hydrides are categorized as LTMH and HTMH based on the temperature at which hydrogen is absorbed and desorbed. $MmNi_{5-x}Al_x$ absorb hydrogen up to 80°C [5] and Mg-based metal hydrides absorb hydrogen up to 500°C [3]. Hence, $MmNi_{5-x}Al_x$ are considered LTHM, and Mg-based metal hydrides are considered HTMH in the present study.

Performance analysis of a metal hydride system provides scope for improving the design and varying the operating conditions. Choudhari et al. [6] studied the performance of thermochemical energy storage based on Lanthanum and Titanium hydrides. The COP of heat storage is observed to be 0.47 and 0.5 for Mm-Ti hydride pair and La-Mm hydride pair respectively. Sarath Babu et al. [7] calculated the COP of thermochemical energy storage system for a concentrated solar power plant. A maximum COP of 0.75 is obtained for Mg-5wt% $LaNi_5$-$La_{0.8}Ce_{0.2}Ni_5$ pair. Malleswararao et al. [8] developed a 3-D model and simulation results has shown that an energy storage efficiency of 89.4 % is obtained at a volumetric energy storage density of 156 kWh /m^3 for $LaNi_5$- Mg_2Ni pair. In the present study, a metal hydride

based polygeneration system is proposed which stores solar energy, upgrades the stored energy and also produces a cooling effect while recovering energy. Though many studies have shown the performance of the thermochemical energy systems based on the first law, studies on the second law performance are limited. Hence, the present article discusses the exergy analysis and compares the exergy performance with the first law performance.

Metal hydride-based polygeneration system

Metal hydride-based polygeneration system consists of a high-temperature metal hydride reactor (HTMHR), a low-temperature metal hydride reactor (LTMHR), and a hydrogen compressor as shown in Figure 1. HTMHR is used to store solar energy which is supplied at source temperature (T_s) and recover the stored energy at recovery temperature (T_r), while LTMHR is used to store hydrogen during the energy storage process and supply hydrogen through the compressor during the energy recovery process. The operation of the complete cycle consists of two stages namely energy storage and energy recovery process. During the energy storage process, both reactors are connected by the pipeline and during the energy recovery process they are connected by the hydrogen compressor. The operation of the cycle is explained below through the thermodynamic cycle, as shown in Figure 2.

Energy storage process: heat energy, Q_s from the available heat source is supplied (at A) at a temperature, T_s, to the HTMHR. HTMH bed desorbs hydrogen by storing supplied energy in the form of chemical potential. Desorbed hydrogen is sent to LTHMR (A-B). LTMH bed absorbs this hydrogen by releasing heat to the ambient (at B). After the energy storage process, both reactors are kept at ambient conditions.

Energy recovery process: HTMHR is heated to recovery temperature, T_r (A-E) and LTMHR is cooled to cooling temperature, T_c. A cooling effect is produced at T_c by desorbing the hydrogen gas from the LTMH bed (at C), this desorbed hydrogen is compressed isentropically by a hydrogen compressor to high pressure and sent to HTMHR (C-D). HTMH bed absorbs compressed hydrogen and releases heat, Q_r at recovery temperature, T_r (at E). To begin with the next cycle, HTMHR is cooled to supply temperature, T_s, and LTMHR is heated to ambient temperature, T_r.
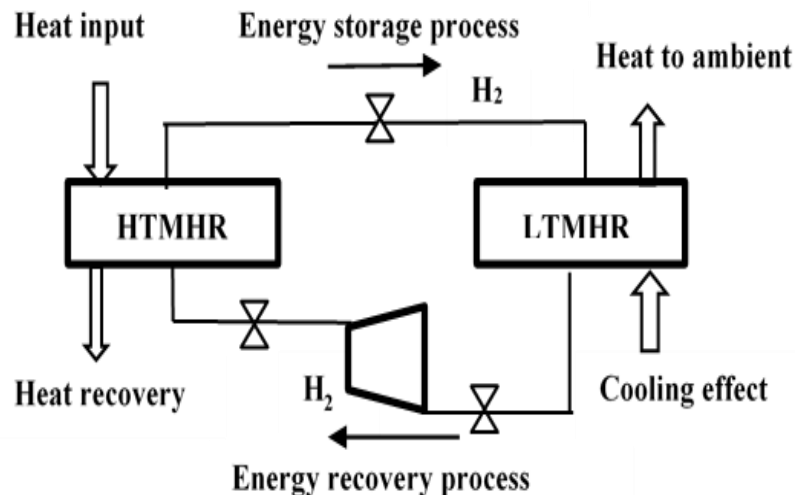
Figure 1: Schematic of metal hydride based polygeneration system
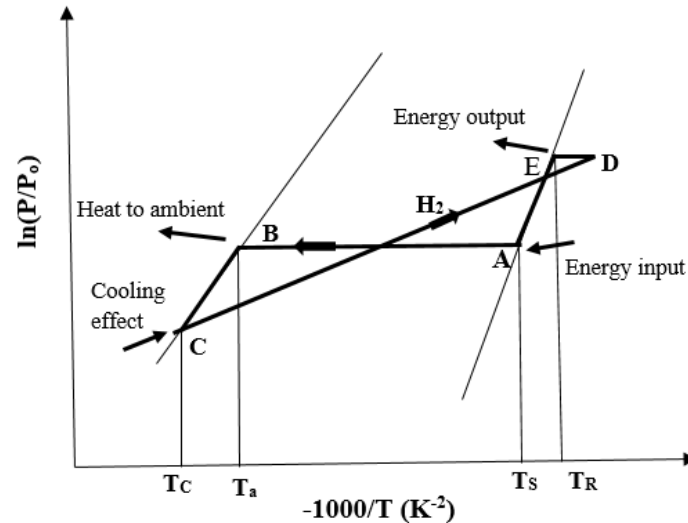
Figure 2: Thermodynamic cycle of metal hydride based polygeneration system

Metal hydride pair selection:

The selection of metal hydrides for the polygeneration system depends on equilibrium P-T relations and reaction enthalpies. Metal hydrides with high reversible storage capacity, flat plateau, minimum hysteresis, and faster kinetics are more suitable for the application [9]. For better system performance, metal hydrides should be selected such that there is a sufficient pressure difference between the two reactors for hydrogen transfer between them. In addition, the reaction enthalpies of the HTMH should be high at high temperatures and LTMH should absorb hydrogen at ambient temperature. As per above mentioned properties, $MmNi_{4.4}Al_{0.6}$ is selected as LTMH and Mg_2Ni, Mg_2Fe, Mg_2Co, Mg_2Cu are selected as HTMH. The thermodynamic properties and equilibrium P-T relations of the selected metal hydrides are given in Table.1

Operating parameters of the metal hydride-based poly generation system:

Energy storage temperature:

The minimum energy storage temperature is obtained from eq (1)

$$\ln\frac{P_{d,HTMH}}{P_o} = \frac{-\Delta H_{d,HTMH}}{RT_S} + \frac{\Delta S_{d,HTMH}}{R} \tag{1}$$

Where, $P_{d,HTMH}$ is the equilibrium desorption pressure of HTMH, $\Delta S_{d,HTMH}$ and $\Delta H_{d,HTMH}$ are reaction entropy and reaction enthalpy of HTMH respectively during desorption. P_o is the reference pressure and R is the universal gas constant.

Energy recovery temperature:

The highest energy recovery temperature of the polygeneration system is obtained from eq (2)

$$\ln\frac{P_{a,HTMH}}{P_o} = \frac{-\Delta H_{a,HTMH}}{RT_R} + \frac{\Delta S_{a,HTMH}}{R} \tag{2}$$

Where, $P_{a,HTMH}$ is the equilibrium absorption pressure of HTMH, $\Delta S_{a,HTMH}$ and $\Delta H_{a,HTMH}$ are reaction entropy and reaction enthalpy of HTMH respectively during absorption.

Table 1: Thermodynamic properties of metal hydrides

Metal hydride	Reaction enthalpy (KJ/mol)		P-T relation		Ref.
	Absorption	Desorption	Absorption	Desorption	
MmNi$_{4.4}$Al$_{0.6}$	29.4	30.1	$\ln\left(\dfrac{P}{P_0}\right) = \dfrac{-3391.87}{T} + 11.98$	$\ln\left(\dfrac{P}{P_0}\right) = \dfrac{-3524.18}{T} + 12.06$	[10]
Mg$_2$Ni	64.0	64.5	$\ln\left(\dfrac{P}{P_0}\right) = \dfrac{-7697.86}{T} + 14.69$	$\ln\left(\dfrac{P}{P_0}\right) = \dfrac{-7758}{T} + 14.74$	[3]
Mg$_2$Fe	77.4	79.2	$\ln\left(\dfrac{P}{P_0}\right) = \dfrac{-9309.59}{T} + 16.16$	$\ln\left(\dfrac{P}{P_0}\right) = \dfrac{-9526.82}{T} + 16.5$	
Mg$_2$Co	69.5	83.2	$\ln\left(\dfrac{P}{P_0}\right) = \dfrac{-8359.39}{T} + 15.58$	$\ln\left(\dfrac{P}{P_0}\right) = \dfrac{-10007.2}{T} + 17.64$	
Mg$_2$Cu	60.6	77.1	$\ln\left(\dfrac{P}{P_0}\right) = \dfrac{-7274.71}{T} + 17.61$	$\ln\left(\dfrac{P}{P_0}\right) = \dfrac{-9274.72}{T} + 17.61$	

Assumptions:

The second law analysis of the metal hydride based polygeneration system is done by considering the following assumptions:

- Hydrogen gas is assumed as an ideal gas.
- The hydrogen compression process is isentropic.
- The ambient temperature is 30°C.
- The LTMH/HTMH, absorb/ desorb hydrogen gas at a constant temperature.
- There is no pressure drop in the pipeline.
- The number of moles of hydrogen transfer between the two reactors is 10.
- The ratio between the mass of the metal reactor and the metal hydride is 0.75 [4].

First law analysis of the polygeneration system:

Heat supplied to the polygeneration system is given in eq (3)

$$Q_S = Q_{d,HTMH} + Q_{S,HTMH} + Q_{S,HTMHR} \tag{3}$$

Where, $Q_{d,HTMH} = n \times \Delta H_{d,HTMH}$, is the total amount of heat required for desorption of hydrogen from HTMH

n is the number of moles of hydrogen

$Q_{S,HTMH} = \int_{T_o}^{T_S} \left[(m \times C_p)_{HTMH} + (m \times C_p)_{H_2} \right] dT$, is total amount of heat supplied to the HTMH to heat from ambient temperature to the supply temperature

$Q_{S,HTMHR} = \int_{T_o}^{T_S}(m \times C_p)_{HTMHR} \, dT$, is the amount of heat supplied to the HTMHR to heat from the ambient temperature to supply temperature

Where, m is mass, kg

C_p is specific heat capacity, KJKg^{-1}K^{-1}

Heat recovered by the polygeneration system is given in eq (4)

$$Q_R = Q_{a,HTMH} - Q_{S,HTMH} - Q_{S,HTMHR} \tag{4}$$

Where, $Q_{a,HTMH} = n \times \Delta H_{a,HTMH}$, is total amount of heat released by HTMH during absorption of hydrogen

$Q_{S,HTMH} = \int_{T_o}^{T_R}(m \times C_p)_{HTMH} \, dT$, is total amount of heat required to heat the HTMH from ambient to recovery temperature

$Q_{S,HTMHR} = \int_{T_o}^{T_R}(m \times C_p)_{HTMHR} \, dT$, is total amount of heat required to heat HTMHR from ambient to recovery temperature

The cooling effect produced by the polygeneration system is given in eq (5)

$$Q_C = Q_{d,LTMH} - Q_{S,LTMH} - Q_{S,LTMHR} \tag{5}$$

Where, $Q_{d,LTMH} = n \times \Delta H_{d,LTMH}$, total desorption heat of LTMH

$Q_{S,LTMH} = \int_{T_o}^{T_C}\left[(m \times C_p)_{LTMH} + (m \times C_p)_{H_2}\right] dT$, is sensible heat load of LTMH and hydrogen gas

$Q_{S,LTMHR} = \int_{o}^{T_C}(m \times C_p)_{LTMHR} \, dT$, is sensible heat load of LTMHR

Hydrogen compressor work which operates between the LTMHR and HTMHR is given by the eq (6)

$$W_C = \frac{nRT_C\left(\frac{\gamma}{\gamma-1}\right)\left[r_P^{\frac{\gamma-1}{\gamma}} - 1\right]}{\eta} \tag{6}$$

Where, R= 8.314 J/mol.K

Index of isentropic compression of hydrogen gas, γ= 1.4

The efficiency of the compressor, η_c=70 %

The energy efficiency of polygeneration system $\eta_e = \frac{Q_R}{Q_S + W_C}$

COP of the cooling effect produced $COP_e = \frac{Q_C}{W_C}$

Exergy analysis of metal hydride based polygeneration system:

Exergy transfer during heat supply to the polygeneration system is given in eq (7)

$$EX_{Q,S} = \int \left(1 - \frac{T_o}{T_S}\right) \delta Q_S \tag{7}$$

Exergy transfer during heat recovery from the polygeneration system is given in eq (8)

$$EX_{Q,R} = \int \left(1 - \frac{T_o}{T_R}\right) \delta Q_R \tag{8}$$

Exergy transfer during cooling effect produced by the polygeneration system is given in eq (9)

$$EX_{Q,C} = \int \left(\frac{T_o}{T_C} - 1\right) \delta Q_C \tag{9}$$

The exergy efficiency of polygeneration system

$$\eta_{ex} = \frac{Ex_{Q,R}}{Ex_{Q,S} + W_C}$$

Exergy COP of the polygeneration system

$$COP_{ex} = \frac{Ex_{Q,C}}{W_C}$$

Discussion and Results

The exergy efficiency of the metal hydride based polygeneration system depends on the storage temperature and recovery temperature. The minimum energy storage temperature depends on the metal hydride pair and the maximum recovery temperature depends on the compression ratio and the temperature at which the cooling effect is produced at LTMHR.

Energy storage temperature:

The minimum energy storage temperature is calculated by allowing LTMH ($MmNi_{4.4}Al_{0.6}$) to absorb hydrogen at ambient temperature. The corresponding absorption equilibrium pressure is 1.8 bar. For hydrogen transfer between HTMR and LTMHR, a minimum pressure difference of 1 bar is maintained. So, the desorption pressure of HTMH is 2.8 bar and the corresponding desorption temperature is the minimum energy storage temperature obtained from eq (1). The minimum energy storage temperature for Mg_2Ni, Mg_2Fe, Mg_2Co and Mg_2Cu are 299 ℃, 349 ℃, 335 ℃ and 292 ℃ respectively. If the storage temperature is less than the minimum storage temperature, the driving pressure difference for hydrogen transfer will be insufficient as the $MmNi_{4.4}Al_{0.6}$ is at ambient. As a result, this polygeneration system cannot store energy below the minimum energy storage temperatures.

Energy recovery temperature:

Energy recovery in the polygeneration system is obtained by the operation of a hydrogen compressor between the LTMHR and HTMHR. LTMHR is connected to the suction side and HTMHR is connected to the delivery side of the compressor. The desorption equilibrium pressure of LTMH at cooling temperature is suction pressure, while delivery pressure is the absorption equilibrium pressure of HTMH at recovery temperature. The energy recovery temperature depends on the cooling temperature and compression ratio of the hydrogen compressor. Cooling temperatures of 5 ℃, 10 ℃, and 15 ℃ and hydrogen compression ratios of 8, 10, and 12 are considered for the study. The calculation of energy recovery temperature is described for the $MmNi_{4.4}Al_{0.6}$ - Mg_2Ni pair for a cooling temperature of 5 ℃ and compression ratio of 8. The desorption equilibrium pressure of $MmNi_{4.4}Al_{0.6}$ is 0.54 bar at 5 ℃ form P-T relations. Hydrogen at this pressure is compressed to 4.32 bar at r_p =8 which is considered as absorption equilibrium pressure of Mg_2Ni. The energy recovery temperature is 308 ℃ which is obtained from eq (2). The energy recovery temperatures increased with cooling temperature and hydrogen compression ratio. A maximum recovery temperature of 399 ℃ is obtained at a cooling temperature of 15 ℃ and a pressure ratio of 12 for Mg_2Fe. Among the four HTMHs chosen, highest and lowest recovery temperatures are obtained for Mg_2Fe and Mg_2Cu, respectively.

Degree of heat upgradation:

The degree of heat upgradation is the difference between the energy recovery temperature and energy storage temperature and it is obtained only when the recovery temperature is greater

Heat Powered Cycles
Conference 2023
Edinburgh
Heat in the new energy system

3rd to 6th of September 2023
The University of Edinburgh, Scotland

than the storage temperature. The degree of heat upgradation depends on cooling temperature and hydrogen compression ratio. A maximum of 50 ℃ heat upgradation is obtained at a cooling temperature of 15 ℃ and a compression ratio of 12 for Mg_2Fe which are shown in Table 2. There is no heat upgradation for Mg_2Cu at all cooling temperatures and compression ratio, and for Mg_2Co at T_c=5 ℃, r_p= 8,10 and T_c=10 ℃, r_p=8.

Table 2: Degree of heat upgradation of polygeneration system

HTMH	T_s °C	T_c=5°C			T_c=10°C			T_c=15°C		
		r_p= 8	r_p= 10	r_p= 12	r_p= 8	r_p= 10	r_p= 12	r_p= 8	r_p= 10	r_p= 12
Mg_2Ni	299	9	19	28	19	30	39	29	40	49
Mg_2Fe	349	11	21	29	21	31	39	30	41	50
Mg_2Co	335	-	-	1	-	3	11	3	13	21
Mg_2Cu	292	-	-	-	-	-	-	-	-	-

The exergy efficiency of energy storage:

The overall performance of the metal hydride based polygenration system is assessed by exergy efficiency. The exergy efficiency of the system is calculated for four different pairs considering $MmNi_{4.4}Al_{0.6}$ as LTMH and Mg_2Ni, Mg_2Fe, Mg_2Co and Mg_2Cu as HTMHs. Exergy efficiency depends on the compression ratio and cooling temperature. The effect of compression ratio and cooling temperature on exergy efficiency are shown in the Figure 3.

For a given cooling temperature, the exergy efficiency decreased with an increase in compression ratio. With an increase in compression ratio, work input and heat input increase. Higher compression ratios result in higher absorption pressure of HTMH thus increasing recovery temperature. So, the amount of energy required to heat the HTMHR from ambient temperature to recovery temperature increases.

For a given compression ratio there is a negligible increase in exergy efficiency with an increase in cooling temperature. The energy recovery temperature is higher at higher cooling temperatures, requiring higher heat input to heat HTMH from ambient to recovery temperature. However, exergy efficiency is based on the second law of thermodynamics which says that the amount of heat recovered at higher temperatures is more qualitative. Hence, exergy efficiency increased inconsiderably even though the heat input increased.

Exergy efficiency at cooling temperature 5 ℃: Maximum exergy efficiencies of 57.6 %, 56.7% and 55.9% are obtained for $MmNi_{4.4}Al_{0.6}$/ Mg_2Fe pair at a cooling temperature of 5 ℃ for pressure ratios 8, 10 and 12 respectively. Minimum exergy efficiencies of 33 %,32.9% and 32.7% are obtained for the $MmNi_{4.4}Al_{0.6}$ /Mg_2Cu pair for pressure ratios 8, 10 and 12 respectively. Variation of exergy efficiency with the pressure ratio of the selected four pairs is shown in Figure 3(a).

Exergy efficiency at cooling temperature 10 ℃: Maximum exergy efficiencies of 57.89 %, 56.93% and 56.12% are obtained for $MmNi_{4.4}Al_{0.6}$/ Mg_2Fe pair at a cooling temperature of 10 ℃ for pressure ratios 8, 10 and 12 respectively. Minimum exergy efficiencies of 33.62%, 33.41% and 33.27% are obtained for the $MmNi_{4.4}Al_{0.6}$ /Mg_2Cu pair for pressure ratios 8, 10 and 12 respectively. Variation of exergy efficiency with the pressure ratio of the selected four pairs is shown in Figure 3(b).

Exergy efficiency at cooling temperature 15 ºC: Maximum exergy efficiencies of 58.12 %, 57.12% and 56.26% are obtained for MmNi$_{4.4}$Al$_{0.6}$/ Mg$_2$Fe pair at a cooling temperature of 15 ºC for pressure ratios 8, 10 and 12 respectively. Minimum exergy efficiencies of 34.2 %, 33.98% and 33.76% are obtained for the MmNi$_{4.4}$Al$_{0.6}$ /Mg$_2$Cu pair for pressure ratios 8, 10 and 12 respectively. Variation of exergy efficiency with the pressure ratio of the selected four pairs is shown in Figure 3(c).
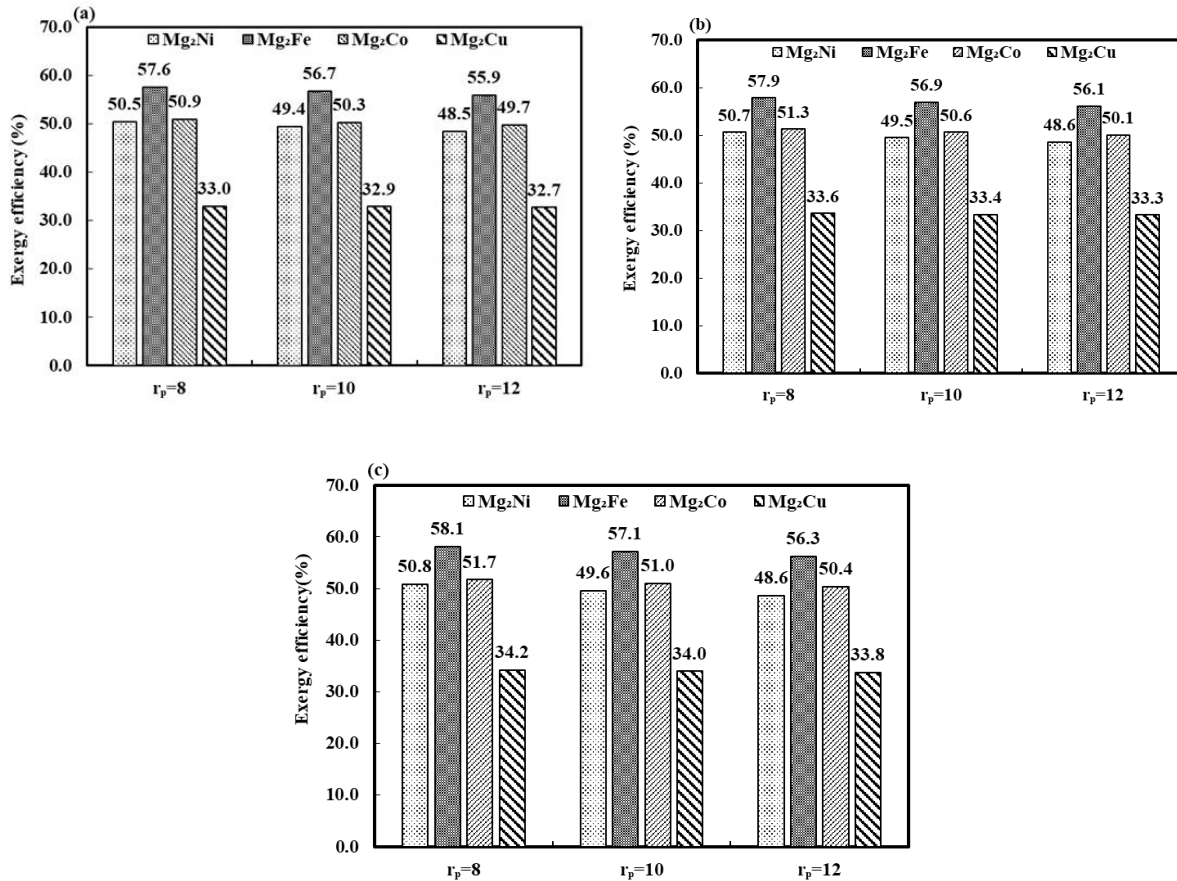
Figure 3: Exergy efficiencies of polygeneration system with working pairs MmNi$_{4.4}$Al$_{0.6}$/ Mg$_2$Ni, MmNi$_{4.4}$Al$_{0.6}$/Mg$_2$Fe, MmNi$_{4.4}$Al$_{0.6}$/Mg$_2$Co and MmNi$_{4.4}$Al$_{0.6}$/Mg$_2$Cu (a) at cooling temperature 5ºC (b) at cooling temperature 10 ºC (c) at cooling temperature 15 ºC

Comparison of exergy efficiency with energy efficiency of the polygeneration system:

The exergy efficiencies obtained with working pair MmNi$_{4.4}$Al$_{0.6}$/Mg$_2$Fe are maximum at all cooling temperatures and hydrogen compression ratios as disused in the above section. Hence, the comparison of exergy efficiencies with energy efficiencies of MmNi$_{4.4}$Al$_{0.6}$/Mg$_2$Fe is shown in Figure 4. It is observed that the exergy efficiencies are greater than energy efficiencies at all operating conditions. The maximum exergy efficiency of 58.1 % is obtained at a cooling temperature of 15 ºC and a hydrogen compression ratio of 12. Whereas a maximum energy efficiency of 49.3 % is obtained at a cooling temperature of 5 ºC and a compression ratio of 8. The main reason for the above results is energy efficiencies are obtained by considering the values of input and output energies. On the other hand, exergy efficiencies depend on the temperatures at which the energy is stored and recovered along with the input and output energies. Energy efficiency is greater than exergy efficiency when the energy recovery temperature is less than the energy storage temperature. For MmNi$_{4.4}$Al$_{0.6}$/Mg$_2$Cu exergy efficiency is less than energy efficiency at all operating conditions as its energy recovery temperatures are less than energy storage temperature. Figure 5 shows the comparison of

Heat Powered Cycles
Conference 2023
Edinburgh
Heat in the new energy system

3rd to 6th of September 2023
The University of Edinburgh, Scotland

energy and exergy efficiencies of all four pairs at a cooling temperature of 15℃ and a hydrogen compression ratio of 12. The exergy efficiency (34 %) is less than the energy efficiency (39 %) for $MmNi_{4.4}Al_{0.6}/Mg_2Cu$ because the energy recovery temperature (202℃) is less than the energy storage temperature (292℃).
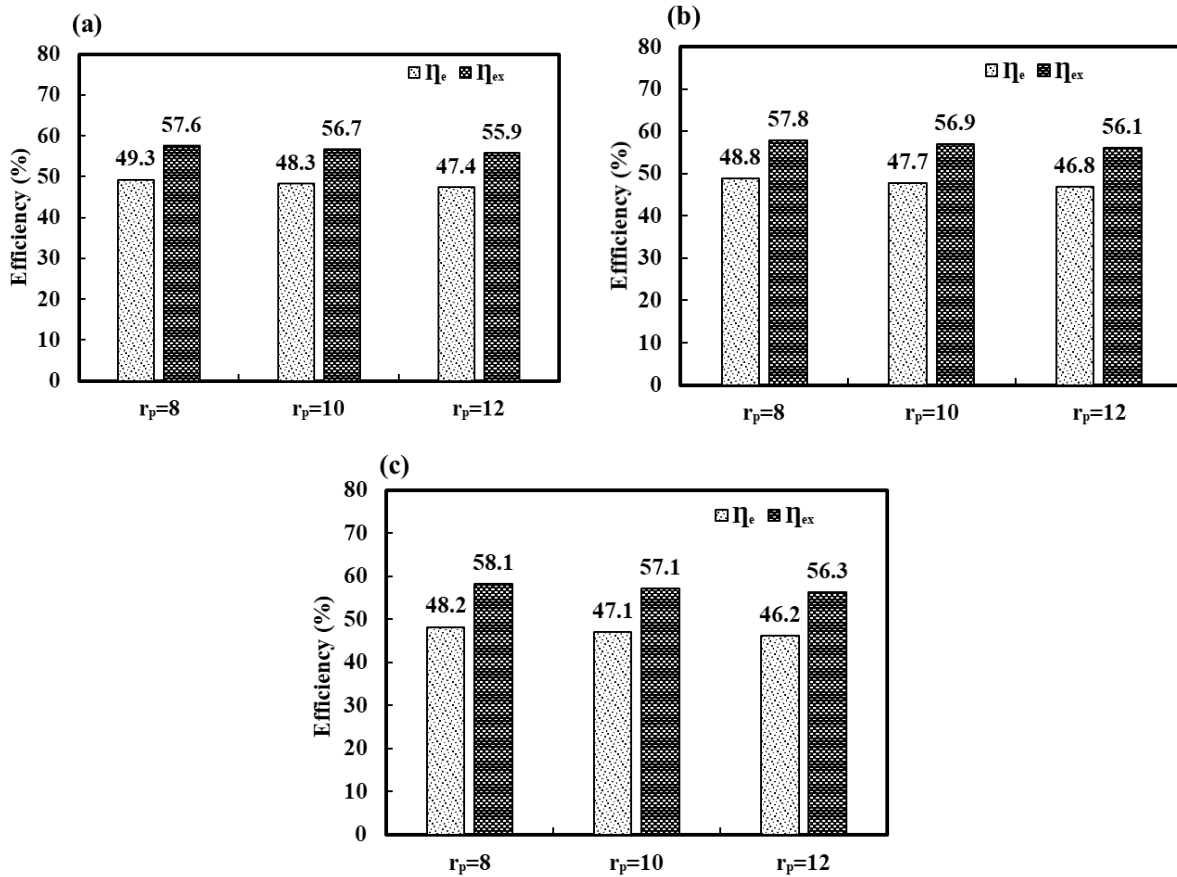
Figure 4: Comparison of exergy and energy efficiencies of polygeneration system with working pairs $MmNi_{4.4}Al_{0.6}/Mg_2Fe$ at (a) cooling temperature 5℃ (b) cooling temperature 10 ℃ (c) cooling temperature 15 ℃
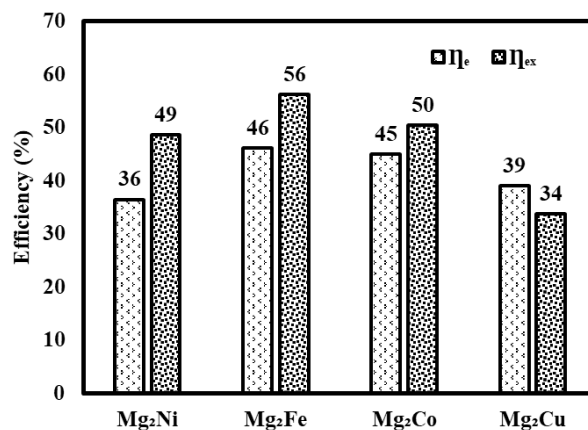
Figure 5: Comparison of exergy and energy efficiencies of polygeneration system with working pairs $MmNi_{4.4}Al_{0.6}/$ Mg_2Ni, $MmNi_{4.4}Al_{0.6}/Mg_2Fe$, $MmNi_{4.4}Al_{0.6}/Mg_2Co$ and $MmNi_{4.4}Al_{0.6}/Mg_2Cu$ cooling temperature 15 ℃ and pressure ratio 12

Comparison of exergy COP with energy COP of the polygeneration system:

The cooling effect in the metal hydride based polygeneration system is produced at LTMHR and it is due to the operation of the hydrogen compressor between HTMHR and LTMHR. Hence, the COP of this system depends on the thermodynamic properties of LTMH and hydrogen compressor work. Hydrogen compressor work depends on cooling temperature and the compression ratio. At a given cooling temperature, with an increase in compression ratio, compressor work increases resulting in a decrease in both energy and exergy COP. At a given compression ratio, with an increase in cooling temperature, energy COP increased while exergy COP decreased. The variation of energy and exergy COP with cooling temperature is explained as follows. Energy output (a cooling effect produced) at 15°C is greater than energy output at 5°C, contrarily exergy output (a cooling effect produced) at 15°C is less than exergy output at 5°C. However, the change in energy COP with respect to cooling temperature and the change in exergy COP with respect to compression ratio is trivial. A maximum energy COP of 2.78 is obtained at a cooling temperature of 15°C and a hydrogen compression ratio of 8. Whereas a maximum exergy COP of 0.26 is obtained at a cooling temperature of 5°C and a hydrogen compression ratio of 8.
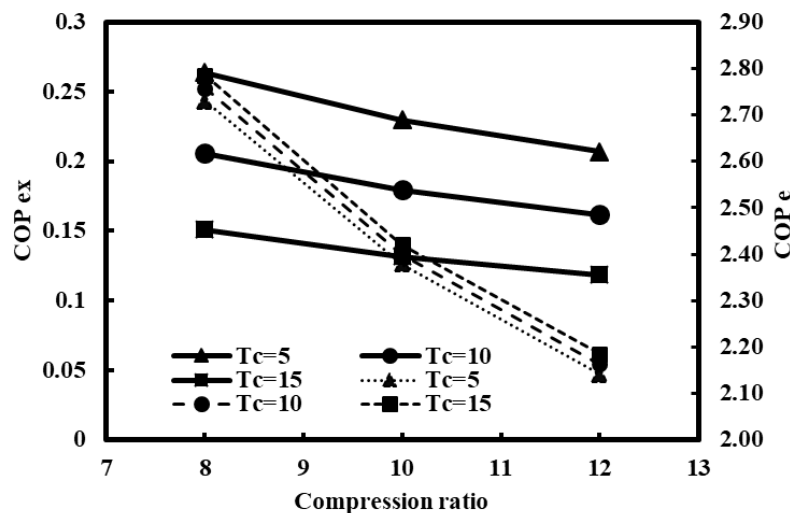
Figure 6: Exergy COP and energy COP of the polygeneration system

Summary/Conclusions

Metal hydride based polygeneration system which can store energy, upgrade energy and produce cooling effect is proposed. The system is analysed thermodynamically for four working pairs namely $MmNi_{4.4}Al_{0.6}/Mg_2Ni$, $MmNi_{4.4}Al_{0.6}/Mg_2Fe$, $MmNi_{4.4}Al_{0.6}/Mg_2Co$ and $MmNi_{4.4}Al_{0.6}/Mg_2Cu$. The exergy efficiency of energy storage and exergy COP of cooling effect are calculated, and the effect of operating parameters on efficiency and COP are studied. In addition, the first law and the second law performances are compared. The following conclusions are made from the present study:

- Heat recovery temperatures obtained for $MmNi_{4.4}Al_{0.6}/Mg_2Fe$ are high, ranging from 360 to 399 °C. And heat upgradation obtained for $MmNi_{4.4}Al_{0.6}/Mg_2Fe$ and $MmNi_{4.4}Al_{0.6}/Mg_2Ni$ is comparable, ranging from 9 to 50 °C.
- The maximum exergy efficiency of 58 % is obtained for $MmNi_{4.4}Al_{0.6}$ - Mg_2Fe at T_r=380°C, T_c=15°C and r_p=8. And a maximum energy efficiency of 49.3 % is obtained at T_c=5°C and r_p=8.

- Exergy efficiency is less than energy efficiency for the pairs whose recovery temperature is less than the source temperature. Other way: Exergy efficiency is higher than the energy efficiency when energy recovery temperature is higher than storage temperature.
- A maximum second law COP of 0.26 is obtained at T_c=5℃ and r_p=8, and a maximum first law COP of 2.78 is obtained at T_c=15℃ and r_p=8. Second law COP is less than first law COP under all operating conditions.

Acknowledgments

References:

[1] Alva G., Lin Y., Fang G., "An overview of thermal energy storage systems", Energy, 2018 Feb 1;144:341-78.

[2] Rong A., Lahdelma R., "Role of polygeneration in sustainable energy system development challenges and opportunities from optimization viewpoints", Renewable and Sustainable Energy Reviews, 2016 Jan 1;53:363-72.

[3] Babu, K.S., Kumar, E.A., "Compressor operated sorption system for high temperature thermochemical energy storage using Mg based hydrides" International Journal of Hydrogen Energy, 2022 Oct 19.

[4] Babu, KS., Kumar, EA., "Thermodynamic analysis of compressor operated resorption thermochemical energy storage system for heat storage, combined cooling and heat upgradation", Journal of Energy Storage, 2022 Jun 1;50:104659.

[5] Sharma, VK., Kumar, EA., Maiya, MP., Murthy, SS., "Experimental and theoretical studies on static and dynamic pressure–concentration isotherms of MmNi5− xAlx (x= 0, 0.3, 0.5 and 0.8) hydride"s", International journal of hydrogen energy, 2014 Nov 11;39(33):18940-51.

[6] Choudhari, MS., Sharma, VK., Paswan, M., "Metal hydrides for thermochemical energy storage applications", International Journal of Energy Research, 2021 Aug;45(10):14465-92.

[7] Babu, KS., Kumar, EA., Murthy, SS., "Thermochemical energy storage using coupled metal hydride beds of Mg-LaNi5 composites and LaNi5 based hydrides for concentrated solar power plants", Applied Thermal Engineering, 2023 Jan 25;219:119521.

[8] Malleswararao, K., Aswin, N., Murthy, SS., Dutta, P., "Performance prediction of a coupled metal hydride based thermal energy storage system", International Journal of Hydrogen Energy, 2020 Jun 11;45(32):16239-53.

[9] Sharma, VK., Kumar, EA., "Thermodynamic analysis of novel multi stage multi effect metal hydride based thermodynamic system for simultaneous cooling, heat pumping and heat transformation", International Journal of Hydrogen Energy. 2017 Jan 5;42(1):437-47.

[10] Mohan, M., Sharma, M., Sharma, V.K., Kumar, E.A., Satheesh, A., Muthukumar, P., "Performance analysis of metal hydride based simultaneous cooling and heat transformation system", International Journal of Hydrogen Energy, 2019 Apr 23;44(21):10906-15.

In-situ Monitoring of two Air-to-Water Hybrid Heat Pumps for Residential Buildings

Camila Dávila[1,*], **Vincent Lemort**[1]

[1]University of Liège, Thermodynamics Laboratory, Liège, Belgium

[*]Corresponding author: cdavila@uliege.be

Abstract

This work describes the methodology used to realize a performance analysis of two hybrid heat pumps (HHP) designed for space heating (SH) and domestic hot water (DHW) production for residential applications. The systems are installed in the same climatical region in the northern part of Belgium. The household composition of both facilities and heat requirements are different between them. Both installations count with sensors that allow to register the appliances gas consumption, electrical consumption, water flows and temperatures. Settings data are known but not monitored. The data collected is daily sent to the Cloud and is used to compute performance indicators. Two years of data are analyzed per site, allowing to quantify the effect of different variables over the system performance. The differences found are described and discussed.

Keywords: Hybrid heat pump, Gas driven systems, Monitoring.

Introduction/Background

In the decarbonization pathway, heat pumps technology can play a main role. Studies point out that heat pumps are a good alternative to reduce the CO_2 emissions and the energy consumption, of which a significant part is destined to buildings in Europe to meet the DHW and SH demands [1,2]. However, an abrupt transition is not possible due to restrictions such as housing requirements, available energy sources, technology cost, etc. That is why when complemented with hybrid solutions, the decarbonization and transition becomes more flexible, cheaper and easier [3]. This, however, could have associated problems. As several studies show, a proper control, correct system integration and monitoring are crucial to properly evaluate the potential and the impact of these technologies under an energetic and economic point of view without diminishing their performance [4-8].

The objective of this work is to compute performance indicators of two appliances under field conditions. The systems are installed in two residential houses in the northern part of Belgium, corresponding to the same climatical region. These locations have sensors that provide information that allows to analyze inputs and outputs to the appliances, enabling to compute performance indicators; sensors to measure indoor and outdoor ambient conditions are also placed. Heat meters are installed to measure the heating energy delivered by the appliances to each circuit that requires it (DHW and SH). Both sites count with photovoltaic panels and the household compositions differ between them, affecting the consumptions.

Both systems have been exhaustively monitored during 2021 and 2022. It is thanks to the monitoring that problems related to both installations were identified and corrected, allowing to quantify the penalization to the performances due to a faulty installation or misunderstanding of parameters. Besides this, changes are applied according to the needs of

the users, achieving a better understanding of the system on their part and adjusting it to their needs.

Description of the systems

The schemes of the monitored appliances are shown in Figure 1 and Figure 2. These hybrid systems are a coupling of an internal module that includes a boiler, and an outdoor module composed by a heat pump. This assembly allows to cover the heat demands of a residential facility with only one module (only boiler, only heat pump) or both (hybrid mode), depending on the thermal demand circuit (DHW or SH) and the delivery water temperature required. The first location in Leest has a heat pump with nominal heating capacity of 7.9 kW under +7°C outdoor air temperature and outlet water temperature of +35°C, with an associated coefficient of performance of 4.34 according to the EN 14511-2. The system provides SH through radiant floor as well as radiators, and counts with a buffer tank of 177 liters in the internal module. Its technical features are shown in Table 1 and Table 2, for the heat pump and the boiler respectively. For Table 2, the values are given for rich gas (H) and lean gas (L).

Table 1. Heating mode: Water outlet temperature +35°C. Performances according to EN 14511-2 (Leest)

	Type of measurement	Unit	AWHP 8 MR-2 model
Outdoor air temperature +7°C	Heating capacity	kW	7.9
	Coefficient of performance (COP)		4.34
	Electrical power absorbed	kWe	1.82
	Rated water flow ($\Delta T = 5K$)	m^3/hour	1.36
Outdoor air temperature +2°C	Heating capacity	kW	6.8
	Coefficient of performance (COP)		3.3
	Electrical power absorbed	kWe	2.06

Table 2. Internal module – Boiler characteristics (Leest)

			Gas H G20	Gas L G25
Rated heating capacity Heating mode (80°C/60°C)	Min-max	kW	3.0-14.9	2.5-12.1
Rated heating capacity Heating mode (50°C/30°C)	Min-max	kW	3.4-15.8	2.8-13.2
Rated heating capacity DHW mode G20 (HHV)	Min-max	kW	3.4-16.7	2.8-13.9
Space heating efficiency at full load (HHV) (80/60°C)		%	86.9	86.9
Space heating efficiency at full load (HHV) (50/30°C)		%	94.8	94.8
Gas consumption G20 (gas H)	Min-max	m^3/h	0.33-1.59	0.32-1.53
Electrical power absorbed – great speed	Max	W	101	101
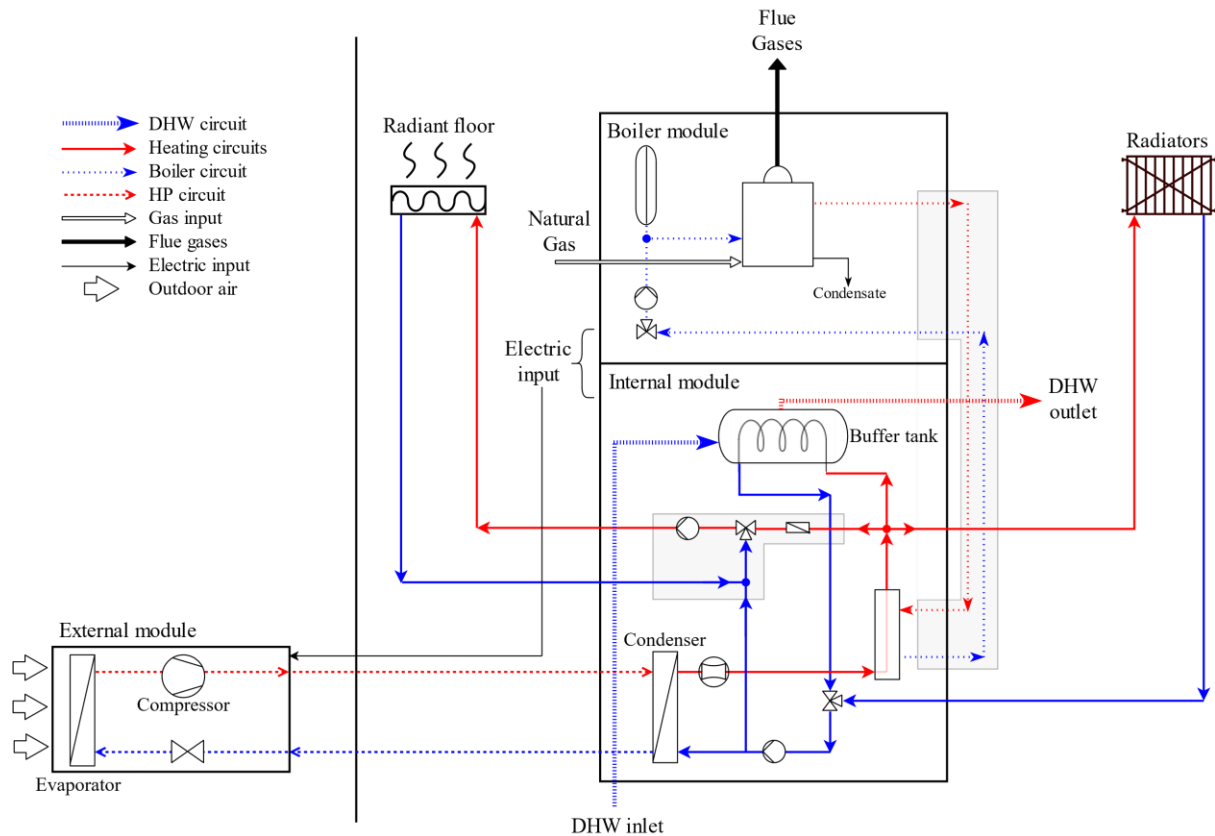
Figure 1. Monitored hybrid heat pump schematic, Leest

For Ruiselede, the SH circuit is based on low temperature radiators and there is no buffer tank embedded or installed in the hydraulic circuit. The technical features are shown in Table 3; for the gas consumption, values are shown for rich gas (G20) and lean gas (G25).

Table 3. Ruiselede monitored hybrid system technical features

External unit: Heat pump			
Rated heating capacity		kW	4.40 / 4.03
Rated power absorbed (heating)		kW	0.87 / 1.13
COP (heating)			5.04 / 3.58
Domestic hot water heating efficiency		%	96
Seasonal efficiency for ambient heating (water temp. outlet 55°C)		%	128
Internal unit: Boiler			
Gas consumption (G20)	Min-max	m³/h	0.78 - 3.39
Gas consumption (G25)	Min-max	m³/h	0.90 - 3.93
Space heating	Heat input (LHV)	Min-max	kW	7.6 - 27
	Output at 80/60°C	Min-Nom.	kW	8.2 - 26.6
	Efficiency	Net calorific value	%	98 / 107
Domestic hot water	Thermal load (LHV)	Min-Nom.	kW	7.6 - 32.7
	Efficiency	Net calorific value	%	105
Power consumption		Stand by / Max	W	2 / 55
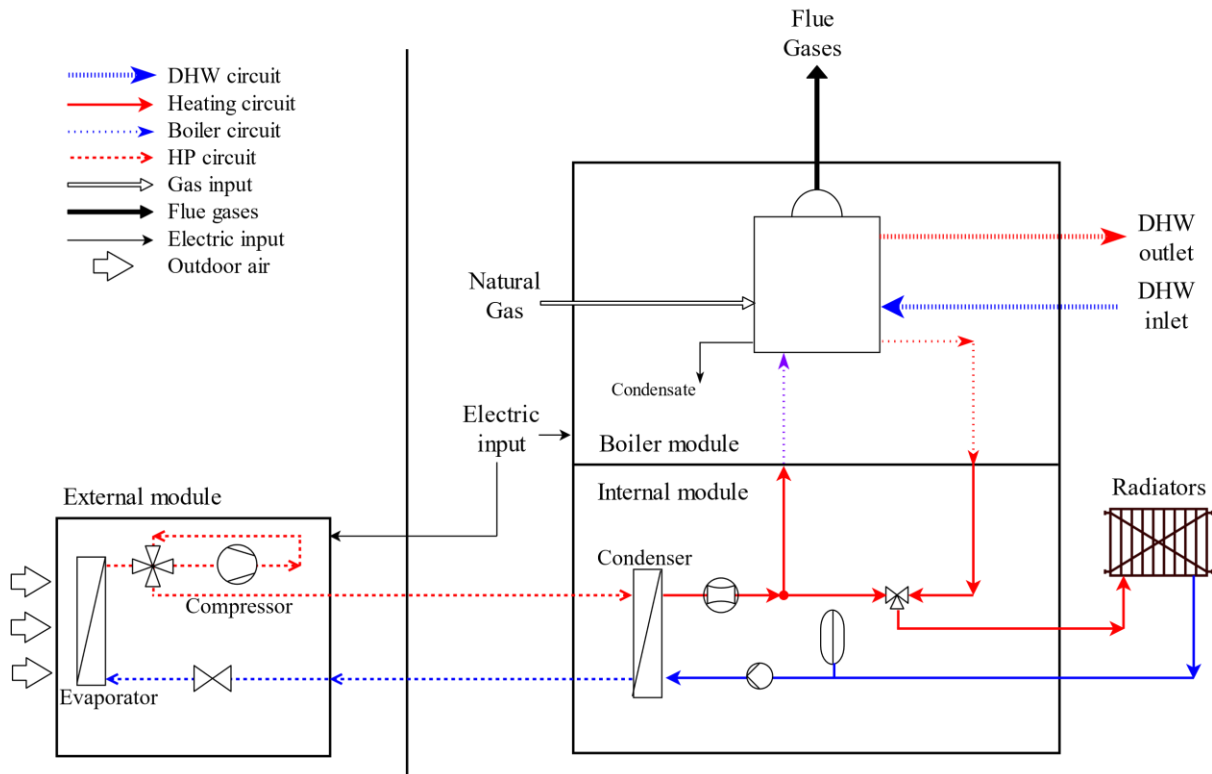
Figure 2. Monitored hybrid heat pump schematic, Ruiselede

Description of the monitored buildings

The monitored hybrid systems are installed in two residential buildings in the northern part of Belgium at Leest and Ruiselede, considered to be in the same climatic region. These locations are equipped with sensors whose collected data is daily sent to the Cloud; their technical features are shown in

Table **4**, and their position can be seen in the installation schemes shown in Figure 3 and Figure 4. Indoor and outdoor ambient conditions are measured, as well as gas and electric consumptions of the system; a heat meter is installed between the inlet and outlet pipes of the machine to measure the heating energy delivered by the appliance to each circuit (DHW or SH) based on the measurement of the water flow rate and its respective inlet and outlet temperatures, allowing to compute performance indicators of both systems.

Some control and internal parameters of the systems such as power modulation or temperature setpoint are not remotely controlled or monitored. This means that changes or modifications made by the user or installer could not be communicated, being difficult or impossible to identify only with the data analysis.

None of the monitored houses counts with a buffer tank for heat storage (besides the one embedded at Leest as shown in Figure 1).; additionally, both sites count with photovoltaic panels. In terms of users, the household composition in Leest correspond to a family (2 adults, 2 kids) while at Ruiselede the household is composed by only one person.

Figure 3. Installation scheme of Leest monitoring site

Figure 4. Installation scheme of Ruiselede monitoring site

Table 4. Reference of the monitoring sensors

Sensors	Reference	Resolution	Accuracy
Ext./Int. temp. ; humidity	Weptech Munia	0,1 K; 0,1%	± 0,3 K; ± 2%
Heat counter	Qalcosonic E1 Qn2,5 qi=0.025m³/h; L=130mm	1 kWh; 1 l; 0,1 K	Accuracy Class 2
Machine 1-way electrical energy counter	Iskraemeco ME162-D1A42-V12G22-M3K0	10 Wh	Accuracy Class 1
Gas volume counter	BK-G4T DN25 Qmax 6 m³/h	10 l	<0.5%
Data logger (cloud connection)	Viltrus MX-9	-	-

From the beginning of the monitoring visits had been made to solve problems linked to the installation and settings at each site, whose consequences are reflected in the monitoring data. These problems and misunderstandings did not allow the appliance to work as a hybrid system before September 2021 at Ruiselede, and the same applies for Leest before December 2021. On the other hand, the electricity consumption of the heat pump was recorded in none of the two facilities before September 2021. Based on these two observations, it is possible to say that both systems worked based only on the boiler thermal production until these dates, and that the electrical measurements registered on each site correspond only to the boiler.

Discussion and Results

Both installations are supplied with natural gas. Along the study, Ruiselede always counted with rich gas (H), while at Leest a transition from lean gas (L) to rich gas was made in June 2022. The mean High Calorific Values (HCV) used for the further analysis, per site and per year, are shown in Table 5.

Table 5. Mean high calorific value used per site, per year

High calorific value [Wh/m3]		Year	
		2021	**2022**
Site	Leest	10.3570 (L)	Until May : 10.3361 (L) From June : 11.5699 (H)
	Ruiselede	11.5376 (H)	11.5612 (H)

From here under, the nomenclature used per graph is shown in Table 6.

Table 6. Nomenclature used in monitoring analysis graphs

L	Leest
R	Ruiselede
Global	Global
Th	Thermal
El	Electrical
DHW	Domestic hot water
SH	Space heating
int	Internal
ext	External
Gas	Gas

The COP_{global} is computed as the ratio of the thermal power output to heat and electric power inputs as defined in Equation (1). The COP_{Th} and COP_{El} are shown in Equation (2) and (3) and correspond to the same definition considering only the thermal or electrical input respectively; the thermal input is considering the high calorific value of the used gas. Similarly, the COP_{Th} and COP_{El} for DHW of SH are computed as shown in Equation (4) and Equation (5), taking into account only the DHW or SH production respectively.

$$COP_{global} = \frac{\dot{Q}_{DHW} + \dot{Q}_{SH}}{\dot{Q}_{gas} + \dot{W}_{El}} \tag{1}$$

$$COP_{Th} = \frac{\dot{Q}_{DHW} + \dot{Q}_{SH}}{\dot{Q}_{gas}} \tag{2}$$

$$COP_{El} = \frac{\dot{Q}_{DHW} + \dot{Q}_{SH}}{\dot{W}_{El}} \tag{3}$$

$$COP_{Th,DHW} = \frac{\dot{Q}_{DHW}}{\dot{Q}_{gas}} \; ; \; COP_{Th,SH} = \frac{\dot{Q}_{SH}}{\dot{Q}_{gas}} \tag{4}$$

$$COP_{El,DHW} = \frac{\dot{Q}_{DHW}}{\dot{W}_{El}} \; ; \; COP_{El,SH} = \frac{\dot{Q}_{SH}}{\dot{W}_{El}} \tag{5}$$

The available number of days to analyze during 2021 is 356 for both sites. For the analysis it must be taken into account that, as previously mentioned, the system worked during some months only based on the boiler thermal production. The most visible effects are due to:

- An electrical meter installation in each facility to measure the heat pump electrical consumption (not registered until then) in early September (day ~250); is worth to mention that the electrical consumption of the boiler (indoor module) was measured all the time.
- Modification of the tariff settings at Leest in mid-December (day ~340), allowing the system to work as a hybrid appliance.
- Modifications in the energy tariffs at Ruiselede in early August (day ~220) and mid-November (day ~320), first to benefit from the PV production and afterwards, to promote the use of natural gas.

These changes are visible in Figure 5, where towards the end of the year the COP global of both facilities increases, as well as the effect in the thermal and electrical COP. These changes are more affected by the SH production during winter since the DHW production remains all over the year as pointed in Figure 7.

At Leest, the datasheets of the appliance do not give an efficiency value for the DHW production based only on the boiler operation as they do for the SH production (Table 2), so no conclusions can be concisely drawn. It can be seen though, that the efficiency for the SH production of the system operation based only on the boiler heat supply (before December 2021) is within the ranges announced by the manufacturer (86.9-94.8% based on HHV, it must be considered that at Leest the installation is powered with lean gas). The seasonal effect is clearly appreciated also in the SH production, while the DHW production remains relatively constant throughout the year. Only a few points above 1 can be seen for the COP global on the second half of December due to the change of tariffs that promotes the use of the heat pump and electricity over natural gas as shown in Figure 8, for an almost identical SH and DHW to that at the beginning of the year 2021. Even more, a switch in the electricity

consumption can be identified (a reduction in the internal electricity consumption linked to the boiler for an increase in the external one liked to the heat pump) as well as a decrease of the natural gas consumed, revealing the change on the internal control of the appliance towards a hybrid mode due to the modifications performed. The effect can be seen also in the change during the start and the end of the year in the thermal and electric COP for DHW and SH production as shown in Figure 6, increasing the efficiency of the gas and diminish the electrical one.

At Ruiselede, the hydraulic system is simpler and direct. The household composition implies that there's almost no DHW production, therefore most of the results are associated to the SH production; however, these results are far from the ones announced in Table 3. It must be considered that they are based on a low calorific value (LHV) for the declared efficiencies, and that the results shown are based on the gas HHV available on site; thus, to be able to compare, it must be considered that the graphic results are ~11% lower in LHV terms.

The gas boiler at Ruiselede is sized for a space heating output range between 8.2 and 26.6 kW; as can be seen in Figure 7, the SH demand is rarely equal or higher than the minimum output of the gas boiler. Thus, it can be said that the gas boiler of the system is oversized for the SH requirements of the household, resulting in poor daily performance indicators before the modifications of August. The heat pump at Ruiselede has a smaller heating capacity that the gas boiler, so after the modifications (around day 220) and since the heat pump is allowed to work, improvements in the COP's are observed due to the fact that now the unit sizing is more suitable for the main demand (SH). Nonetheless, these values decrease drastically after the change of tariffs in mid-November (day 320). This can be observed also by correlating the results shown in Figure 8.
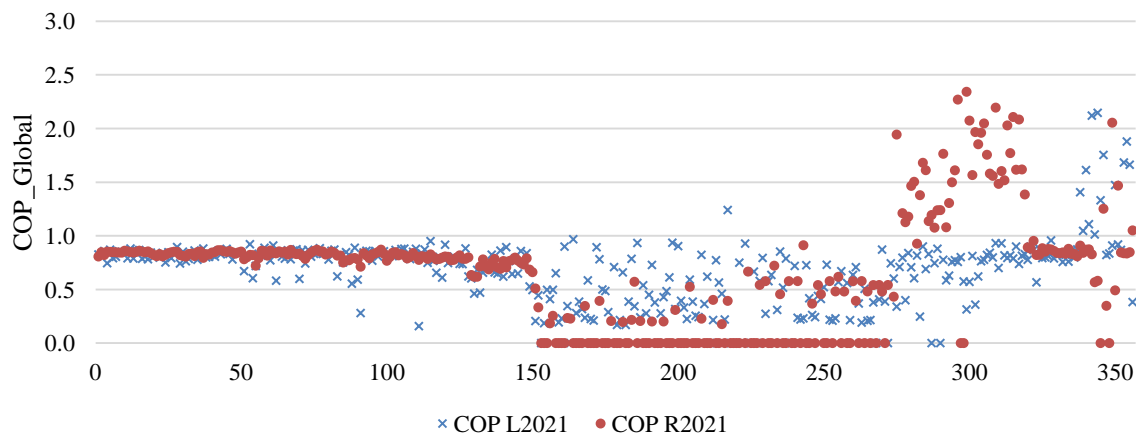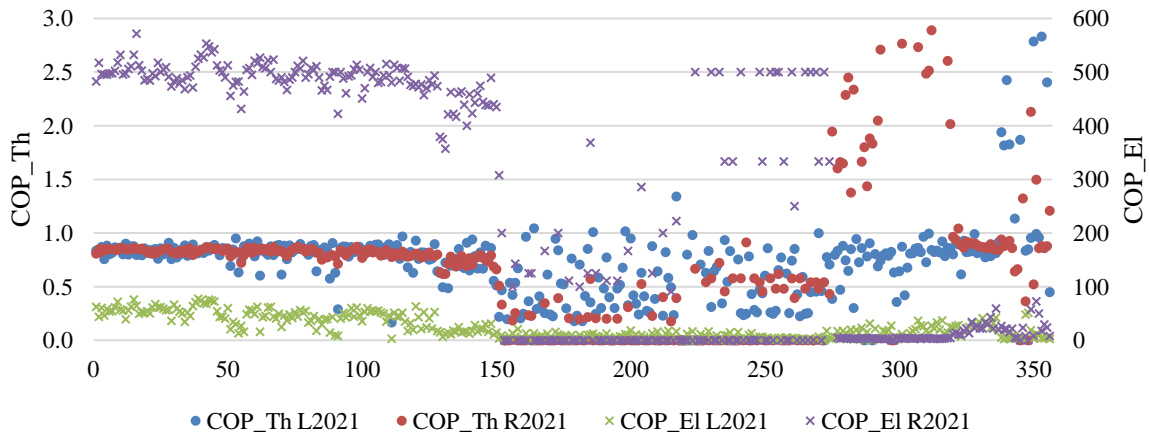
Figure 5. Daily global COP for both sites during year 2021 (top); Daily Th and El COP for both sites during year 2021 (bottom)
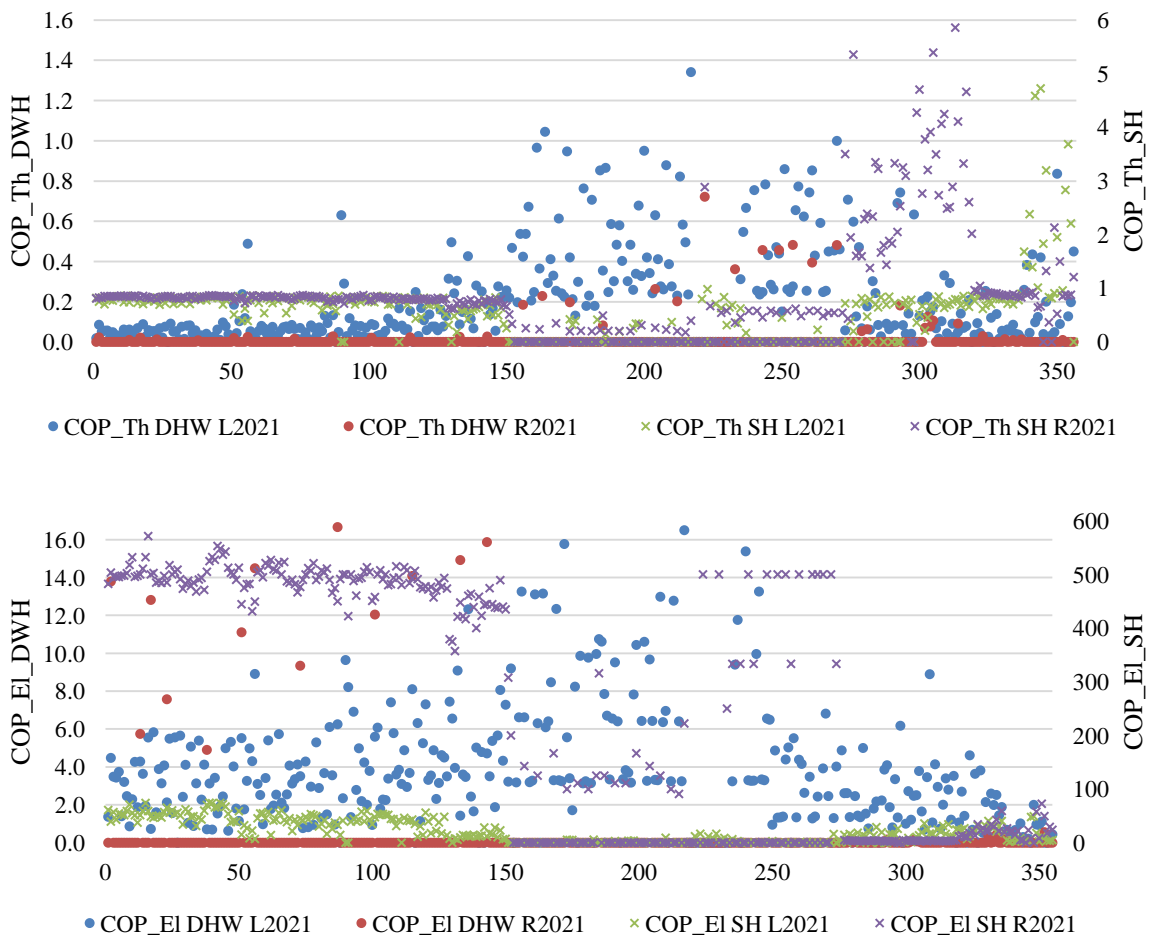
Figure 6. Daily COP Th for DHW and SH for both sites during year 2021 (top); Daily COP El for DHW and SH for both sites during year 2021 (bottom)
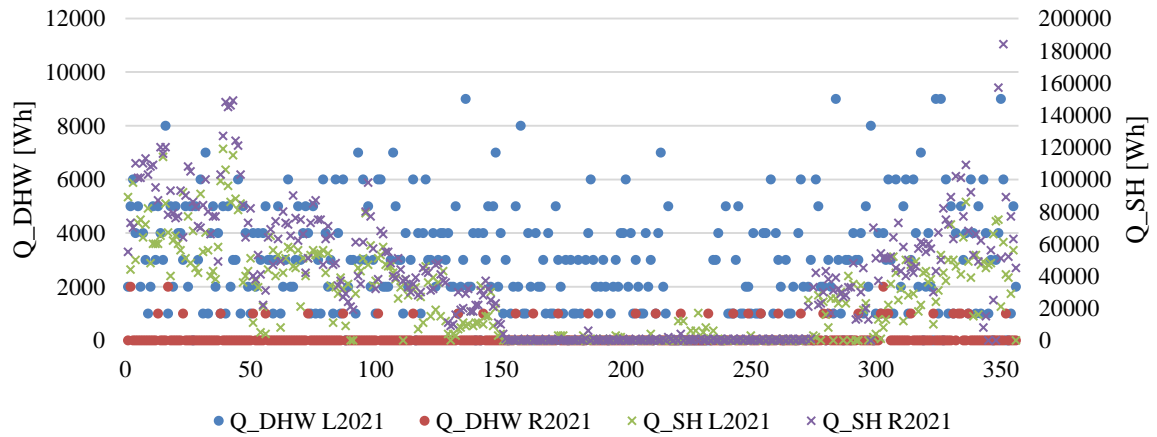
Figure 7. DHW and SH production for both sites during 2021
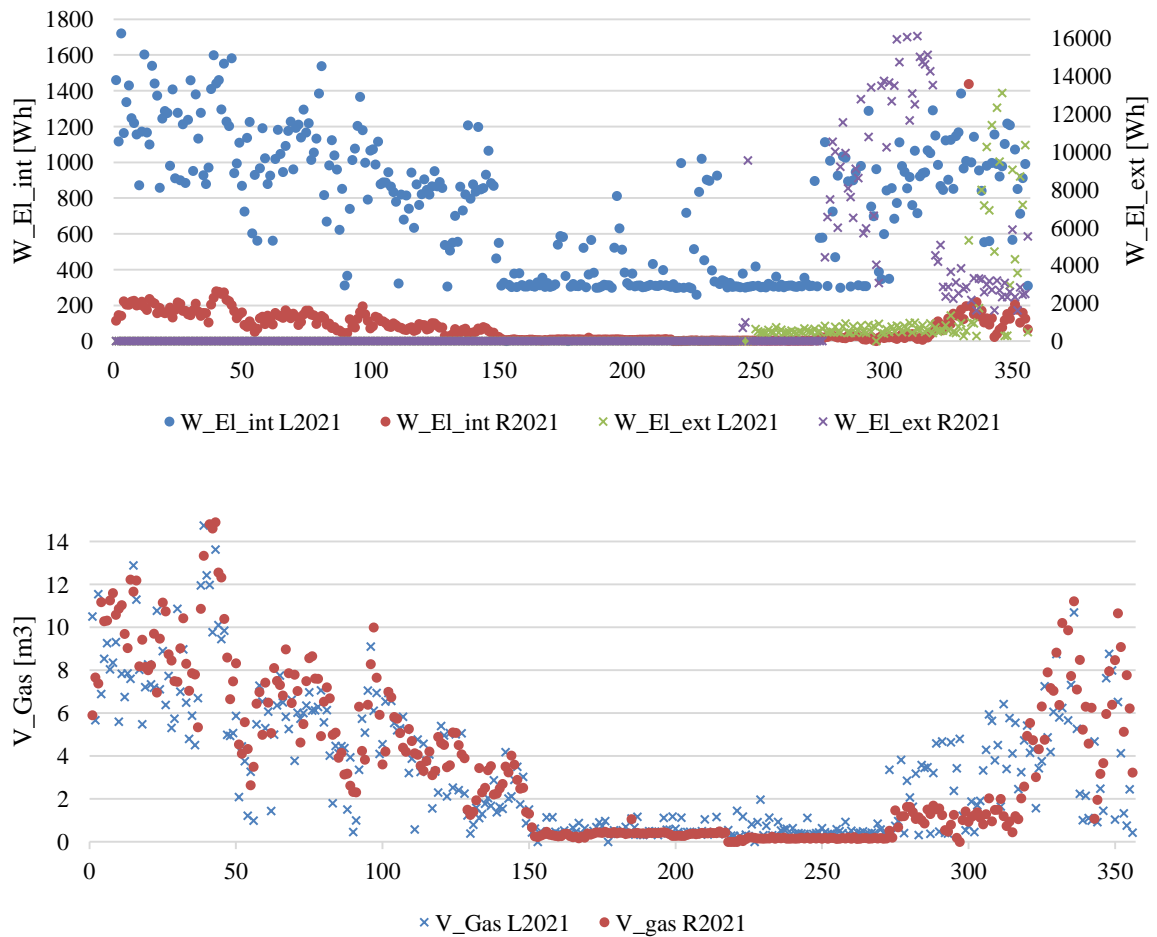
Figure 8. Internal and external electricity consumption for both sites during 2021 (top); gas consumption for both sites during year 2021 (bottom)

For year 2022, the available number of days to analyze is 364 days for both sites. Compared to year 2021, better daily results are observed in Figure 9 (top) for Leest through the first cold months, result of the last modifications performed in December 2021; these improvements, once again, are mostly related to the SH production as shown in Figure 11, where the DHW is a small part of the total. Figure 12 (bottom) shows that the gas consumption decreased

compared to the previous year, effect that is inline with the increase of the external electrical consumption during 2022 compared to 2021 (Figure 12, top).

At Ruiselede and as shown in Figure 9, until the end of summer the results are in line with the change of tariff performed in November 2021, decreasing the COP's; however, this changes when the cold season starts in October (around day 270). There are no variations observed in the behavior of the demand of the household (Figure 11), yet the energy consumption changes with electricity having a main role and most of all, the heat pump (Figure 12, top); this also matches the gas consumption behavior shown in Figure 12 (bottom).

The changes on the external electrical consumption are difficult to explain for the last months of the year; the observed behavior is similar to what is expected from a change of tariff as it was observed in 2021 to promote the heat pump utilization, but there is no record about a change in this respect informed by the user.
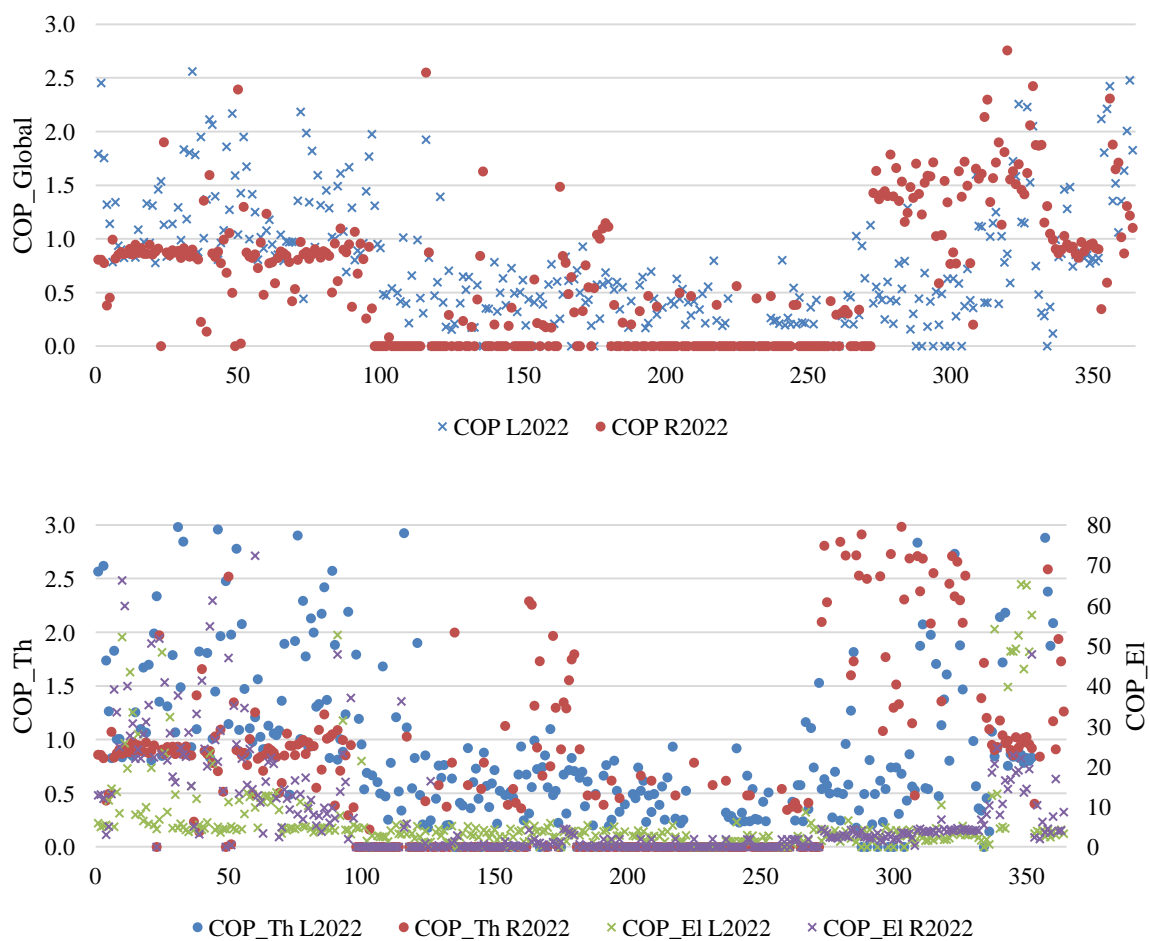
Figure 9. Daily global COP for both sites during year 2022 (top); Daily Th and El COP for both sites during year 2022 (bottom)
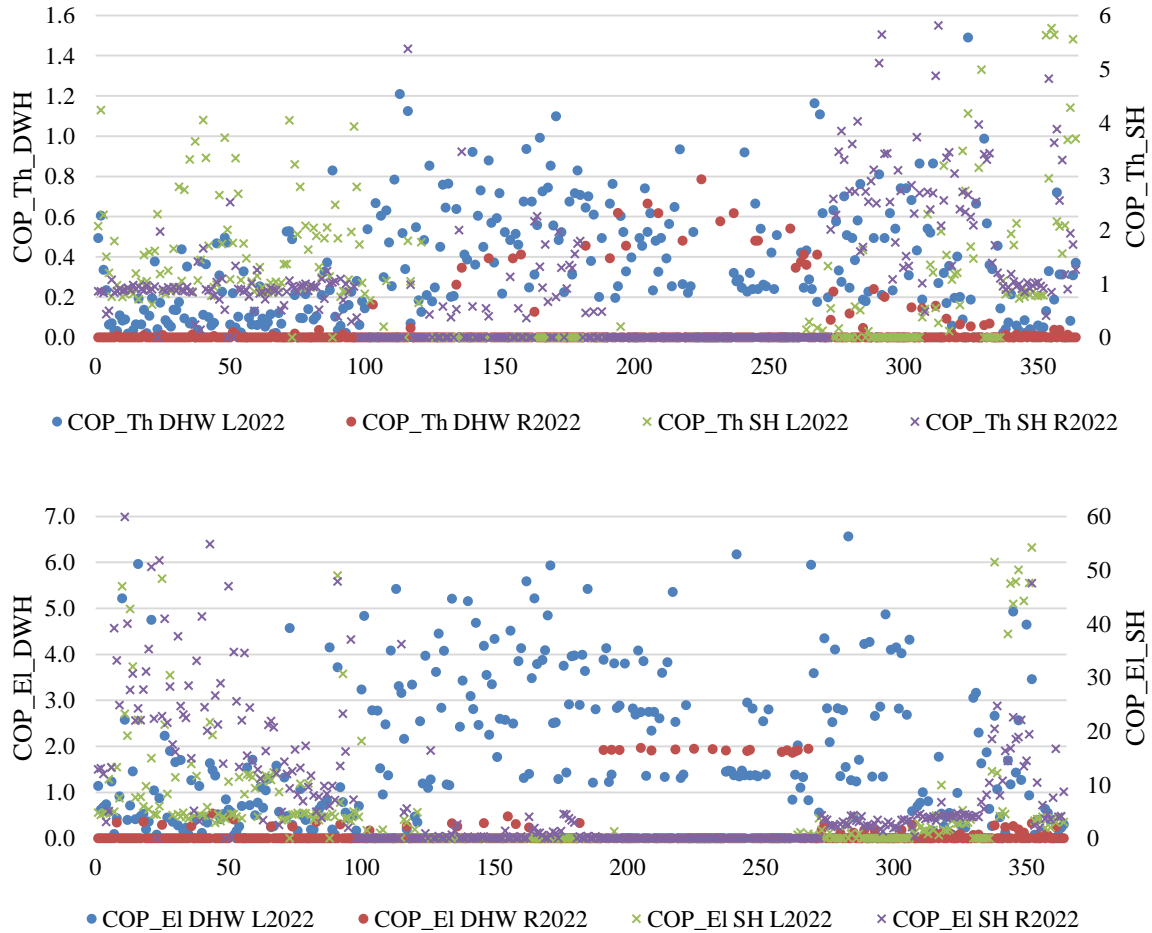
Figure 10. Daily COP Th for DHW and SH for both sites during year 2022 (top); Daily COP El for DHW and SH for both sites during year 2022 (bottom)
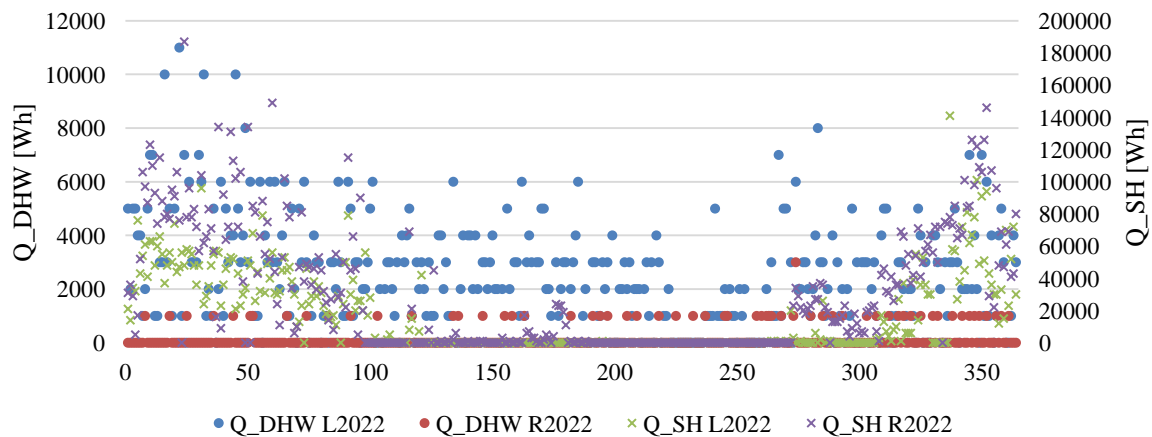
Figure 11. DHW and SH production for both sites during 2022
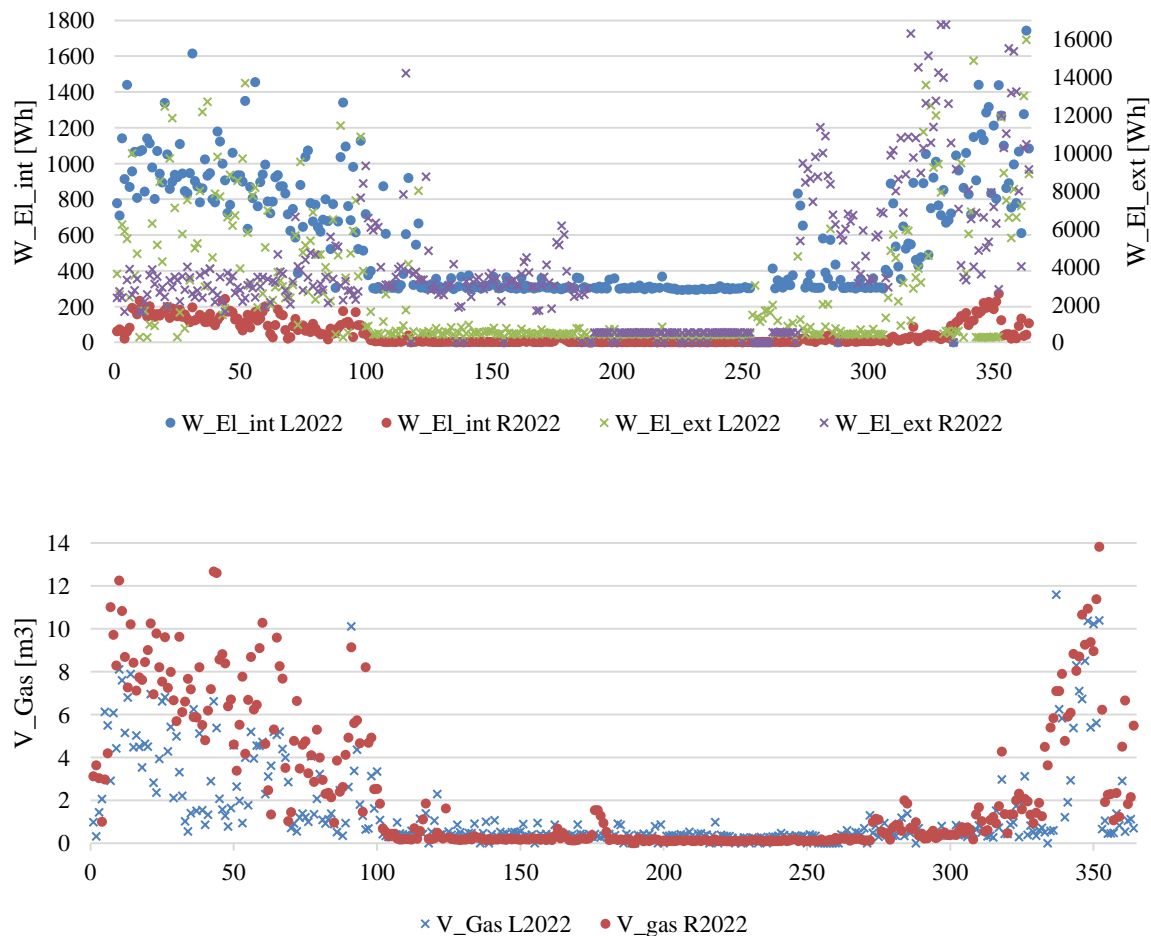
Figure 12. Internal and external electricity consumption for both sites during 2022 (top); gas consumption for both sites during year 2022 (bottom)

Conclusions

The results obtained from two years monitoring of two hybrid heat pumps have been presented and findings discussed.

The results shown along this work evidence that the appliances in the field are not exempt from presenting problems starting from the installation phase made by qualified technicians until the daily use phase made by the owners. These problems are hard to identify without a proper comprehension of the systems and communication with the final user, making the monitoring and follow up of the installations crucial to obtain, at least, acceptable performance results.

The correct parameter setting has a great impact on the system performance and mode of operation, especially when the control is based under energy prices. A misunderstanding or a bad setting can make the difference between a system that works under efficient conditions or not, affecting the performance results, pointing out the vulnerabilities of hybrid technologies and special attention to reach the maximum profit possible. Therefore, installation and parametrization must never be neglected; it can even be stated that monitoring the performance seems necessary until the technology (and the way it is installed and used) has statistically demonstrated its robustness in field-tested applications.

Finally, the results obtained along both years and the modifications that have been implemented point out the fact that the solutions must be adapted to the specific needs of each site, being possible to achieve benefit from the coupling with other systems such as PV panels.

Acknowledgments

References

[1] M.B. Blarke. *Towards an intermittency-friendly energy system: Comparing electric boilers and heat pumps in distributed cogeneration*. Applied Energy, 2011.

[2] K.J. Chua, S.K. Chou, W.M. Yang. *Advances in heat pump systems: A review*. Applied Energy, 2010.

[3] Reiser, M., Klerks, K., Hermelink, A., *Decarbonisation pathways for the European Building sector*, Guidehouse Germany GmbH, 2022.

[4] Hommelberg, M., Janssen, G., Friedel, P., *Final report Installation monitor: practical presentations of heat pumps*, BDH consultancy, 2022.

[5] Beccali M., et al., *Electrical hybrid heat pumps assisted by natural gas boilers: a review*, Applied Energy, 2022.

[6] Sun, M., et al., *Benefits of smart control of hybrid heat pumps: An analysis of field trial data*, Applied Energy, 2019.

[7] Dongellini, M., et al., *Influence of sizing strategy and control rules on the energy saving potential of heat pump hybrid systems in a residential building*, Energy Conversion and Management, 2021.

[8] Miara, M., Russ, C., *Field test results for brine and air source heat pumps*, Fraunhofer Institute for Solar Energy Systems ISE, 2010.

Unlocking the scalable potential for sorbent-based DAC technologies (USorb-DAC)

Jin-Yu Wang[1], Johannes Schilling[2], Elias Moubarak[3], Eva Sanchez-Fernandez[4], Laura Herraiz[1], Charithea Charalambous[1,5], Fergus Mcilwaine[1], John Young[1], Mijndert Van der Spek[1], Shaohan Chen[2], Vincent Dufour-Décieux[2], Sauradeep Majumdar[3], Kevin Jablonka[3], Joren van Herck[3], André Bardow[2], Berend Smit[3], and Susana Garcia[1,*]

[1]The Research Centre for Carbon Solutions (RCCS), School of Engineering and Physical Sciences, Heriot-Watt University, EH14 4AS Edinburgh, United Kingdom
[2]Laboratory of Energy and Process Systems Engineering (EPSE), ETH Zurich, 8092 Zurich, Switzerland
[3]Laboratory of Molecular Simulation (LSMO), Institut des Sciences et Ingénierie Chimiques, École Polytechnique Fédérale de Lausanne (EPFL), Rue de l'Industrie 17, CH-1951 Sion, Valais, Switzerland
[4]Solverlo Limited, 6 Westpoint, Dunbar, East Lothian, Scotland
[5]RMI, 22830 Two Rivers Road, 81621 Basalt, Colorado, United States

[*]Corresponding author: s.garcia@hw.ac.uk

Abstract

While reducing greenhouse gas (GHG) emissions is paramount, it is becoming clear that reductions alone are unlikely to be enough; removing GHGs from the atmosphere will also be necessary to meet agreed climate targets. The IPCC's latest report outlines the scale of the challenge, saying that limiting global warming to 1.5 °C translates into around 6 $GtCO_2$ of carbon dioxide removal (CDR) per year by 2050 [1]. A portfolio of leading CDR solutions, such as natural climate solutions (NCS), bioenergy with carbon capture and storage (BECCS) and direct air carbon capture and storage (DACCS), can meet the need for CDR in a sustainable way.

The carbon removal market needs to grow significantly in the next years and only DACCS has the potential to operate at scale surpassing other CDR options, with a nearly unlimited capacity to capture CO_2 from the atmosphere, provided that the captured CO_2 can be permanently stored in deep geological formations. Moreover, DACCS has the smallest land and water usage and are location-independent, meaning they can be located closer to storage sites.

DACCS technology faces however several challenges, including large energy requirements of producing a high purity CO_2 gas stream and the system's significant capital and operating cost. Early cost estimates for DAC exceed 600 USD/t CO_2, though more recent estimates suggests that a price below 200 USD/t CO_2 may be possible [2].

This project addresses these challenges by using and extending our integrated technology platform 'PrISMa'[1] for material screening, process design, cost estimation and assessment of environmental impacts of sorbent-based carbon capture technologies to de-risk and maximise the benefits of direct CO_2 capture from air, contributing to accelerate the scale-up and speed of deployment of DACCS technologies.

---

[1] 'Process-Informed design of tailor-made Sorbent Materials for energy efficient carbon capture' (PrISMa) funded by ERA-NET Accelerating CCS Technologies (ACT)

An example of the screening results obtained from the PrISMa platform for two different CO_2 sources, an onshore Natural Gas Combined Cycle (NGCC) plant and a coal-fired power plant, is provided in Figure 1. In these cases, the power plants are based in the UK and the CO_2 that is captured is sent for subsequent CO_2 storage. Results show how the materials ranking significantly changes depending on the selected Key Performance Indicator: either from the process (productivity), Technoeconomic- TEA (Cost of CO_2 avoided – CAC), or Life Cycle Analysis – LCA (Climate Change) layer. Our findings for point-source CO_2 capture highlight the need for our integrated approach when screening sorbent materials for any separation application, including DACCS.
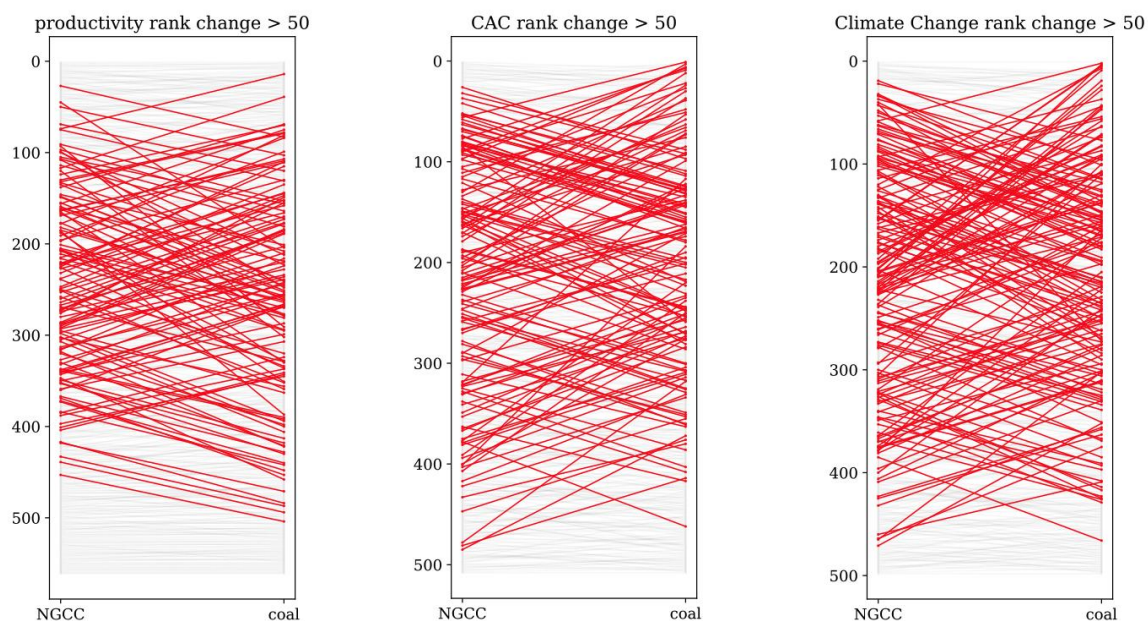
Figure 1 Material screening results from the PrISMa platform: ranking and performance change of Metal-Organic Frameworks (MOF) materials across different layers (process, TEA, and LCA, respectively) depending on the CO_2 point-source capture scenarios: an onshore Natural Gas Combined Cycle Plant (NGCC) or a coal-fired power plant.

The ultimate aim of this project is to unlock the scalable potential of DAC by addressing its affordability issue while maintaining its scalability, flexibility, and ease of capture verification. By coupling basic science with engineering and environmental aspects, an in-depth understanding of materials structure-property-performance relationships will be developed across different time scales and under relevant and realistic DAC operation conditions. This approach will maximise the impact of novel and advanced breakthrough materials by aligning and optimizing the features of the materials and their integration for DAC processes, in order to decrease the time to market of affordable, cost-competitive, low environmental impact, and resource-efficient DAC technologies.

Keywords: Direct Air Capture, Carbon Dioxide Removal, Negative Emissions Technology, Metal-Organic Frameworks, sorbents screening.

Acknowledgments

References:

[1]   IPCC, "Climate Change 2022: Impacts, Adaptation and Vulnerability. Working Group II contribution to the Sixth Assessment Report of the Intergovernmental Panel on Climate Change.," 2022. [Online]. Available: http://www.mdpi.com/2073-8994/7/2/488

[2]   D. W. Keith, G. Holmes, D. st. Angelo, and K. Heidel, "A Process for Capturing CO2 from the Atmosphere," *Joule*, vol. 2, no. 8, pp. 1573–1594, Aug. 2018, doi: 10.1016/J.JOULE.2018.05.006.

Techno-economic evaluation and optimisation of a transcritical ejector CCHP system for district heating applications

F. Schittl[1,2*]**, A. Kührer**[1]**, S. Buchner**[3]**, J. Krail**[1]**, R. Krotil**[1]

[1]University of Applied Sciences Burgenland, Steinamangerstraße 21, 7423 Pinkafeld, Austria

[2]Graz University of Technology, Inffeldgasse 25/A, 8010 Graz, Austria

[3]Wien Energie GmbH, Thomas-Klestil-Platz 14, 1030 Vienna, Austria

*Corresponding author: florian.schittll@fh-burgenland.at

Abstract (12-pt Times New Roman)

In this paper, a new efficient concept for a district heating driven transcritical ejector CHP system is proposed. The process is composed of a Rankine top cycle for the production of electrical energy and an ejector refrigeration cycle as a bottom cycle for the production of cooling energy. A joint medium-pressure condenser serves as the connection between the two sub-processes, which, together with an external heat exchanger, further cools the primary district heating flow and provides useful heat for e. g. space heating or domestic hot water production. In the course of the numerical investigations, critical regulating variables for the process are identified. With the help of simple optimisation calculations, optimal operating points for a cold-controlled or a power-controlled operation are derived. The results are analysed on the basis of technical and economic parameters for an organic working fluid (R507A). With constant heat extraction at the condenser, exergy efficiencies of about $41\,\%$ can be achieved when maximising the cooling capacity, while in power-controlled operation this can even be increased to $55\,\%$.

Keywords: CCHP, numerical modelling, district heating, multi-objective optimisation.

Introdution

Combined cooling, heating, and power (CCHP) systems have been gaining increasing attention as a promising solution for enhancing energy efficiency and reducing greenhouse gas emissions in district heating and cooling networks [1]. In recent years, various studies have focused on investigating the optimal design, operation, and control strategies of CCHP systems [2, 3] to achieve maximum economic and environmental benefits in district energy systems. However, challenges still remain, including the integration of intermittent renewable energy sources, the uncertainty of energy demand and supply, and the trade-off between economic and environmental objectives [4]. Therefore, further research is needed to address these challenges and improve the performance of CCHP systems in district energy systems.

In recent years, a number of studies have already dealt with the coupled supply of heating, cooling and electrical energy by thermodynamic processes. The use of a CHP system in combination with a marine gas turbine was investigated by [5]. The system consists of a supercritical CO_2 recompression cycle, two transcritical CO_2 refrigeration cycles and a steam generator, which allows the waste heat from the ship's gas turbine to be used for the production of cooling energy, steam and power. Furthermore, an exergo-economic analysis and a multi-parameter optimisation were carried out, according to which almost $72\,\%$ of the entire system costs are linked to exergy destruction. Wang et al. [6] developed a solar CCHP system consisting of an ORC and an ejector refrigeration cycle. The system is analysed in terms of the hour angle and the inclination angle of the collector's opening plane, with parameter optimisation being carried out using an GA optimisation algorithm. The optimal tilt angle for the collector is approximately $60°$, while the optimal system performance occurs at a $45°$ tilt angle at midday.

Heat Powered Cycles
Conference 2023
Edinburgh
Heat in the new energy system

3rd to 6th of September 2023
The University of Edinburgh, Scotland

The maximum efficiency of $60.3\,\%$ is achieved at the optimal hour and tilt angle. The authors [7, 8, 9] focus on the applications of CCHP systems in Tehran, with differences in terms of configuration and individual subsystems. Javan et al. [8] conducted investigations with different refrigerants (R134a, R600, R123 and R11) regarding techno-economic modelling and multi-parameter optimisation of a CCHP system for a residential building. The CCHP system contains an internal combustion engine, an ORC, an ejector refrigeration cycle and a water heater. R11 is identified as the most suitable refrigerant, although the nominal load case (day with largest total energy demand) is not completely covered here either. The CHP system examined by [9] for supplying a residential building consists of an ejector refrigeration circuit, an ORC process, a solar collector and a heat and cold storage tank. In the simulation, the influences of the environment are taken into account in order to realise an evaluation over the entire year. Compared to the designs of [8], the system was found to be able to cover the cooling load and sell excess heat in the form of hot water to the district heating network. The annual system efficiency is $25.2\,\%$. Ebrahimi et al. [7] have modified the system of Wang et al. [6] in such a way that the waste heat of the condenser is used for heating water and steam is diverted via a branch before the turbine to increase the cooling capacity. The system is designed for use in a residential building with 20 residential units. Furthermore, a micro gas turbine, a steam-air heat exchanger and an ejector condenser are used in the system. The overall efficiency of the system is $25\,\%$ in summer and $61\,\%$ in winter. Wang et al. [10] developed and investigated a transcritical CO2 process for low-grade energy recovery, which should simultaneously meet the requirements for the delivery of cooling, heating and power. The process combined an ejector refrigeration cycle with a CHP system. Furthermore, the new cycle is compared with a conventional cycle using a throttle valve instead of the ejector. The result of this comparison shows that the ejector cycle can generate more electrical power and achieve a slightly higher exergy efficiency.

System Description and Modelling Approach

Ejector CCHP System

Figure 1 shows the ejector CCHP circuit, whereby the process can be divided into a bottom cycle for the production of cooling energy and a top cycle for the generation of electricity. The shared condensation of the working fluid acts as the connection between the two sub-cycles, whereby this condensation heat is used to provide heat for space heating or domestic hot water supply. The zeotropic mixture R507A ($50\,\%$ R125 and $50\,\%$ R143a) is used as the working medium.

The drive energy of the top cycle is provided by the primary district heating network, which is operated at high temperatures. The top cycle consists of an evaporator pump (P), an internal heat exchanger for preheating the working fluid (IHEX), a steam generator (SG) and a scroll expander (T). After increasing the pressure of the medium to transcritical conditions ($p > p_{\mathrm{cr}}$) in the pump, heat is added isobarically in the two following heat exchangers to raise the temperature to approx. $130\,^\circ\mathrm{C}$. The expander converts the enthalpy drop into mechanical energy and transfers it to an asynchronous generator via a conversion gear. After the steam has been expanded and recuperated in the IHEX, mixing takes place at medium pressure level in the condensation circuit.

In the evaporator (EVA) of the bottom cycle, the working fluid is first evaporated with the addition of heat in order to cool the cold water, which can be used for air conditioning, for instance. The liquid refrigerant supplied to the ejector (EJE) as a motive flow then draws in the suction vapour generated by the evaporator according to the principle of momentum exchange,

thus causing a slight increase in the pressure level (compared to the evaporation pressure) of the resulting mixed vapour. The two-phase mixture emitted by the ejector is then divided into its liquid and gaseous components in a separator (SEP) according to the vapour quality. The latter is taken in by a low-pressure compressor (COM), raised to the appropriate condensation pressure and then mixed with the exhaust steam from the top cycle. The liquid phase from the separator is returned to the evaporator via an expansion valve.

In the middle section of the process, the refrigerant vapour coming from the top and bottom cycle is now mixed and fed to a heat exchanger (CON). There, the working fluid flow is liquefied while releasing heat and fed back to the two circuits according to the operating point. The condensation heat is used to preheat the heating water, which flows in at approx. $28\,°C$ from a storage reservoir. Depending on the condensation pressure and the working medium, this heating water leaves the condenser at between 30 and $45\,°C$. In the case of floor heating systems, this temperature level would already be sufficient. Nevertheless, an additional heat exchanger (DH-HEX) is added to achieve a further temperature increase to $65\,°C$, so that domestic hot water preparation is also supported. This residual heat is provided by the primary district heating medium, which leaves the steam generator of the top cycle at approx. $70\,°C$.
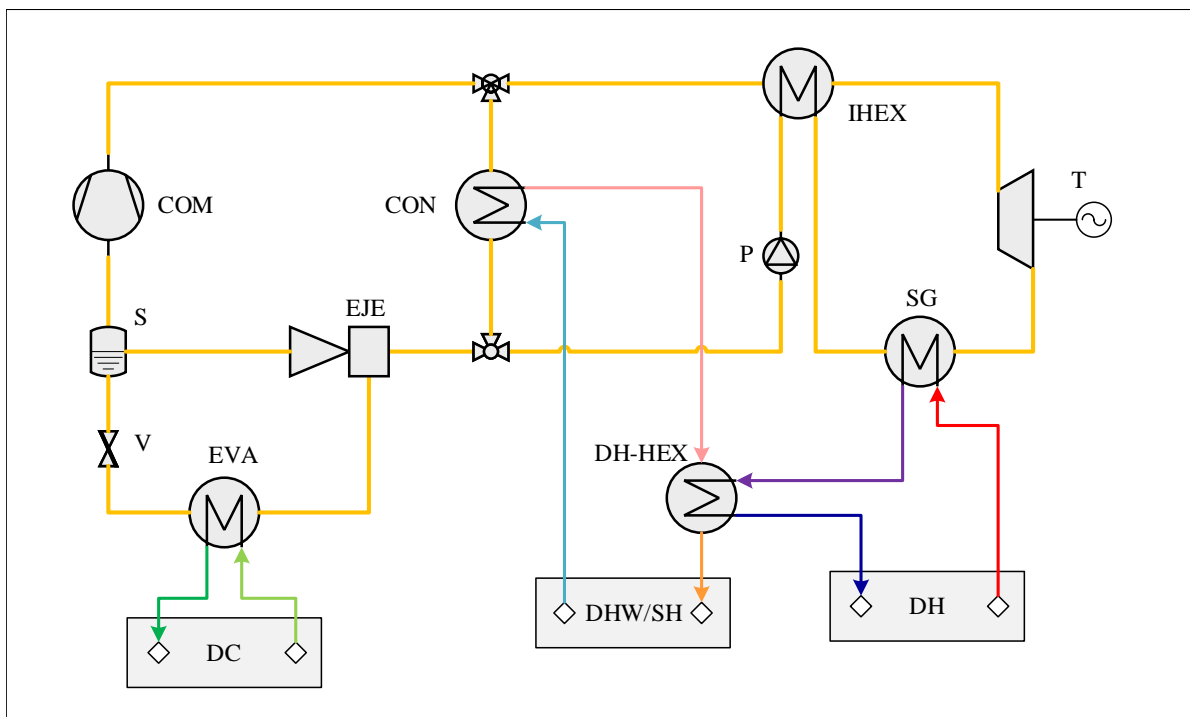
Figure 1. Schematic representation of the ejector CCHP and its integration into a district heating supply infrastructure

Thermodynamic Modelling

For the investigation of the proposed system, a steady-state process model of the plant is created using the software package IPSEpro [11]. As the name implies, this modelling approach neglects all time-dependent variables (e. g. $\mathrm{d}T/\mathrm{d}t$), which leads to a considerable simplification of the set of equations to be solved. By balancing over a plant component k, one finally obtains the stationary conservation equations for mass and energy. Equation 1 shows a special form of the continuity equation and states that the number of mass elements entering the component $\dot{m}_i$ is equal to the number leaving. Another conservation equation results after applying the

first law of thermodynamics (see equation 2). This states that the quantity of heat $\mathrm{d}Q_k$, technical work $\mathrm{d}W_k$ and the energy transported by the mass elements $\mathrm{d}m_i$, which are supplied or released across the system j or component boundaries k, are equal to the change in the internal and external energy of the system $\mathrm{d}U$ and $\mathrm{d}E_a$, respectively. The terms on the right-hand side of the equation can be eliminated due to the steady-state approach and the stationarity of the system.

$$\sum_j \dot{m}_i = 0 \tag{1}$$

$$\sum_j \dot{Q}_j + \sum_j \dot{W}_i + \sum_j \dot{m}_i \left(h_i + \frac{w_i^2}{2} + g \cdot z \right) = 0 \tag{2}$$

To model the heat exchangers in the system (EVA, CON, IHEX, SG), further equations are needed in addition to the two conservation laws. The calculation of the heat transport is done in analogy to Fourier's law, according to which the heat flow transferred from one fluid to another is proportional to the heat transport factor (kA-value) as well as to the logarithmic mean temperature difference $\Delta T_{m,12}$.

$$\dot{Q}_{12} = k_{12} \cdot A \cdot \Delta T_{m,12} \tag{3}$$

The total heat transport coefficient k_{12} is composed of the heat conduction in the partition wall and the two convective heat transport coefficients between the fluid flow and the heat exchanger wall. A reasonable assumption is that the convective part dominates the heat transfer due to conduction ($1/\alpha_1 + 1/\alpha_2 \gg \delta/\lambda$), which means that the heat transfer coefficient can be calculated in a simplified way according to equation 4. For the values for alpha, reference is made to literature data [12].

$$\frac{1}{k_{12}} = \frac{1}{\alpha_1} + \frac{1}{\alpha_2} \tag{4}$$

It is assumed that the change of state in the compressor, pump and turbine takes place without heat exchange with the environment (adiabatic), whereby only the heat loss occurs due to mechanical friction on the shaft. The mechanical efficiency of the apparatus is defined in equation 5.

$$\dot{m}_k \cdot (h_{\text{out}} - h_{\text{out}}) = \eta_{\text{m}} \cdot \dot{W}_k \tag{5}$$

The change of state is modelled following the ideal case of an adiabatic, isentropic change of state. The enthalpy is known for the fluid flow as a function of pressure and entropy. In this way, the isentropic efficiency of compression or expansion is used as follows (equation 6 and 7).

$$h_{\text{is,P,C}} = \frac{h_{\text{is,out}} - h_{\text{in}}}{h_{\text{out}} - h_{\text{in}}} \tag{6}$$

$$h_{\text{is,T}} = \frac{h_{\text{in}} - h_{\text{out}}}{h_{\text{in}} - h_{\text{is,out}}} \tag{7}$$

In modelling the ejector, it is divided into a total of four subsections, which are as follows: nozzle section, mixing section, shock wave section and diffuser section. Furthermore, constant pressure conditions in the respective sections are assumed for the one-dimensional flow model. It is also assumed that the primary and secondary flows do not mix before reaching the mixing chamber. Furthermore, the correlation of [13] is used to predict the sound speed velocity in the mixing chamber, since a homogeneous two-phase condition of the fluid flow is to be expected

**Heat Powered Cycles
Conference 2023**
Edinburgh

Heat in the new energy system

3rd to 6th of September 2023
The University of Edinburgh, Scotland

here. The efficiencies of the nozzles, the mixing chamber and the diffuser are also taken as constant. Based on the assumptions just mentioned and the conservation equations for each section, the relationship between the entrainment ratio of the ejector μ and its efficiencies as well as inlet and outlet conditions shown in equation 8 can finally be established.

$$\mu = \sqrt{\eta_{\mathrm{is,n}}\eta_{\mathrm{is,m}}\eta_{\mathrm{is,d}}\left(\frac{h_{\mathrm{pn,in}} - h_{\mathrm{pn,out,is}}}{h_{\mathrm{d,oust,is}} - h_{\mathrm{m,out}}}\right) - 1} \tag{8}$$

Boundary Conditions

The necessary component-specific boundary conditions are first determined for the numerical simulation as well as the subsequent optimisation study of the ejector CCHP process driven by primary district heating (see Table 1). Pressure losses Δp_k of the equipment are taken into account. Geometrical information is often required for the exact calculation of heat transport processes. Here, the application of the minimum temperature gradient is used, which is also called pinch point $\Delta T_{\mathrm{PP},k}$. This temperature difference limits the exchange of heat between the two separate working media. In order to take the deviations from adiabatic and reversible changes of the fluid state in e. g. turbines into account, so-called isentropic efficiencies $\eta_{\mathrm{is},k}$ are introduced. These are formed from the ratio of real to ideal change of state and can be taken from relevant scientific literature [14, 15].

Table 1. Assumed component-specific boundary conditions for the simulation of the ejector CCHP

quantaty	unit	value
$\Delta T_{\mathrm{PP,SG,IHEX}}$	K	10
$\Delta T_{\mathrm{PP,EVA}}$	K	3
$\Delta T_{\mathrm{PP,CON,DH-HEX}}$	K	5
$\Delta p_{\mathrm{PP,HEX,ext}}$	bar	0.1
$\Delta p_{\mathrm{PP,HEX,int}}$	bar	0.01
$\eta_{\mathrm{el,mech}}$	-	0.98
$\eta_{\mathrm{is,P}}$	-	0.70
$\eta_{\mathrm{is,COM,T}}$	-	0.80
$\eta_{\mathrm{is,n}}$	-	0.90
$\eta_{\mathrm{is,m}}$	-	0.95
$\eta_{\mathrm{is,d}}$	-	0.80

The quantities and value ranges shown in Table 2 refer to the boundary conditions derived for the simulations with regard to operation in the primary district heating network. The process shall be able to convert a district heating load $\dot{Q}_{\mathrm{DH}}$ of about $1.2\,\mathrm{MW}$ at nominal system temperatures $140/50\,^{\circ}\mathrm{C}$ into cooling energy, heating energy for space heating and domestic hot water supply as well as electricity. The temperature levels on the condenser side and on the evaporator side are set at around $65/10\,^{\circ}\mathrm{C}$ and $6/12\,^{\circ}\mathrm{C}$, respectively. The mass flow rates of the two sinks are left free due to the mathematical structure of the optimisation algorithm. A guideline value for the cooling mass flow of this use case was evaluated on the basis of measurement data with approximately $23.7\,\mathrm{kg\,s^{-1}}$.

Energy and Exergy Efficiency Analysis

The technology investigated in this paper provides heating, cooling and electrical energy, which in turn means that conventional key performance indicators such as COP or EER according to

**Heat Powered Cycles
Conference 2023**
Edinburgh

Heat in the new energy system

3rd to 6th of September 2023
The University of Edinburgh, Scotland

Table 2. Derived boundary conditions for the simulation of the ejector CCHP for the application in peripheral areas of district heating and cooling infrastructures at nominal operating conditions (based on the measured data from Wien Energie GmbH)

quantaty	unit	value	lower bounds	upper bounds
$T_{\mathrm{DH,sup}}$	°C	140	120	140
$T_{\mathrm{DH,ret}}$	°C	50	48	54
$\dot{m}_{\mathrm{DH}}$	kg s^{-1}	3.36	0.25	3.36
$T_{\mathrm{H,sup}}$	°C	65	-	-
$T_{\mathrm{H,ret}}$	°C	28	-	-
$\dot{m}_{\mathrm{H}}$	kg s^{-1}	4	-	-
$T_{\mathrm{C,sup}}$	°C	6	6.3	11.7
$T_{\mathrm{C,ret}}$	°C	12	10.1	13.2

the conventions of the "1st Law Analysis" described above are not sufficient to comprehensively evaluate the system. To obtain precise information about the overall efficiency of the process, the overall efficiency, which is subsequently referred to as η_{tot}, is considered in addition to the efficiencies for heating, cooling and electricity production. The total efficiency for this system is obtained by taking into account all heat or power quantities flowing across these boundaries (see equation 9). The effort is thus supplemented by the thermal drive energy of the process, which is supplied in the form of primary district heating $\dot{Q}_{\mathrm{DH}}$ (incl. drive energy for e. g. pumps $\dot{W}_{\mathrm{aux}}$). The output, on the other hand, includes both heat flows, i. e. heating $\dot{Q}_{\mathrm{H}}$ and cooling $\dot{Q}_{\mathrm{C}}$ energy as well as the generated electrical power of the turbine $\dot{W}_{\mathrm{T}}$.

$$\eta_{\mathrm{tot}} = \frac{\dot{Q}_{\mathrm{H}} + \dot{Q}_{\mathrm{C}} + \dot{W}_{\mathrm{T}}}{\dot{Q}_{\mathrm{DH}} + \dot{W}_{\mathrm{aux}}} \qquad (9)$$

Exergy can be transported across the boundaries of a system or component in several ways. The steady-state exergy balance equation (10) for an open, non-adiabatic system, is composed of the transferred work $\dot{W}$, the exergy flux due to heat transfer processes $\dot{E}_q$, and the exergy transfer due to an inflowing or outflowing mass flow $\dot{E}_k$. All these transport terms are evaluated in relation to the reference quantities T_0 and p_0 used to define the exergy. Furthermore, an additional term $\dot{E}_D$, which describes the dissipation of exergy due to irreversibilities within the system, is added.

$$0 = \sum_i \dot{W} + \sum_i \dot{E}_q + \sum_i \dot{E}_k - \sum_i \dot{E}_D \qquad (10)$$

According to authors such as [16], the exergetic evaluation of a system serves to identify thermodynamic inefficiencies of components. According to [17, 18], the performance indicators required for this purpose include the exergetic efficiency $\eta_{\mathrm{ex},k}$ as well as the absolute and relative exergy dissipation ratios $y_{D,k}$ and $y_{D,k}^{\star}$, respectively. The exergetic efficiency is defined by the so-called product $\dot{E}_P$ and the expended resource (fuel) $\dot{E}_F$ (see equation 11). The term $\dot{E}_P$ describes the desired result which the system produces. The resource $\dot{E}_F$ is used as an hypernym for all the resources needed to generate the product. The exergy destruction ratio $y_{D,k}$ of a component k is defined by the ratio of exergy destruction of a component $\dot{E}_{D,k}$ to the exergy resource $\dot{E}_{F,tot}$ supplied to the entire system. In the case of the relative exergy dissipation ratio $y_{D,k}^{\star}$, the total exergy resource dissipated by the system is used instead of $\dot{E}_{F,\mathrm{tot}}$. The

Heat Powered Cycles
Conference 2023
Edinburgh

Heat in the new energy system

3rd to 6th of September 2023
The University of Edinburgh, Scotland

calculation is carried out using equation 12 and 13.

$$\eta_{\text{ex},k} = \frac{\dot{E}_{P,k}}{\dot{E}_{F,k}} \tag{11}$$

$$y_{D,k} = \frac{\dot{E}_{D,k}}{\dot{E}_{F,\text{tot}}} \tag{12}$$

$$y_D^\star = \frac{\dot{E}_{D,k}}{\dot{E}_{D,\text{tot}}} \tag{13}$$

Techno-economic Analysis

In order to ensure an optimal economic operation of a system, the information regarding the energetic or exergetic efficiency of a system is often not sufficient as the sole characteristic. Therefore, in addition to the performance indicators, a further objective function is set up that reflects the economic aspect of the system. In the literature, this methodology is also known as techno-economic analysis and subsequently leads to a multi-criteria optimisation problem, where not only the energy efficiency is maximised, but also the costs are minimised. The basis for this techno-economic analysis is the estimation of investment costs of the plant. In this work, so-called cost correlations, which can be found in Table 3, are used. The total cost rate $\dot{Z}_k$ of a component k, consisting of investment costs as well as operating and maintenance costs, can then be calculated according to equation 14 using the Capital Recovery Factor (CRF) from equation 15. The annual usage time N and the maintenance factor φ are determined by values of $8000\,\text{h}$ and 1.06, respectively. [19]

$$\dot{Z}_k = Z_k \frac{\text{CRF} \cdot \varphi}{N} \tag{14}$$

$$\text{CRF} = i \cdot \frac{(1+i)^\tau}{(1+i)^\tau - 1} \tag{15}$$

The annual interest rate i is assumed to be $5\,\%$, while the life cycle time τ is assessed to be 20 years.

Table 3. Cost correlations of the different circuit components for the techno-economic analysis of the CCHP ejector cycle [19, 20]

component k	component investment costs Z_k
EJE	$Z_{\text{EJE}} = 10^3 \cdot 16.14 \cdot 0.989 \cdot \dot{m}_{\text{sec}} \cdot \left(\frac{T_{\text{pri}}}{p_{\text{pri}}}\right)^{0.05} \cdot p_{\text{sec}}^{-0.75}$
COM	$Z_{\text{COM}} = 44.71 \cdot \frac{\dot{m}_{\text{COM}}}{0.95 - \eta_{\text{is},\text{COM}}} \cdot \left(\frac{p_{\text{out}}}{p_{\text{in}}}\right) \cdot \ln\left(\frac{p_{\text{out}}}{p_{\text{in}}}\right)$
S	$Z_{\text{S}} = 280.3 \cdot \dot{m}_{\text{S}}^{0.67}$
V	$Z_{\text{V}} = 114 \cdot \dot{m}_{\text{V}}$
DH-HEX	$Z_{\text{DH}-\text{HEX}} = 6,200 \cdot (10.76 \cdot A_{\text{DH}-\text{HEX}})^{0.42}$
P	$\log_{10} Z_{\text{P}} = 3.3892 + 0.0536 \cdot \log_{10} \dot{W}_{\text{P}} + 0.1538 \cdot \left(\log_{10} \dot{W}_{\text{P}}\right)^2$
T	$\log_{10} Z_{\text{T}} = 2.2476 + 1.4965 \cdot \log_{10} \dot{W}_{\text{T}} - 0.1618 \cdot \left(\log_{10} \dot{W}_{\text{T}}\right)^2$
EVA,IHEX	$\log_{10} Z_{\text{EVA}} = 4.6656 - 0.1557 \cdot \log_{10} A_{\text{EVA}} + 0.1547 \cdot (\log_{10} A_{\text{EVA}})^2$
CON	$Z_{\text{CON}} = 12,300 \cdot \left(\frac{\dot{Q}_{\text{CON}}}{50}\right)^{0.76}$

**Heat Powered Cycles
Conference 2023**
Edinburgh

Heat in the new energy system

3rd to 6th of September 2023
The University of Edinburgh, Scotland

Multi-Objective Optimisation Method

As described in the section above, the mathematical representation of a process model of this kind is, in most cases, a set of nonlinear equations $\mathbf{f}(\mathbf{x})$. Without loss of generality, the non-linear optimisation problem to be solved can be described as follows, in accordance with the notation commonly used in the mathematical literature ([21], see equation 16). In it, $\mathbf{x}$ denotes the variable vector to be optimised, $\mathbf{x}^L$ and $\mathbf{x}^U$ its lower and upper bounds, $\mathbf{f}(\mathbf{x})$ the objective function, $g(\mathbf{x})$ the inequality constraint and $h(\mathbf{x})$ the equality constraint. The objective functions are to be minimised by satisfying all equality and inequality constraints. If a particular objective function is to be maximised ($\max f$), one can redefine the problem accordingly to minimise its negative value $\min -f$. The gamulitobj algorithm available in MATLAB [22] is used to solve the multiobjective optimisation problem consisting of energy and cost efficiency.

$$
\begin{aligned}
\min \quad & \mathbf{f}(\mathbf{x}) \\
\text{s.t.} \quad & g(\mathbf{x}) \leq 0 \\
& h(\mathbf{x}) = 0 \\
& \mathbf{x}^L \leq \mathbf{x} \leq \mathbf{x}^U
\end{aligned}
\tag{16}
$$

Discussion and Results

Table 4 shows the results regarding the investigated operation modes of the process, distinguishing between the two cases (i) maximisation of the cooling energy $\max \dot{Q}_C$ and (ii) maximisation of the electrical energy output ($\max \dot{W}_{\text{netto}}$). In both cases, the problem represents a simplified form of the previously described optimisation problem, as only one target variable is considered. The simulations show that the process can be operated flexibly between these two operating conditions and can be switched to cold-led or power-led operation depending on requirements. The heat at the condenser, on the other hand, is constant at both operating points. The variables of the optimisation algorithm considered as independent degrees of freedom are the first three variables in the table, namely the turbine inlet pressure $p_{T,\text{in}}$ and the mass flow ratios $\dot{m}_H/\dot{m}_C$ and $\dot{m}_H/\dot{m}_{\text{DH}}$.

In cold-controlled operation, the ejector CCHP process achieves a cooling capacity $\dot{Q}_C$ of approx. $257\,\text{kW}$. This results in an efficiency of $90.5\,\%$ for the supply of cooling with a primary district heating input power $\dot{Q}_{\text{DH}}$ of $197\,\text{kW}$ and a negative net power of $89\,\text{kW}$ (for compressor and pump). If the heat released at the condenser is also taken into account, the overall efficiency or COP increases to 3. The balancing of the exergy flows results in an exergy destruction rate $E_{D,\text{tot}}$ of just under $84\,\text{kW}$. Nevertheless, an exergy efficiency $\eta_{\text{ex,tot}}$ of approx. $41\,\%$ can be achieved due to the high residual heat utilisation.

In the second operating state, mainly electrical energy is produced in the top cycle, which is why the cooling capacity also drops to a negligible value ($\dot{Q}_C < 5\,\text{kW}$). The majority of the mass flow now flows through the expander, which generates a total of around $28\,\text{kW}$ of net electrical power output. The overall efficiency decreases noticeably due to the significantly lower $\dot{Q}_C/\dot{W}_{\text{netto}}$ ratio and totals only 1.44, since the relatively high heating energy is regarded as a fixed boundary condition. However, it should be noted that the exergy destruction rate as well as the exergy efficiency are significantly improved compared to the cold-led operation. $E_{D,\text{tot}}$ and $\eta_{\text{ex,tot}}$ are $54\,\text{kW}$ and $55\,\%$, respectively.

Figure 2 shows the results of the multi-objective optimisation. Unlike the previous results, both the exergy efficiency $\eta_{\text{ex,tot}}$ and the investment costs of the entire system Z_{tot} were declared as objective functions. The associated degrees of freedom remained unchanged. The graph on

Table 4. Optimised operating points of the ejector CCHP process for cold- and power-controlled operation

quantity	unit	max $\dot{Q}_\mathrm{C}$	max $\dot{W}_\mathrm{netto}$
$p_\mathrm{T,in}$	bar	40.33	59.67
$\dot{m}_\mathrm{H}/\dot{m}_\mathrm{C}$	-	0.39	19.94
$\dot{m}_\mathrm{H}/\dot{m}_\mathrm{DH}$	-	4.51	2.14
$\dot{Q}_\mathrm{C}$	kW	257.36	5.05
$\dot{Q}_\mathrm{H}$	kW	618.54	618.54
$\dot{W}_\mathrm{netto}$	kW	-86.93	27.89
$\dot{Q}_\mathrm{DH}$	kW	197.56	446.30
η_tot	-	3.00	1.44
$\eta_\mathrm{ex,tot}$	-	0.41	0.55
$E_{D,\mathrm{tot}}$	kW	83.52	54.25

the left shows the development of the so-called Pareto front. On this frontier curve are optimal solutions for the ejector CCHP's system design. As can be clearly seen, increasing exergy efficiency is always associated with an increase in plant costs. It is also shown that with the help of the optimisation algorithm, only the power-guided variant is associated with achieving the objective function. For additional maximisation of the cooling capacity, the problem formulation must include this or a separate system design must be calculated.

The diagrams on the right show the percent contributions to the exergy destruction rate $y_D^\star$ (top) and the relative costs $Z^\star$ (bottom) of the most important system components. From this it can be seen that the heat exchanger for further district heat extraction respectively heating of domestic hot water leads to an increase in the overall efficiency, but also to a significant reduction in the 2nd law efficiency. The second half of the exergy destruction is divided among the remaining components, whereby the components of the top cycle (SG: $12\,\%$, T: $8\,\%$ and IHEX: $5\,\%$) together account for another quarter. The remainder is distributed to the bottom cycle including the condenser, with the heat exchangers again accounting for the majority with a combined $14\,\%$. The graph below shows the approximate distribution of investment costs among the individual system components. It should be pointed out once again that this is a rough estimate of the investment costs based on empirical cost correlation and is therefore subject to considerable uncertainty.

Conclusions

The results of the numerical investigation of the ejector CCHP process show that by using the newly developed technology, sufficient cooling or heating power can be provided for an individual consumer, depending on the operating mode. Furthermore, a higher heat amount can be transported in already existing district heating systems and thus new consumers can be integrated more easily due to the higher network capacity. The application of multi-objective optimisation algorithms shows the correlation between an efficient system and its investment costs. In addition, the 2nd law analyses show that a large part of the exergy destruction ($85\,\%$ in total) is due to the heat transfer in the heat exchangers. The system is characterised by its high exergy efficiency (41 to $55\,\%$) and thus represents an alternative to, for example, heat pumps or other P2H solutions.

Acknowledgement
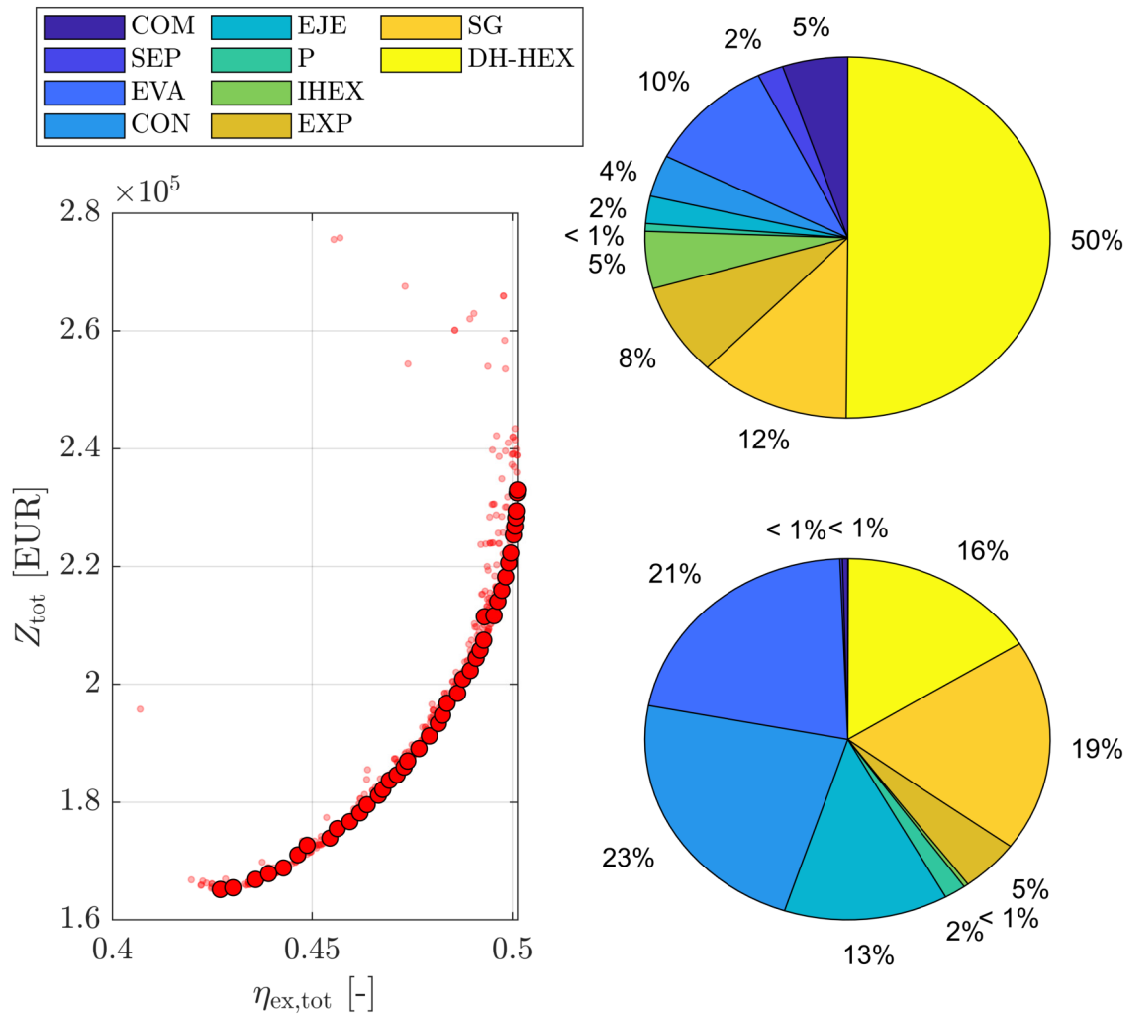
Figure 2. Left: system solutions of the ejector CCHP circuit optimised according to exergy efficiency and investment costs. Top right: exergy destruction rates of every component. Bottom right: relative component investment costs

References

[1] Mohsen Salimi, Morteza Hosseinpour, Shabnam Mansouri, and Tohid N.Borhani. Environmental aspects of the combined cooling, heating, and power (cchp) systems: A review. *Processes*, 10(4):711, 2022.

[2] Mohammad Ameri and Zahed Besharati. Optimal design and operation of district heating and cooling networks with cchp systems in a residential complex. *Energy and Buildings*, 110(3):135–148, 2016.

[3] Qinghua Wang, Jizhen Liu, Yang Hu, and Xiaoning Zhang. Optimal operation strategy of multi-energy complementary distributed cchp system and its application on commercial building. *IEEE Access*, 7:127839–127849, 2019.

Heat Powered Cycles
Conference 2023
Edinburgh

Heat in the new energy system

3rd to 6th of September 2023
The University of Edinburgh, Scotland

[4] Richard Büchele, Lukas Kranzl, Michael Hartner, and Jeton Hasani. Opportunities and challenges of future district heating portfolios of an austrian utility. *Energies*, 13(10):2457, 2020.

[5] Shengya Hou, Fengyuan Zhang, Lijun Yu, Sheng Cao, Yaodong Zhou, Yuandan Wu, and Lingyi Hou. Optimization of a combined cooling, heating and power system using co2 as main working fluid driven by gas turbine waste heat. *Energy Conversion and Management*, 178(9):235–249, 2018.

[6] Jiangfeng Wang, Yiping Dai, Lin Gao, and Shaolin Ma. A new combined cooling, heating and power system driven by solar energy. *Renewable Energy*, 34(12):2780–2788, 2009.

[7] Masood Ebrahimi, Ali Keshavarz, and Arash Jamali. Energy and exergy analyses of a micro-steam cchp cycle for a residential building. *Energy and Buildings*, 45(5):202–210, 2012.

[8] Saeed Javan, Vahid Mohamadi, Pouria Ahmadi, and Pedram Hanafizadeh. Fluid selection optimization of a combined cooling, heating and power (cchp) system for residential applications. *Applied Thermal Engineering*, 96(2):26–38, 2016.

[9] Hassan Jafari Mosleh, Ali Hakkaki-Fard, and Mohammadreza DaqiqShirazi. A year-round dynamic simulation of a solar combined, ejector cooling, heating and power generation system. *Applied Thermal Engineering*, 153:1–14, 2019.

[10] Mingtao Wang, Juan Zhang, and Huanwei Liu. Thermodynamic analysis and optimization of two low-grade energy driven transcritical co2 combined cooling, heating and power systems. *Energy*, 249:123765, 2022.

[11] SimTech GmbH. Ipsepro, 2021.

[12] Ramesh K. Shah and Dušan P. Sekulić. *Fundamentals of heat exchanger design*. Wiley-Interscience, Hoboken, NJ, 2003.

[13] D. L. Nguyen, E.R.F. Winter, and M. Greiner. Sonic velocity in two-phase systems. *International Journal of Multiphase Flow*, 7(3):311–320, 1981.

[14] Fang Liu and Eckhard A. Groll. Study of ejector efficiencies in refrigeration cycles. *Applied Thermal Engineering*, 52(2):360–370, 2013.

[15] Tailu Li, Haiyang Gao, and Xiang Gao. Synergetic mechanism of organic rankine flash cycle with ejector for geothermal power generation enhancement. *Journal of Cleaner Production*, 375(5):134174, 2022.

[16] Bhavik R. Bakshi, Dušan P. Sekulić, and Timothy George Peter Gutowski, editors. *Thermodynamics and the destruction of resources*. Cambridge University Press, Cambridge, 2011.

[17] Adrian Bejan, George Tsatsaronis, and Michael J. Moran. *Thermal design and optimization*. A Wiley-Interscience publication. Wiley, New York, 1996.

[18] Adrian Bejan and Eden Mamut. *Thermodynamic Optimization of Complex Energy Systems*. Springer Netherlands, Dordrecht, 1999.

[19] Ibrahim Dincer, Marc A. Rosen, and Pouria Ahmadi. *Optimization of Energy Systems*. Wiley, 2017.

[20] Sanne Lemmens. Cost engineering techniques and their applicability for cost estimation of organic rankine cycle systems. *Energies*, 9(7):485, 2016.

[21] Kaisa Miettinen. *Nonlinear multiobjective optimization*, volume 12 of *International series in operations research & management science*. Kluwer, Boston, Mass., 4. print edition, 2004.

[22] The Math Works Inc. Matlab (2021a), 2023.

Thermal Energy Storage and Upgrade Using an Integrated Absorption-Adsorption System

Allannah M. Duffy, Kristian T. Lockyear, Matthew T. Hughes, and Srinivas Garimella[*]

Sustainable Thermal Systems Laboratory, GWW School of Mechanical Engineering, Georgia Institute of Technology, Atlanta, GA 30332

[*]Corresponding author: sgarimella@gatech.edu

Abstract

This paper presents a novel sorption-based cycle combining energy storage with energy upgrade to store low-grade heat for long periods and transform it on demand to useable energy at elevated temperatures. A transient system model of an ammonia-water absorption cycle for seasonal heat storage is modeled. This cycle is coupled to a transient solid-gas adsorption cycle for end-use heat transformation. The thermal generator uses two different halide salts with ammonia as the refrigerant. A lumped parameter approach is used to model the chemical kinetics of the salt reactors in the adsorption cycle, including hysteresis effects. This novel system overcomes the significant temperature drop typically associated with thermal storage. Key performance parameters evaluated in this paper are the coefficient of performance and temperature lift between the input and output. The system modeled in this study takes in heat at 85°C during the hot season, and stores it at ambient conditions, before upgrading it to 88°C during the cold season. The storage efficiency of the combined cycle is 12.8% with scope for further improvement.

Keywords: Heat transformation, thermochemical heat storage, adsorption, absorption, seasonal storage

Introduction

Heating is the world's largest energy end use, accounting for almost half of global final energy consumption [1]. Forecasts indicate that heating demand will increase by 6% and reach 14 EJ in the period from 2022-2027 [1]. This demand is satisfied predominantly by non-renewable sources. The implementation and use of renewable energy sources and waste heat will be a significant enabler to facilitate a transition towards cleaner energy.

Commercial buildings in the US generate 765 million metric tons of carbon dioxide emissions annually (16% of all US carbon dioxide emissions), with 37% of the end-use energy consumption going towards space heating and water heating (736 billion kWh annually) [2, 3]. Meanwhile, low-grade thermal energy is wasted every day, with a potential to recover 3.3 EJ of waste heat across all US buildings [4]. Thermal energy storage can store this potential for later use and offset an imbalance between generation and utilization.

In addition to waste heat, solar power is another characteristically under-utilized energy source and considered a highly sustainable alternative to fossil fuels for building heating, due to its pollution-free, inexhaustible, and affordable nature. Nevertheless, one of its main limitations is that it is an intermittent energy source. Additionally, the largest availability of solar energy coincides with the lowest demand. To address this imbalance, thermal energy storage is essential. While diurnal solar energy storage can successfully shift loads during summer, it has limited utility due to low heating demand at night in some applications. Seasonal energy storage is significantly more valuable as the cold season demands the most space heating and hot water, coinciding with the lowest availability of solar energy. In a study conducted by Fisch et al. (1998), it was found that seasonal storage is capable of meeting 50–70% of the annual heat

demand, whereas the diurnal pattern could only satisfy 10–20% of it [5]. This paper presents a novel sorption-based cycle combining energy storage with energy upgrade to store low-grade heat (e.g., waste industrial heat or solar energy) and transform it on demand to energy at useable temperatures.

Current methods for seasonal thermal energy storage can be classified as sensible, latent, and thermochemical heat storage. Sensible heat storage involves storing heat in the form of a temperature differential. Latent heat storage involves storing heat by utilizing a phase change material. Lastly, thermochemical heat storage involves storing heat from a chemical reaction. Thermochemical energy storage has a higher energy density (433-1380 kJ kg^{-1}) in comparison with latent (174 kJ kg^{-1}) and sensible (0.9-1.13 kJ kg^{-1}) energy storage [6]. Thermochemical energy storage (TCES) is also capable of near-lossless long-term storage over a wide range of operating temperatures. Despite the fact the energy "quantity" is largely conserved in TCES, the energy "quality" is significantly reduced. A techno-economic literature review by Yang et al. (2021) of seasonal TCES revealed an average temperature differential between charge and discharge temperatures of -98°C [7]. Another drawback of a conventional sorption storage system is the necessity of a low-temperature heat source for the evaporator coupling to achieve appreciable delivery temperatures. Garimella et al. (2020) proposed a sorption-based thermal storage system integrated with a phase-change material (PCM) to address this limitation. The system utilized a liquid-liquid mixer to recombine the sorption constituents with a storage efficiency of 15.3% for delivery of 1 GJ after 40 days. Furthermore, this study compared the sorption-PCM storage system with sensible and latent storage methods and reported that for well-insulated storage systems, sensible storage remains most efficient for storage durations up to 25 days, while latent is more efficient for storage durations up to 80 days, and thereafter, sorption-based storage is the most efficient [8].

TCES can be further classified into chemical adsorption (chemisorption), chemical absorption, and chemical reaction (without sorption). Solid-gas adsorption such as $MgCl_2$-NH_3 and $CaCl_2$-NH_3, has a wider range of working pairs and applicable temperature ranges compared to liquid-gas absorption such as LiBr-H_2O and NaOH-H_2O [9]. However, liquid-gas sorption requires less heat exchanger surface area as the liquid solution can be stored in tanks and pumped through the heat exchangers as needed. Liquid-gas absorption storage systems have a better potential for long-term storage applications than short-term storage because they retain capacity after equilibrating with the ambient [8]. For short term storage, the separated constituents will not lose a significant proportion of their sensible heat after charging but will encounter losses as a result of desorption and absorption processes. Several studies that propose absorption storage for short term applications integrate heat exchangers in the storage tanks to provide sensible heat for short term applications, and thermochemical heat for long term storage [10, 11].

The present study investigates the coupling of a liquid-gas absorption cycle for storage to a solid-gas adsorption cycle for end-use heat transformation as depicted in Figure 1. Note that by convention, "concentrated solution" refers to the ammonia–water mixture with high ammonia content, and "dilute solution" refers to that with low ammonia content [12].

Working Principle

Waste industrial heat or heat from a solar collector desorbs ammonia from the concentrated solution in the absorption cycle. Once the supply of waste heat is no longer present, the system stores energy in the form of a dilute solution and ammonia in separate tanks. During storage, the tanks are isolated from the rest of the system and allowed to reach equilibrium with ambient conditions. When heat is needed, the dilute solution and ammonia recombine, releasing the heat of reaction. However, due to storage losses, the maximum heat output from the absorber

is lower than the initial heat input. To achieve higher useful temperatures, a heat transformer is required.

Heat transformation is achieved by coupling the absorber of the absorption cycle to a two-bed halide salt-ammonia resorption cycle. A salt pairing of calcium chloride, $CaCl_2$, as the low-temperature salt (LTS) and manganese chloride, $MnCl_2$, as the high-temperature salt (HTS) is chosen for the upgrade system. Ammonia is the refrigerant that flows between the two salt beds. During the charging of the absorption cycle, the waste heat simultaneously also desorbs the high-temperature salt. The desorbed ammonia adsorbs to the low-temperature salt at that pressure and releases heat to the ambient, charging the adsorption cycle. During the discharge phase, heat from the absorption cycle drives the desorption of the low-temperature salt and the adsorption of the high-temperature salt at a higher temperature. In this way, the combined cycle acts as a two-stage sorption cycle, combining the respective advantages of liquid-gas and solid-gas sorption to achieve both storage and upgrade. Figure 1 shows a schematic of the combined cycle with representative temperatures. A lumped parameter approach is used to model the chemical kinetics of the salt reactors, including hysteresis effects, and the absorption cycle. A system-level transient model is developed to integrate the absorption storage and adsorption transformation cycles and evaluate the relevant figures of merit.
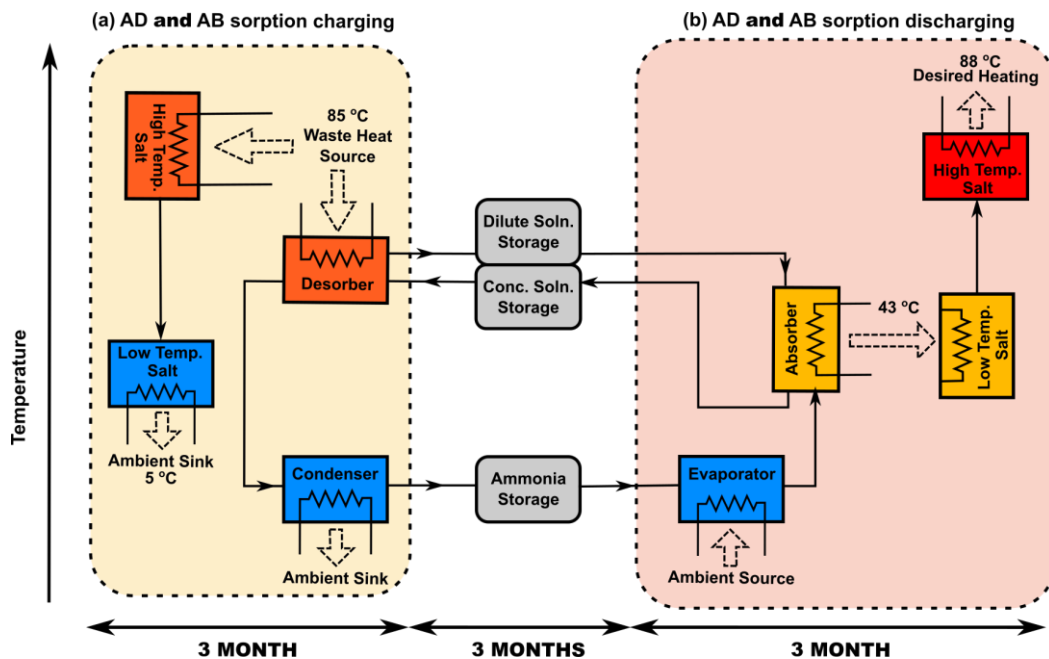
Figure 1. Schematic of the integrated absorption-adsorption cycle

Heat Storage Cycle

The absorption thermal storage cycle is analyzed to establish state points and incorporate the transient behavior of the emptying and filling of the solution tanks. It is assumed that the ambient temperature is 5°C and heat at this temperature is available at all stages of the combined cycle. For ammonia to evaporate and condense at ambient temperature, the high and low side pressures in the system should be relatively close to each other. A closest approach temperature (CAT) of 3°C is chosen for both the evaporator and condenser, and the high and low side pressures are set accordingly for the absorption cycle.

The parameters required to fully specify the size of the system are the volumes of storage tanks and the time for charge and discharge. Although intended for seasonal thermal energy storage, a time scale of four hours is chosen to capture the transience of the components, which can be extrapolated for the entire period of charge and discharge. For example, on any given day

during the hot season, solar energy is directed to the storage system for four hours. This continues for the entire hot season (two to three months), and each day part of the system is charged. Table 1 lists the mass filled (or emptied) in each tank daily, and also the total mass required over the three-month period.

Table 1. Absorption tank sizing parameters

	Daily mass required (kg)	Seasonal mass required (kg)	Discharge flow rate (kg s^{-1})	Ammonia concentration (kg kg^{-1})
Concentrated solution tank	12.5	1125	8.7×10^{-4}	0.5100
Dilute solution tank	8.5	774	6×10^{-4}	0.2849
Refrigerant tank	4.0	360	2.7×10^{-4}	0.9998

The assumptions in the absorption model are listed below:

- The pressure losses through the system components and pipes are negligible
- The time response of the heat-exchanging components is negligible compared to the time response of the tanks
- During the storage phase, the tanks equilibrate fully with ambient conditions (5°C)
- The tanks are well mixed so that the ammonia concentration is constant throughout
- The same mass flow rates are applied for charge and discharge

Component Modeling

The component level modeling of the absorption cycle considers the desorber, rectifier, absorber, condenser, evaporator, expansion tank, and pump, each with corresponding mass, species, and energy balance equations. The desorber is modeled as a control volume with one inflow stream and two outflow streams. The maximum temperature attained in the desorber (state point 6 in Figure 2) is set equal to the temperature of the waste heat input (85°C). A rectifier is necessary to purify the ammonia refrigerant before it is condensed and evaporated. The ammonia stream in the condenser and evaporator is assumed to be at a concentration of 0.9998 after rectification. The rectifier is modeled as an ideal rectifier, with the saturated liquid and vapor stream exiting the desorber in thermodynamic equilibrium. Furthermore, the ammonia mass fraction of the liquid reflux re-entering the desorber equals that of the concentrated solution.

The absorber is modeled analogous to the desorber with two inflow streams and one outflow stream. The inflow streams first undergo adiabatic premixing followed by heat exchange. The maximum temperature in the absorber (state point 16 in Figure 2) is the adiabatic mixing temperature and is the upper limit of the temperature that can drive the discharge of the low temperature salt. The condenser and evaporator both operate at ambient temperature with a closest approach temperature of 3°C; hence, the refrigerant condenses at 8°C and evaporates at 2°C. The expansion tank is modeled as an isenthalpic throttling process. Figure 2 shows the temperatures and heat duties during the middle of both the charge and discharge phases. The upper right-hand side illustrates the charge phase, while the lower left side shows the discharge phase.

There are three storage vessels depicted in Figure 2. The fluids are each stored at the ambient temperature (5°C). During the charge and discharge phases, the governing energy equation is:

$$m_{\text{tank}} \frac{\partial u}{\partial t} + u \frac{\partial m_{\text{tank}}}{\partial t} = \dot{m}_{\text{in}} h_{\text{in}} \tag{1}$$

The solution and refrigerant tanks are isobaric, and an explicit Euler time integration scheme is used to model the filling and emptying of the tanks, followed by an infinitesimal volume step

Heat Powered Cycles
Conference 2023
Edinburgh

Heat in the new energy system

3rd to 6th of September 2023
The University of Edinburgh, Scotland

change to maintain constant pressure. The resulting flow properties are carried throughout the system.

There are two separate storage phases in this cycle; the first occurs after charging (Autumn is the representative season for this phase), and the second occurs after discharging (Spring is the representative season for this phase). During the storage phase following charge, the dilute solution tank and refrigerant tank equilibrate with ambient conditions and the concentrated solution tank is empty. During the storage phase following the discharge, the concentrated solution tank is full and the other two are empty.
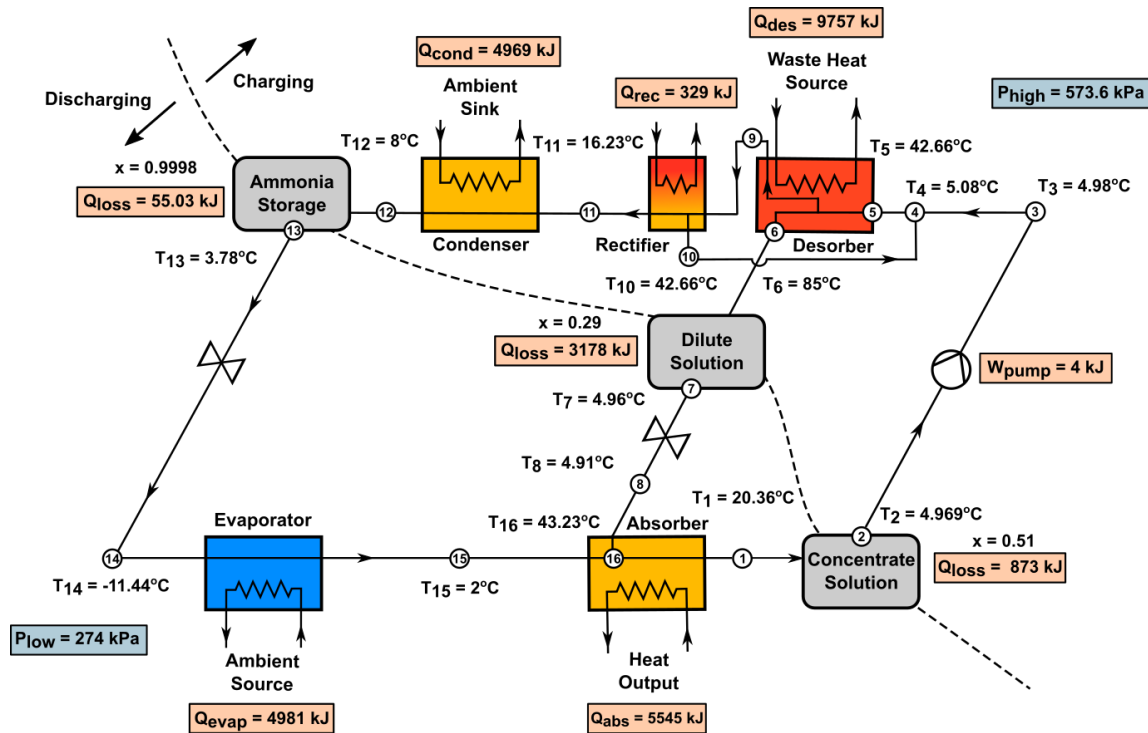
Figure 2. Absorption schematic with state points

Heat Upgrade Cycle

Heat upgrade is achieved by a chemisorption cycle. The chemisorption cycle takes advantage of the wide range of halide salt pairs that can be chosen for purpose-specific applications. The selection of salt pairing for the adsorption cycle is constrained by the waste heat available and the ambient conditions. The present study investigates a salt pairing of $CaCl_2$ and $MnCl_2$ as potential candidates for the heat upgrade cycle. The constraints on selecting an appropriate LTS are that it must adsorb at ambient temperature and desorb at the temperature output of the absorption cycle. The HTS must desorb at the temperature of the waste heat supplied, and the equilibrium pressure of the LTS at ambient temperature as shown in Figure 3. By combining $CaCl_2$ as the low-temperature salt with different high-temperature salts such as BaI_2, $MnCl_2$, and $CaBr_2$, along with their corresponding waste heat temperatures, various heat output temperatures can be achieved at a 5°C ambient temperature. $MnCl_2$ was chosen in this study as it is widely investigated and data relating to hysteresis and rates of this reaction are available from the literature (Table 3).

Figure 4 depicts the charging and discharging processes.

1. During charging, waste heat is supplied to the HTS. This causes the HTS to desorb, and release ammonia vapor. Simultaneously, the LTS undergoes adsorption at ambient temperature.

2. During discharge, the reverse process occurs. The heat output from the absorption cycle is coupled to the LTS, and ammonia is desorbed from the LTS. At the higher pressure, the HTS adsorbs and releases heat.

The heat upgrade cycle is modeled using a lumped parameter analysis. The salt temperature and pressure are uniform throughout the reactive blocks. The two salt beds are connected and hence have equal pressure. The lumped parameter model assumes the uptake is uniform throughout the reactive blocks.
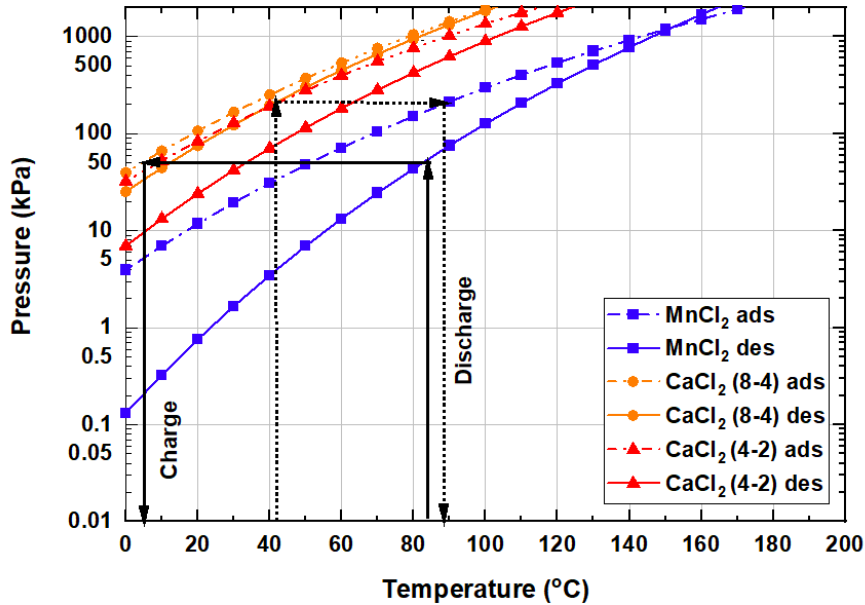
Figure 3. Van't Hoff diagram for MnCl₂ and CaCl₂ including hysteresis

Figure 4. Schematic of the lumped parameter model of resorption

Component Modeling

Three control volumes of the heat upgrade system are modeled; the HTS reactor containing a mixture of expanded natural graphite (ENG) and $MnCl_2$, the LTS reactor containing ENG and $CaCl_2$, and the ammonia vapor flowing between the two reactors. The salts are impregnated in an ENG matrix to improve stability and heat transfer performance, owing to the high thermal conductivity, high surface area, and high permeability of the graphite. T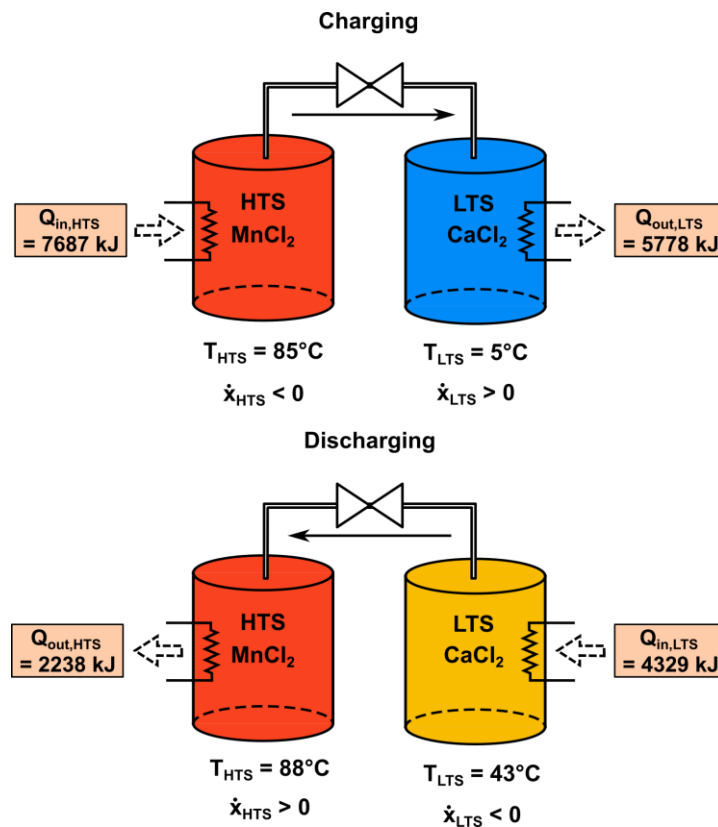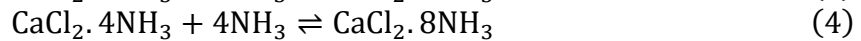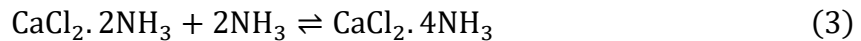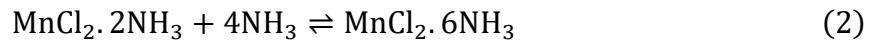he mass fraction of ENG in both blocks is one-quarter [13]. This paper includes the effects of simultaneous multistep reactions occurring within the salts. The reaction between $CaCl_2$ and NH_3 involves four steps (octa- to tetra-ammoniate, tetra- to di-ammoniate, di- to mono-ammoniate, and mono-ammoniate to pure $CaCl_2$). The di- to mono-ammoniate, and mono-ammoniate to pure $CaCl_2$ reactions only occur at temperatures above 150°C and 200°C, respectively, for the pressure range under consideration in this study. Similarly, the decomposition of $MnCl_2$ and NH_3 occurs in three steps (hexa- to di-ammoniate, di- to mono-ammoniate, and mono-ammoniate to pure $MnCl_2$), where the di- to mono-ammoniate, and mono-ammoniate to pure $MnCl_2$ reactions occur at temperatures outside the range of this paper. The applicable reactions are described in Equations 2, 3, and 4.

$$MnCl_2.2NH_3 + 4NH_3 \rightleftharpoons MnCl_2.6NH_3 \tag{2}$$

$$CaCl_2.2NH_3 + 2NH_3 \rightleftharpoons CaCl_2.4NH_3 \tag{3}$$

$$CaCl_2.4NH_3 + 4NH_3 \rightleftharpoons CaCl_2.8NH_3 \tag{4}$$

Equations 5 and 6 described the energy balance of the low and high temperature salt beds respectively, undergoing ad- and desorption:

$$
\left[m_{ENG} \cdot c_{v,ENG} + M_s \cdot n_s \cdot c_{v,s} + M_{NH_3} \cdot n_s \cdot c_{v,NH_3,ads} \cdot (2 \cdot x_{s,2} + 4 \cdot x_{s,4} + 8 \cdot x_{s,8}) \right] \cdot \frac{\partial T_s}{\partial t}
$$
$$
+ \left[M_{NH_3,ads} \cdot n_s \cdot c_{v,NH_3,ads} \cdot T_s \right] \cdot \left(2 \cdot \frac{dX}{dt} + 4 \cdot \frac{dY}{dt} \right)
$$
$$
= \dot{Q}_{HTF} + \dot{Q}_{gen} + \dot{m}_g \cdot h_g + H(\dot{m}_g) \cdot \dot{m}_g \cdot c_{p,g} \cdot (T_{s,ads} - T_g) \tag{5}
$$

$$
\left[m_{ENG} \cdot c_{v,ENG} + M_s \cdot n_s \cdot c_{v,s} + M_{NH_3} \cdot n_s \cdot c_{v,NH_3,ads} \cdot (2 \cdot x_{s,2} + 6 \cdot x_{s,6}) \right] \cdot \frac{\partial T_s}{\partial t}
$$
$$
+ \left[M_{NH_3,ads} \cdot n_s \cdot c_{v,NH_3,ads} \cdot T_s \right] \cdot \left(4 \cdot \frac{dX}{dt} \right)
$$
$$
= \dot{Q}_{HTF} + \dot{Q}_{gen} + \dot{m}_g \cdot h_g + H(\dot{m}_g) \cdot \dot{m}_g \cdot c_{p,g} \cdot (T_{s,ads} - T_g) \tag{6}
$$

The left-hand side of the energy equation represents the energy storage in the salts, where m is mass of the substance in kg, M is the molar mass in kg kmol^{-1}, c_v is the specific heat capacity at a constant volume, and n is the molar amount of salt. The first term on the left-hand side is composed of three distinct parts: the ENG, the pure inorganic salt, and the ammonia in the adsorbed phase. Lower case x in this equation is the molar fraction of salt in any given state divided by the total moles of salt in the bed. Upper case X and Y represent the reaction progression and is a measure of the extent of any given reaction. As the HTS undergoes only one reaction, the reaction progression is represented by a single value, X_{HTS} (Equation 7a). The reaction progression of the LTS is captured by both X_{LTS}, and Y_{LTS}, representing the extent of the reactions described in Equations 3 and 4 respectively. The use of upper- and lower-case letters indicate the current molar fractions (lowercase) and the cumulative history (uppercase) of the different adsorbed phases.

Heat Powered Cycles
Conference 2023
Edinburgh

Heat in the new energy system

3rd to 6th of September 2023
The University of Edinburgh, Scotland

$$X_{\text{HTS}} = \frac{n_{MnCl_2.6NH_3}}{n_{MnCl_2.6NH_3} + n_{MnCl_2.2NH_3}} \tag{7a}$$

$$X_{LTS} = \frac{n_{CaCl_2.4NH_3}}{n_{CaCl_2.2NH_3} + n_{CaCl_2.4NH_3}} \tag{7b}$$

$$Y_{LTS} = \frac{n_{CaCl_2.8NH_3}}{n_{CaCl_2.4NH_3} + n_{CaCl_2.8NH_3}} \tag{7c}$$

There are conflicting results in the literature on the modelling of the specific heat capacity of ammonia in the adsorbed phase. The additive property of specific heats has been used incorporating ammonia in the gas [14, 15] and condensed phases [16], as well as an intermediate phase. Following the model by Fujioka et al. [16], this system is modeled using a constant specific heat of ammonia in the solid state estimated by applying Neumann-Kopp's law. Table 2 lists the physical parameters used in this model.

Table 2. Physical parameters used in the theoretical model

	Daily mass required (kg)	Seasonal mass required (kg)
CaCl$_2$	6.5	587
MnCl$_2$	9.0	810

The right-hand side of the energy balance in Equations 5 and 6 includes the heat generated from the reaction, $\dot{Q}_{\text{gen}}$, and the heat supplied or removed by the heat transfer fluid (HTF), $\dot{Q}_{\text{HTF}}$. Equation 8 describes the heat absorbed or released from the reaction. ΔH_R is the heat of reaction per mole of ammonia, and v is the stoichiometric number of moles of ammonia adsorbed or desorbed per mole of salt.

$$\dot{Q}_{\text{gen}} = v \cdot n_s \cdot \Delta H_R \cdot \frac{dX}{dt} \tag{8}$$

The third and fourth terms on the right-hand side of the energy equation represent the energy associated with the inflow (or efflux) of ammonia vapor into (or out of) the reactor during adsorption (desorption). The mass flow rate of ammonia vapor is assumed to match the rate of change of uptake exactly, although in a more precise model, the differences in adsorption and desorption rates must be considered. The enthalpy term is calculated based on the temperature of the vapor if the salt is adsorbing, or the temperature of the salt if the salt is desorbing. Due to the upwind scheme applied to the system, if ammonia is desorbing from the bed, it is assumed to leave at the temperature of the salt, and if ammonia is being adsorbed, it is assumed to enter at the temperature of the vapor. Therefore, an additional term must be included to account for the increase or decrease in temperature between the ammonia entering the bed and the salt bed itself. H is a unit step function defined as follows:

$$H(\dot{m}_g) := \begin{cases} 1, & \dot{m}_g > 0 \\ 0, & \dot{m}_g \leq 0 \end{cases} \tag{9}$$

This upwind scheme is also reflected in the energy balance of the ammonia vapor, which is written as follows (on a molar basis):

$$n_g \cdot c_{v,g} \cdot \frac{dT_g}{dt} = \left(n_s \cdot v \cdot \frac{dx}{dt} \right)_{\text{des}} \cdot \left(u_g - h_{g,T_{s,\text{des}}} \right) + \left(n_s \cdot v \cdot \frac{dx}{dt} \right)_{ads} \cdot \left(u_g - h_{g,T_g} \right) \tag{10}$$

The pressure in the system is constant across all three control volumes and is modeled by Equation 11, assuming ammonia behaves as an ideal gas.

$$\frac{dP}{dt} = \frac{R}{V_\text{g}} \left(\frac{dn_\text{g}}{dt} \cdot T_\text{g} + \frac{dT_\text{g}}{dt} \cdot n_\text{g} \right) \tag{11}$$

Reaction Kinetics

Chemical adsorption kinetic models can be classified as local, global, or analytical methods as proposed by Stitou and Crozat (1997) [17]. The global reaction model proposed by Mazet (1991) [18] decoupled the kinetic and thermal equations and resolved the kinetic equations. This model is chosen in this paper as it is most commonly cited in the literature for consideration of multi-step reactions. Ar and b are measured constants used in the kinetic reaction model.

For synthesis:

$$\frac{dX}{dt} = Ar \cdot (1 - X)^b \cdot \left(1 - \frac{p_\text{eq}}{p} \right) \tag{12}$$

For decomposition:

$$\frac{dX}{dt} = Ar \cdot X^b \cdot \left(1 - \frac{p_\text{eq}}{p} \right) \tag{13}$$

For CaCl$_2$, a second reaction occurs from tetra- to di-ammoniate. This reaction is reliant on the progression of the octa- to tetra-ammoniate transition. Mazet et al. (1991) propose a model for multistep reactions, governed by the equation [18]:

$$\frac{dY}{dt} = Ar \cdot \left(X(1 - Y) \right)^b \cdot \left(1 - \frac{p_\text{eq}}{p} \right) \tag{14}$$

Where the equilibrium pressure, p_eq, is determined by the relation:

$$\ln \left(\frac{p_{eq}}{p_0} \right) = -\frac{\Delta H}{RT} + \frac{\Delta S}{R} \tag{15}$$

Adsorption hysteresis is a mismatch between adsorption and desorption pressure concentration isotherms at the same temperature, and has been reported in several studies [19-22]. The values recorded in Table 3 indicate the pseudo reaction enthalpies and entropies that govern the equilibrium pressure for adsorption or desorption to occur. It is assumed that when the pressure falls between the two equilibrium lines, no reaction occurs.

Table 3. Reaction rate parameters for Equations 7, 8, and 9 [20, 23, 24]

Reaction	CaCl$_2$.8/4NH$_3$		CaCl$_2$.4/2NH$_3$		CaCl$_2$.6/2NH$_3$	
	Adsorption	Desorption	Adsorption	Desorption	Adsorption	Desorption
ΔH [kJ mol^{-1}]	32,844.620	36,365.790	31,699,720	41,202,320	36,611.107	58,196.253
ΔS [kJ mol^{-1} K^{-1}]	208.302	217.432	202,390	224,432	202.865	253.641
ΔH_R [kJ mol^{-1}]	42,080.324		39,948,772		42,523.900	
Ar [s^{-1}]	0.0125	0.0195	0.0287	0.0045	0.0010187	0.0010187
b [$-$]	2.104	1.005	1.78	0.468	1.185	1.185

Storage Model

Similar to the storage model of the absorption cycle, the process of solid-gas adsorption storage can be divided into two distinct storage phases, namely, the first phase that occurs after charging and the second phase that occurs after discharging. During the first storage phase, the

valves from each tank are closed. The LTS tank, already at ambient conditions, remains stable. The HTS tank, on the other hand, as it decreases in temperature towards ambient, will favor adsorption. However, by closing the valve, the ammonia supply to the HTS is disrupted, rendering it incapable of adsorbing any additional ammonia, except what exists in the free volume of the reactor vessel. The HTS adsorbs a portion of the small quantity of ammonia in the free volume of the reactor, and although the reaction regresses by the amount adsorbed from free volume, this change is small in comparison to the full uptake swing of the cycle, but it results in a large decrease in the pressure of the closed vessel. At the start of discharge, the HTS is isosterically heated so that it does not adsorb instantaneously at the low pressure. Although the reaction kinetics taking place in this phase are not modeled in this study, the initial conditions of the discharge assume that the temperature of the HTS has previously been isosterically heated. The establishment of these initial conditions can be considered in future studies by including specific modules devoted to these phases.

During the second storage phase, both valves remain open. As both the LTS and HTS tanks are at an elevated temperature as they cool down, the regeneration of the cycle will be initiated without a supply of waste heat. Again, the reaction kinetics of the cooling to ambient has not been analyzed in this study.

Numerical Model

The resulting set of equations for both the heat storage and upgrade cycles were modeled on the Engineering Equation Solver (EES) software platform, employing a forward difference Euler time integration scheme [25]. For the ammonia-water mixture in the absorption cycle, three independent thermodynamic properties are required to fully specify any given state. For each state during charging and discharging, an appropriate combination of vapor quality, ammonia mass fraction, enthalpy, and temperature is used. During the storage period, the volume of the tank, and the ammonia concentration are set as constant and only the temperature changes. At the end of the storage phase when the temperature is at 5°C, the state is fully specified.

For the adsorption system, the initial conditions are $MnCl_2$ in the adsorbed state ($X_{HTS} = 1$), and $CaCl_2$ in the desorbed state ($X_{LTS} = 1, Y_{LTS} = 0$). The system is initially at ambient temperature and a pressure determined by the isochoric cooling of ammonia vapor during the storage phases. The cycle time is set to equal the charge (and discharge) time of the absorption cycle. The time step for the numerical integration is limited to a minimum of 0.1 s for the first 0.5% of the half-cycle time due to the rapid transient behavior following storage, increasing to 0.5 s for the remainder of the half-cycle.

System Coupling

The results of the absorption cycle indicate approximately constant heat duties from the major heat-exchanging components. To couple the output from the absorber to the LTS during discharge, a fixed heat duty of 0.302 kW is specified. At this duty, the temperature of the LTS does not exceed the temperature output of the absorber. The heat duty from the absorber cannot be fully realized as the heat duty into the LTS. During discharge, the absorber raises the temperature of the HTF from ambient to a maximum of 43°C. This stream is coupled to the LTS reactor; however, the exit stream of the heat transfer fluid from the LTS will not reach ambient temperatures again. This results in wasted heat and hence $Q_{abs} > Q_{in,LTS}$.

Results and Discussion

The temperature profiles of the main components in the combined cycle are illustrated in Figure 5. The left-hand side of the plot depicts the charging phase, while the right-hand side shows

the discharge phase, each for one day per season. During charging, waste heat at 85°C is delivered to both the desorber and the HTS. It takes one hour for the HTS to reach this elevated temperature as a constant heat duty is supplied to it (labelled point 1). Once the HTS reaches 85°C, it begins to desorb. The LTS rejects heat to the ambient at 5°C for the duration of the charging phase. The heat duty into the desorber is specified so that the HTS does not exceed the temperature of waste heat (point 2).

During discharge, the absorber of the absorption storage system delivers a constant output temperature of 43°C, which is directed to the LTS. The temperature of both the LTS and HTS increase throughout the discharge phase, reaching a maximum at 43°C. An important figure of merit for this system is the combined temperature lift. For the salt pairing chosen in this analysis, the combined temperature lift between the waste heat for charging and the delivery temperature is 3°C. This can be seen as the difference between the temperature of the HTS on the right- and left-hand side of Figure 5 (the difference between points 2 and 4). Without the addition of the chemisorption heat transformer, the absorption system discharges 42°C lower than the charging temperature. One important assumption included in the results of the discharge phase is the initial condition of the HTS at the start of discharging (point 3). Figure 5 shows the HTS starts at a temperature of 40°C. It is assumed here that the HTS is initially isosterically heated by the heat output from the absorber. In the absence of isosteric heating, the HTS adsorbs instantaneously at a low temperature and does not reach its maximum temperature potential. This phase should be accounted for in future modeling iterations.
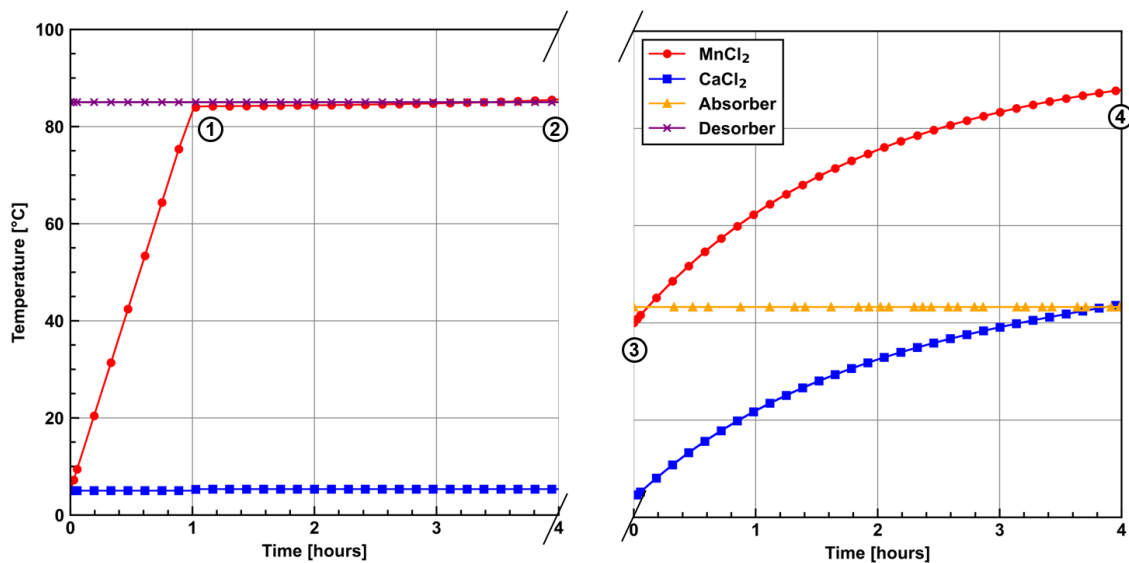
Figure 5. Representative temperature profile of charge and discharge phase

Figure 6 shows the equilibrium pressures and adsorption system pressure profile. The trends in the reaction progression profile (Figure 7) of the salts with time can be understood when viewed in parallel with the pressure profile of the cycle in Figure 6. The first hour of the charging phase indicates when the pressure lies between the equilibrium isotherms on the Van't Hoff plot (Figure 3). During this period, neither desorption nor adsorption take place. When the pressure of the system rises above the LTS equilibrium adsorption line, the reaction progresses approximately linearly (from point 1). For the discharge phase, the system pressure always lies between the HTS adsorption line and the LTS desorption line and hence there is no initial stagnant phase. The second step reaction of the LTS does not occur throughout the charge or discharge phase due to the initial conditions specified ($X_{LTS} = 1, Y_{LTS} = 0$). The model must run several times to achieve a steady state between the uptake at the start of charging and the

end of discharging (i.e., the right- and left-hand sides of Figure 8 match) and show adequate progression of the secondary reaction.
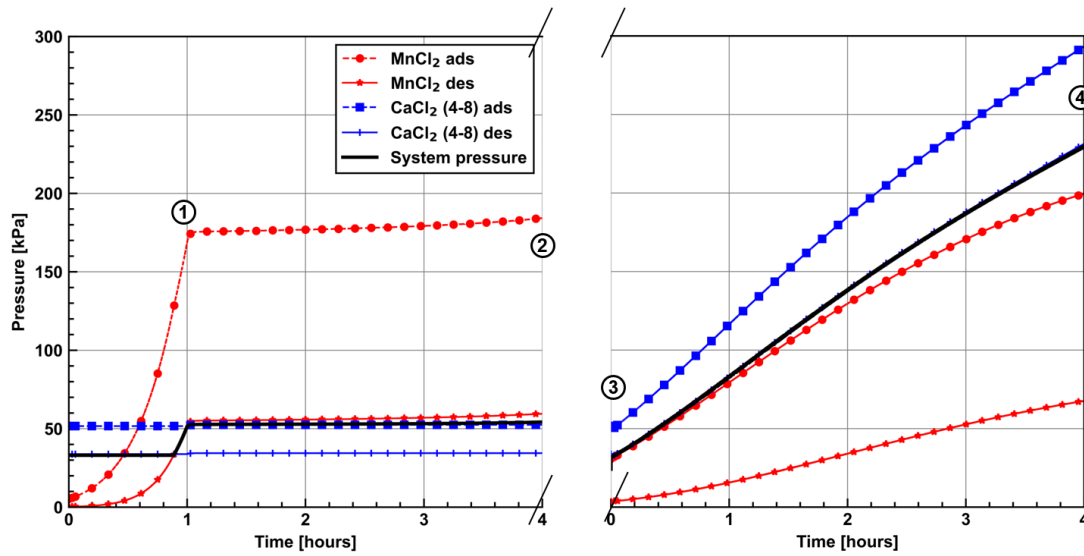
Figure 6. Equilibrium pressure isotherms
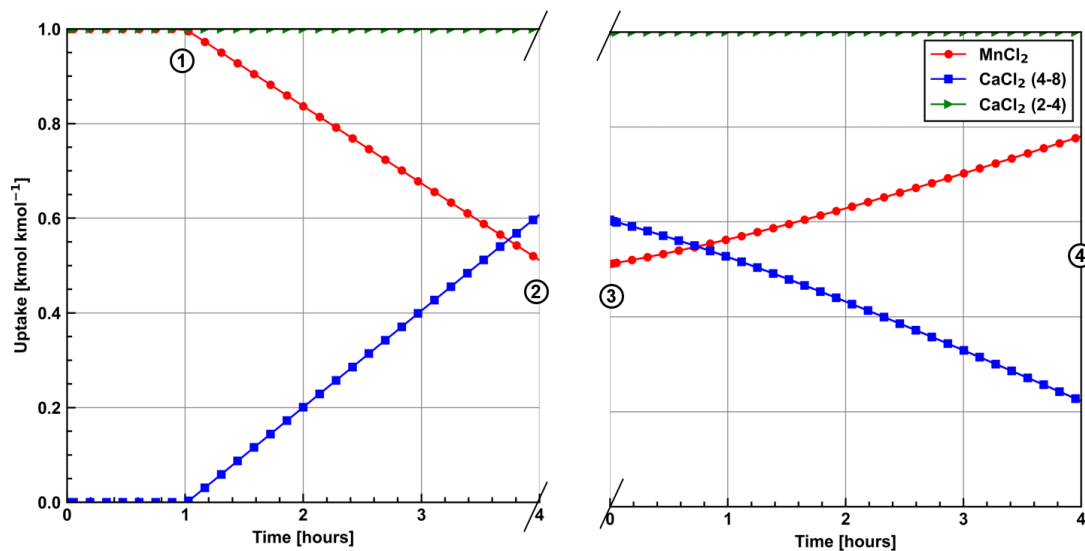
Figure 7. Uptake profile of charge and discharge phase

Figure 8 shows the heat duties of the main components during charge and discharge. The heat-exchanging components of the absorption cycle remain relatively constant for both the charge and discharge phases and can be seen as the straight lines in Figure 8. During the charge phase, there is a constant heat duty input to the HTS. The LTS releases heat after 1 hour (point 1) following the onset of adsorption. During discharge, a constant heat duty is fed into the LTS, and the heat duty of the HTS increases as the adsorption reaction progresses and pressure and temperature increase. The storage losses that occur during the latent phases of the system are recorded in Table 4. During the first storage period, the concentrated solution tank is empty, and the greatest losses occur in the HTS bed and the dilute solution tank as they are both close to the temperature of the waste heat input. During the second storage phase, both the dilute solution tank and refrigerant tank are empty and more significant losses occur from the HTS and LTS as they are both at elevated temperatures.

Heat Powered Cycles
Conference 2023
Edinburgh
Heat in the new energy system

3rd to 6th of September 2023
The University of Edinburgh, Scotland
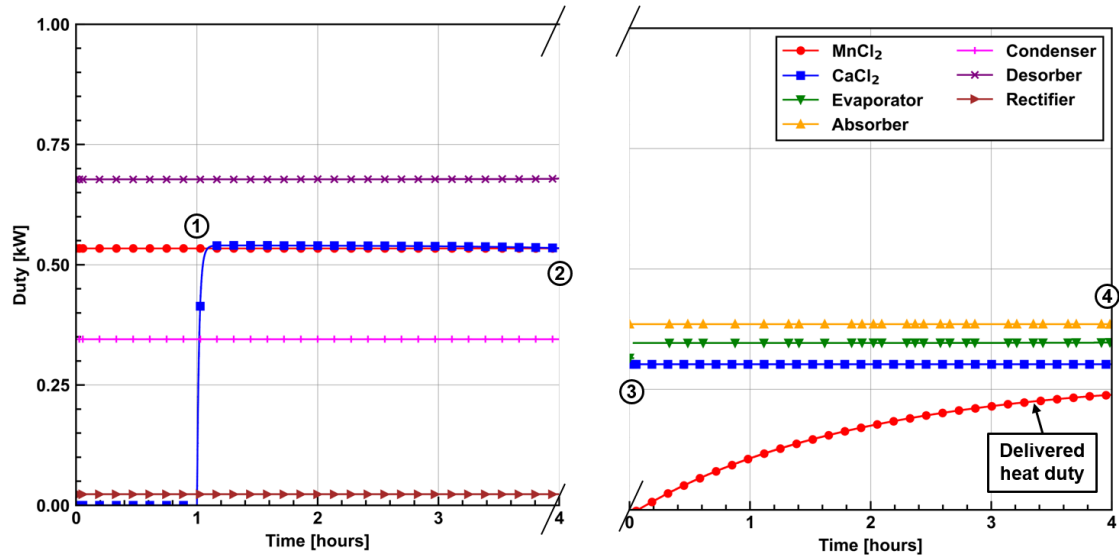
Figure 8. Representative heat duty profile of charge and discharge phase

Table 4. Storage losses over one full cycle

Component	Storage losses phase 1 [kJ]	Storage losses phase 2 [kJ]
Concentrated solution tank	0	873
Dilute solution tank	2979	0
Refrigerant tank	55	0
High temperature salt	775	1796
Low temperature salt	2	640
Ammonia vapor	3	16

The coefficient of performance of this system can be analysed separately on a per cycle basis as described by Equations 16 and 17. The associated heat inputs and outputs to each cycle are calculated as the integral of the heat duties shown in Figure 8.

$$COP_{\mathrm{abs}} = \frac{Q_{\mathrm{abs}}}{Q_{\mathrm{des}} + W_{\mathrm{pump}}} = 0.568 \tag{16}$$

$$COP_{\mathrm{ads}} = \frac{Q_{\mathrm{out,HTS}}}{Q_{\mathrm{in,HTS}} + Q_{\mathrm{in,LTS}}} = 0.186 \tag{17}$$

The overall efficiency of this system is defined as the stored and upgraded heat output divided by the driving heat input to the system in Equation 18. Table 4 shows the losses that occur during the two storage phases in one complete yearly cycle.

$$\eta_{\mathrm{combined}} = \frac{Q_{\mathrm{out,HTS}}}{Q_{\mathrm{des}} + W_{\mathrm{pump}} + Q_{\mathrm{in,HTS}}} = 12.8\% \tag{18}$$

The total energy released in the system per day is 2024 kJ and based on an additive relationship, the energy released over the entire discharge season is 182 MJ. The resulting energy storage density of the combined system is 72 kJ kg^{-1}. The heat duty out from the HTS increases as the system is discharged up to a maximum of 0.25 kW as shown in Figure 8. In comparison to other alternatives for seasonal thermal energy storage, this cycle has the unique advantage of providing temperatures at least as high as the originally supplied temperature. Seasonal TCES systems typically exhibit a large negative temperature differential between discharge and charge temperature [7, 26]. Comparison with the storage efficiency of other seasonal thermal energy storage systems that focus on improving delivery temperatures without reliance on other low-grade heat sources indicates this system is competitive. The combined sorption-PCM-

based system of Garimella et al. had a storage efficiency of 15.3%, and at its maximum discharge temperature had a temperature difference between delivery and charge of -45°C.

The coefficient of performance (COP) of the absorption cycle has potential for significant improvement through the addition of a two- stage absorber. This modification reduces heat losses and also achieves 7.32 times higher energy storage densities than the single stage cycle [27]. Furthermore, the addition of recuperative heat exchangers between concentrated and dilute solutions has the potential to increase the absorption system COP.

Improvements are also possible to the adsorption system. Hysteresis has a large effect on the temperature required for ad- and de-sorption. However, results from Van der Pal and Critoph [28]show that hysteresis can be reduced in a modified large temperature jump reactor. Specific tailored salt pairings can facilitate alternative ambient conditions and temperature outputs from the salt adsorption system. Judicious salt pairing can yield further improvements and capacities to this cycle.

Conclusion

Seasonal thermal energy storage will be a key enabler for the decarbonization of building heating by substituting fossil-fuel-based heat supply with renewable heat sources, such as solar thermal energy, or waste heat generated from industries. This paper presents the result of a novel combined ab- and adsorption cycle for integrated thermal energy storage and upgrade. A method for transient modeling of both an ab- and adsorption thermal storage cycle is presented, as well as an approach to couple the two systems. The model results indicate a temperature lift of 3°C and a storage efficiency of 12.8%. This system overcomes the significant temperature degradation typically associated with thermal storage, however, at the expense of the storage efficiency.

Further investigation is needed to improve the COP of both the ab- and adsorption cycles. The effect of cyclical charging, discharging, and storage phases requires experimental validation, in addition to reactor-specific pseudo-reaction rate constants and hysteresis isotherms. Future work should also consider seasonal temperature fluctuations and accurate modeling of salt reactor beds during the storage phase.

Acknowledgments

The authors would like to extend thanks to Dr. Robert Critoph, Dr. Steven Metcalf, Dr. Stan Shire, Dr. Angeles Rivero Pacho, and Dr. George Atkinson for their valuable insight and discussions related to the development of this concept.

References

[1] International Energy Agency, "Renewables 2022: Analysis and forecast to 2027", 2022.
[2] U.S. Energy Information Administration, "Commercial Buildings Energy Consumption Survey: Energy Consumption and Expenditure Tables", 2018.
[3] U.S. Energy Information Administration, "Annual Energy Outlook 2020: Energy-Related Carbon Dioxide Emissions by Sector and Source", 2020.
[4] Ragoowansi E. A., Garimella S., Goyal A., "Realistic utilization of emerging thermal energy recovery and storage technologies for buildings", Cell Reports Physical Science, 2023.
[5] Fisch M. N., Guigas M., Dalenbäck J. O., "A review of large-scale solar heating systems in Europe", Solar Energy, 1998.
[6] Aydin D., Casey S. P., Riffat S., "The latest advancements on thermochemical heat storage systems", Renewable and Sustainable Energy Reviews, 2015.
[7] Yang T., Liu W., Kramer G. J., Sun Q., "Seasonal thermal energy storage: A techno-economic literature review", Renewable and Sustainable Energy Reviews, 2021.

[8] Garimella S., Keniar K., Rattner A. S., Kini G., "Conceptualization and analysis of a novel combined sorption and phase-change material thermal storage system", Journal of Energy Storage, 2020.

[9] Li T. X., Wang R. Z., Yan T., Ishugah T. F., "Integrated energy storage and energy upgrade, combined cooling and heating supply, and waste heat recovery with solid–gas thermochemical sorption heat transformer", International Journal of Heat and Mass Transfer, 2014.

[10] Fumey B., Weber R., Gantenbein P., Daguenet-Frick X., Williamson T., Dorer V., "Development of a Closed Sorption Heat Storage Prototype", Energy Procedia, 2014.

[11] Quinnell J. A., Davidson J. H., "Heat and mass transfer during heating of a hybrid absorption/sensible storage tank", Solar Energy, 2014.

[12] Viswanathan V. K., Rattner A. S., Determan M. D., Garimella S., "Dynamic model for a small-capacity ammonia–water absorption chiller", HVAC&R Research, 2013.

[13] Valkov V., Kelleher M. D., Sreenivasan K. R., Shah R. K., Joshi Y. Measurement technique for determination of thermophysical properties of thermochemical storage materials. Experimental Heat Transfer, Fluid Mechanics and Thermodynamics 1993. Amsterdam: Elsevier; 1993.

[14] Lourdudoss S., Schuler T., Raldow W., "Determination of the heat capacity of calcium chloride octa- and tetraammines", Inorganica Chimica Acta, 1981.

[15] Marty A., "Etude par microcalorimétrie de la réactivité de deux ammoniacates de chlorure de manganese", Journal of Thermal Analysis and Calorimetry, 1991.

[16] Fujioka K. K., Shin-ichi; Fujiki, Shigehire; Hirata, Yushi, "Variations of molar volume and heat capacity of reactive solids of $CaCl_2$ used for chemcial heat pumps", Journal of Chemical Engineering of Japan, 1996.

[17] Stitou D., Crozat G., "Dimensioning nomograms for the design of fixed-bed solid-gas thermochemical reactors with various geometrical configurations", Chemical Engineering and Processing: Process Intensification, 1997.

[18] Mazet N., Amouroux M., Spinner B., "Analysis and experimental study of the transformation of a non-isothermal solid/gas reacting medium", Chemical Engineering Communications, 1991.

[19] Jabbari-Hichri A., Bennici S., Auroux A., "$CaCl_2$-containing composites as thermochemical heat storage materials", Solar Energy Materials and Solar Cells, 2017.

[20] Hinmers S., Atkinson G. H., Critoph R. E., van der Pal M., "Resorption Thermal Transformer Generator Design", Energies, 2022.

[21] An G., Li Y., Wang L., Gao J., "Wide applicability of analogical models coupled with hysteresis effect for halide/ammonia working pairs", Chemical Engineering Journal, 2020.

[22] Wu S., Li T. X., Wang R. Z., "Experimental identification and thermodynamic analysis of ammonia sorption equilibrium characteristics on halide salts", Energy, 2018.

[23] Hinmers S., Atkinson G. H., Critoph R. E., Van der Pal M., "Modelling and Analysis of Ammonia Sorption Reactions in Halide Salts", International Journal of Refrigeration, 2022.

[24] Han J. H., Lee K.-H., Kim D. H., Kim H., "Transformation Analysis of Thermochemical Reactor Based on Thermophysical Properties of Graphite−$MnCl_2$ Complex", Industrial & Engineering Chemistry Research, 2000.

[25] Klein S. A., Alvarado F. L., "EES - Engineering Equation Solver", 2020.

[26] Weber R., Dorer V., "Long-term heat storage with NaOH", Vacuum, 2008.

[27] Xu Z. Y., Wang R. Z., "Absorption seasonal thermal storage cycle with high energy storage density through multi-stage output", Energy, 2019.

[28] Van der Pal M., Critoph R. E., "Performance of $CaCl_2$-reactor for application in ammonia-salt based thermal transformers", Applied Thermal Engineering, 2017.

![Heat Powered Cycles Conference 2023 logo] Heat Powered Cycles Conference 2023 Edinburgh — Heat in the new energy system

3rd to 6th of September 2023
The University of Edinburgh, Scotland

Green ammonia fuelled combined system integrating solid oxide fuel cell with cathode recycling and Kalina cycle

Dibyendu Roy, Samiran Samanta, Sumit Roy*, Andrew Smallbone and Anthony Paul Roskilly

Department of Engineering, Durham University, Durham DH1 3LE, UK

*Corresponding author: sumit.roy@durham.ac.uk

Abstract

The search for cleaner and more efficient sources of energy has driven the development of new technologies and the optimization of existing ones. One of the promising areas in this field is the integration of solid oxide fuel cells (SOFCs) with waste heat recovery systems such as the Kalina cycle. This approach has the capability to enhance the overall efficiency of power generation and lower greenhouse gas emissions. In the present investigation, a combined system utilizing green ammonia as fuel and integrating solid oxide fuel cell with cathode recycling and Kalina cycle is suggested. The proposed system consumed 515.76 kW of energy through liquid ammonia as fuel input. The SOFC unit generated 289.43 kW of power and 159.24 kW of waste heat at the downstream, which was supplied as the heat input to the Kalina cycle. The Kalina cycle generated 124 kW of power, but the associated pump consumed 57.7 kW of power, resulting in a net power output of 66.3 kW. The total net power output from the SOFC unit and the Kalina cycle was 349.84 kW, with an overall energy efficiency of 67.83%. The sensitivity analysis carried out in this study revealed that the highest power output and energy efficiency of the system were 490.6 kW and 70.43%, respectively, at fuel utilization factors of 0.6 and 0.9. Overall, the integration of solid oxide fuel cells with waste heat recovery systems such as the Kalina cycle holds promise for increasing the efficiency and reducing the emissions of power generation.

Keywords: Solid oxide fuel cell, Kalina cycle, Green ammonia, Decarbonising power generation.

Introduction

The growing demand for energy and concerns over climate change have led to an increased interest in clean and renewable energy sources. One such source is ammonia, which is a sustainable and carbon-free fuel that can be produced from renewable energy sources such as wind and solar. Green ammonia is considered 100% renewable as it is carbon free. It can be utised as a fuel source, in various technologies such as internal combustion engines, turbines, and various types of fuel cells. Out of the available alternatives, the solid oxide fuel cell (SOFC) technology has emerged as one of the most prospective solutions, owing to its elevated efficiency and almost negligible emissions. The solid oxide fuel cells are able to transform chemical energy into electrical energy with high efficiency, while also releasing minimal pollutants. The use of ammonia in SOFCs provides an opportunity to generate electricity with minimal environmental impact while achieving high energy conversion rates. Ammonia has several advantages over other gases commonly used in SOFC applications, such as hydrogen, methane, propane etc. Hydrogen can be difficult to handle and store safely, and it is highly

flammable, and it also has a low volumetric energy density compared to ammonia. On the other hand, methane produces carbon dioxide and other pollutants as by-products, which can be harmful to the environment. Propane has a low hydrogen content and produces carbon dioxide as by-product and more difficult to handle and store safely than ammonia. Ammonia has the potential to revolutionize the energy industry and contribute to the development of sustainable and clean energy systems.

SOFC is considered high temperature fuel cells which operates at temperature levels of 600-1000°C [1]. As it operates at such high temperatures, reformer is often not required thus it reduces the overall capital cost of the system [2]. The practice of recirculating off-gasses from solid oxide fuel cells is a widely recognized approach documented in literature to enhance efficiency. Nonetheless, research into this method has been restricted to examining methane [1], natural gas [3] or syngas [4] only. Furthermore, SOFC also produces high temperature waste heat, which can be utilised in producing additional power in bottoming cycles.

Kalina cycle introduced in the early 1980s, is an alternative to conventional organic Rankine cycle [5] which is suitable for operation with heat source temperature between 100°C–250°C [6]. The Kalina cycle is a thermodynamic cycle used to convert heat energy into electrical power. It is similar to the Rankine cycle, which is used in conventional power plants. The working fluid in the Kalina cycle is typically a mixture of ammonia and water, which has a lower boiling point and a higher specific heat than pure water. This allows for better heat transfer and improved efficiency compared to the Rankine cycle. The exact composition of the working fluid can be adjusted to optimize the cycle for specific operating conditions. The Kalina cycle involves several processes, including evaporation, compression, mixing, and expansion. The basic processes of the Kalina cycle are as follows: (1) Evaporation: The working fluid is heated in a heat exchanger, or boiler, to produce a high-pressure, high-temperature vapor. (2) Compression: The vapor is then compressed to a higher pressure and temperature, which increases its enthalpy. (3) Mixing: The compressed vapor is then mixed with a lower-pressure, lower-temperature vapor from the evaporation process, typically at a ratio determined by the specific cycle design. (4) Expansion: The mixture is then expanded through a turbine, which extracts work from the fluid and converts it to mechanical energy. (5) Condensation: The low-pressure, low-temperature vapor is then condensed back into a liquid state, typically in a separate heat exchanger. Such cycles can be effectively used for integration with SOFC based systems as bottoming cycle.

Previously many researchers investigated SOFC based energy systems. The utilization of methane as fuel was studied by Mojaver et al. [7] in a combined heat and power system, which resulted in reported electrical energy efficiency and exergy efficiency of 48.03% and 46.33%, respectively. Roy [8] conducted a thermodynamic analysis of a hybrid system that combined SOFC, externally fired gas turbine (EFGT), and Stirling engine (SE), and reported a net power output of 572.07 kW and an exergy efficiency of 51.54%. Alns and Sleiti [9] investigated methane fuelled SOFC based electricity and cooling system and reported optimum overall efficiency of 73%. The performance of SOFC-GT integrated systems using different fuels were investigated by Rupiper et al. [10]. According to their findings, the hybrid configuration displayed maximum electrical efficiencies of 64.7% for H_2 fuel, 60.3% for CH_4 fuel, 60.9% for C_3H_8 fuel, 61.7% for JP-4 fuel, 61.0% for JP-5 fuel, and 61.2% for JP-10 fuel. Zhang et al. [11] examined an integrated system that combined a plasma gasification facility, SOFC, supercritical CO_2 cycle, and double-effect absorption refrigeration (ARC), and reported net electrical and exergy efficiencies of 50% and 47%, respectively. Mei et al. [12] investigated a combined system that integrated SOFC, thermoelectric generator, and absorption heat pump

and reported the highest electrical efficiency of 44.7%. Quach et al. [13] investigated ammonia fed SOFC system for distributed power generation. They investigated anode gas recirculation and reported highest system efficiency of 67.5%. In their research, Shafie et al. [14] analysed the incorporation of an SOFC-GT system with a CO_2-to-ethanol conversion facility and determined that the system can attain an overall efficiency of 72.5% and an electrical efficiency of 66.5%. Quyang et al. [15] investigated biomass gasification facility integrated SOFC-dual loop ORC- SCO_2 cycle and heat recovery system and reported 52% energy efficiency can be achieved. Kasaeian et al. [16] studied an integrated system combining gasification facility, SOFC, Rankine cycle and ORC, and reported electrical and overall efficiencies are 51.43% and 81.13%, respectively. Song et al. [17] investigated thermodynamic performance assessment of combination of SOFC, Rankine cycle and Kalina cycle and reported and exergy efficiency of 39.34%.

From the previous discussion it can be seen that though SOFC- Kalina based systems were previously investigated, effect of cathode gas recycling fuelled by ammonia was not extensively investigated. In this study a hybrid system has been proposed integrating SOFC at the toping cycle and Kalina cycle at the bottoming cycle. Cathode off gas recirculation has also been applied in the system arrangement. The proposed was investigated with the aid of energy and exergy analyses.

System description

Figure 1: Schematic of SOFC- Kalina based integrated system with cathode recycling fuelled by Ammonia

The proposed system consists of a SOFC unit, a Kalina cycle unit, and a cathode recycling system. The SOFC unit converts the ammonia fuel into electrical energy and waste heat, which

is then supplied to the Kalina cycle unit to generate additional electrical energy. The cathode recycling system recycles the unused cathode air back to the anode side of the SOFC unit to increase the fuel utilization and improve the overall efficiency of the system. Figure 1 illustrates the schematic of the proposed integrated system based on SOFC-Kalina. In this study, a Co-flow planar SOFC is considered. The air is preheated in the air heater (AHE) and is supplied to the cathode channel of the SOFC with a blower. A separate blower is considered for cathode stream recirculation. The fuel used in the system is liquid ammonia stored at -33°C, which is supplied by a pump and heated by a fuel heater (FHE) before being supplied to the anode channel of the SOFC in the gaseous form. The flue gas produced by the afterburner is utilized to heat up the incoming air and fuel to the SOFC. Additionally, the waste heat from the heat exchanger (HEX1) is utilized to operate a Kalina cycle.

The following assumptions were considered in the model development [13, 18]:

a) Negligible ammonia decomposition reaction in the heat exchanger.

b) Identical temperature for the inlet and outlet of the anode and cathode streams.

c) Steady-state conditions were assumed, with no consideration for changes in kinetic and potential energies.

d) Neglecting pressure losses in the pipelines.

e) Assuming that the gas mixtures behave as ideal gas mixtures.

f) Assuming that unreacted gases are fully combusted in the afterburner.

System Modelling

Solid oxide fuel cell:

The current density distribution in the x-direction across the cell area is computed in the SOFC model. Assuming negligible losses in the electrochemical reactions taking place in a particular cross-section x of the fuel cell, the voltage can be determined using the Nernst equation, and it would be equal to the reversible cell voltage.

$$V_{x,R} = V^0 + \frac{RT}{2F} ln \left(\frac{y_{O_2,ca}^{0.5} \times y_{H_2,an}}{y_{H_2,an}} \times p_{cell}^{0.5} \right) \qquad (1)$$

The actual cell voltage of fuel cell can be estimated by the following relations

$$V_{cell} = V_{x,R} - \Delta V_{loss} \qquad (2)$$

The current density is now assumed to be directly proportional to the voltage loss, and the proportionality constant is denoted by the equivalent cell resistance, R_{ECR}, drawing an analogy with Ohm's law. If it follows, then current density in the cross-section x is defined as

$$j_x = \frac{\Delta V_{loss}}{R_{ECR}} \qquad (3)$$

The cell current can be estimated as follows

$$I_{cell} = \frac{U_f \times \varphi_{m,an,in}}{M_{mol,an}} \times \left(y_{H_2}^0 + y_{CO}^0 + y_{CH_4}^0 \right) \times 2F \qquad (4)$$

The power produced by the SOFC module can be determined by using the following equation:

$$\dot{W}_{SOFC} = N_{cell} \times I_{cell} \times V_{SOFC} \times \eta_{inv} \qquad (5)$$

where N_{cell} denotes the number of cells and η_{inv} is invertor efficiency.

Kalina cycle:

The power output from the turbine is estimated by the following relation

$$\dot{W}_T = \dot{m}_{KC}(h_{in} - h_{out})$$

where, $\dot{m}_{KC}$ and h represent mass flowrate in the Kalina cycle and specific enthalpy, respectively. The subscripts "in" and "out" represents inlet and outlet streams

Performance parameters:

The net power developed from the proposed SOFC-Kalina system is estimated as follows:

$$\dot{W}_{sys} = \dot{W}_{SOFC} + \dot{W}_T - \dot{W}_{Auxiliary} \qquad (6)$$

where $\dot{W}_T$ and $\dot{W}_{Auxiliary}$ are power output from turbine and auxiliary power requirement, resepetively.

Energy efficiency of the integrated system is estimated by the following equation

$$\eta_{sys} = \frac{\dot{W}_{sys}}{\dot{m}_{fuel} \times LHV_{Ammonia}} \qquad (7)$$

The exergy efficiency of the integrated system is evaluated using the following equation.

$$\eta_{exergy} = \frac{\dot{W}_{sys}}{Ex_{sys,in}} \qquad (8)$$

where, $Ex_{sys,in}$ denotes exergy inlet to the system.

Results

Based on the given thermodynamic model as depicted in the previous section a performance evaluation of the proposed plant has been estimated to get the essence how the system exhibits its energetic performances. The overall detailed thermodynamic performances are depicted in Table 1 and Figure 2.

Table 1: Performance parameters of the system at base case

| Name of the Parameter	Value	Unit
Fuel input	515.76	kW
SOFC power output	289.43	kW
Waste heat from SOFC	159.24	kW
Auxiliary power consumption in SOFC unit	5.89	kW
Heat input into Kalina cycle	159.24	kW
Turbine output of Kalina cycle	124	kW
Auxiliary consumption by Pump of Kalina cycle	57.7	kW
Total Net Power Output	349.84	kW
Overall Energy efficiency of the plant	67.83	%

It can be observed that the proposed plant is consuming 515.76 kW of energy through liquid ammonia as fuel input. The SOFC unit generates 289.43 kW of power and 159.24 kW of waste heat at the downstream which is going to be supplied as the heat input to the Kalina cycle. However, the SOFC unit has a total 5.89 kW of auxiliary power consumption to run its fuel compressor, air compressor and other auxiliary devices. Without the incorporation of Kaina cycle, the overall electrical efficiency of the system is estimated to be 54.98%. On the other hand, the turbine of the proposed Kalina cycle generates 124 kW of power. But the pump associate with the

proposed Kalina cycle consumes 57.7 kW of power. As a result, the net power output from the Kalina cycle is only 66.3 kW. Taken together the net power output from the SOFC unit of about 283.54 kW, the whole plant generates a total net power output of 349.84 kW. It can be observed from Table 1 that the proposed plant's total energy efficiency is 67.83%.
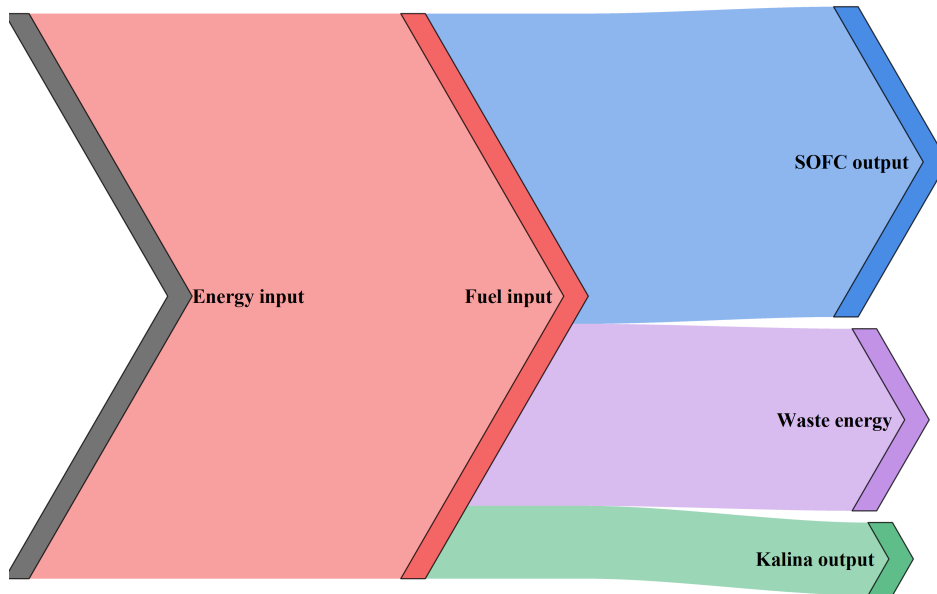
Figure 2: Energy flow of the proposed system

By altering the fuel utilization factor, a sensitivity analysis was conducted on the system, and the total power generated, and energy efficiency of the system are illustrated in Figure 3. The system's maximum power output and energy efficiency were calculated to be 490.6 kW and 70.43%, respectively, which occurred at UF values of 0.6 and 0.9, respectively.
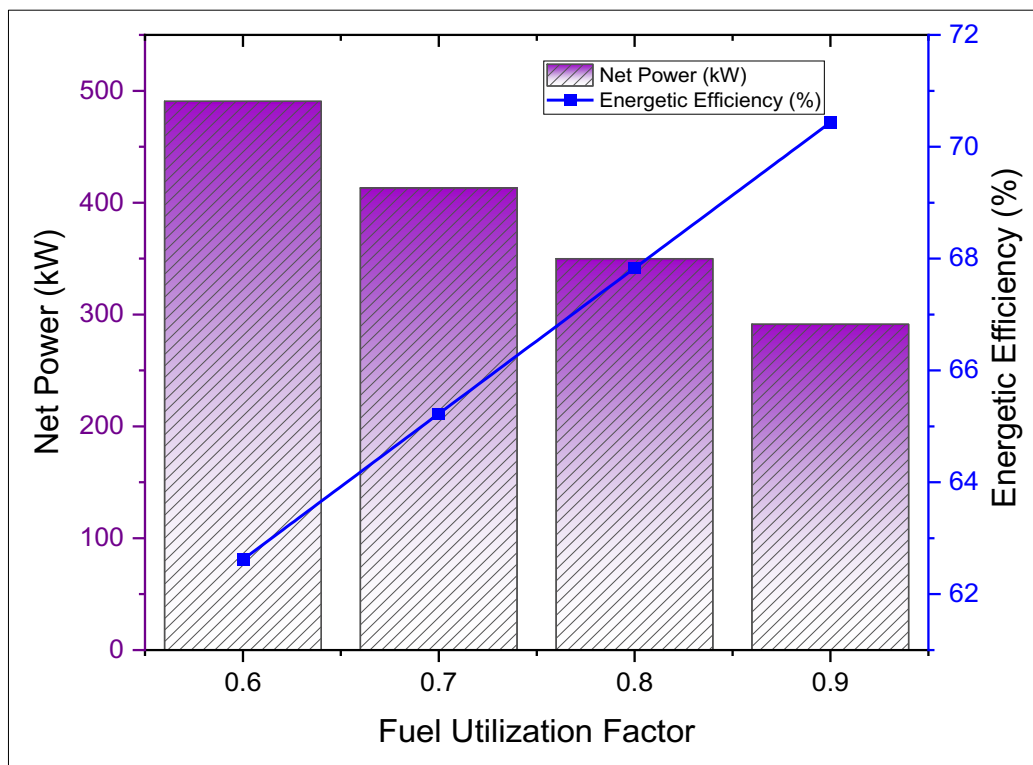
Figure 3: Effect of Fuel Utilization Factor on Net Power output and Energetic Efficiency of the system

Discussions

The results obtained from this study showed that the proposed system is a promising alternative for generating green energy, with an overall energy efficiency over 70%. The combination of the SOFC and the Kalina cycle offers a highly efficient way of generating electricity from ammonia, a sustainable and green energy source. Ammonia has emerged as a potential fuel for SOFCs due to its high hydrogen content and the ability to be easily stored and transported. Ammonia is also a green alternative to fossil fuels and offers a promising solution for reducing greenhouse gas emissions. This analysis highlights the potential for further optimization of the proposed system to achieve even higher efficiency and power output.

The integration of SOFC with cathode recycling in the proposed system offers several benefits. The cathode recycling mechanism allows for the recovery of the excess oxygen and reduces the need for air supply. This reduces the auxiliary power consumption of the SOFC unit, which was observed to be 5.88 kW in this study. The reduction in auxiliary power consumption increases the overall efficiency of the system and reduces operating costs.

The proposed system offers a promising and efficient approach for generating green energy through the integration of SOFC and Kalina cycle, fueled by green ammonia. The high energy efficiency and power output of the system make it a potential candidate for commercial applications, and further optimization can lead to even higher efficiency and power output. The use of green ammonia as a fuel for the system offers a sustainable alternative to fossil fuels, reducing greenhouse gas emissions and contributing to a greener future.

Conclusions

The proposed green ammonia fuelled combined system integrating solid oxide fuel cell with cathode recycling and Kalina cycle is a promising and efficient approach to generate power from a renewable source. The base case performance results show that the system is able to generate a net power output of 349.84 kW with an overall energy efficiency of 67.83%. The sensitivity analysis shows that the system's performance can be further improved by increasing the fuel utilization factor, which can result in a higher power output and energy efficiency. The system's maximum power output and energy efficiency were calculated to be 490.6 kW and 70.43%, respectively, which occurred at UF values of 0.6 and 0.9, respectively. Overall, this research provides valuable insights into the potential of green ammonia as a fuel and the benefits of integrating various technologies to generate clean energy. The findings of this study can be used to inform the development of more sustainable and efficient power generation systems in the future. Further research is needed to optimize the design of these systems and to investigate their economic viability.

Acknowledgments

References:

[1] Mojaver P, Abbasalizadeh M, Khalilarya S, Chitsaz A. Co-generation of electricity and heating using a SOFC-ScCO2 Brayton cycle-ORC integrated plant: Investigation and multi-objective optimization. International Journal of Hydrogen Energy. 2020;45:27713-29.
[2] Eisavi B, Chitsaz A, Hosseinpour J, Ranjbar F. Thermo-environmental and economic comparison of three different arrangements of solid oxide fuel cell-gas turbine (SOFC-GT) hybrid systems. Energy Conversion and Management. 2018;168:343-56.

[3] Chen J, Liang M, Zhang H, Weng S. Study on control strategy for a SOFC-GT hybrid system with anode and cathode recirculation loops. International Journal of Hydrogen Energy. 2017;42:29422-32.

[4] Wang X, Lv X, Weng Y. Performance analysis of a biogas-fueled SOFC/GT hybrid system integrated with anode-combustor exhaust gas recirculation loops. Energy. 2020;197:117213.

[5] Kumar P, Choudhary T, Ansari MZ. Thermodynamic assessment of a novel SOFC and intercooled GT integration with ORC: Energy and exergy analysis. Thermal Science and Engineering Progress. 2022;34:101411.

[6] Victor RA, Kim J-K, Smith R. Composition optimisation of working fluids for Organic Rankine Cycles and Kalina cycles. Energy. 2013;55:114-26.

[7] Mojaver P, Khalilarya S, Chitsaz A, Assadi M. Multi-objective optimization of a power generation system based SOFC using Taguchi/AHP/TOPSIS triple method. Sustainable Energy Technologies and Assessments. 2020;38:100674.

[8] Roy D. Performance evaluation of a novel biomass-based hybrid energy system employing optimisation and multi-criteria decision-making techniques. Sustainable Energy Technologies and Assessments. 2020;42:100861.

[9] Alns A, Sleiti AK. Combined heat and power system based on Solid Oxide Fuel Cells for low energy commercial buildings in Qatar. Sustainable Energy Technologies and Assessments. 2021;48:101615.

[10] Rupiper LN, Skabelund BB, Ghotkar R, Milcarek RJ. Impact of fuel type on the performance of a solid oxide fuel cell integrated with a gas turbine. Sustainable Energy Technologies and Assessments. 2022;51:101959.

[11] Zhang J, Cui P, Yang S, Zhou Y, Du W, Wang Y, et al. Thermodynamic analysis of SOFC–CCHP system based on municipal sludge plasma gasification with carbon capture. Applied Energy. 2023;336:120822.

[12] Mei S, Lu X, Zhu Y, Wang S. Thermodynamic assessment of a system configuration strategy for a cogeneration system combining SOFC, thermoelectric generator, and absorption heat pump. Applied Energy. 2021;302:117573.

[13] Quach T-Q, Giap V-T, Keun Lee D, Pineda Israel T, Young Ahn K. High-efficiency ammonia-fed solid oxide fuel cell systems for distributed power generation. Applied Energy. 2022;324:119718.

[14] Mohammad shafie M, Ali r, Mehrpooya M. Investigation of an electrochemical conversion of carbon dioxide to ethanol and solid oxide fuel cell, gas turbine hybrid process. Renewable Energy. 2022;184:1112-29.

[15] Ouyang T, Zhang M, Qin P, Liu W, Shi X. Converting waste into electric energy and carbon fixation through biosyngas-fueled SOFC hybrid system: A simulation study. Renewable Energy. 2022;193:725-43.

[16] Kasaeian A, Hadavi H, Amirhaeri Y, Pourfayaz F. Thermodynamic analysis of a wood chips-based cycle integrated with solid oxide fuel cell. Renewable Energy. 2022;195:1174-93.

[17] Song M, Zhuang Y, Zhang L, Li W, Du J, Shen S. Thermodynamic performance assessment of SOFC-RC-KC system for multiple waste heat recovery. Energy Conversion and Management. 2021;245:114579.

[18] Gholamian E, Zare V. A comparative thermodynamic investigation with environmental analysis of SOFC waste heat to power conversion employing Kalina and Organic Rankine Cycles. Energy Conversion and Management. 2016;117:150-61.

Analysis of two bed adsorption heat pump with a stratified storage to supply heating demands in a house for retrofitting of multi-family buildings

Alireza Sadeghlu[1*], Ferdinand Schmidt[1]

[1] Karlsruhe Institute of Technology (KIT), Institute of Applied Thermofluidics (IATF)

[*]Corresponding author: alireza.sadeghlu@kit.edu

Abstract

Gas driven heat pumps can contribute to a decarbonization of the building stock. A two-bed adsorption gas heat pump (TAGH) for multi-family buildings has been developed based on validated model. Due to the chosen sorption pair SAPO34/water, the heat pump can provide a temperature lift up to 42 °C, which is not sufficient for domestic hot water (DHW) preparation in stock buildings with circulation systems. Thus, the DHW preparation was achieved in a direct gas burner mode in order to prevent legionella contamination in the DHW circuit. This contribution analyses system aspects of hydraulic integration of a stratified heat storage and adapted controls for achieving two goals. First, a pre-heating of DHW in heat pump mode. Second, an increase in the seasonal system-level gas utilization efficiency (SGUE). In this regard, the analysis consists of three steps. First, the effect of system environment such as weather condition and design parameters have considered. Second, the hydraulic design, which includes the selection of extraction and insertion layers, plays its role in heat consumption and production. Finally, finding proper control strategy is a key factor in the analysis. To further increase of the SGUE, the system hydraulic configuration is redesigned with the help of second thermodynamic efficiency.

Keywords: Two bed adsorption heat pump, stratified storage, heating demands, control strategy, second thermodynamic efficiency, seasonal gas utilization efficienc

Introduction

The primary objective of the AdoSan project was to develop a two-bed adsorption gas heat pump (TAGHP) [1-3]. This was achieved through experimental validation and calibration of its individual components [4]. The specific focus of the project was to supply the heating demand in a space heating circuit, considering the guidelines mentioned in the VDI 4650-2 [5], with a nominal supply temperature of 55°C and a return temperature of 45°C [6]. The researchers sought to improve the gas utilization efficiency of the TAGHP at the system level by integrating various low temperature sources, including a borehole heat exchanger or building exhaust air [7]. The primary focus of the study was to assess the applicability of the two-bed adsorption gas heat pump (TAGHP) in a middle multi-family house (MMFH) [6] setting. In this context, a specialized storage unit called " hydraulic separator " was employed.

The study further evaluated the system's performance and achieved an annual gas utilization efficiency of 1.21 when utilizing a borehole heat exchanger. However, it is important to note that the TAGHP with a SAPO-34/water working pair in sorption mode has limitations in heating water beyond temperatures of 42°C. To fulfill higher temperature requirements, as specified in standards like VDI 4650-2 with 45/55°C [5], the heating process necessitates a "direct heating mode" where the gas burner directly supplies heat, bypassing the adsorption modules.

Given this context, the purpose of the investigation is to explore a system that addresses both water heating and space heating requirements by utilizing a two-bed adsorption gas heat pump (TAGHP). The main objective is to identify an integrated combi storage system and control scheme that enables the TAGHP to efficiently preheat domestic hot water (DHW), while simultaneously achieving gas savings in comparison to the reference configuration where DHW is consistently provided through direct heating mode.

System description

In the overall system configuration of the case study, two main components are considered. Firstly, there is the heat production component, which consists of TAGHPs utilizing both a high temperature source and a low temperature source, specifically a borehole heat exchanger. The TAGHP, composed of two modules, comprises one adsorber and one evaporator/condenser within a single casing. Its primary function is to generate heat. Secondly, there are two heat consumption components: a space heating circuit and a water heating circuit. These components make use of the heat generated by the TAGHP for their respective purposes.

In the case study configuration, there is also a combi-storage with 16 layers that acts as a central point of connection between the heat consumption and heat production components (see Figure1). This combi-storage is designed to store the excess heat and distribute it as needed.

To utilize the high-temperature source of TAGHP for heating the upper part of the combi-storage, a heat exchanger called HX_BRN_Stor is used. It links the combi-storage to the high-temperature source, transferring heat from BRN_HX_HT to the upper part of the tank. Moreover, HX_MTS connects TAGHP to the combi-storage, providing heat for the space heating circuit In Figure 1, it can be observed that the supply temperature is derived from layer 8 and is divided using a three-way valve. Approximately 0.1[kg/s] of the fluid is directed towards BR_HX_MT, while the remaining portion is directed towards HX_MTS. The return fluid from both HX_MTS and BR_HX_MT is then reintroduced into the combi-storage using an ideal inserter. This inserter ensures that the fluid is inserted into the nearest temperature layer within the tank, optimizing the heat distribution process. On the other hand, connecting the heat consumption parts to the combi-storage involves two steps. Firstly, there is a fresh water station (FWS) positioned between the user component and the combi-storage. The supply water is taken from the top layer of the combi-storage and directed to the FWS. The return fluid then flows back to the combi-storage with the help of an ideal inserter.

For the heat consumption component specific to a middle multi-family house (MMFH), it is connected to layer 6 of the combi-storage for the supply fluid and using an ideal inserter for return fluid to the combi-storage. This means that the heat produced by TAGHP and stored in the combi-storage is used to supply and circulate heat within the MMFH.
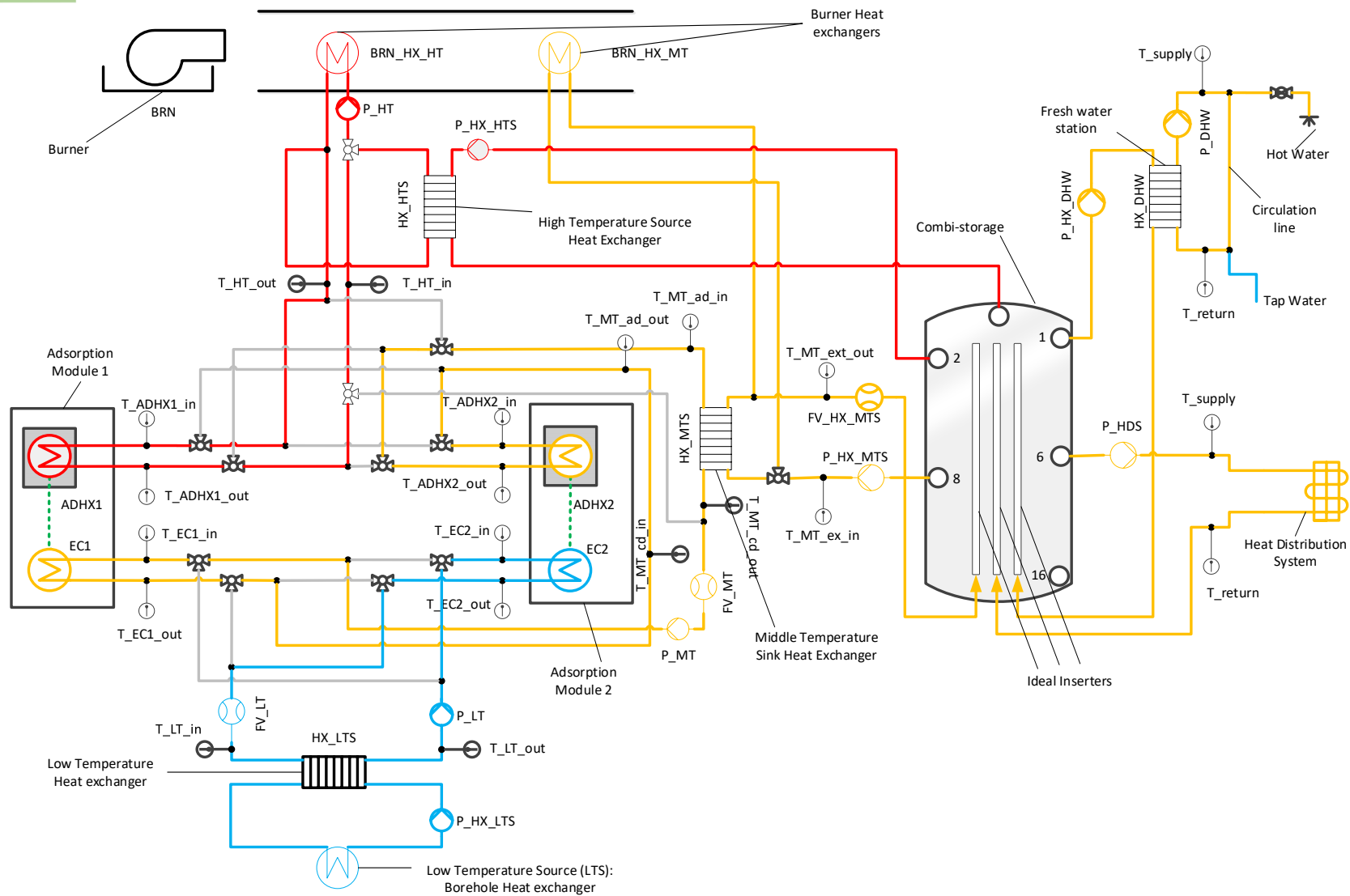
Figure 1: Schematic configuration in system level

Control Strategy

In this case study, there are three levels of control: component level, module level, and system level. At the component level, the mass flow rate of the pump for the user side of the Fresh Water Station (FWS) follows a loading profile every 10 minutes. The FWS serves a multi-family house (MMFH) with 12 apartments (4 with 1 occupant and 8 with 2 occupants). The mass flow rate on the user side of the system exhibits two distinct values. The first value corresponds to instances when tap water is being drawn off, and this value is determined based on the power profile for a multi-family household (MMFH). The second value is applicable when there is no demand for tap water, and in this case, the mass flow rate is set to 0.015 kg/s.

On the storage side, water is extracted from the top layer to create a temperature difference of 5°C in both sides of the heat exchanger. The mass flow rate of the pump in the storage side is controlled by a PI controller to maintain a user-side temperature of 60°C. The PI controller considers the user temperature as the measured value and the set point as 60°C. The output of the PI controller is multiplied by the maximum mass flow rate required for the user side. The return fluid from the FWS is directed to the combi-storage using an ideal inserter to store the lowest return temperature in the bottom part of the storage. In this case, the maximum temperature in the storage is 65°C, while the lowest temperature is around 16°C.

Moving to the other component control level, the space heating circuit is controlled by a PI controller that adjusts the mass flow rate of the supply water, extracted from layer 6, to maintain a room temperature of 20°C. The return water from the radiator is inserted back into the storage using another ideal inserter. For the heat production component, water is extracted from layer 2 and heated in HX_HTS, and then the return hot water is inserted into the top of the storage. Both pumps are controlled at the system level when the temperature of the top layer falls below 65°C.

At the module level, the control strategy of the heat pump (GHP) involves multiple processes such as adsorption, desorption, heat recovery, and direct heating mode. The GHP is activated based on two specific conditions. Firstly, the return temperature from the heating circuit should be below 34°C, considering the characteristics of the working pair SAPO-34/Water. Secondly, the evaporator inlet temperature needs to exceed 7°C. Once the outlet temperature in the adsorber reaches 90°C, the desorption process is ceased, and the heat recovery mode is initiated. During this mode, heat is transferred between the two modules to raise the temperature of the adsorption module while simultaneously cooling down the desorption module in preparation for the subsequent cycle. In the direct heating mode, the BRN_HX_HT is directly connected to the HX_MTS. This mode is activated when the power supplied to the space heating circuit falls below the power demanded. In such cases, the TAGHP exclusively focuses on heating up the storage using the high-temperature source until the supplied heat exceeds the heating demand. At the system level, the priority is to maintain a user temperature of 60°C. If the temperature in layer 1 falls below 63°C, the system prioritizes supplying the water heating circuit over the space heating circuit.

Discussion and Results

Figure 2 illustrates the RC (Resistor-Capacitor) diagram, providing a visual representation of the thermodynamic processes and heat transfer within the TAGHP system. In this diagram, each capacitor corresponds to the thermal mass of the materials, while each resistor represents the specific heat transfer mechanism, including conduction or convection. The diagram helps to understand the flow of energy and identify the various components involved. To further analyze the system's efficiency and identify areas of irreversibility, Table 1 provides a comprehensive list of factors and phenomena contributing to losses within each component of the TAGHP. This information enables a detailed assessment of the system's performance. In addition, a mathematical model has been implemented in Dymola to evaluate and quantify the system's overall efficiency and behavior. This modeling approach allows for in-depth analysis and optimization of the TAGHP system.
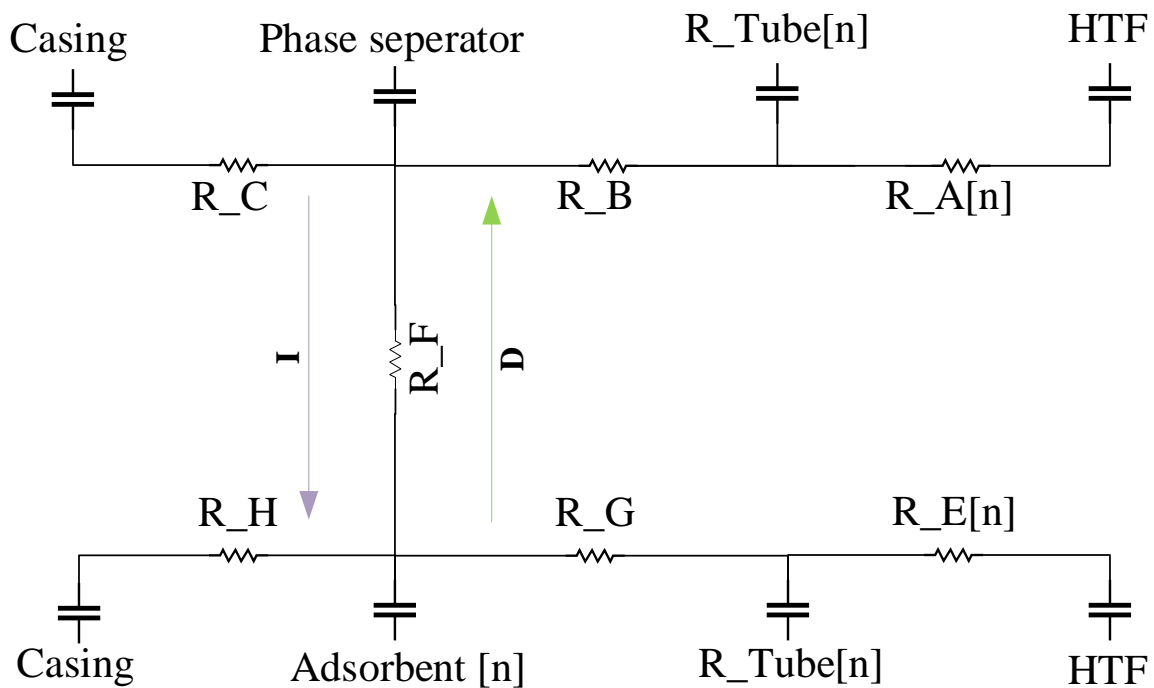
Figure 2. RC Diagram of the adsorber and Evaporator/Condenser

Table 1	
Ireversibility source originate from	
A	Mass and heat transfer between HTF and tube in Evaporator/Condenser
B	Heat transfer between Tube and Phase Separator
C	Heat transfer between Phase Separator and Casing
D	Desuperheat in Evaporator
E	Mass and heat transfer between HTF and tube in Adsorber
F	Heat transfer between Adsorber and Evaporator/Condenser
G	Heat transfer between working pair and Tube
H	Heat transfer between Tube and Casing
I	Superheat in Adsorber

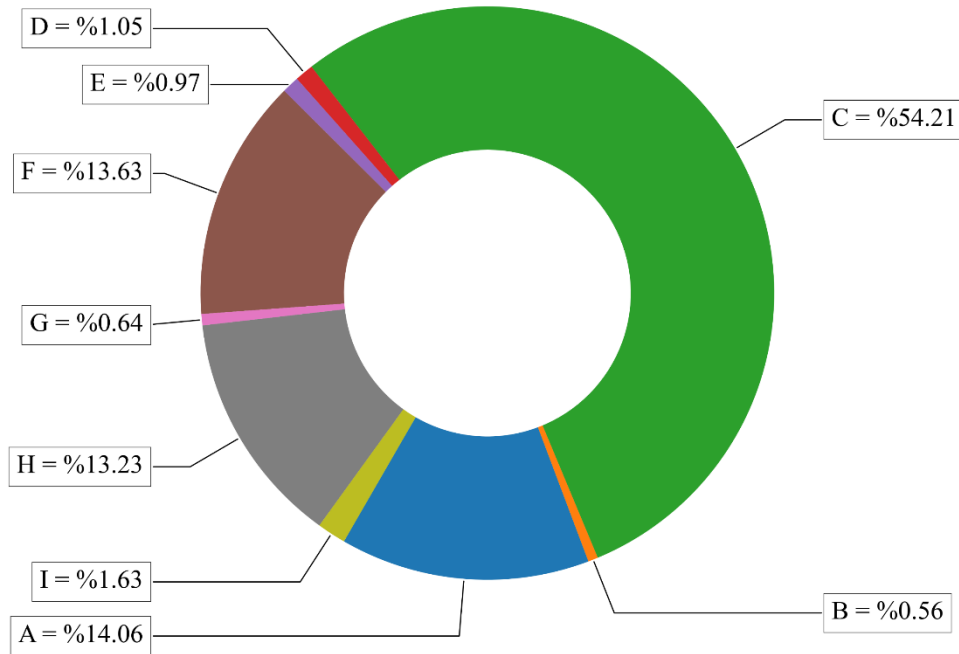Relative Irreversibility for Two-Bed Adsorption Gas Heat Pump

Figure 3: Ralative Irreversibility for various parts in Two-Bed Adsorption Gas Heat pump (TAGHP)

Figure 3 displays the annual relative irreversibilities for different parts of two bed adsorption gas heat pump.

It is clear that the largest source of irreversibility in the TAGHP system arises from the mass and heat transfer processes occurring between the Heat Transfer Fluid (HTF) and the tubes in the Adsorber. This particular aspect contributes significantly to the overall irreversibility within the system. Furthermore, the second-largest portion of relative irreversibility can be attributed to the presence of a finite temperature difference between the adsorber and the evaporator/condenser, as well as between the working pair and the tube. Additionally, the mass and heat transfer processes occurring between the HTF and the tubes, specifically within the evaporator and condenser heat exchanger pipes, play a significant role in comparison to other sources of irreversibility in the overall annual relative irreversibilities of the system.

$$RI = \dfrac{\dot{S}_{gen,i}}{\dot{S}_{gen,total,Module}}$$	(1)
$$\eta_{TAGHP} = \int_{0}^{365} \frac{p_{out}}{p_{in}} dt$$	(2)
$$\eta_{TAGHP} = \int_{0}^{365} \frac{p_{AGHP\_to\_stor\_for\_whc} + p_{AGHP\_to\_stor\_for\_shc}}{p_{in,ncv}} dt$$	(3)

$$\eta_{system} = \int_0^{365} \frac{p_{stor\_to\_whc} + p_{stor\_to\_shc}}{p_{in,ncv}} dt$$	(4)
$$\eta_{storage} = \int_0^{365} \frac{p_{stor\_to\_whc} + p_{stor\_to\_shc}}{p_{AGHP\_to\_stor\_for\_whc} + p_{AGHP\_to\_stor\_for\_shc}} dt$$	(5)
$$\dot{Ex}_i = \dot{m} * (h_i - h_0 - T_0(s_i - s_0))$$	(6)
$$\psi_{storage} = \frac{Ex_{output}}{Ex_{input}} = 1 - \frac{X_l + I}{Ex_{input}}$$	(7)
$$\psi_{storage} = 1 - \int_0^{365} \frac{\left(1 - \frac{T_0}{T_{ave,stor}}\right) p_{stor,loss} + T_0 \dot{S}_{gen}}{\dot{Ex}_{AGHP\_to\_stor\_for\_whc} + \dot{Ex}_{AGHP\_to\_stor\_for\_whc}} dt$$	(8)

| Table 2	
$\dot{S}_{gen,i}$	Rate of Entropy generation in each component
$\dot{S}_{gen,total,Module}$	Sum of Entropy generation rates in condenser/evaporator and adsorber
$p_{AGHP\_to\_stor\_for\_whc}$	Power insert to the storage from HX_HTS to supply power for water heating circuit
$p_{AGHP\_to\_stor\_for\_shc}$	Power insert to the storage from HX_MTS to supply power for space heating circuit
$p_{stor\_to\_whc}$	Power insert to the water heating circuit from storage
$p_{stor\_to\_shc}$	Power insert to the space heating circuit from storage
$p_{in,ncv}$	Power source in net caloric value
$\dot{Ex}_{AGHP\_to\_stor\_for\_whc}$	Rate of Exergy transfer by mass to the storage from HX_HTS to supply power for water heating circuit
$\dot{Ex}_{AGHP\_to\_stor\_for\_whc}$	Rate of Exergy transfer by mass to the storage from HX_MTS to supply power for space heating circuit
X_l	Exergy loss through heat loss
I	Entropy loss through Heat and Mass transfer inside of the storage
$T_{ave,stor}$	Average storage temperature
$p_{stor,loss}$	Power loss from the storage
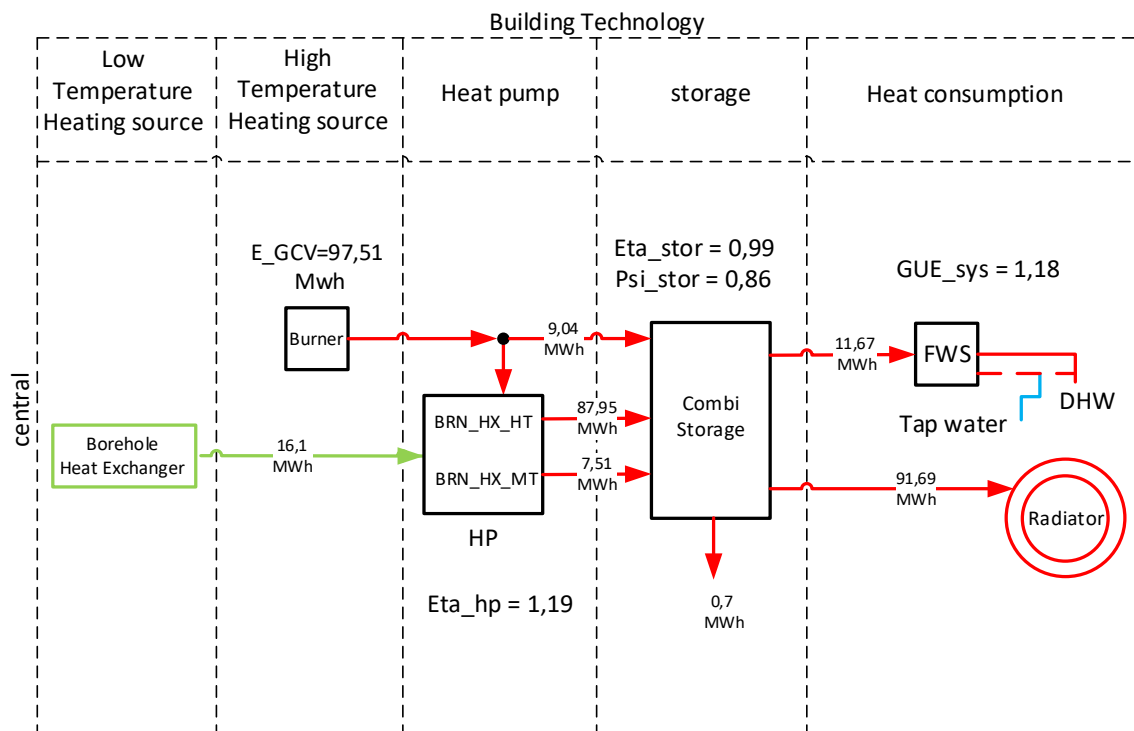
Figure 4: Annual energy flow in case study

The Annual Energy Flow diagram in Figure 4 provides a comprehensive overview of the energy production and consumption within the system. It clearly illustrates the energy generated by the Adsorption Gas Heat Pump (AGHP) and the burner, as well as the energy consumed by the various components. One of the primary objectives of this research is to pre-heat the water for the water heating circuit using the AGHP. Figure 4 highlights that the HX_HTS heat exchanger transfers 9.04 MWh of energy to the upper part of the storage tank, which is then utilized for the water heating circuit. However, the annual energy demand of the water heating circuit is 11.67 MWh, indicating a shortfall in energy supply. To bridge this gap, the AGHP steps in and supplies the remaining energy required for the water heating circuit.

The performance of both the system and the AGHP is assessed using two key parameters: the first law of thermodynamics and the second law of thermodynamics. The first law efficiency considers the net caloric value of the input gas power to determine the efficiencies of the system and the AGHP. On the other hand, the second law of thermodynamics considers the ratio of exergy output to exergy input, providing insights into the system's thermodynamic performance.

Additionally, to gain a more comprehensive understanding of the system's performance, the annual storage efficiencies have been calculated. These efficiencies, depicted in Figure 4 and Table 3, provide valuable insights into how effectively the system stores and distributes heat over the course of a year. By considering these storage efficiencies, a deeper understanding of the system's overall performance can be obtained.

Table 3	
Efficiency	Value [-]
$\eta_{system,annual}$	1.18
$\eta_{TAGHP,annual}$	1.19
$\eta_{storage,annual}$	0.99
$\psi_{storage,annual}$	0.86

Figure 5 provides important temperature information for each layer, including the minimum, maximum, quartile, and median values. In this case study, the return fluid from each component is directed into the storage tank using an ideal inserter, except for the component that heats the upper part of the tank. The supply water for the high temperature source is obtained from layer 2, while the return temperature is directed to the top of the storage tank. Layer 1 represents the supply temperature for the Water Heating Circuit, whereas layer 6 corresponds to the supply temperature for the Space Heating Circuit. Layer 8 supplies the water for the GHP, enabling the utilization of the condenser and adsorption process heat. It's worth noting that the lowest temperature of the return fluid from the fresh water station determines the bottom temperature of the storage tank, and this temperature is also shown in figure 5.
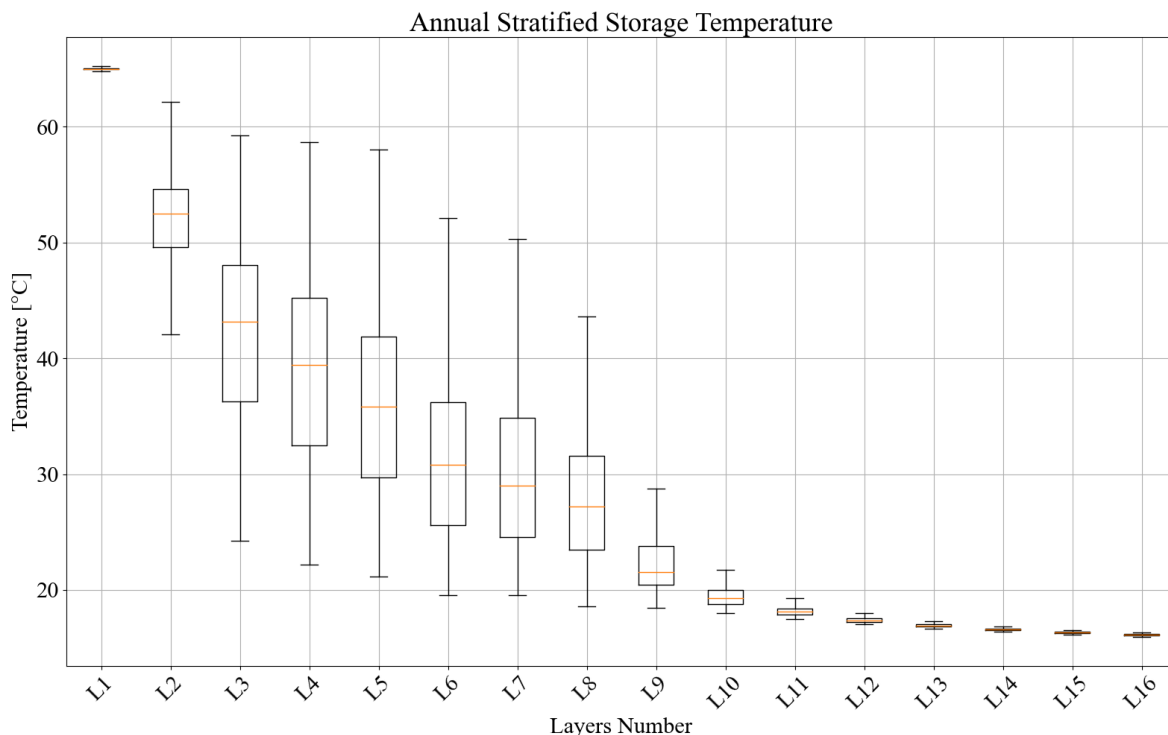

Figure 5: Annual storage temperature in different layers.

To prevent Legionella contamination in the water heating circuit, the system incorporates circulation to maintain a temperature of 55°C for the water inside the pipes when there is no water consumption. As a result, as shown in figure 6, the annual water temperature on the user side of the fresh water station (FWS) is consistently around 60°C. This measure helps ensure the water remains at a temperature that discourages the growth of Legionella bacteria.
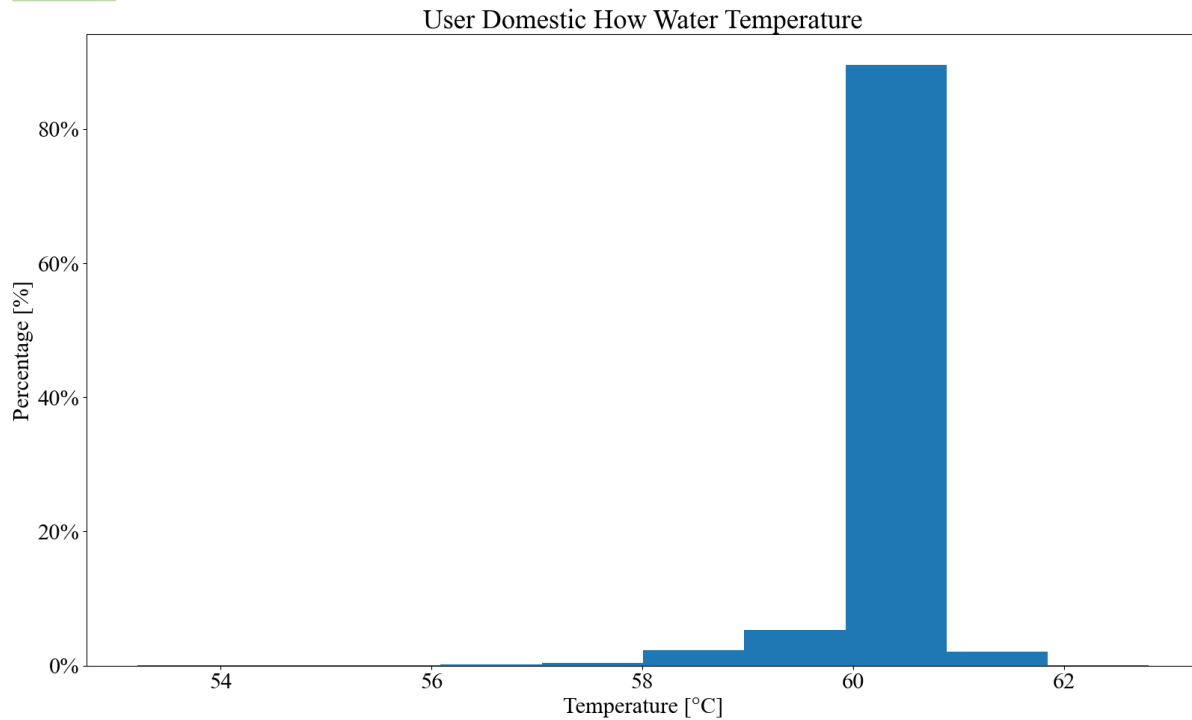
Figure 6: Supply temperature to the user in water heating circuit

Figure 7 presents the correlation between room temperature and outside temperature throughout the span of one year in Potsdam. The graph depicts this relationship by using lighter colors to indicate instances when the room temperature remains relatively stable at around 20°C, particularly during the cold season when the outside temperature drops below 15°C. It is worth noting that the annual simulation of the case study does not consider the presence of air conditioning. Therefore, as the outside temperature rises, the room temperature also experiences a corresponding increase.
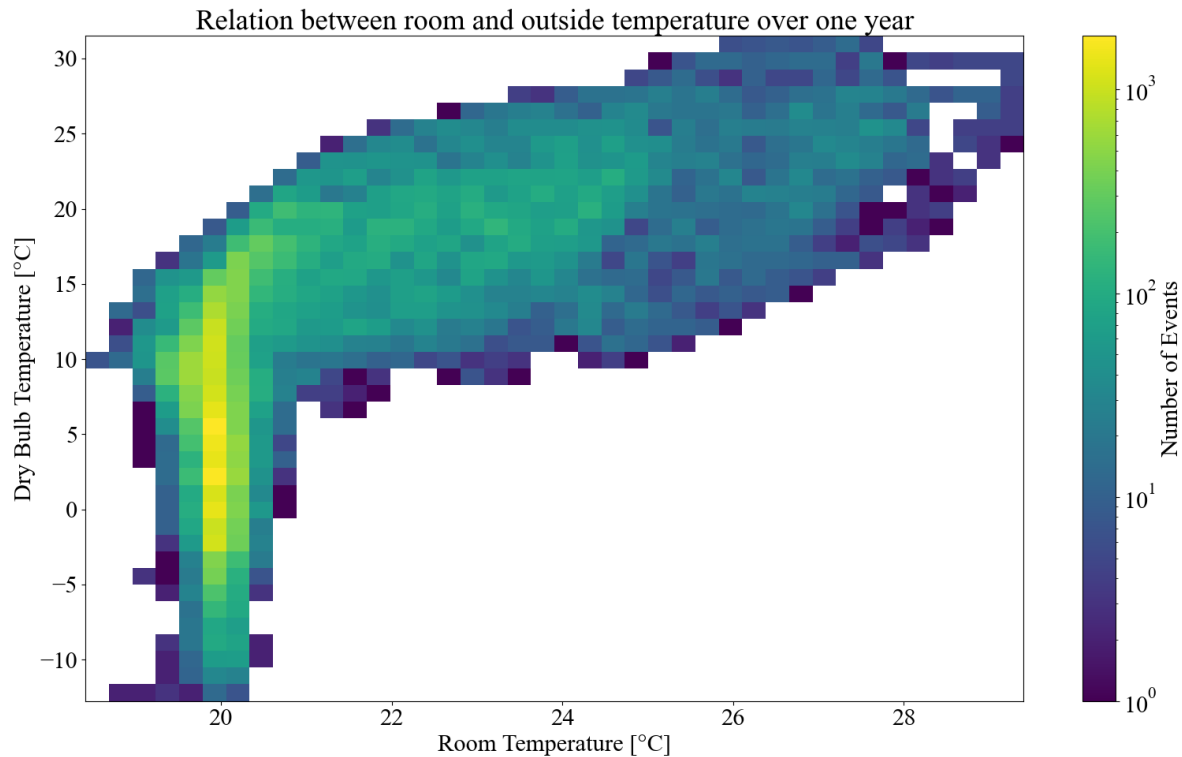
Figure 7: Change of room temperature with respect to the outside temperature over one year

Acknowledgements

References

[1] Wittstadt, U., Füldner, G., Laurenz, E., Warlo, A., Große, A., Herrmann, R., Schnabel, L., Mittelbach, W., "A novel adsorption module with fiber heat exchangers:
Performance analysis based on driving temperature differences", Renewable Energy, 2017.

[2] Freni, A., Bonaccorsi, L., Calabrese, L., Caprì, A., Frazzica, A., Sapienza, A., "SAPO-34 coated adsorbent heat exchanger for adsorption chillers", Applied Thermal Engineering, 2015.

[3] Bendix, P., Füldner, G., Möllers, M., Kummer, H., Schnabel, L., Henninger, S., Henning, H. M., "Optimization of power density and metal-to-adsorbent weight ratio in coated adsorbers for adsorptive heat transformation applications", Applied Thermal Engineering, 2017.

[4] Riffel, D. B., Wittstadt, U., Schmidt, F. P., Núñez, T., Belo, F. A., Leite, A. P. F., Ziegler, F., "Transient modeling of an adsorber using finned-tube heat exchanger", International Journal of Heat and Mass Transfer, 2010.

[5] *Kurzverfahren zur Berechnung der Jahresheizzahl und des Jahresnutzungsgrads von Sorptionswärmepumpenanlagen Gas-Wärmepumpen zur Raumheizung und*

Warmwasserbereitung, VDI 4650 Blatt 2, Verein Deutscher Ingenieure, Jan., 2013.

[6] Andersen, O., Dörr, H., Füldner, G., Groddeck, P., Herrmann, R., Herrmann, S., Kostmann, C., Sadeghlu, A., Schmalzried, H., Schmidt, F., Velte, A., Volmer, R., Wittstadt, U., *LowEx-Konzepte für die Wärmeversorgung von Mehrfamilien-Bestandsgebäuden; Entwicklung einer GasAdsorptionswärmepumpe für die Bestandssanierung: gemeinsamer Abschlussbericht AdoSan-LXB: Berichtszeitraum: 01.08.2018-28.02.2022 (FKZ 03ET1554A, B, C, E und F), 01.08.218-30.06.2022 (FKZ 03ET1554D), [Online], Available*: **https://www.tib.eu/de/suchen/id/TIBKAT%3A182328843X**.

[7] Velte, A., Laurenz, E., Leisner, S., Weber. J., Wittstadt, U., Füldner, G., "Experimental Results of a Gas Fired Adsorption Heat Pump and Simulative Prediction of Annual Performance in a Multi-Family House", Applied Thermal Engineering, 2022.

Retrofit strategy for greenhouse gas reduction in institutional buildings

Milad Ebadi[1], Bernard Chan[2], and Majid Bahrami[1]*

1) *Laboratory for Alternative Energy Conversion* (LAEC), School of Mechatronic Systems Engineering,

Simon Fraser University, Surrey, BC V3T 0A3, Canada

2) *Maintenance and Services, Facility Service*,

Simon Fraser University, 8888 University Dr, Burnaby, BC V5A 1S6

*Corresponding author email address: mbahrami@sfu.ca

Introduction

More than 50% of greenhouse gas emission in the City of Vancouver is due to the heating of buildings [1]; with a growing trend due to extreme weather events caused by Climate Change. Simon Fraser University (SFU) has buildings constructed from the 1960s to 2020 scattered in three regions of Metro Vancouver. A large number of these buildings are equipped with out-of-date facilities, piping, and insulations, whose operations may be also inefficiently scheduled. There is a potential to decelerate the increasing rate of energy consumption and as a result the greenhouse gas emissions and air pollution. An intuitive but costly approach to improve the existing buildings is to replace them with new green buildings. However, due to the investment limit, no more than 1% to 3% of the buildings can be replaced by green buildings annually A popular way to improve energy performance is building energy efficiency retrofit (BEER) [2], which not only can provide energy savings with less investment than replacement, but also, can reduce the fossil fuel consumption, greenhouse gas emissions as well as improving the building market value [3]. However, as there exist several retrofit solution scenarios and numerous variables, it will be difficult to solely design the systems based on experience. As such, there is a need to use a systematic approach to establish an optimized solution.

In this study, our goal is to design a custom Optimized Building Retrofit Strategy Tool (OBRST) focusing on regenerative ventilation systems for the HVAC systems to be used in the targeted existing SFU buildings aiming to reach the 2025 target for greenhouse gas reduction. The proposed approach uses several theoretical models to simulate the heating, cooling, and ventilation load based on the building geometry and geographical location, then, using the models, the emission reduction for each retrofit scenario will be evaluated. Finally, using an optimization tool the optimized combination of the scenario for a case study building will be presented.

Methods and data collected

A systematic approach has been adopted to perform this study, which consists of three steps: i) building information collection, ii) building modeling, and iii) feasible scenario selection.

SFU Discovery 2 Building: characteristic and history

The building is located at the SFU's Burnaby campus, 8900 Nelson Way, Burnaby, BC V5A 4B5, shown in Fig. 1 a. The building was constructed in 1990 and has a lot area of 1,800 m^2 and a total floor area of 3,000 m^2. It has two floors and a mechanical room located at the rooftop of the building. The outside envelope of the building is a metal plate colored light brown with thermal insulation inside them, and 25% of the total surface is glazed. The building had two retrofit projects, one in 2006 and another one in 2015. The 2006 retrofit included redesigning the lighting system, HVAC ducting, room redesigning and

1

implementation. Currently, almost 60% of the electricity consumption and 95% of natural gas consumption of this building are due to its HVAC system. In terms of emissions, the situation is even worse. The HVAC system is responsible for 90% of the total yearly emission, where the total emission of the building is 37 ton CO_2 per year. Two condensing boilers are used for the building heating system to generate hot water which is used for i) domestic hot water, ii) heating the ventilation air, and iii) 38 water source heat pumps to heat the building. To cool the building, there is one cooling tower on the roof that cools water for the 38 heat pumps to air condition the building.

Retrofit scenarios

To find feasible retrofit scenarios, we included the following factors in our analysis: i) technology readiness level (TRL), ii) geographical suitability; and iii) market availability and cost. To measure each of the above-mentioned factors, research was performed and consultations were conducted with the experts in the field as well as the suppliers of each technology. The following scenarios were simulated to establish a roadmap to net-zero, i) envelope upgrading, ii) installation of solar photovoltaic panels, iii) use of biomass boiler, iv) heat recovery system, v) heat pump upgrading, vi) CO_2 capturing system, vii) seasonal heat storage, and viii) the following three combinations.

- Heat recovery ventilator (HRV) + seasonal thermal energy storage + heat pump change
- HRV + biomass boiler + upgrading to heat pumps to new generation water sourced heat pump + carbon capture
- HRV + air source heat pump

Building modeling approach

Building model is based on a new modelling approach developed in our lab, based on machine learning, and was presented in our previous publication [4]. The method utilizes the temperature, relative humidity, air quality (particle concentration, CO_2 concentration, humidity and total chemicals concentrations) and electricity consumption of the heat pump using the data gathered from one zone of the building and is generalized the zone consumption to the entire building based on the orientation of the walls, solar zenith, and azimuth angle and plant coverage. The model has been validated using the measured natural gas and electricity consumption of the building by factoring out the non-heating and non-cooling energy demands during monthly energy consumption. Based on the results, the relative difference of less than 10% was observed between the model and collected data. To evaluate the current envelope performance, an Energy-plus Model [5] was also developed and used [6].

Results and outcomes

To validate the data driven modeling results, monthly natural gas and electricity consumption of the building were used as a reference for energy consumption. Based on the results, the monthly predicted consumption overestimates both the electricity and natural gas consumption. Because, the occupancy of the building is not as reported and some zones are unoccupied, we have planned to add CO_2 concentration measurement to the model to make the result more accurate. Even with this uncertainty, the average relative difference of the model is less than 10% for electricity and 12% for natural gas consumption.
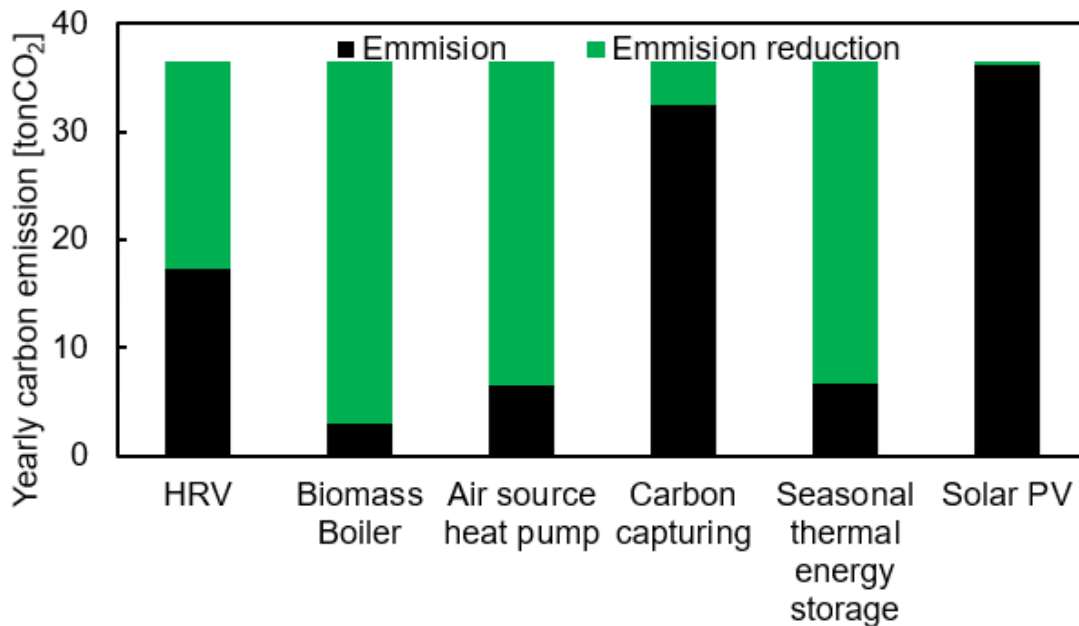
The emission reduction potential for Discovery 2 Building is shown in Fig. 1 b, emission reduction potential are, in order, i) usage of biomass boiler, with 33.5 ton CO_2 reduction per year; ii) air source heat pump, with 30 ton CO_2 reduction per year; iii) seasonal energy storage systems, with 29.8 ton CO_2 reduction per year. The least will be installation of solar PV system (10 kW as a feasible power based on technology and market availability).

These results can be expected due to, i) the electric grid in British Columbia is mostly clean (~90% from hydropower [7]), and ii) high availability of biomass as a fuel. The other parameter that was probed was the cost of emission reduction. Figures 1c and d show the cost (in CAD dollars) of GHG emission reduction per ton for each technology and scenario. The cost of emission reduction per ton of CO_2 is an order of

2

magnitude higher for seasonal battery energy storage and PV. Heat recovery ventilators and biomass plants have a minimum value of almost \$4,000 per ton (based on a 10 kW power plant; quoted by a Canadian supplier, Solarom Inc). Along with the energy reduction scenarios, building application management has also great impact on building energy consumption. Based on a survey, the remote working days in the building is not consistent and there are several air conditioned rooms empty during the working days. Moreover, the zone temperature control of the building is based on the previous application and the current residence scattering cannot make use of zone control system due to scattered departments between zones. Managing the application to make one empty zone each day, can reduce the energy consumption up to 5%.
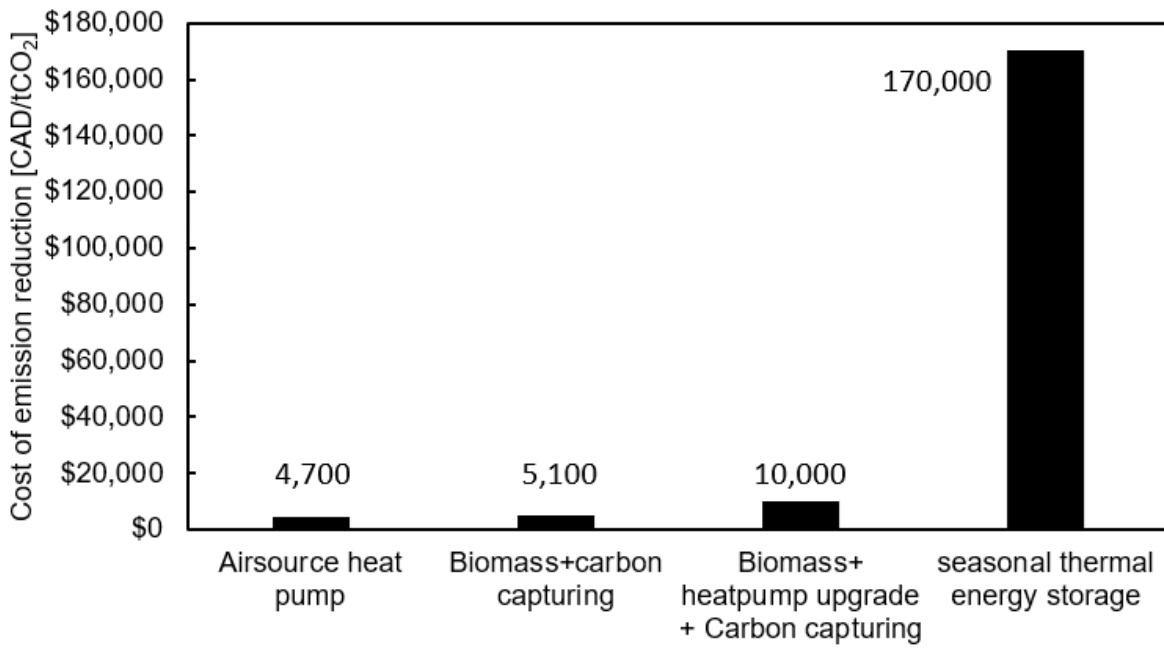

a

b

3
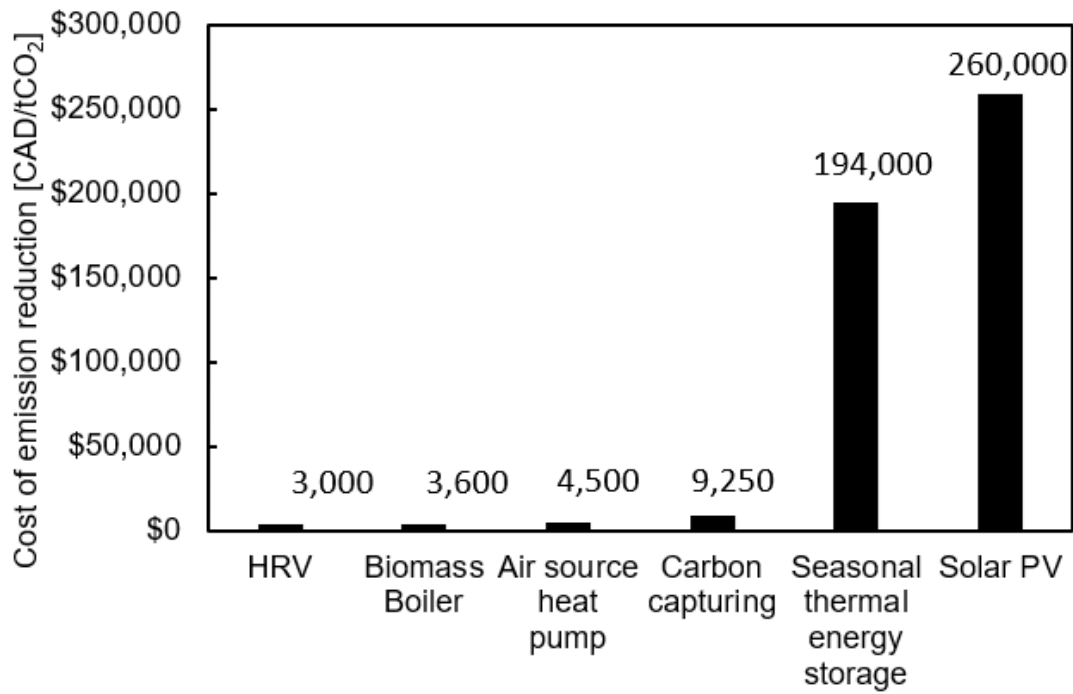
c

d

Figure 1: a) The case study building, SFU Discovery 2 Building. b) Emission reduction potential of each retrofit scenario. c) Cost of emission reduction based on each scenario. d) Cost of emission reduction based on blending of scenarios to reach net zero.

Summary and conclusion

Almost 60% of electricity consumption and 95% of natural gas consumption is dedicated to the heating, ventilation, and air conditioning (HVAC) system in SFU Discovery 2 building. The HVAC system alone is responsible for 90% of the building's total yearly CO_2 emissions, which is 37 tones. The findings of this study can be highlighted as:

1) Biomass boilers have the maximum emission reduction potential at an affordable cost. Furthermore, adding a carbon capturing system to the biomass boiler will eliminate the carbon footprint of the building's electricity usage and make it a net-zero building.

2) Air source heat pumps can reduce the carbon footprint of the building and reduce the emissions to the 2030 targets.

3) Managing the building's working schedules by keeping the remote working days consistent for the occupants and make use of the zone temperature control of the building can affect the building energy performance with negligible cost.

Selected references

1. City of Vancouver, Climate Emergency Action Plan Summary 2020-2025
2. Ma, Z., et al., *Existing building retrofits: Methodology and state-of-the-art.* Energy and buildings, 2012. **55**: p. 889-902.
3. Shao, Y., P. Geyer, and W. Lang, *Integrating requirement analysis and multi-objective optimization for office building energy retrofit strategies.* Energy and Buildings, 2014. **82**: p. 356-368.
4. Wu, Z., B. Wang, and X. Xia, *Large-scale building energy efficiency retrofit: Concept, model and control.* Energy, 2016. **109**: p. 456-465.
5. U.S. Dept. of Energy, EnergyPlus v22.01.00, EnergyPlus, Copyright (c) 1996-2021, available from https://energyplus.net/downloads
6. Milad; Ebadi, Majid Bahrami, *Data-driven Modeling of the City of Surrey District Energy System Heating Load*, in *The Sixth International Symposium on Innovative Materials and Processes in Energy Systems (IMPRES2022).* 2022: Barcelona, Spain.
7. BC hydro, Electricity emission intensity factors for grid-connected entities, available from: https://www2.gov.bc.ca/gov/content/environment/climate-change/industry/reporting/quantify/electricity

5

3rd to 6th of September 2023
The University of Edinburgh, Scotland

Heat Powered Cycles
Conference 2023
Edinburgh

Heat in the new energy system

Molten-salt thermocline thermal energy storage with a temperature booster

S. Funayama[1*], T. Kato[1], S. Tamano[2], K. Mochizuki[3], T. Sugiyama[3], T. Izaki[2], H. Takasu[1] and Y. Kato[1]

[1]Laboratory for Zero-Carbon Energy, Institute of Innovative Research, Tokyo Institute of Technology, 2-12-1-N1-22, O-okayama, Meguro-ku, Tokyo, 152-8550, Japan

[2]Graduate Major in Nuclear Engineering, Department of Transdisciplinary Science and Engineering, Tokyo Institute of Technology, 2-12-1-N1-22, O-okayama, Meguro-ku, Tokyo, 152-8550, Japan

[3]Graduate Major in Nuclear Engineering, Department of Chemical Science and Engineering, Tokyo Institute of Technology, 2-12-1-N1-22, O-okayama, Meguro-ku, Tokyo, 152-8550, Japan

[*]Corresponding author: funayama.s.aa@m.titech.ac.jp

Abstract

Thermocline sensible thermal energy storage is a promising option for large-scale energy storage applications. In this study, a thermocline tank was combined with an indirect thermochemical energy storage (TCES) reactor as a temperature booster during thermal discharge. Molten salt was used as a sensible storage material for the thermocline and heat transfer fluid of the indirect TCES reactor. A TCES composite was synthesized using calcium oxide and silicon-impregnated silicon carbide foam. The molten salt discharged from the thermocline tank was heated from 504 to 566 °C using the exothermic hydration of calcium oxide performed at a pressure of 0.6 MPa, demonstrating the temperature boost operation using the TCES reactor. The proposed hybrid system can potentially offer cost-effective sensible storage with a temperature booster and flexible discharge performance.

Keywords: Thermocline thermal energy storage, Thermochemical energy storage, Molten salt, Calcium hydroxide.

Introduction

Thermal energy storage (TES) has applications in cost-effective large-scale energy storage owing to the low cost of TES media. Furthermore, thermocline sensible storage is inexpensive compared to the two-tank molten salt storage systems. However, sensible heat storage systems require improvements in the flexible discharge temperature; hence, this study combined a thermocline tank with a thermochemical energy storage (TCES) reactor based on a calcium oxide/water reaction system. Herein, we aimed to demonstrate the temperature-boost operation using a TCES reactor.

Materials, systems and methods

Molten salt, known as HITEC [1], was employed as the sensible storage medium in the thermocline tank and heat transfer fluid (HTF) of the TCES reactor. A TCES composite (55 mm in diameter and 1 m in length) was prepared using calcium hydroxide and silicon-impregnated silicon carbide foam [2]. The thermocline tank and the TCES reactor were connected in series (Fig. 1(a)). During thermal discharge, the molten salt flowed from the bottom of the thermocline tank (Fig. 1(b)) and top of the TCES reactor (Fig. 1(c)). Thermocouples were installed inside the thermocline tank and TCES reactor, as shown in Fig. 1(b) and (c), respectively.
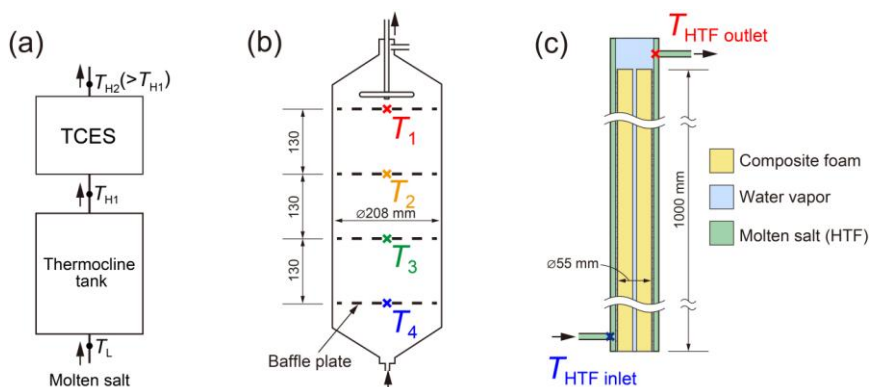
Figure 1 Experimental setup: (a) hybrid TES unit; (b) thermocline tank; (c) indirect fixed-bed TCES reactor.

Discussion and results

The molten salt at approximately 483 °C was stored in the thermocline tank at the beginning of thermal discharge, except for the lowest baffle plate on which T_4 was placed. During thermal discharge, the temperature inside the tank decreased because low-temperature molten salt at approximately 300 °C was supplied from the bottom (Fig. 2(a)). Before reaching the HTF inlet of the TCES reactor, the molten salt from the thermocline tank was preheated to 504 °C using auxiliary heaters. The center temperature of the composite exceeded 600 °C during hydration at a pressure of 0.61 MPa, and $T_{HTF\ outlet}$ attained 566 °C, thereby demonstrating a temperature boost using the TCES reactor.
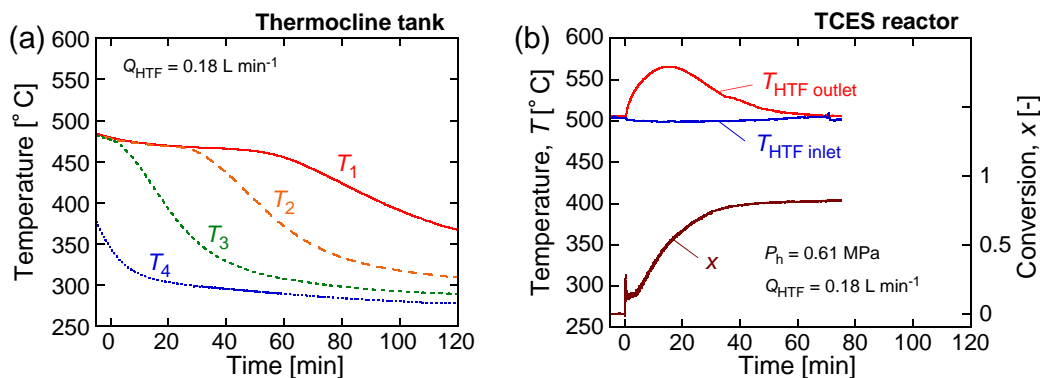
Figure 2 Thermal discharge using the hybrid TES: (a) temperatures inside the thermocline tank; (b) temperatures and hydration conversion of the TCES reactor.

Conclusions

This study investigated a hybrid TES system wherein molten-salt thermocline storage was combined with thermochemical energy storage as a temperature booster during thermal discharge. The temperature boost was successfully performed using the TCES reactor and the molten salt was heated from 504 to 566 °C. The results indicate that the hybrid system can be applied to large-scale TES with a flexible discharge performance.

References:

[1] Olivares, R.I., "The thermal stability of molten nitrite/nitrates salt for solar thermal energy storage in different atmospheres." Solar Energy, 86 (2012), 2576–2583.
[2] Funayama, S., Takasu, H., Zamengo, M., Kariya, J., Kim, S.T., Kato, Y., "Composite material for high-temperature thermochemical energy storage using calcium hydroxide and ceramic foam." Energy Storage, 1 (2019), e53.

Heat Powered Cycles
Conference 2023
Edinburgh

Heat in the new energy system

3rd to 6th of September 2023
The University of Edinburgh, Scotland

Enhanced Solar Evaporation by Superhydrophilic Copper Foam Graphene Coated Inverted 3D Cone

F.Y. Lv[1] *, J. Miao[1], J. Hu[2], D. Orejon[3,4] *

[1]School of Urban Construction and Safety Engineering, Shanghai Institute of Technology, Shanghai, China

[2]School of Perfume and Aroma Technology, Shanghai Institute of Technology, Shanghai 201418, China

[3]Institute for Multiscale Thermofluids, School of Engineering, University of Edinburgh, UK

[4]International Institute for Carbon-Neutral Energy Research (WPI-I2CNER), Kyushu University, 744 Motooka, Nishi-ku, Fukuoka, Japan

*Corresponding author: fengyonglv@alumni.sjtu.edu.cn & d.orejon@ed.ac.uk

Abstract

Solar evaporators are an excellent example where efficient heat utilisation can empower water treatment and desalination contributing to ease one of the pressing United Nations Sustainable Development Goals that of Clean Water and Sanitation for all. Despite the wealth of research carried out on the topic, thermally localised evaporators current production rates are far from theoretical thermodynamic limits. For efficient solar evaporation, water transport from the bulk to the evaporator as well as unimpeded diffusion of the vapour away from the evaporator must be facilitated. In this work, we report on the solar evaporation enhancement owing to the synergistic cooperation of a superhydrophilic copper foam coated and graphene oxide with evaporation rates reported up to 10% higher than current ones. Design reported here benefits this and other heat power cycles where fluid transport in both phases must be maximisied.

Keywords: solar evaporator, phase-change, superhydrophilic copper foam, graphene oxide, synergistic cooperation.

Introduction

Sunlight is unexaustable and provides the necessary energy to power solar evaporators for the production of clean water [1]. The production rates of thermally localized evaporator range from 1 L m^{-2} h^{-1} to 10 L m^{-2} h^{-1}, which are far away from their thermodynamic limit [2]. For efficient utilisiation of the sunlight, thermal localisation avoiding heat loses into the bulk liquid, high light adsorption empowered by the presence of graphene oxide and enhanced water transport via wetting along the superhydrohoilic skeleton and diffusion of its vapour through the pores, are needed. These shortcomings are addressed here by the implementation of a superhydrophilic copper foam skeleton coated with graphene oxide in an inverted cone shape.

Results and Discussion

A 3D inverted conical evaporator was proposed empowering thermal localisation and high light absorption at the interface as sketched in **Figure 1a**. The evaporator comprises a copper foam, which has been further etched to create the micro- and nano-structures as represented in **Figure 1c**. And thereafter coated by graphene oxide by immersion. The functional evaporator was then wrapped up in an air-laid paper ensuring the transport of water towards the evaporaot interface, and monted a top of an insulating layer of air and polyethylene foam separating the evaporator fro mthe bulk water so to meinimise heat loses towards the bulk water as in **Figure 1b.**
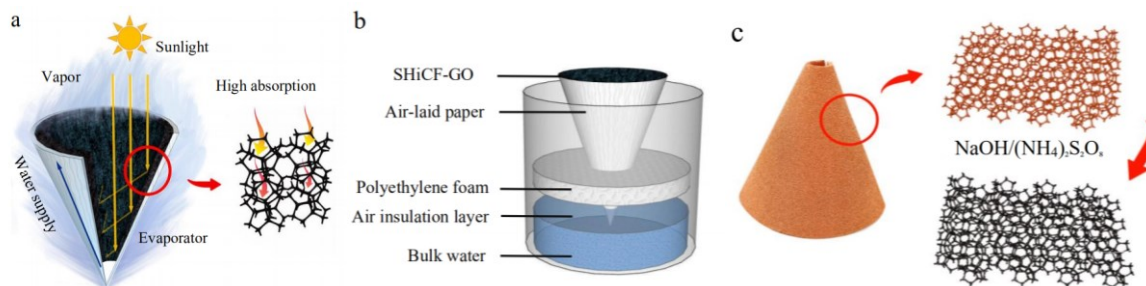
Figure 1 – (a) Schematics of 3D inverted conde solar evaporator proposed with black micro-/nano-structures empowering enhanced water transport and light absorption, **(b)** Schematics of the 3D evaporator including air-laid paper, polyethylene foam and air insulation layers, and bulk water, **(c)** black micro-/nano- superhydrophilic copper foam via wet etching treatment [3].

The different configurations fabricated as superhydrophilic, pristinie copper foam with and withouth air laid paper, and superhydrophilic configurations coated with graphene oxide at different concentrations were tested in the setup represented in **Figure 2a** with evaporation rates results over a period of 9 hours reported in **Figure 2b**. Overall, superhydrophilic configuration enhances wetting and liquid transport while the presence of micro- and nano-structures enhances light absorption. Graphene oxide also enhances light adsorption, water transport and vapour diffusion through the pores. Though immersion in an optimum concentration of 2.5 yields the best results with a maximum efficiency of 93% and a maximum evaporation rate per unit area of 1.71 kg·m^{-2}·h^{-1} under 1 -Sun illumination [3].
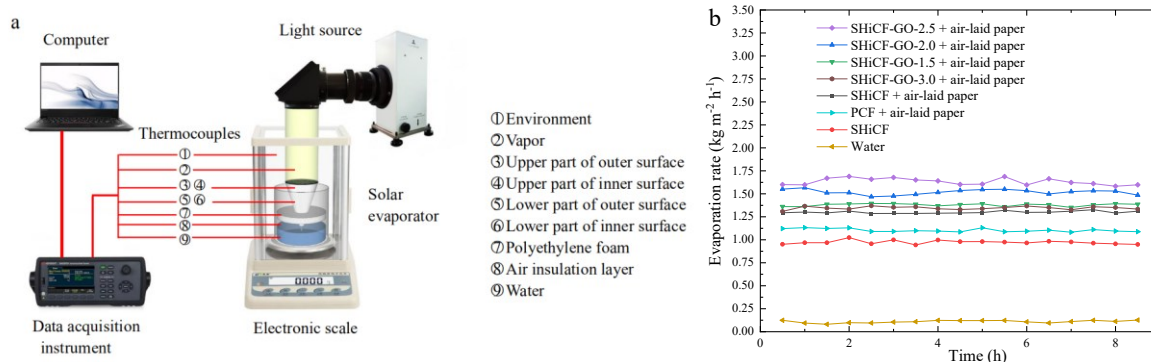
Figure 2 – (a) Solar evaporator experimental setup schematics including light surce, electronic balance, data aquisision system and 9 thermocouples. **(b)** Evaporation rate results in kg m^{-2} h^{-1} for the different configurations studied with the best performance for the SHiCF-GO-2.5.

Summary/Conclusions

The synergistic explotation of the enhanced wetting and liquid transport ensuing in superhycrophilic micro-/nano-structured copper foam and graphene oxide coupled to the unimpeded vapour diffusion through the graphene oxide pores, the insulation of the evaporator from the main bulk water and the high light absorption empowered by the micro-/nano-structures and the graphene oxide is demonstrated with evaporation rates per unit area as high as 1.71 kg·m^{-2}·h^{-1} under 1-Sun illumination. Such synergistic cooperation may be explored in other heat power cycle applications were fluid transport needs to be maximised.

Acknowledgments

References:

[1] Ni, G.; Li, G.; Boriskina, Svetlana V.; Li, H.; Yang, W.; Zhang, T.; Chen, G., "Steam Generation under One Sun Enabled by a Floating Structure with Thermal Concentration", Nature Energy, 2016, **1**, 16126.
[2] Zhang, L.; Xu, Z.; Zhao, L.; Bhatia, B.; Zhong, Y.; Gong, S.; Wang, E. N., "Passive, High-Efficiency Thermally-localized solar desalination", Energy & Environmental Science 2021, **14**, 1771-1793.
[3] Lv, F. Y.; Miao, J.; Hu, J.; Orejon, D. "Three-dimensional solar evaporation enhancement by superhydrophilic copper foam inverted cone and graphene oxide synergistic cooperation", Small 2023, **19**, 2208137.

Experimental and theoretical analysis of alginate-based hydrogel kinetics on sorption and desorption of atmospheric water vapor

M. Calò[1], **V. Gentile**[1]

[1]Energy Department, Politecnico di Torino, C.so Duca degli Abruzzi, 24, 10129, Italy

[*]Corresponding author: matteo.calo@polito.it

Abstract

Hydrogels are highly versatile polymer networks with the remarkable capability to uptake and release substantial amounts of water vapor, making them well-suited for utilization in atmospheric water harvesting applications. This investigation examines an alginate-based hydrogel from both experimental and theoretical perspectives, with a focus on identifying the key factors that contribute to the optimization of sorption/desorption cycles, including water capacity, kinetics, temperature, and vapor diffusion. The impact of the concentration of alginate networks and the reticulation initiator, calcium chloride, was assessed through an experimental investigation in which the material experienced controlled desorption and sorption cycles. The results revealed that higher concentrations of salt and lower levels of alginate within the composition led to enhanced sorption kinetics. The acquired data was subjected to fitting via three distinct models to quantify and compare the transport properties of various samples.

Keywords: Hydrogel, alginate, biopolymer, diffusion.

Introduction

Hydrogels are three-dimensional hydrophilic networks of polymer chains with the remarkable capability to uptake and release substantial amounts of water [1-2]. Due to their properties, hydrogels have been widely used in biomedical applications such as drug delivery [3-4] and tissue engineering [5]. Hydrogels can also be used for water remediation of oil contaminations [6], the removal of heavy metals [7-8], and other pollutants [9].

Currently, extensive research is being conducted on bio-derived hydrogels, to develop composite sorbents with superior hygroscopic properties for applications such as agriculture [10-11]. These hydrogels can reduce water consumption by conditioning the ground to augment water-holding capacity [12-13].

In particular, these hydrogels are being investigated for atmospheric water harvesting, where the biocompatibility of materials is crucial to produce drinkable water from the available moisture in the atmosphere [14-15]. Thermal cycling is utilized for this application, which requires heat input to regenerate the sorbent material. As with other thermally-driven sorption cycles, an optimal trade-off between the sorbent's water capacity and kinetics properties is critical. The regeneration temperature of the sorbent material is a crucial element that greatly impacts the overall energy efficiency of sorption/desorption cycles and diffusion rates. The duration of the sorption/desorption cycles is typically limited by diffusional resistance during both phases, whereas process-level maximization of kinetics is crucial to increase the number of cycles per day, resulting in higher moisture harvesting and water production. This analysis requires the use of the main theories of vapor diffusion through porous media, which involve mathematical modeling to predict and optimize moisture transport [16-17]. On the other hand, experimental techniques such as gravimetric analysis, dynamic vapor sorption, and scanning electron microscopy can also provide valuable information about the sorption and desorption behavior of the hydrogel, helping to improve the efficiency and effectiveness of moisture harvesting and water applications.

This work investigates the potentiality of a calcium alginate (CaAlg) hydrogel employing an experimental approach to evaluate the influence of $CaCl_2$ concentration and the amount of sodium alginate (NaAlg) on the hydrogel's equilibrium water uptakes and respective kinetic performance. CaAlg is a hydrogel obtained through the cross-linking of NaAlg with Ca^{2+} as a linking agent. NaAlg is the sodium salt of alginic acid, a natural polysaccharide extracted from brown seaweeds, and it is commonly used in food, pharmaceuticals, and other industrial applications where gelling agents are required. Ionotropic gelation is the mechanism by which crosslinking occurs between various chains of sodium alginate and Ca^{2+} cations in the hydrogel [18–20]. When the multiple chains of NaAlg come into contact with a solution containing divalent cations (e.g., $CaCl_2$ water solution contains Ca^{2+} ions) the Na^+ present in the chain is substituted with the cation. The presence of Ca^+ initiates the generation of free radicals that react with the crosslinking agent, forming a crosslinked polymer network usually called "egg-box" structure [21]. This analysis entails conducting experimental tests to determine the water vapor capture and release rates during the sorption and regeneration of the material and subsequently utilizing Fickian diffusion theory and the Linear Driving Force potential to derive and quantify the diffusion coefficients of the different hydrogel samples and formulations.

Materials and Methods

Sample Preparation and Testing

Following the aforementioned reaction, a setup was devised wherein a mixture of sodium alginate (NaAlg) and deionized water was dripped into a bath solution of calcium chloride ($CaCl_2$), resulting in the formation of beads comprising the final polymer. This composition was designed to isolate and assess the impact of only two parameters, NaAlg concentration and $CaCl_2$ concentration, based on the material preparation procedure.

Four different samples of NaAlg gel were prepared, mixing the mass of NaAlg with a fixed amount of deionized water (150 mL), obtaining two sets of samples respectively with 1%wt and 2%wt of NaAlg concentration. To obtain a homogeneous solution, the components were mixed with a magnetic stirrer at 500 rpm for two hours and then degassed under a vacuum between 200-500 mbar for 20 minutes. In parallel, 4 different $CaCl_2$/water solutions were prepared using 3 L of deionized water, two with 5%wt and the other two with 10%wt of anhydrous $CaCl_2$ (99% purity). The solution was mixed with a magnetic stirrer at 3000 rpm until the heat of the exothermic reaction was completely rejected to the environment, obtaining a final solution temperature equivalent to the lab environment. The NaAlg was ejected with a peristaltic pump through a 2 mm nozzle, dropping spheres of the gel directly into the reticulation bath. Once the gel interacts with the bath, the reticulation reaction occurs immediately for the outer surface of the sphere, preserving the geometry of the bead, while the complete reticulation of the internal part is constrained by the diffusion of Ca^{2+} ions through the radius of the beads. Then, to obtain a stabilized configuration, the solution was conventionally let rest for 24h. The resulting beads of CaAlg were drained and deeply rinsed with deionized water to remove the excess solution from the external surface. Finally, the beads were dried at 70 °C for 24 h removing the excess water resulting from their preparation. Four different samples were produced: sample S1 with NaAlg at 1%wt and $CaCl_2$ at 5%wt; sample S2 with NaAlg at 1%wt and $CaCl_2$ at 10%wt; sample S3 with NaAlg at 2%wt and $CaCl_2$ at 5%wt; sample S4 with NaAlg at 2%wt and $CaCl_2$ at 10%wt. Figure 1 reports a group of magnifications of the final result focused on the outer surface and the transversal section of sample S2, obtained through an FEI Quanta Scanning Electron Microscope. For each sample, the experimental tests followed the same procedure to evaluate both the maximum equilibrium water uptake at fixed conditions of regeneration/adsorption and the respective kinetics during both stages. Samples were first conditioned in a closed environment at 21°C and 50% of relative humidity, for more than 24 h to reach equilibrium with the conditioning

Heat Powered Cycles
Conference 2023
Edinburgh

Heat in the new energy system

3rd to 6th of September 2023
The University of Edinburgh, Scotland

environment. Then samples were regenerated at 100 °C and ambient vapor pressure, in a thermal balance (KERN DBS60-3, with a linearity error of 3 mg) to evaluate mass variation during the transient, for 180 minutes. Right after the regeneration the sample was conditioned again in the closed environment and weighed every 10 minutes per 6 times, then every 15 minutes per 8 times, and finally every 30 minutes per 4 times, covering an entire period of 5 hours. This experimental procedure was repeated for each sample and results are reported in terms of water uptake in Figure (2).

Data Analysis Procedures

Experimental tests were analyzed using two different theoretical approaches: the Fickian diffusion (FD) theory and the Linear Driving Force (LDF) potential.
The FD model is based on the empirical observation of diffusive processes characterized by a proportionality between the mass flux J [kg/(m^{2}s)] and the opposite of the gradient of concentration C [kg/m^3] of a substance, fluid or gas, over a direction n, and the diffusivity D [m^2/s] of the diffusing substance in a specified medium [17]. Under the hypotheses of isotropic material, constant and not deformable volume, isothermal process, independency of diffusivity over time, and geometry with spherical symmetry (quantities do not vary with the angular coordinates, but only along the radius r [m]), the formulation of variation of concentration over time is:

$$\frac{\partial C}{\partial t} = \nabla \cdot (D\nabla C) = D \cdot \left(\frac{\partial^2 C}{\partial r^2} + \frac{2}{r} \cdot \frac{\partial C}{\partial r} \right) \tag{1}$$

Given the big difference between the diffusivity of the same substance in free air when compared to a porous sorbent (e.g., the diffusivity of water vapor in the air is around 2×10^{-5} m^2/s, while this value dramatically drops down to the order of 10^{-11} m^2/s when the medium is silica gel [22]) the boundary layer generated by the diffusion around the sorbent sphere can be neglected. Therefore, the most external surface of the sorbent brings immediately to the bulk concentration of the surrounding environment. As a consequence and in addition to the other mentioned hypotheses, the outer layer is considered in equilibrium with gas-side concentrations.
When the gas-side volume is sufficiently large, the presence of the adsorbent does not influence the gas concentration, which can be considered constant (C_∞), and the same concentration is found at the radius $r = R_p$ (radius of the particle of volume V_p). With the hypothesis of an initial uniform concentration different from zero, the initial and boundary conditions associated to eq. (1) are: $C|_{r,t=0} = C_0$; $C|_{r=R_p,t} = C_\infty$; $\left.\frac{\partial C}{\partial r}\right|_{r=0} = 0$. The solution is [17]:

$$C(r,t) = C_0 + (C_\infty - C_0) \cdot \left\{ 1 + \frac{2R_p}{\pi r} \cdot \sum_{n=1}^{\infty} \left[\frac{(-1)^n}{n} \cdot \sin\left(\frac{\pi n r}{R_p}\right) \cdot e^{-\pi^2 n^2 \left(\frac{D \cdot t}{R_p^2}\right)} \right] \right\} \tag{2}$$

Within eq. (2), the concentration depends on time and space. For practical applications the detailed knowledge of the spatial distribution is less useful than the total amount within the particle volume. For this reason, it is more convenient to formulate the eq. (2) in terms of the spatial average of sorbate concentration $\bar{C}$ as defined in equation (3) over a particle p, obtaining the resulting formulation in eq. (4):

$$\bar{C}(t) = \frac{1}{V_p} \cdot \int_p C(r,t) \cdot dV = \frac{3}{R_p^3} \cdot \int_0^{R_p} C(r,t) \cdot r^2 dr \tag{3}$$

Heat Powered Cycles
Conference 2023
Edinburgh
Heat in the new energy system

3rd to 6th of September 2023
The University of Edinburgh, Scotland

$$\bar{C}(t) = C_0 + (C_\infty - C_0) \cdot \left\{ 1 - \frac{6}{\pi^2} \sum_{n=1}^{\infty} \left[\frac{e^{-\pi^2 n^2 \left(\frac{D \cdot t}{R_p^2} \right)}}{n^2} \right] \right\} \tag{4}$$

On the contrary respect to FD, the LDF model assumes the proportionality of the sorption driving force to the difference between the gas-side bulk concentration (C_∞) and the average sorbate concentration $\bar{C}(t)$ within the material:

$$\frac{d\bar{C}(t)}{dt} = K \cdot [C_\infty(t) - \bar{C}(t)] \tag{5}$$

K is a proportionality factor equal to:

$$K = \frac{F_0 \cdot D}{R_p^2} \tag{6}$$

, where F_0 is a shape factor, equal to 15 for spheres [23]. Note that the diffusivity D here reported is the very same diffusivity defined through Fick's first law. Applying the same initial and boundary conditions as for the FD, the LDF solution can be easily derived by integration of eq. (5), and it results:

$$\bar{C}(t) = C_0 + (C_\infty - C_0) \cdot \left(1 - e^{-\frac{F_0 \cdot D}{R_p^2} \cdot t} \right) \tag{7}$$

It is important to remember that eq. (7) follows by integrating eq. (5) under the hypothesis of constant coefficient K over time. In reality diffusivity depends, among the others, on temperature, which may change over time. It has been proposed a modified version (LDF$_m$) of the LDF model [22] in which the adimensional test temperature normalized to a reference value T_C and adimensional time $(D/R_p^2)t$ are corrected with exponents n and m, respectively, as in eq. (8):

$$\bar{C}(t) = C_0 + (C_\infty - C_0) \cdot \left(1 - e^{-F_0 \cdot \left(\frac{T}{T_C} \right)^n \left(\frac{D}{R_p^2} \cdot t \right)^m} \right) \tag{8}$$

Given the typical gravimetric approach used for experimental tests, the use of concentration as the main variable is less useful than the definition of water uptake (w) as the amount of sorbate within the material over the dry mass of the sorbent. When the volume of the particle is constant, the ratio of the instantaneous concentrations over the equilibrium concentration can be translated in terms of water uptake as:

$$\frac{\bar{C}(t) - C_0}{C_\infty - C_0} = \frac{w(t) - w_0}{w_\infty - w_0} = \begin{cases} \text{for Fickian Diffusion (FD):} & 1 - \frac{6}{\pi^2} \sum_{n=1}^{\infty} \left[\frac{e^{-\pi^2 n^2 \left(\frac{D \cdot t}{R_p^2} \right)}}{n^2} \right] \\ \\ \text{for Linear Driving Force (LDF):} & 1 - e^{-\frac{F_0 \cdot D}{R_p^2} \cdot t} \\ \\ \text{for modified LDF (LDF}_m\text{):} & 1 - e^{-F_0 \cdot \left(\frac{T}{T_C} \right)^n \cdot \left(\frac{D}{R_p^2} \cdot t \right)^m} \end{cases}$$

Since the experimental campaign involved adsorptions and regenerations at constant temperatures (21 °C and 100 °C respectively), for the purpose of this paper it is supposed $(T/T_C)^n = 1$. Thus, the modified version of LDF (LDF$_m$) only involves parameters D and m. Additionally, the formula can be extended to desorption, making it even more useful.

These three models (FD, LDF, and LDF$_m$) have been applied to the experimental results reported in the following section, using a fitting procedure. The main purpose is to evaluate and compare the diffusive coefficient to discuss the influence of the two main parameters analyzed in the design of the experiment process: the concentration of the crosslinking initiator CaCl$_2$, and the concentration of alginate monomers chains NaAlg. Further on, models are used to analyze the influence of cycle duration on the maximization of the water uptake variation over time.

The quantification of the model parameters was performed through the minimization of the least square root error [24]. This consists in searching for the values of the model parameters which minimize the sum of the squares of the differences between each experimental point and the model output evaluated at the same input. Given a generic function f to model experimental data, dependent on time and on multiple parameters such as $f(t, p_1, p_2, \ldots, p_M)$, the error function err is:

$$err(p_1, p_2, \ldots, p_M) = \sum_{i=1}^{N} [f(t_i, p_1, p_2, \ldots, p_M) - y_i]^2$$

, where (t_1, y_1), (t_2, y_2), $\ldots$, (t_N, y_N) are the coordinates of the N experimental points of the test to be fitted, while err is a function of the sole model parameters. In this research the function f is the water uptake w while t is the time of the experiment. The list of parameters, as well as the function w, change according to the selected model:

- for LDF, $M = 1$, $p_1 \equiv D$
- for LDF$_m$, $M = 2$, $p_1 \equiv D$, $p_2 \equiv m$
- for FD, $M = 1$, $p_1 \equiv D$.

The identification of the best fitting model parameters follows the objective research of values p_1, p_2, $\ldots$, p_M which minimize err. The minimization algorithm used is the Nelder-Mead simplex [25-26], in particular:

- for the fitting of the LDF model, it was searched the positive value of D which minimizes the function $err(D)$, starting from a 1st-iteration value of $D = 10^{-11} \, m^2/s$;
- for the fitting of the LDF$_m$ model, the positive values of D and m which minimize the function $err(D, m)$, starting from 1st-iteration values of $D = 10^{-11} \, m^2/s$ and $m = 1.0$;
- for the fitting of the FD model, the positive value of D which minimizes the function $err(D)$, starting from a 1st-iteration value of $D = 10^{-11} \, m^2/s$.

Discussion and Results

In Figure 1 three SEM magnifications show the external surface of a bead of CaAlg dried polymer and its transversal section. The polymer has a pseudo spherical shape, with an equivalent radius of $0.969 \, mm$, and has a highly rugged surface with multiple openings. Additionally, concentric traces are visible from the outer surface to the inner surface, presumably linked to the progression of the diffusion front and crosslinking of Ca^{2+} ions. The openings start from the outer surface, and they go through the radial direction involving a thickness lower than 200 µm. In the grain inner section, a predominantly solid microstructure exists, apart from the occurrence of

regions exhibiting significant void spaces which can be attributed to inadequate removal of air during the degassing process.
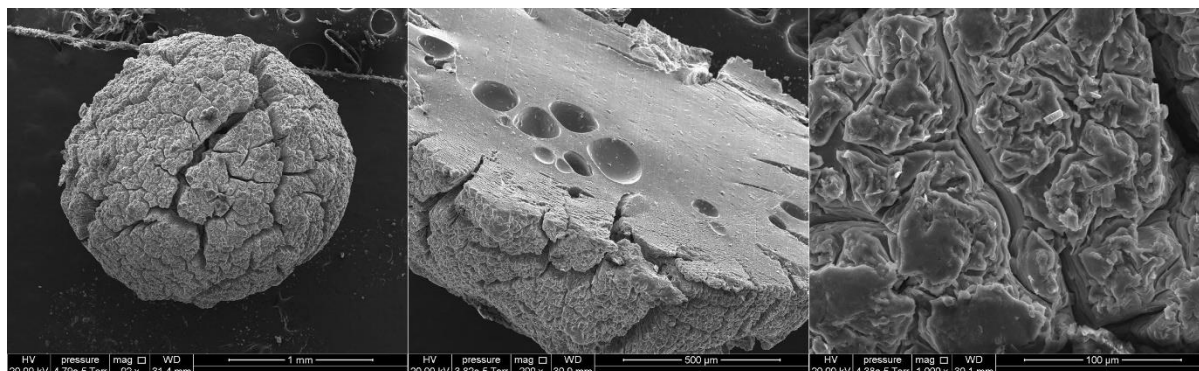

Figure (1). SEM magnifications of a grain of sample S2. (left) a view of the external surface of a pseudo-spherical particle of dried CaAlg; (center) transversal section of a particle of dried CaAlg with the same composition of S2; (right) magnification of the image at the center, focused on the external surface structure.

Figure (2) displays the results of adsorption and regeneration tests as variations in water uptake. The graph on the left presents the results of the test conducted on sample S1, which consisted of a desorption cycle (first 3 hours) followed by an adsorption cycle (next 5 hours), illustrated by a solid line. The points on the adsorption curve correspond to the experimental measurements, while during desorption, the mass of the sample was measured every 5 seconds. The adsorption process was terminated after 5 hours before the material attained its equilibrium mass, which requires approximately 12 hours. However, after 5 hours, the water uptake reached a value w_{5h} of approximately 80% of the equilibrium value, as shown in Table 1.

The dotted line depicts the relative humidity (RH) during the experiment, while the RH after the box is left to evolve for a sufficiently long time (RH$_{eq}$) is illustrated above with the horizontal line. The RH in the conditioning chamber varies over time because the box was opened to place the sample and the conditioning chamber is not large enough to avoid being affected by the adsorption process. The combination of these factors causes the equilibrium concentration experienced by the material to change over time. This suggests that the use of the models should involve a time-dependent function of $C_\infty(t)$ rather than a constant value. The graph on the right of the same figure reports the same kind of test for all four different samples.

The sample composition affects the adsorption and regeneration behaviors. For example, sample S2 shows a greater equilibrium water uptake, while sample S3 has a weaker adsorption capacity. Sample S1 performs better in desorption, exhibiting a steeper behavior. Increasing the CaCl$_2$ content (at a fixed alginate content) the equilibrium value increases. The same conclusion applies to the comparison of S2 with S1 and S4 with S3. Conversely, increasing the alginate content (at a fixed salt content) reduces the steepness of the adsorption process and the equilibrium water uptake at regime conditions, as shown by the comparison between tests S2 and S4, and tests S1 and S3.

It should be noted that the steepness of a sorption/desorption curve is correlated to the diffusive coefficient value as well as to the equilibrium value. If the LDF is used to model the phenomenon, the D/R_p^2 parameter acts as the inverse of a characteristic time τ in a generic exponential expression in the form: $x(t) = A + B \cdot \exp(-t/\tau)$. Sorption/desorption tests with steeper behavior at fixed equilibrium value will be fitted using lower transient characteristic times, which in turn correspond to higher diffusive coefficients.
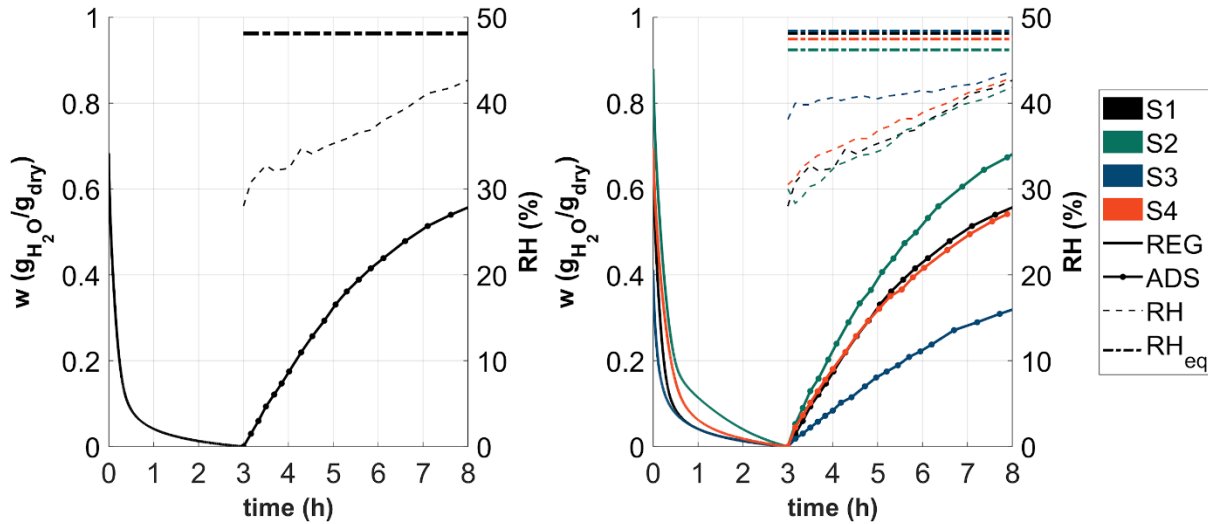
Figure (2). (left) test results of sample S1: time t on the x-axis, water uptake w on the left y-axis, relative humidity RH on the right y-axis; (right) comparison of test results for all the samples S1, S2, S3, S4. The graphs report a regeneration at 100°C and adsorption at 21°C and RH=50%.

Table 1 shows the numerical values of water uptakes alongside the initial and equilibrium RH values measured in the conditioning chamber during the adsorption process. The value of w at the beginning of the regeneration is denoted as w_0, which is equivalent to the equilibrium value that the sample in adsorption would have reached if the experiment had not been interrupted after 5 hours. For each sample, the water uptake at the end of the regeneration process corresponds to the initial water uptake of the adsorption process, given the experimental procedure. This value was assumed as the "zero" point to define the dry mass and for the definition of water uptakes.

Table 1. Initial and final water uptakes and RHs, for tests S1, S2, S3 and S4.

Test	REGENERATION	ADSORPTION		
	$w_0\ (g/g)$	$w_{5h}(g/g)$	$RH_0(\%)$	$RH_{eq}(\%)$
S1	0.683	0.562	28.0	48.1
S2	0.880	0.706	30.0	46.2
S3	0.412	0.326	38.1	48.4
S4	0.695	0.542	30.5	47.5

The analytical solutions provided above (FD, LDF, LDFm) are valid for a fixed geometry where the radius is constant, while a real process on hydrogel spheres, or other polymers, may lead to a significant change in the volume of particles. For this reason, and to reach better fittings between the models and real data, the R_p was the average (avg) value of the equivalent spherical particle over the entire transient:

$$V_{avg} \approx \frac{V_0 + V_\infty}{2} \quad \rightarrow \quad R_p \equiv R_{p,avg} = \sqrt[3]{\frac{R_0^3 + R_\infty^3}{2}}$$

Where the subscripts 0 and ∞ represent the initial and the equilibrium condition of each adsorption and regeneration stage. One average value between the four samples was used to fit regenerations and one for adsorptions. In particular, the average value of the radius during regeneration was

**Heat Powered Cycles
Conference 2023**
Edinburgh

Heat in the new energy system

3rd to 6th of September 2023
The University of Edinburgh, Scotland

$R_{p,avg,reg} = 0.937\ mm$ ($\sigma_{R,reg} = 0.130\ mm$), while the average value of the radius during adsorption was $R_{p,avg,ads} = 1.12\ mm$ ($\sigma_{R,ads} = 0.097\ mm$).

The proposed analytical solutions assume constant concentration on the gas-side. However, because changes in relative humidity affected the concentration in the conditioning chambers, this assumption is not acceptable for this kind of experiment. For this reason, the FD model was properly manipulated by incorporating a step-wise change in gas-side concentration that reflects the varying relative humidity (RH) levels during the experiment. Initially, the concentration would be lower than the equilibrium value due to lower RH levels, but it would increase as the RH levels rise. Assuming that the relationship between concentration C_∞ and RH is linear, one could model the increase in $C_\infty(t)$ over time as being proportional to RH(t). Thus, when RH=RH$_{eq}$, C_∞ would be equal to w_∞.

The time interval is subdivided into N steps, and the FD model is used in its original expression at each step with the same diffusivity to evaluate the new increment in concentration. By increasing the resolution of the step-wise approach (by increasing the number N of discrete subdivisions of testing time) the resulting approximation is expected to improve. This is confirmed by Figure (3), which shows on the left how the step-wise FD (swFD) model better fits experimental data as N increases. For N=1, the swFD model degenerates into an ordinary FD model applied on the whole test time interval, with a consistent overestimation of the water uptake during the first part of the transient, and a symmetrical underestimation for the second part of the transient. When the number N of discrete increases in RH is set to 2 the approximation improves, as the model predicts a lower equilibrium value at the start of the adsorption process. As N increases, the curve becomes even closer to the experimental data, and the fitted value of diffusivity D (as shown in Figure (3) on the right for all four tests) varies more slowly, except for numerical oscillations at higher N resulting from interpolation algorithm. The value of D for N=100 is assumed as the outcome of the fitting procedure with the swFD model. The deviation of the curve from the experimental data may be due to the violation of other hypotheses of the FD model, such as constant particle volume and constant diffusivity, as well as the assumption about the linear relationship between C_∞ and RH.
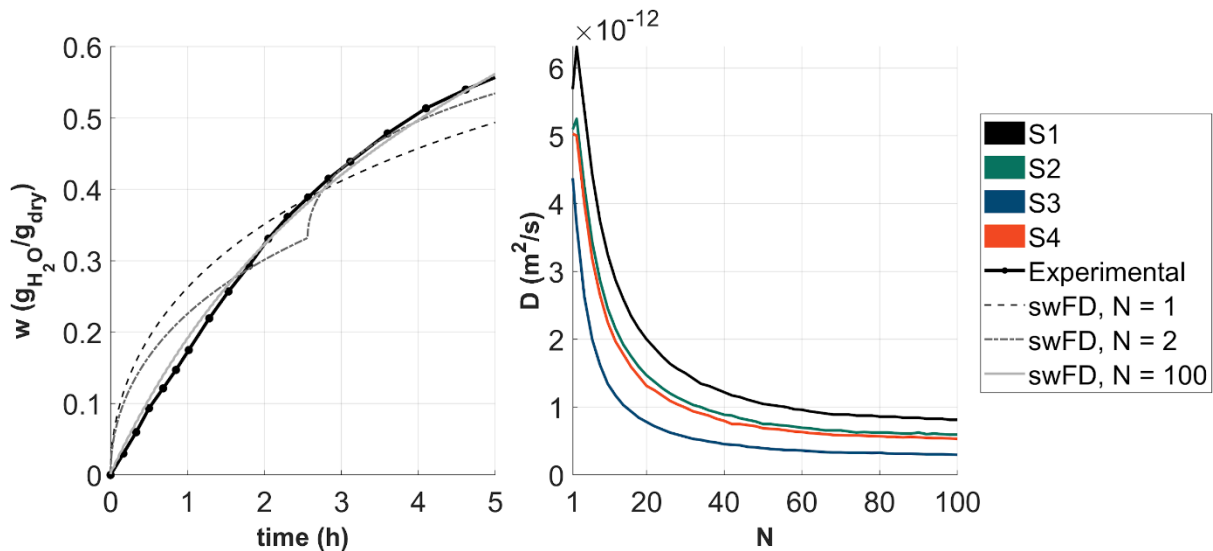

Figure (3). (left) experimental data of test S1 and step-wise FD (swFD) model for a different number of steps N; (right) change in the fitted value of coefficient D with increasing N, for tests S1, S2, S3, S4. For N=1, swFD is equivalent to the original FD model.

The final results of the FD model calculations are reported in Table 2 and Table 3, where the infinite sum was approximated using its first 300 items since the contributions beyond the first 50 terms of the sum were insignificant. Indeed, the additional iterations after the 50th affect the total

Heat Powered Cycles
Conference 2023
Edinburgh
Heat in the new energy system

3rd to 6th of September 2023
The University of Edinburgh, Scotland

water uptake with a magnitude of approximately 0.01 g/g, and similarly, the contributions on the fitted diffusion coefficient are negligible dropping below 1e-14 m^2/s.

The modified equation of LDF is versatile and can be applied to fit experimental data for both adsorption and regeneration. However, it should be noted that the coefficients in the LDF$_m$ model do not have an immediate physical interpretation. Indeed, the corrective coefficient causes the deformation of the resulting curve to better fit the experimental data. The introduction of new mathematical degrees of freedom reduces the overall error, but at the expense of an unclear interpretation of the diffusivity coefficient D. This creates consistency problems when it is carried out a comparison of diffusivities between the different modelling approaches. For this reason, it is more appropriate to use a model based on physical principles, such as the FD or classic LDF, which have a clear physical interpretation.

Figure (4), for example, reports the fitting obtained through each of the different models (LDF, LDF$_m$, and swFD) shown above, in comparison with the experimental data. The absolute error over time is shown below.
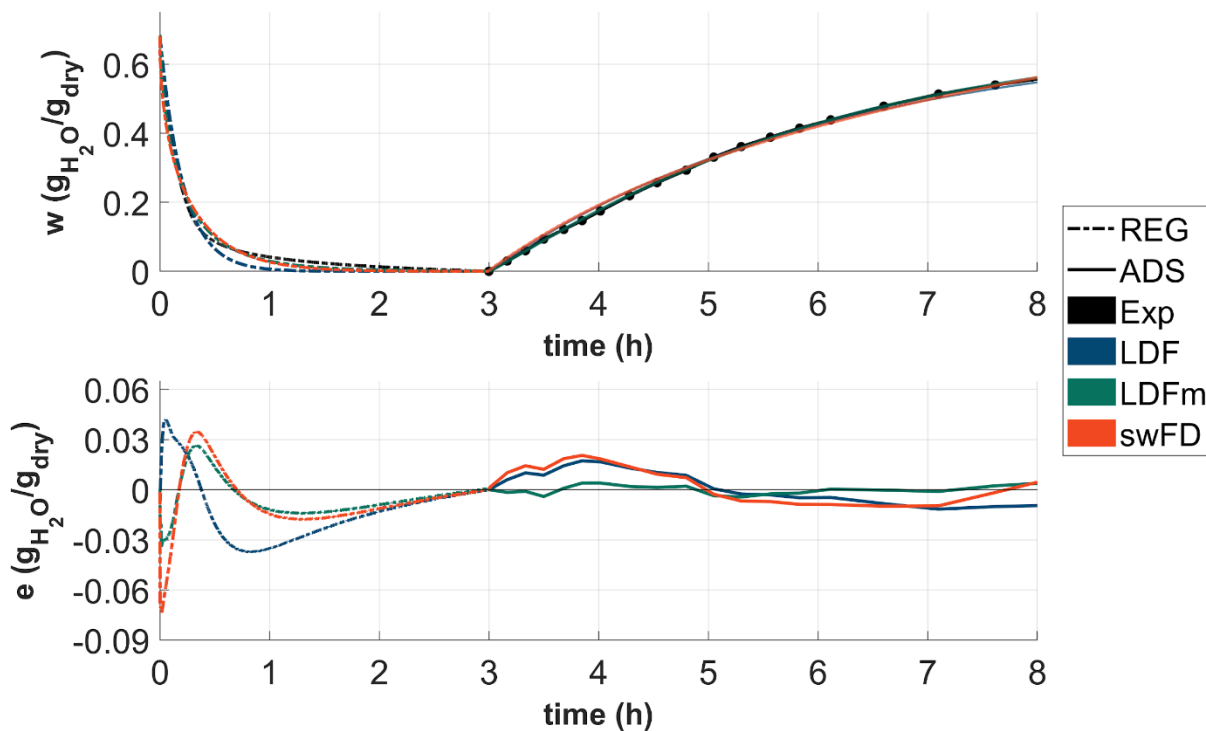
Figure (4). (above) LDF, LDF$_m$, and swFD$_{N=100}$ models in comparison and against the experimental data of the test on sample S1; (below) absolute error over time made by each model, in regeneration and adsorption.

It can be observed that all three models perform well in modeling the adsorption process, while the regeneration phase exhibits higher errors. The LDF$_m$ model is the most precise in both adsorption and desorption, but this could be simply related to the introduction of an additional degree of freedom (i.e., the exponent m) with respect to the other model versions.

Table 2 reports the numerical values of diffusion coefficient D obtained from fitting the different models with regeneration tests (REG), while Table 3 reports the same data for adsorption tests (ADS). Additionally the average absolute error $\bar{e}$ (average of the instantaneous differences between the estimated and the experimental values) and its standard deviation over time σ_e are reported.

Higher values of D are associated with samples containing less alginate (S1 and S2), coherently with what was observed above. Such samples show a steeper behavior, i.e., a faster sorption/desorption process. Regarding the fitting of the LDF$_m$ model, the corrective coefficient

m was observed to have specific values for regeneration and adsorption. For the regeneration, the tests S1, S2, S3, and S4 had m values equal to 0.708, 0.687, 0.555, and 0.795 respectively. On the other hand, for adsorption m had values of 1.09, 1.00, 1.16, and 0.996 respectively. It is noteworthy that in these last cases the coefficients reached proximity to unity values. This indicates a scenario where the ordinary LDF model is already more than sufficient to effectively represent the material's behavior. For example, this is evident in the test of S2 where the value of m rounded to the 2nd decimal place is 1.00, as consequence the value of D coincides with the one evaluated with the simple LDF. On the contrary, desorption requires a more substantial adjustment of the coefficient m to minimize the error that occurs during the LDF fitting process. The reason why adsorption is better suited to LDF modeling than desorption may be attributed to the fact that the linear potential is more suitable for simulating the sorption phenomena at lower temperatures.

Table 2. REG diffusion coefficients and errors resulting from LDF, LDF$_m$, and swFD$_{N=1}$ fittings.

Test	LDF			LDF$_m$			swFD		
	D $\left(\frac{m^2}{s}\right)$	$\bar{e}$ $\left(\frac{g}{g}\right)$	σ_e $\left(\frac{g}{g}\right)$	D $\left(\frac{m^2}{s}\right)$	$\bar{e}$ $\left(\frac{g}{g}\right)$	σ_e $\left(\frac{g}{g}\right)$	D $\left(\frac{m^2}{s}\right)$	$\bar{e}$ $\left(\frac{g}{g}\right)$	σ_e $\left(\frac{g}{g}\right)$
S1	7.6 e-11	-1.29 e-2	1.83 e-2	2.7 e-11	-5.05 e-3	1.10 e-2	6.8 e-11	-6.65 e-3	1.62 e-2
S2	4.4 e-11	-1.95 e-2	3.72 e-3	1.4 e-11	-3.33 e-3	1.82 e-2	3.9 e-11	-5.94 e-3	2.56 e-2
S3	6.5 e-11	-1.14 e-2	2.21 e-2	8.9 e-12	-2.87 e-4	4.74 e-3	5.5 e-11	-4.64 e-3	1.14 e-2
S4	4.8 e-11	-9.23 e-3	1.65 e-2	2.5 e-11	-3.19 e-3	8.29 e-3	4.4 e-11	-2.57 e-3	1.95 e-2

Table 3. ADS diffusion coefficients and errors resulting from LDF, LDF$_m$, and swFD$_{N=100}$ fittings.

Test	LDF			LDF$_m$			swFD		
	D $\left(\frac{m^2}{s}\right)$	$\bar{e}$ $\left(\frac{g}{g}\right)$	σ_e $\left(\frac{g}{g}\right)$	D $\left(\frac{m^2}{s}\right)$	$\bar{e}$ $\left(\frac{g}{g}\right)$	σ_e $\left(\frac{g}{g}\right)$	D $\left(\frac{m^2}{s}\right)$	$\bar{e}$ $\left(\frac{g}{g}\right)$	σ_e $\left(\frac{g}{g}\right)$
S1	7.5 e-12	2.66 e-3	9.61 e-3	9.5 e-12	2.35 e-5	2.67 e-3	8.1 e-13	4.10 e-3	1.13 e-2
S2	7.0 e-12	3.34 e-3	5.51 e-3	7.0 e-12	-8.21 e-4	4.56 e-3	5.9 e-13	5.66 e-4	5.92 e-3
S3	6.3 e-12	3.63 e-3	9.35 e-3	9.3 e-12	-8.14 e-4	3.62 e-3	3.0 e-13	3.38 e-3	8.89 e-3
S4	7.0 e-12	-2.11 e-3	3.77 e-3	7.0 e-12	-7.25 e-4	4.01 e-3	6.3 e-13	-9.37 e-4	3.86 e-3

**Heat Powered Cycles
Conference 2023**
Edinburgh

Heat in the new energy system

3rd to 6th of September 2023
The University of Edinburgh, Scotland

Even if its parameters do have not a direct physical interpretation, the LDF$_m$ best models the curves of water uptake over time. For this reason, it has been selected to simulate the behavior of the material when it is subject to cyclic desorption and adsorption processes.

For example in real applications requiring the harvesting of atmospheric water vapor, the thermal cycle can undergo short fixed times, and repeated many times per day. As a result, materials will hardly reach equilibrium conditions over multiple cycles. Nonetheless, after a few repetitions, the process will reach a regime behavior in which the water uptake, at the beginning of each regeneration, is reduced to a new value lower than the maximum potential related to actual atmospheric conditions. Here, the chosen durations of regeneration and adsorption cycles are such that the decrease in water uptake during regeneration is identical to its increase during adsorption. Initial water uptake, regeneration time, and adsorption time at a given regime are not independent, as one follows the other two (once they are fixed). If the initial water uptake is established as a percentage of the equilibrium water uptake (e.g. 85% of the equilibrium value), the variation in water uptake (Δw) observed during each cycle reaches a regime which is solely determined by the regeneration time and cycling conditions (such as temperatures and relative humidities), as evidenced by the results in Figure 5 (graph on the left).

Moreover, the total cycling time Δt, which encompasses both regeneration and adsorption processes, is limited by the regeneration time since adsorption only restores the material's water uptake to the value obtained at the beginning of regeneration. It can be useful to evaluate the quantity of water uptake rate (i.e., the ratio between the Δw and Δt of each cycling option, for each partial regeneration time), which is a crucial performance metric if the goal of the application is to maximize the water vapor collection in a fixed duration. In Figure (5) (on the right) this metric is plotted against each possible partial regeneration time, for different initial water uptakes.
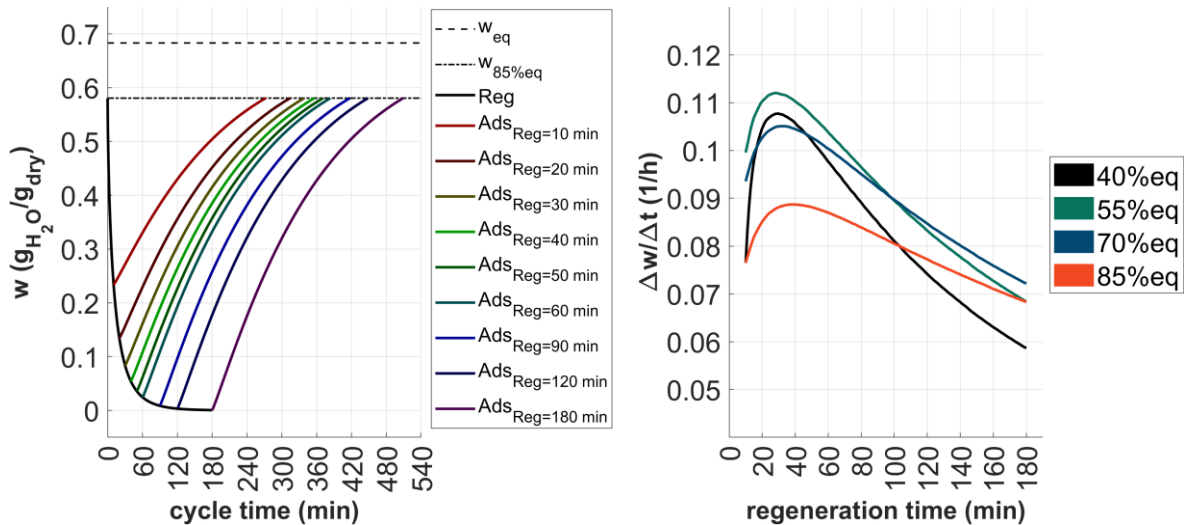
Figure (5). (left) settled cycling curves (simulated through LDF$_m$ for regeneration at 100°C and adsorption at 21°C and RH=50%) at different fixed regeneration times, in fixed environmental conditions and for sample S1; (right) the water uptake rate on the y-axis plotted against each partial chosen regeneration time, for different initial water uptakes expressed as a fraction of the equilibrium value.

The graph on the right of Figure (5) reveals two interesting observations. Firstly, the curve of water uptake rate varies with the initial value (expressed as a percentage of the equilibrium value), with a maximum reached around 55% of w_{eq}. Secondly, each curve achieves a peak value for an intermediate partial regeneration time of around 30-35 minutes. These effects are attributed to the changing steepness of the regeneration and adsorption curves. An optimal regeneration time and an optimal reg starting value can be identified such that the regeneration is long enough to yield a high Δw but not too long to result in a high Δt due to the adsorption time.

Conclusions

This paper explored the influence of composition on the sorption and desorption performances of a family of alginate-based hydrogels and how the kinetics of such processes can be modeled.

It was observed that higher contents of calcium chloride in the composition of the hydrogel imply better adsorption capacities; higher contents of alginate in the composition imply, on the other hand, worse adsorption capacities and longer characteristic times: this is confirmed by the values of the fitted diffusivities, which are higher in case of samples containing less alginate (S1 and S2).

The models used to fit diffusivity were the Fickian diffusion (FD), the Linear Driving Force (LDF), and a modified version of the Linear Driving Force (LDF_m). The latter resulted in the most accurate description of the kinetics of both regeneration and adsorption, but the resulting diffusivity value may be distorted by the introduction of a corrective coefficient, which does not allow a simple physical interpretation of the results. On the other hand, the FD and the LDF models both provided diffusivity values of the order of magnitude 10^{-11} m^2/s in regeneration and values around 10^{-13} - 10^{-12} m^2/s in adsorption.

The LDF_m model, given its mathematical accuracy, was used to simulate the cyclic behavior of one of the studied hydrogels, when non equilibrium cycles are applied with a fixed initial water uptake and at various regeneration times. The water uptake rate was defined as the amount of Δw gained in one complete cycle divided by the cycle time: such quantity is a key indicator in an application that requires to maximize the amount of water extracted in a fixed amount of time. The simulations allowed us to find that it exists an optimal initial water uptake, as well as an optimal regeneration time for each initial water uptake, in order to maximize the water uptake rate.

Future research can investigate the potential of enhancing the adsorption and desorption performance of alginate-based hydrogels by incorporating other materials and additives, while also focusing on developing more accurate models that can account for transient environmental factors, volumetric variations, and the presence of multiple materials.

Acknowledgments

References:

[1] E. Caló and V. V. Khutoryanskiy, "Biomedical applications of hydrogels: A review of patents and commercial products," Eur. Polym. J., vol. 65, pp. 252–267, 2015.

[2] N. A. Peppas, P. Bures, W. Leobandung, and H. Ichikawa, "Hydrogels in pharmaceutical formulations," Eur. J. Pharm. Biopharm., vol. 50, no. 1, pp. 27–46, 2000.

[3] K. Y. Lee and D. J. Mooney, "Alginate: Properties and biomedical applications," Prog. Polym. Sci., vol. 37, no. 1, pp. 106–126, 2012.

[4] M. N. V. R. Kumar, "A review of chitin and chitosan applications," React. Funct. Polym., vol. 46, pp. 1–27, 2000.

[5] J. L. Drury and D. J. Mooney, "Hydrogels for tissue engineering: Scaffold design variables and applications," Biomaterials, vol. 24, no. 24, pp. 4337–4351, 2003.

[6] Z. Xue et al., "A novel superhydrophilic and underwater superoleophobic hydrogel-coated mesh for oil/water separation," Adv. Mater., vol. 23, no. 37, pp. 4270–4273, 2011.

[7]   O. Ozay, S. Ekici, Y. Baran, N. Aktas, and N. Sahiner, "Removal of toxic metal ions with magnetic hydrogels," Water Res., vol. 43, no. 17, pp. 4403–4411, 2009.

[8]   F. Ge, M. M. Li, H. Ye, and B. X. Zhao, "Effective removal of heavy metal ions Cd 2+, Zn 2+, Pb 2+, Cu 2+ from aqueous solution by polymer-modified magnetic nanoparticles," J. Hazard. Mater., vol. 211–212, pp. 366–372, 2012.

[9]   X. Zhou, F. Zhao, Y. Guo, B. Rosenberger, and G. Yu, "Architecting highly hydratable polymer networks to tune the water state for solar water purification," Sci. Adv., vol. 5, no. 6, pp. 1–8, 2019.

[10]   M. R. Guilherme et al., "Superabsorbent hydrogels based on polysaccharides for application in agriculture as soil conditioner and nutrient carrier : A review," Eur. Polym. J., vol. 72, pp. 365–385, 2015.

[11]   B. Ni, M. Liu, S. Lü, L. Xie, and Y. Wang, "Environmentally friendly slow-release nitrogen fertilizer," J. Agric. Food Chem., vol. 59, no. 18, pp. 10169–10175, 2011.

[12]   B. Song, H. Liang, R. Sun, P. Peng, Y. Jiang, and D. She, "Hydrogel synthesis based on lignin/sodium alginate and application in agriculture," Int. J. Biol. Macromol., vol. 144, pp. 219–230, 2020.

[13]   N. Thombare, S. Mishra, M. Z. Siddiqui, U. Jha, D. Singh, and G. R. Mahajan, "Design and development of guar gum based novel, superabsorbent and moisture retaining hydrogels for agricultural applications," Carbohydr. Polym., vol. 185, no. October 2017, pp. 169–178, 2018.

[14]   F. Zhao, X. Zhou, Y. Liu, Y. Shi, Y. Dai, and G. Yu, "Super Moisture-Absorbent Gels for All-Weather Atmospheric Water Harvesting," Adv. Mater., vol. 31, no. 10, pp. 1–7, 2019.

[15]   R. Li, Y. Shi, M. Alsaedi, M. Wu, L. Shi, and P. Wang, "Hybrid Hydrogel with High Water Vapor Harvesting Capacity for Deployable Solar-Driven Atmospheric Water Generator," Environ. Sci. Technol., vol. 52, no. 19, pp. 11367–11377, 2018.

[16]   D. M. Ruthven, "Douglas M. Ruthven. Principles of Adsorption and Adsorption processes.", 1984.

[17]   J. Crank, "The mathematics of diffusion", Clarendon Press Oxford, 2nd ed., 1975.

[18]   C. Hu, W. Lu, A. Mata, K. Nishinari, and Y. Fang, "Ions-induced gelation of alginate: Mechanisms and applications," Int. J. Biol. Macromol., vol. 177, pp. 578–588, 2021.

[19]   S. Paoletti and I. Donati, "Comparative Insights into the Fundamental Steps Underlying Gelation of Plant and Algal Ionic Polysaccharides: Pectate and Alginate," Gels, vol. 8, no. 12, 2022.

[20]   P. A. Kallenberger and M. Fröba, "Water harvesting from air with a hygroscopic salt in a hydrogel–derived matrix," Commun. Chem., vol. 1, no. 1, pp. 6–11, 2018.

[21]   I. Braccini and S. Pérez, "Molecular basis of Ca2+-induced gelation in alginates and pectins: The egg-box model revisited," Biomacromolecules, vol. 2, no. 4, pp. 1089–1096, 2001.

[22]   I. I. El-Sharkawy, "On the linear driving force approximation for adsorption cooling applications," Int. J. Refrig., vol. 34, no. 3, pp. 667–673, May 2011.

[23]   E. Glueckauf, "Theory of chromatography. PART lO.-FORMULA FOR DIFFUSION INTO SPHERES AND THEIR APPLICATION TO CHROMATOGRAPHY," Trans. Faraday Soc. Superseded by J. Chem. Soc., Faraday Trans., I II, vol. 51, no. 3851, p. 220, 1955.

[24]   Bickel J.P., Doksum A.K., "Mathematical statistics", vol. 1. 2013.

[25]   J. C. Lagarias et al., "Convergence properties of the Nelder-Mead simplex method in low dimensions", Society for Industrial and Applied Mathematics, 1998.

[26]   J. A. Nelder and R. Mead, "A simplex method for function minimization", The Computer Journal, vol. 8, 1965.

A multi-scale optimization tool for the design of Organic Rankine Cycles for fluctuating heat source and sink

Donghoi Kim[1*], Lasse Borg Anderson[2],Rubén M. Montañés[1], Johan Raftevold Espelund[1], Lars O. Nord[2] and Luca Riboldi[1]

[1]SINTEF Energy Research, Sem Sælands vei 11, 7034, Trondheim, Norway

[2]NTNU - The Norwegian University of Science and Technology, Department of Energy and Process Engineering, 7491, Trondheim, Norway

[*]Corresponding author: Donghoi.kim@sintef.no

Abstract

Organic Rankine Cycles (ORC) are efficient technologies for waste heat recovery (WHR). In principle, the most important factors affecting the performance of ORC are working fluid selection and expander design. Process design and optimization of heat-to-power cycles is a developed research area. Several studies dealt with the conversion of various sources of waste heat into power by means of different cycles and working fluids [1]. For low temperature heat sources, organic Rankine cycles demonstrated to be an advantageous technology [2]. When considering ORC design, several thermodynamic parameters should be considered, as well as a several organic working fluids and process configurations. Optimization could be performed both on thermodynamic and techno-economic parameters [3]. A main challenge related to small scale (<50kW) ORC cycles is to define the optimal process given a specific application when there is frequent variability in heat source. Many relevant applications will require robust ORC systems to perform under varying heat source [4]. This is an area where the body of knowledge is less developed.

In order to facilitate technology maturation and support future deployment, we are developing a multi-scale optimization tool for optimal design of ORC systems considering fluctuating heat source and sink (Figure 1). The goal is to identify ORC designs that maximize the performance at the expected operating conditions specific to the selected waste heat-to-power application. The first focus will be on small-scale distributed energy systems (DES) but the methodology can be theoretically extended to any application.

The first important characteristic of the proposed tool is to include off-design considerations into design optimization. Especially in distributed settings, ORC systems are required to operate in changing conditions, e.g., waste heat source conditions. Traditional design approaches target optimal performance at a selected design point but, often, lead to poor performance at other relevant operating conditions. In a previous study, we achieved an increase in accumulated power production of 5 % by considering the range of expected operations already during cycle design phase [5]. In this first implementation, the tool included a model for simulation of ORCs as well as simplified off-design models for predicting part load performances of key elements of the cycle.

In this work, we further refined the methodology with a multi-scale approach. The tool is conceived as a flexible platform that allows including fit-for-purpose models of the key elements of the cycle. This brings two main advantages. First, it allows a more accurate representation of the cycle by including in-depth design considerations of critical equipment coupled to a holistic optimization procedure. One example is the design of the geometry of the expander, which is normally performed a posteriori, based on the boundary conditions

provided by the cycle optimization. In this case, the design of the cycle and of the expander are integrated, allowing to intrinsically explore their mutual influence. The second advantage is that the utilization of fit-for-purpose models of certain equipment ensures a more accurate description of their off-design performance. For example, a description of the expander characteristics allows a better estimation of the expected off-design behaviour.
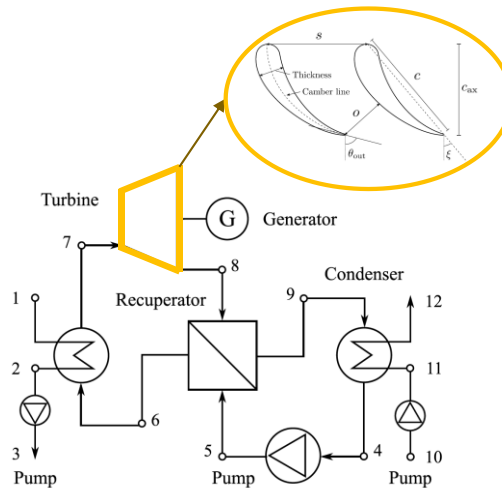

Figure 1. Multi-scale apporach to ORC design.

The Rankine Lab tool is used as the underlying thermodynamic steady-state process model for the simulation and optimization of ORC systems [6]. It is an open-source tool coded in MATLAB that allows the analysis and optimization of several cycle configurations. The numerical optimization is conducted based on a gradient-based approach (i.e., SQP). Thermodynamic properties are retrieved by connections to relevant property databases, such as CoolProp or REFPROP. The expander model follows a mean-line approach, which assumes that the flow at the mean radius represents the flow at all radii [7]. This method adopts the conservation equations of mass, momentum, and energy, in addition to an equation of state and a loss model to predict the performance of the expander.

The type of expander considered in this case is the single-stage axial turbine and the loss model described by the authors Benner, Sjolander, and Moustapha is adopted [8, 9]. This model represents modern trends in turbine design compared to conventional loss models such as [10], while also considering off-design performance due to incidence. These are important traits when analysing small-scale ORC systems for fluctuating heat sources. Other off-design aspects for the ORC are based on the correlations and approaches described in [11]. The inputs to the off-design model are the design parameters obtained by the solution of Rankine Lab at the design tested.

As a case study of the multi-scale simulation tool, this work investigates ORC applications for low-temperature heat sources such as deep geothermal energy wells. Considering the heat source temperature of around 120 °C, a natural working fluid (a600a) is applied to the ORC. The maximum capacity of the ORC and the expander is in the range of 1 to 50 kWe to focus on small-scale applications. During the case study, variations in heat source and sink are applied to the multi-scale tool to identify an ORC design that maximizes the power output under a targeted time span. In this work, the fluctuations of heat and power demand can be taken into account for energy-efficient ORC design. The multi-scale tool also demonstrates the modular design approach where external expander and heat exchanger models can be connected to the framework.

Keywords: ORC, multi-scale simulation, part-load, optimization.

Acknowledgments

References:

[1] S. Quoilin, et al., "Techno-economic survey of organic rankine cycle (ORC) systems", Renewable and Sustainable Energy Reviews. 2013.

[2] Macchi, E., Astolfi, M., *Organic Rankine Cycle (ORC) Power Systems: Technologies and Applications*, Woodhead Publishing, 2016.

[3] Colonna, P. et al., "Organic Rankine Cycle Power Systems: From the Concept to Current Technology, Applications, and an Outlook to the Future", Journal of Engineering for Gas Turbines and Power, 2015.

[4] Petrollese, M., Cocco, D., "Robust optimization for the preliminary design of solar organic Rankine cycle (ORC) systems", Energy Conversion and Management, 2019.

[5] Kim D, Montañés RM, Riboldi L, Nord LO, Spale J, Novotny V., "Design optimization of small-scale ORC cycles for fluctuating heat source", Scandinavian Simulation Society, 2022.

[6] Agromayor, R., Nord, L. O., "Fluid selection and thermodynamic optimization of organic Rankine cycles for waste heat recovery applications", Energy Procedia, 2017.

[7] Dixon, A.L., Hall, C.A., *Fluid Mechanics and Thermodynamics of Turbomachinery,* Elsevier Inc, 2014.

[8] Benner, M.W., Sjolander, S.A., Moustapha, S.H., "An Empirical Prediction Method for Secondary Losses in Turbines-Part I: A New Loss Breakdown Scheme and Penetration Depth Correlation", Journal of Turbomachinery, 2006.

[9] Benner, M.W., Sjolander, S.A., Moustapha, S.H., "An Empirical Prediction Method for Secondary Losses in Turbines-Part II: A new Secondary Loss Correlation", Journal of Turbomachinery, 2006.

[10] Kacker, S.C., Okapuu, U., A Mean Line Prediction Method for Axial Flow Turbine Efficiency, Journal of Enigneering for Power, 1982.

[11] Riboldi, L., Nord, L., "Offshore Power Plants Integrating a Wind Farm: Design Optimisation and Techno-Economic Assessment Based on Surrogate Modelling", Processes, 2018.

Particle Properties of CaO/Ca(OH)₂ Throughout Cyclisation in a Fluidized Bed for Thermochemical Energy Storage – Consequences for Fluidization

L. Morgenstern[1],[*], S. Ohmstedt[1], F. Kerscher[1] and H. Spliethoff[1]

[1] Chair of Energy Systems, Technical University of Munich, Boltzmannstr. 15, 85748 Garching b. München, Germany

[*]Corresponding author: leander.morgenstern@tum.de

Abstract

Calciumoxide/Calciumhydroxide is a promising storage material system for thermochemical energy storage at temperatures between 400 °C and 600 °C. Its main advantages are a high storage density, broad abundance, low cost, nontoxicity and chemical stability. The low heat conductivity of the material is challenging. It restricts the power in- and output of the system. But it can be maximized by using fluidized bed technology. This results in special requirements regarding material stability throughout storage cycles.

Decreasing mechanical stability of the material limits the applicability of the fluidized bed technology. Particle breakage with increasing number of storage cycles leads to an increasing share of fines in the fluidized bed and therefore an increasing risk of defluidization. This knowledge on particle properties and their changes throughout the storage cycles is crucial for reactor design. Of the numerous particle properties relevant in fluidization technology, in this work especially the Sauter mean diameter $d_{3,2}$ and the particle density ρ_p are accounted for.

Both parameters are studied experimentally in laboratory and pilot-scale reactors. The laboratory reactor has a fluidized bed volume of up to 1.8 L and a height to diameter ratio of up to 4. The pilot-scale system has a reactor volume of up to 30 L at a height to diameter ratio of up to 2.3. The results are analyzed regarding fluidization charachteristics based on Geldart classification and theoretical minimal fluidization velocity. A theoretical transition from Geldart A to C through B is observed accompanied by decreasing minimal fluidization velocities. However, due to the broad particle size distributions in the system, solely Geldart B fluidization behavior is observed in the reactor systems. High deviations in calculated theoretical minimal fluidization velocities and theoretical bed porosities at minimal fluidization impede further experimental investigation.

Keywords: Thermochemical Energy Storage, Calcium Hydroxide, Calcium Oxide, Heat, Fluidized Bed, Particle Properties, Reactor Development

Introduction/Background

Heat generation and storage, e.g. to balance fluctuating generation of renewables in industrial applications, is often overlooked although heat applications play a major role in the grid of most countries. Thermal energy storage is favorable because of probable higher efficiencies and lower specific cost compared to other storage types for electrical energy. [1]

Thermal energy storage can be subdivided into sensible, latent and thermochemical systems. Sensible heat storage is widely applied, e.g. as warm water storage in residential buildings [2]. It is based on the heat capacity of materials to store thermal energy by changing the temperature of the storage material [2]. This limits the applicability of the storage system due to the dependence of the storage power on the temperature of the storage material itself. The inherently needed high temperature difference of the charged storage material to the environment requires high insulation efforts to minimize heat losses [3].

Latent energy storage utilizes the phase change enthalpy of a storage material. Different technological applications have reached a commercial technology readiness level, especially for low temperature applications. High temperature applications are more limited in their implementation. A smaller temperature difference at approx. melting/evaporation temperature of the used material likely results in higher storage efficiency because of smaller heat losses. Latent heat storage output temperature is dependent on the phase change temperature of the used storage material. Latent heat storage is therefore still prone to self-discharge due to heat losses and technological difficulties linked to the phase change itself. Applications focusing on elevated temperatures from 20 °C to 300 °C are reported in literature. [2]

Thermochemical energy storage uses reversible chemical reactions with high reaction enthalpy. Typically, gas-solid-reactions are applied due to the easily possible separation of products in the charged state. This allows practically no energy losses during storage periods. Depending on the material system high application temperatures of up to 1500 °C are possible [2]. For providing process heat (300 - 500 °C) multiple materials (e.g. $Ca(OH)_2/CaO$, MgH_2/Mg [4,5]) have been suggested in literature [6]. Thermochemical heat storage therefore has the potential to close a gap in flexibilization of process heat technologies.

Calciumoxide/Calciumhydroxide is a promising storage material system for thermochemical energy storage at temperatures between 400 °C and 600 °C recently gaining interest in literature [7]. Its main advantages are a high storage density, broad abundance, low cost, nontoxicity, and chemical stability [7]. Two challenges have been identified for its application. These are the low heat conductivity of the material system and the decreasing mechanical particle stability throughout multiple storage cycles [8].

The low heat conductivity restricts the power in- and output of the system. It can be maximized by using fluidized bed technology [8,9]. The decreasing mechanical stability of the material however is limiting the applicability of the fluidized bed technology. Particle breakage with increasing number of storage cycles leads to an increasing share of fines in the fluidized bed and therefore a higher risk of defluidization [8,10]. This limits the overall number of storage cycles that can be performed on one batch of storage material. Knowledge on particle

properties and their development throughout the storage cycles are therefore crucial for reactor development.

Development of fluidized bed reactor systems is complex. Multiple material and fluid properties are relevant and interlock in ways not yet fully understood [9,11]. Of the numerous particle properties relevant in fluidization technology, investigations for technical applications are often started with determination of an equivalent particle diameter such as the Sauter mean diameter $d_{3,2}$ and the particle density ρ_p. With these particle properties a first classification of the fluidization characteristics is possible. Based on the material classification according to Geldart [12] these define the fluidizability and indicate the fluidization behavior that is most likely to occur. From there the minimal fluidization velocity is to be determined and can be analyzed theoretically [11,13,14]. However, in most applications an experimental evaluation for this parameter is necessary due to the not yet fully understood correlations between minimal fluidization and particle properties especially for technical grade materials [9].

Additional challenges arise when the particle properties (e.g. $d_{3,2}$, ρ_p) are not constant throughout the storage cycles of thermochemical energy storage using $CaO/Ca(OH)_2$ as reported in literature for $d_{3,2}$ [8,10,15]. In this manuscript the presented data on $d_{3,2}$ from a recent study [10] is expanded by correlating data on ρ_p. Additionally, the presented storage procedure is scaled from a lab-scale to a pilot-scale [16] reactor. Multiple storage cycles are performed. Aim is to push the knowledge on performance and fluidization characteristics of the technical, particulate $CaO/Ca(OH)_2$ system for application in fluidized bed thermochemical energy storage.

Material

$CaCO_3$ ($d_{3,2} = 219$ μm) from the technical limestone product Kalksteinedelbrechsand provided by Märker Holding GmbH (purity of approx. 94 w-% $CaCO_3$) is used as precursor. It is calcined within the respective experimental setup according to the conditions given in the respective section to produce the raw material CaO while CO_2 is released. Water (conductivity σ < 5μS) or nitrogen (Grade 5.0) is used for fluidization.

Experimental Setups

The experimental setups operated here are described in detail by Morgenstern et al. [10] for the laboratory reactor and by Wuerth et al. [16] for the pilot reactor. Here, a short overview of the most important design parameters is presented in Table 1.

Table 1: Design properties of the laboratory- and pilot scale reactors.

Property	Laboratory Reactor	Pilot Reactor
Diameter	80 mm	257 mm
Max. height to diameter	4,08	2,33
Temperature	Up to 850 °C	Up to 700 °C
Pressure Range	1 - 5 bar$_a$	1 - 7 bar$_a$
Maximal gas velocity	0.3 m/s	0.39 m/s
Fluidization Media	Nitrogen/water vapor	Nitrogen/water vapor/air

The reactors are built as cylindrical fluidized beds for operation in nitrogen or pure superheated steam atmosphere at varying superficial gas velocities u_0, temperatures T, and pressures p. In both reactors tuyere-nozzle fluidization plates that are similar to the ones described by Ostermeier et al. [17] are used. The laboratory scale reactor is specialized for fast, high throughput experiments to efficiently reach high storage cycle numbers with a relatively small batch size of up to 1.8 L. The pilot reactor is used for material characterization in conditions close to application conditions and features a bed volume up to 30 L.

Scaling in between the two reactors is performed to achieve a similar identity of the geometric values. Therefore, the bed height to reaction zone diameter can be kept identical in both reactors. An often-used measure for scaling relationships is the Reynolds number. [18] The setup periphery is designed to reach the same values for fluid flow at laboratory and pilot scale.

In literature, the most commonly used scaling laws are presented in the *full set* by Glicksman et al. [19] Due to the same energy storage material used in both reactors the system is scaled based on the first and the fourth defined dimensionless number to achieve the maximal possible similarity. The first dimensionless number incorporates the Reynolds number around a single particle. The flow rate is to remain constant between the two setups during cyclization. The fourth dimensionless number by Glicksman et al. sets the bed height (H) in relation to the reaction zone diameter (D). The material volume used in each setup should result in a constant D/H-value for both setups.

Experimental procedures

The experimental procedure has been reported in detail for the laboratory reactor [10]. Results presented here are additional analytics on the samples reported there. The experiment conditions have been transferred to the pilot-scale reactor from feasible experiments at laboratory-scale using scaling numbers according to Glicksman et al. The Reynolds number is kept at 0.6 and the diameter to bed height ratio at 1.55 at the start of the experimental procedures. During the experimental procedure the bed height varies in both setups due to particle attrition, discharge of fine material, and particle sampling. The most important information about the procedure is summarized here.

The storage material is produced by in-situ calcination in superheated steam atmosphere at bed temperatures of around 690 °C (Pilot) and 705 °C (Laboratory reactor) at fluidization velocities of 0.15 m/s and 0.27 m/s respectively. The discharging reaction (hydration) and the charging reaction (dehydration) are both performed in pure superheated steam atmosphere at reaction temperatures of 505 ± 5 °C and 540 ± 5 °C in both reactors respectively at atmospheric pressure. Each step of charging and discharging is carried out for defined times while ensuring full conversion. Full conversion was verified using thermogravimetric analysis on spot samples.

The main difference in terms of experimental procedure between the two setups is the control of the fluidization velocity. In the pilot plant it is regulated according to the momentary temperature and pressure within the fluidized bed. A fluidization velocity of 20 cm/s is set

throughout the cyclisation procedure. In the laboratory reactor a fixed mass flow of water (1.4 kg/h) is set and the true fluidization velocity is dependent on reactor temperature and pressure ranging from 0.18 to 0.26 cm/s during cyclization. Additionally, in the pilot reactor it is possible to take samples of the charged storage material (CaO) due to the advanced sampling system. This is not possible in the laboratory reactor due to construction limits. The sampling system of the pilot reactor consists of a probe to penetrate the fluidized bed via a linear guide system and is connected to a venturi nozzle, which creates a negative pressure relative to the reactor pressure. This leads to ejection of storage material via a piping system. The material is split from the gas stream via a cyclone. Therefore, in the pilot reactor samples can be taken during operation and fluidization. The nomenclature for describing the storage process cycle is presented in [10].

Analytical Equipment and Methods

The particle size distribution is measured with the Camsizer X2 from *Retsch GmbH* using the X-Jet module with a dispersion pressure of 30 kPa. The evaluation is based on the particle volume that results in the sum curve Q_3. $d_{3,2}$ is calculated as described in [10]. A sample divider is used for sample preparation.

The particle density is measured using the mercury porosimeter Auto Pore IV 9500 in combination with the Pore-Cor program by *Micromeritics Instrument Corp.*. The volume intruded into the particle pores is measured at increasing pressure steps. Intrusion curves with 53 logarithmically spaced pressure steps from 0.5 psi to 59989 psi are measured at equilibration times of 10 s for each step. Particle densities are calculated based on the intrusion volume by the algorithms provided by the supplier of the equipment. The volume attributed to a pore size (cylinder equivalent) smaller than 4 µm is regarded as pore volume.

Discussion and Results

The focus of the presented results is on the consequences that are to be expected from the changes of the Sauter mean diameter $d_{3,2}$ and the particle density ρ_p throughout the cyclisation of the storage material on its fluidization properties. Both are shown in the Geldart-diagram in Figure 1 for Ca(OH)$_2$ (laboratory and pilot reactor) and CaO (pilot reactor only).

Comparing the results from laboratory and pilot reactor similar trends in terms of particle size and particle density are observed. Both decrease with increasing cycle number while showing comparable development of particle density and breakage behavior. Thereby the range of particle densities are observed to be 1.97 g/cm^3 (start of cyclisation) to 0.65 g/cm^3 (end of cyclisation) while the Sauter mean diameter is observed to range from 355 µm to 14 µm.
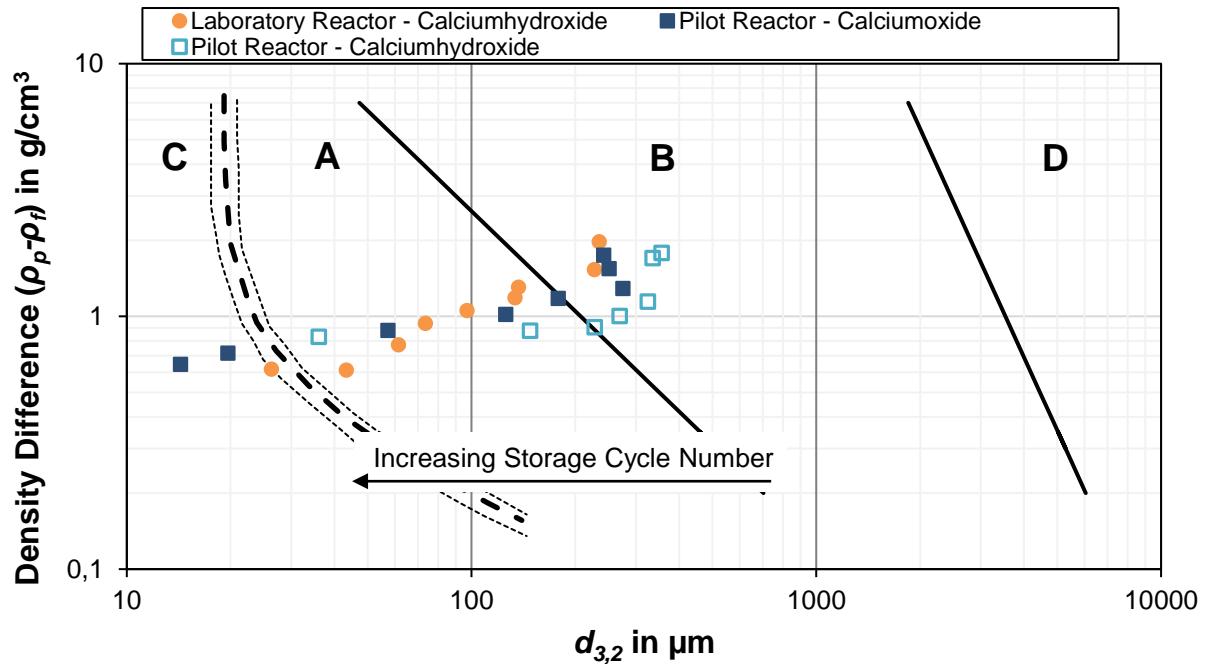
Figure 1: Geldart diagram adapted from [12] for transition A-B and B-D, evaluated for water vapor at 500 °C and 1.5 bar and from [9] for the C-A transition. Experimental results on cyclisation of CaO/Ca(OH)$_2$ in pure steam are depicted for laboratory scale reactor (0.6 kg Ca(OH)$_2$) and the pilot scale reactor (26.4 kg Ca(OH)$_2$).

These high ranges indicate significant consequences for the design of storage reactors as fluidization characteristics may significantly change. The Geldart classification starts at B (bubbling) and proceeds through A (areatable) to C (cohesive). All three classes have different characteristics. Besides the general fluidizability, that is typically very difficult for Geldart C material in contrast to A and B, the main difference is in the horizontal mixing and heat transfer behavior [9]. Reactors which can operate on three of the four Geldart classes are difficult to design. However, the presented laboratory and pilot scale reactor can fully fluidize all presented samples.

Following the classification in the second step of reactor development, the minimal fluidization velocity needs to be analyzed. Due to unavailability of sufficient sample amounts this is approached theoretically as a first step. An experimental investigation on u_{mf} and ε_{mf} is necessary and will be performed in future work.

The analytical approach using the Ergun equation at minimum fluidization velocity as described by Kunii and Levenspiel [11] and an empirical model for particulate materials with broad PSD (d_{10}/d_{90} down to 0,031 after C40.5 [10]) according to Anantharaman et al. [13] is applied. For the first method ε_{mf} is either estimated according to the approximation $\varepsilon_{mf,1} = \varepsilon_0 = 1 - \rho_{bulk}/\rho_p$ [9] or Gibson et al. [20]. Calculations are performed for the Geldart A and B samples only. The results are shown in Figure 2.
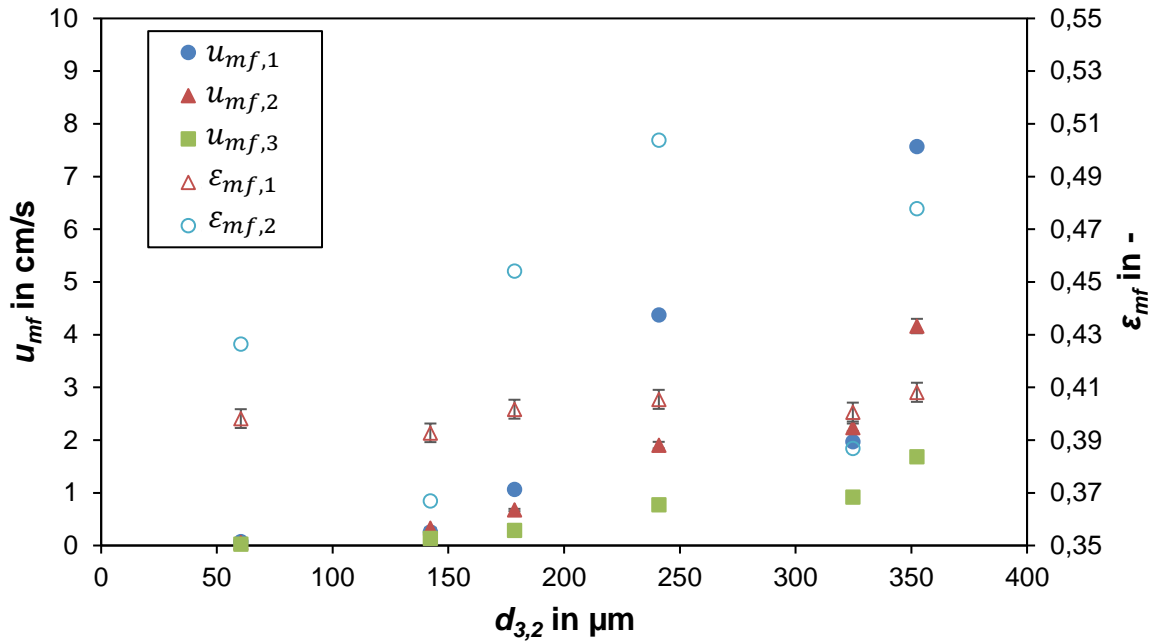
Figure 2: Theoretical minimal fluidization velocity calculated according to Kunii and Levenspiel ($u_{mf,1}$ and $u_{mf,2}$, [11]) and Anantharaman et al. ($\boldsymbol{u_{mf,3}}$, [13]) based on the particle density and Sauter mean diameter presented in Figure 1. For $u_{mf,1}$ the theoretical bed porosity $\varepsilon_{mf,1}$ according to $\varepsilon_{mf,2} = \varepsilon_0 = 1 - \rho_{bulk}/\rho_p$ [9] and for $u_{mf,2}$ the $\varepsilon_{mf,2}$ according to Gibson et al [20]. Gas properties are determined at the temperature and the pressure of the respective storage cycle.

Regarding ε_{mf} differences of up to 19.5 % depending on the estimation approach are determined transferring to deviations in u_{mf} of up to 56.5 % calculated using the theoretical approach presented by Kunii and Levenspiel [11]. Thereby the approach by Gibson for ε_{mf} results in lower values for the theoretical ε_{mf}. From there the ε_{mf} values calculated for the empirical correlation by Anantharaman et al. [13] are again significantly lower. The high deviations in the calculated values are expected for technical material systems with broad particle size distributions as pictured here. This reinforces the need for specific experimental investigations of u_{mf} and ε_{mf} in dependence of the material properties of the cycled storage material. The exceptionally low theoretical values smaller than 0.02 cm/s at $d_{3,2}$ of 60 µm affirm this.

Besides the absolute values the overall ranges and trends are as expected. Decreasing $d_{3,2}$ and ρ_p result in lower u_{mf} and ε_{mf}. This has consequences for the process design regarding material hold-up in the reactor (bed porosity) and mechanical stress applied to the storage material through fluidization. The latter is typically characterized by the fluidization number (u_0/u_{mf}) [9]. A higher number relates to higher mechanical stress for the particles. Since the minimal fluidization velocity decreases with decreasing $d_{3,2}$ the fluidization number increases with progressing storage cycle number if the fluidization velocity is kept constant and is not controlled dynamically during the cyclisation process. This may lead to a mutually reinforcing

effect as the particle stability likely decreases with decreasing particle density (compare to Figure 1).

Conclusions

The description of the particle properties $d_{3,2}$ and particle density ρ_p, which is performed in this work, is crucial for the development of fluidized bed reactors. It could be shown that laboratory scale data of these properties are likely directly scalable. However, the broad ranges within $d_{3,2}$ and ρ_p reported as well as the theoretically calculated u_{mf} and ε_{mf} may lead to significantly changing fluidization characteristics of the storage material throughout the storage cycles. Especially the Geldart C type material possesses high challenges in further technology development. It is aimed to develop technologies and operation strategies that allow relative constant material properties throughout the operation. In this work the first successful step in the pilot-scale reactor is presented. Further analysis of the results from the trials presented and following experimental investigations will be performed. Experimental characterization and strategies for handling of the changing material properties need to be pursued.

CRediT Authorship Contribution Statement

Leander Morgenstern: Conceptualization, Investigation, Validation, Formal analysis, Visualization, Writing – original draft, Writing - review & editing. *Sören Ohmstedt*: Data analysis, Formal analysis, Writing – original draft, Writing – review & editing. *Florian Kerscher*: Writing – review & editing, Supervision, Project administration. *Hartmut Spliethoff*: Resources, Supervision, Project administration, Funding acquisition.

Acknowledgments

References:

[1] H. Lund, P. A. Østergaard, D. Connolly, I. Ridjan, B. V. Mathiesen, F. Hvelplund, J. Z. Thellufsen, P. Sorknæs, in press. DOI: 10.5278/ijsepm.2016.11.2.

[2] M. Sterner, I. Stadler, *Energiespeicher - Bedarf, Technologien, Integration*, Springer Berlin Heidelberg, Berlin, Heidelberg **2017**.

[3] G. Li, *Renewable and Sustainable Energy Reviews* **2016**, *53 (8)*, 897–923. DOI: 10.1016/j.rser.2015.09.006.

[4] A. H. Abedin, *TOREJ* **2011**, *4 (1)*, 42–46. DOI: 10.2174/1876387101004010042.

[5] T. Bauer, W.-D. Steinmann, D. Laing, R. Tamme, *Annual Rev Heat Transfer* **2012**, *15 (15)*, 131–177. DOI: 10.1615/AnnualRevHeatTransfer.2012004651.

[6] A. A. Hawwash, H. Hassan, K. E. feky, *Applied Thermal Engineering* **2020**, *168*, 114776. DOI: 10.1016/j.applthermaleng.2019.114776.

[7]   K. Wang, T. Yan, R. K. Li, W. G. Pan, *Journal of Energy Storage* **2022**, *50 (11)*, 104612. DOI: 10.1016/j.est.2022.104612.

[8]   M. Becker, *Thermochemische Energiespeicherung mit Calcium-Oxid und -Hydroxid: Entwicklung eines Reaktorkonzeptes*. Dissertation, München **2020**.

[9]   J. Grace, X. Bi, N. Ellis, *Essentials of Fluidization Technology*, Wiley **2020**.

[10]   L. Morgenstern, E. Talebi, F. Kerscher, H. Spliethoff, *Fuel,* in press. DOI: 10.1016/j.fuel.2023.128220.

[11]   L. O. Kunii D., *Fluidization Engineering*, Butterworth-Heinemann **1991**.

[12]   D. Geldart, *Powder Technology* **1973**, *7 (5)*, 285–292. DOI: 10.1016/0032-5910(73)80037-3.

[13]   A. Anantharaman, R. A. Cocco, J. W. Chew, *Powder Technology* **2018**, *323*, 454–485. DOI: 10.1016/j.powtec.2017.10.016.

[14]   C. Y. Wen, Y. H. Yu, *AIChE J.* **1966**, *12 (3)*, 610–612. DOI: 10.1002/aic.690120343.

[15]   E. Talebi, L. Morgenstern, M. Würth, F. Kerscher, H. Spliethoff, *Fuel* **2023**, *344 (3)*, 128060. DOI: 10.1016/j.fuel.2023.128060.

[16]   M. Wuerth, M. Becker, P. Ostermeier, S. Gleis, H. Spliethoff, *Journal of Energy Resources Technology* **2019**, *141 (7)*, 51. DOI: 10.1115/1.4043629.

[17]   P. Ostermeier, A. Vandersickel, S. Gleis, H. Spliethoff, *Powder Technology* **2017**, *312 (Part A)*, 89–102. DOI: 10.1016/j.powtec.2017.02.015.

[18]   M. Rüdisüli, T. J. Schildhauer, S. M.A. Biollaz, J. R. van Ommen, *Powder Technology* **2012**, *217 (3)*, 21–38. DOI: 10.1016/j.powtec.2011.10.004.

[19]   L. R. Glicksman, M. R. Hyre, P. A. Farrell, *International Journal of Multiphase Flow* **1994**, *20*, 331–386. DOI: 10.1016/0301-9322(94)90077-9.

[20]   I. A. Gibson, C. J. Slim, Y. Zheng, S. A. Scott, J. F. Davidson, A. N. Hayhurst, *Chemical Engineering Research and Design* **2018**, *135*, 103–111. DOI: 10.1016/j.cherd.2018.05.009.

Photo-upcycling of CO_2 toward energy-dense hydrocarbons using MOF-based materials

N. Poudineh[1], M. Garvin[1], R. McIntosh[2], and S. Garcia[1*]

[1]Research Centre for Carbon Solutions, Heriot-Watt University, Edinburgh EH14 4AS, United Kingdom

[2]Institute of Chemical Sciences, School of Engineering and Physical Sciences, Heriot-Watt University, Edinburgh EH14 4AS, UK

[*]Corresponding author: s.garcia@hw.ac.uk

Abstract

Photoreduction of CO_2 into value-added chemicals and energy-dense hydrocarbons is an appealing technology to address the energy crisis and global warming issue. Metal-organic framework materials (MOFs) with their permanent porosity and tuneable band gap structures attracted great attention as promising materials for CO_2 photocatalysis. However, low stability and low catalytic performance resulting from fast charge recombination of MOF materials present ongoing challenges. In this study, Al-PMOF and Mg-MOF-74 were synthesized via microwave and solvothermal methods, respectively. Both MOFs showed good light absorption in the visible range of 380-780 nm, which is one of the important photonic properties in photocatalysis. The wider range of visible light absorption for Al-PMOF comes from the TCPP linker which is introduced as a good photosensitizer organic material. Al-PMOF and Mg-MOF-74 have narrow direct band gap energies of 1.85 eV and 2.73 eV. Next, their conduction bands (CBs) and valance bands (VBs) will be determined to further assess their potential for CO_2 photoreduction.

Keywords: CO_2 utilization, photoreduction, MOFs

Background

Human civilization strongly depends on providing energy from fossil fuel supplies such as natural gas, coal, and crude oil. However, consecutive and long consumption of these non-sustainable sources due to population growth and economic expansion has not only made a serious energy dependence but has also caused environmental pollution specifically global warming. One of the most serious consequences is the emission of greenhouse gases (GHGs) with carbon dioxide (CO_2) as the most prominent gas which contributes as one of the main reasons for this environmental concern [1, 2].

To address this challenge, carbon capture and storage (CCS) has been considered as one of the possible technologies that could help decrease the concentration of CO_2 in the atmosphere [3]. Utilization of captured CO_2 (CCU) has significant growth along with CCS to produce value-added chemicals or fuels such as carbon monoxide, ethanol, formic acid, and methanol [4, 5].

Currently, some commercialized technologies such as the dry reforming process, reverse water gas shift (RWGS), and methanol synthesis reaction are used for CO_2 conversion [6]. However, as CO_2 is a very stable molecule, breaking C=O bonds requires high activation energy ($\Delta_f H^{298}$ = -393.51 kJ/mol), hence to overcome the energy barrier, commercial-scale technologies use harsh operating conditions using fossil fuels as an energy source [6], [7].

3rd to 6th of September 2023
The University of Edinburgh, Scotland

**Heat Powered Cycles
Conference 2023**
Edinburgh

Heat in the new energy system

Therefore, a sustainable and green technology that can overcome the challenges of conventional routes is highly required. Catalytic photoreduction of CO_2 using solar energy and water could potentially resolve the current shortcomings associated with conventional CO_2 conversion technologies [3]. Although CO_2 photoreduction has many thermodynamic and kinetic challenges, it has emerged as an encouraging approach for addressing both energy supply shortage and global climate change, as it uses renewable energy without further producing CO_2 [8].

Photocatalysis is based on two half-reactions which are oxidation and reduction. Under light illumination, a semiconductor material can be excited if the energy of light is equal to or higher than the energy of the band gap (Eg) (the energy difference between the valance band and conduction band) of the semiconductor. This promotes the electrons in the valance band (VB) to the conduction band (CB) and leaves holes (h^+) in VB. The photogenerated holes and excited electrons ($e^- – h^+$) are responsible for the oxidation of water and the reduction of CO_2 respectively [3].

Metal-organic framework materials (MOFs), a class of porous crystalline materials assembled by coordination between organic linkers and inorganic metal clusters or metal ions, have gained much attention in photocatalysis [9]. In addition to the intrinsic properties of MOFs, the high surface area, permanent porosity, and tuneable structure and their ability to absorb visible light and transfer charges make them interesting and promising materials for various catalytic applications including CO_2 photoreduction [10]. However, low stability and low catalytic performance due to the short lifetime of charge carriers in MOF materials present ongoing challenges. Different combinations of MOF materials with metal or metal-free components (known as cocatalysts) have been studied with the aim of improving the stability, charge separation, charge transfer, and conductivity of MOFs [3].

The research presented here focuses on two objectives, first the synthesis of cocatalyst-based MOFs as photocatalysts for CO_2 photoreduction. Second, the study of the performance of the photocatalysts in the photoreduction of CO_2 into value-added chemicals. Based on a survey of the literature two MOFs, Al-PMOF and Mg-MOF-74 were selected due to their good CO_2 capture capacities, and visible light absorption [11, 12]. In order to improve the photonic properties and stability of these materials silver (Ag) nanoparticles were selected as cocatalysts to be loaded on the surfaces of the MOFs. Ag was chosen as it is a noble metal and has been demonstrated to increase charge production and transfer due to its localized surface plasmon resonance (LSPR) property, which further results in enhancing the efficiency of the reaction by decreasing charge recombination [3].

Discussion and Results

Al-PMOF and Mg-MOF-74 were synthesized using a microwave reactor and solvothermal method, respectively, using modified literature procedures [13, 14]. Powder diffraction X-ray (PXRD) results showed a successful crystal formation. The main peaks at 7.5 θ and 13.5 θ for Al-PMOF and 6.7 θ and 11.7 θ for Mg-MOF-74 match well with samples previously reported [13, 14] (**Figure 1a**).
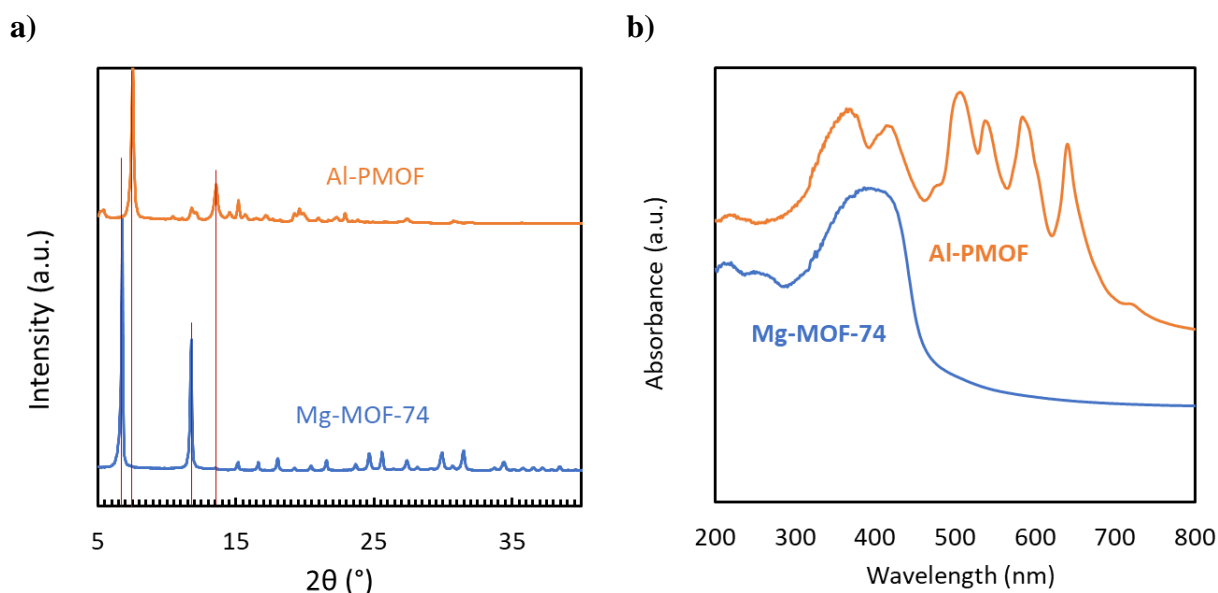
a)

b)

Figure 1. a) P-XRD pattern for MOF materials, b) UV-vis absorption spectra

UV-vis absorption spectrum of these MOFs is illustrated in **Figure 1b**, both two MOFs showed well visible light absorption (380-780 nm) with absorption edges of 450 nm and 700 nm for Mg-MOF-74 and Al-PMOF, respectively. Considering the fact that 43% of the sunlight that reaches Earth's surface is visible light, therefore, providing a photocatalyst that can absorb more light in the visible range is crucial. The band gap energy of these two MOFs was calculated using the Tauc plot method. The narrow direct band gap of Mg-MOF-74 and Al-PMOF (2.73 and 1.85 eV, respectively) can decrease charge recombination. Next, more studies on band gap structure will be performed to determine the energy levels of the valance band and conduction band for the MOFs in order to confirm if they are able to carry out the oxidation of water and reduction of CO_2, along with performing tests for CO_2 photoreduction.

Conclusions

In this work, two MOF materials have been selected with the aim of increasing CO_2 capture capacity and improving visible light absorption for CO_2 photoreduction applications. Silver as a cocatalyst has been selected to be loaded onto the MOFs to improve the photocatalysts' photonic characteristics and performance. The MOF materials were synthesized successfully and their light absorption capacity and band gap energies were measured. Next, after loading the cocatalyst materials, the performance of the photocatalysts will be studied in a bespoke photo-reactor setup using under simulated sunlight. The photonic properties of the photocatalysts will be studied using a three-electrode photoelectrochemical reactor.

References:

[1] Intergovernmental Panel on Climate Change, Climate Change 2013 – The Physical Science Basis, Cambridge University Press, 2014.

[2] Nandal N, Prajapati PK, Abraham BM, Jain SL., "CO2 to ethanol: A selective photoelectrochemical conversion using a ternary composite consisting of graphene oxide/copper oxide and a copper-based metal-organic framework", Electrochimica Acta, 2022 .

[3] Li X, Yu J, Jaroniec M, Chen X., "Cocatalysts for selective photoreduction of CO2 into solar fuels", Chemical reviews, 2019.

[4] Yu KM, Curcic I, Gabriel J, Tsang SC., "Recent advances in CO2 capture and utilization", ChemSusChem: Chemistry & Sustainability Energy & Materials. 2008.

[5] Song C., "Global challenges and strategies for control, conversion and utilization of CO2 for sustainable development involving energy, catalysis, adsorption and chemical processing", Catalysis today, 2006.

[6] Saravanan A, Vo DV, Jeevanantham S, Bhuvaneswari V, Narayanan VA, Yaashikaa PR, Swetha S, Reshma B. A., "Comprehensive review on different approaches for CO2 utilizatio n and conversion pathways", Chemical Engineering Science, 2021.

[7] White JL, Baruch MF, Pander III JE, Hu Y, Fortmeyer IC, Park JE, Zhang T, Liao K, Gu J, Yan Y, Shaw TW., "Light-driven heterogeneous reduction of carbon dioxide: photocatalysts and photoelectrodes", Chemical reviews, 2015.

[8] Habisreutinger SN, Schmidt-Mende L, Stolarczyk JK., "Photocatalytic reduction of CO2 on TiO2 and other semiconductors", Angewandte Chemie International Edition, 2013.

[9] Mo F, Zhou Q, Wang Q, Hou Z, Wang J., "The applications of MOFs related materials in photo/electrochemical decontamination: An updated review", Chemical Engineering Journal, 2022.

[10] Bathla A, Lee J, Younis SA, Kim KH,. "Recent advances in photocatalytic reduction of CO2 by TiO2–and MOF–based nanocomposites impregnated with metal nanoparticles. Materials Today Chemistry", 2022.

[11] Fateeva A, Chater PA, Ireland CP, Tahir AA, Khimyak YZ, Wiper PV, Darwent JR, Rosseinsky MJ., "A water-stable porphyrin-based metal–organic framework active for visible-light photocatalysis", Angewandte Chemie, 2012.

[12] Jiao Y, Morelock CR, Burtch NC, Mounfield III WP, Hungerford JT, Walton KS., "Tuning the kinetic water stability and adsorption interactions of Mg-MOF-74 by partial substitution with Co or Ni", Industrial & Engineering Chemistry Research, 2015.

[13] Boyd PG, Chidambaram A, García-Díez E, Ireland CP, Daff TD, Bounds R, Gładysiak A, Schouwink P, Moosavi SM, Maroto-Valer MM, Reimer JA., "Data-driven design of metal–organic frameworks for wet flue gas CO2 capture", Nature, 2019.

[14] Caskey SR, Wong-Foy AG, Matzger AJ., "Dramatic tuning of carbon dioxide uptake via metal substitution in a coordination polymer with cylindrical pores", Journal of the American Chemical Society, 2008 .

Heat and mass transfer analysis of an aqueous sodium hydroxide based thermal storage system

Sai Yagnamurthy[1*], Steven Metcalf[1] and Robert Critoph[1]

[1]School of Engineering, University of Warwick, Coventry, CV47AL, United Kingdom

[*]Corresponding author: sai.yagnamurthy@warwick.ac.uk

Abstract

To meet the global thermal energy demands, thermal storage system integration is necessary to cater to peak demands as well as to cater to fluctuating loads from renewables. Thermochemical storage systems are seen to offer amongst the highest energy densities in this regard. To contribute to the ongoing efforts in realising compact thermal energy storage systems, the present study carries out a heat and mass transfer evaluation on a spiral finned heat exchanger with aqueous sodium hydroxide solution. A parametric experimental study with varying solution flow rates and operating temperatures is carried out, wherein a temperature jump of around 10°C between the absorber and evaporator is observed to be optimal. Further, the heat and mass transfer coefficients are evaluated based on the experimental data, through a lumped parameter approach. The impact of the heat and mass transfer coefficient variation on the discharge power is studied to determine the maximum discharge power attainable. Further, the impact of a design modification viz. preheating section removal is studied through a lumped parameter approach. It is observed that without the preheating section the discharge power is lower by 10.9 % and beyond an overall heat transfer coefficient value of 1800 $W/m^2.K$, there is no need of a preheating section. An improvement of up to 34.5% over the experimental discharge power is estimated to be attainable with the heat transfer coefficient improvement. Similarly, an improvement of up to 31.6% is observed with a mass transfer coefficient increase. Finally, the impact of fin height improvement is experimentally investigated with and without the preheating sections to identify the critical parameter for performance. The present study helps to identify the design targets for maximising the discharge power and storage density of the thermal storage.

Keywords: Absorption, Thermal storage, Sodium hydroxide, Heat transfer, Mass transfer

Introduction

Heating end use contributes to at least 50% of global energy consumption, out of which at least 46% was consumed for domestic heating applications [1]. In order to achieve the objectives set by the Paris agreement 2015 to keep the rise in global average temperature to below 1.5°C above pre-industrialised levels, there is a need for the adoption of renewables and alternate energy sources. In this regard, thermal energy storage plays an important role in the renewable energy integration of buildings for short term or inter-seasonal load reduction applications (IEA SHC Task 42). Among the various storage options, thermochemical storage is seen to have the highest energy density, lower heat losses and offers flexibility in storage temperature [2]. Absorption based thermochemical storage materials such as LiCl, NaOH, CaCl2, etc. are seen to offer higher energy densities over their adsorption counterparts, with their operating temperatures suitable for building applications [2] and also seen to improve heat transfer when used as salt solutions [3]. Further, liquid media based salt solutions are seen to improve heat transfer during discharging phases. The LiCl-H_2O pair has been commercialised for heat storage applications, but has been restricted for short term applications due to the high cost. Crystallisation of salts has been shown to significantly

increase the storage density, but poses a challenge for the system design to manage the crystallisation [4]. The widely used NH_3-H_2O pair in absorption cooling systems, poses toxicity concerns when considered for a long-term storage application (due to the large quantity of ammonia required). Among the other widely used pairs in absorption systems, LiBr-H_2O pair has been extensively studied for use in long-term storage applications and has shown to yield better performance over other water based pairs [5]. A relatively inexpensive option over the LiBr-H_2O (4750 Euro/tonne) pair suitable for long-term storage applications is seen to be NaOH-H_2O (1000 Euro/tonne) [6]. The pair has also been tested for long-term storage applications and it is seen to improve the storage density by 3 and 6 times for domestic hot water supply and space heating applications, respectively [7]. $CaCl_2$-H_2O pair is regarded as the most inexpensive option for long-term thermal storage but is seen to be limited by the temperature jump during absorption [8]. Thus, the NaOH-H_2O pair can be considered to have significant scope for long term storage in domestic heating applications and is explored in the present study.

The heat exchanger design plays a crucial role in determining the system's performance and storage density [2]. N'Tsoupkoe et al. [3] carried out a dynamic analysis on a LiBr-H_2O thermal storage system and studied the impact of varying heat exchanger area and solution flow rate on storage density. It is observed that solution flow rate is the most critical parameter and a low flow rate with good wettability are desirable for high storage density. Tube bundle heat exchangers with solution falling film have been used for their low cost and simple design [5,9]. However, the absorption performance of these heat exchangers have been reported to be limited by low surface wettability and solution exposure duration for the NaOH-H_2O pair [10]. Other falling film based compact heat exchanger designs such as plate, membrane, etc., shown to be effective for cooling systems aren't observed to be beneficial for improving the storage density for thermal storage systems. This is due to the lower concentration difference observed in these designs between the inlet and outlet streams. To address these issues Fumey et al. [11] proposed a spiral fin heat exchanger design which ensures sufficient exposure duration for the solution for absorption to maximise the concentration change over a single pass. The present study attempts to further the analysis on the spiral heat exchanger through a parametric investigation of the heat exchanger's design, operation and heat and mass transfer characteristics. This can help to understand the impact of the critical parameters on the performance as well as the identification of the optimal operating and design conditions.

System description

The experimental test setup consists of two vessels with spiral heat exchangers for the solution and distilled water for absorption and evaporation processes, respectively, as shown in Figure 1 and described by Fumey et al.[11]. The solution heat exchanger specifications are shown in Table 1. The finned portion of the tube is around 1 m in length, of which the initial 15 cm is insulated from the heat transfer fluid through a hollow PTFE tube of 2 mm thickness fitted internally. This insulation serves to achieve a rapid increase in the solution temperature to enhance the heat transfer rate, as shown in Figure 2. Figure 2 shows the typical temperature profiles of the thermocouples recorded at various heights of the heat exchanger, with thermocouple 2 being at the end of the preheating section. It can be seen that highest temperatures are recorded for thermocouple 2, with a temperature rise of up to 15°C over the inlet.

Table 1. Spiral finned heat exchanger specifications

Length (m)	Outer diameter (mm)	Pitch (mm)	Fin height (mm)
1.2	12.7	1.9	3
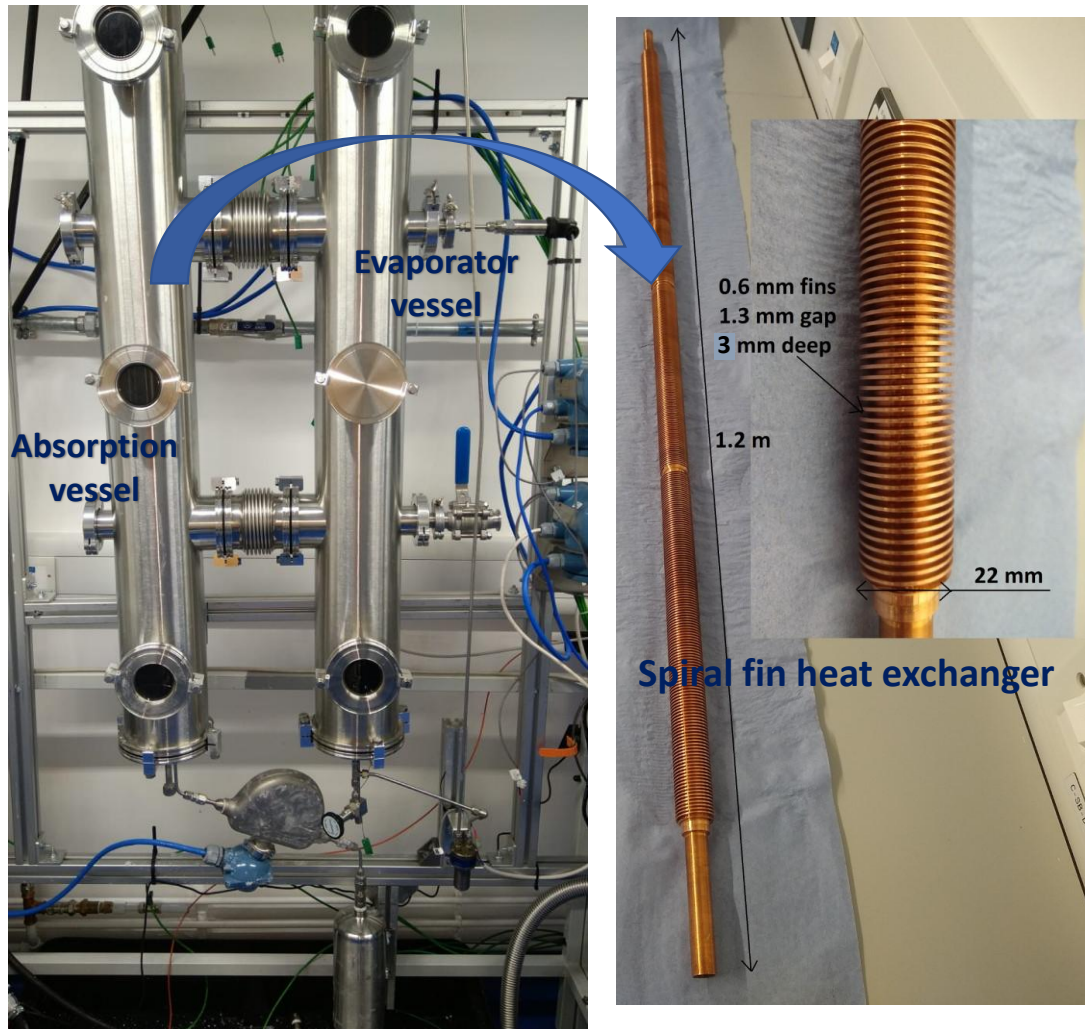
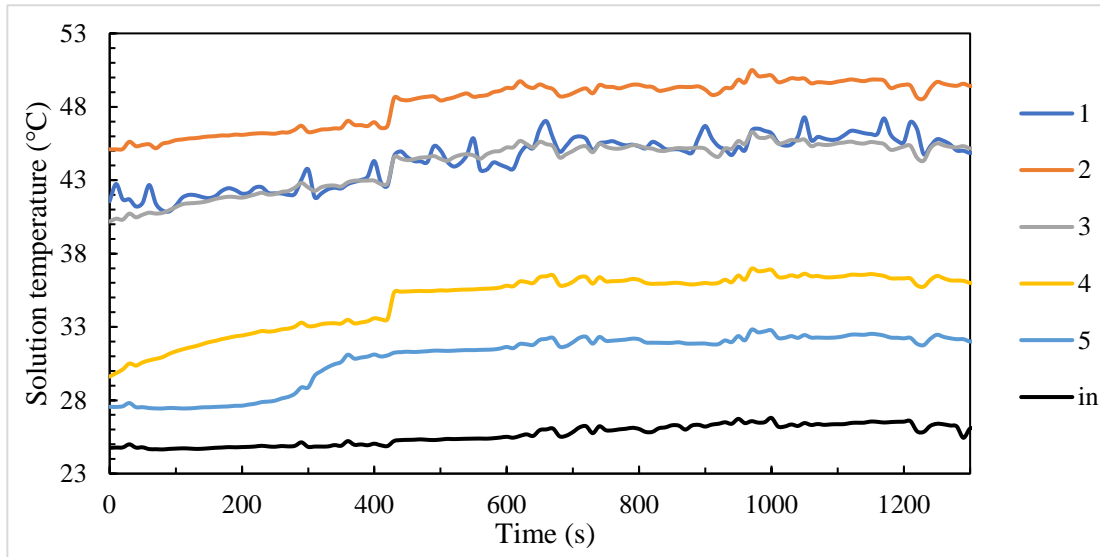*Figure 1. Absorption and evaporator test vessels*

Figure 2. Typical temperature profiles of thermocouples positioned at various lengths along the solution heat exchanger

The solution flow rate to the absorption vessel is regulated with a microflow Microflex® peristaltic pump with an accuracy of ±1% as shown in Figure 3. The solution flow rates are measured using Coriolis meters of ±1% accuracy. The solution temperatures are recorded at 5 equidistant locations on the heat exchanger and the heat transfer fluid's (water) temperatures are recorded at the inlet and outlet using thermocouples of 0.1°C accuracy. The outlet solution concentration is assessed from the density and temperature measurements of the sampled solution from the outlet tank, which can be substituted into the concentration correlation mentioned in Fumey et al.[11].
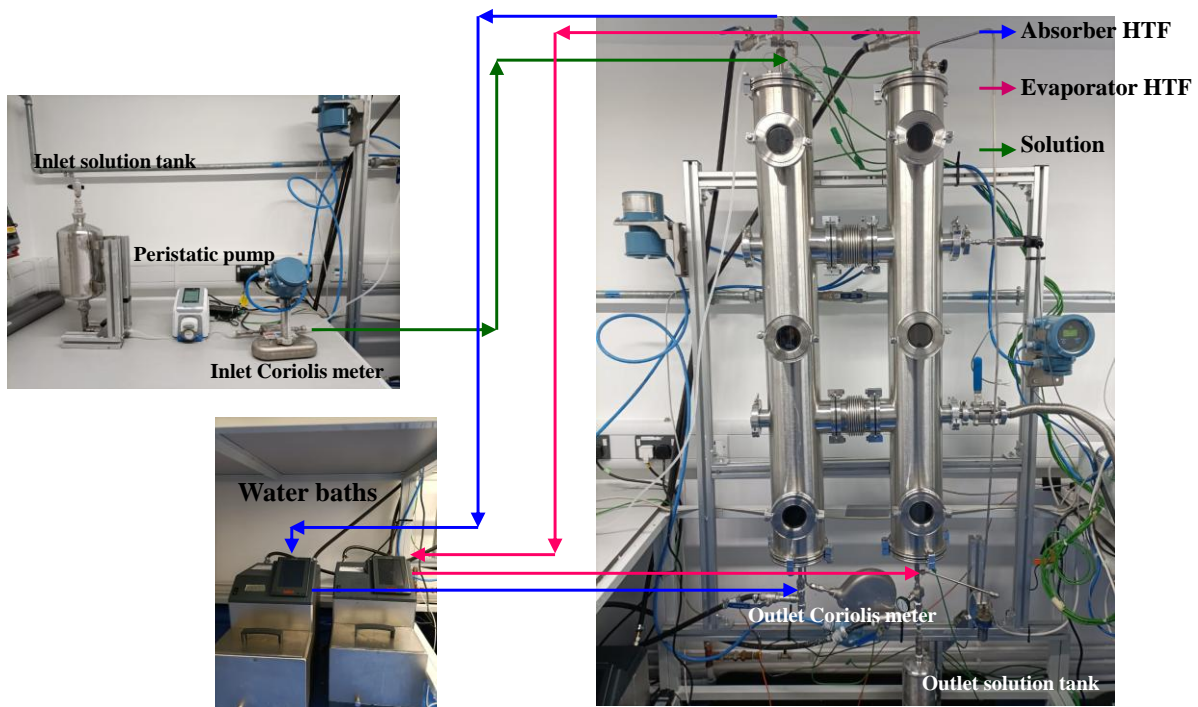
Figure 3. Absorption test setup layout

Results and discussion

Parametric studies

The solution inlet concentration has been maintained at 50% for all of the absorption experiments.

Impact of varying evaporator temperatures

Table 2 shows the heat exchanger's heating power and outlet concentration with varying evaporator temperatures. The absorption rate is seen to be nearly equal for evaporator temperatures between 12-20 °C and is seen to reduce for the case with 7°C. This can be attributed to the relatively higher outlet equilibrium concentration limit for this case over the others, resulting in slower absorption kinetics.

Table 2. Absorption performance with varying evaporator temperature

Evaporator temperature (°C)	Solution flow rate (g/min)	Cooling water inlet temperature(°C)	Heating power	Solution outlet concentration
20	6.2	27.9	141.4	31%
15.5	6.8	25.0	151.8	31%
11	6.0	21.3	150.7	31%
7	5.7	17.8	124.4	32%

Impact of varying cooling water inlet temperatures

The impact of cooling water temperature variation for an evaporator temperature of 11°C and the inlet solution concentration of 50% is shown in Table 3.

Table 3. Absorption performance with varying cooling water inlet temperatures

Case	Solution flow rate (g/min)	Cooling water inlet temperature(°C)	Heating power	Solution outlet concentration
1	5.8	21.3	150.7	30%
2	7.5	25.4	99.0	37%
3	6.5	29.6	69.9	39%

The heating power is observed to decline rapidly with the cooling water inlet temperature increase from 21°C to 25°C and then decrease at a lower rate. This can be primarily attributed to the trend of the vapor diffusion coefficient for the three cases as shown in Figure 4, which in turn depends on the solution's viscosity.
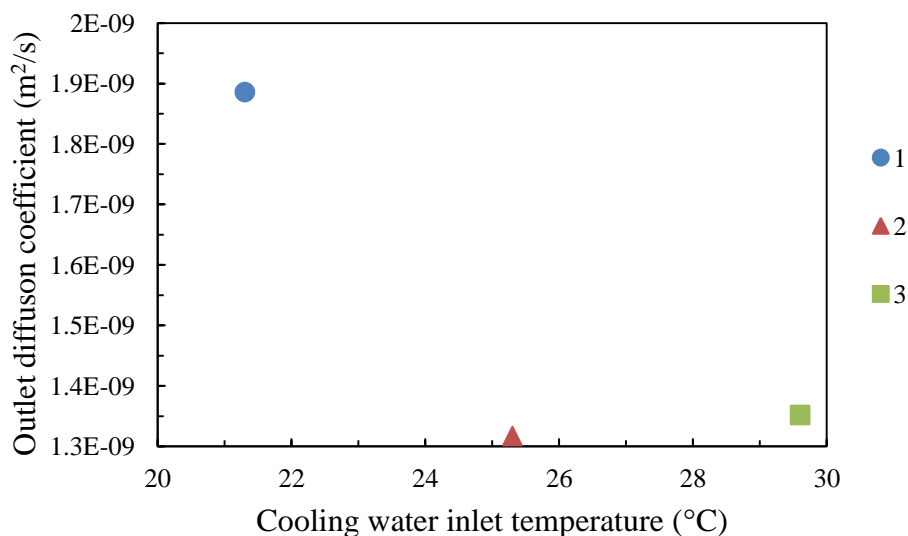
Figure 4. Diffusion coefficient variation for the three cases of cooling water inlet temperatures

Impact of varying solution flow rates

Table 4 shows the impact of solution flow rate variation, with the evaporator temperature at 11°C, the inlet solution concentration at 50% and the cooling water inlet temperature at around 25°C.

Table 4. Impact of solution flow rate variation on absorption performance

Case	Solution flow rate (g/min)	Heating power	Solution outlet concentration	Average solution temperature (°C)
1	5.7	80.7	36%	34.4
2	7.5	99.0	37%	36.4
3	9	61.1	42%	32.3

The fins are observed to be flooded for all the flowrates. The heating power can be said to be primarily dependent on the temperature difference between the solution and the cooling water, as is evident from the average solution temperature trend in the table. The solution temperature in turn depends on an interplay between the absorption heat generation rate and convection heat transfer to the cooling water. The absorption heat generation rate depends on the solution's concentration profile at any given length of the tube. While the exposed surface can be assumed to be at equilibrium concentration, the concentration increases towards the tube wall. This concentration difference at any given lenght is expected to be lower for a lower solution flow rate owing to the higher absorption duration per unit mass of the solution

within the test rig. This can be confirmed from the trend shown in the table, where the outlet solution concentration increases with the increasing solution flow rate. For Case 3 with the highest solution flow rate of 9 g/min, the lowest heating power is observed despite a high concentration difference within the solution. It can be said that the convection heat transfer from the higher solution flow rate dominates over the absorption heat generation in this case. The optimal balance between both the heat transfer rates is observed for Case 2.

Impact of heat and mass transfer coefficients

From the results discussed in section 3.1, the optimal temperature jump between the evaporator and the absorber is seen to be 10°C. For these conditions, the average heat and mass transfer coefficients shown in equations (1)-(2) are computed as shown in Table 5. The energy and mass balance equations are given as follows:

$$\dot{m}_{htf} \times 4.18 \times \left(T_{htf,out} - T_{htf,in}\right) = UA \frac{\left(T_{htf,out} - T_{s,in}\right) - \left(T_{htf,in} - T_{s,out}\right)}{\log\left(\frac{\left(T_{htf,out} - T_{s,in}\right)}{\left(T_{htf,in} - T_{s,out}\right)}\right)} =$$

$$\dot{m}_s\left(h_{in} + \left(\frac{X_{in}}{X_{out}} - 1\right)h_v - \frac{X_{in}}{X_{out}}h_{out}\right) \tag{1}$$

$$\dot{m}_s\left(\frac{X_{in}}{X_{out}} - 1\right) = kA\frac{(X_{in}-X_{eq,in})+(X_{out}-X_{eq,out})}{2} \tag{2}$$

Where $\dot{m}$ is the mass transfer rate (kg/s), U is the overall heat transfer coefficient (W/ m^2.K), A is the heat exchanger surface area (m^2), k is the mass transfer coefficient (kg/m^2.s), T is the temperature (K) and h is the enthalpy (kJ/kg.K). The subscripts *htf* stands for heat transfer fluid, *in* stands for inlet, *out* stands for outlet, *eq* stands for equilibrium, *s* stands for solution and *v* for vapor.

Table 5. Heat and mass transfer coefficient evaluation

Case No.	Evaporator temperature (°C)	Solution flow rate (g/min)	Cooling water inlet temperature(°C)	Heat transfer coefficient (W/m^2.K)	Mass transfer coefficient (kg/m^2.s)$\times 10^{-2}$
1	20	6.2	27.9	606.0	4.2
2	15.5	6.8	25.0	669.0	4.9
3	11	6.0	21.3	724.9	3.8
4	7	5.7	17.8	667.0	3.4
Average				666.7	4.1

The impact of the heat transfer coefficient variation on the discharge power is analysed from equation (1) using Matlab® 2021 platform. The results for the operating conditions shown for Case 3 in Table 5 is shown in Figure 5. It can be seen that the discharge power tends to saturate at around 169 W with an increase in the overall heat transfer coefficient beyond 1266 W/m^2.K. This implies that the mass transfer coefficient becomes the limiting factor for the

heat exchanger's performance beyond a certain heat transfer coefficient value for various operating conditions.
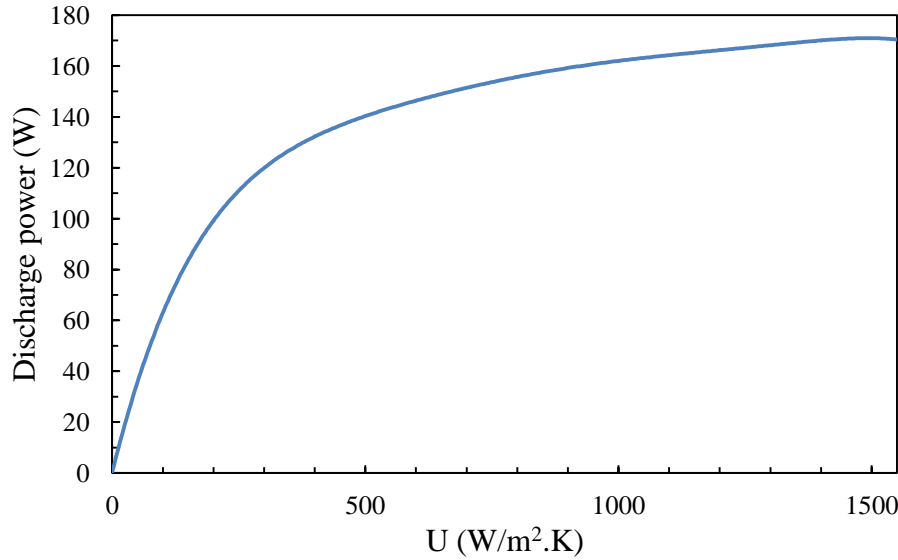

Figure 5. Impact of heat transfer coefficient variation on discharge power

An interesting aspect worth exploring in this context is the impact of the elimination of the preheating section on the discharge power, with varying overall heat transfer coefficient of the tube. For this purpose, the heat and mass transfer processes are analysed across two sections of the solution heat exchanger. The starting section involves a solution temperature rise where the enthalpy gain due to absorption dominates over the heat loss to the heat transfer fluid as shown in equations (3)-(5). It is assumed that the heat transfer fluid outlet temperature equals that of the solution temperature within a short span from the entry point and can be neglected in comparison to the length of the heat exchanger. The solution attains a temperature increase until the point of the outlet enthalpy of the solution being equal to that of the inlet enthalpy and the heat transfer area of this section is indicated by A1 as shown in the equations. In the preceding section of the heat exchanger, the heat loss to the heat transfer fluid dominates over the enthalpy gain due to absorption. The mass and energy balances across this section are shown in equations (6)-(7). The equations (3)-(7) are solved using an iterative approach such that the total surface area of the heat exchanger nearly equals its actual surface area as shown in equation (8). Equation (9) shows the correlation between the heat transfer coefficients of the heat exchanger with and without preheating sections considered in this evaluation. Since the heat exchanger with preheating section has only 85% of its surface area available for heat exchange with the heat transfer fluid (due to 15cms of preheating section length), a compensation factor of 0.85 is considered for the heat exchanger without a preheating section.

$$\dot{m}_{htf} \times 4.18 \times \left(T_{htf,out} - T_{htf,1}\right) = \dot{m}_s \left(\frac{x_{in}}{x_1} - 1\right) h_v \tag{3}$$

$$\dot{m}_s \left(\frac{X_{in}}{X_1} - 1\right) h_v = kA_1 h_v \frac{(x_{in} - x_{eq,in}) + (x_1 - x_{eq,1})}{2} = U_{np}A_1 \frac{(T_{s,1} - T_{htf,1})}{2} \tag{4}$$

$$h_1 = \frac{x_1}{0.5} h_{in} \tag{5}$$

$$\dot{m}_s \frac{x_{in}}{x_1} \left(\frac{x_1}{x_{out}} - 1\right) = kA_2 \frac{(x_{out} - x_{eq,out}) + (x_1 - x_{eq,1})}{2} \tag{6}$$

Heat Powered Cycles
Conference 2023
Edinburgh

Heat in the new energy system

3rd to 6th of September 2023
The University of Edinburgh, Scotland

$$U_{np}A_2 \frac{(T_{s,1}-T_{htf,1})-(T_{s,out}-T_{htf,in})}{\log\left(\frac{(T_{s,1}-T_{htf,1})}{(T_{s,out}-T_{htf,in})}\right)} = \dot{m}_{htf} \times 4.18 \times (T_{htf,1}-T_{htf,in}) = \dot{m}_s \frac{x_{in}}{x_1}(h_1 +$$

$$\left(\frac{x_1}{x_{out}}-1\right)h_v - \frac{x_1}{x_{out}}h_{out}) \tag{7}$$

$$A_1 + A_2 = A \tag{8}$$

$$U_{np} = U_p/0.85 \tag{9}$$ The subscript *np* represents no-preheating section and *p* represents with preheating section in this context. The subscript *1* represents the section having the enthalpy rise of the solution dominant, *2* represents the section having the heat transfer rate to the heat transfer fluid dominant.

The discharge power estimation from the heat exchanger without the preheating section for varying overall heat transfer coefficients is shown in Table 6. As shown in Table 6, the discharge power for each condition is evaluated such that the total heat exchanger surface area combining both the sections remains nearly equal. It can be seen that without the preheating section, the discharge power is lower by 10.9% over that with the preheating section for the same heat transfer coefficient. Upon improvement in the heat transfer coefficient the discharge power is seen to rise beyond that of the heat exchanger without the preheating section and saturates at around 200 W as shown in Figure 6. This improvement in the discharge power without the preheating section can be attributed to the increase in heat exchanger surface area for the latter case.

Table 6. Impact of heat transfer coefficient on discharge power and surface areas for heat exchanger without preheating section

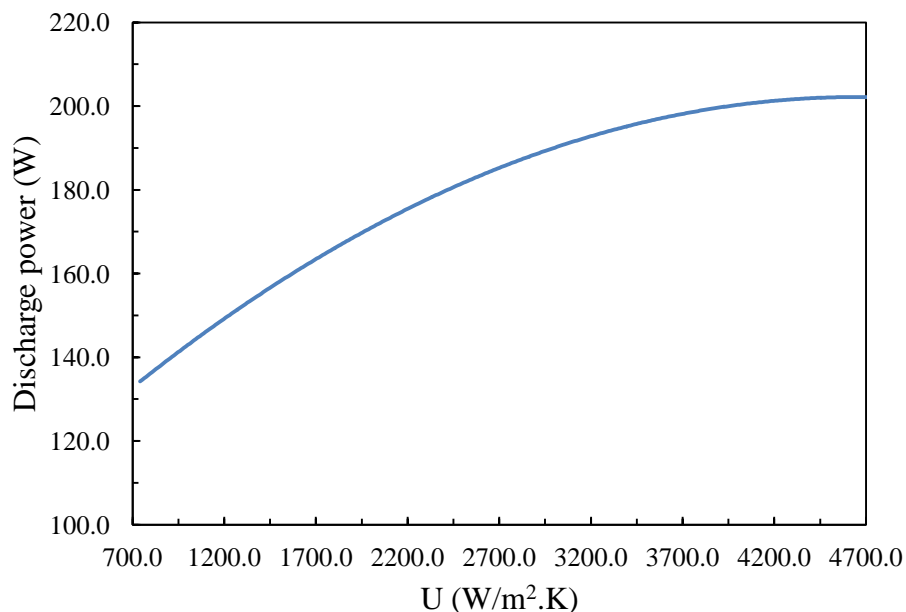| U (W/m².K)	Discharge power (W)	A_1 (m²)	A_2 (m²)	A (m²)
741.8	132.4	0.006	0.036	0.042
940.8	137.9	0.005	0.033	0.038
1112.7	147.7	0.004	0.036	0.040
1411.2	160.2	0.003	0.037	0.040
1881.6	170.0	0.002	0.037	0.039
2116.8	174.2	0.002	0.036	0.038
2508.9	179.7	0.002	0.036	0.038
2665.7	185.3	0.002	0.038	0.040
3214.5	189.5	0.001	0.037	0.038

Figure 6. Impact of heat transfer coefficient on discharge power for heat exchanger without preheating section

Impact of mass transfer coefficient variation

Figure 7 shows the impact of mass transfer coefficient increase for the heat exchanger with preheating section with the same heat transfer coefficient and operating conditions of Case 3 shown in Table 5. It can be seen that the discharge power saturates at around 180 W with an increase in the mass transfer coefficient beyond 0.2 kg/m^2.s. This is due to the first order dependence of the uptake rate, wherein it reduces as the concentration approaches that of the equilibrium value.
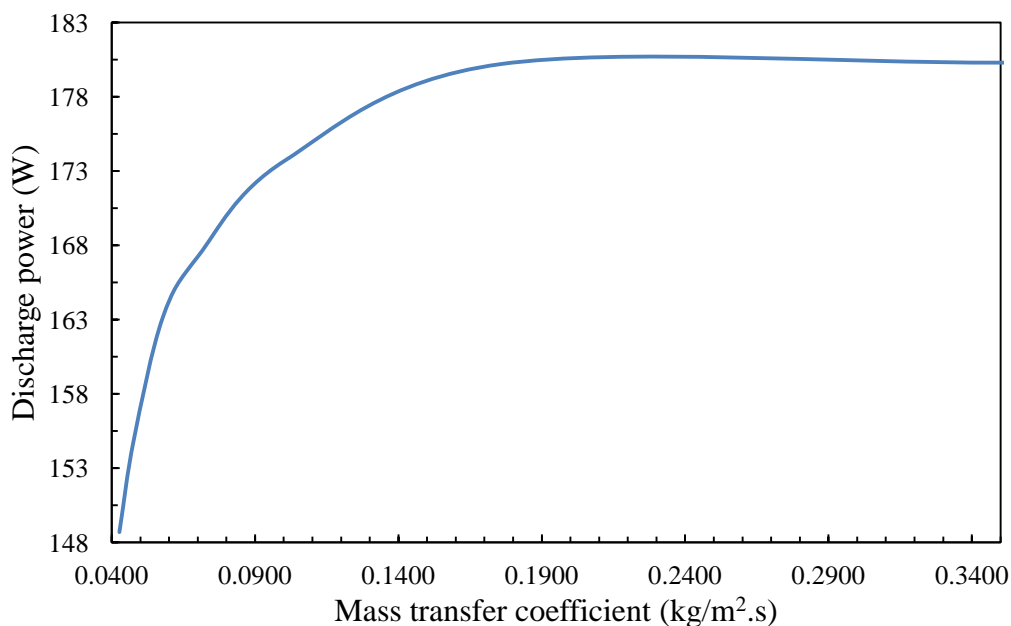
Figure 7. Impact of mass transfer coefficient variation on discharge power

Impact of fin height improvement

The absorption performance has been tested on a heat exchanger with wider fins whose dimensions are shown in Table 7, to study the impact on the heat and mass transfer rates across the solution film. The testing has been carried out on a heat exchanger with and without preheating sections and the results are as shown in Table 8, where a performance reduction over the previous heat exchanger is seen. Further, it can be observed that the preheating section reduces the discharge power, implying that the reduction in the heat transfer surface area dominates over the heat transfer enhancement due to temperature rise. The reduction in performance with wider fins can be attributed to the increase in the solution film thickness, which increases the heat and mass transfer resistances of the film.

Table 7. Wider finned heat exchanger dimensions

Length (m)	Outer diameter (mm)	Pitch (mm)	Fin height (mm)
1.04	15.8	1.9	6.35

Table 8. Absorption performance of wider finned heat exchanger

Preheating	Solution flow rate (g/min)	Cooling water inlet temperature(°C)	Discharge power	Solution outlet concentration
Without	8	27.7	138.6	36%
With	6.7	28.0	127.5	36%

Conclusions

An experimental evaluation of a finned heat exchanger tube is carried out through a parametric evaluation of solution flow rates, evaporator and absorber temperatures. The key observations from the experimental study are as follows:

- The diffusion coefficient of the solution is critical to vapor absorption, which further depends on the temperature jump between the absorber and evaporator. A temperature jump of 10°C is observed to be optimal.
- A low solution flow rate is preferred over higher solution flow rates, owing to the dominance of absorption heat generation rate and a larger absorption duration.

A heat and mass transfer analysis is further carried out using a lumped parameter approach and the experimental heat and mass transfer coefficients are determined. The observations of the heat and mass transfer analysis are as follows:

- A discharge power improvement of up to 12.1% is observed with the heat transfer coefficient increase of the heat exchanger with preheating section. A higher heat transfer coefficient is observed to facilitate a further discharge power improvement by up to 34.15%, with the elimination of the preheating section.
- A mass transfer coefficient of over 0.2 $kg/m^2.s$ and a heat transfer coefficient over 4000 $W/m^2.K$ (without preheating section) are desirable to maximise the discharge power and storage density of the thermal storage system.

Further experimentation with wider finned heat exchanger has revealed that narrow fins yield higher performance owing to the lower solution film thickness. The findings of the present study anticipate identifying the appropriate design parameters and operating conditions for the solution heat exchangers of long term thermal storage applications.

References

[1]   International Energy Agency, *Global Energy and CO2 Status Report*, 2017.

[2]   J. Lizana, R. Chacartegui, A. Barrios-Padura, J.M. Valverde, *Advances in thermal energy storage materials and their applications towards zero energy buildings: A critical review*, Applied Energy. Volume 203, 2017.

[3]   K.E. N'Tsoukpoe, N. Le Pierrès, L. Luo, *Numerical dynamic simulation and analysis of a lithium bromide/water long-term solar heat storage system*, Energy. Volume 37, 2012.

[4]   K.E. N'Tsoukpoe, N. Le Pierrès, L. Luo, *Experimentation of a LiBr–H2O absorption process for long-term solar thermal storage: Prototype design and first results*, Energy. Volume 53, 2013.

[5]   X. Zhang, M. Li, W. Shi, B. Wang, X. Li, *Experimental investigation on charging and discharging performance of absorption thermal energy storage system*, Energy conservation and management, 2014.

[6]   X. Daguenet-Frick, P. Gantenbein, J. Müller, B. Fumey, R. Weber, *Seasonal thermochemical energy storage: Comparison of the experimental results with the modelling of the falling film tube bundle heat and mass exchanger unit*, Renewable Energy. Volume 110, 2017.

[7]   R. Weber, V. Dorer, *Long-term heat storage with NaOH*, Vacuum. Volume 82, 2008.

[8]   L. Hui, N.K. Edem, L.P. Nolwenn, L. Lingai, *Evaluation of a seasonal storage system of solar energy for house heating using different absorption couples*, Energy Conversation and Management, Volume 52, 2011.

[9]   X. Daguenet-Frick, P. Gantenbein, E. Frank, B. Fumey, R. Weber, *Development of a numerical model for the reaction zone design of an aqueous sodium hydroxide seasonal thermal energy storage*, Solar Energy. Volume 121, 2015.

[10]   B. Fumey, R. Weber, P. Gantenbein, X. Daguenet-Frick, S. Stoller, R. Fricker, V. Dorer, *Operation Results of a Closed Sorption Heat Storage Prototype*, Energy Procedia. Volume 73, 2015.

[11]   B. Fumey, R. Weber, L. Baldini, Liquid sorption heat storage – A proof of concept based on lab measurements with a novel spiral fined heat and mass exchanger design, Applied Energy, Volume 200, 2017.

3rd to 6th of September 2023
The University of Edinburgh, Scotland

Heat Powered Cycles
Conference 2023
Edinburgh

Heat in the new energy system

Experimental investigation on the thermal performance of low-temperature OM55/GNPs/SPAN80 nanocomposites

Elisangela J. D'Oliveira[1]*, Tomas Costa[1], Dominika Zabiegaj[1] Ulugbek Azimov[1], Dominic Groulx[2], and Sol Carolina Costa Pereira[1]

[1]Northumbria University, Newcastle, NE1 8ST, UK

[2]Dalhousie University, Halifax, NS B3H 4R2, Canada

*Corresponding author: elisangela.doliveira@northumbria.ac.uk

Abstract

The increasing energy consumption in buildings and its contribution to greenhouse gas emissions have created a pressing energy problem worldwide. As a result, there is a growing global demand for sustainable energy technologies and storage, and latent heat thermal energy storage (LHTES) based on phase change materials (PCMs) is one of the most promising technologies. Although PCMs have suitable thermal properties, they possess low thermal conductivity, a critical parameter determining how efficiently the material can absorb or transfer heat. This study investigates the thermal properties of a commercial mixture of fatty acids (OM55) as PCM enhanced with Graphene nanoplatelets (GNPs), mixed with Sorbitan monooleate (SPAN80) as a surfactant. The results of the thermal conductivity measurements concluded that the inclusion of the GNPs did not increase the thermal conductivity of the NePCMs as expected. Several factors, including potential agglomeration of the nanoparticles, may have contributed to this outcome, resulting in a thermal barrier. Furthermore, the results indicated that the addition of the surfactant had a negative impact on the thermal conductivity enhancement obtained from the inclusion of GNPs into the OM55; the SPAN80 has possibly caused a thermal resistance within the NePCMs, cancelling out the slight thermal conductivity enhancement obtained from the GNPs.

Keywords: Phase change material; Graphene nanoplatelets; Thermal storage; bio-based.

Introduction

Energy consumption in buildings has increased yearly, contributing significantly to greenhouse emissions, resulting in an imminent energy problem. Thus, there is a growing demand for sustainable energy technologies worldwide. Thermal energy storage (TES) based on phase change materials (PCMs) is a promising technology. These systems offer several benefits over other types of TES systems (e.g., sensible heat), including increased energy density [1], making them ideal for applications where space is limited; also, their ability to store high amounts of heat at a quasi-constant temperature makes them suitable for temperature sensitive applications [2]. Although PCMs have suitable thermal properties, they possess low thermal conductivity, which is a critical parameter that determines how efficiently heat can be transferred to or from the material.

Several studies have investigated the thermal properties of different types of PCMs to properly design LHTES systems which have significant discrepancies in the reported results [3]. Moreover, recently there has been a growing interest in bio-based materials, including PCMs, as they offer a sustainable alternative to traditional petroleum-based PCMs as paraffins [4]. Bio-based PCMs are often made from renewable resources such as vegetable oils, beeswax, and other natural sources; they are biodegradable and can provide the same benefits as the PCMs extracted from non-renewable resources. Murphy and Gumtapure [5] analysed the

thermal and volume-dependent behaviour of commercially available organic Bio-PCM OM55. OM55 is thermally stable within the operating temperature of 45-60ºC, with a degradation temperature of 154.6ºC, much higher than its operating temperature range. The authors suggested that for the optimum amount of energy storage and discharge in OM55, operating the LHTES unit over a temperature range between 46-59ºC for domestic hot water (DHW) applications would be recommended. Rolka et al. [6] conducted experimental tests of the thermophysical properties of the OM55, and two other medium-temperature PCMs, OM65 and RT55. The two studies conducted on the thermophysical properties of OM55 were in good agreement.

Although OM55 is an excellent material for DHW applications and heating systems, its low thermal conductivity affects its overall performance and limits its commercial application. Different methods have been used to improve the thermal conductivity of PCMs, such as adding high-conductive particles. Adding nanoparticles, such as graphene nanoplatelets (GNPs) or carbon nanotubes (CNTs), can result in a faster and more efficient heat transfer within the PCM. The increase in the thermal conductivity of nano-enhanced phase change materials (NePCMs) is due to the high surface area-to-volume ratio of the nanoparticles [7], which creates a network of high-conductive pathways, allowing heat to transfer quickly and efficiently through the storage media material.

Harish et al. [8] evaluated the improvement in the thermal conductivity of lauric acid with GNPs; the results showed that the inclusion of GNP improved the thermal conductivity of the base material by 230% at a loading of 1 vol%. The results showed an insignificant effect of the inclusion of GNPs in the latent heat or the melting temperature of the PCM. The microstructure, chemical and thermophysical properties of RT70/GNP composites were investigated by Liu et al. [9]. The thermal conductivity of the RT70 was improved by 21.6%, and the latent heat of fusion decreased by 10.5%, with 0.2 wt.% of GNPs. The synthesis process implemented in this study involved a two-step preparation method, where the NePCMs samples were mechanically stirred for 2 h, followed by ultrasonication for another 2 h, both at constant temperatures of 80°C. The author conducted suspension stability tests for 6 days, concluding that the strength of the ultrasonication treatment substantially impacts the dispersion of the nanoparticles into the base material; the best stability results were obtained with a magnetic stirring at 400 rpm and ultrasonication at 200 W. Although the two studies described previously used similar synthesis processes and materials to prepare the NePCMs, there are significant discrepancies between the reported results for the thermal conductivity. It can be attributed and influenced by a complex interplay of various factors, including the size, shape, and orientation of the nanoparticles, to differences in the measurement methods and conditions used to evaluate the resulting different thermal conductivity values.

Although the inclusion of nanoparticles enhance the thermal conductivity of NePCMs, due to the difference in density between the base material and the nanoparticles, challenges related to the stability and sedimentation have to still be solved [10]; and their susceptibility to Brownian motion further affects it. Different methods could be employed to mitigate the sedimentation issue, such as using surfactants or nucleating agents to prevent the aggregation of nanoparticles and maintain a homogeneous dispersion within the base PCM [3].

Recently in literature, different surfactants have been used to prepare NePCMs, including anionic, cationic and non-ionic surfactants; their selection depends on the specific properties of the PCM and the nanoparticles [11]. Some of these surfactants include polyvinyl alcohol (PVA)[12], cetrimonium bromide (C-TAB) [13-16] , polysorbate 80 (Tween-80) [15], sorbitan monooleate (SPAN80) [16, 17] and sodium dodecyl sulfate (SDS) [13-15]. The thermal characteristics of various NePCMs incorporated with GNPs and different surfactants were

investigated by Sheikh et al. [18] to enhance the cooling properties and chemical stability of commercially available PCM. In their research, they evaluated surfactants such as sodium dodecyl sulfate (SDS), sodium dodecylbenzene sulfonate (SDBS), and sodium stearoyl lactylate (SSL). The results demonstrated different trends; for instance, the latent heat capacity decreases at high concentrations of GNPs when using SSL and SDS as surfactants. The highest thermal conductivity observed was for the NePCM with SDS and 5wt.% of GNPs, reaching a value of 1.03 W/m. K, with an enhancement of 368%.

To the best knowledge of the authors from an extensive literature review, no study has been conducted examining the effectiveness of thermal conductivity enhancement through the incorporation of graphene nanoplatelets (GNPs) in the commercially available bio-based PCM supplies by PLUSS Technologies, OM55. The present study aims to investigate the thermal properties of the NePCMs based on OM55 and GNPs using Sorbitan monooleate (SPAN80) as the surfactant. A preliminary comparison study was conducted also with a cationic, industrial commercially available surfactant CTAB; a short chain water-soluble, biocompatible, and biodegradable Polymer with surface activity, PVA; as well as SDS and Tween-80.

Methodology

Materials

In this work, the base PCM is OM55, a commercial mixture of fatty acids provided by PLUSS Technologies. Graphene nanoplatelets (GNPs, purity = 99.5 %) were purchased from Iolitec, with a specified thickness of 2 nm. Sorbitan monooleate (SPAN80), a non-ionic surfactant purchased from BLD Pharmatech Ltd., was used to improve the stability of the NePCMs. The raw materials were used as received without further purification.

Table 1. Thermophysical properties of the Phase Change Material [19]

Properties	OM55
Density [solid] [kg/m^3]	935
Density [liquid] [kg/m^3]	941
Specific heat capacity [solid] [kJ/kg. K]	2.68
Specific heat capacity [liquid] [kJ/kg. K]	2.76
Latent heat of fusion [kJ/kg]	188
Thermal conductivity [solid] [W/m. K]	0.16
Thermal conductivity [liquid] [W/m. K]	0.1
Phase change temperature [ºC]	55

Table 2. Key thermal properties of graphene nanoplatelets [20]

Properties	Values
Thickness [nm]	2
Specific Surface Area (SSA) [m^2/g]	750

Preparation methods

The NePCMs were prepared using a two-step method described in Figure 1, as it offers better incorporation of the particles into the base PCM, as reported by many studies [21-23]. Firstly, 70 grams of PCM in the solid state was melted using a hot plate stirrer (IKA TM RCT) at a

constant temperature of 80°C. After being completely melted, 2, 4 and 6 wt.% GNPs were added to the PCM. Then, the NePCM was magnetically stirred at the speed of 800 rpm, keeping the temperature at 80°C for 30min. Afterwards, the molten samples were sonicated in an ultrasonic bath (BANDELIN "Sonorex digitec") for 30 min at 80°C; to improve the dispersion of GNPs in the liquid PCM. The time for the ultrasonication was determined based on previous studies that reported favourable outcomes. An additional NePCM was prepared, mixing 4wt.% of GNPs with SPAN80 to investigate the thermal stability of the material; to properly disperse the nanoparticles in fluid and obtain a stable suspension, 28ml of SPAN80 was slowly added and continuously stirred for a period of 15 min. During the preparation process, the temperature was maintained at ambient temperature. After this, the nanoparticle with the surfactant mixture was added to the melted PCM, the synthesis process described previously was performed. The total mass fraction of the surfactant used is 40 wt.%. Figure 1 illustrates a complete schematic representation of the preparation of the NePCMs.
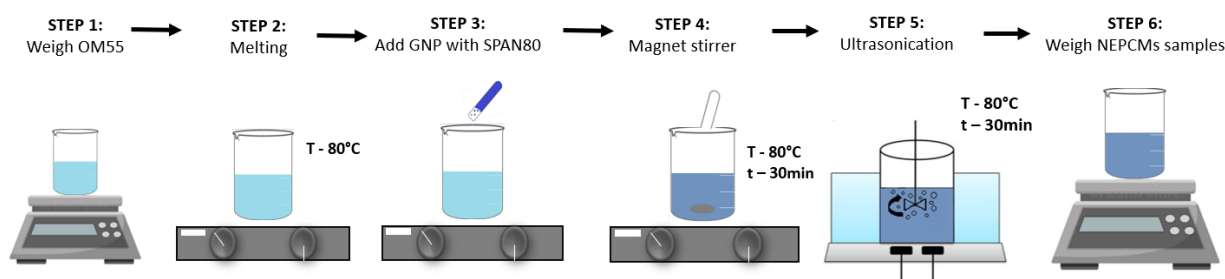
Figure 1. Two-step method synthesis process on the preparation of the NePCMs through magnetic stirring and ultrasonication

Characterisation measurements

Morphology: The morphology and microstructure of the pure OM55, GNPs and nano-enhanced OM55 were observed using scanning electron microscopy (SEM, TESCAN MIRA3) at room temperature. The samples were coated with a platinum coating (Quorum Q150V), 5nm in thickness, to increase the electrical conductivity of the samples. The SEM images were taken at an accelerating voltage of 3.5kV and the same view field to allow a better comparison between the samples. A lower accelerating voltage was used to capture the images as it offers many advantages for the type of samples we investigated (i.e., non-conductive specimens), such as reducing the potential damage of the sample, allowing a more accurate and reliable imaging; however, that can also reduce the penetration depth and signal intensity, limiting the imaging depth.

Latent and specific heat, phase-change temperature: Thermal properties of the PCM and NePCMs, such as melting and crystallisation temperature, latent heat, and specific heat capacity, were measured using Differential Scanning Calorimetry (DSC, 131 SETARAM). The DSC measurements were performed at two heating and cooling rates, 2 K/min and 10 K/min, in a temperature range of 15 to 90°C for heating and 90 to 15°C for cooling, under a constant stream of argon gas atmosphere and nitrogen to control heating and cooling rates better. Three samples of 7-9 mg of each NePCM were prepared using a balance with a precision of 0.1 mg.

Thermal Conductivity: The solid thermal conductivity of nanocomposites was measured by a thermal conductivity instrument (Linseis THB 100), with a measurement accuracy of 5%. The samples prepared were 50 mm ×25 mm with an average thickness of 5mm. The THB/B sensor with a measuring rate of 0.01 to 2 W/m. K was placed between the two solid block samples, and a weight of about 3 kg was used to improve the contact with the sensor. For a single-point

calibration, the sensor was calibrated using Polymethyl methacrylate (PMMA) with a thermal conductivity of 0.194 W/m.K. The solid thermal conductivity was measured at room temperature. Several measurements were taken for each sample, and the reported values were average.

Discussion and Results

Morphology analysis

The morphology of the NePCMs based on OM55/GNPs/SPAN-80 was examined using the SEM to gain insights into the distribution and arrangement of the GNPs within the OM55 matrix. The analysis aims to establish a relationship between the NePCMs morphology and the thermal properties, including the thermal conductivity. The images obtained are presented in Figure 2.
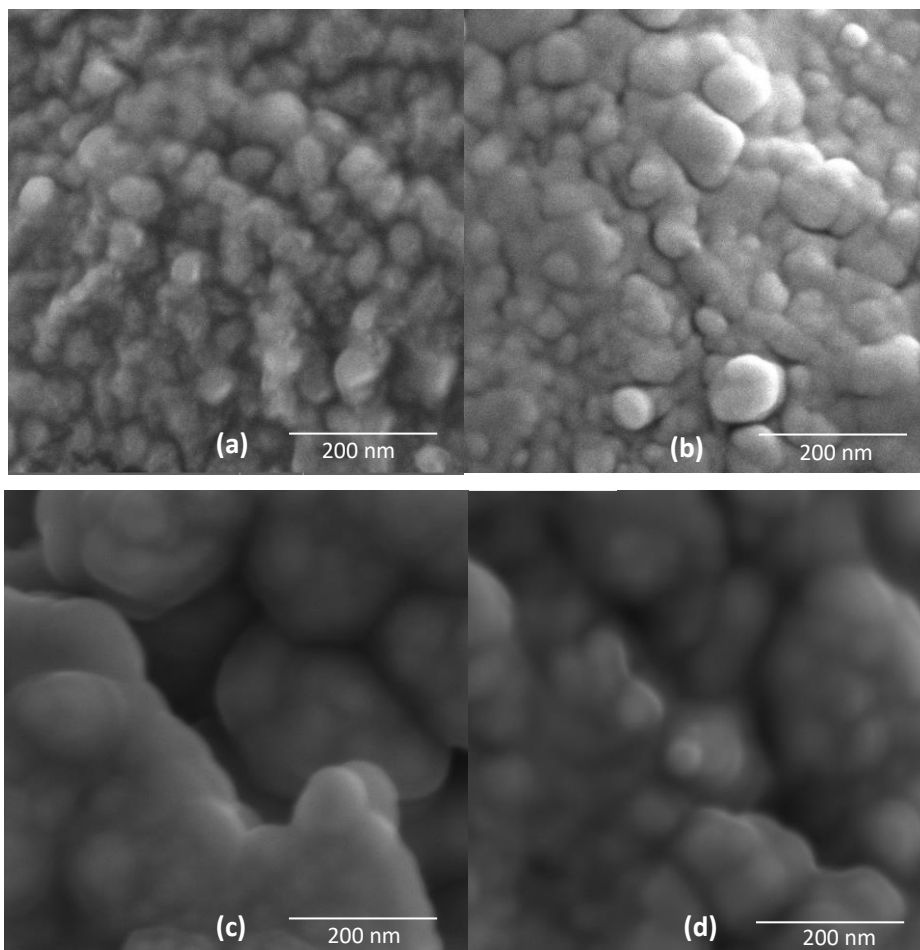
Figure 2. Microscopic structures for: a) OM55 with 2 wt.% GNPs; b) OM55 with 4wt.% GNPs; c) OM55 with 6wt.% GNPs; and d) OM55 with 4wt.% GNPs/SPAN80 at a view field of 1.2 μm and scale bar of 200nm

In the SEM images can be observed a substantial agglomeration of the GNPs within the four prepared NePCMs, indicating that the dispersion of the GNPs within the OM55 matrix is not uniform. This agglomeration can have various implications for the thermal properties of the prepared NePCMs, potentially affecting properties and factors such as thermal conductivity and heat transfer efficiency. Further investigation is required to evaluate the impact of this issue on the thermos-physical properties of the NePCMs and techniques to avoid it.

Thermal property characterization of OM55/GNPs/SPAN80 NePCMs

The following thermal properties of the pure OM55 and NePCMs were obtained, including the onset temperature and latent heat capacity for both the endothermic and exothermic processes, using the Differential Scanning Calorimeter (DSC). One cycle at a scanning rate of 10 K/min was included at the beginning of the cycling temperature programme to eliminate the thermal history of the samples before the measurements and reduce discrepancies and outliers from the measurements obtained. The measurements for the latent heat capacity were taken at 10 K/min, as at this scanning rate the error is minimized ensuring reliable and consistent results, while at 2 K/min, the phase change transition (onset temperature) value tends to be more accurate; testing the samples at both heating rates allowed more accurate measurements of thermal properties stated [24]. The detailed data obtained by the DSC measurements are shown in Table 3, and the DSC curve of the pure OM55 is shown in Figure 3 (b).

Table 3. Variation on the latent heat capacity and phase change temperature for both melting and solidification processes in regard to loading content of GNPs and SPAN80

Material	Wt. %	Melting temperature [ºC]	Latent heat of melting [kJ/kg]	Latent heat difference [%]	Solidification temperature [ºC]	Latent heat of solidification [kJ/kg]
OM55	**0**	54.1	164.3	-	53.2	158.7
	2	53.9	160.0	-2.6%	53.5	156.7
	4	53.6	153.5	-6.7%	53.8	159.2
	6	52.9	144.1	-13.1%	53.4	142.9
OM55/ 40wt. % SPAN80	**0**	52.5	124.7	-27.4%	51.7	128.3
	4	49.1	76.9	-72.5%	51.2	81.02

As expected, the latent heat capacity of the NePCMs is reduced due to the incorporation of the GNPs and SPAN80 into PCMs; however, the reduction is slightly bigger than the reduction of PCM mass. Figure 3 (b) displays the melting and solidification processes of the pure PCM. During the melting process, the slope change in the heating curve reaches the endothermic peak/or the maximum point at 56.8ºC, and the end of the melting process is at 57.8ºC. The melting point of the OM55 was measured using the onset temperature of 54.1ºC, with the measured latent heat being 164.3 kJ/kg.

The latent heat from incorporating the 2, 4 and 6 wt.% of GNPs during the melting process were 160.0, 153.5 and 144.1 kJ/kg and -156.7, -159.2 and -142.9 kJ/kg during the solidification process. There is a slight decrease in the latent heat capacity with the inclusion of the GNPs. However, it is not directly proportional to the inclusion of the nanoparticles; for instance, with the inclusion of 4wt.% of GNPs, there is a reduction of 6.7% of the latent heat capacity. SPAN80 was added to improve the sedimentation/stability issues between the base PCM and the graphene nanoplatelets. However, a considerable impact was observed on the latent heat capacity compared with pure PCM, melting at 76.9 kJ/kg and solidification at 81.02 kJ/kg, respectively.
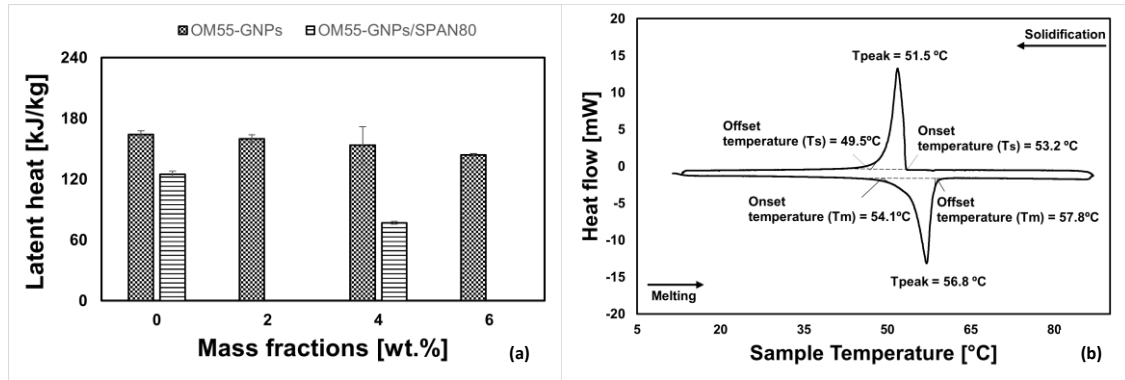
Figure 3. (a) Effects of the inclusion of GNPs into the latent heat capacity of the NePCMs and (b) DSC curve of pure OM55 at a heating rate of 10 K//min

Thermal conductivity

Table 4 summarises the variation of the solid thermal conductivity of the OM55 and NePCMs with different mass fractions, 2-6 wt.%, and enhancement rates. The thermal conductivity measurements of the OM55/4wt.% GNPs and SPAN80 were also included. The solid thermal conductivity measurements were taken at approximately 20°C, and the tests were repeated 3 times for each sample. The reported values are the average measurements obtained from multiple data points, and the corresponding standard deviations are included to indicate the variability observed among the measurements.

Table 4. Effect of the mass fraction of GNPs on the Thermal conductivity of the NePCMs

Material	Wt. %	Thermal conductivity [W/m. K]	Thermal conductivity enhancement [%]	Standard deviation [W/m. K]
OM55	0	0.222	-	0.017
	2	0.252	12.7	0.009
	4	0.256	14.2	0.002
	6	0.259	15.4	0.011
OM55/40wt. % SPAN80	4	0.222	-	0.009

Figure 4 shows the thermal conductivity results obtained from the different NePCMs prepared with the inclusion of the SPAN80. It is generally expected that the addition of graphene nanoplatelets would increase the thermal conductivity of the nano-enhanced OM55 due to their high thermal conductivity (range of 3000-6500 W/m.K [25]) and a high specific surface area. However, the thermal conductivity of the NePCMs did not increase as expected. Many reasons could explain this unexpected behaviour, including the possibility that the GNPs have formed agglomerations, which can create thermal barriers, reducing the thermal conductivity enhancement of the NePCMs. The thermal conductivity results of the OM55 with 2, 4 and 6wt.% of GNPs, were 0.252 W/m.K, 0.256 W/m.K and 0.259 W/m.K, where the thermal

conductivity enhancement is 12.7, 14.2 and 15.4% when comparing with the thermal conductivity of the pure OM55, 0.222 W/m.K.
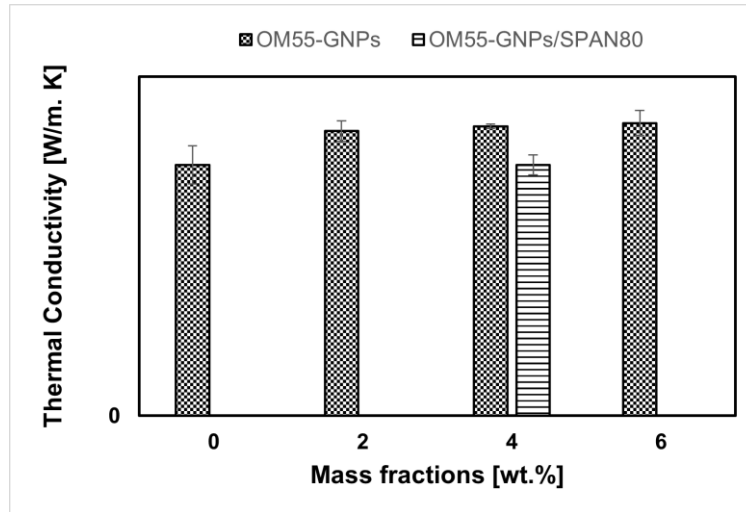
Figure 4. Thermal conductivity of the NePCMs

Table 5 presents a comparison of the thermophysical properties (i.e., latent heat of fusion, thermal conductivity and phase change temperature) among the supplier data, two different studies published in literature [5, 6], and the findings of the current study. The results obtained show a slight difference between the different sources. For instance, the measured latent heat of fusion differs by approximately 13.5% between the current study and data provided by the supplier, 164.3 and 188 kJ/kg, respectively. Many factors can be attributed to these discrepancies including the testing conditions to which the materials were subjected as well as the measurements methods implemented. In the current study, the DSC equipment was used to determine the latent heat of fusion and phase change temperature of the pure material, and the supplier used the T-history method. Besides, the latent heat of fusion and phase change temperature, evidently there are clear differences on the results obtained from the thermal conductivity. The difference between the two, measured data and supplier is 27%, 0.16 and 0.22 W/m. K, respectively. As the latter properties, the equipment used does have a significant impact on the results obtained, for the current study the transient hot bridge (THB-100, Linseis) method was used. Conversely, the supplier used the KDS-Pro equipment, which uses a transient line heat source to measure thermal conductivity at a 60ºC temperature for the testing conditions.

Table 5. Comparison of thermophysical properties between supplier data, literature review and current study

Properties	Supplier	Ref. [5]	Ref. [6]	Current study
Latent heat of fusion [kJ/kg]	188	175	170.00±13.61	164.30±3.42
Thermal Conductivity [W/m. K]	0.16	0.210±0.018	0.16	0.220±0.017
Phase Change Temperature [°C]	55	54.8	55.30±0.80	54.10±0.22

Investigation and selection of different surfactants

This sub-section presents the investigation of six different surfactants, including Tween-80, SPAN80, Chitosan, PVA, C-TAB and SDS based upon the composition of the polarity of the head group (non-ionic, anionic, and cationic) in the stability of the NePCMs. The preparation process for all samples was identical, 4wt.% of carbon particles (graphite powder, 20 µm size, supplied by Sigratherm Carbon) were weighed, and the same concentration of surfactants was gradually added to the carbon particles. The samples were thoroughly mixed until a slurry

consistency was obtained. Subsequently, the melted PCM at 80°C was added to the carbon and surfactant mixture using the method outlined in Figure 1. Table 6 shows the type of surfactant, their charging type and product specification, including critical micellar concentration (CMC) which is defined as the surfactant concentration at which micelle starts to form in the solution [26]. All information is available from the suppliers.

Table 6. Type of surfactants, their charging type and product specification

Surfactant	Charge	CMC	Molecular weight	pH	Viscosity	Ref.
Tween-80	Non-ionic	13-15 mg/liter (25ºC)	-	5.5-7.5	400-620 cps	[27]
SPAN80	Non-ionic	-	428.62 g/mol	-	-	[28]
Chitosan	Cationic	-	-	-	200-800 cps	[29]
PVA (87-89% hydrolized)	Non-ionic	-	13-23k	5.0-7.0	11.6-15.4 cps	[30]
C-TAB	Cationic	0.92 to 1.0 mM (25ºC)	364.45 g/mol	6.0-7.5	-	[31]
SDS	Anionic	-	288.38 g/mol	9.1	-	[32]

Subsequently, all the samples, including the one without any surfactant added, were subjected to a heating and cooling cycle ranging from 20 to 80°C in an oven. During this process, the sedimentation of the particles was continuously monitored. Figure 5, illustrates the initial state of the seven different samples before the heating and cooling cycles. Most of the samples exhibit a homogeneous mixture, except the sample prepared with C-TAB, which displayed a distinct behaviour, as it appears the inclusion of C-TAB surfactant has caused a separation between the liquid solution and the mixture of PCM with carbon particles. This can be explained due to the unique surfactant properties. C-TAB is a cationic surfactant that is effective in solubilising and dispersing hydrophobic substances [33]; thus, when the hydrophilic part of C-TAB interacts with the water molecules, it results in a decrease in the wettability of the carbon particles by water, contributing to the separation of the surfactant solution from the PCM and carbon particles mixture [34, 35]. Figure 6 displays the image of the seven samples after undergoing seven heating and cooling cycles with a temperature programme ranging from 20 to 80°C and 80 to 20°C. Noticeably, it illustrated the separation between the PCM and carbon particles. The sample (a) prepared without surfactants exhibit a noticeable separation between the carbon particles and the PCM. This sample served as the baseline for comparison against the sample containing different phase change materials with carbon particles. Interestingly, the sample (e) which is the mixture prepared with PVA, a non-ionic surfactant which in literature has been reported to have good properties to improve the sedimentation between the particles and PCM has exhibited the most significant separation compared to the other mixtures prepared. The sample (f) with C-TAB as the surfactant continuous to show a separation between the water and PCM and carbon mixture. Despite the clear separation between the PCM and particles observed in sample (c), the mixture prepared with SPAN-80, a non-ionic surfactant, this mixture exhibited the most favourable behaviour among the mixtures. Notably, the separated PCM region still contained a higher concentration of carbon particles. Thus, while the sedimentation is evident, the presence of SPAN-30 improves the dispersion of the carbon particles. For this reason, this was the mixture selected to be taken forward.
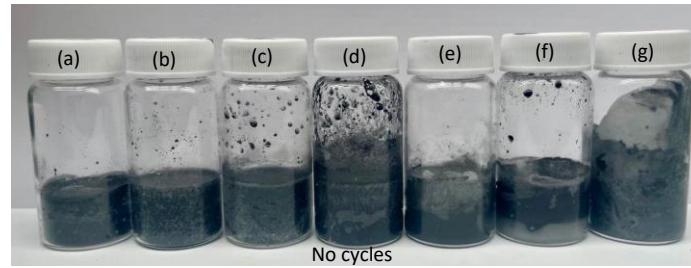
Figure 5. Samples prepared with carbon particles and (a) No surfactant; (b) Tween-80; (c) Span-80; (d) chitosan; (e) PVA; (f) C-TAB; (g) SDS before any heating and cooling cycles were applied.
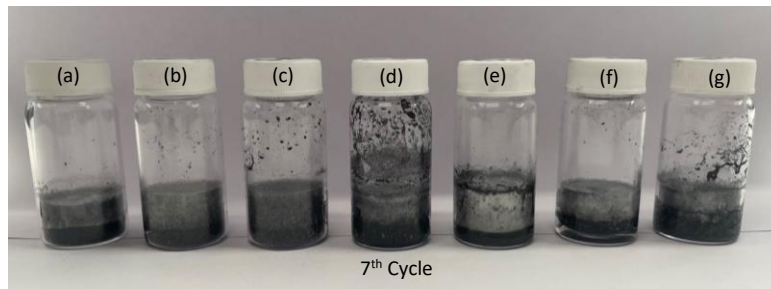
Figure 6. Samples prepared with carbon particles and (a) No surfactant; (b) Tween-80; (c) Span-80; (d) chitosan; (e) PVA; (f) C-TAB; (g) SDS before any heating and cooling cycles were applied.

The addition of surfactants is crucial to enhance the stability of carbon solutions. However, the type of surfactant used, whether cationic or anionic, depends heavily on the charge of the particles. To provide clarity on this matter, zeta potential measurements were performed for a bare solution of graphite carbon particles in a pure DI water. In addition, to understand the nature and character of the used particles, hydrophilic or hydrophobic, the surface tension measurements of a bespoke particles dispersed in a pure DI water by using a Profile Analysis Tensiometer (PAT 1) was performed.

Surface tension Measurement

The surface tension of the solutions, γ, was measured by the Profile Analysis (drop shape analysis) Tensiometer (PAT) technique [36]. This method is based on the acquisition of the drop/bubble shape under gravity effect [37]. The surface tension is determined by fitting the theoretical profile of an axis-symmetric drop calculated through the Gauss- Laplace equation to each experimentally acquired drop profile. The Gauss-Laplace equation (Equation 1) describes the relationship between the curvature of the liquid meniscus and the surface tension:

$$\Delta p = \gamma \left(\frac{1}{R_1} + \frac{1}{R_2} \right)$$

Equation 1

where Δp is the pressure difference across the interfacial layer, γ is the surface/interfacial tension of the solution, and R_1 and R_2 are the principal radii of curvature [38].

The interfacial tension of each solution was measured using a profile analysis tensiometer (PAT1M, SINTERFACE Technologies, Germany). The instrument allows the surface tension versus time, with an accuracy of 0.1 mN/m, to be measured using a pendant drop formed at the tip of a Teflon capillary of a 2 mm in diameter. The instrument allowed the drop/bubble surface area during the surface tension measurement to be automatically controlled by means of an automatic dosing system equipped with a precision syringe pump. In this study, the drop surface area was maintained at a constant value of 25 mm^2 while the surface tension was

Heat Powered Cycles
Conference 2023
Edinburgh
Heat in the new energy system

3rd to 6th of September 2023
The University of Edinburgh, Scotland

acquired over time until the achievement of the equilibrium value. All the measurements were performed at 25°C. Each solution and dispersion were put in an ultrasonic bath at room temperature for 30 min to maintain stability of dispersions during the measurements (avoiding precipitation). Then, the interfacial tension of each sample was measured and repeated three times to obtain the average amount and calculate the standard deviation. It is worth mentioning that prior to every single set of measurements the surface tension of pure water was checked. The water for the solution preparation was deionised and purified by a multi-cartridge system (Elix plus Milli-Q, Millipore) providing a resistivity greater than 18 M$\Omega\cdot$ cm and a surface tension of 72.5 mN/m without any appreciable kinetics over several hours.

Zeta Potential Measurement

The surface charge of the investigated solutions of carbon was obtained by zeta-potential measurements, using a SZ-100 Nano Partica Analyser (Horiba, Japan). The zeta-potential was calculated from measurements of electrophoretic mobility (μe) obtained by laser Doppler electrophoresis technique [36]. All measurements were performed in disposable capillary cells at a fixed controlled temperature of 25°C (room temperature).

The particle solutions have been prepared using a pure DI water added drop by drop to precisely weighted particle powder to obtain 0.1wt% dispersions. This concentration allows dispersions to be subjected for surface tension and z-potential measurements without visual precipitation, maintaining the tests at the appreciable stability level. The measurements of the surface tension of micro-scaled graphite with the concentration of 0.1 wt% in the pure water, reviled the value of the surface tension of 70.6382 $\pm$0.2213 mN/m. No appreciable kinetics has been observed over time. The surface tension of the solution maintains a rather constant value close to that of pure water (70.6382 $\pm$ 0.2213 mN/m) for several hundred of seconds, as shown on the Figure 7.
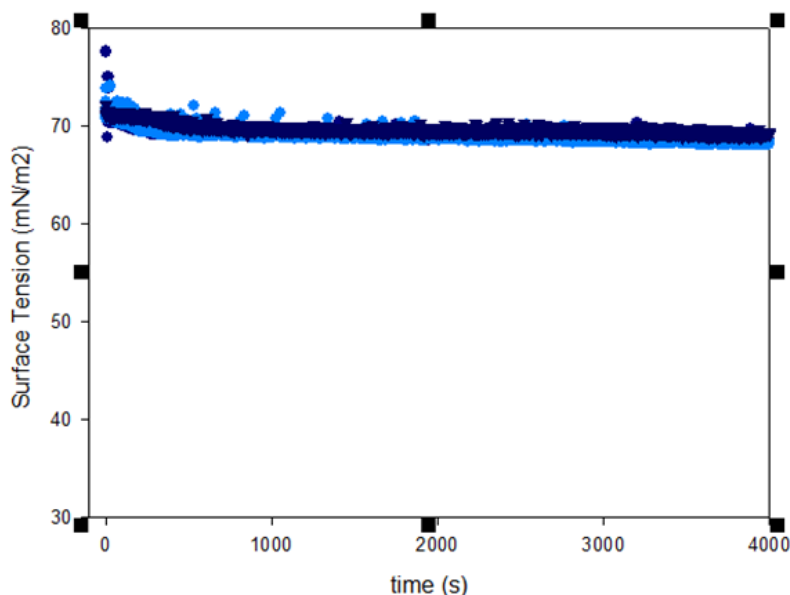
Figure 7. Equilibrium surface tension of micro-scaled graphite 0.1wt% dispersion. The dash line represents the value of surface tension the pure water in the temperature of 25 ºC.

The ξ-potential measurements reviled the positive charge of the micro-scaled graphite surface being +27.9 $\pm$1,09mV. The value of surface tension was determined and compared with the

literature values whereas available. The obtained results are in agreement with the literature data [36].

Bespoke particles used for infusion with PCM were micron-scaled graphite particles as they were used to stabilize particles in water dispersion, and, to refine the mixing with PCM. The micron-scaled graphite was tested for zeta potential, and it was determined that the charge on the particles is positive, thus it revealed that reverse interaction of particles with C-TAB and its evident separation, can be explained by possible repulsion between positively charged carbon particles and surfactant molecules of the same electric sign (cationic surfactant). Moreover, it would be expected that SDS (anionic, negatively charged surfactant) would be the most suitable surfactant to use with already mentioned carbon particles. All above data confirm that the surfactant interaction with oppositely charges particles might be a potential way to improve PCM formulation and mixing, however it remains a lot of open questions, and to answer them more systematic research using a colloidal perspective is required.

Conclusions

This study aimed to characterise the thermophysical properties of a commercially available bio-based fatty acid mixture, OM55, enhanced by incorporating different mass fractions of GNPs. Additionally, the stability of the NePCM was preliminarily assessed by preparing samples with several surfactants into the mixtures. Based on the characterisation measurements, the following conclusions can be drawn:

- The DSC results reveal a slight decrease in the latent heat capacity for the melting and solidification processes when the different mass fractions of GNPs are incorporated. For instance, the measured latent heat capacity for melting in the case of OM55 was found to be 164.3 kJ/kg, whereas for the NePCM with 6wt.% of GNP was extrapolated as 144.8 kJ/kg; representing a decrease of approximately 13%.
- The results show that adding SPAN80 surfactant significantly decreased the latent heat capacity of the NePCMs, for the melting process a decrease of approximately 73%.
- The thermal conductivity measurements indicate no direct correlation between the mass fraction of the GNPs and the thermal conductivity enhancement. This could have resulted due to many factors, including a possible agglomeration of the nanoparticles, acting as a thermal barrier. Further investigations are required.
- The results demonstrated that the addition of the surfactant had a negative impact on the thermal conductivity enhancement obtained from the inclusion of GNPs into the OM55; the SPAN80 has possibly caused a thermal resistance within the NePCMs, cancelling out the slight thermal conductivity enhancement obtained from the GNPs.
- The SEM analysis shows significant agglomeration of GNPs within the NePCMs. A systematic investigation is necessary to evaluate the impact of the preparation methods, mass fractions, and surfactant in the agglomeration of particles and improve the dispersion of the GNPs within the NePCMs.
- The NePCM mixture containing SPAN-80 exhibited the most favourable behaviour in terms of sedimentation compared to the other surfactant mixtures studied.
- The surfactant interaction with oppositely charges particles might be a potential way to improve PCM formulation and mixing. Further investigation of the charge of nanoparticles is required.
- Surfactants could potentially be effective in improving the thermal stability of the NePCMs. However, it is essential to optimise the concentration of surfactants used, as excessive amounts can also negatively impact the thermal properties (i.e., latent heat capacity and thermal conductivity). Thus, selecting the appropriate surfactant and volume

concentration is extremely important to achieve the desired stability and thermal properties of the NePCMs.

Acknowledgements

References

1. Khudhair, A.M. and M. Farid, *A review on energy conservation in building applications with thermal storage by latent heat using phase change materials.* Thermal Energy Storage with Phase Change Materials, 2021: p. 162-175.
2. Jouhara, H., A. Żabnieńska-Góra, N. Khordehgah, D. Ahmad, and T. Lipinski, *Latent thermal energy storage technologies and applications: A review.* International Journal of Thermofluids, 2020. **5**: p. 100039.
3. D'Oliveira, E.J., S.C.C. Pereira, D. Groulx, and U. Azimov, *Thermophysical properties of Nano-enhanced phase change materials for domestic heating applications.* Journal of Energy Storage, 2022. **46**: p. 103794.
4. Li, D., B. Zhuang, Y. Chen, B. Li, V. Landry, A. Kaboorani, Z. Wu, and X.A. Wang, *Incorporation technology of bio-based phase change materials for building envelope: A review.* Energy and Buildings, 2022: p. 111920.
5. Gumtapure, V., *Thermal property study of fatty acid mixture as bio-phase change material for solar thermal energy storage usage in domestic hot water application.* Journal of Energy Storage, 2019. **25**: p. 100870.
6. Rolka, P., R. Kwidzinski, T. Przybylinski, and A. Tomaszewski, *Thermal Characterization of Medium-Temperature Phase Change Materials (PCMs) for Thermal Energy Storage Using the T-History Method.* Materials, 2021. **14**(23): p. 7371.
7. NematpourKeshteli, A., M. Iasiello, G. Langella, and N. Bianco, *Enhancing PCMs thermal conductivity: A comparison among porous metal foams, nanoparticles and finned surfaces in triplex tube heat exchangers.* Applied Thermal Engineering, 2022. **212**: p. 118623.
8. Harish, S., D. Orejon, Y. Takata, and M. Kohno, *Thermal conductivity enhancement of lauric acid phase change nanocomposite with graphene nanoplatelets.* Applied thermal engineering, 2015. **80**: p. 205-211.
9. Liu, Y., R. Zheng, T. Tian, and J. Li, *Characteristics of thermal storage heat pipe charged with graphene nanoplatelets enhanced organic phase change material.* Energy Conversion and Management, 2022. **267**: p. 115902.
10. Williams, J.D. and G. Peterson, *A Review of Thermal property enhancements of low-temperature nano-enhanced phase change materials.* Nanomaterials, 2021. **11**(10): p. 2578.
11. Leong, K.Y., M.R.A. Rahman, and B.A. Gurunathan, *Nano-enhanced phase change materials: A review of thermo-physical properties, applications and challenges.* Journal of Energy Storage, 2019. **21**: p. 18-31.
12. Khezri, A., M. Sahebi, and M. Mohammadi, *Fabrication and Thermal properties of graphene nanoplatelet-enhanced phase change materials based on paraffin encapsulated by melamine–formaldehyde.* Journal of Thermal Analysis and Calorimetry, 2022. **147**(14): p. 7683-7691.
13. Sarsam, W.S., A. Amiri, S. Kazi, and A. Badarudin, *Stability and thermophysical properties of non-covalently functionalized graphene nanoplatelets nanofluids.* Energy conversion and management, 2016. **116**: p. 101-111.
14. Krittayavathananon, A., X. Li, C. Batchelor-McAuley, M. Sawangphruk, and R.G. Compton, *Comparing the effect of different surfactants on the aggregation and electrical contact properties of graphene nanoplatelets.* Applied Materials Today, 2018. **12**: p. 163-167.

15. Palanichamy, S. and K. Athiimoulam, *Influence of various additives on stability and phase change characteristics of DI water-GnP-based NFPCM for cold thermal energy storage systems.* Environmental Science and Pollution Research, 2022. **29**(44): p. 66935-66949.

16. Al-Janabi, A.S., M. Hussin, and M. Abdullah, *Stability, thermal conductivity and rheological properties of graphene and MWCNT in nanolubricant using additive surfactants.* Case Studies in Thermal Engineering, 2021. **28**: p. 101607.

17. Wu, X., M. Gao, K. Wang, Q. Wang, C. Cheng, Y. Zhu, F. Zhang, and Q. Zhang, *Experimental study of the thermal properties of a homogeneous dispersion system of a paraffin-based composite phase change materials.* Journal of Energy Storage, 2021. **36**: p. 102398.

18. Sheikh, Y., M.F. Orhan, M. Umair, E. Mehaisi, and A. Azmeer, *Variation in cooling performance of a bio-based phase change material by adding graphene nanoplatelets with surfactants.* International Journal of Thermofluids, 2022. **16**: p. 100201.

19. PLUSS. *Technical Data Sheet of Save OM55*. 2018 2018; Available from: https://pluss.co.in/upload/technical-datasheets/2019/Doc%20418%20TDS_OM55.pdf.

20. GmbH, I.I.L.T. *IoLiTec Nanomaterials*. 2021 [cited 2021 05]; Available from: https://nanomaterials.iolitec.de/sites/nanomaterials.iolitec.de/files/downloads/2017-01-25-SP%20Price%20List%20Nano2017_V1.pdf.

21. Fang, X., L.-W. Fan, Q. Ding, X. Wang, X.-L. Yao, J.-F. Hou, Z.-T. Yu, G.-H. Cheng, Y.-C. Hu, and K.-F. Cen, *Increased thermal conductivity of eicosane-based composite phase change materials in the presence of graphene nanoplatelets.* Energy & Fuels, 2013. **27**(7): p. 4041-4047.

22. Masoumi, H. and S. Mirfendereski, *Modification of physical and thermal characteristics of stearic acid as a phase change materials using TiO2-nanoparticles.* Thermochimica Acta, 2019. **675**: p. 9-17.

23. Ezhumalai, D., G. Sriharan, and S. Harikrishnan, *Improved thermal energy storage behavior of CuO/palmitic acid composite as phase change material.* Materials Today: Proceedings, 2018. **5**(6): p. 14618-14627.

24. Müller, L., G. Rubio-Pérez, A. Bach, N. Muñoz-Rujas, F. Aguilar, and J. Worlitschek, *Consistent DSC and TGA Methodology as Basis for the Measurement and Comparison of Thermo-Physical Properties of Phase Change Materials.* Materials, 2020. **13**(20): p. 4486.

25. Kim, S.Y., Y.J. Noh, and J. Yu, *Thermal conductivity of graphene nanoplatelets filled composites fabricated by solvent-free processing for the excellent filler dispersion and a theoretical approach for the composites containing the geometrized fillers.* Composites Part A: Applied Science and Manufacturing, 2015. **69**: p. 219-225.

26. Esmaeili, H., S.M. Mousavi, S.A. Hashemi, C.W. Lai, W.-H. Chiang, and S. Bahrani, *Application of biosurfactants in the removal of oil from emulsion*, in *Green Sustainable Process for Chemical and Environmental Engineering and Science*. 2021, Elsevier. p. 107-127.

27. KGaA, M. *Product Information - TWEEN80*. 2023 [cited 2023 25].

28. BLDpharm. *(2R,3R,4R,5S)-Hexane-1,2,3,4,5,6-hexaol mono-(9Z)-9-octadecenoate, Saponification Value 140-160*. 2023 [cited 2023 25]; Available from: https://www.bldpharm.com/products/1338-43-8.html.

29. KGaA, M. *Product information - Chitosan*. 2023 [cited 2023 25]; Available from: https://www.sigmaaldrich.com/specification-sheets/328/923/448877-BULK.pdf.

30. KGaA, M. *Product Specification - Poly (Vinyl alcohol)*. 2023 [cited 2023 25]; Available from: https://www.sigmaaldrich.com/specification-sheets/241/801/341584-BULK_____ALDRICH__.pdf.

31. KGaA, M. *Product Information - Hexadecyltrimethylammonium bromide*. 2023 [cited 2023 25]; Available from: https://www.sigmaaldrich.com/deepweb/assets/sigmaaldrich/product/documents/234/832/h6269pis.pdf.

32. KGaA, M. *Sodium dodecyl sulfate*. 2023 [cited 2023 25]; Available from: https://www.merckmillipore.com/GB/en/product/Sodium-dodecyl-sulfate,MDA_CHEM-817034#documentation.

33. Peetla, C. and V. Labhasetwar, *Effect of molecular structure of cationic surfactants on biophysical interactions of surfactant-modified nanoparticles with a model membrane and cellular uptake.* Langmuir, 2009. **25**(4): p. 2369-2377.

34. Adeleke, O.A., M.R. Saphira, Z. Daud, N. Ismail, A. Ahsan, N.A. Ab Aziz, A. Al-Gheethi, V. Kumar, A. Fadilat, and N. Apandi, *Principles and mechanism of adsorption for the effective treatment of palm oil mill effluent for water reuse*, in *Nanotechnology in Water and Wastewater Treatment*. 2019, Elsevier. p. 1-33.

35. Li, T., J. Wang, F. Wang, L. Zhang, Y. Jiang, H. Arandiyan, and H. Li, *The effect of surface wettability and coalescence dynamics in catalytic performance and catalyst preparation: a review.* ChemCatChem, 2019. **11**(6): p. 1576-1586.

36. Loglio, G., P. Pandolfini, L. Liggieri, A. Makievski, and F. Ravera, *Determination of interfacial properties by the pendant drop tensiometry: Optimisation of experimental and calculation procedures.* Bubble Drop Interfaces, 2011. **2**(7).

37. Javadi, A., N. Mucic, M. Karbaschi, J. Won, M. Lotfi, A. Dan, V. Ulaganathan, G. Gochev, A. Makievski, and V. Kovalchuk, *Characterization methods for liquid interfacial layers.* The European Physical Journal Special Topics, 2013. **222**: p. 7-29.

38. Zholob, S., A. Makievski, R. Miller, and V. Fainerman, *Optimisation of calculation methods for determination of surface tensions by drop profile analysis tensiometry.* Advances in colloid and interface science, 2007. **134**: p. 322-329.

Heat Powered Cycles Conference 2023
Edinburgh

Heat in the new energy system

Dropwise Condensation on Silicone Oil Grafted and Impregnated Surfaces

A. Abbas[1,2*], **G. G. Wells**[1] , **G. McHale**[1] **and K. Sefiane**[1]**, D. Orejon**[1,3*]

[1]Institute for Multiscale Thermofluids, School of Engineering, University of Edinburgh, UK

[2]Department of Mechanical Engineering, University of Engineering and Technology Lahore, Pakistan

[3]International Institute for Carbon-Neutral Energy Research (WPI-I2CNER), Kyushu University, 744 Motooka, Nishi-ku, Fukuoka, Japan

[*]Corresponding author: d.orejon@ed.ac.uk, a.abbas-7@sms.ed.ac.uk

Abstract

We introduce here an optimised silicon grafted method to create hydrophobic coatings on silicon substrate to promote dropwise condensation and hence heat transfer rate. This can be achieved by making use of different fabrication parameters during silicone oil grafting (oil viscosity and/or volume/method, temperature, etc.) onto silicon substrates henceforth referred to as grafted surfaces and further oil impregnation to create Lubricant Infused Surfaces (LISs). We observe dropwise condensation behaviour on these grafted surfaces and LISs when compared to filmwise on bare substrates, which in turns shall increase the heat transfer rate. This study provides an understanding on various techniques that can be applied to create surfaces with high condensation heat transfer rates.

Keywords: Heat transfer, Silicone oil grafting, Dropwise condensation, Droplet size distribution, LIS

Introduction/Background

Depending on the surface wettability, different condensation behaviours can be achieved. On hydrophobic surfaces, dropwise condensation has gained increasing attention due to enhanced heat transfer rates ensuing on these surfaces. It has been reported in literature that approximately 6-8 times higher heat transfer rate can be achieved if the condensation occurs in a dropwise manner instead of a filmwise manner [1]. Efforts have been carried out ever since to modify the surface to promote dropwise condensation [2, 3]. In this work, we prepare surfaces via an optimised grafting method utilising different silicone oils viscosities with varying volumes and deposition methods [4]. In addition, LISs are prepared by impregnating the grafted surfaces with silicone oils varying in viscosity (5-100 cSt). In this work we demonstrate that dropwise condensation mode is favoured on on silicone oil grafted surfaces as well as LISs when compared to the bare hydrophilic substrates typically displaying filmwise condensation behaviour.

Results and Discussion

Substrate fabrication and characterisation

Surfaces prepared via grafting various viscosity (5, 20 and 100 cSt) and varying volumes deposited prior to grafting (up to 10 μL) via pipette and dip coating method of the silicone oils showed hydrophobic behaviour. In addition, these surfaces were impregnated further

with silicone oil (5, 20 and 100 cSt) to create LISs. **Table 1** below includes the different configurations and fabrication details studied:

Table 1: Summary of grafting and impregnation parameters for various viscosity oils

Oil Viscosity (cSt)	Oil application method	Oil volume deposited per layer for grafting (µL)	Number of layers grafted	Viscosity of oil impregnated (cSt)	
				with pipette	Dip-coating
5	Pipette	5	1 & 5	5	20 & 100
100	Dip-coating	0.185	1 & 3	5	20 & 100

Characterisation of the optimised silicone oil grafted surfaces as well as LISs show non-wetting behaviour with contact angles (CA) of 105° - 108° and contact angle hysteresis (CAH) ranging from 1° to 7° (**Figure 1a**) [4]. In addition, the stability of the coatings was also addressed under various stability tests (**Figure 1b**) including mechanical vibration, solvent immersion and coupled mechanical vibration and solvent immersion. While these coatings showed good stability after such stability tests;, however coatings deteriorate when subjected to high temperature humid environment for more than 10-15 minutes.
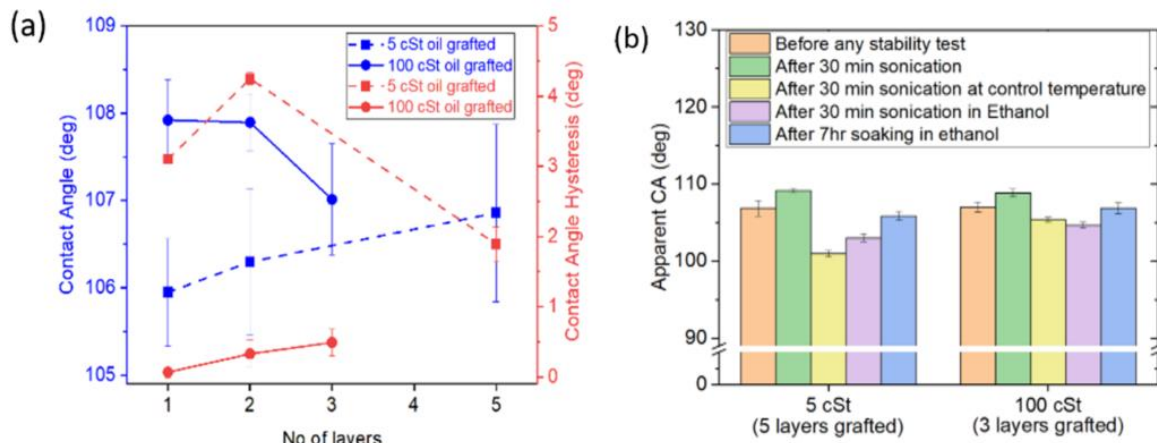
Figure 1 – (a) Contact Angle and Contact Angle Hysteresis of surfaces grafted with 5 cSt and 100 cSt oil[4] **(b)** Apparent CA variation of 3 µL water droplet on grafted samples after various stability tests.

Condensation setup

Condensation experiments are yet to be performed on these novel surfaces, however based on previous research work [5-7], we anticipate condensation on these grafted surfaces as well as on LISs ensuing in a dropwise manner. **Figure 2** shows the schematics of the condensation setup including a controlled humidity chamber and a temperature controlled Peltier stage, copper block and insulating block around, and the fabricated samples.
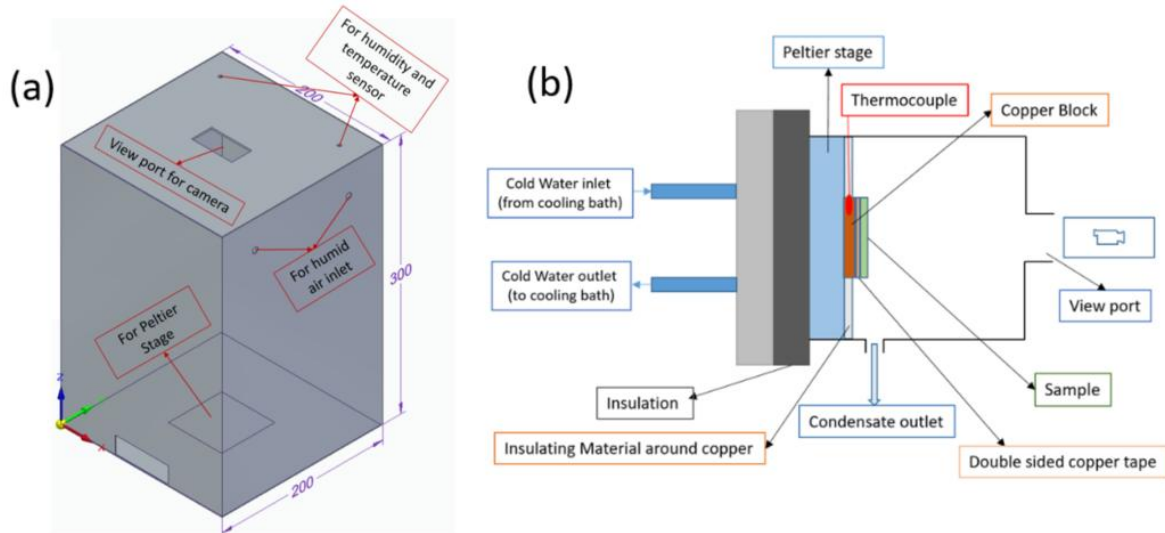
Figure 2 – (a) Schematic of humidity chamber design to perform condensation experiments. The different inlets and outlets for the humid air, humidity and temperature sensors, view port, and Peltier stage location are included **(b)** Set-up inside the chamber including Peltier stage and sample under observation.

To perform the condensation experiments, the thermodynamic parameters inside the chambers are considered as follows: ambient temperature T_{amb} = 25 °C, Peltier stage temperature or substrate temperature T_{surf} = 1, 5 and/or 10 °C, and relative humidity RH = 50, 70 and/or 80%. Inlet humid air parameters are controlled via custom-built temperature & humidity control setup with a temperature and humidity sensor inside the chamber. **Table 2** provides a summary of the different thermodynamics parameters utilised in this study:

Table 2 – List of conditions and thermodynamics parameters utilised for condensation experiments

Conditions	T_{amb} (°C)	T_{surf} (°C)	RH (%)
Values	25	1, 5, 10	50, 70, 80

A cooling bath is also attached to the Peltier stage to absorb excess heat and to keep the temperature of the Peltier stage constant. Samples are attached to the Peltier stage via double sided copper tape so to enhance the heat transfer between sample and the cold Peltier stage.

The following issues may be encountered when setting up the condensation experimental chamber and when carrying out the experimental campaign:

- The chamber size may need to be enlarged depending on the strength of the variation of the relative humidity inside the chamber so to avoid any air flow inside, which may incur in additional ambient convection.
- The Peltier stage temperature might vary more than ±1 °C. This occurrence should be unlikely as other research works have approximated the temperature of the Peltier stage to that of the surface T_{surf} since minor differences within ± 1 °C were found between these. [7].
- There might be some variation and dynamic influence of local RH changes as the setup is custom build and may take a bit longer to reach a set value.

Heat Transfer Resistance Based Model

Experimental observations of water condensing on these samples will be recoded using high speed camera and will be analysed to observe the droplet nucleation, droplet size distribution and growth on the silicone oil grafted surfaces and LISs. We then coupled the droplet size distribution with a thermal resistance based heat transfer model shown in **Figure 3**, to provide a quantification on the heat transfer performance as reported in the literature [3,7,8]. In addition, the experimental setup allows for quantifying the amount of condensate collected during experiments, which can be further utilised to compare and/or validate the heat transfer model adopted.
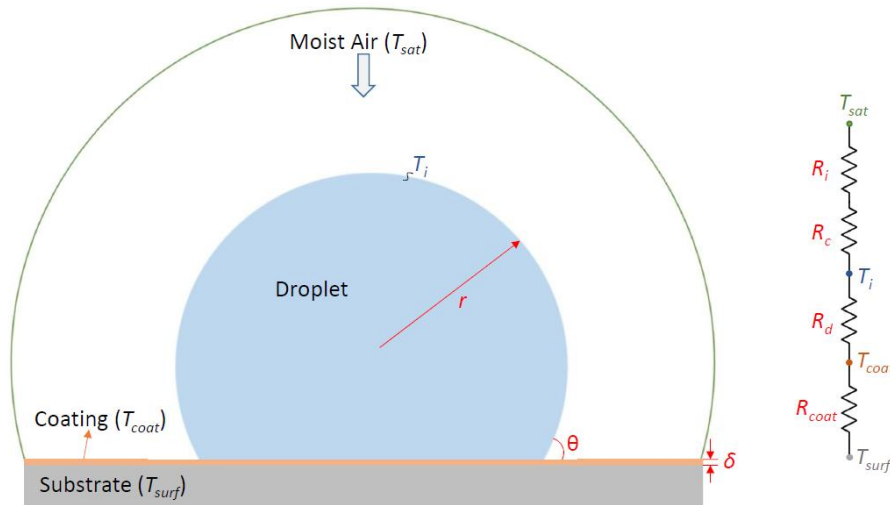
Figure 3 – Heat Transfer through single droplet of radius r condensing on our silicone oil grafted surface where T_{coat} is the temperature of the coating, T_{surf} is the temperature of substrate, T_i is the temperature at liquid vapor interface, T_{sat} is the temperature of saturated moist air, θ is contact angle of droplet on coated substrate, δ is the coating thickness. R_i, R_c, R_d, R_{coat} are the interfacial resistance, resistance due to droplet curvature, conduction resistance through droplet and resistance due to coating respectively.

By making use of the heat transfer resistance based model reported in **Figure 3** adding all the different resistances in parallel, the following heat transfer equation, Equation 1, through a single condensing droplet can be established as:

$$q_d = \frac{\Delta T \, \pi r^2 (1 - \frac{r_{min}}{r})}{\frac{\delta}{k_{coat} sin^2\theta} + \frac{r\theta}{4k_c sin\theta} + \frac{\delta}{2h_i(1 - cos\theta)}}$$

Where r_{min} is critical (minimum) nucleation radius, ΔT is temperature difference between moist air and substrate, k_{coat} and k_c are the thermal conductivity of coating and condensate (water) respectively, h_i is the interfacial heat transfer coefficient.

Droplet pinning to a surface is typically related to the contact angle hysteresis CAH, where higher CAH yields higher degree of pinning. In our previous study, we tailored an approach to control the interaction of water droplet on silicone oil grafted surfaces by means of changing the viscosity, volume of oil and/or oil application method [4]. This led to different behaviour in terms of CA and CAH. On one hand, changes in CA were not apparent, while on the other hand, CAH hysteresis changed significantly, which altered the pinning behaviour (sliding) of droplets.

For low CAH surfaces, sliding angles of water droplets (3μL) are small and within few degrees, which anticipates that droplets will be very mobile during condensation on such low CAH surfaces. Whereas for higher CAH surfaces, presumably larger droplets will remain on the surface requiring grater growth, i.e., gravitational forces, to shed from the surface. The different droplet surface interactions anticipates then a different droplet nucleation and growth and hence a different droplet size distribution, which ultimately impacts the heat transfer performance.

Conclusions

A simple and easy coating method is introduced here to prepare hydrophobic surfaces and LISs on which dropwise condensation is promoted opposed to filmwise condensation ensuing on a hydrophilic surface. The different affinity of droplets to the various coated surfaces anticipates differences on the nucleation, droplet growth and shedding, i.e., on the droplet size density, which ultimately has an impact on the heat transfer rates. This work provides further fundamental insights to select the grafting parameters for preparing surfaces on which dropwise condensation is favourable. In addition, a control of droplet distribution and growth may also be achieved as discussed above.

Acknowledgments

References:

[1] Schmidt E., Schurig, W. & SellschoppW., *Versuche über die Kondensation von Wasserdampf in Film- und Tropfenform,* Technische Mechanik und Thermodynamik, 1930, **1**, 53–63.

[2] Miljkovic, N., Enright, R., and Wang, E.N., *Effect of Droplet Morphology on Growth Dynamics and Heat Transfer during Condensation on Superhydrophobic Nanostructured Surfaces*, ACS Nano, 2012, **6 (2)**, 1776-1785.

[3] Weisensee, P.B., Wang, Y., Qian, H., Schultz, D., King, W.P., Miljkovic, N., *Condensate droplet size distribution on lubricant-infused surfaces*. International Journal of Heat and Mass Transfer, 2017, **109**, 187-199.

[4] Abbas, A., Well, G.G., McHale, G., Sefiane, K., Orejon, D., *Silicone Oil-Grafted Low-Hysteresis Water-Repellent Surfaces,* ACS Applied Materials & Interfaces, 2023, **15**, 11281-11295.

[5] Anand, S., Paxson, .A.T., Dhiman, R., Smith, J.D., Varanasi, K.K., *Enhanced Condensation on Lubricant ImpregnatedNanostructured Surfaces,* ACS Nano, 2012, **6 (11)**, 10122-10129.

[6] Phadnis, A., and Rykaczewski, K., *Dropwise Condensation on Soft Hydrophobic Coatings,* Langmuir, 2017, **33**, 12095-12101.

[7] Maeda, Y., Lv, F.Y., Zhang, P., Takata, Y., Orejon, D., *Condensate Droplet Size Distribution and Heat Transfer on Hierarchical Slippery Lubricant Infused Porous Surfaces*, Applied Thermal Engineering, 2020, **176**, 115386.

[8] Kim, S., and Kim, K. J. *Dropwise Condensation Modeling Suitable for Superhydrophobic Surfaces*, ASME Journal of Heat and Mass Transfer, 2011, **133(8)**, 081502.

Materials screening, lab-scale testing and simulation for high-efficiency adsorption desalination

Y. Zhang[1], V. Brancato[1], D. Palamara[2], L. Calabrese[1,2], V. Palomba[1], W. Mittelbach[3], A. Frazzica[1,*]

[1]Istituto di Tecnologie Avanzate per l'Energia "Nicola Giordano" – CNR ITAE. Via S. Lucia Sopra Contesse, 5, 98126, Messina, Italy

[2]Department of Engineering, University of Messina, Contrada di Dio Sant'Agata, 98166, Messina, Italy

[3]Sorption Technologies GmbH, 79144 Freiburg, Germany

[*]Corresponding author: andrea.frazzica@itae.cnr.it

Abstract

This study aims to develop a high-efficiency adsorption desalination system by materials screening, lab-scale testing and simulation. Silica gel-30% LiCl and vermiculite-45% LiCl composites were synthesized and characterized. Silica gel-30% LiCl was selected as the material candidate for higher predicted specific daily water production (SDWP). A T-LTJ (thermal-large temperature jump) apparatus was utilized to test the ad-desorption dynamics under various operating conditions. The influences of evaporation/condensation and desorption temperature on performances were analysed. The performance indicators- specific daily water production (SDWP) and optimized cycle time were calculated. Moreover, three design strategies, namely, 2-bed, 3-bed and 4-bed systems were proposed and compared. Finally, a mathematical model describing a general AD system is planned to be developed, which will be used to extensively evaluate the application potential of other composites that were developed in the lab.

Keywords: Adsorption desalination, Dynamics, Composite sorbents, Water production.

Introduction

Adsorption desalination (AD) is a novel technology to supply high-quality freshwater driven by renewable energy. It has the possibility of cogenerating freshwater and cooling effect. Sorption materials are the core components, they extract the water vapour from the fed brine inside the evaporator during the adsorption process, and release the adsorbed water in the form of water vapour which is then condensed in the condenser to get the portable water during the desorption process. Composite adsorbents are promising candidates for high water uptake and tunable working operating temperature and pressure ranges. However, only a few composite sorbents have been developed and tested in adsorption desalination (AD) systems [1].

In this study, two types of composites with different pore structures, silica gel-30% LiCl and vermiculite-45% LiCl were selected and measured. Their ad/desorption dynamics were tested and analyzed in a thermal-large temperature jump (T-LTJ) apparatus.

Materials characterizations

Silica gel-30% LiCl and vermiculite-45% LiCl composite were synthesized through the dry impregnation method. The sorption isobars and sorption kinetics under the selected typical operating conditions were measured by the dynamic vapor sorption (DVS) instrument. Sorption isobars show that both composites experience three adsorption stages: physisorption, hydration reaction + deliquescence and solution absorption. Vermiculite-45% LiCl presents higher equilibrium water uptake, but has stronger mass transfer resistance; On the contrary, silica gel-

30% LiCl possesses better mass transfer, but the equilibrium water uptake is lower. The main reason for these phenomena is their different pore sizes. The calculation of the theoretical SDWP indicated that silica gel-30% LiCl can contribute to higher water production ranging from 43 to 60 m^3/tonne/day for the selected typical conditions.

Lab-scale testing of the adsorption desalination device

The thermal large temperature jump (T-LTJ) apparatus (see **Figure 1**) consists of a vacuum chamber, an evaporator/condenser, four thermostats and a vacuum pump. A finned flat-tubes aluminum heat exchanger serves as the ad/desorber, and 74.4 g sorbent particles were packed between the fins. Fast temperature jumps/drops are operated by quickly switching the valves after reaching desorption/adsorption equilibrium, aiming to simulate practical adsorption and desorption process. The differential temperature of the inlet and outlet heat transfer fluid (HTF) contributes to calculating the adsorption/desorption characteristic time by:

$$\Delta T_{ad/de}(t) = \Delta T_\infty + \Delta T_0 \cdot \exp(-\frac{t}{\tau_{ad/de}})$$

1)

where ΔT_∞ and ΔT_0 are fitting parameters. $\tau_{ad/de}$ refers to the characteristic time, reflecting the ad/desorption rates. The analysed results under various conditions ($T_{eva/cond}$=5, 10, 15, 20, 25°C, T_{de}=60,70,80,85^{o}C) reveal that the $\tau_{ad/de}$ of silica gel-30% composite increases with the raised $T_{eva/cond}$ and decreased T_{de}. Furthermore, the obtained $\tau_{ad/de}$ and adsorption equilibrium were used to calculate the maximum SDWP for different system designs (2-bed, 3-bed and 4-bed). It shows that the SDWP can reach 69 m^3/tonne/day when $T_{eva/cond}$=20 ^{o}C and T_{de}=80 ^{o}C by adopting the 3-beds-configuration.
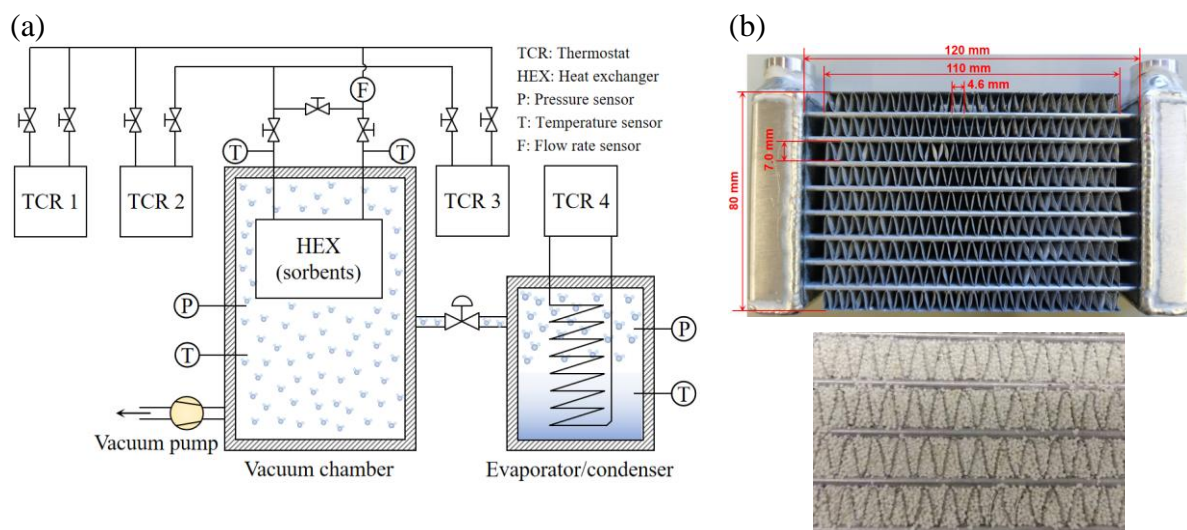
Figure 1 (a) Schematic diagram of the T-LTJ testing system and (b) pictures of the blank heat exchanger and the heat exchangers packed with silica gel-30% LiCl.

Mathematical modelling

The model is planned to be developed from the SorpLib, which is a library of components modelled using Modelica language and realised by the Institute of Technical Thermodynamics at RWTH Aachen university [2]. Its validation will be verified by the lab-scale testing results, and then further estimations on the influencing factors on performance will be conducted.

Conclusions

In summary, silica gel-30% LiCl was selected as a better candidate for adsorption desalination than vermiculite-45% LiCl, it has better mass transfer and can reach higher SDWP. Its practical ad/desorption dynamic in reactors was measured by a lab-scale adsorption desalination device. Results reveal that the ad/desorption rates are more sensitive to evaporation/condensation temperature than the desorption temperature. Both material characterizations and system performance indicate that silica gel-30% LiCl is an excellent material to build high-efficiency adsorption desalination systems.

Acknowledgements

References:

[1] Zhang, Y., Palomba, V., Frazzica, A.. *Understanding the effect of materials , design criteria and operational parameters on the adsorption desalination performance – A review.*, Energy Conversion and Management, 2022.
[2] Gibelhaus, A., Tangkrachang, T., Bau, U., Seiler, J., Bardow, A.. *Integrated design and control of full sorption chiller systems*. Energy, 2019.

Design and experimental evaluation of a thermochemical energy storage system for mid-term energy storage

Valeria Palomba[1*], Vincenza Brancato[1], Yannan Zhang[1], Andrea Frazzica[1], Gabriele Penello[2], Walter Mittelbach[2]

[1]National Research Council of Italy – Institute for Advanced Energy Technologies (CNR-ITAE), Salita S.Lucia sopra Contesse 5, 98126 Messina, Italy. e-mail:valeria.palomba@itae.cnr.it
[2]Sorption Technologies GmbH, Christaweg 52, 79114 Freiburg im Breisgau, Germany
[*]Corresponding author: valeria.palomba@itae.cnr.it

Abstract

This paper presents the design and lab-scale testing of a thermochemical storage reactor that utilizes composite adsorbents, i.e. silica gel/$CaCl_2$. The development included the preparation and characterization of the storage materials and the identification of the optimal packing ratio of the reactor. The lab-scale testing was performed to evaluate the performance of the reactor and the composite adsorbent under various conditions, in terms of operating temperature and dynamic response. The results show that the reactor is capable of efficiently storing and retrieving thermal energy, with high energy storage densities and fast response times. The reactor design and performance results presented provide a valuable foundation for future work aimed at developing practical, large-scale systems for integration into the district heating network.

Keywords: thermochemical storage; composite adsorbents; district heating; monthly storage

Introduction

The use of sorption storage for mid to long-term applications is gaining interest, not only for the residential areas but also in combination with district heating and cooling (DHC). Indeed, one of the most interesting fields of application is thermal-electric sector coupling. In this case, it is possible to use sorption storages as decentralized storages at district/substation levels or even at building levels, charging them directly from the main district heating/cooling ring or in combination with heat pumps. This is especially useful in the new generation of DHC, that approach the concept of "temperature neutral" network, in which the temperature is kept as close to ambient temperature as possible. At the same time, the new generation of DHC is intended to accommodate a larger share of renewables inside the grids (thermal and electric), which requires suitable storage systems for peak shaving and load shifting.

Sorption storage allows to answer to such challenges, thanks to its high flexibility (it can be operated for heating and cooling purposes), virtually lossless operation and possibility of being installed also in residential areas or in buildings (differently from underground storage or aquifer storage). The main challenges that sorption technology has to face for the specific application are: possibility of using non-toxic materials and refrigerants, that would hinder installation in buildings; the need for high energy density and a charging temperature lower than the state-of-art application of sorption system, usually intended for charging with solar heat or industrial heat at temperatures higher than 80°C.

Starting from such basis, the complete development of a thermochemical storage for the application in DHC was carried out, starting from the selection and preparation of the composite material and the lab-scale testing to evaluate its performance in terms of response time, power output and energy storage density. Results were also used for the calibration of an existing model of the storage.

Material selection and preparation

The material selection was carried out thanks to a dedicated preparation and characterization campaign at CNR-ITAE. Initially, 3 ionic liquids, namely [emim][Ac], EMIM DEP and DMIM DMP,

and different salt hydrates, K_2CO_3, $FeCl_2$, LiCl and $CaCl_2$ were selected. Experimental tests were carried out on the pure materials using the Dynamic gravimetric vapor sorption analyzer (DVS) equipment from Surface Measurement Systems. Results from the tests, highlighted that the ionic liquids show a higher sorption capacity at lower relative pressures (up to 0.9 kg/kg for a 40°C isotherm for the DMIM DMP and up to 0.6 kg/kg considering the application in heat pump-assisted operation), but their cost is still too high for large scale application. The salt hydrates showed up to 1.6 kg/kg of sorption capacity, but the vast majority of adsorption is shifted towards higher pressures (3 to 4 kPa for the K_2CO_3 isotherm at 40°C), thus indicating that a higher charging temperature might be needed.

However, since salt hydrates showed leakage issues already during the small-scale testing, composite adsorbents using silica gel and LiCl and $CaCl_2$ were prepared using the wet impregnation method. The composite prepared were tested in the DVS equipment and showed up to 0.6 kg/kg water adsorption.

Due to cost and corrosion issues, the silica gel/$CaCl_2$ (25% wt) composites were selected for the lab-scale testing of the prototype.

Experimental testing of the lab-scale prototype

Testing facilities

The experimental testing was carried out in a testing rig dedicated to the testing of thermal systems. It includes a 36 kWelectric heater connected to a 1 m^3 water storage, and two air/water chillers connected to 0.75 m^3 storages that act as heat sinks/sources at different temperature levels. The temperature inside the 0.75 m^3 are also regulated by means of immersed heaters. Fast-response 3 way valves connected to a custom-made PID control in LabVIEW allow the continuous control of the inlet temperatures of the circuits. All circuits are thermally insulated. Temperature inlet/outlets are measured using Pt100 class 1/10 DIN sensors, temperatures inside the storage are measured using class A type T thermocouples, flow rates are measured using magnetic flow meters with ±2.5 % full scale accuracy.

Heat exchanger preparation

The composite material prepared was used for filling a heat exchanger (HEX) with external dimensions of 266 x132 x 445 (l x w x h) having aluminum fins and copper tubes coated with an epoxy resin to avoid possible corrosion from salt leakage. The heat exchanger was filled with a mixture of silica gel (Siogel® from Oker Chemie) and the composite, in 3 different ratios in volume: 50(siogel)-50(composite), 40(siogel)-60(composite), 30(siogel)-70(composite). As shown in Figure 1 , the heat exchanger was subsequently closed by means of a metallic frame.

Figure 1: the heat exchanger with the composite material.

Testing methodology and results

The tests were carried out considering the possible operating boundaries for the system, listed in Table 1.

Table 1: Testing conditions.

CHARGE	DISCHARGE
Heat source: 85°C / Condensation: 30°C	Adsorption: 30°C / Evaporation: 15°C
Heat source: 75°C / Condensation: 30°C	Adsorption: 35°C / Evaporation: 15°C
Heat source: 85°C / Condensation: 35°C	Adsorption: 30°C / Evaporation: 10°C
Heat source: 75°C / Condensation: 35°C	Adsorption: 35°C / Evaporation: 10°C

An example of the results during the discharge of the prototype is shown in Figure 2. It is possible to notice that there is a ΔT ranging between 6 and 2 K for about 2000 s, corresponding to a power of 0.5 kW to 2.5 kW. If the system is used for contemporary cooling provision, a useful effect is also available at the evaporator.

Figure 2: results of a discharge test.

(a)   (b)
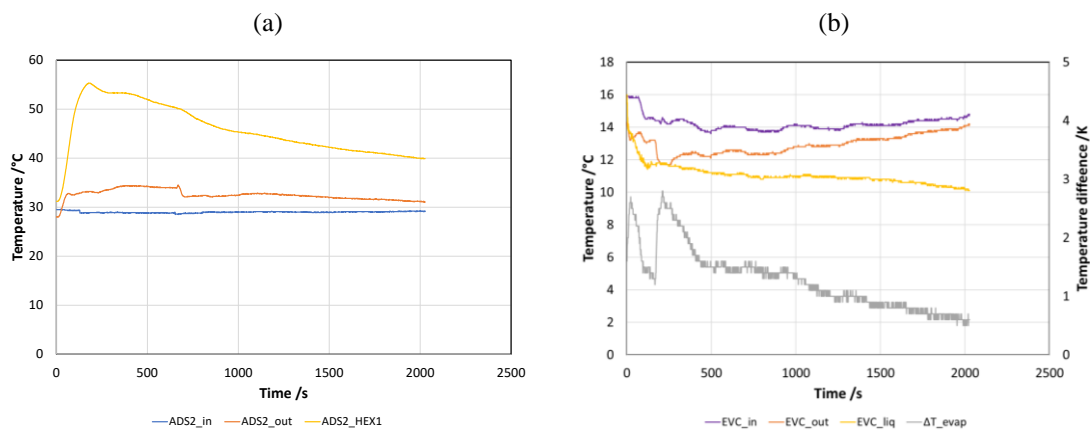
Results were also further analysed considering the achievable energy storage density in the various conditions. In the first preliminary tests carried out, up to 300 J/$g_{adsorbent}$ were achieved, which is about 30% less than the theoretical energy storage density of the material, but still represents a promising result.

Conclusions

In conclusion, this paper presents the design and initial lab-scale testing of a thermochemical storage reactor that utilizes composite adsorbents. The results show that the reactor is capable of efficiently storing and retrieving thermal energy. The study provides important insights into the potential of composite adsorbents for thermochemical energy storage and highlights the need for further efforts to get close to the theoretical energy density of the material. Overall, this work represents a significant step towards the development of sustainable and efficient energy storage solutions for the district heating sector.

Acknowledgements

Screening and experimental evaluation of materials for water harvesting within Direct Air Capture thermally-driven cycles

Valeria Palomba[1*], Vincenza Brancato[1], Andrea Frazzica[1]

[1]National Research Council of Italy – Institute for Advanced Energy Technologies (CNR-ITAE), Salita S.Lucia sopra Contesse 5, 98126 Messina, Italy. e-mail:valeria.palomba@itae.cnr.it

[*]Corresponding author: valeria.palomba@itae.cnr.it

Abstract

Direct Air Capture (DAC) of CO_2 from atmospheric air is becoming a crucial topic. One of the main requirements for DAC systems to drive their practical application is the low energy needed for the process and the possible integration with other energy processes. Among the different routes, physical adsorption of CO_2 from air has a promising potential, but still suffers some limitations, since its technological and economical feasibility is linked to the possibility of using low-temperature heat for driving the process with relevant efficiency. One of the main issues encountered in these type of systems is the presence of humidity in the air. Due to the much higher partial pressure of water compared to CO2, this leads to a negligible CO_2 adsorption if a proper pre-treatment to reduce air humidity is not carried out. Within this paper, we discuss the materials screening and first experimental testing in relevant scale for a water harvesting pre-treatment for the integration of DAC units. To this aim, the theoretical water uptake to significantly reduce humidity is evaluated and different commercial and composite materials have been evaluated. Subsequently, the tests in a dedicated bench at CNR-ITAE to actually evaluate the dynamic of the process are presented.

Keywords: direct air capture; water harvesting; materials screening; composite materials

Introduction

The increasing concentration of carbon dioxide (CO_2) in the atmosphere due to human activities has led to significant concerns about global warming and climate change. Direct air capture (DAC) of CO_2 has emerged as a promising technology to mitigate the effects of anthropogenic CO_2 emissions on the environment.

Thermally-driven DAC is a type of DAC that uses heat to drive the CO_2 capture process, by means of a temperature swing between an adsorption and desorption step. The use of heat in the capture process makes thermally-driven DAC particularly attractive since it allows for the use of low-grade heat sources, such as waste heat from industrial processes, solar thermal energy, or geothermal energy.In recent years, thermally-driven DAC has received increasing attention due to its potential for high CO_2 capture rates, low energy consumption, and the utilization of renewable energy sources. However, significant research efforts are still required to optimize and scale-up thermally-driven DAC processes, and improve their economic feasibility.

One of the main limiting issues is the need to significantly reduce the amount of water in the air before CO2 adsorption. Indeed, the amount of water needed in the is order of magnitudes less than the amount in the inlet air, therefore highlighting the need for deep air drying.

Aim of the present paper is to discuss the selection of materials suitable for such deep drying stage. To this aim, dedicated equilibrium curves measurements were carried out and the results of a thermodynamic and dynamic analysis are presented.

Material selection and preparation

The material selection was carried out in vision of the practical application of such pre-treatment units in the specific context of a DAC system. Therefore, the following constraints were considered:

- Low regeneration temperature;
- Commercial availability of the material or its main components (in the case of composites);
- Possible integration within heat exchangers either as a coated layer or loose grains.

To this aim, a preliminary selection was carried out starting from either results of previous tests are CNR-ITAE or dedicated measurements. The materials selected include: Siogel® from OkerChemie, SAPO34 zeotype , SAPO5 zeotype, and two composites made using silica gel as matrix and $CaCl_2$ and LiCl inorganic salts. The preparation method for the composites is described in (Frazzica et al., 2020).

Experimental tests were carried out using the Dynamic gravimetric vapor sorption analyzer (DVS) equipment from Surface Measurement Systems. In particular, the effect of low relative pressure (corresponding to the case of low relative humidity in the air) was evaluated with dedicated testing.

Thermodynamic evaluation

Thermodynamic evaluation was carried out by evaluating the achievable water uptake for the selected materials. In order to get a correspondence between the water uptake in the adsorbent and the relative humidity of the air, the methodology proposed in (Aristov & Gordeeva, 2022) was used, which consists in the superposition of the isosteric curves of the adsorbent with the prsychrometric chart of humid air. The method mainly consists of the following steps:

1. Measurement of equilibrium curves (isobars or isotherms) for the adsorbent;
2. Calculation of isosteric lines $P_{wa}(T)|_{w=const}$, where P is the pressure (bar), T is the temperature (K) and w is the water uptake (g/g). In order to calculate them, a fitting on the isotherms or isobars was carried out using Python software and Scipy package.
3. Calculation of the lines at constant relative humidity $T(x)|_{RH=const}$, where x is the humidity ratio (g/g) and can be calculated starting from equilibrium data of the material as $x = \frac{M_{wa}P_{wa}}{M_{da}P_{da}}$, where M is the molar mass (g/mol) and "wa" and "da" refer to water and dry air, respectively.
4. Superposition of these lines on the psychrometric chart of the air. This step was carried out in Python using the psychrochart package.

An example of the results is shown in Figure 1, where the initial and final conditions for the theoretical process are also identified. Initial conditions selected (air temperature of 35°C and 60%RH) are considered representative of summer conditions in Mediterranean climates. As exiting condition, a relative humidity of 1% was considered, which would allow for an efficient adsorption of CO_2 in the subsequent step of the process, thus expecting up to 4.5 $mol_{CO2}/kg_{sorbent}$.
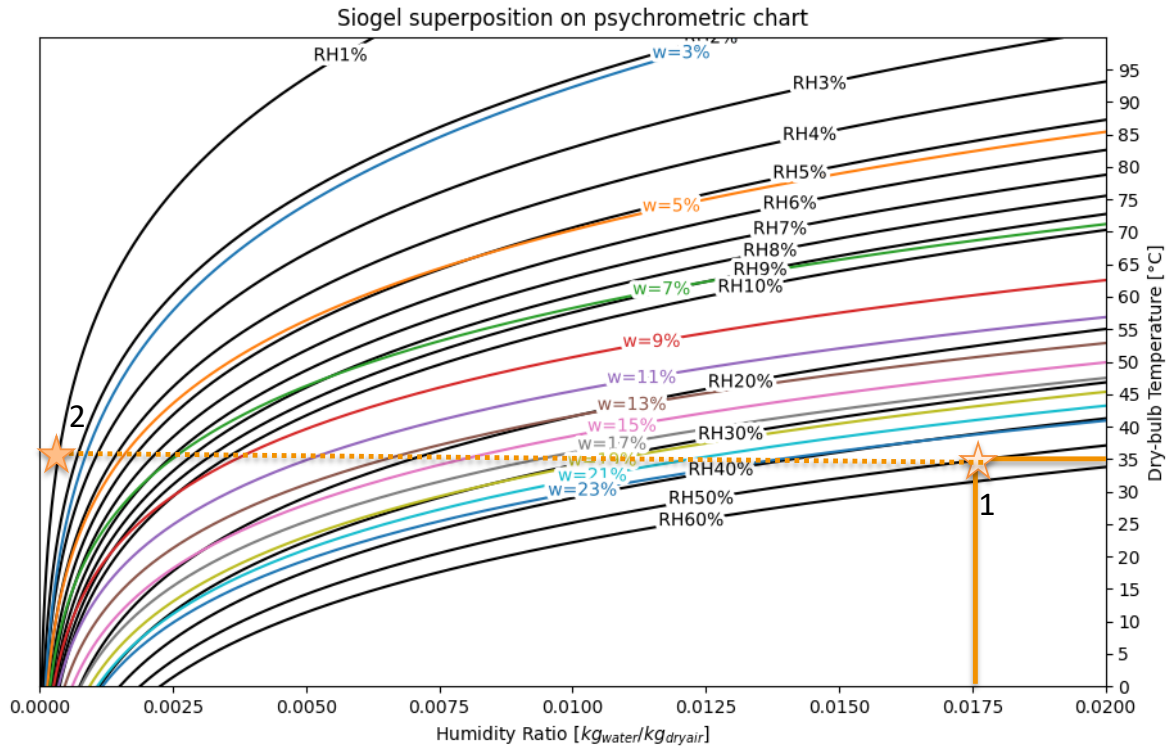
Figure 1. Thermodynamic evaluation by combination of isosteric lines and psychrometric chart. The case of Siogel.

Using this methodology, a comparison of the materials selected was carried out. The results are reported in Table 1. As it is possible to notice, the Silica gel/CaCl$_2$ composite shows the highest differential uptake and, at the same time, the lower regeneration temperature to reach the expected w_{dry}. SAPO5 could also represent an interesting alternative, wheres SAPO34 and Siogel® would need extremely high regeration temperatures. Moreover, Siogel® is also the material with the lowest differential uptake under the expected conditions.

Table 1. Results of the thermodynamic screening.

	w_humid, g/g	w_dry, g/g	Δw, g/g	Expected regeneration T
Siogel®	0.22	0.03	0.18	140°C
Silica gel/CaCl$_2$ 25%wt	0.39	0.07	0.32	100°C
SAPO34 (Fahrenheit)	0.29	0.03	0.26	150°C
SAPO5 (Fahrenheit)	0.25	0.03	0.22	120°C

Dynamic evaluation

Dynamic evaluation will be carried out at CNR-ITAE using a dedicated testing rig, whose rendering is presented in Figure 2. It mainly consists of a channel for the air to be pre-treated, which can be assembled in different sections, in order to have the flexibility of testing heat exchangers in different sizes. Since the regeneration of the adsorbent will be carried out using water as HTF for heating up

the material, hydraulic connections for thermostatic baths have been foreseen. Sensors to be installed include temperature, %RH, pressure difference and air velocity. The desired air flow rate will be guaranteed using a fan connected to a variable speed controller. The first testing activity will be carried out on a heat exchanger with Siogel in loose grains, which will represent the benchmarking material, followed by dedicated experiments with SAPO5/ SAPO34 coatings and the composites with loose grain configuration.
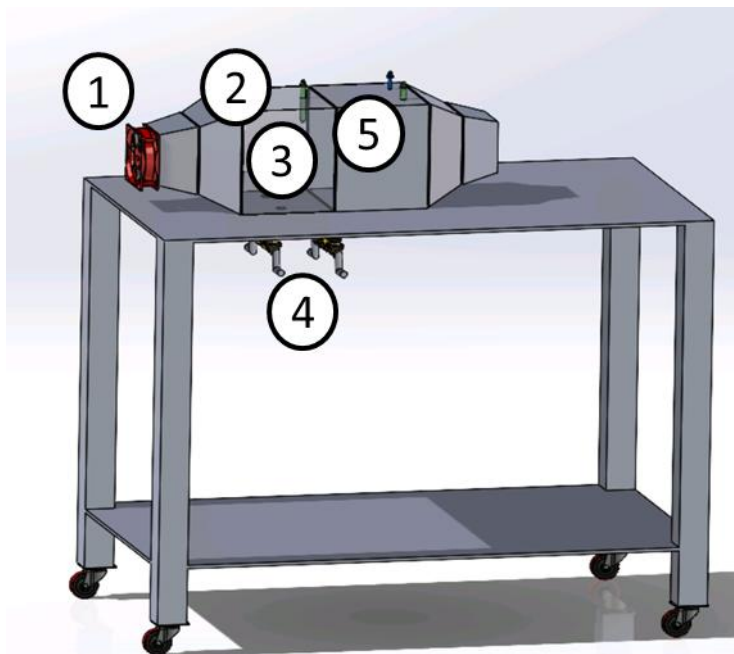
Figure 2. The testing rig for dynamic evaluation of materials at CNR ITAE. 1. Fan; 2. Channel for the air in different sections, selected according to the dimension of the heat exchanger to be tested; 3. Heat exchanger to be tested; 4 hydraulic connections to thermostatic baths; 5. Sensors.

On—going activities and future perspectives

In conclusion, this paper presents the preliminary activity for the selection of an adsorbent material for air pre-treatment in a DAC unit. To this aim, several candidates were selected and their equilibrium properties were measured. Subsequently, a thermodynamic analysis was carried out to identify the expected Δw under the operating conditions, i.e. inlet air of 35°C and Δ%RH=59%. Results indicated that silica gel/CaCl2 composite and SAPO5 have a promising potential, but their dynamic performances need to be assessed. Tests are on-going in a dedicated testing bench and will complete the characterization procedure, including also the selection of loose grains or coating configuration.

Acknowledgements

Microfibrous hygroscopic materials for water adsorption

at high RH

L. Bonaccorsi[1,3*], S. De Antonellis[2], A. Freni[3], A. Malara[1], A. Fotia[1]

[1]Department of Civil, Energetic, Environmental and Materials Engineering, Mediterranean University of Reggio Calabria, Reggio Calabria, Italy

[2]Department of Energy, Politecnico di Milano, Milano, Italy

[3]CNR - Institute of Chemistry of Organo Metallic Compounds (ICCOM), Pisa, Italy

[*]Corresponding author: lucio.boncaccorsi@unirc.it

Abstract

The objective of this work is to prepare, characterize and compare silica gel/polymer and magnesium sulphate/polymer microfibers produced by electrospinning. Such microfibrous hygroscopic materials have been specifically conceived for open-cycle adsorption applications, in which water is adsorbed at medium/high Relative Humidity (RH). The adsorbent microfibers characterization was carried out by scanning electron microscopy (SEM), thermogravimetric analysis and differential scanning calorimetry (TGA-DSC), adsorption/desorption isotherms measurement, permeation test. Hydrothermal stability of realized samples was verified by repeated ad/desorption aging test.

Keywords: Adsorption, Silica Gel, Magnesium Sulphate, Electrospinning, Open Cycles.

Introduction

Materials for water adsorption can be designed for a wide range of applications based on open or closed adsorption/desorption cycles in which the range of RH and temperatures can vary in a significant way. Adsorption closed cycles are commonly used in chillers and heat pumping systems which operating conditions require low partial pressures (low RH) and regeneration temperatures that depend on the heat source available, from medium (T = 350-150 °C) to low (T < 150 °C) temperatures. Open cycles are typically used in air treatment (desiccant cooling), in adsorption desalination and thermal energy storage and are characterized by a wide range of RH and, generally, are characterized by low regeneration temperatures [1,2]. Recently, for instance, De Antonellis et al. demonstrated that silica gel-based compounds can be employed to achieve an efficient air dehumidification and humidification processes [3]. The efficiency of these systems is strongly dependent on the adsorbing materials in terms of thermodynamic properties but also in the dynamic characteristics of the adsorption phenomenon, which is also connected to the transport properties of mass and heat through the adsorbent. One typical material used in these applications is silica gel for the satisfying adsorption capabilities and the low cost and large availability on the market. Silica gel, however, is generally used in granular or powdered form whit limitation in heat and mass transfer. Zeolites or hygroscopic salts suffer of the same limitation because synthesized in powder or pellets. Hygroscopic salts, moreover, are difficult to use because they can easily give rise to deliquescence or fusion in the most hydrated states even at low temperatures. In this work, a new generation of adsorbent materials for open cycles is presented, based on the synthesis of polymeric microfibers in which the adsorbent, silica gel or magnesium sulphate, is incorporated in the form of microcrystals. The particular microstructure of the hybrid microfibers allows to increase the surface area of the adsorbent bed compared to the granular configuration and, the most

important result, to hinder coalescence and fusion phenomena of the hygroscopic component [4].

Discussion and Results

The production of hybrid microfiber mats was achieved by electrospinning, a simple, inexpensive and easily scalable process. The apparatus consists of a syringe, a grounded collector and a high voltage power supply. In the spinning process, the syringe is filled with a polymer solution and a high voltage is applied between the syringe nozzle and the collector. The interaction between the charged polymer solution and the applied electric field provides the extrusion force. The microfibers were realized starting from a polyacrylonitrile (PAN) polymer solution added with different weight concentrations of MgSO4 or silica gel. The solution is then electrospun against an aluminum foil target on which layers of randomly oriented microfibers are formed. Finally, the hybrid microfibers are let drying at 80 °C overnight. The adsorbing mats were characterized by scanning electron microscopy, SEM, thermogravimetric analysis and differential scanning calorimetry (TGA-DSC), adsorption/desorption cycles, permeation test.

SEM images of hybrid microfibers (in Figure 1) show the typical morphology of the electrospun layers, in which the adsorbing particles, MgSO4 or silica gel, are embedded and homogeneously distributed inside the fibrosus matrix. This configuration contributes to maintain a high permeability to vapor diffusion through the adsorbent bed, a large reactive surface area due to the micrometric size of the particles and a high structural stability of the hygroscopic phase as it hinders sintering and granules growth.
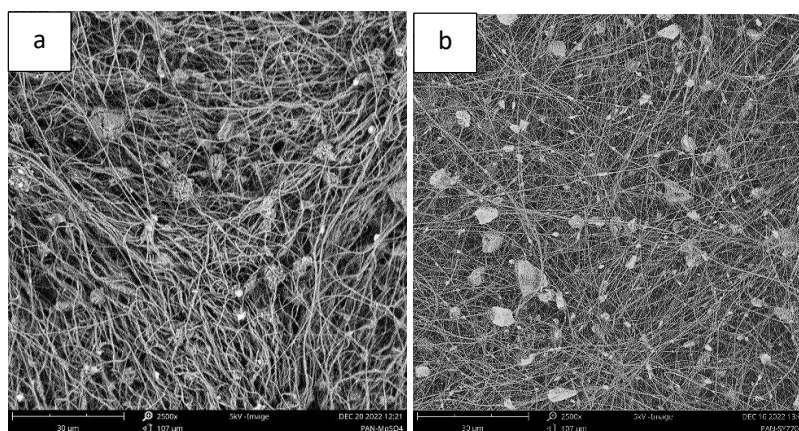
Figure 1. SEM images of PAN microfibers with MgSO4 (a) and silica gel (b).

In Figure 2 the sorption capacity of the same samples at 50°C is reported. Results highlight that MgSO4 and silica gel particles are able to properly adsorb water vapor. The sorption capacity of the samples keeps high and only a limited part doesn't work due to the presence of the polymer.
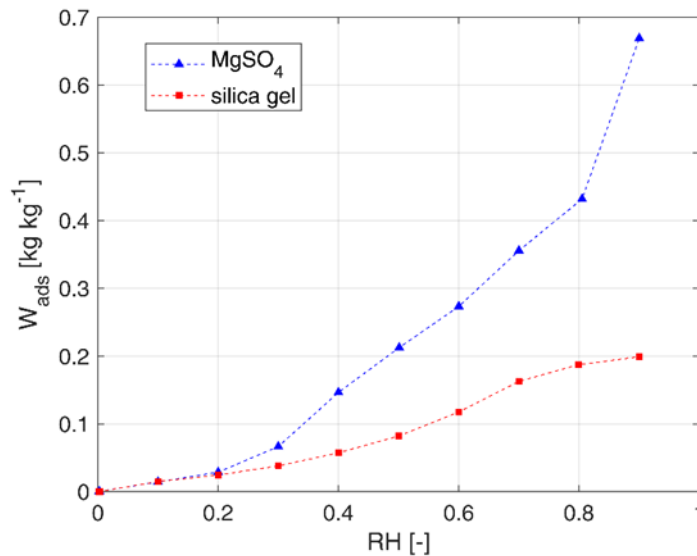
Figure 2. Adsorption isotherms (T=50°C) of microfibers with MgSO4 (triangle) and silica gel (square).

Conclusions

Morphological and functional characterization of electrospun hybrid microfibers have shown that the adsorption properties of silica gel and magnesium sulfate have been preserved and no negative impacts due to microfibers structure have been observed. The stability of microfibers to adsorption/desorption cycles is under evaluation but preliminary results are encouraging. Finally, the electrospinning technique is easily scalable and easily automatable for the production of self-supporting adsorbent sheets or coatings on metals.

References:

[1] Sahlot, M., Riffat, S.B., "Desiccant cooling systems: a review", Int. J. Low-Carbon Technol. 11, 489–505, 2016.

[2] Zhao, L.H., Wang, R.Z., Ge, T.S., "Desiccant coated heat exchanger and its applications", International Journal of Refrigeration, 130, 217-232, 2021.

[3] De Antonellis, S., Bramanti, E., Calabrese, L., Campanella, B., Freni, A., "A novel desiccant compound for air humidification and dehumidification", Applied Thermal Engineering, 214, 118857, 2022.

[4] Malara A., Bonaccorsi L., Frontera P., Freni A., Calabrese L., "Microfiber Textiles of Adsorbing Materials for Heat Transformations". Heat Transf Eng 43, 1652–63, 2021.

3D adsorbent lattice structure based on SAPO-34/S-PEEK composite material obtained by additive manufacturing for energy storage applications

Gabriele Marabello[1], Emanuela Mastronardo[1], Andrea Frazzica[2], Luigi Calabrese[1,2*]

[1] Department of Engineering, University of Messina, Contrada di Dio Sant'Agata, 98166 Messina, Italy

[2] CNR - ITAE "Nicola Giordano", Via Salita S. Lucia sopra Contesse 5, 98126 Messina, Italy,

[*]Corresponding author: lcalabrese@unime.it

Abstract

In this paper, an innovative three-dimensional structure, constituted by SAPO-34 zeolite as filelr and sulphonated polyether ether ketone (S-PEEK) as matrix was obtained by using additive manufacturing (AM) technology, for thermochemical energy storage application. The lattice structure was tailored in order to optimize the synthetsi procedure and material stability. The complex three-dimensional lattice structure was obtained without a metal or plastic reinforcement support. The composite structure was evaluated to assess its structural integrity by morphological and mechanical analysis. Funrthermore, the adsorption/desorption capacity was evaluated by water vapor adsorption isobars at 11 mbar at equilibrium in the temperature range 30-120°C, confirming good adsorption/desorption capacity.

Keywords: zeolite, composite sorbent, sulfonated poly(ether ether ketone), additive manufacturing

Introduction/Background

The growing need to propose more sustainable energy systems, based on a synergistic integration of different energy sources and the consequent development of technologies aimed at optimizing the recovery of waste heat has led to the investigation of innovative thermal energy storage technologies [1]. In this context, thermochemical heat storage represents a promising and viable technology, especially for long-term storage applications. However, its development on large-scale and realistic contexts has been partially limited by the need for more performing and suitable materials for fast and reliable storage design and tailoring.

In previous works [2,3], a composite material was proposed consisting of a high content of zeolite (up to 90% by weight of SAPO-34) and a sulphonated poly(ether-ether-ketone) (S-PEEK) binder. The S-PEEK matrix has a high water vapor permeability, thereby minimizing mass diffusion limits within the adsorbent composite bulk. Furthermore, this composite material has shown promising results in terms of mechanical, thermal and ad/desorption stability.

Based on these promising results, the present paper aims to investigate the use of this material for the realization of three-dimensional lattice structures entirely made of adsorbent composite material (without metal support) with the aid of the additive manufacturing technique.

Discussion and Results

A summary of samples/experiments/theories/simulations and a succinct discussion of key results presented in figures and/or tables should appear in this section.

Figure 1 shows the proposed steps for the manufacturing of the 3D printed lattice sorbent structure. In particular:

- CAD Design: Parametric design of the unitary lattice cell. Spatial replica 2x2x2 (Figure 1a).
- Molding: Design of the negative molding of the lattice structure (Figure 1b) and subsequent additive manufacturing by using PVA support.
- Composite filling: Preparation of the composite SAPO-34/S-PEEK slurry. The slurry is filled in the channel of the negative mold by using a micro-syringe. The slurry was added until the mold was fully filled (Figure 1c). The drying is performed in oven at 40°C for 1 day.
- Mold dissolution. To remove the negative PVA mold a dissolution procedure in water was applied. In particular, the materials were placed un an ultrasonic bath at 70°C for 5h until the complete dissolution of PVA support occurred. The residual material is the solid zeolite-S-PEEK sorbent material with the shape of the chosen lattice structure (Figure 1d).

| a) | b) | c) | d) |
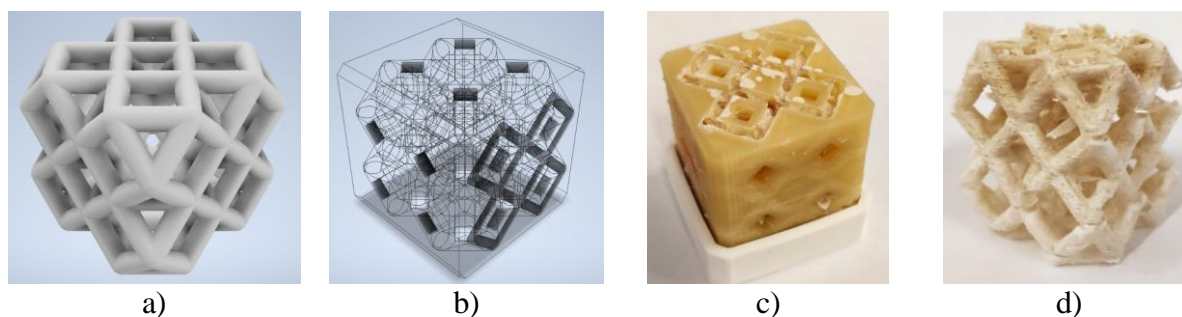
Figure 1. Manufacturing of the 3D printed lattice sorbent structure: a) parametric definition of the 3D cell; b) negative molding of the cell c) negative molding (PVA polymer) filled with composite SAPO-34/S-PEEK slurry; d) demolded lattice sorbent structure.

The 3D lattice structure thus obtained was morphologically and structurally assessed with the purpose to well define the synthesis characteristic, structural homogeneity and integrity. The adsorption/desorption capacity was performed by water vapor adsorption isobars at 11 mbar measured at equilibrium in the temperature range 30-120°C (by using a DVS equipment). The results reported in Figure 2 , confirm that the matrix does not hinder the mass flow of water vapor and the zeolite filler participates in the adsorption/desorption process, indicating this material potentially suitable for thermochemical storage by sorption technology.
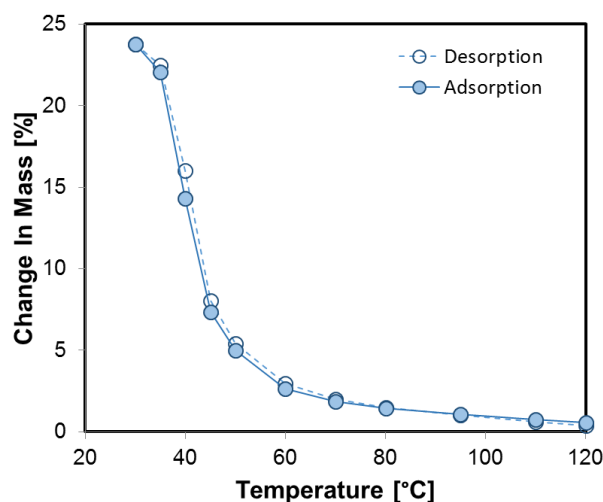
Figure 2. Water adsorption (filled marker) and desorption (empty marker) isobars at 11 mbar for 80% SAPO-34 zeolite filled in S-PEEK polymer material

Conclusions

The present work investigated the synthesis and characterization of an innovative three-dimensional lattice structure, exclusively constituted by an adsorbent composite material (SAPO34 zeolite and S-PEEK as filler and matrix, respectively), for thermal storage. The results highlight that:

- The composite has an effective adsorption/desorption capacity, indicating that the polymeric matrix does not hinder the diffusion of water vapor towards the zeolite.
- The additive manufacturing, by using a negative PVA mold, is a suitable technology in order to procedure adsorbent tridimensional lattice structures.
- The 3D structure is structurally stable, regular, homogeneous and with a high surface area, indicating it as a promising solution for the construction of reactors for energy storage.

References:

[1] G. Sadeghi, Energy storage on demand: Thermal energy storage development, materials, design, and integration challenges, *Energy Storage Mater*. 46 (2022) 192–222. https://doi.org/https://doi.org/10.1016/j.ensm.2022.01.017.

[2] D. Palamara, V. Palomba, L. Calabrese, A. Frazzica, Evaluation of ad/desorption dynamics of S-PEEK/Zeolite composite coatings by T-LTJ method, *Appl. Therm. Eng.* 208 (2022). https://doi.org/10.1016/j.applthermaleng.2022.118262.

[3] D. Palamara, P. Bruzzaniti, L. Calabrese, E. Proverbio, Effect of degree of sulfonation on the performance of adsorbent SAPO-34/S-PEEK composite coatings for adsorption heat pumps, *Prog. Org. Coatings.* 154 (2021) 106193. https://doi.org/https://doi.org/10.1016/j.porgcoat.2021.106193.

Multi-objective performance and cost optimisation of the adsorption chiller for Saudi Arabia's climate

Bawazir, Abdullah[1,2]; AL-Hasni, Shihab[1,3]; Santori, Giulio[1] and Friedrich, Daniel[1] *

[1]The University of Edinburgh, School of Engineering, Institute for Energy Systems, Faraday Building, The King's Buildings, Mayfield Road, EH9 3BF, Edinburgh, Scotland, UK

[2]King Abdulaziz City for Science and Technology Institute for Energy and Water Research, P.O. Box 6086, Riyadh 11442, Saudi Arabia

[3]Department of Engineering, The University of Technology and Applied Sciences, Suhar 311, Oman

*Corresponding author: (D.Friedrich@ed.ac.uk)

Abstract

In recent years, the imperative to develop sustainable cooling systems has grown considerably as a result of increasing concerns over the impact of climate change and increasingly stringent regulatory standards for carbon emissions. Adsorption chillers powered by solar thermal energy have the potential to provide sustainable cooling for many hot regions with good solar irradiance. However, adsorption chillers need to be further optimized to be economically competitive. The objective of this study is to perform a thorough analysis of the the performance of two-bed adsorption chiller by implementing multiobjective optimization techniques that prioritise cost minimization in both the operational and design phases. The present study involved an analysis of a general optimisation for a specific model that utilised the same amount of adsorbent weight and validated it with experimental data from the published literature. A benchmark cost of 2100 \$/kW was established, and optimisation results indicated improvements in Specific Cooling Power (SCP), Coefficient of Performance (COP), and cooling capacity, as well as a price reduction to 1100 \$/kW.

Keywords: Adsorption chiller, dynamic model, SCP analysis, capital cost, Multi-objective optimization

Introduction/Background

The issue of global warming has become a concern worldwide, leading to a growing demand for cooling systems [1]. Traditional refrigeration systems rely on burning fossil fuels, which harm the environment and indirectly raise energy bills.[2]. In 2016, the partner nations agreed to reduce hydrofluorocarbon production and consumption by 80% over the next three decades as part of the Kigali amendment, which is expected to prevent global warming by up to 0.5 °C by the end of this century [3]. Water is considered an ideal refrigerant due to its non-toxic nature and lack of environmental impact [4]. Chilled water is widely used to cool air in buildings and equipment in industrial processes. Various methods are employed to produce chilled water, including cooling towers, compression refrigeration chillers, absorption chillers, and adsorption chillers, among others. Adsorption chillers, like absorption chillers, use water as the refrigerant fluid, but they use a solid adsorbent instead of an absorbent solution [5]. Adsorption chillers have several advantages over absorption chillers, including ease of maintenance and control due to the use of a solid adsorbent and no moving parts. They are also safer, as solid adsorbents do not leak and have no environmental impact during operation [6]. However, the capital cost of adsorption chillers is high [7]. Bawazir and Daniel [8] developed a simulation model that takes into account the energy, economic, and environmental aspects. The model compares the performance of solar-driven adsorption

chillers (ADCs) with the performance of VCCs in Riyadh, the capital city of Saudi Arabia. The aim of the study was to assess the efficiency of large-scale ADS using a TRNSYS simulation. The study findings suggest that the use of ADC leads to a reduction in annual energy cost and CO_2 emissions compared to VCC, with reductions of 74% and 75%, respectively. Hong et al. [9] carried out an optimization study on a fin tube adsorption chiller, employing an experimental design approach to maximise specific cooling power (SCP) and coefficient of performance (COP). Li et al. [10] performed multiobjective optimisation (MOO) of a solar-powered adsorption chiller integrated with a heat pump with the aim of reducing the dependency on fossil fuels and improving the stability of the system. The authors used the curve-fitting method to calculate the SCP and COP of the adsorption chiller and optimised the primary energy consumption and annual cost objective functions using a genetic algorithm based on the Pareto front technique. Djubaedah et al. [11] performed the MOO of a solar-powered, two-bed adsorption chiller to determine the optimal operating cost and exergy destruction, with the area of the solar collector and the flow rates of the utility streams serving as decision variables. Although these studies compare and optimise the operating costs and performance of adsorption chillers, there is a lack of studies that also the capital costs of the system. However, adsorption chillers, like most low-carbon technologies, are capital intensive and it is crucial to include these costs in the optimisation.

This investigation represents a pioneering effort in analysing the performance of a two-bed adsorption chiller by means of a cycle time study together with the reduced-temperature approach. To achieve a novel design solution that minimises the total cost of the adsorption chiller unit, the study will employ multiobjective optimization with genetic algorithms. Furthermore, this study will produce an estimate of the adsorption chiller technology, including an optimal cost with auxiliary devices per cooling capacity. The main focus of the study will be the Saudi Arabian market, which exhibits a high potential for adoption of this technology, facilitating a shift to cleaner cooling alternatives in the arabian peninsula region.

Description of the evaluated system

To benchmark the cost of silica gel for adsorption chillers, we used the experimental model developed by Saha et al. [12]. This model was developed in MATLAB and has been validated. **Figure 1** illustrates the simulation results and their comparison with the experimental data obtained from the original work by Saha et al. [12].
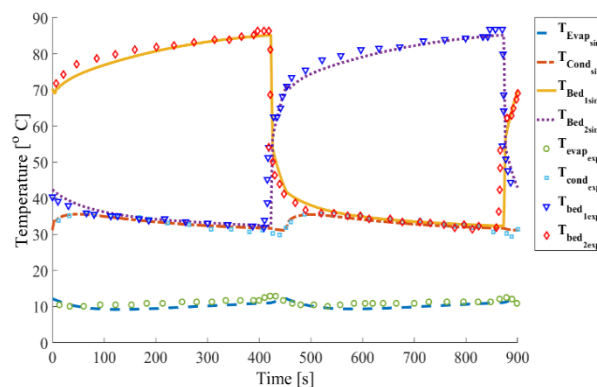
Figure 1 Comparison of the simulation results obtained in this work with the experimental data obtained from [12]

Heat Powered Cycles
Conference 2023
Edinburgh
Heat in the new energy system

3rd to 6th of September 2023
The University of Edinburgh, Scotland

To ensure the precision of a mathematical model using MATLAB software, we evaluated the agreement between the simulation and experimental results. The simulation results exhibited an excellent fit to the experimental data as shown in **Figure 1**. According to the MATLAB simulations, the temperatures in the adsorption system were the same as in the experimental data. Only a minor deviation in the predicted adsorption bed temperature was observed at the end of the cycle time.

To capture the full performance spectrum of the adsorption chiller, a straightforward reduced-temperature method (T_{red}), can be utilised and represented as follows:

$$T_{red} = \frac{T_{cond} - T_{chill}}{T_{hot} - T_{cond}} \tag{1}$$

T_{red} involves using two of the three variables as constant while varying the third variable within a specific range that depends on the cooling system operation. To capture the full performance spectrum of an adsorption chiller, the T_{red} study is performed for a range of cycle times. The results obtained are presented in a graph to show the relationship between the SCP and COP as shown in **Figure 2.**
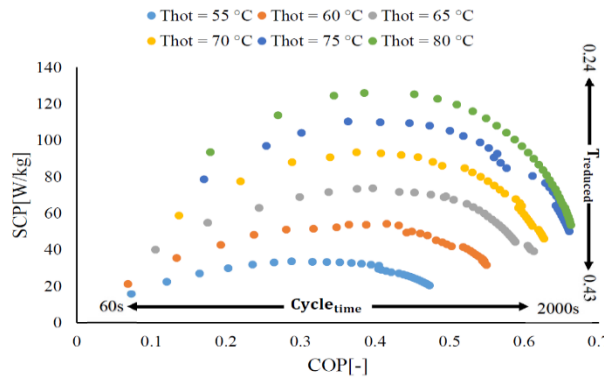
Figure 2 T_{red} based on inlet temperatures T_{chilld} =12°C with T_{cond} =25°C and Thot are variable

The analysis started with the performance mapping of the adsorption chiller design in [13]. The study of T_{red} was carried out on the basis of the the effect of hot temperature range of 55 ° C to 80 °C; with a cooling temperature 25°C; chilled temperature 12°C; T_{red} range of 0.24 to 0.43 and a cycle time study from 60s to 2000s, as shown in **Figure 2**.

This study uses MOO to achieve the objectives of this study and generate new performance values for the two-bed adsorption chiller including cost, SCP, and COP. The optimisation used the decision variables within the specified range except for the weight of the adsorbent, which was kept constant at the level used in the original experimental data. Through iterations of optimization, a larger search space is explored and better solutions are discovered. This is because the adsorption chiller has a multitude of decision variables that possess a good range for each input parameter, allowing the algorithm to provide new solutions based on the best prior best answer and attempt to improve upon it with each iteration. The simulation generated an optimised design that has a lower specific cost per kilowatt of cooling capacity with better performance compared to the benchmark system [12].

The multi-objective optimisation strategy of the adsorption chiller has decision variables aimed at optimising various design and operational parameters, as presented in **Table 1**, such

as the heat transfer areas of the evaporator, condenser, and adsorption beds, as well as the inlet temperatures of chilled water, cooling, and hot water, and the cycle time.

Table 1 The decision variables influence the optimisation of the adsorption chiller.

Variable	Unit	Range
A_{evap}	m^2	1- 10
A_{cond}	m^2	1- 10
A_{ADS}	m^2	1- 10
t_{cycle}	s	60-800
$T_{chilled}$	$°C$	8-20
T_{cond}	$°C$	25-35
T_{hot}	$°C$	55-90
$\dot{m}_{chilled}$	m^3/s	0.5-2
$\dot{m}_{cond}$	m^3/s	0.5-2
$\dot{m}_{cw}$	m^3/s	0.5-2
$\dot{m}_{hot}$	m^3/s	0.5-2

A flow chart of the optimisation algorithm for the adsorption chiller system, which was based on the work of Reddy and Kumar [14], is presented in Figure 3 .This method captures tlowest to highest performance of the adsorption chiller and allows the optimisation of the existing design in terms of operation and physical design parameters.
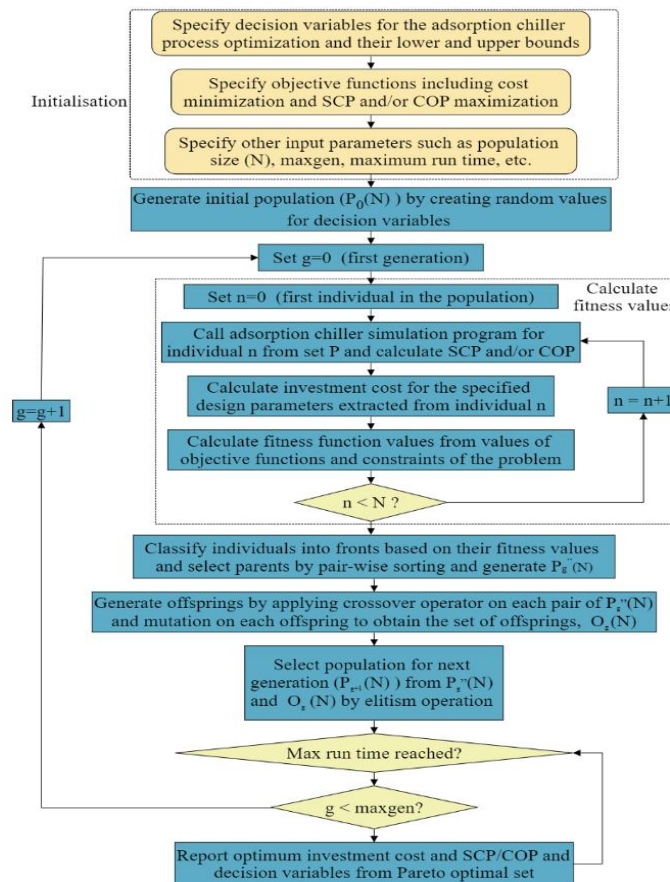
Figure 3 Flow chart of multi-objective optimisation of the adsorption chiller process using the genetic algorithm based on the work of Reddy and Kumar [14].

Heat Powered Cycles
Conference 2023
Edinburgh

Heat in the new energy system

3rd to 6th of September 2023
The University of Edinburgh, Scotland

Discussion and Results

The principal objective of the optimisation process is to enhance the SCP by increasing the cooling capacity of the adsorption chiller and reducing the associated costs. As can be seen in **Erro! Fonte de referência não encontrada.** (a), it is evident that the application of optimisation techniques resulted in a 40% increase in SCP, particularly in the worst-case scenario of a chilled temperature of 8 ° C. The maximum SCP was observed at a chilled temperature of 15 °C, which is consistent with the temperature used in the experimental model. It is possible to achieve a substantial reduction in the capital cost of the adsorption cooling system by applying optimisation techniques. The data presented in Figure 4 (b) show a significant decrease in specific cost percentages for cold temperatures between 8 °C and 20 ° C, compared to the benchmarked price. This reduction suggests that optimisation can lead to a decrease in the cost per kilowatt of cooling capacity. The largest reduction in price per kW of cooling capacity occurs at 20 ° C due to the relatively lower stress on the evaporator resulting from the condenser temperature being around 27 ° C and the hot temperature being approximately 86 ° C. However, it should be noted that a price decrease is still effective even at lower chilled temperatures.
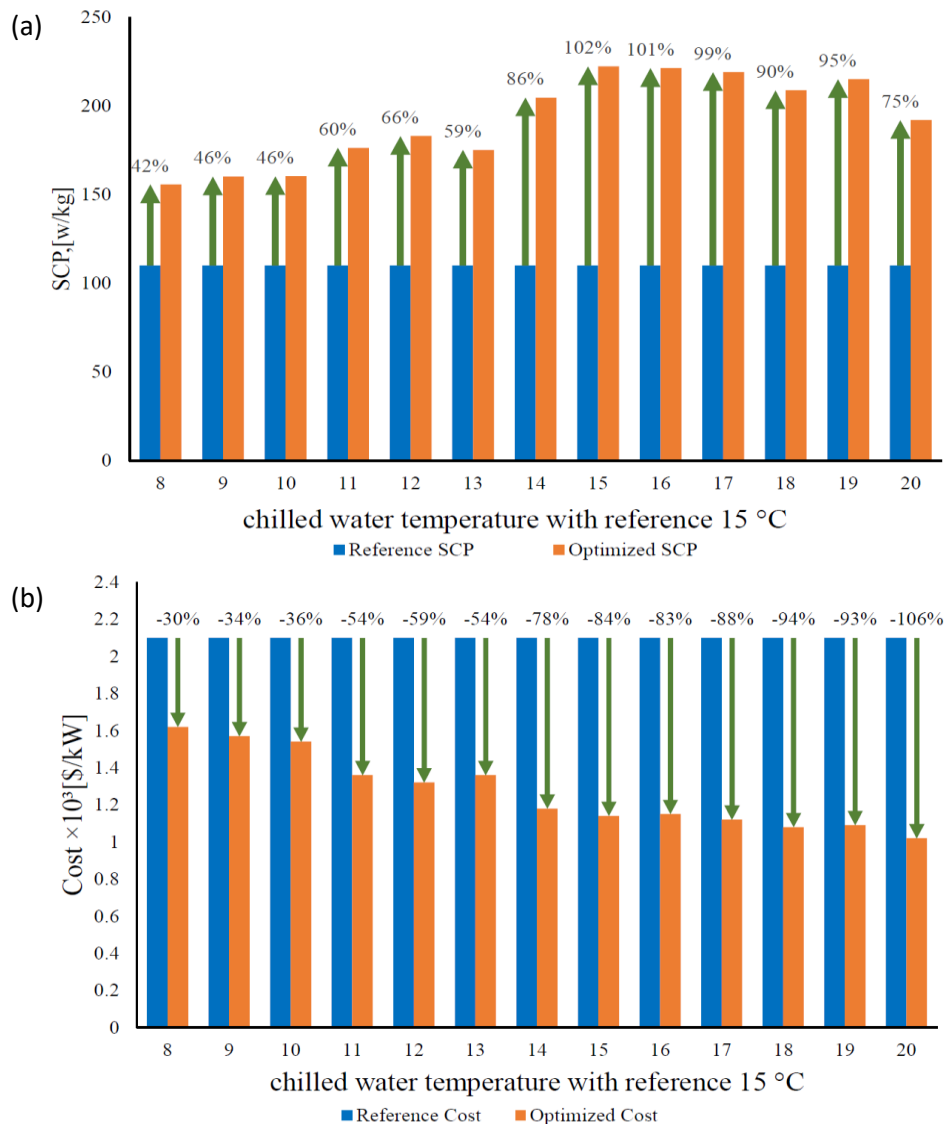
Figure 4 Optimization for two-bed adsorption chiller system (a) SCP and (b) cost per kW

Conclusions

In this study, a multiobjective optimization approach is employed to analyse the performance of a two-bed adsorption cooling system. The goal is to optimise the existing system design by improving the SCP and decreasing the associated specific costs per kilowatt of cooling capacity by increasing the cooling capacity. To achieve this objective, the optimisation process involves exploring a range of operational and physical design parameters. Following the establishment of a benchmark cost of 2100 $/kW, the optimisation process resulted in notable improvements in SCP, COP, and cooling capacity. Furthermore, optimization led to a significant reduction in the price of the system, which was reduced to 1100 $/kW. The next phase of this study will be to evaluate a range of operational and design parameters to optimise for a special case study specifically targeting the Middle East and Saudi Arabian chiller markets.

References

[1]   The Royal Society, 'Low-carbon heating and cooling : overcoming one of world ' s most important net zero challenges', pp. 1–12, 2021.

[2]   Christina Ospina, 'Cooling Your Home but Warming the Planet: How We Can Stop Air Conditioning from Worsening Climate Change', *Clim. Inst.*, pp. 1–8, 2018.

[3]   E. A. Heath, 'Amendment to the Montreal Protocol on Substances that Deplete the Ozone Layer (Kigali Amendment)', *Int. Leg. Mater.*, vol. 56, no. 1, pp. 193–205, 2017.

[4]   R. H. Mohammed, O. Mesalhy, M. L. Elsayed, M. Su, and L. C. Chow, 'Revisiting the adsorption equilibrium equations of silica-gel/water for adsorption cooling applications', *Int. J. Refrig.*, vol. 86, pp. 40–47, 2018.

[5]   E. Elsayed, R. AL-Dadah, S. Mahmoud, P. A. Anderson, A. Elsayed, and P. G. Youssef, 'CPO-27(Ni), aluminium fumarate and MIL-101(Cr) MOF materials for adsorption water desalination', *Desalination*, vol. 406, pp. 25–36, 2017.

[6]   H. T. Chua, H. K. Toh, and K. C. Ng, 'Thermodynamic modeling of an ammonia-water absorption chiller', *Int. J. Refrig.*, vol. 25, no. 7, pp. 896–906, 2002.

[7]   A. Alahmer, X. Wang, and K. C. A. Alam, 'Dynamic and economic investigation of a solar thermal-driven two-bed adsorption chiller under Perth climatic conditions', *Energies*, vol. 13, no. 4, 2020.

[8]   A. A. Bawazir and D. Friedrich, 'Evaluation and Design of Large-Scale Solar Adsorption Cooling Systems Based on Energetic, Economic and Environmental Performance', *Energies*, vol. 15, no. 6, pp. 1–24, 2022.

[9]   S. W. Hong, S. H. Ahn, O. K. Kwon, and J. D. Chung, 'Optimization of a fin-tube type adsorption chiller by design of experiment', *Int. J. Refrig.*, vol. 49, pp. 49–56, 2015.

[10]   R. Li, Y. Dai, and G. Cui, 'Multi-objective optimization of solar powered adsorption chiller combined with river water heat pump system for air conditioning and space heating application', *Energy*, vol. 189, p. 116141, 2019.

[11]   E. Djubaedah, A. Rachmat, N. Aisyah, Nasruddin, and A. Kurniawan, 'Multi-objective optimization of a two-bed solar adsorption chiller based on exergy and economics', *Int. J. Technol.*, vol. 9, no. 6, pp. 1276–1284, 2018.

[12]   B. B. Saha, E. C. Boelman, and T. Kashiwagi, 'Computer simulation of a silica gel-water adsorption refrigeration cycle - the influence of operating conditions on cooling output and COP', *ASHRAE Trans.*, vol. 101, no. Pt 2, pp. 348–357, 1995.

[13]   M. Gado, E. Elgendy, K. Elsayed, and M. Fatouh, 'Parametric Study of an Adsorption Refrigeration System Using Different Working Pairs', *J. Eng. Sci. Mil. Technol.*, vol. 17, no. 17, pp. 1–15, 2017.

[14]   M. J. Reddy and D. N. Kumar, 'Optimal reservoir operation using multi-objective evolutionary algorithm', *Water Resour. Manag.*, vol. 20, no. 6, pp. 861–878, 2006.

Heat Powered Cycles
Conference 2023
Edinburgh

Heat in the new energy system

SolDAC: Full Spectrum Solar-Powered Direct CO₂ Capture from Air and Conversion in Ethylene

N. M. Beltrán[1], V. Brancato[2], S. Brandani[3], N.M. Carretero[4], E. Contreras[5], D. Chemisana[6], A. Frazzica[2], M. Gracia[1], I. Herraiz[5], H. Kaur[7], E. Loscos[8], J. Madrid[6], S. Maestro[6], M. N. Mohammed[3], A. Moreno[6], S. Murcia-Lopez[4], L. Navarro-Tovar[3], J. Núñes[1], V. Palomba[2], I.C.C Quaranta[3]*, A. Solans[6], G. Soley[1], V.S.R.K. Tandava[4], O. Teixidó[6], M. Tovar-Oliva[3], I. Tudela-Montes[3], P.A. Wright[7], Z. Xu[3], G. Santori[3]

[1] Comet Global Innovation S.L., Gran de Gràcia, 1 - 4º 3ª- 08012 Barcelona

[2] CNR Institute for Advanced Energy Technologies (CNR ITAE), 98126 Messina, Italy

[3] The University of Edinburgh, School of Engineering, Institute for Materials and Processes, Robert Stevenson Road, Edinburgh, EH9 3FB, United Kingdom

[4] Catalonia Institute for Energy Research (IREC), C/Jardins de les Dones de Negre 1, 08930, Barcelona, Spain

[5] LOMARTOV S.L., C/Párroco Miguel Tarín 16 Bajo Dcha., 46035, Valencia, Spain

[8] University of Lleida. Applied Physics Section of the Environmental Sci. Dept., c/ Jaume II, 69. 25001, Lleida, Spain

[7] University of St Andrews, School of Chemistry, EaSTCHEM, Purdie Building, North Haugh, St Andrews, KY16 9ST, United Kingdom

[8] European Innovation Marketplace ASBL. 49 rue de Treves 1040 Bruxelles, Belgique

*Corresponding author: i.c.cavalcante-quaranta@sms.ed.ac.uk

Abstract

CO_2-derived chemicals are expensive and only few will be able to meet the current market expectations, settled in decades of fossil fuel economy. Ethylene can be one of the few chemicals that can be produced from a 100% renewable route to the condition that specific targets are achieved. The SolDAC project endeavours in all scientific challenges preventing the demonstration of a sustainable route for renewable Ethylene. A process is proposed that captures CO_2 from the air and convert it to Ethylene in an electrochemical unit. The process is powered by a highly efficient solar energy technology that collects the full spectrum of solar radiation.

Keywords: Full Spectrum Solar Energy, Direct Air Capture, Photo-electrochemical conversion, carbon dioxide.

Introduction

Reducing carbon emissions also requires finding alternative pathways for producing organic chemical compounds derived from fossil fuels. Ethylene is an essential chemical intermediary for plastics, with an annual global production rate of 185 Mt [1]. Traditionally, its production is by steam cracking of crude oil in a high energy-demanding process, resulting in a global carbon footprint of 0.2 Gt [1] emitted annually. Renewable Ethylene can be obtained by electrochemical reduction of atmospheric CO_2 using electricity from renewable sources that is a promising production route to close the carbon loop and mitigate CO_2 emissions [2]. However, the technological viability of this process relies on the efficiency of the renewable source, on the

purification of extremely dilute CO_2 and on affordable electrochemical catalysts that overcome critical factors such as poor activity, selectivity, and energy efficiency [3]. The Full Spectrum Solar Direct Air Capture and Conversion project (SolDAC) gathers eight research institutions and companies from four countries (UK: The University of Edinburgh and University of St Andrews; Spain: IREC, University of Lleida, LOMARTOV SL, Comet; Italy: CNR-ITAE; Belgium: EIM) and aims at demonstrating the sustainable production of renewable Ethylene from atmospheric CO_2 and water through an innovative process.

Overall process

The process is organised into three sections: a Full Spectrum Solar collector (FSS), a Direct Air Capture unit (DAC), and a Photo-Electrochemical Conversion stack (PEC). The main energy and mass fluxes and the interrelations among units are depicted in Fig 1.
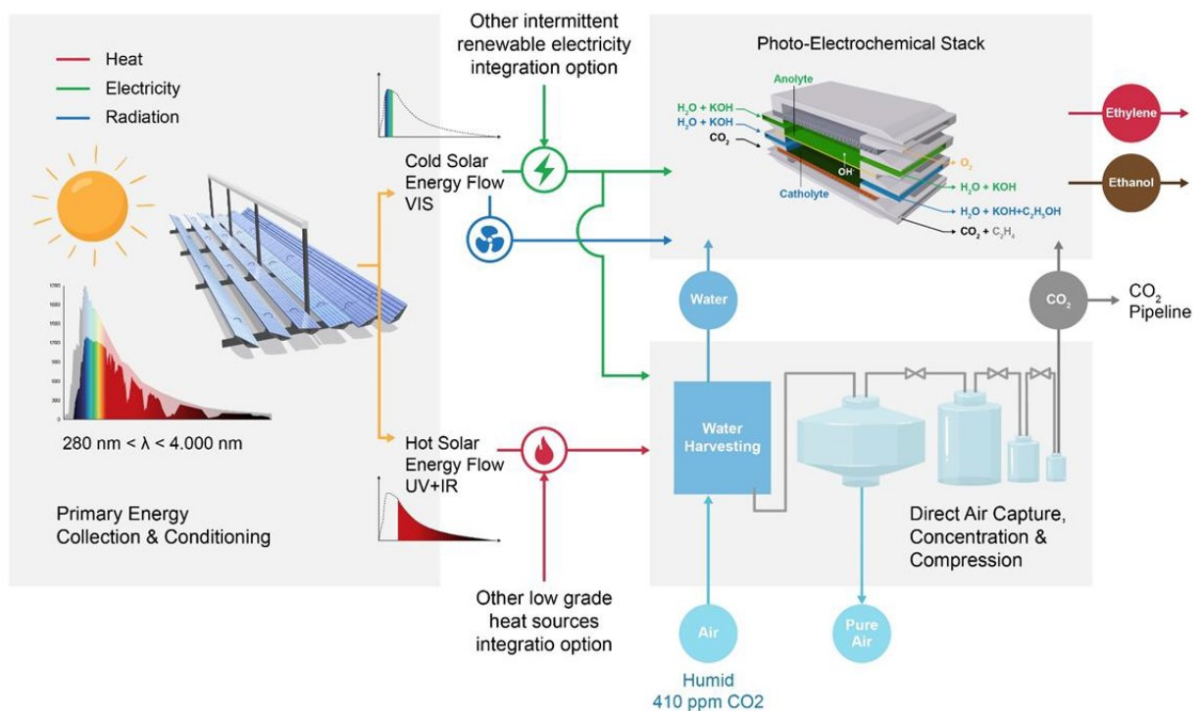
Fig. 1 - The SolDAC process for conversion of atmospheric CO_2 into Ethylene.

Full Spectrum Solar Collector (FSS)

A solar energy collection system able to capture the full spectrum of solar energy powers both DAC and PEC. The power from the FSS comes to the downstream processes in three forms: electrical, thermal, and optical. Ultraviolet light and infra-red are absorbed and transported in form of thermal energy. The visible spectrum wavelengths are collected and converted in electrical power and voltage saving. The overall process efficiency depends on the efficiency of the acceptance angle and the optical efficiency of the Fresnel Concentrator [4]. However, the efficiency needs to be evaluated from the receiver to the thermal and photo-voltaic (electric). Regarding the thermal efficiency, it is strongly dependent on the temperature of the carrier [5]. A higher thermal efficiency is observed in lower temperatures, due to the reduction of heat losses by convection to the ambient. The photo-voltaic (PV) efficiency is related to the photo-carrier, like an optical fiber, and to the photo-voltaic cell, that converts light into electricity. The goal of FSS in terms of electrical efficiency is to convert the 22% of the incident power by

selecting the most efficient photons based on the PV spectral response. On the other hand, the foreseen thermal efficiency to be achieved by the hybrid receiver is expected to reach 38%, which means a target global efficiency of 60%. This figure goes beyond the state-of-the-art by increasing the efficiency of the reference system by 10% [4].

Direct Air Capture Unit (DAC)

A DAC unit consisting of a combination of capture and concentration adsorption beds [6] embedding different nanoporous materials is able to capture ultra-dilute CO_2 (410 ppm) from ambient air and concentrate it before it is used in the PEC to produce ethylene. Usually, nanoporous materials with good CO_2 affinity also present affinity for water. Due to that, a material with good CO_2 capacity and step isotherm for water (H_2O) is preferable in the process. To ensure a low water adsorption, a water harvesting step is considered to reduce relative humidity before the capture bed. A fraction of the water removed from air can be used in electrochemical conversion. The energy consumption in the DAC unit primarily comes from the temperature swings. Therefore, using low-temperature-heat (below the current state-of-the-art 80 °C [7]) to regenerate the sorbent is preferable to make the process more economically attractive [8]. The project targets a regeneration at 60 °C, reducing the primary energy consumption to purify and compress CO_2 from 8.51 MJ/kg_{CO2} (adapted from [9]) to 3 MJ/ kg_{CO2}.

Photo-Electrochemical Conversion stack (PEC)

Previous studies have demonstrated that Cu is the only pure metal that can produce C2+ products with substantial selectivity [10]. For this reason, there have been several investigations on tuning the composition and morphology of Cu catalysts to optimise the conversion of CO_2 [11]. The PEC unit uses an energy flow (in the form of photons and/or electricity) in a copper-based catalyst to convert CO_2 to Ethylene. Cu-based catalysts (e.g. Ag, Bi, Sn) were prepared through optimised electrodeposition and wet-chemistry methods. The catalysts were deposited onto carbon paper (Gas Diffusion Layer) and were used as gas diffusion electrodes (GDEs). The use of GDEs has demonstrated the capacity to obtain high current densities (>200 mA cm^{-2}) by supporting the catalyst on a microporous substrate at a gas-liquid interface [12]. For characterising the electrochemical performance of the catalysts, a flow electrolyser has been used to reduce the captured CO_2 into the targeted renewable chemicals such as Ethylene with targeted faradaic efficiencies > 70%. Liquid products such as ethanol are also expected as by-products, giving a combined C2+ efficiency > 85%. Moreover, the PEC unit foresees the integration of photoelectrodes in the anode side, able to provide additional photovoltage under illumination, in order to decrease the overall energy requirement and to directly utilise photons from the FSS unit.

Process Thermodynamics

Likewise, many other renewable energy-powered chemicals from CO_2, Ethylene can result unbearably expensive, with no real market acceptation. Furthermore, the life-cycle emissions for the construction of the sub-processes have to at least be compensated by the emissions avoided and by those stored underground (geological storage is one of the options present in in Fig. 1). The mass and energy balances of each one of the sub-processes and of the overall SolDAC process can help to identify if the SolDAC project has chances to be sustainable.

Aiming to achieve a defined production rate of ethylene, the process mass balance starts from the PEC stack. A simplified mass balance was implemented based on the Faradaic efficiencies

for ethanol, ethylene and hydrogen, the electrode area and the current density used. An excess factor for the CO_2 demand was introduced to ensure a reaction tending to ethylene and not the by-product (ethanol or hydrogen). The electrical energy required for reaction was calculated based on the specific energy to convert CO_2 to ethylene and the overall process efficiency.

For the DAC unit, a mass balance was used to relate CO_2 purity, recovery, and flowrate at the end of the separation with the air composition and feed flowrate. Air composition was simplified in H_2O, CO_2 and N_2. All other gases present in air were lumped in N_2 concentration. An excess factor for CO_2 was used in the Direct Air Capture, and the CO_2 that surpasses the PEC demand was used for geological storage and consider in the economic analysis as carbon credits. The DAC unit is powered by electrical and thermal energy simultaneously. Electrical energy is used to power fans to move air through the system. The total electricity demand was calculated from the fan efficiency, pressure drop across the system, and the processed volumetric flowrate. Thermal energy is used to regenerate the beds and recover CO_2 that was adsorbed. The heat power was obtained from the minimum work of separation and the efficiency of this process.

The FSS area was calculated to supply the energetic requirements determined in the previous units. As discussed, the full spectrum solar is able to generate electrical, thermal, and photovoltaic power. The total electrical power needs to adequate the PEC and the DAC process requirements, while the thermal power complies with only the DAC unit. Solar energy (photons) is directly used in the anode side of the electrochemical stack with adapted photovoltaics to decrease cell potential and reduce electric energy demand. An energy balance for the FSS was developed to relate the energy generation with the Fresnel area. The calculations considered the conversion efficiency of light to electricity and to heat, the overall efficiency of the Fresnel, and the mean beam irradiance, to relate the energy generation with the Fresnel area.

From the mass and energy balances described, a small plant with capacity to produce 1 kg/day of ethylene needs to process 34 ton/day of air, capturing about 17kg/day of CO_2. To power that pilot-plant, an area of 32 m² is required for the full spectrum solar. In this configuration, 9% of the CO_2 that was captured is used for geological storage.

In addition to the balances done, an economical and environmental check was performed to evaluate the feasibility of the proposal. Fig. 2 depicts the results from those studies. For the environmental analysis, the carbon footprint values of each unit were set at: 0.32 kg of CO_2 emitted per kg of CO_2 removed for the DAC unit, 3.05 kg of CO_2 emitted per m2 of the PEC unit, and 0.025 kg of CO_2 emitted per kWhel generated in the FSS unit. These were based on the Life Cycle Assessments of similar technologies, published in other works [13, 14, 15]. For the economic analysis, chemical prices were assumed at their current market value. The costs of the technologies were estimated from published data to observe the price cost to accomplish a carbon-neutral process that is economically viable.
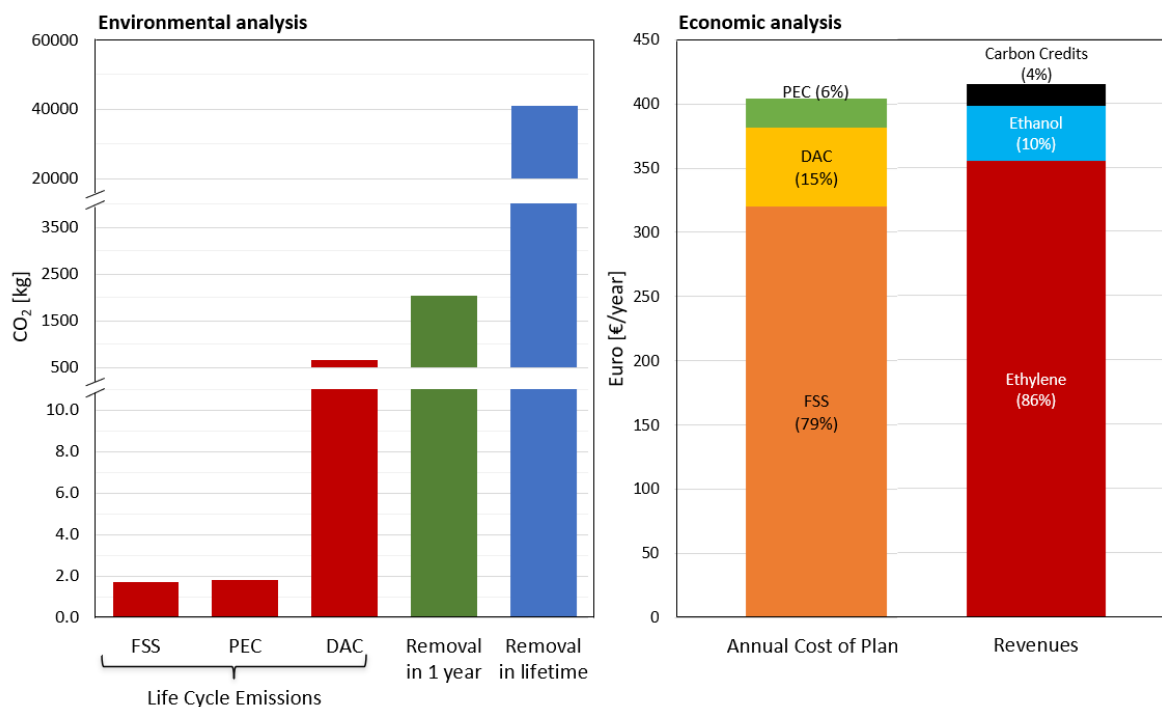
Heat Powered Cycles
Conference 2023
Edinburgh
Heat in the new energy system

3rd to 6th of September 2023
The University of Edinburgh, Scotland

Fig. 2 – Results from the pilot plant to produce 1 kg/day of ethylene and 0.2 kg/day of by-product ethanol.

If the objectives of the project are met, a total life cycle emission of 0.66 ton of CO_2, sourced mainly by DAC emissions (99.4%). However, the CO_2 removed from atmosphere by the process is counterbalanced in less than 6 months of operation. After 20 years of lifetime, the CO_2 removed is more than 62 times greater than the amount emitted in a life cycle.

The highest costs involved in the process are related with the full spectrum solar, representing 79% of the plant total cost. For the current technology price [16], FSS costs surpass the total revenues, showing a necessity to reduce this price in half for a feasible process. This reduction can be achieved by buying down the technology specific cost or by reducing the area requirement of the FSS. In which, the area is a consequence of the individual process efficiencies and the energy conversion in the FSS. Therefore, by tuning the energy efficiency of the process, the calculations showed that the pilot-plant can be economically balanced while having a great carbon-negative potential.

Conclusions

The SolDAC project has an ambitious objective to prove a carbon neutral production of Ethylene by removing CO_2 from air. The preliminary results obtained from the mass and energy balance shows the possibility to go beyond carbon neutrality and achieve a carbon-negative process, with 9 % of the CO_2 captured being used for geological storage. Coupling a Direct Air Capture unit to the Photo-Electrical Chemical stack is a mandatory measure to produce ethylene from a non-fossil-fuel-derivative that is also zero-carbon emission. Finally, by using power obtained from an independent and renewable energy source, the project benefits from not adding pressure on the energy system while relying in a replicable setting of energy production (solar energy). Overall, the project shows promising results to be a pioneer in producing Ethylene with 100% renewable route, that is energetically sufficient and modular carbon neutral, and it is replicable in a wide range of locations. The SolDAC project aims to reinvent the Ethylene industry by replacing the current carbon-positive routes.

Acknowledgments

References:

[1]   P. De Luna, C. Hahn, D. Higgins, S. A. Jaffer, T. F. Jaramillo, and E. H. Sargent, "What would it take for renewably powered electrosynthesis to displace petrochemical processes?," *Science*, vol. 364, no. 6438. American Association for the Advancement of Science, 2019. doi: 10.1126/science.aav3506.

[2]   G. Zhang, Z. J. Zhao, D. Cheng, H. Li, J. Yu, Q. Wang, H. Gao, J. Guo, H. Wang, G. A. Ozin, T. Wang, J. Gong. "Efficient CO2 electroreduction on facet-selective copper films with high conversion rate.", *Nature communications*, vol. 12, no. 5745, 2021, doi: 10.1038/s41467-021-26053-w

[3]   W. Ju, A. Bagger, G.P. Hao, A. S. Varela, I. Sinev, V. Bon, B. R. Cuenya, S. Kaskel, J. Rossmeisl, P. Strasser, "Understanding activity and selectivity of metal-nitrogen-doped carbon catalysts for electrochemical reduction of CO2", *Nature communications*, vol. 8, no. 944, 2017, doi: 10.1038/s41467-017-01035-z.

[4]   G. Huang, K. Wang, and C. N. Markides, "Efficiency limits of concentrating spectral-splitting hybrid photovoltaic-thermal (PV-T) solar collectors and systems," *Light Sci. Appl.*, vol. 10, no. 1, Dec. 2021, doi: 10.1038/s41377-021-00465-1.

[5]   C. Lamnatou, R. Vaillon, S. Parola, and D. Chemisana, "Photovoltaic/thermal systems based on concentrating and non-concentrating technologies: Working fluids at low, medium and high temperatures," *Renewable and Sustainable Energy Reviews*, vol. 137. Elsevier Ltd, Mar. 01, 2021. doi: 10.1016/j.rser.2020.110625.

[6]   G. Santori, C. Charalambous, M. C. Ferrari, and S. Brandani, "Adsorption artificial tree for atmospheric carbon dioxide capture, purification and compression," *Energy*, vol. 162, pp. 1158–1168, Nov. 2018, doi: 10.1016/j.energy.2018.08.090.

[7]   C. Beuttler, L. Charles, and J. Wurzbacher, "The Role of Direct Air Capture in Mitigation of Anthropogenic Greenhouse Gas Emissions," *Front. Clim.*, vol. 1, pp. 1–7, 2019, doi: 10.3389/fclim.2019.00010.

[8]   K. Madhu, S. Pauliuk, S. Dhathri, and F. Creutzig, "Understanding environmental trade-offs and resource demand of direct air capture technologies through comparative life-cycle assessment," *Nat. Energy*, vol. 6, no. 11, pp. 1035–1044, Nov. 2021, doi: 10.1038/s41560-021-00922-6.

[9]   D. W. Keith, G. Holmes, D. St. Angelo, K. Heidel, "A Process for Capturing CO2 from the Atmosphere", *Joule*, vol. 2, no. 8, pp. 1573–1594, 2018, doi: 10.1016/j.joule.2018.05.006.

[10] S. Nitopi, E. Bertheussen, S. B. Scott, X. Liu, A. K. Engstfeld, S. Horch, B. Seger, I. E. L. Stephens, K. Chan, C. Hahn, J. K. Nørskov, T. F. Jaramillo, I. Chorkendorff "Progress and perspectives of electrochemical CO2 reduction on copper in aqueous electrolyte", *Chemical reviews*, vol. 119, no. 12, pp. 7610-7672, 2019, doi: 10.1021/acs.chemrev.8b00705

[11] T. T. H. Hoang, S. Verma, S. Ma, T. T. Fister, J. Timoshenko, A. I. Frenkel, P. J. A. Kenis, A. A. Gewirth, "Nanoporous copper–silver alloys by additive-controlled electrodeposition for the selective electroreduction of CO2 to ethylene and ethanol". *Journal of the American Chemical Society*, vol. 140, no. 17, pp. 5791-5797, 2018, doi: 10.1021/jacs.8b01868.

[12] M. Sassenburg, R. de Rooij, N. T. Nesbitt, R. Kas, S. Chandrashekar, N. J. Firet, K. Yang, K. Liu, M. A. Blommaert, M. Kolen, D. Ripepi, W. A. Smith, T. Burdyny. "Characterizing CO2 Reduction Catalysts on Gas Diffusion Electrodes: Comparing Activity, Selectivity, and Stability of Transition Metal Catalysts", *ACS Applied Energy Materials*, vol. 5, no. 5, pp. 5983-5994, 2022, doi: 10.1021/acsaem.2c00160.

[13] T. Terlouw, K. Treyer, C. Bauer, M. Mazzotti, " Life Cycle Assessment of Direct Air Carbon Capture and Storage with Low-Carbon Energy Sources", *Environmental Science & Technology*, vol. 55, no. 16, pp. 11397-11411, 2021, doi: 10.1021/acs.est.1c03263.

[14] H. H. Khoo, I. Halim, A. D. Handoko, "LCA of electrochemical reduction of CO2 to ethylene", *Journal of CO2 Utilization*, vol. 41, pp. 101229, 2020, doi: 10.1016/j.jcou.2020.101229.

[15] Y. Hang, K. Balkoski, P. Meduri, "Life Cycle Analysis of Linear Fresnel Solar Power Technology." *Proceedings of the ASME 2013 Power Conference. Volume 2: Reliability, Availability and Maintainability (RAM)*, pp. POWER2013-98147, Boston, Massachusetts, USA. July 29–August 1, 2013. V002T09A007. https://doi.org/10.1115/POWER2013-98147

[16] O. Z. Sharaf, M. F. Orhan, "Concentrated photovoltaic thermal (CPVT) solar collector systems: Part II – Implemented systems, performance assessment, and future directions", *Renewable and Sustainable Energy Reviews*, vol. 50, pp. 1566-1633, 2015, doi: 10.1016/j.rser.2014.07.215.

Optimization of thermochemical heat storage systems by controlling operating parameters and using two reactors

Dongyu Meng[1,*], **Abdalqader Ahmad**[1,*], **Yulong Ding**[1] **and Martin Freer**[2]

[1] Birmingham Centre for Energy Storage (BCES), School of Chemical Engineering, University of Birmingham, Birmingham, B15 2TT, United Kingdom

[2] School of Physics and Astronomy, University of Birmingham, Birmingham, B15 2TT, United Kingdom

*Corresponding author: dxm126@student.bham.ac.uk; A.Y.H.Ahmad@bham.ac.uk

Abstract

Direct CO_2 emissions from space heating and hot water production in buildings has been on a rising trend in recent decades. It is increasingly urgent to develop efficient and low-carbon heating technologies that can reduce energy consumption and shift the load to off-peak times. This work concerns thermochemical heat storage (TCHS), which has the potential to offer flexibility to bridge the energy supply and demand mismatches, and help with load shifting. One of the technical barriers for the use of TCHS is the variation of the outlet conditions for discharge process, which limits the implementation and competitiveness of the technology. Here we propose a new method to overcome the barrier. By using packed-bed based thermochemical reactors packed with silica gel, as an example, we use a Computational Fluid Dynamic (CFD) tool to understand the effectiveness of controlling and optimising the outlet conditions of the TCHS reactor. We demonstrated that, by optimizing the packed bed, a stable outlet temperature could be achieved. Furthermore, the whole TCHS performance could be enhanced, doubling the discharging power and prolonged discharge time by 4 times while keeping the same outlet temperature.

Keywords: Thermochemical heat storage, Silica-gel, Decarbonization, Optimization.

Introduction

Heating and cooling for residential, commercial, and industrial purposes accounts for a significant share of total final energy demand [1]. In the European Union, these systems are responsible for about half of the energy consumed by buildings and industries. In 2021, fossil fuels accounted for over 60% of the energy used for heating buildings, resulting in a new high of 2500 Mt of direct CO_2 emissions [2]. Hence, it is urgent to develop more efficient and low-carbon heating technologies that can reduce energy consumption and shift the load to off-peak times [3]. Many innovative approaches, such as solar thermal heat and heat pumps have been proposed for the provision of options for the load shifting and efficiency improvement of heating systems. However, many of these technologies are unable to overcome the scale of the unbalanced demand with supply.

Thermal Energy Storage (TES) provides a solution to address such a mismatch, which is particularly effective for balancing between energy demand and supply in heating and cooling systems. There are three main categories of TES technologies: sensible, latent and thermochemical. This work is concenred with thermochemical energy storage (TCES), which has the advantages of 5~10 times higher storage capacity [4] and negligibe heat loss during storage period. Such a technology, however, has several technical barriers such as varying outlet conditions, limiting the effectiveness of the technology and system efficiency. Research

efforts are therefore needed to develop new approaches for obtaining a more stable thermal output and a higher efficiency.

Several lab-scale testing rigs and prototypes have been reported in the literature [5–7], but the system efficiency and thermal power were very low. For example, a lab-scale thermochemical heat storage with about 1 kg strontium bromide hexahydrate ($SrBr_2 \cdot 6H_2O$) was established through an European project "thermal battery". The system achieved a thermal capacity of 65 kWh with an efficiency of 0.77 [8]. However, the thermal output power was unstable. Jaehnig et al. [9] tested a closed system containing ~200 kg of silica gel as part of the Modestore project. Their experimental results showed that the system could provide a maximum output heating power of 400 W and achieve a temperature lift of only 5°C during discharge process. The AEE-Institute for Sustainable Technologies in Austria developed a closed and integrated sorption heat storage system for a single-family house [10]. Their experimental results showed that the storage density was much smaller than both theoretical one and that measured one under the laboratory conditions. Zongdag et al. [11] built an open system based laboratory prototype containing 17 dm^3 of Magnesium chloride ($MgCl_2 \cdot 6H_2O$) for space heating. The system generated a maximum thermal power of 150 W with only 50 W transferred to the load. The low heat transfer might be due to large heat losses of the system. An open sorption system designed by Zettl et al. [12] consisted of a rotating drum reactor filled with 50-53 kg zeolites. The system showed an energy density of 0.55-0.53 GJ/m^3 only when the desorption temperature was higher than 230°C with very low initial water content in the material.

Two major observations can be drawn from the above on thermochemical heat storage systems: first, the present thermochemical energy storage systems have shown low efficiencies compared to the theoretical one; second, very few studies were found on obtaining a stable thermal output. Here we report our work on controlling and optimising the outlet conditions of a TCHS reactor. A CFD modelling was conducted using COMSOL Multiphysics v6.0 environment. The system was optimized , and we show that a stable outlet temperature could be achieved. Also, we showed that, the whole TCHS performance could be enhanced, e.g. enhanced discharging power and prolonged discharge time while maintaining the same outlet temperature.

System description

Figure 1 and **Table 1** depicts the system diagram and provides process details for controlling operation parameter of a single reactor and using two reactors. The first objective of this paer, controlling the operation parameters of a reactor packed with 0.8 kg silica gel. The system was running in two modes: (a) charging mode, where the inlet air was heated up to 130°C and passed through the reactor to dehydrate the materials; (b) discharging mode, where the air flows through a humidifier and carries moisture to the reactor for hydration; heat released during this process which can be used for heating applications. Thermochemical materials, such as silica gel, exhibit a peculiar behaviour during discharge process. Initially, the outflow temperature increases sharply before eventually decreasing. However, a more stable output temperature is desirable for practical applications. In the proposed system, if the temperature drops below the desired setting (in our case, 40°C), the inlet relative humidity (RH) is increased or decreasing the flowrate (V) to maintain the outflow temperature.

To investigate the effects of different control strategies on the output temperatures during discharge, we simultaneously studied the following five approaches:

a) Constant_RH_V: Constant inlet relative humidity of 80% and flowrate of 33 LPM.

b) Control_RH: The inlet flow rate held constant at 3 m³/h while inlet relative humidity varies from 20% to 80%.

c) Control_V: Constant relative humidity at 80%, while flow rate varies from 25 LPM to 87 LPM.

d) Control_RH_V: Firstly, the inlet flow rate held constant at 50 LPM while inlet relative humidity varies from 20% to 80% for a certain time , then, gradually reducing the flowrate (minimum flowrate of 25 LPM).

e) Control_V_RH: Firstly, keeping the relative humidity constant at 80%, while inlet flow rate varies from 25 LPM to 87 LPM for a certain time, then, gradually increasing the relative humidity (to a maximum value of 95%).

The second objective of this paper is using two reactors for optimization, the reactors can be charged or discharged in series or parallel, which controls the flowrate through the reactors. In the proposed cases, during discharge, reactor 1 can be operated first. When the outflow temperature drops below 40℃, the exit air can be introduced to the reactor 2 to continue the discharging process. Using this control strategy, the mass ratio in both reactors can be optimized to achieve a maximum adsorption heat. In this case study, the total mass of materials in 2 reactors was 1.6 kg. The diameters of both reactors were the same while the mass ratio was varied from the heights.
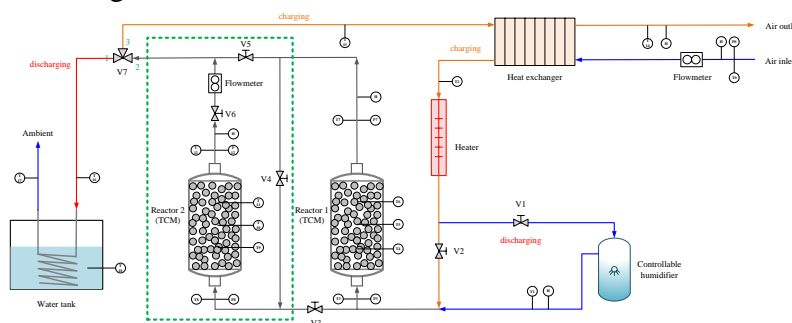
Figure 1 System diagram and operation modes by cotrolling inlet parameters and using two reactors.

Table 1 The operation modes for controlling inlet parameters and using two reactors.

Controlling inlet parameters (only reactor 1, reactor 2 in green box is not applicable)						
Valves	V1	V2	V3	V4	V5	V6	V7
Charging	×	√	×	n/a	n/a	n/a	2-3
Discharging	√	×	×	n/a	n/a	n/a	2-1
Using two reactors						
Valves	V1	V2	V3	V4	V5	V6	V7
Charging	×	√	×	√	×	√	2-3
Discharging	√	×	×	T7>40℃, × T7<40℃, √	T7>40℃, √ T7<40℃, ×	T7>40℃, × T7<40℃, √	2-1

Energy conversion and sorption equilibrium

This section presents the energy balance of the system and sorption equilibrium of silica gel. The adsorption heat Q_{ads} for discharging is calculated by

$$Q_{ads} = \int_0^t (\dot{m}_{out}h_{out} - \dot{m}_{in}h_{out})dt \qquad (1)$$

The adsorption rate of packed bed is given by the linear driving force (LDF), expressed as a function of time [13,14]

$$\frac{dw}{dt} = K(w_e - w) \tag{2}$$

where w is the vapor amount absorbed by the absorbents and w_e is the vapor amount absorbed under equilibrium conditions. K is the overall mass transfer coefficient that is calculated by

$$K = \frac{15 D_{so} \, exp(-\frac{E_a}{RT})}{r_p^2} \tag{3}$$

where r_p is particle radius, D_{so} is the pre-exponential constant, E_a is the activation energy and R refers to the universal gas constant [14].

The equilibrium water concentration w_e is calculated using Temperature-Dependent Toth isotherm [14]. The fitted Toth parameters are given in **Table 2**.

$$w_e = \frac{aP_w}{[1 + (bP_w)^n]^{1/n}} \tag{4a}$$

$$a = a_0 \, exp(E/T) \tag{4b}$$

$$b = b_0 \, exp(E/T) \tag{4c}$$

$$n = n_0 + c/T \tag{4d}$$

P_w means the partial pressure of water vapor in the airflow.

The required input parameters to solve the above equations in Comsol model are given in **Table 3**. The model geometry has a cylindrical shape with inlet and outlet ports as shown in the left side of **Figure 2**. The reactor is fully insulated and three thermocouples have fitted in the centre of the reactor at different locations to monitor the temperature.
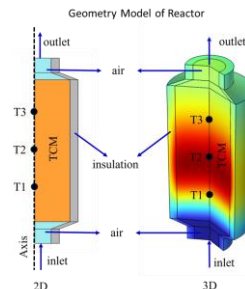
Figure 2 Single reactor geometry of COMSOL modeling.

Table 2 Temperature-dependent Toth isotherm parameters for water vapor on silica gel [14,15].

Parameter	Value
a_0 (mol/kg Pa)	0.1767
b_0 (1/Pa)	2.78E-8
n_0	-0.00119
c (K)	22.13
E (K)	1093

Table 3 Input parameters for the numerical model [13,14,16].

Parameters	Value
Average particle radius (r_p)	1.5 mm
Bed height (L)	200 mm
Bed diameter	86 mm
Activation energy (E_a)	4.2E4 J/mol
Gas constant (R)	8.314 J/mol/K
Pre-exponential term (D_{so})	2.54E-4 m^2/s

Discussion and Results

Figure 3 depicts a temperature contour during discharging in CFD modelling and reactor temperature profiles. The moist air at room temperature flows from the bottom to the top of reactor, heat released during adsorption process and then carried out by air flow for the application. The materials hydrated layer by layer, and the temperature first increases then decreases with absorbing more moisture.
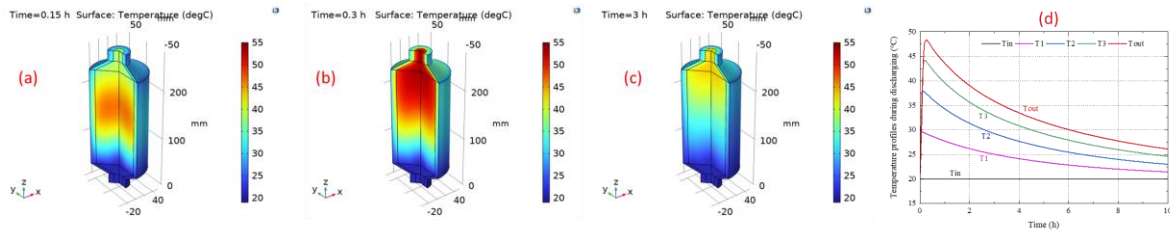
Figure 3 Temperature contours at (a) 0.15 hours, (b) 0.3 hours and (c) 3 hours of discharge; (d) temperature profiles of reactor at discharge process.

Figure 4 shows the reactor outlet temperature and thermal power during discharging under various control strategies. By controlling the inlet relative humidity and flowrate, the system shows more stable output temperatures and higher than 40°C for longer time though the thermal power reduce. For instance, with a constant relative humidity and flowrate (case a), the outflow temperature drops sharply lower than 40°C after 1.75 hours that can not reach the target temperature for applications. However, by adopting control strategies (b) and (c), the output temperature remains stable at 40°C for about 4 hours. Moreover, by applying control strategies (d) and (e), the output temperature remains stable at 40°C for more than 6~7.6 hours. The discharge period extends more than 4 times compared to the constant inlet conditions, regardless themal power is low during extended period. Thus, the total adsorption heat at acceptable temperature, as shown in **Figure 5**, is increased of 88% to 174% with controlling of inlet relative humidity and flowrate leading to increase the total system effeciency.
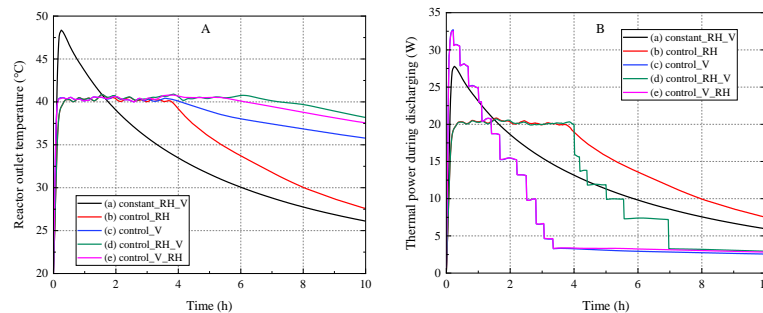
Figure 4 (A) Reactor outlet temperatures and (B) thermal power of discharging under various controlling strategies.
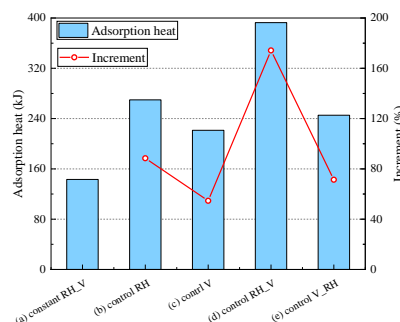
Figure 5 Usable adsorption heat under various control strategies.

By using two reactors, **Figure 6** illustrates the temperature profiles of the reactor outlet and usable adsorption heat under various mass ratios during discharging. Using double reactors with any mass ratio extends the discharge period within the required temperature compared to a single long reactor scenario. For example, while the discharge period with a single reactor is approximately 5.4 hours, it is extended by 22% when using double reactors with mass ratios of (R1:R2) 70%:30%. Because the inlet temperature of reactor 2 is higher than ambient temperature which can activcate the adsorption process of silica gel. Therefore, the adsorption heat of double reactors with any mass ratio is higher than that of a single reactor. Moreover, it foud that the optimum mass ratio of the double reactors system is 40%:60%, that increases the adsorption heat by approximately 14%. This is because of using double reactors can reduce the pressure drop and improves the heat and mass transfer in the system.
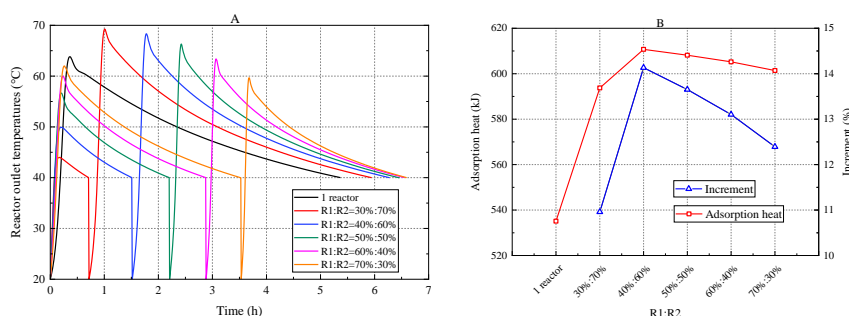
Figure 6 (A) Reactor outflow temperature profiles and (B) usable adsorption heat for various mass ratios durging discharging.

Summary/Conclusions

This study focuses on thermochemical heat storage (TCHS) for heating applications. One of the technical barriers for TCHS is the variability of outlet conditions during the discharge process. To overcome this, we proposed a new method of controlling the inlet parameters so that we can control the reaction process, subsequently controlling the outlet conditions. The results show that by optimizing the inlet relative humidity and flowrate, rather than using constant conditions, the discharge period within the desired temperature can be extended by up to four times with a 174% increase in the usable adsorption heat. Additionally, optimizing the mass ratios of double short reactors, rather than using a single long reactor, can also extend the discharge period and increase the released heat. Compared to a single reactor, using double reactors results in 14% more heat released during discharging with optimum mass ratio of 40%:60%.

Acknowledgments

References:

[1] IRENA (2021), World Energy Transitions Outlook: 1.5°C Pathway, International Renewable Energy Agency, Abu Dhabi. n.d.

[2] Heating – Analysis - IEA n.d. https://www.iea.org/reports/heating (accessed April 20, 2023).

[3] Ahmad, A., Ding., Y., "A thermochemical energy storage based cooling and heating system: Modelling, experimental validation and lab-scale demonstration", Energy Conversion and Management, 2021.

[4] Jarimi, H., Aydin, D., Yanan, Z., Ozankaya, G., Chen, X., Riffat, S., "Review on the recent progress of thermochemical materials and processes for solar thermal energy storage and industrial waste heat recovery", International Journal of Low-Carbon Technologies, 2019.

[5] Mauran, S., Lahmidi, H., Goetz, V., "Solar heating and cooling by a thermochemical process. First experiments of a prototype storing 60kWh by a solid/gas reaction", "Solar Energy", 2008.

[6] Casey, S.P., Aydin, D., Riffat, S., Elvins, J., "Salt impregnated desiccant matrices for 'open' thermochemical energy storage—Hygrothermal cyclic behaviour and energetic analysis by physical experimentation", Energy and Buildings, 2015.

[7] Michel, B., Mazet, N., Neveu, P., "Experimental investigation of an innovative thermochemical process operating with a hydrate salt and moist air for thermal storage of solar energy: Global performance", Applied Energy, 2014.

[8] Fopah-Lele, A., Rohde, C., Neumann, K., Tietjen, T., Rönnebeck, T., N'Tsoukpoe, K.E., et al, "Lab-scale experiment of a closed thermochemical heat storage system including honeycomb heat exchanger", Energy, 2016.

[9] Jaehnig, D., Hausner, R., Wagner, W., Isaksson, C., "Thermo-chemical storage for solar space heating in a single-family house".

[10] Bales, C., Gantenbein, P., Jaenig, D., Essen, M., Weber, R., "Laboratory tests of chemical reactions and prototype sorption storage units. A Report of IEA Solar Heating and Cooling Programme - Task 32 Advanced Storage Concepts for Solar and Low Energy Buildings".

[11] Zondag, H., Kikkert, B., Smeding, S., Boer, R., Bakker, M., "Prototype thermochemical heat storage with open reactor system", Applied Energy, 2013.

[12] Zettl, B., Englmair, G., Steinmaurer, G., "Development of a revolving drum reactor for open-sorption heat storage processes", Applied Thermal Engineering, 2014.

[13] Deshmukh, H., Maiya, M.P., Srinivasa Murthy, S.,"Study of sorption based energy storage system with silica gel for heating application", Applied Thermal Engineering, 2017.

[14] Helaly, H.O., Awad, M.M., El-Sharkawy II, Hamed, A.M., "Theoretical and experimental investigation of the performance of adsorption heat storage system", Applied Thermal Engineering, 2019.

[15] Wang, Y., LeVan, M.D., "Adsorption Equilibrium of Carbon Dioxide and Water Vapor on Zeolites 5A and 13X and Silica Gel: Pure Components", J Chem Eng Data 2009.

[16] Chua, H.T., Ng, K.C., Chakraborty, A., Oo, N.M., Othman, M.A., "Adsorption Characteristics of Silica Gel + Water Systems", J Chem Eng Data, 2002.

Dynamic use of SOFC for flexible heat & electricity supply in industrial processes

Michel van der Pal[1], Robert de Smidt[1], Martien Koppes[1]

[1]TNO, Energy and Material Transition Unit, Petten, The Netherlands

Summary

This paper investigates the dynamic behavior of a BlueGen BG15 solid-oxide fuel cell (SOFC) using natural gas or mixtures of natural gas and hydrogen as fuel. The measurements shows good repeatability of full-load and part-load operation. Rapid ramp up/down from minimum to maximum load (and vice versa), show this can be achieved within 30 minutes without considerable impact on its performance. These results make SOFC an interesting option as a combined heat and power unit for industrial processes.

Introduction

Currently the majority – approximately 80% - of energy used in industry is in the form of heat. This heat is often generated from natural gas. With increasing amounts of renewable electricity from wind and solar, a shift can be expected towards electrification of processes in periods of low electricity prices. However, as most industrial processes are designed to operate 24/7, a solution must be found during periods of low energy supply from renewables. Solid-oxide fuel cells (SOFC) can form an attractive solution as it can efficiently generate electricity whilst the excess heat can generate steam to drive industrial processes. This, however, requires dynamic use of the SOFC. In this paper a commercially available SOFC unit is tested under dynamic conditions where its response time to go from minimum to maximum load and its performance during this transition is determined together with its steady-state performance over a range of intermediate conditions. The current data is based on natural gas as fuel as well as hydrogen-natural gas mixtures with up to 40% hydrogen (v/v). Measurements using mixtures with higher hydrogen fractions and pure hydrogen will be done in the near future.

Experimental setup

A BlueGen BG15 is used as SOFC unit. This unit consists of a fuel cell with a maximum power output of 1500W electricity, a heat exchanger to provide hot water and a steam reformer to allow operation with natural gas. Various parameters including electric power output, fuel and steam use are monitored and made accessible through a Grafana web application. A Julabo thermostatic bath is connected to the BlueGen unit to measure the amount of heat extracted at 20°C. Using a mass flow controller the amount of hydrogen can be controlled as a fraction of natural gas used. The setup is schematically shown in Fig 1.

The experiments consisted of steady-state measurements where the power output of the unit was changed in 250W steps between 1500 and 500W over a period of nine hours followed by 15 hours of steady operation at set power level. For the dynamic measurements, the power output setting was changed between minimum and maximum setting over a 15-minute interval, which the unit follows

as quickly as possible. This change was followed by a near 24 hour period of steady-state operation – resulting in one setting measured each day.
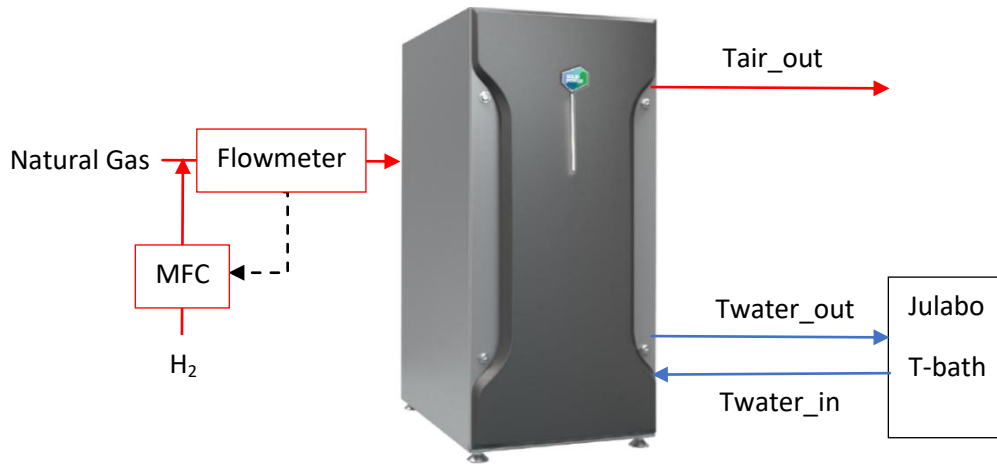
Figure 1: Experimental setup containing BlueGen BG15 unit where a mass flow controller (MFC) controls fraction of hydrogen added to natural gas to create desired mixture(s).

Results

Fig. 2 shows the two measurements of thermal and electric power output and the fractions energy (electricity, heat and lost/unaccounted) as a function of time for the increase from 500W part-load operation to 1500W full load operation in 250W steps. It can be observed that the differences between the two sets of measurements are minor with only some variations in thermal efficiency and energy lost/unaccounted at the beginning of each measurement. The overall efficiency of the system is up to 90%. The increase in energy lost/unaccounted at the 1500W setpoint is due to insufficient cooling power of the Julabo thermostatic bath resulting in higher water temperatures.
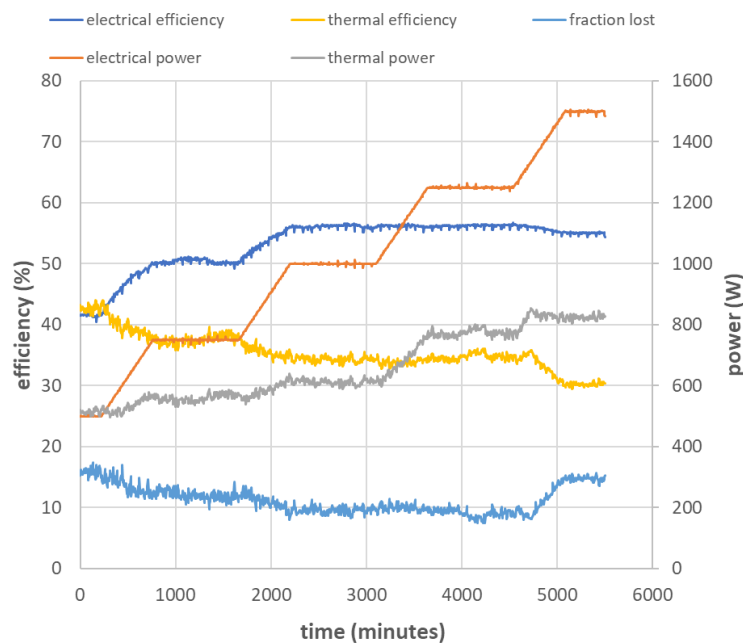
Figure 2. Electrical and thermal output and efficiencies of BG15

Fig. 3 shows the repeated change between 500W and 1500W load. The three colors (red, green and blue) show three separate measurements with otherwise identical conditions. The measurements show good reproducibility. The fraction lost drops to nearly zero during the change from maximum to minimum load. This is due to residual heat taken away whilst the unit is already operating at lower power settings. Similar to Fig. 2, the electrical efficiency is reduced on minimum loading operation.
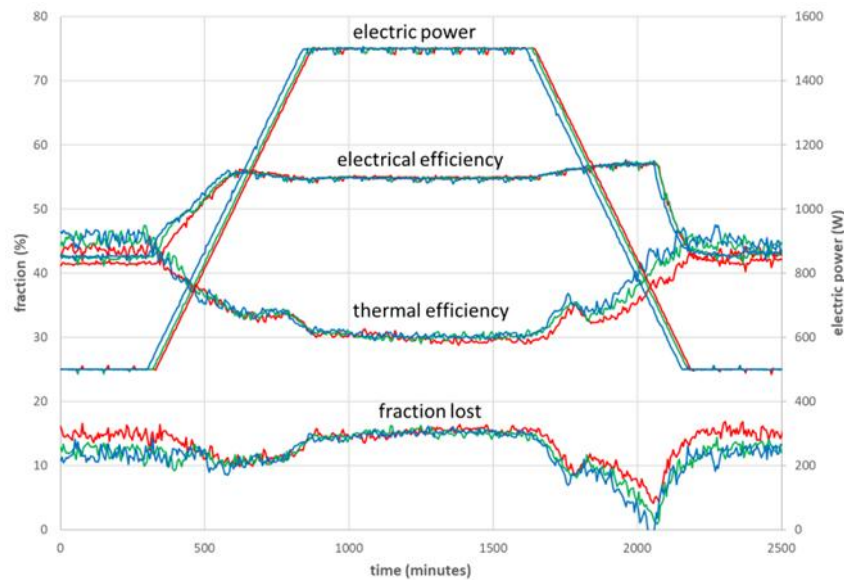
Figure 3. Repeated change from minimum to maximum load

Fig. 4 shows the relation between the thermal and electric power for all measurements conducted with gas mixtures varying from 100% natural gas to 60% natural gas with 40% hydrogen (v/v). The conditions at 1500W have been omitted due to the cooling limits of the thermostatic bath. The results show with increasing amount of hydrogen, increasing amounts of heat are extracted. This is possibly related to a reduced need for heat to reform the natural gas. The thermal output is less strongly correlated to the electric power for the lower range (electric power <1000W) compared to higher electric outputs.

Heat Powered Cycles Conference 2023
Edinburgh

Heat in the new energy system
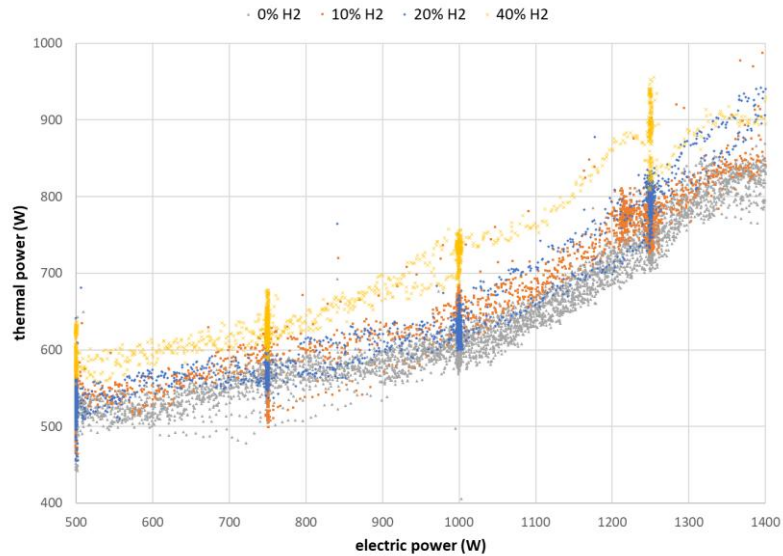
Figure 4. Thermal power as function of electric power

Fig. 5 shows the dynamic behavior of the BG15 (100% natural gas) when rapidly changing the power setting from 1500W to 500W and back. From this figure it can be observed that power output change takes about 30 minutes to increase from 500W to 1500W and about 15 minutes to decrease from 1500W to 500W. The electrical efficiency shows no extreme variations and stays between 50 and 60%. The thermal efficiency calculation suffers again from the lack of cooling power as part of the heat extracted is due to cooling of the bath rather than additional heat from the exhaust air.
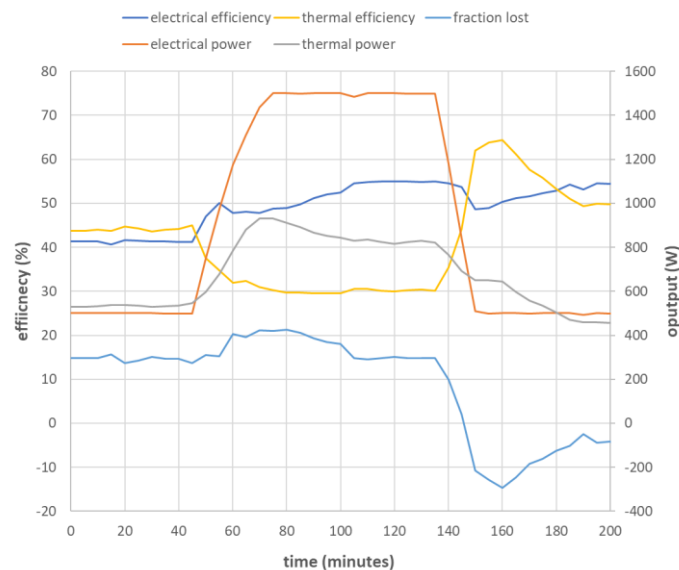
Figure 5. Dynamic behavior of BG15: power output and efficiencies as a function of time.

Discussion and conclusions

The results so far show good repeatability of performance using 100% natural gas. Increasing the fraction hydrogen from 0% to 10%, 20% and 40%, results in an increase in the available heat. This is possibly due to the reduced heat demand for the conversion of natural gas to hydrogen.

The unit is also capable of changing from minimum to maximum load (500W to 1500W electrical output) within half an hour, allowing sufficient flexibility to follow changes in sustainable electricity production from wind and solar and thereby able to take advantage of the variation in electricity prices. The decrease in electric efficiency at minimum load is acceptable as this setting will be used for periods of low electricity prices.

The feasibility of the BG15 to operate with different gas mixtures, achieve high efficiency (>50%) and to quickly change power setting (approximately half an hour), makes SOFC a future proof option for application as Combined Heat and Power unit for industrial applications that require 24/7 operation. Using SOFC technology, the electrical output can be adjusted in accordance to electricity demand and supply, both on-site as well as on the electricity market. When operating using 100% hydrogen or by using CO_2 capture, the carbon footprint of the industrial process can be minimized without being dependent on fluctuating electricity supply from renewable sources.

For determining the business case, a more detailed cost analysis is required. Not only CAPEX and OPEX calculations and optimization, including dynamic electricity prices, is required to determine the economic feasibility. This analysis should also include a comparison with other technologies capable of shifting electricity supply and/or demand such as large (battery) energy storage to determine whether SOFC is an attractive technology for a sustainable industry.

Heat Powered Cycles Conference 2023
Edinburgh
Heat in the new energy system

A standard characterisation method using thermal response for the dynamics of temperature swing adsorption-packed beds

Shihab AL-Hasni[1,2*] and Giulio Santori[1]

[1]The University of Edinburgh, School of Engineering, Institute for Materials and Processes, Sanderson Building, The King's Buildings, Mayfield Road, EH9 3BF, Edinburgh, Scotland, UK

[2]Department of Engineering, The University of Technology and Applied Sciences, Suhar 311, Oman

[*]Corresponding author: email address (s.n.s.al-hasni@sms.ed.ac.uk)

Abstract

This study proposes an experimental protocol to identify the suitability of packed adsorbers in temperature swing adsorption processes. A set of experimental steps allow the identification of the dynamics of the heat exchanger (HEX) with and without an adsorption material and the consequent calculation of typical adsorber parameters that can be used to rank the quality of an adsorber design before its testing within the temperature swing adsorption process. The experiments are based on the theory of identification of dynamic systems and involve the utilisation of step changes in the inlet temperature. The resulting time constants for the HEX with and without adsorption material reveal the influence of the thermal mass of the heat exchanger on the whole adsorber dynamics and the influence that the addition of the adsorbent has on it.

Keywords: Adsorption, Sorption, Temperature swing adsorption, System dynamics.

Nomenclature	
a_f	The angle of fin [°]
B_H	Core height [m]
Bt	Core thickness [m]
B_w	Core width [m]
F_h	Fins height [m]
F_l	fin length [m]
F_p	Fin pitch [m]
F_t	Fins thickness [m]
F_w	Fin width [m]
N_{ct}	Number of coolant tubes in one row
N_f	number of fins per meter
N_p	Number of profiles
N_r	Number of rows of tubes in core depth dimension [-]
R_f	Fin end radius [m]
R_t	Coolant tube end radius [m]
Y_{cl}	Coolant tube cross-section length [m]
Y_{cw}	Coolant tube cross-section width [m]
Y_l	Coolant tube length [m]
Y_p	Coolant tube pitch [m]
Y_t	Coolant tube thickness
η_a	Fins efficiency - air side

Introduction

Prior research examining the impact of grain size on the overall efficacy of adsorption chillers has focused mainly on improving specific cooling power while overlooking the influence of the adsorber design [1]. An investigation of the thermodynamic properties of

1

adsorption heat exchangers used experimental measurements of thermal masses as design metrics, omitting to isolate the contribution of the adsorption material from the contribution of the heat exchanger in the overall thermal responsiveness of the adsorber [2]. This study offers the advantage of conducting a step-by-step replicable analysis of any variety or dimension of heat exchanger with a control volume, thereby expanding the range of potential applications. The present investigation puts forward an approach for assessing the dynamics of the adsorber, both in the absence of an adsorption material, with an adsorption material present but no adsorption taking place. The analysis uses an overall temperature of the adsorber, facilitating the description of the adsorber as a linear dynamic system when no adsorption takes place and the understanding of the non-linear effects when adsorption is present. Following the methodology will help classify adsorber designs, driving towards the most efficient, reducing the time and financial resources for the design and testing without the need to move to the test of the complete heat transformer. Here we show the application of the protocol to two packed bed adsorbers of different sizes to highlight how the results can change across the scales.

Methodology and system description

Calculation of relevant heat transfer areas

To achieve standardisation of heat transfer area calculations, we propose an analytical approach that has been extensively detailed in [3]. Using this approach, we have compiled a table summarising the relevant heat transfer areas (refer to Table 1) for the small heat exchanger illustrated in Figure 1.b. Note that this methodology can be replicated for any sized heat exchanger. Additionally, this study covers the heat transfer area of both headers and tubes. These areas play a pivotal role in the overall performance of the heat exchanger, as they are in direct contact with heat transfer fluid (HTF). Therefore, this section of the protocol is of utmost importance, as any inaccuracies in heat transfer area calculations can significantly affect the heat transfer coefficient. To initiate the calculations, we begin with the fin length. Further details on the geometrical aspects of the heat exchanger can be found in reference [3].

Fin length, F_l

$$F_l=\pi R_f+(F_h-2R_f)/\cos\alpha_f \tag{1}$$

Radiator core frontal area, $A_{fr,\,r}$

$$A_{fr,r}=B_H B_W \tag{2}$$

Coolant tube frontal area, $A_{fr,\,t}$

$$A_{fr,\,t}=Y_{CW}\,Y_l\,N_{CT} \tag{3}$$

Fin frontal heat transfer area, $A_{fr,\,f}$

$$A_{fr,\,f}=F_t\,F_l\,N_f\,Y_l\,N_p \tag{4}$$

Fin heat transfer area, A_f

$$A_f=2B_T\,F_l\,N_f\,Y_l\,N_p \tag{5}$$

Total heat transfer area on the air side, A_a

$$A_a=A_f+2N_{ct}\,Y_l\,N_r\,[(Y_{cl}-2R_t)+(2\pi R_t)] \tag{6}$$

2

Total heat transfer area on the coolant side, A_c

$$A_c = [2\pi(R_t - Y_t) + 2(Y_{cl} - 2R_t)] \, Y_1 \, N_{ct} \, N_r \tag{7}$$

Total air pass area, $A_{p,a}$

$$A_{p,a} = Af_{r,r} - Af_{r,f} - Af_{r,t} \tag{8}$$

Total coolant pass area, $A_{p,c}$

$$A_{p,c} = [\pi(R_t - Y_t)^2 + (Y_{cw} - 2Y_t)(Y_{cl} - 2R_t)] N_{ct} N_r \tag{9}$$

Table 1: Summary of the relevant heat transfer areas.

	Component	Symbol	Value in m^2
1	Fin Length	F_l	0.0090
2	Radiator core frontal area	$A_{fr,r}$	0.0028
3	Coolant tube frontal area	$A_{fr,t}$	0.0004
4	Fin frontal heat transfer area	$A_{fr,f}$	0.0001
5	Fin heat transfer area	A_f	0.0427
6	Total heat transfer area on the air side	A_a	0.0545
7	Total heat transfer area on the coolant side	A_c	0.0097
8	Total air pass area	$A_{p,a}$	0.0023
9	Total coolant pass area	$A_{p,c}$	0.0001
10	Total heat transfer area, including the headers and tubes	A_{total}	0.093

Description of the evaluated system

Initially, the weight of the heat exchangers (HEX) was recorded. This should be executed using both an empty HEX and one that has been filled with an adsorption material and water. The size of the HEX surface area is crucial in determining heat loss and thus should be calculated through the use of dimensional analysis of its constituent parts and with the assistance of 3D computer-aided design. The naked HEX (HEX without adsorption material) should be carefully installed within its clean vessel and cleaned using an alcohol solution. The same procedure should then be repeated with the HEX filled with the adsorption material. During each experiment, it is imperative to regulate and record the water flow rate. The connected thermal sensors will continuously monitor the inlet (T_{in}) and outlet (T_{out}) temperature change, and these data is then stored on a computer for subsequent analysis.
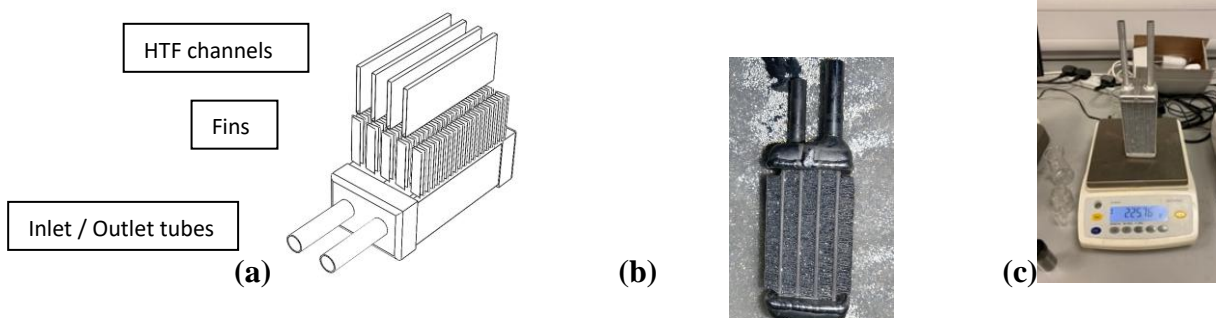
Figure 1: (a) Type of Aluminium heat exchangers tested in this study. The first on the right is the adsorber filled with Silca-Gel Siogel. (b): The small-scale heat exchanger (Hex1) has a heat transfer surface area of each heat exchanger of 0.093 m2 (47.10±0.01 g), and the (c) larger-scale heat exchanger (Hex2) has a heat transfer area of 0.494 m2 (225.76 ±0.01 g).

Table 2: Experimental settings

Equipment	Data	Value/Unit	Error	ref
Rotameters (Nixon, UK)	Water flow rate	0.4 L/minutes	2%	Experimental
T-type thermocouples (Omega UK)	Cooling tempreture	25 /°C	0.25 °C	Experimental
	Heating temperatures	40-50-60 /°C	0.25 °C	Experimental
Vacuum sensor (WIKA, UK)	Pressure level	- / kPa	0.01 kPa	Experimental

3

Balance (Adams, UK)	masses	-./ grams	0.01 grams	Experimental

Before starting any experimental study involving a Heat Exchanger (HEX), it is crucial to undertake a comprehensive cold (25°C) and hot (60°C)purging under a vacuum.
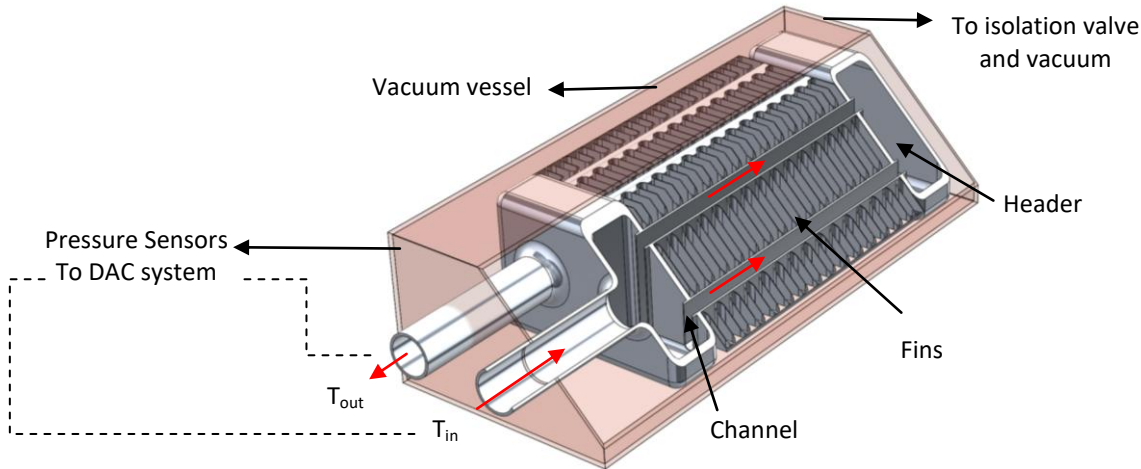
Figure 2: System description. Evaluated heat exchanger enclosed by an evacuated vessel

These purges involve the circulation of a Heat Transfer Fluid (HTF) throughout the HEX, with concurrent vacuum application to ensure the successful elimination of any trapped gases. Furthermore, the HEX is subjected to an evacuation process until no observable pressure increase is detected while also taking into account the initial outgassing before initiating performance testing. The first temperature swings have to be exclusive on the metal heat exchanger without adsorption material to distinguish the heating contributions. The water inlet temperature (Tin_{ads}) and the water outlet temperature ($Tout_{ads}$) are the values recorded by the data acquisition system (DAQ), as depicted in Figure 2.

Static and dynamic heat transfer quantities of a naked heat exchanger and packed bed

Steady-state tests can provide an initial set of quantities (static quantities) related to the heat transfer and heat capacity of the overall adsorber. The energy balance at a steady state is:

$$(\dot{m}\,c_p)_{water}(T_{out} - T_{in}) = (UA)_{Amb} \frac{(T_{in}-T_{amb})-(T_{out}-T_{amb})}{ln\left(\frac{T_{in}-T_{amb}}{T_{out}-T_{amb}}\right)} \qquad (10$$

From this, we obtain the following.

$$T_{out} = T_{amb} + (T_{in} - T_{amb})e^{\frac{(UA)_{Amb}}{(\dot{m}\,c_p)_{water}}} \qquad (11)$$

With the number of transfer units (NTU_{Amb}) of the heat exchanger with the surroundings: $NTU_{Amb} = \frac{(UA)_{Amb}}{(\dot{m}\,c_p)_{water}}$

The equation above can be rewritten as:

$$\frac{T_{out}-T_{amb}}{T_{in}-T_{amb}} = e^{NTU_{Amb}} \qquad (12)$$

where NTU is defined as the number of transfer units. NTU_{Amb} allows one to assess the quality of the insulation with the surroundings. Its value is usually small for systems operating under a vacuum.

To determine the parameters that affect the dynamic behaviour of the heat exchanger (dynamic quantities) and, consequently, the net heat to the naked heat exchanger, the following linear differential equation can be used.

$$\left(m\,c_p\right)_{HEX}\frac{dT_{HEX}}{dt} = (\dot{m}\,c_p)_{water}(T_{in} - T_{out}) - (UA)_{amb}(T_{hex} - T_{amb}) \qquad (13)$$

4

where the term *(m c_p)$_{HEX}$* is the heat capacity of the overall heat exchanger, including all its parts, such as water and any other subcomponent that might be heated due to contact with heated parts. By dividing the term $(\dot{m}\,c_p)_{water}$, Eq. (12) can also be written as follows:

$$\tau_{HEX}\frac{dT_{HEX\,(t)}}{dt} = (T_{in} - T_{out}) - NTU_{Amb}(T_{HEX} - T_{amb}) \qquad (14)$$

Where the variable T_{HEX} [K] is a time-dependent overall temperature of the heat exchanger, $(T_{in} - T_{out})_{exp}$ [K] is the time-dependent difference between the inlet and outlet temperature of the heat transfer fluid measured experimentally, τ_{HEX} is the ratio between the actual heat capacity of the heat exchanger *(mc$_p$)$_{HEX}$* and the heat capacity rate *(ṁc$_p$)$_{htf}$* of the heat transfer fluid and can be represented as follows:

$$\tau_{HEX} = \frac{(m\,c_p)_{HEX}}{(\dot{m}\,c_p)_{water}} \qquad (15)$$

Similarly, for the packed bed:

$$\tau_{dry-ads} = \frac{(m\,c_p)_{dry-ads}}{(\dot{m}\,c_p)_{htf}} \qquad (16)$$

where the variable $T_{dry\text{-}ads}$ [K] is the time-dependent overall temperature of the adsorber without adsorption (dry condition) and $(T_{in} - T_{out})_{exp}$ [K] is as in the previous experiment, the measured values of inlet and outlet temperature of the heat transfer fluid (water), $\tau_{dry\text{-}ads}$ is the ratio between the actual heat capacity of the dry adsorber *(mc$_p$)$_{dry\text{-}ads}$* and the heat capacity rate *(ṁc$_p$)$_{htf}$* of the heat transfer fluid (water). Both τ_{HEX} and $\tau_{dry-ads}$ are experimental parameters determined through regression of the results from temperature step experiments encompassing both transient and steady-state, with the values reported in Figure 3. Figure 3 presents a summary of the experimental results of temperature swings that were performed on two distinct sizes of the same type of heat exchanger (as shown in Figure 1). The smaller heat exchanger has a volume of 17.83 cm^3, while the larger heat exchanger has a volume of 83.3 cm^3. These graphs show the correlation between the definite integral [T$_{in}$ - T$_{out}$] over a specific time period [t$_0$-t$_{end}$] versus inlet temperature changes [ΔT [14.33°C - 33.10 ° C]]. To extract τ_{HEX} and $\tau_{ads-dry}$, the data were plotted using three distinct coordinates.

$$\tau_{HEX} = \frac{N_1}{\Delta T_{in,HEX,1}} = \frac{N_2}{\Delta T_{in,HEX,2}} = \frac{N_3}{\Delta T_{in,HEX,3}} \qquad (17)$$

Similarly,

$$\tau_{ads-dry} = \frac{N_1}{\Delta T_{in,ads,1}} = \frac{N_2}{\Delta T_{in,ads,2}} = \frac{N_3}{\Delta T_{in,ads,3}} \qquad (18)$$
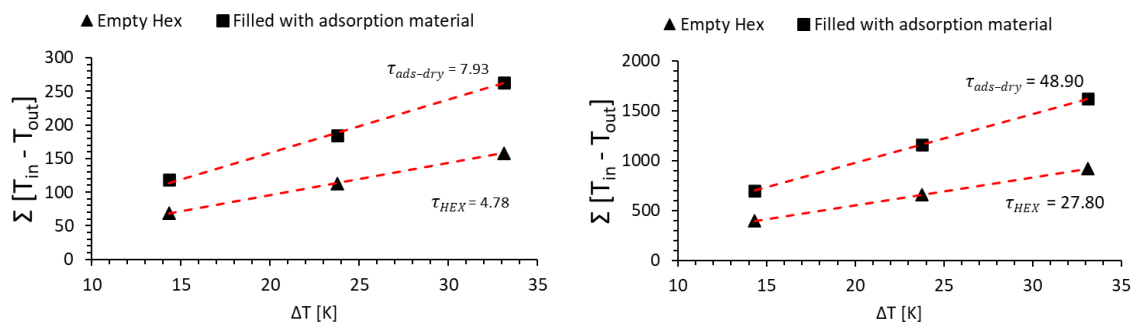
Figure 3:(a): small-scale heat exchanger (Hex1). (b): Larger-scale heat exchanger (Hex2).

5

Residence time and optimal flow rate

The residence time functions as a metric to quantify the duration for which a fluid is detained within a heat exchanger and can be represented as follows.

$$\tau_{res} = \frac{wate\ mass\ flow\ rate\ in\ kg/s}{mass\ of\ water\ in\ kg} \qquad (19)$$

Table 3 documents all time constants, including the dimensional time constant θ, which represents the ratio between the experimental time constant and the residence time of the heat transfer fluid in the heat exchanger.

$$\theta_{HEX} = \tau_{HEX}/\tau_{res} \qquad (20)$$

$$\theta_{dry-ads} = \tau_{dry-ads}/\tau_{res} \qquad (21)$$

Table 3: Summary of the time constants of the two different HEX sizes used in this study.

Contributor	Hex 1	Hex 2
Volume [cm3]	17.38	83.3
τ_{HEX} [s]	4.78	27.80
$\tau_{dry-ads}$ [s]	7.93	48.90
τ_{res} [s]	3.93	14.14
θ_{HEX} [−]	1.22	1.97
$\theta_{dry-ads}$ [−]	2.02	3.46

The experimental time constant ($\tau_{HEX}; \tau_{dry-ads}$) is a reflection of the performance of the real system and its response to the applied flow rate ($\dot{m}$) with a specific temperature difference(ΔT). The residence time represents the expected duration for the amount of water to circulate the heat exchanger based on its water volume inside. Establishing the ratio between the time constants is a useful tool that can be used to enhance the overall time response of a heat exchanger.

$$optimum\ flow\ rate\ =\ mass\ flow\ rate\ (actual)\ \theta \qquad (22)$$

Table 4 presents an overview of the optimal flow rates to enhance residence time in both the naked heat exchanger and the packed bed containing the adsorption material. From the experimental data, the overall heat transfer coefficient for the small-scale heat exchanger is 2.26 W m^2 K^{-1}, and the larger-scale exchanger has a U value of 1.21 W m^2 K^{-1}, which confirms that at least 82% extra mass flow rate is required for the larger heat exchanger as depicted in Table 3 and Table 4. The ratio of the experimental time constant and the theoretical residence time serve as a valuable metric to improve the heat transmission of the empty heat and the filled heat exchanger with adsorption material. This can help engineers size and operate properly in the early stages of commissioning the adsorption chiller.

Table 4: Optimal flow rate investigation

	Empty Hex [L/m]	Hex filled with Siogel [L/m]
Hex1-17.38[cm^3]	0.40	0.40
Hex1-optimum flow rate	0.49	0.80
Improvement required	18%	78%
Hex2-83.3[cm^3]	0.40	0.40
Hex2- optimum flow rate	0.79	1.39
Improvement required	82%	197%

Optimisation of a naked heat exchanger using CFD

The present study utilised Computational Fluid Dynamics (CFD) as a tool integrated into the Solidworks 3D CAD environment developed by Dassault Systemes, United States. Initially, a

6

small-scale heat exchanger with a volume of 17.38 cm^3 was measured using a vernier calliper, and a two-dimensional sketch was subsequently drawn in Solidworks. The final product was then constructed using three-dimensional features in Solidworks, as depicted in Figure 4. To begin the CFD studies on the heat exchanger, the flow simulation tool was activated. The analysis type selected was internal, which means that only the heat exchange within the heat exchanger was considered, and the outer wall condition was set to adiabatic, replicating the dry characterisation test experimental conditions. Furthermore, the selected liquid type was water, with an initial ambient temperature of 25 ° C. The initial metal temperature was also set at 25°C, and three different metal materials, namely aluminium, copper, and stainless steel, were examined.
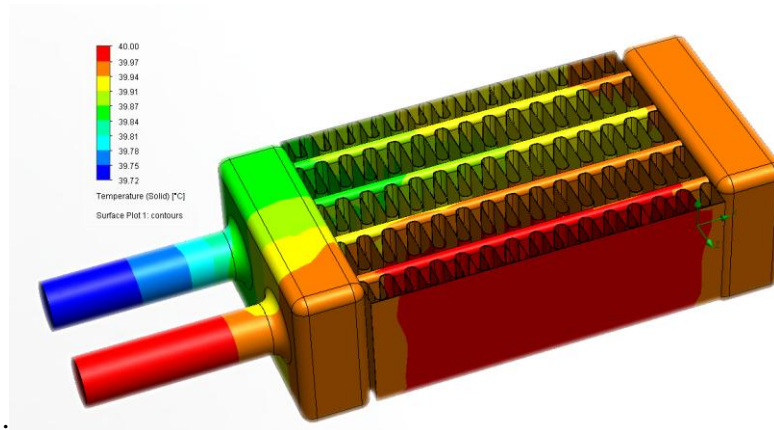
Figure 4:Tempreture gradient distribution of one of the solved cases by CFD. ΔT=15 °C, 0.4 L/m.

The temperature gradient of one of the cases solved in Figure 4 shows the effect of the hot water flow within the heat exchanger passing through its tubes, headers and channels to the outer skin of the heat exchanger. The tests were carried out on the basis of specific settings of mass flow rates with a specific temperature difference (T_{in}-T_{out}), similar to the experimental approach explained in an earlier section. Each heat response experiment from CFD was based on a temperature difference of 15°C; 25°C; and 35°C, as shown in Figure 5.a. The sensitivity or validation of the mesh results of the CFD was achieved on the basis of a close agreement on the time constant acquired experimentally and from the CFD study, as described in Figure 5.b.
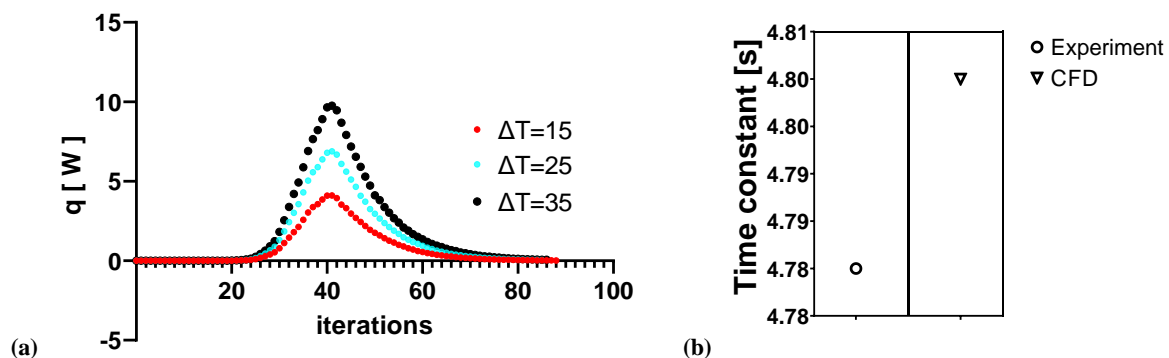
Figure 5: Validation of CFD results

The results presented in Table 4 indicate that the optimal theoretical flow rate of the small-scale heat exchanger with a volume of 17.38 cm^3 is 0.49 litres per minute. This finding is consistent with data obtained through computational fluid dynamics (CFD), which show a high degree of agreement with a flow rate of 0.5 litres per minute. Moreover, Figure 6 reveals

7

that the overall heat transfer coefficient (U value) reaches a plateau at this flow rate, with an average value of 2 W m^2 K^{-1}. The aforementioned U-value characterises the internal resistances of the heat exchanger up to the external wall in a vacuum environment devoid of air or water vapour on the outer side. Consequently, these results have enabled us to investigate the effects of employing alternative materials, such as copper and stainless steel, for the empty heat exchanger. While both materials are commonly employed, there is little or no information on the static characterisation of adsorption cooling applications under vacuum conditions in the absence of water.
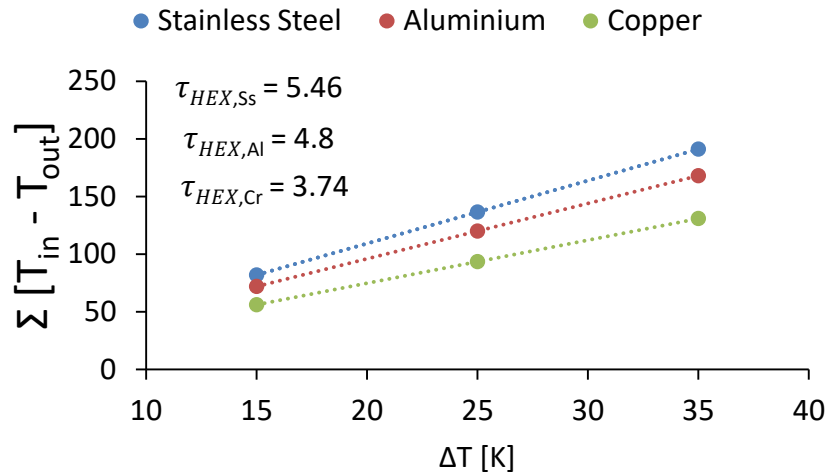
Figure 6:Time constants of the naked heat exchanger using different popular materials

According to the CFD data, it was observed that copper exhibited the shortest time constant of 3.74 seconds (as depicted in Figure 5) for the naked heat exchanger, along with a notable 43% improvement in the internal overall heat transfer coefficient when compared to aluminium (refer to Figure 6). On the other hand, stainless steel exhibited an elongated time constant of 5.46 seconds and a poor heat transfer coefficient of 0.35 W m^2 K^{-1}, making it the least desirable choice among the three materials. It is worth noting that the obtained results are not surprising, given the stark differences in thermal conductivity between the three materials, with copper exhibiting a thermal conductivity of 398 Wm^{-1}K^{-1}, while stainless steel has a considerably lower thermal conductivity of 16.2 Wm^{-1}K^{-1}. The information pertaining to the time constants of different naked heat exchanger materials for temperature swing adsorption applications is a valuable and novel tool for decision-making in terms of selecting an optimal material based on performance and budget constraints. However, it should be emphasised that stainless steel, although not a desirable choice, is still a relatively not cheap material. Therefore, the competition should mainly be between aluminium and copper, as supported by the evidence presented in Figures 6 and 7.

8
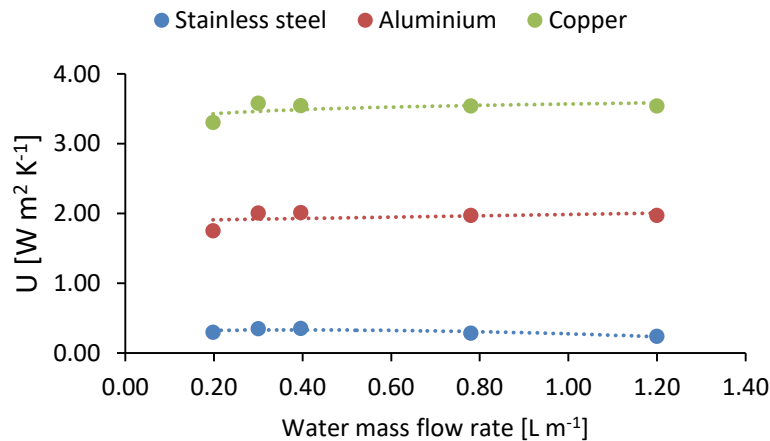
Figure 7:The overall heat transfer coefficients of different materials of the dry tests.

Experimental research is often impeded by constraints such as limited resources and time. In contrast, computational fluid dynamics (CFD) can serve as an extension of empirical methodologies and lead to a greater understanding of the optimal threshold for time-constant optimisation. In this study, three primary materials for heat exchangers, namely aluminium, copper and stainless steel, while varying the inlet water mass flow rates of 0.2, 0.4, and 0.8 L min^{-1}. Previous research[4–6] provided a deeper understanding of the intricacies involved in the design of complex adsorption chillers, which typically entail higher initial expenses[7]. Surprisingly, there exists a paucity of knowledge regarding the optimisation level of the time constants associated with the different heat exchangers' materials. The duration of the adsorption chiller cycle is a pivotal variable influencing the system's performance, and its reduction is dependent on the heat exchanger's response rate to alterations in temperature and inlet mass flow rate.

This study employs the dimensionless group $Nu = h \, L \, k^{-1}$ as a performance metric, which represents the ratio of convective to conductive heat transfer, where h denotes the coefficient of convective heat transfer obtained from CFD analyses, L denotes the characteristic length (that is, the ratio of the volume of the heat exchanger to its surface area) and k denotes the thermal conductivity of the water used in each study case. Figure 8 depicts the influence of the thermal conductivity of the metal used to construct the heat exchanger on the modification of more turbulent flow inside the heat exchanger geometry. The CFD findings reveal that a more turbulent flow regime inside the heat exchanger lowers the time constant; however, an unlimited increase in the inlet mass flow beyond 0.8 L m^{-1} has a negligible impact on the overall heat transfer coefficient (as depicted in Figure 7), thus resulting in higher pump purchase costs but no commensurate gain in heat transfer efficiency. In this case, the small-scale heat exchanger reached the maximum overall heat transfer coefficient at 0.5 Litre per minute.

9
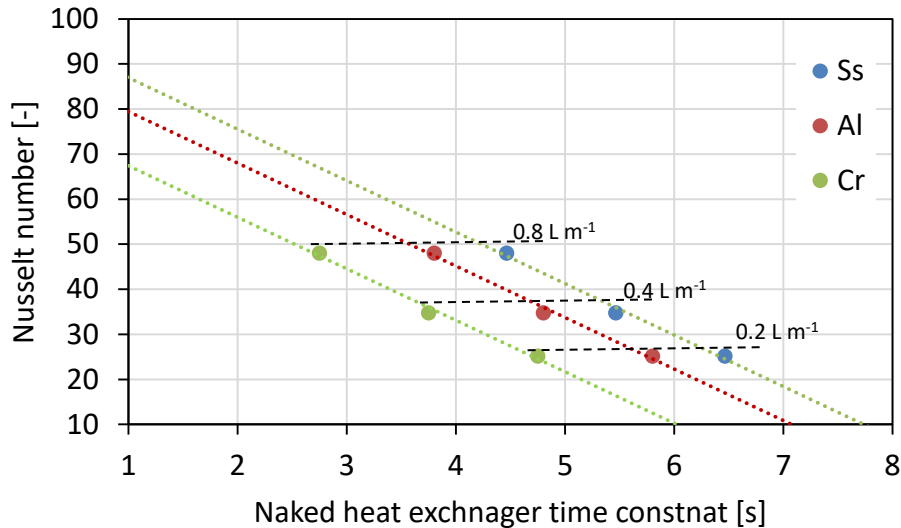
Figure 8: The impact of the metal thermal conductivity and flow regime on the time constant. Cr stands for Copper, AL is Aluminium, and SS is stainless steel.

Furthermore, Figure 8 serves as an optimisation map of different heat exchanger materials, demonstrating that a higher metal conductivity translates into a lower time constant, with copper showing a 22% improvement in time constant compared to aluminium (i.e., from 4.78 seconds to 3.74 seconds at an input mass flow rate of 0.4 L/m). However, increasing the flow rate beyond the optimal level should be avoided, as the gain in heat transfer efficiency is offset by the waste of pumping power. Alternatively, the Nusselt number of the heat exchanger can be used to forecast the extreme threshold of the time constant of one second, as depicted in Figure 8. In most cases, for the small-scale heat exchanger, 44% of the extra pumping power is required when the stainless-steel heat exchanger is used, and 27 % for the aluminium heat exchanger is used instead of copper. This should be taken into account because the pumping power is not free for adsorption cooling applications. It should be emphasised that each heat exchanger design requires meticulous investigation, as the internal geometry and heat transfer through the metal components dictates the time constant. The CFD study concludes that there is a theoretical limit on how fast each heat exchanger can respond to changes in temperature, which is controlled by the heat exchanger material and the flow regime inside the heat exchanger geometry.

Conclusions

The present study proposes a testing protocol for temperature swing adsorption packed beds, which offers a standardised and reliable methodology for evaluating the key heat transfer performance of adsorbers before their testing within a complete temperature swing adsorption technology. The methodology is applicable to every adsorber design, and its adoption would allow comparison among different designs, expediting the identification of the limitations of the adsorber and allowing to single out the adsorber performance from those of the whole technology. Adsorber time constants, as introduced in this study, prove to be a crucial tool in extracting the empty heat exchanger performance and the packed-bed performance through a rigorous experimental approach. Simple thermal mass analysis alone may not be sufficient to identify any internal design issues, such as increased void volume, that can impede the heat transfer process. Notably, the study's findings demonstrate that the packed bed requires an extended residence time and quantifies it.

10

References

[1]   A. Sharafian, S.M. Nemati Mehr, P.C. Thimmaiah, W. Huttema, M. Bahrami, Effects of adsorbent mass and number of adsorber beds on the performance of a waste heat-driven adsorption cooling system for vehicle air conditioning applications, Energy. 112 (2016) 481–493. https://doi.org/10.1016/J.ENERGY.2016.06.099.

[2]   K.R. Gluesenkamp, A. Frazzica, A. Velte, S. Metcalf, Z. Yang, M. Rouhani, C. Blackman, M. Qu, E. Laurenz, A. Rivero-Pacho, S. Hinmers, R. Critoph, M. Bahrami, G. Füldner, I. Hallin, Experimentally Measured Thermal Masses of Adsorption Heat Exchangers, Energies 2020, Vol. 13, Page 1150. 13 (2020) 1150. https://doi.org/10.3390/EN13051150.

[3]   E.Y. Ng1, P.W. Johnson1, S. Watkins1, An analytical study on heat transfer performance of radiators with non-uniform airflow distribution, (2005). https://doi.org/10.1243/095440705X35116.

[4]   C. Olkis, S. AL-Hasni, S. Brandani, S. Vasta, G. Santori, Solar powered adsorption desalination for Northern and Southern Europe, Energy. (2021) 120942. https://doi.org/10.1016/j.energy.2021.120942.

[5]   U. Bau, P. Hoseinpoori, S. Graf, H. Schreiber, F. Lanzerath, C. Kirches, A. Bardow, Dynamic optimisation of adsorber-bed designs ensuring optimal control, Appl Therm Eng. 125 (2017) 1565–1576. https://doi.org/10.1016/J.APPLTHERMALENG.2017.07.073.

[6]   I.S. Girnik, Y.I. Aristov, Effect of residual air on dynamics of temperature- and pressure-initiated adsorption cycles for heat transformation, Appl Therm Eng. 200 (2022) 117629. https://doi.org/10.1016/J.APPLTHERMALENG.2021.117629.

[7]   S. AL-Hasni, G. Santori, The cost of manufacturing adsorption chillers, Thermal Science and Engineering Progress. 39 (2023) 101685. https://doi.org/10.1016/J.TSEP.2023.101685.

11

3rd to 6th of September 2023
The University of Edinburgh, Scotland

Heat Powered Cycles
Conference 2023
Edinburgh

Heat in the new energy system

Fabrication of Gas-Diffusion Electrodes for CO_2 Conversion: Effect of Sputtering Parameters

V.S.R.K. Tandava[1], D. Sylla[1], N.M. Carretero[1] and S. Murcia-Lopez[1*]

[1]Catalonia Institute for Energy Research (IREC), C/Jardins de les Dones de Negre 1, 08930, Barcelona, Spain

[*]Corresponding author: smurcia@irec.cat

Abstract

Low-temperature electrochemical CO_2 reduction (ECO_2R) is proven to be one of several promising strategies to valorise CO_2 through its conversion into value-added products and fuels. In fact, it is the only alternative for the direct conversion of CO_2 into ethylene, with Cu being the only metal exhibiting any selectivity and activity towards the conversion of CO_2 to C_2 products. However, developing functional materials as electrocatalysts and electrodes is imperative to achieve industrially relevant performances and efficiencies. In this sense, besides the necessary improvements in terms of decreased energy consumption at high current densities, it is important to improve the faradaic efficiencies towards desired carbon products, while hindering the competitive hydrogen evolution reaction (HER). Gas-diffusion electrodes (GDE) based on carbon paper and cloth are the standard approach used in ECO_2R; however, during operation, the surface properties (e.g. wettability) of such carbon-based GDEs might change, ultimately favouring the HER and, thus, affecting the efficiency of the process. As alternative, few examples proposing the use of PTFE-based porous structures on which metallic Cu layers are used as both conductive support and catalyst[1], have demonstrated to be a promising approach to avoid the use of carbon-based electrodes. In the context of SolDAC project, we have developed a systematic study on the deposition conditions of sputtered Cu on PTFE structures. Therefore, we have observed that these physical features have a significant effect not only on the electrical conductivity of the electrodes, but also on the ECO_2R performance towards specific products, as show in Figure 1. As observed, different pressure conditions during sputtering modify the texture of the surface and might induce crack formation. This variation leads to different operation cathode potentials, that can decrease up to 400 mV at 200 mA·cm^{-2} in the electrodes with smoother surfaces, while the product distribution is also significantly affected by the current density on electrodes with varied physical properties. Finally, faradaic efficiencies to ethylene >50% are attained with these developed electrodes at cathode potentials of -1 to -1.2 V_{RHE}, showing the potential of as-prepared GDEs based on Cu-PTFE.

Keywords: CO_2 conversion, electrocatalysis, ethylene, copper.
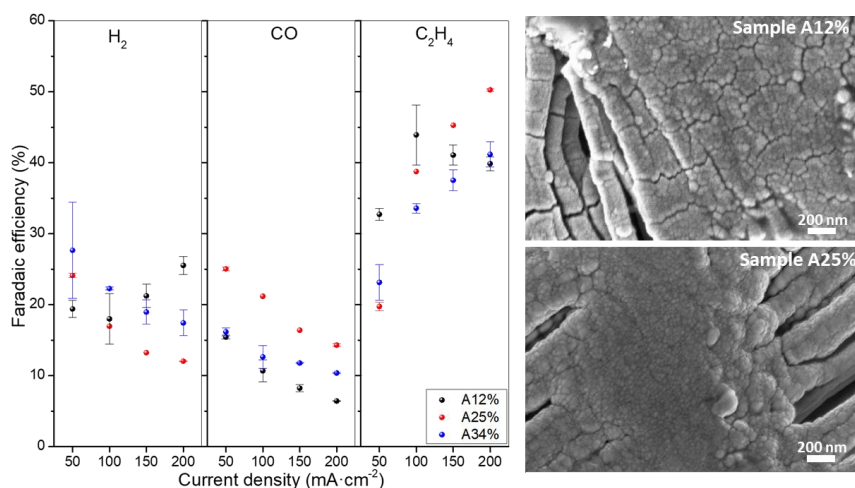
Fig. 1 – Variation of faradaic efficiencies with current density with sputtered materials prepared under different aperture conditions (left), and SEM images showing the microstructure variation of Cu-sputtered samples on PTFE membranes.

Acknowledgments

References:

[1] Kim, C., Bui, J.C., Luo, X., Cooper, J.K., Kusoglu, A., Weber, A.Z., Bell, A.T., *Tailored catalyst microenvironments for CO₂ electroreduction to multicarbon products on copper using bilayer ionomer coatings*, Nature Energy 6, 1026–1034, 2021.

3D simulation of a compact counter-flow dew-point indirect evaporative cooler

BC. Wang[1,2], M. Garcia[1], T. Duc[1,2*], GG. Cheng[1,2], W. Pang[1], JN. Ding[1,2,3]

[1]School of Mechanical Engineering, Jiangsu University, Zhenjiang 212013, China

[2]Institute of Intelligent Flexible Mechatronics, Jiangsu University, Zhenjiang 212013, China

[3]Institute of Technology for Carbon Neutralization, Yangzhou University, Yangzhou 225127, China

[*]Corresponding author: 1000005420@ujs.edu.cn

Abstract

Global warming has led countries around the world to rely more on air-conditioning during the summer times. However, due to the refrigeration principle of most traditional air conditioners is mechanical vapor compression cycle, the huge energy consumption and environmental pollution of them obviously do not meet the current international background of energy conservation and emission reduction. Recently, we have developed a compact counter-flow indirect dew-point evaporative cooler, which is based on a new design that enable the working air to flow to the wet channels without changing its direction. This paper reports a 3D numerical modelling analysis of the cooler. The simulation is validated with the experimental data. The discrepancies of the input pressure and product air temperature between simulation and experimental data are within 8% and 4%, respectively. A parametric study is carried out to evaluate the performance of the cooler at different working ratio, air flowrate, temperature, and humidity. Finally, the cooler performance is studied with the input air conditions in the hottest month of the year in several cities in the world. The key findings of this study are: (1) The cooling COP is reduced from 42.23 to 4.4 when the air flowrate is increased from 316 to 950 m^3/h under typical tropical weather conditions; (2) the cooler performance is enhanced with higher temperatures and lower relative humidity; (3) The cooler cooling COP is highest when the working ratio is 0.5-0.6; (4) This cooler is best for dry and hot cities such as Dubai (UAE) and Xi'an(China).

Keywords: dew-point indirect evaporative cooler, counter-flow, cooling capacity, cooling COP.

1 Introduction

Global warming is a worldwide problem. According to Song et al. [1], from 1980 to 2019, the surface equivalent potential temperature increased by 1.48 °C, while in tropical regions, this number can reach to 4°C. Additionally, with the acceleration of urbanization and the increase of urban population, the temperature in urban areas is higher than that in rural areas, even at night due to the urban heat-island effect [2]. Therefore, to create a comfortable thermal environment, the dependence on air conditioners will be increased thorough year, especially in summertime. However, because most traditional air conditioners work on the vapor compression cycle [3], extensive use of air conditioners inevitably increases electricity consumption. Therefore, the energy consumption by air conditioners obviously does not conform to the current world trend of 'carbon neutrality'. Therefore, research on alternative refrigeration technologies is significantly important.

Heat Powered Cycles
Conference 2023
Edinburgh

Heat in the new energy system

3rd to 6th of September 2023
The University of Edinburgh, Scotland

Among all the alternative technologies, the potential of dew-point evaporative cooling technology is regarded as the greatest [4]. There are mainly two types of indirect dew-point evaporative cooler: crossflow and counter flow. The basic working principle of the cooler is shown in Figure 1. The process air is sensibly cooled in the dry channels of the evaporative heat exchanger. A part of the process air is diverted from the dry channels to the wet channels to be the working air. The working air contacts water and induces the evaporation in the wet channels for the cooling process and is discharged as the humid exhaust air at the end of the wet channels. The rest of the process air coming out at the end of the dry channel is the product air. As the working air is pre-cooled, its cooling potential is increased, and the product air can be cooled below the wet-bulb temperature and near the dew-point temperature. Other advantages of dew-point evaporative cooler are low energy consumption, no heat rejection and no harmful chemical refrigerants.
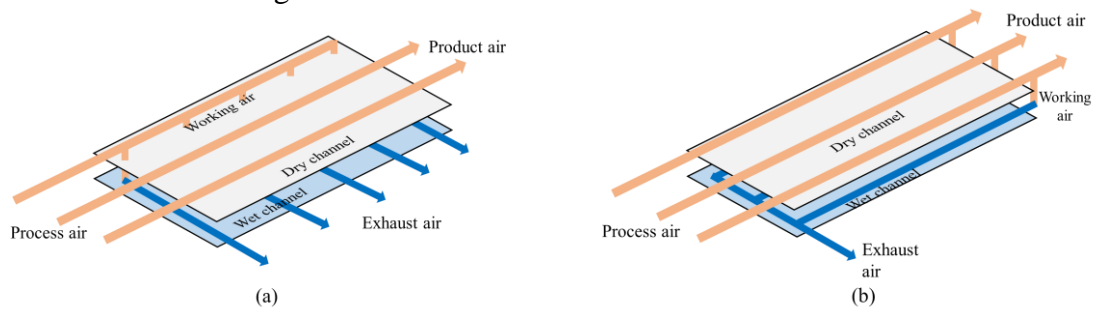
Figure 1: Air configurations and operation principle of (a) crossflow and (b) counter-flow dew-point indirect evaporative coolers.

There are a large number of studies on the development and performance of indirect dew-point evaporative coolers [5]. It is reported that counter-flow dew-point indirect evaporative cooler has higher cooling effectiveness and higher energy efficiency than the crossflow ones [6]. However, both types of the dew-point indirect evaporative coolers with the air configurations and operation principle shown in Figure 1, have an intrinsic problem. That is the working air takes an abrupt turn when it is diverted from the dry channels to the wet channels. This causes a high pressure drop of the working air, which increases the power consumption to drive the airflows. Recently, we have developed a new compact counter-flow dew-point indirect evaporative cooler that enables the working air to enter the wet channels without changing its direction. The photo and air configuration of our cooler are shown in Figure 2.
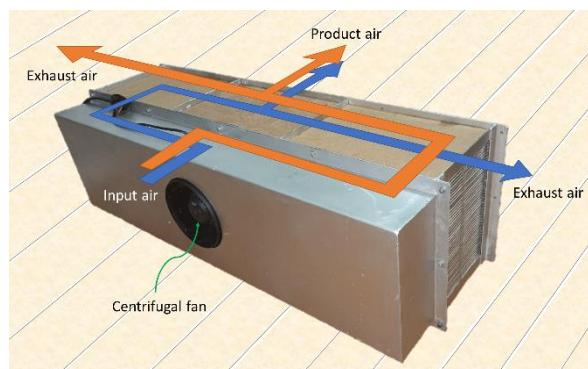
Figure 2: Our recently developed compact counter-flow dew-point indirect evaporative cooler that enables the working air to enter the wet channels without changing its direction.

Heat Powered Cycles
Conference 2023
Edinburgh

Heat in the new energy system

In this work, a 3D numerical simulation is developed by using COMSOL Multiphysics platform version 5.6 to study the cooling performance and energy efficiency of the cooler at different operating conditions. The simulation model is validated with the experimental performance data of the cooler. The effects of the input air flowrate, temperature and humidity and the working ratio are studied. The performance of the cooler under weather conditions of different cities in the world is evaluated and compared.

2 Simulation model and validation

2.1 The evaporative heat exchanger design and the model geometry

The evaporative heat exchanger of the cooler is a stack of 85 air channels as shown in Figure 2. The channels are separated by aluminium separators. Each air channel comprises of a dry half channel and a wet half channel. The wet channels are made of thin layers of wet cloths glued on the separators. The air channels are stacked in the way that a wet half channel is sandwiched between two adjacent dry half channels, and vice versa. The input process air enters the heat exchanger from its two ends. It first passes through the dry half channels. At the middle of the air channels, a part of process air exits the air channels as the product air. The rest of the process air continue pass through the wet half channels to be the working air without changing its direction. The exhaust air is discharged out at the end of the wet half channels.
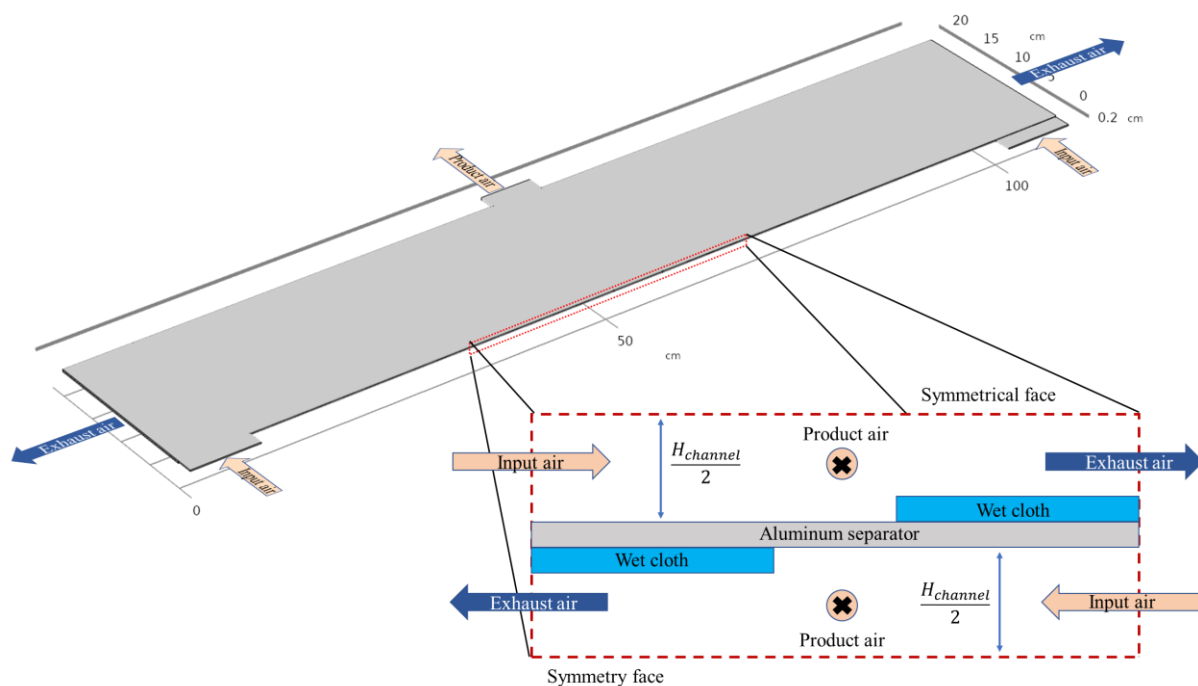
Figure 3: Geometry of the simulation model

Table 1: Dimensions of the simulation geometry

Parameters	Value
Total length of the air channel	108 cm
Width of the air channel	20 cm
Height of the air channel	3 mm
Thickness of the aluminium separator	0.15 mm
Thickness of the wet cloth	0.1 mm
Length of the wet cloth	48 cm
Width of the air inlet	8 cm
Width of the outlet	6cm

Because the heat exchanger is symmetrical, in order to simplify the calculation process, the 3D geometry of the model is constructed to include a half channel of an upper channel, separator with the attached wet cloth layers and a half of a lower channel, as shown in Figure 3. The detailed dimensions are shown in Table 1.

2.2 Mathematical model and calculation method

In this model, the coupling of fluid flow, heat and mass transfer, water evaporation is solved by using COMSOL Multiphysics platform. To simplify the calculation, the following assumptions is made: (1) There is not heat loss and air leak from the air channels and the outside environment and (2) Air is the incompressible ideal gas.

The continuity equation for the air in dry channel is:
$$\rho \nabla \mathbf{u} = 0 \tag{1}$$

The momentum equation for the air in dry channel is:
$$\rho (\mathbf{u} \cdot \nabla) \mathbf{u} = \nabla \cdot [-p\mathbf{I} + \mu(\nabla \mathbf{u} + (\nabla \mathbf{u})^T)] + \mathbf{F} \tag{2}$$

Energy conservation equation of air in dry channel is:
$$c_{d,p} m_d \Delta t_d = k_d (t_d - t_{wa}) \Delta A_d \tag{3}$$

The heat transfer of moist air in wet channel is solved by the following equations:
$$\rho C_p \mathbf{u} \cdot \nabla \mathrm{T} + \nabla \cdot \mathbf{q} = Q + Q_p + Q_{vd} \tag{4}$$
$$\mathbf{q} = -k \nabla T \tag{5}$$

The moisture transport happened in wet channel is:
$$M_v \mathbf{u} \cdot \nabla c_v + \nabla \cdot \boldsymbol{g}_w = G \tag{6}$$
$$\boldsymbol{g}_w = -M_v D \nabla c_v \tag{7}$$
$$c_v = \phi c_{sat} \tag{8}$$

Energy conservation equation of air in wet channel is:
$$c_{w,p} m_w \Delta t_w = h_w (t_{wa} - t_w) \Delta A_w + r h_m (\rho_{wa} - \rho_w) \Delta A_w \tag{9}$$

Mass conservation equation of air in wet channel is:
$$m_w \Delta d = h_m \rho_w (d_{wa} - d_w) \Delta A_w \tag{10}$$

Mass conservation equation of water film is shown as follows:
$$\Delta m_{wa} = h_m \rho_w (d_{wa} - d_w) \Delta A_w \tag{11}$$

Air pressure drop is shown as follows:
$$\Delta p = \Delta p_l + \Delta p_{fr} \tag{12}$$

2.4 Model validation

**Heat Powered Cycles
Conference 2023**
Edinburgh

Heat in the new energy system

3rd to 6th of September 2023
The University of Edinburgh, Scotland
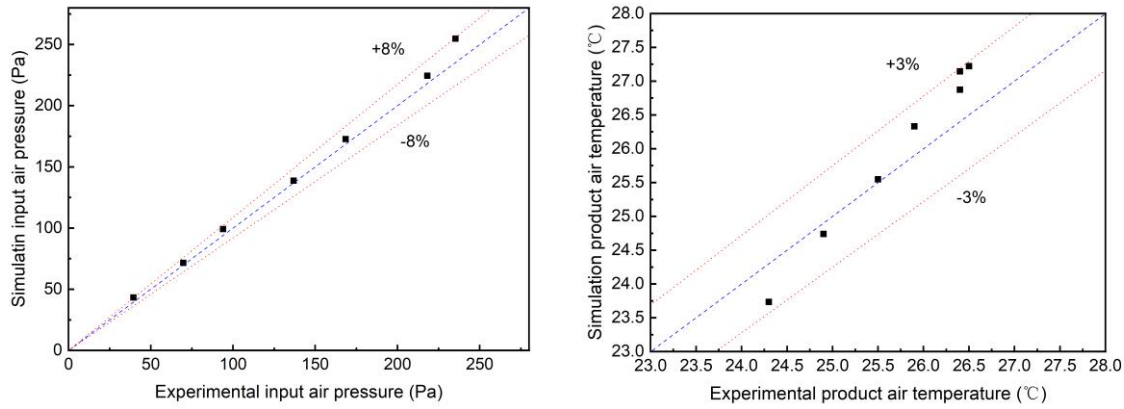
Figure 4: Validation of (a) input air pressure and (b) product air temperature

The developed model is validated with the performance testing data of the physical prototype under the input air temperature and relative humidity conditions of 32.5 – 33 ℃ and 56 – 58 %, respectively, at different input air flowrates ranging from 316 to 950 m³/h, and the working ratio of 0.5. The comparisons between simulation and experimental input pressure and output temperature are shown in Figure 4.

Figure 4 shows that the deviations of the simulation input pressure and output temperature from the experimental data are within 8% and 3%, respectively. Therefore, the simulation model used in this paper is reliable and can be used for further parametric studies.

2.5 Performance evaluation of the cooler

The working air ratio is the ratio of working air volume flowrate to the input air volume flowrate:

$$r = \frac{\dot{V}_{in} - \dot{V}_{pro}}{\dot{V}_{in}} \tag{13}$$

The cooling effectiveness of the developed cooler is evaluated by the wet-bulb effectiveness, ξ_{wb}, and dew-point effectiveness, ξ_{dp}:

$$\xi_{wb} = \frac{T_{in} - T_{pro}}{T_{in} - T_{wb}} \times 100\% \tag{14 a}$$

$$\xi_{dp} = \frac{T_{in} - T_{pro}}{T_{in} - T_{dp}} \times 100\% \tag{14 b}$$

The cooling capacity, Q, of the cooler is calculated by the equation below:

$$Q = (T_{in} - T_{pro}) \times \dot{m}_{pro} \times 1.006 \frac{kJ}{kg \cdot K} \tag{15}$$

The air blower power consumption, E, is calculated from the volume flowrate, $\dot{V}$, the static pressures of the input air, P_{in}, and the motor efficiency, $\eta = 0.4$.

$$E = \frac{P_{in} \dot{V}_{in}}{\eta} \tag{16}$$

The energy efficiency of the developed cooler is evaluated via the cooling coefficient of performance (COP) following below equation.

$$COP = \frac{Q}{E} \tag{17}$$

Heat Powered Cycles
Conference 2023
Edinburgh
Heat in the new energy system

3rd to 6th of September 2023
The University of Edinburgh, Scotland

3 Results and discussion

3.1 Effect of the working ratio

The effect of the working ratio is studied under typical tropical input air conditions. The inlet air temperature is 33 ℃, the relative humidity is 56.14%, and the inlet air volume flowrate is 680m³/h. The changes in the cooler performance are shown in Figure 5 when the working ratio is varied from 0.1 to 0.9.

Figure 5 (a) shows that lower product air temperature is achieved when the working ratio is increased.

Figure 5 (b) shows that the cooling COP, which is the ratio of the cooling capacity and fan power consumption. The cooling COP peaks at the working ratio of 0.5-0.6. Both lower and higher working ratios result in lower cooling COP. It is because either the cooling capacity is low, or the fan power consumption is high.

(a)   (b)
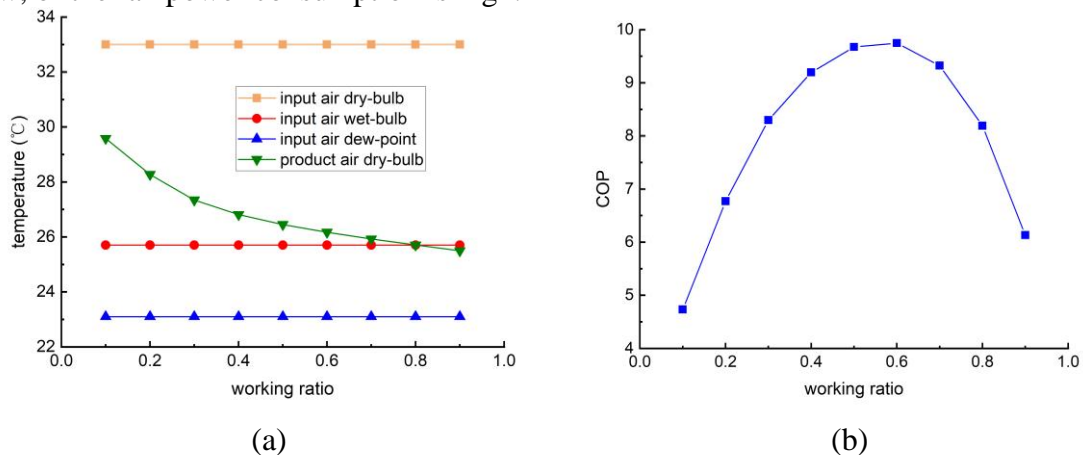
Figure 5: The change in the (a) product air temperature (b) COP with the variation of the working ratio

3.2 Effect of air flowrate

The effect of air flowrate on the performance of the cooler is studied by changing the air volume flow rate from 316.3 to 950 m³/h when the inlet air temperature and relative humidity are 33 °C and 56.14%, and the working ratio is kept at 0.5.

Figure 6 (a) shows that the product air temperature increases with higher input air flowrate. It is attributed to the shorter contact time between the air and the heat exchanger plates. This result in the decrease in the wet-bulb and dewpoint effectiveness as shown in Figure 7 (b). The product air temperature can reach below the wet-bulb temperature and approach the dew-point temperature when the air flowrate is smaller than 530 m³/h. Within the air flowrate range, the wet-bulb effectiveness and dew-point effectiveness achieve 75-122% and 55-90%, respectively.

Figure 6 (c) shows that lower cooling COP when the air flowrate is increased. It is because the power needed to maintain the air flow is increasing drastically with higher air flowrate.
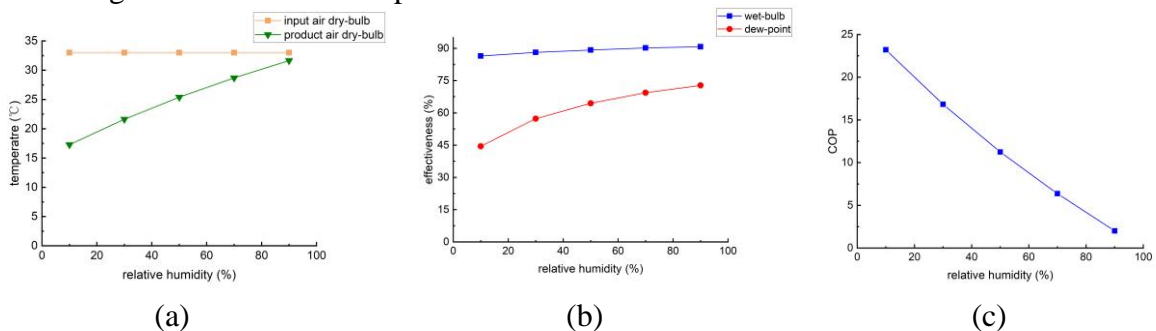

(a)   (b)   (c)
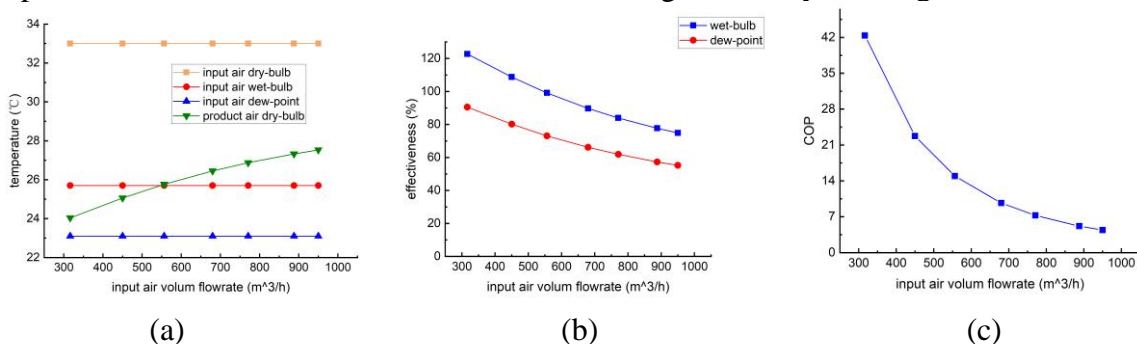
Figure 6: the change in the (a) air temperatures, (b) wet-bulb effectiveness and dew-point effectiveness, (c) COP when the input air volume flow rate is varied.

3.3 Effect of input temperature

In order to study the effect of input temperature on the performance of the cooler, the model is run with the input air dry-bulb temperature varying from 30 to 46 °C while the input wet-bulb temperature is kept at 25°C, the inlet air volume flowrate is 680m³/h, and the working ratio is 0.5.

Figure 7 (a) shows that although the input air temperature is varied in a wide range from 30 to 46 ℃, the product air temperature changes from 25.5-27.5 ℃, near the wet-bulb temperature. This results in the stable wet-bulb and dewpoint effectiveness at 87-88% and 60-62%, respectively, as shown in Figure 7 (b).

Figure 7 (c) shows that the cooling COP is proportional to the input temperature. It means that the developed cooler is more right for hot weather conditions.

(a)   (b)   (c)
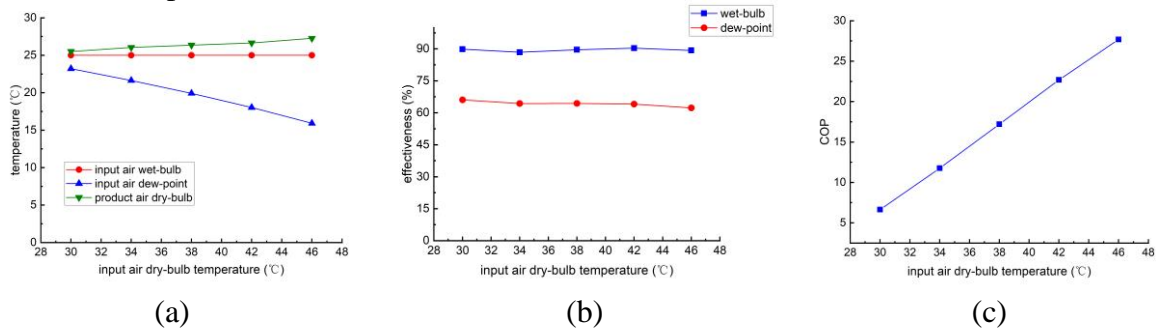
Figure 7: The change in the (a) product air temperature, (b) wet-bulb effectiveness and dew-point effectiveness, (c) COP with the increase of input air temperature.

3.4 Effect of humidity conditions

In this study, the relative humidity is varied from 10 to 90% while the inlet air volume flowrate is 680m³/h, the working ratio is 0.5, and the input air dry-bulb temperature is 32.5 ℃.

It is seen from Figure 8 (a) that with the increase in the relative humidity, the product air temperature decreases. It is because the cooling temperature of the cooler is limited by the dew-point temperature which increases with higher relative humidity. Figure 8 (b) shows that the wet-bulb and dewpoint effectiveness increase from 82 to 88% and from 43 to 75%, respectively, when the relative humidity is changed from 10 to 90%. Figure 8 (c) shows that the cooler can achieve higher COP when the input air is drier.

(a)   (b)   (c)

Figure 8: The change in the (a) product air temperature (b)wet-bulb effectiveness and dew-point effectiveness, (c) COP with the increase in relative humidity.

3.5 Performance in different cities

In this study, the cooler is subjected to typical weather conditions in the daytime (10:00 a.m. to 17:00 p.m.) of the hottest month in the year in several cities in the world. The inlet air volume flowrate is kept at 680m³/h and the working ratio is 0.5.

The results show that the performance of this cooler is different in different cities. Its performance is highest in hot and dry cities such as Dubai and Xi'an, with the temperature drop and cooling COP of 10 -12.5 ℃ and 15-19, respectively. The performance is lower in hot and humid cities such as Singapore, Monterrey, New York, London and Beijing, with the temperature drops and COP of 5-8 ºC and 8-12, respectively.
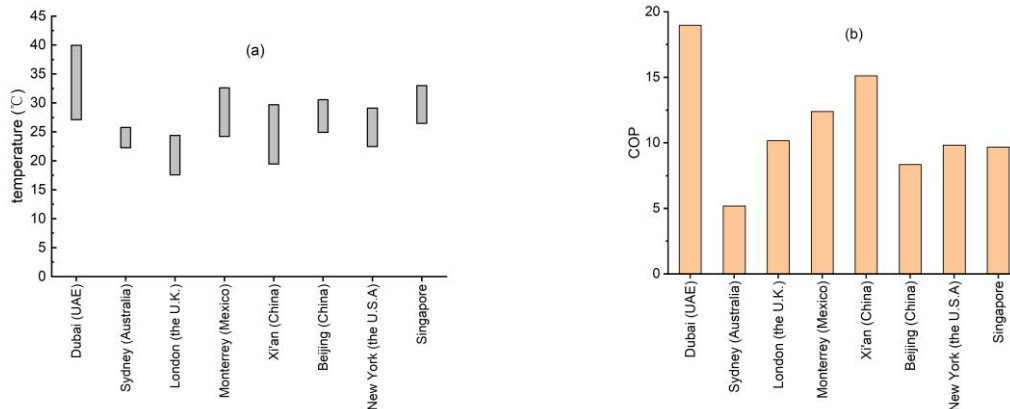
Figure 9: (a) the temperature drop (from the input air temperature to the product air temperature), and (b) the cooling COP of the cooler in different cities.

4 Conclusion

In this work, a 3D simulation model based on the heat and mass transfers in moist air coupled with fluid dynamic transport is developed to study a new compact dew-point indirect evaporative cooler that enables the working air to enter the wet channel without changing its direction. The mathematical model is validated with the experimental performance data of a physical prototype. The errors of the input air pressure and output air temperature between the simulation and experimental data are within 8% and 4%, respectively. The parametric studies show that:

- The cooler has highest cooling COP with the working ratio of 0.5-0.6
- Under typical tropical weather conditions, when the air flowrate is varied from 316 to 950 m³/h, the cooler COP is decreases from 42.23 to 4.4.
- The cooling COP, as well as temperature drop, is enhanced by higher temperature and lower relative humidity of the input air.
- The cooler is best for using in hot and dry regions, such as Dubai (UAE) and Xi'an (China) with the cooling COP of 15-19.

References

[1] F. Song, G. J. Zhang, V. Ramanathan, and L. R. Leung, "Trends in surface equivalent potential temperature: A more comprehensive metric for global warming and weather extremes", PNAS, 2022.

[2] Y. Kikegawa, Y. Genchi, H. Kondo, and K. Hanaki, "Impacts of city-block-scale countermeasures against urban heat-island phenomena upon a building's energy-consumption for air-conditioning," Applied Energy, 2006.

[3] M. H. Mahmood, M. Sultan, T. Miyazaki, S. Koyama, and V. S. Maisotsenko, "Overview of the Maisotsenko cycle – A way towards dew point evaporative cooling," Renewable and Sustainable Energy Reviews, 2016.

[4] J. Lin, R. Z. Wang, M. Kumja, T. D. Bui, and K. J. Chua, "Multivariate scaling and dimensional analysis of the counter-flow dew point evaporative cooler," Energy Conversion and Management, 2017.

[5] G. Zhu, T. Wen, Q. Wang, and X. Xu, "A review of dew-point evaporative cooling: Recent advances and future development," Applied Energy, 2022.

[6] C. Zhan, Z. Duan, X. Zhao, S. Smith, H. Jin, and S. Riffat, "Comparative study of the performance of the M-cycle counter-flow and cross-flow heat exchangers for indirect evaporative cooling - Paving the path toward sustainable cooling of buildings," Energy, 2011.

Heat Powered Cycles
Conference 2023
Edinburgh
Heat in the new energy system

Testing of an adsorption chiller prototype for data center cooling

A.J. Di Cicco[1][*], W. Mittelbach[2], T. Toppi[1], A. Freni[3] and M. Aprile[1]

[1]Department of Energy, Politecnico di Milano, Italy

[2]Sorption Technologies GmbH, 79144, Freiburg, Germany

[3]CNR – Institute of Chemistry of Organo Metallic Compounds (ICCOM), Pisa, Italy

[*]Corresponding author: alejandrojose.dicicco@polimi.it

Abstract

The main objective of this study is to present a novel adsorption chiller prototype (designed and realized by the company Sorption Technologies GmbH) that is suitable for cooling of data center servers. This prototype has been designed to fit into commercially-available data center racks. This adsorption prototype has been designed to cool down the rack servers by means of liquid cooling. Furthermore, an air-cooler heat exchanger is also integrated into the adsorption machine to cool down the rest of the rack components (i.e., patch panels, HDD). This way, the adsorption system is able to cool down all rack components. Phase-change chambers are integrated into the adsorption modules for direct evaporation/condensation, removing the need of large vacuum valves and allowing to have a more simpler and compact vacuum system. This also means that the refrigerant distribution is completely done in liquid phase. The prototype is installed at the Department of Energy at the Politecnico di Milano and testing will be carried out using cooling water temperatures in the range 25 – 30 °C and hot water temperatures in the range 55 – 65 °C.

Keywords: adsorption, cooling, data center, energy efficiency.

Introduction

Adsorption cycles are refrigeration systems that can produce a cooling effect using low-temperature heat sources (lower than 90 °C), such as waste heat [1] and hot water from solar collectors [2]. The core system of an adsorption unit is generally composed by an evaporator, a condenser and two adsorption beds; these sorption beds are devices that carry out the thermo-chemical compression of the refrigerant. The working principle of an adsorption cycle contemplates simultaneous adsorption/evaporation and desorption/condensation processes. Since the evaporator's performance can represent a bottleneck situation for the overall performance of the machine, different configurations have been studied in literature, such as pool boiling [3] and falling-film evaporators [4].

Considering that different applications may produce waste heat at a temperature high enough to drive the adsorption machine, their range of application can always be increased, and one of these applications can be using waste heat from data centers to produce the required cooling for the server racks. Data centers energy consumption has become an important topic to discuss and analyze [5]. Their biggest energy consumption is related to IT equipment power (e.g., computer hardware and severs) and cooling, with the latter being responsible for 40 % of the total energy consumption of a data center [6]. For an air-cooled data center, the cooling plant is composed by the installed mechanical equipment and the heat rejection system. Direct expansion systems using a computer room air conditioner can be used for data center cooling, with air-cooled condensers as the heat rejection system [6]. Chilled water systems can also be used for high IT power densities, but the introduction of fans and chillers results in extra energy costs [7]. Cooling systems that employ air also present some

disadvantages related to air management, such as cold-air bypass and generation of hot spots. Liquid cooling possesses several advantages that can help to reduce the cooling system energy consumption. The most important advantage of a liquid cooling system is a higher heat transfer capacity per unit, which means a reduction in required equipment, facility cost and a higher reliability of the cooling system [7]. Adsorption chillers for data center cooling were first proposed by the company Fahrenheit GmbH (SorTech) with the Leibniz Supercomputer Center (LRZ), where direct liquid cooling for the SuperMUC-NG supercomputer is done by means of a centralized adsorption system [8]. This installation proves the feasibility of the concept along with energy savings, with the only disadvantage for broad applications being the centralized system piping design and complexity.

The aim of this work is to present the concept of an adsorption chiller prototype that could be used for cooling individual racks from a data center. The prototype, designed and realized by the company Sorption Technologies GmbH, is located at the Department of Energy at the Politecnico di Milano. This adsorption chiller design has been patented by Sorption Technologies GmbH and its inventor Walter Mittelbach under publication number WO 2021/089818 (European Pattent Office EP4055330) [9]. The core system of the adsorption chiller includes two adsorption modules each integrated with a phase-change chamber for direct evaporation/condensation. The use of direct evaporation/condensation means that refrigerant distribution within the cycle is done completely in liquid phase, with no refrigerant transport in vapor phase nor large vacuum valves; furthermore, this also means a more simpler and compact design. The analysis of the energy balance of this new machine is shown in Figure 1. As can be seen from said figure, this prototype provides the idea of a rack-integrated adsorption chiller, where the heat removed from the servers by means of liquid cooling is used as driving heat source in the adsorption modules (this driving heat from the servers is referred to as high-temperature energy source in Figure 1, HT). Heat from other components from the rack (i.e., patch panels, HDD) can also be removed by means of an air-cooler installed at the top of the modules (referred to as low-temperature energy source in Figure 1, LT). This way, the adsorption machine is able to remove all heat from all the components of the rack. Another important highlight of this prototype is that heat rejection can be done through a cooling water loop that can be directly connected to a cooling tower without any components in between.
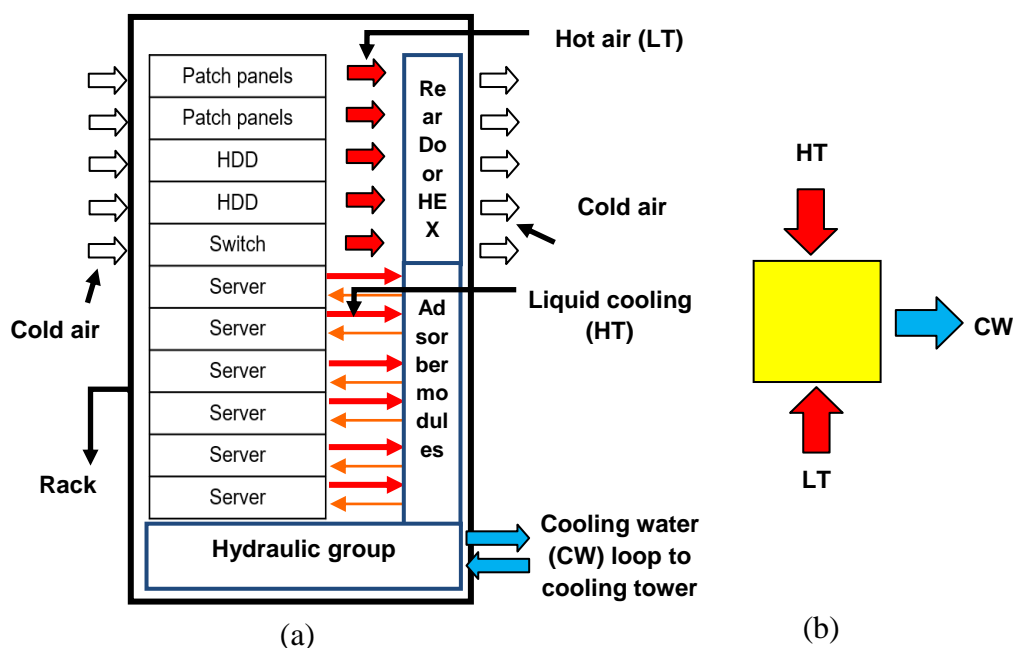
Figure 1. Rack-integrated adsorption chiller: (a) scheme, (b) energy balance

Discussion and Results

The experimental set-up of this study contemplates the adsorption chiller prototype as well as the external water circuits connected to it, as shown in the scheme from Figure 2. A picture of the assembled adsorption prototype and its components is shown in Figure 3.
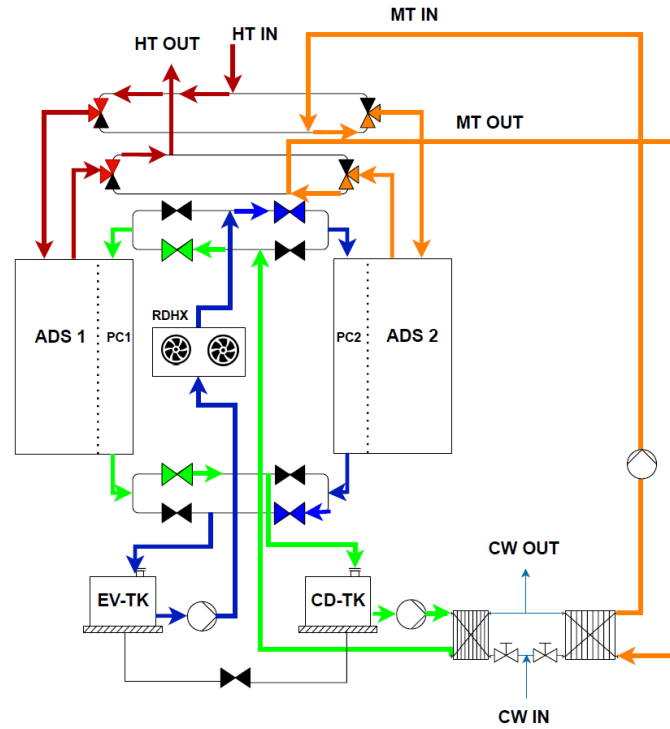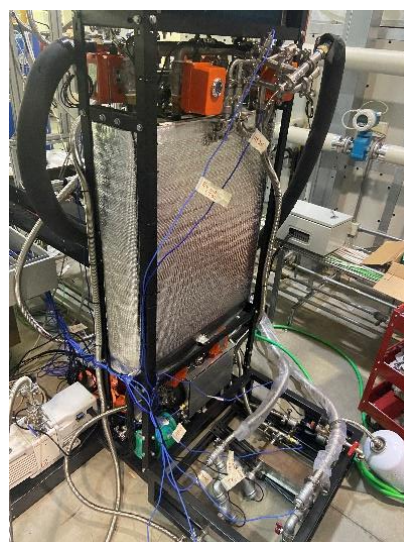

Figure 2. Experimental set-up scheme

(a)   (b)

Figure 3. Adsorption chiller protype: (a) back (b) front

As detailed in Figure 2, the adsorption chiller prototype is composed by two adsorption modules (employing silica gel pellets as adsorbent media) with two internal phase-change chambers ("PC1", "PC2"), an air-cooler heat exchanger ("RDHX"), two small refrigerant tanks (one for the condenser, "CD-TK", and one for the evaporator, "EV-TK"), circulating pumps for the condenser and evaporator loops, and two plate heat exchangers. Both the refrigerant and water flowrates are redirected accordingly using three-way and two-way valves. The two tanks "CD-TK" and "EV-TK" are also connected between them for refrigerant mass transfer. Furthermore, the external water circuits are identified as hot water (HT) and cooling water (CW) temperature circuits, while an internal medium-temperature (MT) water circuit is used to cool down the adsorbers during adsorption/evaporation. Water temperatures are measured on different points of the system using PT-100 and PT-1000 temperature sensors, while pressure from one module can be measured through a vacuum pressure transmitter (range: 0 – 20 kPa, accuracy 0.5 % FS). The water from the CW circuit is prepared at a given setpoint temperature using two flowrates from a 4000 L hot water tank (heated up with a 15 kW electric resistance) and a 3000 L cold water tank. The HT water is prepared using a separate water circuit with a 200 L tank and a 9 kW electric resistance. The working principle of this new adsorption chiller contemplates cyclic adsorption/desorption processes, as well as heat recovery stages, which are all organized into four phases. These four phases are illustrated in Figure 4, while the description of each phase is detailed as follows:

1) **Desorption in module 1 and adsorption in module 2:** during the first phase, shown in Figure 4.a, the hot water directly enters module 1 for desorption/condensation. Once the refrigerant is desorbed, it condenses on the bottom of the "PC1" chamber and falls to the "CD-TK" tank; it is then pumped to the "PHE2" heat exchanger and rejects heat to the CW circuit, before going back to the "PC1" chamber to carry more condensed refrigerant. Simultaneously, adsorption/evaporation happens inside module 2. A fraction of the liquid refrigerant entering the "PC2" chamber evaporates and is adsorbed, while the rest falls to the "EV-TK" tank. The refrigerant is then pumped and circulates through the "RDHX" heat exchanger before entering again into the "PC2" chamber for further evaporation/adsorption. The water circulating inside module 2 is heated up by the adsorption process and rejects heat to the CW circuit through the MT loop.

2) **Mass transfer and heat recovery (cooling of module 1):** when phase 1 is over, the pressure inside the modules needs to be readjusted to switch their operation from adsorption to desorption, and vice versa. As can be noticed from Figure 4.b, hot water begins to circulate in module 2, to increase its pressure. The cooled down water from module 2 flows (through the MT loop) to module 1 to decrease its pressure. During this phase, the refrigerant circulation is interrupted (i.e., pumps are turned off). Furthermore, the remaining refrigerant to in the phase-change chambers exit to either "EV-TK" or "CD-TK".

3) **Desorption in module 2 and adsorption in module 1:** this phase analysis is similar to that of phase 1, with the only difference being the internal operation of the modules. Hot water now circulates inside module 2 for desorption/condensation, while water from the MT loop is redirected to module 1 for adsorption/evaporation. Considering the refrigerant loop, circulating pumps are turned on again and the refrigerant circulates through the "RDHX" and "PC1" for adsorption, and also through "PC2" for desorption. This phase is visually presented in Figure 4.c.

4) **Mass transfer and heat recovery (cooling of module 2):** the final phase, shown in Figure 4.d, follows the same principle of phase 2, in which there is heat recovery to adjust the pressure within the modules. The HT loop is redirected to module 1, and the

resulting cooled down water enters module 2. Circulating pumps are turned off, and the remaining refrigerant exits to the "EV-TK" and "CD-TK" tanks.
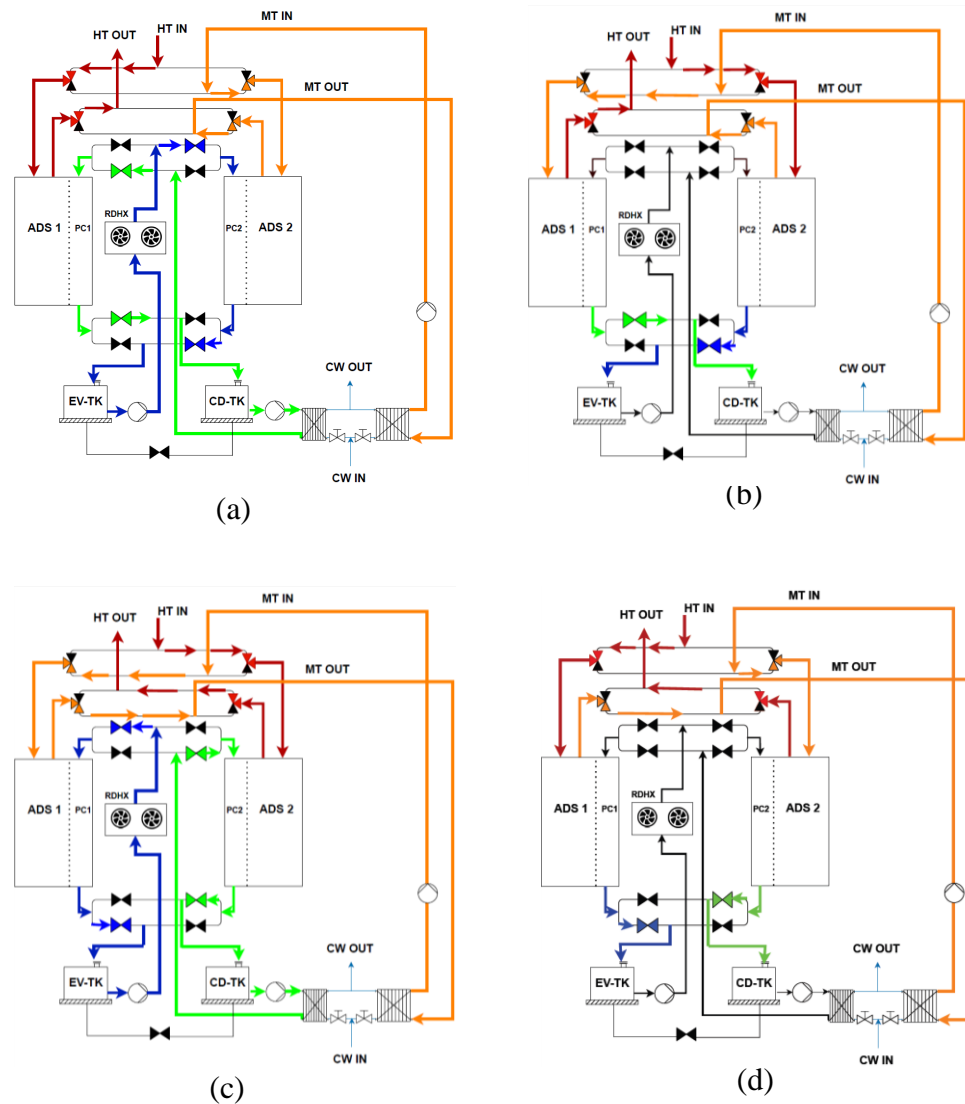

Figure 4. Working phases: (a) Phase 1, (b) Phase 2, (c) Phase 3, (d) Phase 4

Experimental tests are scheduled to be performed considering an inlet HT temperature of 65 °C and inlet CW temperature of 25. Furthermore, HT flowrate is set to 2.3 m³/h while the CW flowrate is set to 2.1 m³/h.

Conclusions

In this article, a novel adsorption chiller configuration for rack-based server cooling is presented, with the first prorotype installed at the Department of Energy of the Politecnico di Milano. This new system contains adsorption modules that have their own phase-change chambers integrated into their architecture. In these chambers, direct evaporation/condensation is carried out, allowing to have the refrigerant distribution completely done in liquid phase. Furthermore, by having the refrigerant distribution completely in liquid phase, the adsorption system can have a more simpler and compact design.

This rack-integrated adsorption chiller is designed to remove the heat from all the components of the rack and use it as heat input to carry out adsorption/evaporation and desorption/condensation. Rack servers can be liquid cooled, while the rest of the rack components (i.e., patch panels and HDD) that cannot be liquid cooled, can be air-cooled with the rear-door heat exchanger (RDHX). The high-temperature (HT) heat source from liquid cooling is used as driving energy source for desorption, while the low-temperature (LT) heat input from the air-cooler (RDHX) is used in the evaporator loop. This way, by means of an air-cooler and liquid cooling all components of the rack can be cooled down.

References:

[1] Pan, Q., Peng, J., Wang, R., "Experimental study of an adsorption chiller for extra low temperature waste heat utilization", Applied Thermal Engineering, 2019.

[2] Roumpedakis, T.C., Vasta, S., Sapienza, A., Kallis, G., Karellas, S., Wittstadt, U., Tanne, M., Harborth, N., Sonnenfeld, U., "Performance results of a solar adsorption cooling and heating unit", Energies, 2020.

[3] Thimmaiah, P.C., Sharafian, A., Rouhani, M., Huttema, W., Bahrami, M., "Evaluation of low-pressure flooded evaporator performance for adsorption chillers", Energy, 2017.

[4] Aprile, M., Di Cicco, A.J., Toppi, T., Freni, A., Motta, M., "Modelling of a falling-film evaporator for adsorption chillers", International Journal of Refrigeration, 2023.

[5] R., Hintemann. Boom führt zu deutlich steigendem Energiebedarf der Rechenzentren in Deutschland im Jahr 2017, Borderstep Institut, (2017).

[6] Capozzoli, A., Primiceri, G., "Cooling systems in data centers: state of art and emerging technologies", Energy Procedia, 2015.

[7] Chi, Y.Q., Summers, J., Hopton, P., Deakin, K., Real, A., Kapur, N., Thompson, H., "Case study of a data centre using enclosed, immersed, direct liquid-cooled servers", Proceedings of the 30th Annual Semiconductor Thermal Measurement and Management Symposium (SEMI-THERM), 2014.

[8] Fahrenheit GmbH. (2021, May 21). Self-Cooling Supercomputer [Press release]. https://fahrenheit.cool/en/self-cooling-supercomputer/

[9] Mittelbach, W. (2021). Adsorption refrigeration machine or heat pump with a liquid-phase refrigerant distribution function, and method for operating the adsorption refrigeration machine or heat pump. (European Patent No. 2021089818). European Pattent Office.

Heat Powered Cycles
Conference 2023
Edinburgh

Heat in the new energy system

Exploring Energy Materials at the Atomic Scale with Solid State Nuclear Magnetic Resonance Spectroscopy

S. Pizzanelli[1], **F. Nardelli**[1], **and A. Freni**[1]

[1] CNR-ICCOM, Institute of the Chemistry of Organometallic Compounds, Via G. Moruzzi 1, 56124 Pisa, Italy

[*]Corresponding author: silvia.pizzanelli@pi.iccom.cnr.it

Abstract

The development of new materials for energy storage and production on porous matrices is the object of intensive research activities in the scientific community. In order to optimize their design, molecular scale phenomena at the basis of their performance should be understood. Solid State Nuclear Magnetic Resonance (NMR) spectroscopy is one of the most powerful techniques to characterize the structure and the dynamics of porous materials as well as of confined guest molecules at the atomic scale. Here, the results obtained by applying NMR techniques for exploring the diffusion of guest molecules within porous matrices of relevance in energy applications will highlight the potential of this technique in this field.

Keywords: solid state NMR, Metal Organic Frameworks, diffusion under confinement, porous matrices

Introduction/Background

Solid State NMR has revealed to be one of the most powerful techniques to characterize different types of materials in terms of structure and dynamics. It is quite versatile in that it is applicable both to crystalline and amorphous phases and also to soft materials, besides being able to probe different nuclei. For example, this technique can reveal structural changes that occur during the service life of the material, the molecular interactions involved in the adsorption/desorption processes, and self-diffusion of guests confined in porous matrices. In this contribution, attention will be focused on diffusion of confined guests and results from two case studies will be shown.

Discussion and Results

The first case study presented here concerns the dynamics of water confined in a microporous metal−organic framework, NH_2-MIL-125. The dynamics was investigated by ^{1}H fast field-cycling NMR relaxometry, a peculiar NMR technique which allows to probe molecular motions over a wide time scale. The data were interpreted within a dynamic model where molecules bind to the surface hopping among preferential binding sites. [1, 2]
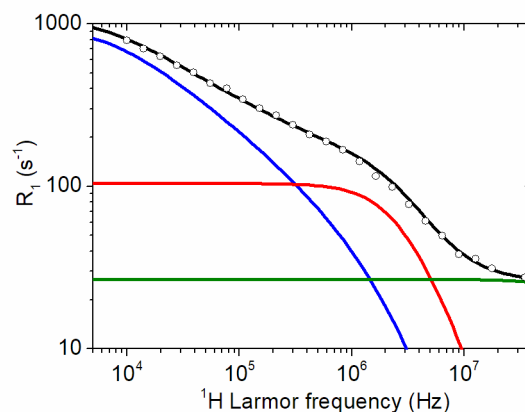
Figure 1. Experimental ^1H longitudinal relaxation rate R_1 as a function of the ^1H Larmor frequency of completely hydrated NH$_2$-MIL-125 at 298 K. Comparison of the experimental (circles) and calculated (black line) curve. Blue, red, and green lines represent contributions to R_1 from different dynamic processes, i.e. reorientations mediated by the translational displacement, and anisotropic and isotropic rotational dynamics, respectively.

A small fraction (about 20%) of water molecules was found to hop among preferential binding sites and reorient as a consequence of the displacement along the surface. This motion occurs on a time scale ranging from several ns to a few µs (Figure 1, blue line). The bound water molecules also experience local restricted molecular reorientations with characteristic times of about 30 ns (Figure 1, red line), whereas free water molecules exhibit isotropic correlation times shorter than 0.4 ns (Figure 1, green line).

In the second study, self-diffusion of methanol impregnating a mesoporous silica gel (average pore size of 7.8 nm) was measured in the 298-316 K temperature interval using ^1H Pulse Field Gradient NMR. Self-diffusion within a silica grain, which is characterized by a size of 0.5-0.8 mm, is measured. The effect of the presence of LiCl dissolved in methanol on the methanol self-diffusion was explored, with LiCl concentrations ranging between 10 and 35 wt %. The self-diffusion coefficient decreases upon increasing the salt concentration in the whole temperature range investigated and its temperature dependence is progressively leveled off upon increasing the salt concentration. The trends at different salt concentrations can be fitted according to an Arrhenius law. The activation energy tends to increase upon increasing the salt concentration.

In addition, the porous matrix induces a slowing down of methanol self-diffusion, as revealed by the comparison of the data obtained under confinement within the porous matrix with those in solution.

Summary/Conclusions

The interpretation of ^1H longitudinal relaxation rate R_1 as a function of the Larmor frequency of water confined in a MOF gives insight into water motions occurring on a time scale ranging between 0.1 ns and a few µs. The self-diffusion data of methanol confined within a silica mesoporous matrix in the presence of LiCl provide a picture of the microscopic behaviour of this guest molecule, revealing the combined role of the matrix and the salt on methanol mobility.

Overall, NMR techniques provide detailed information at the molecular level on molecular motions within different types of porous systems. This knowledge is potentially useful for the optimization of the processes in which these materials are employed.

References:

[1] Pizzanelli, S., Freni, A., Farmahini, A. H., Gordeeva, L. G., Sarkisov, L., Solovyeva, M. V., Forte, C., "Water Dynamics in NH_2-MIL-125: Insights from a Combined ^1H NMR Relaxometry and Computational Investigation", Journal of Chemical Physics, 2021.

[2] Stapf, S., Kimmich, R., Niess, J., "Microstructure of Porous Media and Field-Cycling Nuclear Magnetic Relaxation Spectroscopy", Journal of Applied Physics, 1994.

Feedheat-based electricity storage system for nuclear plant

James W Lazenby[1*]**, Eugene Shwageraus**[1]**, Alexander J White**[1]

[1]University of Cambridge, Department of Engineering, Trumpington Street, Cambridge CB2 1PZ, UK

*Corresponding author: jwl47@cam.ac.uk

Abstract

An energy storage concept which links thermal stores to the feedwater heating system of a nuclear-powered steam plant is described. The storage scheme allows the plant's electricity output to be varied while keeping reactor power constant, thereby enabling the nuclear plant to take on a load-following role. This type of 'generation-integrated' energy storage uses existing hardware to reduce storage costs and provides the equivalent of a high-efficiency electricity storage system. Surplus feedwater is generated during charge, which may be either stored directly or used to transfer energy to a 'sensible-heat' medium. By exploiting the multiple pressure bleed flows, this process is conducted with very little exergetic loss. The paper discusses (1) the off-design behaviour of steam cycle components and (2) the effect of storage heat-transfer effectiveness.

Keywords: energy storage, nuclear, generation-integrated, feedwater heating, dispatchable

Introduction

Conventional fossil-fired electricity generators are highly dispatchable; they can easily vary power output to match demand. However, due to the increasing decarbonisation of the electricity system, these conventional generators are being replaced by intermittent renewable energy sources, such as wind and solar. The increasing uptake of variable and non-dispatchable generators is resulting in difficulties balancing the electricity system [1].

Energy storage systems are one solution for balancing electricity grids with a high share of intermittent generators (other options include, gas-fired peaking power plants, interconnectors, demand-side response, etc.). However, the amount of required energy storage remains very uncertain, with order-of-magnitude differences between estimates within the literature. For example, in a survey of 400 future energy scenarios, Cebulla *et al.* show that estimated power capacity rises linearly with the fraction of electricity generated by variable renewable sources, whereas estimated energy capacity rises exponentially [2]. As such, a moderate amount of 'baseload' nuclear may reduce the quantity of required storage (and therefore total system cost). In addition to reducing the amount of storage, nuclear plants also provide an effective means for 'generation-integrated energy storage', whereby existing electricity conversion pathways can be exploited for sizeable energy storage systems (see Ref. [3] for further discussion on conventional versus generation-integrated energy storage).

The concept of feedheat-integrated storage is not new, being first proposed by Marguerre in a series of German patents filed in the 1920s and 1930s [4, 5, 6]. A full account of its history is given in Ref. [7]. However it appears to have been overlooked in the recent literature on flexing nuclear plant, and it is timely to revisit it in the context of increased renewable penetration.

A detailed thermodynamic analysis of an integrated feedheating storage system is provided in Ref. [7]. One of the main attractive features of this system is that the feedwater going through the steam generator and the reactor power are fixed – i.e., the most expensive piece of the plant (the reactor) has a 100% capacity factor. The scope of the present paper is to (1) describe

the concept and its key features on the basis of previously conducted analysis and (2) extend the previous analysis to study the impact of the type of thermal storage on the overall system performance. The latter is interesting as it highlights the compromises the plant designer will have to make between cycle performance, round-trip storage efficiency, and overall system cost.

Discussion and Results

Description of feedheat storage system

A detailed description of this concept has been presented elsewhere (Ref. [7]) but is summarised here for completeness. The layout for a typical thermal storage system integrated with nuclear plant is shown in Fig. 1. The main features are as follows:

i. During charge a surplus of feedwater, f, is heated by increasing turbine bleed flows, thereby reducing the work output. Thus, as indicated in Fig. 1, the mass flow of feedwater is increased to $1 + f$ per unit mass flow through the steam generator.

ii. The excess fraction of feedwater, f, can either be stored directly in pressurised vessels or used to transfer heat into a thermal storage system, such as tanks of thermal oil or (via an intermediary heat-transfer fluid) packed beds of gravel. Irrespective of the storage method, this process is modelled here by means of a heat-transfer effectiveness, ϵ, which is assumed to have the same value in each direction (i.e., into and out of storage).

iii. The system is discharged by reducing the quantity of feedwater generated below its nominal value (i.e., f is made negative). This is achieved by reducing turbine bleed flow rates. The work output from the turbine therefore increases. The extent to which this is possible depends on the turbine swallowing capacity and is essentially a design choice.

iv. The round trip efficiency for the system may be defined as:

$$\eta_{\mathrm{RT}} = \frac{\Delta W_{\mathrm{dis}}}{\Delta W_{\mathrm{chg}}} \tag{1}$$

where ΔW_{dis} and ΔW_{chg} are respectively, the surplus electrical work output during discharge and the deficit in electrical work output during charge, for a cycle that returns the storage system to its initial state.

Recent thermodynamic analysis

Work to-date has focused on modelling the integration of storage with a steam cycle representative of a large ($\approx 1\mathrm{GWe}$) pressurised water reactor nuclear power station. The layout and nominal operating conditions (design-point) are closely based on the Sizewell B station, detailed in Ref. [8]. Since PWRs are the most prevalent existing and new-build reactor type, the following analysis will be relevant for most nuclear plant designers. The key results are:

i. The process of extracting heat during charge is achieved in an exergetically efficient manner because multiple-pressure bleed flows are exploited. This enables a good match between the temperature profiles of the condensing steam and the heated water, as shown in the *T-Q* diagram of Fig. 2. Note that this would not be the case for some current technologies which focus on extracting heat from live steam, frequently with storage in phase-change materials.
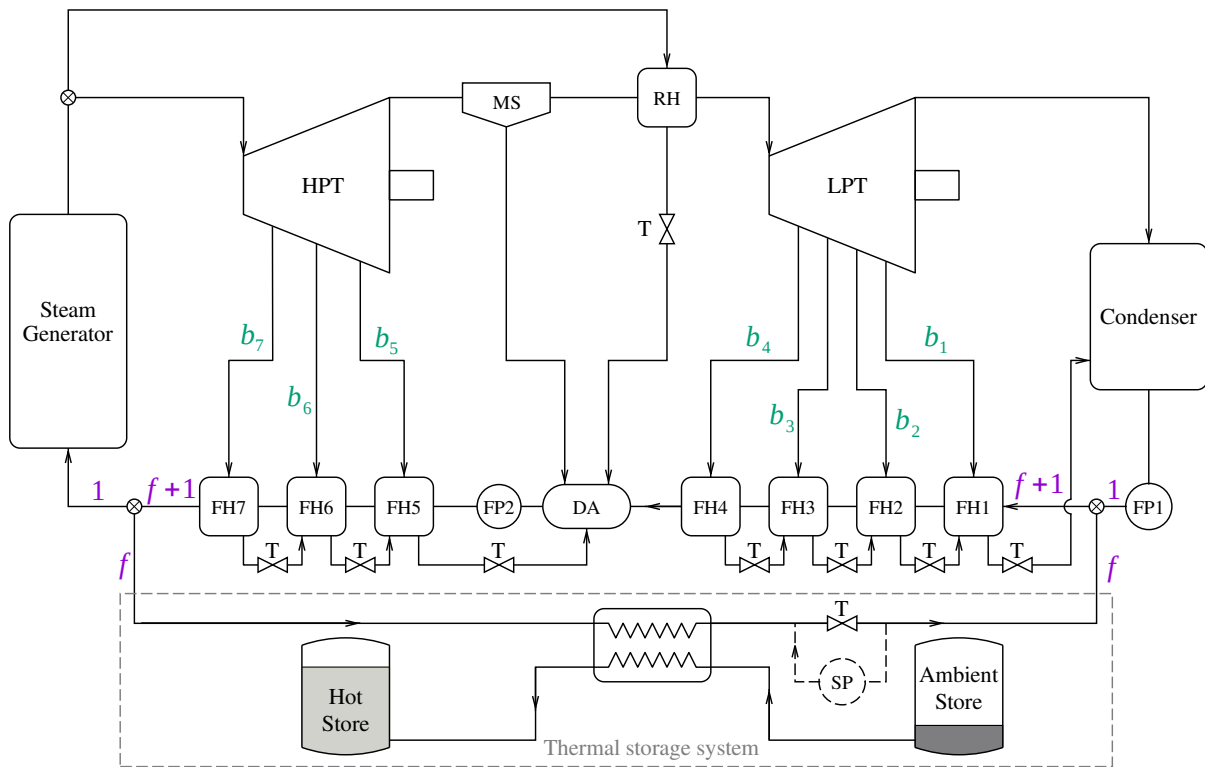
Figure 1. Schematic of plant with thermal storage during charge. HPT = high pressure turbine; LPT = low pressure turbine(s); MS = moisture separator; RH = reheater; FH = feedheater; FP = feed pump; DA = deaerator; T = throttle; SP = storage pump (replaces throttle downstream of the heat exchanger during discharge). Purple text indicates flow fractions through the feedheat train and storage system. Green text indicates the bleed flows. All flows are represented as a fraction of steam generator inlet. Reproduced from Fig. 2 in Ref. [7].
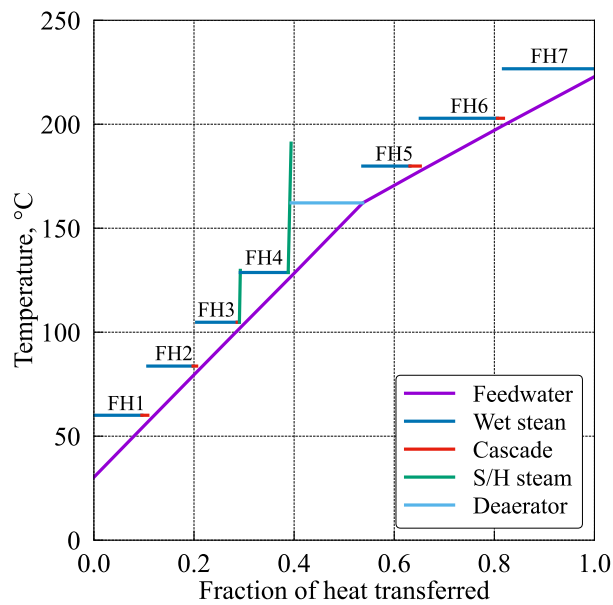
Figure 2. *T-Q* plot of the feedheating train, showing the closely matched bled steam and feedwater temperature profiles. 'S/H' refers to superheated steam. Reproduced from Fig. 2 in Ref. [7].

ii. Changing the feedwater generation rate (i.e., varying f) causes the feedheaters to operate at off-design conditions, which has a knock-on effect for storage temperatures and turbine flow rates. However, results demonstrate that departures from the nominal design-point have only a small impact on feedheat operation and hence on the performance of the system.

iii. For a simplified system without moisture separation and reheat, there is a simple relationship (derived in Ref. [7]) between the f and the deficit / surplus of net work generated by the turbines, Δw, namely

$$\frac{\Delta w}{w_0} = f \left(\frac{\Delta h_t}{w_0} - 1 \right) \tag{2}$$

where w_0 is the net work output under normal operation, and Δh_t is the drop in specific enthalpy across the turbine. Typically this gives around 0.3% decrease / increase in work output for each 1% change in feedwater flow rate.

iv. The addition of reheating and moisture separation between the turbines means this simple relationship is no longer true, and the high-pressure and low-pressure feedheaters are affected to different degrees. As f decreases, the quantity of steam extracted from the HPT bleeds decreases, leading to an increase in its exhaust flow rate. To maintain the desired degree of superheating at the LPT inlet, the proportion of live steam diverted to the reheater must also increase. As a result, the hot drain flows from the moisture separator and reheater to the deaerator increase. This leads to a rise in the temperature of the feedwater entering the first feedheater in the high-pressure train (FH5).

v. Throughflow calculations have indicated that modest changes to the turbine bleed flows can be accommodated without incurring a significant penalty on turbine efficiency [7]. This is important because varying the bleed flows will evidently impact the 'velocity triangles' and the aerodynamic performance of the turbines. This is important as it ensures the reduction in efficiency resulting from such off-design conditions is not significant enough to outweigh the amount of stored work.

Principle exergy transfers and lost work

Fig. 3(a) shows the main exergy transfers to and from the cycle as well as the total lost work term, as f is varied from -0.5 to 0.5 (i.e., the flow in the train is $50\% - 150\%$ of nominal). In this case, the storage system was modelled with a constant effectiveness, $\epsilon = 0.95$, and all values were normalised by exergetic input from the steam generator. Note that the exergy input, e_{in}, comprises input from the steam generator and from storage. Hence, values are greater than 1 during discharge and less than 1 during charge. The net work term, w_{n}, is defined as the work output from the turbines minus the work input to the feed pumps (and the storage pump during discharge). It is apparent that at maximum discharge ($f = -0.5$) the net work output increases by 10% and at maximum charge ($f = 0.5$) the net work output decreases by 12%. This can roughly be expressed as a '$\Delta w_{\text{n}}/\Delta f$' term, where each 1% change in feedwater through the feedheating train results in a 0.20% change in net work output during discharge and a -0.24% change in net work output during charge.

Fig. 3(b) shows how the 'lost work' terms vary with f. These are the exergetic losses due to irreversibility ($T_0 \Delta s_{\text{irr}}$) in the various cycle components and have also been normalised by exergetic input from the steam generator. As expected, when the flow through the feedheat train increases (as f become more positive), so do irreversibilities associated with the feedheating
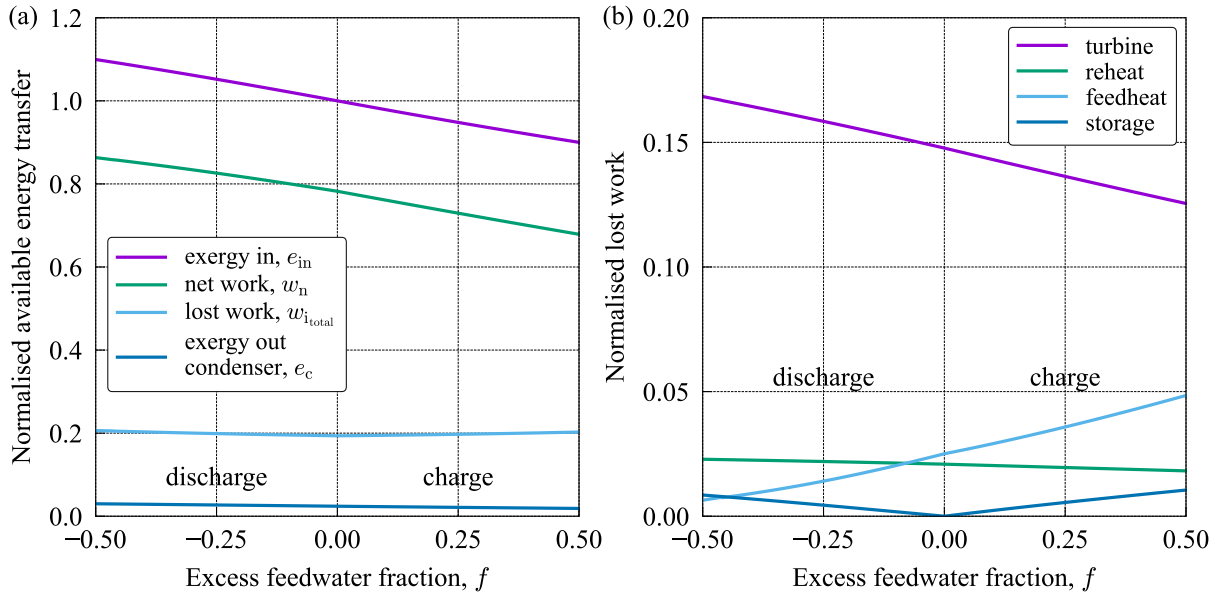
Figure 3. (a) Principal exergy transfers as a function of f, normalised by steam generator exergy input; (b) Lost work processes, also normalised by steam generator exergy input. Note that e_{in} is the net exergy input from both the steam generator and storage. Values are for a storage system with effectiveness of 0.95.

processes. However, this loss is almost perfectly balanced by a decrease in turbine irreversibilities. Turbine losses are lower due to greater bleed flows, which means less flow undergoes the irreversible expansion process. The opposite occurs during discharge, where feedheat losses are reduced, but turbine losses increase.

Impact of effectiveness on plant performance

So far the analysis has been conducted with a constant effectiveness ($\epsilon = 0.95$), to model thermal storage losses. However, in reality, ϵ will depend on the type of storage. Possible options include:

i. Direct pressurised feedwater storage – does not require an additional heat-exchange process and so, barring heat leakage losses, should achieve an effectiveness very close to unity.

ii. Indirect liquid-tank storage – as shown in Fig. 1, requires a storage heat exchanger but by balancing the heat carrying capacity of the two streams, high effectiveness can be achieved. As an example, $\epsilon = 0.90$ corresponds to an approximately $17°\mathrm{C}$ uniform temperature difference between the streams and requires an $\mathrm{NTU} \approx 9$ (counterflow heat exchanger).

iii. Packed-bed storage – requires an intermediate heat-transfer fluid in order to avoid pressuring the containment. This causes an extra level of heat transfer so values of ϵ are likely to be lower.

On the basis of the above, we consider ϵ in the range of 0.85 to 0.99. Note that this is for each direction of the heat exchange – i.e., charge and discharge. (It is also worth noting that 'off-design' factors, such as varying f, will also affect ϵ.) Roughly speaking, $\epsilon = 0.99$ corresponds to direct feedwater storage, $\epsilon = 0.90$ to indirect oil storage, and $\epsilon = 0.85$ to packed-bed storage. Clearly the plant designer must compromise between increased effectiveness (moderately analogous with efficiency) and costly heat exchange equipment, pressure vessels, and/or heat-transfer fluids. Further discussion of storage options can be found in [7].

Fig. 4 characterises general changes in cycle performance as the excess feedwater fraction is varied for different values of ϵ. Broadly, this illustrates the differences between thermal storage options. Fig. 4(a) shows how ϵ impacts the exergy input to the cycle and net work output from the cycle. Again, note that values are normalised by steam generator input and that e_{in} is the sum of exergy input from the steam generator and the storage system. (The lost work term and exergy rejected by the condenser are not shown due to maximum variations of only 0.4% and 1.25% at the lowest case $\epsilon = 0.85$.)

As expected, higher values of ϵ result in greater exergy transfer to and from storage, which causes a greater flex of the net work output. For each 1% increase in ϵ, the change in net work output increases by 0.26% during discharge and decreases by 0.08% during charge. The difference between these values occurs because as the feedheaters move away from their design points, their feedwater outlet temperatures vary. The last feedheater before the steam generator (FH7) experiences a higher temperature rise as f is decreased (discharge) and a lower temperature rise as f is increased (charge). As such, not only is the magnitude of f contributing to the transfer of exergy with storage, so is the temperature of the flow entering the storage heat exchanger, which sets the maximum amount of possible heat transfer (and exergy transfer).

This analysis assumes the storage system is charged and discharged with f values of equivalent magnitude – i.e., $f_{\text{dis}} = -f_{\text{chg}}$ (note that this is not required, and is just for ease of presentation). Barring heat leakage losses, the energy storage capacities in MW and MWh will be equal for f of the same magnitude. However, as shown and explained in a later figure, the temperature difference between the thermal stores and cycle integration points decreases with lower values of ϵ. As such, there is a loss of exergy in the storage heat exchanger and it makes sense to define an 'exegetic effectiveness' term as

$$\epsilon_{\text{2nd}} = \frac{e_{\text{act}}}{e_{\text{max}}} \tag{3}$$

where e_{max} is the maximum possible exergy transfer between cycle and storage, and e_{act} is the actual amount of exergy transfer.

Fig. 4(b) shows how ϵ_{2nd} varies as a function of 'first law' effectiveness, ϵ. As expected, for a perfect storage system both $\epsilon = 1$ and $\epsilon_{\text{2nd}} = 1$. This is not the case at lower values of ϵ where ϵ_{2nd} decreases at a faster rate for both the charge and discharge lines. Lower values occur because of reduced temperatures in the storage heat exchanger (a full discussion on storage heat exchanger temperatures is included later).

Fig. 4(c) shows η_{RT}, previously defined in Eq.(1), as a function of f and contains contours of ϵ values. (Note, again, that for this analysis it was assumed the storage system was charged and discharged at f values of the same magnitude. Further discussions on efficiency and the affect of different charge and discharge magnitudes can be found in Ref. [7].) As f approaches ≈ -0.45, the hot drain flows of the reheater and moisture separator increase the inlet feedwater temperature of the first high-pressure feedheater (FH5) beyond the temperature of its bled steam. This causes it to 'shut down' and results in a small decrease in efficiency due to greater heat-transfer losses in the subsequent feedheater (FH6). This give rise to the discontinuity in Fig. 4(c) at $|f| \approx 0.45$.

As previously illustrated in Fig. 3(b), turbine and feedheating irreversibilities are the dominant lost work terms. Fig. 4(d) shows the absolute change in these values from their nominal design point (values are still normalised by steam generator exergy input). As can be seen, these losses are inversely proportional to each other and similar in magnitude. This aids system
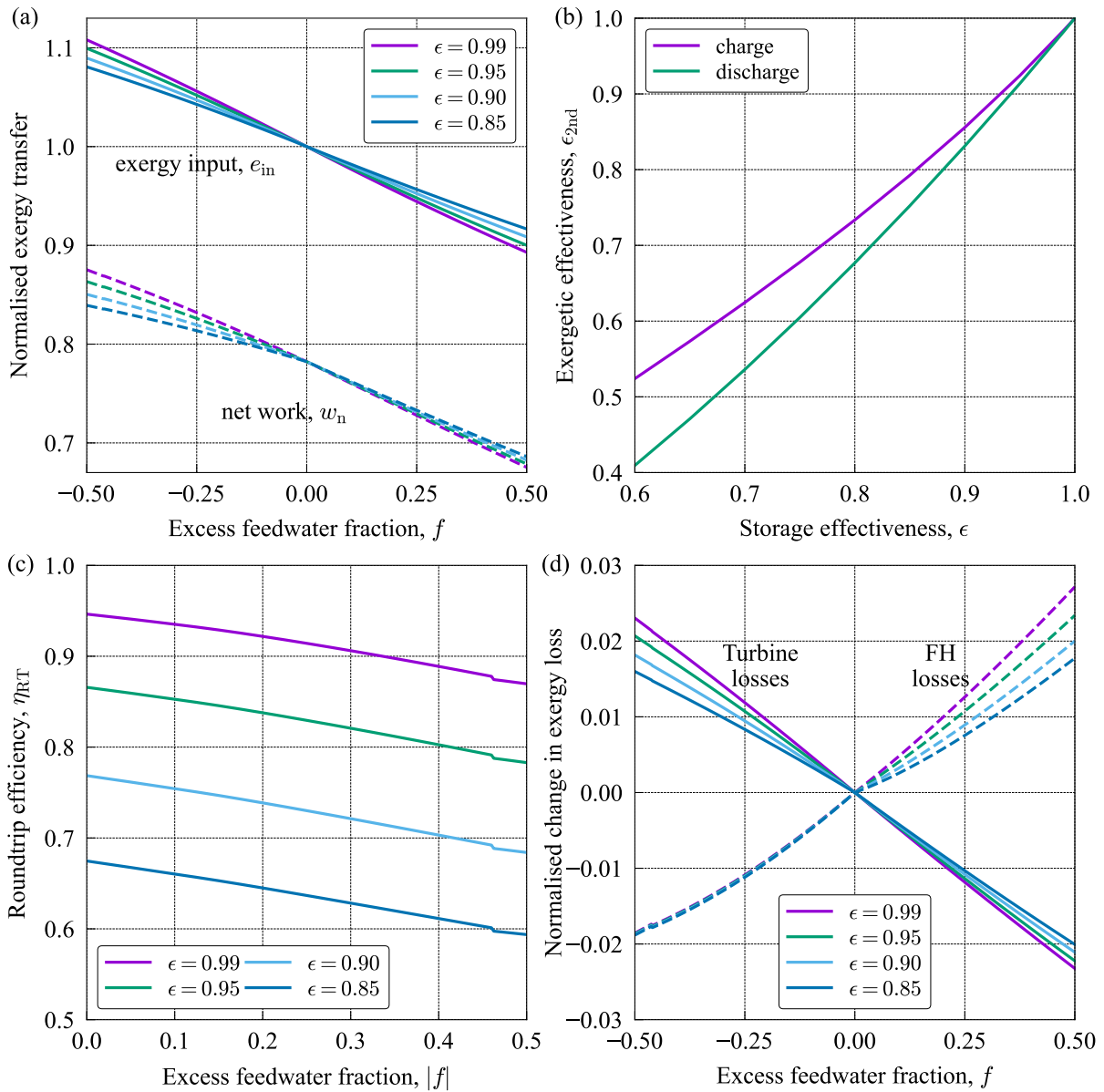
Figure 4. Plant performance at varying values of storage effectiveness: (a) total exergy in (solid lines) and net work output (dashed lines), as a function of f; (b) equivalent exegetic effectivenesses as a function of 'first law' heat-transfer effectiveness; (c) round trip storage efficiency; (d) comparison of lost work in turbine expansion (solid lines) and feedheaters (dashed lines).
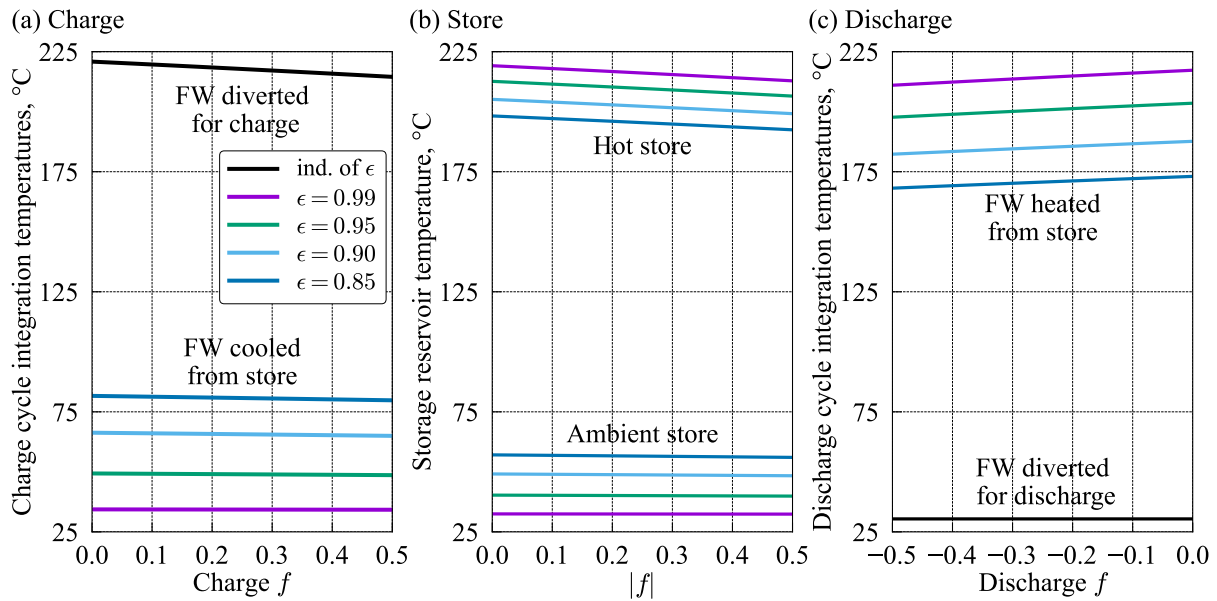
Figure 5. Cycle and storage temperatures at varying values of storage effectiveness: (a) charge temperatures of the feedwater diverted from cycle (split from FH7 exit) and feedwater returned to cycle (mixed at FH1 inlet); (b) storage temperatures; (c) discharge temperatures of the feedwater diverted from cycle (split from FH1 inlet) and feedwater returned to cycle (mixed at FH7 exit). Black lines indicate values are independent (ind.) of storage effectivenesses.

performance as, even at maximum charge and discharge rates, the total lost work term remains approximately constant.

Impact of effectiveness on storage temperatures

The thermal storage process can be divided into three main 'temperature pairs' – i.e., the cycle-side integration temperatures during charge, the storage reservoir temperatures (same for charge and discharge), and the cycle-side integration temperatures during discharge. These temperature profiles, and how they vary with ϵ, are shown in Fig. 5. The charge process begins by diverting hot feedwater from the exit of the final feedheater (FH7). Its outlet temperature decreases by $0.13°C$ for each 1% increase in f, this is due to reduced NTUs at off-design charge conditions. However, this temperature profile is independent of ϵ and, as such, is denoted by the black line in Fig. 5(a). As expected, the temperature of the feedwater cooled from the store, is directly proportional to ϵ. For each 1% decrease in storage effectiveness, the feedwater returned to the cycle increases by $3.3°C$.

Fig. 5(b) shows the temperatures of the hot and ambient stores. It is worth noting that the temperature difference between the hot store and ambient store decreases by $3°C$ for every 1% reduction in storage effectiveness. The temperature variation of the hot side varies more with f since the level of allowable heat transfer is set by the feedwater diverted for charge, which is dependant on f.

The cycle-side integration temperatures during discharge are shown in Fig. 5(c). The feedwater diverted to storage for heating is denoted by the black line, since it remains constant, as its conditions are set by the condenser exit which always maintains saturated liquid at its outlet. As expected, ϵ is directly proportional to the temperature of the feedwater returned during discharge. For each 1% increase in ϵ, the returned feedwater increases by $3.1°C$. The variation of the returned feedwater temperature with respect to f is due to the existing dependence of the hot store temperature on f; it sets the limit for maximum allowed heat transfer.
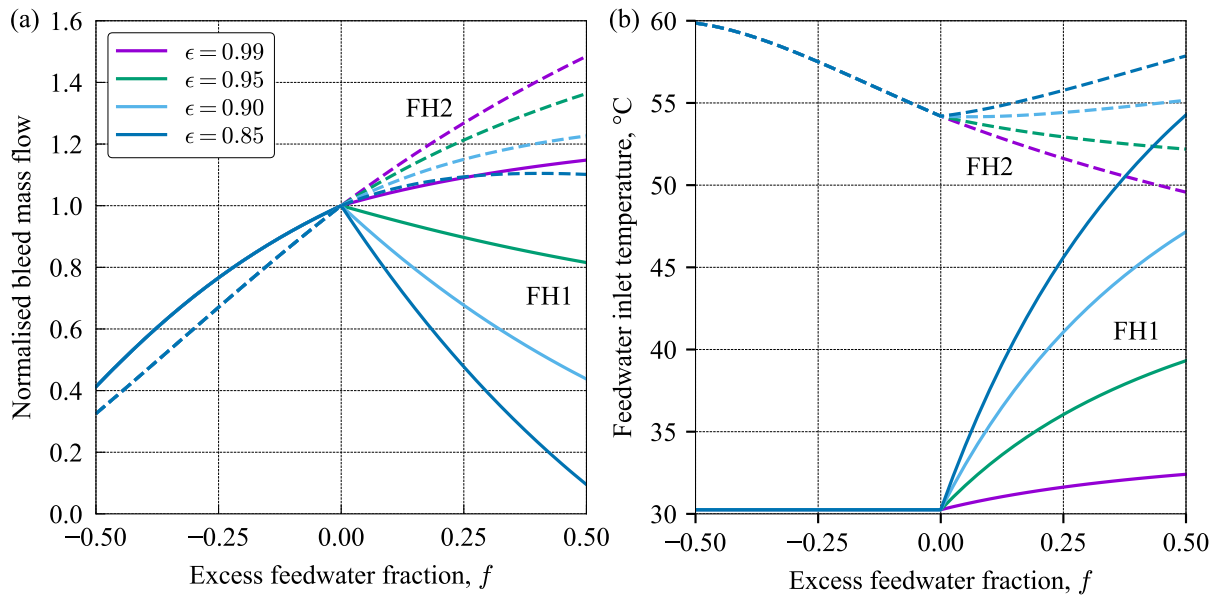
Figure 6. Impact of storage effectiveness on the first feedheater (FH1) and second feedheater (FH2): (a) bleed flow rates normalised by design point; (b) inlet feedwater temperature. Solid lines are FH1, dashed lines are FH2.

Impact of effectiveness on bleed flows

The proposed storage scheme relies on sufficient off-design performance of the feedheaters, to ensure exergetically efficient heat transfer. It has been demonstrated for $\epsilon = 0.95$, that off-design operation does cause non-uniform bleed flows and temperature rises across the feed-heat train Ref. [7]. However these deviations do not result in excessive degradation of system performance. Fig. 6(a) and Fig. 6(b) show respectively, how the bleed flow rates and inlet temperatures vary for the very first feedheater (FH1, solid lines) and the second feedheater (FH2, dashed lines) when $\epsilon = 0.85, 0.90, 0.95$, and 0.99. As shown for the discharge processes, the normalised bleed flow fractions and inlet temperatures are independent of ϵ. This is because the storage flow is reintroduced to the cycle before the inlet to the steam generator.

During charge, the feedwater which enters the first feedheater (FH1) is a mix of the condenser outlet flow and flow re-integrated from storage. As such, when ϵ is reduced, the returned flow is hotter (unable to transfer as much heat to storage) and its inlet feedwater temperature increases. This is similar to second feedheater (FH2) which also sees an increase in its inlet temperature with a reduction in ϵ, but to a lesser extent. The increase in temperature means less flow must be bled from the corresponding bleed ports. This trend propagates throughout the low-pressure train. After mixing of the moisture separator and reheater drains in the deaerator, the inlet to the high-pressure train has stabilised – i.e., the high-pressure feedheaters are independent of ϵ, but are still dependant on f.

Conclusions

The paper presented the integration of thermal energy storage with the feedwater heating system of a nuclear steam plant. The aim was to increase plant dispatchability while maintaining constant power output from the reactor; thereby enabling nuclear plant to perform a 'load-following' role (replacing the function of fossil-fired generators in low-carbon energy systems). Detailed consideration was given to the thermodynamic off-design modelling of the feedheaters, as well as understanding the impact of storage heat-transfer effectiveness. The following conclusions can be made:

i. By transferring heat with the proposed storage system, the net work output of nuclear plant can flex by $\pm 10\%$ while maintaining constant reactor power. Since the system exploits existing hardware and the efficient feedwater heating system, the equivalent of a low-cost electricity storage system can be achieved.

ii. The generation-integrated energy storage system incurs exegetic losses through two mechanisms: (1) off-design operation of components in the steam cycle as the excess feedwater fraction, f, is varied and (2) heat transfer to/from the storage system. For an ideal storage system ($\epsilon = 1.0$), each 1% change in feedwater through the feedheating train results in a 0.24% (discharge) and -0.29% (charge) change in net work output. This $\Delta w_{\mathrm{n}}/\Delta f$ figure falls at greater rates as ϵ is reduced, due to increasing exergetic loss in the heat exchange processes. (e.g. when $\epsilon = 0.95$, $\Delta w_{\mathrm{n}}/\Delta f$ is 0.20% for discharge and -0.25% for charge, for each 1% change in feedwater.)

iii. The cycle calculations for a storage system with $\epsilon = 0.95$, showed that an effective round-trip storage efficiency of around 80% can be achieved. This is relatively high for a thermo-mechanical storage system and reflects the fact that heat storage occurs prior to conversion to electricity, so that exergetic losses that would occur anyway are simply deferred.

iv. Off-design analysis of the feedheating system demonstrates that departures from the nominal conditions has only a small impact on feedheat operation and hence on the performance of the cycle.

v. The effectiveness of the storage system directly sets the temperatures of the hot and ambient stores, as well as the temperature of the feedwater re-integrated with the cycle. The temperature difference between the hot store and ambient store decreases by $3°\mathrm{C}$ for every 1% reduction in storage effectiveness. Moreover, during charge, lower effectiveness results in warmer feedwater reintroduced to the cycle which causes additional non-uniform bleed flows in the LPT.

Future work will include: optimisation of the condenser vacuum to minimise required cooling water while maximising the net work output; integrating storage around only the high-pressure train or low-pressure train; implementing storage with small module reactors and co-generation plants; detailed cost estimates, both per KW and per kWh capacity.

References

[1] National Grid ESO. Future energy scenarios. Technical report, July 2022.

[2] Felix Cebulla, Jannik Haas, Josh Eichman, Wolfgang Nowak, and Pierluigi Mancarella. How much electrical energy storage do we need? A synthesis for the U.S., Europe, and Germany. *Journal of Cleaner Production*, 181:449–459, April 2018.

[3] S.D. Garvey, P.C. Eames, J.H. Wang, A.J. Pimm, M. Waterson, R.S. MacKay, M. Giulietti, L.C. Flatley, M. Thomson, J. Barton, D.J. Evans, J. Busby, and J.E. Garvey. On generation-integrated energy storage. *Energy Policy*, 86:544–551, November 2015.

[4] Fritz Marguerre. Improvements in or relating to steam power plants, UK Patent 359140, Oct. 1931.

[5] Fritz Marguerre. Improvements in or relating to steam power plants, UK Patent 381924, Oct. 1932.

[6] P.H. Margen. Thermal energy storage in rock chambers - a complement to nuclear power. In *Fourth United Nations International Conference on the Peaceful Uses of Atomic Energy - September, 1971*, Geneva, Switzerland, 1971.

[7] James Lazenby, Eugene Shwageraus, and Alexander White. An integrated energy-storage system for nuclear-powered steam plant. *Manuscript submitted for publication*, 2023.

[8] J A Hesketh and J Muscroft. Steam turbine generators for Sizewell B nuclear power station. *Proceedings of the Institution of Mechanical Engineers, Part A: Journal of Power and Energy*, 204(3):183–191, August 1990.

Adsorption heat and mass conversion cycles for direct air capture

L. Jiang[1,*], W. Liu[1], T. Wang[2] and X. J. Zhang[1]

[1]Institute of Refrigeration and Cryogenics. Zhejiang University, Hangzhou. 310027, China

[2] Key Laboratory of Clean Energy and Carbon Neutrality of Zhejiang Province, Zhejiang University, Hangzhou. 310027, China

[*]Corresponding author: email address jianglong@zju.edu.cn

Abstract

Direct air capture is gathering the momentum to achieve the target of carbon neutrality. However, common amine scrubbing technologies may lead to some issues, e.g., degradation of sorption capacity and high regeneration energy consumption. Comparably, adsorptive carbon capture draws more attention has a reasonable energy input, especially considering the integration of other potential technologies. This work aims to present adsorption heat and mass conversion cycles for direct air capture (DAC). Two typical adsorbents are selected for the approaches of DAC, i.e., amine-functioned and commercial quaternate resin which are used to illustrate temperature swing adsorption (TSA) and moisture swing adsorption (MSA), respectively. Then, the integrated DAC systems with heat pumps and compressed air energy storage (CAES) are proposed to provide the improved capture performance. It is demonstrated that the integrated adsorption DAC may be a promising solution to reduce energy consumption in the near future.

Keywords: Adsorption, Heat and mass conversion, Direct air capture, Thermodynamics

Introduction

The urgency to address global climate change has been correlated to the increasing levels of carbon dioxide (CO_2) in the atmosphere, which generates an alarm all over the world [1]. To limit the global 2 °C temperature rise as a consensus reached in the Paris Agreement, the united efforts and effective actions are indispensable [2, 3]. Adsorption capture technology has received widespread attention in recent years due to the advantages of low cost and high efficiency [4]. Direct air capture (DAC), as one of the negative emission technologies (NETs) that combines the characteristics of safety, efficiency, and cost-effectiveness [5, 6], is highly recommended. In addition, DAC technology is not limited by geographical sites, and it can even be located near the site of CO_2 employment and storage without transport costs [7]. CO_2 sources of DAC are also much cleaner.

It is paramount to design an efficient DAC process to meet energy and cost requirements for commercialization. Adsorption DAC processes could be mainly classified into temperature swing adsorption (TSA) [8], vacuum swing adsorption (VSA), humid swing adsorption (HSA) [9]. TSA is a heat driven process which is quite attractive with its simple system design, whereas its production CO_2 is diluted [10]. VSA is not practical for DAC due to the extremely low vacuum levels [10]. As the combination of vacuum and temperature swing processes, temperature-vacuum swing adsorption (TVSA) is a cost-effective process, and it has been used widely in DAC applications [11]. Moreover, for the single-bed cycle using activated carbon, Plaza et al. [12] found that the productivity and the recovery of desorbed CO_2 followed the order: TVSA>VSA>TSA. Hence, the cyclic operation of TVSA would also be energy efficient and is adopted in this work. To optimize TVSA cycle, many attempts have been conducted. For instance, Sinha et al. [13] performed a modeling study and economic

assessment on a five-step TVSA process for DAC by using steam as the stripping agent during the desorption process. Elfving et al. [14] studied the effects of cold conditions and humidity (2 vol% H_2O) on the equilibrium CO_2 working capacities in PSA, TSA, and TVSA. The results implied that TVSA was only considered when requiring a high-purity CO_2. The current researches mainly lies in both materials and process modelling. The basic mechanism of working cycles of DAC is not clear especially for heat and mass conversion processes as well as the intergration with other current energy saving technologies.

The objective of this work is to present adsorption heat and mass conversion cycles for DAC. Thermal cycle of MSA is first proposed as a mass conversion cycle for DAC which is also compared with TSA as a heat conversion cycle. Also two types of the integrated systems for DAC, i.e., heat pump assisted cycle and compressed air energy storage (CAES) assisted cycle are proposed and compared in terms of cycle concept, thermal performance and future potential.

General concepts

Fig. 1 indicates a schematic diagram of a basic 4-step TSA cycle, which could be classifed as a heat conversion cycle due to that fact that only heat is inputted to drive the working cycle. It is generally composed of adsorption, preheating, desorption and precooling. The complete thermal cycle is 1-2-3-4-1. Step 1-2 is an adsorption process. In this process, gas mixture, i.e., N_2/CO_2 flow into adsorption reactor. Then CO_2 is adsorbed by adsorbent, and cooling medium will take away adsorption heat. Theoretical adsorption process could reach point 5 for adsorption stautration. Step 2-3 is a preheating process. The temperature of adsorption reactor is increased but no CO_2 is desorbed. Step 3-4 is a desorption process. Temperature of adsorption reactor is increased and N_2 purge is used sequentially. After temperature reaching T_3 of point 3, CO_2 adsorption capacity for the reactor is higher than the maximum value with the increasing temperature and constant pressure. Step 4-1 is a precooling process. Cooling medium flows into the inner tube for removing the heat from adsorption reactor. Until temperature of reactor decreasing to the original adsorption temperature, the operating conditions are resumed hereafter and a new 4-step TSA cycle will start.

Fig. 2 demonstrate a schematic diagram of a basic 4-step MSA cycle, which is assumed as a mass conversion cycle since the whole process is not concerned with heat input. The sorption and desorption processes are driven by the difference of relative humidity (RH), i.e., the periodic control of partial pressure of water vapor. It is generally composed of adsorption, humidification, desorption, dehumidification. The complete thermal cycle is 1-2-3-4-1. Step 1-2 is an adsorption process. After dehumification process, the adsorbent is ready to adsorb CO_2 at a low RH. Step 2-3 is an humidification process which aims to provide the potential for desorption later. Step 3-4 is an desorption process, which is usually mixed with water vapour. Thus the purity of MSA cycle is not as high as that of TSA. Step 4-1 is an dehumidification process for the regeneration of MSA sorbent by using fan. It is worth noting that energy consumption of MSA can be ideally just meted by free energy of evaporation and just slightly larger than flue gas capture. This method gives the chance of an isothermal sorbent swing, which avoids the sensible heat of working pairs and eliminate reliance on heating, cooling, and pressure-related facilities. It caters to the demands on cost, space, and energy saving.
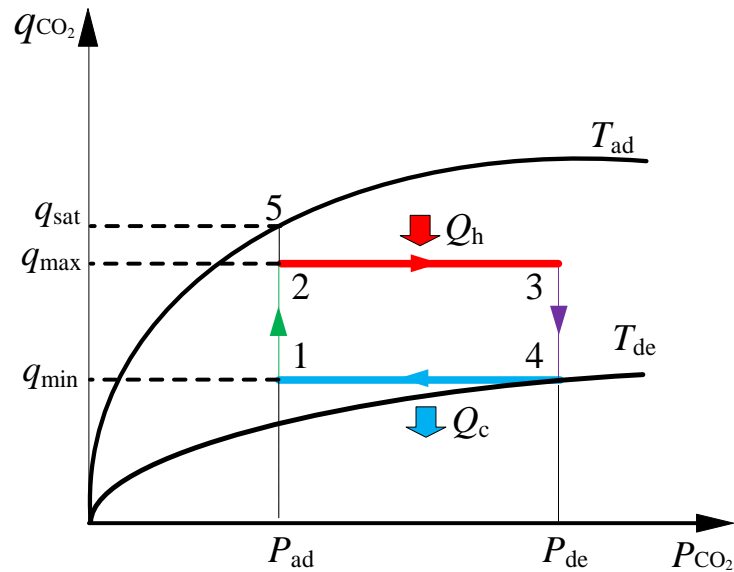
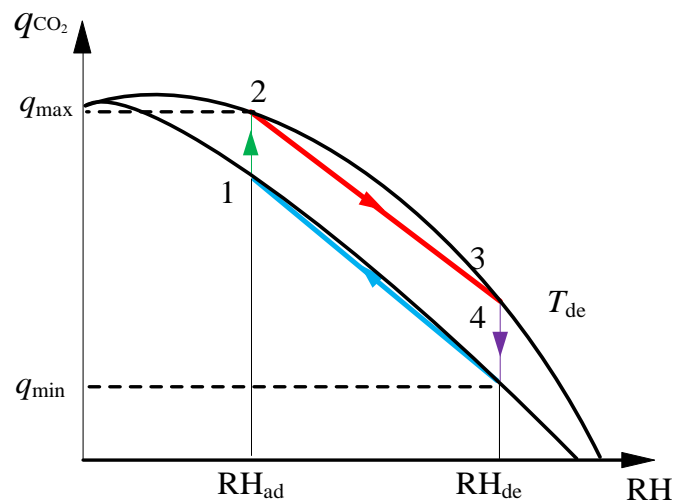Fig. 1. Schematic diagram of a heat conversion cycle: an example of TSA [15, 16].

Fig. 2. Schematic diagram of a mass conversion cycle: an example of MSA [17, 18].

Except for above basic sorption heat and mass conversion cycles, two concepts of the integration systems are presented. Fig. 3 indicates a typical case of heat pump-assisted TSA system in which vapour compression heat pump is used as a case for assistance [19]. Heat output of heat pump could be used to compensate for the regeneration heat whereas evaporation cooling power can be used to reduce the sorption temperature for a high sorption uptake. Temperature ranges of heat pump should well match the adsorption and regeneration temperature ranges of carbon capture. It is worth noting that for DAC, some senarios may happen when considering various extenal working conditions. For the cases with the external heat sources or renewables, e.g., solar energy, a second-type absorption heat pump could be used for DAC technologies since enough heat could be upgraded to meet the requirements in the generation process. If the temperature of heat source is not enough for the regeneration processes, vapour compression heat pump is used as the first stage and absorption heat pump could be used as the second stage for heat supply.

Comparably, Fig. 4 indicates a typical case of MSA with the integration of CAES. Also the heat consumption of regeneration process of MSA is quite low. However, energy consumption, espeically for the fan is also required. Thus the outlet gas of the CAES system after the expander is enough to be utilised as a air source to drive MSA for a low energy consumption of DAC.
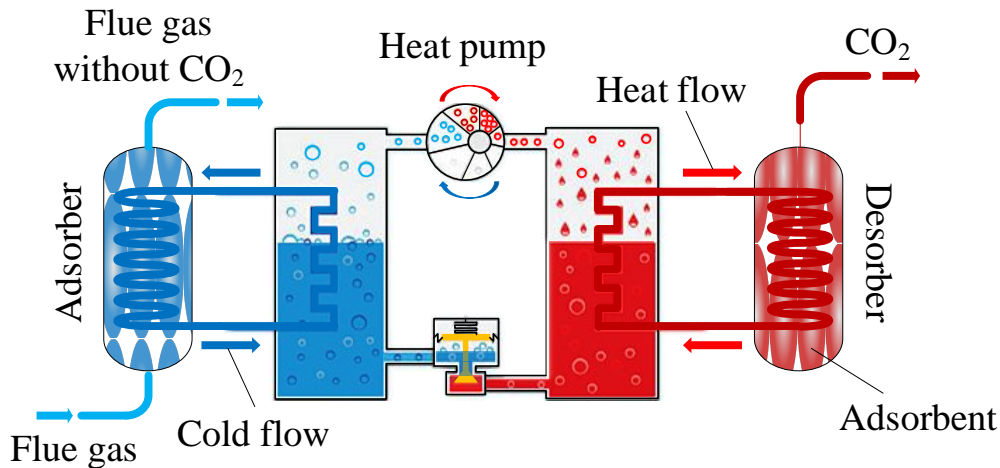
Fig. 3. Schematic diagram of adsorption carbon capture integrated with vapour compression heat pump [19].
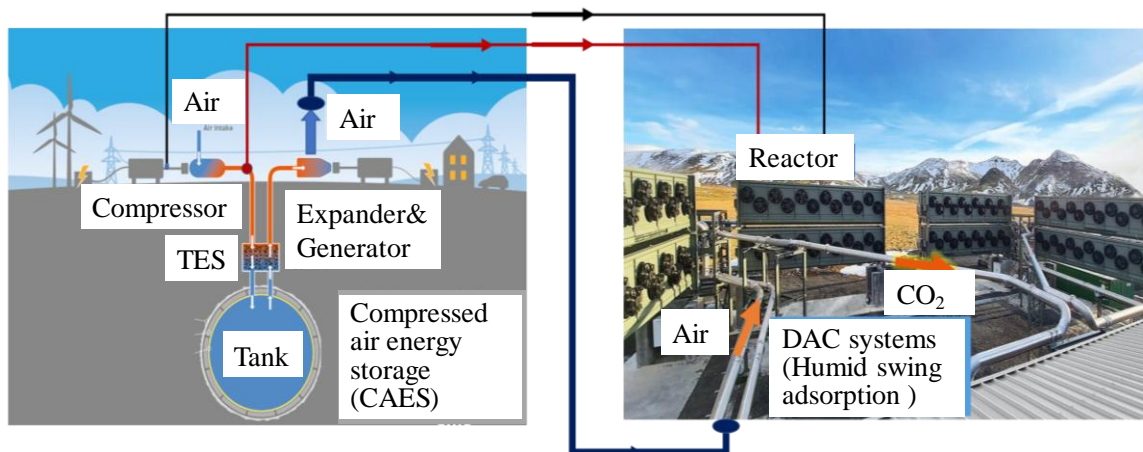
Fig. 4. A typical case of adsorption carbon capture integrated with CAES.

Methodology

In this work, zeolite 13X and Mg-MOF-74 are selected for TSA cycle due to their relativel high sorption capacity among the physical adsorbents. A multi-temperature Toth model is used for CO_2 especially on zeolite 13X and Mg-MOF-74 in low CO_2 partial pressure of DAC [20]. Temperature-dependent form of Toth isotherm are expressed as equation 1.

$$q = \frac{aP_{CO_2}}{[1+(bP_{CO_2})^t]^{1/t}}$$

(1)

where q is the amount of CO_2 adsorbed at equilibrium, mol·kg^{-1}; P_{CO2} is CO_2 partial pressure, kPa; E is a measure of the heat of adsorption, K; b is an equilibrium constant; a is a parameter

related to b and the saturation capacity; t is the Toth isotherm exponent related to surface heterogeneity.

The isotherm parameters of Toth model could refer to the reference [20]., which are fitted from experimental data.

The minimum separation work (W_{min}) for DAC could be calculated by Gibbs free energy equation as a state function. W_{min} is only relevant with heat input temperature T_{in}, CO_2 fraction in the gas mixture y_{CO2} and CO_2 recovery Re_{CO2}, which could be defined as equation 2.

$$W_{min} = G(T_{in}, y_{CO_2}, Re_{CO_2})$$

(2)

Exergy efficiency is the ratio of the minimum separation work to the consumption of the actual work (W_r), which is defined as equation 3, referring to the reference [21].

$$\eta_{ex} = \frac{W_{min}}{W_r} = \frac{W_{min}}{W_{min} + W_{loss}}$$

$$= \frac{W_{min}}{W_s + Q_H(1 - \frac{T_0}{T_H}) - Q_L(1 - \frac{T_0}{T_L})}$$

(3)

where W_s is input work, which is not considered in TSA process due to no extra power apparatus in this study. Q_H is heat input of high temperature heat source; Q_L is heat output of low temperature heat source; T_L is temperature of low temperature heat source, namely adsorption temperature. Similarly, T_H is the desorption temperature.

Heat input of TSA cycle Q_H is composed of latent heat i.e. reaction heat and sensible heat. It could be defined by equation 4.

$$Q_H = (Q_{s,CO_2} + Q_{s,ad} + Q_{s,re} + Q_{L,ad}) / (q_c - q_d)$$

$$= (Q_{s,CO_2} + Q_{s,ad} + Q_{s,re}) / (q_c - q_d) + H_{ad}$$

(4)

where $Q_{s,CO2}$ is sensible heat consumed by adsorbed phase of CO_2, $Q_{s,ad}$ is sensible heat consumed by adsorbent; $Q_{s,re}$ is sensible heat consumed by sorption reactor; $Q_{L,ad}$ is reaction heat.

For MSA, sorption model of the commercial quaternate resin is selected for the analysis which could refer to the reference with experimental data [17, 18]. The electricity consumption of the fan can be calculated as equation 5.

$$W_{fan} = \int_{v_1}^{v_2} \Delta P V_{air}$$

(5)

where ΔP is the pressure drop from inlet to outlet, V_{air} is the volume of air in a cycle.

For calculating energy consumption of evacuation, it is recommended that evacuation is regarded as compression under vacuum to ambient pressure. The electricity consumption of vacuum pump W_{vac} is calculated as equation 6 [22]. For the exergy efficiency could be evaluated by equation 3 in a similar way.

$$W_{vac} = \int_{p_L}^{p_H} V \mathrm{d}p \tag{6}$$

where p_L and p_H is evacuation pressure and ambient pressure in a MSA cycle.

Discussion and Results

Fig. 5 indicates the working performance of 4-step TSA cycle under DAC condition in which regeneration heat and exergy efficiency are described, respectively. It is demonstrated that regeneration heat of zeolite 13X and Mg-MOF-74 increases with the increase of desorption temperature. The regeneration heat of Mg-MOF-74 increases rapidly at the temperature of 35-50 °C, and then is significantly higher than Mg-MOF-74 when temperature is higher than 50 °C. When the temperature increases from 35-70 °C, reaction heat of Mg-MOF-74 has the largest change rate from 63 kJ·mol^{-1} to 899 kJ·mol^{-1}. Also, it could be observed that exergy efficiency increases with the decrease of desorption temperature. Exergy efficiencies of zeolite 13X and Mg-MOF-74 have the similar trends with the increase of the temperature. The highest exergy efficiency of 4-step TSA cycle is able to reach 0.82 which could be obtained at the lowest desorption temperature of 35 °C for zeolite 13X. Exergy efficiency of zeolite 13X is the highest in the range of 35-55 °C, which increases from 0.16 to 0.82. These results could be still reasonable and competitive among common physical sorbents e.g. activated carbon or silica gel.

Fig. 6 indicates the working performance of 4-step MSA cycle under DAC condition in which energy consumption and exergy efficiency are described, respectively. The RH are selected in the common ranges between 55% and 90% since the lower RH cannot generate enough CO_2 below this RH. It is demonstrated that energy consumption of the commercial quaternate resin for 4-step MSA decreases with the increase of RH, which ranges from 151 kJ·mol^{-1} and 260 kJ·mol^{-1}. This is mainly because the cycle working CO_2 become extremely low at a RH of 55% and the increase of electricity device e.g. fan is not high. Comparably, exergy efficiencies of the commercial quaternate resin for MSA show a reverse trend due to the fact that the minimum work doesn't much which is related with inlet gas state according to equation 2. The highest exergy efficiency of 4-step MSA cycle is able to reach 0.33 which could be obtained at the highest RH of 90 °C. For different RHs, exergy efficiencies range from 0.19 to 0.33. It could be observed that thermal efficiency range of MSA is less than that of TSA. This is mainly because the electricity and heat are consumed for MSA and TSA respectively which accounts for the different grade of energy.

In order to generally compare MSA with TSA, Table 1 illustrates the performance of CO_2 capture for DAC in terms of capture energy consumption, regeneration temperature, CO_2 product purity and CO_2 recovery rate. It is indicated that capture energy consumption of TSA or TVSA is 60% high than that of MSA. This is mainly because heat consumption for the regeneration accounts fro a large amount of energy consumption for TSA or TVSA while no heat input is required for MSA theoretically. With the integration of heat pump, TSA or TVSA could reduce up to 50% energy consumption. By integrated with CAES, MSA could reduce more than 50% energy consumption since electricity of fan could be covered by the CAES which leave less electricity requirements for MSA. Also MSA could regeneration at ambient temperature around 20-25°C while TSA or TSVA have a regeneration temperature range of 70-160°C. One of the shortcomings of MSA is that CO_2 product purity is usually lower than 85% which is not suitable for carbon conversion processes. A good way of carbon utilization for MSA is to use the product CO_2 to greenhouse for the plants. Comparably, TSA or TVSA could reach both high CO_2 product purity and CO_2 recovery rate.
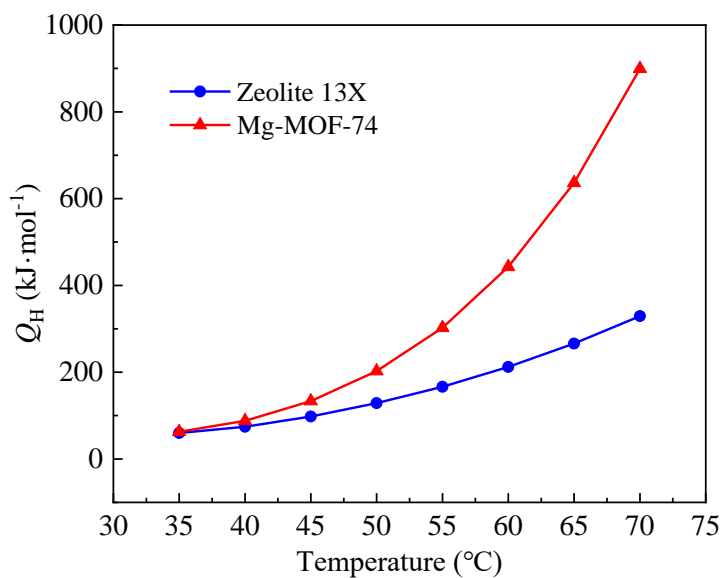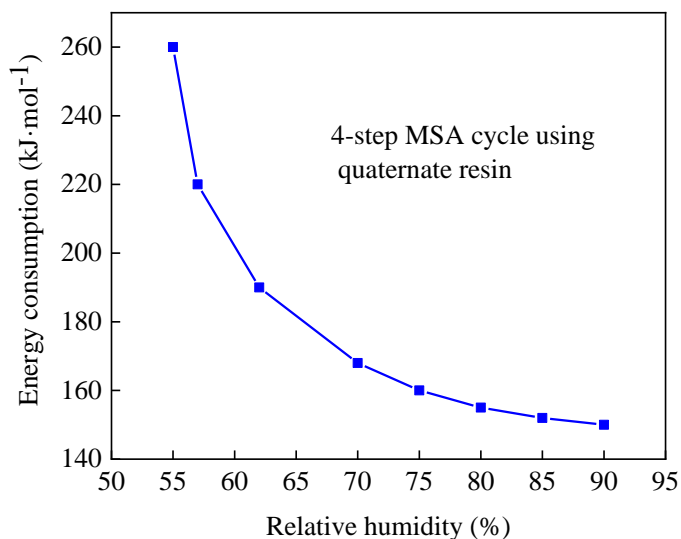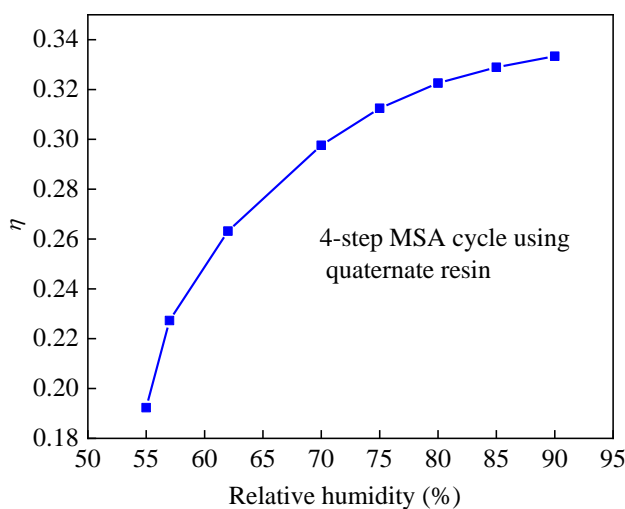
(a)
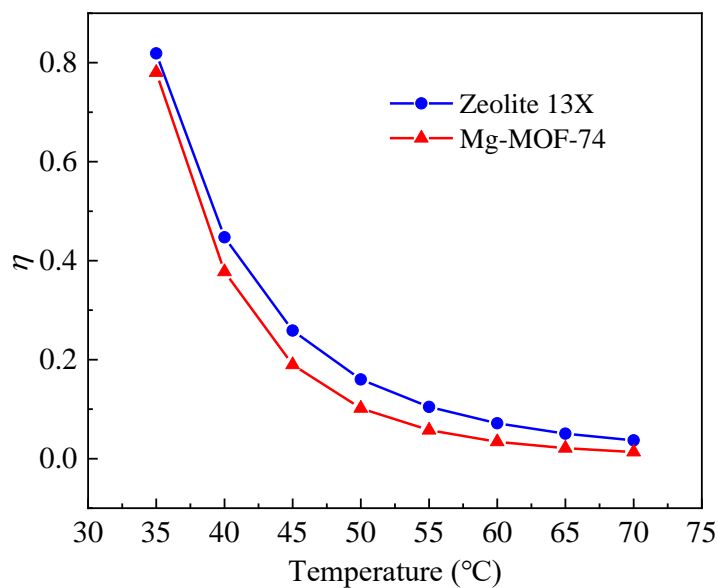
(b)

Fig. 5. Thermal performance of 4-step TSA cycle under DAC condition (a) regeneration heat; (b) exergy efficiencies.

(a)

(b)

Fig. 6. Thermal performance of 4-step MSA cycle under DAC condition (a) energy consumption; (b) exergy efficiencies.

Table 1. Comparison of TSA and MSA for DAC [23, 24].

Types	Energy consumption	Regeneration temperature	CO_2 purity	CO_2 recovery rate
TSA/TVSA	6-8 GJ·t_{co2}	70-160 ^{o}C	>95%,	>90%
TSA/TVSA with heat pump or other heat source	3-4 GJ·t_{co2}	70-160 ^{o}C	>95%,	>90%
MSA	4-5 GJ·t_{co2}	20-25 ^{o}C	>55%; <85%,	>90%
MSA with CAES	1.8-3 GJ·t_{co2}	20-25 ^{o}C	>55%;<85%,	>90%

Conclusions

In this work, adsorption heat and mass conversion cycles are presented for DAC in which TSA and MSA are exemplified as the compared cases, respectively. The main parameters e.g. energy consumption and exergy efficiency are determined by using different adsorbents. Conclusions are yielded as follows:

For TSA cycle of DAC, when the temperature increases from 35-70 ℃, reaction heat of Mg-MOF-74 has the largest change rate from 63 kJ·mol^{-1} to 899 kJ·mol^{-1}. Exergy efficiency of zeolite 13X is the highest in the range of 35-55 °C, which increases from 0.16 to 0.82. These results could be still reasonable and competitive among common physical sorbents e.g. activated carbon or silica gel. For MSA, energy consumption of the commercial quaternate resin ranges from 151 kJ·mol^{-1} and 260 kJ·mol^{-1}. For different RHs, exergy efficiencies of MSA range from 0.19 to 0.33 which is less than that of TSA.

Capture energy consumption of TSA or TVSA is 60% high than that of MSA. With the integration of heat pump, TSA or TVSA could reduce up to 50% energy consumption. By integrated with CAES, MSA could reduce more than 50% energy consumption since electricity of fan could be covered by the CAES which leave less electricity requirements for MSA. One shortcoming of MSA is that CO_2 product purity is usually lower than 85% which is not suitable for carbon conversion processes which is better to use the product CO_2 to greenhouse for the plants. Comparably, TSA or TVSA could reach both high CO_2 product purity and CO_2 recovery rate.

Acknowledgments

References:

[1] Jiang, L., Gonzalez-Diaz, A., Ling-Chin, J., Malik, A., Roskilly, A.P., Smallbone, A.J.. *PEF plastic synthesized from industrial carbon dioxide and biowaste*. Nature Sustainability. 2020;3:761-7.
[2] Liu, W., Lin, Y.C., Ji, Y., Yong, J.Y., Zhang, X.J., Jiang, L. *Thermodynamic study on two adsorption working cycles for direct air capture*. Applied Thermal Engineering. 2022;214.
[3] Jiang, L., Wang, R.Q., Gonzalez-Diaz, A., Smallbone, A., Lamidi, R.O., Roskilly, A.P. *Comparative analysis on temperature swing adsorption cycle for carbon capture by using internal heat/mass recovery*. Applied Thermal Engineering. 2020;169.
[4] Liu, W., Lin, Y.C., Jiang, L., Ji, Y., Yong, J.Y., Zhang, X.J. *Thermodynamic exploration of two-stage vacuum-pressure swing adsorption for carbon dioxide capture*. Energy. 2022;241.
[5] Sabatino, F., Grimm, A., Gallucci, F., van, Sint Annaland M., Kramer, G.J., Gazzani, M. *A comparative energy and costs assessment and optimization for direct air capture technologies*. Joule. 2021;5:2047-76.
[6] Jiang, L., Liu, W., Wang, R.Q., Gonzalez-Diaz, A., Rojas-Michaga, M.F., Michailos, S., et al. *Sorption direct air capture with CO2 utilization*. Progress in Energy and Combustion Science. 2023;95.

[7] von der Assen, N., Muller, L.J., Steingrube, A., Voll, P., Bardow, A.. *Selecting CO2 Sources for CO2 Utilization by Environmental-Merit-Order Curves*. Environ Sci Technol. 2016;50:1093-101.

[8] Jiang, L., Roskilly, A.P., Wang, R.Z. *Performance exploration of temperature swing adsorption technology for carbon dioxide capture*. Energy Conversion and Management. 2018;165:396-404.

[9] Lee, T.S., Cho, J.H., Chi, S.H.. *Carbon dioxide removal using carbon monolith as electric swing adsorption to improve indoor air quality.* Building and Environment. 2015;92:209-21.

[10] Zhu, X., Ge, T., Yang, F., Wang, R.. *Design of steam-assisted temperature vacuum-swing adsorption processes for efficient CO2 capture from ambient air*. Renewable and Sustainable Energy Reviews. 2021;137, 134-135.

[11] Zhao, R.K., Zhao, L., Deng, S., Li, H.L. *Thermodynamic exploration of temperature vacuum swing adsorption for direct air capture of carbon dioxide in buildings.* Energy Conversion and Management. 2019;183:418-26.

[12] Plaza, M.G., García, S., Rubiera, F., Pis, J.J., Pevida, *C. Post-combustion CO2 capture with a commercial activated carbon: Comparison of different regeneration strategies*. Chemical Engineering Journal. 2010;163:41-7.

[13] Sinha, A., Darunte, L.A., Jones, C.W., Realff, M.J., Kawajiri, Y. *Systems Design and Economic Analysis of Direct Air Capture of CO2 through Temperature Vacuum Swing Adsorption Using MIL-101(Cr)-PEI-800 and mmen-Mg2(dobpdc) MOF Adsorbents.* Industrial & Engineering Chemistry Research. 2017;56:750-64.

[14] Elfving, J., Bajamundi, C., Kauppinen, J., Sainio, T. *Modelling of equilibrium working capacity of PSA, TSA and TVSA processes for CO 2 adsorption under direct air capture conditions*. Journal of CO2 Utilization. 2017;22:270-7.

[15] Zhao, R., Liu, L., Zhao, L., Deng, S., Li, S., Zhang, Y. *A comprehensive performance evaluation of temperature swing adsorption for post-combustion carbon dioxide capture*. Renewable and Sustainable Energy Reviews. 2019;114:109285.

[16] Zhao, R., Deng, S., Zhao, L., Li, S., Zhang, Y., Liu, B. *Performance analysis of temperature swing adsorption for CO2 capture using thermodynamic properties of adsorbed phase.* Applied Thermal Engineering. 2017;123:205-15.

[17] Wang, T., Lackner, K.S., Wright, A. *Moisture Swing Sorbent for Carbon Dioxide Capture from Ambient Air*. Environmental Science & Technology. 2011;45:6670-5.

[18] Wang, T., Liu, J., Huang, H., Fang, M., Luo, Z. *Preparation and kinetics of a heterogeneous sorbent for CO2 capture from the atmosphere*. Chemical Engineering Journal. 2016;284:679-86.

[19] Liu, W., Ji, Y., Wang, R.Q., Zhang, X.J., Jiang, L. *Analysis on temperature vacuum swing adsorption integrated with heat pump for efficient carbon capture*. Applied Energy. 2023;335:120757.

[20] Wang, Y., LeVan, M.D. *Adsorption Equilibrium of Carbon Dioxide and Water Vapor on Zeolites 5A and 13X and Silica Gel: Pure Components*. Journal of Chemical & Engineering Data. 2009;54:2839-44.

[21] Zhao, R., Deng, S., Liu, Y., Zhao, Q., He, J., Zhao, L. *Carbon pump: Fundamental theory and applications.* Energy. 2017;119:1131-43.

[22] Stampi-Bombelli V., van der Spek M., Mazzotti M. Analysis of direct capture of CO2 from ambient air via steam-assisted temperature–vacuum swing adsorption. Adsorption. 2020;26:1183-97.

[23] Hou, C.L., Wu, Y.S., Jiao, Y.Z., Huang, J., Wang, T., Fang, M.X., et al. *Integrated direct air capture and CO2 utilization of gas fertilizer based on moisture swing adsorption*. Journal of Zhejiang University-SCIENCE A. 2017;18:819-30.

[24] Liu, W., Lin, Y.C., Ji, Y., Yong, J.Y., Zhang, X.J., Jiang L. *Thermodynamic study on two adsorption working cycles for direct air capture*. Applied Thermal Engineering. 2022;214:118920.

Hollow Fibre Technology: The Key to the Designing Compact Systems to Facilitate Transport Decarbonisation

C. Larkin[1], F. Oliva[2,] and F. García-García[1*]

[1] The University of Edinburgh, School of Engineering, Sanderson Building, The King's Buildings, Mayfield Road, EH9 3JL, Edinburgh, Scotland, UK

[2] Repsol S.A., Calle Méndez Álvaro, 44, 28045 Madrid, Spain

[*]Corresponding author: francisco.garcia-garcia@ed.ac.uk

Abstract

CCS is already regarded as a central pillar of industrial decarbonisation and could play a critical role in reducing transport CO_2 emissions. However, for it to be retrofitted to all surface transport modes, it must be made as compact as possible. Currently, it suffers from being limited to only fitting large vehicles. Therefore, the goal of this paper is to develop a holistic approach using hollow fibre technology to produce a smaller and lighter on-board hollow fibre-based CCS system. The holistic approach proposed considers the effect diesel and green NH_3 fuel blends have on the design of a truck's fuel tanks, aftertreatment architecture and on-board hollow fibre-based CCS system. In this respect, the breakthrough of this paper is highlighting the importance of hollow fibre technology and how it is the key to decarbonising transport.

Keywords: on-board CCS, hollow fibres, TSA, blue transport

Introduction/Background

Additional decarbonisation solutions are required in the short-to-mid-term to reduce surface transport CO_2 emissions. A solution that can be retrofitted to existing vehicles is on-board carbon capture and storage (CCS). In this instance, a CCS system is retrofitted in the same way a CCS system can be retrofitted to a hydrogen plant, transforming transport from grey to blue. However, CCS technologies developed for blue transport applications are traditionally too big to be retrofitted as they consist of packed bed units. To combat this, hollow fibre-based CCS systems should be implemented instead as the high surface area-to-volume ratios inherent to hollow fibres produces a more compact, lightweight and cheaper on-board CCS system [1,2].

However, despite hollow fibres generating more compact systems, the on-board hollow fibre-based systems proposed so far are limited to large surface transport modes. Thus, in order to retrofit on-board hollow fibre-based CCS systems to all surface transport modes, a different methodology is needed. Hence, this work proposes a new holistic approach that considers the effect of diesel and green NH_3 fuel blends on the sizing of a truck's fuel tanks, aftertreatment architecture and on-board hollow fibre-based CCS system. With this, short-hand design calculations were completed for the following scenarios: (i) diesel-powered truck retrofitted with on-board CCS; (ii) diesel-green NH_3-powered truck retrofitted with on-board CCS; and, (iii) hydrogen fuel cell-powered truck fuelled by green NH_3.

Discussion and Results

A series of short-hand design calculations were completed for each scenario and were carried out using the data reported in our previous work [1], the data published by Reiter and Kong [3,4] and the findings of Mazzone *et al* [5].

For scenario one, an on-board hollow fibre-based CCS system was designed without any modifications to the truck's fuel tank or aftertreatment architecture. The on-board hollow fibre-based CCS system obtained was 2,500 L and weighed ~4,000 kg. An on-board CCS system of this size would be limited to larger surface transport modes.

Hence, in scenario two, different diesel-green NH_3 fuel blend ratios were studied to reduce the size of the on-board hollow fibre-based CCS system. It was noticed that there was a trade-off between lowering the diesel loading and reducing the on-board hollow fibre-based CCS system volume. This can be explained by the CO_2 concentration becoming so dilute that the CO_2 capture performance of the sorbent material decreased, and therefore, a bigger on-board hollow fibre-based CCS system was needed. With this, the optimum fuel blend ratio at 20:80 diesel-green NH_3 gave a 40% reduction in the on-board hollow fibre-based CCS system volume, presenting an opportunity for the technology to be retrofitted to small surface transport modes.

Finally, the third scenario contemplated the cracking of green NH_3 instead of the combustion of green NH_3. In this scenario, no aftertreatment architecture or on-board CCS system was required. Instead, a pretreatment unit in the form of an NH_3 cracking reactor was needed. Hollow fibre technology was implemented in the design of the NH_3 cracking reactor to ensure the reactor could be feasibly installed on-board the vehicle. The volume of the overall system obtained for this scenario was approximately eight times smaller than that of scenario one and five times smaller than that of scenario two.

Summary/Conclusions

Blue transport is currently limited to large surface transport modes because the on-board hollow fibre-based CCS systems proposed thus far are too big to be retrofitted onto small surface transport modes. However, the results of this work have shown that the volume of the on-board hollow fibre-based CCS system can be decreased by 40% by co-feeding green NH_3 at a fuel blend ratio of 20:80 diesel-green NH_3. Thus, allowing on-board hollow fibre-based CCS systems to be retrofitted to all surface transport modes. Additionally, the findings of this paper show that hollow fibres can play an important role in green NH_3 cracking for hydrogen fuel cell-powered vehicles. Overall, the work presented herein demonstrates how hollow fibres are key to developing blue transport for all surface transport modes and facilitating the deployment of green transport.

Acknowledgements

References:

[1]   C. Larkin *et al*, *Retrofitting hollow fibre carbon capture systems to decarbonise surface transport*, J. CO2 Util. 67 (2023).

[2]   C. Larkin *et al*, *Hollow Fibre Adsorption Unit for On-board Carbon Capture: The Key to Reducing Transport Emissions*, Carbon Capture Sci. Technol. 2 (2022) 100034.

[3]   A.J. Reiter and S.C. Kong, *Demonstration of compression-ignition engine combustion*

using ammonia in reducing greenhouse gas emissions, Energy and Fuels. 22 (2008)

[4]   A.J. Reiter and S.C. Kong, *Combustion and emissions characteristics of compression-ignition engine using dual ammonia-diesel fuel*, Fuel. 90 (2011) 87–97.

[5]   S. Mazzone *et al*, *A compact non-PGM catalytic hollow fibre converter for on-board hydrogen production*, Sustain. Energy Fuels. 6 (2022) 1554–1567.

An overview of performance and viability of nanofluids in thermal energy systems

S.M.S. Murshed[1], Roger R. Riehl[2,*]

[1]IDMEC, Department of Mechanical Engineering,
Instituto Superior Técnico, University of Lisbon, 1049-001 Lisbon, Portugal

[2]GamaTech Thermal Solutions, São José dos Campos, SP Brazil 12235-390

[*]Corresponding author: roger.riehl@gtts.com.br

Abstract

Nanofluids are defined as heat transfer fluids with enhanced heat transfer properties by the addition of nanoparticles. Nanofluid's stability, nanoparticles' type, and chemical compatibility with the base fluid are essential not only to increase their thermophysical properties but also to ensure the long-lasting and thermally efficient use of the equipment in which these new fluids are used. Some of these key aspects are briefly discussed in this paper. Likewise, the improvement in terms of the heat transfer capacity (thermal resistance) that the use of nanofluids has on the heat pipes-thermosyphons is demonstrated. On the other hand, the improvement in energy efficiency that nanofluids cause in a vapor compression system is also presented.

Keywords: nanofluid, heat pipe, vapor compression, battery refrigeration

Introduction

In an increasingly digitized society with a growing trend in the interconnection of things (e.g., IoT and AI), the volume of information circulating through the network and being processed is constantly growing. This information must be processed in high-speed processing and storage servers, which means that the density of heat to be dissipated has increased considerably in recent decades. This heat flux increase, together with technological advances that allow the miniaturization of electronics, forces thermal engineers to seek advanced solutions for heat dissipation. Advances in the field of electronics, and particularly power electronics, have resulted in a significant increase in heat flux density at the component level. Meeting component temperature requirements and ensuring maximum system performance and longevity require more efficient, lower-volume cooling technologies. As a result, thermal management is becoming increasingly critical to the electronics industry and data centres. The need for thermal management has increased over the past decade and the prediction is that a steeper increase is yet to come in the coming years.

In parallel, other applications have demanded an increasing thermal management capability that was not even considered less than a decade ago. The advent of electric vehicles with the use of Li-Ion batteries has become a new edge for the development of reliable and high-performance thermal management systems. Since this type of battery can be charged within minutes and present a high density of energy that can be delivered to the vehicle's systems, overheating became an issue that can potentially cause accidents, which unfortunately have already been reported in some applications. This type of issue is generally caused by heat concentration in specific areas of the battery resulting in temperature overshooting with consequent potential fire and loss of the device. Such an issue has been reported with more

frequency as new vehicles that utilize electric propulsion are gaining interest from different markets, which require proper addressing using reliable thermal management systems. As a potential solution for this issue, temperature homogenization can be applied to minimize heat concentration, which also contributes to increasing the battery's lifetime.

On the other hand, conventional vapor compression refrigeration has, in recent years, suffered from the consequences of international environmental legislation relating to fluorinated refrigerants "HFCs". In this regard, Europe has adopted the "F-GAS" regulation, which establishes deadlines for the use of these refrigerants due to their negative impact on the climate. The climate impact of a substance is commonly expressed as the global warming potential (GWP). The lower the GWP, the more climate-friendly the substance. Most of the HFCs have a very high GWP and are hence potent greenhouse gases. Most of the HFCs are used as refrigerants in refrigeration and air conditioning. To mitigate emissions of substances with a high GWP and comply with the F-Gas Regulation, each sector needs to find solutions to quickly switch to low GWP refrigerants. The F-gas regulation is committed to so-called clean refrigerants (hydrocarbons, CO_2, HFOs) due to their zero or very low GWP. However, the use of these refrigerants often implies a reduction in the efficiency of the refrigerators as well as an extra effort to redesign them.

Under this scenario, thermal and refrigeration engineers are forced to find solutions, not only in terms of the type of refrigerant (more respectful of the environment) but also in terms of new refrigeration technologies (acoustic, thermocaloric, thermoelectric, nanofluids …) that meet new challenges in heat dissipation and cooling. Nanofluids are envisioned as one of these solutions. Although there is little bibliography in this regard, recent works show the interest in nanofluids as a key enabling technology to meet the environmental challenges vapor compression systems must face. For example, Gokulnath [1] presents an analysis of the effect of different nano-refrigerants on domestic refrigerator performance. Haque [2] analyzes the behavior of a domestic refrigerator when using a polyester-based nano-lubricant.

Nanofluids are defined as heat transfer fluids with enhanced heat transfer properties by the addition of nanoparticles. When formulating a nanofluid, a fundamental aspect to consider is its stability, since its thermophysical properties pretty much depend on it. Adding dispersants in the two-phase systems is an easy and economical method to enhance the stability of nanofluids. Although surfactant addition is an effective way to enhance the dispersibility of nanoparticles, surfactants might cause several problems [3]. In this paper, an analysis of the effect of nanoparticles not only on the stability of the nanofluid but also on its thermal conductivity is carried out. The use of nanofluids is already being seen in different applications - technologies, some application cases are also summarised in this paper.

Results and Discussion

Nanofluids [4] are a type of fluid made up of a base fluid to which nanoparticles (typically <100 nm) are added to increase their thermophysical properties. Nanoparticles manipulation and in turn, nanofluid formulation requires high-security measures and therefore must be handled in controlled environments.

Metallic nanoparticles are among the most interesting ones due to their high thermal conductivity. This nanoparticle addition makes the nanofluid thermal conductivity increase [5, 6] as well as its viscosity which is a negative effect as far as pressure drop is concerned. Despite the volume of research carried out so far, which shows that the use of nanofluids increases the heat transfer coefficients, there is still much to understand in the area of nanofluids, for example, depending on which cooling technology (LHP, HP) the nanofluid is used in, other forces

**Heat Powered Cycles
Conference 2023**
Edinburgh

Heat in the new energy system

3rd to 6th of September 2023
University of Edinburgh, Scotland

(capillarity) apart from the viscous and gravitational forces come into play requiring a better fluid–structure interaction understanding [7]. This interaction is given, among others, by the surface tension and the contact angle between the fluid and the porous medium. Since the contact angle is affected by the addition of nanoparticles [8–10] the capillary forces are altered and with them the LHP capillary pumping. From a theoretical point of view, the phenomena that take place at the nanoparticle level (Brownian movement, plasma) that make the heat transfer coefficients improve are not clear. In the bibliography, there are several theoretical models [11–19] that try to shed light on the matter but their predictions differ from the experimental values [20–22]. This theoretical field requires a greater research effort to be able to give answers to the real behavior of nanofluids. Nanoparticles not only increase the thermal conductivity of the base fluid but also act as sources of bubble generation in boiling processes, thus increasing the boiling performance such as critical heat flux, important in LHPs and HPs [23, 24]. Nanoparticle stability [3, 25, 26] in the fluid is key to having a nanofluid that ensures an enhancement of the device's thermal performance over time. Different techniques are used for such purposes: surfactant addition, sonication, and surface charge change. The addition of nanoparticles to a base fluid, as mentioned above in the section, basically alters its viscosity and its thermal conductivity. These alterations depend pretty much on the nanoparticle size and concentration as shown in the following sections. This influence is reflected in the following analysis carried out for the base fluid polyolester when it is doped with different types of nanoparticles (CuO, Al_2O_3, and TiO_2).

Nanoparticles size - viscosity and thermal conductivity

As mentioned above, nanofluid viscosity [27] is an important property as far as thermal performance and fluid flow are concerned. As shown by the rheological analyzes carried out by different researchers [28, 29]. Among the several works regarding oil-based nanofluids, Resiga et al. [30] investigated the rheological properties of highly concentrated transformer oil-based magnetic nanofluids; the results confirmed that the nanofluids were Newtonians in all concentrations except at the highest concentration of 20.8 vol.%. Murshed et al. [31] experimentally studied the viscosity of silicone oil (SO) based TiO_2 and SiO_2 nanofluids confirming the nanofluids' Newtonian nature. Chen and Xie [32] reached the same conclusion for carbon nanotubes (TCNT)-nanofluids. At low shear rates, Newtonian behavior of silicone oil (Syltherm 800) based diamond-graphene nanofluid was observed by Yang et al. [33]. Further researchers [34-36] investigated the effects of multi-walled carbon nanotubes (MWCNT) loading, surfactant concentration, and dispersion energy (ultrasonication) on the thermal conductivity and steady shear viscosity of oil (PAO6)- based-nanofluids. Polyisobutene succinimide (PIBSI) was used as the surfactant. The results showed that at low shear conditions, the nanofluid viscosity was governed by the PIBSI, observing a 0.1 to 0.07 Pa shear stress decrease. They also analyzed the concentration of CNT versus viscosity, it was observed that the viscosity increased for any concentration other than 3% by weight.

Saeedinia et al. [37] investigated the thermal conductivity of CuO/oil nanofluid. The authors measured the thermal conductivity at different temperatures ranging between 24 and 70 °C and at two concentrations of 1 wt.% and 2 wt. %. The results showed a remarkable enhancement in the thermal conductivity of the studied nanofluid with temperature. With increasing the temperature, the agglomeration of nanoparticles is hindered, and thus the thermal conductivity is enhanced because of the more uniform nanoparticles dispersion.

When analyzing the Ti_2O_3 nanoparticles size on the 1 wt. % polyol-ester nanofluid, Figure 1, it is observed that viscosity increases with the increase of NP size. This increase becomes steeper for a specific size (180 nm). This result agrees with other researchers' work [38, 39]. Although it could be expected that viscosity would decrease with increasing NP size [40], this performance

Heat Powered Cycles
Conference 2023
Edinburgh
Heat in the new energy system

3rd to 6th of September 2023
University of Edinburgh, Scotland

depends to a great extent on the NP concentration, which can cause a decrease or an increase in viscosity as the size of the NPs increases [41-45]. In any refrigeration application, the nanofluid must be pumped to flow through the pipe and this pumping work is greater the higher the viscosity. In terms of efficiency, this work must be as low as possible and consequently the nanofluid viscosity.
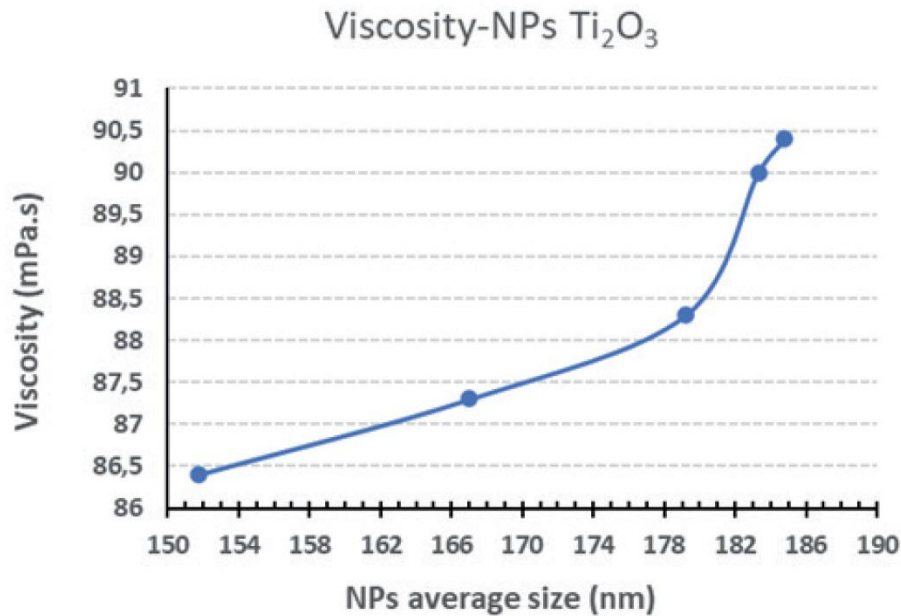
Figure 1. Influence of NPs size on viscosity. 1 wt% nanofluid of Ti_2O_3 NPs in polyol-ester.

Figure 2 shows the thermal conductivity variation with variation in nanoparticle concentration from 0.1 wt.% to 1.1 wt.% at ambient temperature. It is apparent that thermal conductivity increases with increasing the NPs concentration [46]. However, in the cases of Al_2O_3 and TiO_2, the thermal conductivity increase is less the higher the concentration. The "CuO" nanofluid exhibits a linearly increasing behavior with concentration.

Application cases

Passive cooling devices

Nanofluids can be potentially applied as working fluids in active (mechanically driven) and passive (capillary action, slug/plug dynamics) systems. Thermal management devices employing either concept can benefit from the advantages of using nanofluids to enhance their heat transport capabilities. Liquid cooling systems use a pump to drive the liquid to the heat source (or sources) in contact with a dedicated heat exchanger (or multiple heat exchangers). Heat is then absorbed by the working fluid and transported by the lines to a condenser (one or multiple), where the heat is rejected to a medium (environmental air, liquid reservoir, etc) with low temperature. Since the liquid cooling system is a closed circuit, the working fluid operates in a cycle absorbing and rejecting heat. As a necessity from its design, liquid cooling systems require a reservoir used to self-control the working fluid being used by the system, which will be determined by the flow rate at which it is operating. Figure 3a presents schematics of a liquid cooling system.
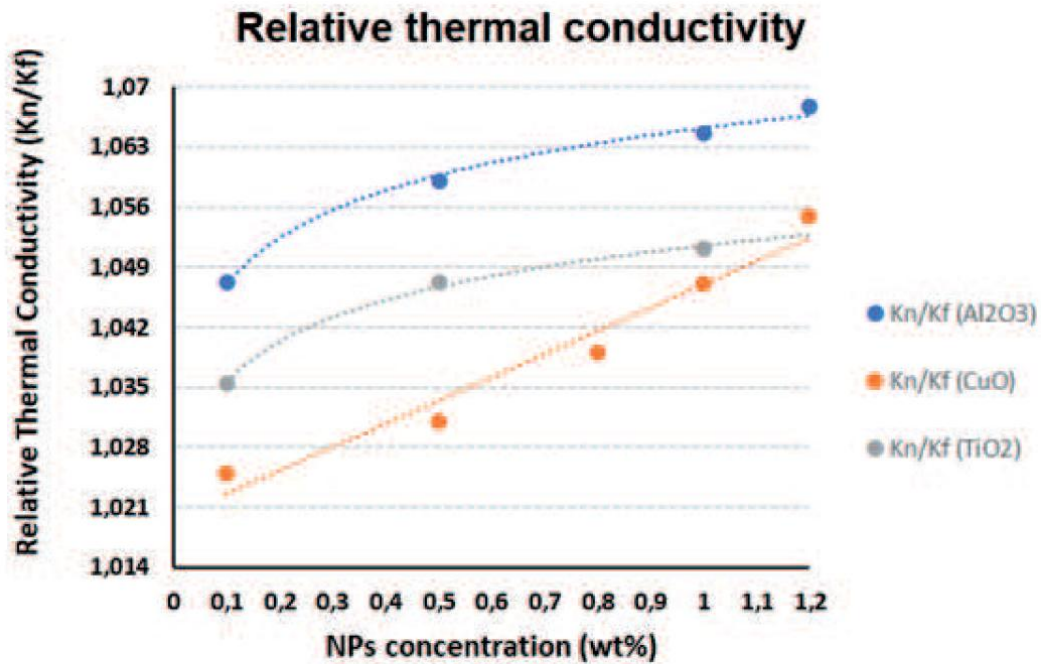
Figure 2. Influence of NPs concentration on thermal conductivity for different NPs (CuO, Ti_2O_3 and Al_2O_3) and concentrations. Polyol-ester as base fluid.

As a promising technology for complex thermal management systems, Pulsating Heat Pipe (PHPs), also known as Oscillating Heat Pipes (OHPs) can potentially use nanofluids as their working fluids, because they do not present a wick structure that could compromise their overall thermal performance. Their simple construction based on a meandering tube bent in several parallel curves operates utilizing liquid slugs and vapor plugs motion [46], transporting the heat absorbed from a source and rejecting it in a sink. This kind of device can be considered a special type of heat pipe and was introduced by Akachi [47].
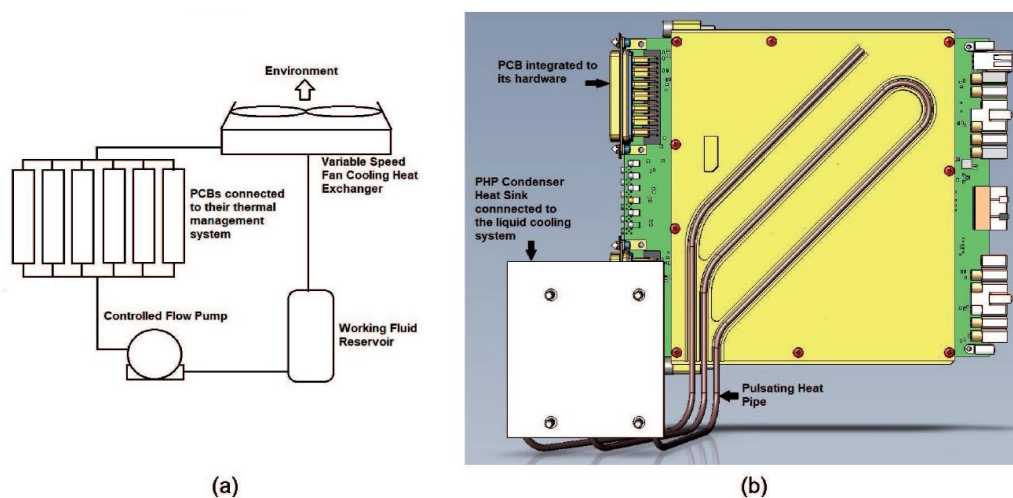
Figure 3. (a) schematic, and (b) CAD representation of the thermal control system arrangement.

Heat Powered Cycles
Conference 2023
Edinburgh
Heat in the new energy system

3rd to 6th of September 2023
University of Edinburgh, Scotland

Moreover, other designs present the application of nanofluids operating with passive thermal control devices like the PHPs [48]. Figure 4 presents another configuration applied to the thermal control of PCBs that operate with nanofluids with f ranging from 2.0 to 3.5% for the same nanoparticle characteristics. For such applications, the PHPs have been designed to homogenize the temperatures throughout the PCBs to maximize the heat dissipation capabilities of the entire system, thus minimizing the risks of undesirable concentrations that could potentially cause the failure of the entire thermal management system.

| (a) | (b) | (c) |
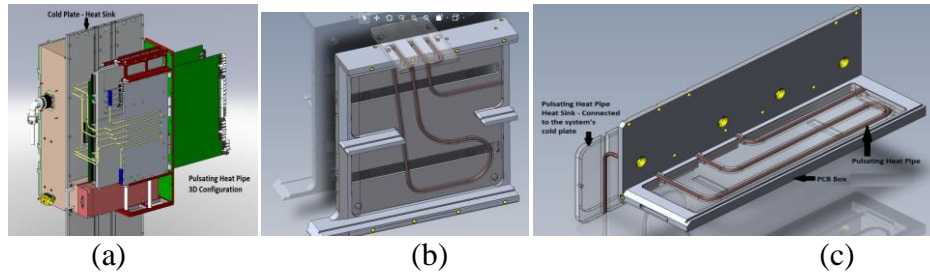
Figure 4. PHPs with nanofluids applied to the thermal control of PCBs.

In the case of thermal management of high heat density equipment, such as computer clusters, avionics, processors, etc, the demand for thermal control using specific devices is also growing. In this case, PHPs are not indicated as they cannot handle high heat fluxes. Therefore, another device called a loop heat pipe (LHP) is the most indicated one for the use of passive thermal control, being able to work with heat fluxes of 100W/cm^2 or above [49-51].

Solutions for thermal control on the equipment mentioned above have been using LHPs with and without nanofluids, which, in general, presented the configuration as shown in Fig. 5.
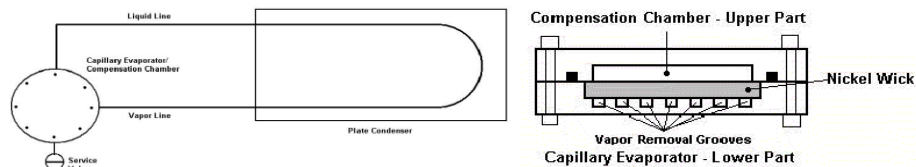
Figure 5. Loop heat pipes applied to computer clusters' thermal control.

In the case of nanofluids, LHPs can present an increase of 20% in their overall heat management capabilities, but there is a penalty in the maximum heat fluxes that they can be operational because the solid nanoparticles imply additional restrictions to the fluid flow (higher pressure drops). Adequate manipulation of the nanofluid is also required to avoid the formation of non-condensable gases (NCGs) that might impact the overall device's performance [52].

Active cooling -vapor compression

Another potential application for nanofluids is vapor compression refrigeration systems "VCS". In these systems, the working fluid is circulated actively through a compressor. The compressor generates the pressure difference necessary for the refrigerant to circulate. During its journey, the refrigerant undergoes a cyclical phase change, condensation-evaporation, which gives it a greater heat transport capacity compared to liquid cooling. The coefficient of performance "COP" of the VCS systems can be improved in two ways: firstly, by increasing the heat

abstraction rate in the evaporator, and secondly, by reducing the work done in a compressor The use of nanoparticles to increase the COP of vapor compression systems is something that has already been confirmed, as evidenced by the research works on the matter [53, 54]. Some works are more focused on the increase of heat transfer rates [55–57] while others are on compressor lubrication improvement [58, 59].

Conclusions

Considering the importance of nanofluids as heat transport media, from this overview of the performance and viability of nanofluids following conclusions can be drawn:

- Nanofluids are a promising science to improve the heat transfer capacity of different technologies particularly used in thermal systems.
- It applies to different sectors with minimal investment cost.
- Nanofluid stability continues to be a challenge and therefore an open door to research.
- A greater understanding of the causes that make the thermophysical properties of nanofluid improve is still necessary and thus more theoretical research is required.
- The large amount of experimental research work carried out to date positions nanofluids as a key enabling technology for the advancement of thermal and cooling management in the immediate future.

References:

[1] Gokulnath, G., Prabhu, A. R. G., Performance Analysis of a Nano Refrigerant Mixtures in a Domestic Refrigeration System, 2017 Applied Science 508-516.

[2] Haque M.E, Bakar Kadirgama K,Noor M, and Shakaib,Performance of a domestic refrigerator using nanoparticles-based polyolester oil lubricant, 2016 J. Mech. Eng. Sci.,1778-1791.

[3] Cacua, K., Buitrago-Sierra, R., Herrera, B., Pabón, E., Murshed, S. M. S., Nanofluids' stability effects on the thermal performance of heat pipes. Journal of Thermal Analysis and Calorimetry 136 (2019) 1597–1614.

[4] Wei Yu and Huaqing Xie. "A Review on Nanofluids: Preparation, Stability Mechanisms, and Applications. Journal of Nanomaterials, 2012.

[5] Murshed, S. M. S., Leong, K. C., Yang, C., A Combined Model for the Effective Thermal Conductivity of Nanofluids, Applied Thermal Engineering, 29 (2009) 2477-2483.

[6] Chein, R. and Huang, G., Analysis of microchannel heat sink performance using nanofluids, Applied Thermal Engineering, 25 (2005) 3104-3114.

[7] Riehl, R. R., Performance evaluation when using nanofluids in loop heat pipe and pulsating heat pipe, in: Proceedings of the 37th International Conference on Environmental Systems (ICES), July 10-15 (2007), Chicago, IL USA, paper 2007-01-3193.

[8] M. Hernaiz, V. Alonso, P. Estellé, Z. Wu, B. Sundén, L. Doretti, S. Mancin, N. Çobanoğlu, Z.H. Karadeniz, N. Garmendia, M. Lasheras-Zubiate el al. The contact angle of nanofluids as thermophysical property. Journal of Colloid and Interface Science, Volume 547, 1 July 2019, Pages 393-406

[9] M.H.Buchmann, N. Garmendia, et al. "The contact angle of nanofluids as thermophysical property". Journal of Colloid and Interface Science. Volume 547, 1 July 2019, Pages 393-406

[10] Gimeno-Furio A., Mancin S. (2020) Effects of Carbon Nanohorn Based Nanofluids Pool Boiling on Optical Properties and Wettability of Different Metal Surfaces, Heat Transfer Engineering, DOI: 10.1080/01457632.2020.1818407

[11] Ghadimi, A., Saidur, R., Metselaar H. S. C., "A Review of Nanofluid Stability Properties and Characterization in Stationary Conditions", International Journal of Heat and Mass Transfer, 4051-4068, Elsevier, Jul. 2011.

[12] Riehl, R. R., Development of Copper-Methanol Heat Pipes: Thermal Performance Evaluation for Electronics Cooling, Heat Powered Cycles Conference, Nottingham, UK, June 26-29, 2016.

[13] Liu, Z. H., and Zhu, Q. Z., "Application of Aqueous Nanofluids in a Horizontal Mesh Heat Pipe", Energy Conversion and management, 292-300, Elsevier, Jul. 2010.

[14] Wang, P. Y., and Chen, X. J., and Liu, Z. H., and Liu, Y. P., "Application of Nanofluid in an Inclined Mesh Wicked Heat Pipes", Thermochimica Acta, 100-108, Elsevier, Apr. 2012.

[15] Kumaresan, G., and Venkatachalapathy, S., Arsivatham, L. G., Wongwises, S., "Comparative Study on Heat Transfer Characteristics of Sintered and Mesh wick heat pipes using CuO Nanofluids", International Communications in Heat and Mass Transfer, 208-215, Elsevier, Aug. 2014.

[16] Liu, Z. H., and Li, Y. Y., and Bao, R., "Thermal Performance of Inclined Grooved Heat Pipes Using Nanofluids", International Journal of Thermal Sciences, 1680-1687, Elsevier, Apr. 2010.

[17] Wang, G. S., and Song, B., and Liu, Z. H., "Operation Characteristics of Cylindrical Miniature Grooved Heat Pipe Using Aqueous CuO Nanofluids", Experimental Thermal and Fluid Science, 1415-1421, Elsevier, Jul. 2010.

[18] Kumaresan, G., and Venkatachalapathy, S., "A Review on Heat Transfer Enhancement Studies of Heat Pipes Using Nanofluids", Frontiers in heat pipes, (FHP) 3-043001, 2012.

[19] Chien, H.-T., Tsai, C.-I., Chen, P.-H., and Chen, P.-Y. "Improvement on Thermal Performance of a Disk-Shaped Miniature Heat Pipe with Nanofluid", ICEPT 2003. Fifth International Conference on Electronic Packaging Technology. Proceedings. (IEEE Cat. No.03EX750), 389. IEEE, Shanghai, China (2003).

[20] Yang, X. F., and Liu, Z. H., and Zhao, J., "Heat Transfer Performance of a Horizontal Micro-Grooved Heat Pipe Using CuO Nanofluid", Journal of Micromechanics and Microengineering, 035038, IOP Pub., Feb. 2008.

[21] Marcelino, E., Oliveira, D., Riehl, R. R., "A Review on Thermal Performance of CuO-water Nanofluids Applied to Heat Pipes and Their Characteristics", ITherm - The Intersociety Conference on Thermal and Thermomechanical Phenomena in Electronic Systems, May 31 - June 3, Las Vegas, NV USA, 2016.

[22] Venkatachalapathy, S., Kumaresan, G., Suresh, S., "Performance analysis of cylindrical heat pipe using nanofluids – An experimental study", International Journal of Multiphase Flow 72 (2015) 188–197.

[23] Tong, B. Y., Wong, T. N., Ooi, K. T., Closed-loop pulsating heat pipe, Applied Thermal Engineering, 21 (2001) 1845-1862.

[24] Murshed, S. M. S., Leong, K. C., Yang, C., A Model for the Thermal Conductivity of Nanofluids–the Effect of Interfacial Layer, Journal of Nanoparticle Research, 8 (2006) 245-254.

[25] Riehl, R. R., "Analysis of Loop Heat Pipe Behaviour Using Nanofluid", Heat Powered Cycle Int. Conf., Newcastle, UK, 2006.

[26] Murshed, S. M. S., Nieto de Castro, C. A., Nanofluids: Synthesis, Properties and Applications, 1sted., Nova Science Inc., New York, 2014.

[27] Murshed, S. M. S., Estellé, P., A state of the art review on viscosity of nanofluids, Renewable and Sustainable Energy Reviews 76 (2017) 1134–1152.

[28] Sharma, A. K, Tiwari, A. K., Dixit, A. R., Rheological behavior of nanofluids: a review. Renewable and Sustainable Energy Reviews 53(2016) 779–791.

[29] Murshed, S. M. S., Leong, K. C., Yang, C., Thermophysical properties of nanofluids. In: Sattler KD, editor. Handbook of nanophysics: nanoparticles and quantum dots. Boca Raton: Taylor & Francis; 2010

[30] Resiga DS, Socoliuc V, Boros T, Borbath T, Marinica O, Han A, Vekas L. The influence of particle clustering on the rheological properties of highly concentrated magnetic nanofluids. J Colloid Interface Sci 2012;373:110–5.

[31] Murshed, S. M. S., Santos, F.J.V., Nieto de Castro, C. A., Investigations of viscosity of silicone oil-based semiconductor nanofluids. Journal of Nanofluids 2 (2013) 261–266.

[32] Chen L, Xie H. Silicon oil based multiwalled carbon nanotubes nanofluid with optimized thermal conductivity enhancement. Colloid Surf A: Physicochem Eng Asp 2009;352:136–40.

[33] Yang Y, Oztekin A, Neti S, Mohapatra S. Particle agglomeration and properties of nanofluids. J Nanopart Res 2012;14:852.

[34] Yang Y, Grulke EA, Zhang ZG, Wu G. Thermal and rheological properties of carbon nanotube-in-oil dispersions. J Appl Phys 2006;99:114307.

[35] Heris SZ, Razbani MA, Estellé P, Mahian O. Rheological behavior of zinc-oxide nanolubricants. J Dispers Sci Techol 2015;36:1073–9

[36] Kole M, Dey TK. Effect of aggregation on the viscosity of copper oxide–gear oil nanofluids. Int J Therm Sci 2011;50:1741–7

[37] Saeedinia M, Akhavan-Behabadi MA, Razi P. Thermal and rheological characteristics of CuO-base oil nanofluid flow inside a circular tube. Int Commun Heat Mass Transf 2012;39:152–9

[38] R. Prasher, et al., "Measurements of nanofluid viscosity and its implications for thermal applications".[J], Appl. Phys. Lett. 89 (13) (2006) 255.

[39] M.H. Esfe, et al. "An experimental investigation, sensitivity analysis and RSM analysis of MWCNT (10)-ZnO(90)/10W40 nanofluid viscosity". Journal of Molecular Liquids 288 (2019) 111020.

[40] Xichen Hu, et, al. "Experimental investigation and mechanism analysis: Effect of nanoparticle size on viscosity of nanofluids". Journal of Molecular Liquids 314 (2020) 113604

[41] S.P. Jang, et. al. "Particle concentration and tube size dependence of viscosity of Al2O3 – water nanofluids flowing through micro-and minitubes". J. Appl. Phys. Lett. 91 (24) (2007) 243112

[42] B. Wang, X. Wang, W. Lou, J. Hao, Thermal conductivity and rheological propertiesof graphite/oil nanofluids, Colloids Surf. A Physicochem. Eng. Asp. 414 (Nov. 2012)125–131

[43] S. Aberoumand, A. Jafarimoghaddam, M. Moravej, H. Aberoumand, K. Javaherdeh,Experimental study on the rheological behavior of silver-heat transfer oil nanofluidand suggesting two empirical based correlations for thermal conductivity and vis-cosity of oil based nanofluids, Appl. Therm. Eng. 101 (May 2016) 362–372.

[44] S. Aberoumand, A. Jafarimoghaddam, Experimental study on synthesis, stability,thermal conductivity and viscosity of Cu–engine oil nanofluid, J. Taiwan Inst.Chem. Eng. 71 (Feb. 2017) 315–322.

[45] G. Colangelo, E. Favale, P. Miglietta, M. Milanese, A. de Risi, Thermal conductivity,viscosity and stability of Al2O3-diathermic oil nanofluids for solar energy systems,Energy 95 (Jan. 2016) 124–136

[46] Ovais Gulzar et. al. "Experimental study on thermal conductivity of mono and hybrid Al2O3–TiO2 nanofluids for concentrating solar collectors". International Journal of Energy Research. (2020), 1–15.

[47] Akachi, H., Polasek, F., Stulc, P., Pulsating Heat Pipes, Proceedings of the 5th International Heat Pipe Symposium, Melbourne, Australia, pp. 208-217, 1996.

[48] Riehl, R. R., Thermal Performance and Development of a Dual Evaporator Loop Heat Pipe, Heat Pipe Science and Technology, An International Journal, 4(1-2), 105–117, 2013

[49] J.Esarte, A. Bernardine, et al. "Performance assessment of a Three-Dimensional printed porous media produced by Selective Laser Melting technology for the optimization of Loop Heat Pipe wicks". Applied Science 2019, 9 2905; doi:10.3390/app9142905.

[50] Riehl, R. R., "Current Developments on Pulsating Heat Pipes and Dual-Evaporators Loop Heat Pipes", 18th Workshop on Thermophysics Applications in Microgravity, March 24, the Aerospace Corporation, El Segundo, CA, USA 2014.

[51] Riehl, R. R. "Utilization of Passive Thermal Control Technologies in Cooling Electronics: A Brief Review, Heat Pipe Science and Technology, An International Journal, 7 (3-4), 161-183, 2016.

[52] Riehl, R. R., Murshed, S. M. S., Life Time Expectancy Prediction and Ageing Process of Heat Pipes Using Nanofluids, Heat Transfer Engineering, DOI: 10.1080/01457632.2020.1818423.

[53] Haque M.E, Bakar Kadirgama K,Noor M M, and Shakaib,Performance of a domestic refrigerator using nanoparticles-based polyolester oil lubricant, 2016 J. Mech. Eng. Sci., 1778–1791.

[54] Kamaraj N, Experimental analysis of Vapour Compression Refrigeration System using the refrigerant with Nano particles,2016 Int journal of mech.engg. 16–25.

[55] Kedarnath B,Enhancement of COP using Nanoadditives in Domestic Refrigerator 2015 Int journal of Applied sci.engg.tech.282–286.

[56] Kamaraj N, Experimental analysis of Vapour Compression Refrigeration System using the refrigerant with Nano particles,2016 Int journal of mech.engg. 16–25.

[57] Soliman AMS Taher SH Abdel-Rahman AK and Ookawara S, Performance enhancement of vapor compression cycle using nano materials, 2015 Int. Conf. Renew. Energy 821–826.

[58] Kannan P and Manivanana A, Theoretical analysis of a vapour compression refrigeration system with R134a , R290 , R600a & various ratio of R290 / R600a, 2016 IJRASET 143–146.

[59] Veera Raghavalu K, Govindha Rasu N. "Review on Applications of NanoFluids used in Vapour Compression Refrigeration System for Cop Enhancement". Materials Science and Engineering 330 (2018).

Assessment of electrospun nanofibrous mats for direct air capture of CO_2

K. Papchenko, L.Curtice, E. Lasseuguette, M.-C. Ferrari and M.G. De Angelis*

Institute for Materials and Processes, School of Engineering, University of Edinburgh, Scotland, UK

*Corresponding author: grazia.deangelis@ed.ac.uk

Abstract

In this work we fabricated nanostructured polymeric material, based on poly(acrylonitrile), and studied the feasibility of its use for low concentration removal of CO_2 directly from air. Polymeric powder was electrospun to prepare nanofibrous mats with high surface area and functionalised with primary amine to promote the CO_2 adsorption capacity of the material.

Keywords: Direct Air Capture, electrospinning, nanofibers, polymers, CO2.

Introduction/Background

There is a clear consensus that human activities result in increasing emission of greenhouse gases and are the major contributors to global warming. Tackling the negative effects of such emissions on the environment calls for the devolepment of the mitigation technologies for deep decarbonisazion both of large concentrated sources and point sources of emission.

Conventional CO_2 capture and storage techniques allow only to decrease emissions from high concentration sources, and so are not enough to reach the decarbonisation target. Instead, negative emission technologies (NETs) are required, such as direct air capture (DAC). Such technology is currently removing thousand of tonnes of CO_2 per year and has already been recognised as the measure to directly address the couse of climate change. Indeed, DAC offers a viable solution to remove CO_2 from ambient air while offering higher flexibility with respect to other technologies in terms of location and scalability [1-2].

Nevertheless, capturing and concentrating CO_2 directly from air presents several limitations, due to very low carbon concentration, presence of moisture, operating temperature and pressure. Thus, together with requirements on high sorption capacity at ambient pressure, stability issues also have to be addressed, when choosing the material for solid sorbent DAC [2]. In this regard, polymeric materials could offer a suitable solution, offering both chemical and physical stability, and ease of manufacturing. Furthermore, it is possible to covalently attach CO_2-philic carriers to the polymeric matrix, creating a material with enhanced carbon selectivity, promoted by the presence of humidity in the stream [3].

In this work, we study the feasibility of creating such material from poly(acrylonitrile) (PAN). Such polymer can be easily functionalised, given the availability of active nitrile groups. At the same time, techniques like electrospinning can be used to increase significantly the surface area and promote CO_2 adsorption. Indeed, it was shown in the previous work that chemical and morphological modification can increase significantly the CO_2 capture ability at relatively high pressures of a conventional polymer such as PAN [3]. Here, we study the feasibility of using electrospun nanofibrous mats based on amine-functionalised PAN for low concentration removal of CO_2.

Discussion and Results

Nanofibrous mats of pure PAN were electrospun from 5wt% polymer solution in N, N-dimethylformamide (DMF) by using IME electrospinner. The spinning procedure was optimised to produce uniform material while maximising the superficial area by controlling the fibre diameter. The obtained non-woven mats were then functionalised through reaction with acqueous solution of Ethylenediamine (EDA), primary amine known to directly interact with CO_2. Samples with different amine contents were obtaines and dried in the oven under vacuum prior to further characterization.

Morphological analysis of pure and functionalised nanomats was performed by using Scanning Electron Microscopy (SEM) technique, allowing to study the uniformity of the fibers and their diameter distribution, as showed in Figure 1. Chemical characterisazion was performed by using Fourier-transform infrared (FT-IR) spectroscopy, allowing to define and determine the nitrile groups conversion after the functionalization of PAN. Finally, dry CO_2 sorption was measured directly in a pressure decay apparatus, at 30°C and pressures up to 1 bar. The solubility values were correlated to the degree of functionalisation and total surface area, related to the mean fibre diameter.
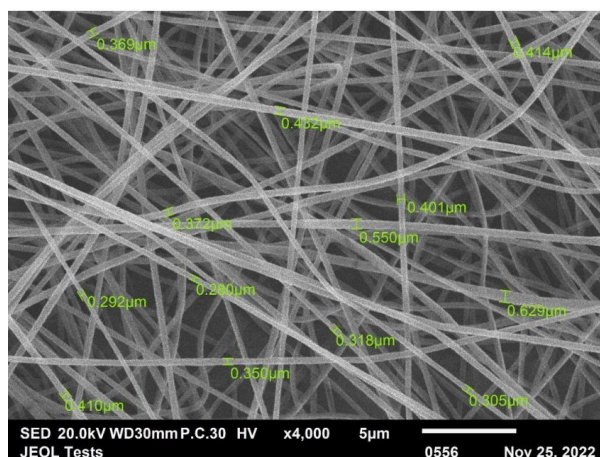
Figure 1: SEM image of pure PAN nanofibrous mat. The image was obtained at 4000x magnification and used for the analysis of diameter distribution.

The results were compared with a previous study, where the PAN powder was functionalised prior to electrospinning [3].

Summary/Conclusions

In conclusion, in this work we investigated the feasibility of using nanostructured polymeric materials for direct carbon capture from air. Fibrous electrospun mats of pure and amine-functionalised PAN were produced at different conditions; their morphological, chemical, and adsorption properties were characterised and compared with previous work, showing promising results for DAC application.

References:

[1] McQueen, N. et al, "A review of direct air capture (DAC): scaling up commercial technologies and innovating for the future", Progress in Energy, 2021.
[2] Goeppert, A., Czaun, M., Prakash, G. K. S., Olah, G. A., "Air as the renewable carbon source of the future: an overview of CO2 capture from the atmosphere", Energy & Environmental Science, 2012.
[3] Olivieri, O., Roso, M., De Angelis M. G., Lorenzetti, A., "Evaluation of electrospun nanofibrous mats as materials for CO2 capture: A feasibility study on functionalized poly(acrylonitrile) (PAN)", Journal of Membrane Science, 2018.

Realistic evaluation of prototypical solid sorbents for temperature swing adsorption CO2 capture processes

Katie Everden[1], Connor Hewson[1], Majid Naderi[1], Daryl Williams[2] and Paul Iacomi[1]

[1]Surface Measurement Systems, Unit 5, Wharfside, HA0 4PE, London, UK

[2]Imperial College London, Department of Chemical Engineering, SW7 2BY, London, UK

[*]Corresponding author: piacomi@surfacemeasurementsystems.com

Abstract

Carbon capture is a crucial technology to mitigate climate change and reduce CO_2 emissions. Solid sorbents are one of the most promising class of materials for developing carbon capture technologies, with their pores or surfaces directly capturing CO_2, or acting a backbone/confining medium for CO_2-capturing functional groups [1].

The most common integrated process in use for post-combustion and direct air capture, is temperature swing adsorption (TSA). TSA operates by alternating between adsorption at low temperature and desorption at high temperature, thus exploiting the temperature-dependent affinity of the sorbent for CO_2. If low to medium grade heat is used for sorbent regeneration, the intensive energy cost of carbon capture can be mitigated, while efficiently exhausting waste heat in the process.

Screening the realistic TSA performance of novel promising solid sorbents requires lab-scale experiments in process relevant conditions: varying relative humidity, presence of oxygen, mass transfer kinetics, and multiple cycle stability. In this work, several prototypical MOFs (MIL-100Fe, UTSA-16, MOF-74Ni), a reference aluminosilicate zeolite (13X) and an ion exchange resin (Lewatit® VP1065) are screened in realistic conditions for CO_2 capture using advanced dynamic gravimetric sorption and packed bed breakthrough methods. After validation of methodology with previous results [2,3], we consider several factors that affect TSA efficiency, such adsorption/desorption temperature and cycle time. Importantly, we show that isobars (uptake at a constant concentration but changing temperature) are more relevant metrics than isotherms. We also identify the challenges and opportunities for further improvement of screening solid sorbents to be used in TSA processes for carbon capture applications.

Keywords: CCUS, solid sorbents, TSA, humidity, realistic conditions

References:

[1] Z. Hu, Y. Wang, B. B. Shah, D. Zhao, *Advanced Sustainable Systems* **2018**, 1800080.
[2] J. A. Mason, T. M. McDonald, T.-H. Bae, J. E. Bachman, K. Sumida, J. J. Dutton, S. S. Kaye, J. R. Long, *Journal of the American Chemical Society* **2015**, *137*, 4787–4803.
[3] N. S. Wilkins, J. A. Sawada, A. Rajendran, *Adsorption* **2020**, *26*, 765–779.

Solar powered hybrid desalination system between adsorption and salt hydrate desalination system

Ehab S. Ali[1], Ahmed S. Alsaman[2], A. M. Farid[3], A. E. Zohir[3], Mohamed Ghazy[2], Ahmed A. Askalany[2],*

[1] Mechanical Engineering Department, Faculty of Engineering, South Valley University, Qena 83511, Egypt.

[2] Mechanical Department, Faculty of Technology and Education, Sohag University, Sohag 82524, Egypt.

[3] Mechanical Engineering Department, Tabbin Institute for Metallurgical Studies, Tabbin, 11421, Cairo, Egypt.

Corresponding author. Email: ahmed_askalany3@yahoo.com

Abstract

This paper presents a simulation model for proposed solar-powered hybrid adsorption desalination and salt hydrate employing silica gel and copper sulfate as adsorbent material and salt hydrate respectively. In the present study, a simulation model of the investigated system utilizing three-bed has been investigated under Egyptian weather conditions. Solar radiation of Assuit city is expressed using TRNSYS software.

1. Introduction

Many countries around the world, especially developing countries and countries in the Middle East region suffer from a shortage of fresh water. Currently, over one-third of the world's population lives in areas where people are unable to meet their water demand of fresh water [1-3]. Many researcher presented many studies trying to improve the performance of ADCS by many methods as investigation new adsorption materials, improving adsorption beds overall heat transfer coefficient and improving adsorption time and adsorption beds arrangements.

2. System description

The proposed SHAD system is consists of three beds with two evaporators as expressed in Figure 1. The first and second beds are backed with silica gel while the third bed is backed with copper sulfate as salt hydrate material. The solar data is modeled by TRNSYS software. Figure 2 shows a schematic diagram for solar-assisted hybrid SHAD cycle using TRNSYS.
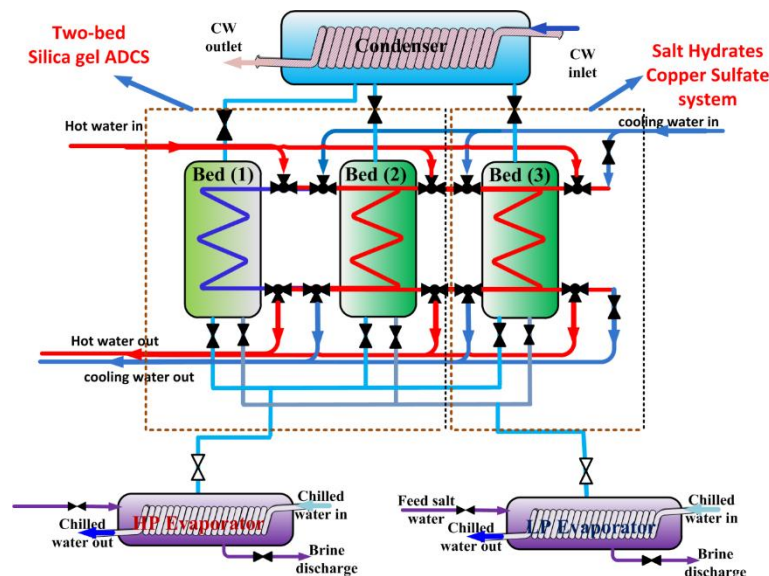
Fig.1. Hybrid salt hydrate and ADCS systems
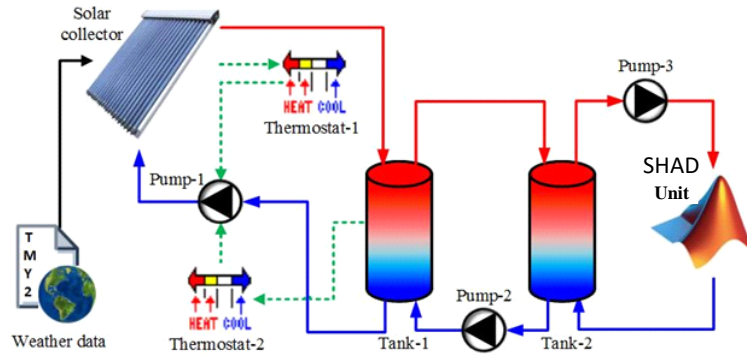
Fig.2. Schematic diagram for solar-assisted hybrid SHAD cycle using TRNSYS.

4. Results

This section presents the simulation results of the solar powered hybrid SHAD system for higher water desalination and cooling power.

Representative average daily SDWP of the solar-powered SHAD system, and SCP for around one-year climate conditions are presented in Fig. 3. It is found that, both SDWP and SCP increase with the increase of inlet HWT therefore, SDWP and SCP decrease with the decrease of the average SR. The average cycle COP increases until they reach their maximum values of about 0.67 for the selected city. The investigated hybrid system has higher performance in SDWP, SCP and COP by 57%, 55%, and 25% respectively compared to conventional AD system with silica gel as adsorbent material.
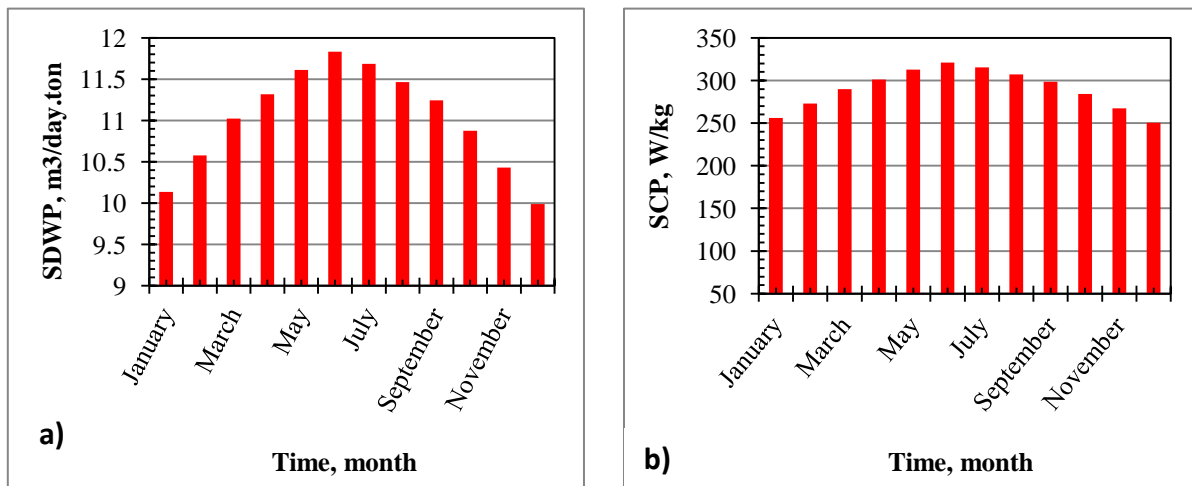
Fig. 3. Average a) SDWP, and b) SCP of the solar powered hybrid SHAD during the year for Assiut.

5- Conclusions

This study expresses the utilizing of solar powered solar hybrid adsorption and salt hydrated desalination systems under Egyptian weather conditions. Solar radiation of Assuit city is expressed using TRNSYS software with Assiut meteorological weather data. The investigated hybrid system has higher performance in SDWP, SCP and COP by 57%, 55%, 25% respectively compared to conventional ADCS system with silica gel as adsorbent material. It can be concluded that the hybrid SHAD system which is driven by solar energy can be used effectively with the Egyptian weather conditions

References

[1] Zejli D, Benchrifa R, Bennouna A, Bouhelal O, A solar adsorption desalination device: first simulation results. Desalination 2004;168:127–35.

[2] Alsaman AS, Askalany AA, Harby K, Ahmed MS. A state of the art of hybrid adsorption desalination–cooling systems. Renewable Sustainable Energy Rev 2016;58:692–703.

[3] Ali ES, Alsaman AS, Askalany AA, Harby K, Diab MR. Recycling brine water of reverse osmosis desalination system employing adsorption desalination system: A theoretical study, Desalination 2017;408:13–24.

Nonequilibrium condensation of supercritical carbon dioxide (sCO₂) in a centrifugal compressor for the Brayton cycle

Hongbing Ding[1], Yuanyuan Dong[1], Yu Zhang[1], Yan Yang[2,*], Chuang Wen[3,*]

[1]School of Electrical and Information Engineering, Tianjin University, Tianjin 300072, China

[2]Faculty of Environment, Science and Economy, University of Exeter, Exeter EX4 4QF, United Kingdom

[3]School of the Built Environment, University of Reading, Reading, RG6 6AH, United Kingdom

[*]Corresponding author: y.yang7@exeter.ac.uk, c.wen@reading.ac.uk

Abstract

The supercritical carbon dioxide (sCO₂) Brayton cycle is a highly efficient potential power propulsion system, providing necessary strategies for reducing pollution emissions and achieving the goal of carbon neutrality. The centrifugal compressor is the core equipment of the sCO₂ system. The efficient design of the supercritical carbon dioxide Brayton cycle requires the compressor to operate near the critical point of carbon dioxide, where the thermophysical properties of carbon dioxide will change significantly, making the flow in the compressor more complex and having the risk of condensation, thus affecting the compressor performance prediction. In this paper, an aerodynamic design method of a supercritical carbon dioxide centrifugal compressor was proposed to reduce the dependence on model experience. Combined with metastable phase characteristics, the cause of blade condensation was clarified, and the impact of impeller passage flow characteristics on compressor performance was systematically analysed.

Keywords: Brayton cycle, Supercritical carbon dioxide (sCO₂), Centrifugal compressor, Non-equilibrium condensation, Transonic flow, Phase change.

Nomenclature

Abbreviations

sCO₂	supercritical carbon dioxide
LE	leading edge
TIT	turbine inlet temperature

Symbols

c	critical
Y	liquid fraction
N	droplet number
I	nucleation rate

Introduction

Due to the global energy shortage and the continuous growth of energy demand, energy structure reform and new power propulsion technology have become urgent engineering problems in the field of energy and electricity. The supercritical carbon dioxide (sCO₂) Brayton cycle is a potential alternative power propulsion system [1]. It can realize efficient and clean

power generation, effectively reduce the pollution emissions of traditional power generation methods, and then make great contributions to achieving the goal of carbon neutrality. At lower turbine inlet temperature (TIT) [2], the sCO2 Brayton cycle can achieve similar efficiency to the steam Rankin cycle. In order to improve the cycle efficiency, the sCO2 Brayton cycle compressor should be close to but slightly higher than the critical point of carbon dioxide. At this critical point, the thermophysical properties of the working fluid change significantly and condensation is easy to occur. The main concern is the sharp change of fluid density, temperature and pressure near the critical point. Secondly, the condensation of the working fluid is easy to occur at the inlet of the compressor impeller due to the local flow acceleration and the accompanying local static pressure and temperature reduction. Therefore, in order to put the supercritical carbon dioxide (sCO$_2$) Brayton cycle system into real industrial utilization, the development and design of its anti-condensation and real gas analysis have quite necessary practical significance.

The concept of the supercritical CO$_2$ Brayton cycle was first proposed by Feher and Angelino [3-4]. In recent years, with the pursuit of higher energy utilization, effective Brayton cycle systems and design optimization have become a research focus again. Some numerical studies on the performance and flow field behavior of CO$_2$ centrifugal compressor have been further advanced. Kim et al. [5] studied the efficiency and pressure ratio of the compressor under different working conditions, and compared the numerical simulation results with the experimental data. Ameli et al. [6] studied the influence of different operating conditions on the compressor performance and the condensation phenomenon at the leading edge of the impeller (LE). On this basis, many researchers have explored the optimal design of centrifugal compressors. Wang et al. [7] designed an axial compressor based on the real gas model and found that the supercritical carbon dioxide compressor is more compact than the helium compressor. Wang et al. [8] adopted the system-component coupling optimization method to obtain the optimal parameters and design results of s CO$_2$ compressor and steam turbine. Li et al. [9] proposed a new design method for the impeller inlet of the sCO$_2$ compressor, and derived the acceleration margin to limit the condensation at the impeller inlet. Moreover, during the rapid cooling stage, the fluid enters a metastable state [10] and exhibits gaseous properties until it reaches the Wilson point, where nucleation begins. Therefore, a detailed explanation of metastable thermodynamic properties remains a key challenge in uncovering non-equilibrium condensation phenomena.

In the present study, an improved NIST real CO$_2$ gas model that can calculate the metastable characteristic values of fluid at a given pressure and temperature data point was developed. The physical and mathematical models of the sCO$_2$ centrifugal compressor were established, and subsequently, the condensation characteristics of CO$_2$ were predicted on the basis of validating the accuracy of the mathematical model. At last, the change of operating parameters in the non-equilibrium condensation process of centrifugal compressor and its influence on condensation were analyzed.

Physical model

The compressor used in this study is composed of blade, hub and shroud, including 24 blades. A clearance gap exists between the blades and the shroud of the compressor. The outer

Heat Powered Cycles
Conference 2023
Edinburgh

Heat in the new energy system

3rd to 6th of September 2023
The University of Edinburgh, Scotland

diameter of the blade row is about 40 cm. The physical structure of the centrifugal compressor is shown in **Fig. 1**.
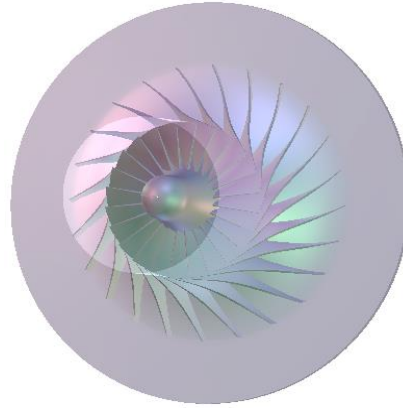
Fig. 1 Impeller geometry of sCO2 centrifugal compressor

Mathematical model

The mass, momentum, and energy conservation equations of the gas-liquid mixture are shown below,

$$\frac{\partial \rho}{\partial t} + \nabla \cdot (\rho \bar{u}) = S_m \tag{1}$$

$$\frac{\partial (\rho \bar{u})}{\partial t} + \nabla \cdot \left(\rho \bar{u}_i \bar{u}_j \right) = -\nabla \cdot p + \nabla \cdot (\bar{\bar{\tau}}) + S_F \tag{2}$$

$$\frac{\partial (\rho E)}{\partial t} + \nabla \cdot [\bar{u} (\rho E + p)] = -\nabla \cdot (\lambda \cdot \nabla T) + S_h \tag{3}$$

where u, p, ρ, and E are the velocity, pressure, density, total energy of the gas phase, respectively. $\bar{\bar{\tau}}$ is the stress tensor, and S_m, S_F, S_h are the mass, momentum, and energy source terms produced by the exchange between two phases. Two transport equations are used to describe the condensation process of CO_2 in supersonic flow. Two scalar equations are used to describe the droplet number (N) and a liquid fraction (Y).

$$\frac{\partial (\rho Y)}{\partial t} + \nabla \cdot (\rho \bar{u} Y) = S_Y \tag{4}$$

$$\frac{\partial (\rho N)}{\partial t} + \nabla \cdot (\rho \bar{u} N) = I \tag{5}$$

The source term S_Y describes the condensation rate of the wet steam and $S_Y = m_v$, where m_v represents mass production rate. N (m^{-3}) is the number of droplets per volume. I (m^{-3}s^{-1}) is the spontaneous condensation nucleation rate, which is defined as:

$$I = \frac{q_c}{1+\theta} \frac{\rho_{CO2}^2}{\rho_l} \sqrt{\frac{2\sigma}{\pi M_m^3}} \exp \left(-\frac{4\pi \sigma r_c^2}{3 k_B T_{CO2}} \right) \tag{6}$$

The condensation of CO_2 in supersonic flow includes the nucleation process and droplet growth process. And m_v is determined by nucleation and droplet growth in the process of non-equilibrium condensation.

$$m_v = \frac{4}{3}\pi\rho_l I r_c^3 + 4\pi\rho_l N r^2 \frac{\partial r}{\partial t} \tag{7}$$

where ρ_l is the liquid density, r (m) is the droplet radius, dr/dt is the growth rate of droplets, the r_c is the critical droplet radius.

Numerical methods

The centrifugal compressor was meshed with three-dimensional structural grids. Single channel grids and local refinement are shown in **Fig. 2**. Both sides of the single channel are set with rotating periodic interface, and the boundary condition of solid wall is anti-slip thermal insulation wall. Viscosity model set to SST k-ω. The solver uses the pressure-based transient solution method to solve the equation. The inlet and outlet conditions are set as pressure inlet and pressure outlet respectively, and the Second-order upwind scheme is used to discrete the turbulent flow energy equation, the turbulent dissipation rate equation, and the flow control equation.

Mesh refinement
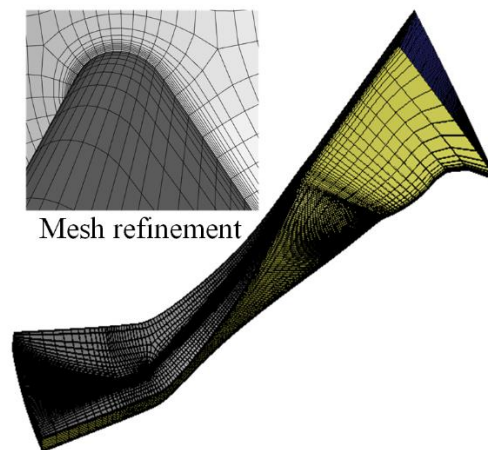
Fig. 2 Computational grid for single-channel impeller

To illustrate the accuracy of the CO_2 condensation model, this paper selects the nozzle structure and experimental data of Claudio Lettieri's for specific validation, which can be obtained in **Fig. 3**. The inlet pressure is 57.24 bar and the inlet temperature is 314.78 K. As shown in **Fig. 4**, a pressure jump occurs behind the nozzle throat, which is caused by the release of latent heat during the process of condensation. It should be emphasized that in this study, based on the cubic spline extrapolation method, the real gas properties calculated by the established mathematical model are extended to the metastable region, achieving a smooth transition during the pressure jump process, which is closer to the experimental results, that can be intuitively observed in the figure. In addition, it can be seen that the condensation position of the ideal gas is relatively backward, and the prediction ability of the ideal gas model for condensation characteristics is also poor. This further confirms that the NIST real gas model based on cubic spline curve extrapolation and equation of state (EOS) is absolutely accurate and stable for simulating the condensation process of CO_2.

3rd to 6th of September 2023
The University of Edinburgh, Scotland

Heat Powered Cycles
Conference 2023
Edinburgh

Heat in the new energy system
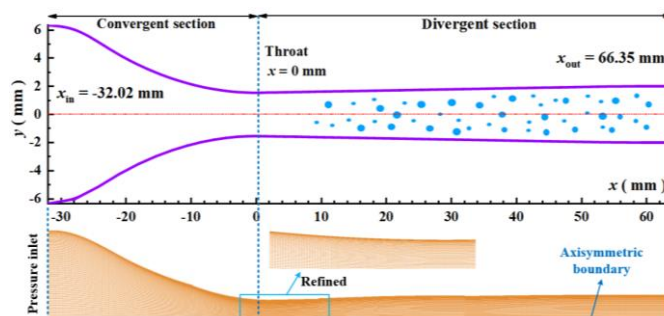
Fig. 3 The geometry and dimensions of the nozzle used for validation
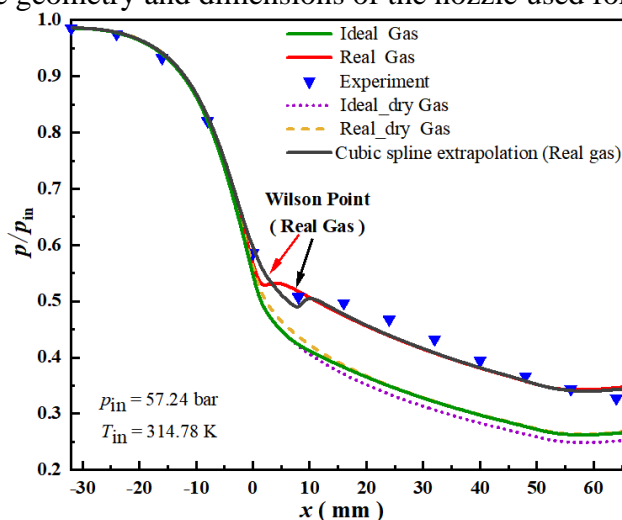
Fig. 4 The validation results of CO_2 models with experiment and simulation

Results and discussion

This section presents the numerical results of the sCO_2 centrifugal compressor and observes the performance and flow characteristics of the sCO_2 centrifugal compressor. Under the action of centrifugal compressor blades, the temperature and pressure values of the working medium will continuously increase with the flow direction. This phenomenon can be found in **Fig. 5** and **Fig. 6**. As shown in **Fig. 5**, the range of static temperature of an CO_2 gas medium centrifugal compressor impeller is about 250-400K. At 10% span, the temperature at the tip of the trailing edge of the blade reaches the maximum value, about 400K. Similarly, the maximum values of temperature at 50% and 90% span appear at the rear end of the blade. As the span of the blade increases, the temperature drop significantly increases. Compared to the wet gas model, the temperature difference under dry gas will be greater.

Heat Powered Cycles
Conference 2023
Edinburgh

Heat in the new energy system

3rd to 6th of September 2023
The University of Edinburgh, Scotland
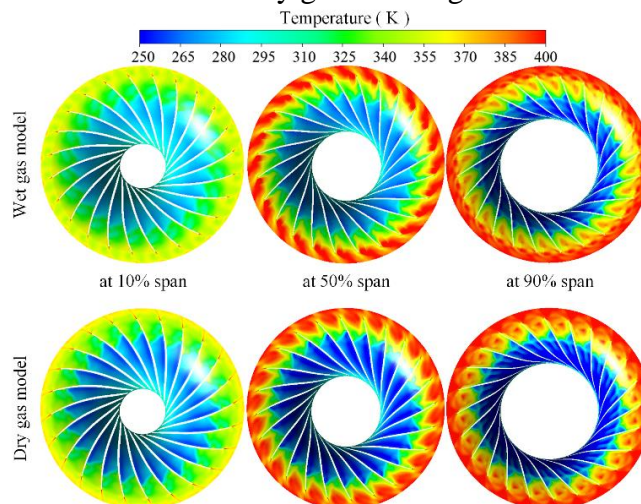
Fig. 5 Distribution of static temperature on compressor blades

Similar to the static temperature distribution, as shown in **Fig. 6**, the static pressure range of an CO_2 gas medium centrifugal compressor impeller is about 10-180 bar, showing a trend of first decreasing and then increasing, with a maximum static pressure value appearing at the rear end of the blade.

Presssure (bar)
0 18 36 54 72 90 108 126 144 162 180

at 10% span   at 50% span   at 90% span
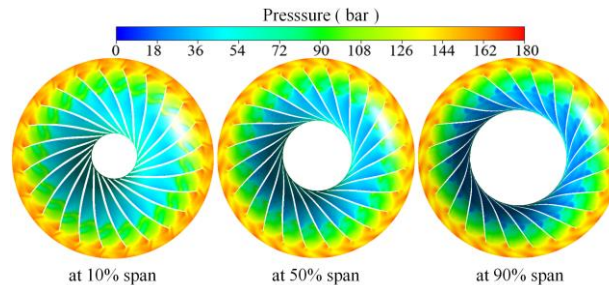
Fig. 6 Distribution of static pressure on compressor blades

Fig. 7 shows the distribution of relative Mach numbers along different leaf height directions under the wet gas model. It can be clearly seen that the overall trend of relative Mach numbers is to increase first and then decrease, with the high-speed region mainly concentrated at the tip of the front edge of the blade suction. At the height of 90% of the blade, the velocity changes are sufficiently intense, and there is a significant presence of supersonic regions and strong shock behavior. That is, the intensity of the shock wave has a significant increase trend with the increase of the blade height. **Table 1** shows the specific data results. The channel shock wave mainly exists at the leading edge and suction slide of the blade, and there is a relatively obvious low speed region at the outlet.

Relative Mach number (-)
0.000 0.225 0.450 0.675 0.900 1.125 1.350 1.575 1.800

at 10% span   at 50% span   at 90% span
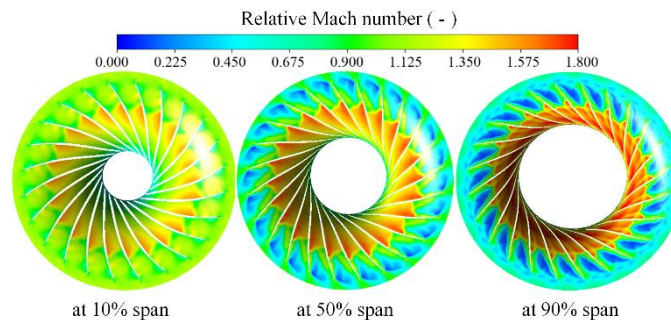
Fig. 7 Distribution of Mach Numbers on Compressor Blades

Table 1 Comparison of Mach Number at different blade span

Mach number	At 10% span	At 50% span	At 90% span
Minimum	0.113	0.106	0.097
Maximum	1.605	1.733	1.867

There are significant differences in ΔT under dry and wet gas models. As shown in **Fig. 8**, under the wet gas model, the higher ΔT occurs at the front end of the blade, while the lower supercooling occurs at the trailing edge of the blade. That is, supercritical CO_2 tends to reach a supersaturated state at the leading edge of the blade, which means condensation is prone to occur there.
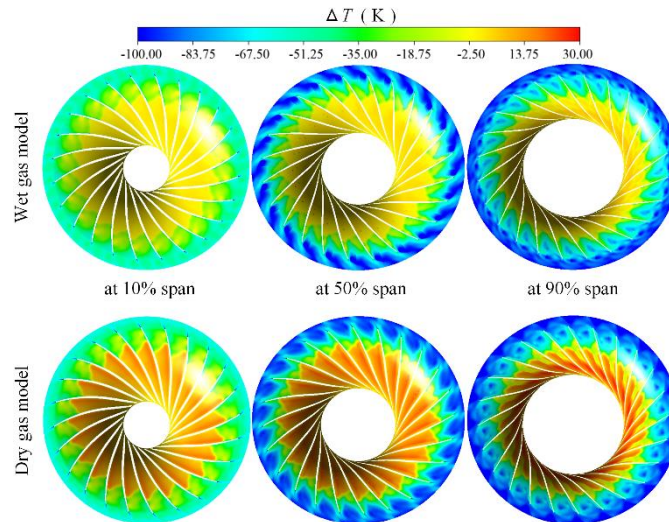
Fig. 8 Distribution of Degree of supercooling (ΔT) of compressor blades

Finally, the liquid fraction of supercritical carbon dioxide in a centrifugal compressor is analyzed, which is a typical parameter for measuring CO_2 condensation. As shown in **Fig. 9**, as the blade height increases, the condensation intensity at the front end of the blade increases, and the variation pattern is very similar to the distribution of the relative Mach number. This distribution pattern indicates that the condensation at the leading edge of the blade in a sCO_2 centrifugal compressor is caused by local flow acceleration. This provides theoretical guidance for blade design aimed at reducing CO_2 condensation.
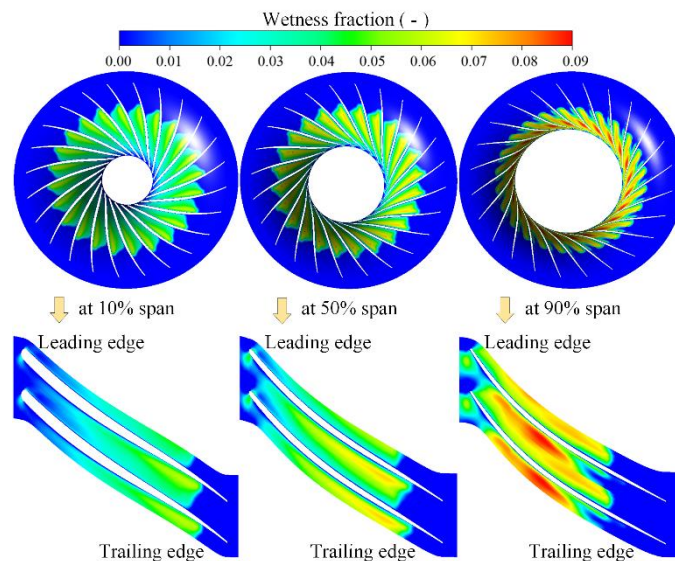
Fig. 9 Distribution of wetness fraction on compressor blades

Table 2 provides specific data on wetness fraction under different blade span. It can be seen that with the increase of blade span from 10% to 90%, the liquid fraction during condensation can increase from 6.0% to 9.1%.

Table 2 Comparison of wetness fraction Data at Different blade span

Wetness fraction	At 10% span	At 50% span	At 90% span

Minimum	0	0	0
Maximum	6.0%	7.3%	9.1%

Conclusions

In this paper, a numerical calculation model for cubic spline curve extrapolation of CO_2 real gas is established. After validation, the model can accurately predict the condensation behavior of CO_2 after passing through the metastable region. Applying this model to a supercritical CO_2 centrifugal compressor, through numerical simulation, the main conclusions are as follows:

1) With the increase of blade span, the temperature and pressure difference of the fluid significantly increases, and the low temperature and pressure regions appear at the leading edge of the blade.

2) A supersonic region appears at the leading edge of the blade, where the Mach number and wetness fraction have a consistent trend, and condensation is extremely prone to occur.

3) As the blade span raises, the condensation intensity increases, and the value of ΔT also increases.

Acknowledgments

References

[1] Ahn Y, Bae SJ, Kim M, Cho SK, Baik S, Lee JI, et al. Review of supercritical CO2 power cycle technology and current status of research and development. Nucl Eng Technol. 2015;47:647-61.

[2] White MT, Bianchi G, Chai L, Tassou SA, Sayma AI. Review of supercritical CO2 technologies and systems for power generation. Appl Therm Eng. 2021;185:1.

[3] Feher EG. The supercritical thermodynamic power cycle. Energy Conversion 1967; 8(2):85–90.

[4] Angelino G. Carbon dioxide condensation cycles for power production. J Eng Gas Turbines Power 1968;90(3):287–95.

[5] Kim SG, Lee J, Ahn Y, Lee JI, Addad Y, Ko B. CFD investigation of a centrifugal compressor derived from pump technology for supercritical carbon dioxide as a working fluid. The Journal of supercritical fluids. 2014;86:160-71.

[6] Ameli A, Uusitalo A, Turunen-Saaresti T, Backman J. Numerical Sensitivity Analysis for Supercritical CO2 Radial Turbine Performance and Flow Field. Energy procedia. 2017;129:1117-24.

[7] Wang Y, Guenette G, Hejzlar P, Driscoll M. Compressor design for the supercritical CO2 Brayton cycle. In: Proceedings of the 2nd international energy conversion engineering conference; 2004.

[8] Wang J, Guo Y, Zhou K, Xia J, Li Y, Zhao P, et al. Design and performance analysis

of compressor and turbine in supercritical CO.sub.2 power cycle based on system-component coupled optimization. Energ Convers Manage. 2020;221.

[9]   Li X, Zhao Y, Yao H, Zhao M, Liu Z. A New Method for Impeller Inlet Design of Supercritical CO2 Centrifugal Compressors in Brayton Cycles. Energies. 2020;13:5049.

[10]   Vijayakumaran H, Lemma TA. CFD modelling of non-equilibrium condensation of CO2 within a supersonic nozzle using metastability approach. J Nat Gas Sci Eng. 2021;85:103715.

CFD simulations on heat transfer performances by a solar thermal energy in a water-based serpentine photovoltaic-thermal collector

Sang Shin Park[1*] and Ji-Hong Moon[2]

[1]Energy AI·Computational Science & Engineering Laboratory, Korea Institute of Energy Research (KIER)
Deajon, South Korea
[2]Clean Fuel Research Laboratory, Korea Institute of Energy Research (KIER), Deajon, South Korea
[*]Sang Shin Park: pss@kier.re.kr

Abstract

In current article, in order to investigate and analysis solar thermal transfer performance in a water-based serpentine PVT collector, three-dimensional computational fluid dynamics (CFD) modeling was carried out. The CFD modeling results were carefully validated with experimental data. The thermal efficiencies of CFD modeling results were in good agreement with experimental data as error scale from 1.4% to 5.76%. After this careful verification, the CFD modeling was also carried out to investigations of solar thermal energy performances by pitch sizes (40 mm, 60 mm, 80 mm, 100 mm, and 120 mm) and water inlet positions. Specifically, significant parameters of a useful thermal energy (Q_u), water outlet temperature, pressure drop, and $Q_u/\Delta P$ (useful thermal energy ($\dot{m}\cdot Cp\cdot\Delta T$)/pressure drop ($\Delta P$)) were numerically derived with the pith sizes and the water inlet positions. Given the selected significant parameters and by considering $Q_u/\Delta P$, the optimal pitch size was found to be 80 mm, while it was shown that the optimal position for the water inlet was on the left side of the unit.

Keywords: Water-based PVT collector; Solar thermal energy; CFD simulation; Solar thermal energy.

Introduction/Background

Fossil fuel resources are seriously depleting due to growing energy demand with increasing population density and technology for the past 30 years [1]. In this paper, experimental results on the solar thermal energy performance of a PVT collector designed and installed according to ISO 9806 [13] were used to validated the CFD model of a water-based serpentine PVT collector. Once verified, CFD modeling was carried out to investigate and analyze solar thermal energy performance for various pitch sizes on a water-based serpentine PVT collector. The optimum designs in the water-based serpentine PVT collector were derived with thermal efficiency as well as pressure drop. Those were disclosed for the first time to our knowledge. The future perspectives of this study include the contribution of a design guide for a carbon-free solar heating and power generation system with PVT water thermal-hydraulic performance results.
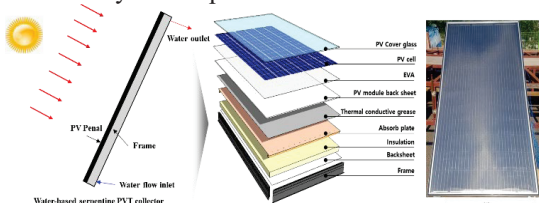

Fig. 1. Schematic diagram of water-based serpentine (PVT) collector

Discussion and Results

The spatial distribution of temperature over the tube, PV module, and insulator obtained by CFD calculations for cases 1 to 4 are shown in Fig. 2. The temperature of the tube gradually increased as we move with the injected water flowing from the inlet to the outlet, while the temperatures of the PV module and insulator in the areas where the tubes carried the flowing water were lower than the surrounding areas with no tubing.
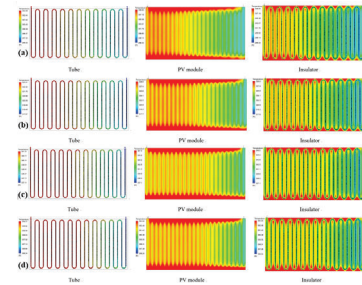

Fig. 2. Spatial distribution of temperature : (a) radiation of 1047.58 W/m² and inlet temp. of 23.18°C, (b) radiation of 1019.08 W/m² and inlet temp. of 44.52°C, (c) radiation of 997.85 W/m² and inlet temp. of 63.96°C, and (d) radiation of 1038.58 W/m² and inlet temp. of 83.09°C.
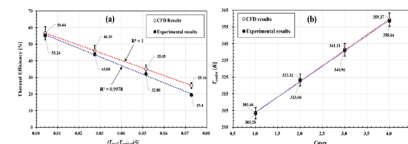

Fig. 3. Validation of CFD with exp. results : (a) Exp. results vs. CFD results for thermal efficiency and (b) Exp. results vs. CFD results for outlet temp..

Summary/Conclusions

In the current paper, a numerical investigation and analysis was achieved to validation with experimental data and assessment for effects of various pitch sizes. Our CFD model was verified by comparing its predictions with real-world experimental results of the same system. Furthermore, the validated our CFD model was significantly applied to assess the solar thermal energy performances by effects of various pitch sizes and positions of the water inlet affected the water-based serpentine PVT collector.

References

[1] Misha A. et al., "Simulation CFD and experimental investigation of PVT water system under natural Malaysian weather conditions" Energy Repo., 2020

[2] ISO 9806 (KS B 8295). Solar Energy – Solar Thermal Collector - Test methods, 2013

Liquid Metals as Heat Transfer Fluids for High-Temperature Heat Storage

Klarissa Niedermeier[1*], Franziska Müller-Trefzer[1] and Thomas Wetzel[1]

[1]Karlsruhe Institute of Technology (KIT), Institute for Thermal Energy Technology and Safety (ITES),
Hermann-von-Helmholtz-Platz 1, 76344 Eggenstein-Leopoldshafen
[*]Corresponding author: klarissa.niedermeier@kit.edu (10-pt. Times New Roman)

Abstract

With a growing share of fluctuating renewables, the use of energy storage systems bridging the gap between supply and demand becomes increasingly important to ensure reliable energy supply. Among such storage systems, thermal energy storage is a simple, low-cost and efficient way to store energy in the form of heat. Thermal energy storage can help balancing the heat grid, can be used in sector coupling or in heat-to-power-to-heat systems. However, especially at high temperatures, storage concepts, configurations and materials are still under research. The poster will give an overview of the current work of the Karlsruhe Liquid Metal Laboratory regarding liquid metal-based high-temperature heat storage.

Keywords: heat storage, packed bed, liquid metal, heat transfer.

Introduction

At the Karlsruhe Institute of Technology (KIT), the Karlsruhe Liquid Metal Laboratory focuses on heat storage systems with liquid metals as the heat transfer fluid and the test of materials and components in contact with liquid metals.

Liquid metals offer a wide liquid temperature range and excellent heat transport rates; therefore, they can act as efficient heat transfer fluids in so-called packed bed thermal energy storage systems, based on cheap, granular solid storage materials [1].

Discussion and Results

The poster will present the current activities of the Karlsruhe Liquid Metal Laboratory regarding high-temperature heat storage:

(1) The results of testing a lab-scale prototype with ceramic filler material and liquid lead-bismuth as heat transfer fluid will be discussed [2].

(2) The design and set-up of a pilot-scale demonstrator (100 kWh) will be presented.

(3) The high-temperature material and component test loop (700°C, liquid lead), which is currently under construction, will be shown.

Summary

Using liquid metals as heat transfer fluid has the advantage of high heat transfer rates and high operating temperatures. The challenges are material compatibility issues at high temperatures above 600°C. Therefore, we focus on demonstrating heat storage systems from lab to pilot scale and test materials and components (e.g. pumps, valves) in contact with liquid metals.

References

[1] Niedermeier, K., Marocco, L., Flesch, J., Mohan, G., Coventry, J., Wetzel, T., "Performance of molten sodium vs. molten salts in a packed bed thermal energy storage", Applied thermal engineering, 141, 368–377, 2018.

[2] Müller-Trefzer, F., Niedermeier, K., Daubner, M., Wetzel, T., "Experimental investigations on the design of a dual-media thermal energy storage with liquid metal", Applied Thermal Engineering, 213, 118619, 2022.

Thermodynamic Analysis of a small-scale Reversible Heat Pump–Organic Rankine Cycle System for residential applications

Zaib Shahid[1], Luca Cioccolanti[2], Sebastiano Tomassetti[1] and Giovanni di Nicola [*1]

[1]Department of Industrial Engineering and Mathematical Sciences,
Università Politecnica delle Marche - 60121 Ancona – Italy

[2]Research Center on Energy, Environment and Landscape, Università degli Studi eCampus - 22060 Novedrate – Italy

[*]Corresponding author: g.dinicola@univpm.it

Abstract

In the present study, a thermodynamic analysis of a reversible Medium-Temperature Heat Pump—Organic Rankine Cycle (MTHP - ORC) system is conducted to evaluate the suitable operating range of different low global warming potential (GWP) working fluids for varying heat source and sink temperatures. The heat source considered in our investigation is derived from solar thermal collectors. Additionally, we assessed eight low GWP working fluids capable of efficient operation in both modes. The correlation between the Coefficient of Performance (COP) and temperature lift in heat pump mode, as well as the relationship between global efficiency and temperature lift in ORC mode, are evaluated. The results unveil that R1336mzz(Z) attains the optimum COP in HP mode, while R1233zd(E) achieves the highest global efficiency in ORC mode, each within their specific temperature ranges of heat sink and source.

Keywords: reverse heat pump—organic Rankine cycle, global warming potential, refrigerants

Introduction

In today's world, finding sustainable energy solutions is more important than ever. The world needs efficient and renewable sources of power, so as to replace the reliance on fossil fuels, due to their scarcity and impact. This shift is a path towards a greener future, which relies on innovations that not only use renewable resources but also integrate them seamlessly into our daily lives.

Combining solar thermal collectors with efficient energy technologies, such as heat pumps [1], is a big step towards this sustainable goal. One of the ideas is to develop an integrated system in which we bring together heat pumps (HPs) and Organic Rankine Cycle (ORC) systems assisted by the solar energy. This creates a versatile system that can generate electricity and provide heating.

In summer, when the heat captured by solar thermal collectors exceeds the one needed for domestic applications, the system turns into an ORC, turning extra heat into electricity. In

winter, it becomes a heat pump, warming up homes or domestic water. This dual function is a smart way to manage energy in residential buildings. This idea has been discussed by few of the peer authors such as Dumont et al [2] and Stefan et al [3],

For better energy solutions, it is important to choose the suitable working fluids as their high global warming potential (GWP), toxicity and flammability, can be harmful to the environment. The choice of these fluids, called refrigerants, are important in both heat pumps and Organic Rankine Cycle (ORC) systems in terms of performance. Hence, in this paper eight low-GWP refrigerants have been selected and a thermodynamic study on the performance of Medium Temperature Heat Pump (MTHP) - ORC system is carried out with varying heat source and sink temperatures, so as to figure out the best temperature range for its optimum performance based on how much heat it gives to the end-user (in heat pump mode) and how much work it generates (in the ORC mode).

The selected eight refrigerants for analysis are as R245fa, R134a, R1233zd(E), R1234ze(Z), R1234ze(E), R1234yf R1224yd(Z), R1336mzz(Z).

System Configuration

The considered system consists of three interconnected loops each serving a distinct purpose. In the first loop, a heat transfer fluid absorbs heat from solar collectors and transfers it to the evaporator. The second loop (in the ORC mode) utilizes the absorbed heat to produce electricity and provide heat through the condenser. Finally, in the third loop, a hot water absorbs heat from the condenser and distributes it to end user, such as a residential building. Figure 1 illustrates the working principle of a reversible MTHP-ORC system.

The system is supposed to operate as solar ORC when the temperature of the fluid in the first loop is high (i.e., summertime) and as solar heat pump mode for lower temperatures (i.e., wintertime). In the second case, the expander of the ORC acts as a compressor. The following ranges for the inlet temperature of the heat transfer fluid in the first loop are analysed: 100-140 °C in the ORC mode and 30-60 °C in the HP mode. Instead, the studied inlet temperatures of hot water in the third loop range from 50 to 70 °C in both operating modes.
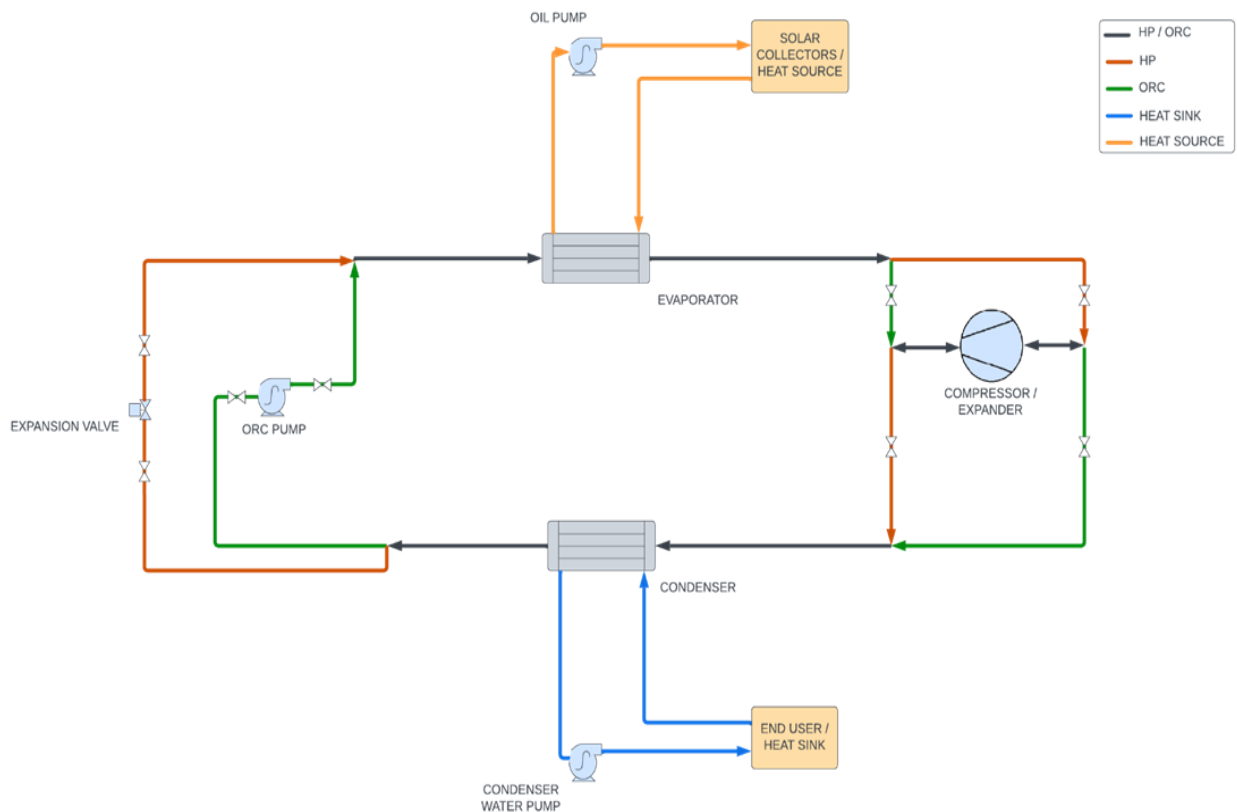
Figure 1: Schematic of solar-powered reversible Heat Pump–organic Rankine cycle system

For the feasibility of analysis, some parameters must be fixed, based on the literature [2], [3], [4]. Table 1 reports the values of parameters that are fixed in the present analysis.

Table 1: Technical data of the components

Component	Parameter	ORC Mode	HP Mode
Evaporator	Oil pump speed at evaporator (rpm)	2500	2500
	Oil pump swept volume at evaporator (m3/rev)	1.95E-05	1.95E-05
	Oil input temperature (°C)	100-140	30-60
	Superheating et evaporator (K)	5	5
	Temperature difference between Toil and Tev (K)	15	10
	Evaporator efficiency (%)	21.79	21.79

	Evaporator pressure ratio drops (-)	0.997	0.967
Condenser	Water flow at condenser (kg/s)	0.846	--
	Water input temperature (°C)	40-60	40-60
	Delta temperature of water (°C)	-	10
	Subcooling at condenser (K)	5	5
	Temperature difference between Tcond and Tw (K)	10	10
	Condenser pressure ratio drops (-)	0.955	0.996
Expander/compressor	Built-in volume ratio (BVR) (-)	2.8	2.8
	Swept volume (m^3/rev)	2.95E-05	8.26E-05
	Overall isentropic efficiency (%)	58	66
ORC pump	ORC pump swept volume (dm^3/rev)	15.1/1725	-
	Pump isentropic efficiency (%)	50	-

Methodology

The numerical model is developed in MATLAB while fluid properties are taken from REFPROP 10.0 library. The ORC modelling originates from a previous work by Moradi et al. [5] considering single-coefficient models for main components. The reverse operation of the system in heat pump mode is developed by the authors of the present paper and main assumptions are taken in accordance with Dumont et al [4].

The selected refrigerants are ranked for each operation mode and eventually the most suitable fluids for the reverse operation are identified for given temperature ranges of heat source and sink temperatures. In this way the work makes possible to preliminary assess the suitability of the different working fluids and their admissible operating range considering the peculiarities of small-scale MTHP-ORC systems based on volumetric machines.

In particular, after fixing above mentioned parameters, (as mentioned in Table 1), the code takes as input the operating temperatures i.e., inlet temperature of thermal oil into evaporator and that of water into condenser. The program then utilizes the thermophysical properties such as pressure, temperature, entropy, specific volume at each state of heat pump / ORC from the REFPROP library and basic thermodynamical relations such as rate of heat transfer, efficiency, coefficient of performance etc. The simulation is run for every inlet temperature increment of 10°C both for thermal oil to evaporator and that of water to condenser, so as to get the running conditions for optimum performance.

Table 2 and 3 shows the minimum and maximum values of the main parameters in HP and ORC mode respectively.

Table 2 - Minimum and maximum values of parameters (HP Mode)

Parameters	Min	Max
Condenser Thermal Power (W)	3393.43	4292.41
Evaporation Pressure (bar)	0.60	13.18
Condensation Pressure (bar)	1.85	21.90
Mass flow rate of Refrigerant [kg/h]	58.39	124.92
Mass flow rate of Water [kg/h]	292.26	369.05
Compressor power consumption [W]	358.80	1300.74
Coefficient of performance	3.30	9.63
Pinch-point - Evaporator (K)	4.83	7.29
Pinch-point - Condenser (K)	0.26	1.86

Table 3 - Minimum and maximum values of parameters (ORC Mode)

Parameters	Min	Max
Evaporator Thermal Power (W)	11181.13	29707.43
Evaporation Pressure (bar)	4.89	30.26
Condensation Pressure (bar)	1.80	21.23
Mass flow rate [kg/h]	210.12	718.18
Expander power generation [W]	70.15	2225.55
Efficiency (%)	0.63	7.52
Pumping Losses (BWR)	0.06	0.73

Pinch-point - Evaporator (K)	5.11	44.78
Pinch-point - Condenser (K)	2.52	3.59

Results and Discussions:

After running the simulations for each refrigerant over the varying temperatures of sink and source, the values for the various parameters are reported. Tables 4 & 5 shows the summarized simulated results for the corresponding parameters along with COP and global efficiency when the system is simulated for HP and ORC mode respectively.

Table 4 : Summarized simulation results for each refrigerant in HP Mode

Refrigerant	T_in_ev (°C)	T_out_ev (°C)	T_in_cond (°C)	T_out_cond (°C)	M_ref (kg/h)	M_water (kg/h)	P_ex_p (bar)	Pressure Ratio_t	W_el_net (W)	Q_con (W)	COPel	PinchP_ev (K)	PinchP_cd (K)
R1224yd(Z)	30.00	27.84	60.00	70.00	92.76	349.99	1.24	4.79	1079.04	4070.71	3.77	6.86	0.78
	60.00	57.84	60.00	70.00	82.05	297.48	3.32	1.79	363.63	3459.97	9.52	6.99	0.42
R1233zd(E)	30.00	27.84	60.00	70.00	75.89	347.35	1.08	4.89	1048.35	4040.02	3.85	4.91	1.02
	60.00	57.84	60.00	70.00	69.15	297.18	2.93	1.80	360.15	3456.49	9.60	7.04	0.46
R1234yf	30.00	27.84	60.00	70.00	124.92	369.05	5.92	3.57	1300.74	4292.41	3.30	7.11	1.45
	40.00	37.84	40.00	50.00	88.32	295.26	7.84	1.72	400.90	3428.26	8.55	7.20	0.69
R1234ze(E)	30.00	27.84	60.00	70.00	99.24	359.20	4.27	3.90	1186.17	4177.84	3.52	6.99	1.25
	60.00	57.84	60.00	70.00	87.69	299.89	9.97	1.67	391.68	3488.01	8.91	7.06	0.76
R1234ze(Z)	30.00	27.84	60.00	70.00	70.67	347.81	1.49	4.67	1053.76	4045.43	3.84	6.88	1.17
	60.00	57.84	60.00	70.00	64.65	297.42	3.91	1.78	362.93	3459.27	9.53	7.07	0.58
R1336mzz(Z)	30.00	27.84	60.00	70.00	90.70	349.78	0.60	5.62	1076.59	4068.26	3.78	4.85	0.54
	60.00	57.84	60.00	70.00	79.41	297.06	1.79	1.89	358.80	3455.14	9.63	6.94	0.26
R134a	30.00	27.84	60.00	70.00	91.34	359.66	5.72	3.83	1191.55	4183.22	3.51	7.06	1.86
	50.00	47.84	50.00	60.00	76.36	297.46	10.17	1.71	393.89	3456.13	8.77	7.16	0.93
R245fa	30.00	27.84	60.00	70.00	79.35	349.67	1.23	5.12	1075.36	4067.03	3.78	6.85	0.81
	60.00	57.84	60.00	70.00	70.39	297.36	3.44	1.83	362.29	3458.62	9.55	6.90	0.43

Table 5: Summarized simulation results for each refrigerant in ORC Mode

Refrigerant	T_in_HF (°C)	T_out_HF (°C)	T_in_CF (°C)	T_out_CF (°C)	M_ref (kg/h)	P_ex_p (bar)	Pressure Ratio_t	BWR	W_el_net (W)	Eff_el_net	Q_ev2 (W)	PinchP_ev (K)	PinchP_cd (K)
R1224yd(Z)	100.00	92.25	60.00	63.18	258.74	8.30	1.44	0.14	217.28	1.89	11483.88	8.59	3.23
	140.00	120.59	40.00	47.75	527.11	19.25	5.78	0.16	2100.99	7.11	29536.51	6.07	3.38
R1233zd(E)	100.00	92.25	60.00	63.18	221.32	7.42	1.45	0.12	225.82	1.97	11489.89	8.45	3.25
	140.00	120.55	40.00	47.73	459.53	17.35	5.90	0.13	2225.55	7.52	29586.11	5.20	3.26
R1234yf	100.00	92.46	60.00	63.13	347.37	27.88	1.36	0.73	70.15	0.63	11181.13	10.05	2.87
	140.00	120.63	40.00	48.09	711.54	27.88	2.13	0.46	789.68	2.68	29467.57	44.78	2.58
R1234ze(E)	100.00	92.36	60.00	63.16	282.70	22.32	1.38	0.46	140.65	1.24	11324.92	9.27	2.99
	140.00	120.72	40.00	47.95	611.00	30.26	3.03	0.38	1174.81	4.00	29344.82	31.34	2.52
R1234ze(Z)	100.00	92.26	60.00	63.18	210.12	9.66	1.43	0.15	218.99	1.91	11470.72	8.52	3.21
	140.00	120.64	40.00	47.72	445.76	22.33	5.69	0.17	2122.50	7.21	29452.08	6.00	3.03
R1336mzz(Z)	100.00	92.26	60.00	63.18	243.27	4.89	1.49	0.09	227.20	1.98	11483.41	8.59	3.39
	140.00	120.47	40.00	47.77	482.10	12.20	6.80	0.10	2199.69	7.40	29707.43	5.65	3.59
R134a	100.00	92.44	60.00	63.13	283.07	29.26	1.38	0.58	111.64	1.00	11211.60	9.51	2.97
	100.00	-	40.00	*expansion in the two phase region*									
R245fa	100.00	92.27	60.00	63.18	222.32	8.93	1.46	0.14	218.15	1.90	11467.14	8.60	3.30
	140.00	120.59	40.00	47.75	455.51	21.32	6.18	0.16	2103.54	7.12	29527.73	6.20	3.34

Interestingly the findings related to performance of low GWP refrigerants are better than that of relatively high GWP refrigerants i.e., R134a & R245fa. Such that, for the same system configuration, R1234yf resulted in highest condenser heat rejection (in Heat Pump Mode) whereas, R1233zd(E) showcased a highest net power output (in ORC Mode). Moreover, R1233zd(E) showcased a highest global efficiency too in ORC Mode whereas R1336mzz(Z) achieved the highest COP in heat pump mode. It is noteworthy that in ORC Mode, the least BWR is exhibited by R1336mzz(Z), along with significant global efficiency making it one of

the best performing refrigerants among others in both the modes. Figure 2 illustrates the COP & Heat delivered by Heat Pump, Figure 3 illustrates the Global Efficiency & Net work done by ORC, and Figure 4 illustrates BWR at Optimum Conditions for each analysed refrigerant respectively.
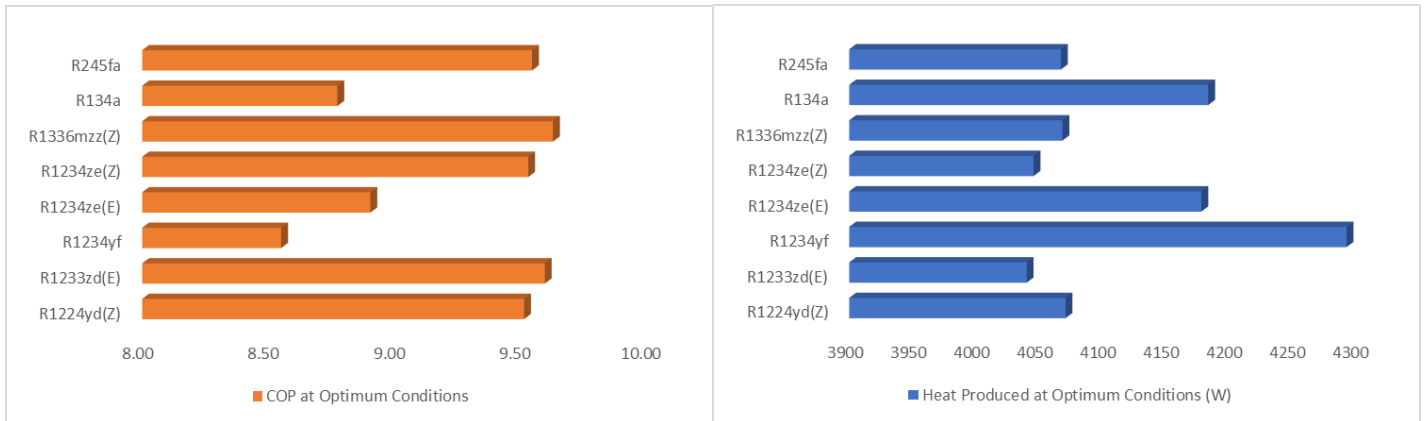

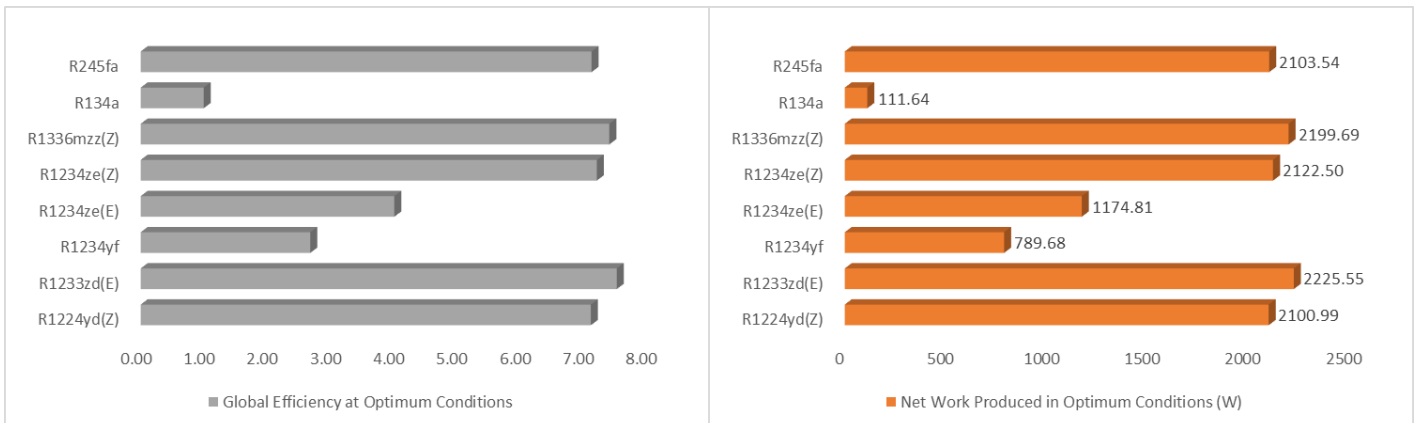*Figure 2: COP & Heat delivered by HP in Optimum Conditions*

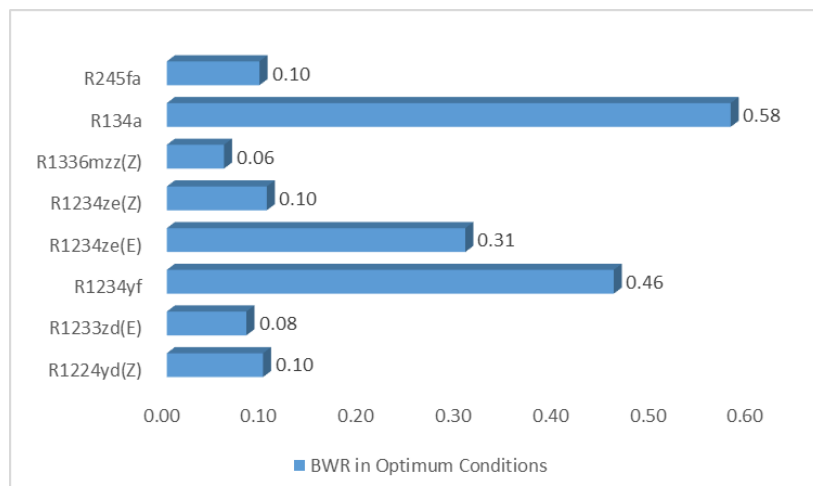*Figure 3: Global Efficiency and Net Work Produced by ORC in Optimum Conditions*

Figure 4: BWR (Pumping Losses) in ORC in Optimum Conditions.

The simulated results provide with deep insights of MTHP-ORC systems with respect to their performance. The results are in accordance with the theory such that in heat pump mode, COP and temperature lift are inversely proportional whereas, in ORC mode, the global efficiency and temperature lift are directly proportional, as shown in the Figure 5 and Figure 6. Figure 7 shows the direct relation of net power output in ORC with the temperature lift. The straight line shows the increasing/decreasing trend of these parameters.
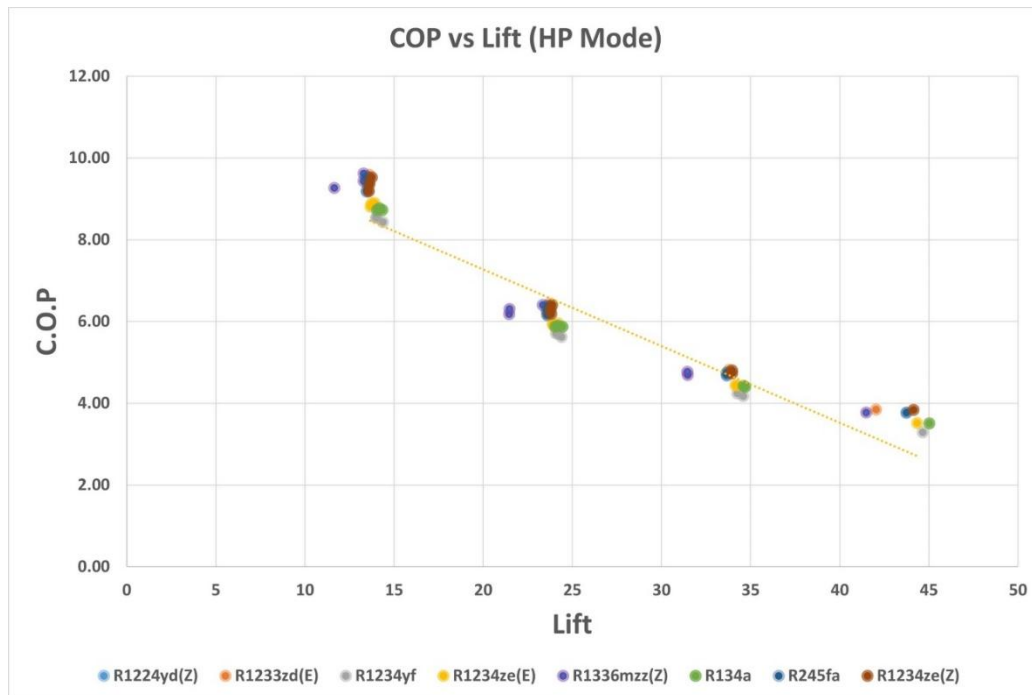
Figure 5: COP vs Lift in HP Mode
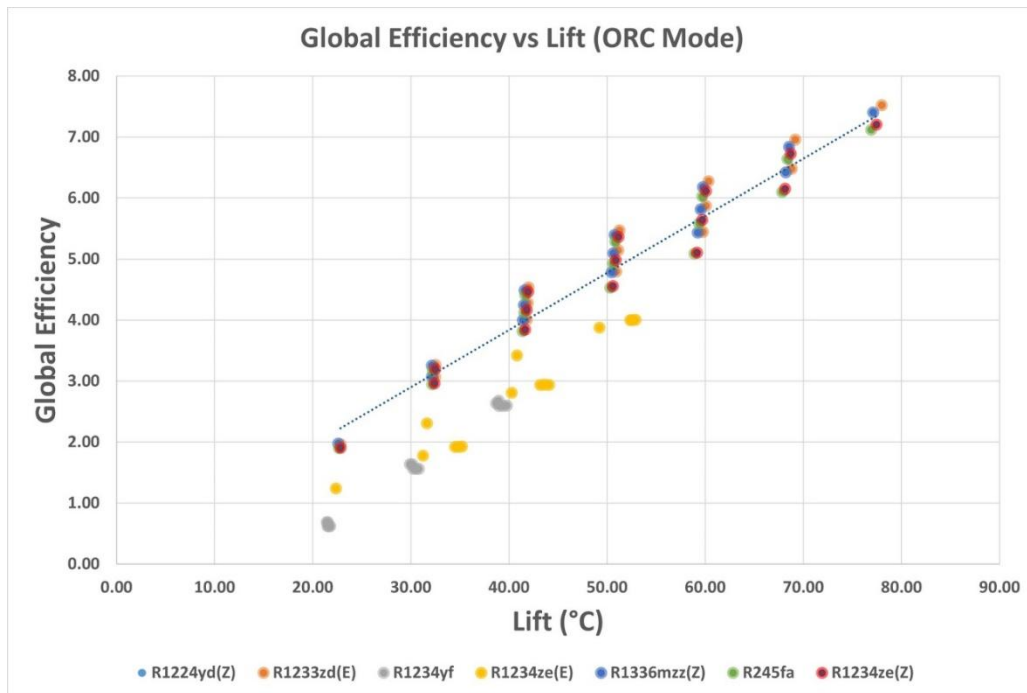
Figure 6: Global Efficiency vs Lift in ORC Mode
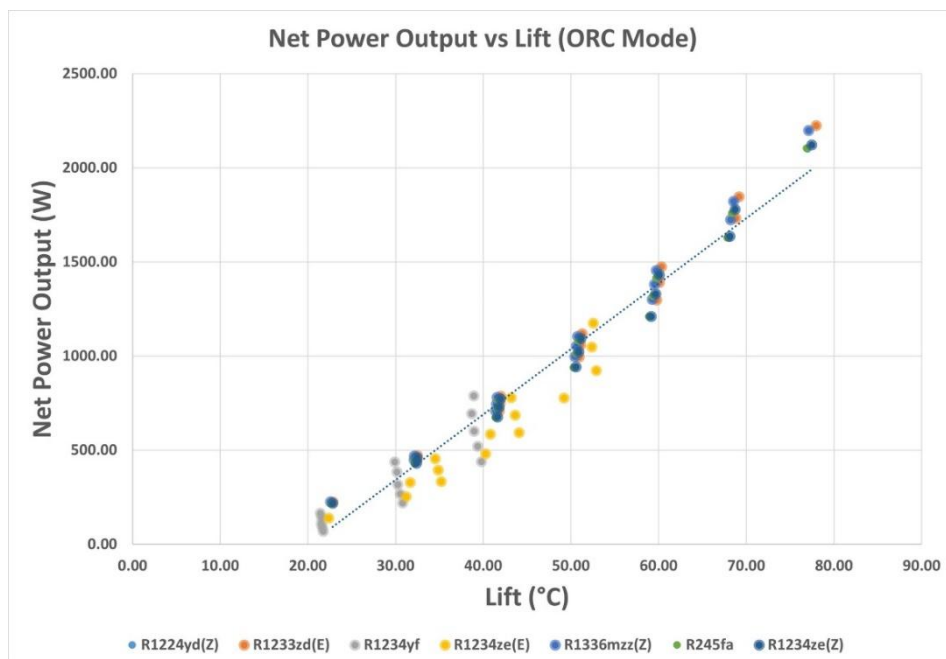
Figure 7: Net power output vs Lift in ORC Mode

Furthermore, in our analysis, out of all 8 refrigerants, R1233zd(E) in ORC Mode has the maximum efficiency of 7.52% whereas R1336mzz(Z) had the best COP of 9.63 in Heat pump mode, in the optimum temperature ranges, considering all the assumptions. These findings

agree with the results reported in various literature studies concerning reversible HP-ORC systems [6,7,8].

Conclusion

The analysis revealed the efficiency and environmental benefits of reversible MTHP-ORC cycles, utilizing low-GWP refrigerants. The research highlighted the optimum temperature ranges for heat source and sink. Amongst the eight refrigerants simulated, R1336mzz(Z) achieved the highest COP of 9.63 in heat pump mode, while R1234yf resulted in highest condenser heat rejection of 4292.4 watts. In ORC mode, R1233zd(E) showcased the highest global efficiency of 7.52 producing a net power output of 2225.55 watts. Notably, in ORC Mode, R1336mzz(Z) demonstrated the lowest BWR of 0.06 and along with substantial global efficiency, making it one of the best performing refrigerants in both the modes. Future development is suggested in terms of experimental verification of these results. These findings emphasize the potential of utilizing sustainable refrigerants and optimized configurations to enhance overall performance.

Nomenclature

T_in_ev = Inlet Temperatures of fluid from heat source (°C)
T_out_ev = Outlet Temperatures of fluid from heat source (°C)
T_in_cond = Inlet Temperatures of fluid from heat sink (°C)
T_out_cond = Outlet Temperatures of fluid from heat sink (°C)
M_ref = Mass flow rate of refrigerant (kg/h)
M_water = Mass flow rate of water across condenser (kg/h)
P_ex_p= Outlet Pressure of pump or expansion valve in ORC or HP Mode respectively (bar)
BVR = Built-in Volume Ratio
BWR = Pumping losses i.e, Ratio between Pump electrical power to Expander electrical power
W_el_net = Net power input or output (Watts)
Q_con = Heat rejection from condenser (Watts)
Q_ev2 = Heat absorbed in Evaporator (Watts)
COPel = Coefficient of Performance of HP
Eff_el_net = Global efficiency of ORC (%)
PinchP_ev = Pinchpoint temperature at evaporator (K)
PinchP_cd = Pinchpoint temperature at condenser (K)

References

[1] Lazzarin, R. (2020). "Heat pumps and solar energy: A review with some insights in the future. International journal of refrigeration", 116, 146-160.

[2] Dumont, O, Quoilin, S, & Lemort, V. "Design, Modeling and Experimentation of a Reversible HP-ORC Prototype." Proceedings of the ASME Turbo Expo 2014: Turbine Technical Conference and Exposition. Volume 3B: Oil and Gas Applications; Organic

Rankine Cycle Power Systems; Supercritical CO2 Power Cycles; Wind Energy. Düsseldorf, Germany. June 16–20, 2014. V03BT26A010. ASME.

[3] Stefan S & Roland S. "Simulation of a solar assisted combined heat pump – Organic rankine cycle system" Energy Conversion and Management, Volume 102, 2015, Pages 151-160, ISSN 0196-8904.

[4] Moradi, R., Campana, P. E., Tascioni, R., & Cioccolanti, L. (2021). "Thermodynamic analysis of the off-design performance of a micro solar organic Rankine cycle trigeneration system". In Proceedings of the 6th International Seminar on ORC Power System

[5] Dumont, O., Quoilin, S., & Lemort, V. (2015). "Experimental investigation of a reversible heat pump/organic Rankine cycle unit designed to be coupled with a passive house to get a Net Zero Energy Building". International journal of refrigeration, 54, 190-203.

[6] D. Steger, C. Regensburger, B. Eppinger, S. Will, J. Karl, E. Schlücker, "Design aspects of a reversible heat pump - Organic rankine cycle pilot plant for energy storage", Energy, Volume 208, 2020, 118216, ISSN 0360-5442

[7] R. Ravindran, M. Huang, N. Hewitt, "Design and modelling of a small-scale reversible high-temperature heat pump—organic Rankine cycle system for industrial waste heat recovery", International Journal of Low-Carbon Technologies, Volume 18, 2023, Pages 482–493, https://doi.org/10.1093/ijlct/ctad038

[8] Carlos Mateu-Royo, Adrián Mota-Babiloni, Joaquín Navarro-Esbrí, Bernardo Peris, Francisco Molés, Marta Amat-Albuixech, "Multi-objective optimization of a novel reversible High-Temperature Heat Pump-Organic Rankine Cycle (HTHP-ORC) for industrial low-grade waste heat recovery", Energy Conversion and Management, Volume 197, 2019, 111908, ISSN 0196-8904, https://doi.org/10.1016/j.enconman.2019.111908.

Evaluation of porous organic polymers and MOFs for direct air capture

Richard Blom*, Giorgia Mondino, and Shreenath Krishnamurthy

ªSINTEF Industry, Forskningsveien 1, 0314 Oslo, Norway

*Corresponding author: Richard.blom@sintef.no

Keywords: Porous polymers, CO_2 capture, direct air capture, DAC, process simulation, Lewatit, VTSA.

Introduction/Background

In the IPCC report on global warming [1], direct air capture of CO_2 from ambient air (DAC) is regarded as one of the technologies that can be used to reduce the concentration of CO_2 in the atmosphere to pre-industrial levels. Due to the low CO_2 concentration in air (423 ppm in 2023), DAC technologies will inherently require more energy for separation than traditional post-combustion technologies which remove CO_2 from industrial flue gas point sources typically containing 4-20 vol% CO_2 [2]. Consequently, the cost of CO_2 captured in a DAC plant will be significantly higher than that of post-combustion CO_2 capture [3].

Several technologies for DAC are under development, including either the use of solvents or solid sorbents. So far, the solid sorbent-based vacuum-temperature-swing adsorption (VTSA) technology developed by Climeworks has gained the most attention and is now demonstrated at 4000-ton CO_2/year scale in Iceland using geothermal energy for sorbent regeneration.

When selecting the adsorbent for a VTSA DAC process, one important criterion is the ability of the material to preferentially adsorb CO_2 at the specific conditions, typically, ambient temperature (5-40°C) and various relative humidity levels (20-80%). Furthermore, the sorbent should withstand repeated pressurization, depressurization cycles, temperatures up to 120°C and the presence of O_2, and to last at least 5 years. Amine based sorbents have been used so far, but they are quite thermally unstable in the presence of O_2 at temperatures above 80-100°C. Therefore, alternative sorbents are needed.

In this presentation we will show preliminary results from a study where we are simulating the performances of a DAC process using either the porous amine based polymer Lewatit [4] or the mmen-M_2(dobpdc) MOFs [5] showing very different isotherm shape (S-shaped). Experimental CO_2, N_2 and H_2O isotherms and kinetic constants are used to simulate a Climeworks type VTSA process for direct CO_2 capture at a typical site in Norway. Based on the simulations we estimated the capture rate and CO_2 purity of the product gas stream, process energy requirements and process footprint.

Methods, Discussion and Results

The first adsorbent chosen for this work is Lewatit VP OC 1065 [4] and assumed to be shaped in the form of filters, similar to the Climeworks technology. A six step VTSA process was chosen for this work. The process schematic is shown in the Figure below. Simulations initially were carried out using a parametric method. The capture process was designed for capturing CO_2 from the Norwegian west coast conditions (5°C and 80% RH). The simulations showed that the process was able to achieve > 95% purity on a dry basis with 60-78.6% recovery values. The column was 1 m long and 2.3 m in diameter. The regeneration temperature was 95°C. The total cycle time was 6220 s.
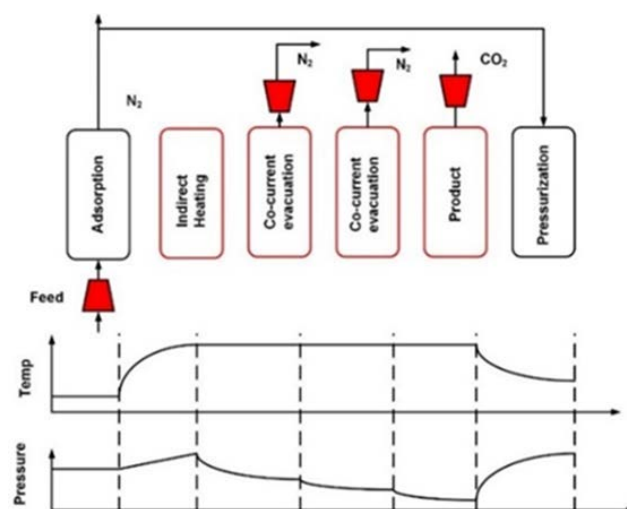

Figure 1: VTSA scheme used in the process simulations

Table 1: Step times for the VTSA DAC process.

Steps	Ads	Heat	Prod	Evac	Press
Duration (s)	4000	1200	800	200	20

Table 2: The performance details from the DAC simulations.

Indicator	Purity (%)	Recovery (%)	Productivity (mol/m³ ads s)	Energy (MJ/kg)
Value	95.4	78.6	0.017	29.5

Scaling the system to 4000 tonnes CO_2/year based on these dimensions shows about 82 parallel trains are required with each column containing about 1.8 tonnes of sorbent. For 100000 tonnes CO_2/year nearly 2000 parallel units are required.

Summary/Conclusions

Preliminary simulations reveal that the Lewatit sorbent is able to achieve high purities (>95%) and recovery values of >70%. Currently work is ongoing with the mmen-M_2(dobpdc) type MOFs. The preliminary simulations also showed that higher purity values are achieved at higher regeneration temperatures. It is worth highlighting that the results reported in this abstract are based on parametric study. Detailed optimization of the cycle configuration and the operating conditions are necessary to improve the productivity as well as lower the energy conditions. One may also consider drying the air before the CO_2 capture to reduce the energy consumption, but at the extent of a lower CO_2 purity.

Acknowledgments

References

[1] IPCC, Ed., 'Strengthening and Implementing the Global Response', in *Global Warming of 1.5°C: IPCC Special Report on Impacts of Global Warming of 1.5°C above Pre-industrial Levels in Context of Strengthening Response to Climate Change, Sustainable Development, and Efforts to Eradicate Poverty*, Cambridge: Cambridge University Press, 2022, pp. 313–444. doi: 10.1017/9781009157940.006.

[2] R. L. Siegelman, E. J. Kim, and J. R. Long, 'Porous materials for carbon dioxide separations', *Nat. Mater.*, vol. 20, no. 8, pp. 1060–1072, 2021.

[3] F. Sabatino, A. Grimm, F. Gallucci, M. van Sint Annaland, G. J. Kramer, and M. Gazzani, 'A comparative energy and costs assessment and optimization for direct air capture technologies', *Joule*, vol. 5, no. 8, pp. 2047–2076, 2021.

[4] R. Veneman, N. Frigka, W. Zhao, Z. Li, S. Kersten, and W. Brilman, 'Adsorption of H2O and CO2 on supported amine sorbents', *Int. J. Greenh. Gas Control*, vol. 41, pp. 268–275, 2015.

[5] J. Park *et al.*, 'Metal–Organic Framework Adsorbent for Practical Capture of Trace Carbon Dioxide', *ACS Appl. Mater. Interfaces*, vol. 12, no. 45, pp. 50534–50540, 2020.

Numerical simulation of the adsorption and desorption process for cooling applications

Szymon Janusz[1,2], Marcin Borcuch[2], Piotr Cyklis[1]

[1] Cracow University of Technology, Mechanical Engineering Department
[2] M.A.S. Ltd., Research and Development Department, Starachowice
Corresponding author: szymon.janusz@doktorant.pk.edu.pl

Abstract

This article outlines a methodology for conducting numerical simulations of the adsorption and desorption cycle using computational fluid dynamics software. These simulations provide insights into the quantity of water vapor absorbed by the adsorbent bed and the heat generated during the adsorption process. Additionally, they illustrate how to model the entire adsorption-desorption cycle and how changes in isotherms can impact the progression of the process.

Keywords: Adsorption, Heat transfer, CFD, Ansys

Introduction/Background

Computational Fluid Dynamics (CFD) is crucial in comprehending how different parameters, including temperature, pressure, and cycle time, influence the adsorption process in cooling devices. It is employed to investigate the impact of variables like silica gel grain size on adsorption efficiency and spatial porosity gradient's effect on cooling performance. The principal objective of using CFD is enhancing heat exchange between the adsorption bed and the cooling/heating medium, a key element in developing efficient adsorption heat exchangers.

CFD Model

➢ The adsorbent layer, which was made of silica gel RD type with a 0.35 mm diameter, was modeled as a porous material (Fig.1).

➢ The kinetics of the adsorption process were modeled using the Linear Driving Force (LDF) model.

➢ The equilibrium concentration is described using isotherms. The choice of the appropriate isotherm depends on the investigated adsorbent-adsorbate pair. Fig.2 shows the influence of changing the isotherm used in the model on the saturation curve for the same adsorbent-adsorbate pair.

➢ As the process shifts from adsorption to desorption, boundary condition change from 30°C to 80°C.

➢ User-Defined Function (UDF) tracks bed pressure, switching the boundary condition from inlet (adsorption) to outlet (desorption).
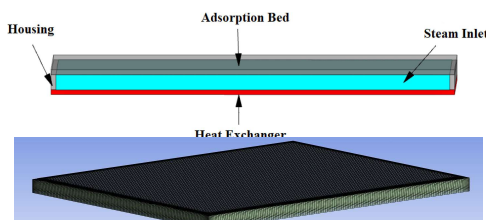
Fig. 1 Geometry and mesh used in the simulation.
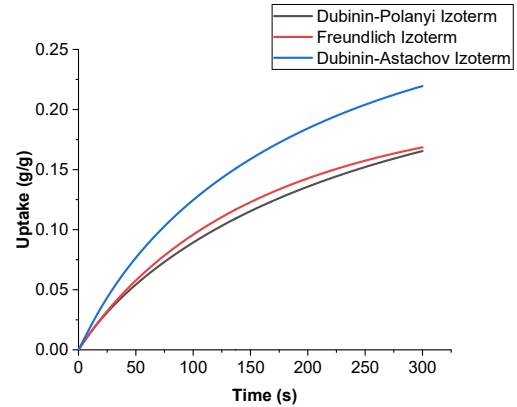
Fig. 2 The amount of water vapor adsorbed by the silica gel bed for different isotherms.
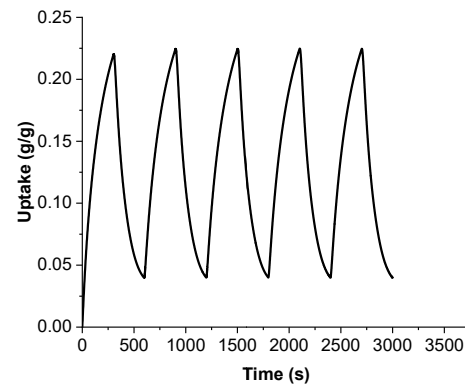
Fig. 3 The amount of adsorbed vapor over the 5 cycles.

Summary/Conclusions

The simulation model presented in this work enables the achievement of qualitative and quantitative results of H2O absorption and desorption from the bed with periodic cooling and heating (Fig.3). Reaction times in actual beds range between 5-10 minutes, which is consistent with the obtained operating period of the bed. The incorporated CFD model further allows for the simulation of various conditions, such as different types of adsorbent material, the influence of cold and hot medium, pressure variations, bed geometry, etc., providing a comprehensive analytical framework for the study.

Experimental setup for the analysis of sorption and desorption phenomena in refrigeration applications

Marcin Borcuch[1], Szymon Janusz[1,2]

[1] M.A.S. Ltd., Research and Development Department, Starachowice
[2] Cracow University of Technology, Mechanical Engineering Department
Corresponding author: marcin.borcuch@mas-sp.pl

Abstract

The presented work describes the design and realization of an experimental setup for analyzing an adsorbent bed's sorption capabilities and heat exchange. The setup simulates the operation of an adsorption refrigeration device on a small scale, thereby allowing for a detailed analysis of the bed's performance under the working conditions of adsorption cooling devices and for the validation of numerical models.

Keywords: Adsorption, Heat transfer, Refrigeration

Introduction/Background

Adsorption cooling devices, favored for their energy efficiency and eco-friendliness, may not yet fully meet efficiency expectations due to various influencing factors. These include the selection of optimal adsorbent-adsorbate pairs, carefully adjusting cooling and heating water temperature, controlling pressure related to the desired evaporation temperature, and managing the adsorption-desorption cycle duration. Hence, an experimental station has been designed to control key simulation parameters and allow for the validation and calibration of numerical models, contributing to process optimization and improving adsorption chiller efficiency.

Experimental setup

Based on the weight-based approach, an experimental setup was designed to operate and monitor the adsorption/desorption process at specific pressure and temperature. The experimental setup consists of two vacuum chambers, four water tanks, flow devices, measuring equipment, and auxiliary equipment (Fig. 1, Fig. 2).

K1 - adsorption chamber, K2 - evaporator/condenser, Z - water tank, Zk - ball valve, ZT - solenoid valve, VP - vacuum pump,
T - temperature sensor, M - pressure sensor, P - pump, G - heater, Fm - flowmeter, ZA - adsorption bed, CP - heat exchanger, W - s

Fig. 1 Experimental setup diagram

Fig. 2 Experimental setup

Experimental procedure

✓ The measured sample is placed on the heat exchanger (CP) within the sealed adsorption chamber (K1).
✓ The bed (ZA) is heated and a vacuum is created in the system.
✓ The cooling system is activated.
✓ Throughout the process, changes in the adsorbent mass are monitored (Fig.2), and temperature shifts at the inlet and outlet of the bed's cooling exchanger and the evaporator are tracked.

Fig. 3 Water vapor adsorbed by the bed

Summary

The research setup enables the study of adsorption and desorption in refrigeration systems, allowing simulation of various conditions such as different types of adsorbent material, the influence of cold and hot medium, pressure, bed geometry, etc. This comprehensive approach facilitates the identification of optimal solutions for refining models and designing devices tailored to the specific aspects of the adsorption process.

Acknowledgments

Norway grants

PARP Grupa PFR

Surface Measurement Systems
World Leader in Sorption Science

Sorption Technologies

Novel Nitrate & Nitrate-Chloride salt mixtures for CSP applications

Siddhesh Pawar   Dr. Zacharie Tamainot-Telto

STET group, Mechanical Engineering, University of Warwick, Coventry, UK

WARWICK
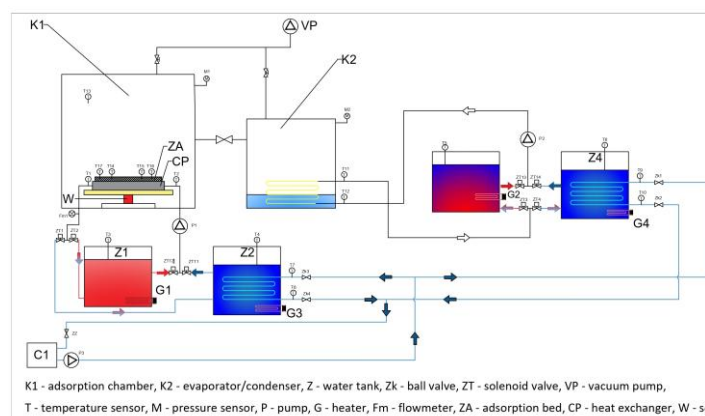THE UNIVERSITY OF WARWICK

Abstract

Molten nitrate salts are widely used for Thermal Energy Storage (TES) in Concentrated Solar Power (CSP) plant. Solar salt, a mixture of 60%NaNO$_3$ -40%KNO$_3$ by weight, with melting point of 220°C is the most commonly used salt material for TES application. The aim of this project is to develop novel salt mixtures with lower melting points and acceptable decomposition points to serve the dual purpose as a Heat Transfer Fluid (HTF) and TES medium in modern CSP's. In this context, two novel salt mixtures are prepared and tested for their short / long duration thermal stability and melting point. The formulation 1 is a ternary salt comprising of 44%KNO$_3$- 32% Ca(NO$_3$)$_2$- 24%NaNO$_3$ (Base Salt) and the formulation 2 is a quinary mixture of 90%Base salt + 5%NaCl + 5%KCl (Base-Chloride). Solar salt is also tested along with the novel mixtures to provide an overall comparison of thermal properties. The observations confirm that, while the solar salt has better thermal stability for short and long durations, the novel formulations have comparatively lower melting points in the range of 136°C-141°C. Thus, provide a wider operating range of temperature.

Keywords- Molten salt, Heat transfer, Energy storage, CSP

Introduction

- Molten Nitrate salts have high temperature stability, low unit cost and non-toxic nature compared to the traditional thermal oils, eutectic mixture of biphenyl and diphenyl oxide
- Use of molten salt increases the live-steam temperatures in the power block to over 400°C, resulting in lower levelized cost of electricity (LCOE)
- The focus now is on development of new salt materials with low melting points, better thermal stability and suitable thermo-physical properties to potentially serve as HTF and TES in generation-3 CSP's

Figure 1. A rendered image of the Central Tower type CSP plant, Noor Energy 1 project, Dubai [1]

Instruments and Procedure

Determination of melting points by Differential Scanning Calorimeter (DSC):
15 to 55 mg of sample is loaded for the test. It is heated at a constant rate of 5°C/minute from 30°C to 400°C in inert atmosphere of nitrogen, flowing at 100mL/minute. Two continuous cycles are performed. The first cycle eradicates moisture and impurities (if any) from the sample, while values from second cycles are analyzed for determination of melting point

Determination of Short duration & long duration stability by Thermogravimetric analysis (TGA) method
The instrument used is a Mettler Toledo, Simultaneous thermal analysis TGA/DSC-III, The standard operating procedure for checking thermal stability for short and long duration is shown in figure 2a and 2b, respectively. All the tests were performed in inert atmosphere of nitrogen flowing at 10mL/minute
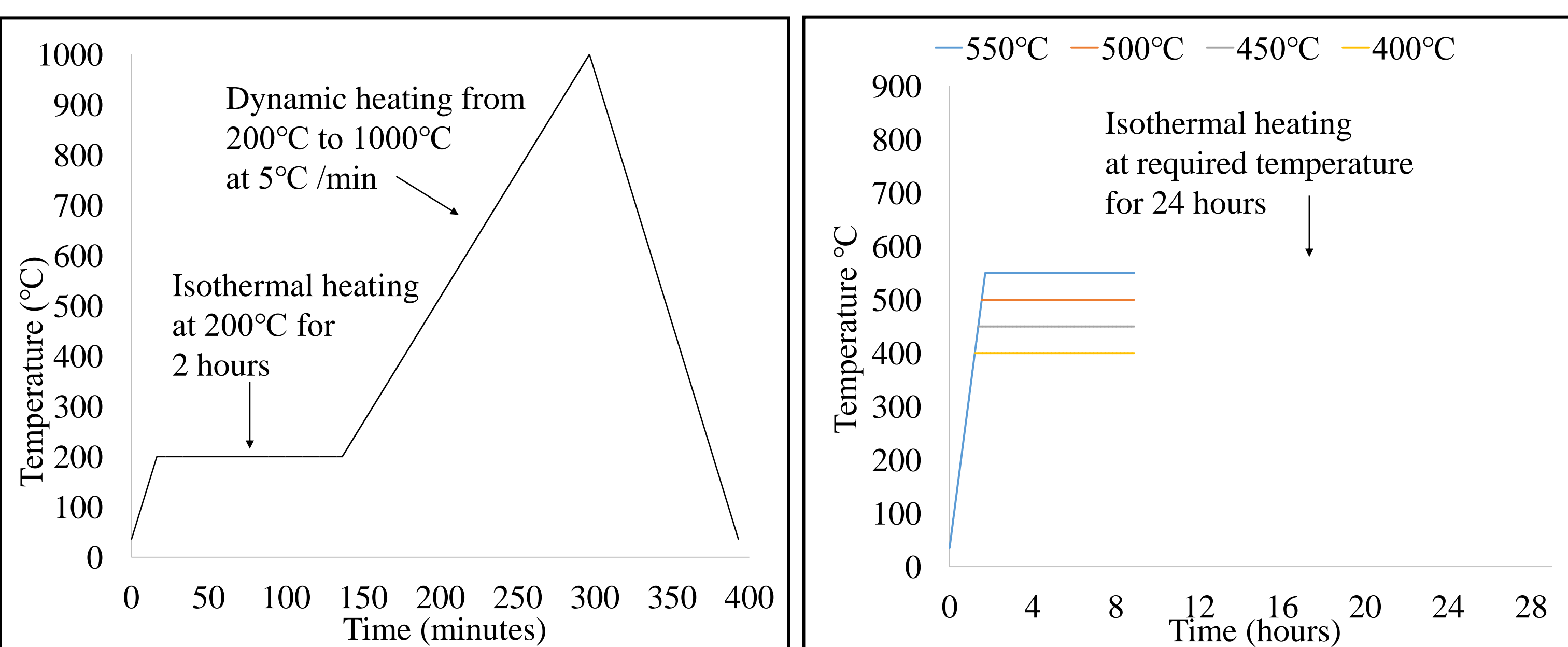
Figure 2a. Standard operating procedure for short duration stability

Figure 2b. Standard operating procedure for long duration stability

Observation and Results

1) The melting of solar salt begins at 218°C, with endothermic peak observed at 222.7°C.
2) Base salt melts over a wide range, melting starts at 106°C and is completed nearly at 163°C. The endothermic peak is observed at 137.3°C.
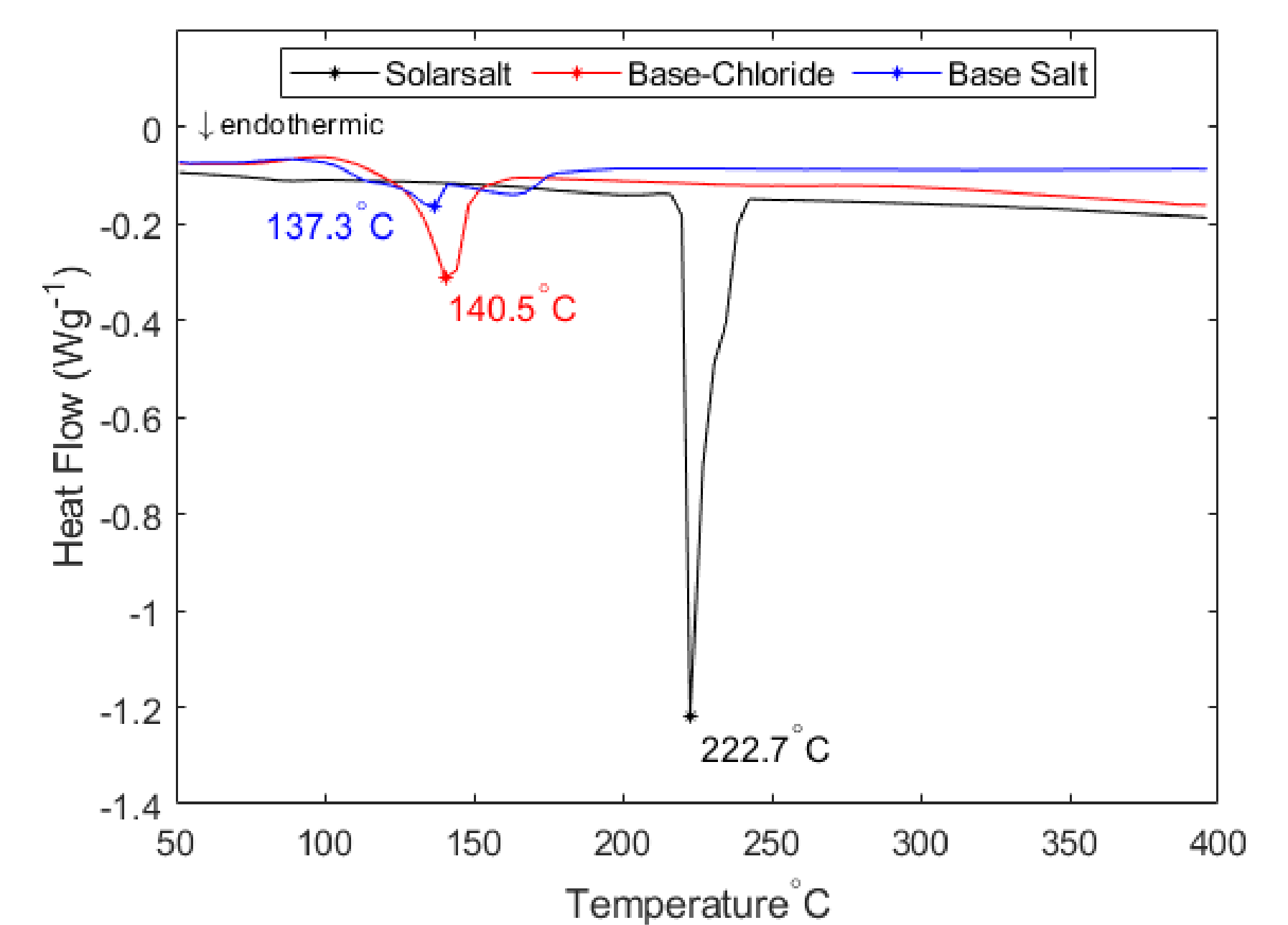3) Base-Chloride melts over a range of 107°C to 148°C, with endothermic peak at 140.5 °C.

Figure 3. DSC results of the mixtures

1) The temperature where sample loses 3% of its original mass is considered to be the decomposition point.
2) The Solar salt decomposes at 631°C.
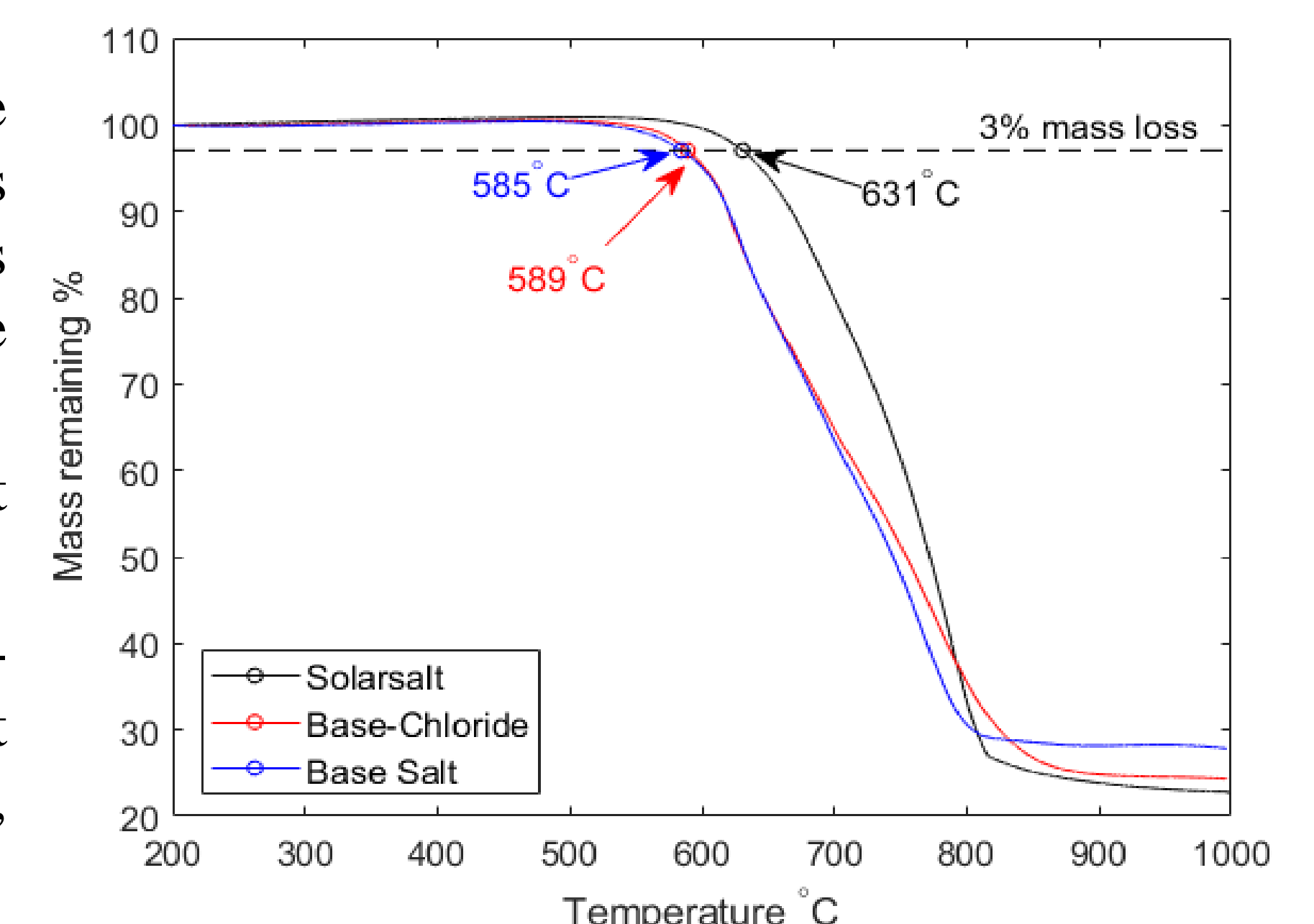3) The Base salt & Base-Chloride decompose at 585°C and 589°C, respectively.

Figure 4. TGA graph showing decomposition points of the mixtures

Figure 5. TGA graph showing mass loss of the mixtures at various temperatures in 24 hours

1) The mass loss over a period of 24 hours is significant at 550°C followed by 500°C and 450°C.
2) At 400°C, no significant mass change is observed suggesting that the mixtures can be operated till 400°C for long duration.

Conclusion

1) In terms of short duration thermal stability, the Solar salt performs better than the new mixtures
2) Operating range= $T_{decomposition} - T_{melting}$. Base salt & Base- Chloride mixtures have an operating range of nearly 448°C, which is greater than Solar salt with a range of around 408°C.
2) The long duration stability test is to understand the potential of the material as a TES medium. All the 3 mixtures are found to be extremely stable at 400°C, for 24 hours, suggesting equal potential to be used as TES till 400°C and below
4) The addition of Chloride components do not have a significant effect on thermal performance of the Base salt. However, its effect on physical properties currently under evaluation
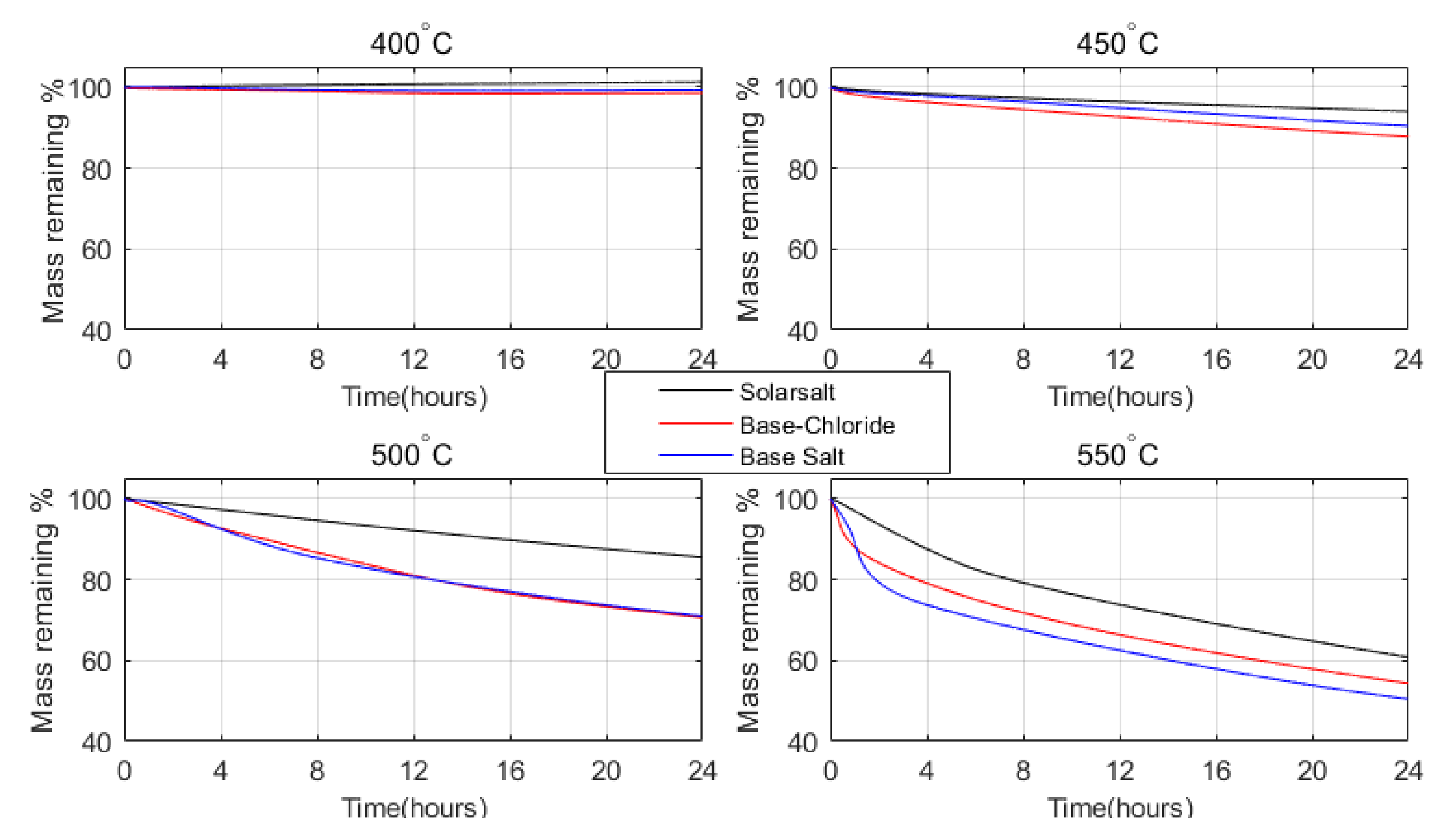
References

[1] helioscsp.com/worlds-largest-concentrated-solar-power-plant
[2] 9) Solarpaces.nrel.gov

Surface Measurement Systems
World Leader in Sorption Science

Sorption Technologies

Heat Powered Cycles
Conference 2023
Edinburgh
Heat in the new energy system

3rd to *6th* of September 2023
The University of Edinburgh, Scotland

Humidification Dehumidification Adsorption System for Water Desalination

M. Luberti[1*], Mauro Capocelli[2]

[1]Department of Chemical Engineering, School of Engineering, The University of Manchester, Oxford Road, M13 9PL, Manchester, United Kingdom
[2]University Campus Bio-Medico di Roma, Department of Science & Technology for Sustainable Development & One Health, Via Alvaro del Portillo, 21 00128, Rome, Italy
[*]Corresponding author: mauro.luberti@manchester.ac.uk

Abstract

An advanced humidification dehumidification (HDH) process integrated with a thermally-driven adsorption (AD) unit is proposed and numerically assessed for sustainable water desalination. The resulting HDH-AD system, also consisting of multiple air extractions and brine recirculation, exhibited the following enhanced performances: gained output ratio (GOR) of 7.0 and specific energy consumption (SEC) of 8.9 kJ$_e$ kg^{-1}.

Keywords: Sustainable Desalination, Humidification Dehumidification, Water Adsorption, Waste Heat.

Introduction and Methodology

Almost half of the world population will be affected by water scarcity by 2040 [1]. Among desalination technologies, HDH is a reliable and energy-efficient method for decentralized and small-scale applications.

Figure 1 – Schematic of the integrated HDH-AD system
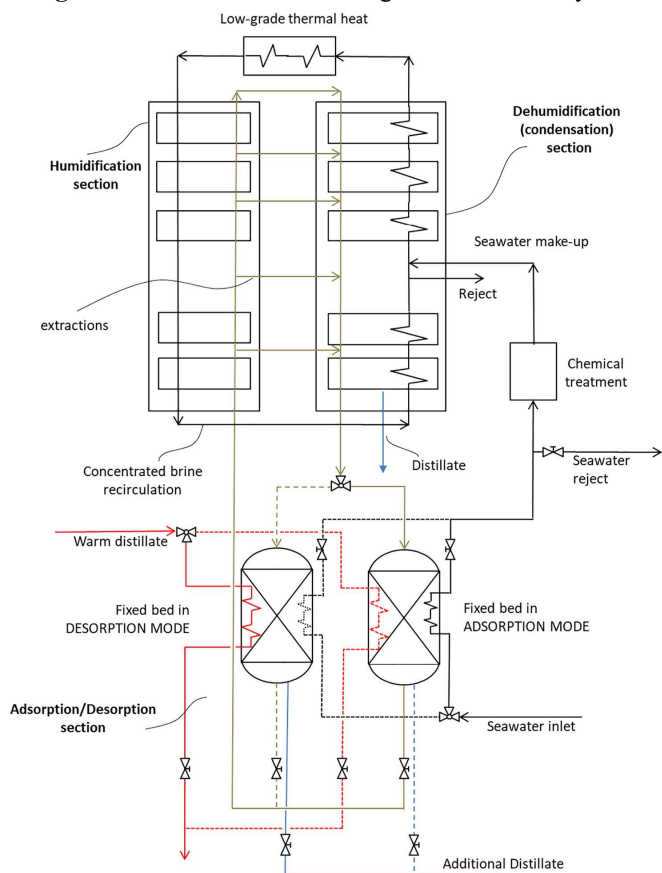
HDH systems can be powered by renewable and low-grade/waste energy sources, with a thermal energy consumption being virtually zero. However, they are usually operated at 1 atm so that humidification and dehumidification are both thermodynamically limited.

Integrated HDH-AD systems are more efficient because the humidity ratio of the air exiting the dehumidifier can be further abated in a temperature swing adsorption (TSA) unit prior to being directed to the humidifier (Figure 1). We developed a mathematical model to assess the performance of the integrated HDH-AD system including intermediate air extractions and brine recirculation [2], as shown in Figure 1.

Results and Conclusions

The integrated HDH-AD system is designed to produce 30 m^3 d^{-1} of freshwater. The system features and KPIs (GOR and SEC) are reported in Table 1. With the same design basis, it is clear from the table that the integrated HDH-AD system outperforms both the conventional HDH system and the variable pressure (VP) HDH system.

Table 1 – Performance comparison of HDH-based systems

System	Features	GOR (–)	SEC (kJ$_e$ kg^{-1})
HDH [3]	$P_H = P_{DH} = 101.3$ kPa	1.1	5.1
VP-HDH [3]	$P_H = 50$ kPa; $P_{DH} = 66.7$ kPa	4.8	640
HDH-AD [4]	$P_H = P_{DH} = 101.3$ kPa; 4 air extractions; RH = 0.2 @ TSA outlet	7.0	8.9

References

[1] World Health Organization. Drinking-water, 2020.
[2] Capocelli, M., Balsamo, M., Lancia, A., Barba, D., *Process analysis of a novel humidification-dehumidification-adsorption (HDHA) desalination method*. Desalination 429: 155–166, 2018.
[3] Siddiqui, O.K., Sharqawy, M.H., Antar, M.A., Zubair, S.M., *Performance evaluation of variable pressure humidification-dehumidification systems*. Desalination 409: 171–182, 2017.
[4] Capocelli, M., Balsamo, M., Mazzeo, L., Luberti, M., *Thermodynamic analysis of the humidification-dehumidification-adsorption (HDHA) desalination process*. Desalination 554: 116510, 2023.

Feedheat-based electricity storage system for nuclear plant

James W Lazenby, Eugene Shwageraus, Alexander J White
(E-mail: jwl47@cam.ac.uk)

Abstract

An energy storage concept which links thermal stores to the feedwater heating system of a nuclear-powered steam plant is described. The storage scheme allows the plant's electricity output to be varied while keeping reactor power constant, thereby enabling the nuclear plant to take on a load-following role. This type of 'generation-integrated' energy storage uses existing hardware to reduce storage costs and provides the equivalent of a high-efficiency electricity storage system. By exploiting the multiple pressure bleed flows, this process is conducted with very little exergetic loss.

Performance of plant

Fig. 2: (a) T-s diagram; (b) T-Q diagram

➤ Note the closely matched bled steam and feedwater temperature profiles.
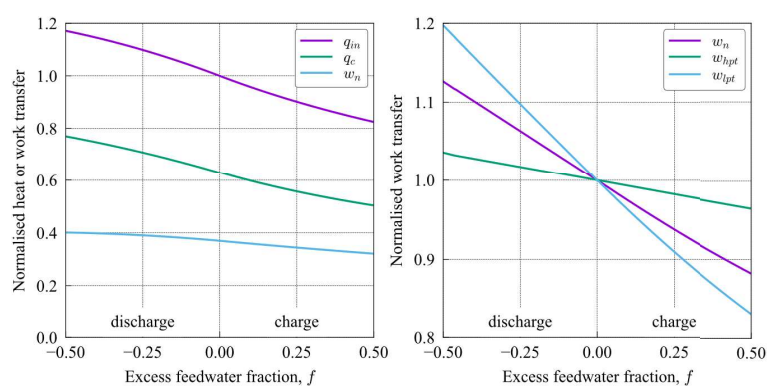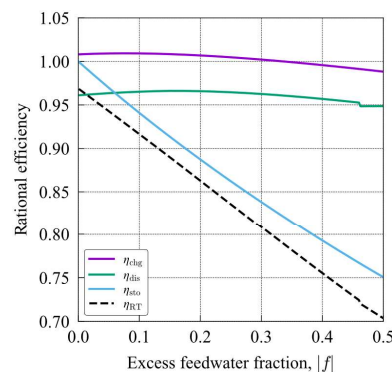

Fig. 3: (a) Principal exergy transfers; (b) Lost work processes.

➤ Integrated storage can **flex net work output by ± 10%**.
➤ Exergy input is from store and steam generator.

System Description

Fig. 1: Proposed system layout.

➤ **Charge:** A surplus of feedwater, f, is heated by increasing turbine bleed flows, thereby reducing the work output. Thus, as indicated in Fig. 1, the mass flow of feedwater is increased to $1 + f$ per unit mass flow through the steam generator.

➤ **Storage:** The excess fraction of feedwater, f, can either be stored directly or used to transfer heat into a thermal storage system.

➤ **Discharge:** The system is discharged by reducing the quantity of feedwater generated below its nominal value (i.e., f is made negative). This is achieved by reducing turbine bleed flow rates.

f = surplus feedwater fraction

Fig. 4: System efficiency.

$$\eta_{chg} = \frac{\text{exergy to store}}{\text{reduction turbine work}}$$

$$\eta_{dis} = \frac{\text{increase turbine work}}{\text{exergy from store}}$$

$$\eta_{sto} = \frac{\text{exergy from store}}{\text{exergy to store}}$$

$$\eta_{RT} = \eta_{chg} \times \eta_{sto} \times \eta_{dis}$$

➤ Charge efficiency over 100%, since the turbine expansion is avoided for a lower-loss heat transfer process.

Heat Powered Cycles
Conference 2023
Edinburgh
Heat in the new energy system

3rd to 6th of September 2023
The University of Edinburgh, Scotland

Additive Manufacturing for Heat Powered Cycle machines.

Drummond Hislop[1]

[1]**Integrated Heat Exchange Ltd (IHE), 63 The Avenue, Lewes, East Sussex, BN7 1QU, UK**
(**drummond@integratedheatexchange.com**).

Abstract

This poster demonstrates how metal additive manufacturing (AM) can greatly reduce the size and mass of heat and mass transfer components of a Heat Powered Cycle machine, and summarises the wider potential.

Keywords: Additive manufacturing, heat/mass transfer, small energy systems, sorption cycles.

Introduction/Background

AM heat exchangers are now used in aero-space [1] and F1, as AM-enabled design freedoms generate new heat transfer surfaces, and core and manifold geometries, that increase heat transfer coefficients, and reduce size and mass by ~30-60%.

IHE designs AM heat and mass transfer components for small energy systems (eg Heat-Powered Cycle machines) that need two or more such components. One is a heat-to-power system, driven by a 3.5 MW_e diesel genset's exhaust heat, with super-critical CO_2 as working fluid. With InnovateUK funding, IHE has carried out initial 1-D sizing and design of a monolith that integrates four main AM heat and mass transfer components of a bottoming cycle. It takes the form of an H_2O/NH_3 absorption cooler that chills cooling water to 12ºC from 25ºC.

Discussion and Results

Fig. 1a is a cutaway concept for the compact, thermally efficient AM monolith that integrates absorber, pre-cooler, condenser, solution heat exchanger and manifolds. Fig. 1b shows fluid inlets and outlets.

Table 1: Results of 1-D sizing of monolith

Component	Volume (litres)	Mass (kgs)
Absorber	0.66	1.60
Condensor	0.66	1.60
Solution HX	2.48	6.40
Pre-cooler	0.66	1.70
Manifolds, casing	2.38	2.54
Total for monolith	6.84	13.84

Table 1 shows initial 1-D sizing results (the evaporator, with size and mass similar to the monolith, is not included in Fig. 1 or Table 1 as the benefits of its thermal integration are less significant).

Summary/Conclusions

We estimate that the size and mass of the AM-enabled cooler are less than 50% of the machine with conventional heat and mass transfer components. We also estimate that emerging AM production technology, combined with novel AM-enabled heat and mass transfer processes and component designs, will further increase heat and mass transfer coefficients. We anticipate up to order-of-magnitude reductions in system size and mass, and significant increases in system efficiency. This approach will provide similar benefits for other Heat Powered Cycle machines. A study for an AM absorption cooler for a refrigerated trailor, powered by the exhaust heat of its tractor's diesel engine, is under way. The aim is to replace the standard compression-vapour cycle cooler, powered by a high emissions, on-board diesel genset.

Acknowledgments

We acknowledge the technical contributions of Morpheus Thermal Designs Ltd.

References

[1] F.Careri et al. *Additive Manufacturing of Heat Exchangers in Aerospace Applications: A Review.* Applied Thermal Engineering August 2023.

Fig. 1a Cutaway of monolith design

Ammonia liquid out   Ammonia vapour in
Water out
Ammonia vapour in
Solution out
Solution in   Water in
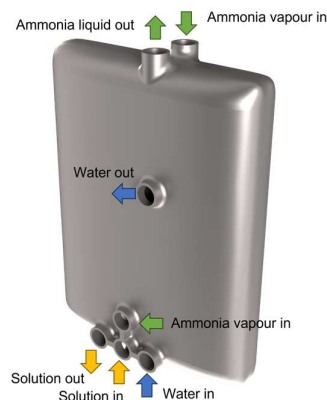
Fig. 1b Fluid inlets & outlets for monolith

Surface Measurement Systems
World Leader in Sorption Science

Sorption Technologies

Economic and Heat & Energy Analysis of Thermochemical and Biological Conversion of Livestock Manure to Hydrogen

Ji-Hong Moon[1*], Sang Jun Yoon[1] and Sang Shin Park[2]

[1]Clean Fuel Research Laboratory, Korea Institute of Energy Research (KIER), Deajon, South Korea

[2]Energy AI·Computational Science & Engineering Laboratory, Korea Institute of Energy Research (KIER) Deajon, South Korea

[*]Ji-Hong Moon: mjh@kier.re.kr

Abstract

In this study, a heat and energy analysis was performed along with an economic analysis of the thermochemical and biological conversion of livestock manure to hydrogen. The thermochemical conversion was based on the gasification process and the biological conversion was analyzed based on the anaerobic digestion process. The hydrogen production yields after reforming livestock manure were analyzed to be 16.2 and 2.8 kg-H_2/ton-manure, and the levelised cost of hydrogen (LCOH) was analyzed to be 2.18 and 4.68 $/kg, respectively. The reason for this difference is that the thermochemical conversion process has a high product gas yield and requires less energy due to an autothermal reaction.

Keywords: Hydrogen, Gasification, Biogas, Livestock manure.

Introduction/Background

Although the use of clean hydrogen is emerging as an alternative for carbon neutrality, water electrolysis-based green hydrogen production technology is not yet economical. As a result, economical hydrogen production methods are being reviewed, and a technology for producing hydrogen by reforming biogas, the main component of which is methane gas, is spreading. However, this method has a low product gas yield and high energy consumption, so a more economical hydrogen production method is required. The thermochemical conversion method is known as a highly economical technology among hydrogen production technologies [1]. In this study, the economic feasibility of the process of producing hydrogen by thermochemical conversion after reducing drying energy by applying high-speed fermentation technology to livestock manure with sufficient supply was considered.

Discussion and Results

Fig. 1 summarizes the energy and heat & mass balances of the biological conversion process and the thermochemical conversion process for hydrogen production from livestock manure. The energy required to produce 1 ton of hydrogen was analyzed as 45 MWh for the biological conversion process and 7.5 MWh for the thermochemical conversion process.
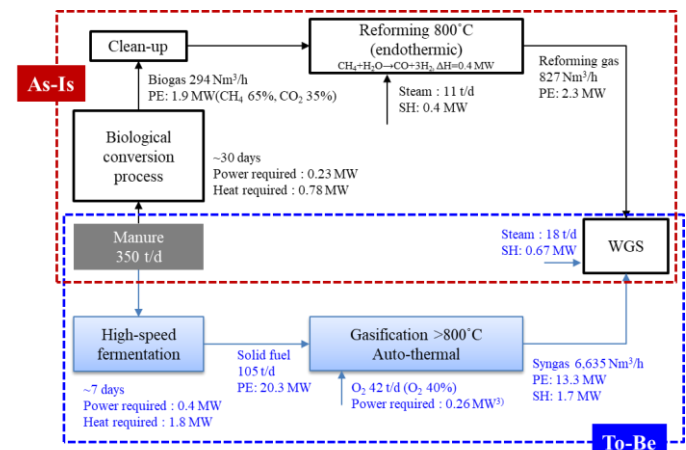

Fig. 1. Energy and Heat & Mass balance (Black: Biological, Blue: Thermochemical conversion)

Summary/Conclusions

In this study, it is analyzed that the thermochemical conversion process is highly economical, and it is expected in terms of expanding clean hydrogen production technology.

References

[1] Nikolaidis P., Poullikkas A., "A comparative overview of hydrogen production process", Renewable and Sustainable Energy Reviews, 2017.

3-6 September 2023
Edinburgh — Scotland

Sorption Technologies

Surface Measurement Systems
World Leader in Sorption Science

Contact: c.wen@reading.ac.uk (C. Wen)

Screening of Working Fluid Pairs for Thermally Integrated Pumped Thermal Electricity Storage System

Heat Powered Cycles Conference 2023
Edinburgh
Heat in the new energy system

Ding Wu[a], Ji Zhang[a], Yan Yang[b,*], Chuang Wen[c,*]
[a]Hunan University, [b]University of Exeter, [c]University of Reading

Context and objectives

A **thermally integrated pumped thermal electricity storage (TI-PTES)** system is a good solution to the power grid peak load shifting and waste heat recovery. **Working fluid pairs are screened** from 24 fluids of heat pump and 21 fluids of ORC.

✓ Considering three working fluid selection strategies: single pure fluid, different pure fluids and different fluids.

✓ Two-layer optimization: multi-optimizaiton with NSGA II and the User-defined single-objective optimization.

Method

First layer: Thermodynamic and economic performance multi-objective optimization by NSGA-II algorithm and TOPSIS method

Second layer: User-defined single-objective optimization function for the screening of optimal fluid selections under different weighting factors
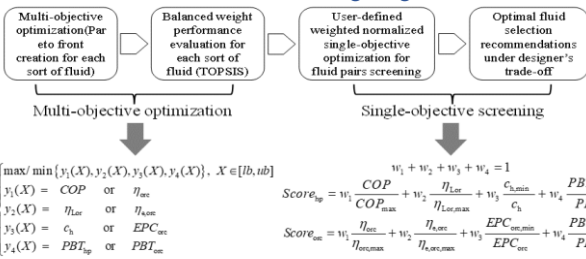
Fig. 1 Two-layer optimization methodology flow of working fluid pair selection

Application example

Thermally Integrated PTES:

✓ Waste heat source: 373.15 K

✓ Waste heat load: 3 MW

✓ Heat storage temperature range: 393.15 K to 423.15 K

Fig. 2 Schematic diagram of the TI-PTES
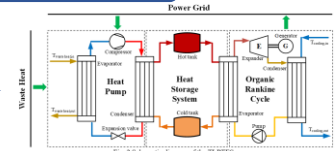
Parameter assumptions

Table 1 Main parameter assumptions for the TI-PTES system

Parameter	Symbol	Unit	Value
Compressor or Turbine efficiency	η_{comp}/η_{tur}	-	0.75
Pump efficiency	η_{pump}	-	0.85
Motor or Generator efficiency	η_{motor}/η_{gen}	-	0.97
Heat storage efficiency	η_{sto}	-	1
Pinch point temperature difference	ΔT_{pp}	K	3
Superheat degree in HP evaporator	$\Delta T_{sup,HP}$	K	5
Superheat degree in ORC evaporator	$\Delta T_{sup,orc}$	K	5
Cooling water inlet temperature	$T_{cooling,inlet}$	K	298.15
Ambient temperature	T_{amb}	K	293.15

Table 2 List of fluids considered for the screening

Cycle	Fluids for screening
HP	R50, R170, R1234, R1150, R1270, R290, Dimethyl ether (DME), Hexane, Heptane, R600, R600a, R601, R601a, R717, R718, R744, Diethyl ether (DEE), R1224yd(Z), R1233zd(E), R1234ze(E), R1234ze(Z), R1234yf, R1243zf, R1336mzz(Z)
ORC	R161, R290, R1270, R152a, R134a, R123, R227ea, R245fa, R600, R600a, R601, R601a, R1224yd(Z), R1233zd(E), R1234ze(E), R1234ze(Z), R1234yf, R1243zf, R1336mzz(Z)

Results

Zeotropic mixtures improve the round-trip efficiency η_{rt}.

✓ Higher *COP* or η_{orc} for thermodynamic cycles.

✓ Significant improvement of η_{rt} based on pure fluids.

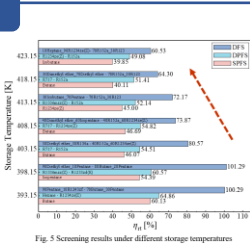✓ Decreasing trend of η_{rt} with Heat storage temperature.

Fig. 5 Screening results under different storage temperatures

Fig. 3 screening results of HP

Fig. 4 screening results of ORC
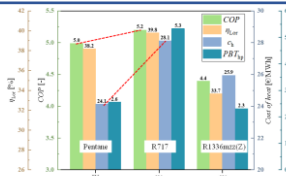

Fig. 6 screening results of HP

Thermo-economic performance analysis under different weighting factors:

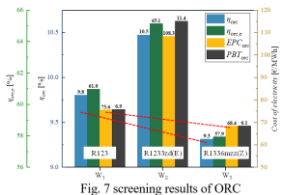✓ Fluid performance is screened under designer's expectation.
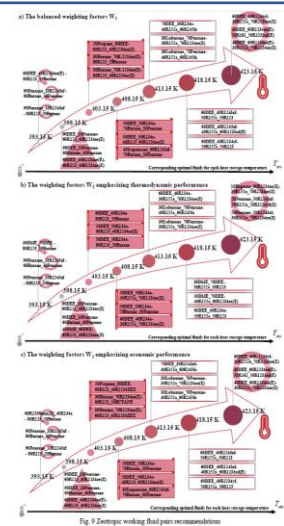

Fig. 7 screening results of ORC

Fig. 9 Zeotropic working fluid pairs recommendations

Fig. 8 Pure working fluid pairs recommendations

Working fluid pairs recommended under 7 storage temperatures and 3 groups of weighting factors:

✓ Variation of screened fluids

✓ Difference among weighting factors

Conclusions and perspective

✓ Utilization of zeotropic fluids promoted the thermodynamic efficiency of HP and ORC respectively based on the pure fluids

✓ Highest round-trip efficiency is improved obviously by Zeotropic fluids

✓ Weighting factors guide the selection of working fluid performance

✓ Screened results varies with storage temperatures to form a better match between working fluids and working conditions.

Full report and references available on https://heatpoweredcycles.eng.ed.ac.uk/

THE UNIVERSITY of EDINBURGH
School of Engineering

The **Heat Powered Cycles Conference** 2023 edition comes home at The University of Edinburgh, where J.C. Maxwell, R. Stirling, W. Rankine and J. Black, the fathers of the theory of heat and heat-powered devices have first moved their steps.